

Pertanika Journal of  
**SCIENCE &  
TECHNOLOGY**

**JST**

**VOL. 30 (1) JAN. 2022**



PERTANIKA  
JOURNALS

A scientific journal published by Universiti Putra Malaysia Press

# PERTANIKA JOURNAL OF SCIENCE & TECHNOLOGY

## About the Journal

### Overview

Pertanika Journal of Science & Technology is an official journal of Universiti Putra Malaysia. It is an open-access online scientific journal. It publishes original scientific outputs. It neither accepts nor commissions third party content.

Recognised internationally as the leading peer-reviewed interdisciplinary journal devoted to the publication of original papers, it serves as a forum for practical approaches to improve quality on issues pertaining to science and engineering and its related fields.

Pertanika Journal of Science & Technology is a **quarterly** (*January, April, July, and October*) periodical that considers for publication original articles as per its scope. The journal publishes in **English** and it is open for submission by authors from all over the world.

The journal is available world-wide.

### Aims and scope

Pertanika Journal of Science & Technology aims to provide a forum for high quality research related to science and engineering research. Areas relevant to the scope of the journal include: bioinformatics, bioscience, biotechnology and bio-molecular sciences, chemistry, computer science, ecology, engineering, engineering design, environmental control and management, mathematics and statistics, medicine and health sciences, nanotechnology, physics, safety and emergency management, and related fields of study.

### History

Pertanika Journal of Science & Technology was founded in 1993 and focuses on research in science and engineering and its related fields.

### Vision

To publish a journal of international repute.

### Mission

Our goal is to bring the highest quality research to the widest possible audience.

### Quality

We aim for excellence, sustained by a responsible and professional approach to journal publishing. Submissions can expect to receive a decision within 90 days. The elapsed time from submission to publication for the articles averages 180 days. We are working towards decreasing the processing time with the help of our editors and the reviewers.

### Abstracting and indexing of Pertanika

Pertanika Journal of Science & Technology is now over 27 years old; this accumulated knowledge and experience has resulted the journal being abstracted and indexed in SCOPUS (Elsevier), Clarivate Web of Science (ESCI), EBSCO, ASEAN CITATION INDEX, Microsoft Academic, Google Scholar, and MyCite.

### Citing journal articles

The abbreviation for Pertanika Journal of Science & Technology is *Pertanika J. Sci. & Technol.*

### Publication policy

*Pertanika* policy prohibits an author from submitting the same manuscript for concurrent consideration by two or more publications. It prohibits as well publication of any manuscript that has already been published either in whole or substantial part elsewhere. It also does not permit publication of manuscript that has been published in full in proceedings.

### Code of Ethics

The *Pertanika* journals and Universiti Putra Malaysia take seriously the responsibility of all of its journal publications to reflect the highest in publication ethics. Thus, all journals and journal editors are expected to abide by the journal's codes of ethics. Refer to *Pertanika's Code of Ethics* for full details, or visit the journal's web link at [http://www.pertanika.upm.edu.my/code\\_of\\_ethics.php](http://www.pertanika.upm.edu.my/code_of_ethics.php)

### Originality

The author must ensure that when a manuscript is submitted to *Pertanika*, the manuscript must be an original work. The author should check the manuscript for any possible plagiarism using any program such as Turn-It-In or any other software before submitting the manuscripts to the *Pertanika* Editorial Office, Journal Division.

All submitted manuscripts must be in the journal's acceptable similarity index range:  
**≤ 20% – PASS; > 20% – REJECT.**

### International Standard Serial Number (ISSN)

An ISSN is an 8-digit code used to identify periodicals such as journals of all kinds and on all media—print and electronic.

Pertanika Journal of Science & Technology: e-ISSN 2231-8526 (Online).

### Lag time

A decision on acceptance or rejection of a manuscript is reached in 90 days (average). The elapsed time from submission to publication for the articles averages 180 days.

### Authorship

Authors are not permitted to add or remove any names from the authorship provided at the time of initial submission without the consent of the journal's Chief Executive Editor.

### Manuscript preparation

Most scientific papers are prepared according to a format called IMRAD. The term represents the first letters of the words *Introduction, Materials and Methods, Results, And Discussion*. IMRAD is simply a more 'defined' version of the "IBC" (*Introduction, Body, Conclusion*) format used for all academic writing. IMRAD indicates a pattern or format rather than a complete list of headings or components of research papers; the missing parts of a paper are: *Title, Authors, Keywords, Abstract, Conclusions, References, and Acknowledgement*. Additionally, some papers include *Appendices*.

The *Introduction* explains the scope and objective of the study in the light of current knowledge on the subject; the *Materials and Methods* describes how the study was conducted; the *Results* section reports what was found in the study; and the *Discussion* section explains meaning and significance of the results and provides suggestions for future directions of research. The manuscript must be prepared according to the journal's **Instruction to Authors** ([http://www.pertanika.upm.edu.my/Resources/regular\\_issues/Regular\\_Issues\\_Instructions\\_to\\_Authors.pdf](http://www.pertanika.upm.edu.my/Resources/regular_issues/Regular_Issues_Instructions_to_Authors.pdf)).

### Editorial process

Authors who complete any submission are notified with an acknowledgement containing a manuscript ID on receipt of a manuscript, and upon the editorial decision regarding publication.

*Pertanika* follows a **double-blind peer-review** process. Manuscripts deemed suitable for publication are sent to reviewers. Authors are encouraged to suggest names of at least 3 potential reviewers at the time of submission of their manuscripts to *Pertanika*, but the editors will make the final selection and are not, however, bound by these suggestions.

Notification of the editorial decision is usually provided within 90 days from the receipt of manuscript. Publication of solicited manuscripts is not guaranteed. In most cases, manuscripts are accepted conditionally, pending an author's revision of the material.

As articles are double-blind reviewed, material that may identify authorship of the paper should be placed only on page 2 as described in the first-4-page format in *Pertanika*'s **Instruction to Authors** ([http://www.pertanika.upm.edu.my/Resources/regular\\_issues/Regular\\_Issues\\_Instructions\\_to\\_Authors.pdf](http://www.pertanika.upm.edu.my/Resources/regular_issues/Regular_Issues_Instructions_to_Authors.pdf)).

### The journal's peer review

In the peer-review process, 2 to 3 referees independently evaluate the scientific quality of the submitted manuscripts. At least 2 referee reports are required to help make a decision.

Peer reviewers are experts chosen by journal editors to provide written assessment of the **strengths** and **weaknesses** of written research, with the aim of improving the reporting of research and identifying the most appropriate and highest quality material for the journal.

### **Operating and review process**

What happens to a manuscript once it is submitted to *Pertanika*? Typically, there are 7 steps to the editorial review process:

1. The journal's Chief Executive Editor and the Editor-in-Chief examine the paper to determine whether it is relevance to journal needs in terms of novelty, impact, design, procedure, language as well as presentation and allow it to proceed to the reviewing process. If not appropriate, the manuscript is rejected outright and the author is informed.
2. The Chief Executive Editor sends the article-identifying information having been removed, to 2 to 3 reviewers. They are specialists in the subject matter of the article. The Chief Executive Editor requests that they complete the review within 3 weeks.

Comments to authors are about the appropriateness and adequacy of the theoretical or conceptual framework, literature review, method, results and discussion, and conclusions. Reviewers often include suggestions for strengthening of the manuscript. Comments to the editor are in the nature of the significance of the work and its potential contribution to the research field.

3. The Editor-in-Chief examines the review reports and decides whether to accept or reject the manuscript, invite the authors to revise and resubmit the manuscript, or seek additional review reports. In rare instances, the manuscript is accepted with almost no revision. Almost without exception, reviewers' comments (to the authors) are forwarded to the authors. If a revision is indicated, the editor provides guidelines for attending to the reviewers' suggestions and perhaps additional advice about revising the manuscript.
4. The authors decide whether and how to address the reviewers' comments and criticisms and the editor's concerns. The authors return a revised version of the paper to the Chief Executive Editor along with specific information describing how they have addressed' the concerns of the reviewers and the editor, usually in a tabular form. The authors may also submit a rebuttal if there is a need especially when the authors disagree with certain comments provided by reviewers.
5. The Chief Executive Editor sends the revised manuscript out for re-review. Typically, at least 1 of the original reviewers will be asked to examine the article.
6. When the reviewers have completed their work, the Editor-in-Chief examines their comments and decides whether the manuscript is ready to be published, needs another round of revisions, or should be rejected. If the decision is to accept, the Chief Executive Editor is notified.
7. The Chief Executive Editor reserves the final right to accept or reject any material for publication, if the processing of a particular manuscript is deemed not to be in compliance with the S.O.P. of *Pertanika*. An acceptance letter is sent to all the authors.

The editorial office ensures that the manuscript adheres to the correct style (in-text citations, the reference list, and tables are typical areas of concern, clarity, and grammar). The authors are asked to respond to any minor queries by the editorial office. Following these corrections, page proofs are mailed to the corresponding authors for their final approval. At this point, **only essential changes are accepted**. Finally, the manuscript appears in the pages of the journal and is posted on-line.

Pertanika Journal of

**SCIENCE  
& TECHNOLOGY**

**Vol. 30 (1) Jan. 2022**



A scientific journal published by Universiti Putra Malaysia Press



## EDITOR-IN-CHIEF

**Luqman Chuah Abdullah**  
*Chemical Engineering*

## CHIEF EXECUTIVE EDITOR

## UNIVERSITY PUBLICATIONS COMMITTEE

### CHAIRMAN

Nazamid Saari

### EDITORIAL STAFF

#### Journal Officers:

Kanagamaral Silvarajoo, *ScholarOne*  
Siti Zuhaila Abd Wahid, *ScholarOne*  
Tee Syn Ying, *ScholarOne*  
Umni Fairuz Hanapi, *ScholarOne*

#### Editorial Assistants:

Ku Ida Mastura Ku Baharom  
Siti Juridah Mat Arip  
Zulinaardawati Kamarudin

#### English Editor:

Norhanisah Ismail

### PRODUCTION STAFF

#### Pre-press Officers:

Nur Farrah Dila Ismail  
Wong Lih Jiun

### WEBMASTER

#### IT Officer:

To be appointed

### EDITORIAL OFFICE

#### JOURNAL DIVISION

Putra Science Park  
1<sup>st</sup> Floor, IDEA Tower II  
UPM-MTDC Technology Centre  
Universiti Putra Malaysia  
43400 Serdang, Selangor Malaysia.

#### Gen Enquiry

Tel. No: +603 9769 1622 | 1616

#### E-mail:

[executive\\_editor.pertanika@upm.edu.my](mailto:executive_editor.pertanika@upm.edu.my)

URL: [www.journals-jd.upm.edu.my](http://www.journals-jd.upm.edu.my)

### PUBLISHER

#### UPM Press

Universiti Putra Malaysia  
43400 UPM, Serdang, Selangor, Malaysia.

Tel: +603 9769 8851

E-mail: [penerbit@putra.upm.edu.my](mailto:penerbit@putra.upm.edu.my)

URL: <http://penerbit.upm.edu.my>



## ASSOCIATE EDITOR

### 2021-2023

#### Adem Kilicman

Mathematical Sciences  
Universiti Putra Malaysia, Malaysia

#### Miss Laiha Mat Kiah

Security Services Sn: Digital Forensic,  
Steganography, Network Security,  
Information Security, Communication  
Protocols, Security Protocols  
Universiti Malaya, Malaysia

#### Saidur Rahman

Renewable Energy, Nanofluids, Energy  
Efficiency, Heat Transfer, Energy Policy  
Sunway University, Malaysia

## EDITORIAL BOARD

### 2020-2022

#### Abdul Latif Ahmad

Chemical Engineering  
Universiti Sains Malaysia, Malaysia

#### Hsiu-Po Kuo

Chemical Engineering  
National Taiwan University, Taiwan

#### Mohd. Ali Hassan

Bioprocess Engineering, Environmental  
Biotechnology  
Universiti Putra Malaysia, Malaysia

#### Ahmad Zaharin Aris

Hydrochemistry, Environmental  
Chemistry, Environmental Forensics,  
Heavy Metals  
Universiti Putra Malaysia, Malaysia

#### Ivan D. Rukhlenko

Nonlinear Optics, Silicon Photonics,  
Plasmonics and Nanotechnology  
The University of Sydney, Australia

#### Najafpour Darzi Ghasem

Bioprocess Technology, Chemical  
Engineering, Water and Wastewater  
Treatment Technology, Biochemical  
Engineering and Biotechnology,  
Bioethanol, Biofuel, Biohydrogen,  
Enzyme and Fermentation Technology  
Babol Noshirvani University of  
Technology, Iran

#### Azlina Harun@Kamaruddin

Enzyme Technology, Fermentation  
Technology  
Universiti Sains Malaysia, Malaysia

#### Lee Keat Teong

Energy Environment, Reaction  
Engineering, Waste Utilization,  
Renewable Energy  
Universiti Sains Malaysia, Malaysia

#### Bassim H. Hameed

Chemical Engineering: Reaction  
Engineering, Environmental Catalysis &  
Adsorption  
Qatar University, Qatar

#### Mohamed Othman

Communication Technology and  
Network, Scientific Computing  
Universiti Putra Malaysia, Malaysia

#### Nor Azah Yusof

Biosensors, Chemical Sensor, Functional  
Material  
Universiti Putra Malaysia, Malaysia

#### Biswajeet Pradhan

Digital image processing, Geographical  
Information System (GIS), Remote  
Sensing  
University of Technology Sydney,  
Australia

#### Mohd Sapuan Salit

Concurrent Engineering and Composite  
Materials  
Universiti Putra Malaysia, Malaysia

#### Norbahiah Misran

Communication Engineering  
Universiti Kebangsaan Malaysia,  
Malaysia

#### Daud Ahmad Israf Ali

Cell Biology, Biochemical, Pharmacology  
Universiti Putra Malaysia, Malaysia

#### Mohd Shukry Abdul Majid

Polymer Composites, Composite  
Pipes, Natural Fibre Composites,  
Biodegradable Composites, Bio-  
Composites  
Universiti Malaysia Perlis, Malaysia

#### Roslan Abd-Shukur

Physics & Materials Physics,  
Superconducting Materials  
Universiti Kebangsaan Malaysia,  
Malaysia

#### Hari M. Srivastava

Mathematics and Statistics  
University of Victoria, Canada

#### Mohd Zulkifly Abdullah

Fluid Mechanics, Heat Transfer,  
Computational Fluid Dynamics (CFD)  
Universiti Sains Malaysia, Malaysia

#### Wing Keong Ng

Aquaculture, Aquatic Animal Nutrition,  
Aqua Feed Technology  
Universiti Sains Malaysia, Malaysia

## INTERNATIONAL ADVISORY BOARD

### 2021-2024

#### CHUNG, Neal Tai-Shung

Polymer Science, Composite and  
Materials Science  
National University of Singapore,  
Singapore

#### Mohamed Pourkashanian

Mechanical Engineering, Energy, CFD  
and Combustion Processes  
Sheffield University, United Kingdom

#### Yulong Ding

Particle Science & Thermal Engineering  
University of Birmingham, United  
Kingdom

#### Hiroshi Uyama

Polymer Chemistry, Organic  
Compounds, Coating, Chemical  
Engineering  
Osaka University, Japan

#### Mohini Sain

Material Science, Biocomposites,  
Biomaterials  
University of Toronto, Canada

## ABSTRACTING AND INDEXING OF PERTANIKA JOURNALS

The journal is indexed in SCOPUS (Elsevier), Clarivate-Emerging Sources Citation Index (ESCI), BIOSIS, National Agricultural Science (NAL), Google Scholar, MyCite, ISC. In addition, Pertanika JSSH is recipient of "CREAM" Award conferred by Ministry of Higher Education (MoHE), Malaysia.





**Pertanika Journal of Science & Technology**  
**Vol. 30 (1) Jan. 2022**

**Contents**

Foreword <i>Chief Executive Editor</i>	
Deep Learning to Detect and Classify the Purity Level of Luwak Coffee Green Beans <i>Yusuf Hendrawan, Shinta Widyaningtyas, Muchammad Riza Fauzy, Sucipto Sucipto, Retno Damayanti, Dimas Firmanda Al Riza, Mochamad Bagus Hermanto and Sandra Sandra</i>	1
<i>Review article</i> Data Acquisition and Data Processing using Electroencephalogram in Neuromarketing: A Review <i>Annis Shafika Amran, Sharifah Aida Sheikh Ibrahim, Nurul Hashimah Ahamed Hassain Malim, Nurfaten Hamzah, Putra Sumari, Syaheerah Lebai Lutfi and Jafri Malin Abdullah</i>	19
Multi-band Antenna with CSRR Loaded Ground Plane and Stubs Incorporated Patch for WiMAX/WLAN Applications <i>Palanivel Manikandan, Pothiraj Sivakumar and Nagarajan Rajini</i>	35
<i>Review article</i> A Survey on Model-based Fault Detection Techniques for Linear Time-Invariant Systems with Numerical Analysis <i>Masood Ahmad and Rosmiwati Mohd-Mokhtar</i>	53
Work Performance of Extension Agents: Skills of Transfer of Technology and Human Resource Development in Cocoa Industry <i>Murni Azureen Mohd Pakri, Salim Hassan, Oluwatoyin Olagunju, Mohd Yusoff Abd Samad and Ramle Kasin</i>	79
Sliding Window and Parallel LSTM with Attention and CNN for Sentence Alignment on Low-Resource Languages <i>Tien-Ping Tan, Chai Kim Lim and Wan Rose Eliza Abdul Rahman</i>	97
The Relationships of Interleukin-33, Ve-Cadherin And Other Physiological Parameters in Male Patients with Rheumatoid Arthritis <i>Khalid F. AL-Rawi, Hameed Hussein Ali, Manaf A. Guma, Shakir F.T. Alaaraji and Muthanna M. Awad</i>	123

Towards Adoption of Smart Contract in Construction Industry in Malaysia <i>Dewi Noorain Bolhassan, Chai Changsaar, Ali Raza Khoso, Loo Siawchuing, Jibril Adewale Bamgbade and Wong Ngie Hing</i>	141
Person Verification based on Multimodal Biometric Recognition <i>Annie Anak Joseph, Alex Ng Ho Lian, Kuryati Kipli, Kho Lee Chin, Dyg Azra Awang Mat, Charlie Sia Chin Voon, David Chua Sing Ngie and Ngu Sze Song</i>	161
Development of Stand-Alone DC Energy Datalogger for Off- Grid PV System Application based on Microcontroller <i>Mohd Ruzaimi Ariffin, Suhaidi Shafie, Wan Zuha Wan Hasan, Norhafiz Azis, Mohammad Effendy Yaacob and Eris Elianddy Supeni</i>	185
Performance of a HAWT Rotor with a Modified Blade Configuration <i>Tabrej Khan, Balbir Singh, Mohamed Thariq Hameed Sultan and Kamarul Arifin Ahmad</i>	201
Acceptance Ratio Analysis in Grid-Connected Photovoltaic System: Is There Any Difference between DC and AC? <i>Fatin Azirah Mohd Shukor, Hedzlin Zainuddin, Jasrul Jamani Jamian, Nurmalessa Muhammad, Farah Liyana Muhammad Khir and Noor Hasliza Abdul Rahman</i>	221
A Dashboard-based System to Manage and Monitor the Progression of Undergraduate IT Degree Final Year Projects <i>Nooralisa Mohd Tuah, Ainnecia Yoag, Dinna@Nina Mohd Nizam and Cheang Wan Chin</i>	235
Pectinase Production from Banana Peel Biomass via the Optimization of the Solid-State Fermentation Conditions of <i>Aspergillus niger</i> Strain <i>Nazaitulshila Rasit, Yong Sin Sze, Mohd Ali Hassan, Ooi Chee Kuan, Sofiah Hamzah, Wan Rafizah Wan Abdullah@Wan Abd. Rahman and Md. Nurul Islam Siddique</i>	257
Compression and Flexural Behavior of ECC Containing PVA Fibers <i>Lee Siong Wee, Mohd Raizamzamani Md Zain, Oh Chai Lian, Nadiyah Saari and Norrul Azmi Yahya</i>	277
The Effect of Quenching on High-Temperature Heat Treated Mild Steel and its Corrosion Resistance <i>Alaba Oladeji Araoyinbo, Ayuba Samuel, Albakri Mohammed Mustapha Abdullah and Mathew Biodun</i>	291
Tensile Behaviour of Slag-based Engineered Cementitious Composite <i>Chai Lian Oh, Siong Wee Lee, Norrul Azmi Yahya, Gajalakshmi Pandulu and Mohd Raizamzamani Md Zain</i>	303

A Comparative Effectiveness of Hierarchical and Non-hierarchical Regionalisation Algorithms in Regionalising the Homogeneous Rainfall Regions <i>Zun Liang Chuan, Wan Nur Syahidah Wan Yusoff, Azlyna Senawi, Mohd Romlay Mohd Akramin, Soo-Fen Fam, Wendy Ling Shinyie and Tan Lit Ken</i>	319
Optical Properties of Cu <sub>2</sub> O Thin Films Impregnated with Carbon Nanotube (CNT) <i>Oluayamo Sunday Samuel, Ajanaku Olanrewaju and Adedayo Kayode David</i>	343
<i>Review article</i>	
A Review on Synthesis and Characterization of Activated Carbon from Natural Fibers for Supercapacitor Application <i>Thilageshwaran Subramaniam, Mohamed Ansari Mohamed Nainar and Noor Afeefah Nordin</i>	351
Esterification of Free Fatty Acid in Palm Oil Mill Effluent using Sulfated Carbon-Zeolite Composite Catalyst <i>Hasanudin Hasanudin, Qodria Utami Putri, Tuty Emilia Agustina and Fitri Hadiah</i>	377
Effect of Water Absorption on Flexural Properties of Kenaf/Glass Fibres Reinforced Unsaturated Polyester Hybrid Composites Rod <i>Bassam Hamid Alaseel, Mohamed Ansari Mohamed Nainar, Noor Afeefah Nordin, Zainudin Yahya and Mohd Nazim Abdul Rahim</i>	397
MYLPHerb-1: A Dataset of Malaysian Local Perennial Herbs for the Study of Plant Images Classification under Uncontrolled Environment <i>Kalananthni Pushpanathan, Marsyita Hanafi, Syamsiah Masohor and Wan Fazilah Fazlil Ilahi</i>	413
<i>Review article</i>	
The Effect of Elevated Temperature on Engineered Cementitious Composite Microstructural Behavior: An Overview <i>Mohamad Hakimin Khazani, Oh Chai Lian, Lee Siong Wee, Mohd Raizamzamani Md Zain and Norrul Azmi Yahya</i>	433
Palaeoecologic and Palaeoclimatic Inferences from Calcareous Nannofossils in Western Lobe Offshore, Niger Delta <i>Bamidele Samuel Oretade and Che Aziz Ali</i>	451
Effect of Chemical Reaction towards MHD Marginal Layer Movement of Casson Nanofluid through Porous Media above a Moving Plate with an Adaptable Thickness <i>Ganugapati Raghavendra Ganesh and Wuriti Sridhar</i>	477

A New Method to Estimate Peak Signal to Noise Ratio for Least Significant Bit Modification Audio Steganography <i>Muhammad Harith Noor Azam, Farida Ridzuan and M Norazizi Sham Mohd Sayuti</i>	497
Formulation of Polyherbal Carbonated Beverage based on <i>Halalan Thoyyiban</i> Principle <i>Puteri Shazleen Izreena Mohd Shahrin, Norhayati Muhammad and Nur Fazira Abdul Rahim</i>	513
Comparative Study on the Social Behavior of Sambar Deer ( <i>Rusa unicolor</i> ) in Three Selected Captive Facilities in Peninsular Malaysia <i>Kushaal Selvarajah, Mohd Noor Hisham Mohd Nadzir and Geetha Annavi</i>	527
Synthesis and Performance of PAFS Coagulant Derived from Aluminium Dross <i>Shiyi Li and Shafreeza Sobri</i>	547
Assessment of Domestic Wastewaters as Potential Growth Media for <i>Chlorella vulgaris</i> and <i>Haematococcus pluvialis</i> <i>Yeong Hwang Tan, Mee Kin Chai, Yang Kai Ooi and Ling Shing Wong</i>	565
FPGA-based Implementation of SHA-256 with Improvement of Throughput using Unfolding Transformation <i>Shamsiah Suhaili and Norhuzaimin Julai</i>	581
Characterization of Polyvinylidene Difluoride-based Energy Harvesting with IDE Circuit Flexible Cantilever Beam <i>Khairul Azman Ahmad, Noramalina Abdullah, Mohamad Faizal Abd Rahman, Muhammad Khusairi Osman and Rozan Boudville</i>	605
<i>Conceptual paper</i> A Conceptual Framework for Road Safety Education using Serious Games with a Gesture-based Interaction Approach <i>Wan Salfarina Wan Husain, Syadiah Nor Wan Shamsuddin and Normala Rahim</i>	621
Arabic Handwriting Classification using Deep Transfer Learning Techniques <i>Ali Abd Almisreb, Nooritawati Md Tahir, Sherzod Turaev, Mohammed A. Saleh and Syed Abdul Mutalib Al Junid</i>	641
<i>Review article</i> Adoption of Cloud Computing in E-Government: A Systematic Literature Review <i>Osama Abied, Othman Ibrahim and Siti Nuur-Ila Mat Kamal</i>	655

Dose Distribution of <sup>192</sup> Ir HDR Brachytherapy Source Measurement using Gafchromic® EBT3 Film Dosimeter and TLD-100H <i>Nor Shazleen Ab Shukor, Marianie Musarudin, Reduan Abdullah and Mohd Zahri Abdul Aziz</i>	691
Development of Attendance and Temperature Monitoring System using IoT with Wireless Power Transfer Application <i>Noramalina Abdullah and Sarah Madihah Mohd Shazali</i>	709
Octave Band Technique for Noise Measurement at the Source, Path, and Receiver of Gas Turbines in Oil and Gas Facilities <i>Akmal Haziq Mohd Yunos and Nor Azali Azmir</i>	725
The Detection of Changes in Land Use and Land Cover of Al-Kut City using Geographic Information System (GIS) <i>Fatima Asaad Tayeb, Ahmed Kareem Jebur and Husham H. Rashid</i>	747
Automation of Psychological Selection Procedures for Personnel to Specific Activities <i>Ihor Prykhodko, Stanislav Horielyshev, Yanina Matsehora, Vasily Lefterov, Stanislav Larionov, Olena Kravchenko, Maksim Baida, Olena Halkina and Olena Servachak</i>	761
Determination of Putative Vacuolar Proteases, PEP4 and PRB1 in a Novel Yeast Expression Host <i>Meyerozyma guilliermondii</i> Strain SO using Bioinformatics Tools <i>Okojie Eseoghene Lorraine, Raja Noor Zaliha Raja Abd. Rahman, Joo Shun Tan, Raja Farhana Raja Khairuddin, Abu Bakar Salleh and Siti Nurbaya Oslan</i>	777
The Asymmetric Impacts of Crude Oil Prices, Inflation, the Exchange Rate, Institutional Quality, and Trade Balance on Tourist Arrivals in Bangladesh: A Nonlinear ARDL Model Approach <i>Rehana Parvin</i>	781
<i>Short communication</i>	
Reinvestigation on Assessing the Stability of Mullagulov Tested Steel Rods under Follower Forces <i>Jakkana Peter Praveen and Boggarapu Nageswara Rao</i>	801
<i>Review article</i>	
A Review of Thermal Design for Buildings in Hot Climates <i>Sahar Najeeb Kharrufa and Firas Noori</i>	813
Accuracy of Ultrasound and Magnetic Resonance Cholangiopancreatography Findings in the Diagnosis of Biliary System Stones <i>Abdullah Taher Naji, Ameen Mohsen Amer, Saddam Mohammed Alzofi, Esmail Abdu Ali and Noman Qaid Alnaggar</i>	841



# Foreword

Welcome to the first issue of 2022 for the *Pertanika Journal of Science and Technology (PJST)*!

PJST is an open-access journal for studies in Science and Technology published by Universiti Putra Malaysia Press. It is independently owned and managed by the university for the benefit of the world-wide science community.

This issue contains 46 articles; six review articles, one short communication, one conceptual paper and the rest are regular articles. The authors of these articles come from different countries namely Bangladesh, India, Indonesia, Iraq, Malaysia, Nigeria, Pakistan, Ukraine and United Arab Emirates.

A review on data acquisition and data processing using electroencephalogram (EEG) in neuromarketing was conducted by Annis Shafika Amran and colleagues from Universiti Sains Malaysia. The invention of EEG has paved the way for diagnosing and studying various neurological disorders and studying human cognitive processes. The signals of an EEG provide subjective sine signal patterns enabling the visualization of changes in brain activity. The flexibility of an EEG system allows manipulation of techniques to best-fit study goals and allow better coverage of the brain area for accurate imaging with the manipulation of electrode number and position. The Revolution of EEG against time has caused EEG to be wearable, portable, and accessible to the masses, allowing extensive use of EEG in research and study, not just for the application in healthcare. Details of this study are available on page 19.

A regular article titled “The Relationships of Interleukin-33, VE-Cadherin and other Physiological Parameters in Male Patients with Rheumatoid Arthritis” was presented by Khalid F. AL-Rawi and co-researchers from the University of Anbar, Iraq. This study used various enzymatic-linked immunosorbent assays, spectroscopic, serological, and hematological methods to quantify blood count, erythrocyte sedimentation rate, C-reactive protein, and rheumatoid factor, lipid profile, kidney function tests, specific enzymes, TGF- $\beta$ 1, vitamin E, VE-cadherin, interleukin 33 and TIMP-1. The results have revealed a significant positive correlation between ESR, RF, VE-cadherin, and vitamin E, specifically type  $\alpha$ -tocopherol that are associated with the non-biochemical parameters such as body mass index, waist length, hip length, thorax, and age. In addition, the study revealed some parameters that would positively affect rheumatoid arthritis (RA) patients, such as TGF- $\beta$ 1, vitamin E, and VE-cadherin, which have shown a decrease in

their values compared to those to the controls. In contrast, other parameters showed an increase in RA patients, and therefore they can be useful biomarkers for RA disease. The detailed information of this study is available on page 123.

An investigation to evaluate the diagnostic accuracy of magnetic resonance cholangiopancreatography (MRCP) and Ultrasound (US) images for the diagnosis of biliary system stones, as well as to assess the consistency between MRCP and US findings, was conducted by Abdullah Taher Naji et al. from University of Science and Technology, Yemen. The study revealed that the most prominent age group with symptoms of biliary system stones was the 33-60-year-old group. It also found that the accuracy of US and MRCP in detecting gallbladder (GB) stones compared with the final diagnosis was 94% and 91%, respectively, with moderate conformity between their results. The accuracy of US and MRCP images in detecting common bile duct (CBD) stones was 61% and 98%, respectively, with fair conformity between their results. In addition, there is a significant agreement between the MRCP and US results in detecting the GB and CBD stones with an agreed percentage of 74% and 71%, respectively. Further details of the investigation can be found on page 841.

We anticipate that you will find the evidence presented in this issue to be intriguing, thought-provoking and useful in reaching new milestones in your own research. Please recommend the journal to your colleagues and students to make this endeavour meaningful.

All the papers published in this edition underwent Pertanika's stringent peer-review process involving a minimum of two reviewers comprising internal as well as external referees. This was to ensure that the quality of the papers justified the high ranking of the journal, which is renowned as a heavily-cited journal not only by authors and researchers in Malaysia but by those in other countries around the world as well.

We would also like to express our gratitude to all the contributors, namely the authors, reviewers, Editor-in-Chief and Editorial Board Members of PJST, who have made this issue possible.

PJST is currently accepting manuscripts for upcoming issues based on original qualitative or quantitative research that opens new areas of inquiry and investigation.

**Chief Executive Editor**

[executive\\_editor.pertanika@upm.edu.my](mailto:executive_editor.pertanika@upm.edu.my)



## Deep Learning to Detect and Classify the Purity Level of Luwak Coffee Green Beans

Yusuf Hendrawan<sup>1\*</sup>, Shinta Widyaningtyas<sup>2</sup>, Muchammad Riza Fauzy<sup>3</sup>, Sucipto Sucipto<sup>2</sup>, Retno Damayanti<sup>1</sup>, Dimas Firmanda Al Riza<sup>1</sup>, Mochamad Bagus Hermanto<sup>1</sup> and Sandra Sandra<sup>1</sup>

<sup>1</sup>Department of Agricultural Engineering, Faculty of Agricultural Technology, Brawijaya University, Veteran St., Malang, East Java, ZIP 65145, Indonesia

<sup>2</sup>Department of Agroindustrial Engineering, Faculty of Agricultural Technology, Brawijaya University, Veteran St., Malang, East Java, ZIP 65145, Indonesia

<sup>3</sup>Department of Industrial Engineering, Faculty of Engineering, Universitas Merdeka, Jl. Terusan Raya Dieng 62-64, Malang, East Java, Indonesia

### ABSTRACT

Luwak coffee (palm civet coffee) is known as one of the most expensive coffee in the world. In order to lower production costs, Indonesian producers and retailers often mix high-priced Luwak coffee with regular coffee green beans. However, the absence of tools and methods to classify Luwak coffee counterfeiting makes the sensing method's development urgent. The research aimed to detect and classify Luwak coffee green beans purity into the following purity categories, very low (0-25%), low (25-50%), medium (50-75%), and high (75-100%). The classifying method relied on a low-cost commercial visible light camera and the deep learning model method. Then, the research also compared the performance of four pre-trained convolutional neural network (CNN) models consisting of SqueezeNet,

GoogLeNet, ResNet-50, and AlexNet. At the same time, the sensitivity analysis was performed by setting the CNN parameters such as optimization technique (SGDm, Adam, RMSProp) and the initial learning rate (0.00005 and 0.0001). The training and validation result obtained the GoogLeNet as the best CNN model with optimizer type Adam and learning rate 0.0001, which resulted in 89.65% accuracy. Furthermore, the testing process using confusion matrix from different sample data obtained the best

### ARTICLE INFO

#### Article history:

Received: 23 March 2021

Accepted: 15 September 2021

Published: 06 December 2021

DOI: <https://doi.org/10.47836/pjst.30.1.01>

#### E-mail addresses:

yusufhendrawan@gmail.com (Yusuf Hendrawan)

shintawidya1435@gmail.com (Shinta Widyaningtyas)

Muchrizafauzi@gmail.com (Muchammad Riza Fauzy)

ciptotip@ub.ac.id (Sucipto Sucipto)

just.ennox@gmail.com (Retno Damayanti)

dimasfirmanda@ub.ac.id (Dimas Firmanda Al Riza)

mbhermanto@ub.ac.id (Mochamad Bagus Hermanto)

sandra.msutan@ub.ac.id (Sandra Sandra)

\* Corresponding author

CNN model using ResNet-50 with optimizer type RMSProp and learning rate 0.0001, providing an accuracy average of up to 85.00%. Later, the CNN model can be used to establish a real-time, non-destructive, rapid, and precise purity detection system.

*Keywords:* Classification, convolutional neural network, Luwak coffee green beans, purity

---

## INTRODUCTION

The two most popular coffee varieties are *Coffea canephora* L. (Robusta) and *Coffea arabica* L. (Arabika) (Skowron et al., 2020). As one of the expensive and popular coffees derived from those two varieties, Civet coffee (also known as Luwak coffee in Indonesia) is produced less than 127 kg per month, and the price ranges from USD 200-400 per kg, creating this a hundred times more costly than regular coffees (Muzaiifa et al., 2019; Jumhawan et al., 2016). Currently, Indonesia has become the main producer of Luwak coffee, followed by East Timor, the Philippines, Thailand, Vietnam, and Ethiopia. Luwak coffee is made of Arabica or Robusta passing through the civet (*Paradoxurus hermaphroditus*) digestive system (Suhandy & Yulia, 2017). Civet can identify the best and ripe coffee beans.

After consuming the beans, the fermentation process occurs on the civet digestive system then changes the chemical structure of coffee beans, which later produces smoother coffee beans and a lesser bitter taste. The high price and scarcity of Luwak coffee trigger producers and retailers to fraud the product by mixing Luwak coffee with another cheaper coffee affecting its purity level; this also affects the coffee taste, quality, pH value, and antioxidant content. It often occurs in Indonesia as the third largest coffee producer after Brazil and Vietnam, and the case gradually increases in the food industry and becomes a serious problem to overcome to assure the quality for consumers' satisfaction (Amirvaresi et al., 2021).

As a conventional method, human sensing by the smelling aroma of coffee is utilized to distinguish between Luwak coffee and regular coffee. However, since the method relies on the human perspective, this may result in different outcomes among panelists. So, human sensing cannot be a standard method, and other procedures need to be developed. Some researchers have been developed to detect Luwak coffee purity, i.e., using electric nose (E-nose) and gas chromatography (Marcone, 2004). Jumhawan et al. (2013) has developed research using citric acid, malic acid, and inositol to distinguish roasted Luwak coffee and roasted regular coffee. However, this method is lengthy, destructive, high cost, and not real-time. Moreover, Jumhawan et al. (2015) have also developed a gas chromatography/flame ionization detector to authentic the Asian palm civet coffee (Luwak coffee).

This research has successfully developed a method to distinguish commercial civet coffee, regular coffee, and coffee blend with 50% civet coffee. Nunez et al. (2021) and Pauli et al. (2014) have also observed the use of non-targeted HPLC-FLD fingerprinting

methods to detect the counterfeiting of Arabica coffee and regular Robusta coffee with prediction error results below 3.4%. Sezer et al. (2018) has used laser-induced breakdown spectroscopy (LIBS) to determine the counterfeiting level of Arabica coffee, with a prediction result showing a coefficient value of the highest determination 0.996. Cebi et al. (2017) researched using rapid ATR-FTIR to detect tea and regular coffee product by accuracy result 100%. Finally, Daniel et al. (2018) detected regular coffee counterfeiting using capillary electrophoresis-tandem mass spectrometry (CE-MS) with a significant prediction, i.e., the highest coefficient of determination value 0.995.

Combes et al. (2018) has successfully developed a rapid DNA-based method to detect counterfeiting of Arabica coffee and regular Robusta coffee. Furthermore, Lopetcharat et al. (2016) has also successful developed the electronic tongue (E-tongue) to differentiate civet coffee and regular coffee. The weakness of E-nose is that it depends on the environmental conditions such as temperature and water content, and the weaknesses of gas chromatography (Ongo et al., 2012), HPLC-FLD, LIBS, ATR-FTIR, CE-MS, DNA-based method, and E-tongue are high cost, need a longer time, and destructive-sensing testing. Yulia and Suhandy's (2017) research developed a coffee authenticity detection method using UV-Visible spectra. Combining the UV-Visible spectra tool and partial least square (PLS) regression method obtained a good prediction result, yet this method requires expensive instrumentation.

Therefore, computer vision is proposed in this research as it is non-destructive, rapid, real-time, low-cost, and accurate. This method has been widely used to detect counterfeiting in various food products. For example, Song et al. (2021) used two smartphone-based low-cost computer vision (Samsung Galaxy C5 and A9s) to detect minced beef counterfeiting with root mean square error ranging from 0.04 to 0.16. Kiani et al. (2017) combined computer vision (CCD digital camera) and E-nose to detect saffron counterfeiting. The result was quite good, with the prediction accuracy up to 89%. Anami et al. (2019) successfully used a commercial digital camera (PENTAX MX-1) to identify and classify bulk paddy grain counterfeiting rate by accuracy value up to 93.31%.

The commercial digital camera was also used in research by Lin et al. (2020), which analyzed the counterfeiting rate of safflower using a Nikon D90 digital SLR camera. Reile et al. (2020), in their research, proved that the effectiveness of low-cost commercial digital camera, i.e., Sony digital camera (model DSC-W830, resolution of 20.1 Mpixels) to detect ketchup product counterfeiting with  $R^2$  value reached 0.96. A low-cost digital camera was also very practical used in the research by Silva and Rocha (2020) to detect the counterfeiting rate of dairy products using an LG K10 Pro smartphone equipped with a 13-megapixel camera. According to several types of research conducted, using a low-cost digital camera was highly possible to detect counterfeiting rates in food products, particularly coffee.

Other than that, some researchers have widely used artificial intelligence (AI) to develop a detection model to understand adulterants on food. For example, Wojcik and Jakubowska (2021) used a deep neural network to predict adulteration in apple juice with an R2 prediction that reached 0.98. Moreover, the AI has successfully detected butter counterfeit with 82.66% accuracy (Iymen et al., 2020). Likewise, Support Vector Machine (SVM) (kind of AI) can detect cassava starch adulteration (86.9% accuracy) (Cardoso & Poppi, 2021) and white rice counterfeiting (90% accuracy) (Lim et al., 2017). Furthermore, an artificial neural network (ANN) was also popular to detect counterfeiting of Muscatel wines (Cancilla et al., 2020), edible bird's nests (90% accuracy) (Huang et al., 2019), and coffee chemical compounds (such as phenol, pH, and coffee purity) up to 90% accuracy and mean square error 0.0442 (Hendrawan et al., 2019). Above that, recent research in convolutional neural networks (CNN), another type of AI, gave more practical results on detecting honey adulteration resulting in up to 97.96% accuracy (Li et al., 2021; Izquierdo et al., 2020a), extra virgin olive oil with 97% accuracy (Izquierdo et al., 2020b), and counterfeiting in Arabica and Robusta coffee with an error below 1% (Lopez et al., 2021). Hence, CNN was more potential to detect coffee quality and authenticity than other learning machines.

The combination of low-cost commercial visible light camera and deep learning is promising as an alternative for rapid, real-time, and non-destructive detection with high prediction accuracy but affordable than other non-destructive methods. Therefore, the research aims to detect and classify Luwak coffee green beans into several purity categories: very low (0-25%), low (25-50%), medium (50-75%), and high (75-100%) using low-cost commercial visible light camera tool tandem with deep learning model. Furthermore, it includes four pre-trained CNN (SqueezeNet, AlexNet, GoogLeNet, and Resnet 50), which have been tested elsewhere (Nayak et al., 2021).

## **MATERIAL AND METHODS**

Two coffee samples, Arabica Luwak coffee green beans, and pure Arabica regular coffee green beans were set. In each image data acquisition, one hundred sixty coffee beans were randomly mixed between Arabica Luwak coffee green beans and pure Arabica regular coffee green beans. The percentage of the mixture was calculated using the beans unit. Several conditions from the sample were then arranged into four different purity mixtures: very low (0-25% or 0-40 Luwak coffee beans), low (25-50% or 40-80 Luwak coffee beans), medium (50-75% or 80-120 Luwak coffee beans), and high (75-100% or 120-160 Luwak coffee beans). Samples of some mixtures of Luwak coffee green beans are shown in Figure 1. The sample images were acquired using a visible light digital camera (Nikon Coolpix A10, 16 megapixels, Japan). The initial image resolution was  $1024 \times 768$  pixels and was cropped into  $500 \times 500$  pixels. Four hundred twenty-eight images were obtained from each mixture, creating 1712 images in total for four mixtures. All samples for CNN analysis

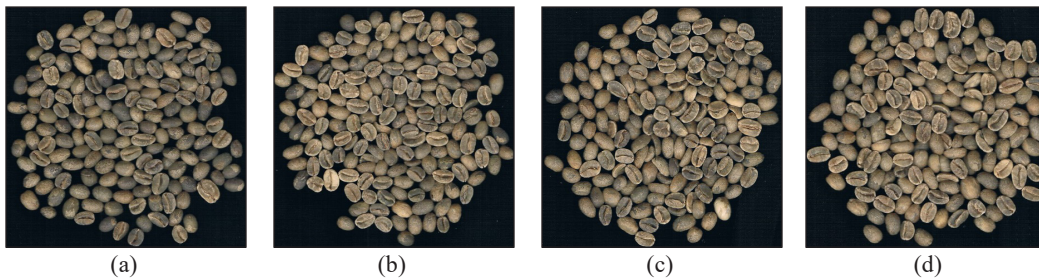


Figure 1.  $500 \times 500$  pixels image of Luwak coffee green beans in several purity levels: (a) high (75-100%); (b) medium (50-75%); (c) low (25-50%); and (d) very low (0-25%)

were then divided into three data set: training, validation, and testing (Bragagnolo et al., 2021). 70% of total data (1200 images) were set as training data, and 30% of total data (512 images) for validation (Medus et al., 2021). The testing data were acquired separately at a different time with 400 images of Luwak coffee green beans at different purity conditions.

CNN has been widely used, and it is a popular deep learning method for detecting food product counterfeiting and purity based on computer vision (Liu et al., 2021). The usage of CNN features could capture the high-level features, which can be the central key for segregating an image's color, morphology, and textural features (Simon & Uma, 2020). The deep CNN can capture the low detail features from the initial convolution layers, and layers are propagated to generate the high-level features in the last layers. Different filters in CNN were generated by efficient convolution and pooling operation to recognize color, morphology, and textural features. The features were extracted from certain layers of the network and later considered for training classifiers. Unlike conventional machine learning, CNN does not require image feature extraction and feature selection process, providing a more efficient, effective, and accurate prediction model (Yu et al., 2021).

CNN can directly process raw images to classify output by tuning parameters in the convolutional and pooling layers. In the classification process, deep learning architecture was used to classify sample images of Luwak coffee green beans at four purity levels (very low, low, medium, and high). The structure of typical CNN can be seen in Figure 2. The CNN structure involves image acquisition, convolutional layer, pooling layer, and fully connected layer. The research used four types of pre-trained CNN models (SqueezeNet (Ucar & Korkmaz, 2020), GoogLeNet (Raikar et al., 2020), ResNet-50 (Mkonyi et al., 2020), and AlexNet (Jiang et al., 2019)) provided in Matlab R2020b. SqueezeNet is a convolutional neural network that is 18 layers deep. It begins with a standalone convolution layer, followed by 8 Fire modules, ending with a final conv layer. The number of filters per fire module gradually increases from the beginning to the end of the network. GoogLeNet is a 22-layer deep convolutional neural network, a variant of the Inception Network, a deep CNN developed by researchers at Google.

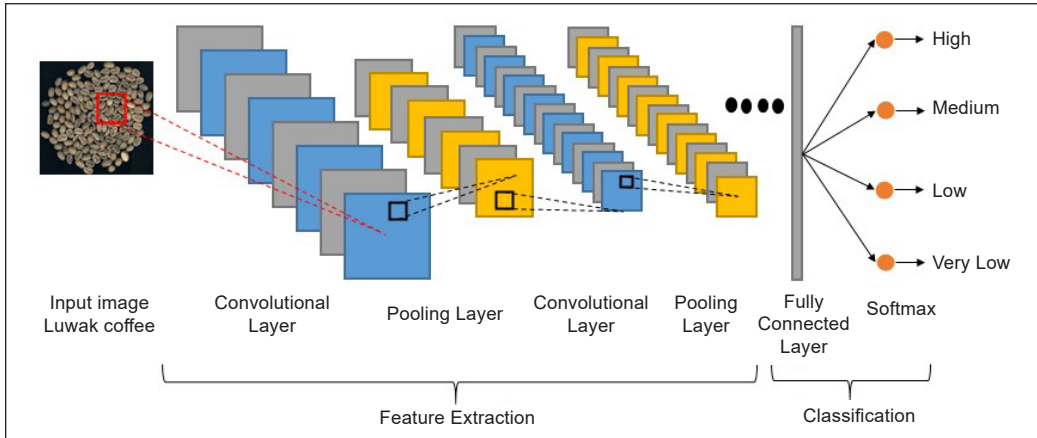


Figure 2. Proposed computer vision to classify the purity level in Luwak coffee green beans using deep learning

This architecture uses techniques such as  $1 \times 1$  convolutions in the middle of the architecture and global average pooling. ResNet-50 is a convolutional neural network that is 50 layers deep. ResNet architecture makes use of shortcut connections to solve the vanishing gradient problem. The basic building block of ResNet is a Residual block that is repeated throughout the network. AlexNet is a convolutional neural network that is eight layers deep. The network consists of 5 convolutional layers and three fully connected layers. The activation used is the Rectified Linear Unit (ReLU). The activation function of ReLU was used in every hidden layer, and the softmax function was applied in the final layer to ensure the output value consistently ranging between 0 and 1, which ReLU and softmax have been described in the research by Lin and Shen (2018). AlexNet addresses the over-fitting problem by using drop-out layers where a connection is dropped during training with a probability of  $p=0.5$ . Figure 3 shows the flow chart of the four pre-trained CNN models used in this study (Hendrawan et al., 2021).

In the training process, the maximum epoch was set at 20 (Eltrass et al., 2021), the mini-batch size was set at 20 (Tian et al., 2020), maximum iteration at 1200, 60 iterations per epoch, momentum 0.9, and loss function used binary cross-entropy. Thenmozhi and Reddy (2019) research obtained the best learning rate in the CNN model at the value of 0.0001 and 0.00005, so the initial learning rate was set at 0.0001 and 0.00005 in this research. The optimization techniques (optimizers) used in the research were stochastic gradient descent with momentum (SGDm) adaptive moment estimation (Adam), and root means square propagation (RMSProp) (Manninen et al., 2021). SGDm accelerated the convergence by changing the actual gradient with an estimate, which was calculated from subset data that was selected randomly. Adam is an algorithm to optimize the learning rate by combining the advantages of RMSProp and SGDm. The CNN program was run on a computer with the following specifications, Intel Core i3-4150 CPU @3.50GHz (4

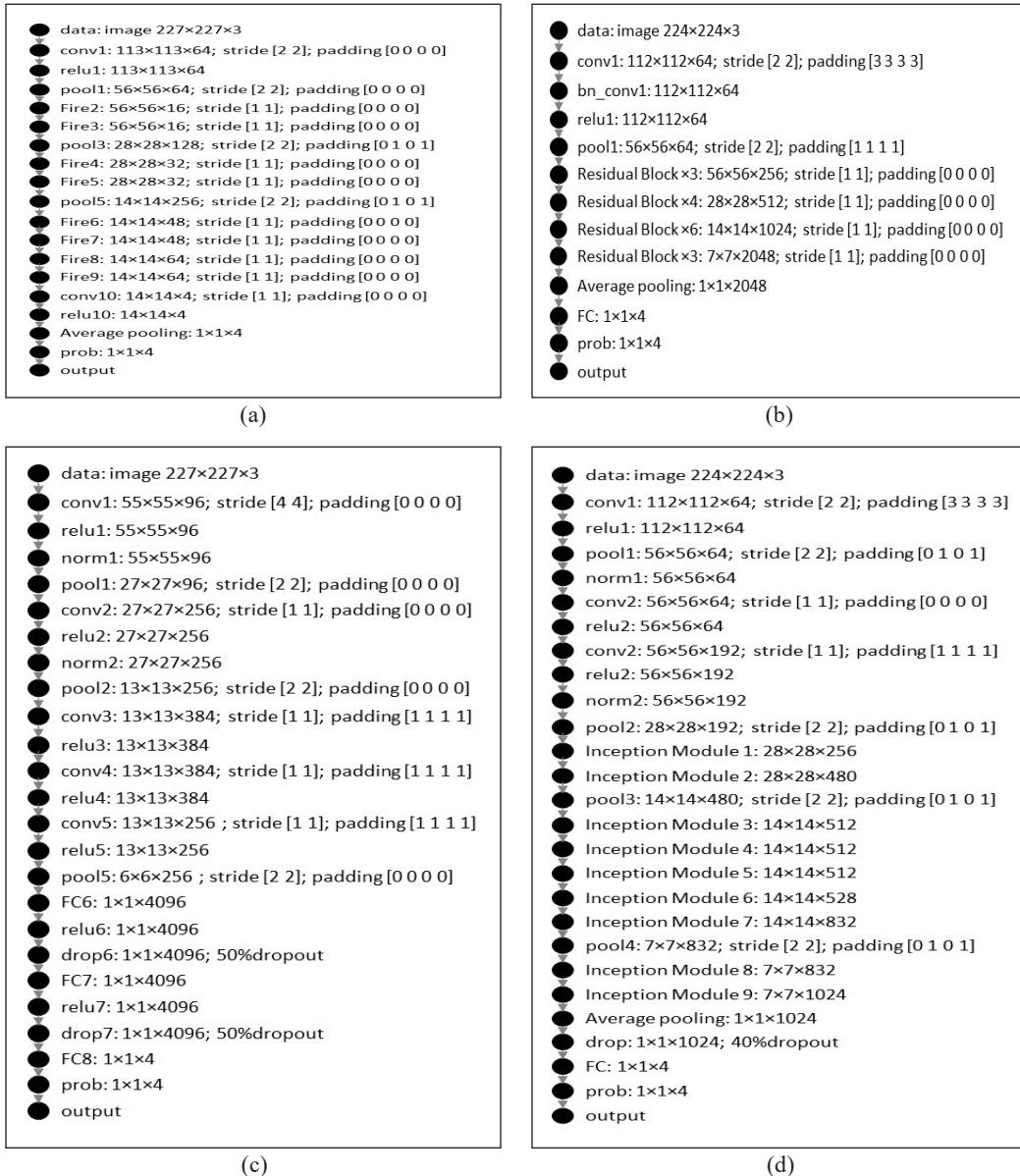


Figure 3. Schematic representation of pre-trained CNN model: (a) SqueezeNet; (b) ResNet-50; (c) AlexNet; (d) GoogLeNet

CPUs) 10 GB of RAM. The 24 types of CNN models built then were evaluated based on the validation data to retrieve the best 5 CNN models. These best five CNN models were later tested using confusion matrix and testing data according to the classification accuracy. The confusion matrix method was implemented to see the prediction error rate in the testing data (Ruuska et al., 2018). The accuracy of each CNN model is the main parameter that determines model performance.

## RESULTS AND DISCUSSIONS

All total 24 CNN models provided accuracy validation ranging from 61.52% to 89.65%, depending on the number of layers and structure. Additionally, the selection of optimization techniques also affected the prediction accuracy. Table 1 shows the accuracy result of validation data obtained from the learning process using deep learning architecture. The sensitivity analysis was done by tuning the optimization technique and learning rate in each CNN model, i.e., SqueezeNet, GoogLeNet, ResNet-50, and AlexNet. Not all CNN models produced high accuracy. The highest accuracy value obtained by each model is presented in Table 1. Five CNN models producing highest accuracy were generated by GoogLeNet (optimizer = Adam; learning rate = 0.0001), ResNet-50 (optimizer = RMSProp; learning rate = 0.0001), GoogLeNet (optimizer = Adam; learning rate = 0.00005), ResNet-50 (optimizer = Adam; learning rate = 0.0001), and GoogLeNet (optimizer = RMSProp; learning rate = 0.0001) with accuracy value of validation data respectively 89.65%, 89.26%, 88.67%,

Table 1  
*Result and parameter used in the deep learning method*

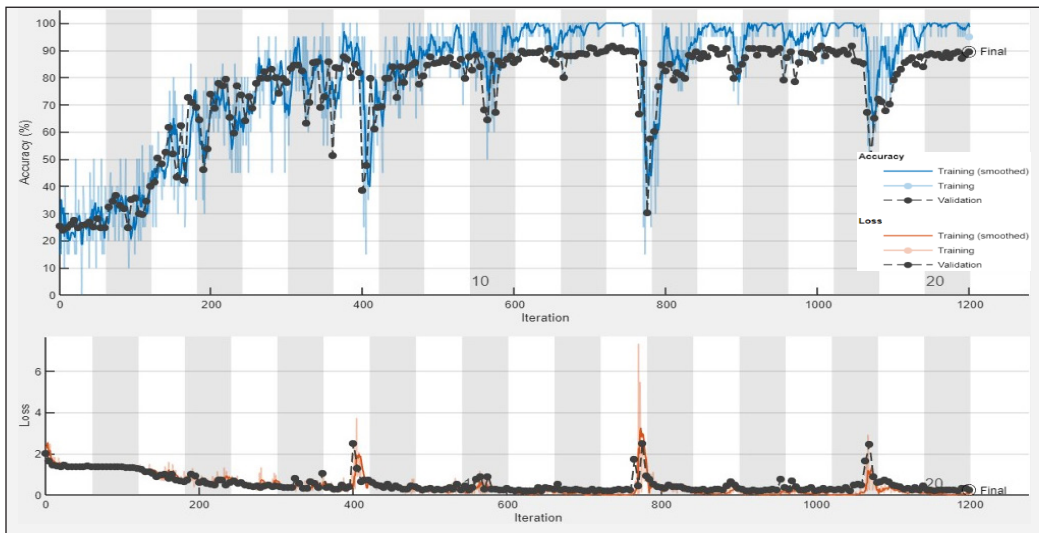
Architecture	Optimizer	Learning Rate	Accuracy (%)	Training Time (minutes)
SqueezeNet	SGDm	0.00005	77.34	118
	Adam	0.00005	75.59	118
	RMSProp	0.00005	73.24	119
	SGDm	0.0001	72.27	118
	Adam	0.0001	80.47	118
	RMSProp	0.0001	77.54	119
GoogleNet	SGDm	0.00005	64.41	241
	<b>Adam</b>	<b>0.00005</b>	<b>88.67</b>	<b>251</b>
	RMSProp	0.00005	78.71	245
	SGDm	0.0001	82.42	242
	<b>Adam</b>	<b>0.0001</b>	<b>89.65</b>	<b>254</b>
ResNet50	<b>RMSProp</b>	<b>0.0001</b>	<b>85.94</b>	<b>268</b>
	SGDm	0.00005	80.66	587
	Adam	0.00005	81.64	605
	RMSProp	0.00005	81.64	641
	SGDm	0.0001	76.95	601
AlexNet	<b>Adam</b>	<b>0.0001</b>	<b>86.52</b>	<b>642</b>
	<b>RMSProp</b>	<b>0.0001</b>	<b>89.26</b>	<b>653</b>
	SGDm	0.00005	66.6	117
	Adam	0.00005	72.85	115
	RMSProp	0.00005	61.52	127
AlexNet	SGDm	0.0001	77.73	108
	Adam	0.0001	69.53	117
	RMSProp	0.0001	27.93	141



86.52%, and 85.94%. In a single layer of GoogLeNet, multiple types of feature extractors were present. It indirectly helps the network perform better, as the network at training itself has many options to choose from when solving the task. It can either choose to convolve the input or pool it directly.

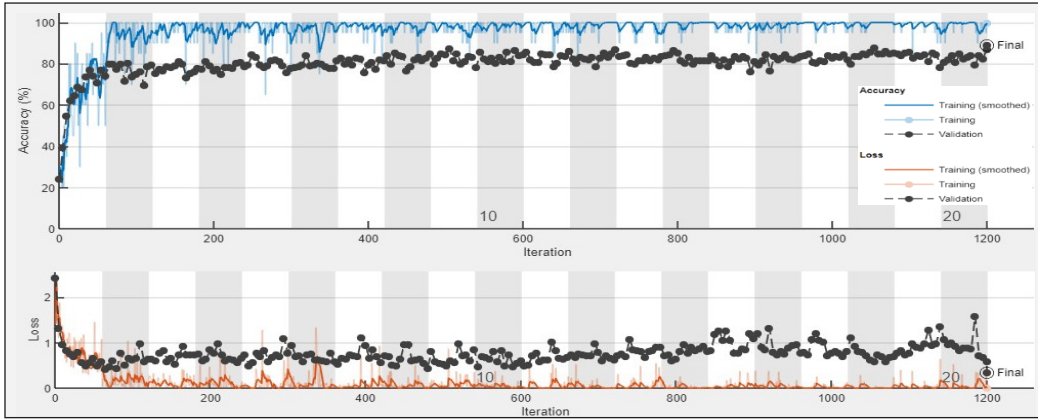
The GoogLeNet architecture contains multiple inception modules as most of the topmost layers have their output layer. It helps the model converge faster compared to other networks. Thus, it is in line with research conducted by Huitron et al. (2021), which detected the disease in the tomato leaves using CNN which the pre-trained model GoogLeNet and ResNet had more superior performance than other pre-trained CNN. However, since the classification of purity level only relies on visual appearance (brownish-black color, morphology, and texture) and the appearance between two mixtures (Arabica Luwak and Arabica regular) is similar, classifying all samples has only reached 89.65% accuracy. However, this accuracy was acceptable and defined as good. The performance of the five best CNN models can be seen in Figure 4. Figure 4 illustrates a comparison between classification accuracy and loss and learning iteration numbers. Based on the performance results, the continuous performance improvement was seen by the increase of iteration.

The CNN performance graph also showed that the accuracy increased with the increase of iteration. The loss graph also reduced with the increase of iteration and gradually became convergent nearing 0. Thus, all CNN models nearly have the same pattern. The performance improvement runs very fast at the initial epoch, i.e., epoch 1 to epoch 10. Then, the accuracy value was increased, followed by minor improvements in training and validation data performance. In Figure 4(a), there were fluctuations in the accuracy and

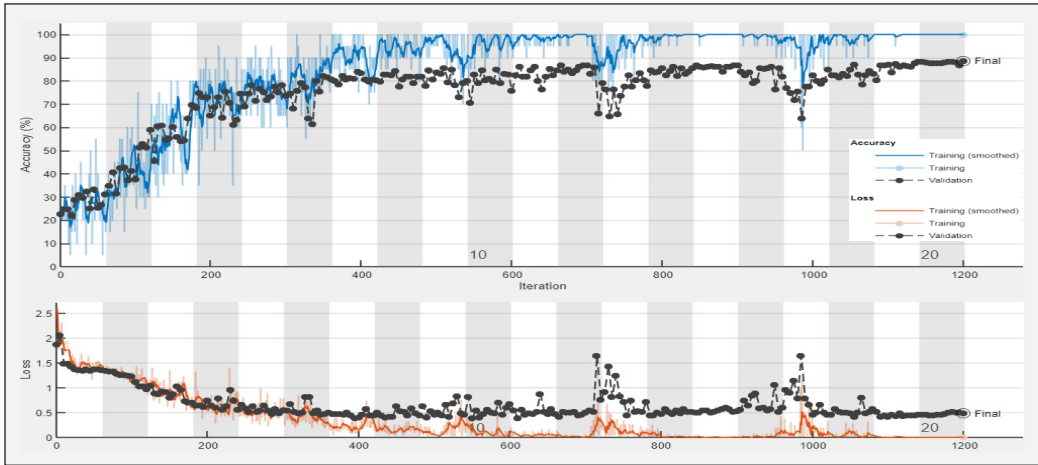


(a)

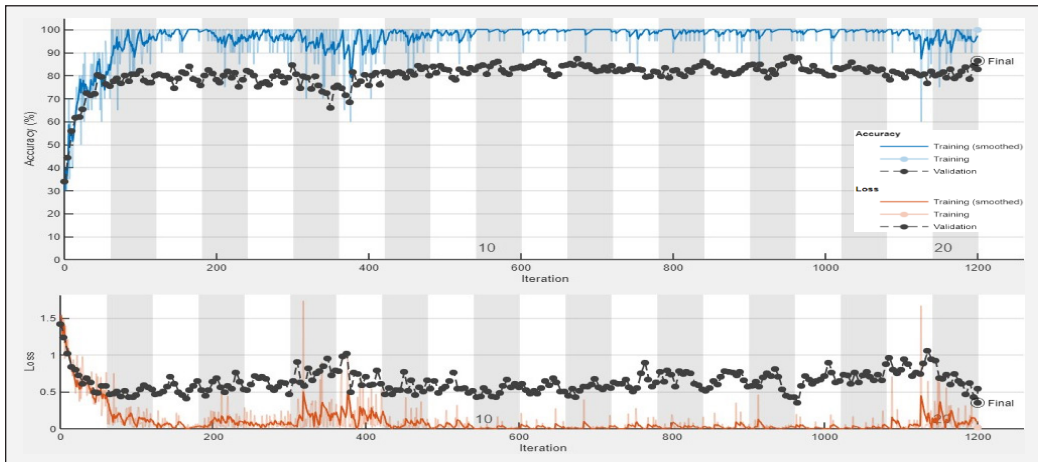
Figure 4. Accuracy and loss versus the number of iterations: (a) GoogLeNet (optimizer = Adam; learning rate = 0.0001)



(b)



(c)



(d)

Figure 4 (continue). Accuracy and loss versus the number of iterations: (b) ResNet-50 (optimizer = RMSProp; learning rate = 0.0001); (c) GoogLeNet (optimizer = Adam; learning rate = 0.00005); (d) ResNet-50 (optimizer = Adam; learning rate = 0.0001)

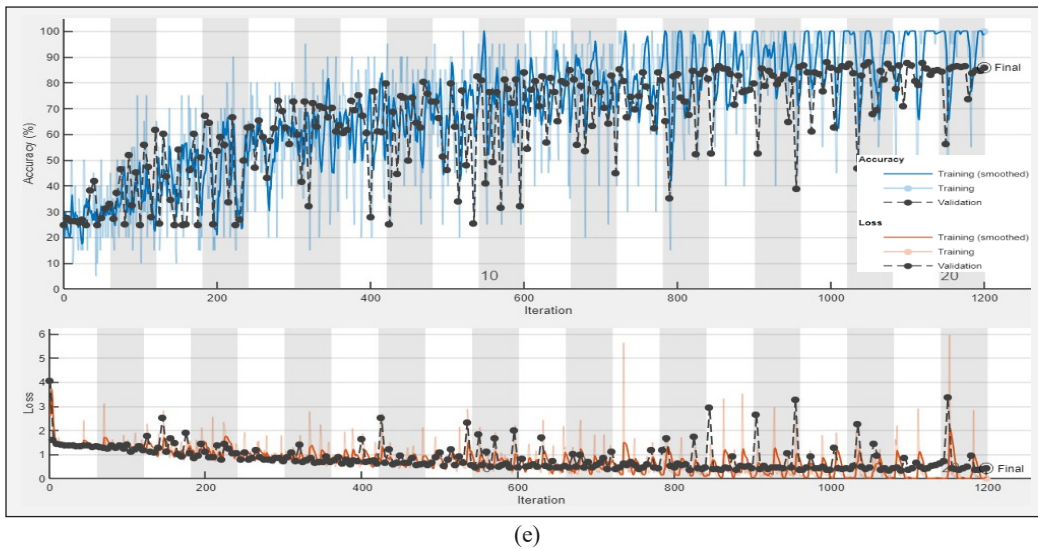


Figure 4 (continue). Accuracy and loss versus the number of iterations: (e) GoogLeNet (optimizer = RMSProp; learning rate = 0.0001)

losses which indicated that some portion of the example was classified randomly, which produced fluctuations. Updating network weights during the training process and noisy data also affected the occurrence of fluctuations. However, validation loss fluctuations during training are natural for most machine learning algorithms as long as the training pattern generally increases steadily during iterations (Takase, 2021). The pattern accuracy and loss graph obtained by CNN in the research was in line with research by Azimi et al. (2021), in which the accuracy value pattern was significantly increased at the initial epoch, but the loss value pattern exhibited the reverse and would be convergent nearing 0. Overall results in Figure 4 show that several parameters such as optimization technique and learning rate also affect the validation accuracy. It was clear that the learning rate value of 0.0001 creates higher accuracy (79.65%) than the learning rate of 0.00005 (75.23%), which was in line with Thenmozhi and Reddy (2019). The study revealed that the 0.0001 learning rate is better than the other (0.00005, 0.0005, and 0.001).

Figure 5 illustrates the confusion matrix result using testing data in five best CNN models namely GoogLeNet (optimizer = Adam, learning rate = 0.00005); GoogLeNet (optimizer = Adam, learning rate = 0.0001); GoogLeNet (optimizer = RMSProp, learning rate = 0.0001); ResNet-50 (optimizer = RMSProp, learning rate = 0.0001); and ResNet-50 (optimizer = Adam, learning rate = 0.0001). Furthermore, the individual classification rate data for every category was described by comparing the predicted value (abscissa) with true value (ordinate). Distribution of value in the confusion matrix in five best CNN models showed that purity mixture of both high (75 to 100%) and very low (0 to 25%) purity performed higher accuracy compared to other two categories which accounted



Figure 5. Confusion matrix of testing data: (a) GoogLeNet (optimizer = Adam, learning rate = 0.00005); (b) GoogLeNet (optimizer = Adam, learning rate = 0.0001); (c) GoogLeNet (optimizer = RMSProp, learning rate = 0.0001); (d) ResNet-50 (optimizer = RMSProp, learning rate = 0.0001); (e) ResNet-50 (optimizer = Adam, learning rate = 0.0001)

for 99.00% and 92.80%, respectively. In fact, in the three CNN models, GoogLeNet (optimizer= Adam; learning rate = 0.00005), ResNet-50 (optimizer = RMSProp; learning rate = 0.0001), and ResNet-50 (optimizer = Adam; learning rate = 0.0001), gave better accuracy to classify high purity reaching 100% accuracy. Therefore, this proved that CNN model could classify accurately (up to 100% accuracy) between Luwak coffee green beans with high purity (75 to 100%) and other purity categories (<75%). Low purity (25 to 50%) provided the lowest classifying accuracy on the testing process, accounting for 65.80%. Meanwhile, medium purity (50 to 75%) provided 72% accuracy. If it is based on the testing data accuracy using a confusion matrix, it can be said that the highest accuracy was reached by the CNN model using ResNet-50 (optimizer = RMSProp, learning rate = 0.0001) with the average accuracy value of testing data that is 85.00%, followed by GoogLeNet (optimizer = RMSProp, learning rate = 0.0001), GoogLeNet (optimizer = Adam, learning rate = 0.0001), GoogLeNet (optimizer = Adam, learning rate = 0.00005), and ResNet-50 (optimizer = Adam, learning rate = 0.0001) with the average accuracy value 83.25%, 82.25%, 82.00%, and 79.50%, respectively. By the highest average of testing, data accuracy reached 85.00%. Thus, it can be concluded that the CNN model produced in the research can effectively classify the purity level of Luwak coffee green beans.

## CONCLUSIONS

This research used four pre-trained CNN models (SqueezeNet, GoogLeNet, ResNet-50, and AlexNet) to classify four purity mixtures consisting of very low (0-25%), low (25-50%), medium (50-75%), and high (75-100%). Based on the training and validation result, the model exhibited an accuracy ranging from 61.52% to 89.65%. The highest accuracy value, 89.65%, was obtained using GoogLeNet pre-trained with optimizer type = Adam and learning rate value = 0.0001. Other than that, according to the testing result, the model provided the highest accuracy, 85.00%, using ResNet-50 with optimizer type = RMSProp and learning rate = 0.0001. Therefore, the CNN model generated from the research was a high potential for field-trial to classify Luwak coffee green beans purity. Moreover, since it was feasible as a rapid, real-time, and accurate method, this can be a basis for further classification study for other crops and agricultural products.

## ACKNOWLEDGEMENTS

The authors wish to acknowledge support from the Laboratory of Mechatronics and Agro-industrial Machineries, Department of Agricultural Engineering, Faculty of Agricultural Technology, University of Brawijaya, for the assistance given during the research. This study was funded by the Research Grant Program, University of Brawijaya, the Ministry of Research, Technology, and Higher Education of the Republic of Indonesia.

## REFERENCES

- Amirvaresi, A., Nikounezhad, N., Amirahmadi, M., Daraei, B., & Parastar, H. (2021). Comparison of near-infrared (NIR) and mid-infrared (MIR) spectroscopy based on chemometrics for saffron authentication and adulteration detection. *Food Chemistry*, *344*, Article 128647. <https://doi.org/10.1016/j.foodchem.2020.128647>
- Anami, B. S., Malvade, N. N., & Palaiah, S. (2019). Automated recognition and classification of adulteration levels from bulk paddy grain samples. *Information Processing in Agriculture*, *6*(1), 47-60. <https://doi.org/10.1016/j.inpa.2018.09.001>
- Azimi, S., Kaur, T., & Gandhi, T. K. (2021). A deep learning approach to measure stress level in plants due to Nitrogen deficiency. *Measurement*, *173*, Article 108650. <https://doi.org/10.1016/j.measurement.2020.108650>
- Bragagnolo, L., Rezende, L. R., da Silva, R. V., & Grzybowski, J. M. V. (2021). Convolutional neural networks applied to semantic segmentation of landslide scars. *CATENA*, *201*, Article 105189. <https://doi.org/10.1016/j.catena.2021.105189>
- Cancilla, J. C., Izquierdo, M., Semenikhina, A., Flores, E. G., Mejias, M. L., & Torrecilla, J. S. (2020). Exposing adulteration of Muscatel wines and assessing its distribution chain with fluorescence via intelligent and chaotic networks. *Food Control*, *118*, Article 107428. <https://doi.org/10.1016/j.foodcont.2020.107428>
- Cardoso, V. G. K., & Poppi, R. J. (2021). Cleaner and faster method to detect adulteration in cassava starch using Raman spectroscopy and one-class support vector machine. *Food Control*, *125*, Article 107917. <https://doi.org/10.1016/j.foodcont.2021.107917>
- Cebi, N., Yilmaz, M. T., & Sagdic, O. (2017). A rapid ATR-FTIR spectroscopic method for detection of sibutramine adulteration in tea and coffee based on hierarchical cluster and principal component analyses. *Food Chemistry*, *229*, 517-526. <https://doi.org/10.1016/j.foodchem.2017.02.072>
- Combes, M. C., Joet, T., & Lashermes, P. (2018). Development of a rapid and efficient DNA-based method to detect and quantify adulterations in coffee (Arabica versus Robusta). *Food Control*, *88*, 198-206. <https://doi.org/10.1016/j.foodcont.2018.01.014>
- Daniel, D., Lopes, F. S., Santos, V. B., & Lago, C. L. (2018). Detection of coffee adulteration with soybean and corn by capillary electrophoresis-tandem mass spectrometry. *Food Chemistry*, *243*, 305-310. <https://doi.org/10.1016/j.foodchem.2017.09.140>
- Eltrass, A. S., Tayel, M. B., & Ammar, A. I. (2021). A new automated CNN deep learning approach for identification of ECG congestive heart failure and arrhythmia using constant-Q non-stationary Gabor transform. *Biomedical Signal Processing and Control*, *65*, Article 102326. <https://doi.org/10.1016/j.bspc.2020.102326>
- Hendrawan, Y., Damayanti, R., Al-Riza, D. F., & Hermanto, B. (2021). Classification of water stress in cultured Sunagoke moss using deep learning. *TELKOMNIKA*, *19*(5), 1594-1604. <http://dx.doi.org/10.12928/telkomnika.v19i5.20063>
- Hendrawan, Y., Widyaningtyas, S., & Sucipto. (2019). Computer vision for purity, phenol, and pH detection of Luwak Coffee green bean. *TELKOMNIKA*, *17*(6), 3073-3085. <http://dx.doi.org/10.12928/telkomnika.v17i6.12689>

- Huang, X., Li, Z., Zou, X., Shi, J., Tahir, H. E., Xu, Y., Zhai, X., & Hu, X. (2019). A low cost smart system to analyze different types of edible Bird's nest adulteration based on colorimetric sensor array. *Journal of Food and Drug Analysis*, 27(4), 876-886. <https://doi.org/10.1016/j.jfda.2019.06.004>
- Huitron, V. G., Borges, J. A. L., Mata, A E. R., Sosa, L. E. A., Pereda, B. R., & Rodriguez, H. (2021). Disease detection in tomato leaves via CNN with lightweight architectures implemented in Raspberry Pi 4. *Computers and Electronics in Agriculture*, 181, Article 105951. <https://doi.org/10.1016/j.compag.2020.105951>
- Iymen, G., Tanriver, G., Hayirlioglu, Y. Z., & Ergen, O. (2020). Artificial intelligence-based identification of butter variations as a model study for detecting food adulteration. *Innovative Food Science & Emerging Technologies*, 66, Article 102527. <https://doi.org/10.1016/j.ifset.2020.102527>
- Izquierdo, M., Mejias, M. L., Flores, E. G., Cancilla, J. C., Perez, M., & Torrecilla, J. S. (2020a). Convolutional decoding of thermographic images to locate and quantify honey adulterations. *Talanta*, 209, Article 120500. <https://doi.org/10.1016/j.talanta.2019.120500>
- Izquierdo, M., Mejias, M. L., Flores, E. G., Cancilla, J. C., Santos, R. A., & Torrecilla, J. S. (2020b). Deep thermal imaging to compute the adulteration state of extra virgin olive oil. *Computers and Electronics in Agriculture*, 171, Article 105290. <https://doi.org/10.1016/j.compag.2020.105290>
- Jiang, B., He, J., Yang, S., Fu, H., Li, T., Song, H., & He, D. (2019). Fusion of machine vision technology and AlexNet-CNNs deep learning network for the detection of postharvest apple pesticide residues. *Artificial Intelligence in Agriculture*, 1, 1-8. <https://doi.org/10.1016/j.aiaa.2019.02.001>
- Jumhawan, U., Putri, S. P., Yusianto, Bamba, T., & Fukusaki, E. (2015). Application of gas chromatography/flame ionization detector-based metabolite fingerprinting for authentication of Asian palm civet coffee (Kopi Luwak). *Journal of Bioscience and Bioengineering*, 120(5), 555-561. <https://doi.org/10.1016/j.jbiosc.2015.03.005>
- Jumhawan, U., Putri, S. P., Yusianto, Bamba, T., & Fukusaki, E. (2016). Quantification of coffee blends for authentication of Asian palm civet coffee (Kopi Luwak) via metabolomics: A proof of concept. *Journal of Bioscience and Bioengineering*, 122(1), 79-84. <https://doi.org/10.1016/j.jbiosc.2015.12.008>
- Jumhawan, U., Putri, S. P., Yusianto, Marwani, E., Bamba, T., & Fukusaki, E. (2013). Selection of discriminant markers for authentication of Asian palm civet coffee (Kopi Luwak): A metabolomics approach. *Journal of Agricultural and Food Chemistry*, 61(3), 7994-8001. <https://doi.org/10.1021/jf401819s>
- Kiani, S., Minaei, S., & Varnamkhasti, M. G. (2017). Integration of computer vision and electronic nose as non-destructive systems for saffron adulteration detection. *Computers and Electronics in Agriculture*, 141, 46-53. <https://doi.org/10.1016/j.compag.2017.06.018>
- Li, Q., Zeng, J., Lin, J., Zhang, J., Yao, L., Wang, S., Du, J., & Wu, Z. (2021). Mid-infrared spectra feature extraction and visualization by convolutional neural network for sugar adulteration identification of honey and real-world application. *LWT*, 140, Article 110856. <https://doi.org/10.1016/j.lwt.2021.110856>
- Lim, D. K., Long, N. P., Mo, C., Dong, Z., Cui, L., Kim, G., & Kwon, S. W. (2017). Combination of mass spectrometry-based targeted lipidomics and supervised machine learning algorithms in detecting adulterated admixtures of white rice. *Food Research International*, 100(1), 814-821. <https://doi.org/10.1016/j.foodres.2017.08.006>

- Lin, G., & Shen, W. (2018). Research on convolutional neural network based on improved Relu piecewise activation function. *Procedia Computer Science*, 131, 977-984. <https://doi.org/10.1016/j.procs.2018.04.239>
- Lin, L., Xu, M., Ma, L., Zeng, J., Zhang, F., Qiao, Y., & Wu, Z. (2020). A rapid analysis method of safflower (*Carthamus tinctorius* L.) using combination of computer vision and near-infrared. *Spectrochimica Acta Part A: Molecular and Biomolecular Spectroscopy*, 236, Article 118360. <https://doi.org/10.1016/j.saa.2020.118360>
- Liu, Y., Yao, L., Xia, Z., Gao, Y., & Gong, Z. (2021). Geographical discrimination and adulteration analysis for edible oils using two-dimensional correlation spectroscopy and convolutional neural networks (CNNs). *Spectrochimica Acta Part A: Molecular and Biomolecular Spectroscopy*, 246, Article 118973. <https://doi.org/10.1016/j.saa.2020.118973>
- Lopetcharat, K., Kulapichitr, F., Suppavorasatit, I., Chodjarusawad, T., Phatthara-aneksin, A., Pratontep, S., & Borompichaichartkul, C. (2016). Relationship between overall difference decision and electronic tongue: Discrimination of civet coffee. *Journal of Food Engineering*, 180, 60-68. <https://doi.org/10.1016/j.jfoodeng.2016.02.011>
- Lopez, S. P., Calabuig, A. M. P., Cancilla, J. C., Lozano, M. A., Rodrigo, C., Mena, M. L., & Torrecilla, J. S. (2021). Deep transfer learning to verify quality and safety of ground coffee. *Food Control*, 122, Article 107801. <https://doi.org/10.1016/j.foodcont.2020.107801>
- Manninen, H., Ramlal, C. J., Singh, A., Rocke, S., Kilter, J., & Landsberg, M. (2021). Toward automatic condition assessment of high-voltage transmission infrastructure using deep learning techniques. *International Journal of Electrical Power & Energy Systems*, 128, Article 106726. <https://doi.org/10.1016/j.ijepes.2020.106726>
- Marcone, M. F. (2004). Composition and properties of Indonesian palm civet coffee (Kopi Luwak) and Ethiopian civet coffee. *Food Research International*, 37(9), 901-912. <https://doi.org/10.1016/j.foodres.2004.05.008>
- Medus, L. D., Saban, M., Villora, J. V. F., mompean, M. B., & Munoz, A. R. (2021). Hyperspectral image classification using CNN: Application to industrial food packaging. *Food Control*, 125, Article 107962. <https://doi.org/10.1016/j.foodcont.2021.107962>
- Mkonyi, L., Rubanga, D., Richard, M., Zekeya, N., Sawahiko, S., Maiseli, B., & Machuve, D. (2020). Early identification of Tuta absoluta in tomato plants using deep learning. *Scientific African*, 10, Article e00590. <https://doi.org/10.1016/j.sciaf.2020.e00590>
- Muzaifa, M., Hasni, D., & Syarifudin. (2019). What is Kopi Luwak? A literature review on production, quality and problems. *IOP Conf. Series: Earth and Environmental Science*, 365, Article 012041. doi:10.1088/1755-1315/365/1/012041
- Nayak, S. R., Nayak, D. R., Sinha, U., Arora, V., & Pachori, R. B. (2021). Application of deep learning techniques for detection of COVID-19 cases using chest X-ray images: A comprehensive study. *Biomedical Signal Processing and Control*, 64, Article 102365. <https://doi.org/10.1016/j.bspc.2020.102365>
- Nunez, N., Saurina, J., & Nunez, O. (2021). Non-targeted HPLC-FLD fingerprinting for the detection and quantitation of adulterated coffee samples by chemometrics. *Food Control*, 124, Article 107912. <https://doi.org/10.1016/j.foodcont.2021.107912>



- Ongo, E., Falasconi, M., Sberveglieri, G., Antonelli, A., Montevecchi, G., Scerveglieri, V., Concina, I., & Sevilla, F. (2012). Chemometric discrimination of Philippine civet coffee using electronic nose and gas chromatography mass spectrometry. *Procedia Engineering*, *47*, 977-980. <https://doi.org/10.1016/j.proeng.2012.09.310>
- Pauli, E. D., Barbieri, F., Garcia, P. S., Madeira, T. B., Junior, V. R. A., Scarminio, I. S., Camara, C. A. P., & Nixdorf, S. L. (2014). Detection of ground roasted coffee adulteration with roasted soybean and wheat. *Food Research International*. *61*, 112-119. <https://doi.org/10.1016/j.foodres.2014.02.032>
- Raikar, M. M., Meena, S. M., Kuchanur, C., Girraddi, S., & Benagi, P. (2020). Classification and grading of okra-ladies finger using deep learning. *Procedia Computer Science*, *171*, 2380-2389. <https://doi.org/10.1016/j.procs.2020.04.258>
- Reile, C. G., Rodriguez, M. S., Fernandes, D. D. S., Gomes, A. A., Diniz, P. H. G. D., & Anibal, C. V. D. (2020). Qualitative and quantitative analysis based on digital images to determine the adulteration of ketchup samples with Sudan I dye. *Food Chemistry*, *328*, Article 127101. <https://doi.org/10.1016/j.foodchem.2020.127101>
- Ruuska, S., Hamalainen, W., Kajava, S., Mughal, M., Matilainen, P., & Mononen, J. (2018). Evaluation of the confusion matrix method in the validation of an automated system for measuring feeding behaviour of cattle. *Behavioral Processes*, *148*, 56-62. <https://doi.org/10.1016/j.beproc.2018.01.004>
- Sezer, B., Apaydin, H., Bilge, G., & Boyaci, I. H. (2018). Coffee arabica adulteration: Detection of wheat, corn and chickpea. *Food Chemistry*, *264*, 142-148. <https://doi.org/10.1016/j.foodchem.2018.05.037>
- Silva, A. F. S., & Rocha, F. R. P. (2020). A novel approach to detect milk adulteration based on the determination of protein content by smartphone-based digital image colorimetry. *Food Control*, *115*, Article 107299. <https://doi.org/10.1016/j.foodcont.2020.107299>
- Simon, P., & Uma, V. (2020). Deep learning based feature extraction for texture classification. *Procedia Computer Science*, *171*, 1680-1687. <https://doi.org/10.1016/j.procs.2020.04.180>
- Skowron, M. J., Franskowski, R., & Grzeskowiak, A.Z. (2020). Comparison of methylxantines, trigonelline, nicotinic acid and nicotinamide contents in brews of green and processed Arabica and Robusta coffee beans - Influence of steaming, decaffeination and roasting processes on coffee beans. *LWT*, *125*, Article 109344. <https://doi.org/10.1016/j.lwt.2020.109344>
- Song, W., Yun, Y. H., Wang, H., Hou, Z., & Wang, Z. (2021). Smartphone detection of minced beef adulteration. *Microchemical Journal*, *164*, Article 106088. <https://doi.org/10.1016/j.microc.2021.106088>
- Suhandy, D., & Yulia, M. (2017). The use of partial least square regression and spectral data in UV-visible region for quantification of adulteration in Indonesian palm civet coffee. *International Journal of Food Science*, *2017*, Article 6274178. <https://doi.org/10.1155/2017/6274178>
- Takase, T. (2021). Dynamic batch size tuning based on stopping criterion for neural network training. *Neurocomputing*, *429*, 1-11. <https://doi.org/10.1016/j.neucom.2020.11.054>
- Thenmozhi, K., & Redy, U. S. (2019). Crop pest classification based on deep convolutional neural network and transfer learning. *Computers and Electronics in Agriculture*, *164*, Article 104906. <https://doi.org/10.1016/j.compag.2019.104906>

- Tian, C., Xu, Y., & Zuo, W. (2020). Image denoising using deep CNN with batch renormalization. *Neural Networks*, 121, 461-473. <https://doi.org/10.1016/j.neunet.2019.08.022>
- Ucar, F., & Korkmaz, D. (2020). COVIDiagnosis-Net: Deep Bayes-SqueezeNet based diagnosis of the coronavirus disease 2019 (COVID-19) from X-ray images. *Medical Hypotheses*, 140, Article 109761. <https://doi.org/10.1016/j.mehy.2020.109761>
- Wojcik, S., & Jakubowska, M. (2021). Deep neural networks in profiling of apple juice adulteration based on voltammetric signal of the iridium quadruple-disk electrode. *Chemometrics and Intelligent Laboratory Systems*, 209, Article 104246. <https://doi.org/10.1016/j.chemolab.2021.104246>
- Yu, H., Yang, L. T., Zhang, Q., Armstrong, D., & Deen, M. J. (2021). Convolutional neural networks for medical image analysis: State-of-the-art, comparisons, improvement and perspectives. *Neurocomputing*, 444, 92-110. <https://doi.org/10.1016/j.neucom.2020.04.157>
- Yulia, M., & Suhandy, D. (2017). Indonesian palm civet coffee discrimination using UV-visible spectroscopy and several chemometrics methods. *Journal of Physics: Conference Series*, 835, Article 012010. <https://doi.org/10.1088/1742-6596/835/1/012010>

*Review article*

## Data Acquisition and Data Processing using Electroencephalogram in Neuromarketing: A Review

Annis Shafika Amran<sup>1</sup>, Sharifah Aida Sheikh Ibrahim<sup>2,3</sup>, Nurul Hashimah Ahamed Hassain Malim<sup>2,3\*</sup>, Nurfaten Hamzah<sup>1,3</sup>, Putra Sumari<sup>2,3</sup>, Syaheerah Lebai Lutfi<sup>2,3</sup> and Jafri Malin Abdullah<sup>1,2</sup>

<sup>1</sup>Department of Neurosciences, School of Medical Sciences, Universiti Sains Malaysia, Kubang Kerian, 15200 USM, Kota Bharu, Kelantan, Malaysia

<sup>2</sup>School of Computer Sciences, Universiti Sains Malaysia, 11800 USM, Pulau Pinang, Malaysia

<sup>3</sup>Brain and Behavior Cluster, School of Medical Sciences, Universiti Sains Malaysia, Kubang Kerian, 15200 USM, Kota Bharu, Kelantan, Malaysia

### ABSTRACT

Electroencephalogram (EEG) is a neurotechnology used to measure brain activity via brain impulses. Throughout the years, EEG has contributed tremendously to data-driven research models (e.g., Generalised Linear Models, Bayesian Generative Models, and Latent Space Models) in Neuroscience Technology and Neuroinformatic. Due to versatility, portability, cost feasibility, and non-invasiveness. It contributed to various Neuroscientific data that led to advancement in medical, education, management, and even the marketing field. In the past years, the extensive uses of EEG have been inclined towards medical healthcare studies such as in disease detection and as an intervention in mental disorders, but not fully explored for uses in neuromarketing. Hence, this study construes the data acquisition technique in neuroscience studies using electroencephalogram and outlines the trend of

revolution of this technique in aspects of its technology and databases by focusing on neuromarketing uses.

*Keywords:* Consumer sciences, EEG advancement, and revolution, EEG technology, future VR-EEG integration, neural signal processing, neuromarketing

### ARTICLE INFO

*Article history:*

Received: 01 April 2021

Accepted: 15 September 2021

Published: 06 December 2021

DOI: <https://doi.org/10.47836/pjst.30.1.02>

*E-mail addresses:*

[annisamran@gmail.com](mailto:annisamran@gmail.com) (Annis Shafika Amran)

[aidaibrahim@usm.my](mailto:aidaibrahim@usm.my) (Sharifah Aida Sheikh Ibrahim)

[nurulhashimah@usm.my](mailto:nurulhashimah@usm.my) (Nurul Hashimah Ahamed Hassain Malim)

[nurfaten@usm.my](mailto:nurfaten@usm.my) (Nurfaten Hamzah)

[putras@usm.my](mailto:putras@usm.my) (Putra Sumari)

[syaheerah@usm.my](mailto:syaheerah@usm.my) (Syaheerah Lebai Lutfi)

[jafrialin@usm.my](mailto:jafrialin@usm.my) (Jafri Malin Abdullah)

\* Corresponding author

### INTRODUCTION

Electroencephalogram (EEG) is a widely used neurotechnology that detects electrical impulses in the brain, passed through

the neurons and axons of the brain to measure brain activity (Casson et al., 2018). The impulses arise from the interactions of one neuron to another, with potassium and sodium ions passing through the synaptic clefts. Electrodes of the EEG are attached to the head to capture the brain impulses, which are later amplified, and potential differences are calculated to represent the brain activity. EEG on Human was initially introduced by Hans Berger, a German Psychiatrist which in the year 1929. This technique follows the principle of an Electrocardiogram (ECG or EKG), which detects the electrical signal triggered by the heartbeats (Tudor et al., 2005). Berger first performed his study of brainwaves using Novocaine injection and electrodes in the periosteum in a 17-year-old boy undergoing neurosurgery by Dr. Nikolai Guleke (Kaplan, 2011). Using this event as a steppingstone, he began developing the non-invasive method used and revolutionised today (Coenen & Zayachkivska, 2013).

### **EEG in Clinical Research and Studies**

According to Deolindo and colleagues, the ability of EEG to detect and measure neuronal oscillations which is also known as magnetic fields, enables access to information of functional and effective connectivity of neurons in the brain (Deolindo et al., 2020). It can also provide deeper understanding on the process of specific information coding, state of brain attention, and providing evidence on cognitive impairments. As EEG depends on event-related potentials (ERP) with time-locked- evoke stimulation or spectral analysis, aside spontaneous potentials, neurocognition in human being can be tested (Xue et al., 2010). Spontaneous EEG has been used as a measure for quite some time in evaluating seizures and epilepsy but rarely in cognitive neuroscience research. However, studies often incorporate ERP as a measuring tool up to this day. It heavily provides insight in the field of science, technology, medicine, education, and marketing. The study of neuroscience with the aid of EEG enables us to understand which region of the brain is responsible for which activity, enhancing understanding on neurodegenerative diseases as well as help in understanding human behaviours and discovery of the effective methods in learning, teaching, and marketing (Casson et al., 2018; Deolindo et al., 2020)The immense importance of the study of brain oscillation study in knowing neuropsychiatric disorders helps in determining disturbances between excitations and inhibitions of the networks between each neuron which can be seen in Schizophrenic and Autistic individuals as well as those with Attention Deficit Hyperactivity Disorder (ADHD)(Deolindo et al., 2020). Abnormal cortical oscillations were also depicted, especially in the attention and control areas of the brain. There is arising question on whether these oscillations can one day be a biomarker in clinical diagnostics or neuro disorders. Besides that, a future that can rely on EEG as an evidence provider in brain inattention is also being investigated and might become a breakthrough in Neuroscience studies.

EEG has been used for various neurology and cognitive science studies, especially in the medical field (Reyes et al., 2019). It includes:

- Monitoring anaesthesia process
- Seizure or epilepsy diagnostics
- Assessment of head injuries
- Brain tumour detection
- Detection of encephalitis
- Determining brain activity of coma patients
- Detection of Alzheimer's Disease onset
- Post-stroke assessments
- Sleep disorders assessment
- Confirmation of brain death
- Brain activity measurements in disordered neuro patients

Among these clinical uses, EEG maintains to execute its vital role in diagnostics of seizures and epileptic episodes with every abnormal brain activity in ictal and interictal conditions characterised by abrupt frequency changes in every measurement, enabling detection and determination of types of seizure which is important in order to determine the suitable medication as well as predicting prognosis (Siuly et al., 2016). The application of EEG in clinical studies has always been vast as it poses multiple advantages compared to other techniques, especially in health care. However, the usage of EEG in neuromarketing is also growing and evolving, especially with the emergence of wearable EEG that is more accessible and affordable to the masses where the study of neuromarketing via EEG can delve into the studies of emotions to study human preferences (Suhaimi et al., 2020).

### **EEG in Neuromarketing and Consumer Neuroscience**

The methodology in this study is composed of data collection and several pre-processing techniques, such as data cleaning, annotations, and eventually, automatic classification by three ML algorithms [Naïve Bayes (NB), Sequential Minimal Optimization (SMO) & Decision Tree (DT)]. The application of neuroscience methods allows unbiased and accurate marketing data to be obtained in response to self-reports which may carry intrinsic biases (Suhaimi et al., 2020). As an alternative, neuroscience allows a more refined understanding of the cognitive process that entrains consumerism and its underlying mechanisms, which cannot be obtained via surveys. Nevertheless, this field of study has not been used widely despite the increasing revolution of techniques and feasibilities, which proves to be beneficial to business owners and consumer brand managers. However, big brands such as Coca-Cola and Campbell's have started to venture into using functional imaging modalities such as functional magnetic resonance imaging (fMRI), which is commonly used, followed by electroencephalogram (EEG) and eye-tracking (Lin et al., 2018).

The application of EEG in marketing is usually focused on Event-Related-Potential (ERP) via time-locked activity or neural oscillations called spectral content, which captures brain responses when triggered by stimuli in the form of brainwave that rises from multiple sensory and cognitive processes, influencing the neural activities (Lin et al., 2018). Following its advantages, EEG proves to be gaining attention in the world of marketing research. Not only is it non-invasive and less costly, but it is also extremely beneficial in capturing objective as well as direct data to understand human cognitive processes and emotions (Suhaimi et al., 2020). ERP allows the identification of branding recognition based on categorisation processes. Whether positive or negative, emotions play an important role in influencing brand preferences and behaviour on good luxury purchases. Furthermore, with the study of EEG, the role of emotions in decision making can be further characterised. The relevant cognitive processes are involved in marketing-based EEG (Lin et al., 2018). These studies are: (i) Affect and emotions; (ii) Attitude and preferences, (iii) Decision making based on available information and (iv) Attention and memory.

### **Data Repositories for EEG Data**

There is an increasing need for Big Data Analytics, especially as we are approaching the Industrial Revolution 4.0 (IR4.0), where we move towards automation (Husain & Sinha, 2020). Hence, increasing the need for data for machine learning algorithms. Big Data is known as the complex dataset library, which provides a variety of datasets retrieved from research studies that can be used as a reference and even benchmarks for upcoming studies (Ibrahim et al., 2020). These libraries are often established with security and privacy, querying, data storing and analysis, as well as data transfers. For example, the data for EEG is mostly archived in databases where some of them are publicly accessible (Bhagchandani et al., 2018).

A database can be a private and closed source as well as open access known as open-source, which is free to be accessed and used. In the aspects of EEG itself, the data recordings of EEG represent various network-wide connections in the brain (Ibrahim et al., 2020). These sanctioned computational processes of the human brain allow extensive studies towards measuring brain functions and applying such knowledge to future innovations such as robotics, artificial intelligence, and automation in machinery. EEG data is stored in the form of “.eeg, .txt and.xls”. A reliable database is important, especially with the robust amount of pre-existing data to make established practices possible, such as determining the best biomarkers for various psychiatric diseases and neurological impairments (Bhagchandani et al., 2018). Unfortunately, a scarce well-known database is designated for EEG, unlike other modalities like fMRI and PET. However, there are a few open-source databases for data storing and sharing made by a group of individuals and institutions (Table 1).

Table 1  
EEG databases

Database	References
OpenNeuro Database	openneuro.org
Collaborative Research in Computational Neuroscience	crcns.org/
NeuroImaging Tools & Resources Collaboratory (NITRC)	nitrc.org
Physionet Database	physionet.org
UCI Machine Learning Repository	archive.ics.uci.edu
BNCI Horizon 2020	bnci-horizon-2020.eu
DEAP Dataset	www.eecs.qmul.ac.uk
European Epilepsy EEG Database	epilepsy-database.eu
Patient Repository of EEG Data	PRED+CT: predictsite.com
Github Sharing Open Access	hgithub.com/meagmohit/EEG-Datasets
MyNeuroDB	myneurodb.cs.usm.my
Temple University Hospital Repository	www.isip.piconepress.com/projects/tuh_eeeg/
IEEE DataPort	ieee-dataport.org
Zenodo EEG and audio dataset	zenodo.org

## Technical Aspects of EEG System

**Forms of EEG Data.** EEG data are often in the form of sinusoidal frequencies, which are repeated wave frequencies. These frequencies can be in rhythmic waves, consisting of stable constant frequencies, arrhythmic waves consisting of unstable, non-patterned waves and dysrhythmic waves that are rarely seen in normal samples (Husain & Sinha, 2020). These frequencies come from neurons which are vital for information transmission and reception of information through synapses. Hence, the electrical currents from information transmission in the neuron give rise to brainwaves of different frequencies that EEG can detect. Each brainwave is represented by different wavelengths, as shown in Figure 1.

Alpha and Beta waves are small sharp waves that are often observed when subjects are induced with interaction, which is the opposite of a relaxed state (Seal et al., 2020). Frequencies of brainwaves are divided into five distinct categories with one additional category for spike potential, as described in Table 2.

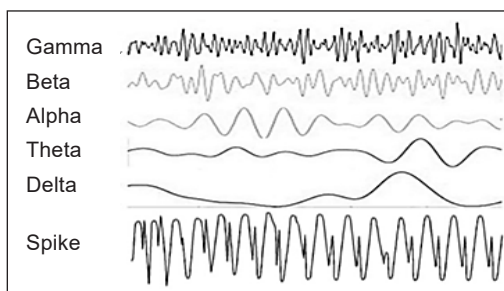


Figure 1. Patterns of brainwave (Reyes et al., 2019)

Table 2  
Waves and frequency (Reyes et al., 2019)

Waves	Frequency (Hz)
Gamma	>30
Beta	13-30
Alpha	8-13
Theta	5-8
Delta	0.5-4
Spike	3

These signals captured through electrodes on the scalp's surface are measured as voltage against actions. These signals are then classified between free-running, hybrid, and evoked components (Koudelková & Strmiska, 2018). Delta waves are low-frequency waves observed when deeply relaxed individuals, such as deep sleep or deep meditation. Technically, when the body is in deep rest. These brainwaves are vital for the rejuvenation of the body and brain (Seal et al., 2020).

Additionally, theta brainwave represents relaxation or sleep, much like delta waves. The difference is that these waves indicate that the individual is dreaming and focusing, which causes the brainwaves to be more energetic. As we begin to be awake, our brain begins to produce alpha waves. Activities that are considered restful such as praying, exhibits alpha waves instead of beta waves. On the other hand, Beta waves are a sharper and higher wave frequency exhibited most during attentive thinking and working. The brain is said to be fully awake and active. During rapid brain activity, gamma waves may occur. Gamma waves are often associated with the brain, which requires attention and perception of cognitive and behavioural processes (Koudelková & Strmiska, 2018; Seal et al., 2020).

### Data Acquisition in EEG System

Previously EEG applied its electrode channels in the deep intracerebral region and later revolutionised to extracranial measuring (Husain & Sinha, 2020). However, it is said that depth study allowed more focal details to be captured but with restrained spatial clarity causing the inability to study the brain function at extensive coverage (Bhagchandani et al., 2018). The versatility of the EEG system enables the employment of various numbers of electrodes to produce a robust neocortical dynamic function measurement with each scalp cap as it can provide an estimation of over mass tissue volume containing around 1 billion neurons (Mosslah et al., 2019).

Generally, the channel employed can be a single or multichannel and incorporate up to 256 channels following a 10 to 20 systems arrangement. A continuous EEG or cEEG uses about 9 to 16 electrodes arranged accordingly following the standardised international 10 to 20 system as shown in Figure 2. This system employs 21 electrodes placed on the scalp surface with nasion and inion as a reference point (Mosslah et al., 2019). Nasion point is situated above the nose, on a par level with the eyes, whereas the lump of bone at the skull's foot is

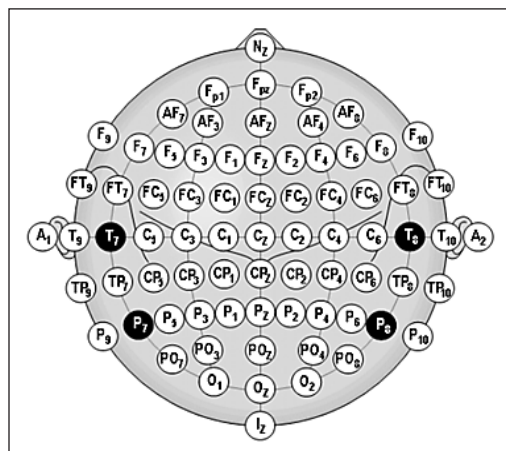


Figure 2. International 10-20 EEG system (Rojas et al., 2018)



between the midlines of the head. Additionally, the Queen Square System has also been applied to record the electrical potential of evoked potentials in clinical testing (Husain & Sinha, 2020).

The traditional EEG system was somewhat invasive and had to implement the penetrative electrodes through the brain, whereas the electrodes are now only applied on the scalp nowadays. Initially, EEG is less portable. Medical grade EEG devices have 16 or 32 channels on the headgear with amplifiers connected to these electrodes. Consumer-grade wearable EEG, on the other hand, only ranges from 2 channels to 14 channels. The two types of EEG follow the international 10-20 standard arrangement system (Mosslah et al., 2019). The decrease in electrodes is associated with a decrease in performance. However, studies show that the easy to set up wearable EEG device could outperform medical-grade EEG and detect artefacts. These artefacts such as muscle and eye blinking movements can be filtered out in pre-processing. Aside from that, the advancement of EEG allowed it to be wearable and wireless, allowing a correct measurement of imagined directional inputs and bodily movements of the user as there will be no constraints to movements. Examples of low to middle-cost EEG devices are Emotiv EPOC+, NeuroSky, MindWave, Ultracortex Mark IV EEG, Interaxon Muse, B-Alert X Series and ENT-Neuro EEG (Abujelala et al., 2016; Lin et al., 2018).

### Structure of EEG System

Generally, the basic steps used in EEG signal processing involves retrieving the raw data and continues with the conditioning and amplification of data, as stated in Figure 3.

The raw data must go through pre-processing steps. First, the signal goes through a measuring rig or amplifier that include a high-pass filter, and then an analogue filter is preceded for low-pass filtering. A high-pass filter, for example, can eliminate a direct current (DC) component or a slow fluctuation. In contrast, undesirable high-frequency components can be removed by “conditioning” the data with a low-pass filter. It is then followed by information acquisition, which involves converting analogue data to digital data to retrieve analysable data using pre-programmed software. Signal processing is then done by passing the data through a filter for data filtering to remove any unwanted noise and suppress certain parts of the signal. Feature extraction then paves the way for the characterisation of signals into distinct frequency classification. Feature selection is an optional step before classification involving many features to specify the

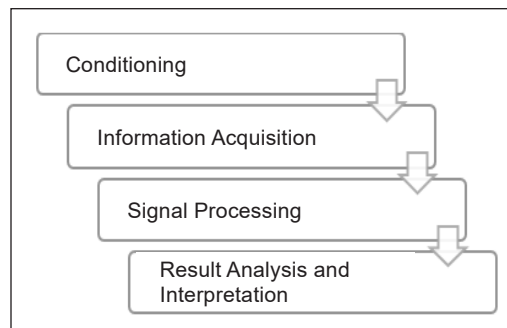


Figure 3. Basic processes in EEG signal processing

signals relevant to the study target. Lastly is frequency analysis and interpretation of results (Reyes et al., 2019).

EEG can process these data through several different programs. For example, there are linear techniques such as Independent Component Analysis (ICA), Eigenvector, Fast Fourier Transform (FFT), Autoregressive (AR), Wavelet Transform (TW), Wavelet Packet Decomposition (WPD), Principal Component Analysis (PCA). In contrast, the non-linear technique includes Fractal Dimension Analysis (FD), Hurst Exponent (H), Higher-Order Spectra (HOS) and Correlation Dimension (CD) (Reyes et al., 2019; Vaid et al., 2015). Additionally, past studies incorporated entropy and complexity measure, EMG signal integration in Brain-Computer-Interface EEG (BCI-EEG) system, computer-aided diagnostic (CAD) system, as well as Emotiv EPOC headphones system for imaginal colour image data (Maddirala & Shaik, 2018; Yu & Sim, 2016).

### **Benefits and Limitations**

Among other modalities, EEG is very much non-invasive, painless, and safe for use even in young children (Casson et al., 2018). Due to its cost-effectivity, it is suitable for usage in large scale studies despite the amount of repetition used. The recorder is often portable, does not involve large types of machinery and is only needed to be applied on the scalp of the head like a cap. However, previous EEG is found to be bulkier with longer cables. Therefore, EEG has been revolutionised into wearable and portable EEG (Lau-Zhu et al., 2019). As it is a simple system, setting up for usage is also non-complex. Due to its versatility, it can be adjusted to a different number of channels with different electrodes installed within the region of interest, enabling researchers to control coverage area and increase data accuracy (Read & Innis, 2017). EEG also has exceptional temporal resolution and supports real-time resolution to track events within the brain at milliseconds. Despite the notable benefits, EEG also presents challenging limitations: poor spatial resolution, inability to penetrate deeper beyond the cortex and subcortical regions from which the signals are derived, to observe activation patterns (Casson et al., 2018). It causes the need to integrate other neurotechnology to provide extensive functional data, such as integrating EEG with fMRI. Not only that, but it also has high noise, and possible data loss may occur during the recording of high-intensity activity (Beres, 2017). Such activities include running or jumping (Hill, 2019).

### **TRENDS IN EEG STUDIES**

The extensive use of EEG in neurological disease is majorly seen in epilepsy and seizures (Reyes et al., 2019). The brain undergoes paroxysm where electrical current changes abruptly, causing a spike in action potential due to excessive depolarization of neurons as shown in Figure 4, causing modified behaviours such as memory loss, convulsions, and continuous

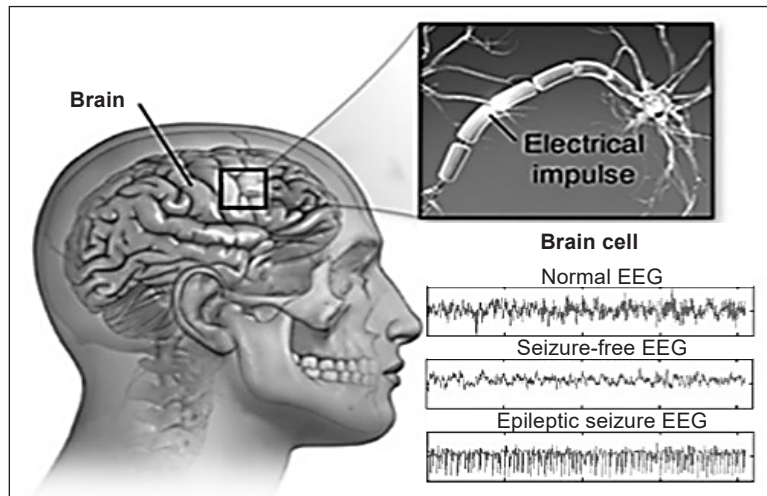


Figure 4. Electrical impulses in normal, epileptic and seizure brain (Siuly et al., 2016)

jerking due to muscle spasms, emotional disarray and may cause unconsciousness (Siuly et al., 2016). This occurrence results from an imbalance in neurotransmitters and brain wiring, causing incorrect signal transmission and distribution, disrupting hormonal release. In addressing this issue, interventions have been made using EEG, and with an increasing number of cases against time, improvements, and modification of EEG technology has continuously been made. Additionally, EEG also provides measures on the effectiveness of the intervention technique with the aid of pre-and post-treatment assessment (Reyes et al., 2019). Additionally, these advancements of technology have been providing means in products manufacturing that are useful and feasible to the community and allowing formulation and improvements of teaching and learning techniques in education.

### EEG Techniques in Clinical and Rehabilitation Use

Reyes et al. (2019) explained that the technological evolution of EEG started with the focus on the early detection of epilepsy. This proposition provided accuracy and sensitivity of data acquisition technique at 64 to 81% and 65 to 81%, respectively, followed by a study focused on focal epilepsy via neural networks of the brain, giving only 47.4% of data sensitivity. Finally, Da Silva produced a newer proposition on reviewing MEG-EEG signal processing technique comparison to demonstrate the epileptic characteristics of the human brain (Deolindo et al., 2020). Later, the technique of EEG signal classification using cross-correlation and spectral power density, resulting in 99.81 to 100% data accuracy and sensitivity. Within the same year, a meta-analysis study was proposed to predict the best periods of medication uptake and reduction of doses and stop intake from reducing medical expenses of epileptic patients. These studies provided evidence for the feasibility of EEG as an important prognostic tool in the clinical field.

## **EEG Techniques Application in Neuromarketing**

Interestingly, there are US-based neuromarketing companies that are constantly growing. These companies are AC Nielsen and Forbes Consulting Group. Nielsen has been outsourcing their services to other companies in market data science analytics (Lin et al., 2018). Consumer Neuroscience has expanded its footprint beyond various fields such as bioengineering, marketing, food technology and industrial designs. In neuromarketing and consumerism, it is important to study human responses towards certain items or products and advertisements (Plassmann et al., 2015). It is to ensure the ability to capture people's attention and engagement, which will provide larger opportunities for effective product and service sales.

Presently, Beta and Gamma brainwaves oscillations have posed importance in predicting box office sales in movie productions by studying the EEG results during movie trailers viewings in studying consumer behaviours (Boksem & Smidts, 2015). Recent studies also took account of the Alpha waves activity in calculating neural activities related to sales of tickets and free recall of the movie storyline (Barnett & Cerf, 2017). The same techniques have been applied in direct studies of television-based marketing ads, enabling calculations of engagement index using a beta, alpha and theta waves. The EEG used in this study was dense-array EEG (Lin et al., 2018).

## **Potential Trends Forward**

Rapid economic and technological growth demands the evolution of intervention techniques and tools to ensure better ways are produced for a better future. In the aspects of EEG in Neuromarketing, a huge potential can be seen with integrating Virtual Reality (VR) (Maples-Keller et al., 2017) and wearable EEG as it allows mimicking of real-life situations and environment to be used in studies (Lin et al., 2018). VR is currently being used in tourism and education (House et al., 2020). Virtual, augmented, and mixed reality has provided diversified and interactive teaching and learning environments to improve students' cognitive ability, especially in terms of information processing and storage and recalling acquired knowledge such as VSI Patient Education (VSI PE), as shown in Figure 5.

In Neuromarketing, VR was integrated with EEG in several studies, especially in 2020. However, it is still in trial studies. Therefore, it has not been used widely in the market, unlike in education, where virtual and augmented reality has been widely used to create immersive studying environments. It may be because VR itself is an expensive technology and requires knowledgeable professionals to create the VR 3D environment using software such as Unity3D or CRYENGINE and VR devices such as Oculus Rift, Playstation VR, HTC Vive and Samsung Gear attached to an EEG like in Figure 6.

Despite that, this mixed-reality convergence eases the process of incorporating computerised virtual graphic objects via 3D environment with ease at any selected location,



Figure 5. VSI PE on brain model (House et al., 2020)

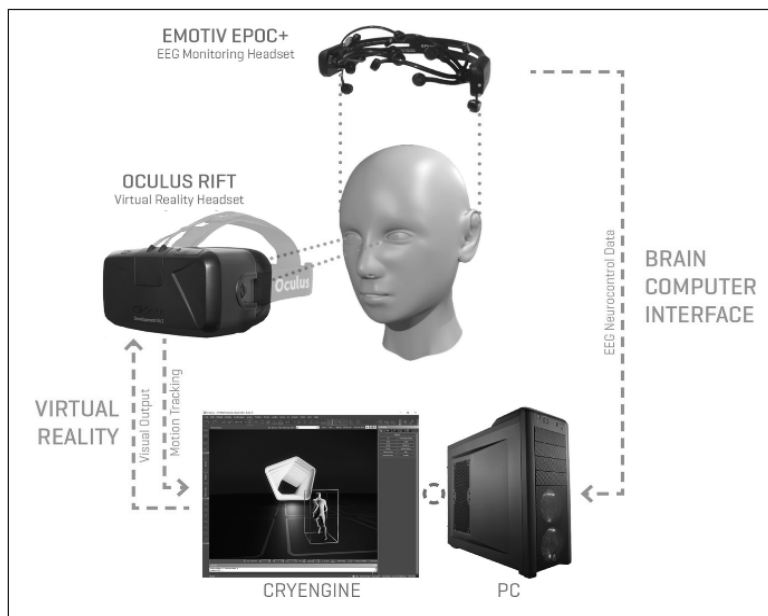


Figure 6. VR 3D environment (Doma, 2019)

be it in a lab, office and even outdoors. Liu and colleagues (2018) have also studied virtual reality in military training by making immersive battlefield environments and weapon production. Additionally, VR has been used to mimic the environment that can boost the health and well-being of military personnel (McIntosh et al., 2019). The same concept can be applied in marketing as it works by providing stimulation to the individual's emotional experience, elucidating reactions through emotional changes and brain activities. A recent study from 2016 to 2020 showed VR being the most effective in evoking emotional engagement by 31.03% compared to music at 24.14%, music videos and clips at 20.69%,

and pictures at 3.45% (Suhaimi et al., 2020). Previous studies have also incorporated the use of virtual reality to remedy anxiety, which provided empirical evidence of its viability (Maples-Keller et al., 2017).

As the beneficial uses of VR are evident, coupling of VRs to EEG systems can provide vast insight to researchers in studying the effectiveness of intervention via brain activity signals imaging. Furthermore, there is a possible application of treatment intervention techniques for various psychiatric disorders to provide more extensive and personalised treatment for each type of disorder. Lastly, to study how human emotion is manipulated through virtual reality choices of various products in the market. The various benefits it carries makes it a viable technique and device to be applied in the future, not just in studies. Thus, the application of VR-EEG is possible in future innovations to ease studies and training in marketing and military, education, and ultimately healthcare.

## CONCLUSIONS

The invention of EEG has paved the way for diagnosing and studying various neurological disorders and studying human cognitive processes. The signals of an EEG provide subjective sine signal patterns enabling the visualisation of changes in brain activity. The flexibility of an EEG system allows manipulation of techniques to best-fit study goals and allow better coverage of the brain area for accurate imaging with the manipulation of electrode number and position. The Revolution of EEG against time has caused EEG to be wearable, portable, and accessible to the masses, allowing extensive use of EEG in research and study, not just for the application in healthcare. Furthermore, the study of consumer neuroscience in neuromarketing has been found important and has received the attention of various business owners, managers, scientists, and technology designers as EEG pave the way for better and more effective marketing of products and services. Despite the innumerable benefits an EEG system possess, there are still limitations that have yet been tackled, warranting the opportunity to explore and improve a better performance in visualising brain functionality. Nevertheless, the vast benefits of EEG outweigh its limitations which can be addressed via multimodal integration.

## ACKNOWLEDGEMENT

We would like to thank Universiti Sains Malaysia for the support given to complete the manuscript.

## REFERENCES

- Abujelala, M., Sharma, A., Abellanoza, C., & Makedon, F. (2016). Brain-EE: Brain enjoyment evaluation using commercial EEG headband. In *Proceedings of the 9th ACM International Conference on*

- Pervasive Technologies Related to Assistive Environments* (pp. 1-5). ACM Publishing. <https://doi.org/10.1145/2910674.2910691>
- Barnett, S. B., & Cerf, M. (2017). A ticket for your thoughts: Method for predicting content recall and sales using neural similarity of moviegoers. *Journal of Consumer Research*, 44(1), 160-181. <https://doi.org/10.1093/jcr/ucw083>
- Beres, A. M. (2017). Time is of the essence: A review of electroencephalography (EEG) and event-related brain potentials (ERPs) in language research. *Applied Psychophysiology Biofeedback*, 42(4), 247-255. <https://doi.org/10.1007/s10484-017-9371-3>
- Bhagchandani, A., Bhatt, D., & Chopade, M. (2018). Various big data techniques to process and analyse neuroscience data. In *2018 5th International Conference on "Computing for Sustainable Global Development"* (pp. 397-402). INDIACOM.
- Boksem, M. A. S., & Smidts, A. (2015). Brain responses to movie trailers predict individual preferences for movies and their population-wide commercial success. *Journal of Marketing Research*, 52(4), 482-492. <https://doi.org/10.1509/jmr.13.0572>
- Casson, A. J., Abdulaal, M., Dulabh, M., Kohli, S., Krachunov, S., & Trimble, E. (2018). Electroencephalogram. In T. Tamura & W. Chen (Eds), *Seamless healthcare monitoring* (pp. 45-81). Springer. [https://doi.org/https://doi.org/10.1007/978-3-319-69362-0\\_2](https://doi.org/https://doi.org/10.1007/978-3-319-69362-0_2)
- Coenen, A., & Zayachkivska, O. (2013). Adolf Beck: A pioneer in electroencephalography in between Richard Caton and Hans Berger. *Advances in Cognitive Psychology*, 9(4), 216-221. <https://doi.org/10.5709/acp-0148-3>
- Deolindo, C. S., Ribeiro, M. W., Aratanha, M. A., Afonso, R. F., Irrmischer, M., & Kozasa, E. H. (2020). A critical analysis on characterising the meditation experience through the electroencephalogram. *Frontiers in Systems Neuroscience*, 14(August), 1-29. <https://doi.org/10.3389/fnsys.2020.00053>
- Doma, O. O. (2019). EEG as input for virtual reality. In N. Lee (Ed.), *Encyclopedia of computer graphics and games* (pp. 1-4). Springer International Publishing. [https://doi.org/10.1007/978-3-319-08234-9\\_176-1](https://doi.org/10.1007/978-3-319-08234-9_176-1)
- Hill, H. (2019). Exploring the limitations of event-related potential measures in moving subjects. Case studies of four different technical modifications in ergometer rowing. *BioRxiv*, 31, 1-23. <https://doi.org/10.1101/578534>
- House, P. M., Pelzl, S., Furrer, S., Lanz, M., Simova, O., Voges, B., Stodieck, S. R. G., & Brückner, K. E. (2020). Use the mixed reality tool "VSI Patient Education" for more comprehensible and imaginable patient education before epilepsy surgery and stereotactic implantation of DBS or stereo-EEG electrodes. *Epilepsy Research*, 159(October 2019), Article 106247. <https://doi.org/10.1016/j.eplepsyres.2019.106247>
- Husain, A. M., & Sinha, S. R. (2020). Continuous EEG monitoring: Principles and practice. *Journal of Clinical Neurophysiology*, 37(3), 274-274. <https://doi.org/10.1097/wnp.0000000000000571>
- Ibrahim, S. A. S., Hamzah, N., Wahab, A. R. A., Abdullah, J. M., Malim, N. H. A. H., Sumari, P., Idris, Z., Mokhtar, A. M., Ghani, A. R. I., Halim, S. A., & Razak, S. A. (2020). Big brain data initiative in universiti sains malaysia: Challenges in brain mapping for Malaysia. *Malaysian Journal of Medical Sciences*, 27(4), 1-8. <https://doi.org/10.21315/mjms2020.27.4.1>

- Kaplan, R. M. (2011). The mind reader: The forgotten life of Hans Berger, discoverer of the EEG. *Australasian Psychiatry*, 19(2), 168-169. <https://doi.org/10.3109/10398562.2011.561495>
- Koudelková, Z., & Strmiska, M. (2018). Introduction to the identification of brain waves based on their frequency. *MATEC Web of Conferences*, 210, 1-4. <https://doi.org/10.1051/mateconf/201821005012>
- Lau-Zhu, A., Lau, M. P. H., & McLoughlin, G. (2019). Mobile EEG in research on neurodevelopmental disorders: Opportunities and challenges. *Developmental Cognitive Neuroscience*, 36(October 2018), Article 100635. <https://doi.org/10.1016/j.dcn.2019.100635>
- Lin, M. H. J., Cross, S. N. N., Jones, W. J., & Childers, T. L. (2018). Applying EEG in consumer neuroscience. *European Journal of Marketing*, 52(1-2), 66-91. <https://doi.org/10.1108/EJM-12-2016-0805>
- Liu, X., Zhang, J., Hou, G., & Wang, Z. (2018). Virtual reality and its application in military. *IOP Conference Series: Earth and Environmental Science*, 170(3), Article 032155. <https://doi.org/10.1088/1755-1315/170/3/032155>
- Maddirala, A. K., & Shaik, R. A. (2018). Separation of sources from single-channel EEG signals using independent component analysis. *IEEE Transactions on Instrumentation and Measurement*, 67(2), 382-393. <https://doi.org/10.1109/TIM.2017.2775358>
- Maples-Keller, J. L., Bunnell, B. E., Kim, S. J., & Rothbaum, B. O. (2017). The use of virtual reality technology in the treatment of anxiety and other psychiatric disorders. *Harvard Review of Psychiatry*, 25(3), 103-113. <https://doi.org/10.1097/HRP.0000000000000138>
- McIntosh, J., Rodgers, M., Marques, B., & Gibbard, A. (2019). The use of VR for creating therapeutic environments for the health and well-being of military personnel, their families and their communities. *Journal of Digital Landscape Architecture*, 2019(4), 185-194. <https://doi.org/10.14627/537663020>
- Mosslah, A. A., Mahdi, R. H., & Al-Barzinji, S. M. (2019). Brain-computer interface for biometric authentication by recording signal. *Computer Science & Information Technology*, 2019, 153-162. <https://doi.org/10.5121/csit.2019.90613>
- Plassmann, H., Venkatraman, V., Huettel, S., & Yoon, C. (2015). Consumer neuroscience: Applications, challenges, and possible solutions. *Journal of Marketing Research*, 52(4), 427-435. <https://doi.org/10.1509/jmr.14.0048>
- Read, G. L., & Innis, I. J. (2017). Electroencephalography (EEG). In J. Matthes (Ed.), *The international encyclopedia of communication research methods* (pp. 1-18). John Wiley & Sons, Inc. <https://doi.org/10.1002/9781118901731.iccrm0080>
- Reyes, L. M. S., Reséndiz, J. R., & Ramírez, G. N. A. (2019). Trends of clinical EEG systems: A review. In *2018 IEEE EMBS Conference on Biomedical Engineering and Sciences, IECBES 2018 - Proceedings* (pp. 571-576). IEEE Publishing. <https://doi.org/10.1109/IECBES.2018.8626680>
- Rojas, G. M., Alvarez, C., Montoya, C. E., de la Iglesia-Vayá, M., Cisternas, J. E., & Gálvez, M. (2018). Study of resting-state functional connectivity networks using EEG electrodes position as seed. *Frontiers in Neuroscience*, 12(APR), 1-12. <https://doi.org/10.3389/fnins.2018.00235>



- Seal, A., Reddy, P. P. N., Chaithanya, P., Meghana, A., Jahnavi, K., Krejcar, O., Hudak, R., & Jiang, Y. Z. (2020). An EEG database and its initial benchmark emotion classification performance. *Computational and Mathematical Methods in Medicine*, 2020, Article 8303465. <https://doi.org/10.1155/2020/8303465>
- Siuly, S., Li, Y., & Zhang, Y. (2016). Significance of EEG signals in medical and health research. In *EEG signal analysis and classification* (pp. 23-41). Springer. [https://doi.org/https://doi.org/10.1007/978-3-319-47653-7\\_2](https://doi.org/https://doi.org/10.1007/978-3-319-47653-7_2)
- Suhaimi, N. S., Mountstephens, J., & Teo, J. (2020). EEG-based emotion recognition: A state-of-the-art review of current trends and opportunities. *Computational Intelligence and Neuroscience*, 2020, Article 8875426. <https://doi.org/10.1155/2020/8875426>
- Tudor, M., Tudor, L., & Tudor, K. I. (2005). The history of electroencephalography. *Acta Medica Croatica*, 59(4), 307-313.
- Vaid, S., Singh, P., & Kaur, C. (2015). EEG signal analysis for BCI interface: A review. In *International Conference on Advanced Computing and Communication Technologies, ACCT* ( pp. 143-147). IEEE Publishing. <https://doi.org/10.1109/ACCT.2015.72>
- Xue, G., Chen, C., Lu, Z. L., & Dong, Q. (2010). Brain imaging techniques and their applications in decision-making research. *Acta Psychologica Sinica*, 42(1), 120-137. <https://doi.org/10.3724/sp.j.1041.2010.00120>
- Yu, J. H., & Sim, K. B. (2016). Classification of color imagination using Emotiv EPOC and event-related potential in electroencephalogram. *Optik*, 127(20), 9711-9718. <https://doi.org/10.1016/j.ijleo.2016.07.074>



## Multi-band Antenna with CSRR Loaded Ground Plane and Stubs Incorporated Patch for WiMAX/WLAN Applications

Palanivel Manikandan<sup>1\*</sup>, Pothiraj Sivakumar<sup>1</sup> and Nagarajan Rajini<sup>2</sup>

<sup>1</sup>Department of Electronics and Communication Engineering, Kalasalingam Academy of Research and Education, Tamilnadu-626126, India

<sup>2</sup>Department of Mechanical Engineering, Kalasalingam Academy of Research and Education, Tamilnadu-626126, India

### ABSTRACT

This paper proposes a novel compact, single structure, multi-band antenna along with tested results for wireless local area networks (WLAN) and Worldwide Interoperability for Microwave Access (WiMAX) applications. In this work, modified complementary split-ring resonators (CSRR) were incorporated in the ground layer of the patch to achieve permeable bands to accommodate multi-resonance frequencies in a single device. The proposed antenna design supported the upgraded performance and led to desirable size reduction. Open stubs were incorporated at the edges of the triangle patch to get the improved reflection coefficient responses. It resulted in specific band spectra of 2.4 / 3.4 / 5.1 / 5.8GHz for WLAN/WiMAX applications. For constructive antenna design, CST microwave studio simulation software was utilized.  $S_{11}$  parameter was observed as -24dB at 2.4GHz, -32dB at 3.4GHz, -15dB at 5.1GHz and -22dB at 5.8GHz bands. Field patterns of each band were observed. The parametric study of the arrangement and positioning of the CSRR unit cell was examined. Excellent consistency between the experimental and simulated results revealed the capability of the projected structure to perform with improved gain.

*Keywords:* CSRR, microstrip, multi-band antenna, WiMAX, WLAN

### ARTICLE INFO

*Article history:*

Received: 12 May 2021

Accepted: 15 September 2021

Published: 06 December 2021

DOI: <https://doi.org/10.47836/pjst.30.1.03>

*E-mail addresses:*

maanip85@gmail.com (Palanivel Manikandan)

sivapothi@gmail.com (Pothiraj Sivakumar)

rajiniklu@gmail.com (Nagarajan Rajini)

\* Corresponding author

### INTRODUCTION

Today's wireless communication systems focus on the enhancement of current techniques using multi-band antennas. The features of multi-band antennas include compact size, low cost, easy fabrication, multiple resonating frequencies, less weight, and low profile (Ali et al., 2018). The

advantages of microstrip antennas are easy accommodation with compact devices due to their planar structure, low profile, less weight, and easy integration with circuits. These features make them highly suitable for communication devices. Developments in the microstrip antenna domain and an increase in the demands of microstrip antennas are transforming the field of communication technology (Peixeiro, 2011). However, microstrip antennas have a few limitations, such as narrowband resonance and poor efficiency. Hence, many techniques were later developed to overcome these limitations (Wong, 2002; Waterhouse, 2003). The performance of microstrip-patch antennas was improved by implementing a cavity structure on the back of the patch with many dielectric layers and shorts. In addition, fractal structures were implemented to provide wideband characteristics (Rahim et al., 2019). Multi-band technique for wireless applications can be achieved by incorporating slots over structures (Zavosh & Aberle, 1996), fractal geometries (Baliarda, 1998), stubs at various locations (Ali & Biradar, 2017), multi-layered structures (Firdausi & Alaydrus, 2016), reconfigurable structures (Sung, 2014), aperture coupling feed, feeding techniques (Casula et al., 2016), insertion of parasitic elements, electronically reconfiguring the antenna using microelectronic switches (Parchin et al., 2020) or by making defected ground structures (DGS). Multi-band antenna is reported in slotted rectangular patch antenna for wireless applications (Malik & Singh 2019).

Recent developments in wireless communications demand multiple bands in the range of 6 to 100 GHz (Ishfaq et al., 2017). In 5G wireless technology, antennas for mobile or other handheld electronic devices are compact and demand operation in multi-resonance frequency bands (Cheng et al., 2020). For ease of fabrication, planar antennas are desirable, while bandwidth limitations can be overcome by following techniques such as incorporating slots in the radiating elements (Zong et al., 2015), metamaterials (Xu et al., 2012; Xu et al., 2013), and making defects in the ground plane (Chiang & Tam, 2008). Many antennas designed using complementary split-ring resonators (CSRR) were allocated for gain and bandwidth enhancement (Ntaikos et al., 2011). CSRR is a unique structure to produce a very firm magnetic field coupling on the source of EM Field than by using conventional materials (Liu et al., 2013). It reduces the geometrical size of the antenna without modifying its properties (Dong & Itoh, 2011; Dong et al., 2012). Multi-band antenna was developed through fractal structure and CSRR based ground plane (Manikandan et al., 2020). A compact dual-band antenna for high-frequency wireless applications was reported (Erentok & Ziolkowski, 2008). A microstrip multi-band antenna was proposed by loading an SRR with slots to miniaturize the structure (Sarkar et al., 2014). Wi-Fi and WiMAX applications can be achieved through CSRR with radiating elements (Nelaturi & Sarma, 2018) through miniaturizing characteristics (Ntaikos et al., 2011) and adaptive frequency reconfigurability (Manikandan et al., 2019). Finding the dimension of an antenna can be done with the help of design equations. However, there is a need to optimize the element's dimensions

or feed to ensure improved results. Currently, many optimization methods exist. Genetic algorithms and evolution strategies were applied to find the dimensions of horn antenna for good results (Deepika et al., 2017). Challenges in designing a 5G communication system antenna to fulfill multi-band requirements were reported (Shaik & Malik, 2021).

This paper presents a multi-band triangular antenna using CSRR with four bands, i.e., 2.4 / 3.4 / 5.1 / 5.8 GHz for WLAN and WiMAX applications. CSRR was introduced on the ground layer of the microstrip to realize the additional bands without making physical changes in the patch. Metallic open stubs were incorporated to shift the existing bands to the desired multi-resonant frequencies with improved reflection coefficients. In this work, a microstrip triangular patch was examined with and without CSRR. A computer simulation technology (CST) software tool was appropriated to design and simulate the constructed antenna. It showed high radiation features at distinct frequencies, making our proposal the correct element for WLAN and WiMAX applications.

## METHODS

### Design of Triangular Patch

The proposed multi-band antenna was designed and fabricated over a commercially available FR4 substrate with a dielectric constant of 4.4, thickness value of 1.60 mm, and loss tangent of 0.02. The designed multi-band antenna had dimensions of 30 mm x 25.98 mm with a 50 Ohm transmission line. An equilateral triangular shape patch was considered because it required less metal area on the substrate compared to existing regular shapes like a rectangle or circle (Garg & Long, 1988). Based on the literature, the dimensions of an equilateral triangle were considered as per Equation 1 for 2.75GHz, which was radiated due to the fringing fields of the patch and simulated with CST microwave studio simulation software.

$$a = \frac{2c}{3f_r\sqrt{\epsilon_r}} \quad [1]$$

Where,  $a$  = side length of the equilateral triangle

$f_r$  = resonance frequency

$\epsilon_r$  = Relative dielectric constant of the substrate used

The triangular patch dimension is considered for 3 GHz. The antenna progressed in numerous stages to attain multi-resonance frequencies by adjusting its parameters. After introducing the large slots on the base sides of the triangle, a fully grounded patch provided two resonance frequencies, such as 2.75 and 4.5GHz, due to effective surface current distribution at a different place at each resonance. At the lower resonance frequency, the maximum surface current is distributed at the center area of the triangle and minimum at the parallel edges. At higher resonance, maximum surface current existed at edges and

the minimum at the center. A microstrip feed was matched with a patch radiator, having a selected dimension of 15 mm and 2.5 mm, respectively. Esteemed reference impedance was 50 ohm. The antenna was fabricated with the dimensions specified in Figure 1.

The proposed triangle was fed with the microstrip feed as an impedance matching transformer to give 50 ohms matching the load. The dimensions of the radiating element are given in Table 1.

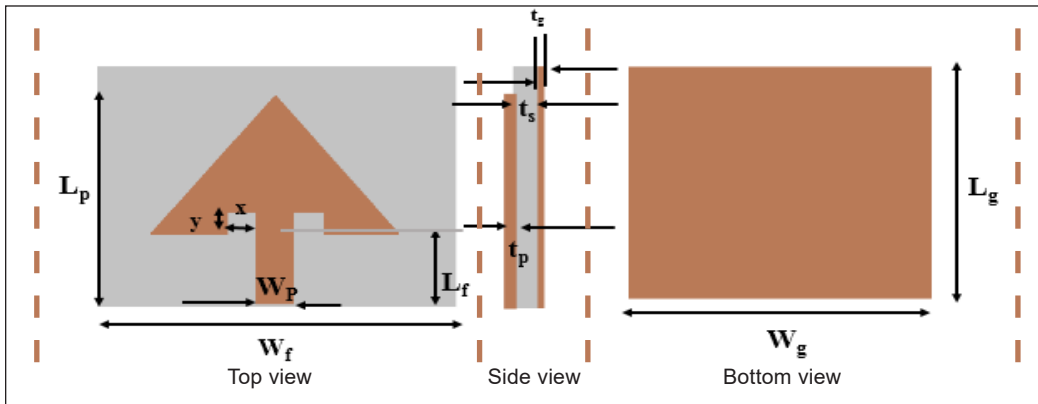


Figure 1. Geometrical parameters of the triangle patch

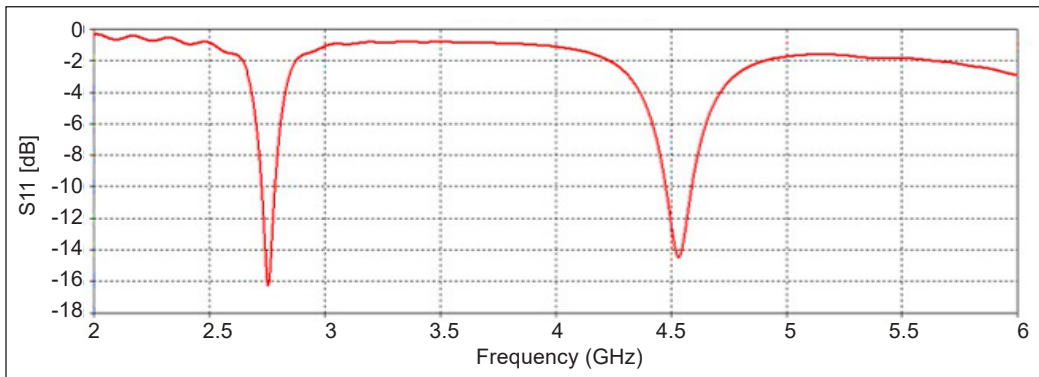


Figure 2. Simulation result of S11 versus frequency

Table 1  
Dimensions of the triangle patch

Antenna	
Parameters	Value
Dimensions of patch ( $W_p \times L_p \times t_p$ )	$30 \times 25.98 \times 0.035 \text{ mm}^3$
Dimensions of slot ( $x \times y$ )	$15 \times 7.5 \text{ mm}^2$
Dimensions of feed ( $W_f \times L_f$ )	$2.5 \times 30 \text{ mm}^2$
Dimensions of ground ( $W_g \times L_g \times t_g$ )	$60 \times 60 \times 0.035 \text{ mm}^3$
Thickness of the substrate ( $t_s$ )	1.6 mm

Figure 1 displays the geometrical parameters, and Figure 2 is the graph of the reflection coefficient (S11 in dB) of the proposed multi-band triangle. The prescribed triangle provided a very minimal S11 response at the frequencies of 2.75 and 4.5GHz.

### Introducing Complementary Slip Ring Resonator on Ground Layer

The complementary split-ring resonator (CSRR) was incorporated into the ground side of the triangle patch antenna. The capacitive nature of CSRR created an electric field when energized. This electric field created an electromotive force (EMF) in CSRR, which generated fluctuating voltage among the slots of CSRR at RF frequencies. The dimensions and the equivalent circuit model of CSRR are given in Figure 3. The boundaries were altered to obtain unit cell scattering parameters. As a result, the appearance of TEM wave broadcasts was in the direction of the y-axis. The E-field of the incident wave was oriented along the direction of the z-axis, and the H-field in the direction of the x-axis, as shown in Figure 4. The effect of proposed resonators can be exhibited on a microstrip patch by promoting the circuit model of the CSRR. Further reduction in the dimensions of these

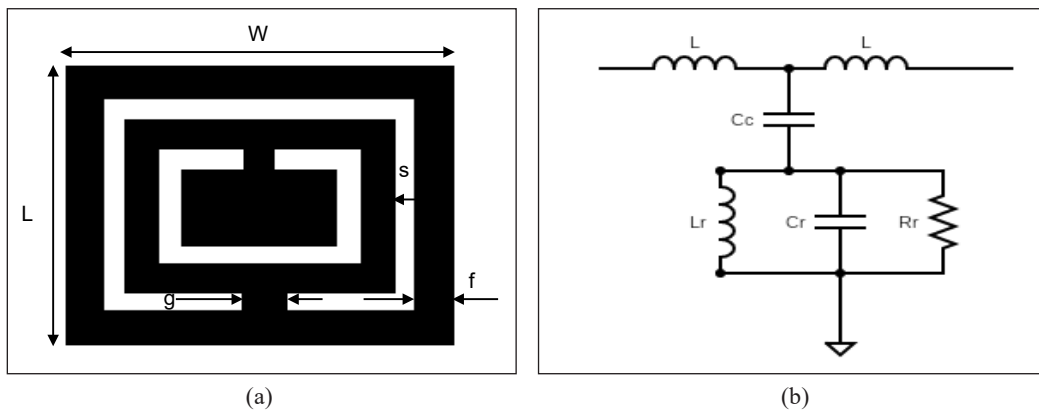


Figure 3. (a) Dimensions; and (b) Equivalent circuit of CSRR

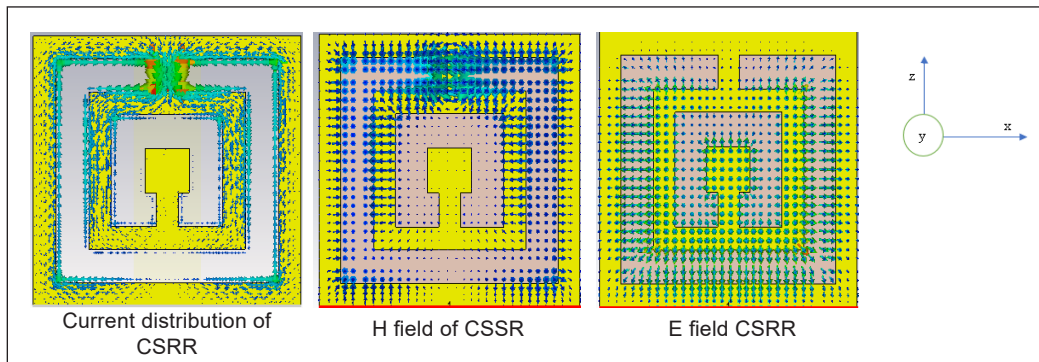


Figure 4. (a) Current distribution; (b) H field; and (c) E field of CSRR

artificial transmission lines was executed through a single cell. Mutual capacitance existed through the electric field in the gap between the conductor of CSRR, and inductance was established due to the current flow across the transmission line. Thus, CSRR acted as a resonance circuit with the parallel  $R_r$ ,  $L_r$ , and  $C_r$  resonating structures, as shown in Figure 3(b).

### Analysis of the Location of CSRR Incorporated Over a Ground Plane

Table 2 demonstrates the dimensions of CSRR to be loaded. In Figure 3, the designed CSRR was loaded with the proposed patch to attain a multi-band resonance (Aminu-Baba et al., 2018).  $L$  represents the inductance of the lines in CSRR. The latter was described through the resonators and designed with the parallel  $R_r$ ,  $L_r$ , and  $C_r$  coupled with the host Conductor, as presented by coupling capacitance  $C_c$ . When the dielectric losses

Table 2  
*Optimal dimensions of CSRR*

CSRR	
Parameters	Value (mm)
Length (L)	7
Width (W)	7
Width of metal (f)	1
Spacing (s)	0.7
Width of metal strip connected ring (g)	0.3

were insignificant (based on the 1<sup>st</sup> order approximation), Multi-resonance was realized with a patch, as shown in Figure 6. It demonstrated the S parameter characteristics of the projected patch with a CSRR incorporated ground plane. Experimentally, it confirmed that it could radiate at 2.45GHz with S11 equal to -34 dB and 4.5 GHz with S11 equal to -10 dB. Thus, it was significant for WLAN applications. The developed element was a type of CSRR used in this design and etched into the ground layer of the patch, as shown in Figure 5.

Figure 5 demonstrates the suitably positioned CSRR in the ground layer, touching the vertical axis  $o$  at the rear of the feed line attached to the proposed patch. This portion determined the positioning of the rectangular unit cell without changing the dimensions.

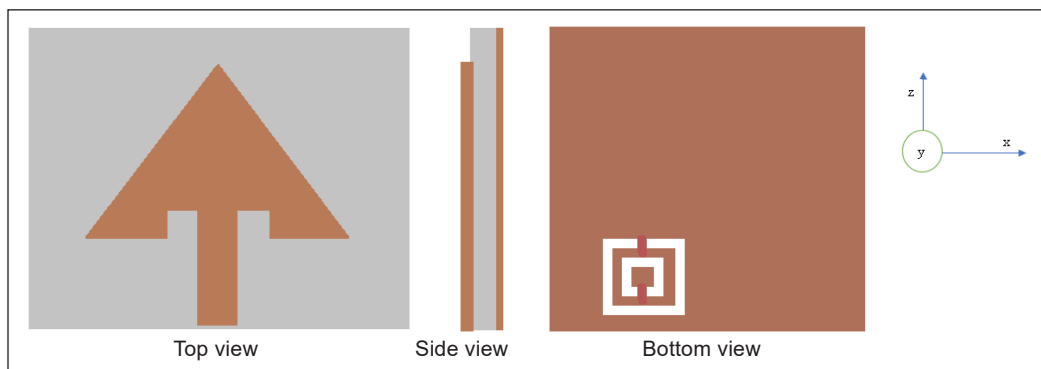


Figure 5. Proposed multi-band triangle with CSRR on the ground plane



The rectangular unit cell that emerged at the patch was positioned with the ground layer, symmetric to the feed of the maximum field to achieve a lower level in the patch.

The rectangular CSRR was placed in the X-direction, -3.5 mm from the feed center and 7 mm from the feed edge in the Y-direction. Thus, the left corner of the CSRR was precisely under the feed line. This positioning of the CSRR made the antenna resonates effectively in a lower band frequency of 2.45 GHz. Furthermore, the results revealed that the acceptable reflection coefficient transpired at the first band itself, as shown in Figure 6.

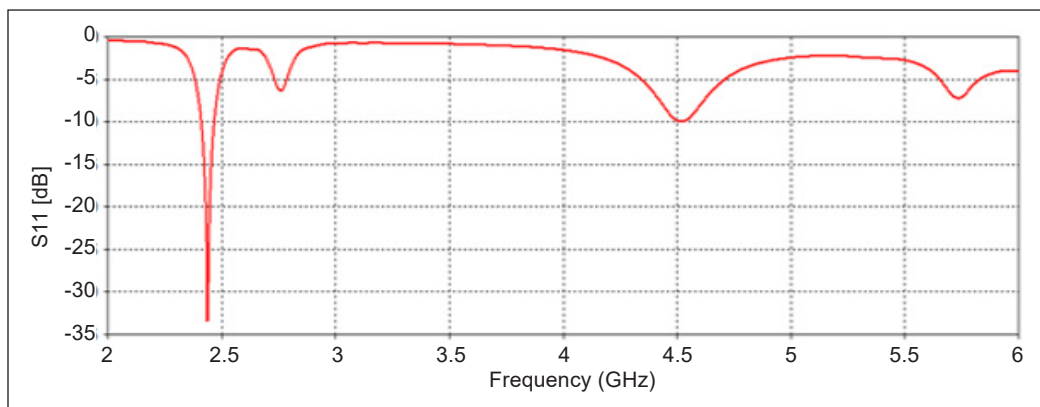


Figure 6. Simulated S11 response of patch with CSRR incorporated ground plane

### Introduction of Stubs to the Edges of the Patch

Stubs were incorporated at the edges of the proposed CSRR loaded patch antenna to shift the frequencies with adequate reflection coefficient value (Deshmukh & Tirodkar, 2013; Deshmukh et al., 2012). When the length of stub was in the order of one by a fourth of the wavelength, it gave different capacitive and inductive reactance in various resonance frequencies of the antenna and accomplished frequency shift with a significant reflection coefficient. Stubs were introduced on the patch edges to alter the current distribution and improve frequency response at 2.4, 3.4, 5.1, and 5.8GHz. We have made a study on stub length to exhibit better performance. When the stub length was increased, surface current flow direction was associated more in the x-direction, the radiation pattern developed was normal to the surface of the patch. Also, cross-polarization levels were eliminated. By varying stub length, surface current distribution, and radiation pattern direction were different to get the significant reflection coefficient. The impedance of the stubs has changed the impedance of the patch at each resonance.

Thus, the open circuit stub altered the frequency of the proposed patch element. As a result, the formulated element of the multi-band triangle shown in Figure 7 was expected to get multiple bands corresponding to one of the wireless applications at 2.4 / 3.4 / 5.1 / 5.8 GHz.

The radiating frequency of the patch excluding CSRR was achieved at 2.75 and 4.5 GHz. Incorporating a CSRR under the patch in the ground plane offers significant resonance at 2.45 and 4.5GHz. In Table 3, the comparison analysis shows that CSRR has brought the two new resonance frequencies at 2.45 GHz and 5.7GHz. However, most of the remaining bands having poor reflection coefficient responses other than 2.45GHz.

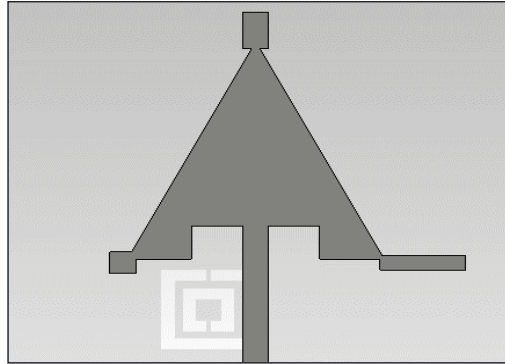


Figure 7. Patch with extended stub on the edges and the CSRR incorporated ground plane

Table 3  
Comparison analysis

	Resonance frequency (GHz)	Reflection Coefficient (dB)
Triangle patch without CSRR and stubs	2.75	-16
	4.5	-14
	2.45	-34
Patch with CSRR incorporated ground plane	2.75	-06
	4.5	-10
	5.7	-07
	2.4	-24.5
Patch with stubs and CSSR incorporated ground plane	3.4	-34
	5.1	-16
	5.8	-23

CSSR grounded patch with stubs have provided the shift on the resonance frequencies of the patch with good reflection coefficient values.

### Optimization

Optimization of various parameters was undertaken to make the obtained frequency bands suitable for wireless applications with enough S11 value. By adjusting the feed width, input impedance was made to resemble an improved reflection coefficient ideally. The width of the feed line was optimized by the Tree-seed Optimization algorithm (Kiran, 2015).

**Tree-seed Algorithm for Feed width Optimization.** This algorithm was implemented as per the following steps:

Step 1: Initial feed width value was calculated from the transmission line equation and was considered the initial Tree location. New feed width values were calculated by using Equation 2,

$$W_{x,y} = L_{y,min} + r_{x,y}(H_{y,max} - L_{y,min}) \quad [2]$$

Where  $L_{y,max}$  is the Lower value of the feed width.

$H_{y,max}$  is the Upper value of the feed width.

$r_{x,y}$  is the Scaling factor randomly selected between 0 and 0.1.

Step 2: The best solution was obtained from populated values (Equation 3).

$$B_y = \min\{f(W_x)\} \quad [3]$$

where  $x=0, 1, 2, 3, 4 \dots N$

$N$  is the number of feed width values in the search range.

Step 3: If the best Optimized feed width was not obtained, New feed width could be considered as per the following Equations 4 and 5

$$S_{xy} = T_{xy} + \alpha_{x,y} * (B_y - T_{r,y}) \quad [4]$$

$$S_{xy} = T_{xy} + \alpha_{i,j} * (T_{x,y} - T_{r,y}) \quad [5]$$

Where;

$S_{xy}$  is the  $y$ -th dimension of  $x$ -th feed width that would be produced at  $i^{\text{th}}$  impedance.

$T_{xy}$  is the  $y$ -th dimension of  $x$ -th impedance,

$B_y$  is the  $y$ -th dimension of the obtained feed width.

$T_{r,y}$  is the  $y$ -th dimension of  $r^{\text{th}}$  impedance randomly chosen from the population.

$\alpha_{x,y}$  is the scaling factor randomly selected in a range of -0.1 to 0.1.

The selection of new feed width was controlled by the patch impedance parameter called Searching Tendency (ST), and its value was in a range of 0 to 0.1.

Step 4: The above steps were repeated until the best seed was obtained or an iteration value of 100.

The feed width dimension was optimized according to the steps specified in the flowchart shown in Figure 8. The best feed width values of sample iterations are listed in Table 4. Feed width of 2.9 mm was the optimized value to realize better reflection coefficient  $S_{11}(\text{dB})$  for the proposed structure.

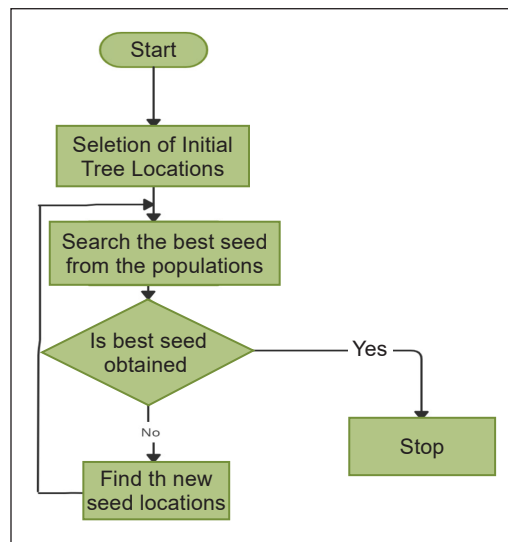


Figure 8. Flow chart of the Tree-Seed Optimization Algorithm

Table 4  
Optimized feed width of sample iterations

Sample Iteration	Optimized Feed width value (mm)	S11 (dB) for different frequency bands		
		2.4 GHz	3.4 GHz	5.8GHz
1	2	-11.03	-22.12	-27.5
2	2.5	-14.858	-24.576	-23.36
3	2.7	-17.02	-17.47	-28.7
4	2.8	-19.37	-26.33	-29.738
5	2.9	-24.485	-33.843	-23.102
6	3.1	-20.9	-12.5	-18

Figure 9 shows the fabricated antenna. The element was fabricated using a commercially available FR4 substrate and loaded with a CSRR incorporated ground layer. The element was attached to the SMA connector to measure the radiating characteristics.

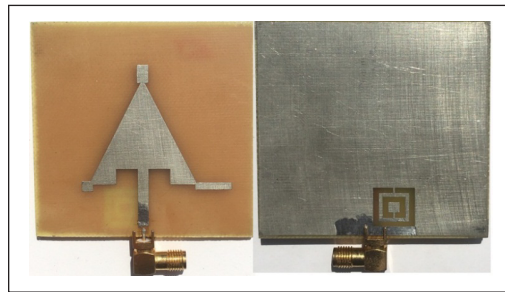


Figure 9. Photograph of fabricated stub incorporated CSRR loaded multiband antenna

**RESULTS AND DISCUSSION**

**Reflection Coefficient**

The designed technique showed sustained results that matched the simulated results. However, the simulated and measured S11 of the projected element varied slightly. It was noted that the developed prototype radiated at 2.4 / 3.4 / 5.1 / 5.8 GHz, respectively.

Due to the placement of the rectangular unit cell near the SMA connector, it was observed that there was a minor change in the reflection coefficient, which affected the antenna’s radiating properties. The experimental results of S11 (in dB) are plotted in Figure 10. It was observed that the frequencies matched precisely. However, the reflection

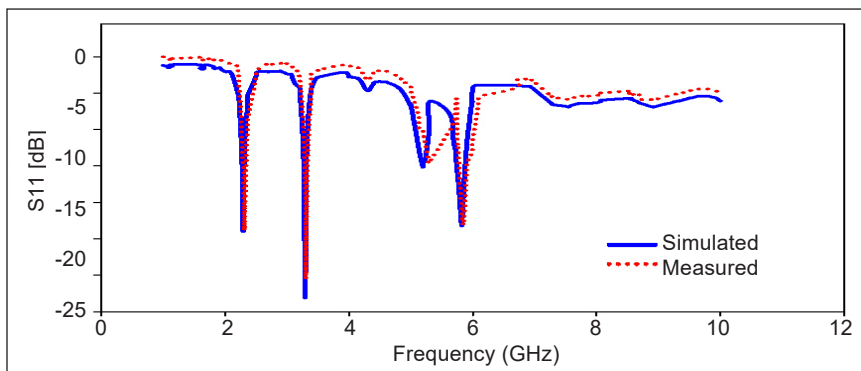


Figure 10. Simulated and measured S11 response

Table 5  
Comparison between simulated and experimental results

Parameters	Frequency band (GHz)	$S_{11}$ Parameter (dB)	Gain (dB)	Efficiency (dB)
Simulated	2.4	-24.5	4.38	-2.85
	3.4	-34	3.46	-3.21
	5.1	-16	1.98	-4.06
	5.8	-23	4.7	-2.53
Measured	2.4	-24	4.25	-2.98
	3.4	-32	3.12	-3.5
	5.1	-15	1.52	-4.2
	5.8	-22	4.58	-2.82

coefficient of the simulated and the measured values varied slightly due to setup limitations like connector loss, excessive soldering and sharp edges in the slots, fabrication tolerances, and improper impedance matching of the driving source for optimum power transfer. The comparison values are tabulated in Table 5.

From the graph in Figure 10, the proposed antenna ensured better performance and was superior compared to existing antennas from literature.

### Gain and Efficiency

Predictable values of gain and efficiency were realized for each resonant frequency. The proposed antenna radiated at 2.4, 3.4, 5.1, and 5.8 GHz with a gain of 4.38, 3.46, 1.28, and 4.79 dB, respectively. The measured gain and efficiency values for each resonance frequency were closely matched with the simulation results, as shown in Table 5. The smaller distance between CSRR and the SMA connector provided excellent gain improvement at 2.4 GHz.

### Radiation Pattern

Figure 11 represents three-dimensional simulated radiation patterns of the projected antenna observed using simulation software. Simulated radiation patterns clearly showed that the patch radiated normal at its plane for all resonance frequencies. However, the shape of the patterns differed slightly among all resonances due to different surface current distributions at each resonance frequency.

Figure 12 demonstrates the measured and simulated radiation patterns for E-Plane and H-plane at 2.4 / 3.4 / 5.1 / 5.8 GHz. Again, the measured and simulated patterns were closely matched. H Plane pattern was observed for all theta values (0 to 360 degrees) by keeping constant  $\phi=90$  degrees. E Plane pattern was observed for all theta values (0 to 360 degrees) by keeping constant  $\phi=0$  degree.

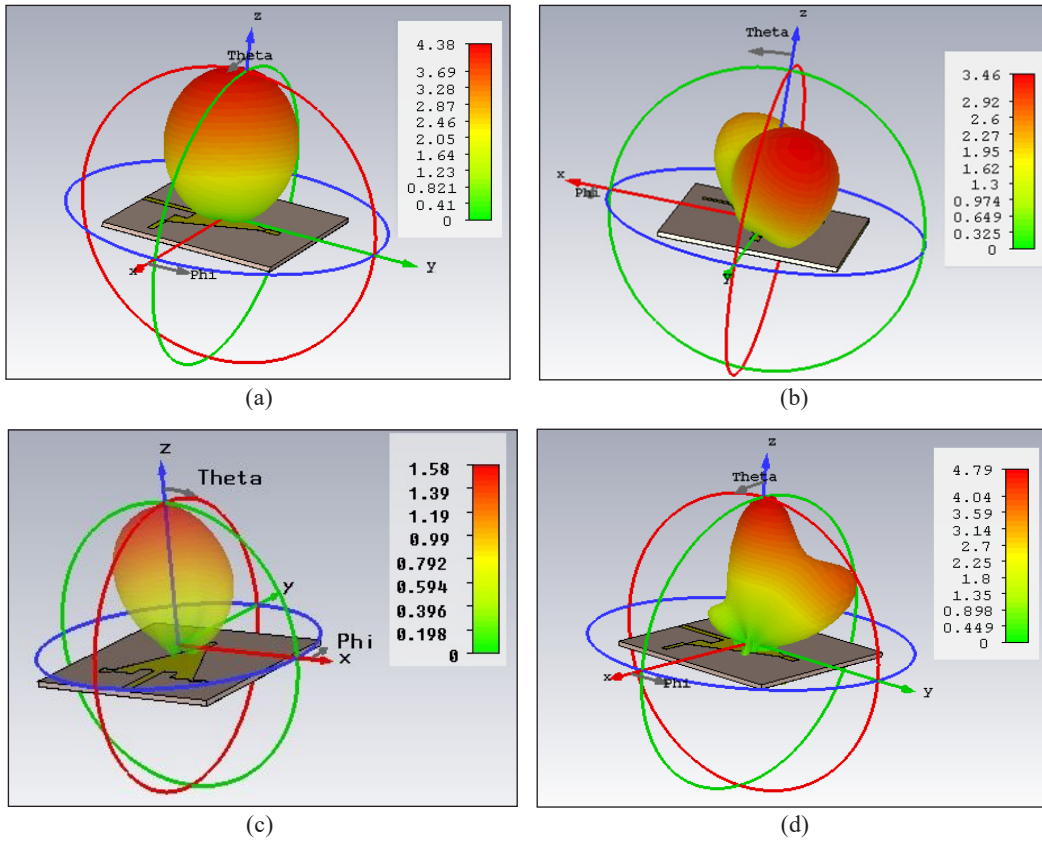


Figure 11. Simulated 3D radiation patterns of (a) 2.4 GHz, (b) 3.4 GHz, (c) 5.1 GHz and (d) 5.8 GHz

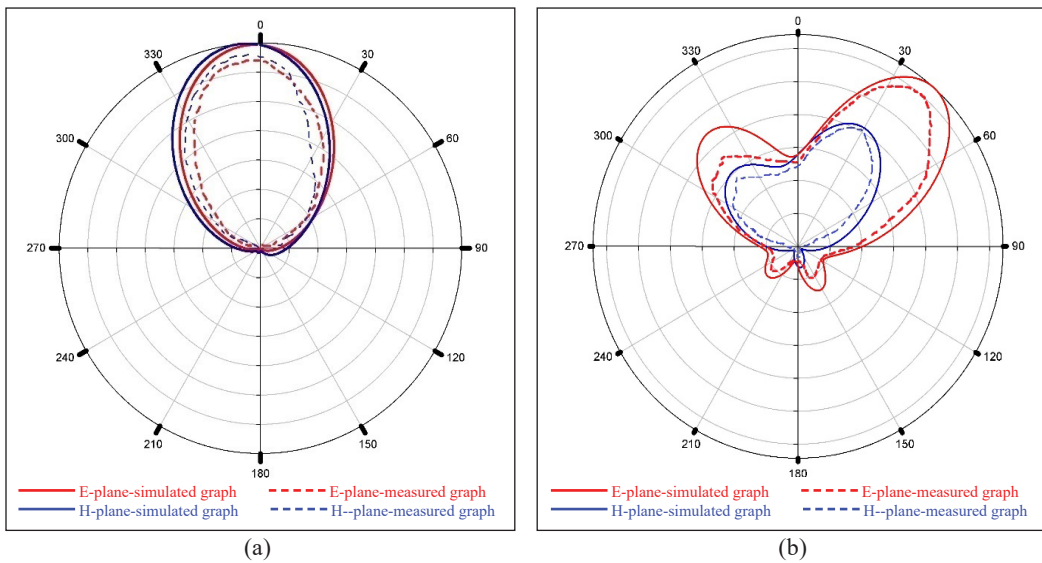


Figure 12. Practical and simulation patterns of (a) 2.4GHz, (b) 3.4GHz, (c) 5.1GHz and (d) 5.8GHz

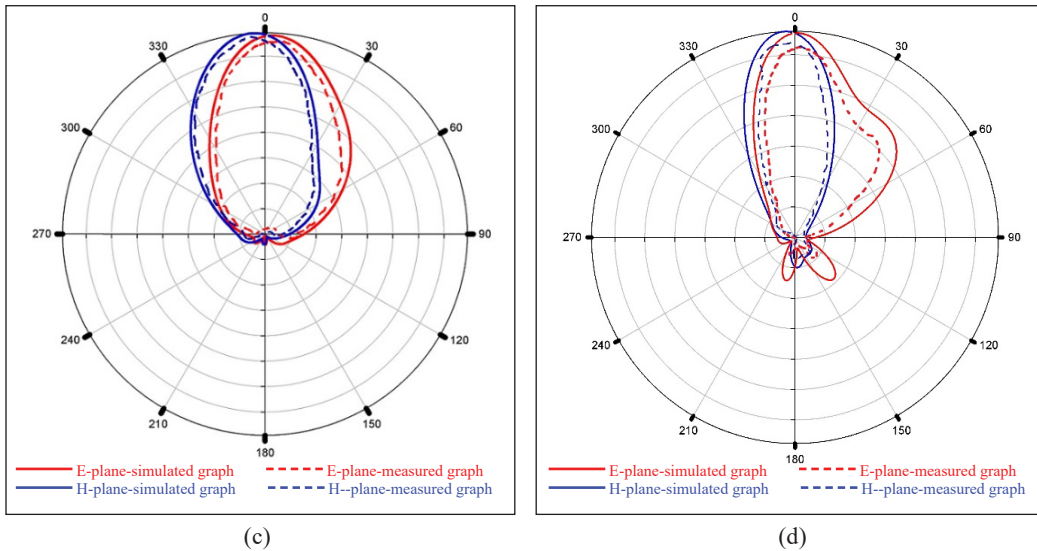


Figure 12 (continue). Practical and simulation patterns of (a) 2.4GHz, (b) 3.4GHz, (c) 5.1GHz and (d) 5.8GHz

### Surface Current Distribution

The surface current distribution of the proposed antenna for each resonance frequency is shown in Figure 13. The following Figure 13 represents the exact current path of the designed antenna. Generally, the resonance frequency of radiation depends on the electrical length of the antenna. Therefore, the current travels in different paths at each resonance frequency, and the structure allows the appropriate current to provide effective radiation.

At the resonance frequency of 2.4 GHz, an appropriate current distribution existed on the sides of the patch, as shown in Figure 13(a). The current phase was reversed at each stub (edges of the patch), while the current direction did not change on each side and provided a low-frequency resonance. At 3.4 GHz frequency, significant current distribution was found at the junction between stubs and the top edge and on the right edge of the patch, as reported in Figure 13(b). The current phase was reversed at the middle of each side of the triangle as frequency and wavelength are inversely proportional to each other. Hence with an increase in the frequency, the length of the wave decreased, and the phase of the current changed in a shorter distance.

Figure 13(c) shows the current distribution of the antenna at 5.1 GHz. A strong current distribution existed on the edge of the patch, and the phase of the current changed by 180 degrees at every 1/3 part of the patch's length formed by side length and stub length. At the resonance frequency of 5.8 GHz, the current phase changed thrice by 180 degrees over the length formed by side length and stub length, as shown in Figure 13(d).

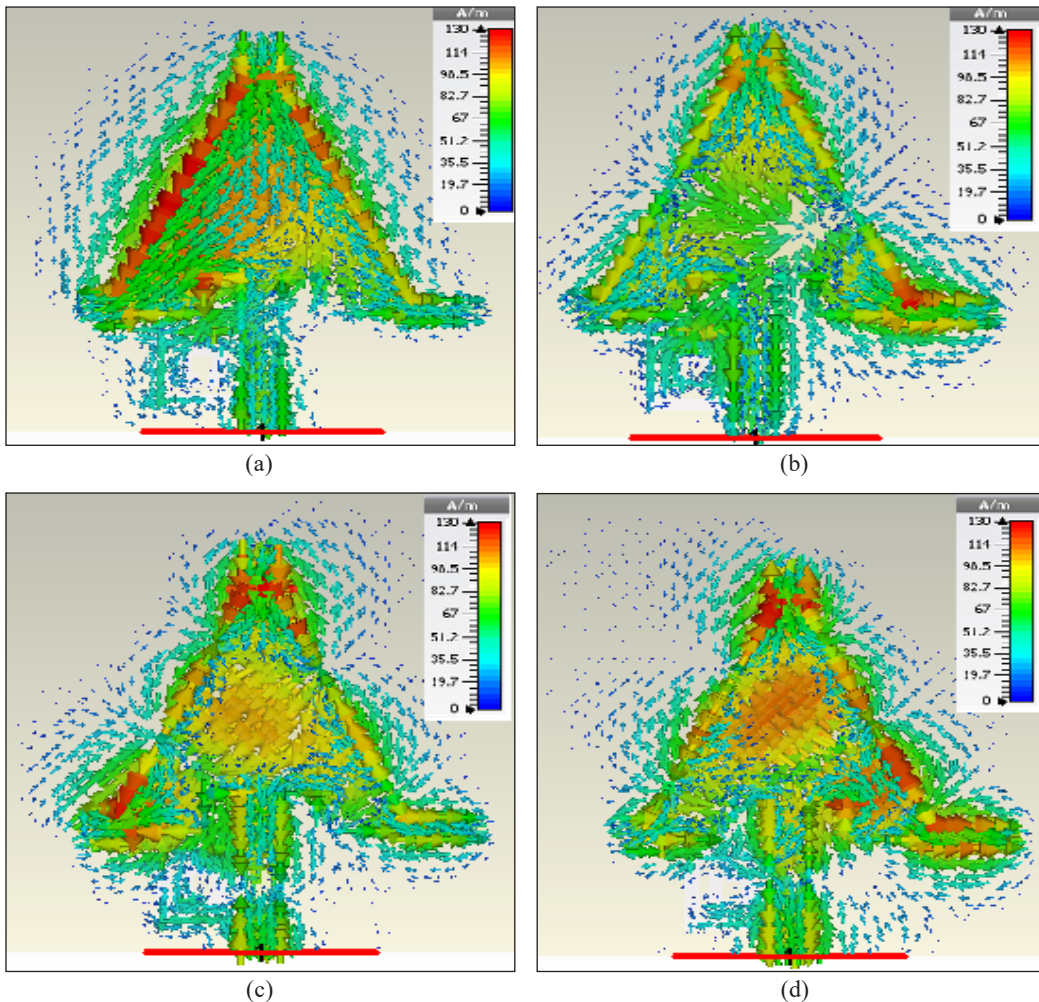


Figure 13. Surface current distribution at (a) 2.4 GHz, (b) 3.4 GHz, (c) 5.1 GHz and (d) 5.8 GHz

### VSWR (Voltage Standing Wave Ratio)

VSWR denotes the power delivered to the antenna from the applied power source. Practical antennas require VSWR values  $\leq 2$ . The proposed antenna reported a VSWR value between 1 and 2 at all four resonance frequencies, as shown in Figure 14. Thus, it ensured that more than 90% of the applied power was delivered to the antenna.

### Input Impedance

The proposed antenna offered a 50-ohm input impedance for all resonance frequencies (2.4 / 3.4 / 5.1 / 5.8 GHz), as shown in Figure 15. Thus, the antenna received maximum power from the appropriate source connected through a 50-ohm connector.



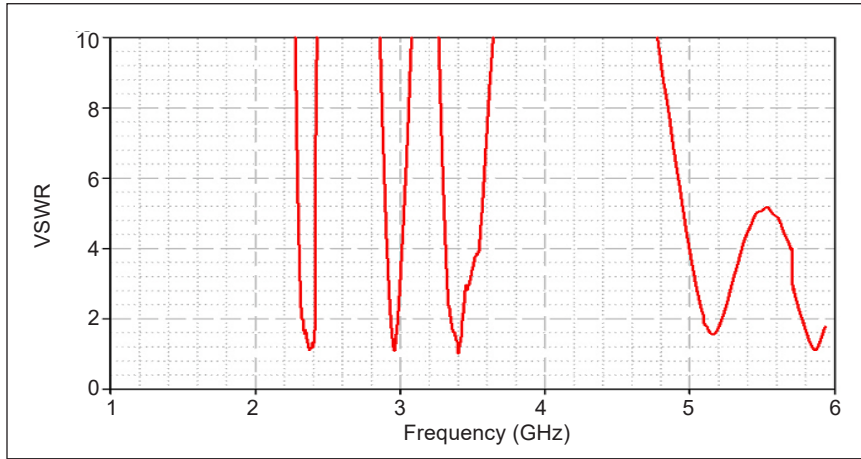


Figure 14. VSWR graph

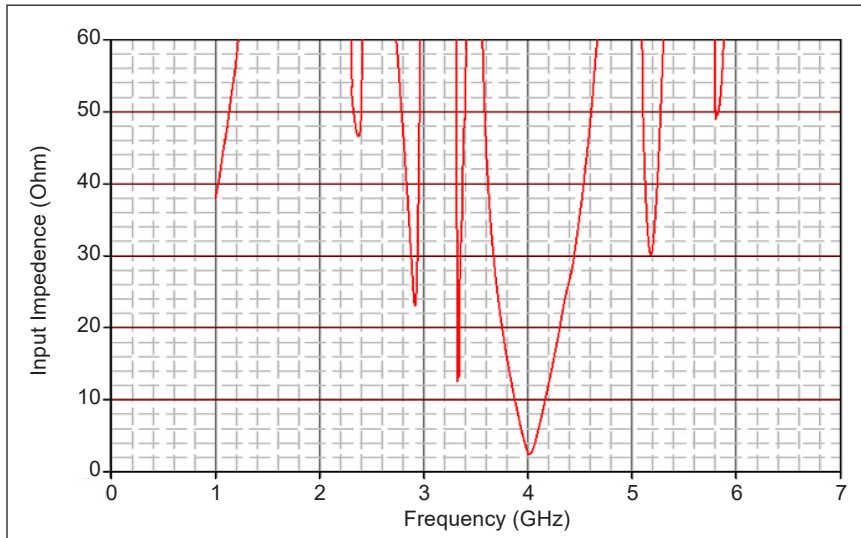


Figure 15. Input impedance graph

## CONCLUSION

A novel CSRR loaded, stub-based microstrip triangle patch antenna for wireless application was proposed and fabricated in this study. As confirmed through simulation and measured results, the proposed antenna design was an authentic novel design for a multi-band microstrip antenna. The proposed antenna provided the reflection coefficient as  $-24\text{dB}$  at  $2.4\text{GHz}$ ,  $-32\text{dB}$  at  $3.4\text{GHz}$ ,  $-15\text{dB}$  at  $5.1\text{GHz}$  and  $-22\text{dB}$  at  $5.8\text{GHz}$  bands. It was observed that the proposed triangle had a functional bandwidth of about  $4.33$ ,  $3.03$ ,  $4.87$ , and  $8.24\%$  at resonance frequencies of  $2.4$ ,  $3.4$ ,  $5.1$ , and  $5.8$  GHz, respectively. It provided a gain of  $4.25$ ,  $3.12$ ,  $1.52$ , and  $4.58$  dB at resonance frequencies of  $2.4$ ,  $3.4$ ,  $5.1$ , and  $5.8$  GHz,

respectively, and thus satisfied the demand for WLAN/WiMAX applications. The projected antenna revealed good E and H plane radiation characteristics. The design also provided a substantial size reduction, making it possible for the antenna to be placed in a single handheld wireless device to operate at four different resonant frequencies. The productive design was simulated using CST Microwave Studio and compared with experimental results. Both results were validated and showed that this antenna was much compact for use in wireless communication systems.

## ACKNOWLEDGEMENT

The authors are thankful to the management of Kalasalingam Academy of Research and Education (KARE) for providing lab facilities during this research.

## REFERENCES

- Ali, T., & Biradar, R. C. (2017). A compact multiband antenna using  $\lambda/4$  rectangular stub loaded with metamaterial for IEEE 802.11 N and IEEE 802.16 E. *Microwave and Optical Technology Letters*, 59(5), 1000-1006. <https://doi.org/10.1002/mop.30454>.
- Ali, T., Pathan, S., & Biradar, R. C. (2018). Multiband, frequency reconfigurable, and metamaterial antennas design techniques: Present and future research directions. *Internet Technology Letters*, 1(6), Article e19. <https://doi.org/10.1002/itl2.19>
- Aminu-Baba, M., Rahim, M. K. A., Zubir, F., & Yusoff, M. F. M. (2018). Design of miniaturized multiband patch antenna using CSRR for WLAN/WiMAX applications. *TELKOMNIKA Telecommunication, Computing, Electronics and Control*, 16(4), 1838-1845.
- Baliarda, C. P. (1998). On the behavior of the Sierpinski multiband fractal antenna. *IEEE Transactions on Antennas and Propagation*, 46(4), 517-524. <https://doi.org/10.1109/8.664115>
- Casula, G. A., Maxia, P., Montisci, G., Valente, G., Mazzarella, G., & Pisanu, T. (2016). A multiband proximity-coupled-fed flexible microstrip antenna for wireless systems. *International Journal of Antennas and Propagation*, 2016, Article 8536058. <https://doi.org/10.1155/2016/8536058>
- Cheng, Y., Lu, J., & Sheng, B. Q. (2020). MIMO handset antenna for 5G/WLAN applications. *Frontiers of Information Technology & Electronic Engineering*, 21(1), 182-187. <https://doi.org/10.1631/FITEE.1900478>
- Chiang, K. H., & Tam, K. W. (2008). Microstrip monopole antenna with enhanced bandwidth using defected ground structure. *IEEE Antennas and Wireless Propagation Letters*, 7, 532-535. <https://doi.org/10.1109/LAWP.2008.2005592>
- Deepika, R., Manikandan, P., & Sivakumar, P. (2017). Optimization of pyramid horn antenna using genetic algorithm and evolution strategy. In 2017 *IEEE International Conference on Electrical, Instrumentation and Communication Engineering (ICEICE)* (pp. 1-4). IEEE Publishing. <https://doi.org/10.1109/ICEICE.2017.8191862>.

- Deshmukh, A. A., & Tirodkar, T. (2013). Formulation of Resonant Length for Triple Band Slot Cut Stub Loaded Rectangular Microstrip Antenna. *International Journal of Computer Applications*, 975-8887, 23-27.
- Deshmukh, A. A., Pranali, S., Nikita, G., Monika, K., & Ray, K. P. (2012). Analysis of stub loaded equilateral triangular microstrip antennas. In *2012 International Conference on Communication, Information & Computing Technology (ICCICT)* (pp. 1-5). IEEE Publishing. <https://doi.org/10.1109/ICCICT.2012.6398154>
- Dong, Y., & Itoh, T. (2012). Metamaterial-based antennas. *Proceedings of the IEEE*, 100(7), 2271-2285. <https://doi.org/10.1109/JPROC.2012.2187631>
- Dong, Y., Toyao, H., & Itoh, T. (2011). Design and characterization of miniaturized patch antennas loaded with complementary split-ring resonators. *IEEE Transactions on Antennas and Propagation*, 60(2), 772-785. <https://doi.org/10.1109/TAP.2011.2173120>
- Erentok, A., & Ziolkowski, R. W. (2008). Metamaterial-inspired efficient electrically small antennas. *IEEE Transactions on Antennas and Propagation*, 56(3), 691-707. <https://doi.org/10.1109/TAP.2008.916949>
- Firdausi, A., & Alaydrus, M. (2016). Designing multiband multilayered microstrip antenna for mm Wave applications. In *2016 International Conference on Radar, Antenna, Microwave, Electronics, and Telecommunications (ICRAMET)* (pp. 99-102). IEEE Publishing. <https://doi.org/10.1109/ICRAMET.2016.7849591>
- Garg, R., & Long, S. A. (1988). An improved formula for the resonant frequencies of the triangular microstrip patch antenna. *IEEE Transactions on Antennas and Propagation*, 36(4), 570. <https://doi.org/10.1109/8.1148>
- Ishfaq, M. K., Rahman, T. A., Chattha, H. T., & Rehman, M. U. (2017). Multiband split-ring resonator based planar inverted-F antenna for 5G applications. *International Journal of Antennas and Propagation*, 2017, Article 5148083. <https://doi.org/10.1155/2017/5148083>
- Kiran, M. S. (2015). TSA: Tree-seed algorithm for continuous optimization. *Expert Systems with Applications*, 42(19), 6686-6698. <https://doi.org/10.1016/j.eswa.2015.04.055>
- Liu, J., Cheng, Y., Nie, Y., & Gong, R. (2013). Metamaterial extends microstrip antenna. *Microwaves & RF*, 52(12), 69-73.
- Malik, P. K., & Singh, M. (2019). Multiple bandwidth design of micro strip antenna for future wireless communication. *International Journal of Recent Technology and Engineering*, 8(2), 5135-5138. <https://doi.org/10.35940/ijrte.B2871.078219>.
- Manikandan, P., Sivakumar, P., & Swedheetha, C. (2019). Design of adaptive frequency reconfigurable antenna for MIMO applications. In *Soft Computing in Data Analytics* (pp. 203-213). Springer. [https://doi.org/10.1007/978-981-13-0514-6\\_21](https://doi.org/10.1007/978-981-13-0514-6_21)
- Manikandan, P., Sivakumar, P., Krishna, K. S. V., Sumanth, P., & Poornesh, T. (2020). A fractal based CSRR loaded multi-band antenna for wireless applications. *International Journal of Advanced Science and Technology*, 29(7s), 4486-4492.
- Nelaturi, S., & Sarma, N. V. S. N. (2018). CSRR based patch antenna for Wi-Fi and WiMAX applications. *Advanced Electromagnetics*, 7(3), 40-45. <https://doi.org/10.7716/aem.v7i3.700>

- Ntaikos, D. K., Bourgis, N. K., & Yioultsis, T. V. (2011). Metamaterial-based electrically small multiband planar monopole antennas. *IEEE Antennas and Wireless Propagation Letters*, *10*, 963-966. <https://doi.org/10.1109/LAWP.2011.2167309>
- Parchin, N. O., Basherlou, H. J., Al-Yasir, Y. I. A., Abdulkhaleq, A. M., & Abd-Alhameed, R. A. (2020). Reconfigurable antennas: Switching techniques - A survey. *Electronics*, *9*(2), Article 336. <https://doi.org/10.3390/electronics9020336>
- Peixeiro C. (2011). Microstrip patch antennas: An historical perspective of the development. In *2011 SBMO/IEEE MTT-S International Microwave and Optoelectronics Conference (IMOC 2011)* (pp. 684-688). IEEE Publishing. <https://doi.org/10.1109/IMOC.2011.6169224>.
- Rahim, A., Malik, P. K., & Ponnappalli, V. A. S. (2019). Fractal antenna design for overtaking on highways in 5g vehicular communication ad-hoc networks environment. *International Journal of Engineering and Advanced Technology*, *9*(1S6), 157-160. <https://doi.org/10.35940/ijeat.A1031.1291S619>
- Sarkar, D., Saurav, K., & Srivastava, K. V. (2014). Multi-band microstrip-fed slot antenna loaded with split-ring resonator. *Electronics Letters*, *50*(21), 1498-1500. <https://doi.org/10.1049/el.2014.2625>.
- Shaik, N., & Malik, P. K. (2021). A comprehensive survey 5G wireless communication systems: Open issues, research challenges, channel estimation, multi carrier modulation and 5G applications. *Multimedia Tools and Applications*, *80*, 28789-28827. <https://doi.org/10.1007/s11042-021-11128-z>
- Sung, Y. (2014). Multi-band reconfigurable antenna for mobile handset applications. *IET Microwaves, Antennas & Propagation*, *8*(11), 864-871. <https://doi.org/10.1049/iet-map.2013.0525>
- Waterhouse, R. B. (2003). Improving the efficiency of microstrip patch antennas. In *Microstrip Patch Antennas: A Designer's Guide* (pp. 167-195). Springer. [https://doi.org/10.1007/978-1-4757-3791-2\\_4](https://doi.org/10.1007/978-1-4757-3791-2_4)
- Wong, K. L. (2002). *Compact and broadband microstrip antennas*. Jon Wiley & Sons. Inc.
- Xu, H. X., Wang, G. M., Lv, Y. Y., Qi, M. Q., Gao, X., & Ge, S. (2013). Multifrequency monopole antennas by loading metamaterial transmission lines with dual-shunt branch circuit. *Progress in Electromagnetics Research*, *137*, 703-725. <http://dx.doi.org/10.2528/PIER12122409>
- Xu, H. X., Wang, G. M., Qi, M. Q., Zhang, C. X., Liang, J. G., Gong, J. Q., & Zhou, Y. C. (2012). Analysis and design of two-dimensional resonant-type composite right/left-handed transmission lines with compact gain-enhanced resonant antennas. *IEEE Transactions on Antennas and Propagation*, *61*(2), 735-747. <https://doi.org/10.1109/TAP.2012.2215298>
- Zavosh, F., & Aberle, J. T. (1996). Improving the performance of microstrip-patch antennas. *IEEE Antennas and Propagation Magazine*, *38*(4), 7-12. <https://doi.org/10.1109/74.537361>.
- Zong, W. H., Yang, X. M., Li, S. D., Wei, X. Y., & Hou, J. C. (2015). Design and fabrication of a wideband slot antenna for Handset Applications. In *2015 IEEE International RF and Microwave Conference (RFM)* (pp. 161-165). IEEE Publishing. <https://doi.org/10.1109/RFM.2015.7587735>

*Review article*

## A Survey on Model-based Fault Detection Techniques for Linear Time-Invariant Systems with Numerical Analysis

Masood Ahmad<sup>1,2</sup> and Rosmiwati Mohd-Mokhtar<sup>1\*</sup>

<sup>1</sup>*School of Electrical and Electronic Engineering, Universiti Sains Malaysia, Engineering Campus, 14300 Nibong Tebal, Pulau Pinang, Malaysia*

<sup>2</sup>*Department of Electrical and Computer Engineering, COMSATS University Islamabad (Lahore Campus) Lahore, Pakistan*

### ABSTRACT

With the ongoing increase in complexity, less tolerance to performance degradation and safety requirements of practical systems has increased the necessity of fault detection (FD) as early as possible. During the last few decades, many research findings have been developed in fault diagnosis that addresses the issue of fault detection and isolation in linear and nonlinear systems. The paper's objective is to present a survey on various state-of-art model-based FD techniques developed for linear time-invariant (LTI) systems for the interested readers to learn about recent development in this field. Model-based FD techniques for LTI systems are classified as parameter-estimation methods, parity-space-based methods, and observer-based methods. The background and recent progress, in context to fault detection, of each of these methods and their practical applications are discussed in this paper. Furthermore, two different FD techniques are compared via analytical equations and simulation results obtained from the DC motor model. In the end, possible future research directions in model-based FD, particularly for the LTI system, are highlighted for prosperous researchers. A comparison and emerging research topic make this contribution different from the existing survey papers on FD.

*Keywords:* Fault detection, Kalman filter, LTI system, model-based techniques, residual generation

### ARTICLE INFO

*Article history:*

Received: 03 May 2021

Accepted: 15 September 2021

Published: 06 December 2021

DOI: <https://doi.org/10.47836/pjst.30.1.04>

*E-mail addresses:*

masoodjaffar@student.usm.my (Masood Ahmad)

eerosmiwati@usm.my (Rosmiwati Mohd-Mokhtar)

\* Corresponding author

### INTRODUCTION

In the era of science and technology, every engineering system demands accuracy, reliability, and safety during its operation. However, to realize such systems, i.e., high-

speed trains, power systems, aircraft, and chemical plants, increases the system complexity and financial cost. Moreover, any abnormal behavior in a safety-critical system causes performance degradation and leads to a dangerous situation. Thus, detecting and locating the fault early is important to ensure safety and reliability by taking necessary measures (Li et al., 2016; Franklin et al., 2019).

A fault is an unexpected event and input to the system that can occur in any part of the system. Concerning the location of occurrence, it is generally classified as an actuator fault (loss of control), a sensor fault (improper functioning of measuring components), and a component fault (variation in the system's internal parameters). Actuator and sensor faults can be considered additive faults, while component faults are multiplicative faults (Frank et al., 2000). Faults can also be classified according to their time behavior, i.e., abrupt fault, incipient fault, and intermittent fault. Any fault in a system causes poor performance and leads the entire system to collapse if it is not timely handled (Jie & Patton, 2012; Liu et al., 2018; Na & Ahmad, 2019).

The fault diagnosis system is composed of three sub-systems. Each subsystem is merged with the capabilities of detection, isolation, and identification (estimation) of the fault. FD is the first step in the fault diagnosis process that indicates the fault and its time of occurrence in the system. Fault isolation determines the location of a fault, and fault identification finds the type and size of a fault (Gao et al., 2015). Generally, fault diagnosis methods are model-based and data-driven methods depending on the system model information (Isermann, 1997). Data-driven-based FD methods solve the FD problem directly from online process data. Therefore, these techniques are more suitable for large-scale complex systems (Ding, 2014). On the other hand, model-based FD techniques utilize the analytical model of the process that reveals the physical meaning of process dynamics through the mathematical description. Ample of research has been done on model-based fault diagnosis and their applications on various linear and nonlinear systems during the last few decades (Gertler, 2017; Jie & Patton, 2012; Isermann, 2006; Ding, 2013). Therefore, model-based techniques are chosen in many practical scenarios, provided that the analytical model of the process is well-established.

The core idea of the model-based FD technique is to reconstruct/estimate the output of a practical system using the analytical model, and the reconstructed output is compared with the actual output of the system measured from sensors. The difference between the two outputs is a residual signal, which indicates fault occurrence in the practical system. The model-based FD system is depicted in Figure 1. Residual evaluation refers to the process of extracting fault information from residuals to differentiate between fault and disturbance. Finally, a binary decision about the occurrence of a fault is made by comparing the evaluated residual signal with the pre-defined threshold. Hence, a model-based fault detection system consists of two subsystems: residual generation, residual evaluation, and

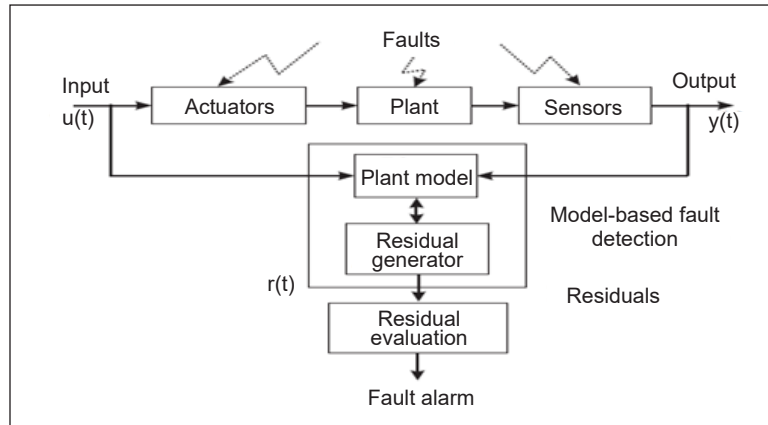


Figure 1. Model-based fault detection system (Chen et al., 2011)

threshold computation (Ding, 2013). In case of fault occurrence, an alarm is generated to intimate the operator, or some control action is taken to compensate the effect of fault for the smooth operation of an entire system. The process of modifying the control action according to fault nature is called fault-tolerant control (FTC). A detailed discussion on FTC is available in Zhang and Jiang (2008).

There are three main types of model-based fault detection techniques according to the way of residual generation. They are known as observer-based FD techniques, parity-space-based FD techniques, and parameter-estimation-based FD techniques (Isermann, 1984). Observer-based fault detection techniques correspond to the design of an observer for estimating system output and residual generation. In the parity-space-based approach, residual is generated by eliminating the initial states of dynamic systems and utilizing only system input and measurement data within a finite time window. The prime objective of both techniques is to ensure the robustness of residual against the process and measurement of unknown inputs. Finally, the parameter-estimation approach is used to detect the slight change/drift in the system parameters by comparing the actual parameters of the nominal process with the estimated parameters.

Considering the massive monetary losses caused by the faults, there is a need to find the solution for FD problems in safety-critical applications in the presence of unknown inputs and system parameter variations. External unknown inputs and parameter variations make the FD more intricated. In addition, FD becomes more complex in the closed-loop configuration because a fault in the system gets buried rapidly by the control actions. Most of the existing survey papers discussed the FD methods for nominal linear systems. This survey paper aims to look at another perspective, in which it presents state-of-art model-based fault detection techniques recently developed for the linear time-invariant (LTI) systems in open and closed-loop configurations and subjected to unknown inputs and uncertainties simultaneously. Also, two well-known FD techniques, Kalman filter (Blanke

et al., 2015) and optimal FD filter (Ding, 2013), are compared using an analogy in observer gain matrices and by simulations in this survey paper to demonstrate the clear picture of the FD process. Sensor and actuator fault in a linear model of DC motor is detected using both FD techniques. Their performance is compared in terms of detectability, computational burden, and design complexity.

Unlike other review papers that focused on the same subject, our paper also included a numerical comparison of fault detection techniques, and the simulation results were shown for verification. Furthermore, based on the review, future research direction in model-based fault detection approach is added to give the readers an idea and way forward to extend the research in this field. It is significant because the review outcome from this paper can be used as a reference for the readers of interest.

### LTI SYSTEM WITH DISTURBANCE AND FAULT

LTI system subject to disturbance and fault can be expressed in the form of state-space representation as Equations 1 and 2:

$$x(k+1) = Ax(k) + Bu(k) + E_d d(k) + E_f f(k) \quad (1)$$

$$y(k) = Cx(k) + Du(k) + F_d d(k) + F_f f(k) \quad (2)$$

$x(k) \in R^n, u(k) \in R^p, y(k) \in R^q$  are state, input, output vectors respectively.  $d \in R^{k_d}$  is  $l_2$ -norm bounded unknown input vector and  $f \in R^{k_f}$  is  $l_2$ -norm bounded unknown fault vector.  $(A, B, C, D, E_d, E_f, F_d, F_f)$  are known matrices with appropriate dimensions. Furthermore,  $E_f$  and  $F_f$  represent the place where the fault occurs and its influence on the system dynamics (Ahmad et al., 2017). Component/process fault or modeling error in the system may cause the change of parameters of process dynamics. Equations 1 and 2 can be represented by incorporating the process fault (Equation 3).

$$x(k+1) = (A + \Delta A)x(k) + (B + \Delta B)u(k) + E_d d(k) + E_f f_a(k)$$

$$y(k) = (C + \Delta C)x(k) + (D + \Delta D)u(k) + F_d d(k) + F_f f_s(k) \quad (3)$$

Where  $(\Delta A, \Delta B, \Delta C, \Delta D)$  represents the component faults/modeling errors. There are normally four types of sensor faults: sensor drift fault, sensor offset fault, fixed scaling factor fault, and sensor stuck fault. In addition, the same type of fault could be categorized for actuators (Franklin et al., 2019). It is important to mention here that this survey only focuses on additive fault detection techniques (sensor/actuator fault).



## PARAMETER-ESTIMATION-BASED RESIDUAL GENERATION

The core of the parameter-estimation technique is based on system identification by utilizing the system's measured input and output data. In this technique, system parameters of a practical system are identified either offline or online under the normal operating condition while assuming that the fault is reflected in the system's physical parameters. In the context of FD, residual is defined as a comparison between nominal parameters of the system in a fault-free case and estimated parameters. The estimated parameters should match with the system parameters in a fault-free situation. Any discrepancy in process parameters indicates the change/fault in the system. Parameters are estimated using parameter-estimation algorithms, i.e., least squares (LS), recursive least squares (RLS), regularized LS, or extended least squares (ELS). These methods can be applied to any engineering system, provide the inherent information of system dynamics. The exploitation of these methods leads to an efficient fault detection and control system (Ding, 2013). Jesica and Poznyak (2018) developed a new technique using the Kalman filter and instrument variable method for parameter estimation in the stochastic system. The proposed technique minimized the influence of Gaussian noise and removed the biases in estimation, which remains available in standard least square methods. The designed scheme also improved the convergence speed.

Bachir et al. (2006) used the offline parameter-estimation technique for stator inter-turn short circuit fault and broken rotor bar detection. In this study, a new model of an induction machine for stator and rotor has been developed for fault detection. They introduced the new parameters in the original model of the induction machine for stator inter-turn fault detection and the design of a new faulty model for broken rotor bars detection.

Generally, the parameter-estimation technique requires one input and output signal, and it provides a more detailed picture of internal process quantities. Therefore, this technique is more suitable for component fault detection. However, it can be used for sensor/actuator fault detection as well. The major disadvantage is that it always needs an excitation signal for initiating the parameter-estimation process, which may not be suitable for the process, operating at a stationary point (Isermann, 2006). In addition, the parameter-estimation technique is less robust to unknown inputs that may affect the estimation process. Nevertheless, the performance of parameter-estimation-based- FD systems has been demonstrated by many successful applications in industrial processes and automatic control systems (Belmokhtar et al., 2015; Ye et al., 2015; Herrera & Yao, 2018; Khang et al., 2018).

## PARITY-SPACE-BASED RESIDUAL GENERATION

In a parity-space-based approach, a residual is generated by eliminating the effect of initial states of a dynamic system and utilizing only the system input and measurement data within

a finite time window. The inconsistency arises in the residual in case of abnormal behavior evolving in the system dynamics. For example, the parity-space-based fault detection system has been studied (Sun et al., 2019; Zhang et al., 2006; Zhong et al., 2018). This section discusses parity-space-based FD for a linear discrete-time system in terms of design and implementation issues.

Consider Equation 1. The following parity relation can be established (Equation 4).

$$y_s(k) = H_{o,s}x(k - s) + H_{u,s}u_s(k) + H_{d,s}d_s(k) + H_{f,s}f_s(k) \quad (4)$$

Where  $\theta_s(k) = [\theta^T(k - s), \theta^T(k - s + 1), \dots, \theta^T(k)]$ , while  $\theta = [y, u, d, f]$  and  $s$  is the order of parity-space and

$$H_{o,s} = \begin{bmatrix} C \\ CA \\ \vdots \\ CA^s \end{bmatrix}, H_{u,s} = \begin{bmatrix} D & 0 & \dots & 0 \\ CB & D & \ddots & \vdots \\ \vdots & \ddots & \ddots & 0 \\ CA^{s-1}B & \dots & CB & D \end{bmatrix}$$

$H_{d,s}, H_{f,s}$  can be obtained by substituting  $(E_d, F_d)$  and  $(E_f, F_f)$  in place of  $(B, D)$  in  $H_{u,s}$ . Residual generator based on parity relation vector can be written as Equation 5.

$$\begin{aligned} r(k) &= M[y_s(k) - H_{u,s}u_s(k)] \\ &= M[H_{d,s}d_s(k) + H_{f,s}f_s(k)] \end{aligned} \quad (5)$$

$r(k)$  is a residual signal and  $M$  is donated as a parity-space matrix, which contains a set of parity vectors and is defined as parity space,  $P_{sk} = [M | MH_{o,s} = 0]$ . Let us denote  $v_s$  is the parity vector and holds the condition  $[v_s \in P_{sk}]$  then residual in Equation 5 can be represented as Equation 6.

$$r(k) = v_s[H_{d,s}d_s(k) + H_{f,s}f_s(k)] \quad (6)$$

Equation 6 clearly shows that parity relation-based residual design only requires the computation of parity vector  $v_s$ . In a fault-free case,  $(f(k) = 0)$ ,  $d_s(k)$  can be perfectly decoupled from the residual if the rank condition is satisfied  $(M[H_{o,s}H_{d,s}] = 0)$ . However, the condition looks stringent and very hard to satisfy for practical systems. In such cases, the preferred solution for residual design is to apply the optimization technique to make an appropriate trade-off between robustness and sensitivity. For this purpose, several objective functions, with the prime aim to achieve the trade-off between robustness against disturbances and sensitivity to faults, have been defined. The following performance index is widely adopted for a parity-space-based residual generation (Equation 7) (Ding, 2013; Gertler, 2017).

$$J_s = \min_{v_s} \frac{\|v_s H_{d,s}\|_2}{\|v_s H_{f,s}\|_2} \quad (7)$$

For successful fault detection, the  $l_2$ -norm of a residual signal in Equation 6 is the most commonly used evaluation function and is defined as Equation 8 (Ding, 2013).

$$\|r(k)\|_2 = \sqrt{\sum_{k=0}^{k=\infty} r^T(k)r(k)} \quad (8)$$

A threshold can be set as  $J_{th} = \|d(k)\|_2^2 = \delta_d$  ( $\delta_d$  is an upper bound of disturbance energy) in a fault-free case. In the last step, the decision logic is used to declare the fault alarm.

An optimized parity-spaced-based fault detection algorithm was developed in (Odendaal & Jones, 2014) for actuator fault detection in Meraka Modular UAV. The study optimized the parity relation, obtained from the standard parity-space approach, using the transformation matrix that forms the residual more sensitive to the fault. The said approach improved the computational burden compared to the online computation of covariance matrices at every instant in the Extended Kalman filter. As compared to FD techniques in an open-loop, fault detection in a closed-loop control system is much complicated because a closed-loop is more robust against exogenous inputs. External inputs surround a fault signal with low amplitude, and closed-loop control input makes the fault signal smaller. The phenomena reduce the fault detection performance and fault detection rate significantly. Sun et al. (2019) proposed a parity-space transformation-based fault detection system for the closed-loop control system. A stable kernel matrix for parity-space transformation was designed to obtain the more accurate parity-space in a closed-loop system that improves the fault detection performance. Furthermore, the fault detection rate has been improved by accumulating the residual in a time window.

Zhong et al. (2018) demonstrated an integrated design of residual generation and residual evaluation for fault detection in a linear discrete-time system subject to unknown input without complete knowledge of probability distribution. The study focuses on parity-space-based FD design to achieve an optimal trade-off between false alarm rate (FAR) and missed detection rate (MDR). Determination of parity-space vector and optimization of FAR and MDR are formulated in the minimum error minimax probability machine (MEMPM) framework. The proposed algorithm delivers an optimal trade-off between MDR and FAR in the worst-case scenario of unknown inputs without the information of stochastic distribution.

Equation 6 demonstrates that the residual generator requires the past data of input and output measurements; hence, this residual generator is preferred for discrete-time dynamic systems only. Furthermore, it is important to mention that parity-space-based residual generators are more sensitive to unknown inputs because of their open-loop structure than the observer-based residual generator, which has a closed-loop configuration and is less sensitive to unknown input and system uncertainties. Despite the advantage of design simplicity, knowledge of previous data and constraints on parity-space order makes the parity-space-based residual generator non-ideal for online implementation. The solution to these two problems is a one-to-one mapping between the design parameters of the observer-based technique and the parity-space-based technique. This scheme is known as parity-space design, observer-based implementation (Ding, 2013; Isermann, 2006). By taking advantage of both designs, less design effort of parity-space vector, and online realization of the observer, this scheme can also be used for continuous-time systems.

The parity-space-based technique is well applied for FD purposes in the induction motor drive system (Dybkowski & Klimkowski, 2017), electromechanical brake systems (Hwang & Huh, 2015), vehicles (Wang et al., 2019), and power systems (Rasoolzadeh & Salmasi, 2020).

## **OBSERVER-BASED RESIDUAL GENERATION**

A survey on observer-based FD techniques for the LTI system is presented in this section. FD system based on Kalman filter is presented first for stochastic LTI systems with Gaussian noise. Next, unknown input observer (UIO) is discussed for perfectly decoupling the unknown input, followed by a discussion on optimal observer design for deterministic LTI systems subjected to norm-bounded unknown inputs and uncertainties.

### **Kalman Filter-based Fault Detection**

A stochastic system is a dynamic system subjected to a stochastic/random noise, i.e., Gaussian noise with mean value and variance. The first stochastic fault detection system was developed using the innovations (residuals) generated by the Kalman filter (Mehra & Peschon, 1971). A well-known Kalman filter, which looks like an observer in a deterministic environment, is used to estimate the system's state based on a series of measurements taken in time, having system inaccuracies and statistical noise. The residual signal contains the information of fault and the mutual effect of uncertainties, process, and measurement noise. Stochastic residual evaluation techniques are used to eliminate these undesired effects and recover the fault information from the residual. These techniques use the residual's statistical properties, i.e., mean, variance, and covariance, and try to detect statistical parameters change. Several statistical methods are available in the literature to evaluate

the residual generated by the Kalman filter for fault detection purposes. A few of these methods are the chi-square test (Da & Lin, 1996), multiple hypothesis tests (Bøgh, 1995), generalized likelihood ratio (GLR) test (Willsky & Jones, 1976), and cumulative sum algorithms (Nikiforov et al., 1993).

Kalman filter provides an optimal estimate of system states, i.e., minimum covariance of error between estimated and actual states of the system. The unified approach is presented in Doraiswami and Cheded (2013) to detect and isolate the fault in a linear discrete-time system with measurement and system noise using the Kalman filter. Switched Kalman filter is designed for sensor fault detection and isolation in power converters (Kleilat et al., 2018). The proposed filter is an extended version of the standard Kalman filter combined with a disturbance decoupling observer and has confirmed satisfactory results disturbance. The incipient sensor fault detection in the continuous stirred-tank reactor benchmark process has been addressed in Gautam et al. (2017) using Kalman filter and GLR test. In this technique, signal to noise ratio (SNR) index is used to determine the threshold for successful fault detection with minimum false alarm and missed detection rate.

As physical and technological constraints arose in the industrial system due to complexity and robustness, many researchers developed modified and enhanced versions of the Kalman filter to cope with the advanced requirements of the system. As a result of dedicated research towards the development of stochastic fault detection techniques, in parallel with ongoing research on deterministic fault detection techniques, improved versions of Kalman filter is obtained, such as extended Kalman filters (EKF), unscented Kalman filters (UKF), adaptive Kalman filters, and augmented state Kalman filters.

An Extended Kalman filter is commonly used for estimating the non-measurable states of a nonlinear dynamic system (Jokic et al., 2018). Extended Kalman filter has shown good results random disturbances; however, owing to nonlinearity in states and measurements of the system, it is imperative to get the linearized and Jacobian matrix of the system model. Moreover, the linearization process reduces the estimation performance of EKF that might lead to instability of the filtering process for fault detection purposes.

Unscented Kalman filter overcomes the drawbacks of the EKF approach. UKF uses the unscented transform, i.e., a good approximation of the stochastic distribution of state rather than nonlinear function. Therefore, this method is straightforward and efficient for estimating the system states for nonlinear dynamic systems leading to better fault detection performance (Khazraj et al., 2016). However, in some cases, EKF requires a precise value of measurement and process noise covariance matrix. This condition is not often practical, leading to another version of the Kalman filter, i.e., adaptive Kalman filter.

An adaptive Kalman filter is used to tune the measurement noise covariance matrix and system noise covariance matrix according to noise conditions to obtain a satisfactory fault diagnosis (Hajiyev & Soken, 2013). According to the literature, researchers classify the

adaptive filters into four types: Bayesian-based, maximum likelihood-based, correlation-based, and covariance matching techniques (Tripathi et al., 2016). In addition, the augmented Kalman filter is often used to estimate the system states and fault and disturbance signals simultaneously (Gannouni & Hmida, 2017). Various applications of Kalman filter-based fault detection system can be found in the gas turbine engine (Pourbabaei et al. 2016), synchronous generator (Nadarajan et al., 2016), power systems (Liu & He, 2017), wind turbine system (Cho et al., 2018), and aircraft (Marzat et al., 2012).

### **UIO-based Fault Detection**

Fault detection system should be robust against all undesired inputs such as process and measurement disturbance. Initially, it was proposed to decouple the unknown input from the state estimation process using the disturbance distribution matrix. If system states are decoupled from unknown disturbance, then residual is, obviously, also independent (Ding & Frank, 1990; Wünnenberg & Frank, 1987). The decoupling observer is known as the unknown input observer (UIO), a type of Luenberger observer, principally to estimate state variables.

In the Eigen structure assignment method, left eigenvectors of the observer gain matrix are assigned so that gain's left eigenvectors are orthogonal to the disturbance distribution matrix to make residual signal robust (Patton & Chen, 2000). In this approach, instead of decoupling unknown input from the state estimation process, the residual signal is made independent of unknown input. The geometric approach is used by (Hur & Ahn, 2014) to decouple the effect of disturbance from the residual. All the above approaches (UIO, Eigen structure assignment approach, and geometric approach) address the problem of disturbance decoupling from the residual. However, these approaches are not capable of handling the model uncertainties. One possible solution to tackle the model uncertainties is to model them as an unknown input and then apply the disturbance decoupling techniques further.

The inverter incipient sensor fault is successfully detected and accommodated in three-phase PWM inverters in the traction system (Zhang et al., 2017). UIO technique has been widely used in many applications of FD, aircraft systems (Hur & Ahn, 2014), gas turbine engines (Dai et al., 2009), cyber-physical systems, and wind energy systems (Zhu & Gao, 2014). However, as stated in Ding (2013), the existing condition of the disturbance decoupling technique is stringent and hard to achieve for many practical systems. Moreover, the decoupling technique is also not suitable for cases where fault vector lies in the same space as disturbance vector that may lead to a decoupling of fault signal from residual as well, just like disturbance. An alternate strategy, widely adopted, is to design an observer to make a suitable compromise between robustness to unknown input and sensitivity to fault. It makes the fault detection problem a multi-objective design problem.

### Optimized Observer/FDF-based Fault Detection

Fault Detection Filter (FDF), a well-known realization of full order state observer, generates the residual for fault detection purposes. FDF structure for Equations 1 and 2 can be represented by the following Equation 9:

$$\begin{cases} \hat{x}(k+1) = A\hat{x}(k) + Bu(k) + L(y(k) - \hat{y}(k)) \\ \hat{y}(k) = C\hat{x}(k) + Du(k) \\ r(k) = V(y(k) - \hat{y}(k)) \\ r(k) = V[Ce(k) + F_d d(k) + F_f f(k)] \end{cases} \quad (9)$$

$\hat{x}(k) \in R^n$ ,  $\hat{y}(k) \in R^q$  is the state estimation vector and measurement estimation vector, respectively.  $r(k)$  is a so-called residual signal.  $L$  and  $V$  are two design parameters of FDF. Observer gain  $L$  is determined in such a way that estimation error asymptotically goes to zero. The residual in Equation 9 can be rewritten in the frequency domain as Equation 10:

$$r(z) = G_{rd}d(z) + G_{rf}f(z) \quad (10)$$

Where

$$G_{rd} = C(zI - A + LC)^{-1}(E_d - LF_d) + F_d$$

$$G_{rf} = C(zI - A + LC)^{-1}(E_f - LF_f) + F_f$$

It can be observed from Equation 9 that residual is dependent on fault and unknown input signal.  $H_\infty$  norm represents the maximum influence of disturbance on residual and is widely used to improve the robustness of residual against the unknown inputs (Zhou & Zhang, 2019). Furthermore, to analytically represent the influence of fault on the residual,  $H_\infty$  norm,  $H_2$  norm, and  $H_-$  index are successfully adopted for FDF design. Robustness to unknown input/disturbance while, at the same time, sensitivity to fault makes the design of FDF a multi-objective optimization problem. This way, optimal observer gain can be obtained by solving the following optimization problem over some specified frequency range (Equation 11).

$$L^*, V^* = \arg \left( \max_{L, V} \left( \frac{\|G_{rf}\|}{\|G_{rd}\|} \right) \right) \quad (11)$$

There are several forms of performance indices (i.e.,  $\frac{H_\infty}{H_\infty}, \frac{H_-}{H_\infty}, \frac{H_2}{H_\infty}$ ) are available for solving Equation 11. In addition,  $L^*, V^*$  are optimal parameters of FDF in Equation 9 that deliver a residual which has maximum robustness to unknown inputs and maximum sensitivity to faults (Ding, 2013).

Optimal FDF design for linear system formulated as a multi-objective optimization problem (Ding et al., 2000) and unified solution for the optimization problem is obtained using factorization technique which is realized by solving the Riccati equation. Aguilera et al. (2016) designed an observer-based fault detection system to detect the current sensor fault in the induction motor drive. A differential geometric approach is used in this study to detect and isolate the single and multiple faults, i.e., disconnection, offset, and constant gain faults.

The prime objective of all techniques developed for the solution of Equation 11 is to obtain an optimal trade-off between robustness and sensitivity. These techniques are well-suited for fault detection in linear systems subjected to unknown disturbances only. However, in model-based FD techniques, another issue often encounters in the residual generation process is model mismatching. A perfect mathematical model of a practical system is never available because of modeling error, process linearization, and component aging issues. Hence, optimization techniques that solve Equation 11 cannot be applied to uncertain systems.

System uncertainty severely affects the output estimation that leads to poor performance of fault detection. Robust FDF has been designed for continuous LTI systems subjected to disturbance and norm-bounded uncertainty (Zhong et al., 2003). Robust FD problem is formulated as  $H_\infty$  model matching problem, and solution of the optimization problem is presented in linear matrix inequality (LMI) form in the said paper. Li et al. (2013) extended the same work discussed in Ding et al. (2000) for continuous-time linear uncertain systems subjected to polytopic uncertainty utilizing the iterative LMI approach. Farhat and Koenig (2015) formulated the proportional integral observer (PIO) design problem as a multi-objective optimization problem for the continuous-time linear uncertain system. The robustness to disturbance and uncertainty has been ensured minimizing the  $H_\infty$  norm of  $G_{rd}$  in the LMI framework.

Although the designed robust FDF, with and without system uncertainty, somehow minimizes the effect of disturbances and uncertainties, these are not completely decoupled from the residual. These unknown inputs still influence the residual. In such cases, the appropriate residual evaluation function and threshold computation selection are integral in successful fault detection. The final decision on the occurrence of a fault is made using a simple comparison between residual evaluation function and threshold.

There are two widely accepted ways to generate evaluation function and threshold depending on the system's dynamics under consideration. Generally, the norm-based residual evaluation function is used for a deterministic system in which the energy of unknown input is bounded under a certain limit ( $\|d(k)\|_2 \leq \delta_d$ ). On the other hand, a statistical-based residual evaluation function is adopted for stochastic systems. For deterministic systems,  $l_2$ -norm is a mostly used evaluation function and is defined in [8]. Peak value, root mean square value, and moving average of residual is also used



for residual evolution function. We refer our esteemed readers to Ding et al. (2003) for more knowledge and computational skills. In case, residual is dependent on disturbance, uncertainty, and fault signal, then residual, generated by any of the methods discussed above, can be represented as Equation 12:

$$\|r(k)\|_2^2 = \|r_d(k) + r_u(k) + r_f(k)\|_2^2 \quad (12)$$

In a fault-free case,  $\|r_f(k)\|_2^2 = 0$ , the threshold can be defined as Equation 13:

$$J_{th} = \sup(\|r(k)\|_2^2) \quad (13)$$

### Other Observer-based Fault Detection Techniques

Besides the previously discussed Kalman filter, UIO, and optimized FDF schemes, other types of fault detection observers in the literature have been investigated for LTI systems. Those are a proportional-integral observer (Do et al., 2018; Yang et al., 2020), sliding mode observer (Zhirabok et al., 2018; Zhang et al., 2019), interval observer (Pourasghar et al., 2020; Zammali et al. 2020), and adaptive observer (Lijia et al., 2019; Perrin et al., 2004). These observers are designed to estimate the system output with minimum output estimation error and fast convergence speed. Then output estimation error is used as a residual to indicate the fault occurrence.

## DISCUSSION

In this section, a comparison among various fault detection techniques discussed so far is given in terms of robustness, complexity, and performance. The robustness of the fault detection method is checked by the measure of sensitivity to noise, disturbance, and uncertainty. Likewise, robustness and the performance of the fault detection method are determined in terms of FAR and MDR. Based on the above survey, the following points are highlighted:

1. An observer generates the residual for fault detection, and it is synthesized to zero in fault-free cases. Observer-based and parity-space-based FD methods produce the alike residual in terms of residual characteristics. However, the observer-based method shows more robustness to uncertainty as compared to the parity-space-based residual generator.
2. FDF is a complete state observer, while an unknown input observer is a reduced-order observer and might be considered where full state estimation is not required. UIO has more robustness to unknown inputs with increased complexity and computational effort.
3. Observer-based and parity-space-based fault detection methods are designed for additive faults and perform well when the plant model is perfect.

4. Observer-based and parity-space-based FD system design requires the knowledge of robust control theory when there is uncertainty and unmodeled disturbance in the linear systems. These unwanted inputs are handled by selecting a higher detection threshold in the second step of the fault detection process. However, a higher detection threshold causes to increase in the FAR, and a lower detection threshold cause to increase in the MDR. Therefore, a feasible trade-off is required between FAR and MDR for successful fault detection.
5. Optimization-based FD methods are formulated so that the sensitivity of residual to unknown inputs is minimized along with improved sensitivity to faults. Such methods provide a solution in terms of mathematical multi-objective functions. There could be one disadvantage: it might not guarantee the usefulness and performance of the solution in some applications. Hence, special care is required while implementing optimized FD methods in the underlying application, which may also increase complexity.
6. Kalman filter-based FD system is used for stochastic systems, and much knowledge of statistical analysis and probability is required. Different versions of the Kalman filter can be applied to nonlinear systems and time-varying systems as well.
7. Fault detection methods relying on system identification are useful for linear and nonlinear systems, but the performance of such FD systems entirely depends on detecting the variation in system parameters. Moreover, these fault detection methods are beneficial for detecting small and incipient faults.
8. The major disadvantage of the model-based FD method is to get the precise mathematical model of the system. This reason restricts the application of the model-based FD methods to industrial systems. In such cases, data-driven techniques are advantageous when the system model is unavailable (Denkena et al., 2020).
9. The parameter-estimation method produced good results in detecting structural damage, while all other model-based methods are well suited for detecting the actuator and sensor faults.
10. The selection of an appropriate detection technique depends on the reliability of the available knowledge of the system.

## COMPARISON OF FAULT DETECTION TECHNIQUES

This section compares two well-known fault detection techniques in terms of detectability, design complexity, and computational load. For this purpose, a linear DC motor model is simulated in MATLAB for sensor and actuator fault detection. First, a unified solution of an optimal FDF developed in Ding (2013) for Equations 1 and 2 subjected to deterministic disturbance is compared with Kalman filter-based optimal estimator for stochastic LTI

system (Blanke et al., 2015). Both FD techniques confirm good performance in terms of fault detection if an unknown disturbance lies within bound and there is no system uncertainty. Second, the state-space model of DC motor in Equations 1 and 2 has the following matrices:

$$A = [0.2231 \ 0.0109; -0.0022 \ 0.5488], \quad B = [0.0047; 0.4512], \quad C = \text{eye}(2), \quad D = 0$$

$$E_d = E_\omega = [-1.5537; 0], \quad F_d = F_f = C, \quad E_f = B$$

### Kalman Filter Design

Residual generation for stochastic LTI system (Equation 14):

$$x(k+1) = Ax(k) + Bu(k) + E_\omega \omega(k) + E_f f(k)$$

$$y(k) = Cx(k) + Du(k) + v(k) + F_f f(k) \quad (14)$$

Let  $\omega(k)$  and  $v(k)$ , be zero-mean process and measurement noise with following covariance matrix,  $E \left( \begin{bmatrix} \omega(k) \\ v(k) \end{bmatrix} \begin{bmatrix} \omega^T(i) & v^T(i) \end{bmatrix} \right) = \begin{bmatrix} \sigma_\omega^2 & S_{ki} \\ S_{ik} & \sigma_v^2 \end{bmatrix}$ . The dynamics of the Kalman filter-based residual generator is represented by Equation 15:

$$\hat{x}(k+1) = A\hat{x}(k) + Bu(k) + K(y(k) - \hat{y}(k))$$

$$r(k) = y(k) - \hat{y}(k) = Ce(k) + v(k) + F_f f(k) \quad (15)$$

$K$  is Kalman filter gain and can be determined as  $K = (APC^T + E_d S)[CPC^T + \sigma_v^2]^{-1}$ , While  $P$  can be obtained by solving the following Riccati Equation 16:

$$P = APA^T - K[CPC^T + \sigma_v^2]K^T + \sigma_\omega^2 \quad (16)$$

The residual evaluation and threshold are given as Equation 17:

$$J(k) = r(k)^T (\sigma_{RES(k)}^2)^{-1} r(k) \quad (17)$$

Where  $\sigma_{RES}^2 = E[r(k)r^T(k)] = CPC^T + \sigma_v^2$ . Threshold could be defined as  $J_{th} = \chi_\alpha^2(n)$ , where  $\alpha$  is given false alarm rate (FAR) and  $n$  is the number of output signals. The threshold is computed using chi-square ( $X^2$ ) test.

### Unified Solution of Optimal FDF

Residual generation for deterministic LTI system in Equations 1 and 2,  $d(k)$  is  $l_2$  norm bounded unknown disturbance, holds ( $\|d(k)\|_2 \leq \delta_d$ ). Optimal FDF of the form in Equation 11, observer gain  $L$  and post-filter  $V$  is obtained using the unified solution

Equation 18:

$$\begin{aligned}
 L &= (AXC^T + E_d F_d^T)(F_d F_d^T + CXC^T)^{-1} \\
 V &= (F_d F_d^T + CXC^T)^{-0.5} \\
 X &= AXA^T - L(F_d F_d^T + CXC^T)L^T + E_d E_d^T
 \end{aligned} \tag{18}$$

Where,  $X$  is a solution of the above Riccati equation. Residual obtained from unified solution is an optimal solution because, in fault-free case, the effect of  $d(k)$  on the residual is uniform in the entire subspace spanned by the disturbance  $d(k)$ . Thus Equation 9 serves as a residual evaluation function, and the threshold is taken as the upper limit of disturbance energy (Equation 19).

$$J_{th} = \delta_d \tag{19}$$

Table 1 describes the comparison in gain matrices of the Kalman filter and optimal FDF. It is shown that the gain of both filters depends on their noise characteristics. The following comparison reveals no difference between these two filters, and they deliver optimal residual in terms of robustness if there is no system uncertainty.

Table 1  
Comparison between FD techniques via gain equations

$K = (APC^T + E_d S)[CPC^T + \sigma_v^2]^{-1}$	$L = (AXC^T + E_d F_d^T)(F_d F_d^T + CXC^T)^{-1}$	
$P = APA^T - K[CPC^T + \sigma_v^2]K^T + \sigma_\omega^2$	$X = AXA^T - L(F_d F_d^T + CXC^T)L^T + E_d E_d^T$	
$J(k) = r(k)^T (\sigma_{RES(k)}^2)^{-1} r(k)$	$J(k) = r^T(k) V^T V r(k)$	
$\sigma_{RES}^2 = CPC^T + \sigma_v^2$	$V = (F_d F_d^T + CXC^T)^{-0.5}$	
$E_d S$	$\longleftrightarrow$	$E_d F_d^T$
$\sigma_v^2$	$\longleftrightarrow$	$F_d F_d^T$
$\sigma_\omega^2$	$\longleftrightarrow$	$E_d E_d^T$
<b>r(k) is zero-mean white noise with the covariance matrix <math>\sigma^2 v</math></b>		<b>r(k) is an all-pass filter in fault-free case, i.e., the beauty of a unified solution</b>

### Comparison by Simulation

For simulation purposes, the following assumptions are considered,  $x(0) = [0,0]^T$ ,  $u(k) = 0.5$ , the covariance of Gaussian noise:  $\sigma_v^2 = 0.0025$ ,  $\sigma_\omega^2 = 0.0012$ , FAR = 10% and  $d(k) \in [-0.01, 0.01]$ .

The following simulation results have been observed: Figure 2 illustrates that system output estimates are close to actual measurement in fault-free cases. Thus, residual obtained from both schemes prove robustness to unknown disturbance/noise. Figure 3 demonstrates a speed sensor fault case in which ramp input as an incipient fault is injected at 2.2 sec. It is observed that the detection time of the Kalman filter is high as compared to optimal FDF. In this case, the Kalman filter has shown less robustness to a time-varying fault in the DC motor speed sensor. Finally, Figure 4 confirms the effectiveness of both schemes in terms of robustness and detection time in actuator stuck fault conditions.

Simulation results confirm that both approaches have shown better performance under unknown inputs. However, they have limited capability of FD in the presence of system uncertainty and may deliver large FAR and MDR. Therefore, a fault-sensitive filter has

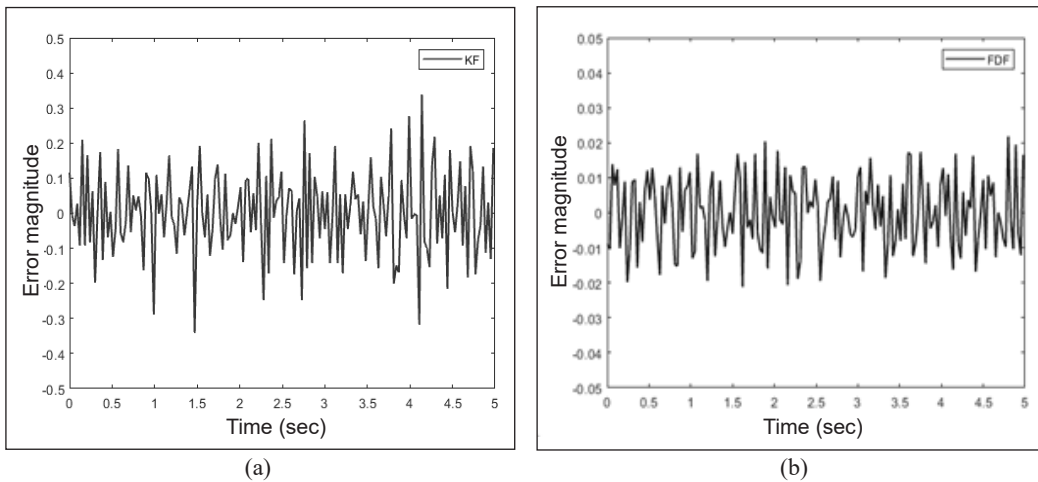


Figure 2. Residual,  $f(k) = 0$  from (a) Kalman filter (left); and (b) optimal FDF

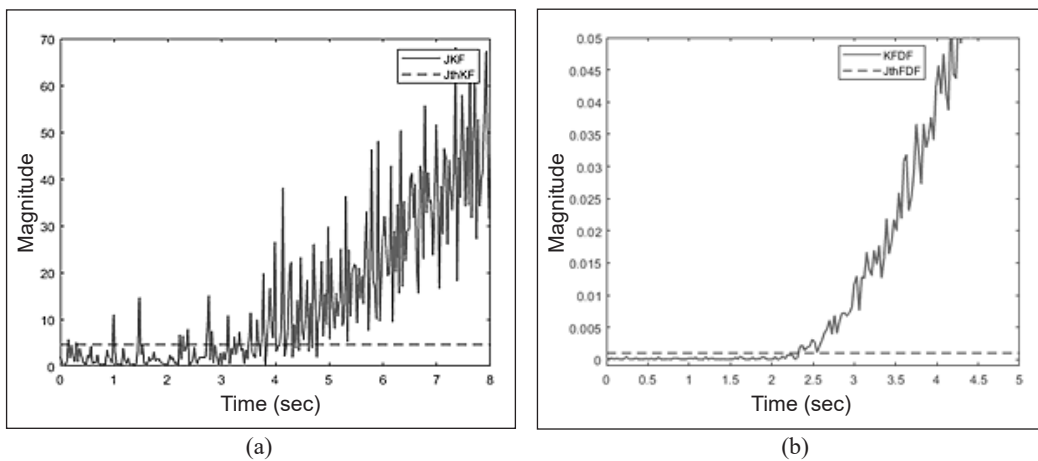


Figure 3. Evaluation function and threshold in incipient fault at  $t=2.2$ sec: (a) Kalman filter; and (b) optimal FDF

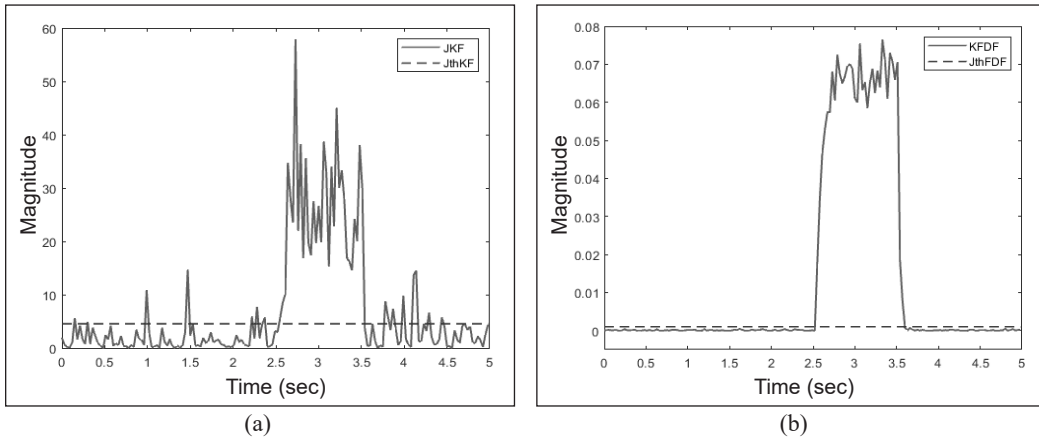


Figure 4. Evaluation function and threshold in actuator stuck fault at  $t = 2.5-3.5$ sec: (a) Kalman filter; and (b) optimal FDF

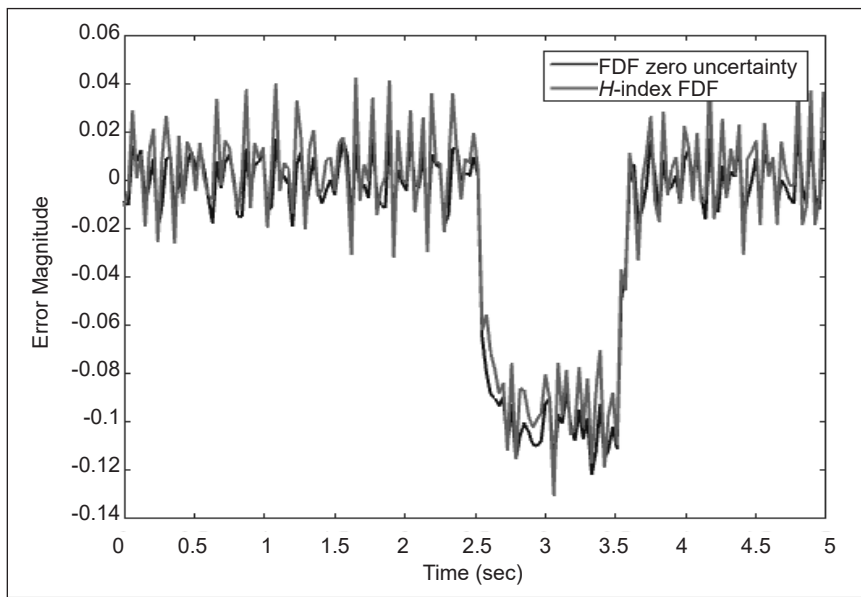


Figure 5. Residual in actuator stuck case with system uncertainty

been designed for LTI uncertain system to handle the uncertainty problem (Ahmad & Mohd-Mokhtar, 2020). Figure 5 shows residual obtained from  $H$ -index FDF for uncertain DC motor system and residual from optimal FDF of nominal DC motor system. It has been shown that  $H$ -index fault-sensitive FDF can minimize the effect of system uncertainties and enhance the fault sensitivity (Ahmad & Mohd-Mokhtar, 2020) and shows the approximate performance of optimal FDF designed for nominal DC motor. Detail comparison of the three FD schemes is given in Table 2.

Table 2  
*General comparison of three FD schemes*

	Kalman Filter	Optimal FDF	<i>H</i> -index FDF
Detectability	Can detect all faults but may increase FAR when the fault has a low fault to noise ratio	Can detect all faults simulated in this paper	Can detect all faults simulated in this paper
Detection time	Fast	Fast	Fast
Computation load	Moderate	Low	Moderate
Robustness to uncertainty	FAR high in the simulation case	MDR high in the simulation case	Acceptable robustness
Robustness to initial states	Less robust than optimal FDF	More robust than other	Least robust

## MODERN TRENDS IN MODEL-BASED FD FOR LTI SYSTEMS

1. As discussed above, a model-based FD system consists of two stages: residual generation and residual evaluation. The prime objective of the residual generation stage is to generate the optimal residual. The objective of the residual evaluation and threshold stage is to ensure maximum fault detectability. Thus, the overall objective of an optimal fault detection system is to achieve the maximum fault detectability and maintain zero false alarm for a deterministic type of system or achieve the fault detectability under some allowable false alarm rate under stochastic noise. Based on the survey, most of the results mentioned above focus on the effort of residual generation. However, little attention is given to the residual evaluation and corresponding threshold computation. Hence, there is an indispensable need to design the residual generation and residual evaluation in an integrated way, rather than dealing with them separately, to optimize certain criteria for better performance of the fault detection system.
2. Even though very nice results are available for model-based fault detection, there is still a scarcity of research for uncertain linear systems. The standalone design of the residual generator and residual evaluator and an optimally integrated fault detection system, as discussed in 1, for the continuous and discrete-time linear uncertain system, is still an open and challenging topic for researchers.
3. The fault should be estimated after it has been detected so that its effect can be compensated to maintain the reliability of a practical system in a faulty situation. An optimal fault estimator and fault-tolerant controller for nominal and uncertain systems is also an ongoing open research topic.
4. It is also observed that minimal effort has been devoted to developing fault detection systems in a closed-loop environment. Open-loop fault detection techniques become ineffective in a closed-loop environment. Thus, it is necessary to work on this topic which is also an emerging topic.

5. Besides the process and measurement noise, there is also multiplicative noise in the system. Due to this, traditional methods could not produce the optimal performance for fault detection. Hence, there is a need to address the fault detection problem for LTI systems involving multiplicative noise.

In some instances, recorded or online data of system inputs and measurements are only available. In such scenarios, model-based fault detection methods cannot be directly applied. Therefore, model-based and data-driven or signal processing-based fault detection methods can be combined to design optimal FD systems for complex systems where the mathematical model of the system is not possible. As technology advances and more techniques are developed regarding fault detection in LTI systems, the combination of data-driven and model-based fault detection methods are the future research directions. The integration of the two methods provides new opportunities and challenges. Furthermore, the integration of robust control and machine learning techniques for observer-based FD and estimation scheme for linear systems open new research directions in the model-based FD framework.

## CONCLUSION

The safety, reliability and desired performance of a practical system must be maintained at all the time during its operation. Fault detection plays a paramount role in accomplishing these objectives. This paper discusses various model-based residual generation techniques, including FDF, UIO, parity-space, optimization-based, Kalman filter, and system identification approach. Three different FD approaches were illustrated to address the FD problem in the DC motor system, and their performance is compared. The arising issues and emerging research topics on fault detection for LTI systems were explained. The outcome from this paper may assist in further research in the future.

## ACKNOWLEDGMENT

The work is supported under the HRDI-UESTPS scholarship program funded by the Higher Education Commission (HEC) of Pakistan and partially supported by the USM RUI Grant: 1001/PELECT/8014093.

## REFERENCES

- Aguilera, F., de la Barrera, P. M., De Angelo, C. H., & Espinoza Trejo, D. R. (2016). Current-sensor fault detection and isolation for induction-motor drives using a geometric approach. *Control Engineering Practice*, 53, 35-46. <https://doi.org/10.1016/j.conengprac.2016.04.014>
- Ahmad, M., & Mohd-Mokhtar, R. (2020). H-indexed fault sensitive filter design for linear discrete-time uncertain DC motor system. *Interciencia*, 45(10), 60-74.



- Ahmad, S., Ali, N., Ayaz, M., & Ahmad, E. (2017). Design of robust fault detection filter using algorithm for a class of LTI systems. In *13th International Conference on Emerging Technologies (ICET)* (pp. 1-5). IEEE Publishing. <https://doi.org/10.1109/ICET.2017.8281720>
- Bachir, S., Tnani, S., Trigeassou, J. C., & Champenois, G. (2006). Diagnosis by parameter estimation of stator and rotor faults occurring in induction machines. *IEEE Transactions on Industrial Electronics*, *53*(3), 963-973. <https://doi.org/10.1109/TIE.2006.874258>
- Belmokhtar, K., Ibrahim, H., & Merabet, A. (2015). Online parameter identification for a DFIG driven wind turbine generator based on recursive least squares algorithm. In *IEEE 28th Canadian Conference on Electrical and Computer Engineering (CCECE)* (pp. 965-969). IEEE Publishing. <https://doi.org/10.1109/CCECE.2015.7129406>
- Blanke, M., Kinnaert, M., Lunze, J., & Staroswiecki, M. (2015). *Diagnosis and fault-tolerant control* (3rd Ed.). Springer.
- Bøgh, S. (1995). Multiple hypothesis-testing approaches to FDI for the industrial actuator benchmark. *Control Engineering Practice*, *3*(12), 1763-1768. [https://doi.org/10.1016/0967-0661\(95\)00191-V](https://doi.org/10.1016/0967-0661(95)00191-V)
- Chen, W., Ding, S. X., Haghani, A., Naik, A., Khan, A. Q., & Yin, S. (2011). Observer-based FDI schemes for wind turbine benchmark. *IFAC Proceedings Volumes*, *44*(1), 7073-7078. <https://doi.org/10.3182/20110828-6-IT-1002.03469>
- Cho, S., Gao, Z., & Moan, T. (2018). Model-based fault detection, fault isolation, and fault-tolerant control of a blade pitch system in floating wind turbines. *Renewable Energy*, *120*, 306-321. <https://doi.org/10.1016/j.renene.2017.12.102>
- Da, R., & Lin, C. F. (1996). Sensitivity analysis of the state chi-square test. *IFAC Proceedings Volumes*, *29*(1), 6596-6601. [https://doi.org/10.1016/S1474-6670\(17\)58741-8](https://doi.org/10.1016/S1474-6670(17)58741-8)
- Dai, X., Gao, Z., Breikin, T., & Wang, H. (2009). Disturbance attenuation in fault detection of gas turbine engines: A discrete robust observer design. *IEEE Transactions on Systems, Man, and Cybernetics, Part C (Applications and Reviews)*, *39*(2), 234-239. <https://doi.org/10.1109/TSMCC.2008.2005845>
- Denkena, B., Bergmann, B., & Stoppel, D. (2020). Reconstruction of process forces in a five-axis milling center with a LSTM neural network in comparison to a model-based approach. *Journal of Manufacturing and Materials Processing*, *4*(3), Article 62. <https://doi.org/10.3390/jmmp4030062>
- Ding, S. X. (2013). *Model-based fault diagnosis techniques: design schemes, algorithms, and tools*. Springer Science & Business Media.
- Ding, S. X. (2014). *Data-driven design of fault diagnosis and fault-tolerant control systems*. Springer. <https://doi.org/10.1007/978-1-4471-6410-4>
- Ding, S. X., & Frank, P. M. (1990). Fault detection via factorization approach. *Systems & Control Letters*, *14*(5), 431-436. [https://doi.org/10.1016/0167-6911\(90\)90094-B](https://doi.org/10.1016/0167-6911(90)90094-B)
- Ding, S. X., Jeinsch, T., Frank, P. M., & Ding, E. L. (2000). A unified approach to the optimization of fault detection systems. *International Journal of Adaptive Control and Signal Processing*, *14*(7), 725-745. [https://doi.org/10.1002/1099-1115\(200011\)](https://doi.org/10.1002/1099-1115(200011))

- Ding, S. X., Zhang, P., & Frank, P. M. (2003). Threshold calculation using LMI-technique and its integration in the design of fault detection systems. In *42nd IEEE International Conference on Decision and Control* (pp. 469-474). IEEE Publishing. <https://doi.org/10.1109/CDC.2003.1272607>
- Do, M. H., Koenig, D., & Theilliol, D. (2018). Robust  $H_\infty$  proportional-integral observer for fault diagnosis: Application to vehicle suspension. *IFAC-PapersOnLine*, *51*(24), 536-543. <https://doi.org/10.1016/j.ifacol.2018.09.628>
- Doraiswami, R., & Cheded, L. (2013). A unified approach to detection and isolation of parametric faults using a Kalman filter residual-based approach. *Journal of the Franklin Institute*, *350*(5), 938-965. <https://doi.org/10.1016/j.jfranklin.2013.01.005>
- Dybkowski, M., & Klimkowski, K. (2017). Speed sensor fault detection algorithm for vector control methods based on the parity relations. In *2017 19th European Conference on Power Electronics and Applications* (pp. 1-5). IEEE Publishing. <https://doi.org/10.23919/EPE17ECCEEurope.2017.8099342>
- Farhat, A., & Koenig, D. (2015). PI robust fault detection observer for a class of uncertain switched systems using LMIs. *IFAC-PapersOnLine*, *48*(21), 125-130. <https://doi.org/10.1016/j.ifacol.2015.09.515>
- Frank, P. M., Ding, S. X., & Koppen-Seliger B. (2000). Current developments in the theory of FDI. *IFAC Proceeding Volumes: 4th IFAC Symposium on Fault Detection, Supervision, and Safety for Technical Processes*, *33*(11), 17-28.
- Franklin, G. F., David-Powell, J., & Emami-Naeini, A. (2019). *Feedback control of dynamic systems* (8th Ed.). Pearson Prentice Hall.
- Gannouni, F., & Hmida, F. B. (2017). Simultaneous state and fault estimation for linear stochastic systems. In *18th International Conference on Sciences and Techniques of Automatic Control and Computer Engineering (STA)* (pp. 59-66). IEEE Publishing. <https://doi.org/10.1109/STA.2017.8314965>
- Gao, Z., Cecati, C., & Ding, S. X. (2015). A survey of fault diagnosis and fault-tolerant techniques-part I: Fault diagnosis with model-based and signal-based approaches. *IEEE Transactions on Industrial Electronics*, *62*(6), 3757-3767. <https://doi.org/10.1109/TIE.2015.2417501>
- Gautam, S., Tamboli, P. K., Patankar, V. H., Duttgupta, S. P., & Roy, K. (2017). Performance evaluation of statistical method for incipient fault detection under noisy environment. *IFAC-PapersOnLine*, *50*(1), 15728-15733. <https://doi.org/10.1016/j.ifacol.2017.08.2415>
- Gertler, J. J. (2017). *Fault detection and diagnosis in engineering systems*. CRC Press. <https://doi.org/10.1201/9780203756126>
- Hajiyev, C., & Soken, H. E. (2013). Robust adaptive Kalman filter for estimation of UAV dynamics in the presence of sensor/actuator faults. *Aerospace Science and Technology*, *28*(1), 376-383. <https://doi.org/10.1016/j.ast.2012.12.003>
- Herrera, L., & Yao, X. (2018). Parameter identification approach to series DC arc fault detection and localization. In *IEEE Energy Conversion Congress and Exposition (ECCE)* (pp. 497-501). IEEE Publishing. <https://doi.org/10.1109/ECCE.2018.8557679>
- Hur, H., & Ahn, H. S. (2014). Unknown input H-infinity observer-based localization of a mobile robot with sensor failure. *IEEE/ASME Transactions on Mechatronics*, *19*(6), 1830-1838. <https://doi.org/10.1109/TMECH.2014.2298034>

- Hwang, W., & Huh, K. (2015). Fault detection and estimation for electromechanical brake systems using parity space approach. *Journal of Dynamic Systems, Measurement, and Control*, 137(1), Article 014504. <https://doi.org/10.1115/1.4028184>
- Isermann, R. (1984). Process fault detection based on modeling and estimation methods - A survey. *Automatica*, 20(4), 387-404. [https://doi.org/10.1016/0005-1098\(84\)90098-0](https://doi.org/10.1016/0005-1098(84)90098-0)
- Isermann, R. (1997). Supervision, fault-detection, and fault-diagnosis methods - An introduction. *Control Engineering Practice*, 5(5), 639-652. [https://doi.org/10.1016/S0967-0661\(97\)00046-4](https://doi.org/10.1016/S0967-0661(97)00046-4)
- Isermann, R. (2006). *Fault-diagnosis systems*. Springer.
- Jesica, E., & Poznyak, A. (2018). Parameter estimation in continuous-time stochastic systems with correlated noises using the Kalman filter and least squares method. *IFAC-PapersOnLine*, 51(13), 309-313. <https://doi.org/10.1016/j.ifacol.2018.07.296>
- Jie, C., & Patton, R. J. (2012). *Robust model-based fault diagnosis for dynamic systems*. Springer. <https://doi.org/10.1007/978-1-4615-5149-2>
- Jokic, I., Zecevic, Z., & Krstajic, B. (2018). State-of-charge estimation of lithium-ion batteries using extended Kalman filter and unscented Kalman filter. In *23rd International Scientific-Professional Conference on Information Technology (IT)* (pp. 1-4). IEEE Publishing. <https://doi.org/10.1109/SPIT.2018.8350462>
- Khang, H. V., Kandukuri, S., Pawlus, W., & Robbersmyr, K. G. (2018). Parameter identification of a winding function-based model for fault detection of induction machines. In *Eighth International Conference on Information Science and Technology (ICIST)* (pp. 200-205). <https://doi.org/10.1109/ICIST.2018.8426188>
- Khazraj, H., Faria da Silva, F., & Bak, C. L. (2016). A performance comparison between extended Kalman filter and unscented Kalman filter in power system dynamic state estimation. In *51st International Universities Power Engineering Conference (UPEC)* (pp. 1-6). IEEE Publishing. <https://doi.org/10.1109/UPEC.2016.8114125>
- Kleilat, I., Al-Sheikh, H., Moubayed, N., & Hoblos, G. (2018). Robust fault diagnosis of sensor faults in power converter used in hybrid electric vehicle. *IFAC-PapersOnLine*, 51(24), 326-331. <https://doi.org/10.1016/j.ifacol.2018.09.597>
- Li, L., Ding, S. X., Zhang, Y., & Yang, Y. (2016). Optimal fault detection design via iterative estimation methods for industrial control systems. *Journal of the Franklin Institute*, 353(2), 359-377. <https://doi.org/10.1016/j.jfranklin.2015.12.002>
- Li, W., Zhu, Z., Zhou, G., & Chen, G. (2013). Optimal  $H_1/H_\infty$  fault-detection filter design for uncertain linear time-invariant systems: An iterative linear matrix inequality approach. *IET Control Theory & Applications*, 7(8), 1160-1167. <https://doi.org/10.1049/iet-cta.2012.0954>
- Lijia, C., Yu, T., & Guo, Z. (2019). Adaptive observer-based fault detection and active tolerant control for unmanned aerial vehicles attitude system. *IFAC-PapersOnLine*, 52(24), 47-52. <https://doi.org/10.1016/j.ifacol.2019.12.379>
- Liu, X., Wang, Z., Wang, Y., & Shen, Y. (2018). Dynamic threshold computation in fault detection for discrete-time linear systems. In *2018 Chinese Control And Decision Conference (CCDC)* (pp. 2241-2246). IEEE Publishing. <https://doi.org/10.1109/CCDC.2018.8407499>

- Liu, Z., & He, H. (2017). Sensor fault detection and isolation for a lithium-ion battery pack in electric vehicles using adaptive extended Kalman filter. *Applied Energy*, 185, 2033-2044. <https://doi.org/10.1016/j.apenergy.2015.10.168>
- Marzat, J., Piet-Lahanier, H., Damongeot, F., & Walter, E. (2012). Model-based fault diagnosis for aerospace systems: A survey. *Proceedings of the Institution of Mechanical Engineers, Part G: Journal of Aerospace Engineering*, 226(10), 1329-1360. <https://doi.org/10.1177/0954410011421717>
- Mehra, R. K., & Peschon, J. (1971). An innovations approach to fault detection and diagnosis in dynamic systems. *Automatica*, 7(5), 637-640. [https://doi.org/10.1016/0005-1098\(71\)90028-8](https://doi.org/10.1016/0005-1098(71)90028-8)
- Na, Y., & Ahmad, M. (2019). A fault detection scheme for switched systems with noise under asynchronous switching. In *9th International Conference on Information Science and Technology (ICIST)* (pp. 258-262). IEEE Publishing. <https://doi.org/10.1109/ICIST.2019.8836838>
- Nadarajan, S., Panda, S. K., Bhangu, B., & Gupta, A. K. (2016). Online model-based condition monitoring for brushless wound-field synchronous generator to detect and diagnose stator windings turn-to-turn shorts using extended Kalman filter. *IEEE Transactions on Industrial Electronics*, 63(5), 3228-3241. <https://doi.org/10.1109/TIE.2016.2535959>
- Nikiforov, I., Varavva, V., & Kireichikov, V. (1993). Application of statistical fault detection algorithms to navigation systems monitoring. *Automatica*, 29(5), 1275-1290. [https://doi.org/10.1016/0005-1098\(93\)90050-4](https://doi.org/10.1016/0005-1098(93)90050-4)
- Odendaal, H. M., & Jones, T. (2014). Actuator fault detection and isolation: An optimized parity space approach. *Control Engineering Practice*, 26, 222-232. <https://doi.org/10.1016/j.conengprac.2014.01.013>
- Patton, R. J., & Chen, J. (2000). On eigenstructure assignment for robust fault diagnosis. *International Journal of Robust and Nonlinear Control*, 10(14), 1193-1208. [https://doi.org/10.1002/1099-1239\(20001215\)10:14<1193::AID-RNC523>3.0.CO;2-R](https://doi.org/10.1002/1099-1239(20001215)10:14<1193::AID-RNC523>3.0.CO;2-R)
- Perrin, O., Basseville, M., Sorine, M., & Zhang, Q. (2004). On-board diesel particulate filter fault detection using an adaptive observer. *IFAC Proceedings Volumes*, 37(22), 367-372. [https://doi.org/10.1016/S1474-6670\(17\)30371-3](https://doi.org/10.1016/S1474-6670(17)30371-3)
- Pourasghar, M., Puig, V., & Ocampo-Martinez, C. (2020). Characterization of interval-observer fault detection and isolation properties using the set-invariance approach. *Journal of the Franklin Institute*, 357(3), 1853-1886. <https://doi.org/10.1016/j.jfranklin.2019.11.027>
- Pourbabae, B., Meskin, N., & Khorasani, K. (2016). Sensor fault detection, isolation, and identification using multiple-model-based hybrid Kalman filter for gas turbine engines. *IEEE Transactions on Control Systems Technology*, 24(4), 1184-1200. <https://doi.org/10.1109/TCST.2015.2480003>
- Rasoolzadeh, A., & Salmasi, F. R. (2020). Mitigating zero dynamic attacks in communication link-enabled droop-controlled hybrid AC/DC microgrids. *IET Cyber-Physical Systems: Theory & Applications*, 5(2), 207-217. <https://doi.org/10.1049/iet-cps.2019.0043>
- Sun, B., Wang, J., He, Z., Qin, Y., Wang, D., & Zhou, H. (2019). Fault detection for closed-loop control systems based on parity space transformation. *IEEE Access*, 7, 75153-75165. <https://doi.org/10.1109/ACCESS.2019.2916785>

- Tripathi, R. P., Ghosh, S., & Chandle, J. O. (2016). Tracking of object using optimal adaptive Kalman filter. In *2016 IEEE International Conference on Engineering and Technology (ICETECH)* (pp. 1128-1131). IEEE Publishing. <https://doi.org/10.1109/ICETECH.2016.7569426>
- Wang, Y., Liu, Q., Li, K., Yin, L., & Chen, H. (2019). Resilient fault and attack detection of DCT vehicles using parity space approach. In *2019 Chinese Automation Congress (CAC)* (pp. 431-436). IEEE Publishing. <https://doi.org/10.1109/CAC48633.2019.8996359>
- Willsky, A., & Jones, H. (1976). A generalized likelihood ratio approach to the detection and estimation of jumps in linear systems. *IEEE Transactions on Automatic Control*, *21*(1), 108-112. <https://doi.org/10.1109/TAC.1976.1101146>
- Wünnenberg, J., & Frank, P. M. (1987). Sensor fault detection via robust observers. In S. Tzafestas, M. Singh & G. Schmidt (Eds.), *System Fault Diagnostics, Reliability and Related Knowledge-Based Approaches* (pp. 147-160). Springer. [https://doi.org/10.1007/978-94-009-3929-5\\_5](https://doi.org/10.1007/978-94-009-3929-5_5)
- Yang, X., Chen, Y., Li, B., & Luo, D. (2020). Battery states online estimation based on exponential decay particle swarm optimization and proportional-integral observer with a hybrid battery model. *Energy*, *191*, Article 116509. <https://doi.org/10.1016/j.energy.2019.116509>
- Ye, H., Wang, W., & Zhai, S. (2015). Fault diagnosis based on parameter estimation in closed-loop systems. *IET Control Theory & Applications*, *9*(7), 1146-1153. <https://doi.org/10.1049/iet-cta.2014.0717>
- Zammali, C., Van Gorp, J., Wang, Z., & Raïssi, T. (2020). Sensor fault detection for switched systems using interval observer with  $L_\infty$  performance. *European Journal of Control*, *57*, 147-156. <https://doi.org/10.1016/j.ejcon.2020.06.004>
- Zhang, K., Jiang, B., Yan, X. G., & Mao, Z. (2017). Incipient sensor fault estimation and accommodation for inverter devices in electric railway traction systems. *International Journal of Adaptive Control and Signal Processing*, *31*(5), 785-804. <https://doi.org/10.1002/acs.2730>
- Zhang, P., Ye, H., Ding, S. X., Wang, G. Z., & Zhou, D. H. (2006). On the relationship between parity space and approaches to fault detection. *Systems & Control Letters*, *55*(2), 94-100. <https://doi.org/10.1016/j.sysconle.2005.05.006>
- Zhang, Y., & Jiang, J. (2008). Bibliographical review on reconfigurable fault-tolerant control systems. *Annual Reviews in Control*, *32*(2), 229-252. <https://doi.org/10.1016/j.arcontrol.2008.03.008>
- Zhang, Z. H., Li, S., Yan, H., & Fan, Q. Y. (2019). Sliding mode switching observer-based actuator fault detection and isolation for a class of uncertain systems. *Nonlinear Analysis: Hybrid Systems*, *33*, 322-335. <https://doi.org/10.1016/j.nahs.2019.04.001>
- Zhirabok, A. N., Shumsky, A. E., & Zuev, A. V. (2018). Sliding mode observers for fault detection in linear dynamic systems. *IFAC-PapersOnLine*, *51*(24), 1403-1408. <https://doi.org/10.1016/j.ifacol.2018.09.540>
- Zhong, M., Ding, S. X., Lam, J., & Wang, H. (2003). An LMI approach to design robust fault detection filters for uncertain LTI systems. *Automatica*, *39*(3), 543-550. [https://doi.org/10.1016/S0005-1098\(02\)00269-8](https://doi.org/10.1016/S0005-1098(02)00269-8)
- Zhong, M., Song, Y., Xue, T., Yang, R., & Li, W. (2018). Parity space-based fault detection by minimum error minimax probability machine. *IFAC-PapersOnLine*, *51*(24), 1292-1297. <https://doi.org/10.1016/j.ifacol.2018.09.568>

- Zhou, J., & Zhang, D. (2019). H-infinity fault detection for delta operator systems with random two-channels packet losses and limited communication. *IEEE Access*, 7, 94448-94459. <https://doi.org/10.1109/ACCESS.2019.2928306>
- Zhu, Y., & Gao, Z. (2014). Robust observer-based fault detection via evolutionary optimization with applications to wind turbine systems. In *9th IEEE Conference on Industrial Electronics and Applications* (pp. 1627-1632). IEEE Publishing. <https://doi.org/10.1109/ICIEA.2014.6931428>

## Work Performance of Extension Agents: Skills of Transfer of Technology and Human Resource Development in Cocoa Industry

Murni Azureen Mohd Pakri<sup>1\*</sup>, Salim Hassan<sup>1</sup>, Oluwatoyin Olagunju<sup>2</sup>, Mohd Yusoff Abd Samad<sup>1</sup> and Ramle Kasin<sup>3</sup>

<sup>1</sup>Department of Agriculture Technology, Faculty of Agriculture, Universiti Putra Malaysia, 43400 UPM, Serdang, Selangor, Malaysia

<sup>2</sup>Department of Agricultural Economics and Extension, Faculty of Agriculture, Adekunle Ajasin University, Akungba-Akoko, Nigeria

<sup>3</sup>Head Office of Malaysian Cocoa Board, Tingkat 5, 6 & 7, Wisma SEDCO, Lorong Plaza Wawasan, 88999, Kota Kinabalu, Sabah, Malaysia

### ABSTRACT

Transfer of technology (ToT) and human resource development (HRD) are essential components to acknowledge extension agents' performance. Understanding the foundations and implications of ToT and HRD is vital for improving agriculture extension agents in research and extension programmes. This study was designed to determine extension agents' ToT and HRD skills to explain the work performance of Malaysian Cocoa Board (MCB) extension agents in East Malaysia. A total of 315 productive cocoa farmers exposed to the extension activities for a minimum of five years and had attended two basic training from the agency were selected to answer the questionnaire within a month. The researcher

applied Krejcie and Morgan formula to determine the sample size based on the population using stratified random sampling. The data were analysed using descriptive statistics, multiple regression and Pearson correlation analysis. Results showed a positive and moderate relationship between ToT and HRD towards work performance. However, from the six variables tested, only three variables were significant towards work performance, namely technical skill ( $p=0.000$ ), leadership skill ( $p=0.015$ )

### ARTICLE INFO

#### Article history:

Received: 5 July 2021

Accepted: 15 September 2021

Published: 24 November 2021

DOI: <https://doi.org/10.47836/pjst.30.1.05>

#### E-mail addresses:

[azureenpakri@gmail.com](mailto:azureenpakri@gmail.com) (Murni Azureen Mohd Pakri)

[salimhassan@upm.edu.my](mailto:salimhassan@upm.edu.my) (Salim Hassan)

[toyinolagunju01@gmail.com](mailto:toyinolagunju01@gmail.com) (Oluwatoyin Olagunju)

[myusoffas@upm.edu.my](mailto:myusoffas@upm.edu.my) (Mohd Yusoff Abd Samad)

[ramle@koko.gov.my](mailto:ramle@koko.gov.my) (Ramle Kasin)

\*Corresponding author

and decision-making skill ( $p=0.000$ ). Therefore, the extension agents' skills must be strengthened, their working knowledge updated, and new concepts for developing agriculture that can fulfil complicated demand patterns, reduce poverty and pressure and increase productivity must be developed. This study also strengthens the iceberg model by adding six characteristics of skills in extension agents. The outcomes would contribute to the policymakers and MCB's management in elevating the extension agents' performance through training and developing ToT and HRD.

*Keywords:* Extension agent; human resource development; training and development; transfer of technology; work performance

## INTRODUCTION

Cocoa bean production has been declining since 1990, while the downstream processing sector shows an upward trend (Malaysian Cocoa Board, 2018). Currently, the major cocoa plantation is owned by smallholders. Therefore, the plan for a large-scale plantation remains unseen because of the loss of interest among the farmers. Other challenges for a large-scale plantation include the competition for land use from oil palm cultivation, labour constraints, low world cocoa prices and the cocoa pod borer's infestation (Lee, 2013). In addition, there is an imbalance between upstream and downstream in the cocoa sector (Figure 1). As a result, the cocoa bean production is still low, and the gap between the current (0.7 tons/ha/year) and targeted production (1.5 tons/ha/year) is more than 50% (Malaysia Cocoa Board, 2018). In this case, the role of extension agents needs to be improved to apply new technologies introduced by the Malaysian Cocoa Board (MCB).

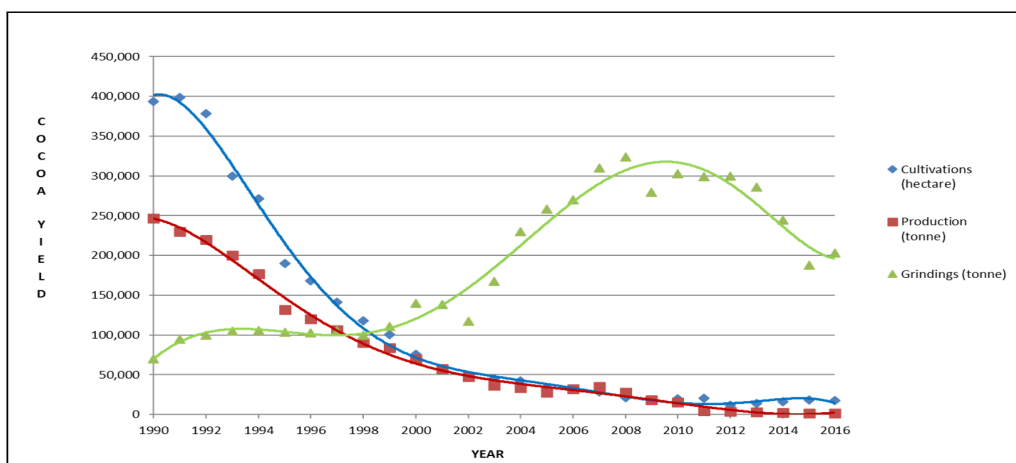


Figure 1. Malaysia: Cultivation, Production and Grinding from 1990-2016 (Malaysian Cocoa Board, 2017)



The work performance of extension agents will reflect the work performance of farmers to increase productivity. As today's organisation endures a parcel of challenges, individuals' work performance should be addressed and emphasised in an organisation's plan to empower them to succeed within the latest work environment or situation. The transfer of technology (ToT) and human resource development (HRD) skills are essential components to acknowledge the performance of extension agents. Conversely, Saleh and Man (2017) mentioned that the low performances by extension agents in the ToT and HRD skills have been attributed to inadequate skills and inadequacies in professional competencies needed to perform the work assigned to them skillfully. In order to transfer the technologies to farmers, extension agents need to have good interaction and relationships with them so that the process of transferring technology is booming. With the development of agriculture, especially cocoa, extension agents' role in supporting cocoa farmers in cocoa technology is vital as the technology itself is already there. Therefore, this study looks at the role of extension agents in predicting the successful adoption of technology among productive cocoa farmers reflected by the productivity of cocoa bean production.

Emerging concepts from present theories will help to explain the theories in the research framework. For example, a quantitative study by Motolani et al. (2017) on the performance of extension agents in MCB, West Malaysia, used the same six variables to determine the work performance in ToT and HRD skills. However, this study was conducted only in West Malaysia. Thus, this current study will cover Sabah to Sarawak as the East area dominates Malaysia's cocoa production. The study will highlight the importance of developing HRD while delivering the technology. Spencer and Spencer (1993) highlighted that by knowledge qualification and skills are vital and thoroughly explained the competence structure. The iceberg model will sufficiently explain the relationship between knowledge, skill and work performance of extension agents in the MCB.

## Model

This research focused on the knowledge and skills of extension agents' work performance. Predicting future job performance or behaviour of a specific criterion or standard is an important quality of competency. For this, Spencer and Spencer (1993) used the iceberg model, which consists of two parts: hidden (containing motives, characteristics and self-concepts) and visible (including motives, traits, self-concepts, knowledge and skills) (Figure 2).

The first part of this study focused on the extension agents' knowledge and skills in ToT and HRD. Knowledge is the information of specific areas, while the capacity to accomplish a specific task is the skill—the iceberg model suits both the extension agents and farmers. In the visible part, knowledge and skills could be learned and practised. First, however, the hidden characteristics need to be brought up. The elements include the motives, traits and

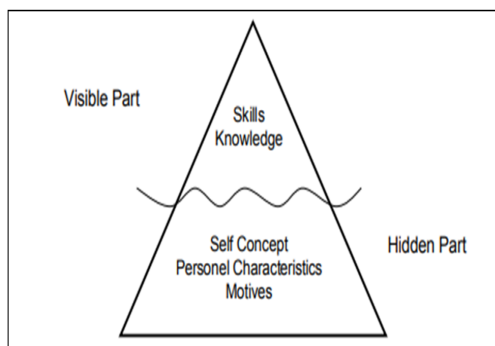


Figure 2. The Iceberg Model of Competence by Spencer and Spencer (1993)

self-concepts in the soul of humanity itself. This hidden part leads to the behaviour of reaching the goals and creates the path for higher productivity of extension agents, especially farmers.

The MCB has established an extension programme to provide farmers with technology in knowledge, and resources to address these issues. This programme was joined by extension agents responsible for sharing the MCB's technologies with the

farmers. The extension agents served as an intermediary between government agencies and farmers to distribute information and convince farmers to adopt relevant technologies (Tiraieyari et al., 2014). This engagement will highlight the extension agents' competencies, which are critical for transferring technology to farmers. Therefore, the objectives of this research were:

1. To determine the level of transfer of technology and human resource development component with work performance.
2. To determine the relationship between the transfer of technology and human resource development with work performance.
3. To identify the most crucial factor contributing to work performance.

This study's goal was to understand better the link between ToT and HRD in terms of job performance. This research will aid extension agents in gaining a better understanding of the topic and serve as a guide or source of information to help them improve their knowledge and skills in transferring the technology to farmers. As a result, extension agents will be able to identify important aspects pertaining to their work performance through a better grasp of ToT and HRD.

This study also strengthens the iceberg model of competencies by adding six characteristics for the skills in extension agents. Therefore, this study aimed to provide knowledge about the skills of extension agents in the MCB to identify the factors influencing the extension agents' work performance. Moreover, the result of this study will serve as an input for the MCB to improve extension services in training cocoa farmers. Also, the knowledge and skills can help improve cocoa farmers' skills to increase their productivity by using proper technology techniques and skills in their farms.

## Literature Review

As today's organisations endured a parcel of challenges, individuals' work performance ought to be addressed and should be in every organisation's plan for them to succeed in any work environment or situation. Work performance is behavioural, measurable, multifaceted and incidental and is additionally a sum of recurrent events which workers have done in a normal range in the association (Chu & Lai, 2011). In this current study, work performance's definition will gauge the extension agents' capabilities on how they conduct the ToT and HRD to farmers and how committed they are to their jobs.

Cocoa plantation needs to be restarted to produce good quality cocoa beans continuously. The ToT is one equipment that needs to be considered necessary to improve cocoa bean production. The function of agricultural extension agents is vital to help in the ToT and HRD (Motolani et al., 2017). Agricultural extension is a continuous process of providing farmers with helpful information and aiding them in obtaining the knowledge, skills and attitudes necessary to effectively employ information and technology to boost productivity (Sail, 2010).

Extension services' effectiveness was also heavily reliant on qualified extension agents who understood their tasks and were competent in them. They were responsible for transferring information to farmers during the entire extension process. Extension services were established worldwide according to various ideas, and in certain nations, extension programmes were used to transfer government directives to rural areas. As a result, the responsibility of extension officers in transferring technology and technical competence to farmers to raise their production is critical to the success of extension services (Rahim, 2008).

Transfer of technology, also known as ToT, transfers the technology to the recipients. ToT is used loosely in public discourse, even though it is tightly defined in academic literature. The ToT encompasses a broad scope of activities that lead to the adoption and practice change, including services from extension agents and the diffusion of knowledge to the clients (Ministry of Primary Industries, 2013). According to Altalb et al. (2015), technology encompasses not only the invention of machines and equipment or the introduction of new objects but also skills, talents, knowledge, systems and procedures. All of these are required for them to function and provide outcomes. Technology should also encompass the knowledge and skill required to carry out procedures, goods and services, along with organisation and operational measures.

Meanwhile, human resource development or HRD encourage and ensure the procurement of competencies required by the individuals. Individuals are the employees, supervisors, pioneers, or people in common to perform certain activities or tasks expected to achieve desired outcomes. Thus, human resource development is a form of systematically planned activity, training and development, career planning and performance

appraisals for organisational development (Salleh & Sulaiman, 2016). This aspect plays a significant role in deciding the efficiency and effectiveness of workers' performance in the organisation. Furthermore, human resource development assumes importance in fast-changing organisational environments and demands new techniques by responding to environmental changes.

### Hypotheses Development

This study tested the following hypotheses:

H1: Technical skill is significantly related to work performance.

H2: Technology delivery skill is significantly related to work performance.

H3: Technology evaluation skill is significantly related to work performance.

H4: Leadership skill is significantly related to work performance.

H5: Decision-making skill is significantly related to work performance.

H6: Social skill is significantly related to work performance.

## MATERIALS AND METHODS

### Research Design

This study was a descriptive correlation that combined descriptive and correlative studies. In this study, work performance was a dependent variable (Figure 3). At the same time, technology transfer, which was made up of three components: technology skill, technology delivery skill and technology evaluation skill, was treated as an independent variable. Additionally, leadership abilities, decision-making skills and social skills were the three components of human resource development.

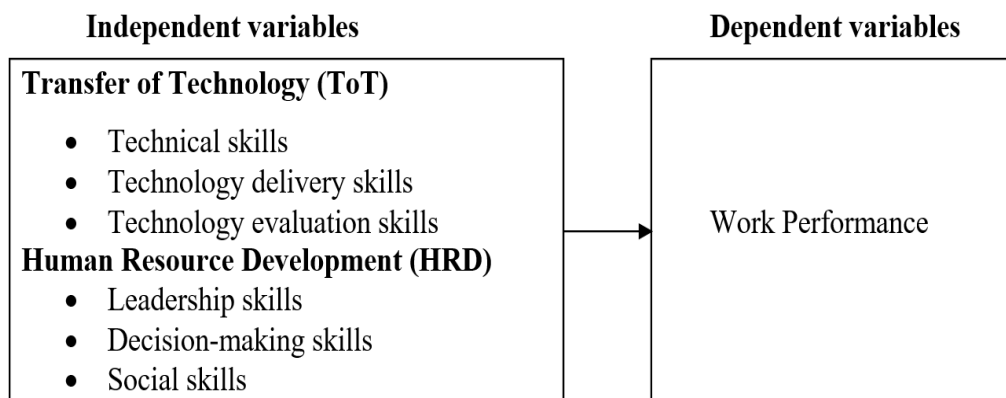


Figure 3. Independent and dependent variables

## Population and Samples

The study's target group was all productive cocoa farmers in East Malaysia exposed to extension activities conducted by the Malaysian Cocoa Board's (MCB's) extension agents for at least five years and has received at least two MCB training. A geographically stratified sample methodology was used in this research. Sabah and Sarawak are the two regions that makeup East Malaysia. The total number of productive cocoa farmers in these two regions is 1360, with 1095 farmers in Sabah and 265 farmers in Sarawak. The list of productive cocoa farmers in each area was obtained from MCB. Based on Krejcie and Morgan's table, a sample size of 297 is needed for a population of 1360 (Krejcie & Morgan, 1970). The questionnaires were then distributed, and we managed to collect more than the sample size needed based on the Krejcie and Morgan's table of 297. Therefore, a final total number of 315 productive cocoa farmers were selected based on the distributed questionnaires.

## Instrument and Measurement

This study utilises an established questionnaire as the instrument to gather data from the respondents. The original questionnaire was initially developed by Motolani et al. (2017). There were four sections to the questionnaire. The first section of the questionnaire was intended to gather information on the respondents' demographic profiles. The extension agents' technical and human resource development skills were measured in three dimensions in the second and third sections. The last part of the questionnaire measured the work performance of extension agents. Six Likert scale points were used to measure respondents' perception of the statement given, consisting of ToT, HRD and work performance on the cocoa technology used. The items in the questionnaire were created in response to the study's research questions and objectives. The pre-test analysis was conducted; reliability, where alpha is more than 0.7, was tested in the final questionnaire development stage (Table 1).

Table 1  
*Reliability test*

Items	No. sub items	Cronbach's Alpha Pre-test	Cronbach's Alpha Final test
Technical skill	9	0.934	<b>0.886</b>
Technology delivery skill	9	0.967	<b>0.881</b>
Technology evaluation skill	9	0.859	<b>0.899</b>
Leadership skill	8	0.899	<b>0.894</b>
Decision-making skill	7	0.825	<b>0.864</b>
Social skill	7	0.785	<b>0.861</b>
Work performance	8	0.950	<b>0.863</b>

**Data Analysis**

For data analysis, SPSS statistics version 23.0 was used:

1. Mean, frequency and percentage statistics were used to perform a descriptive analysis of the respondents’ profiles.
2. The range level as in Table 2 (low, moderate and high) was used to describe the ToT, HRD and work performance levels based on mean, frequency and percentage values.
3. The associations between ToT and HRD with work performance were examined using Pearson’s correlation coefficients.
4. A multiple regression analysis was carried out to determine the most important elements influencing ToT, HRD and work performance.

Table 2  
*Level of mean score*

Likert Scale Level	
1 - 2.669	<b>Low</b>
2.67 – 4.339	<b>Moderate</b>
<b>4.34 – 6</b>	<b>High</b>

**RESULTS AND DISCUSSION**

Table 3 shows the demographic characteristics of the respondents. The descriptive analysis used in the study was based on the frequency and percentage of respondents’ distribution.

Table 3  
*Respondents’ and farm profiles*

Profile	Frequency	Percent (%)	Profile	Frequency	Percent (%)
<b>Race</b>			<b>Gender</b>		
Malay	55	17.5	Male	269	85.4
Chinese	8	2.5	Female	46	14.6
Orang Asli	4	1.3	<b>Age</b>		
Kadazan	126	40	≤30	15	4.8
Murut	16	5.1	31-40	44	14
Bajau	1	0.3	41-50	66	21
Iban	69	21.9	51-60	104	33
Bidayuh	9	2.9	≥ 61	86	27.3
Sungai	10	3.2	<b>Occupation</b>		
Idahan	2	0.6	Full time	163	51.7
Others	15	4.8	Part time	152	48.3

Table 3 (Continued)

<b>Profile</b>	<b>Frequency</b>	<b>Percent (%)</b>
<b>Farm Profile</b>		
<b>Year of Cocoa Planting</b>		
2010-2006	262	83.2
2005-2001	17	5.4
At/Before 2000	36	11.4
<b>Clone/Farm</b>		
< 3 clones	183	58.1
3-5 clones	118	37.5
≥ 5 clones	14	4.4
<b>Hectarage</b>		
< 1	29	9.2
1-3.	277	87.9
3.1-5	7	2.2
5.1-7	2	0.6
<b>Source of Cocoa Information</b>		
MCB Officers	292	41.4
Family	106	15
Friends	154	21.8
Brochure	57	8.1
Radio	13	1.8
TV	37	5.2
Newspaper	14	2
Internet	26	3.7
Others	6	0.9

### **Transfer of Technology (ToT)**

Table 4 shows the distribution of technical skills, technology delivery skills and technology evaluation skills. Again the distribution was categorised in low, medium and high levels, as in Table 4.

91.7% showed high-level technical skills for technical skills, followed by 7.9% in the medium and 0.3% in the low level. It means that most farmers mentioned that the extension agents had knowledge and skills about the technology. Therefore, technical skills were vital as the main component of the extension agents' work. The results align with a study by Al-Rimawi et al. (2016) concluded that technical skills and attitudes increased the chance of success in extension work.

Table 4  
*Transfer of technology skills*

(A) Technical skill	Frequency	Percent
Low	1	0.3
Medium	25	7.9
High	289	91.7
Total	315	100
Mean = 5.318	SD = 0.827	
(B) Technology delivery skill	Frequency	Percent
Low	2	0.6
Medium	32	10.2
High	281	89.2
Total	315	100
Mean = 5.323	SD = 0.854	
(C) Technology evaluation skill	Frequency	Percent
Low	1	0.3
Medium	35	11.1
High	279	88.6
Total	315	100
Mean = 5.191	SD = 0.852	

In Table 4B, 89.2% showed a high level for technology delivery skills, followed by the medium at 10.2% and low at 0.6%. Technology delivery skills function as the way the technology is being transferred to the farmers. Therefore, extension agents were needed to master the process of delivering the technology. Somehow, the technology will be not understood without the right delivery technique, and they will refuse the technology itself.

The level of technology evaluation skill had the same trend as technical skill and technology delivery skill (Table 4C). About 88.6% showed a high level of technology evaluation skill, 11.1% at medium and 0.3% at low. Evaluation is needed to confirm the technology that has been used, and farmers needed the extension agents who were able to evaluate their work. Thus, extension agents must suggest a suitable technology according to the problem encountered by farmers in the field. The performance in any activity requires specific knowledge competencies to identify or solve problems (Melak & Negatu, 2012). Also, agriculture extension has a role to play in agricultural development. According to



Anaeto et al. (2016), the role of extension agents can be well-defined as norms, values and interaction patterns associated with a specific group of people.

### Human Resource Development (HRD)

Leadership skills, decision-making skills and social skills are the three sub-variables of HRD, as stated in Table 5.

Table 5

*Human resource development skills*

(A) Leadership skill	Frequency	Percent
Low	1	0.3
Medium	34	10.8
High	280	88.9
Total	315	100
Mean = 5.281	SD = 0.891	
(B) Decision-Making skill	Frequency	Percent
Low	1	0.3
Medium	29	9.2
High	285	90.5
Total	315	100
Mean = 5.238	SD = 0.816	
(C) Social skill	Frequency	Percent
Low	3	1.0
Medium	55	17.5
High	257	81.5
Total	315	100
Mean = 5.05	SD = 1.047	

In the leadership skills, 88.9% showed a high level, while only 10.8% for medium and 0.3% for low (Table 5A). Leadership was important for extension agents to develop leadership skills among farmers. Farmers need to increase their knowledge and skills in leadership, especially those who need to develop their ability to administer and manage the farm. If these were not implemented, the clients would continue to rely on extension agents, and the goal of getting them to work will not be accomplished.

The results in Table 5B show that the decision-making skill level was high (90.5%), 9.2% for medium and 0.3% for low level. Decision-making was necessary for the farmer to

decide without waiting for the extension agents’ instructions. Extension agents are needed to assist and train farmers to make decisions precisely according to the problems faced. This skill was also crucial for farmers to understand their situation in detail and make an effort to generate the right decision.

For social skills, 81.6% showed a high level, 17.5% at medium level and 1.0% at low level (Table 5C). Social skill was vital as it was a way of interaction between extension agents and farmers. Without good interaction or social skills, the process of transferring technology will be affected. Extension work will be more accessible when social networking disseminates the technology from extension agents to farmers.

### Work Performance

The extension agents’ work performance level was high at 91.1%, while medium and low were 8.6% and 0.3%, respectively (Table 6). These numbers indicated that the extension agents performed well in their extension work. Therefore, the extension agents’ performance is reflected in the performance of farmers and increased productivity.

Table 6  
*Work performance*

Work Performance	Frequency	Percent
Low	1	0.3
Medium	27	8.6
High	287	91.1
Total	315	100
Mean = 5.244	SD = 0.879	

Work engagement and workplace self-efficacy were both associated with work performance, according to Alessandri et al. (2015), and workplace self-efficacy was linked to work engagement. However, Okwoche et al. (2015) found that most agricultural extension agents were moderately satisfied at work, followed by a low level of satisfaction and finally a high level of satisfaction. The satisfaction levels experienced by agricultural extension agents were due to lack of training, welfare package and salary.

### Relationship between Transfer of Technology (ToT), Human Resource Development (HRD) and Work Performance

The ToT and HRD, when associated with the respondent’s work performance, were found to have a positive and moderate relationship, with each having a value of  $r = 0.673$  and  $0.654$ , respectively (Table 7).

Table 7

*Relationship between ToT and HRD with work performance*

Variables	X1	X2	Y
X1 Transfer of Technology	1	0.714**	0.673**
X2 Human resource development		1	0.654**
Y Work performance			1

\*\* . Correlation is significant at the 0.01 level (2-tailed)

Every component within the ToT and HRD skills was analysed to determine its relationship to work performance. Table 8 shows the six components having a positive and moderate relationship with work performance.

Table 8

*Relationship between ToT and HRD skills with work performance*

	X1	X2	X3	X4	X5	X6	Y
X1 Technical Skill	1	0.788**	0.639**	0.640**	0.680**	0.574**	0.652**
X2 Technology Delivery Skill		1	0.695**	0.690**	0.708**	0.625**	0.633**
X3 Technology Delivery Skill			1	0.638**	0.646**	0.586**	0.528**
X4 Leadership Skill				1	0.729**	0.670**	0.634**
X5 Decision-Making Support Skill					1	0.763**	0.701**
X6 Social Skill						1	0.611**
Y Work Performance							1

\*\* Correlation is significant at the 0.01 level (2-tailed)

This analysis showed that the ToT components, technical skill ( $r = 0.65$ ), technology delivering skill ( $r = 0.63$ ) and technology evaluation skills ( $r = 0.53$ ), affected the extension agents' work performance. Likewise, leadership skills ( $r = 0.63$ ), decision-making skills ( $r = 0.70$ ) and social skills ( $r = 0.61$ ) for HRD also affected their work performance. The

results indicated that the extension agents should have the skills to do the job to efficiently and effectively build the farmers’ capability and potential. Motolani et al. (2017) revealed positive and strong connections between agricultural extension agents’ technical skills, technology delivery skills, technology evaluation skills, leadership skills, social skills and work performance.

Furthermore, each extension strategy has its characteristics, features and properties (Baig & Aldosari, 2013). As a result, the degree to which clients accept various strategies varies. On the other hand, extension agents must do or have the knowledge and skills of all available technologies. According to Anandajayasekeram et al. (2008), the fundamental difficulty faced by agricultural extension was that the extension team was not adequately equipped with sufficient skills to function optimally. Therefore, the extension agents’ skills must be strengthened, their working knowledge updated, and new concepts for developing agriculture that can fulfil complicated demand patterns, reduce poverty and pressure and increase productivity must be developed.

According to Wahab et al. (2012), the relationship between technology transfer features and technology delivery significantly impacts extension agents’ and farmers’ performance. The ability to acquire and use transferred technologies can boost average performance. As a result, the extension organisation’s competitive advantage will be maximised. The crucial role of human resources provided an answer to the evolution of confidence in worker relations to their clients to achieve strategic objectives and performance (Deadrick & Stone, 2014). The practices that work synergistically to enhance employee’s skills, commitment and productivity cultivate a strategic edge due to effective and efficient implementation of HRD. Human capital elements, combined with the employee’s skills, commitment and productivity, would result in high-performance systems (Gerhart, 2012; Chapman et al., 2016).

### Analysis of Coefficient for Work Performance

From the regression analysis, most contributed components on the extension agents’ work performance were identified.

Table 9  
*Estimated coefficient for work performance model*

Performance dimension	Unstandardized Coefficients		Standardized Coefficients	t	Sig.
	B	Std. Error	Beta		
Constant	0.752	0.235		3.202	0.002

Table 9 (Continued)

Performance dimension	Unstandardized Coefficients		Standardized Coefficients	t	Sig.
	B	Std. Error	Beta		
<b>Transfer of Technology</b>					
Technical Skill	0.270	0.069	0.249	3.890	0.000
Technology Delivery Skill	0.074	0.071	0.074	1.051	0.294
Technology Evaluation Skill	-0.047	0.058	-0.046	-0.813	0.417
<b>Human Resource Development</b>					
Leadership Skill	0.146	0.059	0.150	2.455	0.015
Decision-Making Skill	0.321	0.070	<b>0.319</b>	4.560	0.000
Social Skill	0.090	0.052	0.104	1.726	0.085

R = 0.754, R<sup>2</sup> = 0.568, Adjusted R<sup>2</sup> = 0.559, Std. Error of the Estimate = 0.445

The highest Beta value explained most of the contributed skills. The components of decision-making skills had the most significant Beta value (0.319) as the extension agents' performance strongest predictor compared to other skills (Table 9). Agricultural extension services have been recognised for improving farmers' knowledge and farming methods and their attitudes toward agricultural advancements. With a rating of 0.270, technical skills had the second-highest Beta value, with leadership skills coming third, having a Beta value of 0.146. Other skills received a small Beta value, allowing them to contribute to work performance computation. It means that decision-making, technical, and leadership skills explained 55.9% (R<sup>2</sup> value adjusted) of the extension agents' work performance.

Three variables that were significantly different ( $p < 0.05$ ) were technical skill ( $p = 0.000$ ), leadership skill ( $p = 0.015$ ) and decision-making skill ( $p = 0.000$ ). Olagunju (2019) also found that decision-making is the most important skill for the extension agents' work performance in Malaysia, with a Beta value of 0.215 ( $t = 5.33$ ,  $p = 0.00$ ). Agricultural extension services are known for improving farmers' knowledge, abilities in farming practice, and attitudes toward agricultural advancements.

The other three variables which showed no significant differences ( $p > 0.05$ ) were technology delivery skills ( $p = 0.294$ ), technology evaluation skills ( $p = 0.417$ ) and social skills ( $p = 0.085$ ) towards work performance. In addition, there were negative numbers in the Beta value of technology evaluation skills. Statistically, if there is a negative coefficient, there will be negative changes in the correlation. However, technology evaluation skill has no significant differences towards work performance. If there is no correlation, there is no association between the changes in independent variables and the shifts in the dependent variables.

## CONCLUSION

Extension agents' work performance reflects the performance of the farmers and will enhance productivity if the performance is excellent. As today's organisations have to face many challenges, individuals' performance should be considered at the highest level of the organisation's plan to make sure that they can succeed in the ever-changing business environment. The limitation of this study emanated from the usage of the sample meant to be representative of the whole population. Even though there is a positive relationship between the dependent and independent variables, the work performance variance of 55.9% explained the three significant independent variables. The use of productive cocoa farmers only serves as a limitation in this study as the numbers of cocoa farmers who were not involved in training may not be representative. There is a need for more diverse samples in future research. The implication in this study focused on the training of extension agents in technology transfer and human resource skills to carry out their responsibilities of transferring technology to farmers, particularly in cocoa cultivation, by providing them with in-service training and new technologies. Findings from this study will contribute to the body of knowledge in ToT and HRD, especially in the Malaysian Cocoa Board that is responsible for cocoa production in Malaysia. Finally, the researcher encourages authorities to reinforce research on farmer and extension agents' connections by giving intensive training to extension agents and farmers. This training will expand the skills and techniques of extension agents and increase the size of farmers to participate outstandingly in the programmes by institutions or on-farm research.

## ACKNOWLEDGEMENTS

The author gratefully acknowledges the Malaysian Cocoa Board staff's commitment and technical assistance during the data collection and School of Graduate Studies (GRF) and Putra IPS Grant (No Grant: 9610900) for financial support.

## REFERENCES

- Alessandri, G., Borgogni, L., Schaufeli, W. B., Caprara, G. V., & Consiglio, C. (2015). From positive orientation to job performance: The role of work engagement and self-efficacy beliefs. *Journal of Happiness Studies*, 16(3), 767-788. <https://doi.org/10.1007/s10902-014-9543-2>
- Al-Rimawi, A., Tabieh, M., & Al-Qudah, H. (2016). Assessing growers' perceptions of effective extension methods and information communication technologies for training vegetable growers in Jordan. *International Journal of Economics and Finance*, 8(8), 229-236. <https://doi.org/10.5539/ijef.v8n8p229>
- Altalb, A. A. T., Filipek, T., & Skowron, P. (2015). The role of agricultural extension in the transfer and adoption of agricultural technologies. *Asian Journal of Agriculture and Food Sciences*, 3(5), 500-507.

- Anaeto, F. C., Asiabaka, C. C., Ani, A. O., Nnadi, F. N., Ugwoke, F. O., Asiabaka, I. P., Anaeto, C. A., & Ihekeronye, N. (2016). The roles of science and technology in national development. *Direct Research Journal of Social Science and Educational Studies*, 3(3), 38-43.
- Anandajayasekeram, P. (2008). *Concepts and practices in agricultural extension in developing countries: A source book*. ILRI (aka ILCA and ILRAD).
- Baig, M. B., & Aldosari, F. (2013). Agricultural extension in Asia: Constraints and options for improvement. *Journal of Animal and Plant Science*, 23, 619-632.
- Chapman, E. F., Sisk, F. A., Schatten, J., & Miles, E. W. (2016). Human resource development and human resource management levers for sustained competitive advantage: Combining isomorphism and differentiation. *Journal of Management & Organization*, 24(4), 533-550. <https://doi.org/10.1017/jmo.2016.37>
- Chu, L. C., & Lai, C. C. (2011). A research on the influence of leadership style and job characteristics on job performance among accountants of county and city government in Taiwan. *Public Personnel Management*, 40(2), 101-118. <https://doi.org/10.1177/009102601104000202>
- Deadrick, D. L., & Stone, D. L. (2014). Human resource management: Past, present, and future. *Human Resource Management Review*, 3(24), 193-195. <https://doi.org/10.1016/j.hrmr.2014.03.002>
- Gerhart, B. (2012). Construct validity, causality, and policy recommendations: The case of high performance work practices systems. *Human Resource Management Review*, 2(22), 157-160. <https://doi.org/10.1016/j.hrmr.2011.12.002>
- Krejcie, R. V., & Morgan, D. W. (1970). Determining sample size for research activities. *Educational and Psychological Measurement*, 30(3), 607-610. <https://doi.org/10.1177/001316447003000308>
- Lee, C. H. (2013). *Planting cocoa-challenges and realities*. Received September 2, 2019, from [www.ipicex.com/doc1/2012/onral/planting cocoa – challenges and reality in malaysia.pdf](http://www.ipicex.com/doc1/2012/onral/planting%20cocoa%20-%20challenges%20and%20reality%20in%20malaysia.pdf)
- Malaysian Cocoa Board. (2018). *Introduction (Target Groups Development)*. Retrieved September 2, 2019, from <https://www.koko.gov.my/lkm/loader.cfm?page=1>
- Malaysian Cocoa Board. (2017). *Statistics. Cultivation, production and grinding*. Received September 2, 2019, from <https://www.koko.gov.my/lkm/loader.cfm?page=10>
- Melak, D., & Negatu, W. (2012). Agricultural education and technical competency of development agents in Ethiopia. *Journal of Agricultural Extension and Rural Development*, 4(11), 347-351. <https://doi.org/10.5897/JAERD12.037>
- Ministry for Primary Industries. (2013). *Survey of technology transfer services to farmers and growers in New Zealand p.27*. Retrieved September 2, 2019, from [www.mpi.govt.nz](http://www.mpi.govt.nz)
- Motolani, M., Hassan, S., Olagunju, O., & Ramle, K. (2017). ToT and HRD competencies and its relationship to extension agents' performance among cocoa smallholders. *IOSR Journal of Agriculture and Veterinary Science (IOSR-JAVS)*, 10(12), 14-21. <https://doi.org/10.9790/2380-1012021421>
- Okwoche, V. A. O., Eziehe, J. C., & Agabi, V. (2015). Determinants of job satisfaction among extension agents in Benue State Agricultural and Rural Development Authority (BNARDA), Benue State, Nigeria. *European Journal of Physical and Agricultural Sciences*, 3(2), 38-48.

- Olagunju, O. (2019). *Perceptions of cocoa growers in Malaysia on relationship between transfer of technology skills, human resource development skills and extension agents' work performance* (Doctoral dissertation). Universiti Putra Malaysia, Malaysia.
- Rahim, M. S. (2008). *Kompetensi dan amalan pendidikan pengembangan* [Concept and practice of extension education]. *Buletin Pengembangan, Bil*, 1.
- Sail, R. M. (2010). Kompetensi pembangunan sumberdaya manusia dan pemindahan teknologi dan kaitannya dengan prestasi kerja agen pendidikan pengembangan [Human resource development and transfer of technology competencies and their relationships to extension agents' job performance]. *Akademika*, 79(1), 127-137.
- Saleh, J. M., & Man, N. B. (2017). Training requirements of agricultural extension officers using Borich needs assessment model. *Journal of Agricultural & Food Information*, 18(2), 110-122. <https://doi.org/10.1080/10496505.2017.1281748>
- Salleh, K. M., & Sulaiman, N. L. (2016). Competencies among human resource development practitioners according to disciplines and levels in Malaysian organizations. *International Journal of Applied Business and Economic Research*, 14(9), 521-533.
- Spencer, L. M., & Spencer, P. S. M. (1993). *Competence at work models for superior performance*. John Wiley & Sons.
- Tiraeyari, N., Hamzah, A., & Samah, B. A. (2014). Extension agents and sustainable cocoa farming: A case study of extension agents in Sabah state, Malaysia. *Modern Applied Science*, 8(6), 210-218. <https://doi.org/10.5539/mas.v8n6p210>
- Wahab, S. A., Rose, R. C., & Osman, S. I. W. (2012). Defining the concepts of technology and technology transfer: A literature analysis. *International Business Research*, 5(1), 61-71. <https://doi.org/10.5539/ibr.v5n1p61>



## **Sliding Window and Parallel LSTM with Attention and CNN for Sentence Alignment on Low-Resource Languages**

**Tien-Ping Tan<sup>1\*</sup>, Chai Kim Lim<sup>1</sup> and Wan Rose Eliza Abdul Rahman<sup>2</sup>**

<sup>1</sup>*School of Computer Sciences, Universiti Sains Malaysia, 11800 USM, Penang, Malaysia*

<sup>2</sup>*School of Humanities, Universiti Sains Malaysia, 11800 USM, Penang, Malaysia*

### **ABSTRACT**

A parallel text corpus is an important resource for building a machine translation (MT) system. Existing resources such as translated documents, bilingual dictionaries, and translated subtitles are excellent resources for constructing parallel text corpus. A sentence alignment algorithm automatically aligns source sentences and target sentences because manual sentence alignment is resource-intensive. Over the years, sentence alignment approaches have improved from sentence length heuristics to statistical lexical models to deep neural networks. Solving the alignment problem as a classification problem is interesting as classification is the core of machine learning. This paper proposes a parallel long-short-term memory with attention and convolutional neural network (parallel LSTM+Attention+CNN) for classifying two sentences as parallel or non-parallel sentences. A sliding window approach is also proposed with the classifier to align sentences in the source and target

languages. The proposed approach was compared with three classifiers, namely the feedforward neural network, CNN, and bi-directional LSTM. It is also compared with the BleuAlign sentence alignment system. The classification accuracy of these models was evaluated using Malay-English parallel text corpus and UN French-English parallel text corpus. The Malay-English sentence alignment performance was then evaluated using research documents and the very challenging Classical Malay-English document. The proposed classifier obtained

### ARTICLE INFO

*Article history:*

Received: 7 July 2021

Accepted: 15 September 2021

Published: 24 November 2021

DOI: <https://doi.org/10.47836/pjst.30.1.06>

*E-mail addresses:*

[tienping@usm.my](mailto:tienping@usm.my) (Tien-Ping Tan)

[chaikimlim@gmail.com](mailto:chaikimlim@gmail.com) (Chai Kim Lim)

[wardah@usm.my](mailto:wardah@usm.my) (Wan Rose Eliza Abdul Rahman)

\*Corresponding author

more than 80% accuracy in categorizing parallel/non-parallel sentences with a model built using only five thousand training parallel sentences. It has a higher sentence alignment accuracy than other baseline systems.

*Keywords:* Attention, CNN, LSTM, parallel text, sentence alignment

## INTRODUCTION

A parallel text corpus is an important resource for building a machine translation (MT) system containing words, phrases, or sentences of two or more languages aligned semantically. An example is the UN parallel text corpus created from official records and parliamentary documents of the United Nations in 6 languages (Ziemski et al., 2016). Table 1 shows a snippet of the English-French parallel text entries. The second column consists of an English word, phrase, or sentence and their corresponding translation in column 3. For instance, entry #1 is the English word “GENERAL,” translated as “GÉNÉRALE” in French. Entry #3 is an English phrase “2. Paragraphs 4, 5 and 6 of the resolution read as follows”, which was translated in French as “2. Les paragraphes 4, 5 et 6 de cette résolution se lisent comme suit.”

Table 1

*UN Parallel Text Corpus (English-French)*

#	English	French
1.	GENERAL	GÉNÉRALE
2.	2 February 1999	2 février 1999
3.	2. Paragraphs 4, 5 and 6 of the resolution read as follows:	2. Les paragraphes 4, 5 et 6 de cette résolution se lisent comme suit :
4.	In the example of approval marks and in the captions below, replace approval number “001234” by “011234”.	Dans les exemples de marques d’homologation et dans les légendes situées en dessous, remplacer le numéro d’homologation “001234” par “011234”.

A parallel text corpus can be constructed manually or automatically. Normally, a parallel text corpus is only manually created for a language pair if existing resources such as translated documents, bilingual dictionaries are not available. For example, Almeman et al. (2013) described an effort to collect a parallel Arabic dialects corpora consisting of parallel sentences and speech utterances in Modern Standard Arabic, Gulf, Egypt, and Levantine dialects. The Modern Standard Arabic text, consisting of more than a thousand sentences, was prepared before being translated to the other three dialects. Another example

is the Malay dialect parallel corpora (Khaw et al., 2021) that contain the Kelantan Malay-Standard Malay and Sarawak Malay-Standard Malay parallel text and speech utterances. The dialect speech was first recorded. The speech was then transcribed before it was translated to Standard Malay.

If a parallel or comparable text is available, parallel sentences can be extracted to construct a parallel text corpus. A text is segmented into a smaller unit first, generally in sentences. For translated documents, such as novels and technical reports, after the text is segmented, the sentences in the source language text and the sentences in the target language text can be aligned to produce a parallel text corpus using a sentence alignment system.

### Sentence Alignment

The sentence alignment system automatically aligns sentences in the source language text and the target language text. The goal of sentence alignment is to match the source and target sentences with similar meanings. The sentence alignment algorithms may use the similarity comparison in terms of the sentence length and co-occurrence of lexical items in the source and target sentences to determine the sentences aligned together.

The early sentence alignment algorithms used sentence length as the heuristics for aligning sentences. Brown et al. (1991) proposed to use the number of words in the sentences for alignment. The basic idea is to align a long source sentence with a long target sentence and vice versa. Another heuristic used in the alignment is that the alignment must be in a monotonic sequence. For example, if source sentence  $i$  is aligned to target sentence  $j$ , source sentence  $i+1$  cannot be aligned to sentence  $j-1$ . The approach aligned source sentences to target sentences with many-to-one or one-to-many relationships, but at most, only two sentences can align with one sentence. The algorithm also used anchor points to reduce the complexity of the alignment algorithm. Gale and Church (1993) also proposed to use sentence length for aligning sentences. However, the approach is based on the character statistics in the sentence. A probabilistic score was calculated for each sentence pair based on the scaled difference of length of the sentence pair and the variance of the difference. Finally, the maximum likelihood alignment of the sentences was calculated to find the best alignment.

The limitation of the previous approaches is that they ignore the lexical items in sentences. Chen (1993) proposed a statistical word-based translation model that captures the word alignment probability of a source word  $w_s$  and a target word  $w_t$ ,  $p(w_s, w_t)$ . The expectation-maximization (EM) algorithm was used to estimate the model. The proposed approach calculated the sentence alignment probability for 1:0, 0:1, 1:1, 2:1, and 1:2 sentences. Sentence alignments with the highest probability were selected, and a minimum threshold was also applied to remove possible sentences without alignment. Another example is Champollion, which is a Chinese-English sentence alignment system. The

approach requires a bilingual word lexicon to be prepared before alignment (Ma, 2006). The bilingual lexicon was created from Chinese-English bilingual dictionaries. Champollion uses the bag-of-words model, and it calculates tf-idf for the words in the source and target segments to determine the similarity of the two segments. A segment consists of one or more sentences. A similarity measure that is based on tf-idf was proposed to calculate the weight of source-target word pairs. The word pairs that appear very frequent but not commonly found in all documents have a higher weight than less frequent and common word pairs. Champollion allows one-to-many and many-to-one alignments, with a maximum of four sentences aligned to one sentence. Dynamic programming was used in the lexical approach to search for the alignments with the highest total similarity.

Sennrich and Volk (2010) proposed an interesting idea to align source sentences and target sentences with the help of an MT system. The MT system was used to generate the translation for the source sentences; the hypothetical target sentences produced were compared with the target sentences using the BLEU metric. BLEU is an evaluation metric used in machine translation to compare the hypothesis translation to the reference translation. The BleuAlign algorithm created a matrix that contains the similarity score in BLEU between the hypothetical target sentence (from the translation of the source sentence) and the target sentences. Sentence pairs with the highest BLEU scores and which appeared in monotonic sequence were selected. Besides, heuristics were used to improve sentence alignment, such as aligning the unaligned sentences using the length-based alignment algorithm. A similar idea was proposed by Wolk and Marasek (2014) that also used MT to create hypothetical target sentences. In addition, they used WordNet to obtain synonyms for words in the target sentences to generate similar target sentences. Finally, a custom similarity metric was proposed that scored the source sentence and target sentences.

Grégoire and Langlais (2017) proposed to use bidirectional recurrent neural networks to extract parallel sentences from Wikipedia. The deep neural network processes a parallel document and outputs sentence alignments. The proposed approach needs a seed parallel text corpus that serves as positive examples for training the classifier. The negative examples were generated by randomly pairing non-parallel sentences. The source and target languages were encoded using bidirectional recurrent neural networks, and the matching information is estimated using their element-wise product and absolute element-wise difference. The cell can be an LSTM or a GRU. The probability that two sentences were a translation of each other was estimated by feeding the matching vectors into fully connected layers. A sentence pair was classified as parallel if the probability score was greater than or equal to a decision threshold.

On the other hand, Luo et al. (2021) presented an unsupervised sentence alignment method using deep neural networks. First, the bilingual pseudo documents were created from parallel documents (Vulić & Moens, 2015). Next, bilingual word embeddings were

extracted using word2vec approaches from pseudo documents. Then, word similarity was calculated using the cosine similarity. Finally, the similarity between two sentences was defined based on word similarity and word position. The sentence alignment problem was then converted into an extended earth mover's distance (EMD) problem. The approach is interesting as it does not require a seed parallel corpus. However, the approach will require a sufficiently large parallel document to learn robust bilingual word embeddings.

Sentence alignment techniques have improved from just sentence length to word translation models and bilingual lexicon. In addition, neural networks are now being used to model word semantics, encoding sentences, and latent word alignments in sentences.

### **Text Classifiers**

The approach using a classifier to align sentences by Grégoire and Langlais (2017) is interesting as classification is the core of machine learning, and the classification algorithms have been improving over the years. Classification is a process that predicts the category/label of a given data. Classification is supervised learning, where the classification algorithm identifies the significant features in the training data that are important in predicting the category of the data. In-text classification, the data being classified is text. The categories that a classifier predicts are task-dependent and depend on the training data. For instance, given a text with sentiment annotation, a classifier will learn to predict the sentiment in a text (Lim et al., 2020). In the case of sentence alignment, the alignment of two sentences of different languages can be solved as a text classification problem. The classifier learns the significant features in two sentences of different languages to predict whether the given sentences are parallel.

Before classification is carried out on a text, the text is first pre-processed, segmented, tokenized, and normalized. The pre-processing step removes the unwanted noise in the text. Next, the sentence segmentation splits a text into sentences. The tokenization step then segments every sentence into tokens that consist of words, punctuations, and numbers. Then, the normalization process standardizes the tokens in the text, such as lowercasing the characters and standardizing the acronyms. Additional steps may be performed depending on the classification problems, such as removing the stop words and lemmatizing/stemming the words.

Next, features are extracted from the normalized text. The types of features used in text classification can be divided into two: bag-of-words and word embedding. The bag-of-words features are used in conventional text classification algorithms such as decision trees, naïve Bayes, support vector machines, and multilayer perceptron. In the bag-of-words approach, a vector is used to store the statistics of every token that appears in the text. The statistics of the words used can be Boolean, word frequency, word probability, and tf-idf. The advantage of the approach is that it is simple to implement, but the disadvantage is

that the contextual information of a word is lost when words are converted to bag-of-words features.

On the other hand, word embedding approaches are techniques where words are represented as real-valued vectors in a vector space. Word embeddings are based on the idea of distributed semantics. The semantic similarities between words are based on their distributional properties in large text samples in distributional semantics. In other words, words that appear in the text with similar contexts have similar semantics. For example, the word “cough” and “sofa” can appear in similar contexts in a sentence. Word embedding is one of the most important advancements in semantic modeling from deep neural networks. Examples of approaches in word embeddings are 1) word embedding layer, 2) word2vec (Mikolov et al., 2013), and 3) count-based word embeddings (Stratos et al., 2015). An embedding layer is the input layer of a neural network that is jointly trained with a natural language processing task, such as sentiment analysis. The word2vec approach, on the other hand, is a standalone neural network approach that learns to convert words to vectors from a large text corpus. Examples of word2vec approaches are Skip-gram and Continuous Bag-of-Words (CBOW). The count-based word embedding is similar to the word2vec approach, where it is a standalone approach and learns from a text corpus. One major difference is that the count-based approach is based on counting the co-occurrence of words. On the other hand, the word2vec approaches do not involve counting words to derive the word to vector mappings.

After a text is converted to the respective features, the classification algorithm is applied to the features. This section discusses a conventional feedforward neural network and two state-of-the-art text classification algorithms: convolutional neural networks (CNN) and bi-directional long short-term memory (LSTM).

**Feedforward Neural Network Classifier.** Feedforward neural network is the earliest neural network used in classification. Figure 1 shows an example feedforward neural network that processes three inputs and produces two outputs. The output neurons convert the scores  $s_i$  to the estimated probabilities  $y_j$  of the corresponding classes. Equation 1 corresponds to the input layers, while Equation 2 corresponds to the output layer. The gradient descent algorithm will estimate the weight matrices during training by minimizing the loss function.

$$h = \phi(xW^T + b) \quad [1]$$

$$y = hU^T + b \quad [2]$$

where  $x$  is the inputs,  $y$  is the outputs,  $\phi$  is the activation function such as ReLU,  $W$  and  $U$  are the weight matrices, and  $b$  is the bias.

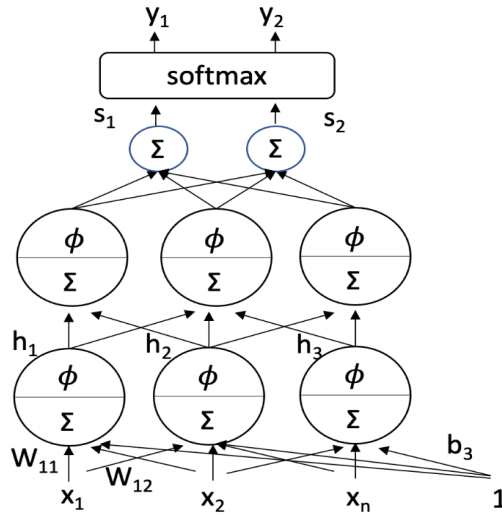


Figure 1. Feedforward neural network with two hidden layers and a Softmax output layer

**Bi-directional Long Short-Term Memory Classifier.** A recurrent neural network (RNN) is like the feedforward neural network, except it has a feedback loop. Long short-term memory (LSTM) is a special type of recurrent neuron. Bi-directional LSTM consists of a layer of LSTM that processes input from left to right and another layer of LSTM that processes the same input in the opposite direction. Many studies showed that bi-directional LSTM gives good results in time series classification problems such as sentiment analysis and text classification (Zhou et al., 2016). Figure 2a shows an LSTM memory cell.  $x_t$  is an input vector;  $\sigma$  and  $\tanh$  are neural network layers with sigmoid and hyperbolic tan activation function respectively, refer to Equation 1,  $c_t$  is the current cell state;  $h_t$  is the hidden state;  $\times$  and  $+$  are the pointwise multiplication and addition operation respectively. Figure 2b shows that input vectors  $x_t$  is input to a layer of forward LSTM,  $LSTM_{fw}$  that processes the input vectors from left to right, and a layer of backward LSTM,  $LSTM_{bw}$  that processes the input in the opposite direction. Refer to Equations 3, 4, and 5.

$$h_{fw,t} = LSTM_{fw}(h_{fw,t-1}, x_t) \tag{3}$$

$$h_{bw,t} = LSTM_{bw}(h_{bw,t-1}, x_t) \tag{4}$$

$$h_t = [h_{fw,t}; h_{bw,t}] \tag{5}$$

The output states,  $h_t$  from both LSTM are concatenated to become a single vector, and the vector goes through a Softmax output layer before classification. One or more dense layers are often added before the output layer.

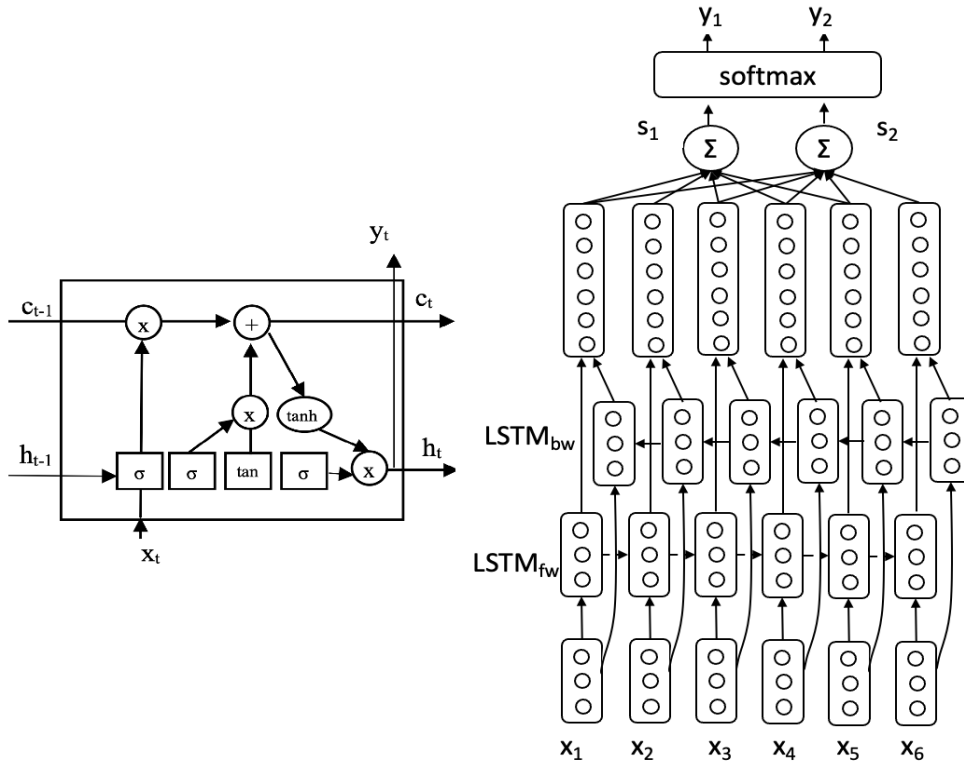


Figure 2. a) Left, an LSTM memory cell. b) Right, a bi-directional LSTM with a SoftMax output layer

**Convolutional Neural Network Classifier.** Convolutional neural network (CNN) emerged from the study of image recognition. Since its introduction, it has achieved state-of-the-art performance in image recognition tasks and later text classification (Kim, 2014). A CNN consists of a convolutional layer and pooling layer. A convolutional layer consists of filters or kernels. The purpose of a filter is to highlight the areas in an image that are most similar to it. The weights for a filter will be learned during training, and the networks learn to combine the filters to recognize complex patterns (Equation 6).

$$h_{i,j,k} = \phi \left( \sum_{u=1}^h \sum_{v=1}^w \sum_{k=1}^n x_{i,j'} w_{u,v,k} + b_k \right) \quad [6]$$

where  $h_{i,j,k}$  is the output of the feature map  $k$ , at row  $i$ , and column  $j$ ;  $w$  is the weights of the filter  $k$ ;  $b_k$  is the bias of feature map  $k$ .



The pooling layer is a downsampling operation that is applied normally after the convolutional layer. There are two types of pooling functions, max-pooling and average-pooling. The max-pooling operation selects the maximum value of the current view, while the average-pooling averages the values of the current view. Max-pooling preserves the detected features, and it is more commonly used.

Figure 3 shows a CNN used for recognizing a written character. It consists of a convolutional layer and a max-pooling layer. The output of a max-pooling has to be flattened to become a one-dimensional vector before it can be input to a layer of dense network for classification.

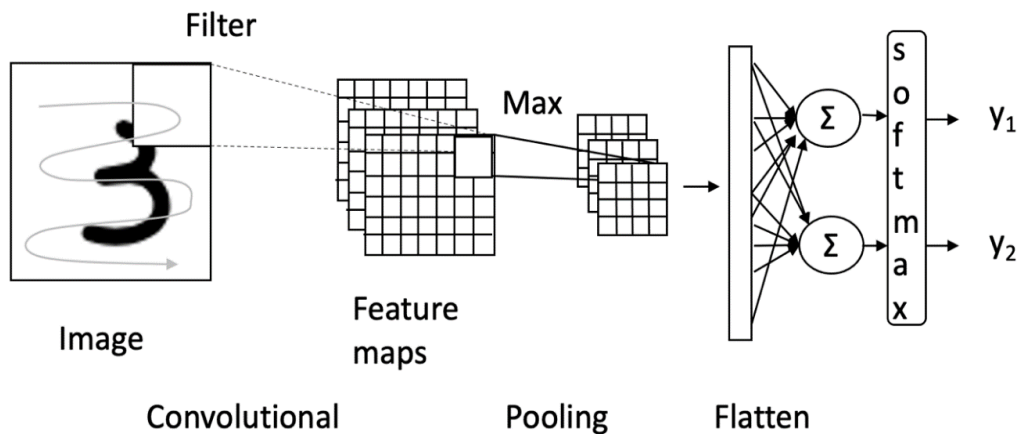


Figure 3. CNN classifier for image recognition. A convolutional layer is followed by a max-pooling layer and a Softmax output layer

## MATERIALS AND METHODS

We solve the problem of aligning two sentences of different languages as a classification problem. The Boolean classifier scores two sentences as parallel/non-parallel sentences given text in the source and the target languages. A sliding window subsequently aligns the source sentences and the target sentences using the scores generated by the classifier.

### Parallel LSTM with Attention and CNN Classifier

We propose a new model, parallel LSTM with attention and CNN, classifying a source sentence and a target sentence as parallel/non-parallel sentences. Thus, the classifier will evaluate a given pair of semantically similar sentences as a parallel sentence and a pair of semantically non-similar sentences as non-parallel. For example, the pairs of words/phrases/sentences in Table 1 are parallel because they are semantically similar. Figure 4

shows our proposed architecture. The encoder-decoder inspires the proposed architecture with attention architecture used in sequence-to-sequence modeling (Luong et al., 2015).

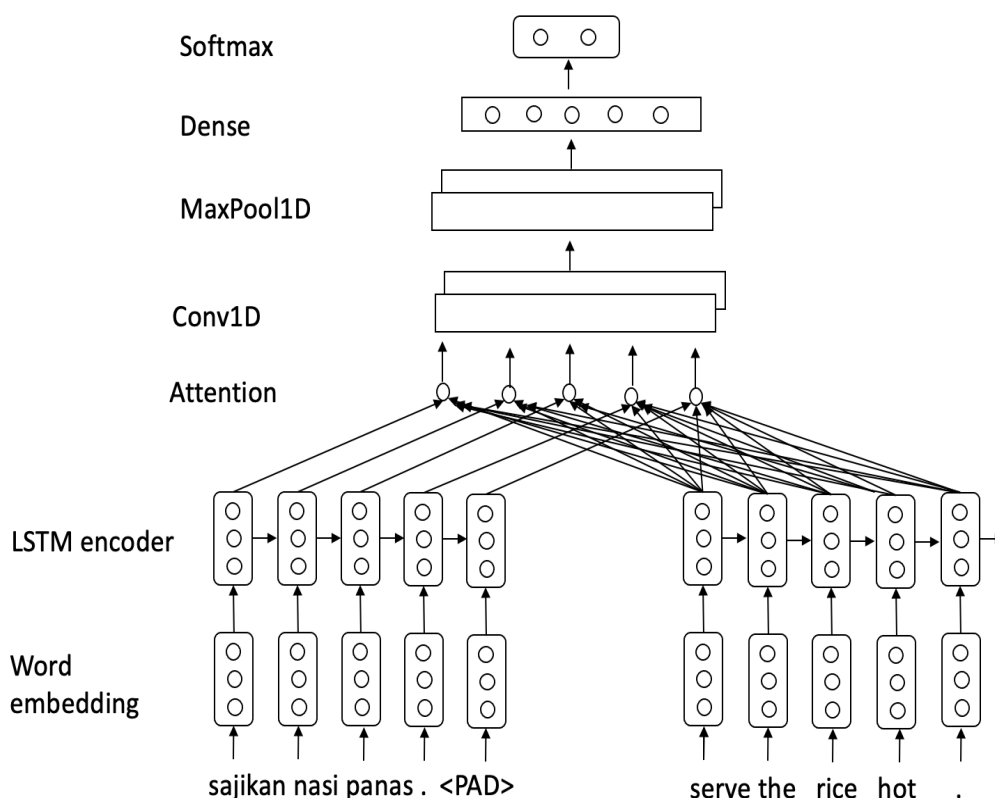


Figure 4. Parallel LSTM with attention and CNN (Parallel LSTM+Attention+CNN)

The sentences will be tokenized and normalized given a source sentence,  $x_s$ , and a target sentence,  $x_t$ . The tokens in the sentences will be converted to embedding vectors,  $v_s$ , and  $v_t$ . In the proposed approach, we use the word embedding model. First, the word2vec approach is preferred since it reduces the time for training the classifier model later. Second, the number of parameters to be tuned during training is reduced. Third, more text can train the word embedding vectors, producing a more robust model. The vocabulary for the word embedding model must be specified. The words that are not in the vocabulary will be mapped to a special tag, <UNK>. The length of a sentence is set to N tokens. If the length of a sentence is less than N, then the sentence will be padded with the tag <PAD>.

After the word embedding models for the source and target languages have been trained, the source sentences and target sentences are converted to the embedding vectors

using the respective model. The source vector  $v_s$  is input to a source LSTM, while the target vector  $v_t$  is input to a target LSTM. For each input vector, the LSTM will output a hidden state. For example, the source LSTM will output hidden states  $h_i$ , while the target LSTM will output hidden states  $s_i$ . The attention scores are calculated using Equation 7 below. In general, the attention mechanism calculates the alignment distribution between the source output hidden states and the target output hidden states. For example, if the length of the source sentence and the target sentence is  $N$ , then an attention matrix of size  $N \times N$  will be produced.

$$e(t, i) = [s(t)^T, h(i = 1) s(t)^T h(2) \dots, s(t)^T h(N)] \quad [7]$$

The attention matrix is input to a layer of a convolutional layer. The purpose of the convolutional layer is to extract high-level features from the attention scores that are important in identifying the semantic similarity between the source sentence and the target sentence. Max-pooling, on the other hand, filters the noise in the data by choosing the prominent features. The matrix output will be flattened before input to a dense layer of neurons. The output from the dense layer will then be sent to the Softmax layer containing two neurons classified as non-parallel or parallel. The Softmax layer gives a probability/score between zero and one for each category. Since there are only two categories for this model, the category that has a probability of more than 0.5 is selected.

For training the classifier to learn to identify non-parallel/parallel sentences, training examples from a seed parallel text corpus is required. Since a parallel text corpus only contains the valid pairs of the parallel sentence, the non-parallel sentence pairs (or semantically non-similar sentence pairs) have to be added to the training data. We generate the non-parallel sentence pairs by pairing for every source sentence a randomly selected target sentence where the sentence length is plus/minus three tokens. If no target sentence meets the requirement can be found, then a random target sentence is paired with the source sentence. The purpose of selecting a sentence with a length close to the valid target sentence is to avoid the classifier from using the sentence length as a criterion to identify non-parallel/parallel sentences and to force it to learn from the similar lexical items in the sentences. Therefore, the parallel pairs are annotated as “1” and the non-parallel pairs as “0”. Table 2 shows an example of generated records from the data in Table 1.

Table 2

*An example of generated records from the data in Table 1*

English	French	Ann.
GENERAL	GÉNÉRALE	1
GENERAL	2 février 1999	0
2 February 1999	2 février 1999	1
2 February 1999	GÉNÉRALE	0
2. Paragraphs 4, 5 and 6 of the resolution read as follows:	2. Les paragraphes 4, 5 et 6 de cette résolution se lisent comme suit :	1
2. Paragraphs 4, 5 and 6 of the resolution read as follows:	2 février 1999	0
In the example of approval marks and in the captions below, replace approval number "001234" by "011234".	Dans les exemples de marques d'homologation et dans les légendes situées en dessous, remplacer le numéro d'homologation "001234" par "011234".	1
In the example of approval marks and in the captions below, replace approval number "001234" by "011234".	2. Les paragraphes 4, 5 et 6 de cette résolution se lisent comme suit :	0

### Source Sentence and Target Sentence Sliding Window

The information on the type of document for sentence alignment can be taken advantage. When the sentences to be aligned are translated texts, for example, the translation of a novel or book, most of the sentences, if not all, in the source text and the target text should be aligned in the same order. Nevertheless, it is possible for a translator to translate a part of a sentence or to translate more than one sentence into a single sentence. Therefore, the heuristics that the source sentences and target sentences appear in the monotonic sequence can be used in aligning the sentences assuming the texts we are aligning are translated materials. Besides, by knowing the type of documents used in alignment, the time complexity of the alignment can be improved by searching the areas for possible targets instead of searching for the target everywhere.

We propose to use a sliding window that will match a source sentence at line  $i$ ,  $x_{s,i}$  to some target sentences at line  $j$ ,  $x_{s,j}$ . The classifier is then used to classify the pair of the source sentence and target sentence as either non-parallel/parallel. Below is the definition of the sliding window (Equations 8, 9, and 10):

$$i' = i + 1 \quad [8]$$

$$j' = \text{round}(i' \times J) \quad [9]$$

$$J = N_t/N_s \quad [10]$$

- $x_{s,i}$ : source sentence at line  $i$ .  $0 < i \leq N_s$
- $\{x_{s,j} : \text{target sentences at line } j, i-d \leq j \leq i+d \cap 0 < j \leq N_t\}$
- $i$ —the current source sentence at line  $i$ .
- $i'$ —the next source sentence at line  $i'$ .
- $j'$ —the next target sentence at line  $j'$ .
- $J$ —incrementing step.  $J > 0 \cap J \in \mathbb{R}$ .
- $d$ —size of the sliding window.  $d \in \mathbb{Z}^{0+} \cap d < N_t$ .
- $N_s$ —the total number of lines in the source text.
- $N_t$ —the total number of lines in the target text.

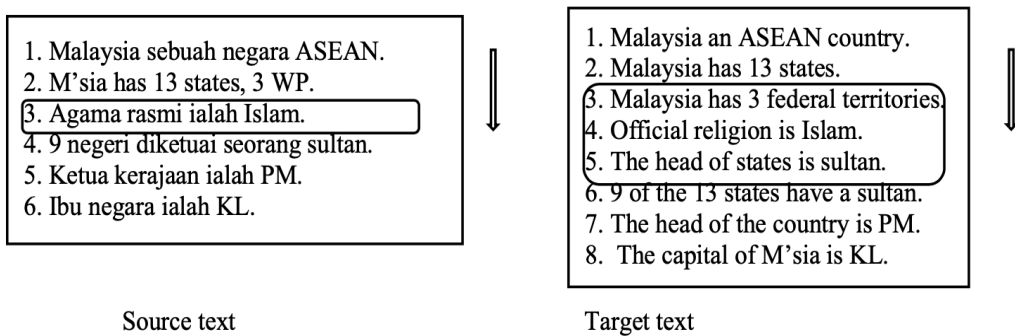


Figure 5. A sliding window matches the source sentence at line three to target sentences at lines three, four, and five, where  $d=1$ ,  $J=1.33$

Figure 5 shows a source text with six sentences and a target text with eight sentences, and the sliding window is based on the definition given in Equations 8, 9, and 10. Two important parameters that have to be set for the sliding window are  $d$ , and  $J$ .  $d$  is manually set, normally in the range of 1 to 5. Step  $J$  can be manually set or set by default calculated as in Equation 10. In Figure 5, the source sentence at line 3 is matched to the target sentences at lines 3, 4, and 5. The classifier is then used to classify every pair of a source-target sentence,  $(x_{s,3}, x_{t,3})$ ,  $(x_{s,3}, x_{t,4})$ , and  $(x_{s,3}, x_{t,5})$ .

For aligning the sentences in the source text and the target text, we use the probability returned by the classifier when it compares a given source sentence  $x_{s,i}$  and a target sentence  $x_{t,j}$ , for classification, instead of using the classification category that is returned by the classifier. Given a source text and a target text, the source sentence, and the target sentence alignment,  $A'$  is the set of the source sentence and target sentence alignment, and  $a'(x_{s,i}, x_{t,j})$  is the tuple that consists of the aligned source sentence and target sentence such as in Equation 11:

$$A' = \underset{0 < j < N_t}{\underset{0 \leq i \leq N_s}{\operatorname{argmax}}} P(x_{s,i}, x_{t,j}) \quad [11]$$

where  $x_{s,i}$  is line/sentence  $i$  of source text, and  $x_{t,j}$  is line/sentence  $j$  of target text.  $N_s$  is the total number of lines in the source text, and  $N_t$  is the total number of lines in the target text. If  $a'(x_{s,i}, x_{t,j})$ ,  $a'(x_{s,p}, x_{t,q})$  and if  $p \geq i \rightarrow q \geq j$ . In other words, we want to find the source-target sentence alignment,  $A'$ , that has the highest overall probability. A source sentence can align to one or more target sentences, and a target sentence can be aligned to one or more source sentences, but the alignments must be in a monotonic sequence.

Dynamic programming is used to find the set of aligned source sentences and target sentences that has the highest overall probability,  $a'(x_{s,i}, x_{t,j})$ . A table is used to store the score of the alignments,  $Sc(x_{s,i}, x_{t,j})$ . The example source text and target text from Figure 5 are used to create Figure 6. The bottom first row of Figure 6 indicates the sentence  $i$  of the source text, while the first column indicates the sentence  $j$  of the target text. A cell in the table stores the alignment probability between a source sentence  $i$  and a target sentence  $t$ ,  $P(x_{s,i}, x_{t,j})$ . The probability  $P(x_{s,i}, x_{t,j})$  is converted to log probability to improve the time complexity and to avoid underflow. Thus, the  $P(x_{s,i}, x_{t,j})$  in Equations 12 and 13 are in log probability. Imaginary  $P(x_{s,i}, x_{t,j})$  were assigned in Figure 6 to show the calculations. The grey cells correspond to source-target sentence pairs that were not evaluated by the classifier because they are outside of the sliding window. Thus, the log probability  $P(x_{s,i}, x_{t,j})$  is set to  $-\infty$ . The algorithm calculates from the bottom left cell to the top right cell. The score for the cell ( $i=1, j=1$ ) is initialize to the value of  $P(x_{s,1}, x_{t,1})$ , while the alignment is set to  $(0, 0)$  (Equations 12 & 14). Equation 13 is used to calculate the rest of the cells. For example score at the cell  $(2,2)$  is calculated as follow:

$$\begin{aligned} Sc(x_{s,2}, x_{t,2}) &= \max(Sc(x_{s,1}, x_{t,2}), Sc(x_{s,2}, x_{t,1}), Sc(x_{s,1}, x_{t,1})) + P(x_{s,2}, x_{t,2}) \\ &= \max(-1.1, -\infty, \underline{-0.1}) + (-0.2) \\ &= -0.1 - 0.2 \\ &= -0.3 \end{aligned}$$

The  $a(x_{s,i}, x_{t,j})$  keep track of the alignment  $i$  and  $j$  that produces the highest score,  $Sc(x_{s,i}, x_{t,j})$ . Refer to Equation 15. After all the scores are calculated from bottom left to top right,  $A'$  can be obtained by backtracking from  $a(x_{s,N_s}, x_{t,N_t})$  until  $a(x_{s,1}, x_{t,1})$  by following along  $a(x_{s,i}, x_{t,j})$  from the top right cell.

8						$P=-2$ $Sc=\max(-\infty, -\underline{3.3}, -\infty)$ $=-5.3$ $a=(5,7)$	$P=-0.5$ $Sc=\max(-5.3, -4.3, \underline{3.3})$ $=-3.8$ $a=(5,7)$
7						$P=-0.1$ $Sc=\max(-\infty, -5.7, \underline{3.2})-0.1$ $=-3.3$ $a=(4,6)$	$P=-1$ $Sc=\max(\underline{3.3}, -\infty, -5.7)-1$ $=-4.3$ $a=(5,7)$
6					$P=-0.5$ $Sc=\max(-\infty, -\underline{2.7}, -4.7)$ $=-3.2$ $a=(4,5)$	$P=-3$ $Sc=\max(-3.2, -\infty, \underline{2.7})-3$ $=-5.7$ $a=(4,6)$	
5				$P=-4$ $Sc=\max(-\infty, -\underline{0.7}, -3.7)-4$ $=-4.7$ $a=(3,5)$	$P=-2$ $Sc=\max(-4.7, -3.2, \underline{0.7})-2$ $=-2.7$ $a=(3,4)$		
4			$P=-3$ $Sc=\max(-\infty, -\underline{0.7}, -\infty)-3$ $=-3.7$ $a=(2,3)$	$P=0$ $Sc=\max(-3.7, -2.3, \underline{0.7})+0$ $=-0.7$ $a=(2,3)$	$P=-2.5$ $Sc=\max(\underline{0.7}, -\infty, -2.3)-2.5$ $=-3.2$ $a=(3,4)$		
3			$P=-0.4$ $Sc=\max(-\infty, -\underline{0.3}, -1.1)-0.4$ $=-0.7$ $a=(2,2)$	$P=-2$ $Sc=\max(-0.7, -\infty, \underline{0.3})-2$ $=-2.3$ $a=(2,2)$			
2		$P=-1$ $Sc=\max(-\infty, -\underline{0.1}, -\infty)-1$ $=-1.1$ $a=(1,1)$	$P=-0.2$ $Sc=\max(-1.1, -\infty, \underline{0.1})-0.2$ $=-0.3$ $a=(1,1)$				
1		$P=-0.1$ $Sc=-0.1$ $a=(0,0)$					
0							
j \ / \ i	0	1	2	3	4	5	6

Figure 6. A table is used to keep track of the alignment score, Sc, in dynamic programming. This table is created based on the sliding window in Figure 5.

Backtracking from the top right cell (6,8) in Figure 6, we get (5,7), (4,6), (4,5), (3,4), (2,3), (2,2), (1,1), (0,0), which correspond to the sentence alignment in Table 3.

Table 3

*An example of generated records for training the classifier from the data in Table 1*

i	Source Text	j	Target Text
1	Malaysia sebuah negara ASEAN.	1	Malaysia an ASEAN country.
2	M'sia has 13 states, 3 WP.	2	M'sia has 13 states, 3 WP.
2	M'sia has 13 states, 3 WP.	3	Malaysia has 3 federal territories.
3	Agama rasmi ialah Islam.	4	Official religion is Islam.
4	9 negeri diketuai seorang sultan.	5	The head of states is sultan.
4	9 negeri diketuai seorang sultan.	6	9 of the 13 states have a sultan.
5	Ketua kerajaan ialah PM.	7	The head of the country is PM.
6	Ibu negara ialah KL.	8	The capital of M'sia is KL.

## RESULTS AND DISCUSSIONS

We evaluated our proposed classifier for classifying tasks using two datasets, our Malay-English parallel text corpus and the French-English parallel sentences from UN parallel text corpus (Ziemski et al., 2016). The setup for training and testing the classifiers for both datasets is as follows. The training set consists of 50 thousand parallel sentences, and the validation set consists of 3 thousand parallel sentences. Since the parallel text corpus consists of only valid pairs of parallel sentences, for every source sentence in the parallel text, a pair of the non-parallel sentence was randomly generated as described in the previous section for the training set and validation set. As a result, the size of the training and validation set double. For testing the classifier performance, a test set that consists of more than 25 thousand parallel/non-parallel sentences that were prepared just like the training and validation set was used.

For evaluating the classifier in aligning sentences, only Malay-English texts were evaluated. For testing the classifier for aligning sentences, we prepared two tasks. The first task was to evaluate the alignment of sentences in research documents. We selected ten postgraduate research thesis documents <http://eprints.usm.my/view/type/thesis.html> that contain abstracts written in Malay and English from different domains such as social science, computer science, and engineering. The abstract texts were selected so that the number of sentences in the source and target documents differed. We combined all the selected texts into a single Malay document and an English document to increase the difficulty further. The resulting Malay document contains 161 sentences, while the English document contains 164 sentences. We aligned sentences in a Classical Malay document



and its translation text in English for the second alignment task. The reason for selecting Classical Malay for alignment is because the result obtained serves as a lower bound for the sentence alignment algorithms as Classical Malay is very different from Standard Malay text. We manually extracted chapter one of “*Hikayat Hang Tuah*” (Ahmad, 2017) and the literature’s English translation “The Epic of Hang Tuah” (Salleh, 2010) for evaluation. The extracted Classical Malay document contains 227 sentences, while the English document contains 184 sentences. Table 4 summarizes the data used for training, validation, and testing.

Table 4  
*Training, validation and testing data*

Data	Size (number of sentences)
Training: Malay-English and French-English (UN)	100,000
Validation: Malay-English and French-English (UN)	6,000
Classification Test: Malay-English and French-English (UN)	25,000
Sentence Alignment Test 1: 10 research articles	161 (Malay), 164 (English)
Sentence Alignment Test 2: <i>The Epic of Hang Tuah</i>	227 (Classical Malay), 184 (English)

Our proposed parallel LSTM classifier with attention and CNN was trained using the word embedding features. The LSTM layer consists of 128 units. The time step of the LSTM was set to the maximum length of the sentence, which is 80 words. The subsequent layer, which is the convolutional layer, consists of 128 filters, and the size of the filter is 3. The dense layer before the output layer consists of 16 neurons with a ReLU activation function. The input for the classifier is GloVe word embedding features (Pennington et al., 2014). The English word embedding was downloaded from the GloVe GitHub page, and the size of the vocabulary is 400 thousand with 100 dimensions. The Malay GloVe word embedding with 100 dimensions and the vocabulary size was 146 thousand words; It was trained using our Malay text corpus that consists of more than 800 MB of clean text. The French GloVe word embedding with 100 dimensions and more than 350 thousand vocabularies was trained using the French text from the UN parallel text corpus. An unknown word embedding, <UNK> was calculated for the source and target languages by averaging all the word embeddings for each corresponding language. The <PAD> word embedding vector was set to zeros.

We compared our proposed classifier with three baseline classifiers. First, a conventional text classifier using the feedforward neural network and bag-of-words model was evaluated. The feedforward neural network consists of two hidden layers. The first layer consists of 128 neurons, while the second layer consists of 32 neurons. The activation function for the neurons is ReLU, and the optimizer was Adam. Our dataset’s source and target sentences were tokenized using NLTK tokenizer and normalized by lowercasing the characters. The stop words were removed from the sentences. The words not in the vocabulary list were mapped to the <UNK> in the source/target language. The tf-idf for the words in the source sentences and target sentences were calculated separately for the source language and target language. Finally, the bag-of-words vector from the source sentence and the target sentence were concatenated to become one. The feedforward neural network with the bag-of-words model was trained using the training set and the above validation set until converged.

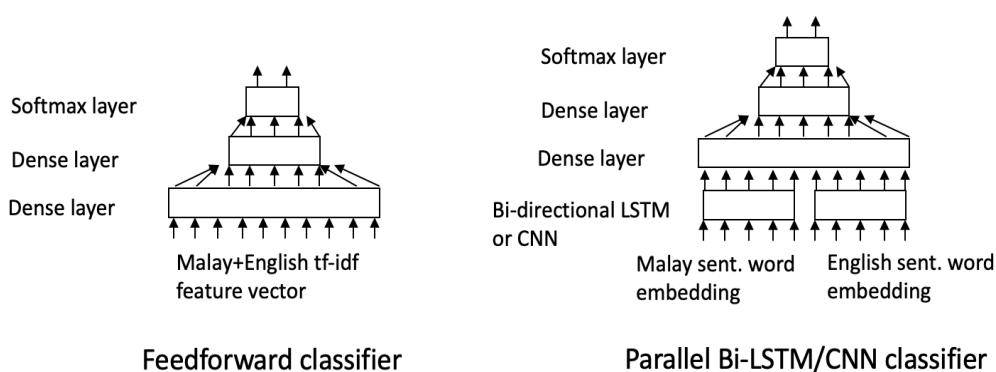


Figure 7. The architecture of the feedforward classifier, parallel bi-directional LSTM, and parallel CNN classifier used.

Two state-of-the-art classifiers using bi-directional LSTM and CNN discussed in the previous section were also compared to the proposed model. Some modifications allowed the classifiers to process two inputs, Malay-English or French-English sentences/word embedding vectors. Refer to Figure 7. The parallel bi-directional LSTM classifier consists of two LSTMs that process Malay and English word embedding feature vectors. Both bi-directional LSTM was set to 128 units. The time step was set to 80. The outputs from the two LSTMs were flattened and concatenated to become a single vector before sending it to two-layer dense neural networks with 64 and 16 neurons, respectively, with ReLU activation function. Finally, the output from the dense layer was sent to the Softmax output layer. For the parallel CNN classifier, two CNNs of the convolutional layer and the max-pooling layer were used to process Malay and English word embedding features. The convolutional layer

consists of 128 filters with the size set to 3. Like the bi-directional LSTM, the CNN layer output was flattened and sent to a two-layer dense neural network before the output went to the Softmax output layer. The number of neurons at the two-layer dense neural network was set to 32 and 8, respectively, with the ReLU activation function. The optimizer used was Adam. The models were trained until they converged.

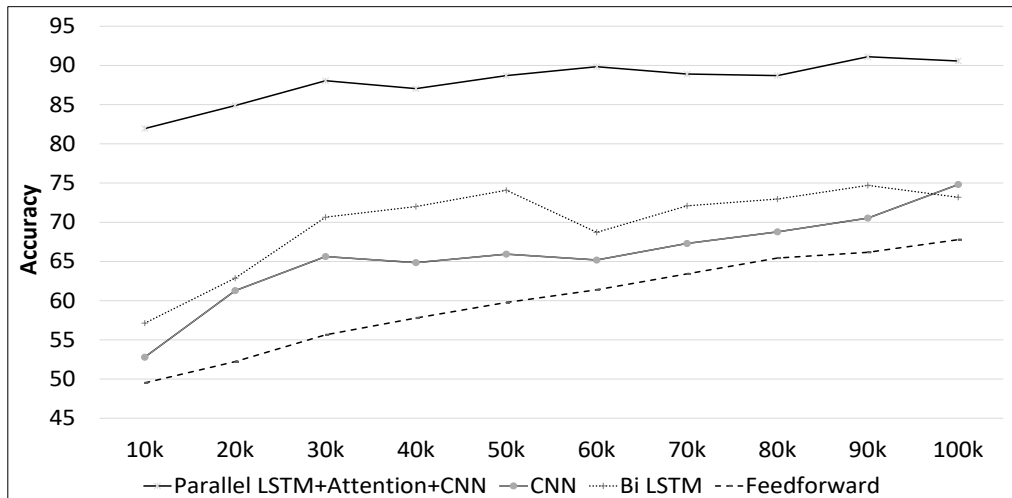


Figure 8. Malay-English parallel/non-parallel sentence classification using different classifiers with different amounts of training data.

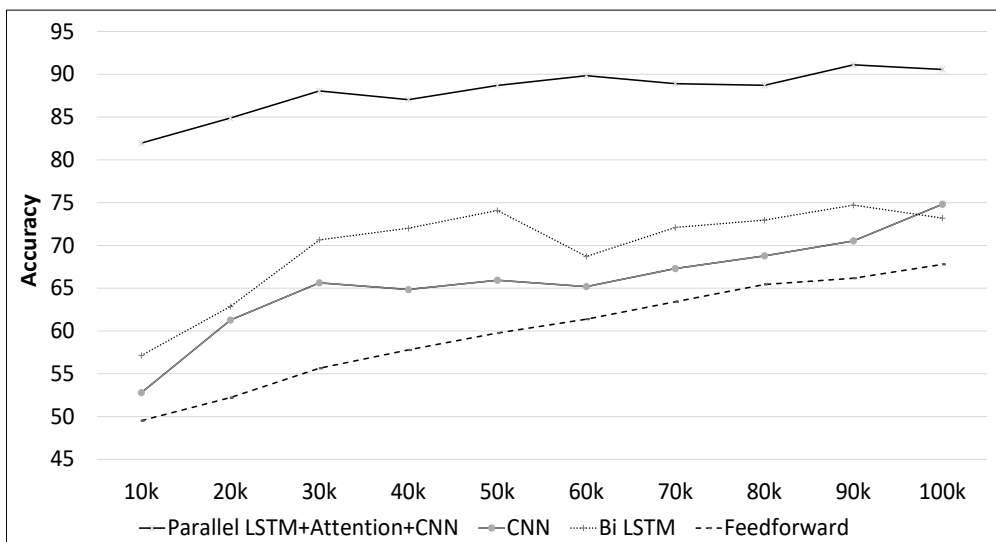


Figure 9. UN French-English parallel/non-parallel sentence classification using different classifiers with different amounts of training data.

Figures 8 and 9 show parallel/non-parallel sentence classification accuracy using different Malay-English models and French-English models. In both the experiments, the training data used to build the models varies from 10 thousand to 100 thousand sentences. The results show that our proposed parallel LSTM+Attention+CNN classifier achieved the highest accuracies under different settings, followed by parallel bi-directional LSTM, parallel CNN, and feedforward neural network in both datasets. The classifier trained and tested on the UN French-English parallel text corpus has higher accuracy than the Malay-English parallel text corpus because the training and testing data are from the same domain. However, the training and testing data in the Malay-English parallel text corpus are from different domains. Adding more training sentences improved the accuracy of all classifiers. The parallel LSTM+Attention+CNN classifier obtained classification accuracies of 81.96% and 87.01% with the Malay-English model and French-English model, respectively, using 10 thousand training sentences. When the number of sentences was 100 thousand, the accuracies of the proposed classifier increased to 90.57% and 96.12% when classifying Malay-English sentences and French-English sentences, respectively. The parallel bi-directional LSTM has the second-best accuracy overall. The parallel CNN classifier was slightly worse than parallel bi-directional LSTM in terms of accuracy. Based on the result, the CNN classifier requires more than 20 thousand parallel sentences to obtain a reasonably good classification accuracy. The feedforward neural network was the worst performer among all the classifiers.

The LSTM, bi-directional LSTM, and CNN in the classifiers encode given sentences to sentence vectors. Encoding sentences using CNN was first proposed by Kim (2014) to be used in sentiment classification. After the sentences are encoded in the parallel bi-directional LSTM and CNN classifier, the subsequent layers compare the encoded sentences in terms of their similarity and classify similar sentences as parallel and vice versa. In the parallel bi-directional LSTM classifier and the parallel CNN classifier, the higher layers were the same, consisting of two dense layers. Based on the results of the parallel bi-directional LSTM classifier and parallel CNN classifier, we observed that the bi-directional LSTM is slightly better in encoding sentences than CNN in this study, as bi-directional LSTM achieved higher accuracy in the classification tasks.

On the other hand, there is an attention mechanism in our proposed LSTM with attention and CNN classifier after the LSTMs encode the sentences to sentence vectors. The attention mechanism learns the relationship between the lexical items between the sentence vectors. Figure 10 shows an interesting visualization of the attention matrix when two test sentences, “*dia benci akan pergaduhan dan pembunuhan*” and “he abhors fighting and killing,” were input to the classifier. The attention weights were normalized and set to brighter color for a higher value. In Figure 10, the attention cells that align between the words ‘*dia*’ and ‘he,’ ‘*pergaduhan*’ and ‘fighting,’ ‘*pembunuhan*’ and ‘killing’ have high

values. During training, the attention mechanism learns to associate between lexical items of the given language pair that frequently appear together by assigning higher weights to them. Often, these are words that are a translation of each other. The attention mechanism is the main contributor to the increment in the classification accuracy because the attention learns the soft lexical alignments in the sentence. Subsequently, the CNN layer then learns the patterns of the attention matrix to classify it as parallel or non-parallel.

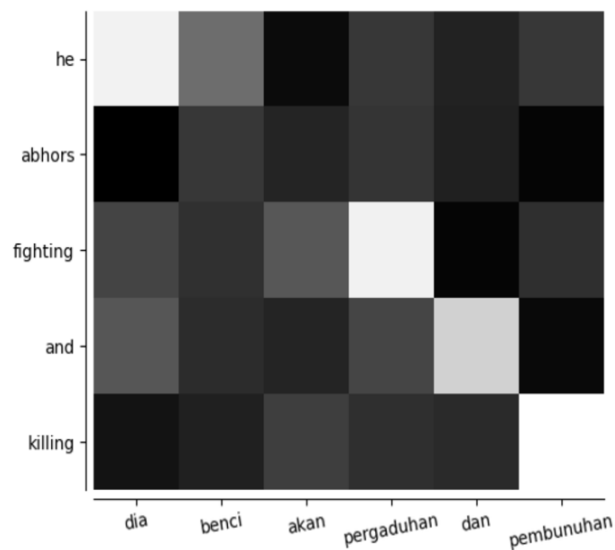


Figure 10. Visualizing the attention matrix

In the second experiment, we evaluated the alignment of Malay and English documents using the proposed sliding window approach with different classifiers. For this study, the classifiers' models that were trained using all the training data were used. The window size  $d$  was set to three for all the experiments, and the step size  $J$  was estimated using Equation 11. Besides the classifiers, we also tested BleuAlign in aligning the documents. BleuAlign needs an MT system to produce hypothetical translation for the source sentences before using sentence alignment. We used a statistical machine translation system (Yeong et al., 2019) for this purpose. Table 5 shows the accuracies of the sentence alignment using different classifiers and the BleuAlign system. In general, the result aligns with the performance of the classifiers, where the classifier with the higher accuracy in the first task achieved a higher sentence alignment accuracy. The proposed parallel LSTM+Attention+CNN classifier obtained the highest sentence alignment accuracy on the research and Classical Malay documents. The accuracies obtained for the two tasks were 95.75% and 51.24%, respectively. The second-best classifier was the parallel bi-directional LSTM, which scored 86.06% and 36.82%, respectively, for the two tasks.

On the other hand, the BleuAlign system achieved 78.18% and 23.01% accuracy for the two-sentence alignment tasks. From the experiment result, using the sliding window approach with the classifiers increased the accuracy of sentence alignments on the research document.

The sliding window limits the search of the sentences to within the search window (which is  $2 \times \text{window size} + 1$ ). It improves the searching time and accuracy when aligning the research document due to the heuristic that sentences are aligning in monotonic order. However, without limiting the search space, the accuracy of the classifier in aligning the sentences may reduce due to the following three reasons. First, a sentence in a source document can be translated to zero or more sentences in the target document, or more than one sentence in the source document can be translated to a single target sentence. Second, when we evaluated the classifiers in the previous experiment, there were no partially matched sentences in the training or testing data since the training and testing data were generated from a parallel corpus. These partially match sentences may increase the error rate of the classifier since the classifier was not specifically trained for it.

Nevertheless, there was no drop in the accuracies in the experiment result when using the sliding window with the classifier, even though about 20% of the source sentences and target sentences were partially matched sentences. Second, when the search space increases, the probability for a classifier to make an error by matching a source sentence to similar target sentences will increase. For instance, consider two target sentences that differ only in one word. The possibility for the classifier to make an error will increase in this case. Third, the difference in testing and training domain may reduce the accuracy of the classifier in the alignment. For instance, in the case of French-English parallel sentence classification, the training and testing data were from the same domain. Thus, it achieved higher classification accuracy than the Malay-English parallel text classification where the training and testing data were acquired from different sources. Finally, the sliding window approach may reduce the effect of domain mismatch. It can be observed in the slight improvement in the accuracy of the sentence alignment when the Malay-English classifier was used with the sliding window. However, if the domain is very different, for instance, in the case of the alignment of sentences in classical Malay documents, the accuracy may also drop.

One of the challenges in aligning Classical Malay sentences is the differences in Classical Malay writing compared to Standard Malay. Besides, the English translation of the Classical Malay literature was written using semantic/free translation, increasing the alignment difficulty. Therefore, Classical Malay and Standard Malay are compared below, with example sentences from *Hikayat Hang Tuah*.

- The use of 'maka' (then) and 'hatta' as the start of the sentence. These words function as punctuation words in Jawi. Example: "*maka baginda pun tersenyum*" (His Majesty smile)

Table 5

*Accuracy of different classifiers and BleuAlign in aligning sentences in Malay document and English document*

Classifier/System	Classical Malay	Research Document
Parallel LSTM+Attention+CNN	51.24%	95.75%
Parallel Bidirectional LSTM	36.82%	86.06%
Parallel CNN	27.36%	82.42%
Feedforward	28.36%	58.79%
BlueAlign	23.01%	78.18%

- Passive sentence is frequent in Classical Malay text. Example: “*maka digelar oleh baginda bendahara paduka raja.*” (He was bestowed by His Majesty bendahara paduka raja.)
- Frequently used of the particle ‘*pun*’ and ‘*lah*’ in Classical Malay text. ‘*pun*’ and ‘*lah*’ form special feature structures in Classical Malay. The ‘*pun-lah*’ structure indexes an event (-*lah*) and the participant (pun) who or which will be under investigation (Ajamiseba, 1983). Example: “*maka segala menteri pun kembalilah ke rumahnya.*”
- Classical Malay sentences are often long and convoluted. The longest test sentence is 80 words long!
- The words/phrases with the same surface form in Malay and Classical Malay have different meanings. For example, the phrase ‘*berapa lamanya ...*’ means “after a while...” in Classical Malay but in Standard Malay, it means “how long...” The corresponding phrase in Standard Malay is “*selepas seketika*”. Example: “*hatta berapa lamanya maka Tuan Puteri Kemala Ratna Pelinggam pun besarlah...*”

## CONCLUSION

In this study, the parallel LSTM with attention and CNN is proposed for classifying two sentences as parallel/non-parallel sentences. The parallel LSTM+Attention+CNN classifier shows a higher classification accuracy than the feedforward classifier, bi-directional LSTM classifier, and CNN classifier. A sliding window that matches the source sentence and target sentences for alignment is also proposed for aligning translated documents. The sliding window selects sentence alignments with the highest overall probability and assumes sentence alignment appears in monotonic order. In aligning Malay-English sentences in the research document and Classical Malay-English document, the parallel LSTM+Attention+CNN approach produced better sentence alignment compared to the other baseline systems. Thus, the sliding window approach is suitable for the proposed classifier to construct a parallel text from translated documents. However, it is not suitable for comparable texts, for example, similar news in different languages by different

publishers or similar Wikipedia topics in different languages where the sentence alignments may appear in a free order, and the only fragment of a sentence may be aligned. Our future work will be to extend our study to this problem.

## ACKNOWLEDGMENT

This research was supported by The Research University Grant (RUI) (1001.PHUMANITI.8016043) from Universiti Sains Malaysia.

## REFERENCES

- Ahmad, K. (2017). *Hikayat Hang Tuah* [The epic of Hang Tuah]. Dewan Bahasa & Pustaka.
- Ajamiseba, D. C. (1983). *A classical malay text grammar: Insights into a non-wester text tradition*. Australian National University.
- Almeman, K., Lee, M., & Almiman, A. A. (2013). Multi dialect Arabic speech parallel corpora. In *Proceedings International Conference on Communications, Signal Processing, and Their Applications (ICCSPA)* (pp. 1-6). IEEE Publishing. <http://dx.doi.org/10.1109/ICCSPA.2013.6487288>
- Brown, P. F., Lai, J. C., & Mercer, R. L. (1991). Aligning sentences in parallel corpora. In *Proceedings of the 29th Annual Meeting of the Association for Computational Linguistics* (pp. 169-176). Berkeley. <http://dx.doi.org/10.3115/981344.981366>
- Chen, S. F. (1993). Aligning sentences in bilingual corpora using lexical information. In *Proceedings of the 31st Annual Meeting of the Association for Computational Linguistics* (pp. 9-16). ACM Publishing. <http://dx.doi.org/10.3115/981574.981576>
- Gale, W. A., & Church, K. W. (1993). A program for aligning sentences in bilingual corpora. *Computational Linguistics*, 19, 75-102. <http://dx.doi.org/10.3115/981344.981367>
- Grégoire, F., & Langlais, P. (2017). *A deep neural network approach to parallel sentence extraction*. ArXiv preprint.
- Khaw, J. Y. M., Tan, T. P., & Ranaivo, B. (2021). Kelantan and Sarawak Malay dialects: Parallel dialect text collection and alignment using hybrid distance-statistical-based phrase alignment algorithm. *Turkish Journal of Computer and Mathematics Education*, 12(3), 2163-2171. <https://doi.org/10.17762/turcomat.v12i3.1160>
- Kim, Y. (2014). Convolutional neural networks for sentence classification. In *Proceedings of the Conference on Empirical Methods in Natural Language Processing (EMNLP)* (pp. 1746-1751). Association for Computational Linguistics Publishing. <http://dx.doi.org/10.3115/v1/D14-1181>
- Lim, S. L. O., Lim, H. M., Tan, E. K., & Tan, T. P. (2020). Examining machine learning techniques in business news headline sentiment analysis. In R. Alfred, Y. Lim, H. Havaluddin & K. O. Chin (Eds.), *Computational Science and Technology* (pp. 363-372). Springer. [https://doi.org/10.1007/978-981-15-0058-9\\_35](https://doi.org/10.1007/978-981-15-0058-9_35)
- Luo, S., Ying, H., & Yu, S. (2021). *Sentence alignment with parallel documents helps biomedical machine translation*. ArXiv preprint.



- Luong, M. T., Pham, H., & Manning, C. D. (2015). Effective approaches to attention-based neural machine translation. In *Proceedings of Conference on Empirical Methods in Natural Language Processing* (pp. 1412-1421). Association for Computational Linguistics Publishing. <http://dx.doi.org/10.18653/v1/D15-1166>
- Ma, X. (2006, May 22-28). Champollion: A robust parallel text sentence aligner. In *Proceedings of Fifth International Conference on Language Resources and Evaluation* (pp. 489-492). Genoa, Italy.
- Mikolov, T., Sutskever, I., Chen, K., Corrado, G. S., & Dean, J. (2013). Distributed representations of words and phrases and their compositionality. In *Advances in Neural Processing Information Systems 26* (pp. 3136-3144). Curran Associates, Inc.
- Pennington, J., Socher, R., & Manning, C. D. (2014). GloVe: Global vectors for word representation. In *Proceedings of Empirical Methods in Natural Language Processing (EMNLP)* (pp. 1532-1543). Association for Computational Linguistics Publishing. <http://dx.doi.org/10.3115/v1/D14-1162>
- Salleh, M. (2010) *The epic of Hang Tuah*. Malaysian Institute of Translation & Books.
- Sennrich, R., & Volk, M. (2010, November 4 - December 14). MT-based sentence alignment for OCR-generated parallel texts. In *The Ninth Conference of the Association for Machine Translation in the Americas (AMTA 2010)* (pp. 1-11). Denver, Colorado.
- Stratos, K., Collins, M., & Hsu D. (2015). Model-based word embeddings from decompositions of count matrices. In *Proceedings of the 53rd Annual Meeting of the Association for Computational Linguistics* (pp. 1282-1291). Association for Computational Linguistics Publishing. <http://dx.doi.org/10.3115/v1/P15-1124>
- Vulić, I., & Moens, M. F. (2015). Bilingual word embeddings from non-parallel document-aligned data applied to bilingual lexicon induction. In *Proceedings of the 53rd Annual Meeting of the Association for Computational Linguistics* (Vol. 2, pp. 719-725). Association for Computational Linguistics Publishing. <http://dx.doi.org/10.3115/v1/P15-2118>
- Wołk, K., & Marasek, K. (2014). A sentence meaning based alignment method for parallel text corpora preparation. *New Perspectives in Information Systems and Technologies, 1*, 229-237. [http://dx.doi.org/10.1007/978-3-319-05951-8\\_22](http://dx.doi.org/10.1007/978-3-319-05951-8_22)
- Yeong, Y. M., Tan, T. P., & Gan, K. H. (2019) A hybrid of sentence-level approach and fragment-level approach of parallel text extraction from comparable text. *Procedia Computer Science, 161*, 406-414. <http://dx.doi.org/10.1016/j.procs.2019.11.139>
- Zhou, P., Qi, Z., Zheng, S., Xu, J., Bao, H., & Xu, B. (2016, December 11-16). Text classification improved by integrating bidirectional LSTM with two-dimensional max pooling. In *Proceedings of the 26th International Conference on Computational Linguistics* (pp. 3485-3495). Osaka, Japan.
- Ziemski, M., Junczys-Dowmunt, M., & Pouliquen, B. (2016, May 23-28). The United Nations parallel corpus v1.0. In *Proceedings of the Tenth International Conference on Language Resources and Evaluation LREC 2016* (pp. 3530-3534). Portorož, Slovenia.



## The Relationships of Interleukin-33, Ve-Cadherin and Other Physiological Parameters in Male Patients with Rheumatoid Arthritis

Khalid F. AL-Rawi<sup>1</sup>, Hameed Hussein Ali<sup>1</sup>, Manaf A. Guma<sup>2\*</sup>, Shakir F.T. Alaaraji<sup>3</sup> and Muthanna M. Awad<sup>4</sup>

<sup>1</sup>Department of Chemistry, College of Science, University of Anbar, Ramadi 31001 Iraq

<sup>2</sup>Department of Applied Chemistry, College of Applied Science- Hit, University of Anbar, Ramadi 31001 Iraq

<sup>3</sup>Department of Chemistry, College of Education for Pure Science, University of Anbar, Ramadi 31001 Iraq

<sup>4</sup>Department of Biology, College of Education for Pure Sciences, University of Anbar, Ramadi 31001 Iraq

### ABSTRACT

Rheumatoid arthritis (RA) is a chronic joint inflammatory disease that involves various pro-inflammatory mediators and cytokines. This study explores the correlation among various biochemical and immunological parameters for the male patients with RA and performs a predictive equation that would correlate these parameters together. The study involved 44 male patients suffering from RA with the same number of healthy controls. Consent was achieved for all patients and controls, together with a general examination including complete blood count, erythrocyte sedimentation rate (ESR), C-reactive protein (CRP), and RF. Moreover, lipid profile, kidney function tests, specific enzymes and the

following parameters have been detected, which were hypothesised to negatively impact RA disease such as TGF- $\beta$ 1, vitamin E, VE-cadherin, interleukin 33 and TIMP-1. Various enzymatic-linked immunosorbent assays (ELISAs), spectroscopic, serological, and haematological methods were used to quantify these parameters. Our results have revealed a significant positive correlation between ESR, RF, VE-cadherin and vitamin E, specifically type  $\alpha$ -tocopherol that are associated with the non-biochemical parameters such as BMI, waist length, hip

### ARTICLE INFO

#### Article history:

Received: 10 July 2021

Accepted: 15 September 2021

Published: 24 November 2021

DOI: <https://doi.org/10.47836/pjst.30.1.07>

#### E-mail addresses:

sc.kfwi72@uoanbar.edu.iq (Khalid F. AL-Rawi)

sc.dr.hameedh.ali@uoanbar.edu.iq (Hameed Hussein Ali)

manafguma@uoanbar.edu.iq (Manaf A. Guma)

esp.shaker.faris@uoanbar.edu.iq (Shakir F.T. Alaaraji)

muthanna.awad@uoanbar.edu.iq (Muthanna M. Awad)

\*Corresponding author

length, thorax and age. The important parameters revealed correlated with RA were used to generate two predictive equations to help the physicians confirm whether a patient is diagnosed with RA directly. In addition, the study revealed some parameters that would have a positive effect on RA patients, such as TGF- $\beta$ 1, vitamin E and VE-cadherin, which have shown a decrease in their values compared to the controls. In contrast, other parameters showed an increase in RA patients, and therefore they can be useful biomarkers for RA disease.

*Keywords:* Immune system, ox-LDL, Rheumatoid arthritis (RA), TGF- $\beta$ 1, TIMP-1

---

## INTRODUCTION

Autoimmunity is one of the most common and chronic disorders of the immune system. Rheumatoid arthritis (RA) is an autoimmune disorder that predominantly influences joints (Kumar et al., 2019). RA might affect many tissues and organs but mainly attacks flexible joints (Saraux et al., 2005). In autoimmune conditions, healthy cells are mistakenly targeted by the immune system. As a result, RA leads to inflammation and the destruction of cartilage and bone that show different symptoms such as warm, swollen, and painful joints and worsen after rest. Commonly, the symptoms include symmetrical arthralgia, mostly shown as loss of physical function in the hands and feet (Corada et al., 2001). Therefore, the dysregulation of the immune system results in damage in the soft and hard tissues, which is the main symptom of RA (Schmalz et al., 2019). Moreover, a decrease in inflammatory activity is the main goal for treating patients diagnosed with RA (Gonzalez-Juanatey et al., 2004). Studies showed that the prevalence of RA is within the range of 0.3% to 1% in the general population and usually affects the middle ages between 35 to 55 (Corada et al., 2001). Although the RA prevalence seems low, an increase of risk factors such as cardiovascular events correlates to RA increase in prevalence (McInnes & Schett, 2011).

Multiple clinical and biochemical methods are used to assess Rheumatoid arthritis: RA is frequently diagnosed by rheumatoid factors test (Shmerling & Delbanco, 1991). RF are antibodies (Ab) that bind specifically to gamma ( $\gamma$ ) globulins and are known as auto-Ab. There are two well-known RF types: agglutinating RF and non-agglutinating RF. They can both be used to diagnose RA. Despite the fact that they are non-specific for RA, the valuation of agglutination of IgM-RF is still the most practical serological test for RA diagnosis. RF blood tests detect the amount of the RF antibody in the blood. Typically, The RF antibody can bind to normal body tissue and damage it. In contrast, antibodies generated by a healthy immune system can destroy and remove attacking bacteria and viruses, causing diseases (Renaudineau et al., 2005). Several factors could affect RA disorder, such as genetic factors, environmental factors and impairment in the autoimmune when the healthy body tissue is attacked by the immune system (McInnes & Schett, 2011).

For instance, Interleukin-33, a new member of the IL-1 family, has been reported to play a key role in arthritis (Iwahana et al., 1999). A recent study showed that IL-33 stimulates the emergence of group 2 innate lymphoid cells from the bone marrow (Riedel et al., 2017). Another study assessed the functions of IL-33 in fibroblast-like synoviocytes (FLS) in RA patients. The study found that IL-33 levels were higher in the plasma of RA patients than in patients with osteoarthritis OA. It suggested that an increase in plasma IL-33 in patients with RA might be a useful biomarker to diagnose RA. It would reflect the possible risks of bone erosion (Lee et al., 2016).

Another factor that could affect RA disorder is VE-cadherin (vascular endothelial cadherin). It is also known as Cadherin 5, type 2 or CD144 (Cluster of Differentiation 144). VE-cadherin is a classical cadherin which is a transmembrane protein belonging to the cadherin superfamily. Cadherins are the adhesion molecules in most cells families. VE-cadherin is the main endothelial-specific adhesion molecule responsible for the endothelial cell barrier's integrity and angiogenesis, forming new blood vessels located at connections between endothelial cells (Vestweber, 2008). VE-cadherin also controls and maintains the permeability of the blood vessel wall for cells and substances in the tissues (Vestweber, 2008). Since IL-33 is present in endothelial cells as a nuclear factor and VE-cadherin is an integrator of endothelial cell barriers, the correlation between IL-33 and VE-cadherin is influenced by other factors such as interleukin-4 and tissue inhibitor of metalloproteinases environments TIMP1 (Bokarewa et al., 2005). TIMP1 is a glycoprotein, and it is a subfamily of four protease inhibitors. TIMP1 is a crucial regulator for growth remodelling and apoptosis in different cells in physiological and pathological conditions. In addition, it is involved in the degradation of extracellular matrix molecules. Previous studies showed an autoimmune response to TIMP1 in RA patients (Verma & Hansch, 2007). In addition, VE-cadherin has been recently significantly correlated to C-reactive protein (Banse et al., 2017).

Another important factor that is associated with RA is Transforming Growth Factor  $\beta$  (TGF- $\beta$ ). TGF- $\beta$  is defined as a multifunctional cytokine involved in numerous biological processes, as it plays fundamental functions in angiogenesis homeostasis, cell proliferation, migration and apoptosis (Gonzalo-Gil & Galindo-Izquierdo, 2014). However, the role of TGF- $\beta$  in RA is a matter of debate (Schiller et al., 2004). Genetic studies showed that TGF- $\beta$  includes three mammalian isoforms for TGF- $\beta$ : TGF- $\beta$ 1, TGF- $\beta$ 2 and TGF- $\beta$ 3. These isoforms have a similar function, but they are expressed in different tissues (Battaglia et al., 2013; Schiller et al., 2004). A study showed that TGF- $\beta$ 1 plays a key role in the immune system, especially in controlling T cells' activation, proliferation, and differentiation (Nowak et al., 2016). However, non-classical risk factors might correlate to patients with RA indirectly, which have not been studied yet. For instance, oxLDL (oxidised low-density lipoprotein) fraction is associated with cardiovascular (CV) disease, indirectly affecting

RA patients. A study showed that a higher fraction of oxLDL was noticed in RA patients (Fernández-Ortiz et al., 2020). The study suggested that the elevated oxLDL is probably correlated to chronic inflammation in RA patients with the acceleration of atherosclerosis (Fernández-Ortiz et al., 2020). A recent study revealed that changes in the HDL-C and ox-LDL-C levels of the lipid profile are associated with high disease activity in early stages arthritis patients (Dai et al., 2018).

Another non-classical risk factor that might correlate indirectly to RA patients is vitamin E. It is a natural antioxidant that can regulate immune responses. It consists of two leading common families: tocopherols and tocotrienols. It has been reported that tocotrienol is an anti-inflammatory agent (Anderson et al., 2011). In addition, a study on neonatal rats showed that supplementation with vitamin E exhibited a synergistic effect with glucosamine against RA (Dai et al., 2018).

All the factors mentioned above seem to be correlated with RA. The diagnosis of the disease activity for RA is based routinely on C-reactive protein (CRP) and erythrocyte sedimentation rate (ESR) assessment (George et al., 2017). A study showed that a greater ESR in women with RA is associated with severe obesity, related to fat mass and greater BMI. However, men with RA have shown greater CRP and ESR with a lower BMI in the general population (Jain et al., 2000). Thus, all these factors appeared to play a part in rheumatoid arthritis collectively. Here, we aim to explore the biological roles of various immune and non-immune factors associated with obesity in Iraqi male patients with RA such as Interleukin-33, VE-cadherin, TIMP-1, TGF- $\beta$ 1, OX-LDL and Vitamin E. The reasons for choosing the male patients are to avoid the complication of women sex hormones that might involve RA formation. Also, males develop RA less than females due to genetics, and hormonal differences, which lead to consequently occurring RA symptoms were more severe in women than in men. Thus, we suggested studying the lowest level that could affect both genders. Also, we aim to reveal a predictor equation from statistical analysis for various parameters measured for RA patients to estimate whether a patient suffers from RA or not. The criteria are mentioned in the next section.

## **METHODS**

### **Methods and Patients**

A total of 88 patients had their blood drawn from the main venous line after admission. At least 3 mL of blood had been collected and placed into a serum separator tube and then centrifuged at 4 °C at 3000 rpm for 15 min. The serum was taken and then stored at -80 °C for later analysis. An additional 2 mL of whole blood were collected for ESR, and complete blood count (CBC) examinations were performed immediately. Patients were selected from the clinic of the main teaching hospitals in Ramadi city and Fallujah city in Iraq.

The study was conducted with critical criteria. First, only males' patients with RA were examined. It is to achieve our goal in this study. Another important criterion was that all patients with chronic and acute diseases such as diabetes and hypertension except RA were excluded in this study. It is to avoid any contradiction that would affect the results. In addition, only middle-aged, 40 to 60 years old, patients were chosen as there was a rare sample size for those out of middle age. The same things followed for control but with no RA disease.

### **Haematology**

Full routine haematological values were obtained using a CBC blood test machine (Auto Haematology analyser MSLAB42 from Guandong, China) in the local governmental and private laboratories., Erythrocyte Sedimentation Rate (ESR) was determined following the procedure described by Sharma and Singh (2000) (as cited in Mu et al., 2010).

### **Serology**

Multiple serological and immunological tests have been studied, such as rheumatoid factor, IL-33, VE-cadherin, TIMP-1, TGF- $\beta$ 1, ox-LDL and alpha-tocopherol vitamin E using commercial kits from My BioSource®.

### **Biochemical Study**

Serum samples were analysed manually following commercial kits procedures from Cromatest® using Colorimetric Assay Kits to detect the following biochemical parameters; urea, creatinine, uric acid, lipid profile; Triglyceride (TG), Cholesterol, high-density lipoprotein HDL, and vitamin E specifically type  $\alpha$ -tocopherol. All samples were processed and examined at the biochemistry laboratory of the main teaching hospitals in Ramadi city and Fallujah city in Iraq.

### **Statistical Analysis**

The data were collected and analysed using SPSS, version 25. Figures were plotted using JASP software version 0.14 and Prism Graph Pad 8.3.1. The descriptive statistic tables for patients and healthy controls were expressed as mean, minimum, maximum, and SD values. In addition, the concentrations of the following parameters (Ox-LDL, TGF- $\beta$ 1, VE-cadherin, vitamin E and IL-33) were plotted versus the duration of the disease, which was expressed in years.

## **RESULTS AND DISCUSSION**

It is a descriptive and predictive study involving patients admitted to the clinic of the main teaching hospitals in both Ramadi and Fallujah cities in Iraq. The study was based on data

collected from 44 orally consented Iraqi male patients aged 40 to 60 years suffering from RA and joint pain. With equal numbers of healthy control. The samples were collected from patients who attended multiple laboratories and clinics at the main teaching hospitals in Ramadi and Fallujah cities in Iraq. All patients were interviewed, clinically examined, and approved according to the signed ethical forms of the responsible committee on humans in the Ramadi and Fallujah institutions that the Ministry of Health directs. Informed consent was obtained from all patients included in this study.

The study was conducted on a total of 44 male patients suffering from RA. An equal total of healthy controls was also included. The general examination included complete blood count, erythrocyte sedimentation rate (ESR), C-reactive protein (CRP), and RF. Most of the biochemical parameters have been examined as well, such as a lipid profile, kidney function, and specific molecules have been detected which were hypothesised to decrease RA diseases such as TGF- $\beta$ 1, vitamin E, VE-cadherin, interleukin 33, and TIMP-1. Some measurable parameters such as waist, age, hip and neck width and blood pressure have also been recorded. In addition, other parameters assumed to affect RA have also been recorded, such as smoking, employment duration, disease duration, academic achievements, and social conditions (Tables 1 & 2). The age range for the patients was from 42 to 62 years with a mean of  $50.66 \pm 6.035$  years, and the duration of their disease ranged from 1 to 10 years, with a mean of  $6 \pm 2$  years (group 2). For the control, the age range was between 40 to 60 years, with a mean of  $48.48 \pm 5.663$  years.

Table 1

*Descriptive statistical analysis of the biochemical, serological, immunological and social measured parameters for males' healthy controls.*

The Parameters	N	Minimum	Maximum	Mean	Std. Deviation
Ox-LDL ng/ml	44	5	15	10.36	3.033
TGF-B1 pg/ml	44	61	196	119.72	42.691
VE- Cadherin ng/ml	44	5	20	12.4	5.016
Vitamin E $\mu$ g/ml	44	2	4	3.1	0.579
IL-33 pg/ml	44	22	175	94.43	46.22
TIMP1 pg/ml	44	52	288	150.95	72.915
Age years	44	40	60	48.48	5.663
BMI kg/m <sup>2</sup>	44	21	29	24.82	2.222
Hip length cm	44	80	105	94.35	7.367
Waist length cm	44	74	104	92.5	6.882



Table 1 (Continued)

The Parameters	N	Minimum	Maximum	Mean	Std. Deviation
Thoracic cm	44	82	114	101.81	7.06
Neck length cm	44	34	45	39.29	2.645
SBP mmHg	44	92	133	119.09	8.263
DBP mmHg	44	66	96	78.64	5.714
ESR (mm/hr)	44	10	26	16.91	3.094
RF (IU/mL)	44	8	16	11.09	3.94
CRP (mg/L)	44	6	24	9.41	4.91
S. Creatinine (mg/dL)	44	1	1	0.89	0.224
S. Uric Acid (mg/dL)	44	3	7	5.11	0.892
S.Urea (mg/dL)	44	13	38	25.89	5.654
T. Cholesterol (mg/dL)	44	97	203	160.45	22.733
Triglycerides (mg/dL)	44	52	136	100.52	23.291
HDL (mg/dL)	44	34	63	48.7	5.381
LDL (mg/dL)	44	27	122	91.65	22.223
VLDL (mg/dL)	44	10	27	20.1	4.658
Hb (g/dL)	44	11	16	13.2	1.123
WBC (10 <sup>3</sup> /L)	44	3	10	7.1	1.349
Smoking	44	0	1	0.07	0.255
Rural OR Urban	44	0	1	0.5	0.506
Employment	44	0	1	0.82	0.39
Academic achievement	44	0	4	1.41	1.127
Valid N (listwise)	44				

Some useful abbreviations : IL-33; interleukin 33, SBP mmHg; Systolic Blood Pressure, DBP; Diastolic blood pressure, Hb; Haemoglobin, WBC; White Blood Cells, Smoking: Yes(1) OR No(0), Employment; Yes (1) Or No(0), Rural (1) OR Urban (0), Academic achievement : Ph. D(4); Master (3); BA(2); Sec(1); Pri (0)

Table 2

*Descriptive statistical analysis of the biochemical, serological, immunological and social measured parameters for males' patients with RA*

The Parameters	N	Minimum	Maximum	Mean	Std. Deviation
OX-LDL ng/ml	44	12	55	31.69	13.007
TGF-B1 pg/ml	44	32	99	60.16	19.521
VE- Cadherin ng/ml	44	2	10	5.33	1.951
Vitamin E µg/ml	44	2	3	2.16	0.471
IL-33 pg/ml	44	49	499	284.57	117.156
TIMP1pg/ml	44	61	300	163.04	70.742
Age years	44	42	62	50.66	6.035
BMI kg/m2	44	23	36	29.74	2.98
Hip length cm	44	90	138	108.17	8.795
Waist length cm	44	90	129	106.58	9.158
Thoracic cm	44	85	117	99.04	7.521
Neck length cm	44	30	46	37.21	3.811
SBP mmHg	44	2	9	5.3	2.268
DBP mmHg	44	115	161	136.55	10.513
ESR (mm/hr)	44	66	109	91.34	10.751
RF (IU/mL)	44	37	111	60.8	14.866
CRP (mg/L)	44	8	32	22.18	8.942
S. Creatinine (mg/dL)	44	6	48	26.32	13.768
S. Uric Acid (mg/dL)	44	1	14	1.81	1.909
S.Urea (mg/dL)	44	5	9	7.1	1.097
T. Cholesterol (mg/dL)	44	27	53	40.55	6.815
Triglycerides (mg/dL)	44	154	291	204.11	30.388
HDL (mg/dL)	44	115	1399	194.18	189.545
LDL (mg/dL)	44	24	59	35.64	9.791
VLDL (mg/dL)	44	-119	237	129.64	46.309
Hb (g/dL)	44	23	280	38.84	37.909
WBC (103/L)	44	10	14	11.67	1.044
Smoking	44	6	15	9.38	1.892
Rural OR Urban	44	0	1	0.16	0.37
Employment	0	0	0	0	0
Academic achievement	44	0	2	1.34	0.645
Valid N (listwise)	0				

A t-test was performed to examine the significant difference between the means of the biochemical parameters in RA patients and control, as seen in Table 3. Moreover, one sample t and Wilcoxon test experiment were performed to examine the significant difference between the variation of the concentrations for the biochemical parameters versus the disease duration for RA patients, as seen in Table 4. The study revealed that five parameters only amongst others had shown significant differences in RA patients compared to the healthy control, which are TIMP-1, TGF-β1, ox-LDL, vitamin D and IL-33. In addition, the concentrations of these parameters are independent of the duration of RA disease, which can be seen in Figure 1.

Table 3

*The statistical analysis of the biochemical and immunological parameters performed using t-test experiment for males' patients with RA verses the healthy control as shown in Figure 1.*

Unpaired t test	Ox-LDL	TGF	VE	Vit E	IL-33
P value	<0.0001	<0.0001	<0.0001	<0.0001	<0.0001
P value summary	****	****	****	****	****
Significantly different (P < 0.05)	Yes	Yes	Yes	Yes	Yes
One- or two-tailed P value?	Two-tailed	Two-tailed	Two-tailed	Two-tailed	Two-tailed
t, df	t=10.59, df=86	t=8.416, df=86	t=8.708, df=86	t=8.424, df=86	t=5.386, df=86
Mean of Patients (B)	10.36	119.7	5.332	2.157	163.0
Mean of Control (A)	31.69	60.16	12.40	3.105	94.43
Difference between means (B - A) ± SEM	21.32 ± 2.014	-59.56 ± 7.077	7.066 ± 0.8114	0.9477 ± 0.1125	-68.61 ± 12.74
95% confidence interval	17.32 to 25.33	-73.63 to -45.49	5.453 to 8.679	0.7241 to 1.171	-93.93 to -43.28
R squared (eta squared)	0.5660	0.4516	0.4686	0.4521	0.2522
<b>F test to compare variances</b>					
F, DFn, Dfd	18.39, 43, 43	4.783, 43, 43	6.611, 43, 43	1.513, 43, 43	2.343, 43, 43
P value	<0.0001	<0.0001	<0.0001	0.1784	0.0062
P value summary	****	****	****	ns	**
Significantly different (P < 0.05)?	Yes	Yes	Yes	No	Yes

Table 4

The statistical analysis of the biochemical and immunological parameters was performed using a one-sample t and Wilcoxon test experiment affected by the duration of RA disease, as shown in Figure 1.

One sample t test	Ox-LDL	TGF	VE	Vit E	IL-33
t, df	t=16.16, df=43	t=20.44, df=43	t=18.13, df=43	t=30.39, df=43	t=15.29, df=43
P value (two tailed)	<0.0001	<0.0001	<0.0001	<0.0001	<0.0001
Discrepancy	31.69	60.16	5.332	2.157	163.0
SD of discrepancy	13.01	19.52	1.951	0.4707	70.74
SEM of discrepancy	1.961	2.943	0.2941	0.07096	10.66
95% confidence interval	27.73 to 35.64	54.22 to 66.09	4.739 to 5.925	2.014 to 2.300	141.5 to 184.5
R squared	0.8586	0.9067	0.8843	0.9555	0.8446

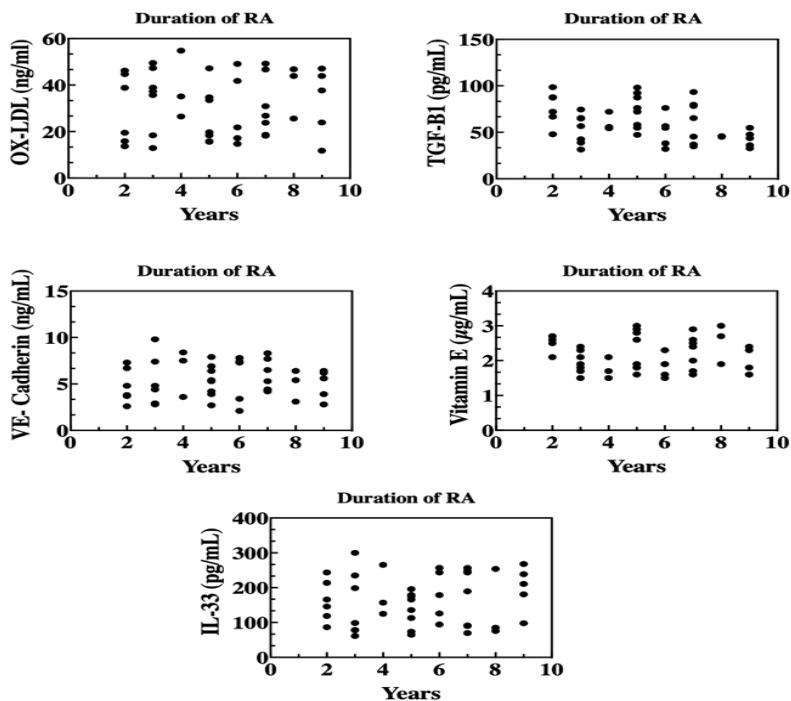


Figure 1. The descriptive statistical analysis of the following quantified biochemical and immunological parameters; TIMP-1, TGF-β1, ox-LDL, vitamin D and IL-33 versus the durations of RA diseases (expressed by years).

Moreover, there seems to be a significant positive correlation between ESR, RF, VE-cadherin, vitamin E with the non-biochemical parameters such as BMI, waist length, hip length, thorax, and age. Other biochemical examined parameters have not shown a direct impact on RA disease (Table 1). Therefore, a predictive equation that links these parameters collectively to calculate rheumatoid factor RF was generated (Equation 1). Standard values were obtained from the statistical analysis to link the most significant parameters in the predictive Equation 1. Another predictive equation was also generated to calculate ESR or any other unknown parameter belonging to the RA (Equation 2). It should be noted that these two equations are only valid if the range of the collected data is within the same conditions of these data's range.

$$\text{RF} = -57.63 + 0.5 \text{ ESR} + 1.26 \text{ BMI} + 0.33 \text{ waist.} \quad (1)$$

$$\text{ESR} = -7.44 + 0.39 \text{ Ox-LDL} - 0.08 \text{ TGF-}\beta\text{1} - 129 \text{ VE-Cadherin} + 1.75 \text{ hip} - 1.59 \text{ Thorax} + 0.06 \text{ IL33} - 7.02 \text{ vitamin E} + 0.39 \text{ waist} + 0.52 \text{ age.} \quad (2)$$

The results showed that serum IL-33 concentrations were two folds higher in RA patients than in healthy controls. These results confirm previous studies which have shown similar output (Hidayat et al., 2019; Salama et al., 2017). Other recent studies have reported that serum IL-33 is linked to RA disease, indicating a brilliant diagnostic performance (Albertsen et al., 2013; Harris & Nelson, 2010). The results indicate that IL-33 is probably involved in the RA pathogenesis, and it might suggest a direct therapy for IL-33 to treat RA patients who have been assessed with high levels of IL-33 (Chen et al., 2019). In contrast, the statistical analysis between the duration of RA disease for each patient and the concentrations of IL-33 showed that IL-33 concentrations remain abnormally high in all the durations. In other words, IL-33 concentration was not back to normal once it had changed. Thus, serum IL-33 assessment can be considered a useful biomarker for evaluating RA disease activity (Figure 1). However, an earlier study found a significant negative association with IL-33 level with disease duration in years (Gonzalo-Gil & Galindo-Izquierdo, 2014). Other biochemical parameters such as ox-LDL showed a significant increase in RA patients than in controls. Ox-LDL concentrations were shown to be about three times higher in RA patients than controls (Figure 2).

However, the concentrations of Ox-LDL remained elevated in all durations of RA patients. Ox-LDL stimulates inflammations, cell damage, generating cytokines, cell adhesion, apoptosis (Bašić et al., 2019). Therefore, it can be said that Ox-LDL is a valuable biomarker for RA disease. Therefore, it was involved in the predictive equation (Figure 2 and Table 3). TGF- $\beta$ 1 was shown to be significantly decreased in RA patients than in controls. The maximum concentration of TGF- $\beta$ 1 was 100 pg/ml in RA patients, while

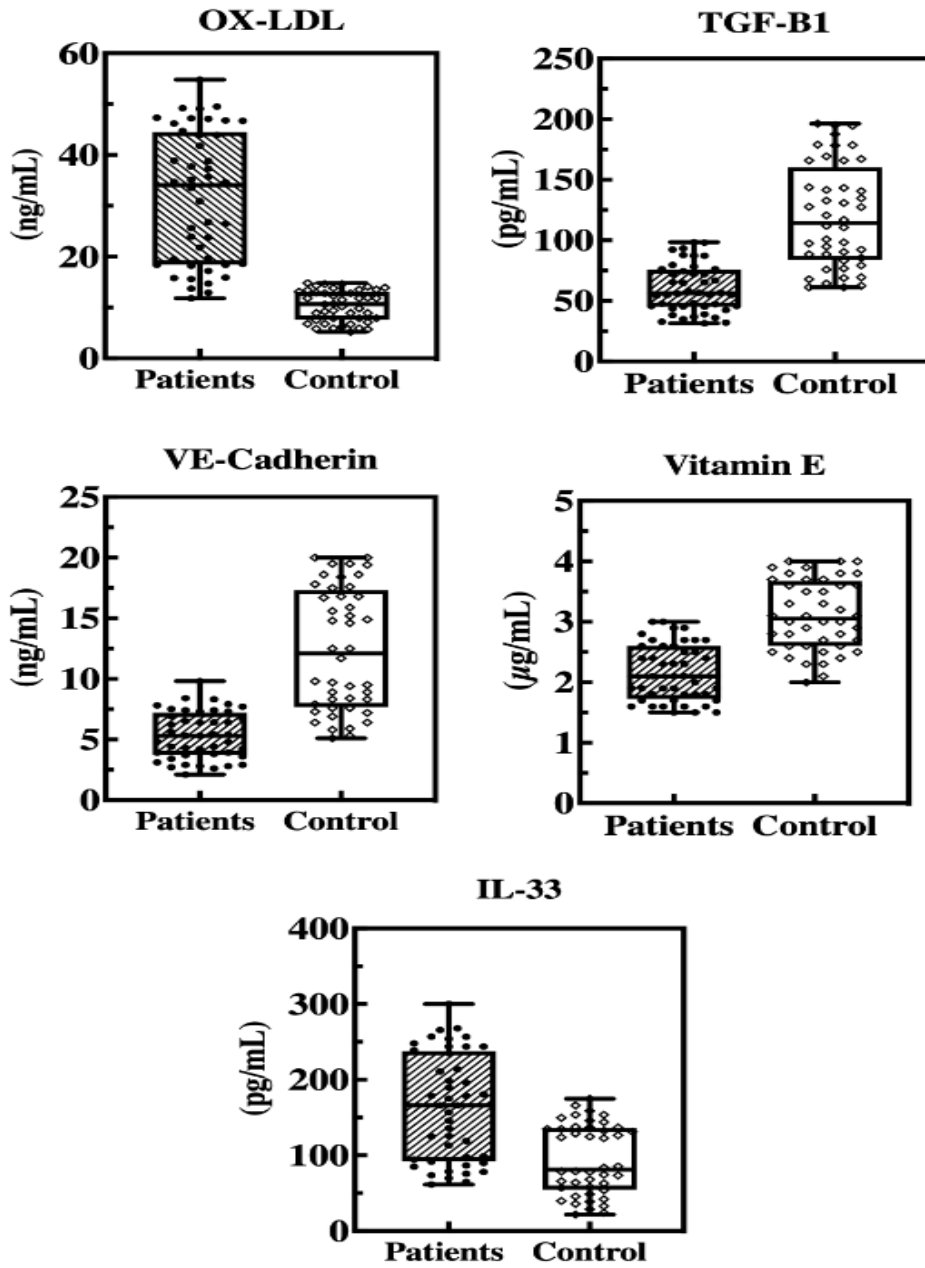


Figure 2. The biochemical and immunological quantification of TIMP-1, TGF- $\beta$ 1, ox-LDL, vitamin D and IL-33 in the serum of RA patients and healthy controls.

the maximum concentration was 200 pg/ml in the healthy controls. Moreover, people who have struggled with RA for 8 and 9 years have shown less TGF- $\beta$ 1 concentrations than the control (Figure 2 and Table 4). These findings are compatible with a recent study that showed that TGF- $\beta$  is an effective therapeutic target (Pap et al., 2000). Another study suggests that blocking the TGF- $\beta$  pathway is correlated with immune tolerance defeat and natural autoimmunity, defective tissue repair, and other effectors (Sakuma et al., 2007). Therefore, an increase in TGF- $\beta$  would reduce RA.

Another important factor that has shown a similar impact to TGF- $\beta$  on RA is VE-cadherin. It has shown a significant decrease in RA patients than in controls. The average range concentration for VE-cadherin was observed between 2-10 ng/ml in RA patients, while it was between 5-20 ng/ml in the healthy controls. Moreover, the duration of the disease was not shown to affect the VE-cadherin concentration for RA patients. It is probably due to the multiple functions of VE-cadherin in the immune system but also due to its behaviour in different cell types: various cellular processes such as apoptosis and cell proliferation are regulated by VE-cadherin, which also regulates vascular endothelial growth key receptor functions (Chen et al., 2019). Therefore, VE-cadherin also regulates cell dynamics and cell cycle progression (Hidayat et al., 2019). The studies have described the correlation between IL-33 and VE-cadherin with other cytokines as follows; IL-33 is released when tissue is injured. IL-33 then warn the immune system, which releases Th2 cells. Thus, increased IL-33 with the association of the growth factors (TGF- $\beta$ ) showed significantly reduced work as a beneficial biomarker for RA disease. Therefore, both measured parameters with IL-4 could reduce endothelial integrity and stimulates permeability, as has been shown previously. It also could escort the downregulation of VE-cadherin mRNA expression. In addition, IL-33 might also lead to less-controlling of endothelial barrier down-regulation process, which is performed to regulate the release of the proteins, solutes and the leukocytes entry into injured tissue that secretes the IL-33 to alarm the immune system (Chalubinski et al., 2015).

A study has suggested that TGF- $\beta$  signalling could be blocked to become a useful strategy for RA treatment (Sakuma et al., 2007). Due to these crucial functions of VE-cadherin, an impairment on such a molecule could result in diseases such as RA. VE-cadherin is associated with an increase in the vasculature, which is one of the most characteristic changes in the synovial tissue of the joints in RA (Jain et al., 2000). Studies suggested that an increase in vasculatures could result from VE-cadherin-dependent angiogenesis and a potential therapeutic target of the disease. VE-cadherin is expressed by synovial fibroblastic cells and form tube-like structures. Recently, non-endothelial cells have expressed VE-cadherin, which mature vasculatures in placental tissue and malignant tumours (Fernández-Ortiz et al., 2020; Nowak et al., 2016).

The last measured biochemical parameter which has shown less impact on RA patients than others is vitamin E. However, it is still a beneficial biomarker that could be taken with other mentioned parameters for RA diagnosis, as in Equation 2. The total average concentration for vitamin E was observed at 3 g/ml in RA patients, while the average concentration was observed at 4 g/ml in the healthy controls. It indicates that a decrease in vitamin E in the blood might increase the probability of rheumatoid arthritis. A preclinical study on a rat model of collagen-induced arthritis showed that the tocotrienol-rich fraction from palm oil containing vitamin E has a beneficial therapeutic and anti-inflammatory activity against the disease (Zainal et al., 2019). Moreover, we have shown that the duration of the disease has a remarkable effect on the concentration of vitamin E (Figure 1). These findings demonstrate the crucial role of vitamin E on the immune system itself, not only during the disease period but also compared to the healthy control. Another study on neonatal rats showed supplementation with vitamin E exhibited a synergistic effect with glucosamine against RA (Hinds et al., 2013).

## CONCLUSION

Rheumatoid arthritis (RA) is a chronic joint inflammatory disease that involves various pro-inflammatory mediators and cytokines. There are various biochemical and immunological parameters associated with RA patients. This study aims to find the most important biochemical and immunological parameters correlated to RA disease and drive an equation that directly guides the diagnosis. Various enzymatic-linked immunosorbent assays (ELISAs), spectroscopic, serological, and haematological methods were used to examine these parameters. Our results have revealed a significant positive correlation amongst ESR, RF, VE-cadherin and vitamin E, associated with non-biochemical parameters such as BMI, waist length, hip length, thorax, and age. All these mentioned parameters were shown to be significantly abnormal in RA patients in comparison to healthy control. The statistical study between the durations of the disease for each patient and the concentrations of the following parameters: TIMP-1, TGF- $\beta$ 1, ox-LDL, vitamin D and IL-33 revealed that their concentrations remain abnormal in all the duration of the disease, which can highlight the importance of these parameters in RA diagnosis.

Thus, we suggest all of the parameters be examined as biomarkers using the two predictive equations generated in this study to confirm whether a patient is diagnosed with RA directly. In addition, the study revealed that the concentrations of most parameters that showed significant differences are independent of the duration of the disease. Moreover, our findings indicated that some parameters that showed significant differences are inversely proportional to each other for RA patients, which need further investigation in the future. Also, the study revealed some useful parameters that would positively affect RA patients and could be targeted therapeutically to obtain an increase in TGF-B1, vitamin E, and VE-



cadherin. In contrast, other biochemical and serological parameters showed an increase with RA patients, and they can be useful biomarkers for RA disease.

## ACKNOWLEDGMENT

We are immensely thankful for:

1. Bilal Altaha, Department of Applied Chemistry, College of Applied Sciences Hit (head), University Of Anbar, Iraq; and
2. Dr Lorenza Francescut, Champion Mental Health First Aider, Department of Molecular and Cell Biology, College of Sciences, Henry Welcome Building, University of Leicester, UK.

## REFERENCES

- Albertsen, H. M., Chettier, R., Farrington, P., & Ward, K. (2013). Genome-wide association study link novel loci to endometriosis. *PLoS One*, *8*(3), Article e58257. <https://doi.org/10.1371/journal.pone.0058257>
- Anderson, J. K., Zimmerman, L., Caplan, L., & Michaud, K. (2011). Measures of rheumatoid arthritis disease activity: Patient (PtGA) and provider (PrGA) global assessment of disease activity, disease activity score (DAS) and disease activity score with 28-joint counts (DAS28), simplified disease activity index (SDAI), et al. *Arthritis Care & Research*, *63*(S11), S14-S36. <https://doi.org/10.1002/acr.20621>
- Banse, C., Polena, H., Stidder, B., Khalil-Mgharbel, A., Houivet, E., Lequerré, T., Fardellone, P., Le-Loët, X., Philippe, P., & Marcelli, C. (2017). Soluble vascular endothelial (VE) cadherin and autoantibodies to VE-cadherin in rheumatoid arthritis patients treated with etanercept or adalimumab. *Joint Bone Spine*, *84*(6), 685-691. <https://doi.org/10.1016/j.jbspin.2016.10.012>
- Bašić, J., Vojinović, J., Jevtović-Stoimenov, T., Despotović, M., Sušić, G., Lazarević, D., Milošević, V., Cvetković, M., & Pavlović, D. (2019). Vitamin D receptor gene polymorphism influences lipid profile in patients with juvenile idiopathic arthritis. *Clinical Rheumatology*, *38*(1), 117-124. <https://doi.org/10.1007/s10067-018-4264-2>
- Battaglia, A., Buzzonetti, A., Baranello, C., Fanelli, M., Fossati, M., Catzola, V., Scambia, G., & Fattorossi, A. (2013). Interleukin-21 (IL-21) synergizes with IL-2 to enhance T-cell receptor-induced human T-cell proliferation and counteracts IL-2/transforming growth factor- $\beta$ -induced regulatory T-cell development. *Immunology*, *139*(1), 109-120. <https://doi.org/10.1111/imm.12061>
- Bokarewa, M., Dahlberg, L., & Tarkowski, A. (2005). Expression and functional properties of antibodies to tissue inhibitors of metalloproteinases (TIMPs) in rheumatoid arthritis. *Arthritis Research & Therapy*, *7*(5), 1-9. <https://doi.org/10.1186/ar1771>
- Chalubinski, M., Wojdan, K., Luczak, E., Gorzelak, P., Borowiec, M., Gajewski, A., Rudnicka, K., Chmiela, M., & Broncel, M. (2015). IL-33 and IL-4 impair barrier functions of human vascular endothelium via different mechanisms. *Vascular Pharmacology*, *73*, 57-63. <https://doi.org/10.1016/j.vph.2015.07.012>
- Chen, Z., Bozec, A., Ramming, A., & Schett, G. (2019). Anti-inflammatory and immune-regulatory cytokines in rheumatoid arthritis. *Nature Reviews Rheumatology*, *15*(1), 9-17. <https://doi.org/10.1038/s41584-018-0109-2>

- Corada, M., Liao, F., Lindgren, M., Lampugnani, M. G., Breviario, F., Frank, R., Muller, W. A., Hicklin, D. J., Bohlen, P., & Dejana, E. (2001). Monoclonal antibodies directed to different regions of vascular endothelial cadherin extracellular domain affect adhesion and clustering of the protein and modulate endothelial permeability. *Blood, The Journal of the American Society of Hematology*, 97(6), 1679-1684. <https://doi.org/10.1182/blood.V97.6.1679>
- Dai, W., Qi, C., & Wang, S. (2018). Synergistic effect of glucosamine and vitamin E against experimental rheumatoid arthritis in neonatal rats. *Biomedicine & Pharmacotherapy*, 105, 835-840. <https://doi.org/10.1016/j.biopha.2018.05.136>
- Fernández-Ortiz, A. M., Ortiz, A. M., Pérez, S., Toledano, E., Abásolo, L., González-Gay, M. A., Castañeda, S., & González-Álvaro, I. (2020). Effects of disease activity on lipoprotein levels in patients with early arthritis: can oxidized LDL cholesterol explain the lipid paradox theory? *Arthritis Research & Therapy*, 22(1), 1-12. <https://doi.org/10.1186/s13075-020-02307-8>
- George, M. D., Giles, J. T., Katz, P. P., England, B. R., Mikuls, T. R., Michaud, K., Ogdie-Beatty, A. R., Ibrahim, S., Cannon, G. W., & Caplan, L. (2017). Impact of obesity and adiposity on inflammatory markers in patients with rheumatoid arthritis. *Arthritis Care & Research*, 69(12), 1789-1798. <https://doi.org/10.1002/acr.23229>
- Gonzalez-Juanatey, C., Testa, A., Garcia-Castelo, A., Garcia-Porrúa, C., Llorca, J., & Gonzalez-Gay, M. A. (2004). Active but transient improvement of endothelial function in rheumatoid arthritis patients undergoing long-term treatment with anti-tumor necrosis factor  $\alpha$  antibody. *Arthritis Care & Research*, 51(3), 447-450. <https://doi.org/10.1002/art.20407>
- Gonzalo-Gil, E., & Galindo-Izquierdo, M. (2014). Role of transforming growth factor-beta (TGF) beta in the physiopathology of rheumatoid arthritis. *Reumatología Clínica (English Edition)*, 10(3), 174-179. <https://doi.org/10.1016/j.reumae.2014.01.006>
- Harris, E. S., & Nelson, W. J. (2010). VE-cadherin: At the front, center, and sides of endothelial cell organization and function. *Current Opinion in Cell Biology*, 22(5), 651-658. <https://doi.org/10.1016/j.ceb.2010.07.006>
- Hidayat, R., Isbagio, H., Alwi, I., Soewondo, P., Setiabudy, R., Jusman, S. W., Immanuel, S., Harimurti, K., & Kalim, H. (2019). The effect of hydroxychloroquine on endothelial dysfunction in patients with rheumatoid arthritis: A double-blind randomized clinical trial. *International Journal of Clinical Rheumatology*, 14(2), 59-64.
- Hinds, D. A., McMahon, G., Kiefer, A. K., Do, C. B., Eriksson, N., Evans, D. M., St Pourcain, B., Ring, S. M., Mountain, J. L., & Francke, U. (2013). A genome-wide association meta-analysis of self-reported allergy identifies shared and allergy-specific susceptibility loci. *Nature Genetics*, 45(8), 907-911. <https://doi.org/10.1038/ng.2686>
- Iwahana, H., Yanagisawa, K., Ito-Kosaka, A., Kuroiwa, K., Tago, K., Komatsu, N., Katashima, R., Itakura, M., & Tominaga, S. (1999). Different promoter usage and multiple transcription initiation sites of the interleukin-1 receptor-related human ST2 gene in UT-7 and TM12 cells. *European Journal of Biochemistry*, 264(2), 397-406. <https://doi.org/10.1046/j.1432-1327.1999.00615.x>
- Jain, S., Sharma, N., Singh, S., Bali, H. K., Kumar, L., & Sharma, B. K. (2000). Takayasu arteritis in children and young Indians. *International Journal of Cardiology*, 75, S153-S157. [https://doi.org/10.1016/S0167-5273\(00\)00180-7](https://doi.org/10.1016/S0167-5273(00)00180-7)

- Kumar, R., Attri, A., Rozera, R., Verma, S., Yadav, A. K., Singh, S. K., & Sudhakar, C. K. (2019). A review on pathophysiology of rheumatoid arthritis in conjunction with modernistic approaches of treatment. *Plant Archives*, 19(2), 2201-2206.
- Lee, E. J., So, M. W., Hong, S., Kim, Y. G., Yoo, B., & Lee, C. K. (2016). Interleukin-33 acts as a transcriptional repressor and extracellular cytokine in fibroblast-like synoviocytes in patients with rheumatoid arthritis. *Cytokine*, 77, 35-43. <https://doi.org/10.1016/j.cyto.2015.10.005>
- McInnes, I. B., & Schett, G. (2011). The pathogenesis of rheumatoid arthritis. *New England Journal of Medicine*, 365(23), 2205-2219.
- Mu, R., Huang, H. Q., Li, Y. H., Li, C., Ye, H., & Li, Z. G. (2010). Elevated serum interleukin 33 is associated with autoantibody production in patients with rheumatoid arthritis. *The Journal of Rheumatology*, 37(10), 2006-2013. <https://doi.org/10.3899/jrheum.100184>
- Nowak, B., Madej, M., Łuczak, A., Małecki, R., & Wiland, P. (2016). Disease activity, oxidized-LDL fraction and anti-oxidized LDL antibodies influence cardiovascular risk in rheumatoid arthritis. *Advances in Clinical and Experimental Medicine*, 25(1), 43-50.
- Pap, T., Müller-Ladner, U., Gay, R. E., & Gay, S. (2000). Fibroblast biology: Role of synovial fibroblasts in the pathogenesis of rheumatoid arthritis. *Arthritis Research & Therapy*, 2(5), 1-7. <https://doi.org/10.1186/ar113>
- Renaudineau, Y., Jamin, C., Saraux, A., & Youinou, P. (2005). Rheumatoid factor on a daily basis. *Autoimmunity*, 38(1), 11-16. <https://doi.org/10.1080/08916930400022574>
- Riedel, J. H., Becker, M., Kopp, K., Düster, M., Brix, S. R., Meyer-Schwesinger, C., Kluth, L. A., Gnirck, A. C., Attar, M., & Krohn, S. (2017). IL-33-mediated expansion of type 2 innate lymphoid cells protects from progressive glomerulosclerosis. *Journal of the American Society of Nephrology*, 28(7), 2068-2080. <https://doi.org/10.1681/ASN.2016080877>
- Sakuma, M., Hatsushika, K., Koyama, K., Katoh, R., Ando, T., Watanabe, Y., Wako, M., Kanzaki, M., Takano, S., & Sugiyama, H. (2007). TGF- $\beta$  type I receptor kinase inhibitor down-regulates rheumatoid synoviocytes and prevents the arthritis induced by type II collagen antibody. *International Immunology*, 19(2), 117-126. <https://doi.org/10.1093/intimm/dx1128>
- Salama, A. A., Mahmoud, A. B., Al-Sharaki, D. R., & Gomah, A. F. (2017). Role of interleukin-33 in rheumatoid arthritis patients from Menoufia University Hospitals. *Menoufia Medical Journal*, 30(3), 952-957. <https://doi.org/10.4103/1110-2098.218272>
- Saraux, A., Guillemin, F., Guggenbuhl, P., Roux, C. H., Fardellone, P., Le Bihan, E., Cantagrel, A., Chary-Valckenaere, I., Euller-Ziegler, L., & Flipo, R. M. (2005). Prevalence of spondyloarthropathies in France: 2001. *Annals of the Rheumatic Diseases*, 64(10), 1431-1435.
- Schiller, M., Javelaud, D., & Mauviel, A. (2004). TGF- $\beta$ -induced SMAD signaling and gene regulation: Consequences for extracellular matrix remodeling and wound healing. *Journal of Dermatological Science*, 35(2), 83-92. <https://doi.org/10.1016/j.jdermsci.2003.12.006>
- Schmalz, G., Davarpanah, I., Jäger, J., Mausberg, R. F., Krohn-Grimberghe, B., Schmidt, J., Haak, R., Sack, U., & Ziebolz, D. (2019). MMP-8 and TIMP-1 are associated to periodontal inflammation in patients with rheumatoid arthritis under methotrexate immunosuppression - First results of a cross-sectional study. *Journal of Microbiology, Immunology and Infection*, 52(3), 386-394. <https://doi.org/10.1016/j.jmii.2017.07.016>

- Shmerling, R. H., & Delbanco, T. L. (1991). The rheumatoid factor: An analysis of clinical utility. *The American Journal of Medicine*, 91(5), 528-534. [https://doi.org/10.1016/0002-9343\(91\)90190-9](https://doi.org/10.1016/0002-9343(91)90190-9)
- Verma, R. P., & Hansch, C. (2007). Matrix metalloproteinases (MMPs): Chemical-biological functions and (Q) SARs. *Bioorganic & Medicinal Chemistry*, 15(6), 2223-2268. <https://doi.org/10.1016/j.bmc.2007.01.011>
- Vestweber, D. (2008). VE-cadherin: The major endothelial adhesion molecule controlling cellular junctions and blood vessel formation. *Arteriosclerosis, Thrombosis, and Vascular Biology*, 28(2), 223-232. <https://doi.org/10.1161/ATVBAHA.107.158014>
- Zainal, Z., Rahim, A. A., Radhakrishnan, A. K., Chang, S. K., & Khaza'ai, H. (2019). Investigation of the curative effects of palm vitamin E tocotrienols on autoimmune arthritis disease in vivo. *Scientific Reports*, 9(1), 1-11. <https://doi.org/10.1038/s41598-019-53424-7>

## Towards Adoption of Smart Contract in Construction Industry in Malaysia

Dewi Noorain Bolhassan<sup>1</sup>, Chai Changsaar<sup>1</sup>, Ali Raza Khoso<sup>2,3\*</sup>, Loo Siawchuing<sup>4</sup>, Jibril Adewale Bamgbade<sup>1</sup> and Wong Ngie Hing<sup>1</sup>

<sup>1</sup>Faculty of Engineering, Computing and Science, Swinburne University of Technology Sarawak Campus, 93350 Sarawak, Malaysia

<sup>2</sup>School of Civil Engineering, Faculty of Engineering, Universiti Teknologi Malaysia, Skudai, 81310 Johor Bharu, Malaysia

<sup>3</sup>Department of Civil Engineering, Mehran University of Engineering & Technology, 76062 Jamshoro, Pakistan

<sup>4</sup>Centre of Building, Construction and Tropical Architecture, Faculty of Built Environment, University of Malaya, 50603 Kuala Lumpur, Malaysia

### ABSTRACT

The revolution of Malaysian Construction 4.0 through emerging technologies has brought a paradigm shift that has digitalized the construction sector. There is a need to adopt a computerized protocol to assist in automating the performance of a contract to meet future digital challenges. Therefore, this paper aims to serve as a pioneer study to investigate the implementation of the Malaysian construction industry to adopt smart contracts. This study adopted a qualitative scientific methodology, whereby a systematic review was conducted to gather the benefits and challenges of implementing smart contracts in the construction

industry. Further, interview sessions were arranged to collect data from the construction contract management experts. The research findings unveil that due to the self-executing attribute of smart contracts, the implementation of smart contracts could provide a better apportionment of risks in a contract. The study also finds that the challenges in implementing smart contracts are severe. For instance, the smart contract is irreversible and immutable and prone to human error. The study concludes that it is more suitable to apply and implement a smart contract to a short-term contract that

### ARTICLE INFO

#### Article history:

Received: 12 July 2021

Accepted: 15 September 2021

Published: 24 November 2021

DOI: <https://doi.org/10.47836/pjst.30.1.08>

#### E-mail addresses:

101218642@students.swinburne.edu.my (Dewi Noorain Bolhassan)

cschai@swinburne.edu.my (Chai Changsaar)

aliraza.khoso@faculty.muett.edu.pk (Ali Raza Khoso)

siawchuing@um.edu.my (Loo Siawchuing)

jbamgbade@swinburne.edu.my (Jibril Adewale Bamgbade)

nhwong@swinburne.edu.my (Wong Ngie Hing)

\*Corresponding author

is not subjected to variation. Furthermore, a smart contract can enhance the efficiency in managing the contracts, such as reducing time and managing the conflicts and disputes that arise during the contract duration. The developed implementation framework is significant for the construction personnel, especially those dealing with the contract administration. The implementation of smart contracts in construction could boost contract administration and management discipline via investment in this new technology.

*Keywords:* Adoption, construction industry, Malaysia, qualitative research, smart contracts

---

## INTRODUCTION

The term *smart contract* was first mentioned by Nick Szabo in 1994, who defined it as “a computerized transaction protocol that executes the terms of a contract” (Li et al., 2020). The general objectives of smart contract design are to satisfy common contractual conditions (such as payments terms), minimize expectations, and the need for trusted intermediaries”. There is a consensus that the term “smart” in smart contracts refers to a kind of artificial intelligence replacing a human endeavor for making tasks easier to complete (Mason & Escott, 2018). A smart contract is generally an executable code that runs on the blockchain to facilitate, execute and enforce the terms of an agreement, where the main aim is to automatically execute the terms of an agreement once the specific conditions are met (Alharby & van Moorsel, 2017). Over the years, the development in blockchain technology has strengthened smart contracts, which are considered secure, further, the use of unstoppable computer programs that are executable automatically within a blockchain network (Wang et al., 2019). Smart contracts and blockchain are technologies that have made a significant contribution in various industries such as the healthcare industry, banking industry, and so on (Ekblaw et al., 2016). These digital contracts are digitally created in a paperless condition and executed, completed, and archived digitally.

Smart contracts are exceptionally valuable to manage construction projects, such as effectively minimizing disputes among parties. However, the global construction dispute grew to a value of USD 33 million in 2019, and it takes an average of 17 months to resolve that dispute (ARCADIS, 2019). This report named the top causes of construction disputes as poor contract administration. Like contract management, discretionary clauses allow for discrepancies and contradict other clauses, leading to construction disputes. The three causes for disputes globally are failing to properly administer the contract, poorly drafted or incomplete unsubstantiated claims, and employer/contractor/subcontractor failing to understand or comply with its contractual obligations (ARCADIS, 2019).

The nature of a construction contract where it has always been a collaboration between either a large or small group of participants necessitates risks of these parties to be allocated; hence the development and utilization of standard conditions of a contract is an important

parameter. Smart contracts digitalize the contract and agreement between these parties and reduce the risks of a traditional contract over disputes. It is because of a smart contract's self-executing attribute, where the terms and conditions are coded. Therefore, it can lead to less interpretation of a contract and reduce the risk in a contract structure.

The construction industry is currently observing continuing growth, and it is forecasted that the volume of construction output will grow to USD 10.1 trillion worldwide by 2021 (GlobalData, 2017). The average global growth is expected to increase at a rate of 3.9% per annum. In Malaysia, the construction industry is also expecting an expansion of about 4.7%. However, the construction industry is lagging in productivity which is a crucial aspect of failure, and conversely has the opportunity to boost volume by \$1.6 trillion (Barbosa et al., 2017). Digitalization in the construction industry can improve productivity and create value by closing gaps in inefficiencies. However, digitalization has not been genuinely embraced in the industry. According to an index of McKinsey Global Institute, the construction sector is among the least digitized sector in the world (Barbosa et al., 2017). Although there is already an awareness that digitalization influences the industry, there is still so much potential that could be done if the industry pursues more on its digitalization initiatives. Nonetheless, over the recent years, the construction industry has etched its step towards various technological advancements, the prominent ones being the Building Information Model (BIM), Internet of Things (IoT), and Electronic tendering (E-tendering), which are the result of client's expectations, new technological capabilities, and growing legal frameworks and requirement from large infrastructure projects (Kaufmann et al., 2018). Moreover, the Government has pushed for a paradigm shift towards a digital economy in Malaysia, in line with the Industrial Revolution 4.0. Hence, a strategic change is expected with a vision to accelerate economic growth by embracing digitalization.

Considering the above and various other strategic development and paradigm shift pushed by the Malaysian Government towards digitalization, the local construction industry must evaluate the various impacts of smart contracts that could be disruptive technology. However, most construction companies' attitude towards digitalization has no impact on their organization, resulting in not approaching and adopting digital innovation as these organizations find it challenging to embrace and work effectively in the digital revolution (McNamara & Sepasgozar, 2020). Hence, there is a need to evaluate the impacts of smart contract implementation on the construction industry in Malaysia. Therefore, this research aims to enhance the construction contract performance in the Malaysian construction industry via identifying the benefits of smart contracts implementation in the Malaysian construction industry and the challenges of smart contracts implementation compared to traditional contracts in Malaysia. Finally, the study develops an implementation framework of smart contracts for the Malaysian construction industry. However, it should be noted that smart contracts are still considered a state-of-the-art technology, and there are many

gaps in the body of knowledge in the implementation of smart contracts in the construction industry in Malaysia. Therefore, this evaluation can serve as a benchmark and a decision tool in gauging and embracing smart contracts in consideration and preparation of its various benefits and challenges.

## LITERATURE REVIEW

### Traditional Contracts Vs. Smart contracts

In a construction context, the relatively complex nature of a construction project necessitates using a carefully written contract to prescribe the legal, financial, and technical aspects of the project (Clough, 1986). The construction contract defines the relationship, including responsibilities between the contracting parties, and spells out commercial terms and general project rules. Before the digital age, contracts are traditionally signed on paper and between parties at the same time. The current practice of traditional contracting allows for paper distribution instead of storing electronically in a contract management system. In Malaysia, contracts are governed by the Contracts Act 1950, which covers the rights of the contracting parties. To enforce a contract in Malaysia, the parties must observe the essential elements of the Contracts Act 1950. However, the evolving digital platform and capabilities of the Information and Communications Technology industry and the emergence of e-commerce allows people to have faith in the online environment, including entering into contract digitally and electronically.

In line with this, Malaysia enforced new legislation, the Electronic Commerce Act 2006, where information in electronic form shall not be denied with legal effect, validity, and enforceability. The Act 2006 also enforces the norm of digital signature where a digital signature bears the same effect as a normal wet- signature required in a traditional contract. Table 1 depicts the fundamental differences between traditional contracts and smart contracts. With smart contracts, trust is distributed across a community on a peer two peer network rather than centralized (England & Moreci, 2012). In other words, “no one can unilaterally take actions on behalf of the community” (Lamb, 2018).

Table 1  
*Differences between smart contract and traditional contract*

Aspects	Smart contract	Traditional contract
Governance/Legal Framework in Malaysia	Contracts Act 1950 Electronic Commerce Act 2006	Contracts Act 1950
Signature	Digital Signing	Wet Signature Mandatory



Table 1 (Continued)

Aspects	Smart contract	Traditional contract
Platform	Peer to Peer (P2P) Network, Distributed Ledger Technology	Paper-based
Storage	Distributed Ledger	Physical storage
Network	Distributed	Centralized
Administration	Self-Executing	Executed and administered by human

### Smart Contracts in Construction

The construction industry, likewise several other industries, is starting to embrace and engage with new technology. It is further assumed that modern technologies are paving their deeper path in the construction industry with the recent technological developments (Khosro et al., 2021). It can be seen with the widespread adoption in Building Information Model (BIM), 3D Modelling, Internet of Things, and many more. However, it can be viewed that smart contracts can be among the technology adopted to enhance the construction industry.

In the execution of a construction project, procurement is among the time-consuming phases of a construction project, and multiple contracts occur within a supply chain. In a construction context, this flows down from supplier, sub-contractor to the main contractor. The trust among the different contracting parties, such as in financial transactions, project management, and others, are usually validities by a contract and amenities such as a Letter of Credit (LC) document where third parties such as banks create trust between the parties (Ahmadisheykhsarmast & Sonmez, 2018). The financial institution's role in this such as banks exist in this financial transaction to ensure trust between both parties and guarantee that the seller will be paid after delivering the predefined conditions. In executing a construction project, payment stability is imperative for avoiding disputes (Mason & Escott, 2018). In a smart contract environment, as the transactions are between parties, there is no need for intermediary involvement other than a traditional contract (Li et al., 2019). Therefore, it is considered advantageous since banks and third-party are involved directly (Crosby et al., 2016). There is also a consensus that overheads in a smart contract can be greatly reduced as it eliminates the need for a 'middle man' for legal costs and administration costs for preparation and supervision of a traditional contract (Giancaspro, 2017).

In the procurement phase of a project, parties can code attributes and clauses such as the amount due to a party. Therefore, it ensures that the transaction between parties is transparent, and both parties cannot access the money up to the due date of payment. It is achieved by taking advantage of the self-executing attribute of smart contracts. However,

it is to be noted that the money and transaction that will be transferred to smart contracts are in a cryptocurrency account as of the present moment. This technology allows the elimination of third-party administration fees and mitigates problems concerning slow processing and verification of payment (Cardeira, 2015). It is important as delayed progress payment has been a significant problem in construction as it contributes to difficulties in cash flow within the construction supply chain (Badroldin et al., 2016). Furthermore, payments are guaranteed and automatically executed with cryptocurrencies, which is considered an enormous contribution to the construction sector (Xue & Lu, 2020).

Apart from the numerous advantages of smart contracts in the modern construction industry, they face setbacks such as collaboration agenda. The construction industry has been regarded as slow in adopting changes, adversarial, and unfair to subcontractors. Therefore, the collaboration agenda has been prominent in the construction industry, where the key to collaboration agenda has always been mutually trusted (Bouchlaghem & Shelbourn, 2011). Moreover, a challenge faced by implementing smart contracts is that once a smart contract is coded, it is immutable and irreversible (Luo et al., 2019). Smart contracts that are coded wrongfully due to human error could result in a disastrous end. Because of the nature of a smart contract, it is self-executing to rely upon the pre-determined conditions and set out all the contracting parties' obligations (Li et al., 2019). Further, a blockchain requires big data, so it is impossible to manage change within the system (Xue & Lu, 2020). Since contracts can run on either public blockchain or private blockchain, but public blockchain consensus of all parties is needed for validation. At present, there is no established blockchain for all project management activities (Yang et al., 2020).

In addition, deviant miners can release malicious blocks at a later stage and attack the blockchain. It can result in acquiring more than 50% of the computational power and resulting in a tampered ledger (Luo et al., 2019). Furthermore, some functions can create malicious notes and libraries in blockchain technology, such as 'self-destruct', which deactivates contracts (Ghosh et al., 2020). In 2016, a malicious user led to a burglary of \$50 million in a smart contract transaction implemented in Ethereum, which is a platform for smart contracts (Dorsala et al., 2020). It suggests that the dependability of smart contracts is doubtful as it has been used for criminal purposes. The vulnerability of smart contracts can also inspire cybercriminals to steal and launder money. Therefore, testing smart contract code is necessary as it is vulnerable to attacks, which can be done using security analysis tools (Yang et al., 2020).

Another big challenge to note regarding the implementation of smart contracts in construction is that as smart contracts utilize cryptocurrency, it still has many barriers to overcome. It is not a mainstream application in Malaysia yet. There are still risks in fluctuation due to cryptocurrency usage, suggesting that cryptocurrencies are not stable at the present moment for use in construction projects. In addition, using cryptocurrencies

requires a considerable amount of data and capacity than the typical payment transaction such as a visa (Zhong et al., 2019).

Contract management is an integral part of contract execution. However, it is believed that construction professionals need to know the intricacies of process and involvement in a project. Concerning implementing smart contracts, there is a need for specialist knowledge in the implementation of smart contracts. It requires participation from various disciplines of the contract management team (McNamara & Sepasgozar, 2020). Presently there is a significant lack of expertise to execute and administer smart contracts (Li et al., 2019). Therefore, before designing the blockchain system for a construction project, there is a multitude of information required from multidisciplinary parties (Yang et al., 2020).

A novel smart contract payment security system by Ahmadiheykhsarmast and Sonmez (2020) was adopted in preparation for this research considering the above facts. The purpose of this adaption is because benchmarking is recognized as “an essential tool for continuous improvement of quality” (Dattakumar & Jagadeesh, 2003). However, it has not been assessed regarding the implementation of smart contracts in Malaysia. The framework includes setting up a secured payment system for smart contract implementation. Their framework has eliminated the problem, resolved the payment security system, and done the practical test on a real construction project. Therefore, it is suitable for this study. It exemplifies the success of the implementation of smart contracts in the construction industry. The recommended smart contract payment security system provides guaranteed security of payments of works under construction and a platform for a secure and transparent platform, as shown in Figure 1.

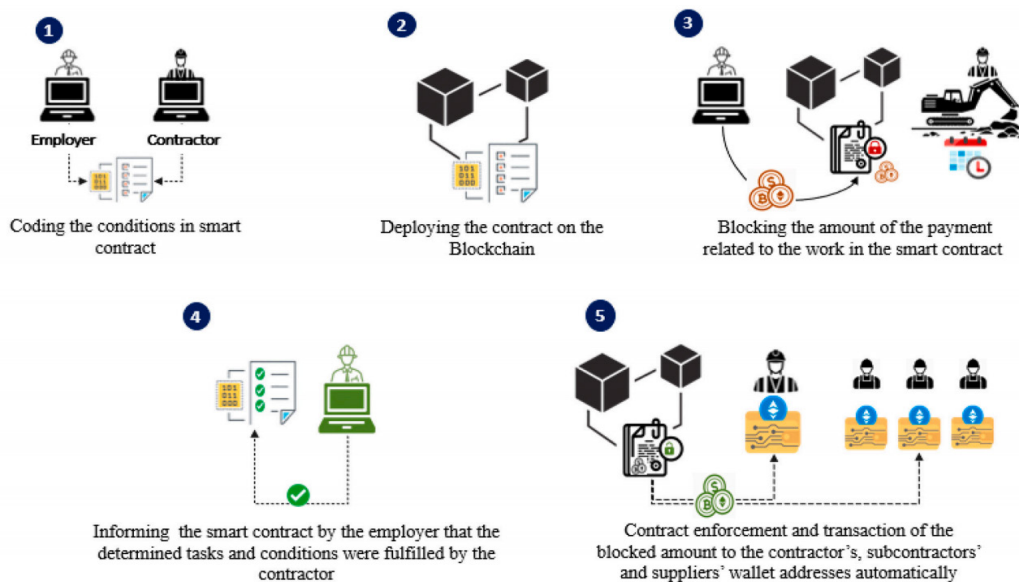


Figure 1. Framework adopted from (Ahmadiheykhsarmast & Sonmez, 2020)

## RESEARCH METHODOLOGY

This research adopts a systematic qualitative approach, as depicted in Figure 2. The advantage of applying a qualitative research approach is mainly inductive and explorative; thus is ideally suited in situations where the nature of impacts of smart contracts is to be investigated. Questions like the current challenges and benefits of smart contracts are examined. Qualitative methods such as semi-structured interviews, content analysis, and framework analysis research methods are applied to achieve each research objective.

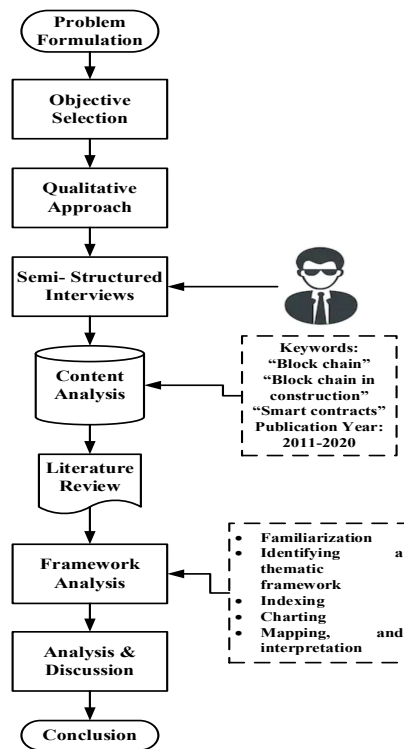


Figure 2. Systematic research methodology

### Semi-Structured Interviews

A semi-structured interview technique was applied based on pre-conceived questions. It provided background knowledge to accomplish the objectives, providing relevant outcomes to confirm and validate the data. A personal interview is adopted as there can be much private and confidential data and information in the interview, which would necessitate approval from the interviewee. The interviewees consisted of various backgrounds that included experts were involved from different backgrounds in contracts administration. The interviews were conducted in May 2021, which consumed around two weeks. The information of interviews is illustrated in Table 2.

Table 2

*Background of interviewees*

Interviewee ID	Profession	Executive Level	Experience
Respondent 1	Contracts Manager	Senior	More than 20 years
Respondent 2	Contracts Manager	Senior	More than 15 years
Respondent 3	Quantity Surveyor	Middle	More than 10 years
Respondent 4	Senior Contracts Administrator	Middle	More than 15 years
Respondent 5	Contracts Administrator	Middle	More than 10 years
Respondent 6	Finance Manager	Senior	More than 15 years

### Content Analysis

The focus of content analysis is the characteristics of language, taking into account the content or contextual meaning of the text (Hsieh & Shannon, 2005). The content analysis aims to provide “knowledge and understanding of the phenomenon under study” (Bengtsson, 2016). A more specific type of content analysis considered here is leaning towards a summative approach of content analysis, where it aims to identify certain words or contexts to understand the contextual use of the words and content (Erlingsson & Brysiewicz, 2017). It allows to attempts not to infer meaning but explore usage. It is deemed as a suitable approach in this research context concerned with the research objectives.

The first step of the research involved the academic literature on the topic of smart contracts in construction. The document survey focused only on electronic journals written in English. A set of selection criteria was applied to gather the relevant data to be reviewed, and the first criteria were to restrict the review period to 2010 until 2020. This eleven-year interval shall address maturity and future trends in a smart contract, blockchain, and construction. As smart contracts run on a blockchain, the search also included blockchain in construction. Due to the novel nature of this technology, there is quite a limited number of documents that explicitly address smart contracts in construction; instead, it addresses blockchain in construction and blockchain and smart contracts. Insights were developed to discuss the surrounding theme and context of the literature. From the literature survey, several themes emerged and were discussed surrounding smart contracts.

### Framework Analysis

Since the smart contract is still considered a ‘state of the art’ technology, there are various gaps in knowledge on the implementation of smart contracts, especially in Malaysia, that would be useful for adoption. There is currently no information available for the

construction sector in the implementation of such a disruptive change. A theoretical framework aims to provide an analytical structure and contextualize formal theories into a guide (Adom & Hussain, 2018). It is in line with the aim of the research to identify the impact of smart contract implementation in Malaysia. The theoretical framework outlined from this research would allow future research to identify the practical implications of smart contracts within the local construction industry.

Later, a framework analysis is used to analyze the interview data. The framework creates a new structure for the data to summarize or reduce the data while contemporaneously, capable of answering the research questions (Gale et al., 2013). Following the framework analysis method, data were analyzed in five stages: familiarization, identifying a thematic framework, indexing, charting, mapping, and interpretation, as shown in the following Table 3.

Table 3  
*Framework analysis stages*

Process	Description
Familiarization	Where the collected data from the interview sessions are familiarized and transcribed, and the overview of the collected data is gained.
Identifying a thematic work	Emerging themes of issues and data set are collected. Key issues, concepts, and themes of participants can form the basis of the framework and be used to classify data.
Indexing	Identification of sections of data that responds to a particular theme.
Charting	Specific indexed data is placed in the framework with headings and subheadings.
Mapping and interpretation	Analysis at this stage guides the interpretation of the data set.

## RESULTS AND DISCUSSIONS

### Benefits of Smart contract Implementation in Malaysian Construction Industry

In a traditional system, the contract is formed between parties which requires a third party (trustee). In contrast, third parties such as banks are not required in a smart contract, as the smart contract attributes are self-executing through the blockchain system. In the interviews, the data revealed that Respondents 1 and 3 were agreed to eliminate the trustee and suggested reducing the processing time for the payment. Thus, there is a necessity to evaluate the benefits of shifting to a smart contract compared to a traditional contract.

Furthermore, it shall provide an overview and basis of migration to a digitalized database. In addition, due to the automation or self-executing attribute, this would also guarantee the payment to the contractor.

In traditional contracts, there is always an emphasis on stakeholder engagement, and construction contracts are usually built on a multi-dimensional party. These stakeholders need to administer the contracts and interpret them based on their disciplines manually. Therefore, it may contribute to inefficient contract procedures and administration. In a smart contract environment, the obligations of the employer and the contractor are coded in the smart contract system that executes automatically in a secure and decentralized platform without third-party involvement. The automation of responsibilities reduces the possibility of disputes between parties, which have been established as a contributing factor in construction disputes. In this current study, Respondents 1, 3, 4, and 6 believe that digitizing the contracts shall improve contract administration. It would decrease the amount to communicate any requirements to the parties as now there is a precise apportionment of responsibility between them. Respondents 4 also believes that the payment part of contract administration benefits greatly from this attribute, where payment automation shall improve payment processing, ensuring that the contractor's cash flow is guaranteed. It is also in line with Respondent 2 views which suggest that a smart contract is an avenue that can replace human intervention in contract execution. Contracts are sometimes entered into without complete knowledge on the potential outcome, and manual contract administration in traditional contracts contributes to tremendous inefficiency, and this can cause disputes with low levels of traceability. Smart contract implementation promotes collaboration between parties with increased transparency than a traditional contract, which will create a stable environment in a project in terms of apportionment of risks.

In addition, as compared to traditional contracts, the smart contract is also indicated as more accessible due to its digital database. Respondent 2 and Respondent 5 commented that a smart contract creates value addition and increases efficiency where parties can easily access the terms and conditions, leaving less room for interpretation. In terms of record-keeping, Respondent 1 believes that a smart contract improves the administration of a contract as terms are now digitized. In addition, the status of a smart contract is automatically updated, and the digital currency will only be deployed after a pre-existing condition is fulfilled. Therefore, it will alleviate concerns on withheld payment and improve efficiency. This efficiency is a product of the smart contract's main attribute, which is self-executing.

Through smart contracts, instant payment is possible as all participants are in the same network to close all payment channels without the involvement of third parties. This problem of late payment can be alleviated as the system could be coded. As soon as the employers verify the work done and the accuracy of the total amount, the payment could be released instantly in a cryptocurrency. Eliminating intermediaries in a smart contract can alleviate the

poor treatment of subcontractors, leading to insolvencies, and payment security will result in a more stable supply chain (McNamara & Sepasgozar, 2020). In summary, the benefits of a smart contract implementation are identified, as demonstrated in Table 4.

Table 4  
*Benefits of implementation of smart contracts*

No	Description	Remarks
1	Better Apportionment of Risks and Responsibilities	Responsibilities are established during the contract formation, and there is better risk apportionment in a multi-dimensional party as obligations are self-executed.
2	Less Room for Disputes	Require less interpretation of parties' obligations.
3	Self-Executing Contract	Automation of contract responsibilities increases efficiency in contract administration and management due to digitalization.
4	Elimination of Third Party	Reduce the processing time and cost of payment to contractors.
5	Guaranteed Payment	It shall improve the contractor's cash flow due to the automation in payment processing.

### **Challenges of Smart Contract Implementation Compared to Traditional Contracts in Malaysia**

A smart contract is still at the forefront of technology, still has several challenges to overcome, improving accessibility and usage of smart contracts compared to traditional contracts. One of the challenges that should be addressed is cybersecurity. Respondents 1, 3, 4, and 5 voiced concerns about using cybersecurity as often there is confidential information in the contract. Usually, there is much effort to preserve the confidentiality of a construction contract. In addition, as viewed by Respondent 6, which is from a banking background, fault transaction and stolen accounts problems in the banking industry are still unresolved. Therefore, they have posed an issue in the banking industry. Hence, handling the cybersecurity risk would be a challenge in managing this smart contract environment.

Considering that smart contracts utilize a peer-to-peer network where data is only distributed between intended parties, and there is no third party involved, it solely depends on the contracting parties and code to pursue the transaction. There should be malicious code between the blockchain; this affects the other nodes in the blockchain system and



ensures transparency in transactions. However, one could not deny that smart contracts can be susceptible to malicious intentions to the coding system. Data uploaded in the ledger needs to be legitimate, and there is a possibility of fraudulent activity that will run through the supply chain (Li et al., 2019). It is different in a traditional contract environment where transactions are conducted manually, and any alleged malicious intentions can be stopped and possibly would not affect subsequent activities.

The irreversibility and immutability of smart contracts are also a challenge for implementation as contracts coded wrongfully due to human error could result in a disastrous end. Respondent 5 is concerned that if a change in law and taxes calls for any extra deduction from the payment, the smart contract could not accommodate this due to its irreversibility trait. Hence, it has been recommended that projects that are prone to variations do not utilize smart contracts. It could pose a problem for long-term projects many external factors could allow for changes in the contract structure. A more straightforward type of contract would be easier to manage. Respondent 1 emphasized that there should be a strong agreement between client and contractor before executing the smart contract due to it being irreversible. Hence, communication and consensus between the parties are essential in implementation. Should any of the parties decide on changes in the contract structure or terms, this shall not be easy to manage in the future. The immutable nature of smart contracts would give rise to its inefficiency as to 'reasonableness' inherent in contract management, usually found in discretionary clauses (Giancaspro, 2017). It gives rise to professionals versed in programming collaborating with lawyers or legal teams to monitor or enforce the contracts.

The utilization of a cryptocurrency is a prominent feature in implementing a smart contract, as the automation of execution shall subsequently release the payment in a cryptocurrency form. However, all respondents agree that they do not know much about cryptocurrency, as it has not been practiced as a form of payment in the construction industry yet. Respondents 1, 2, and 4 were concerned about the flexibility in using cryptocurrency in the construction industry. However, Respondent 2 believes that it may be possible to exchange the goods if other services and works also use cryptocurrency. Respondent 5 also could not provide opinions on cryptocurrency usage due to the lack of knowledge of cryptocurrency usage in the construction world. Respondent 6, from a finance and banking background, thinks that cryptocurrency is a fast and secure form of transaction; it is still an unrecognized method in the worldwide banking industry. In addition, cryptocurrency is an unstable currency and has a high fluctuation range. The unpredictability of price fluctuation in cryptocurrency constitutes a high risk in the transaction. Therefore, it exhibits a gap that needs to be closed in implementing smart contracts. There should be more training construction professionals need to educate practitioners should cryptocurrency is used in the construction industry.

In addition, the usage of cryptocurrencies requires a considerable amount of data. From the data obtained, most respondents agree that the novelty in implementing smart contracts such as the infrastructure and acceptability of the industry players is the main concern. It was unanimously agreed that the proper training of construction professionals is a major issue. Respondent 1 commented that there should be multiple test cases before the comprehensive implementation of the smart contract first. Hence, a smart contract environment must be implemented in a project, and the contract management team needs to be equipped with technology-based knowledge.

Another challenge from the implementation of smart contracts is the lack of legal precedence. The interviewees (Respondent 4 and Respondent 5) believed finding legal precedence and cover the legal jurisdictions would be challenging. As informed by Respondent 6, a cryptocurrency that has yet to be formally recognized by any government as an authorized transaction might pose a legal risk, and there is no legal entity to enforce and authenticate these transactions. It is important as contracts are heavily reliant upon terms and conditions to administer and enforce the regulation. Hence, contracts written in a more understandable language by the vast majority of the construction practitioners are preferred compared to contracts written in a traditional ‘legalese’ language (Boon et al., 2019). Respondent 6 believes that there is a gap in the industry’s competent personnel and IT infrastructure to execute the smart contract. Smart contracts are developed in a different environment, and their terms must be read, understood, and soon coded into a computer. Therefore, it supports the notion of novelty in smart contract implementation, where there are many gaps in training and execution before implementation in the construction industry. There is also a requirement for a certain level of technological advancement in the construction industry to implement a smart contract successfully. The construction industry’s digitalization level is not sufficient to implement new technology such as a smart contract. In summary, the challenges of smart contract implementation are summarized in Table 5.

Table 5  
*Challenges of implementation of smart contracts*

No	Description	Remarks
1	Novelty	Lack of legal precedence and infrastructure.
2	Human Error in Coding	Prone to human error in coding that might provide a disastrous end to the system.
3	Irreversible and Immutable	It is not suitable for long-term projects, where it will be prone to changes or variables as smart contracts are irreversible.

Table 5 (Continued)

No	Description	Remarks
4	Cybersecurity Issues	Risk of cybersecurity issues in the contract administration, as information in the contract, are confidential.
5	Uncertainty in Cryptocurrency	Have not been practiced in construction payment, and there is not much knowledge on the stability of the cryptocurrency.

### Smart Contract Framework for the Malaysian Construction Industry

The Employer (E) and Main Contractor (MC) need to agree on payment terms in the proposed framework. The agreed terms are presented as a computerized protocol through a smart contract deployed on a blockchain system. A monthly progress payment is assumed to be made. In the smart contract, a projected payment is pre-determined in relation to the planned progress of the project. Then, after payment approval, the smart contract automatically transfers the amount to the contractor's subcontractors and suppliers' wallets according to the agreed terms. It is to be noted that this transaction utilizes cryptocurrency. It is unique for each project, and this has to include a contingency amount to cover the potential fluctuations in cryptocurrency. There is a consensus that integrating hardware and software, including scalability, security, and privacy, is essential in selecting a blockchain. The suggested platforms to execute these smart contracts on blockchain include; Ethereum, Hyperledger Fabric, Corda, Stellar, and Rootstock as major smart contract developer platforms based on popularity. It is to be noted that among those companies, Ethereum is the only one that has a base in Kuala Lumpur, Malaysia. It also has the largest market influence among others. The smart contract procedure enables releasing a blocked amount.

In this system, data is provided and coded into the smart contract. The data required are schedule payment data, actual completion dates, budgeted and actual payment, and parties' information such as contractor, sub-contractor, and suppliers. During the cut-off period, the contractor can update the planned and actual schedule and the payment data for the employer's approval and payment. Employers can click on an authorization button ('approve,' 'pay'). The payment amount will simultaneously be transferred to the main contractor's, subcontractors', and any specified suppliers' wallets through a smart contract. If the Contractor/supplier/subcontractor receives the payment notification, they will convert the currency into any local cryptocurrency amount. The primary framework of the proposed framework is depicted in Figure 3.

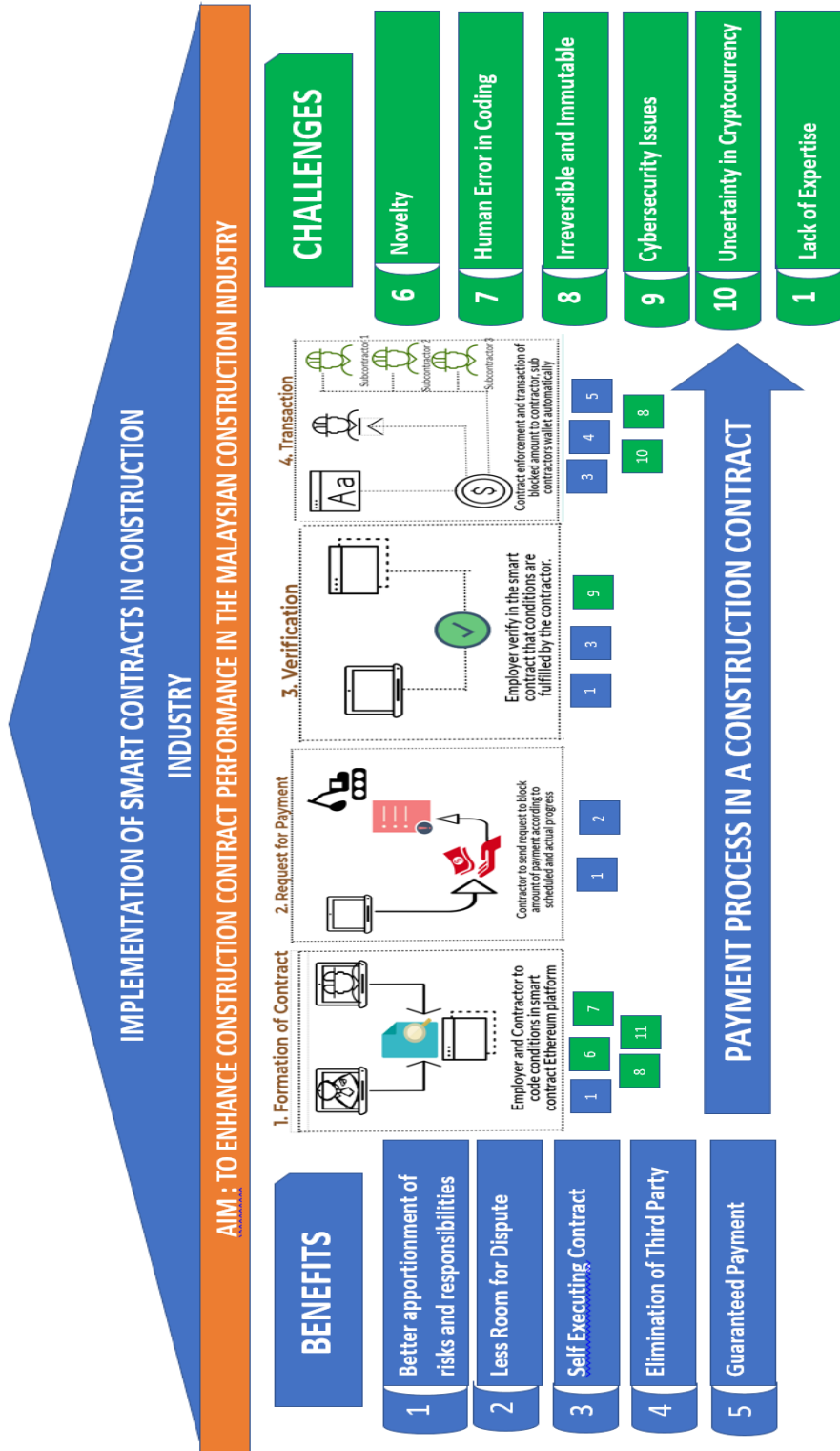


Figure 3. Smart contracts implementation framework

## CONCLUSION AND RECOMMENDATION

The construction sector is embracing and pushing the Industry Revolution 4.0, and digitization of contracts fits in rightly in this agenda. Digitization of contracts fits perfectly as a follow-up to introducing modern technologies in the industry, where this generation of practitioners and future generations are more susceptible to technological adventures. The findings and discussion suggest several benefits of smart contracts that could potentially provide efficiency in contract management. It is by several avenues, one of them and the more important one is by greatly reducing disputes in payment processing and improve contractor's cash flow all through the supply chain by automation of payment. The findings on the benefits of the implementation of smart contracts point to possible improvement in the contract management part of a construction project. However, evaluating the implementation of the smart contract includes various challenges. Considering that this technology is still embryonic, it is prudent that the identified challenges be evaluated thoroughly to ensure that it is not detrimental to the successful implementation. For example, overcoming concerns and challenges regarding the irreversible and immutable coding in smart contracts needs to be identified before implementing a construction project.

Hence, referring to the framework developed, it is prudent that all scenarios are taken into consideration, and as respondents have pointed out, there should be a strong and mutual agreement. The mapping of benefits and challenges in the framework suggests that at the moment, it is more suitable to apply and implement a Smart contract to a short-term contract that is not subjected to variation. There are inevitably systemic problems in contract management in the construction industry as it yields a huge number of disputes which also takes a long time to manage. The time spent by the contract management team managing disputes could be reduced or eliminated by introducing a smart contract, where obligations are coded in the system, leaving less room for interpretation. This technology's clarity may add efficiencies in the contract management process and allow for a paradigm shift to proactive and efficient project delivery rather than a defensive approach when disputes arise. This new approach of smart contract implementation could enhance the contractor's contract performance, and more focus can be provided on the quality of the works.

## ACKNOWLEDGEMENT

The authors wish to pay gratitude to Swinburne University of Technology Sarawak Campus for providing a conducive research environment.

## REFERENCES

- Adom, D., & Hussain, E. K. (2018). Theoretical and conceptual framework: Mandatory ingredients engineering. *International Journal of Scientific Research*, 7(1), 438-441.

- Ahmadisheykhsarmast, S., & Sonmez, R. (2018). Smart contracts in construction industry. In *5th International Project and Construction Management Conference (IPCMC2018)* (pp. 767-774). ACADEMIA.
- Ahmadisheykhsarmast, S., & Sonmez, R. (2020). A smart contract system for security of payment of construction contracts. *Automation in Construction*, 120(October 2019), Article 103401. <https://doi.org/10.1016/j.autcon.2020.103401>
- Alharby, M., & van Moorsel, A. (2017). A systematic mapping study on current research topics in smart contracts. *International Journal of Computer Science and Information Technology*, 9(5), 151-164. <https://doi.org/10.5121/ijcsit.2017.9511>
- ARCADIS. (2019). Laying the Foundation for success. In *Global Construction Disputes Report 2019* (pp. 1-31). ARCADIS
- Badroldin, M. K. A. M., Hamid, A. R. A., Raman, S. A., Zakaria, R., & Mohandes, S. R. (2016). Late payment practices in the Malaysian construction industry. *Malaysian Journal of Civil Engineering*, 28(3), 149-162. <https://doi.org/10.11113/mjce.v28.16005>
- Barbosa, F., Woetzel, J., Mischke, J., Ribeirinho, M. J., Sridhar, M., Parsons, M., Bertram, N., & Brown, S. (2017). *Reinventing construction: A route of higher productivity*. McKinsey Global Institute.
- Bengtsson, M. (2016). How to plan and perform a qualitative study using content analysis. *NursingPlus Open*, 2, 8-14. <https://doi.org/10.1016/j.npls.2016.01.001>
- Boon, K. S., Sector, I., Firms, C., & Contracting, C. (2019). *Transforming the Singapore built construction project budget*. PAQS Congress Kuching Malaysia.
- Bouchlaghem, D., & Shelbourn, M. (2011). Introduction. In *Collaborative Working in Construction* (p. 5). Routledge.
- Cardeira, H. (2015). Smart contracts and possible application to the construction industry. *New Perspectives in Construction Law Conference*, 1, 19-21.
- Clough, R. H. (1986). *Construction contracting*. John Wiley & Sons Ltd.
- Crosby, M., Nachaippan, Pattanayak, P., Verma, S., & Kalyanaraman, V. (2016). Blockchain technology: Beyond bitcoin. *Applied Innovation Review*, 2(6), 6-19.
- Dattakumar, R., & Jagadeesh, R. (2003). A review of literature on benchmarking. *Benchmarking: An International Journal*, 10(3), 176-209. <https://doi.org/10.1108/14635770310477744>
- Dorsala, M. R., Sastry, V. N., & Chapram, S. (2020). Fair payments for verifiable cloud services using smart contracts. *Computers and Security*, 90, Article 101712. <https://doi.org/10.1016/j.cose.2019.101712>
- Ekblaw, A., Azaria, A., Halamka, J. D., & Lippman, J. D. H. A. (2016). A case study for blockchain in healthcare: "MedRec" prototype for electronic health records and medical research data. In *Proceedings of IEEE open & big data conference* (Vol. 13, p. 13). IEEE Publishing.
- England, K., & Moreci, J. (2012). *Contingency - Are you Covered?* Project Management Institute.
- Erlingsson, C., & Brysiewicz, P. (2017). A hands-on guide to doing content analysis. *African Journal of Emergency Medicine*, 7(3), 93-99. <https://doi.org/10.1016/j.afjem.2017.08.001>

- Gale, N. K., Heath, G., Cameron, E., Rashid, S., & Redwood, S. (2013). Using the framework method for the analysis of qualitative data in multi-disciplinary health research. *BMC Medical Research Methodology*, 13(1), 1-8. <https://doi.org/10.1186/1471-2288-13-117>
- Ghosh, A., Gupta, S., Dua, A., & Kumar, N. (2020). Security of cryptocurrencies in blockchain technology: State-of-art, challenges and future prospects. *Journal of Network and Computer Applications*, 163(April), Article 102635. <https://doi.org/10.1016/j.jnca.2020.102635>
- Giancaspro, M. (2017). Is a 'smart contract' really a smart idea? Insights from a legal perspective. *Computer Law and Security Review*, 33(6), 825-835. <https://doi.org/10.1016/j.clsr.2017.05.007>
- GlobalData. (2017). *Global construction outlook 2021*. GlobalData UK Ltd.
- Hsieh, H. F., & Shannon, S. E. (2005). Three approaches to qualitative content analysis. *Qualitative Health Research*, 15(9), 1277-1288. <https://doi.org/10.1177/1049732305276687>
- Kaufmann, D., Ruaux, X., & Jacob, M. (2018). *Digitalization of the construction industry: The revolution is underway*. OliverWyman.
- Khoso, A. R., Yusof, A. M., Chai, C., & Laghari, M. A. (2021). Robust contractor evaluation criteria classification for modern technology public construction projects. *Journal of Public Procurement*, 21(1), 53-74. <https://doi.org/10.1108/JOPP-06-2020-0053>
- Lamb, K. (2018). *Blockchain and smart contracts: What the AEC sector needs to know* (Issue July). Centre for Digital Built Britain Publication. <https://doi.org/10.17863/CAM.26272>
- Li, J., Greenwood, D., & Kassem, M. (2019). Blockchain in the built environment and construction industry: A systematic review, conceptual models and practical use cases. *Automation in Construction*, 102(February), 288-307. <https://doi.org/10.1016/j.autcon.2019.02.005>
- Li, T., Chen, Y., Wang, Y., Wang, Y., Zhao, M., Zhu, H., Tian, Y., Yu, X., & Yang, Y. (2020). Rational protocols and attacks in blockchain system. *Security and Communication Networks*, 2020, Article 8839047. <https://doi.org/10.1155/2020/8839047>
- Luo, H., Das, M., Wang, J., & Cheng, J. C. P. (2019). Construction payment automation through smart contract-based blockchain framework. In *Proceedings of the 36th International Symposium on Automation and Robotics in Construction, ISARC 2019* (Vol. 36, pp. 1254-1260). IAARC Publications. <https://doi.org/10.22260/isarc2019/0168>
- Mason, J., & Escott, H. (2018, May 06-11). Smart contracts in construction: Views and perceptions of stakeholders. In *Proceedings of FIG Conference*. Istanbul, Turkey.
- McNamara, A. J., & Sepasgozar, S. M. E. (2020). Developing a theoretical framework for intelligent contract acceptance. *Construction Innovation*, 20(3), 421-445. <https://doi.org/10.1108/CI-07-2019-0061>
- Wang, S., Huang, C., Li, J., Yuan, Y., & Wang, F. Y. (2019). Decentralized construction of knowledge graphs for deep recommender systems based on blockchain-powered smart contracts. *IEEE Access*, 7, 136951-136961. <https://doi.org/10.1109/access.2019.2942338>
- Xue, F., & Lu, W. (2020). A semantic differential transaction approach to minimizing information redundancy for BIM and blockchain integration. *Automation in Construction*, 118(May), Article 103270. <https://doi.org/10.1016/j.autcon.2020.103270>

- Yang, R., Wakefield, R., Lyu, S., Jayasuriya, S., Han, F., Yi, X., Yang, X., Amarasinghe, G., & Chen, S. (2020). Public and private blockchain in construction business process and information integration. *Automation in Construction*, 118(May), Article 103276. <https://doi.org/10.1016/j.autcon.2020.103276>
- Zhong, L., Wu, Q., Xie, J., Guan, Z., & Qin, B. (2019). A secure large-scale instant payment system based on blockchain. *Computers and Security*, 84, 349-364. <https://doi.org/10.1016/j.cose.2019.04.007>



## Person Verification Based on Multimodal Biometric Recognition

Annie Anak Joseph<sup>1\*</sup>, Alex Ng Ho Lian<sup>1</sup>, Kuryati Kipli<sup>1</sup>, Kho Lee Chin<sup>1</sup>, Dayang Azra Awang Mat<sup>1</sup>, Charlie Sia Chin Voon<sup>2</sup>, David Chua Sing Ngie<sup>1</sup> and Ngu Sze Song<sup>1</sup>

<sup>1</sup>Department of Electrical and Electronics Engineering, Faculty of Engineering, Universiti Malaysia Sarawak, 94300 UNIMAS, Kota Samarahan, Sarawak, Malaysia

<sup>2</sup>Faculty of Engineering, Computing and Science, Swinburne University of Technology Sarawak Campus Jalan Simpang Tiga, 93350 Kuching, Sarawak, Malaysia

### ABSTRACT

Nowadays, person recognition has received significant attention due to broad applications in the security system. However, most person recognition systems are implemented based on unimodal biometrics such as face recognition or voice recognition. Biometric systems that adopted unimodal have limitations, mainly when the data contains outliers and corrupted datasets. Multimodal biometric systems grab researchers' consideration due to their superiority, such as better security than the unimodal biometric system and outstanding recognition efficiency. Therefore, the multimodal biometric system based on face and fingerprint recognition is developed in this paper. First, the multimodal biometric person recognition system is developed based on Convolutional Neural Network (CNN) and ORB (Oriented FAST and Rotated BRIEF) algorithm. Next, two features are fused

by using match score level fusion based on Weighted Sum-Rule. The verification process is matched if the fusion score is greater than the pre-set threshold  $t$ . The algorithm is extensively evaluated on UCI Machine Learning Repository Database datasets, including one real dataset with state-of-the-art approaches. The proposed method achieves a promising result in the person recognition system.

**Keywords:** Biometric, convolutional neural network, Oriented FAST and Rotated BRIEF (ORB), person recognition

### ARTICLE INFO

#### Article history:

Received: 22 July 2021

Accepted: 15 September 2021

Published: 24 November 2021

DOI: <https://doi.org/10.47836/pjst.30.1.09>

#### E-mail addresses:

Jannie@unimas.my (Annie Anak Joseph)

alexngg1129@gmail.com (Alex Ng Ho Lian)

kkuryati@unimas.my (Kuryati Kipli)

lckho@unimas.my (Kho Lee Chin)

amdazra@unimas.my (Dayang Azra binti Awang Mat)

cvsia@swinburne.edu.my (Charlie Sia Chin Voon)

csndavid@unimas.my (David Chua Sing Ngie)

ssngu@unimas.my (Ngu Sze Song)

\*Corresponding author

## INTRODUCTION

Nowadays, the security system has become crucial to protect someone or an organization from burglars and intruders. However, traditional security systems have several limitations. In the past few years, it has been confirmed that conventional security systems will lead to a rising crime rate of cyber-attacks. It also has many flaws, such as passwords that may be lost, hacked, or passed, plastic IDs may be duplicated, and RFID cards can be copied. All these flaws occur because it does not provide strong security in data protection. Therefore, it is easy for unauthorized people to access or invade the system.

In recent years, human behavioral and physiological parameters are getting popular in the security system because these parameters are exclusive and human-specific than conventional ones. Physiological characteristics refer to human traits, such as fingerprint, face, hand, and iris recognition, while behavioral refers to keystrokes, signatures, and sounds. This way of security system is called biometric authentication. Biometric authentication is introduced to make cybersecurity more effective and respond to growing threats and improve an organization's cybersecurity posture to solve the problems in traditional security systems (Yang et al., 2018). It provides high accuracy and confident automatic recognition to identify the person based on biometric traits such as hand, finger-vein, iris, face, voice, fingerprint, and signature. Moreover, it provides a high accessibility system for the user without memorizing the passwords. Therefore, it is difficult for cybercriminals because they cannot access the entry points and devices of the network efficiently (Devi & Sujatha, 2017).

However, most biometric security systems are based on unimodal systems (Zhao et al., 2020; Zhu et al., 2020). Single trait recognition leading to various issues, such as noisy data, non-universality, mutations within the class, uniqueness, and deceptive attacks. For example, a facial structure such as hairstyle, facial expression, facial angles, and age changes will be a problem in facial recognition. In recognition of fingerprints, the valleys and ridges of the fingerprint will change due to human age. It is also a serious problem if there is a biometric trait disfigured. These problems can be tackled by using a multimodal biometrics security system.

A multimodal biometric system is a system that can use multiple physiological or behavioral characteristics for registration, identification, and verification. Multimodal biometric recognition has become the latest technology in human attention (Guo et al., 2019; Huang et al., 2018). One of the most important reasons for combining different biometrics is to improve recognition accuracy. However, there are other reasons for combining two or more biometrics. For example, different biometrics are more suitable for various deployment scenarios, and it became essential to protect sensitive data (Parkavi et al., 2017).

On the other hand, the traditional learning methods always face challenges such as posture changes, facial camouflage, scene lighting, image background complexity, and

facial expression changes. Methods based on shallow learning only adopt some image features and rely on artificial experience to extract the characteristics of the sample. Deep learning methods can excerpt more complex face attributes. Deep learning has made a significant breakthrough in figuring out the problems plaguing the AI industry's best attempts for many years. The practice has proved that it is very good at revealing the intricate structure in the high-dimensional dataset. Thus, it is applicable for many fields such as government, business, and science. Deep learning involves some methods, such as deep belief networks (DBN) (Song & Kim, 2017), stacked autoencoders (Liu et al., 2018), and convolutional neural networks (CNN) (Ismail et al., 2020).

Therefore, in this paper, multimodal person recognition by integrating face and fingerprint biometrics is developed. Classic CNN is carried out for face images after pre-processing, considering that CNN can extract more complex face attributes. However, the same learning algorithm may not produce the optimum results for the different biometric traits. Therefore, Oriented FAST and Rotated BRIEF (ORB) is adopted for fingerprint images because they are resistant to noise and rotation invariant. ORB extracts and describes feature points very quickly. The score level fusion is performed to match the recognition of both biometric traits after both recognition is performed. For multimodal biometrics systems, fusion is essential to improve learning accuracies. Here, face and fingerprint biometrics traits are fused using match score level fusion based on weighted Sum-Rule. There are four main categories of fusion techniques: sensor level fusion, feature level fusion, match score level fusion, and decision level fusion (Peng et al., 2020). First, match score level fusion is adopted to fuse both biometrics traits. The match scores contain the richest information for all input data, less noise, and are relatively easy to implement. It also includes the wealthiest information about the input pattern.

On the other hand, sensor level and feature level fusion are hard to execute when the size of the features is not the same. The relationship between all features is not known in advance, and in most cases, it is noisy and redundant (Somashekhar & Nijagunarya, 2018). The performance of decision level fusion is low because not much information is available at this level (Mwaura et al., 2017). Based on the combination models explained above, the proposed person identification achieved satisfactory results.

The rest of the paper is organized as follows. The related works are exposed in section II. Section III present the materials used and the methodology conducted to accomplish the objectives. The results, analysis, and discussion data are discussed in section IV. Finally, section V is devoted to the conclusion and future work.

## RELATED WORKS

In this section, some past researches related to biometrics systems and any relevant topics are further discussed. For example, recently, there have been numerous researches on person identification based on biometrics characteristics.

Kurban et al. (2017) proposed a multimodal biometric system based on face and body gestures. In their research, the VGG face model in Convolution Neural Network (CNN) is adopted for face feature extractor while body gesture feature is extracted using energy imaging method. Both modalities were fused using the score level fusion technique, and then Principal Component Analysis (PCA) was adopted to reduce the dimensionalities for both features. Finally, standard deviation Euclidean distance is utilized to produce the similarity scores. Their proposed method shows promising results.

Mwaura et al. (2017) proposed a face and fingerprint biometric-based on the match score level fusion method. Both individual biometric traits are developed using Scale Invariant Feature Transform Features (SIFT). The distance between the key points is measured by hamming distance. K-Nearest Neighbor (KNN) is adopted for the matching by comparing the images in the databases. Their method achieved the performance of 92.5% of accuracy.

Somashekhar and Nijagunarya (2018) proposed a face and fingerprint multimodal biometric system by integrating two fusion methods: feature level fusion and decision level fusion. The accuracy is studied based on Gabor and Scale Invariant Feature Transform Features (SIFT) extraction for both biometric traits. First, a fusion of face and fingerprint is carried out at the feature level using all possible combinations of feature vectors. Then the feature vectors are later fed into the fusion classifier, which is Support Vector Machine (SVM), K-Nearest Neighbor (KNN), Radial Basis Function (RBF), and Naïve Bayes (NB). Their method achieves an accuracy of more than 90%.

In the same year, Xin et al. (2018) proposed another person identification system based on face, fingerprint, and finger vein images. The algorithm is carried out based on the Fisher vector, and the biometric traits are fused using feature-level fusion. In their works, the fake feature is also investigated to improve the learning accuracy. Their results achieved an excellent recognition rate compared to the unimodal approach.

Alazawi et al. (2019) proposed a multimodal biometrics method for face and fingerprint traits using general feature fusion vectors. Their approach involved two main processes in which fused share features of both biometric characteristics are extracted first. In contrast, Euclidean distance is adopted to recognize these features for the right person at the second step. The same algorithm is used for both biometrics traits. The method achieved an accuracy of 86%.

In Gavisiddappa et al. (2019), face, fingerprint, and iris are fused using feature-level fusion. In their approach, Bi-directional Empirical Mode Decomposition (BEMD) and Grey Level Co-occurrence Matrix (GLCM) algorithm are adopted for the feature extraction. After the feature extraction, the Hilbert-Huang transform (HHT) is carried out to obtain local features. The performance of their proposed method is based on False Acceptance Ratio (FAR), False Rejection Ratio (FRR), and accuracy. Their approach gave 96% of accuracy.

Ammour et al. (2020) developed multimodal person identification based on face and iris traits. An efficient multi-resolution 2D Log-Gabor filter carries the textural information from the iris attribute, and the Singular Spectrum Analysis (SSA) is adopted for facial features. Two biometric traits are united at a hybrid fusion level, and their results show the robustness of the proposed method.

Alay and Al-Baity (2020) discussed the multimodal biometrics system combining face, iris, and finger-vein traits, and the proposed method was implemented using deep learning techniques. VGG-16 CNN is adopted. Adam optimization method is applied where categorical cross-entropy is adopted as loss function. The biometric traits are fused based on feature-level fusion and score-level fusion. The results from the experimental works showed that their proposed method is outperformed state-of-the-art methods.

Lv et al. (2020) presented feature-level fusion based on fingerprint and finger-vein biometrics. Fingerprint and finger vein feature-layer fusion recognition algorithm is investigated based on a single ICNIR finger image. Their proposed method shows that person identification using multimodal biometrics is better than the unimodal biometric system.

Aleem et al. (2020) proposed another multimodal biometric identification system by fusing both biometric traits using score level fusion. Fingerprint matching is done using an alignment-based elastic algorithm, while extended local binary patterns (ELBP) are used for facial feature extraction. In their proposed method, local non-negative matrix factorization is carried out for dimensionality reduction. The proposed method achieved the recognition of 99.59%.

Recently, Kumar et al. (2021) proposed an improved biometrics system based on face and fingerprint. Whale optimization is adopted with minutiae feature for fingerprint recognition and Maximally Stable External Regions (MSER) for face recognition. In addition, Support Vector Machine (SVM) is carried out along with pattern net to improve the classification accuracy. As a result, the proposed method achieved averaged more than 90% accuracy.

Next, Pawar et al. (2021) have described works on biometrics systems based on face and fingerprint biometrics. Scale-invariant feature transform (SIFT) is adopted for feature extraction. The particle swarm is used to optimize features while the ridges and minutiae extractions are carried out for fingerprint biometrics. Both biometric traits are fused by using the summing rule. Their approach attains more than 99% accuracy.

Based on the comprehensive literature review explained above, recently developed biometrics systems based on face and fingerprint traits are summarized in Table 1.

Table 1

*Recently developed biometrics system based multimodal biometric traits*

Authors	Method Applied	Advantages	Disadvantages
Mwaura et al. (2017)	Match score level fusion	Scale Invariant Feature Transform (SIFT) is introduced for feature extraction. SIFT method has the advantages of rotation invariance; scale invariance has strong robustness for occlusion problem and noise and affine invariance	KNN is used where time and space complexity is enormous, which is a significant disadvantage of KNN.
Somashekhar and Nijagunarya (2018)	Feature level fusion and Decision level fusion	A new method has been proposed where face images and fingerprint are processed with compatible feature extraction algorithms to extract features from the dataset	This method may heavily depend on the physical nature of the input in a real application scenario
Xin et al. (2018)	Feature level fusion	Use of the Discrete Cosine Transform (DCT) algorithm for bioassay that produces better accuracy and effectively improves the anti-forgery capability in-person identification.	PCA is used for face recognition where this is an ancient technique for feature extraction
Alazawi et al. (2019)	Feature level fusion	The method has good performance in terms of precision using invariant moments to extract shape features vectors and the direct Euclidean distance for similarity measurement.	Using the same learning algorithm for face and fingerprint biometrics, which in reality may not produce the optimum results for different biometric traits.

Table 1 (Continued)

Authors	Method Applied	Advantages	Disadvantages
Gavisiddappa et al. (2019)	Feature level fusion	Combination of Bi-directional Empirical Mode Decomposition (BEMD), Hilbert-Huang transforms (HHT) and Grey Level Co-occurrence Matrix (GLCM) to form the MMB-BEMB-HHT method. MMB-BEMD-HHT method was constructed to identifying the individual biometric features of fingerprint, face, and iris to improve the security of the desired system	The proposed method is applied to a limited dataset
Aleem et al. (2020)	Score level fusion	Histogram equalization is adopted to improve the intensity level of the face images; Extended Local Binary Pattern (ELBP) and Local Non-Matrix Factorization (LNMF). is adopted for face images in which it is a pixel-based texture extraction method that has achieved remarkable performance along with low computational cost.	It does not mention the criteria or threshold to set the most significant base information for LNMF. The optimum result depends on the size of the choices of dimensionality in LNMF.
Alay and Al-Baity (2020)	Feature Level Fusion and score level fusion	The first study is to investigate deep learning algorithms for a multimodal model with three biometric traits.	Adopted CNN (VGG) for all biometric traits in which, in the actual case, different biometric characteristics may not produce the optimum results in all biometric features.

Table 1 (Continued)

Authors	Method Applied	Advantages	Disadvantages
Kumar et al. (2021)	Feature level fusion	Their paper proposed a novel approach to improve the accuracy and maximizes the accuracy of biometric traits for noisy data	This work is carried by using an SVM classifier where the SVM algorithm is not suitable for large datasets.
Pawar et al. (2021)	Fusion using summing rule	The features are extracted using scale-invariant feature transform (SIFT), and the feature optimization is done using particle swarm optimization.	The fusion technique is not clearly explained in the paper.

From Table 1, the most recently developed works focus on the feature level method as a fusion method and SIFT for feature extraction. Not many works have been carried out using CNN. Even though Alay and Al-Baity (2020) also use CNN for their work, they focus on the combination of feature-level and score-level fusion. In addition, their works focused on three modalities: face, iris, and finger vein. It is the first work focusing on face recognition based on CNN and fingerprint recognition based on ORB, then fused by score level fusion to the best of our knowledge. The process of the ORB algorithm is faster than SIFT. Based on the advantages of CNN, match score level fusion, ORB, and the motivation why the different algorithms should be used for the different biometric traits explained in the previous section. Hence, this paper aims to develop a multimodal biometric system using classic CNN for face recognition and ORB for fingerprint. The recognition of both biometric traits is fused using score level fusion considering the advantages of score level fusion stated in the previous section.

## METHODOLOGY

In this section, the development of the system is explained and illustrated clearly with a block diagram, as shown in Figure 1.

The system consists of three main processes that involve face recognition, fingerprint recognition, and score level fusion. First, face recognition involves image pre-processing, feature extraction, and classification. The second process is fingerprint recognition, and the process includes pre-processing and feature matching. Finally, two biometric features are combined into the same domain for the last operation, executed in the decision-making process.



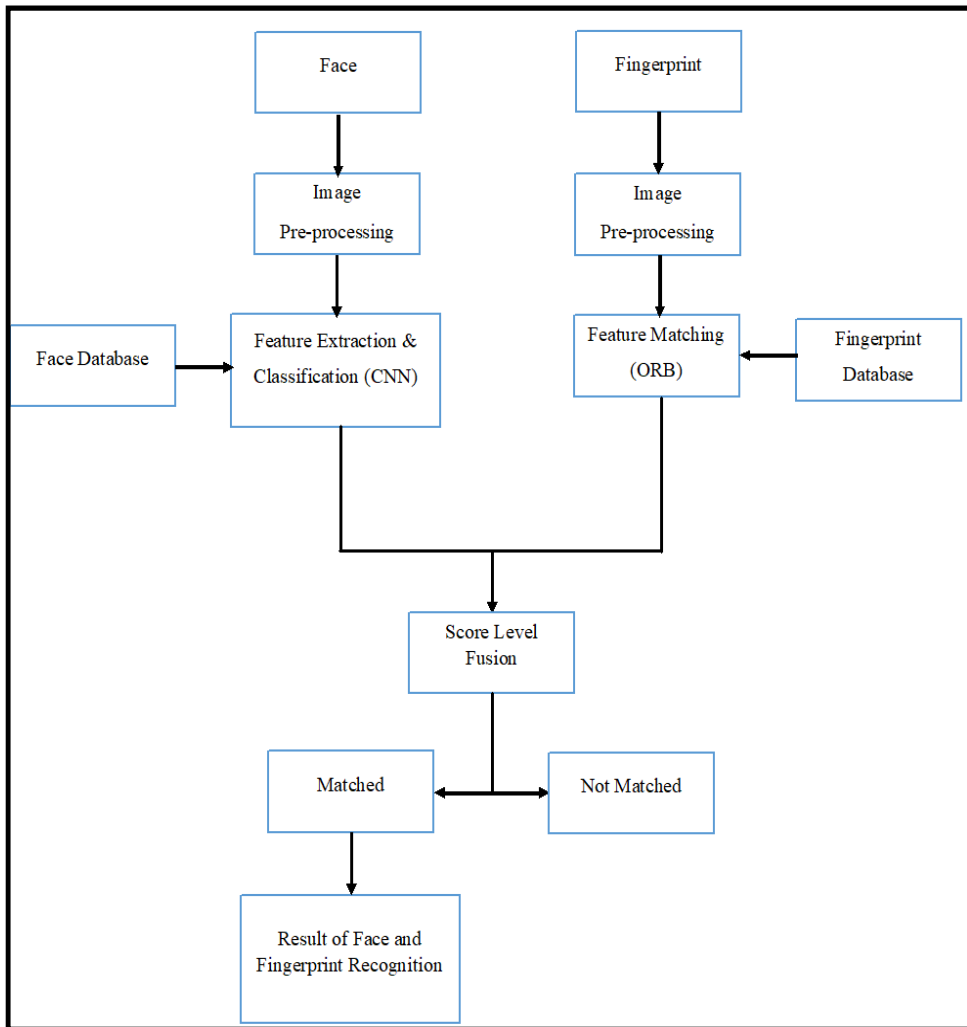


Figure 1. Multimodal biometric system diagram

Based on Figure 1, the pre-processing and feature extraction steps are first applied to face images, and classic CNN is adopted to train the face images. The pre-processing stage is also applied to fingerprint datasets and feature matching by using the ORB algorithm. Then, two biometrics are fused with score level fusion based on the weighted sum rule. The verification process is matched if the fusion score is higher than the pre-specified threshold  $t$ . In this case,  $t$  is set to 0.57. Otherwise, the verification process indicates a mismatch. Therefore, there is an opportunity for fraud in a unimodal biometric system, but this problem can be solved if we integrate multiple functions. For an instant, fingerprint data can be easily stolen if the system is only used fingerprint biometric. However, if

fingerprint recognition and facial recognition are combined, identification and verification will be more promising, where the system will be challenging to crack.

The software used in this paper is Python 3.7.3. The Desktop-NJTDRNO PC is used to run the software and the program. The processor provides Intel(R) Core (TM) i5-4460M 3.20 GHz, and the memory of this laptop is 8GB RAM. NVIDIA GeForce GTX 1650 Graphic card is used. This laptop also contains 240GB SSD and 1TB HDD.

## **Image Dataset**

In this paper, two biometrics image datasets are obtained from the UCI machine learning repository database. There are 400 face images and 120 fingerprint images. Three hundred sixty images are adopted as a training set for face recognition, while 40 images are used as a testing set. One hundred images are adopted as a training set for fingerprint recognition, and 20 are used as a testing set. ORB is used to define descriptors around key points with Hamming distance, and the matching is decided based on the threshold set initially. The dataset for face and fingerprint is not equal because in the actual case, faces may face various conditions such as different lighting conditions, different angles, and facial expressions. However, these condition does not affect the fingerprint ridges too much. Therefore, more dataset is needed to train the face images.

## **Face Recognition**

Face recognition consists of three steps. First, it starts from the pre-processing step: color space conversion and image resizing. They were then followed by facial features extraction by CNN before the classification by using Softmax Classifier.

In a pre-processing step, the collected datasets are first converted from BGR to RGB before being resized to 200x200. Next, essential features from datasets are extracted by using CNN and classification by Softmax classifier. CNN is a neural network that has been established to be very valuable in feature extraction and classification. The structure of CNN consists of convolution functions, pooling functions, and ReLU functions. Simultaneously, the Python library is adopted to implement the multi-layer perceptron MLP to complete the connection and classification layers. The Fully Connected Layer (FCL) stacks the convolutional layer, pool, and ReLU layer to simplify the CNN model. Thus, the CNN model comprises a convolutional, pooling, ReLU, FCL, and Softmax classifier to train face datasets.

## **Fingerprint Recognition**

The fingerprint recognition process consists of two stages. It starts from the pre-processing stage, which is Oriented Gabor Filter, binarization, and thinning. Next, the ORB algorithm

is performed in three steps: feature point extraction, generating feature point descriptors, and computing feature point matching. Before a detail-based function is completed, it is necessary to perform image enhancement processing on the fingerprint images. It can make the image clearer and adjust the picture to an appropriate resolution. If image enhancement is not performed, noise may be generated. In addition, the process creates a sharp contrast between the ridges and valleys. Therefore, enhancement processing is vital to improve recognition accuracy. The enhancement step is adopted by using Oriented Gabor Filters. The direction of the Gabor filter is determined by the direction of the ridges in the input image, as shown in Figure 2. Thus, there are two steps of the minutiae-based feature used in fingerprint recognition: binarization and thinning.

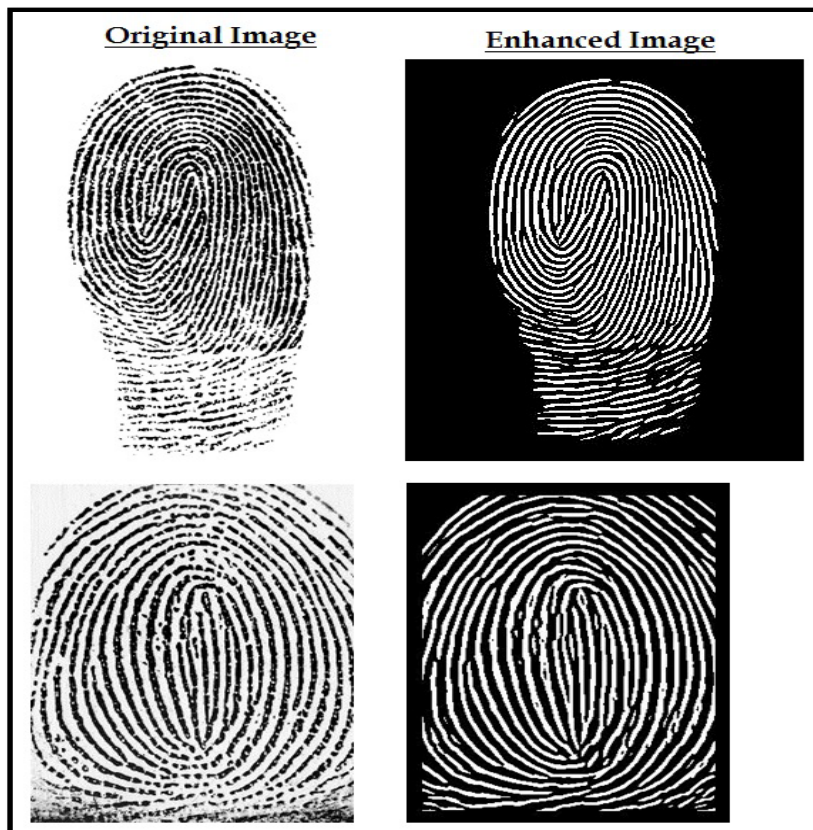


Figure 2. Left side: original image, right side: enhanced image (Chanklan et al., 2015)

### **Binarization**

Binarization is one of the pre-processing methods based on the minutiae-based method. The binarization process converts the image from 8-bit grayscale to a 1-bit grayscale image, as shown in Figure 3.

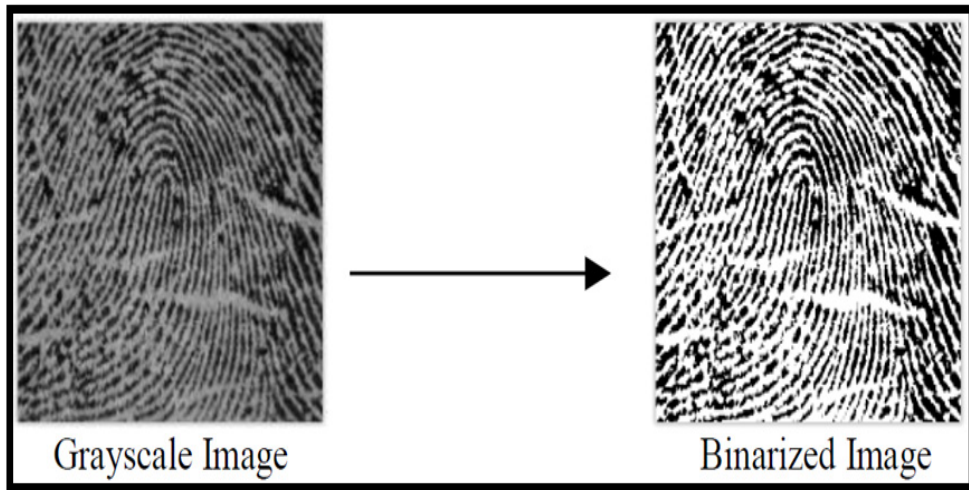


Figure 3. Result of binarization of fingerprint (Fatt et al., 2017)

### Thinning

The thinning process is applied to the binarized image to reduce the thickness of the ridge pattern. This process is essential to ensure the exact location of the thorough extraction. The thinning therefore maintains the position of the minute points in comparison with the original fingerprint. Finally, the result of the thinning process is obtained, as shown in Figure 4.

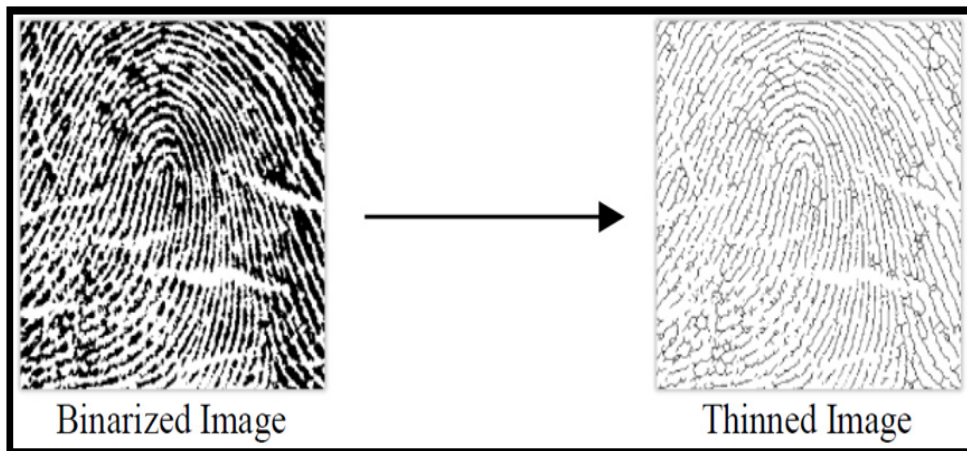


Figure 4. Result of thinning of fingerprint (Fatt et al., 2017)

### Fingerprint Matching with ORB (Oriented FAST and Rotated BRIEF)

Oriented FAST and Rotated BRIEF (ORB) algorithm consists of three steps: feature point extraction, defining feature point descriptors, and calculating feature point matching. ORB uses an improved FAST (Accelerated Testing Function) algorithm to detect fingerprint image features (Rosten et al., 2010). If the pixels in the picture are different from nearby pixels, this is likely to be a corner point. The detected image feature point is screened after the feature point is extracted. Scale invariance is added to the features after FAST features are extracted. Finally, the direction point of the feature is determined. Updated Brief algorithm (Calonder et al., 2010) is adopted to generate descriptors after the directional FAST feature points are extracted. The ORB algorithm then uses the updated Brief algorithm (Calonder et al., 2010) to create descriptors after extracting the directional FAST feature points.

After the fingerprint feature point descriptor is generated, it is necessary to find similar feature points in two different fingerprint images to determine the matching, as shown in Figure 5. Suppose the image  $I_t$  is extracted from feature points  $x_t^m, m = 1, 2, \dots, M$ , and the image  $I_{t+1}$  is extracted from feature points  $x_t^n, n = 1, 2, \dots, N$ . A brute force matcher is adopted to determine the distance on every feature point  $x_t^m$  and all  $x_{t+1}^n$  descriptors. The nearest one is selected as the matching point. Hamming distance is applied for the Brief binary descriptor to estimate the number of different characters between two strings of the same length character (Luo et al., 2019).

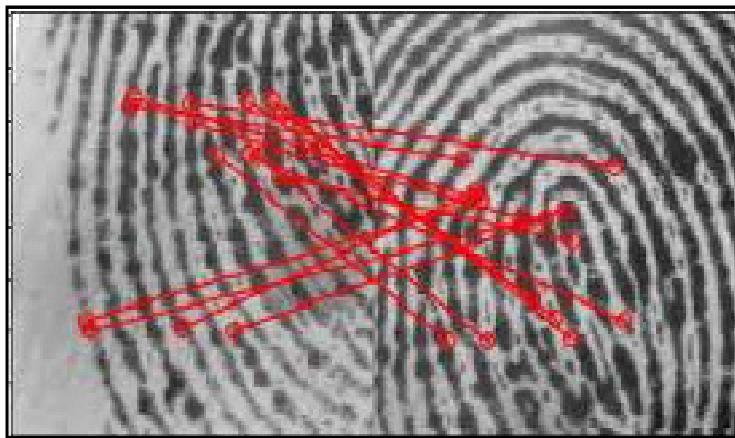


Figure 5. Result of brute force matcher (Luo et al., 2019)

After the recognition training is performed on both biometrics data set, the score level fusion is used as a final stage to match the two types of recognition—the adopted weighted sum rule for the fusion score levels. The rule sets the weighted sum of all scores generated by the matcher is given in Equation 1.

$$S_{fusion} = \sum_{i=1}^N w_i S_i \quad (1)$$

Here,  $w_i$  are weights assigned to the  $S_i$  score generated by the matcher and  $w$  sum of the weights assigned to the matcher that meet the conditions (Equation 2).

$$w = \sum_{i=1}^N w_i = 1 \quad (2)$$

Equation 1 can be written in Equation 3 since there are two biological features, “face” and “fingerprint”.

$$S_{fusion} = w_1 S_1 + w_2 S_2 \quad (3)$$

where  $w_1 + w_2 = 1$ ,  $w_1$  and  $w_2$  are weights assigned to face and fingerprint matching scores. The weights are calculated based on Equation 4,

$$w_m = \frac{1}{\frac{\sum_{m=1}^M \frac{1}{a_m}}{a_m}} \quad (4)$$

Here,  $w_m$  is weighted associated with matcher  $m$  and  $a_m$  is the accuracy of matcher  $m$ . The different parts of the model are illustrated in details in Figure 6.

Finally, a multimodal person identification system based on face and fingerprint biometrics is developed using GUI in Python IDE, as shown in Figure 7. The accuracy of the system is displayed on the GUI.

## RESULT AND DISCUSSION

In this section, the performance of the person identification based on face and fingerprint biometrics is discussed. Score level fusion generated by the Face and Fingerprint matcher is then combined using the weighted sum rule, and the performance is further discussed in the rest of this section.

### Face Recognition

For face recognition, the datasets for 20 people are obtained from UCI Machine Learning Repository Database, including images for one real person. Thus, twenty photos are obtained from each person. Figure 8 shows the face recognition based on one testing image.

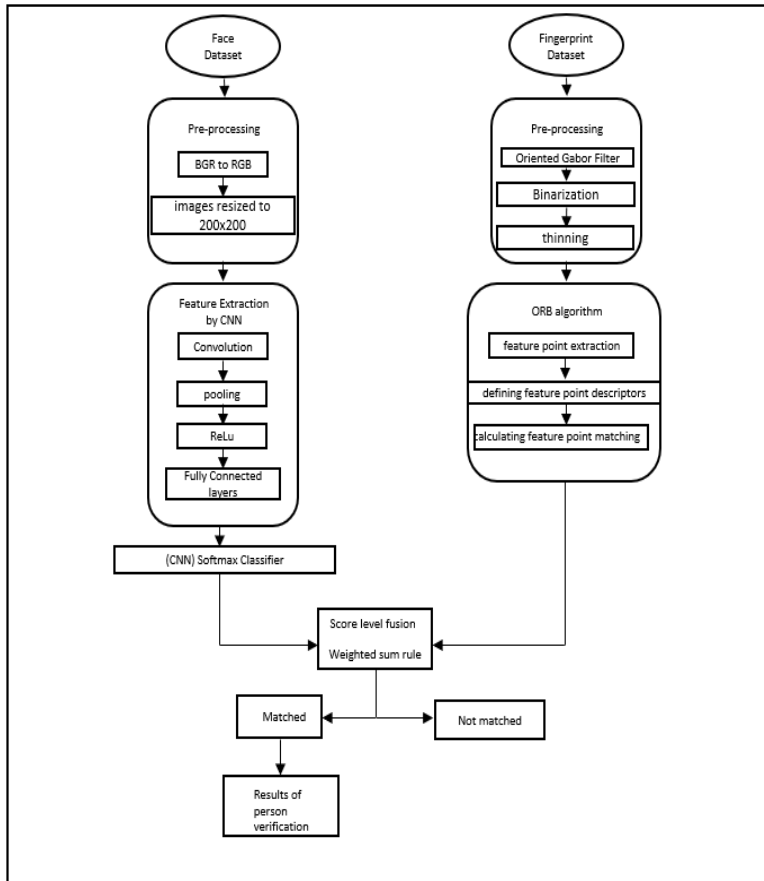


Figure 6. The details flowchart of the face and fingerprint recognition system

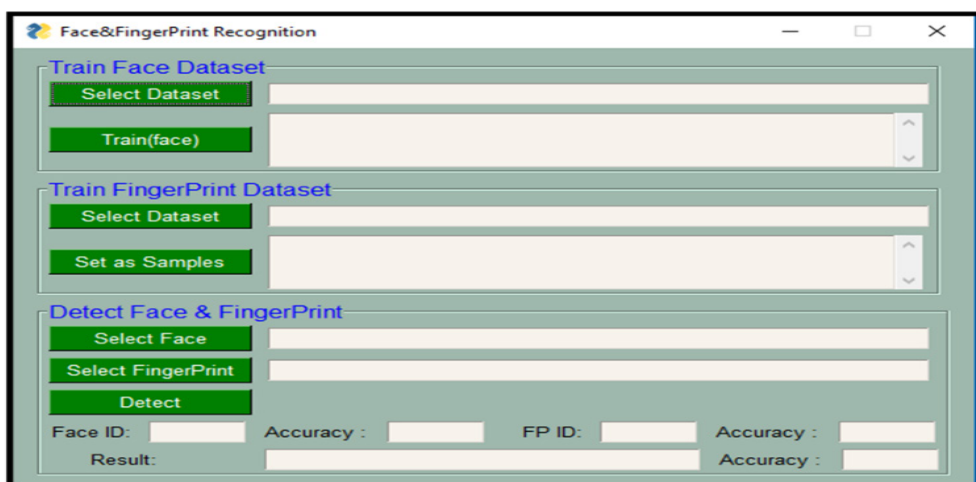


Figure 7. Python GUI for multimodal biometric recognition

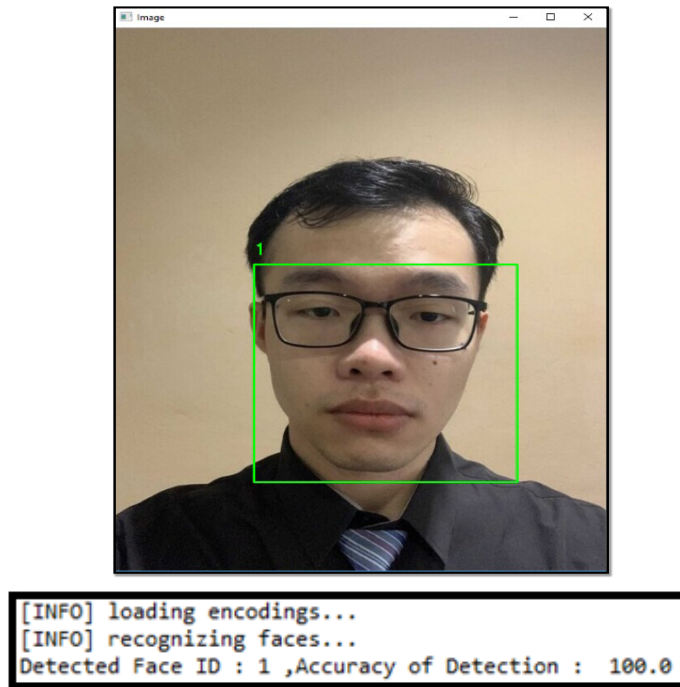


Figure 8. Recognition accuracy based on one testing sample

As mentioned in the previous section, 360 images are adopted as a training set, while 40 images are used as a testing set. The average recognition accuracy and standard deviation based on the testing datasets are illustrated in Table 2.

Table 2

*Accuracy for face recognition based on testing data*

Mean accuracy, $\bar{X}$	Standard Deviation, s
95.57	5.97

### Fingerprint Recognition

There are 120 fingerprint images for fingerprint recognition obtained from UCI Machine Learning Repository Database, where 100 datasets are adopted as training set while 20 as testing datasets. These images are obtained from 20 people, including one real person in which every one of them consists of six shots. The pictures for fingerprints are processed using the ORB algorithm, and the recognition accuracy for one fingerprint image is shown in Figure 9.



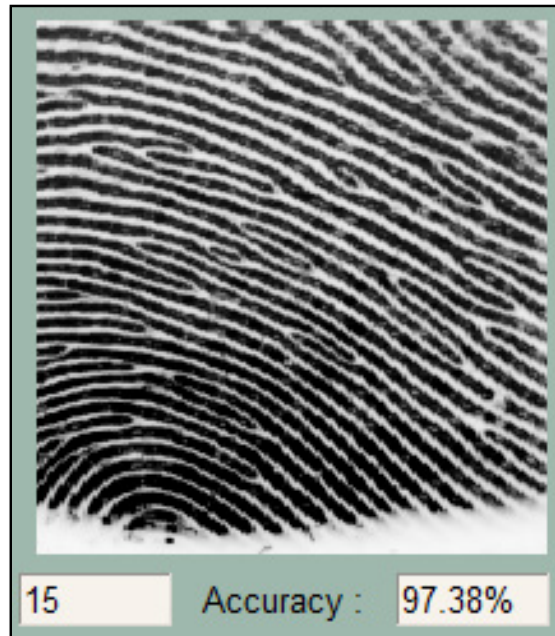


Figure 9. The result of sample 1

The average recognition accuracy and standard deviation based on the testing datasets are illustrated in Table 3.

Table 3  
Accuracy for fingerprint recognition based on ORB algorithm

Mean accuracy, $\bar{x}$	Standard Deviation, s
97.28	0.61

### Multimodal Biometric Recognition (Face and Fingerprint)

After both recognition results were obtained, score level fusion is adopted to combine the two biometrics based on the weighted sum rule. The development of the multimodal biometric system is shown in Figure 10. Python IDE is adopted to develop GUI for multimodal biometric recognition. Results of samples 1, 8, 11, and 18 show that face ID and fingerprint ID are matched with 98.77%, 98.56%, 99.44%, and 87.53%. Figure 11 shows that the matching for both biometrics is not successful if both biometrics are not from the same person.

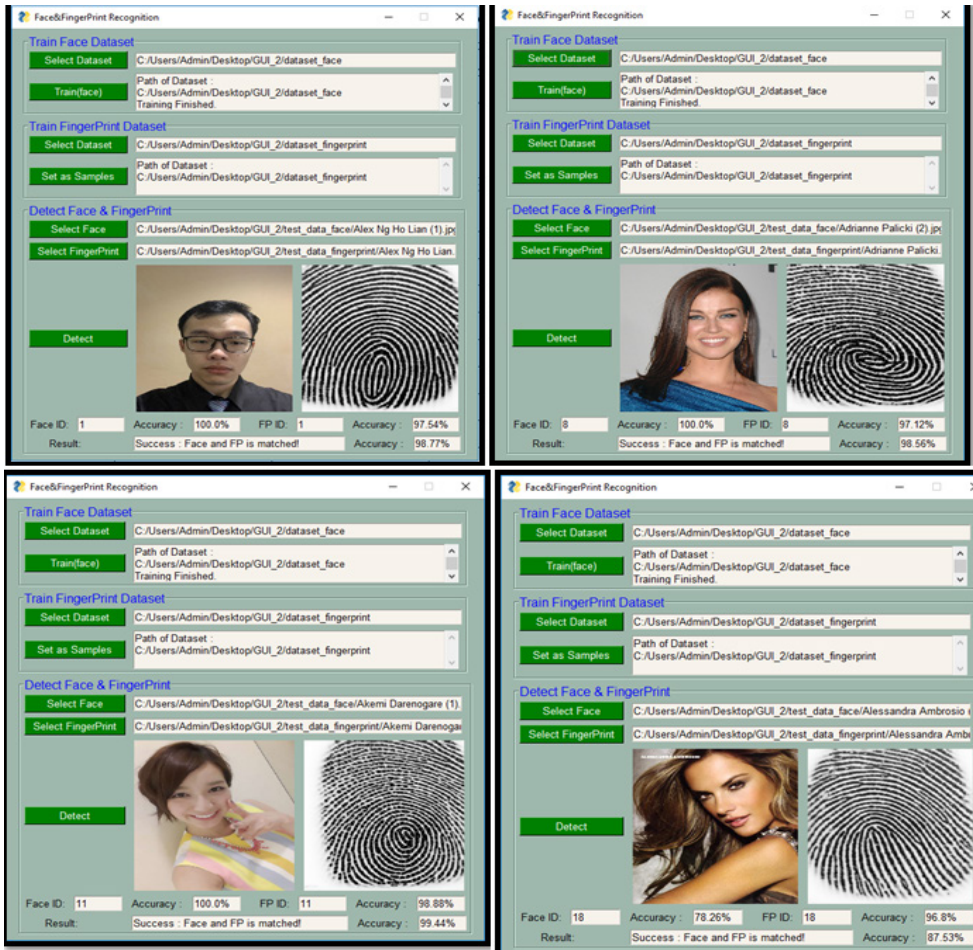


Figure 10. The result of several samples after fusion

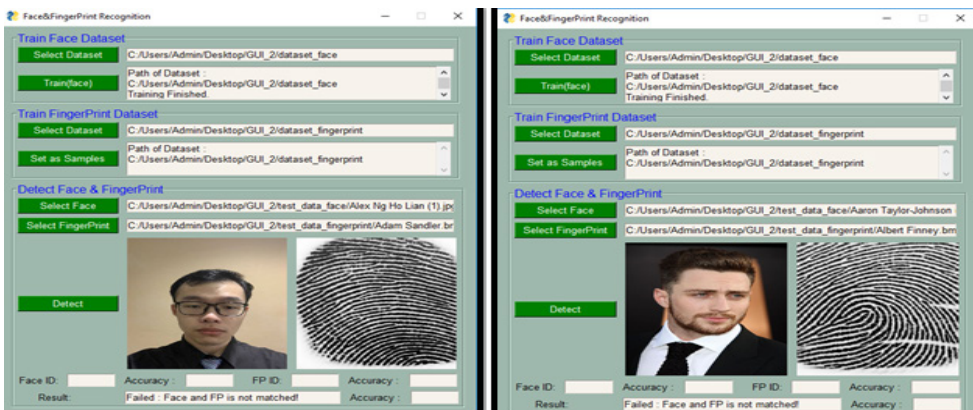


Figure 11. The results of several samples if the biometrics are not matched

Table 4

*The matching results for 20 samples*

No of Samples	Face Recognition (%)	Fingerprint Recognition (%)	Fusion (%)
1	100	97.41	98.7
2	94.74	97.48	96.11
3	100	96.32	98.16
4	94.44	96.92	95.68
5	94.74	97.23	95.98
6	100	97.31	98.66
7	81.82	97.59	89.7
8	100	97.08	98.54
9	100	96.66	98.33
10	90	98.63	94.32
11	100	98.77	99.38
12	100	96.56	98.28
13	94.44	96.98	95.71
14	100	97.56	98.78
15	87.5	97.28	92.39
16	100	97.48	98.74
17	100	97.25	98.62
18	78.26	96.73	87.5
19	100	96.81	98.4
20	100	97.62	98.81

The face, fingerprint, and fusion recognition based on 20 datasets are shown in Table 4. Multimodal Biometric systems achieve 87.5% to 99.38%. It shows that overall accuracy in multimodal biometric accuracy recognition is consistent and precise. Average recognition accuracy based on the proposed method and the baseline approaches with face and fingerprint biometric traits to validate the proposed method are shown in Table 5.

Table 5

*Comparison of accuracy for various multimodal methods*

Authors	Method Applied	Accuracy
Proposed method	Match score level+CNN+ORB	96.54%

Table 5 (Continued)

Authors	Method Applied	Accuracy
Mwaura et al. (2017)	Match score level fusion+SIFT	92.5%
Somashekhar and Nijagunarya (2018)	Feature level fusion and Decision level fusion	91.47%
Alazawi et al. (2019)	Feature level fusion +Euclidean distance	86%
Aleem et al. (2020)	Score level fusion+LBP	99.60%
Kumar et al. (2021)	Feature level fusion+SVM	99.60%
Pawar et al. (2021)	Fusion using summing rule+SIFT	99.2%

In Table 5, it is shown that the accuracy of the proposed method is better than Mwaura et al. (2017), Somashekhar and Nijagunarya (2018) as well as Alazawi et al. (2019). The result of the proposed method is slightly lower than Aleem et al. (2020), Kumar et al. (2021), and Pawar et al. (2021) because of the two samples: sample 7 and sample 18, as shown in Table 4. Overall, the result of the proposed method is comparable to Aleem et al. (2020), Kumar et al. (2021) and Pawar et al. (2021). As mentioned in the previous section, match score level fusion contains the richest information for all input data, less noise, and is relatively easy to implement. It also includes the wealthiest information about the input pattern compared to feature-level fusion. Both Kumar et al. (2021), and Pawar et al. (2021) are using feature-level fusion, where in most cases, feature-level fusion is hard to execute when the size of the features is not the same. In most conditions, the relationship between all features is not known in advance, noisy and redundant. Even though Aleem et al. (2020) use score level fusion to fuse face and fingerprint, the optimum results vary depending on the choices of dimensionality in LNMF. The proposed method is superior to the baseline approaches taking into account various aspects.

In summary, the result of a multimodal biometric system is successfully obtained. The score level fusion based on weighted sum-rule is used to fuse the scores of the face matcher samples and the fingerprint matcher samples, and it is observed that the weighted sum rule with optimized weight provides excellent performance. It is concluded that the multimodal biometric system achieves more than 96% accuracy.

## CONCLUSION AND RECOMMENDATIONS

In conclusion, an effective and efficient face and fingerprint multimodal biometric system has been developed. Fingerprint recognition is performed using directed FAST and Rotated Brief (ORB), while face recognition is achieved using the Classic CNN model. The

combination of two biometrics produces a robust multimodal biometric system. Score level fusion is adopted to perform the fusion of facial and fingerprint features. The experiment is performed on the UCI Machine Learning Repository database, including one real dataset. Experimental results show that the proposed multimodal biometric system provides better security compared to single biometric recognition. The best recognition rate is obtained through the weighted sum rule, and the higher recognition rate is 99.38%, as shown in Table 4 for sample 11. The recognition rate is based on the average of the recognition rate of face and fingerprint. The result of the proposed method is slightly lower than Aleem et al. (2020), Kumar et al. (2021), and Pawar et al. (2021) because of the two samples: sample 7 and sample 18, as shown in Table 4. Overall, the proposed method is comparable to those baseline approaches. Thus, there remain some future works that need to be done in the future. More training is set to be included for the training process with cross-validation to improve learning accuracy. In the future, a balanced dataset will be included for both multimodal face and fingerprint recognition systems. Different type of CNN models is to be included to check the performance of the system.

## ACKNOWLEDGMENT

This work is supported by Universiti Malaysia Sarawak (UNIMAS) through research grant F02/SpTDG/1772/2018.

## REFERENCES

- Alay, N., & Al-Baity, H. H. (2020). Deep learning approach for multimodal biometric recognition system based on fusion of iris, face, and finger vein traits. *Sensors*, 20(19), Article 5523. <https://doi.org/10.3390/s20195523>
- Alazawi, S. A., Abdulaaliabdulbaqi, H., & Mohialden, Y. M. (2019). New authentication model for multimodal biometrics based on shape features vectors. *Journal of Southwest Jiaotong University*, 54(6). <https://doi.org/10.35741/issn.0258-2724.54.6.18>
- Aleem, S., Yang, P., Masood, S., Li, P., & Sheng, B. (2020). An accurate multi-modal biometric identification system for person identification via fusion of face and finger print. *Springer*, 23(6), 1299-1317. <https://doi.org/10.1007/s11280-019-00698-6>
- Ammour, B., Boubchir, L., Bouden, T., & Ramdani, M. (2020). Face-iris multimodal biometric identification system. *Electronics*, 9(1), Article 85. <https://doi.org/10.3390/electronics9010085>
- Calonder, M., Lepetit, V., Strecha, C., & Fua, P. (2010). BRIEF: Binary robust independent elementary features. In *Lecture Notes in Artificial Intelligence Lecture Notes Bioinformatics* (Vol. 6314, No. 4, pp.778-792). Springer. [https://doi.org/10.1007/978-3-642-15561-1\\_56](https://doi.org/10.1007/978-3-642-15561-1_56)
- Chanklan, R., Chaiyakhon, K., Hirunyanakul, A., Kerdprasop, K., & Kerdprasop, N. (2015). Fingerprint recognition with edge detection and dimensionality reduction techniques. In *Proceedings of the 3rd*

- International Conference on Industrial Application Engineering* (pp. 569-574). The Institute of Industrial Applications Engineers. <https://doi.org/10.12792/ICIAE2015.098>
- Devi, R., & Sujatha, P. (2017). A study on biometric and multi-modal biometric system modules, applications, techniques and challenges. In *Proceedings of Conference on Emerging Devices and Smart Systems (ICEDSS)* (pp. 267-271). IEEE Publishing. <https://doi.org/10.1109/ICEDSS.2017.8073691>
- Fatt, W. K., Kushsairy, A. K., Nasir, H., Safie, S. I., & Noor, N. M. (2017). Fingerprint and face recognition: Application to multimodal biometrics system. *Journal of Telecommunication, Electronic and Computer Engineering*, 9(2-2), 81-85.
- Gavisiddappa, C. M. P., Shivakumar, M., & Pramod, K. S. (2019). Multi-modal biometric: Bi-directional empirical mode decomposition with hilbert-hung transformation. *International Journal of Advanced Computer Science and Applications (IJACSA)*, 10(6), 528-537. <http://dx.doi.org/10.14569/IJACSA.2019.0100669>
- Guo, Z., Li, X., Huang, H., Guo, N., & Li, Q. (2019). Deep learning-based image segmentation on multimodal medical imaging. *IEEE Transactions on Radiation and Plasma Medical Sciences*, 3(2), 162-169. <https://doi.org/10.1109/TRPMS.2018.2890359>
- Huang, L., Yu, C., & Cao, X. (2018). Bimodal biometric person recognition by score fusion. In *Proceedings of 5th International Conference on Information Science and Control Engineering (ICISCE)* (pp. 1093-1097). IEEE Publishing. <https://doi.org/10.1109/ICISCE.2018.00225>
- Ismail, A., Ahmad, S. A., Soh, A. C., Hassan, M. K., & Harith, H. H. (2020). Deep learning object detector using a combination of convolutional neural network (CNN) architecture (minivggnet) and classic object detection algorithm. *Pertanika Journal of Social Science and Humanities*, 28(S2), 161-171. <https://doi.org/10.47836/pjst.28.s2.13>
- Kumar, T., Bhushan, S., & Jangra, S. (2021). An improved biometric fusion system of fingerprint and face using whale optimization. *International Journal of Advanced Computer Science and Applications (IJACSA)*, 12(1), 664-671. <http://dx.doi.org/10.14569/IJACSA.2021.0120176>
- Kurban, O. C., Yildirim, T., & Bilgic, A. (2017). A multi-biometric recognition system based on deep features of face and gesture energy image. In *Proceedings of IEEE International Conference on Innovations in Intelligent Systems and Applications (INISTA)* (pp. 361-364). IEEE Publishing. <https://doi.org/10.1109/INISTA.2017.8001186>
- Liu, G. F., Bao, H. Q., & Han, B. K. (2018). A stacked autoencoder-based deep neural network for achieving gearbox fault diagnosis. *Mathematical Problems in Engineering*, 5, 1-10. <https://doi.org/10.1155/2018/5105709>
- Luo, C., Yang, W., Huang, P., & Zhou, J. (2019). Overview of image matching based on ORB algorithm. *Journal of Physics Conference Series*, 1237(3), Article 032020. <https://doi.org/10.1088/1742-6596/1237/3/032020>
- Lv, G. L., Shen, L., Yao, Y. D., Wang, H. X., & Zhao, G. D. (2020). Feature-level fusion of finger vein and fingerprint based on a single finger image: The use of incompletely closed near-infrared equipment. *Symmetry*, 12(5), Article 709. <https://doi.org/10.3390/sym12050709>

- Mwaura, G., Mwangi, W., & Otieno, C. (2017). Multimodal biometric system: Fusion of face and fingerprint biometrics at match score fusion level. *International Journal of Scientific & Technology Research*, 6(4), 41-49.
- Parkavi, R., Babu, K. R. C., & Kumar, J. A. (2017). Multimodal biometrics for user authentication. In *Proceedings of 11th International Conference on Intelligent Systems and Control (ISCO)* (pp. 501-505). IEEE Publishing. <https://doi.org/10.1109/ISCO.2017.7856044>
- Pawar, M. D., Kokate, R. D., & Gosavi, V. R. (2021, June 28-29) An optimize multimodal biometric authentication system for low classification error rates using face and fingerprint. In *Proceedings of the International Conference on IoT Based Control Networks & Intelligent Systems*. Kottayam, India. <http://dx.doi.org/10.2139/ssrn.3883852>
- Peng, J., Wu, J. Y., & Chen, Y. (2020). A score level fusion method on fingerprint and finger vein. *E3S Web of Conferences*, 185(14), Article 03035. <https://doi.org/10.1051/e3sconf/202018503035>
- Rosten, E., Porter, R., & Drummond, T. (2010). Faster and better: A machine learning approach to corner detection. *IEEE Transactions on Pattern Analysis and Machine Intelligence*, 32(1), 105-119. <https://doi.org/10.1109/TPAMI.2008.275>
- Somashekhar, B. M., & Nijagunarya, Y. S. (2018). Face and fingerprint fusion system for identity authentication using fusion classifiers. *International Journal of Computer Science & Engineering Survey*, 9(1/2/3), 1-12. <https://doi.org/10.5121/IJCSES.2018.9301>
- Song, S. H., & Kim, D. K. (2017). Development of a stress classification model using deep belief networks for stress monitoring. *Healthcare Informatics Research*, 23(4), 285-292. <https://doi.org/10.4258/hir.2017.23.4.285>
- Xin, Y., Kong, L. S., Liu, Z., Wang, C. H., Zhu, H. L., Gao, M. C., Zhao, C. S., & Xu, X. K. (2018). Multimodal feature-level fusion for biometrics identification system on IOMT platform. *IEEE Access*, 6, 21418-21426. <https://doi.org/10.1109/ACCESS.2018.2815540>
- Yang, W., Wang, S., Hu, J., Zheng, G., Chaudhry, J., Erwin, A., & Craig, V. (2018). Securing mobile healthcare data: A smart card based cancelable Finger-Vein Bio-Cryptosystem. *IEEE Access*, 6, 36939-36947. <https://doi.org/10.1109/ACCESS.2018.2844182>
- Zhao, J., Yan, S., & Feng, J. (2020). Towards age-invariant face recognition. In *IEEE Transactions on Pattern Analysis and Machine Intelligence*. IEEE Publishing. <https://doi.org/10.1109/TPAMI.2020.3011426>
- Zhu, N., Yu, Z., & Kou, C. (2020). A new deep neural architecture search pipeline for face recognition. *IEEE Access*, 8, 91303-91310. <https://doi.org/10.1109/ACCESS.2020.2994207>





## Development of Stand-Alone DC Energy Datalogger for Off-Grid PV System Application based on Microcontroller

Mohd Ruzaimi Ariffin<sup>1\*</sup>, Suhaidi Shafie<sup>1,2</sup>, Wan Zuha Wan Hasan<sup>1,2</sup>,  
Norhafiz Azis<sup>1,2</sup>, Mohammad Effendy Yaacob<sup>3</sup> and Eris Elianddy Supeni<sup>4</sup>

<sup>1</sup>Institute of Advanced Technology, Universiti Putra Malaysia, 43400 UPM, Serdang, Selangor, Malaysia

<sup>2</sup>Department of Electrical and Electronic Engineering, Faculty of Engineering, Universiti Putra Malaysia, 43400 UPM, Serdang, Selangor, Malaysia

<sup>3</sup>Department of Food and Processing Engineering, Faculty of Engineering, Universiti Putra Malaysia, 43400 UPM, Serdang, Selangor, Malaysia

<sup>4</sup>Department of Mechanical & Manufacturing Engineering, Faculty of Engineering, Universiti Putra Malaysia, 43400 UPM, Serdang, Selangor, Malaysia

### ABSTRACT

This article presents a microcontroller-based direct current (DC) energy data logger developed by adapting low-cost ATmega328 by measuring the PV system DC and voltage characteristics while simultaneously recording the measured value over time to compute the energy production Watt-hour (*Wh*). The prototype logger has been tested on a live 1 kW standalone PV system where the voltage sensor detects PV series array output voltage ranging between 0–50 VDC by a voltage divider sensing circuit. For accurate sensing of the current output measurement from the PV array, 50A ACS756 hall effect IC was integrated as the current sensor. The data was measured and saved in text format with comma-separated values (CSV) in an SD card, read using Microsoft Excel software. The liquid crystal display (LCD) showed the actual value of the recording process's current, voltage, power, and duration in minutes. The recorded data has been compared to the standard laboratory

digital multimeter for calibration manually to justify the measurement value. The error is minimized to 0.6% average by varying the constant float value in the programming code. The advantage of developing this logger is that the development cost is much cheaper than the standard commercial PV energy meter, can be reproduced for other DC application energy measurements, and easily modify the voltage and current range

#### ARTICLE INFO

##### Article history:

Received: 31 January 2021

Accepted: 05 July 2021

Published: 14 December 2021

DOI: <https://doi.org/10.47836/pjst.30.1.10>

##### E-mail addresses:

[mohdruzaimi@gmail.com](mailto:mohdruzaimi@gmail.com) (Mohd Ruzaimi Ariffin)

[suhaidi@upm.edu.my](mailto:suhaidi@upm.edu.my) (Suhaidi Shafie)

[wanzuha@upm.edu.my](mailto:wanzuha@upm.edu.my) (Wan Zuha Wan Hassan)

[norhafiz@upm.edu.my](mailto:norhafiz@upm.edu.my) (Norhafiz Azis)

[m\\_effendy@upm.edu.my](mailto:m_effendy@upm.edu.my) (Mohammad Effendy Ya'acob)

[eris@upm.edu.my](mailto:eris@upm.edu.my) (Eris Elianddy Supeni)

\* Corresponding author

to suit the application. Apart from that, this logger also provides high accuracy performance, and its independent characteristic is practical for off-grid or off-site PV system use.

*Keywords:* Direct current logger, energy logger, off-grid photovoltaic, photovoltaic

---

## INTRODUCTION

The increase in electrical energy power consumption of the declining fossil fuel resources, the environmental pollution issue, and increasing power utility prices have led humanity to depend more on a clean and sustainable energy source. For a long time, solar energy has been a huge renewable energy source that light and heat can be transformed directly into electricity. The photovoltaic system was used globally in various applications, such as buildings, space, agriculture, defense, telecommunications, and electrical gadgets, to reduce costs and easy access to its harvesting process. A complete PV system was equipped with an energy meter or monitoring device. This system is normally equipped or integrated with a larger scale or expensive charge controller and inverters with a dedicated external software system and interfaces. In several situations, off-grid or standalone PV systems normally did not have a data logger system, assessing the power generation generated because of the complexity and higher hardware costs. In the end, the user cannot trace long-term power production, system losses, and failure in the operation of the PV system.

Ronay et al. (2014) and Gertz and Di Justo (2012), in their research, agreed to the term that the solar energy monitoring system is a system that instantly assesses the magnitude of PV system energy characteristics by its embedded potential with an amperage sensor. However, the data can be continuously obtained or stored for long-term use with limited power consumption, either on grid-connected or standalone PV systems. An energy logger can be used in either system, consuming minimal energy and easily accessible by the user. PV system status is commonly monitored using a few types of control and communication technologies. Wired and wireless networking systems are usually used to obtain measuring data from a power meter. Han et al. (2015) developed a microcontroller-based PV control and monitoring device that incorporated a GSM communication module as the way of transmission between the device and a personal computer. However, the whole system is still costly, where the control and monitoring system did not provide a convenient method to retrieve the recorded data, and this device still dissipates extra or external power, which is not practical for remote areas.

In another study, Hadi et al. (2018) built a standalone power logger to measure a solar panel power output by applying Arduino modules proving that such a standalone device is known to be the perfect solution for remote or off-grid PV energy measurement systems and also much cheaper than those on the market for commercial products. However, this method is best used to measure individual or single solar panels in low voltage and current range, limited by the Arduino commercial modules (i.e., 0-25V<sub>DC</sub> B25 voltage module,

0-20A ACS712 current module) and not suitable for a bigger system. Finally, Mahzan et al. (2017) outline the construction of a data logger for PV monitoring systems that store bulk data from input channels using the Arduino Mega 2560 board, which adapts the ATmega2560 chip. According to their findings, a data logger with an Arduino-based microcontroller is reliable in controlling the PV device. Furthermore, by comparing the data obtained from the proposed data logger with an existing data logger on the market, the proposed data logger achieved about 5% accuracy.

Another power data logger for a PV system, which has been developed by using a microcontroller (micro-C), has been presented by Rehman and Iqbal (2020) adapting ESP32-S2 micro-C, while Gupta et al. (2017) adapted the Arduino UNO, and Borza and Kaplani (2019) adapted the atmega328P board. Figure 1 shows the commercial measurement and monitoring device of PV systems available on the market, with a price starting from RM 600.00 and above.



Figure 1. Commercial PV energy meter and monitoring device

The construction of a prototype DC energy logger was presented in this study, which was developed utilizing a low-cost microcontroller to measure the DC and voltage of a PV system while recording the calculated data over time to calculate the solar energy generated (in kWh). This prototype was then tested and implemented to an established one kWp standalone PV Hybrid Agrivoltaic (HAV) greenhouse system for energy monitoring (Ariffin et al., 2017). The energy logger was integrated by connecting the voltage sensor from the PV array at the PV charge controller's input voltage terminal in parallel, while the current sensor connected in series at the PV array's negative input cable. The logger saved the collected data in an SD card, while the LCD screen displays the voltage, current, power, and duration of the logging progress in real-time. The logged data from the SD card can easily be accessed via MS Excel and will be explained in detail in the next section. Complete PV system for the testing purpose and application is specified in Table 1.

## MATERIALS AND METHODS

In this prototype development, the system comprises four elements: the microcontroller as the brain part, voltage detector, current sensor, and data storage. The logger reads the data

Table 1  
*HAV greenhouse PV system specification*

<b>PV Panel Maximum Power</b>	<b>100 W</b>
<b>PV Cell Technology</b>	Mono-crystalline Silicon
<b>Panel Quantity</b>	10
<b>Array Configuration</b>	2 panel strings, 5 string parallel
<b>Total Maximum Power (Pmax)</b>	1000 Wp
<b>Maximum Voltage (Vmp)</b>	35.64V in series
<b>Maximum Current (Imp)</b>	28.5A in parallel
<b>Installation Method</b>	Roof-mounted

in the one-minute interval from the sensor circuits and records the data into an SD card. In the meantime, the value measured was displayed on an LCD screen for ease of use to get the PV system information in real-time. This energy logger prototype is specifically designed to measure up to 50 V<sub>DC</sub> and from 0-50A current using a specific hall effect sensor from the PV array. Table 2 lists out the component used in developing the energy logger, the cost for each component, and the total cost for the whole prototype. Figure 2 represents the process flow in developing the system programming and hardware prototype. Figure 3 exhibits the logger’s hardware architecture based on the four main elements above.

Table 2  
*Component list and cost in Ringgit Malaysia (RM)*

No	Item	Qty	U/Price (RM)	Total (RM)
1	Atmel Atmega328P Microcontroller (Arduino UNO)	1	30.00	30.00
2	ACS756 50A current sensor	1	50.00	50.00
3	IIC I2C LCD 2004 (20x4) display	1	25.00	25.00
4	W5100 Ethernet and SD card shield	1	25.00	25.00
5	Voltage divider (100kΩ & 10kΩ resistors)	1	1.00	1.00
6	Plastic Casing	1	10.00	10.00
7	Push button switch	2	4.00	8.00
8	12V cooling fan	1	4.00	4.00
9	Cable & connectors	1	10.00	10.00
			<b>G/Total</b>	<b>153.00</b>

**Microcontroller System Hardware and Software**

This energy prototype logger uses the ATmega328P-based microcontroller boards (Arduino UNO) consisting of 14 digital input/output (DIO) pins and six analog inputs (AI) for the analog sensor and can be programmed with the IDE (Integrated Development Environment) via a USB type B cable. The measured value is written into an SD card with the built-in SD library by integrating the SD module. The board can be programmed with its specific

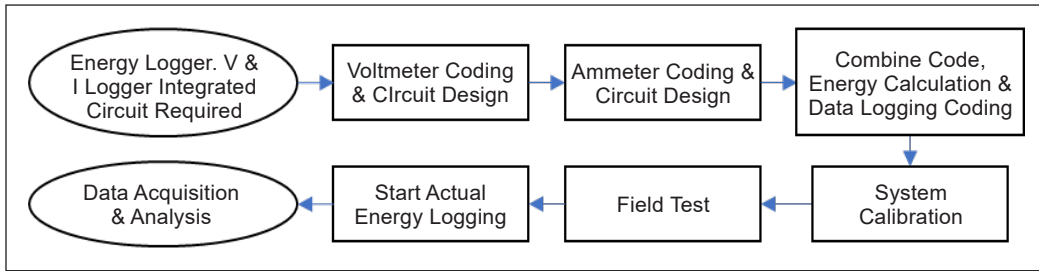


Figure 2. Energy logger design flow showing the steps in developing the software and hardware prototype

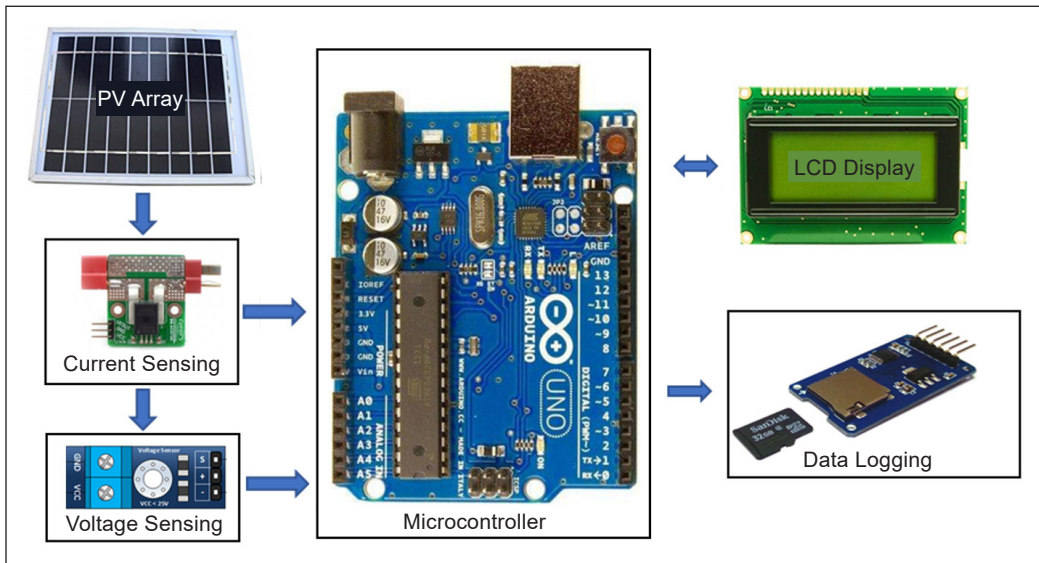


Figure 3. Energy logger hardware architecture, which consists of a microcontroller, current sensor, voltage sensor, and data logger component

software, and usually, the program code is called a sketch. Functionality is placed in the file of the library and applied within the program. The name of their file header with its pre-processor directive is included in the program. For example, float variables are used when calculating voltage, current, and power. This function tends to store real numbers.

Figure 4 represents the programming flow as the system evolves. The first initialization is to test for SD card absence and storage capacity. If the card is not found, it returns to the initialization of the SD card. After the initialization is complete, the system will go into ready mode. The first trigger pulse instruction code will begin measuring and displays the value of voltage, current, and power in real-time. Then, the second trigger pulse is a set of instructions to start the data recording. Next, the microcontroller begins writing the datasets into text format of comma-separated values (CSV) with a pre-programmed string filename. Simultaneously, the LCD screen will show the same information as the above with additional information, duration time in minutes. At any time, once the required data

logging time reaches, the data logging cycle will be stopped by giving a third trigger pulse, and the system will be returned to steady mode.

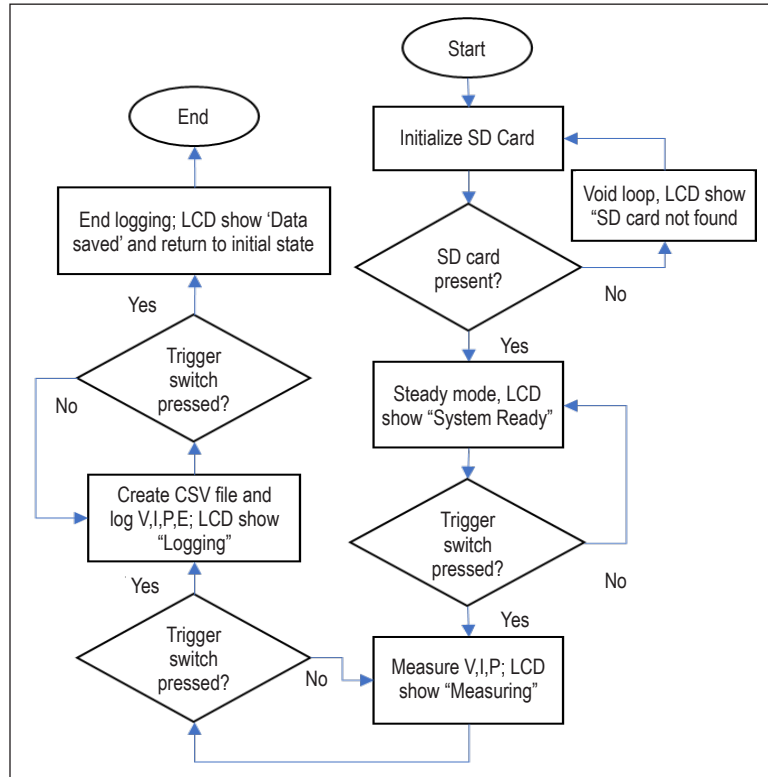


Figure 4. Prototype logger programming flow

### Prototype Hardware

The energy logger prototype with LCD, a memory storage module, and the sensor are shown in Figure 5. It has high reliability for embedded systems and very low power consumption.

**Voltage Detection.** A voltage divider circuit was used as the voltage sensor. Since the ADC analog pin of the microcontroller (for voltage input) is limited to 5V, the divider’s voltage output must not be more than that. The voltage divider circuit divides the voltage into two parts, from which one is fed to the Arduino analog input terminal. For a voltage range of 0-50 V<sub>DC</sub>, the sensor circuit comprises of 100kΩ (R1) and 10kΩ (R2) resistors, where for precise output accuracy, the ratio of both resistors must be minimal. The R2 output voltage was referred to as input for ADC pin A0 on the microcontroller. Figure 6 represent the voltage divider circuit diagram, and R2 output voltage can be written as Equation 1:

$$V_{out} = V_{in} \frac{R_2}{R_1 + R_2} \quad [1]$$

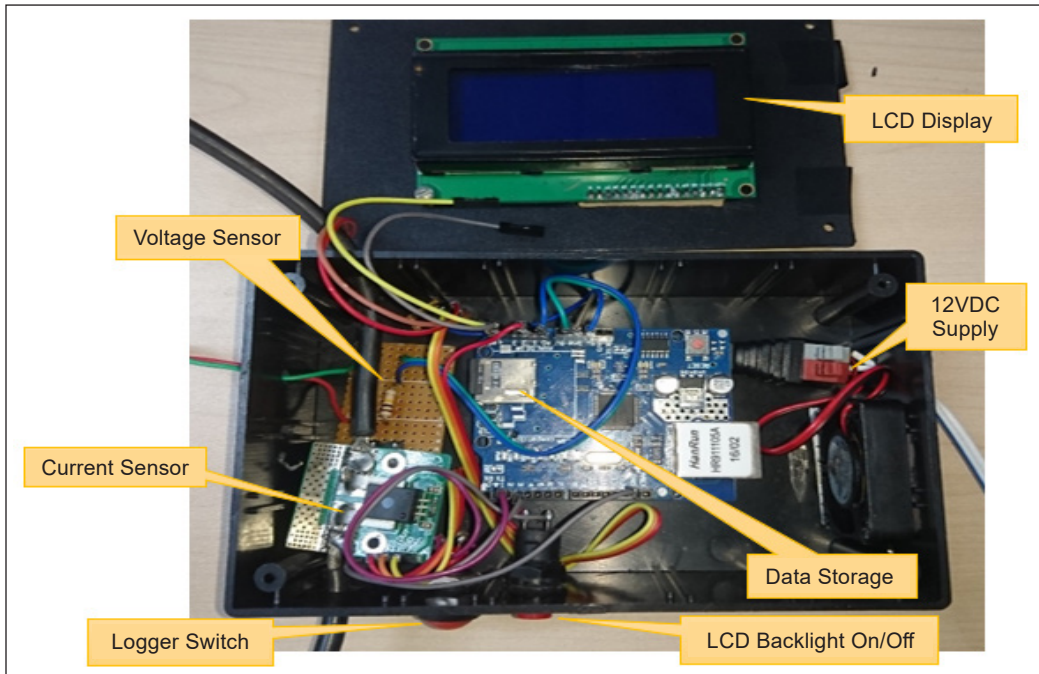


Figure 5. Developed energy logger prototype with memory modules, LCD, and sensors based on ATmega328P microcontroller

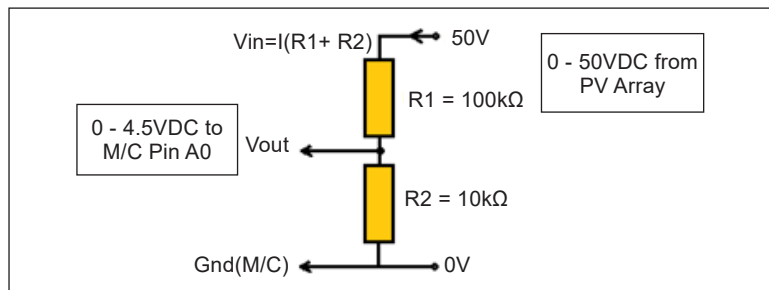


Figure 6. Voltage divider circuit developed for voltage sensing

In this application, if  $V_{in}=50V$  maximum, then:

$$V_{out} = 50 \frac{10000}{110000} = 4.545V = 4545mV$$

The analog input ADC resolution can be calculated using Equation 2:

$$ADC_{resolution} = \frac{V_{ref}}{(1024-1)} \quad [2]$$

$$ADC_{resolution} = \frac{4545 mV}{1023} = 4.442 mV$$

Therefore, 4.442mV will be converted to 1V in the programming code. To protect the microcontroller analog pin, a Zener Diode can be used to avoid high voltage.

**Current Sensing.** ACS756 Hall Effect current sensor IC has been adapted for DC measurement for high precision sensing. It can measure current up to 50A maximum and can be applied in both DC and AC applications. ‘Hall effect’ means generating a voltage difference (the Hall voltage) across an electrical conductor, a transverse to an electrical current in the conductor, and a perpendicular magnetic field to the current. A major benefit of adapting this sensor in a system is that its conductive path terminals are electrically isolated from the signal line. Figure 7 exhibits the pinout of the IC module and its standard use. The sensor has a sensitivity of 40mV/A, according to its datasheet. Initially, it produces between 2.4–2.5V analog output from the Vout pin at 0A current (no load) depending on environmental conditions. Since the module can sense up to ±50A current range, the highest voltage output is 4.5V for positive +50A and 0.5 V for negative -50A current measurement.

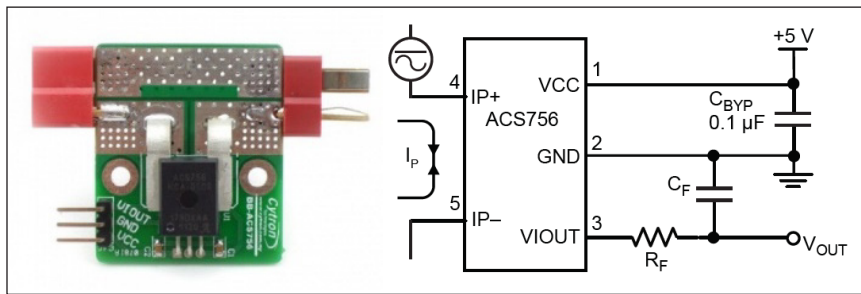


Figure 7. ACS756 Module and typical application

Figure 8 illustrates the schematic diagram for hardware design, which shows the voltage divider and the current sensor connection. IP+ terminal of the ACS756 is connected to the solar charge controller, and the IP- terminal is connected to the negative line from the PV array. The sensor’s Vcc pin is connected to the microcontroller’s 5V pin. In contrast, Vout is connected to an A1 analog input pin (pin A0 occupied by voltage sensor). The microcontroller converts the analog to a digital signal via its 10 bits ADC, similar to the voltage sensor conversion.

As mentioned earlier, the sensor’s sensitivity is 40mV/A, which describes every increment of 1A by PV system array will increase 40mV to Vout pin of ACS756 IC. The sensor output is a voltage that needs to be calculated to transform it to the current value (Ang, 2012). Considering the sensor’s ratio and sensitivity in Equation 3:

$$\frac{\text{Change of Voltage}}{I(mA)} = \frac{0.04V}{I(mA)} \quad [3]$$



which the change of voltage can be written as the following:

$$\text{Change of voltage} = (\text{Sensor reading} - \text{Initial reading}) \text{ bits} \frac{5V}{1024 \text{ bits}}$$

The change of voltage is different at the time between the output voltage (sensor reading) and the initial state output voltage, which is about 2.5V. Because 2.5V in Arduino give 510 in 10 bits of ADC, the voltage change can therefore be written as Equation 4:

$$\text{Change of voltage} = (\text{Sensor reading} - 510) \text{ bits} \frac{5V}{1024 \text{ bits}} \quad [4]$$

Combining Equations 3 and 4 gives:

$$I(mA) = \frac{(\text{Sensor Reading} - 510) \text{ bits}}{0.04 V} \left( \frac{5V}{1024 \text{ bits}} \right) (1000mA)$$

Hence,

$$I(mA) = (\text{Sensor Reading} - 510)(122)$$

$$I(mA) = (\text{Sensor Reading} - 510)(122)$$

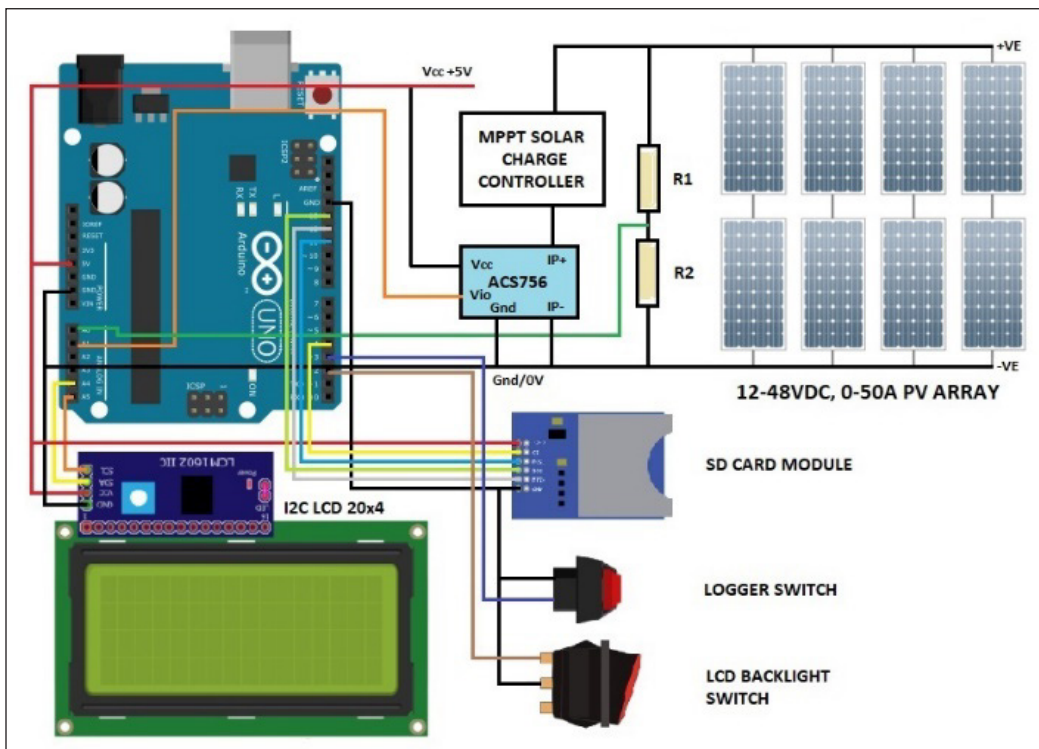


Figure 8. System schematic drawing

**Data Logging.** The energy logger developed is integrated with an ethernet module with a microSD card slot for storing data with a reading capability of 32 GB to enable bigger data storage and memory backup. When the second trigger button is pressed, this will start the data recording process, and when pressed again, it will stop logging. Measurement's current, voltage, power, and energy values are written to a CSV file in the SD card. By reading the microSD card using the Microsoft Excel application, several files can be found in series based on how many logging cycles a person has taken the readings, each with the filename starting with "datalog" followed by running number as pre-set during programming development.

**Power and Energy Calculation.** Measurement of power and energy is written in program code performed by the system and automatically written with the measured data in the SD card. For example, to calculate power (Equation 5):

$$P = V \times I \quad [5]$$

For energy calculation (Equation 6):

$$E = \frac{P(\text{average}) \times t(\text{duration in minutes})}{60} = kWh \quad [6]$$

**LCD Screen.** The LCD screen is the device output panel to display the measured value of voltage, current, power, and duration in real-time. The LCD backlight can be turned on and off by the toggle switch to reduce the power consumption of the logger when not needed (i.e., during daytime).

## RESULTS AND DISCUSSIONS

### Voltage and Current Sensor Calibration

Once the program was uploaded to the microcontroller, the logger's sensor system was tested using a variable DC power supply and digital multimeter, calibrated for the laboratory instrument standard. A 50W 12VDC bulb as a dummy load was applied to calibrate the current reading. The logger's voltage measurement reading on the LCD is almost similar to the laboratory's power supply voltage display.

Because of ACS756 module produce floating voltage ranging from 2.4 to 2.5V. At the same time, the current is 0A, and a different output sensitivity of 20~40 mV/A due to varying operating temperature, it takes a long procedure to match the readings by repeatedly tuning the constant float value in the programming code. Figure 9 exhibits a dummy load's voltage and current being measured for calibration. The final adjustment calculation between the prototype logger and the laboratory standard instruments resulted in an average deviation of 0.6%, acceptable for most certified calibrated measuring devices where meters cannot

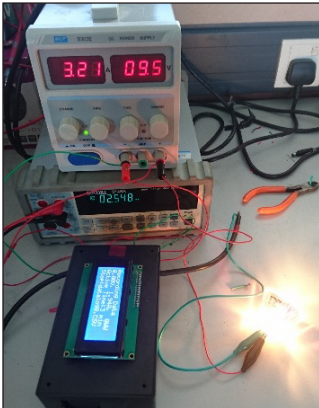


Figure 9. Manual calibration process by comparing prototype logger's voltage and current sensor measurement with standard laboratory DC power supply and current meter

exceed 3% inaccuracy when tested (IEC, 2020; Energy Commission, 2021).

### Field Sampling

After the calibration work has been done in the laboratory, a field test experiment has been carried out to assess the energy logger's stability and reliability in real-time and actual conditions. The prototype logger has been installed in line with a specific commercial energy logger to analyze the measured data accuracy. The setup is shown in the Figure 10 schematic diagram below. The commercial energy meter measures the voltage by tapping the positive and negative terminal of the PV array, similar to the prototype logger.

While the prototype logger measures the current through the Hall effect sensor, the commercial energy

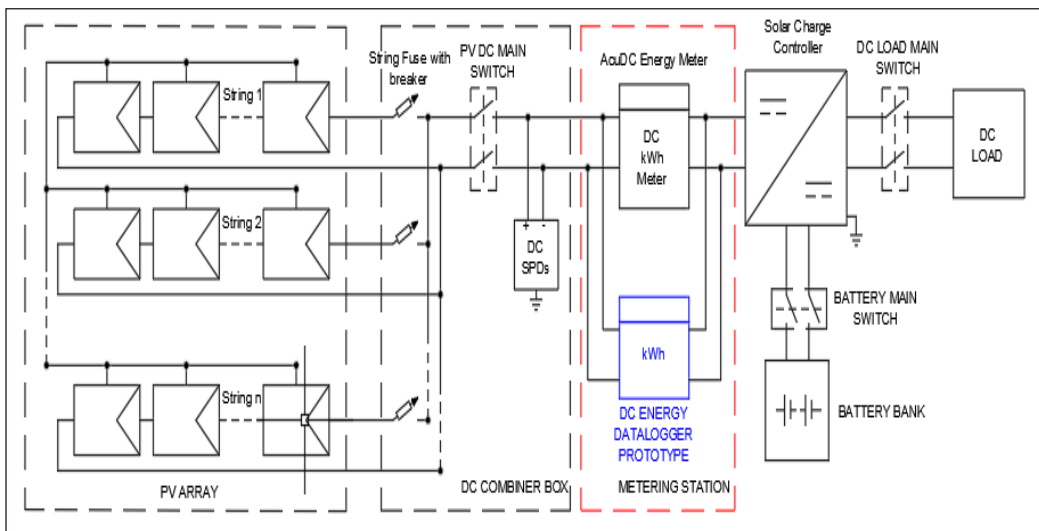


Figure 10. Schematic diagram of measurement setup for prototype logger and commercial energy meter on an existing 1kWp DC PV greenhouse system

meter uses the shunt resistor to measure the current in series at the negative line of the PV array before connecting to the solar charge controller. Figure 11(a) shows the data samples presented using MS Excel, which was copied from the SD memory card, and Figure 11(b) shows the MS Excel data extracted from the commercial energy meter through its specific user interface software, which shows more parameters being measured and calculated by the meter.

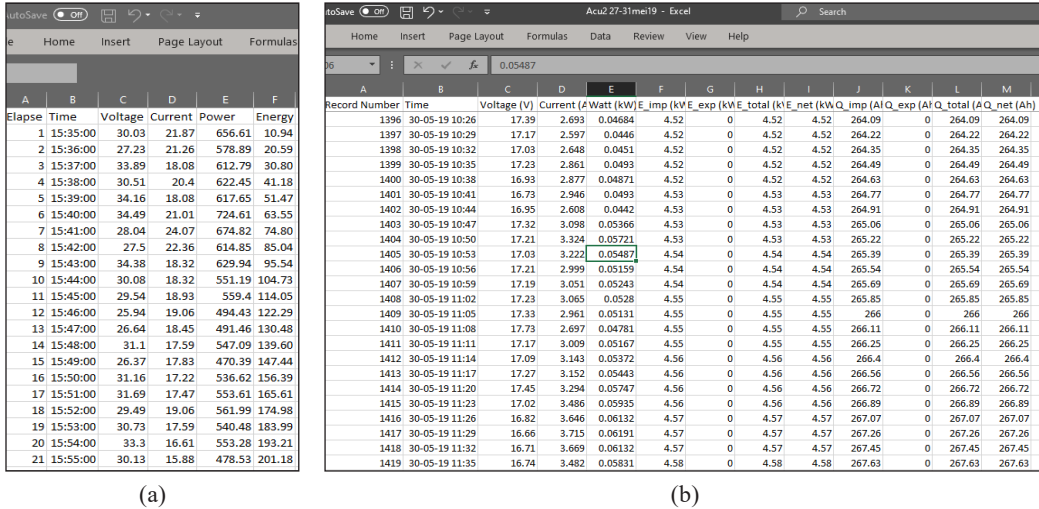


Figure 11. (a) Prototype energy logger’s CSV data extracted from the SD card read in MS Excel; (b) Extracted data from commercial energy meter user interface software

### Energy Analysis

A sample measurement of energy generation from a PV system was recorded using the energy logger for one day from 9:15 AM with 1 minute time interval until 7:00 PM. From the prototype logger’s CSV saved data and the commercial energy meter’s data, the voltage ( $V$ ) and current ( $I$ ) graph plot has been plotted by MS Excel in Figures 12 and 13, respectively showing small errors between the prototype and the actual energy meter reading.

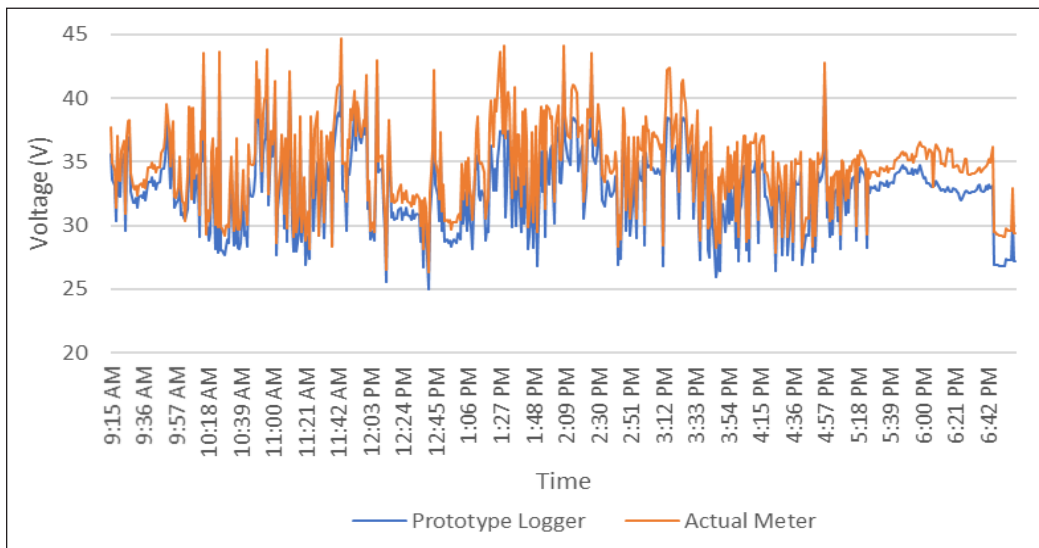


Figure 12. Prototype logger and actual energy meter voltage output over time

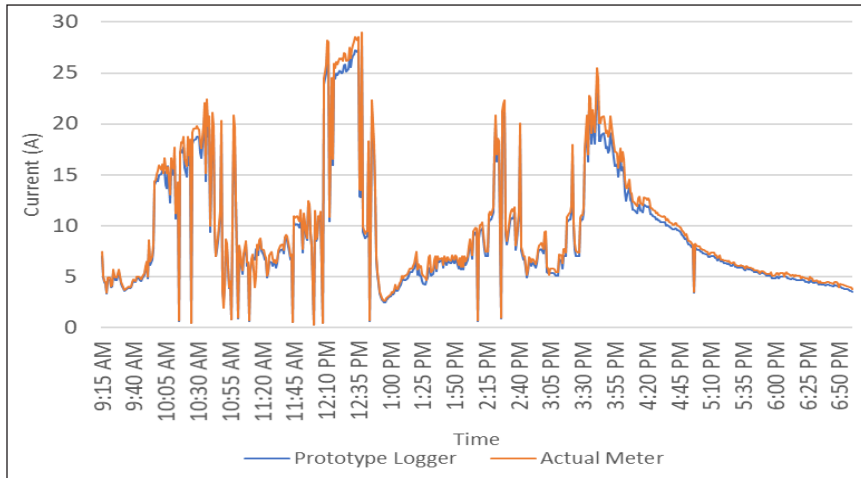


Figure 13. Prototype logger and actual energy meter current output over time

Figure 14 shows the power and cumulative energy in Watt ( $W$ ) & Watt-hour ( $Wh$ ) from prototype and energy meter data. Based on the observation, logged data of the voltage and current characteristic on the prototype logger compared to the actual energy meter is not much different. The deviation calculated was at 0.574% for voltage and 0.531% for current, which is tolerable for standard instrument measurement. Minimizing the voltage divider resistor error tolerance and larger range of ADC bit is suggested to get a more precise value. For the ACS756 current sensor, the error can be reduced more by fine-tuning the constant value in the programming code to match the floating voltage sensitivity due to environmental conditions.

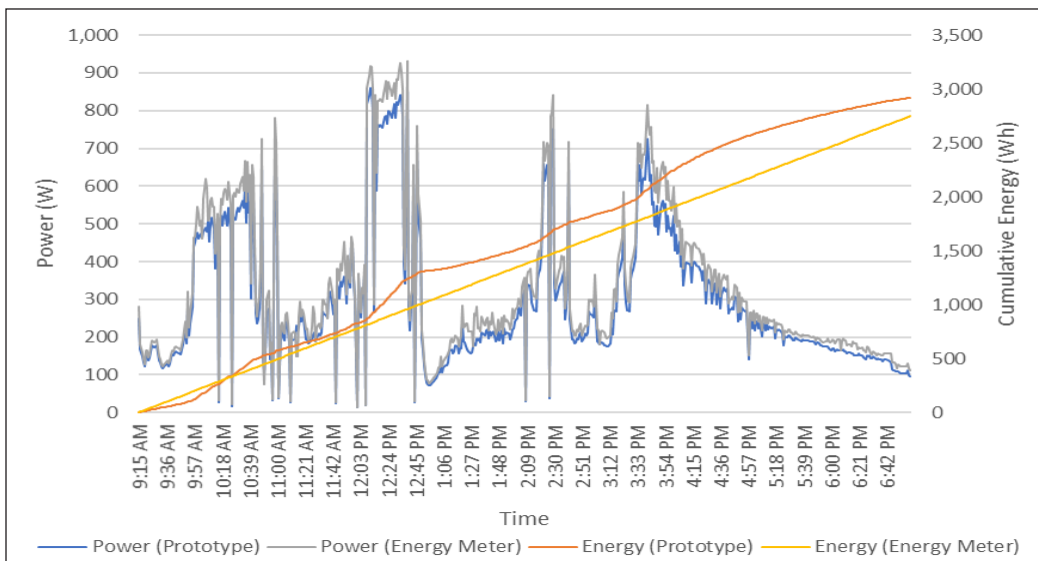


Figure 14. Power and Energy output file from both prototype logger and commercial energy meter.

## CONCLUSION

In this article, a microcontroller-based DC energy data logger has been developed using a low-cost ATmega328 microcontroller by measuring the PV system DC and voltage characteristics while simultaneously logging the measured data over time to calculate the energy production in watt-hour (*Wh*). The prototype logger has effectively proven recording and actual DC voltage, current, and power generation on a live one kWp 24V<sub>DC</sub> standalone PV system continuously for a period required. The prototype logger can be reproduced for other DC application energy measurements and easily modified to a larger voltage and current range to suit the application by adjusting the voltage divider circuit and replacing the current sensor module with a higher current limit type. The measured value has been verified using the manual calibration method by comparing the recorded data with the standard laboratory digital multimeter. The error is minimized to  $\pm 0.6\%$  average by varying the constant float value in the programming code. The advantage of this logger is that the hardware cost was much cheaper than the standard commercial PV logger, and apart from that, this logger also provides high accuracy performance. Its independent characteristic is very relevant for standalone or off-grid PV system use. Improvement, such as combination with GSM, Bluetooth, or WiFi module for wireless data acquisition (DAQ) and graphical user interface (GUI) development, is being considered for commercialization.

## ACKNOWLEDGMENT

These works were supported by the Universiti Putra Malaysia Research Management Centre [grant number GP-IPS/2018/9626800].

## REFERENCES

- Ang, J. Y. (2012). *Current measuring using BB-ACS756 with SK28A*. Retrieved January 25, 2021, from <http://tutorial.cytron.com.my/2012/08/08/current-measuring-using-bb-acs756-with-sk28a/>
- Ariffin, M. R., Shafie, S., Hassan, W. Z. W., Azis, N., & Ya'acob, M. E. (2017). Conceptual design of hybrid photovoltaic-thermoelectric generator (PV/TEG) for automated greenhouse system. In *2017 IEEE 15th Student Conference on Research and Development (SCORED)* (pp. 309-314). IEEE Publishing. <https://doi.org/10.1109/SCORED.2017.8305373>
- Borza, P., & Kaplani, E. (2019). An embedded microcontroller unit for PV module monitoring and fault detection. In *2019 8th International Conference on Renewable Energy Research and Applications (ICRERA)* (pp. 557-562). IEEE Publishing. <http://dx.doi.org/10.1109/ICRERA47325.2019.8996874>
- Energy Commission. (2021). *Licensee supply regulations, 1990 arrangement of regulations, sub-regulation 12(2)*. Retrieved May 6, 2020, from [https://www.st.gov.my/en/details/policies\\_details/12/2](https://www.st.gov.my/en/details/policies_details/12/2)
- Gertz, E., & Di Justo, P. (2012). *Environmental monitoring with Arduino: Building simple devices to collect data about the world around us*. O'Reilly Media Inc.

- Gupta, V., Raj, P., & Yadav, A. (2017). Design and cost minimization of PV analyzer based on Arduino UNO. In *2017 IEEE International Conference on Power, Control, Signals and Instrumentation Engineering (ICPCSI)* (pp. 1337-1342). IEEE Publishing. <http://dx.doi.org/10.1109/ICPCSI.2017.8391928>
- Hadi, M. S., Afandi, A. N., Wibawa, A. P., Ahmar, A. S., & Saputra, K. H. (2018). Stand-alone data logger for solar panel energy system with RTC and SD card. In *Journal of Physics: Conference Series* (Vol. 1028, No. 1, p. 012065). IOP Publishing. <https://doi.org/10.1088/1742-6596/1028/1/012065>
- Han, J., Lee, I., & Kim, S. H. (2015). User-friendly monitoring system for residential PV system based on low-cost power line communication. *IEEE Transactions on Consumer Electronics*, *61*(2), 175-180. <https://doi.org/10.1109/TCE.2015.7150571>
- IEC. (2020). *Electricity metering equipment - Particular requirements - Part 21: Static meters for AC active energy (classes 0,5, 1 and 2)*. International Electrotechnical Commission.
- Mahzan, N. N., Omar, A. M., Rimon, L., Noor, S. M., & Rosselan, M. Z. (2017). Design and development of an arduino based data logger for photovoltaic monitoring system. *International Journal of Simulation: Systems, Science and Technology*, *17*(41), 15.1-15.5. <http://dx.doi.org/10.5013/IJSSST.a.17.41.15>
- Rehman, A. U., & Iqbal, M. T. (2020). Design of an Ultra-Low Powered Data-Logger for Stand-Alone PV Energy Systems. *European Journal of Electrical Engineering and Computer Science*, *4*(6), 1-6. <http://dx.doi.org/10.24018/ejece.2020.4.6.26>
- Ronay, K., Dorin, B. I. C. A., & Dumitru, C. (2014). Energy monitoring and load control application for an off-grid PV system. *Scientific Bulletin of the Petru Maior University of Targu Mures*, *11*(2), 30-33.





## Performance of a HAWT Rotor with a Modified Blade Configuration

Tabrej Khan<sup>1</sup>, Balbir Singh<sup>1,2</sup>, Mohamed Thariq Hameed Sultan<sup>1,3,4</sup> and Kamarul Arifin Ahmad<sup>1,5\*</sup>

<sup>1</sup>Department of Aerospace Engineering, Faculty of Engineering, Universiti Putra Malaysia, 43400 UPM, Serdang, Selangor, Malaysia

<sup>2</sup>Department of Aeronautical and Automobile Engineering, Manipal Institute of Technology, Manipal Academy of Higher Education, Manipal 576104, India

<sup>3</sup>Laboratory of Biocomposite Laboratory, Institute of Tropical Forestry and Forest Products (INTROP), Universiti Putra Malaysia, 43400 UPM, Serdang, Selangor, Malaysia

<sup>4</sup>Aerospace Malaysia Innovation Centre (944751-A), Prime Minister's Department, MIGHT Partnership Hub, Jalan Impact, Cyberjaya 63000, Selangor, Malaysia

<sup>5</sup>Aerospace Malaysia Research Centre, Faculty of Engineering, Universiti Putra Malaysia, 43400 UPM, Serdang, Selangor, Malaysia

### ABSTRACT

As the world focuses more on clean and green Earth, wind energy plays a significant role. Wind energy is a renewable source of energy that can cope with the ongoing global fossil fuel crisis. The wind energy converters like wind turbines have been studied a lot in terms of design and performance. The current work includes analyzing the output effects of a horizontal axis wind turbine (HAWT) with a modified blade configuration at specific wind speeds. A numerical investigation is carried out using two different numerical software on the chosen airfoil used in blade design validated with the analysis carried out in open-loop wind tunnels. The study is divided into two phases: first, the selected airfoil is tested experimentally and using CFD, and then the findings are compared to those of the University of Illinois Urbana Champaign wind tunnel tests at low Reynolds numbers. The second phase includes the numerical analysis based on the blade element momentum method and non-linear lifting line simulations of modified blade design at high Reynolds number.

The numerical results of rotor performance analysis have been compared to existing experimental results. The findings of all numerical investigations agree with those of the experiments. An optimal value of the power coefficient is obtained at a particular tip speed ratio close to the desired value

### ARTICLE INFO

#### Article history:

Received: 04 May 2021

Accepted: 09 August 2021

Published: 14 December 2021

DOI: <https://doi.org/10.47836/pjst.30.1.11>

#### E-mail addresses:

tabrejkhani279@gmail.com (Tabrej Khan)

balbir.s@manipal.edu (Balbir Singh)

thariq@upm.edu.my (Mohamed Thariq Hameed Sultan)

aekamarul@upm.edu.my (Kamarul Arifin Ahmad)

\* Corresponding author

for large wind turbines. For maximum power, this study investigates the optimum pitch angle. The work demonstrated the improved HAWT rotor blade design to produce better aerodynamic lift and thus improve performance.

*Keywords:* Aerodynamics, computational fluid dynamics, pitch angle, turbine blade, wind energy, wind speed

## INTRODUCTION

Wind energy has evolved considerably for decades and established its role as an essential substitute for developing renewable energy (Pinto et al., 2020). In tropical climates with reasonably constant wind speed, wind energy has very significant potential. A summary of various numerical studies performed in the past shows that micro-siting, modeling and estimation, rotor and turbine optimization, modeling in terms of blade and flow, and structural analysis are the highest priority fields of study (Sudhamshu et al., 2016). Figure 1 shows the wind turbine classification between the horizontal axis (HAWT) and the vertical axis (VAWT) wind turbine. There is a range of benefits of the horizontal axis wind turbine (HAWT) compared to the vertical axis wind turbine. In the case of HAWT, the rotor angle plays a significant role in rotating the turbine to generate the aerodynamic impact for the rotor coupled with the generator to produce power. Therefore, the drag force that induces reverse flow and rotor speed reduction must be reduced to enhance performance. In addition, the vortex on the blade's tip is decreased by the winglets, increasing the output by flow separation of the tip (Satwika et al., 2019). By diffusing the vortices from the blade tips,

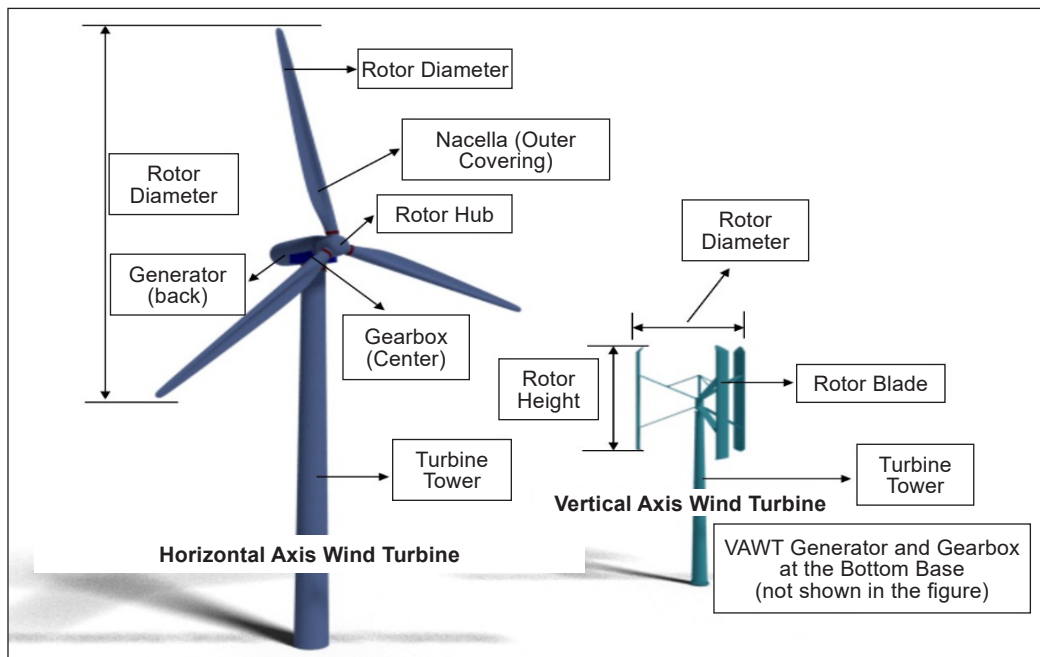


Figure 1. Typical configurations of horizontal and vertical axis turbines

winglets will reduce the impact of wingtip vortices on the turbine performance (Farhan et al., 2019).

In wind turbines, the lift force creates the rotor torque due to pressure distribution, which slotting can alter. However, this distribution change keeps the rotational velocity under control even in extreme wind speeds (Navinkumar et al., 2021). A HAWT is outstanding in energy efficiency, producing relatively constant torque and demonstrating higher power coefficients. The nacelle is hard to maintain and repair because it is heavy and accommodates the gearbox and generator. The yaw instrument rotates the nacelle completely 360 degrees to align the blade front in the wind direction (Kim & Suh, 2019). For the HAWT configuration, the aerodynamic efficiency under the yaw is very critical. With the rise in yaw angle, the wind turbine's power reduces as per cosine law (Ye et al., 2020). CFD analysis is essential for precise performance research of these blades, including flow physics.

However, Blade Element Momentum Theory is used to estimate performance compared to CFD to do it reasonably quickly (Kumar et al., 2019). The coupling between wall-resolved large eddy simulation (LES) and the blade element momentum theory (BEM) is the basis of the structure. It helps to understand the aerodynamics of the airfoil and the wind turbine and enables a wide range of turbine operating conditions to be addressed with reduced computational costs (Revaz et al., 2020). Fluid-Structure Interaction reveals that in a velocity shear state, deformation of the turbine blades enhances relative to uniform flow (Hafeez et al., 2019). FSI has been conducted many times before on wind turbines, covering various applications and interests. For instance, the  $k-\epsilon$ -SST turbulence model uses 2D and 3D computational fluid dynamics (CFD) simulations of a vertical axis wind turbine (VAWT) (Santo et al., 2019). Most current airfoils maximize the sub-atmospheric pressure by altering the airflow from the leading edge through a slat. At elevated pressure, the air movement is from the leading edge to the trailing edge until it is pushed at the corner of the vent (Yang et al., 2020). However, aerodynamic efficiency is significantly impaired by disturbances of any kind, such as ice accretion on the blades (Jin et al., 2020).

The past research indicates that HAWT has higher performance than VAWT (Albuquerque & Matos, 2016). In this paper, a new approach is used to assess the performance of a HAWT wind turbine blade. Three different airfoils are chosen to design the turbine blade to reduce the design complexity, cost, followed by aerodynamic and performance analysis. The Clark Y airfoil used as one of the airfoils is first tested numerically and experimentally and is then used in the fabrication process. Experimental validation is performed in both airfoil and blade analysis to ensure the accuracy of the results. The numerical investigation uses blade element momentum (BEM) Theory and non-linear lifting line (LLT) algorithms to analyze the blade performance. In addition, in terms of optimal pitch angle, the efficiency of the blade and the rotor is checked. The

primary objective of this research is to analyze the performance of the new modified design of a wind turbine blade and rotor at a high Reynolds number using numerical and experimental methods.

### DESCRIPTION OF PROBLEM

The performance of the HAWT turbine rotor blade is studied here. The use of low Reynolds number airfoil for 30% of the blade towards the tip is first studied numerically using computational fluid dynamics with wind speeds of 7 m/s and 14 m/s, at different angles of attack and Reynolds number. The findings are compared to the Universiti Putra Malaysia and University of Illinois Urbana Champaign open-circuit wind tunnel experimental data. The blade profile is then designed using three different airfoils, DU84132V, NACA643618, and Clark-Y, modeled based on parameters, such as increased Reynolds number, wind speed, and optimized using the profile, tip speed, and maximum lift to drag ratios. The simulations are performed in Qblade and validated with experimental data from already published work. The turbine blade profile is shown in Figure 2, with the corresponding chord lengths at each section. For the turbine, the cut-in wind speed is 3 m/s. The rotor blade is also analyzed structurally.

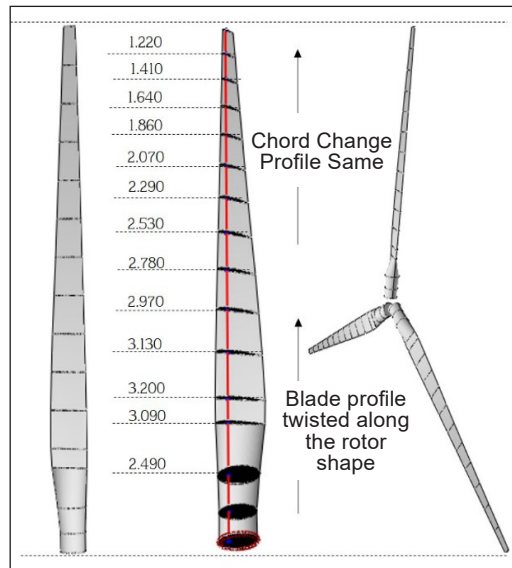


Figure 2. Blade design and section twist

### BACKGROUND AND GOVERNING EQUATIONS

A traditional approach to solving a wind turbine blade design or control problem is to minimize the actual, complex configuration into a simple mechanical model that depends only on significant parameters. Then analytical, semi-analytical, and numerical methods are used (Li et al., 2014). At a high Reynolds number, the flow is turbulent across the blades. Steady Reynolds averaged continuity and momentum equations are solved at given flow conditions (Sudhamshu et al., 2016).

The sectional schematic diagram of the airfoil with the corresponding forces and angles associated with it is shown in Figure 3. As seen in the diagram, the blades rotate in the turbine’s plane of rotation (POR). The twist angle  $\beta$  is the chord line’s sectional twist angle concerning the plane of rotation. From the reference (Sudhamshu et al., 2016), for dynamic blade control, it is again helpful to use an additional twist angle called the global

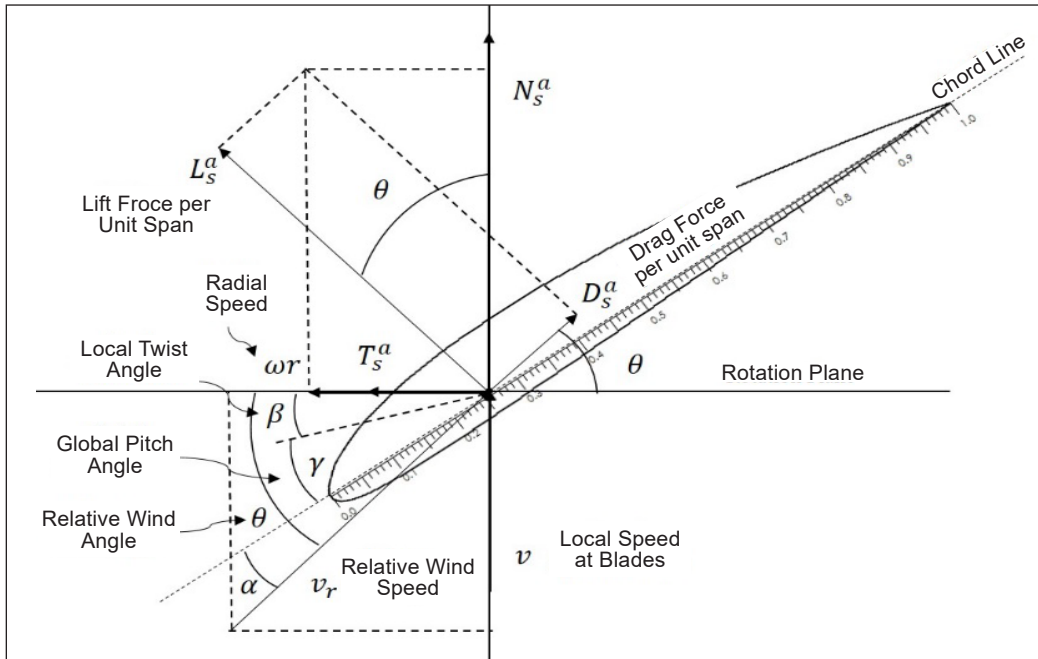


Figure 3. Forces acting on the aerofoil (Sudhamshu et al., 2016)

pitch angle  $\phi$ , which changes the twist of every cross-section by  $\phi$ . Rigid configurations of a HAWT blade and a blade section are shown in Figure 4. Due to the twisted blade profile and inclination, there is a bias 'e' between the center of mass of the hub and the centroid of the blade root. This bias includes the effect of the hub radius. There is no symmetry of the blade section concerning the chord line (Li et al., 2014). The blade system is complicated in its rotation as it moves along with a huge twist towards the blade's tip, as shown in Figure 2. As shown in Figures 4 and 5,  $U_\infty$  is the oncoming wind speed, and  $\omega$  is the angular rotation,  $\hat{u}_z$  into the wind,  $\hat{u}_r$  along with the blade profile, and  $\hat{u}_\theta$  is in the direction of rotation. Airfoil is moving in the  $\hat{u}_\theta$  direction. The radial speed is  $\omega r$  where  $r$  is the distance from the center of the hub.  $\omega_\infty$  creates some force on the airfoil section.  $L_s^a$  and  $D_s^a$  are the sectional lift and drag forces, respectively, perpendicular to each other. For designing a wind turbine rotor blade, it is essential to estimate the amount of moment this force on the blade is generating.  $F_\theta^a$  and  $F_z^a$  are the forces in the  $\hat{u}_\theta$  and  $\hat{u}_z$  (Equations 1, 2 & 3).

$$F_\theta^a = L_s^a \cos \theta - D_s^a \sin \theta \quad [1]$$

$$F_z^a = -L_s^a \sin \theta - D_s^a \cos \theta \quad [2]$$

$$M = r \cdot F_\theta^a = r \cdot (L_s^a \cos \theta - D_s^a \sin \theta) \quad [3]$$

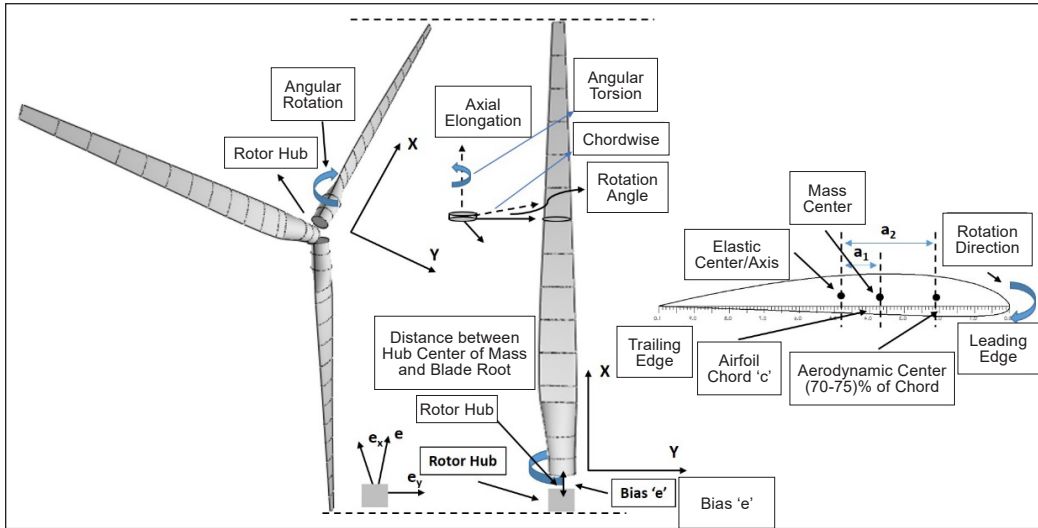


Figure 4. The detailed rigid geometry of our HAWT design

As per reference (Sudhamshu et al., 2016), the coefficient of pressure  $C_P$  can be used to quantify the pressure distribution across the airfoil in a non-dimensional way, defined as Equation 4

$$C_P = \frac{(P - P_\infty)}{\left[ \frac{1}{2} \rho (U_\infty^2 + \omega r^2) \right]} \quad [4]$$

### DETAILED METHODOLOGY

The methodology used in this study includes selecting appropriate airfoils for design and fabrication and numerical and experimental investigations to comprehend blade performance completely. Though it is standard practice in the industry to build

high Reynolds number wind turbine blades with standard DU84-132V3 and NACA 64(3)-618 airfoils, or even a combination of the two, the design is complex, the fabrication process is complicated, and the turbine blade is heavy. Therefore, we strive to improve the design by incorporating a simple low Reynolds number airfoil known as the Clark Y at least 30% until the tip end. This airfoil has a high glide ratio in subsonic flow conditions. The base and the middle portion remain the combination of the standard airfoils, which reduces the design's complexity and weight to some extent.

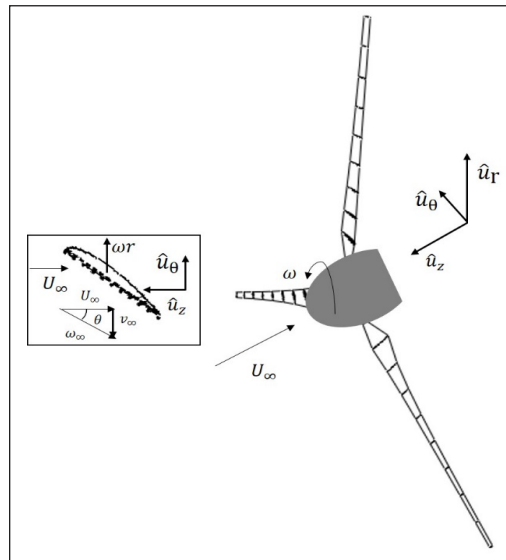


Figure 5. Rotor blade velocity profile

Incorporating Clark Y airfoil in the design needs thorough investigation by adequate aerodynamic analysis using open-circuit wind tunnels, computational fluid dynamics, and structural analysis. The properties of all these selected airfoils chosen are listed in Table 1.

Qblade software was used to calculate the pressure distribution, lift and drag characteristics of the selected airfoils, as shown in Figure 6. Due to wind tunnel limitations, aerodynamic analysis was performed on Clark Y for Re value of 200k and 400k typically associated with a wind speed of 7 m/s and 14 m/s. In the aerodynamic laboratory, the Clark Y airfoil used in this experiment was fabricated. Tests were carried out in the UPM subsonic wind tunnel with an operational speed range of 0.01-0.15 Mach with stagnation pressure varying from 120 kPa to 1200 kPa. The UPM wind tunnel test section is 1 meter square with a maximum velocity of 50 m/s, illustrated in Figure 7(a). A six-component internal balance is used to measure all forces and moments. The angle blade's attack on which the lift depends is determined by the relative wind direction, the current blade length, and the line angle (Yang et al., 2020). The combination of experimental results assisted by the numerical results from computational fluid dynamics gave sufficient evidence of its fabrication and was used in the blade design. To further confirm the findings, the experimental outcomes were also compared with UIUC wind tunnel data ([https://m-selig.ae.illinois.edu/uiuc\\_lsar.html](https://m-selig.ae.illinois.edu/uiuc_lsar.html)).

The numerical investigation of Clark-Y was carried out in a Phoenix-VR environment to support the experimental part, and the airfoil was modeled using CATIA V5. As shown in Figure 7(b), C-H type mesh is always adopted for this type of study (Yan et al., 2019), but in Phoenix-VR, the grid dimension is total cell number along a single direction. As

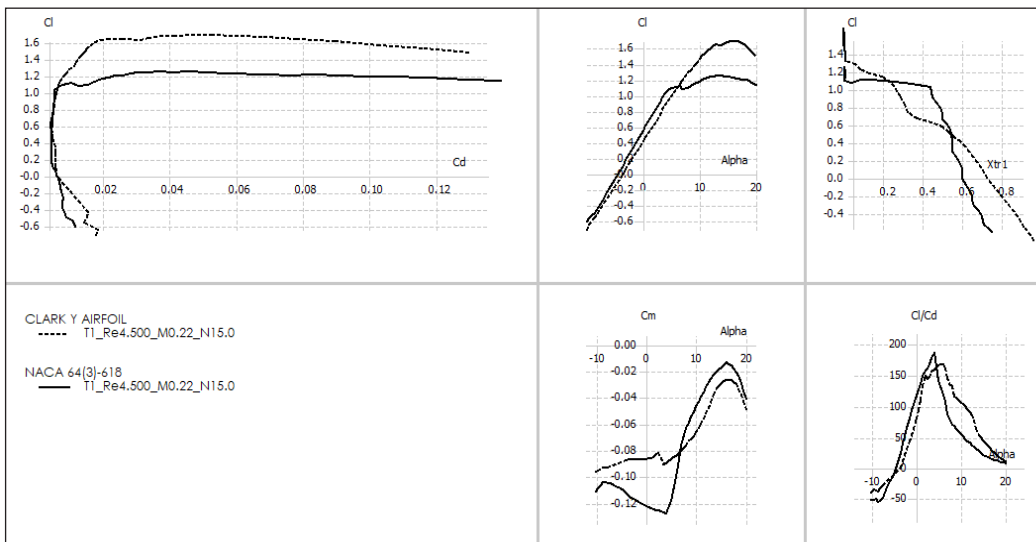


Figure 6. The performance simulations of airfoils in Qblade at  $M = 0.22$  with  $N_{crit}$  (free flow turbulence measuring parameter) of 15

shown in Figures 8(a) and 8(b), the airfoil meshed with open and closed wall domains, and flow is incompressible. The boundary outside is typically 15 chord lengths from the surface. Suitable boundary conditions were applied, and nonslip wall conditions were set up. A periodic condition is enforced in the spanwise direction as in (Yan et al., 2019). The turbulence model ‘KEMODL’ was used in simulation-based on ‘elliptic-staggered’ equation formulation. The numerical findings were then compared with the University of Illinois at Urbana-Champaign (UIUC) data considered a benchmark for such cases.

The turbine blade modified with three airfoils is then imported into the QBlade to optimize and model the large turbine blade rotor in the second phase. A complete analysis of the designed rotor was carried out in QBlade, which includes blade design and optimization with 3D visualization, rotor performance concerning tip speed ratio, turbine performance over a wind speed range, use of blade element momentum (BEM) algorithms, linear lifting line simulations, structural blade design, and analysis. Optimum pitch angle value

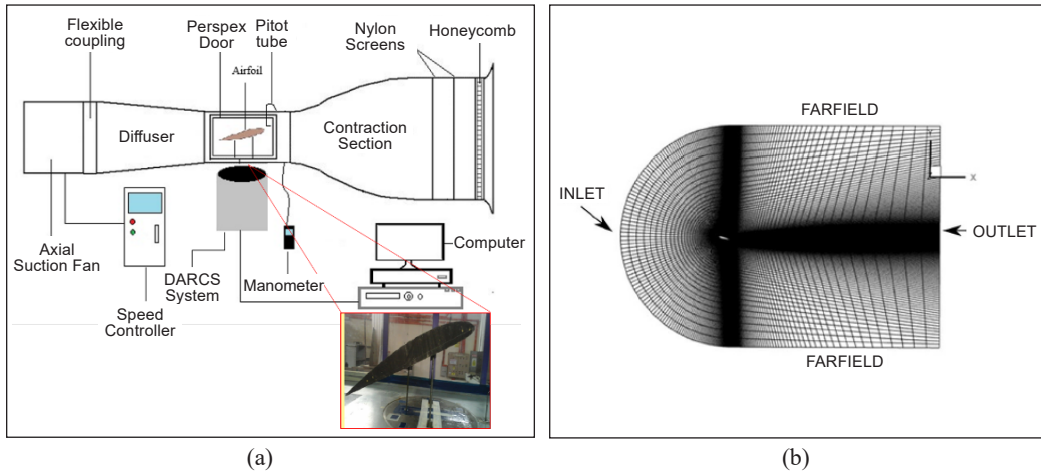


Figure 7. (a) UPM wind tunnel layout and Clark Y model in the test section; (b) C-H type computational domain. Reprinted from (Yan et al., 2019), with the permission of AIP Publishing.

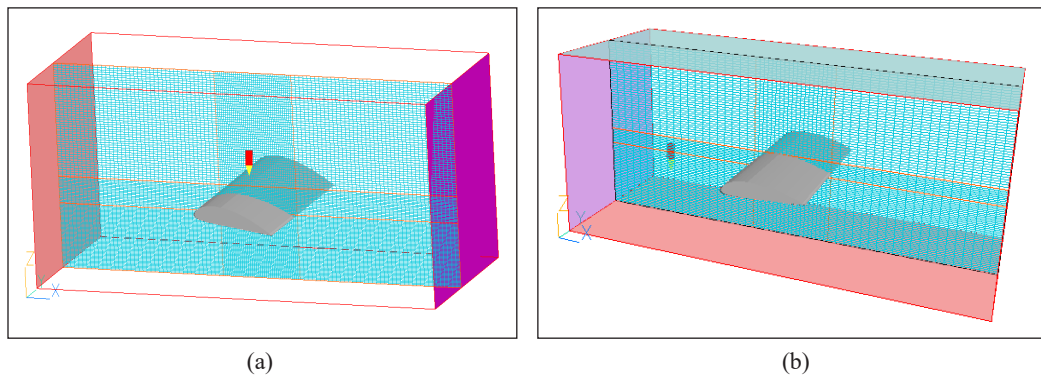


Figure 8. (a) Open wall meshed domain setup; and (b) closed wall meshed domain setup



can be determined based on the lift and drag coefficient values gained from several blade segments (Satwika et al., 2019). It is important to note that the effectiveness of lift force is always more significant than the drag force increase, and also, the addition of a winglet on the tip of the turbine blade gives good performance in low tip speed ratio conditions (Satwika et al., 2019).

Table 1  
*Properties of the selected airfoils used in modeling*

Airfoil	Chord Length	Maximum Thickness	Camber
Clark Y	28%	11%	3.4%
	42%	11%	3.4%
NACA643618	34.7%	17.9%	3.3%
	50.0%	17.9%	3.3%
DU84132V	33.9%	13.6%	3.3%
	45.3%	13.6%	3.1%

## RESULTS AND DISCUSSIONS

### Airfoil Analysis

The effect of velocity and pressure in the airfoil vicinity is clearly shown in pressure and velocity contours obtained from the CFD simulation. It is observed that pressure has both negative and positive values. Negative pressure means that the pressure is lower than the ambient pressure and vice versa. In Figure 9(a), for velocity 7 m/s at a -4 degrees angle of attack, the highest pressure region is found at the upper surface's leading edge. It is also the location of the stagnation point where the local velocity of the fluid ceases. Therefore, the negative pressure region on the airfoil's upper surface is more significant than that on the lower surface.

This change in pressure distribution causes lifts to increase. The maximum pressure at the leading edge is 33.15187 Pa, while the minimum pressure at the trailing edge is 16.24748 Pa, which gives a pressure drag of 16.90439 Pa. The variation in pressure drag depends on the maximum and minimum pressures at leading and trailing edges. The average pressure around the airfoil is between 0 Pa and 3 Pa. Referring to Figure 9(b), for velocity 7 m/s at -4 degrees angle of attack, it is observed that the highest velocity is 8.890738 m/s at the middle of the upper surface and the vicinity of the leading edge of the lower surface. Therefore, in the region of minimum pressure, the velocity is maximum.

The trailing edge velocity is found in the range of 3 to 5, which is still less than the values on the upper and lower surfaces of the airfoil. For velocity 7 m/s at the trim angle of attack, the more significant negative pressure suction at the upper surface can be observed than at the lower surface. The highest pressure is 32.65910 Pa at the leading-edge stagnation point. The velocity contour also shows that velocities of around 4 m/s are found at the

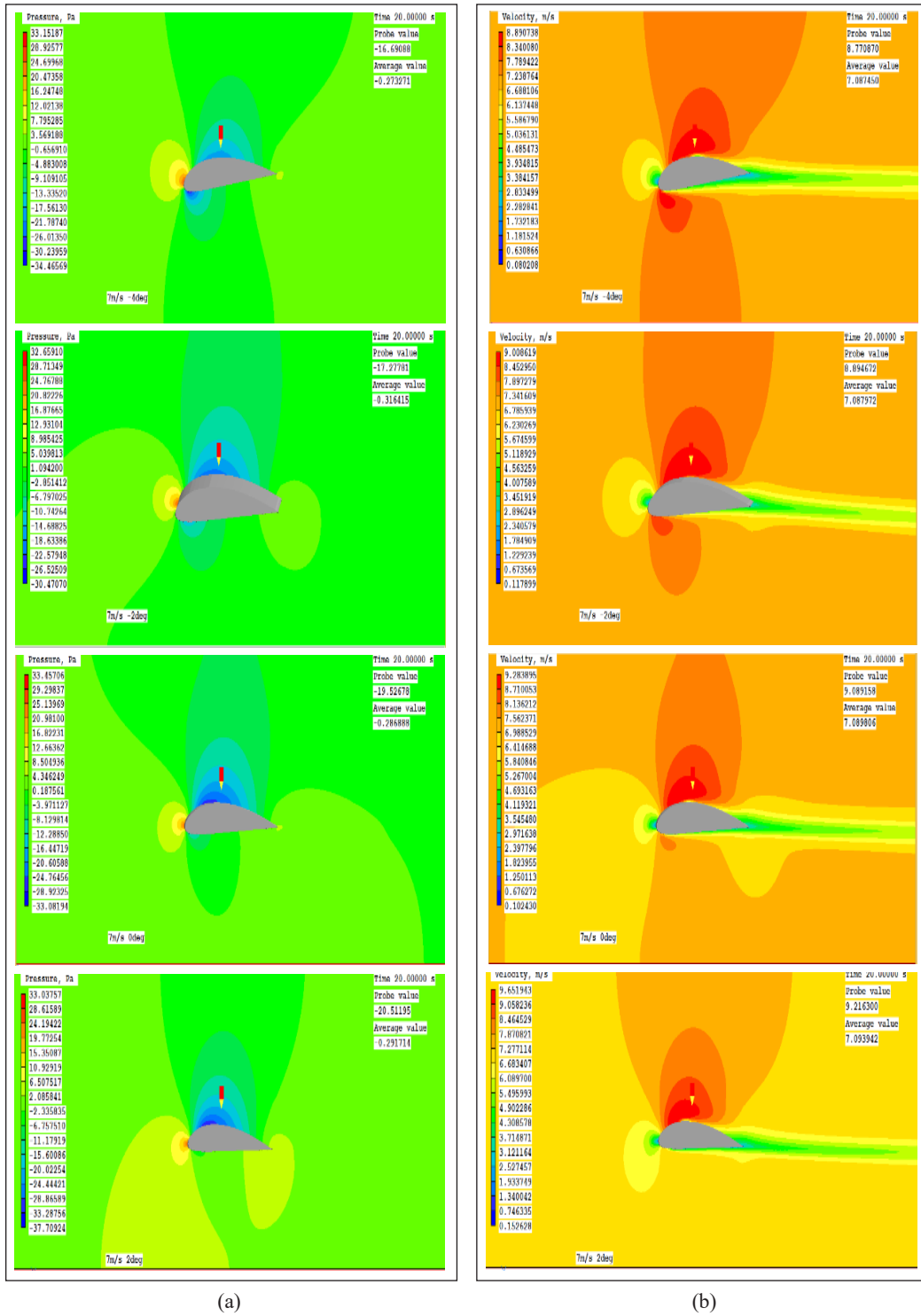


Figure 9. Clark Y airfoil (a) Pressure and (b) Velocity Contours for 7 m/s at -4, -2, 0 and 2 degrees AOA

leading and the trailing edges. The airfoil's upper surface is the highest velocity region with a velocity over 9 m/s due to the lowest pressure gradient. Contours also show the wake production at the back of the airfoil.

For velocity 7 m/s at 2 degrees angle of attack, as the angle of attack increases, the pressure on the upper surface is more significant than that on the lower surface. The pressure suction on the lower surface is smaller than the -4 and -2 degrees angle of attack. The lowest pressure is -33.08194 Pa, whereas most of the pressure in the domain is around 4.346249 Pa. The highest velocity is 9.283895 m/s, and it is found in the upper region of the airfoil.

A velocity value of around 4 m/s is found at both the leading and trailing edges. Referring to Figure 10(a), the lower pressure region under the airfoil disappeared for a velocity of 14 m/s at a -4 degrees angle of attack. The negative pressure suction can be seen only on the upper surface. Two moderate pressure values are observed in front of the airfoil and behind it. The pressure difference becomes high, and so does the pressure drag. The corresponding velocity values are found in the airfoil's upper region, with higher velocity gradients. The difference in velocities on the top and bottom of the airfoil becomes large. When the angle of attack is higher, we can see that the streamlines above the airfoil become denser than those under the airfoil. For velocity 14 m/s at a -2 degrees angle of attack, it can be observed that there is more significant negative pressure suction at the upper surface than that at the lower surface. The highest pressure is 129.8730 Pa occurring at the leading-edge stagnation point. Referring to Figure 10(b), the velocity contour at a -2 degree angle of the attack shows that velocities of around 9 m/s are found at the leading and the trailing edge. The highest velocity is 18 m/s, and it is found in the region of the lowest pressure gradient. For velocity 14 m/s at trim degrees angle of attack, the pressure on the upper surface is more significant than on the lower surface. The lowest pressure is around -88 Pa, whereas most of the domain's pressure is around -14 Pa. The highest velocity is 18.70307 m/s at the upper region of the airfoil.

### Validation of Airfoil Results

Referring to Figures 11(a) and 11(b), at Reynolds number  $2 \times 10^5$ , the CFD results are in good agreement with the experimental data obtained from wind tunnels; the higher the alpha, the larger the lift coefficient. Subsequently, the slopes are almost linear. The data-related lift coefficients obtained from the experiments in the UPM wind tunnel are lower than the values of the UIUC wind tunnel experiment and CFD data with relevancy at angles of attack of -4 to 0 degrees. The lift coefficients of CFD analysis are slightly larger than those of UIUC wind tunnel data. The maximum lift coefficient for UIUC wind tunnel data is 1.309 at an AoA of 12.35 degrees, while that of UPM wind tunnel data is 0.743 at an AoA of 13 degrees.

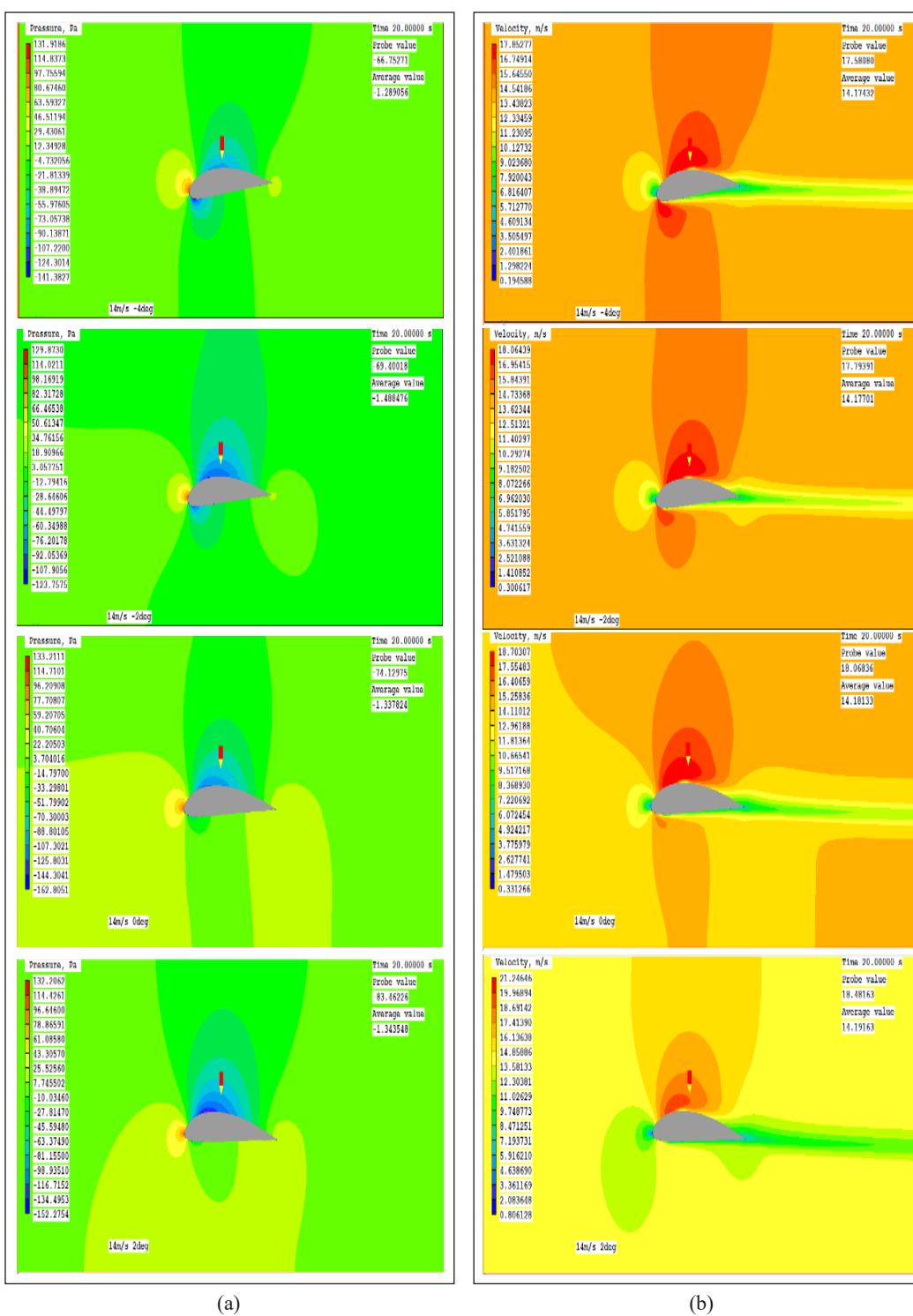


Figure 10. Clark Y airfoil (a) Pressure and (b) Velocity Contours for 14 m/s at -4, -2, 0 and 2 degrees AOA

The CFD analysis gives a maximum lift coefficient of 1.456 at an AoA of 14 degrees. The maximum drag coefficient occurs at AoA of 12.35 degrees, and the value is 0.0225 for the UIUC wind tunnel data. From Figures 11(c) and 11(d), at Reynolds number 399,900, both lift and drag coefficients increase. The maximum lift coefficient is 1.332 at AoA of 12.35 degrees from UIUC wind tunnel data. Thus, for the Coefficient of Drag  $C_D$  versus AoA, all the results from CFD, UIUC, and UPM wind tunnels are in good agreement with each other. The modest discrepancy in lift coefficient between the UPM and UIUC wind tunnels is due to changes in wind tunnel flow quality, measurement methods, model accuracy (i.e., significant uncertainties of parameters and model geometry during the experiment, between all three measurements. This error is also caused by a model mounting limitation, where the brace used to modify the angle of attack passes through the airfoil model, preventing the whole lift force experienced by the airfoil from being appropriately communicated to the transducer. Though this problem is wholly rectified now, this also explains the minimum error from -6 to 0 degrees angle of attack.

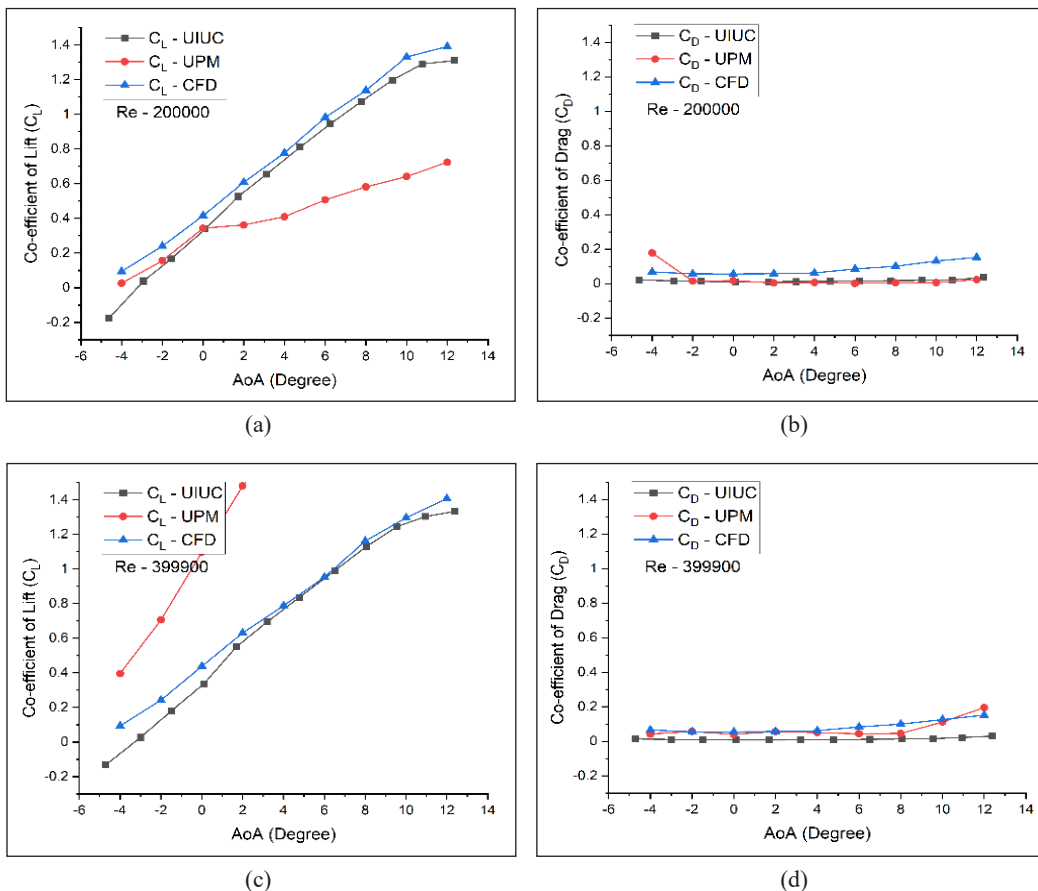


Figure 11. Numerical and experimental comparisons (a) – (b) Coefficients of lift and drag versus AoA at  $Re = 200000$  (c) – (d) Coefficients of lift and drag versus AoA at  $Re = 399900$

### Turbine Rotor Analysis

QBlade is used to design the blade using the selected airfoils listed in Table 1 and the rotor with three blades. The blade geometry optimization was completed in the optimization module. Optimization based on the tip-speed ratio is used in this analysis, rather than the lift-to-drag ratio, which sets the corresponding twist at a specific tip-speed ratio. Therefore, it is necessary to investigate the section solidity that depends on the section chord and should be between 0 and 1 when designing the blade. The Blade Element Momentum algorithm will not converge if any segment solidity increases beyond this range of values. The blade design parameters are given below in Table 2. Computational simulations, using fluid dynamic equations and algorithms, have been widely used to predict, overcome and analyze problems involving fluid flows (Akansu et al., 2017). The blade element momentum theory combined with the lifting line method with guaranteed convergence in QBlade was used for the blade study. The airfoil coordinates were entered into the structural analysis as part of the profile (Barrett & Ning, 2016).

The structural part also takes input from Blade Element Momentum/Lifting Line Theory Analysis.

Table 2  
Wind turbine rotor blade design parameters

Blade Parameter	Value
Rated Power	1.5 – 2.5 MW
No. of Blades	3 blades, upwind
Transmission	Single
Blade radius (m)	42.20
Hub Radius (m)	1
Maximum speed (rpm)	15
Cut-in wind speed (m/s)	3
Cut-out wind speed (m/s)	25
Hub Height (m)	100
Rotor Overhang (m)	7.03

**Rotor BEM and Non-linear Lifting Line Analysis.** A significant advantage of the Lifting Line Theory over the Blade Element Momentum approach is that it is possible to obtain velocity distribution in the flow field around the rotor. In addition, as shown in Figure 12, integrated velocity planes make it possible to access the 3D velocity field information in general.

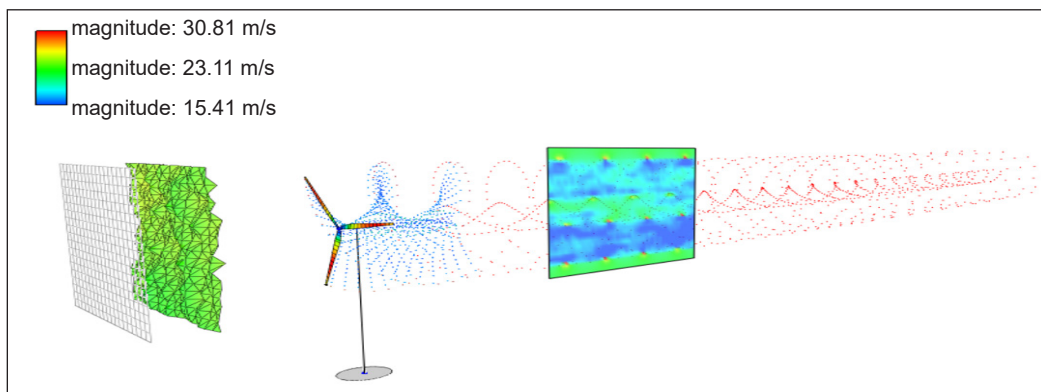


Figure 12. Velocity distribution in the rotor (side view)

A finite number of blade components are discretized into the blade. Two parts connect an element that sweeps the rotor plane on a circular track. The radial location, profile, chord, twist, and length of the blade cross-sections characterize them. It is possible to compute the relative wind speed for every section using momentum theory. Next, the normal and tangential components are calculated with these coefficients and the area of an element, thereby calculating an element's thrust and torque.

The inputs of the various components can then be applied together to obtain the total rotor thrust and torque. For different wind speeds and angular speed ratios, characteristic curves can be helpful. It is important to note that BEM looks at two crucial iteration factors related to the respective blade design for understanding. The relative wind angle  $\theta$  and power of the rotor  $\sigma$  depends on the chord and  $N$  number of the blade (Equation 5).

$$\sigma = \frac{CN}{2\pi r} \quad [5]$$

The relative wind angle depicts the angle of attack, the angle between the chord line, and the relative wind speed experienced by the rotor blade (Equation 6). Figure 13 shows the power in megawatts with the wind speed for the current rotor blade. The optimal rated power is close to 2 MW.

$$\alpha = \theta - (\beta + \gamma) \quad [6]$$

Qblade also can examine blades using lifting line algorithms. As a result, it has an advantage in vortex core modeling, computational efficiency criteria, multi-threading, and wake connectivity monitoring.

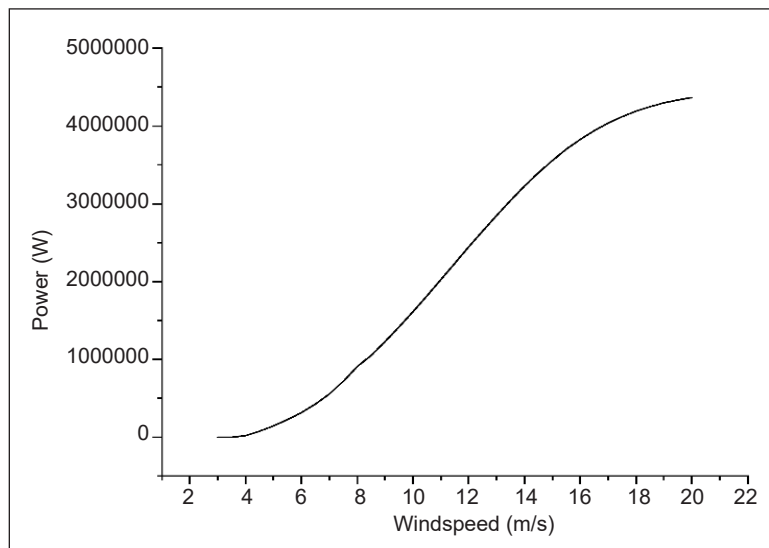


Figure 13. Power versus wind speed for the current analysis

**Structural Blade Design and Analysis.** The Horizontal-Axis Wind Turbine (HAWT) has a rotor with a radius of 42.2 meters and starts at the root tending with a cylindrical shape and progressing to the body and tip using Clark-Y. As a function of the radius, this wind blade often has a pitch to differ, giving it a twist and pitch angle at the blade’s tip. As a result, the strength of the e-glass used on the outer shell determines the blade’s maximum stress. At 15 m/s, a typically rated wind speed for a turbine at this scale, the turbulent wind flows towards the negative z-direction. It is believed that this incoming flow makes the blade rotate around the z-axis.

Therefore, the optimal tip velocity ratio equals 8, a good value for a giant wind turbine and the TSR point at which the power coefficient is maximum.

The GFRP E-Glass, widely used in wind turbine blades, is the material chosen for the other shell construction, and the inner structure is Polymethacrylimide foam (PMI). The material characteristics of each of these are given in Table 3. From the BEM/LLT studies conducted before, QBlade takes each part of the blade’s load values. The blade root is offset by 1.2 meters from the rotation axis. A method for calculating average loads on a wind turbine is given in this study.

Nevertheless, the BEM theory presented several significant steady-state and dynamic effects that trigger increased loads or reduced power output, significantly increased transient loads. In Figure 14, the structural load analysis is shown.

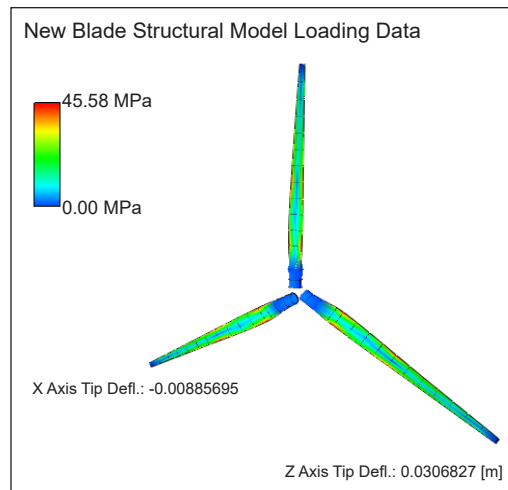


Figure 14. Structural blade modal and deflection analysis

Table 3  
Blade element material properties

Blade Element	Material	Young’s Modulus (GPa)	Density (kg/m <sup>3</sup> )
Blade outer shell	GFRP (E-Glass)	7.2	2580
Blade inner Shell	PMI Foam	0.03 – 0.39	30 - 300

**Validation of Results.** Without validation, the second step of blade design and rotor output analysis cannot be considered successful. Wang et al. (2011) used the same blade configuration (but different airfoils) with rotor diameter and power almost identical to the current study; this was taken as a validation benchmark. For their designed rotor and turbine, Wang et al. (2011) used experimental, CFD, and FVM studies. For the full-scale 3-bladed NH1500 wind turbine, the measurement of both CFD and FVM was performed.



Figure 15 shows their comparison of the power coefficient  $C_p$  with tip-speed ratio (TSR) variance based on experimental performance, CFD measurements, and FVM estimation.

The  $C_p$  versus TSR results from the current study show a reasonably good agreement with Wang et al. (2011) in Figure 16. The overall  $C_p$  was obtained at an optimal TSR of around 9.5, compared to 8.0 in the current study. The mean  $C_p$  for the experiment was 0.492, 0.505 for the CFD calculation, 0.528 for the FVM calculation, and 0.525 for the current analysis. The higher maximum  $C_p$  of both the reference and current research is very similar to the well-known limit of Betz 0.593. The maximum outcome of 0.525 from the study can therefore be persuasive.

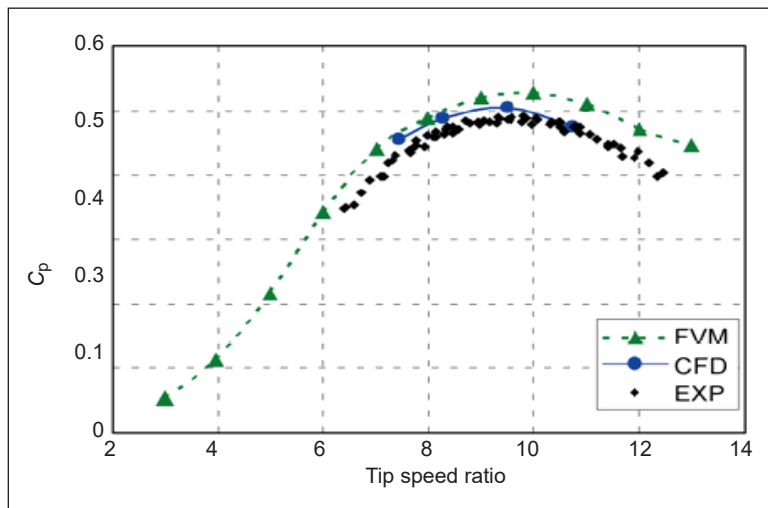


Figure 15. Relation of  $C_p$  with TSR (Wang et al., 2011)

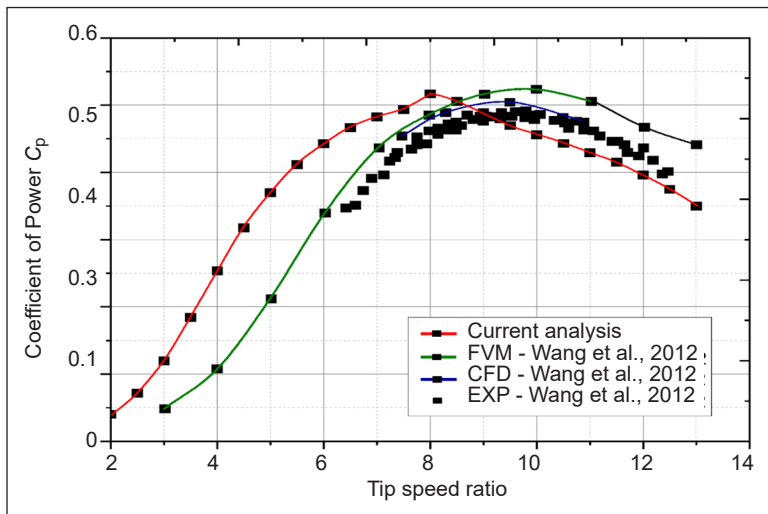


Figure 16.  $C_p$  versus TSR for experimental validation (Wang et al., 2011)

## CONCLUSION

This study designed and checked the performance and brief structural analyses of the Horizontal-Axis Wind Turbine (HAWT) rotor blade. The goal of studying large wind turbine blades at a high Reynolds number with a modified blade design made from three airfoils was fulfilled. Although this is a preliminary study, the outcomes are satisfactory, but it requires more extensive experimentation in the future. The first part of the paper focused on the wind turbine geometry modeling, including the airfoil selection and performance numerically and experimentally using open-circuit wind tunnels. The second part looked at the modified blade design, optimization, and performance analysis based on Blade Element Moment Theory and Lifting Line Theory using Qblade and later on validation with the experimental results. Aerodynamic equations based on selected parameters and the efficiency of selected airfoils determine a practical blade shape, according to the current study on blade design. Aesthetics has a small part to play.

The most efficient shape is made up of airfoil parts that increase in width, thickness and twist angle as they approach the hub. The paper demonstrated that the chosen 1.5–2.5 MW turbine with a diameter of more than 80 m and a hub height of 100 m has an optimal power coefficient of 0.525 at a tip speed ratio of 8, which is an excellent value for large wind turbines with this modified design. Aeroelastic uncertainty is always associated with large and flexible wind turbine blades that need thorough analysis and could be valuable to future study. The displacement of the blade tip at the nominal wind speed reduces the turbine's rated power. In the future, it is observed that the use of intensive computational BEM/LLT, fluid-structure interaction, and CFD studies with experimental analysis for new designs will help to analyze the giant wind turbine performance in detail.

## ACKNOWLEDGEMENTS

The authors gratefully acknowledge the contributions of FAAS ENGINEERING AND CONSULTANCY SDN. BHD in providing opportunities to flourish and make engineering and energy-related research a reality through grant no: 6300248. The authors would also like to convey their gratitude to UPM for providing the necessary facilities required for this research work.

## REFERENCES

- Akansu, S. O., Dagdevir, T., & Kahraman, N. (2017). Numerical investigation of the effect of blade airfoils on a vertical axis wind turbine. *Isi Bilimi Ve Teknigi Dergisi/ Journal of Thermal Science and Technology*, 37(1), 115-125.
- Albuquerque, I., & Matos, F. (2016). A characterization of vertical axis wind turbines. *IEEE Latin America Transactions*, 14(10), 4255-4260. <https://doi.org/10.1109/tla.2016.7786302>

- Barrett, R., & Ning, A. (2016). Comparison of airfoil precomputational analysis methods for optimization of wind turbine blades. *IEEE Transactions on Sustainable Energy*, 7(3), 1081-1088. <https://doi.org/10.1109/tste.2016.2522381>
- Farhan, A., Hassanpour, A., Burns, A., & Motlagh, Y. G. (2019). Numerical study of effect of winglet planform and airfoil on a horizontal axis wind turbine performance. *Renewable Energy*, 131, 1255-1273. <https://doi.org/10.1016/j.renene.2018.08.017>
- Hafeez, N., Badshah, S., Badshah, M., & Khalil, S. J. (2019). Effect of velocity shear on the performance and structural response of a small-scale horizontal axis tidal turbine. *Marine Systems & Ocean Technology*, 14(2-3), 51-58. <https://doi.org/10.1007/s40868-019-00057-0>
- Jin, J. Y., Virk, M. S., Hu, Q., & Jiang, X. (2020). Study of ice accretion on horizontal axis wind turbine blade using 2D and 3D numerical approach. *IEEE Access*, 8, 166236-166245. <https://doi.org/10.1109/access.2020.3022458>
- Kim, S. H., & Suh, K. (2019). Experimental and numerical investigation on power characteristics of 300 W class horizontal axis wind turbine with wave winding type AFPM generator. *International Journal of Precision Engineering and Manufacturing-Green Technology*, 7(4), 837-848. <https://doi.org/10.1007/s40684-019-00160-y>
- Kumar, P. M., Seo, J., Seok, W., Rhee, S. H., & Samad, A. (2019). Multi-fidelity optimization of blade thickness parameters for a horizontal axis tidal stream turbine. *Renewable Energy*, 135, 277-287. <https://doi.org/10.1016/j.renene.2018.12.023>
- Li, L., Li, Y., Liu, Q., & Lv, H. (2014). A mathematical model for horizontal axis wind turbine blades. *Applied Mathematical Modelling*, 38(11-12), 2695-2715. <https://doi.org/10.1016/j.apm.2013.10.068>
- Navinkumar, B., Parammasivam, K., Rajendran, S., & Mohanavel, V. (2021). CFD analysis of horizontal axis wind turbine braking system using chordwise spacing. *Materials Today: Proceedings*, 37, 542-552. <https://doi.org/10.1016/j.matpr.2020.05.564>
- Pinto, M. L., Franzini, G. R., & Simos, A. N. (2020). A CFD analysis of NREL's 5MW wind turbine in full and model scales. *Journal of Ocean Engineering and Marine Energy*, 6(2), 211-220. <https://doi.org/10.1007/s40722-020-00162-y>
- Revaz, T., Lin, M., & Porté-Agel, F. (2020). Numerical framework for aerodynamic characterization of wind turbine airfoils: Application to miniature wind turbine WiRE-01. *Energies*, 13(21), Article 5612. <https://doi.org/10.3390/en13215612>
- Santo, G., Peeters, M., Van Paepegem, W., & Degroote, J. (2019). Dynamic load and stress analysis of a large horizontal axis wind turbine using full scale fluid-structure interaction simulation. *Renewable Energy*, 140, 212-226. <https://doi.org/10.1016/j.renene.2019.03.053>
- Satwika, N. A., Hantoro, R., Sarwono, S., & Nugroho, G. (2019). The experimental investigation and numerical analysis on horizontal axis wind turbine with winglet and pitch variations. *Engineering Journal*, 23(6), 345-360. <https://doi.org/10.4186/ej.2019.23.6.345>
- Sudhamshu, A. R., Pandey, M. C., Sunil, N., Satish, N. S., Mugundhan, V., & Velamati, R. K. (2016). Numerical study of effect of pitch angle on performance characteristics of a HAWT. *Engineering Science and Technology, an International Journal*, 19(1), 632-641. <https://doi.org/10.1016/j.jestech.2015.09.010>

- Wang, T., Wang, L., Zhong, W., Xu, B., & Chen, L. (2011). Large-scale wind turbine blade design and aerodynamic analysis. *Chinese Science Bulletin*, 57(5), 466-472. <https://doi.org/10.1007/s11434-011-4856-6>
- Yan, Y., Avital, E., Williams, J., & Cui, J. (2019). CFD analysis for the performance of micro-vortex generator on aerofoil and vertical axis turbine. *Journal of Renewable and Sustainable Energy*, 11(4), Article 043302. <https://doi.org/10.1063/1.5110422>
- Yang, Y. K., Kim, M. Y., Song, Y. W., Choi, S. H., & Park, J. C. (2020). Windcatcher louvers to improve ventilation efficiency. *Energies*, 13(17), Article 4459. <https://doi.org/10.3390/en13174459>
- Ye, Z., Wang, X., Chen, Z., & Wang, L. (2020). Unsteady aerodynamic characteristics of a horizontal wind turbine under yaw and dynamic yawing. *Acta Mechanica Sinica*, 36(2), 320-338. <https://doi.org/10.1007/s10409-020-00947-2>

## Acceptance Ratio Analysis in Grid-Connected Photovoltaic System: Is There Any Difference Between DC and AC?

Fatin Azirah Mohd Shukor<sup>1</sup>, Hedzlin Zainuddin<sup>1,2\*</sup>, Jasrul Jamani Jamian<sup>3</sup>, Nurmalessa Muhammad<sup>1,2</sup>, Farah Liyana Muhammad Khir<sup>1,2</sup> and Noor Hasliza Abdul Rahman<sup>2,4</sup>

<sup>1</sup>Faculty of Applied Sciences, Universiti Teknologi MARA, 40450 UiTM, Shah Alam, Selangor, Malaysia

<sup>2</sup>Faculty of Applied Sciences, SPECTRA Research Interest Group, Universiti Teknologi MARA, 40450 UiTM, Shah Alam, Selangor, Malaysia

<sup>3</sup>Faculty of Engineering, Universiti Teknologi Malaysia, 81310 UTM, Johor Bahru, Johor, Malaysia

<sup>4</sup>College of Engineering, Universiti Teknologi MARA, Cawangan Johor, Kampus Pasir Gudang, 81750 UiTM, Masai, Johor, Malaysia

### ABSTRACT

The performance status of a grid-connected photovoltaic (GCPV) system is denoted by performance indices, namely performance ratio, capacity factor, and even through power acceptance ratio (AR), as documented in Malaysia Standard (MS) procedures for acceptance test of GCPV testing and commissioning (TNC). Even though AR analysis can be either on the DC or AC side, the MS TNC procedures implemented analysis on the AC side. Therefore, the question arises whether there is any significant difference when using AC AR analysis compared to DC AR analysis in evaluating the system performance. Thus, this paper evaluates the differences between applying DC AR analysis and AC AR analysis in accessing the performance of the ten kW<sub>p</sub> GCPV system in Malaysia. The AR analytical analysis employed the 2019 one-year historical data of solar irradiance,

module temperature, DC power, and AC power. The results demonstrated that the monthly AC AR were consistently lower than DC AR with a percentage difference of approximately 3%. The percentage discrepancy was due to the variation of actual inverter efficiencies compared to the declared constant value by the manufacturer used in the AR prediction model. These findings have verified a significant difference between DC AR analysis and AC AR

### ARTICLE INFO

#### Article history:

Received: 21 May 2021

Accepted: 13 October 2021

Published: 14 December 2021

DOI: <https://doi.org/10.47836/pjst.30.1.12>

#### E-mail addresses:

azirahshukor@gmail.com (Fatin Azirah Mohd Shukor)

hedzl506@uitm.edu.my (Hedzlin Zainuddin)

jasrul@utm.my (Jasrul Jamani Jamian)

nurmalessa@uitm.edu.my (Nurmalessa Muhammad)

farah668@uitm.edu.my (Farah Liyana Muhammad Khir)

noorhasliza@uitm.edu.my (Noor Hasliza Abdul Rahman)

\* Corresponding author

analysis. Most importantly, this study has highlighted the significance of AC AR analysis compared to DC AR analysis as a tool to evaluate GCPV system performance because AC AR has taken an additional factor into consideration, which is the inverter efficiency variation.

*Keywords:* AC acceptance ratio, DC acceptance ratio, grid-connected photovoltaic (GCPV), inverter efficiency, performance

---

## INTRODUCTION

A photovoltaic (PV) energy system is widely used to generate energy by converting sunlight into electrical energy. PV systems can be divided into three types, which are grid-connected (GC), off-grid (OG), and hybrid systems (Appiah et al., 2019; Khatib et al., 2017). Monitoring the output power generated by the PV system is necessary to ensure the shortest return-on-investment (ROI), reduce maintenance costs, and extend the PV system's lifetime. Besides, monitoring PV system's performance is required as the output power generated by a PV system might be reduced due to several factors, such as heat effect, light input, accumulation of dirt, and aging factor (Yusoff et al., 2017). There were also studies conducted on partial shading (Humada et al., 2014) and dirt accumulation due to high pollution in the city center of Krakow, Poland (Jaszczur et al., 2019).

A few performance parameters were introduced in international standard of IEC 61724 for monitoring the PV system, including final yield, performance ratio, efficiency, and capacity factor (OFA, 2010; IEC TS 61724, 2016). Final yield is defined as a ratio of total AC energy output by the PV system during a specific period to the nominal power of the installed PV system; meanwhile, performance ratio represents the overall losses effect on the power output of a PV system (Wittkopf et al., 2012). Unlike the final yield and performance ratio, efficiency represents the net conversion efficiency of a PV module, PV system, and inverter, while capacity factor is the comparison of actual energy to the predicted energy generated by the PV system (Nurdiana et al., 2020).

In Southeast Asia, numerous studies on the performance evaluation of GCPV systems have been reported (Hussin et al., 2013; Nurdiana et al., 2020; Wittkopf et al., 2012). Analytical performance of a 142.5 kW<sub>p</sub> rooftop GCPV system using polycrystalline Silicon (p-Si) in Singapore was carried out by (Wittkopf et al., 2012). The performance ratio was about 81%, while the final yield and PV module efficiency were 3.12 kWh/kW<sub>p</sub> and 11.8%, respectively. In Serpong, Indonesia, a study conducted by Nurdiana et al. (2020) showed that the performance ratio was 82.42%, with the average value of the final yield, 3.38 kWh/kW<sub>p</sub>/d. Meanwhile, the average values of the PV module efficiency, system efficiency, inverter efficiency, and capacity factor were 15.29%, 14.77%, 96.63%, and 14.07%, respectively, during the eight-month monitoring period. Another study on the performance of a GCPV system was reported by Hussin et al. (2013). Three GCPV

systems of different PV module technologies (monocrystalline, polycrystalline, and thin-film) installed in Selangor, Malaysia, were used for the analysis. The results showed that the performance ratios for monocrystalline, polycrystalline, and thin-film PV modules were 81.0%, 78.2%, and 94.6% respectively. Besides, the study found that thin-film PV modules exhibit higher energy production, reliability, and conversion efficiency in Malaysia (Hussin et al., 2013).

In the tropical region of Malaysia, the Acceptance Ratio (AR) is one of the parameters used to evaluate the GCPV system under the system acceptance procedure for testing and commissioning (TNC). AR is known as a ratio of actual power to predicted power. According to Malaysian Standard (MS2692:2020), a benchmark range of AR equal to 0.9 up to 1.3 has been documented as the requirement for a GCPV system to be accepted in the TNC procedure (SIRIM, 2020). Notably, the TNC acceptance procedure for designated AR is the AC AR, which utilizes AC power (output power from the inverter) inside the developed mathematical equation instead of DC power.

Several existing studies have shown a relationship between AC AR with failure detection in the GCPV system (Muhammad et al., 2019; Shukor et al., 2021). Firstly, an algorithm comprised of failure detection on AC power by using AR determination (AC AR) has been developed (Muhammad et al., 2019). The analysis was conducted on two GCPV systems of different PV module technologies, polycrystalline and monocrystalline, installed under the tropical climate of Malaysia. The minimum AR threshold of 0.9 introduced in the Malaysian Standard was used as a benchmark in the analysis to identify a fault-free and a failure GCPV system. The result showed that a fault-free GCPV system recorded 31.4% of  $AR < 0.9$ ; meanwhile, a failure GCPV system demonstrated 93.38% of  $AR < 0.9$ . Thus, the study has highlighted the utilization of AR analysis as a significant early fault indicator for PV systems (Muhammad et al., 2019).

Another similar study that used AC AR as an early failure indicator in the GCPV system was reported by Shukor et al. (2021). The analysis was conducted on three GCPV systems installed at different locations in Malaysia. It was found that System 1 under investigation showed an early failure symptom where the cumulative percentage of  $AR < 0.9$  ranges between 34% to 71%, meanwhile System 2 and 3 were identified as fault-free GCPV systems with cumulative percentage  $AR < 0.9$  ranging from 5% until 19% (Shukor et al., 2021). Likewise, a study was also conducted on failure detection at the PV array level, which involved DC AR (Kim et al., 2021). The study proposed that DC AR must range between 0.93 until 1.02 for a normal operating condition. Otherwise, the system will be identified as a failure. In addition, various type of failure was diagnosed from this study, such as series, parallel and total failure. These identified failures were the factors that led to the decrease in the electrical output of the system (Kim et al., 2021).

From the literature on AR, numerous studies have focused on AC power analysis; meanwhile, there were also studies conducted on DC power analysis that would eventually

lead to the determination of DC AR and AC AR. However, an issue arises on whether there is any significant difference between these two ratios to evaluate the performance of a GCPV system. Therefore, this study aims to evaluate the percentage discrepancy of DC AR compared to AC AR analysis in evaluating the performance of a GCPV system.

From this point onwards, this study will be elucidated through three sections: methodology, results, discussions, and conclusion. The methodology section contains the information of the selected GCPV system, detailed descriptions of the PV module and inverter used in the studies. A flowchart for DC and AC AR analysis with their explanation is also included in this section. The following section, which is results and discussions, presents the discrepancy in the form of percentage differences between DC and AC AR. Finally, the last section draws out the conclusion for the whole study.

## METHODOLOGY

### System Descriptions

The study was performed for a ten kW<sub>p</sub> GCPV system installed on the rooftop with an inclination angle of 30°. The system was installed and commissioned in December 2015 under the Feed-in-Tariff (FiT) scheme, an initiative introduced by the Government of Malaysia (GoM). The general information of the system is tabulated in Table 1.

Table 1  
*General information of selected GCPV system*

Subjects	Descriptions
Location	Terengganu, Malaysia
Latitude and Longitude	5.2077° N and 103.2049° E
Nominal array power	10 kW <sub>p</sub>
Mounting type	Retrofitted (RF)

### PV Module and Inverter Descriptions

The GCPV system comprises polycrystalline PV modules connected to an inverter. The related specifications are as described in Table 2.

Table 2  
*PT-P660250WB module and Blueplanet 9.0 TL3 specification*

	Specification
PV technology	Polycrystalline
PV module model	PT-P660250WB
Maximum power, P <sub>mod_STC</sub>	250 W
Module efficiency, $\eta_{PV}$	15.37%
Inverter model	Blueplanet 9.0 TL3
Nominal power, P <sub>nom</sub>	9000 W
Inverter efficiency, $\eta_{inverter}$	98.30 %



A few other components were connected to the GCPV system, such as a module temperature sensor, ambient temperature sensor, relative humidity sensor, and pyranometer. A data logger (WebBox) was also installed at the inverter to record the system’s DC and AC power output and the data coming from the sensors. Each data was recorded in every 5 minutes interval consecutive per day. In addition, historical data of DC and AC power output ( $P_{DC\_actual}$  and  $P_{AC\_actual}$ ), solar irradiance, and module temperature from 1 January 2019 to 31 December 2019 were collected for further analysis.

### DC and AC AR Analysis

This section presents the methodology applied for AR analysis between DC and AC. A flow of work is presented in Figure 1.

First, a few parameters, such as solar irradiance, module temperature, DC and AC power output ( $P_{DC\_actual}$  and  $P_{AC\_actual}$ ), were extracted from the data logger meanwhile  $P_{DC\_predict}$  and  $P_{AC\_predict}$  were obtained through a mathematical model as shown in Equations 1 and 2 (SEDA, 2016):

$$P_{DC\_predict} = P_{mod\_STC} \times N_T \times f_g \times f_{temp} \times f_{mm} \times f_{age} \times f_{dirt} \times \eta_{cable} \quad (1)$$

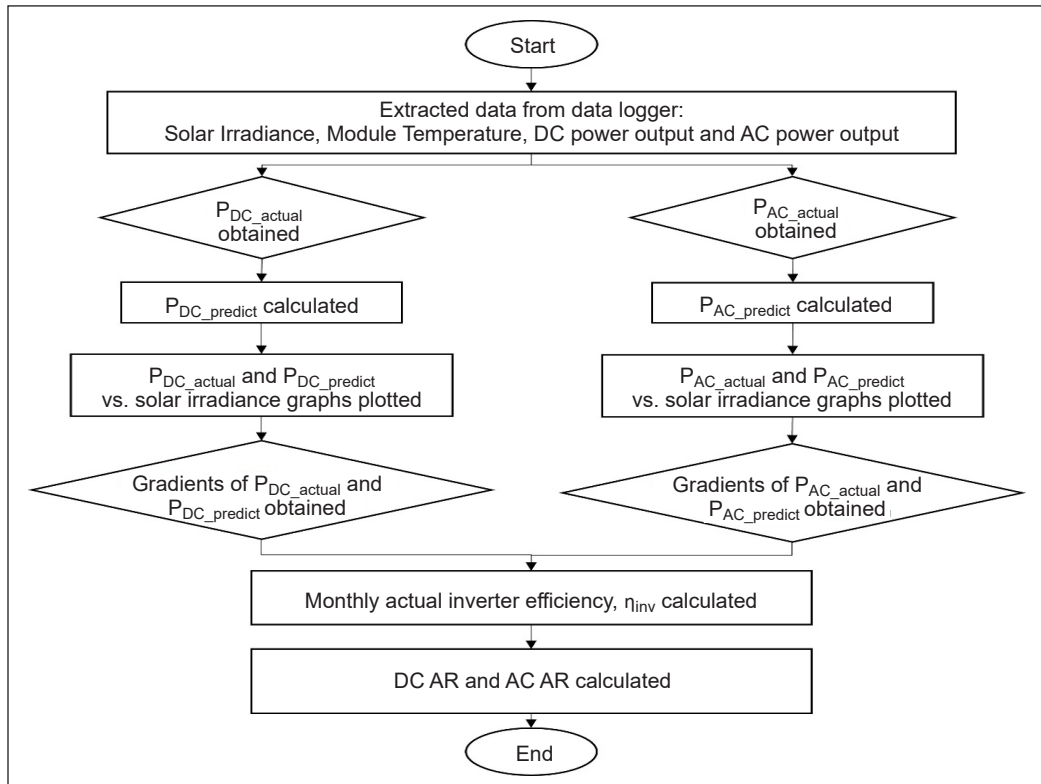


Figure 1. A flowchart of DC AR and AC AR analysis in the GCPV system

For  $P_{AC\_predict}$ :

$$P_{AC\_predict} = P_{mod\_STC} \times N_T \times f_g \times f_{temp} \times f_{mm} \times f_{age} \times f_{dirt} \times \eta_{cable} \times \eta_{inverter} \quad (2)$$

Where  $P_{mod\_STC}$  is the maximum power of a PV module at Standard Test Condition, STC (W).  $N_T$  is the total amount of PV modules. Next,  $f_g$  is the peak sun factor, which can be calculated using Equation 3:

$$f_g = \frac{G}{G_{STC}} \quad (3)$$

Where the solar irradiance at the instant time,  $G$  ( $Wm^{-2}$ ), is divided by the solar irradiance at STC,  $G_{STC}$  rated at  $1 \text{ kWm}^{-2}$ . The value of the temperature coefficient factor for power,  $f_{temp}$ , can be determined based on Equation 4.

$$f_{temp} = 1 + \left[ \left( \frac{\% \gamma_{pmp}}{100} \right) \times (T_m - 25) \right] \quad (4)$$

Where  $\gamma_{pmp}$  is the temperature coefficient of power ( $\%/^{\circ}C$ ), and  $T_m$  is the temperature of the PV module ( $^{\circ}C$ ).

Table 3 shows the parameters and references related to the determination of other de-rating factors.

Table 3  
*Determination of de-rating factors*

Parameters	References
Module mismatch, $f_{mm}$	Module datasheet
Aging factor, $f_{age}$	Module datasheet / Duration of PV system installation
Dirt factor, $f_{dirt}$	0.97 (Marion et al., 2005)
Efficiency of cable, $\eta_{cable}$	0.97 (Marion et al., 2005)
Efficiency of inverter, $\eta_{inv}$	Inverter datasheet (refer Table 2)

Next, monthly DC power graphs ( $P_{DC\_actual}$  and  $P_{DC\_predict}$ ) and AC power ( $P_{AC\_actual}$  and  $P_{AC\_predict}$ ) were plotted and analyzed. The linear equation and Pearson correlation coefficient ( $R^2$ ) were also determined. Finally, the gradients obtained from the linear equations were tabulated. Monthly actual inverter efficiency, DC, and AC AR with their respective percentage differences were also calculated and discussed in the next section.

## RESULTS AND DISCUSSIONS

For this study, the data of actual DC and AC power output for the system was collected in 2019. It is best to note that the data used were recorded every 5 minutes because a shorter

time interval (15 minutes or less) will have minor errors than hourly-averaged data (Hansen et al., 2012). These data were then analyzed by using Excel and Matlab software. Figures 2 until 13 show that the red and blue data markers represent the actual and predicted DC and AC power, respectively. Meanwhile, yellow and green lines refer to the linear regression line for actual and predicted data.

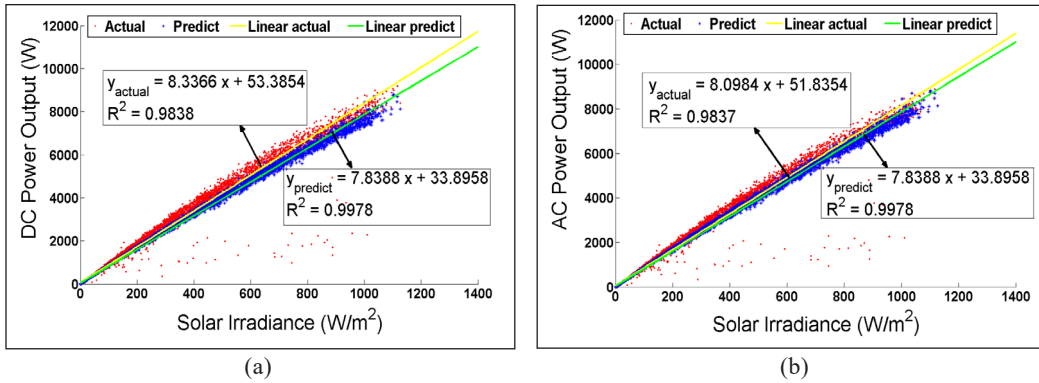


Figure 2. Power output versus solar irradiance in January 2019 for (a) DC power and (b) AC power

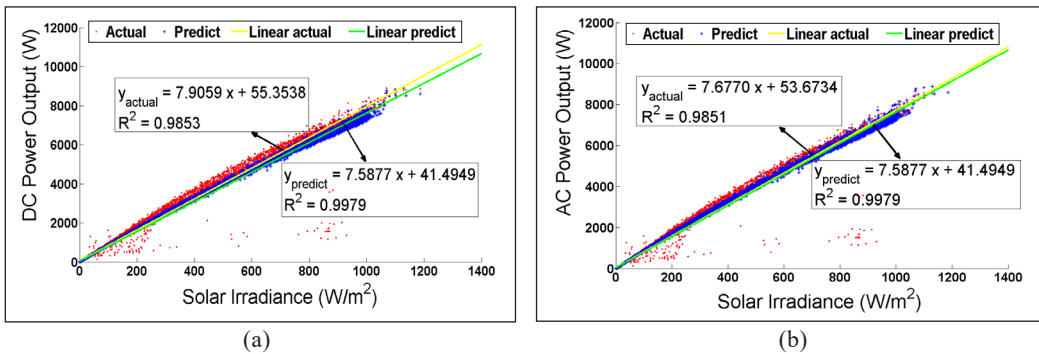


Figure 3. Power output versus solar irradiance in February 2019 for (a) DC power and (b) AC power

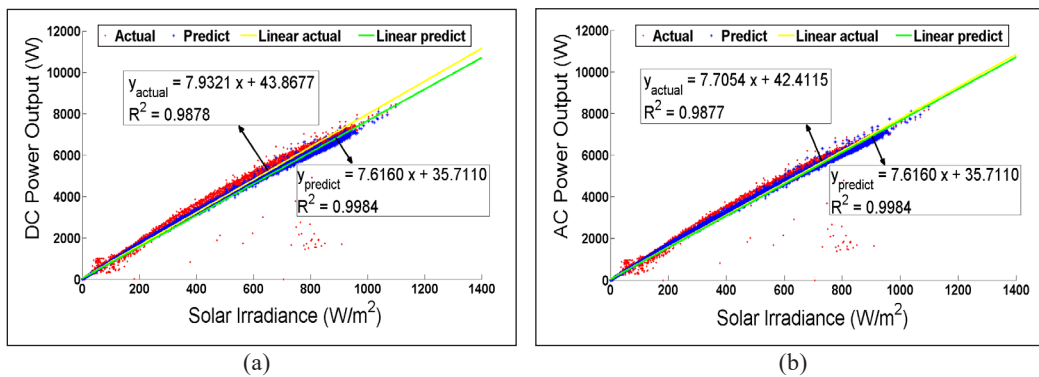


Figure 4. Power output versus solar irradiance in March 2019 for (a) DC power and (b) AC power

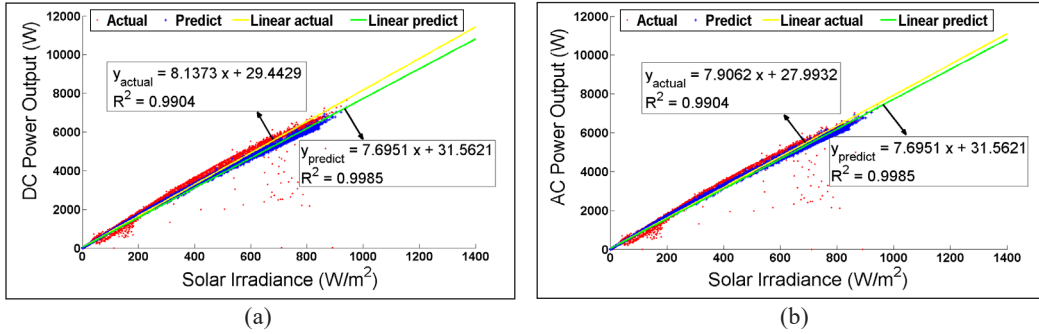


Figure 5. Power output versus solar irradiance in April 2019 for (a) DC power and (b) AC power

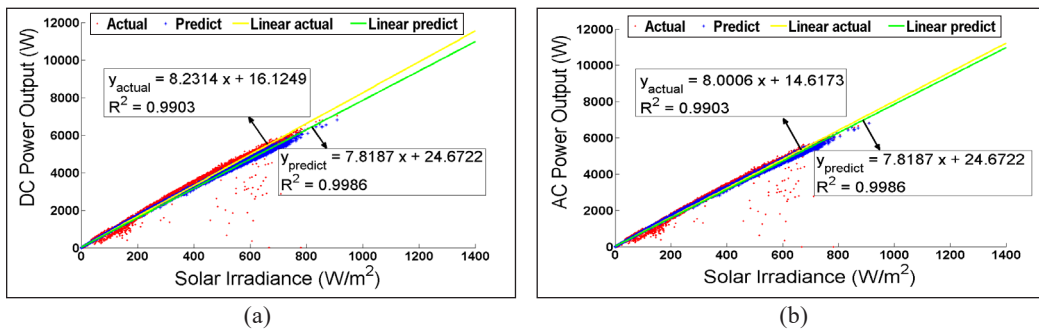


Figure 6. Power output versus solar irradiance in May 2019 for (a) DC power and (b) AC power

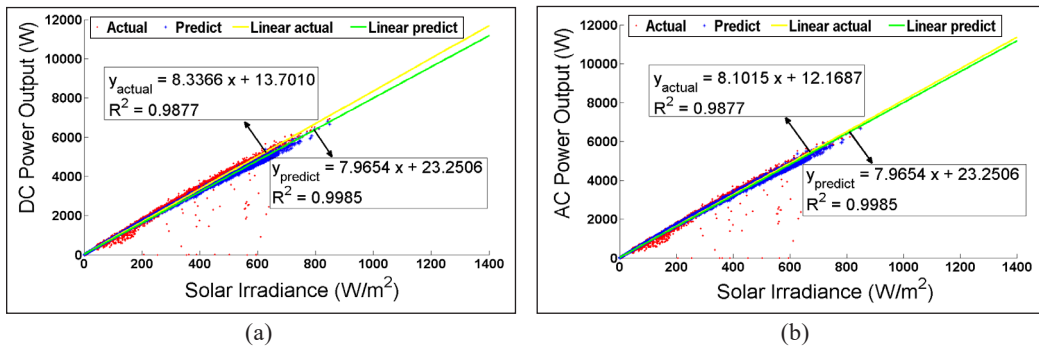


Figure 7. Power output versus solar irradiance in June 2019 for (a) DC power and (b) AC power

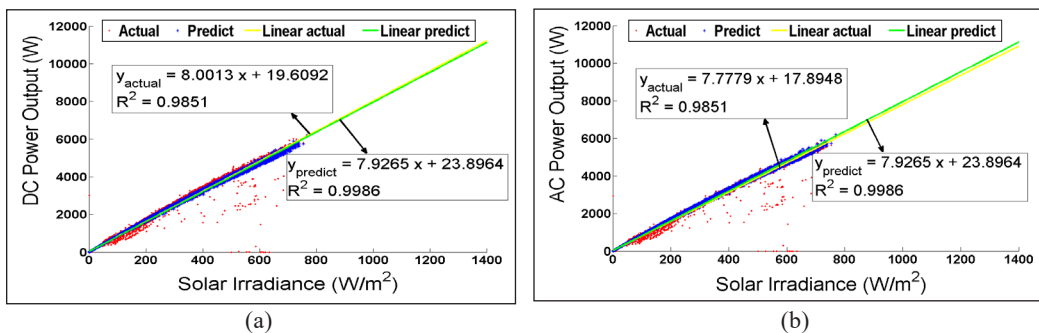


Figure 8. Power output versus solar irradiance in July 2019 for (a) DC power and (b) AC power

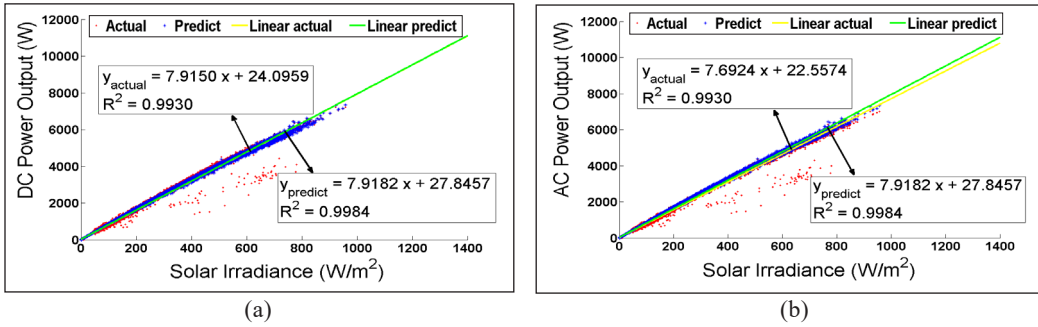


Figure 9. Power output versus solar irradiance in August 2019 for (a) DC power and (b) AC power

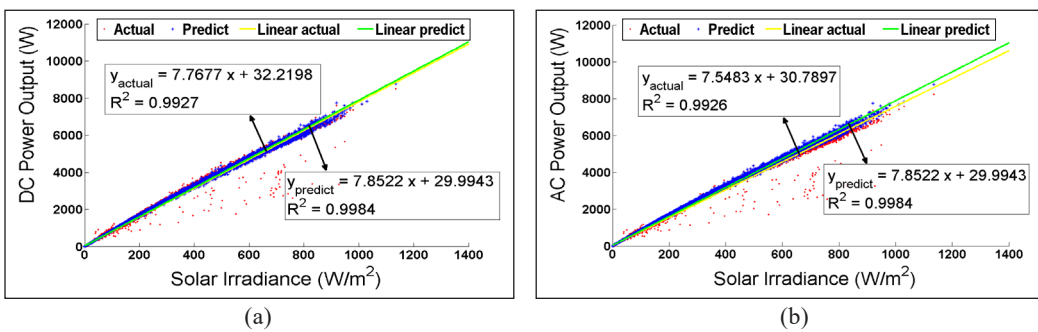


Figure 10. Power output versus solar irradiance in September 2019 for (a) DC power and (b) AC power

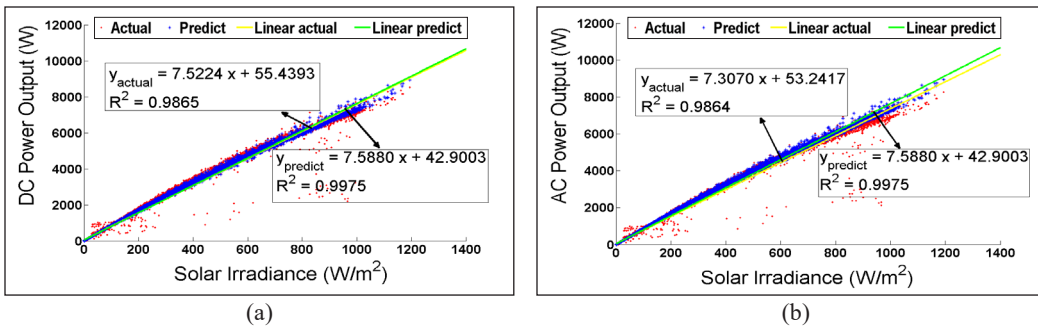


Figure 11. Power output versus solar irradiance in October 2019 for (a) DC power and (b) AC power

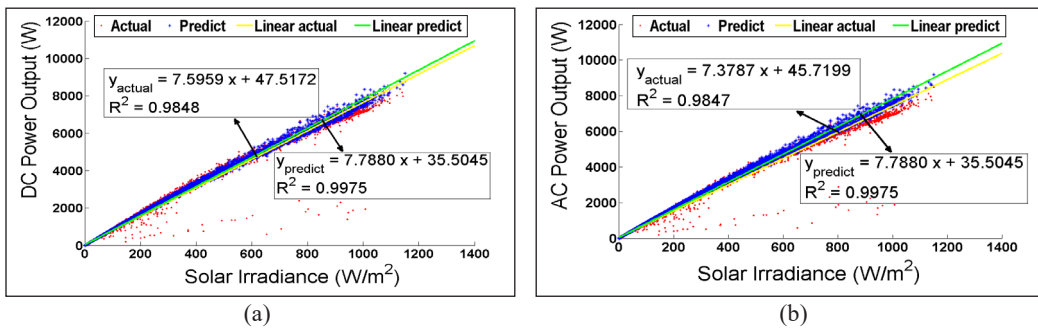


Figure 12. Power output versus solar irradiance in November 2019 for (a) DC power and (b) AC power

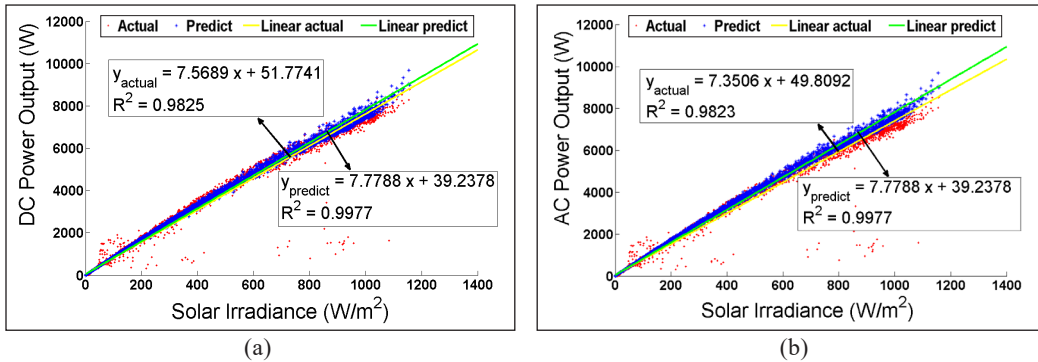


Figure 13. Power output versus solar irradiance in December 2019 for (a) DC power and (b) AC power

For DC power analysis, it can be observed that the predicted DC power ( $P_{DC\_predict}$ ) is slightly lower than the actual DC power ( $P_{DC\_actual}$ ) in the month January until June 2019, as shown in Figures 2 (a), 3(a), 4(a), 5(a), 6(a), and 7(a). It is proposed that some of the de-rating factors for output power were underpredicted, causing slightly lower predictions. It is also interesting to observe that the  $P_{DC\_actual}$  and  $P_{DC\_predict}$  graphs have a good agreement as to the solar irradiance increases from July to December, as shown in Figures 8(a), 9(a), 10(a), 11(a), 12(a), and 13(a). It is suggested that based on the data, the system is working properly. However, several of the  $P_{DC\_actual}$  and  $P_{AC\_actual}$  were observed to be abnormally low despite relatively high solar irradiance (in each month of the year 2019), and they fluctuated from the prediction. Lower power production at high solar irradiance might be due to recorded data inside cloud server storing not being synchronized with the actual measurement generated by the inverter (Platon et al., 2015).

For AC power analysis, the predicted AC power ( $P_{AC\_predict}$ ) was observed to be slightly lower than the actual AC power ( $P_{AC\_actual}$ ) in January 2019, as illustrated in Figure 2(b). It is found that some of the de-rating factors were underpredicted, same as for DC power. Starting from February until August, the graphs of AC power ( $P_{AC\_predict}$  and  $P_{AC\_actual}$ ) are quite aligned, as shown in Figures 3(b), 4(b), 5(b), 6(b), 7(b), 8(b), and 9(b). On the contrary,  $P_{AC\_actual}$  were underpredicted from September until December 2019, as depicted by Figures 10(b), 11(b), 12(b), and 13(b).

Some  $P_{DC\_actual}$  and  $P_{AC\_actual}$  values were recorded as zero from March until July 2019 (Figures 4 until 8). Based on the anomaly observed, we proposed that the anomaly resulted from a system technical problem. Thus, an in-depth investigation needs to be done in the future to understand the root cause of the anomaly.

Table 4 shows the monthly values for actual inverter efficiency, DC, and AC AR with their percentage differences from January until December 2019 of the installed GCPV system. From Table 4, the monthly inverter efficiency can be determined by calculating the ratio of actual measurements between  $P_{AC\_actual}$  (output power from the inverter) to  $P_{DC\_actual}$  (input power to the inverter), expressed by the following Equation 5:

$$\eta_{inv} = \frac{P_{AC\_actual}}{P_{DC\_actual}} \approx \frac{\text{gradient of } P_{AC\_actual}}{\text{gradient of } P_{DC\_actual}} \tag{5}$$

From the calculation, the maximum and minimum  $\eta_{inv}$  were recorded as 97.21% and 97.10%, respectively (Table 4). Therefore, the average monthly actual inverter efficiency of the system,  $\eta_{inv}$ , was 97.16% compared to 98.30%, which is the maximum  $\eta_{inv}$  declared by the manufacturer. These findings prove that the inverter is not working at a constant maximum of 98.30% efficiency, but the actual efficiency varies and is slightly lower than 98.30% on average during the operation.

Table 4  
Average monthly inverter efficiency with DC AR and AC AR

Month	Gradient, m				Monthly actual inverter efficiency, $\eta_{inv}$ (%)	AR		Percentage differences of AR (%)
	$P_{DC\_predict}$	$P_{DC\_actual}$	$P_{AC\_predict}$	$P_{AC\_actual}$		DC	AC	
Jan	7.8388	8.3366	7.8388	8.0984	97.14	1.06	1.03	2.90
Feb	7.5877	7.9059	7.5877	7.6770	97.10	1.04	1.01	2.94
Mar	7.6160	7.9321	7.6160	7.7054	97.14	1.04	1.01	2.90
Apr	7.6951	8.1373	7.6951	7.9062	97.16	1.06	1.03	2.88
May	7.8187	8.2314	7.8187	8.0006	97.20	1.05	1.02	2.84
Jun	7.9654	8.3366	7.9654	8.1015	97.18	1.05	1.02	2.86
Jul	7.9265	8.0013	7.9265	7.7779	97.21	1.01	0.98	2.83
Aug	7.9182	7.9150	7.9182	7.6924	97.19	1.00	0.97	2.85
Sep	7.8522	7.7677	7.8522	7.5483	97.18	0.99	0.96	2.86
Oct	7.5880	7.5224	7.5880	7.3070	97.14	0.99	0.96	2.91
Nov	7.7880	7.5959	7.7880	7.3787	97.14	0.98	0.95	2.90
Dec	7.7788	7.5689	7.7788	7.3506	97.12	0.97	0.94	2.93

Since the study aims to evaluate whether there is any significant difference using DC AR compared to AC AR, the AR analysis was conducted. AR is just the ratio of measured power to the predicted power as calculated by the following Equation 6:

$$AR = \frac{\text{actual power}}{\text{predicted power}} \approx \frac{\text{gradient of actual power}}{\text{gradient of predicted power}} \tag{6}$$

The AR on the DC side was calculated, followed by the AR on the AC side. Finally, a comparison was made between DC AR and AC AR. The results presented in Table 4 shows that the AC AR were consistently lower than DC AR for the whole 12 months with a percentage difference of approximately 3%. These findings were as expected based on the understanding that AC AR has included one additional variable, which is  $\eta_{inv}$  that was declared a constant in the prediction calculation as 98.30%.

In summary, the results and analysis above have proven a significant difference between DC AR and AC AR. More than that, it is found that AC AR is more reliable to access GCPV system performance because it takes into consideration the inverter efficiency performance.

## CONCLUSION

The study has succeeded in achieving the aim by proving that DC AR significantly differs compared to AC AR by 3% when analyzed based on one-year historical data for a GCPV system located in tropical Malaysia. The discrepancy was due to the additional factor in AC AR analysis compared to DC AR analysis, which refers to the inverter efficiency that varies during actual operation compared to constant manufacturer declared inverter efficiency used in the AC AR prediction. Thus, an in-depth investigation should be conducted to delve into the typical yet anomaly behaviors of the daily operating inverter efficiency compared to the constant declared inverter efficiency by the manufacturer.

## ACKNOWLEDGEMENT

The authors wish to thank Solar Photovoltaic Energy Conversion Technology and Research Application (SPECTRA) and Green Energy Research Center (GERC) for their support and guidance throughout the project. The Ministry of Education funded this work was under research grant 600-IRMI/FRGS 5/3 (446/2019).

## REFERENCES

- Appiah, A. Y., Zhang, X., Ayawli, B. B. K., & Kyeremeh, F. (2019). Review and performance evaluation of photovoltaic array fault detection and diagnosis techniques. *International Journal of Photoenergy*, 2019, Article 6953530. <https://doi.org/10.1155/2019/6953530>
- Hansen, C., Stein, J., & Riley, D. (2012). *Effect of time scale on analysis of PV system performance*. Sandia National Laboratories. <https://doi.org/10.13140/2.1.1150.3368>
- Humada, A. M., Hojabri, M., Mohamed, M. B., Sulaiman, M. H., & Dakheel, T. H. (2014). A proposed method of photovoltaic solar array configuration under different partial shadow conditions. In *Advanced Materials Research* (Vol. 983, pp. 307-311). Trans Tech Publications LTD. <https://doi.org/10.4028/www.scientific.net/AMR.983.307>
- Hussin, M. Z., Omar, A. M., Zain, Z. M., & Shaari, S. (2013). Performance of grid-connected photovoltaic system in equatorial rainforest fully humid climate of Malaysia. *International Journal of Applied Power Engineering (IJAPE)*, 2(3), 105-114. <https://doi.org/10.11591/ijape.v2i3.2090>
- IEC TS 61724. (2016). *Photovoltaic system performance - Part 3: Energy evaluation method*. International Electrotechnical Commission.
- Jaszczur, M., Teneta, J., Styszko, K., Hassan, Q., Burzyńska, P., Marcinek, E., & Łopian, N. (2019). The field experiments and model of the natural dust deposition effects on photovoltaic module efficiency.



*Environmental Science and Pollution Research*, 26(9), 8402-8417. <https://doi.org/10.1007/s11356-018-1970-x>

- Khatib, T., Yasin, A., Mohammad, A. A., & Ibrahim, I. A. (2017). On the effectiveness of optimally sizing an inverter in a grid-connected photovoltaic power system. In *14th International Conference on Smart Cities: Improving Quality of Life Using ICT & IoT (HONET-ICT)* (pp. 48-52). IEEE Publishing. <https://doi.org/10.1109/HONET.2017.8102220>
- Kim, G. G., Lee, W., Bhang, B. G., Choi, J. H., & Ahn, H. (2021). Fault Detection for Photovoltaic Systems Using Multivariate Analysis With Electrical and Environmental Variables. *IEEE Journal of Photovoltaics*, 11(1), 202-212. <https://doi.org/10.1109/JPHOTOV.2020.3032974>
- Marion, B., Adelstein, J., Boyle, K. E., Hayden, H., Hammond, B., Fletcher, T., Canada, B., Narang, D., Kimber, A., Mitchell, L., Rich, G., & Townsend, T. (2005). Performance parameters for grid-connected PV systems. In *Conference Record of the Thirty-first IEEE Photovoltaic Specialists Conference* (pp. 1601-1606). IEEE Publishing. <https://doi.org/10.1109/PVSC.2005.1488451>
- Muhammad, N., Zainuddin, H., Jaaper, E., & Idrus, Z. (2019). An early fault detection approach in grid-connected photovoltaic (GCPV) system. *Indonesian Journal of Electrical Engineering and Computer Science*, 17(2), 671-679. <https://doi.org/10.11591/ijeecs.v17.i2.pp671-679>
- Nurdiana, E., Subiyanto, I., Indarto, A., Wibisono, G., & Hudaya, C. (2020). Performance analysis and evaluation of a 10.6 kWp grid-connected photovoltaic system in Serpong. In *IOP Conference Series: Materials Science and Engineering* (Vol. 909, No. 1, p. 012019). IOP Publishing. <https://doi.org/10.1088/1757-899X/909/1/012019>
- OFA. (2010). *MS IEC 61724:2010 Photovoltaic system performance monitoring-Guidelines for measurement, data exchange and analysis*. Online Finding Aid.
- Platon, R., Martel, J., Woodruff, N., & Chau, T. Y. (2015). Online fault detection in PV systems. *IEEE Transactions on Sustainable Energy*, 6(4), 1200-1207. <https://doi.org/10.1109/TSTE.2015.2421447>
- SEDA. (2016). *Malaysia grid-connected design course*. Sustainable Energy Development Authority Malaysia.
- Shukor, F. A. M., Zainuddin, H., Muhammad, N., & Khir, F. L. M. (2021). Acceptance ratio analysis: An early fault indicator for grid-connected photovoltaic system. *International Journal on Advanced Science Engineering Information Technology*, 11(3), 1214-1223.
- SIRIM. (2020). *MS 2692:2020 testing and commissioning of grid-connected photovoltaic system*. Department of Standards Malaysia.
- Wittkopf, S., Valliappan, S., Liu, L., Seng, K., Chye, S., & Cheng, J. (2012). Analytical performance monitoring of a 142.5 kWp grid-connected rooftop BIPV system in Singapore. *Renewable Energy*, 47, 9-20. <https://doi.org/10.1016/j.renene.2012.03.034>
- Yusoff, N. F., Zakaria, N. Z., Zainuddin, H., & Shaari, S. (2017). Mounting configuration factor for building integrated photovoltaic and retrofitted grid-connected photovoltaic system. *Science Letters*, 11(1), 1-6.



## A Dashboard-based System to Manage and Monitor the Progression of Undergraduate IT Degree Final Year Projects

Nooralisa Mohd Tuah\*, Ainnecia Yoag, Dinna@Nina Mohd Nizam and Cheang Wan Chin

*Creative Computing Research Group (CCRG), Faculty of Computing and Informatics, Universiti Malaysia Sabah, Jalan UMS, 88400 Kota Kinabalu, Sabah, Malaysia*

### ABSTRACT

Having a system to process and store information securely is crucial for an e-learning environment in a higher learning institute. Data recorded manually is deemed unsuitable as it may lead to mishandling of documents, poor record of documents movements, and even missing documents. A final year project (FYP) subject for a particular university's course would need a specific management system to alleviate the work processes of supervision and monitor student progress. This system would reduce cost, paperwork, staffing and even simplify the workflow process. Therefore, introducing a student dashboard-based system for the FYP course is proposed in this study. This paper presents a smart system utilizing data analytics and a dashboard that enables the students to self-monitor, track progress and manage important information related to their FYP. The system development followed stepwise Rapid Application Development (RAD) methodology in developing the system. The developed system has been designed, developed, and tested by university students taking FYP courses. A Technology Acceptance Model (TAM) was adopted in the testing phase to examine the system acceptance and user behavior intention in using the proposed system. The results showed a significant effect on a positive implementation in the faculty's

course management and monitoring the student's FYP progress. For the dashboard-based system to reach its full potential, it is highly recommended to implement the system in its course management fully.

### ARTICLE INFO

#### Article history:

Received: 30 May 2021

Accepted: 15 September 2021

Published: 15 December 2021

DOI: <https://doi.org/10.47836/pjst.30.1.13>

#### E-mail addresses:

[alisa.tuah@ums.edu.my](mailto:alisa.tuah@ums.edu.my) (Nooralisa Mohd Tuah)

[ainnecia@ums.edu.my](mailto:ainnecia@ums.edu.my) (Ainnecia Yoag)

[dinna@ums.edu.my](mailto:dinna@ums.edu.my) (Dinna@Nina Mohd Nizam)

[chloecheang97@gmail.com](mailto:chloecheang97@gmail.com) (Cheang Wan Chin)

\*Corresponding author

**Keywords:** Dashboard, final year project, rapid application development, technology acceptance model

## INTRODUCTION

Leveraging an online learning tool is a significant way of delivering a course effectively. Online learning tools, such as e-learning Massive Open Online Courses (MOOC), Moodle, and learning management system (LMS), have been widely implemented in online course content. Online learning tool plays an important role in higher education. It is also beneficial for managing a student's Final Year Project (FYP) course other than being used for course delivery.

For IT students in many universities in Malaysia, the FYP is a crucial course that structured for the students to undertake in their final year before they can be graduated. The FYP course is challenging as the students need to exhibit their ability to apply the knowledge and skills throughout their tenure as undergraduate students. Moreover, they must demonstrate their proficiency in designing and developing a fully functional system at the end of the semester. This process involves several parties: the course coordinator or committee, supervisors, examiners, and the students themselves. FYP systems have been researched in the literature, for example in (Ismail et al., 2017; Khamaruddin et al., 2017); however, they are not general and limited to a specific implementation. Thus, it seems not enough to manage the project course itself. The limitation is most probably due to the following problem:

1. progress-tracking has hardly been conducted, and the current implementation processes seem not transparent enough to the students and the instructors, and data for analysis may not be supported as different parties may provide various input,
2. Students hardly manage their work, and thus, the progress of students cannot be seen and analyzed as a whole and
3. management wise where a manual process could cause inaccurate data and analysis, and the process requires much work to manage.

Following the previous research articles related to FYP in higher education, several types of FYP systems have been developed and implemented locally (within particular faculty or university use only). The FYP system is mostly related to the management and the process of FYP (Ismail et al., 2017; Khamaruddin et al., 2017; Roberts et al., 2017; Vakaloudis et al., 2020). The system includes the submission of a proposal, report, and the FYP product resources (Ismail et al., 2017; Vakaloudis et al., 2020), a platform for the coordinator, supervisors, examiners, and students to communicate with each other (Roberts et al., 2017), monitoring processes (Khamaruddin et al., 2017; Mohamed et al., 2017; Vakaloudis et al., 2020), students and supervisor's allocation as well as the evaluation process (Kar et al., 2017). For monitoring purposes, an online logbook is usually adopted, which in the logbook, the features are mainly related to supervision activities and the progress of report writing. However, it is argued that monitoring how far the software,

system, or application has been developed might not properly be captured and analyzed through the online logbook. Furthermore, less interactive applications that can provide communication between lecturers and students are available in the current FYP application. Visualizing students' progress interactively, such as using a dashboard-type application, may help to improve the learning environment (Safsouf et al., 2021). Some of the related applications from previous research works are summarized in Table 1 to comprehend the implementation of the FYP system further. The title of the existing FYP problems, the proposed system application, the users, the system functionality, and any related dashboard-type application in the system was extracted.

Among the existing application for FYP in Table 1, it can be summarized that the systems were revolving on a similar feature, which is to the FYP project management, it is related to supervisor and student project allocation, student progress tracking, logbook, and supervision monitoring, and evaluation of the project. These features are essential for providing an effective management system, particularly for administering the FYP course. Moreover, moving from a manual to a systematic approach in the era of IR4.0 is indispensable considering the advancement of technology and changes in the learning environment these days. A dashboard that can provide real-time information and support the learning experiences becomes a significant challenge to the learning environment (Safsouf et al., 2021). In managing a course, other than providing a function to ease the course management process, it is also essential to have a function that can act as a tool to communicate the work being conducted between the lecturer and the student, as well as a tool to visualize the information meaningfully (Safsouf et al., 2021; Sarikaya et al., 2019). This information will provide guidance for the student to monitor and make progress on their performance (Mehmet & Arif, 2021).

Based on the existing FYP applications in Table 1, the current dashboard-style has been implemented in some ways. For example, the systems summarize the student information (i.e., name, course, program, credit hours), the student's FYP thesis submission status, a list of work, and comments from examiners or supervisors on one page. However, the type of implemented dashboard was not designed with data semantics and with enough visual features. According to Sarikaya et al. (2019), some characteristics of a dashboard for motivation and learning, particularly that tailored to an individual's achievement, should be designed with interactive interfaces and with alert features. However, the existing FYP applications did not emphasize these elements in their application. Apart from that, following the provided solution to the problem in FYP in Table 1, one solution to the FYP problems that the existing application might not give enough attention to is the implementation of the element of progression in assessing the student's FYP performance. The implementation of progress tracking merely in the form of a list of records (Ismail et al., 2017; Mohamed et al., 2017) and submission of files (Abdulkareem et al., 2013;

Table 1

*The summary of available FYP system in literature*

Article	Title	Current problems	Proposed FYP System	User	Main Function/ Features	Implementation of Any kind of Dashboard types
Kar et al. (2017)	Integrated Supervision and Evaluation System for Final Year Project	The FYP was managed manually (paper-based). Several internal problems occur using a manual approach, mostly related to limited time for supervisors to update the respective students' progress. Also, a manual approach requires much effort in sorting out the student's work.	The system provides a centralized unit for all person-in-charge (PIC)	Students, supervisors, panels, and coordinator	The research offered an integrated supervision and assessment system, which could efficiently manage the FYP system.	The system has a summary of the projects in terms of student details, status on submitted final thesis, and comments from examiner were shown on one page. None of them related to FYP progression.
Abdulkareem et al. (2013)	Design and Development of a University Portal for the Management of Final Year Undergraduate Projects	The manual process sometimes leads to time-wasting, delaying progress as the students cannot update their supervisor (lecturer) on the project's accomplishment.	The system is a portal used to automate the processes associated with the management of final-year projects.	Students and supervisors.	The online system would be able to work on the following functions: identify duplication of projects systematize supervisors and students' allocation students and supervisor interaction submit reports online evaluation and feedback to students.	The portal does not show any summarization related to student details and their FYP progress.

Table 1 (Continue)

Article	Title	Current problems	Proposed FYP System	User	Main Function/ Features	Implementation of Any kind of Dashboard types
Chik and Rafi' (2016)	Interactive Evaluation System for Final Year Project (FYP)	The Program Coordinator (PC) has a problem with processing the student's marks. Presently, all the marks are processed and stored manually using Microsoft Excel.	A systematic evaluation system enables the Final Year Project evaluators to evaluate the FYP during the evaluations simultaneously.	Students and evaluators.	The system enables the evaluators to log the student's scores, significantly generating the results in real-time.	The proposed system does not show any summarization of information or visualization of Information. For example, the marking system could be in the form of a table list.
Buhari et al. (2017)	A Streamlined Approach to Enhance the Capacity of Undergraduate IT Students to Deliver High Quality and Demand-Driven Final Year Project: A Conceptual Framework on Collaboration between Industry and University	They were using a manual approach to managing FYP activities. Hence, the common problems faced are poor planning and management of a project, unstructured documentation, students' problem not related to the project, and inadequate or negligent supervision.	The proposed system is a web-based system that systematizes all FYP activities.	Students and supervisors.	The system includes all student's FYP processes from the selection process until the evaluation process. Also, the system provides a secure and fastest approach in managing the FYP processes.	The system is only a proposal to design an FYP system. No proposal related to dashboard or information visualization was mentioned in the paper.

Table 1 (Continue)

Article	Title	Current problems	Proposed FYP System	User	Main Function/ Features	Implementation of Any kind of Dashboard types
Leung et al. (2015)	The Development of a Final Year Project Management System for Information Technology Programs	It is kind of hard for students to communicate with their supervisor out of the consultation hours. All communication depends on the email. The students usually get a longer response time, which has caused the project to be progressed and be finished on time.	A system that can significantly improve the management and communication problem in the FYP program	Students and supervisors.	The developed system has five modules. The modules are: <ul style="list-style-type: none"> <li>• Distribution of Project</li> <li>• Communication</li> <li>• Project Management</li> <li>• File Sharing and Repository</li> <li>• Submission &amp; Grading Module.</li> </ul>	The system has a one-stop information page for students to check on their FYP tasks and to-do lists. However, none of the features shows on the students' FYP progression.
Mohamed et al. (2017)	An Implementation of Final Year Project Management System: A Case Study at Universiti Sultan Zainal Abidin	The FYP is manually processed and managed using hardcopy forms and a booklet. The student's common problem was arranging appointments with supervisors and presenting their project assignments every week. Since there is no integrated system, the supervisor finds it challenging to track the project, particularly when the student misses the appointment.	This project aims to smoothen the communication process between the students and their supervisors, and the coordinator.	Students, supervisors, and head of department.	A web application was developed in which the application can be used to supervise and track the student's FYP progress.	The system has no implementation of any dashboard-style information. Also, the system does not show any information related visualization to students' FYP progress.



Table 1 (Continue)

Article	Title	Current problems	Proposed FYP System	User	Main Function/ Features	Implementation of Any kind of Dashboard types
Ismail et al. (2017)	Online Project Evaluation and Supervision System (oPENs) for Final Year Project Proposal Development Process	FYP is managed manually. There is no provided system or tools that can ease the administration of Student's FYP.	With the development of oPENs, students' data retrieval will be more straightforward and practical. It significantly can save much time.	Coordinator, supervisors, examiners, and students.	The oPENs system is provided with more secured features whereby in the system, it included safe storage for all the project's documentation as well as the student's marks. Also, it will be no errors in the final marks uploading process.	The system has no implementation of any dashboard-style information. The system does not show any information visualization related to students' FYP progress.
Khamaruddin et al. (2017)	Using Moodle as an Integrated Final Year Project Management System	The number of students and academic staff is increasing every year. The situation has caused some difficulties for the FYP coordinator to manage the FYP processes. The manual method does not help the coordinator to ease the management process. Thus, it is plausible to have a system that effectively enables the FYP's users to contribute to the whole process.	An online management system includes the students' final year project evaluation process by utilizing Moodle.	Students, supervisors, internal moderators, and examiners.	Moodle is used to organize the students' FYP submissions and their evaluations. The evaluation also could be conducted online. The system made it easier for the students to download and upload their files before the due date. Also, the functions available to the supervisors and examiners,	Using standard Moodle application in managing the FYP course. None of the functions showed any information visualization related to students' FYP progress.

Khamaruddin et al., 2017). In this view, the available progress monitoring processes may not be sufficient to assess how well the students have done for their project. Therefore, it might have a minimal effect on the student's performance towards completing their FYP works within the given time. The element of progression for project-based IT courses can give autonomy to the students in managing their project deliverables (Szynkiewicz et al., 2020). It will also make the project processes get more engagement from the students and academic supervisors (Buhari et al., 2017).

Regarding this, implementation of a Dashboards-based system could be an effective option to monitor the project progress and the student's system (Buhari et al., 2017). A dashboard provides a simple descriptive statistic of students' progress visualized for monitoring and decision process (Gutiérrez et al., 2020). Furthermore, following the previous implementation, as in Table 1, there is a limited Dashboard-based application in the FYP system. Research in dashboard analytics has generated considerable recent research interest (Buhari et al., 2017; Chik & Rafi'i, 2016). It shows that the student data analytics and the dashboard have an important role in advancing learning intervention in higher education (Aljohani et al., 2019; Buhari et al., 2017). In general, the dashboard and data analytics is a platform that presents a collection of data, reports, and analysis about learners and their learning contexts with the aims to comprehend and optimize the learning environment (Asli et al., 2019; Buhari et al., 2017; Leitner et al., 2017). It has many possible uses in a learning environment. It has also been investigated as a potential tool in students' learning patterns and behaviors and supports students' learning achievement (Abdulkareem et al., 2013; Aljohani et al., 2019).

Through dashboard and data analytics, it mainly summarizes the learners' learning achievement and progression. Thus, it helps to provide further insight into the students current learning progress status, list of any completed and incomplete tasks, their learning achievement so far, performance prediction, and related learning information in their educational context. The information presented in the dashboard indirectly allows the students to effectively manage their own time and space to conduct the courses (Abdulkareem et al., 2013). Thus, it will nurture the students to be more self-regulated towards their learning process. Furthermore, using a dashboard-based system in e-learning courses requires two-way content delivery. The courses allow the instructor to provide the content and the students' input to generate the analysis. Thus, they can be reported accordingly. Therefore, a dashboard can be a powerful tool supporting the learning environment involving students, instructors, system developers, and implementers to better implementation in learning and educational processes (Buhari et al., 2017).

Review articles have highlighted several types of research on dashboard applications in higher education (Buhari et al., 2017; Chik & Rafi'i, 2016). However, although the use of the dashboard in teaching and learning has increased, little attention has been paid to

research its practicality and applicability, mainly implementation in the FYP system. In these five years, research on dashboard and data analytics have been conducted primarily on 1) the application design and framework (Asli et al., 2019; Klačnja-Milićević & Ivanović, 2018), and 2) student's perceptions and acceptance (Sønderlund et al., 2019), 3) learning motivation and engagement (Kim et al., 2016), and 4) teaching and learning effectiveness (Abdulkareem et al., 2013). Meanwhile, for the effectiveness of the delivery of the FYP course, recent research had focused on the integrated web application that transformed manual workflow into more systemize processes (Ismail et al., 2017; Khamaruddin et al., 2017). Thus, apart from a web system, adapting a dashboard to simplify the process of managing and monitoring the progress of the final year project course could significantly affect teaching and learning activities in higher education. Therefore, a different type of FYP system that is not only about management system but a system that emphasizes graphical progression to indicate the completeness of the student's project is introduced. Furthermore, it is considered another approach that might gain more involvement from the students and the academic supervisors towards on-time project completion. Thus, the objectives of this study are 1) to design and develop the dashboard-based system for the students to manage and track their progress, as well as a tool to self-regulated, and 2) to assess the system accordingly.

In this paper, the groundwork of the system's development and implementation is presented. The development process and examine the system acceptance, and behavioral intention using a modified version of the TAM is described (Leung et al., 2015). This paper is organized as follows: Section 2 describes the material and methodology used in this study; Section 3 presents the system and dashboard developed for the FYP system; the result and findings are presented in Section 4; Finally, in section 5 offered discussion, concluding remarks, and future work.

## **MATERIALS AND METHODS**

### **The Methods**

This research adopts the Rapid Application Development (RAD) methodology to achieve this research's objectives. The methodology was chosen because it emphasizes rapid system development through prototype and reusable codes. Developers will work closely with the users in designing and developing the system. Quick responses during the user design cycle can expedite the design process. Reusable codes that are available in the open-source platform helps in speeding up the development process in the construction phase. Furthermore, the cutover phase helps finalize the system features and functions with suitable testing conducted within a short time. With that in mind, all the phases in RAD system development were followed. The phases include System Requirements Planning Phase, User Design Phase, Construction Phase, and Cut-Over Phase. The phases are shown

in Figure 1. RAD focuses on developing a prototype that provides rapid response during the cycles of development and testing. RAD processes were adopted mainly to accelerate the duration of application development, with high-quality results towards the system functions and features.

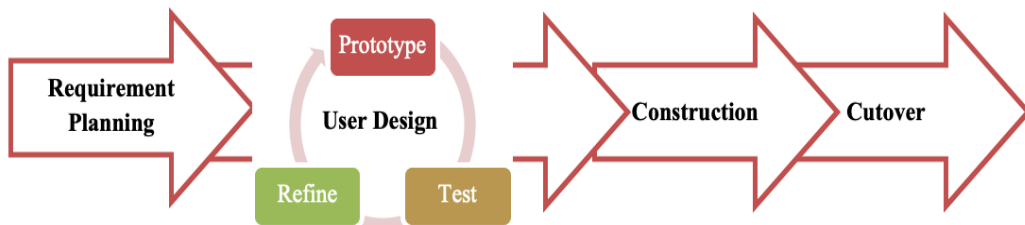


Figure 1. Rapid Application Development (RAD) methodology

Based on the model in Figure 1, details for each step performed are explained as follows.

1. System Requirement Planning: In the first phase, the researcher collected and analyzed system requirements and reconfirmed them with the users. In this case, the researchers collected FYP materials and data from the course instructor and conducted a focus group interview participated by the instructor, two lecturers, and two students' representatives.
2. User Design: This second phase involved an iterative system design process through prototyping, testing, and refining. In the first iterative process, a low fidelity prototype (storyboard/sketch, i.e., Figures 2a & 2b) was designed beforehand and sent to the focus group participants (same as in the previous phase) to get feedback. Then, based on the feedback, a high fidelity prototype (system design with minimum workable function, i.e., Figures 2c & 2d) is developed and tested with similar focus group participants. Following the second feedbacks, the hi-fidelity prototype was refined accordingly. Finally, in the third iteration process, another testing with the focus group participants was conducted again, and based on the testing, it resulted in a consensus among them. Thus, the confirmed system design was sent for construction.
3. Construction: At this stage, the refined prototype in the previous phase is improved into a fully developed system. Other than the functions and interfaces, the databases are the essential components to be accomplished. Hence, the integration of the system and its databases is made synchronously until the system development phase is completed.
4. Cut Over: This is the finalization phase. At this stage, the exclusive features, functions, and interfaces are finalized through system evaluation. For that purpose,

system testing with the expert users is conducted, and this testing is conducted to ensure all the functions work correctly. Following the system testing, user acceptance testing is conducted with the FYP’s students. The testing is to examine the system acceptance and user behavior intention of using the system.

The next section will further explain the detail of the system requirement, design, application, and testing conducted in this study.

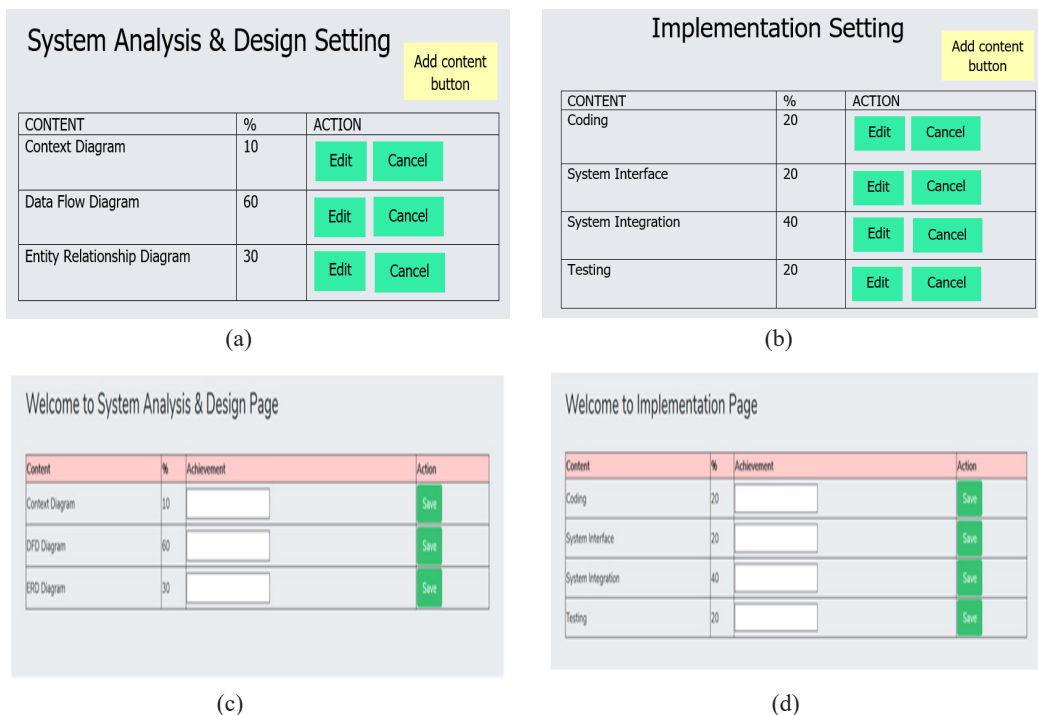


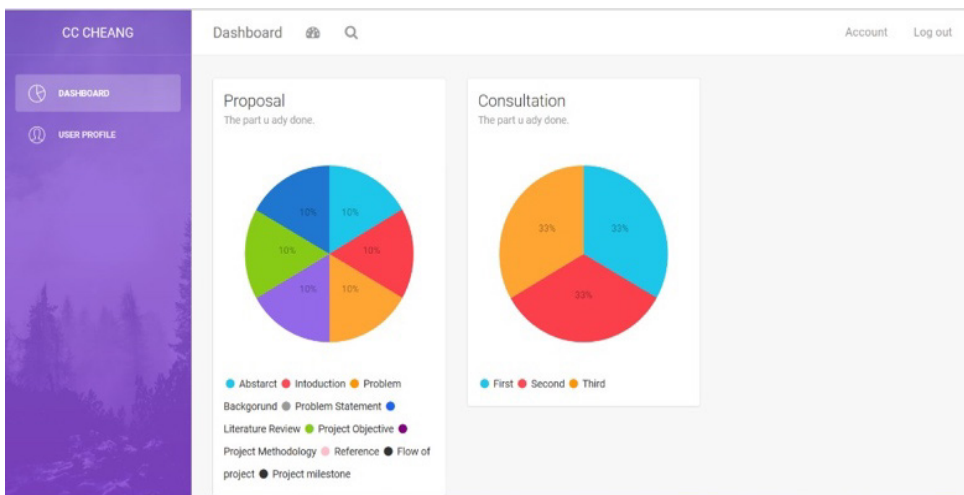
Figure 2. (a) low fidelity for system analysis & design setting; (b) low fidelity for implementation setting; (c) high fidelity for system analysis & design setting; (d) high fidelity for implementation setting.

### The System Requirement, Design, and Application

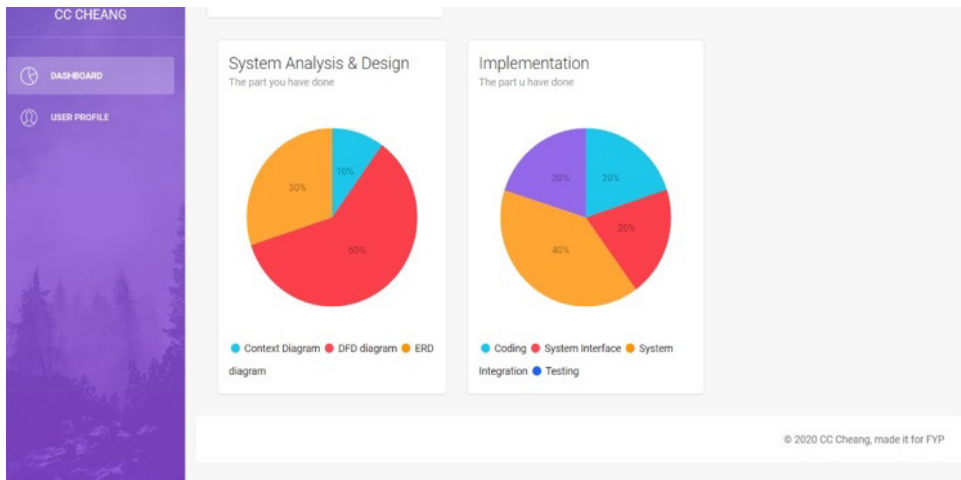
The developed FYP system in this study was purposely for computing and information technology students, whereby the features in the system are related to the nature of a system development itself. In this study, the FYP system was designed to be aligned with promoting the data analytics and dashboard into the course. There are a few important functions developed for that purpose. As the main objective of dashboard implementation in FYP was to enable the student to track their progress in completing the course, the dashboard will mainly show the information. The student progresses from 1) auto form completion, 2) student’s file submission through the system, and 3) instructor remarks (coordinator or supervisor).

For the system to reach its potential, the FYP requirement and processes beforehand are summarized. This requirement is summaries based on the system requirement gathered in the first phase of the RAD system development. The FYP course is divided into two semesters, where in the first semester, the system will be designed and analyzed, and a prototype will be developed accordingly. In the second semester, the prototype system will be fully developed, tested, and deployed. However, the students were required to develop their project proposal a semester before the students registered for their FYP course. Therefore, the use of a dashboard will cover students’ progress for all phases in both semesters. Figures 3(a) and 3(b) show the example of a student’s dashboard for each phase in FYP. In addition, the details for each achievement are presented on another page, where information can be updated as required in the FYP processes. Following the progress of the FYP processes, once the faculty’s committee approves the student’s project, the students must submit their proposals through the system. The completion of the proposal can also be seen through the dashboard.

In FYP, consultation sessions are important to provide a platform for the students to allocate time for progress meetings with their supervisor and discuss ideas, issues, problems, and solutions related to their project. The supervisors can add the consultations, and the details for each consultation also will be recorded in the system. During the consultation, the students will present and submit the designs and analyses of their systems. In this sense (depending on the design method agreed by the supervisor and the student), the context diagram/use cases and the data flow diagram/sequence diagram. The respective supervisor will update the performance progress report for each student.



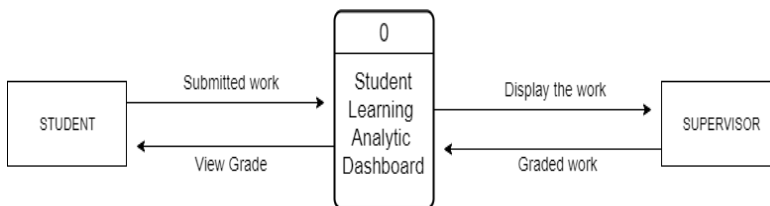
(a)



(b)

Figure 3. (a) Dashboard interfaces for proposal and consultation; (b) Dashboard interfaces for system analysis and design and implementation

The progress of students' performance is similar to the progress of implementation. The students are required to submit their material to the supervisors, and their progress will be recorded in the system. This performance progress monitoring-based function using a dashboard is transparent to the student and supervisor. The students can practically identify the gap in their progress, work on it, and accomplish them. The supervisor and instructor could also monitor how far the student has achieved at a particular time. With the implementation of a dashboard in the FYP course, it is expected that at the end of the course, the students are able to plan, design, develop and test an IT-related project very well structured. With all the required processes in mind, the system is designed accordingly. The design of the system processes is illustrated as in the context diagram in Figure 4a and Data Flow Diagram in Figure 4b.



(a)

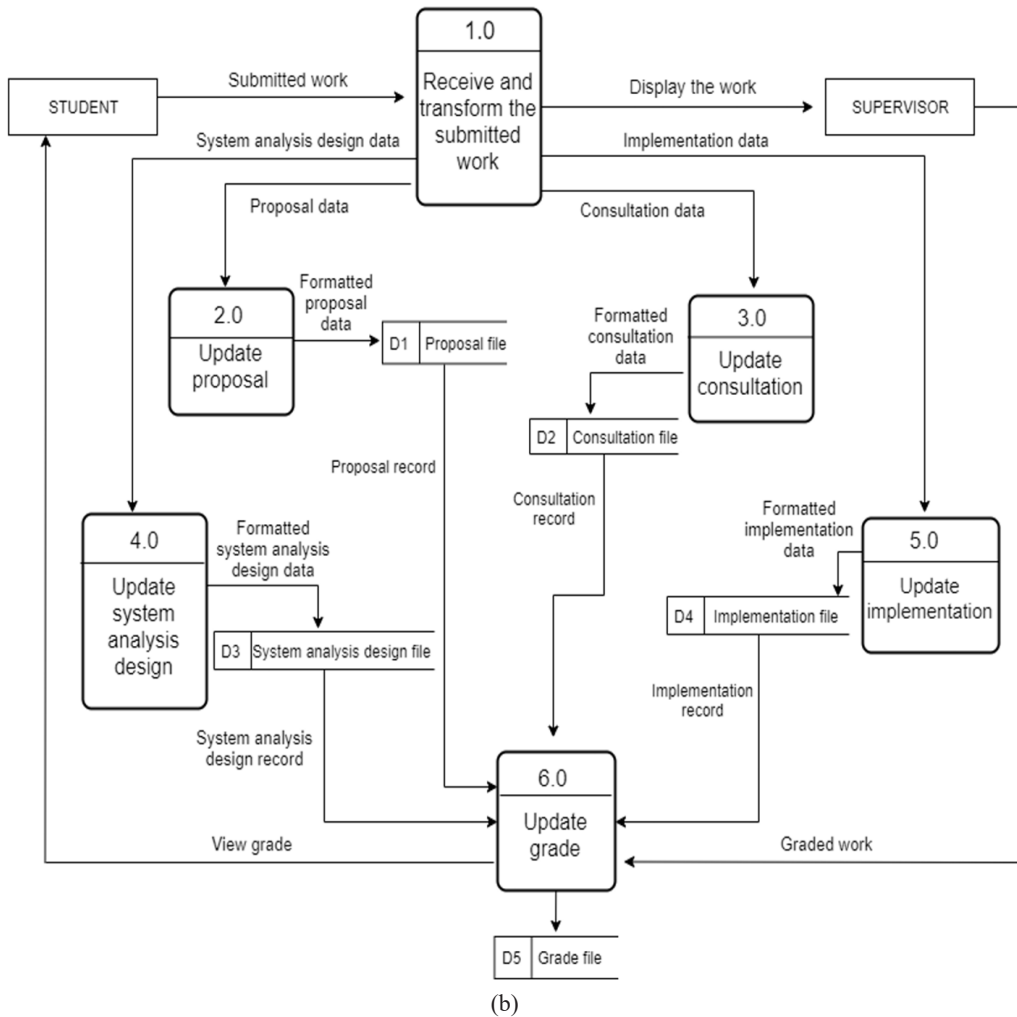


Figure 4. (a) System context diagram; (b) System data flow diagram

### Development and Testing Material

The system was developed utilizing the Laravel framework, Apache server, MySQL databases and coded using PHP languages. All development tools are open source-based, easy to use, and maintainable. For the evaluation purposes, the TAM, as previously studied in (Ifenthaler & Schumacher, 2016; Revyathi & Tselios, 2019; To & Tang, 2019), has been used to verify the students’ behavioral intention to use the FYP system is affected by the student’s perception of using the system. The constructs adopted from the TAM model consist of perceived usefulness, perceived ease of use, and behavioral intention. Each of the constructs is defined and its related items for this study. The model, as in Figure 5, and details of each construct are explained in Table 2. The questionnaire item is rated using the Likert Scale from 1 (Strongly disagree) to 5 (Strongly Agree).



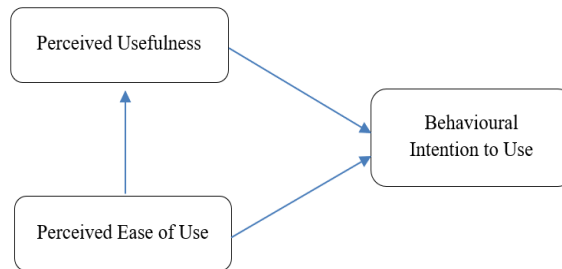


Figure 5. Adapted Technology Acceptance Model (TAM)

Table 2

Construct definition of Technology Acceptance Model

Construct	Operational Definition	Items
Perceived usefulness	The construct reflects the students' perception of whether the use of dashboard and data analytics (DDA) in the FYP system will enhance their FYP performance.	Using dashboard and data analytics in the FYP system would enable me to see my progress more quickly.
		Using dashboard and data analytics in the FYP system would improve my academic performance.
		Using dashboard and data analytics in the FYP system will enhance the effectiveness of learning.
		I find the use of dashboards and data analytics in the FYP system useful.
Perceived ease of use	The construct refers to the student's responses towards the ease of understanding the use of dashboard and data analytics in the FYP system.	I find dashboard and data analytics in the FYP system easy to use.
		Learning to use the dashboard and data analytics in the FYP system is easy for me.
		It is easy to become skillful in using the dashboard and data analytics in the FYP system.
		I would find dashboard and data analytics in the FYP system to be flexible to interact with.

Table 2 (Continue)

Construct	Operational Definition	ITEMS
Behavioral intention to use	The construct refers to the student's intention to use the FYP system, dashboard, and data analytics in monitoring their progress.	I intend to continue using the system for my FYP course. I will always try to use the system for my FYP course. I plan to continue using the FYP system throughout the semester.

## RESULT AND DISCUSSION

### System Testing

System testing was conducted to ensure the system functionalities were working accordingly and following the user's requirements. For the testing, the test plan was developed for every function. Following the plan, testing was conducted on five expert users. These experts were the individuals who work closely with the FYP processes and those who are proficient in system development and user interface design. Table 3 shows the detailed demographic of the experts. The distribution of the expert users is considered reasonable based on their years of experience in the subject matter, the field of expertise, and their employment status.

Table 3

*Expert demographic*

Demographic	No	Demographic	No
<b><i>Gender</i></b>		<b><i>Field of Expertise</i></b>	
Female	3	User Interface	1
Male	2	System Development	2
<b><i>Age</i></b>		FYP processes + User Interfaces	2
30 - 40	2	<b><i>Years of experience in the field</i></b>	
41 - 50	2	3 - 5	2
51 - 60	1	6 - 9	2
<b><i>Employment Status</i></b>		10 and Above	1
Senior Lecturer	3		
IT Officer	2		

During the testing, the expert users were explained every feature in the system and how the features for each user of the system are linked together. The experts were given one day to test the system personally, and they were asked to report back to the researcher of their findings with comments for improvement. As a result of the testing, no errors have been found, and all functions work correctly. However, the expert users have made a few suggestions to ensure the information is presented clearly and the system is easy to use and more user-friendly. The suggestions are summarized in Table 4.

Table 4  
*Suggestions from evaluators*

Suggestions for Improvement	
System Functions	<ul style="list-style-type: none"> <li>• The input text should be re-designed (for bigger text size) and scrollable</li> <li>• Visibility of the user profile at the left panel with options to update directly</li> <li>• To change the upload button for multiple file uploaded function.</li> </ul>
User Interface	<ul style="list-style-type: none"> <li>• The use of color for the chart</li> <li>• The legends ordered</li> <li>• Update button should be more obvious</li> <li>• To add student avatar (changeable depends on student's achievement)</li> </ul>
Others	<ul style="list-style-type: none"> <li>• Registration can be arranged into a more straightforward mode as some of the student's information can be found in the university's Student Information System (SMP).</li> </ul>

### Acceptance Testing

A questionnaire survey to 25 users was conducted to ensure the system was accepted and practically used. They were students who had passed the course (20%), are currently taking the course (40%), and will be registering for the course in the following semester (40%). For the latter category of the student, these students are in the pre-process of taking the FYP course in their current semester. During this pre-process, they were asked to develop a proposal, and they had several consultation sessions with the course coordinator. Thus, they would also be able to reflect the processes of the system. In the acceptance testing, the users were asked to use the system following the given instructions (Register, update/

upload proposal, and add/update consultation). Once completed, a postal questionnaire survey using TAM, as detailed in Table 2, is conducted.

As a result, the mean score and *SD* for perceived usefulness, perceived ease of use, and behavioral intention to use are shown in Table 5. The result indicates that the student's responses are primarily towards "strongly agree" in using dashboard and data analytics in the FYP system. Reliability analysis was conducted to ensure the consistency of the items used in the questionnaire. Generally, the construct should achieve .70 and above to indicate that the items are measuring the same constant. The result in Table 6 shows that overall Cronbach's Alpha is .68, whereby each of the constructs obtained more than .70. Correlation between the construct was also tested to verify the student's intention in using the FYP system. This intention is affected by the student's perceived usefulness and perceived ease of use of the system. For that, Table 7 reports the correlation coefficients between the constructs.

Table 5  
*Mean and standard deviation responses*

	N	Min	Max	Mean	SD
Perceived usefulness	25	3.00	5.00	4.26	0.68
Perceived ease of use	25	3.00	5.00	4.42	0.61
Behavioral intention to use	25	3.00	5.00	4.35	0.63

Table 6  
*Construct reliability*

Construct	Cronbach's Alpha	No. of Item
Perceived of Usefulness	.75	4
Perceived Ease of Use	.70	5
Behavioral Intention to Use	.73	3

Table 7  
*Correlation between the constructs*

Construct	Perceived of Usefulness	Perceived Ease of Use	Behavioral Intention to Use
Perceived of Usefulness	1	.328**	.406**
Perceived Ease of Use	.328**	1	.969*
Behavioral Intention to Use	.406**	.969*	1

\*\* : Correlation is significant at the 0.01 level (2-tailed)

Perceived of usefulness is significantly correlated to perceived ease of use ( $r = 0.328$  at  $p = 0.005$ ) and the intention to use the system ( $r = 0.406$  at  $p = 0.005$ ). Also, the perceived ease of use is significantly correlated to the intention of using the system. Thus, the use of a dashboard in the FYP system was perceived as useful and easy to be used, and because of that, the students intend to use the system for their FYP course. This result added to the contribution of dashboard application in teaching and learning activities, whereby it further supports the previous works on the effectiveness of dashboard and data analytics in learning and teaching and on course delivery by Ismail et al. (2017), Klačnja-Milićević and Ivanović (2018), and Leitner et al. (2017). Besides, using a dashboard is a good strategy for learning analytics implementation in teaching and learning (Gutiérrez et al., 2020; Tsai et al., 2020). This work also supports the requirement and needs of dashboard and data analytics implementation for other types of university courses like the student's e-community project (Ahmad et al., 2019).

## CONCLUSION

The use of student data analytics dashboards can help monitor and improve the student's performance and benefit the structure and management of the course itself—the FYP system aims to stimulate students' psychological changes by improving self-regulated and social awareness. Moreover, by providing a dashboard-based system, the instructors can monitor and evaluate the progress of the students' performance and get the best result from it. Hence, using an analytic data dashboard could help achieve the FYP system's aims in general. From our study, the implementation of a dashboard for the FYP course indicates that students intended to use the system for their FYP because it is perceived as beneficial for their academic progress and effective for the course. For future work, the system will be expanded with more features that enable the students to showcase their system and allow the instructor to manage the evaluation process through the system. In conclusion, the data analytics dashboard significantly affects course delivery where course materials were collected and analyzed accordingly. Thus, this research has contributed to learning efficiency as well as to learning management research.

## ACKNOWLEDGEMENTS

The authors would like to thank the Universiti Malaysia Sabah for all the supports in the research, and special thanks go to the participants who participated in the data collection, thus helping in the completion of this research.

## REFERENCES

- Abdulkareem, A., Adewale, A. A., & Dike, I. U. (2013). Design and development of a university portal for the management of final year undergraduate projects. *International Journal of Engineering and Computer Science*, 2(10), 2911-2920.
- Ahmad, W. N. W., Rodzuan, A. R. A., Teong, K. V, Jamil, N., & Tuah, N. M. (2019). E-community program: A study on ICT knowledge transfer to Labuan community. In H. B. Zaman, A. F. Smeaton, T. K. Shih, S. Velastin, T. Terutoshi, N. M. Ali & M. N. Ahmad (Eds.), *IVIC: International Visual Informatics Conference* (pp. 729-740). Springer. [https://doi.org/10.1007/978-3-030-34032-2\\_65](https://doi.org/10.1007/978-3-030-34032-2_65)
- Aljohani, N. R., Daud, A., Abbasi, R. A., Alowibdi, J. S., Basher, M., & Aslam, M. A. (2019). An integrated framework for course adapted student learning analytics dashboard. *Computers in Human Behavior*, 92, 679-690. <http://doi.org/10.1016/j.chb.2018.03.035>
- Asli, M. F., Hamzah, M., Ibrahim, A. A. A., & Embug, A. J. (2019). Visual analytics: Design study for exploratory analytics on peer profiles, activity and learning performance for MOOC forum activity assessment. *International Journal on Advanced Science, Engineering and Information Technology*, 9(1), 66-72. <http://doi.org/10.18517/ijaseit.9.1.7542>.
- Buhari, A., Valloo, S., & Hashim, H. (2017). A Streamlined approach to enhance the capacity of undergraduate IT students to deliver high quality and demand-driven final year project: A conceptual framework on collaboration between industry and university. In *Proceedings of 7th World Engineering Education Forum (WEEF)* (pp. 910-914). IEEE Publishing. <http://doi.org/10.1109/WEEF.2017.8467126>
- Chik, R., & Rafi'i, M. (2016). Interactive evaluation system for final year project (FYP). In *Proceedings of International Conference on Information and Communication Technology (ICICTM)* (pp. 203-208). IEEE Publishing. <http://doi.org/10.1109/ICICTM.2016.7890801>
- Gutiérrez, F., Seipp, K., Ochoa, X., Chiluzza, K., De Laet, T., & Verbert, K. (2020). LADA: A learning analytics dashboard for academic advising. *Computers in Human Behavior*, 107, Article 105826. <http://doi.org/10.1016/j.chb.2018.12.004>
- Ifenthaler, D., & Schumacher, C. (2016). Student perceptions of privacy principles for learning analytics. *Educational Technology Research and Development*, 64(5), 923-938. <http://doi.org/10.1007/s11423-016-9477-y>
- Ismail, S. I., Abdullah, R., Kar, S. A. C., Fadzal, N., Husni, H., & Omar, H. M. (2017). Online project evaluation and supervision system (oPENs) for final year project proposal development process. In *Proceeding of the IEEE 15th Student Conference on Research and Development (SCOREd)* (pp. 210-214). IEEE Publishing. <http://doi.org/10.1109/SCORED.2017.8305392>
- Kar, S. A., Fadzal, N., Ismail, S. I., Abdullah, R., & Omar, H. M. (2017). Integrated supervision and evaluation system for final year project. In *Proceeding of the IEEE 15th Student Conference on Research and Development (SCOREd)* (pp. 198-203). IEEE Publishing. <http://doi.org/10.1109/SCORED.2017.8305394>.
- Khamaruddin, P. F. M., Sauki, A., Othman, N. H., & Kadri, A. (2017). Using moodle as an integrated final year project management system. In *Proceeding of the IEEE 9th International Conference on Engineering Education (ICEED)* (pp. 238-242). IEEE Publishing. <http://doi.org/10.1109/ICEED.2017.8251200>.

- Kim, J., Jo, I. H., & Park, Y. (2016). Effects of learning analytics dashboard: Analyzing the relations among dashboard utilization, satisfaction, and learning achievement. *Asia Pacific Education Review*, 17(1), 13-24. <http://doi.org/10.1007/s12564-015-9403-8>
- Klašnja-Milićević, A., & Ivanović, M. (2018). Learning analytics - New flavor and benefits for educational environments. *Informatics in Education*, 17(2), 285-300. <http://doi.org/10.15388/infedu.2018.15>
- Leitner, P., Khalil, M., & Ebner, M. (2017). Learning analytics in higher education - A literature review. In A. Pena-Ayala (Ed.), *Learning analytics: Fundamentals, applications, and trends* (pp. 1-23). Springer. [https://doi.org/10.1007/978-3-319-52977-6\\_1](https://doi.org/10.1007/978-3-319-52977-6_1)
- Leung, C., Lai, C., Yuan, T., Pang, W., Tang, J. K., Ho, W., & Wong, T. (2015). The development of a final year project management system for information technology programmes. In K. C. Li, T. L. Wong, S. K. S. Cheung, J. Lam & K. K. Ng (Eds.), *Technology in education. Transforming educational practices with technology* (pp. 86-97). Springer. [https://doi.org/10.1007/978-3-662-46158-7\\_9](https://doi.org/10.1007/978-3-662-46158-7_9)
- Mehmet, K., & Arif, A. (2021). Effects of learner interaction with learning dashboards on academic performance in an e-learning environment. *Behaviour & Information Technology*, 40(2), 161-175.
- Mohamed, M. A., Abidin, A., Jamal, A. A., Amin, M., Rozaimée, A., & Wahab, F. A. (2017). An implementation of final year project management system: A case study at Universiti Sultan Zainal Abidin. *World Applied Sciences Journal*, 35(8), 1246-1251.
- Revythi, A., & Tselios, N. (2019). Extension of technology acceptance model by using system usability scale to assess behavioral intention to use e-learning. *Education and Information Technologies*, 24(4), 2341-2355. <http://doi.org/10.1007/s10639-019-09869-4>
- Roberts, L. D., Howell, J. A., & Seaman, K. (2017). Give me a customizable dashboard: Personalized learning analytics dashboards in higher education. *Technology, Knowledge and Learning*, 22(3), 317-333. <http://doi.org/10.1007/s10758-017-9316-1>
- Safsouf, Y., Mansouri, K., & Poirier, F. (2021). Experimental design of learning analysis dashboards for teachers and learners. In *Proceedings of the Eighth ACM Conference on Learning@ Scale* (pp. 347-350). ACM Publishing. <http://doi.org/10.1145/3430895.3460990>
- Sarikaya, A., Correll, M., Bartram, L., Tory, M., & Fisher, D. (2019). What do we talk about when we talk about dashboards? *IEEE Transactions on Visualization and Computer Graphics*, 25(1), 682-692. <http://doi.org/10.1109/TVCG.2018.2864903>
- Sønderlund, A. L., Hughes, E., & Smith, J. (2019). The efficacy of learning analytics interventions in higher education: A systematic review. *British Journal of Educational Technology*, 50(5), 2594-2618. <http://doi.org/10.1111/bjet.12720>
- Szynkiewicz, J., Munkvold, R. I., & Kolas, L. (2020). Progression of tool usage in project-based IT courses. In *Proceedings of the Frontiers in Education Conference* (Vol. 2020-October, pp. 1-5). IEEE Publishing. <http://doi.org/10.1109/FIE44824.2020.9274171>
- To, W. M., & Tang, M. N. F. (2019). Computer-based course evaluation: An extended technology acceptance model. *Educational Studies*, 45(2), 131-144. <http://doi.org/10.1080/03055698.2018.1443797>

- Tsai, Y. S., Rates, D., Moreno-Marcos, P. M., Muñoz-Merino, P. J., Jivet, I., Scheffel, M., Drachsler, H., Kloos, C. D., & Gašević, D. (2020). Learning analytics in European higher education - Trends and barriers. *Computers and Education*, 155, Article 103933. <http://doi.org/10.1016/j.compedu.2020.103933>
- Vakaloudis, A., Cahill, B., O'Leary, C., & Challa, D. (2020). Preparation and execution of final year student projects on the cloud. In *2020 IEEE Frontiers in Education Conference (FIE)* (pp. 1-7). IEEE Publishing. <http://doi.org/10.1109/FIE44824.2020.9273971>



## Pectinase Production from Banana Peel Biomass via the Optimization of the Solid-state Fermentation Conditions of *Aspergillus niger* Strain

Nazaitulshila Rasit<sup>1,2\*</sup>, Yong Sin Sze<sup>2</sup>, Mohd Ali Hassan<sup>1</sup>, Ooi Chee Kuan<sup>2</sup>, Sofiah Hamzah<sup>2</sup>, Wan Rafizah Wan Abdullah@Wan Abd. Rahman<sup>2</sup> and Md. Nurul Islam Siddique<sup>2</sup>

<sup>1</sup>Department of Bioprocess Technology, Faculty of Biotechnology and Biomolecular Sciences, Universiti Putra Malaysia, 43400 UPM, Serdang, Selangor, Malaysia

<sup>2</sup>Faculty of Ocean Engineering Technology and Informatics, Universiti Malaysia Terengganu, 21030 UMT, Kuala Nerus, Terengganu, Malaysia

### ABSTRACT

In this study, the biomass of banana peel was used to produce pectinase via optimization of solid-state fermentation conditions of the filamentous fungi *Aspergillus niger* (*A. niger*). The operating conditions of solid-state fermentation were optimized using the method of full factorial design with incubation temperature ranging between 25 °C and 35 °C, moisture content between 40% and 60%, and inoculum size between 1.6 x 10<sup>6</sup> spores/mL and 1.4 x 10<sup>7</sup> spores/mL. Optimizing the solid-state fermentation conditions appeared

crucial to minimize the sample used in this experimental design and determine the significant correlation between the operating conditions. A relatively high maximal pectinase production of 27 U/mL was attained at 35 °C of incubation, 60% of moisture content, and 1.6 x 10<sup>6</sup> spores/mL of inoculum size with a relatively low amount of substrate (5 g). Given that the production of pectinase with other substrates (e.g., pineapple waste, lemon peel, cassava waste, and wheat bran) generally ranges between 3 U/mL and 16 U/mL (Abdullah et al., 2018; Handa et al., 2016; Melnichuk et al., 2020;

### ARTICLE INFO

#### Article history:

Received: 15 June 2021

Accepted: 21 October 2021

Published: 15 December 2021

DOI: <https://doi.org/10.47836/pjst.30.1.14>

#### E-mail addresses:

nazaitulshila@umt.edu.my (Nazaitulshila Rasit)

p3312@pps.umt.edu.my (Yong Sin Sze)

alihas@upm.edu.my (Mohd Ali Hassan)

9w2ckq@gmail.com (Ooi Chee Kuan)

sofiah@umt.edu.my (Sofiah Hamzah)

wanrafizah@umt.edu.my (Wan Rafizah Wan Abdullah@Wan Abd.

Rahman)

m.nurul@umt.edu.my (Md. Nurul Islam Siddique)

\*Corresponding author

Thangaratham and Manimegalai, 2014; Salim et al., 2017), thus the yield of pectinase derived from the banana peel in this study (27 U/mL) was considered moderately high. The findings of this study indicated that the biomass of banana peel would be a potential substrate for pectinase production via the solid-state fermentation of *A. niger*.

*Keywords:* Banana peel, biomass, full factorial design, optimization, pectinase, solid-state fermentation

---

## INTRODUCTION

The pectinolytic enzymes, or more commonly known as pectinases, are normally found in plant cell walls. They break down the polysaccharide pectin through the reactions known as hydrolysis and de-esterification (Sudeep et al., 2020). Based on the mechanism of actions of their pectin molecules, they are classified into three groups, namely pectolyase, pectozyme, and polygalacturonase (Jayani et al., 2005). Given its capability to degrade plant materials, pectinase has a wide range of industrial uses, such as in the food processing industry (Ribeiro et al., 2010), textile manufacturing (Aggarwal et al., 2020), agricultural application (Al-Rousan et al., 2019) and environmental cares (Kamaruddin et al., 2019). However, the key role for the application is the capability of the enzyme to act as a catalyzing reaction in degrading a long and complex molecule presented in the cell wall of a plant cell, thus improving further related processes (Jayani et al., 2005; Ribeiro et al., 2010).

In the food processing industry, pectinase is combined with other enzymes, such as xylanases and cellulases, to increase juice extraction and clarity (Ribeiro et al., 2010, Dal Magro et al., 2018; Cerreti et al., 2016). Meanwhile, in the textile industry, pectinase is used to pre-treat the cotton fibers by bioscouring to increase their absorbency, making them suitable for subsequent staining (Aggarwal et al., 2020; Erdem & Bahtiyari, 2018). Furthermore, in agricultural application, pectinase is widely used in the extraction of olive oil to prevent emulsification by dispersing the oils droplets from peel extracts, thus facilitating its extraction later in the aqueous process (Al-Rousan et al., 2019; Caporaso, 2016). On the other hand, in the environmental application, pectinase is commonly used in wastewater treatment, whereby pretreatment of wastewater with pectinase could remove oil and grease from kitchen greywater, thereby reducing its biological oxygen demand (Kamaruddin et al., 2019).

Although pectinase occurs naturally in many terrestrial plants, in industrial applications, the microbial systems are used for pectinase production because they provide a higher yield at less cost (Ribeiro et al., 2010; Sudeep et al., 2020). There are various pectinase-producing microorganisms, such as bacteria, fungi, nematodes, and protozoans (Sudeep et al., 2020). The most widely used microorganism in pectinase production is the filamentous fungi, particularly the *Aspergillus niger* that the United States Food and Drug Administration (FDA) has classified under the Generally Recognized as Safe (GRAS) category (Jayani

et al., 2005). Also, the development of the fermentation technique, known as solid-state fermentation (SSF), has helped *A. niger* gain wide acceptance in industrial applications (Kapilan, 2015).

The SSF is an economical fermentation technique because the amount of water used is low, thereby reducing the chance of contamination. Also, the yield of SSF is higher than that of the conventional methods, such as liquid and submerged fermentation, because a high biomass ratio is used in the SSF (Doriya et al., 2007; Webb & Manan, 2017). In SSF fermentation, the substrate provides the nutrients that act as carbon and nitrogen sources for the microorganisms to grow on the culture medium (Kapilan, 2015). Thus, in the production of industrial pectinase, the selection of substrate and its availability has become a crucial factor in determining the production cost and efficiency (Abdullah et al., 2018; El Enshasy et al., 2018; Handa et al., 2016; Thangaratham & Manimegalai, 2014). In this respect, cheap carbon sources are commonly acquired from agro-industrial waste because they are highly abundant (Melnichuk et al., 2020; Salim et al., 2017). In this study, the biomass of banana peel, an underutilized agro-waste, was used as a substrate for pectinase production. The biological and physico-chemical factors are important in affecting the performance of SSF. Among the factors are temperature, moisture content, pH, aeration rate, and particle size of the substrate. The development of the SSF method varies according to the factors used, and each factor selected has its advantages and disadvantages (Webb & Manan, 2017).

In Malaysia, banana is the second-largest cultivated fruit, with a total production of about 530,000 metric tons in 2007, together with a substantial amount of banana peel (Mekhilef et al., 2011). The banana peel, comprising approximately 40% of the banana's weight, contains a relatively high amount of pectin (10-21% of its total biochemical content) (Mohapatra et al., 2010), making it a suitable substrate for the production of pectinase. In this study, the fungi *A. niger* was used to hydrolyze pectin in the banana peel for the production of pectinase using the SSF method. The objective of this study was to determine the optimal operating conditions for the SSF of *A. niger* in producing the maximum yield of pectinase at a specific amount of substrate. Thus, the use of banana peels would contribute toward more effective sustainable management of agro-waste in the country.

## **MATERIALS AND METHODS**

### **The Experimental Design and Optimization of Solid-state Fermentation**

In this study, the SSF with *A. niger* was used to produce pectinase, and the operating conditions of SSF were optimized for the maximum production of the enzyme. Three major factors influence the performance of SSF: biological factors, physico-chemical factors, and mechanical factors. However, only the biological and physico-chemical factors are frequently manipulated to enhance the productivity of SSF. Meanwhile, the latter can be further designed during the commercial stage (Webb & Manan, 2017).

Thus, this study selected three fermentation parameters for optimization, namely moisture content, temperature, and inoculum size. They are among the most commonly reported contributory biological and physico-chemical factors that control the dynamics of enzyme production. For example, the moisture content is known as the limiting factor for which *A. niger* grows optimally in the moisture content of 40% - 60% (Jayani et al., 2005; Manpreet et al., 2005) and in the inoculum size of  $1.59 \times 10^6$  spores/ml to  $1.43 \times 10^7$  spores/ml (Sandoval-Contreras et al., 2017). Meanwhile, the enzymatic reactions are dependent on incubating temperatures with high reactivity between 25 °C and 35 °C (Kapilan, 2015; Pandey et al., 2001).

The full factorial design incorporated in the Minitab Statistical Software (*Minitab LLC, Sydney, Australia*) was used to list all the possible interactive combinations of SSF parameters while determining the number of samples to be run. In addition, this study employed the 2k-level design, where k denoted the number of parameters examined in the experiment (Awad et al., 2011; Bouchekara et al., 2011). Altogether, this study experimented with 24 samples run in triplicates on three parameters.

### **The Substrate, Microorganisms, and Culture Conditions**

In this study, the biomass of banana peel served as the substrate for pectinase production. The banana peel collected from the local market was washed with tap water, sliced, and dried in an oven at 45 °C for 24 hours to remove the water content. The dried peel was grounded into fine masses, sieved through a standard mesh sieve of 75 µm, and stored at room temperature before using it as the solid substrate. Meanwhile, the CFR335 strain of *A. niger* used in this study to hydrolyze pectin in the substrate was obtained from the microbiological laboratory of Universiti Malaysia Terengganu. The fungi strain was inoculated on the potato-dextrose agar medium and incubated at 30 °C for six days to produce enough mature spores. Spores were then collected by flooding the surface of PDA with distilled water. Then, they were removed by scratching away from the PDA gently with a spatula and diluting with 500 mL of distilled water. The spores in the suspension were calculated as an inoculum size using a Neubauer Chamber (Sandoval-Contreras et al., 2017). These spores were then stored at 4 °C before they were used for pectinase production.

### **The Preparation of *A. niger* for Pectinase Production via Solid-State Fermentation**

The SSF technique used in this study was similar to the method described in Mansor et al. (2019). A series of 24 aqueous fermentation media with varying moisture contents were prepared. In the preparation of each fermentation medium, 5 g solid substrates were placed in each 100-mL Erlenmeyer flask and mixed with the corresponding amount of distilled water to produce the projected moisture content. Specifically, 5.5 mL and 7.5 mL of distilled water were added to generate a moisture content of 40% and 60%, respectively. These fermentation media were then sterilized at 121 °C for 20 minutes. Each fermentation

medium was inoculated with 2 mL of diluted *A. niger* at varying inoculum sizes upon cooling. Specifically, the fermentation medium of 40% and 60% were inoculated with *A. niger* at an inoculum size of  $1.59 \times 10^6$  spores/ml to  $1.43 \times 10^7$  spores/ml, respectively. The inoculum size of the mature spores *A. niger* was prepared by diluting 1 petri dish in 500 mL of distilled water and was calculated as  $1.59 \times 10^6$  spores/mL. Meanwhile, spores were collected from the PDA of 9 petri dishes, diluted with 500 mL of distilled water, and calculated as  $1.43 \times 10^7$  spores/ml. These inoculated fermentation media were then incubated at different temperatures for 120 hours. Specifically, 40% and 60% fermented medium were incubated at 25 °C and 35 °C, respectively. Table 1 shows the design matrix of the factors in the binary systems, and the coded values for the selected parameters are randomized. For each selected parameter, the low level and high level were coded -1 and +1, respectively.

Table 1

*The design matrix of aqueous fermentation for the optimization of pectinase*

Run Number	Coded Values of Variables			Pectinase Activity (U/ml)
	Temperature	Moisture Content	Inoculum Size	
1	-1	-1	-1	4.264
2	+1	-1	-1	16.116
3	-1	+1	-1	6.251
4	+1	+1	-1	27.678
5	-1	-1	+1	5.348
6	+1	-1	+1	20.813
7	-1	+1	+1	2.909
8	+1	+1	+1	16.477
9	-1	-1	-1	5.348
10	+1	-1	-1	15.935
11	-1	+1	-1	9.413
12	+1	+1	-1	23.704
13	-1	-1	+1	4.354
14	+1	-1	+1	17.019
15	-1	+1	+1	3.631
16	+1	+1	+1	19.368
17	-1	-1	-1	5.980
18	+1	-1	-1	17.019
19	-1	+1	-1	9.142
20	+1	+1	-1	25.510
21	-1	-1	+1	3.722
22	+1	-1	+1	19.368
23	-1	+1	+1	4.444
24	+1	+1	+1	18.284

## **Pectinase Extraction and Activity**

Upon the completion of fermentation, each of the inoculated fermentation mediums was added with 20 mL of 0.01 M sodium acetate buffer at pH 5.8. The Erlenmeyer flasks containing fermentation media were shaken at 120 rpm for 30 minutes. The suspension of each flask was filtered, and each filtrate was transferred into a separate Falcon tube. The cultured filtrate was cooled to 4 °C and centrifuged at 4000 rpm for 15 minutes. The supernatants were collected as crude pectinase. The extracted pectinase was analyzed for enzymatic activity using the method of dinitrosalicylic acid (DNS). The enzymatic concentration was defined as the amount of enzyme that catalyzes the  $\mu\text{mol}$  of substrate per minute under the assay condition (U/mL). Pectinase produced catalyzes the degradation of pectic substances in two reactions, which are depolymerization and desertification (Miller, 1959). Pectinase produced catalyzes the degradation of pectic substances in two reactions, which are depolymerization and desertification. The biological factors used in this study are related to the reproduction and metabolic process of the microorganism used in the SSF. On the other hand, the physico-chemical factors are related to the conditions inside the bioreactors during the SSF process.

## **Statistical Analyses, the Relative Importance, and Standardized Effects of Individual Parameter and their Interactions with other Parameters**

The underlying assumptions of ANOVA and outliers were examined with the residual plot, evaluating the difference between the predicted response value and observed response value (El-Zaher & Mahrouse, 2013). Also, the normal probability plot of residual analysis was used to check the normality of data (Hasan et al., 2009).

Meanwhile, the relative importance of each parameter was assessed with a Pareto chart, in which a statistical-based acceptance limit equivalent to 95% confidence level was used for ranking the effect of each parameter and their interactions (Van Hecke, 2016). Also, the normal probability plot was used to examine if the effect of a parameter by itself or in interaction with others was significant. The effect of a parameter or an interaction is significant if the plot is close to the normal line, but if the plot is centered on the zero value, the effect is deemed negligible (Kukreja et al., 2011; Regti et al., 2017). Besides, the main effect plot was used to determine the magnitude of each parameter for the optimized production of pectinase (Kukreja et al., 2011). On the other hand, the response surface and contour plots were used to determine the relationship and interaction between all the parameters on their responses to pectinase activity while establishing the desirable response values and operating conditions (Hank et al., 2014). Finally, the experimental results were validated with the optimization plots from Minitab Statistical Software.

## RESULTS AND DISCUSSION

### The Individual Effect and Interaction of Parameters

The main effect plot in Figure 1 shows that the plots for all the three parameters, namely incubation temperature, moisture content, and inoculum size, were not parallel with the reference line, suggesting that these parameters would affect the pectinase production. For the temperature plot, the highest pectinase activity was attained at 35 °C, and raising the incubation temperature from 25 °C to 35 °C increased the pectinase activity by 14 U/mL. Meanwhile, the moisture content of 60% yielded a pectinase activity of about 4 U/mL higher than the moisture content of 40%. Besides, an increase of inoculum size from  $1.59 \times 10^6$  spores/ml to  $1.43 \times 10^7$  spores/ml resulted in a decrease of 3 U/mL of pectinase activity. Together, the incubation temperature appeared to have the greatest effect on pectinase activity with the steepest plot slope than the moisture content and inoculum size.

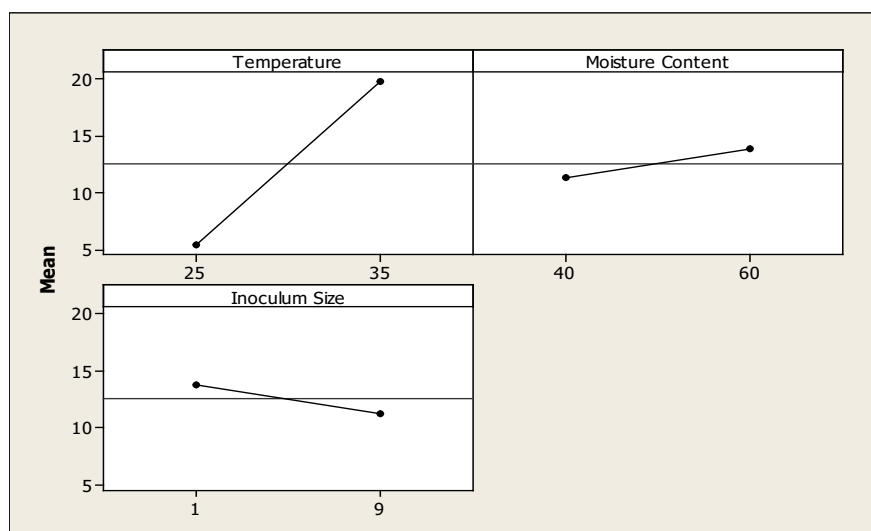


Figure 1. The main effect plots for pectinase activity

Meanwhile, the interaction between moisture content and inoculum size, with plots deviating more from parallel (Figure 2, bottom right), was greater than the interaction between incubation temperature and moisture content (Regti et al., 2017). Besides, the interaction plot of temperature and moisture content (Figure 2, top left) shows that the maximum pectinase activity was attained at an incubation temperature of 35 °C and a moisture content of 60%. For the interaction plot of moisture content and inoculum size, the highest pectinase activity was reached at a moisture content of 60% and an inoculum size of  $1.59 \times 10^6$  spores/ml. On the other hand, the interaction between incubation temperature and inoculum size was insignificant, with two nearly parallel lines (Figure 2, top right) (Hank et al., 2014).

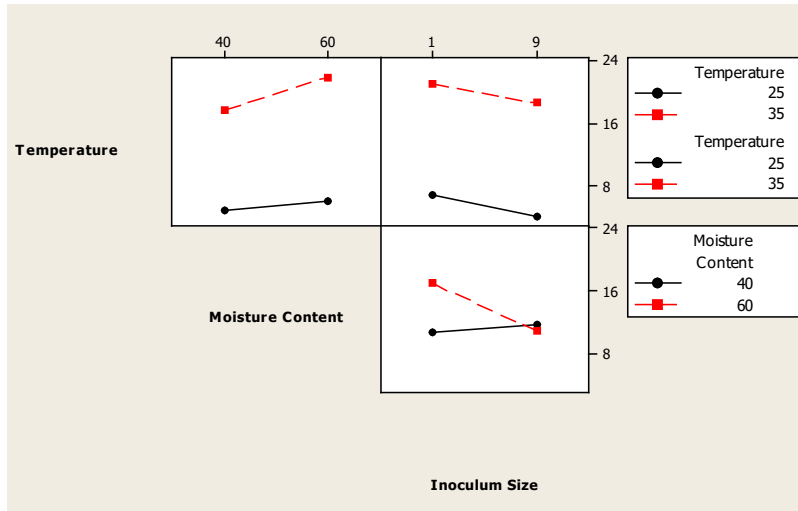


Figure 2. The interaction plots for pectinase activity

### Statistical Analysis, Residual Analysis, and the Relative Importance of Various Parameters

Pectinase produced from *A.niger* by using 5g banana peel as solid substrate in 24 experiment runs were conducted as suggested by the design matrix of Minitab for the selected parameter. The selected parameters with their corresponding low and high level were moisture content (40%, 60%), inoculum size ( $1.59 \times 10^6$  spores/ml,  $1.43 \times 10^7$  spores/ml) and incubation temperature (25 °C, 35 °C). Table 2 shows the effects of the individual parameter ( $X_1$ ,  $X_2$ , and  $X_3$ ) and their interactions ( $X_1X_2$ ,  $X_1X_3$ ,  $X_2X_3$ , and  $X_1X_2X_3$ ), the regression coefficients (RCs), standard error of RCs, and  $P$  value, i.e., the probability of statistical tests. Except for the interaction between temperature and inoculum size, the effects of each parameter and the remainders of their interactions were significant with  $P$  values  $<0.05$ . Equation 1 gives the regression of the interacting parameters with a coefficient of determination ( $R^2$ ) of 97.9% and a predicted  $R^2$  of 95.3%.

$$Y=12.587+7.187X_1+1.314X_2-1.276X_3+0.749X_1 X_2+0.057X_1X_3-1.773X_2X_3-0.802X_1X_2X_3 \quad (1)$$

The residuals of ANOVA show a normal distribution with a straight line with no outliers, skewness, or unknown variables detected (Figure 3). Furthermore, the histogram of residuals shows a similar pattern with a bell-shaped curve, suggesting that the errors were normally distributed with a mean value of zero. On the other hand, the plot of residuals versus fitted values shows that the residuals were scattered randomly around zero, indicating a constant variance for the errors. Finally, the plot of residuals in the



order of corresponding observation shows that the residuals ranged between 2 and -2 and were randomly scattered around zero. Thus, the residual analysis suggested that the model adequately explained the data.

Table 2

The estimated effects and regression coefficients for the optimization of pectinase

Term	Effect	Regression Coefficient (RC)	SE of RC*	T**	P value
Constant (average value of the enzyme yield from the total run)		12.587	0.2812	44.76	0
Temperature ( $X_1$ )	14.374	7.187	0.2812	25.56	0
Moisture Content ( $X_2$ )	2.627	1.314	0.2812	4.67	0
Inoculum Size ( $X_3$ )	-2.552	-1.276	0.2812	-4.54	0
$X_1X_2$	1.498	0.749	0.2812	2.66	0.017
$X_1X_3$	0.113	0.057	0.2812	0.2	0.843
$X_2X_3$	-3.546	-1.773	0.2812	-6.3	0
$X_1X_2X_3$	-1.603	-0.802	0.2812	-2.85	0.012

S=1.37761\*\*\* PRESS=68.3210§

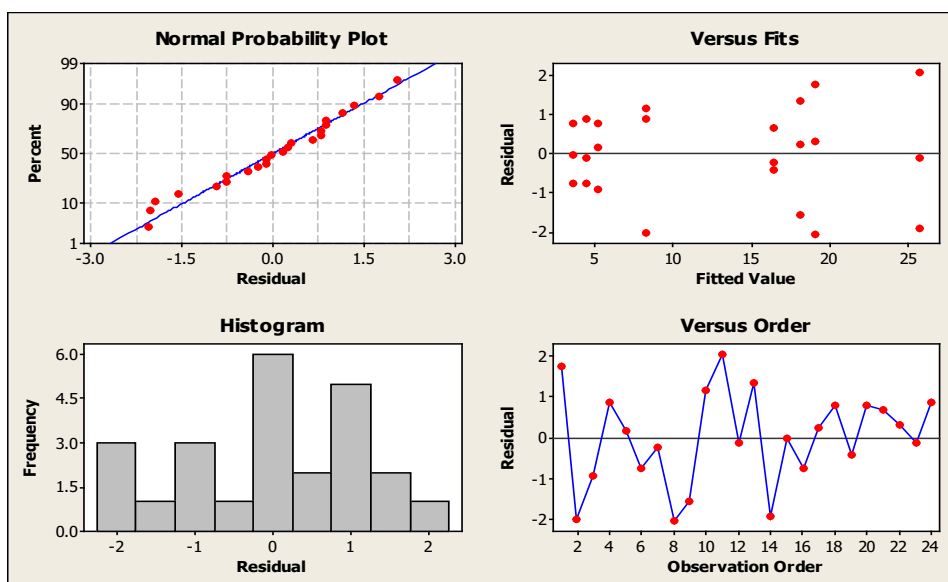
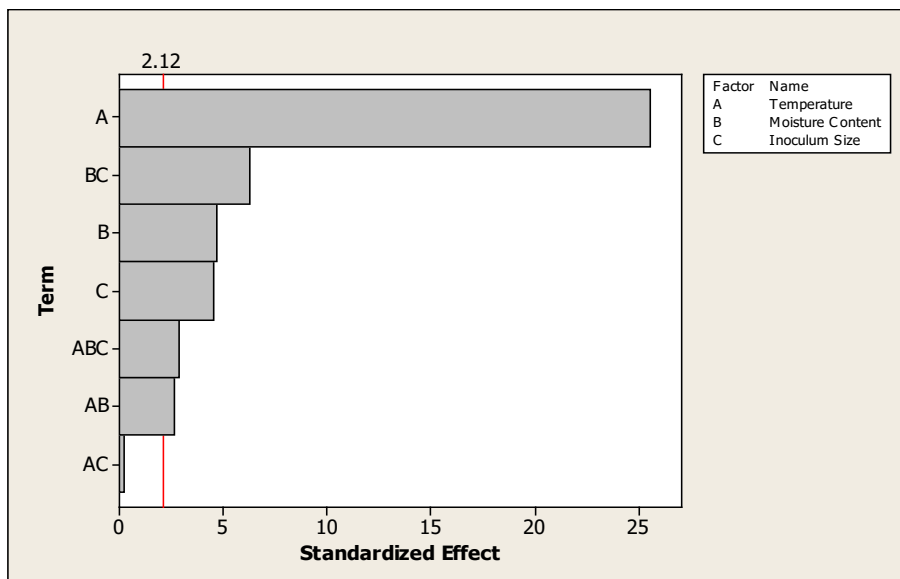


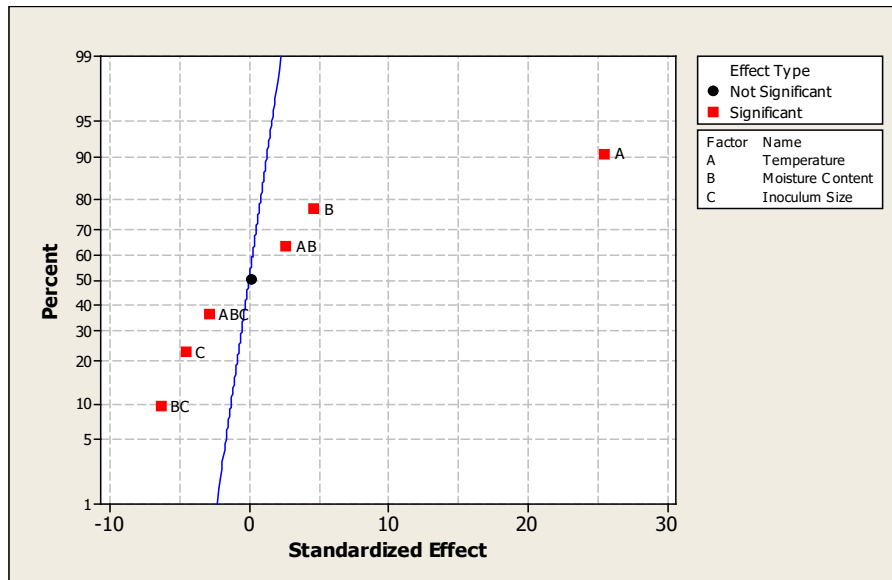
Figure 3. The residual plots for pectinase activity

Meanwhile, the Pareto chart (Figure 4a) shows a similar result to the Full Factorial Analysis (Table 2), i.e., except for the interaction between temperature and inoculum size (AC), all other standardized effects, inclusive each parameter by itself and its interaction with other parameters, were significant with values exceeding the threshold of 2.1 at 95% confidence level. Also, the Pareto chart indicates that the incubation temperature (A) was the most influencing parameter on the pectinase activity, followed by the interaction of moisture content and inoculum size (BC), moisture content by itself (B), inoculum size by itself (C), the interaction of temperature, moisture content, and inoculum (ABC), and interaction between temperature and moisture content (AB).

Also, the results of the normal probability plot (Figure 4b) were in congruence with that of the statistical tests and the Pareto chart, i.e., except for the interaction between temperature and inoculum size (AC), all other standardized effects, inclusive a parameter by itself and its interaction with other parameters, were significant with plots centered around the zero value. Besides, the incubation temperature (A), with the largest plot value and locating the farthest from the normal line, appeared to have the greatest effect on the SSF. In addition, the standardized effects of incubation temperature (A), moisture content (B), and interaction between incubation temperature and moisture content (AB) occurred on the right of the normal line, indicating a positive effect of these factors on the SSF. In contrast, the standardized effects of inoculum size (C), interactions of incubation temperature, moisture content, and inoculum size (ABC), and interaction between moisture content and inoculum size (BC) occurred on the left of the normal line, showing a negative effect of these factors on the SSF.



(a)



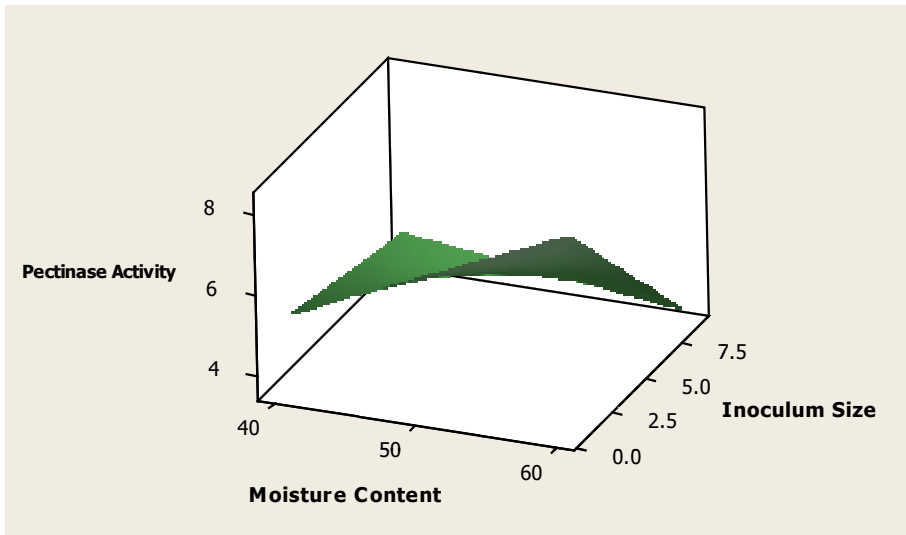
(b)

Figure 4. The (a) Pareto chart; and (b) normal probability plot of standardized effects

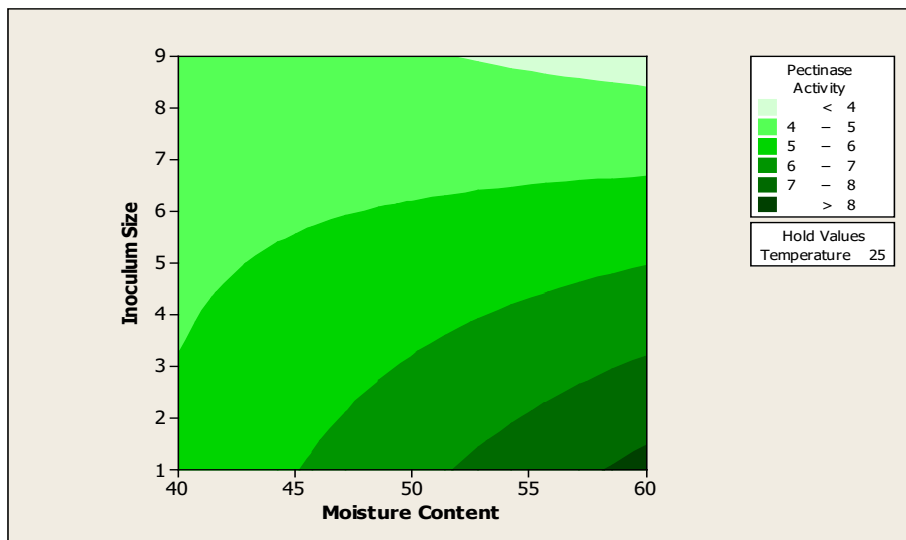
### The Response Surface, Contour Plots, and Optimization

As a starting point, the hold value of response surface for each parameter was set to the lowest level, i.e., 25 °C for incubation temperature, 40% for moisture content, and  $1.59 \times 10^6$  spores/ml for inoculum size. For the interaction between moisture content and inoculum size, a relatively high pectinase activity was attained at a combination of high moisture content of 60% and low inoculum size of  $1.59 \times 10^6$  spores/ml (Figure 5a). A similar trend is shown in the contour plot of this interaction (Figure 5b). The maximum pectinase activity was attained at increasing moisture content in combination with decreasing inoculum size. Thus, the responses of moisture content appeared to be inhibited by high inoculum size, i.e., however high the moisture content increased, the maximal pectinase activity would remain unachievable if the inoculum size were not reduced.

Meanwhile, the surface plot for the interaction (Figure 6a) between temperature and moisture content shows that the maximum pectinase activity was achieved when the moisture content and incubation temperature were at their respective highest magnitude, namely 60% and 35 °C. Also, the contour plot for this interaction (Figure 6b) shows a directly proportional relationship, and the pectinase activity was the highest at 60% moisture content and 35 °C incubation temperature. Thus, the temperature plays an important role in the SSF process because it will determine the occurrence of protein denaturation, enzymatic inhibition, and cell death. Furthermore, the temperature will affect the germination of fungi, production of primary and secondary metabolites, and sporulation (Melnichuk et al., 2020; Thangaratham & Manimegalai, 2014).

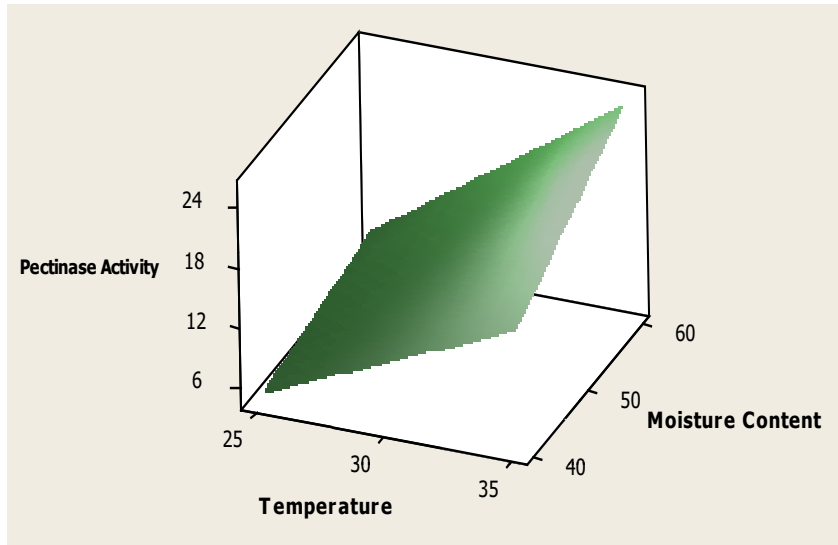


(a)

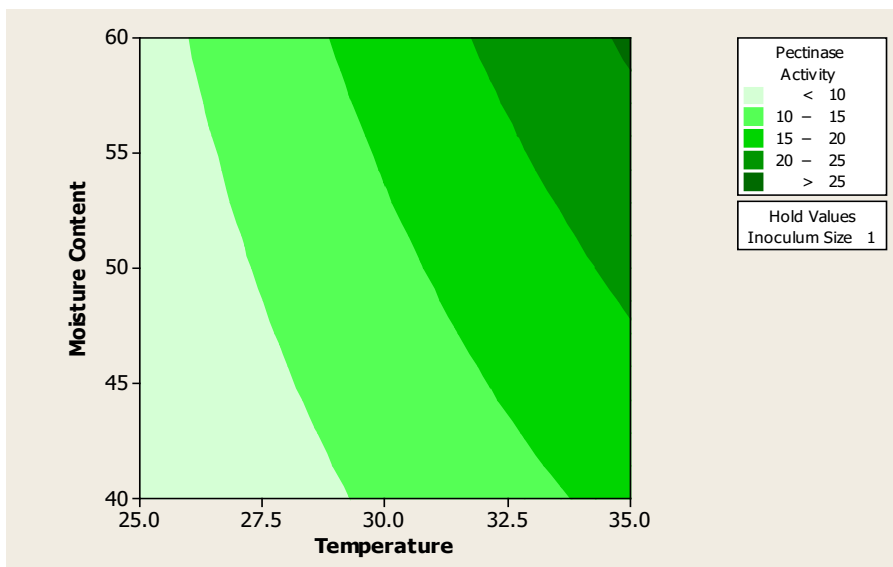


(b)

Figure 5. The surface plot (a) and contour plot (b) for the interaction between moisture content and inoculum size on pectinase activity



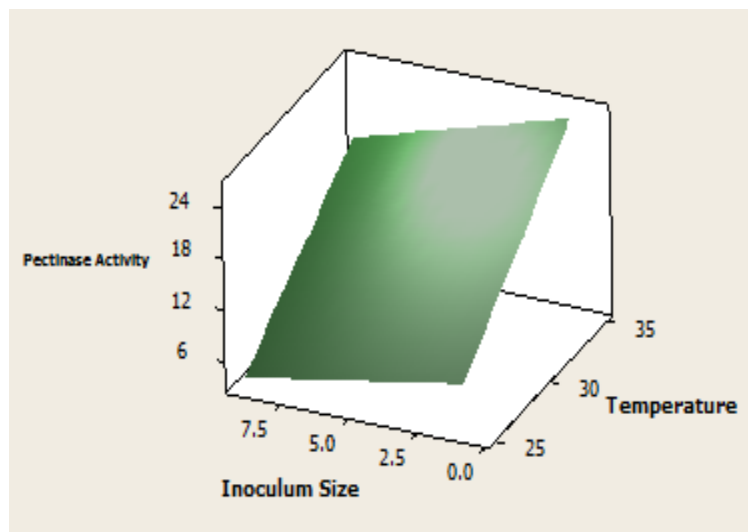
(a)



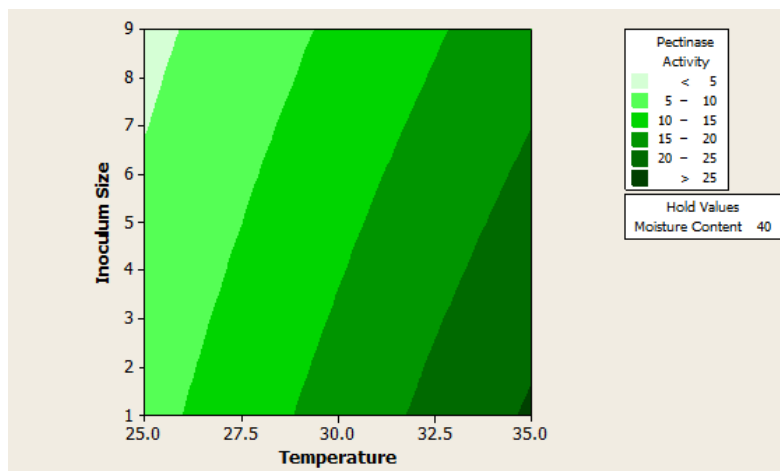
(b)

Figure 6. The surface plot (a) and contour plot (b) for the interaction between moisture content and temperature on pectinase activity

On the other hand, the surface plot for the interaction between inoculum size and temperature (Figure 7a) shows that a combination of low inoculum size ( $1.59 \times 10^6$  spores/ml) and high temperature ( $35^\circ\text{C}$ ) yielded high pectinase activity. The contour plot for this interaction (Figure 7b) shows that the highest pectinase activity was achieved at  $35^\circ\text{C}$  incubation temperature and  $1.59 \times 10^6$  spores/ml inoculum size. However, the interaction between incubation temperature and inoculum size was relatively mild since the curvature of its plot (Figure 7b) was not as pronounced as those of the other two interactions (Figures 5b and 6b). Together, the optimum conditions for the maximum pectinase activity were  $35^\circ\text{C}$  incubation temperature, 60% moisture content, and  $1.59 \times 10^6$  spores/ml of inoculum size.



(a)



(b)

Figure 7. The surface plot (a) and contour plot (b) for the interaction between temperature and inoculum size on pectinase activity.

Finally, in the validation of experimental results, the minimum and maximum pectinase activity were set to 20 U/ml and 30 U/ml, respectively, yielding an average of 25 U/ml as the target value (Ayed et al., 2012). The optimization plot (Figure 8) shows that the target pectinase activity was predicted to achieve at 35 °C incubation temperature, 58.6% moisture content, and  $1.59 \times 10^6$  spores/ml of inoculum size, and the desirability to achieve the target was 1. Besides, the plot's desirability shape shows that a higher temperature and moisture content with a lower inoculum size was optimal for a maximum yield of pectinase production. On the other hand, other than banana peel biomass, agro-industrial residues used in the SSF are sugar cane bagasse, wheat bran, rice husk, coconut coir pith, banana waste, tea waste, apple pomace, and many more (Kapilan, 2015). Therefore, other than the parameters used in the study, a few factors affect the selection of substrate for producing an enzyme: the cost and availability of substrate (Pandey et al., 2001).

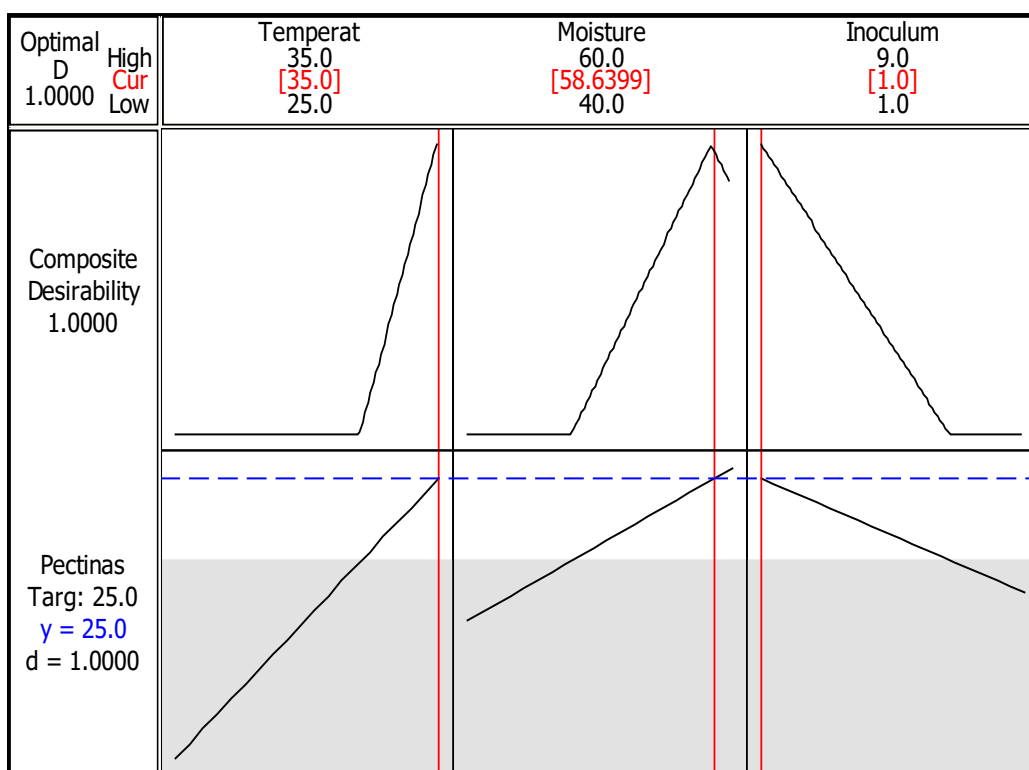


Figure 8. The process optimization curve

## CONCLUSION

In this study, the incubation temperature was the most crucial parameter in driving for the maximum production of pectinase. However, the interaction between incubation temperature and inoculum size did not affect the pectinase activity. A weak interaction was found between the incubation temperature and inoculum size, whereas a strong interaction occurred between the moisture content and inoculum size. Therefore, the optimum conditions for the pectinase production in SSF were 35 °C incubation temperature, 60% moisture content, and  $1.59 \times 10^6$  spores/ml of inoculum size, with the highest pectinase activity at 27 U/mL. Given that the production of pectinase with other substrates (e.g., pineapple waste, lemon peel, cassava waste, and wheat bran) generally ranges between 3 U/mL and 16 U/mL (Abdullah et al., 2018; Handa et al., 2016; Melnichuk et al., 2020; Thangaratham & Manimegalai, 2014; Salim et al., 2017), thus the yield of pectinase derived from the banana peel in this study (27 U/mL) was considered moderately high. Therefore, the biomass of banana peel has the potential to be used as a substrate in SSF for pectinase production. If this design of optimum operating conditions could be commercialized, it would enhance the efficiency of managing agro-industrial waste for sustainable development.

## ACKNOWLEDGEMENTS

The Fundamental Research Grant Scheme (FRGS-Vot. No. 59437) of the Ministry of Higher Education Malaysia provided financial support for this study. In addition, the authors would like to thank Universiti Malaysia Terengganu for the assistance provided during this study.

## REFERENCES

- Abdullah, R., Jafer, A., Nisar, K., Kaleem, A., Iqtedar, M., Iftikhar, T., Saleem, F., & Naz, S. (2018). Process optimization for pectinase production by locally isolated fungal strain. *Bioscience Journal*, 34(4), 1025-1032. <https://doi.org/10.14393/BJ-v34n1a2018-39947>
- Aggarwal, R., Dutta, T., & Sheikh, J. (2020). Extraction of pectinase from *Candida* isolated from textile mill effluent and its application in bio-scouring of cotton. *Sustainable Chemistry and Pharmacy*, 17, Article 100291. <https://doi.org/10.1016/j.scp.2020.100291>
- Al-Rousan, W. M., Al-Marazeeq, K., Abdullah, M. A., Khalailah, N., & Ajo, R. Y. (2019). Use enzymatic preparations to enhance olive oil extraction and their quality. *Journal of Food and Nutrition Research*, 7(4), 311-318. <https://doi:10.12691/jfnr-7-4-8>
- Awad, G. E. A., Elnashar, M. M. M., & Danial, E. N. (2011). Optimization of phytase production by *Penicillium funiculosum* NRC467 under solid state fermentation by using full factorial design. *World Applied Sciences Journal*, 15(11), 1635-1644. <https://doi.org/10.1016/j.sjbs.2013.06.004>
- Ayed, L., Ksibi, I., Cheref, A., & Bakhrouf, A. (2012). Response surface methodology for optimization of the treatment of textile wastewater by a novel bacterial consortium: Enzymes and metabolites characterization. *Journal of Biotechnology*, 11(59), 12339-12355. <https://doi:10.5897/AJB11.3506>



- Boucekara, H. R. E. H., Boucherma, M., & Allag, H. (2011). Interactive implementation of experimental design method-application to engineering optimal design. *American Journal of Computational and Applied Mathematics*, 1(2), 78-85. <https://doi.org/10.5923/j.ajcam.20110102.15>
- Caporaso, N. (2016). Virgin olive oils: Environmental conditions, agronomical factors and processing technology affecting the chemistry of flavor profile. *Journal of Food Chemistry & Nanotechnology*, 2(1), 21-31. <https://doi.org/10.17756/jfcn.2016-007>
- Cerreti, M., Liburdi, K., Benucci, I., & Esti, M. (2016). The effect of pectinase and protease treatment on turbidity and on haze active molecules in pomegranate juice. *LWT-Food Science and Technology*, 73, 326-333. <https://doi.org/10.1016/j.lwt.2016.06.030>
- Dal Magro, L., Silveira, V. C. C., de Menezes, E. W., Benvenuto, E. V., Nicolodi, S., Hertz, P. F., & Rodrigues, R. C. (2018). Magnetic biocatalysts of pectinase and cellulase: Synthesis and characterization of two preparations for application in grape juice clarification. *International Journal of Biological Macromolecules*, 115, 35-44. <https://doi.org/10.1016/j.ijbiomac.2018.04.028>
- Doriya, K., Jose, N., Gowda, M., & Kumar, D. S. (2016). Solid-state fermentation vs submerged fermentation for the production of L-Asparaginase. *Advances in Food and Nutrition Research*, 78, 115-135. <https://doi.org/10.1016/bs.afnr.2016.05.003>
- El Enshasy, H. A., Elsayed, E. A., Suhaimi, N., Malek, R. A., & Esawy, M. (2018). Bioprocess optimization for pectinase production using *Aspergillus niger* in a submerged cultivation system. *BMC Biotechnology*, 18(71), 1-13. <https://doi.org/10.1186/s12896-018-0481-7>
- El-Zaher, A. A., & Mahrouse, M. A. (2013). A validated spectrofluorimetric method for the determination of nifuroxazide through coumarin formation using experimental design. *Chemistry Central Journal*, 7, 90-102. <https://doi.org/10.1186/1752-153X-7-90>
- Erdem, A., & Bahtiyari, M. I. (2018). Ultrasonic-bioscouring and ozone based bleaching of cotton slivers and coloration of them with natural dye sources. *Journal of Cleaner Production*, 188, 670-677. <https://doi.org/10.1016/j.jclepro.2018.03.166>
- Handa, S., Sharma, N., & Pathania, S. (2016). Multiple parameter optimization for maximization of pectinase production by *Rhizopus* sp. C4 under solid state fermentation. *Fermentation*, 2(4), Article 10. <https://doi.org/10.3390/fermentation2020010>
- Hank, D., Azi, Z., Hocine, S. A., Chaalal, O., & Hellal, A. (2014). Optimization of phenol adsorption onto bentonite by factorial design methodology. *Journal of Industrial and Engineering Chemistry*, 20, 2256-2263. <https://doi.org/10.1016/j.jiec.2013.09.058>
- Hasan, S. H., Srivastava, P., & Talat, M. (2009). Biosorption of Pb (II) from water using biomass of *Aeromonas hydrophilia*: Central composite design for optimization of process variables. *Journal of Hazardous Materials*, 168, 1155-1162. <https://doi.org/10.1016/j.jhazmat.2009.02.142>
- Jayani, R. S., Saxena, S., & Gupta, R. (2005). Microbial pectinolytic enzymes: A review. *Process Biochemistry*, 40, 2931-2944. <https://doi.org/10.1016/j.procbio.2005.03.026>
- Kamaruddin, M. A., Ibrahim, M. H., Thung, L. M., Emmanuel, M. I., Niza, N. M., Shadi, A. M. H., & Norashiddin, F. A. (2019). Sustainable synthesis of pectinolytic enzymes from citrus and *Musa acuminata* peels for biochemical oxygen demand and grease removal by batch protocol. *Applied Water Science*, 9(4), 1-10. <https://doi.org/10.1007/s13201-019-0948-2>

- Kapilan, R. (2015). Solid state fermentation for microbial products: A review. *Archives of Applied Science Research*, 7(8), 21-25.
- Kukreja, A., Chopra, P., Aggarwal, A., & Khanna, P. (2011). Application of full factorial design for optimization of feed rate of stationary hook hopper. *International Journal of Modeling and Optimization*, 1(3), 205-209.
- Manpreet, S., Sawraj, S., & Sachin, D. (2005). Influence of process parameters on the production of metabolites in solid-state fermentation. *Malaysian Journal of Microbiology*, 1(2), 1-9.
- Mansor, A., Ramlia, M. S., Rashida, N. Y. A., Samat, N., Lani, M. N., Sharifudin, S. A., & Raseetha, S. (2019). Evaluation of selected agri-industrial residues as potential substrates for enhanced tannase production via solid-state fermentation. *Biocatalysis and Agricultural Biotechnology*, 20, Article 101216. <https://doi.org/10.1016/j.bcab.2019.101216>
- Mekhilef, S., Saidur, R., Safari, A., & Mustafa, W. E. S. B. (2011). Biomass energy in Malaysia: Current state and prospects. *Renewable and Sustainable Energy Reviews*, 15(7), 3360-3370.
- Melnichuk, N., Braia, M. J., Anselmi, P. A., Meini, M. R., & Romanini, D. (2020). Valorization of two agroindustrial wastes to produce alpha-amylase enzyme from *Aspergillus oryzae* by solid-state fermentation. *Waste Management*, 106, 155-161. <https://doi.org/10.1016/j.wasman.2020.04.016>
- Miller, G. L. (1959). Use of dinitrosalicylic acid reagent for determination of reducing sugar. *Analytical Chemistry*, 31(3), 426-428. <https://doi.org/10.1021/ac60147a030>
- Mohapatra, D., Mishra, S., & Sutar, N. (2010). Banana and its by-product utilization: An overview. *Journal of Scientific & Industrial Research*, 69, 323-329.
- Pandey, A., Soccol, C. R., & Rodriguez-Leon, J. A. (2001). *Aspects of design of fermenter in solid-state fermentation. Solid-state fermentation in Biotechnology: Fundamentals and Application* (1st Ed.). Asistech Publishers.
- Regti, A., El Kassimi, A., Laamari, M. R., & El Haddad, M. (2017). Competitive adsorption and optimization of binary mixture of textiles dyes: A factorial design analysis. *Journal of the Association of Arab Universities for Basic and Applied Sciences*, 24, 1-9. <https://doi.org/10.1016/j.jaubas.2016.07.005>
- Ribeiro, D. S., Henrique, S., Oliveira, L. S., Macedo, G. A., & Fleuri, L. F. (2010). Enzymes in juice processing: A review. *International Journal of Food Science Technology*, 45(4), 635-641. <https://doi.org/10.1111/j.1365-2621.2010.02177.x>
- Salim, A. A., Grbavčić, S., Šekuljica, N., Stefanović, A., Tanasković, S. J., Luković, N., & Knežević-Jugović, Z. (2017). Production of enzymes by a newly isolated *Bacillus* sp. TMF-1 in solid state fermentation on agricultural by-products: The evaluation of substrate pretreatment methods. *Bioresource Technology*, 228, 193-200. <https://doi.org/10.1016/j.biortech.2016.12.081>
- Sandoval-Contreras, T., Marín, S., Villarruel-López, A., Gschaedler, A., Garrido-Sánchez, L., & Ascensio, F. (2017). Growth modeling of *Aspergillus niger* strains isolated from citrus fruit as a function of temperature on a synthetic medium from lime (*Citrus latifolia* T.) Pericarp. *Journal of Food Production*, 80(7), 1090-1098. <https://doi.org/10.4315/0362-028X.JFP-16-408>
- Sudeep, K. C., Upadhyaya, J., Joshi, D. R., Lekhak, B., Chaudhary, D. K., Pant, B. R., & Raghavan, V. (2020). Production, characterization, and industrial application of pectinase enzyme isolated from fungal strains. *Fermentation*, 6(2), Article 59. <https://doi.org/10.3390/fermentation6020059>

- Thangaratham, T., & Manimegalai, G. (2014). Optimization and production of pectinase using agro waste by solid state and submerged fermentation. *International Journal of Current Microbiology and Applied Science*, 3(9), 357-365.
- Van Hecke, T. (2016). Pareto plot threshold for multiple management factors in design of experiments. *Journal of Statistics and Management Systems*, 20(2), 235-244. <https://doi.org/10.1080/09720510.2016.1231967>
- Webb, C., & Manan, M. A., (2017). Design aspects of solid state fermentation as applied to microbial bioprocessing. *Journal of Applied Biotechnology & Bioengineering*, 4(1), 511-532. <https://doi: 10.15406/jabb.2017.04.00094>



## Compression and Flexural Behavior of ECC Containing PVA Fibers

Lee Siong Wee<sup>1\*</sup>, Mohd Raizamzamani Md Zain<sup>2</sup>, Oh Chai Lian<sup>2</sup>, Nadiah Saari<sup>2</sup>  
and Norrul Azmi Yahya<sup>2</sup>

<sup>1</sup>*School of Civil Engineering, College of Engineering, Universiti Teknologi MARA Cawangan Johor, Kampus Pasir Gudang Campus, 81750 UiTM, Masai, Johor, Malaysia*

<sup>2</sup>*School of Civil Engineering, College of Engineering, Universiti Teknologi MARA Shah Alam, 40450 UiTM, Shah Alam, Selangor, Malaysia*

### ABSTRACT

Research on Engineered Cementitious Composites (ECC) is overwhelming owing to its wide structural applications that can serve multi-functional purposes in civil and environmental infrastructures. Compared to other high-performance fiber reinforced concrete, ECC yields superior tensile ductility and multiple cracking behaviors when subjected to tensile loadings even with low to moderate volume of fibers. This paper presents the flexural properties of ECC made of cement, an industrial by-product, such as ground granulated blast-furnace slags (GGBS), local silica sand, polyvinyl alcohol (PVA) fiber, water, and superplasticizer (SP). Two series of ECC mixtures (ECC-G50 series and ECC-G60 series) and one control mixture were designed. The effect of two different fiber contents in volume

fraction was investigated for the two series of ECC mixtures. The compression and flexural tests were conducted on ECC and control specimens after 28 days of curing. A compression test revealed that almost all ECC mixtures improved compressive strength between 20% to 30% compared to the control specimens. In addition, all ECC plate specimens demonstrated excellent strain-hardening states (i.e., displacement capacity at least ten times greater than the control specimens) and multiple fine-cracks failure modes after the three-point bending

### ARTICLE INFO

#### Article history:

Received: 12 June 2021

Accepted: 28 September 2021

Published: 15 December 2021

DOI: <https://doi.org/10.47836/pjst.30.1.15>

#### E-mail addresses:

leesiongwee@uitm.edu.my (Lee Siong Wee)

raizam@uitm.edu.my (Mohd Raizamzamani Md Zain)

chailian@uitm.edu.my (Oh Chai Lian)

nadia903@uitm.edu.my (Nadiah Saari)

norrulazmi@uitm.edu.my (Norrul Azmi Yahya)

\*Corresponding author

test. The increase in fiber content slightly reduced the compressive strength but enhanced the flexural behavior of the ECC-G50 series. However, this observation is not discovered in the ECC-G60 series. Outcomes of this research assist material scientists on the content of PVA fiber and GGBS used in making ECC.

*Keywords:* Compressive strength, cracking, ductility, engineered cementitious composites (ECC), flexural strength, ground granulated blast-furnace slag (GGBS), polyvinyl alcohol (PVA) fiber

---

## INTRODUCTION

Engineered Cementitious Composites (ECC) appeared to solve the problem of normal concrete, which is commonly known as brittle material under tension loads. ECC is similar to high-performance fiber-reinforced cementitious composites. However, the main focus of this material relies on its ability to achieve tensile ductility and strain hardening rather than on compressive strength. According to Li et al. (2001), ECC can achieve strain capacity up to 5% under tensile stress depending on the design of ECC mixtures and selection of ingredients. Furthermore, unlike concrete, ECC exhibits multiple fine cracking of equal or lesser than 100  $\mu\text{m}$  width (Li et al., 2001); this shows a remarkable damage tolerance feature that requires minor repair to none (Parra-Montesinos et al., 2005). A compatible deformation and improved bond-slip behavior were also observed in steel-reinforced ECC (Lee et al., 2016). With all these reliable features, ECC is suitable for earthquake resistance structures, as demonstrated by previous studies (Qudah & Maalej, 2014; Said & Razak, 2016; Lee et al., 2018a). In addition, ECC can be designed to cater to different functionalities, such as self-sensing and self-healing, as it is subjected to different types of loading and different exposure conditions or environments.

In terms of durability, ECC is recognized as superior compared to other high-performance fiber-reinforced cementitious composites because of its multiple tight crack widths that can provide better protection of steel reinforcement from corrosion. Therefore, it is important to ensure ECC infrastructures maintain their strength, stiffness, and serviceability throughout their design life span. Previous studies have confirmed that the use of ECC is feasible for more durable and sustainable development (Adesina & Das, 2021; Kewalramani et al., 2017; Li et al., 2004; Liu et al., 2017; Nemecek et al., 2006; Sahmaran & Li, 2007; Sahmaran & Li, 2008; Suthiwarapirak et al., 2002; Wang & Li, 2006).

Another interesting fact about ECC is the number of fibers incorporated in cementitious composites. Typically, a low to the moderate volume fraction of between 1.5% to 3% of fibers is sufficient to ensure ECC attains its desirable displacement capacity. Therefore, the additional cost of this material due to the use of fibers is still bearable if the purpose of using ECC is served. There are few types of fibers commonly employed in ECC mixtures,

and it is found that ECCs that contain polyvinyl alcohol (PVA) fibers have consistently exhibited excellent durability, greater mechanical properties as well as enhanced structural performances (Meng et al., 2017; Pakravan et al., 2018; Yang & Li, 2014). Some researchers explored the use of polypropylene (PP) fibers instead of PVA in the making of ECC, together with some of the locally available materials (Zhang et al., 2014; Zhang et al., 2015; Lee et al., 2018b; Lee et al., 2019a, Lee et al., 2019b; Zhu et al., 2020). In one of these studies, PP fibers of volume fractions 1.5%, 2.0%, and 2.5% were employed in ECC with GGBS to study the flexural strength and ductility (Lee et al., 2018b). The results showed that ECC with PP fibers could not achieve the strain-hardening behavior under the three-point bending test. Another investigation by Lee et al. (2019a) reported that tensile softening behavior of ECC specimens was observed under direct tensile test. Therefore, this study aims to investigate the performance of ECC under compression and flexural loadings by substituting PP fibers with PVA fibers in the ECC design mix, as stated in Lee et al. (2018b). A compression test is accepted as the most basic test to determine the compressive strength for any cementitious material. Even though a direct tensile test is the best way to demonstrate the tensile ductility of ECC, this test setup is complicated and time-consuming. Therefore, as an alternative, the flexural bending test was conducted to provide equivalent flexural ductility of ECC. Flexural behaviors of ECC were evaluated through the first cracking strength, the ultimate flexural strength, and its corresponding displacement.

## MATERIALS AND METHODS

### Materials

The design method of ECC is based on micromechanics-strain hardening criteria, as mentioned in Yang et al. (2007). The composition mixture of ECC-GGBS in this study includes cement, GGBS, PVA fiber, silica sand, water, and SP, as shown in Table 1. There are two series of ECC, namely G50 and G60, that represent 50% and 60% of cement substitution with GGBS. In each series, two different contents of PVA fibers at 2.0% and 2.5% of volume fraction were investigated, represented by F2.0 and F2.5, respectively. The amount of water, superplasticizer, and silica sand were almost identical for all ECC design mixes, as shown in Table 1. Moreover, Table 1 also indicated the design mix proportions from the previous study compared to the design mixtures of ECC in this study (Lee et al., 2018b). With an exception for the river sand, which was substituted with silica sand and PVA fibers were replaced by PP fibers, all other ingredients were identical under the same series of ECC design.

The amount of water used was calculated based on the water to binder ratio (0.27). Binder refers to the total unit weight of cement and GGBS. It is worthy of mentioning that the fresh density of all ECC mixtures was designed in the range of 2133 to 2159 kg/m<sup>3</sup>,

which were comparable to standard ECC mixtures studied in the literature. Local silica sand with a grain size of an average of 285  $\mu\text{m}$  was used in the ECC mixtures, and its physical properties are shown in Table 2. For PVA fibers, the diameter and the length were 40  $\mu\text{m}$  and 8 mm, respectively. The tensile strength of this fiber was 1600 MPa, a density of 910  $\text{kg}/\text{m}^3$  were employed, and local river sands below 600  $\mu\text{m}$  were incorporated in the cementitious matrix (Lee et al., 2018b).

Table 1

*Design mix proportion for control and ECC ( $\text{kg}/\text{m}^3$ )*

Mixture	Cement	GGBS	Water	PVA fiber	Superplasticizer	Silica sand	Density
Control	1444	0	390	0	10	289	2133
G50F2.0	722	722	390	26	10	289	2159
G50F2.5	719	719	388	32	10	288	2156
G60F2.0	575	863	388	26	10	288	2150
G60F2.5	572	858	386	32	10	286	2144
G50S0.2F2.0*	723	723	390	18 (PP fiber)	10	289	2153
G50S0.2F2.5*	719	719	388	23 (PP fiber)	10	288	2147
G60S0.2F2.0*	575	863	388	18 (PP fiber)	10	288	2142
G60S0.2F2.5*	572	858	386	23 (pp fiber)	10	286	2135

\*ECC mix proportions employed in the previous study (Lee et al., 2018b).

Table 2

*Physical properties of silica sand*

Physical percentage (%)	Properties
Loss of ignition	< 0.5
10 Mesh Residue	< 0.2
40 Mesh Residue	> 75

Table 3

*Chemical composition of GGBS and silica sand*

Chemical composition	GGBS (%)	Silica sand (%)
Silica ( $\text{SiO}_2$ )	33.2	> 98.0
Alumina ( $\text{Al}_2\text{O}_3$ )	12.1	< 0.3
Titanium Oxide ( $\text{TiO}_2$ )	0.54	-
Calcium Oxide ( $\text{CaO}$ )	44.2	-
Magnesia ( $\text{MgO}$ )	5.5	< 0.5
Sulphide Sulphur $\text{S}^2$	0.7	-



Table 3 (Continue)

Chemical composition	GGBS (%)	Silica sand (%)
Sulphate (SO <sub>3</sub> )	2.0	-
Potassium Oxide (K <sub>2</sub> O)	0.42	< 0.3
Sodium Oxide (Na <sub>2</sub> O)	0.18	-
Alkalis	0.46	-
Ferric Oxide (Fe <sub>2</sub> O <sub>3</sub> )	-	< 0.3

### ECC Mixing Procedure and Test Method

For the first step, the three dry ingredients—GGBS, cement, and silica sand, were placed and mixed for about three minutes in a standard concrete mixer of 40-liter capacity. Then, the liquid ingredients, i.e., SP and water, were added to the dry ingredients in the mixer while the mixing process was still running at a lower speed. After a few minutes, a mortar was formed, and when the mortar was uniformed and achieved certain fluidity, PVA fibers were carefully added. Special care was required in this step to avoid balling PVA fibers due to the fibers that were not evenly distributed yet. Fiber dispersion is very important to ensure the excellent workability of ECC. The overall mixing of ECC ended when all fibers were well-mixed in the mortar.

For each ECC mixture, three-cylinder specimens of size 50 mm diameter × 100 mm height were cast and cured for 28 days for the compression test. A Universal Testing Machine (UTM) of 1000 kN capacity was used to test the specimens under compression loads. Five plate specimens of 300 mm × 75 mm × 12 mm were cast according to the size employed in the previous study for a three-point bending test after 28 days of curing (Li & Yang, 2017). UTM of 50 kN capacity was used to test the flexural behavior of these ECC plates. The displacement control method at 0.5 mm/minute was employed in this test.

## RESULTS AND DISCUSSIONS

### Compressive Strength

Table 4 indicates the average compression strength and enhancement factor for each ECC mixture. It is worth mentioning that the average compressive strength of the ECC and control mixture was calculated based on three samples tested on the 28th day of curing. Generally, the compressive strengths of all ECC specimens are greater than the control specimen. The enhancement factors by incorporating the different variations of GGBS and PVA fibers into the mixtures are in the range of 1.2 to 1.3, as shown in Table 4. However, ECC G60F2.0 exhibits a relatively lower compressive strength of 35.92 MPa compared to the other mixtures. It could be due to some shortcomings during the mixing or casting of ECC, as this mixture was the first batch. The G50 series (replacement of cement by 50%

of GGBS) performs better than the G60 series under compression due to the higher cement content in the mixtures. On the other hand, the increase in fibers content from 2.0% to 2.5% of volume fraction slightly decreases the compressive strength for the G50 series, and this result agrees well with findings reported by Lee et al. (2018b).

Table 4  
*Result of compressive strength (28 days)*

Mixture	Average Compressive Strength (MPa)	Enhancement Factor (compared with control)
Control	44.02	1.00
G50F2.0	57.02	1.30
G50F2.5	54.82	1.25
G60F2.0	35.92	0.82
G60F2.5	52.70	1.20

### Comparison of Compressive Strength with Previous Study

Figure 1 shows the comparison of compressive strength on 28th days for the current study and the study carried out by Lee et al. (2018b). As described in the experimental program and shown in Table 1, the design mix compositions of both studies are similar except for the types of fibers and sand. Sahmaran et al. (2009) reported that aggregate characteristics, such as the surface texture and maximum aggregate size, did not influence the compressive strength in the case of ECC. Therefore, by neglecting the effect of sand, only the effect of types of fibers on the compressive strength of ECC is discussed. As shown in Figure 1, for the G50 series, the compressive strengths are identical when 2.0% of the volume fraction of either PVA or PP fibers were incorporated in ECC mixtures. However, when the number of fibers is increased to 2.5% of volume fraction, the compression strength of ECC with PVA fibers has improved by 24%. On the other hand, ECC with 60% of GGBS behaved differently under compression when PVA fibers increased from 2.0% to 2.5% of volume fraction. As mentioned earlier, the lower compressive strength obtained by ECC G60F2.0 in this study is possibly due to faults during the mixing or casting of this design mix. For the same mixture, ECC with PP fibers yields better compression capacity compared to ECC that contains PVA fibers. Nevertheless, for ECC mixtures with a 2.5% volume fraction of fibers and 60% GGBS, the incorporation of PVA fibers shows slightly enhanced compression capacity by 3.9% compared to PP fibers.

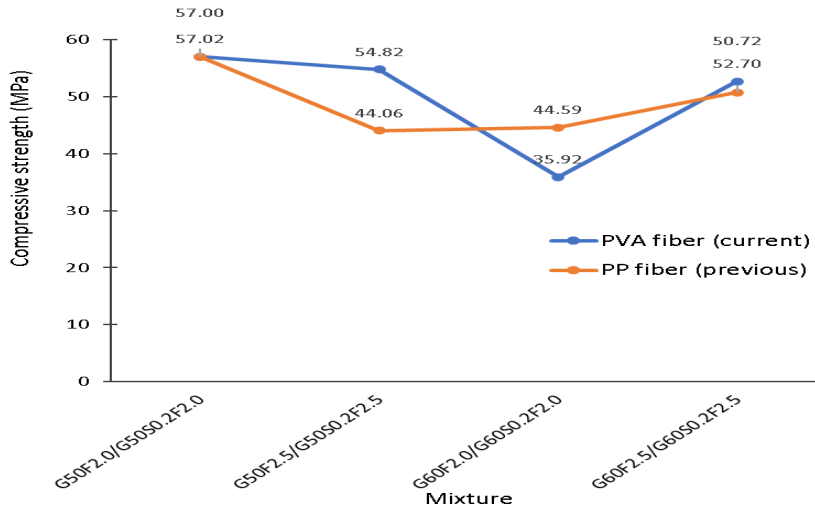


Figure 1. Comparison of compressive strength at 28 days

### Flexural Behavior

The results of ECC plates under the three-point bending test are presented by the flexural stress-displacement curves as shown in Figure 2. It should be noted that each curve represents a typical flexural behavior of each ECC mixture. Apparently, the control specimen demonstrates brittle behavior in which the plate specimen failed directly upon reaching its first cracking strength. This behavior is similar to normal concrete, as demonstrated in a study by Lee et al. (2019b). For the control specimen, neither GGBS nor PVA fibers were incorporated in the cementitious matrix, and it consisted of only cement mortar. The high cement content can improve flexural strength compared to normal concrete, but no significant effect was discovered in terms of ductility.

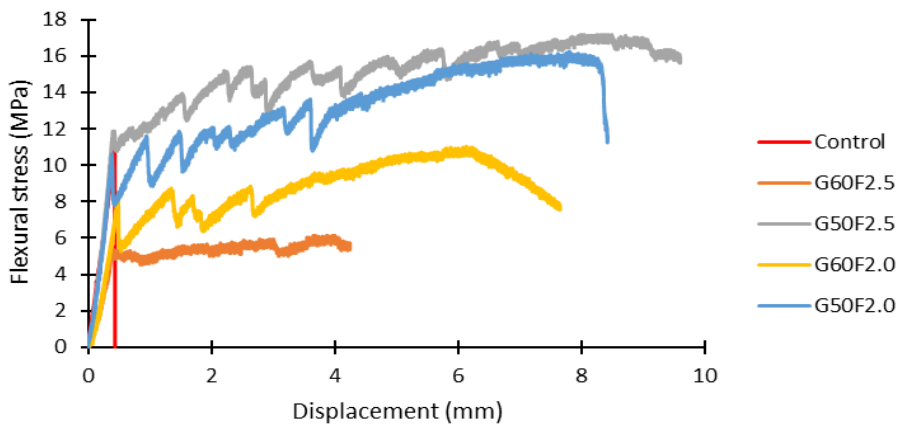


Figure 2. Flexural behavior of ECC-PVA

The G50 series yields greater flexural strength and a larger displacement capacity than the G60 series, as presented in Figure 2. ECC G50F2.5 shows the highest first cracking and ultimate strength of 11.34 MPa and 16.65 MPa, respectively. The displacement corresponds with the ultimate strength is 8.54 mm, which indicates that this mixture can undergo a good strain-hardening behavior of ECC. In this series, it is observed that increasing the PVA fibers content to 2.5% of volume fraction has improved the modulus of toughness (area under the curve). A similar observation was also noted in the study by Lee et al. (2018b).

For the G60 series, G60F2.0 demonstrates relatively greater flexural behavior compared to G60F2.5 despite the fact that its compressive strength is merely at 35.92 MPa. The enhancements in the ultimate strength and the displacement corresponding to the ultimate strength are 79% and 57%, respectively. However, these series give a contradicting result when compared to the G50 series. The increase of PVA fiber content in the G60 mixture had a detrimental effect on flexural strength and ductility. The poor performance of G60F2.5 could be attributed to the shortcomings during the preparation of specimens or test setup, and more tests are required to achieve a solid conclusion.

Table 5  
*Performance of ECC-PVA under three-point bending test*

Mixture	First cracking strength (MPa)	Ultimate strength (MPa)	Displacement corresponding to ultimate strength (mm)
Control	11.24	11.24	0.43
G50F2.0	10.15	15.66	7.94
G50F2.5	11.34	16.65	8.54
G60F2.0	8.06	10.87	6.27
G60F2.5	5.36	6.09	4.00

Table 5 shows the first cracking strength, the ultimate flexural strength, and the displacement that correspond with the ultimate strength of ECC plates. The first cracking strength is defined as the first drop in stress in which the flexural stress-deflection response deviates from linearity. In contrast, the ultimate strength refers to the maximum flexural strength before the specimens fail. In the current study, ECC-PVA fibers have shown significant improvement, especially in the strain-hardening behavior of ECC as compared to ECC-PP fibers in another study by Lee et al. (2018b). In addition, all ECC mixtures successfully demonstrate good flexural ductility, by at least ten times better than the control mixture. For example, the displacement corresponding to ultimate strength for G60F2.5 is 4.00 mm, while only 0.43 mm can be obtained in the control mixture, as shown in Table 5.

### Comparison of Flexural Behavior with Previous Study

The effect of types of fibers in flexural behavior can be examined through comparison with a previous study (Lee et al., 2018). Figures 3 and 4 demonstrate the comparisons of flexural behavior of the ECC G50 and ECC G60 series, respectively. Apparently, PVA fibers play a significant role in achieving the flexural ductility of ECC as compared to ECC-PP fibers of similar design mix proportion. As shown in Figure 3, the modulus of toughness measured by the area under the curve for ECC-PVA fibers of the G50 series (ECC G50F2.0 and ECC G50F2.5) are significantly higher than that of ECC-PP fibers (ECC G50S0.2F2.0 and ECC G50S0.2F2.5). For the ECC G60 series, the flexural strength obtained by ECC G60F2.5 in the current study was lower than ECC-PP fibers in Lee et al. (2018b) (G60S0.2F2.0 and G60S0.2F2.5), the modulus of the toughness of this mixture is greater than its counterpart. Therefore, the PVA fibers employed in the design mix compositions of this current study are more effective compared to PP fibers in terms of flexural performance. The findings in this study confirm that PVA fibers are better than PP fibers to be used in developing ECC that exhibit strain hardening and multiple fine cracking behaviors, and this is parallel with the evidence found in previous investigations (Huang & Zhang, 2014; Li et al., 2001; Li et al., 2004; Liu et al., 2018; Pakravan et al., 2018; Yang & Li, 2014; Yang et al., 2007).

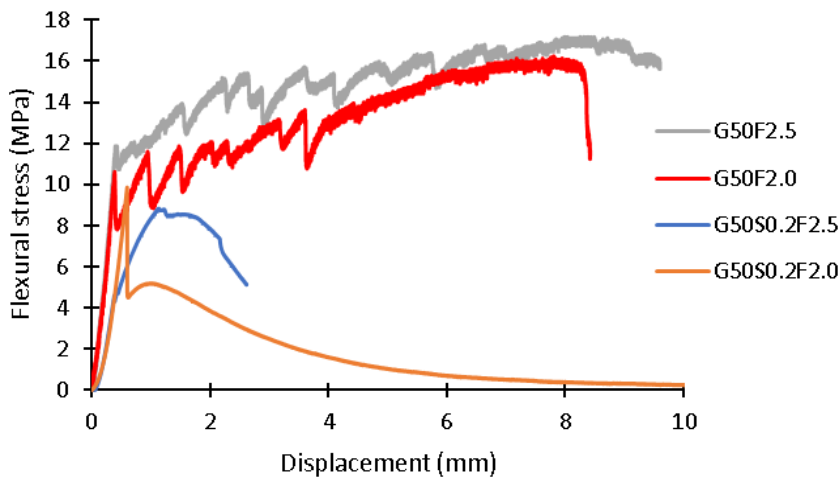


Figure 3. Comparison of flexural behavior for ECC G50 series

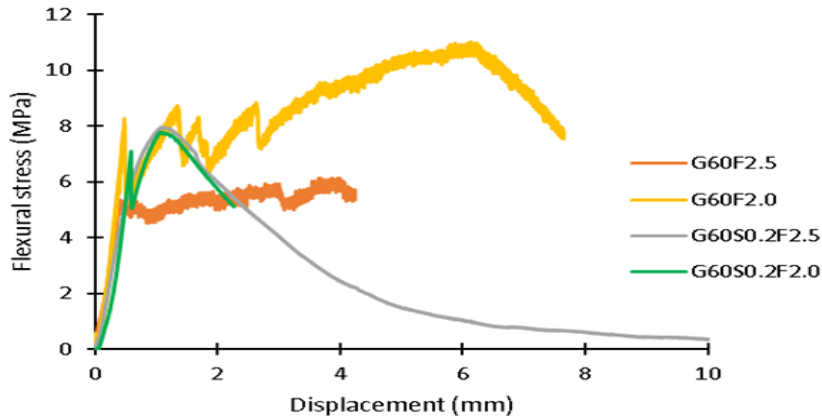


Figure 4. Comparison of flexural behavior for ECC G60 series

### Failure Mode of Specimens

As shown in Figure 2, all ECC mixtures in the current study were able to go beyond their first cracking strength until they achieved the ultimate strength and finally failed under increasing applied point load. All ECC specimens failed in ductile modes, as shown in Figure 5b. Unlike the control specimens, ECC specimens exhibit multiple cracking with very fine crack widths, which required minor or no repair. As indicated in Figure 5a, the control specimens showed a single big crack at the mid-span of the plate. This mode is considered a brittle failure, even though the average compressive strength of 44.02 MPa is obtained from this mixture.



Figure 5. Failure modes under three-point bending test

### CONCLUSION

The performances of ECC mixtures are found to be satisfactory for both compression and flexural tests in this study. From the compression test results, all ECC specimens except

G60F2.0 demonstrated greater compressive strength compared to control specimens. On the other hand, all ECC plate specimens demonstrated good strain-hardening and multiple cracking behaviors under the three-point bending test. The ECC G50 series performed better than the G60 series in both compression and flexural tests, as observed in this study. Among all, ECC G50F2.5 is considered the best mixture as it achieves the highest flexural strength of 16.65 MPa with the ultimate displacement of 8.54 mm, while its compressive strength is 54.82 MPa. Even though increasing the content of PVA fibers up to 2.5% of volume fraction is not beneficial in improving the compressive strength, it slightly enhances the flexural properties of the ECC G50 series. This observation is not discovered in the ECC G60 series. Hence, more experimental studies are required to confirm this trend. Compared to the previous study by Lee et al. (2018b), incorporating PVA fibers instead of PP fibers in ECC has improved flexural ductility and modulus of toughness under the same design mix proportion. However, the trend in the compressive behavior of ECC is inconsistent when the results of these two fibers are compared. Hence, the effect of the type of fibers (PVA or PP) on the compressive strength of ECC is less significant.

## ACKNOWLEDGEMENTS

This research was financially supported by the Universiti Teknologi MARA Johor under “Geran Penyelidikan Bestari Fasa 1/2021 (600-UiTM CJ (PJIA. 5/2)).”

## REFERENCES

- Adesina, A., & Das, S. (2021). Evaluation of the durability properties of engineered cementitious composites incorporating recycled concrete as aggregate. *Journal of Materials in Civil Engineering*, 33(2), Article 04020439. [https://doi.org/10.1061/\(asce\)mt.1943-5533.0003563](https://doi.org/10.1061/(asce)mt.1943-5533.0003563)
- Huang, T., & Zhang, Y. X. (2014). Mechanical properties of a PVA fiber reinforced engineered cementitious composite. *Proceedings of International Structural Engineering and Construction*, 1(1), 439-444. <https://doi.org/10.14455/isec.res.2014.40>
- Kewalramani, M. A., Mohamed, O. A., & Syed, Z. I. (2017). Engineered cementitious composites for modern civil engineering structures in hot arid coastal climatic conditions. *Procedia Engineering*, 180, 767-774. <https://doi.org/10.1016/j.proeng.2017.04.237>
- Lee, S. W., Kang, S. B., Tan, K. H., & Yang, E. H. (2016). Experimental and analytical investigation on bond-slip behaviour of deformed bars embedded in engineered cementitious composites. *Construction and Building Materials*, 127, 494-503. <https://doi.org/10.1016/j.conbuildmat.2016.10.036>
- Lee, S. W., Tan, K. H., & Yang, E. H. (2018a). Seismic behaviour of interior reinforced-concrete beam-column sub-assemblages with engineered cementitious composites. *Magazine of Concrete Research*, 70(24), 1280-1296. <https://doi.org/10.1680/jmacr.17.00359>
- Lee, S. W., Oh, C. L., & Zain, M. R. M. (2018b). Evaluation of the design mix proportion on mechanical properties of engineered cementitious composites. In A. M. Korsunsky, C. Makabe & E. Wang (Eds.), *Key*

- Engineering Materials* (Vol. 775, pp. 589-595). Trans Tech Publications Ltd. <https://doi.org/10.4028/www.scientific.net/kem.775.589>
- Lee, S. W., Oh, C. L., & Zain, M. R. M. (2019a). Mechanical properties of engineered cementitious composites using local ingredients. *Journal of Mechanical Engineering (JMechE)*, 16(2), 145-157.
- Lee, S. W., Oh, C. L., Zain, M. R. M., Yahya, N. A., & Rahman, A. A. (2019b). Mechanical performances of green engineered cementitious composites incorporating various types of sand. In A. M. Korsunsky (Ed.), *Key Engineering Materials* (Vol. 821, pp. 512-517). Trans Tech Publications Ltd. <https://doi.org/10.4028/www.scientific.net/kem.821.512>
- Li, J., & Yang, E. H. (2017). Macroscopic and microstructural properties of engineered cementitious composites incorporating recycled concrete fines. *Cement and Concrete Composites*, 78, 33-42. <https://doi.org/10.1016/j.cemconcomp.2016.12.013>
- Li, V. C., Horikoshi, T., Ogawa, A., Torigoe, S., & Saito, T. (2004). Micromechanics-based durability study of polyvinyl alcohol-engineered cementitious composite. *ACI Materials Journal*, 101(3), 242-248. <https://doi.org/10.14359/13120>
- Li, V. C., Wang, S., & Wu, C. (2001). Tensile strain-hardening behavior of polyvinyl alcohol engineered cementitious composite (PVA-ECC). *ACI Materials Journal-American Concrete Institute*, 98(6), 483-492. <https://doi.org/10.14359/10851>
- Liu, H., Zhang, Q., Li, V., Su, H., & Gu, C. (2017). Durability study on engineered cementitious composites (ECC) under sulfate and chloride environment. *Construction and Building Materials*, 133, 171-181. <https://doi.org/10.1016/j.conbuildmat.2016.12.074>
- Liu, Y., Zhou, X., Lv, C., Yang, Y., & Liu, T. (2018). Use of silica fume and GGBS to improve frost resistance of ECC with high-volume fly ash. *Advances in Civil Engineering*, 2018, 1-11. <https://doi.org/10.1155/2018/7987589>
- Meng, D., Huang, T., Zhang, Y. X., & Lee, C. K. (2017). Mechanical behaviour of a polyvinyl alcohol fibre reinforced engineered cementitious composite (PVA-ECC) using local ingredients. *Construction and Building Materials*, 141, 259-270. <https://doi.org/10.1016/j.conbuildmat.2017.02.158>
- Nemecek, J., Kabele, P., Kopecký, L., & Bittnar, Z. (2006). Micromechanical properties of calcium leached engineered cementitious composites. In G. Fischer & V. C. Li (Eds.), *International RILEM Workshop on High Performance Fiber Reinforced Cementitious Composites in Structural Applications* (Vol. 49, pp. 205-211). RILEM Publications SARL.
- Pakravan, H. R., Jamshidi, M., & Latifi, M. (2018). The effect of hydrophilic (polyvinyl alcohol) fiber content on the flexural behavior of engineered cementitious composites (ECC). *The Journal of The Textile Institute*, 109(1), 79-84. <https://doi.org/10.1080/00405000.2017.1329132>
- Parra-Montesinos, G. J., Peterfreund, S. W., & Shih-Ho, C. (2005). Highly damage-tolerant beam-column joints through use of high-performance fiber-reinforced cement composites. *ACI Structural Journal*, 102(3), 487-495. <https://doi.org/10.14359/14421>
- Qudah, S., & Maalej, M. (2014). Application of engineered cementitious composites (ECC) in interior beam-column connections for enhanced seismic resistance. *Engineering Structures*, 69, 235-245. <https://doi.org/10.1016/j.engstruct.2014.03.026>



- Şahmaran, M., & Li, V. C. (2007). De-icing salt scaling resistance of mechanically loaded engineered cementitious composites. *Cement and Concrete Research*, 37(7), 1035-1046. <https://doi.org/10.1016/j.cemconres.2007.04.001>
- Şahmaran, M., & Li, V. C. (2008). Durability of mechanically loaded engineered cementitious composites under highly alkaline environments. *Cement and Concrete Composites*, 30(2), 72-81. <https://doi.org/10.1016/j.cemconcomp.2007.09.004>
- Sahmaran, M., Lachemi, M., Hossain, K. M., Ranade, R., & Li, V. C. (2009). Influence of aggregate type and size on ductility and mechanical properties of engineered cementitious composites. *ACI Materials Journal*, 106(3), 308-316. <https://doi.org/10.14359/56556>
- Said, S. H., & Razak, H. A. (2016). Structural behavior of RC engineered cementitious composite (ECC) exterior beam–column joints under reversed cyclic loading. *Construction and Building Materials*, 107, 226-234. <https://doi.org/10.1016/j.conbuildmat.2016.01.001>
- Suthiwarapirak, P., Matsumoto, T., & Kanda, T. (2002). Flexural fatigue failure characteristics of an engineered cementitious composite and polymer cement mortars. *Doboku Gakkai Ronbunshu*, 2002(718), 121-134. [https://doi.org/10.2208/jscej.2002.718\\_121](https://doi.org/10.2208/jscej.2002.718_121)
- Wang, S., & Li, V. C. (2006). High-early-strength engineered cementitious composites. *ACI Materials Journal*, 103(2), 97-105. <https://doi.org/10.14359/15260>
- Yang, E. H., & Li, V. C. (2014). Strain-rate effects on the tensile behavior of strain-hardening cementitious composites. *Construction and Building Materials*, 52, 96-104. <https://doi.org/10.1016/j.conbuildmat.2013.11.013>
- Yang, E. H., Yang, Y., & Li, V. C. (2007). Use of high volumes of fly ash to improve ECC mechanical properties and material greenness. *ACI Materials Journal*, 104(6), 620-628. <https://doi.org/10.14359/18966>
- Zhang, R., Matsumoto, K., Hirata, T., Ishizeki, Y., & Niwa, J. (2015). Application of PP-ECC in beam–column joint connections of rigid-framed railway bridges to reduce transverse reinforcements. *Engineering Structures*, 86, 146-156. <https://doi.org/10.1016/j.engstruct.2015.01.005>
- Zhang, R., Matsumoto, K., Hirata, T., Ishizeki, Y., & Niwa, J. (2014). Shear behavior of polypropylene fiber reinforced ECC beams with varying shear reinforcement ratios. *Journal of JSCE*, 2(1), 39-53. [https://doi.org/10.2208/journalofjsce.2.1\\_39](https://doi.org/10.2208/journalofjsce.2.1_39)
- Zhu, H., Zhang, D., Wang, T., Wu, H., & Li, V. C. (2020). Mechanical and self-healing behavior of low carbon engineered cementitious composites reinforced with PP-fibers. *Construction and Building Materials*, 259, Article 119805. <https://doi.org/10.1016/j.conbuildmat.2020.119805>



## The Effect of Quenching on High-temperature Heat Treated Mild Steel and Its Corrosion Resistance

Alaba Oladeji Araoyinbo<sup>1\*</sup>, Ayuba Samuel<sup>1</sup>, Albakri Mohammed Mustapha Abdullah<sup>2</sup> and Mathew Biodun<sup>1</sup>

<sup>1</sup>Department of Mechanical Engineering, College of Engineering, Covenant University, Ota, Ogun State, Nigeria

<sup>2</sup>Center of Excellence Geopolymer and Green Materials (CEGeoGTech), School of Materials Engineering, Universiti Malaysia Perlis, 01000 UniMAP, Perlis, Malaysia

### ABSTRACT

Steel is extensively used in many applications that include construction because of its unique properties and the ease with which its properties can be enhanced for improved performance. Due to its high malleability and strength, it can be easily machined and welded compared to other types of steel. However, the susceptibility to low performance has been associated with its low resistance to environmental degradation when exposed to corrosive or polluted environments. This study focuses on mild steel heat treatment quenched in four mediums of engine oil, water, palm oil, and air, along with its properties and corrosion susceptibility. The high temperature used for the procedure is 800 °C, 900 °C, and 1000 °C, respectively.

After the heat treatment procedure, the test samples undergo corrosion testing in the sodium chloride solution for two weeks to observe the presence of corrosion products rust on its surface. The tensile machine was utilized to obtain the mechanical properties, including yield strength, tensile strength, and percentage elongation. The hardness values were obtained using the Rockwell hardness machine, and the optical microscope (OM) was used to observe the effect of the corrosion activity on the sample surface. The results obtained indicate an

### ARTICLE INFO

#### Article history:

Received: 25 June 2021

Accepted: 15 September 2021

Published: 15 December 2021

DOI: <https://doi.org/10.47836/pjst.30.1.16>

#### E-mail addresses:

[alaba.araoyinbo@covenantuniversity.edu.ng](mailto:alaba.araoyinbo@covenantuniversity.edu.ng) (Alaba Oladeji Araoyinbo)

[ayuba.samuelpgs@stu.cu.edu.ng](mailto:ayuba.samuelpgs@stu.cu.edu.ng) (Ayuba Samuel)

[mustafa\\_albakri@unimap.edu.my](mailto:mustafa_albakri@unimap.edu.my) (Albakri Mohammed Mustafa Abdullah)

[matthewbiodun@yahoo.com](mailto:matthewbiodun@yahoo.com) (Mathew Biodun)

\*Corresponding author

increase in the hardness, yield, and tensile strength, but the elongation reduces as the temperature increases.

*Keywords:* Heat treatment, mechanical properties, mild steel, quenching, sodium chloride

---

## INTRODUCTION

Carbon steel, due to its extensive use, can be classified into three different categories based on its carbon content: low carbon steel (mild steel); medium carbon steel; and high carbon steel (Fadara et al., 2011). Mild steel is a type of low-carbon steel, which is cheap and easy to alter its mechanical properties (Hassan, 2016). The low carbon content of this steel gives lower tensile strength when compared with high carbon alloy steel (Alves et al., 2013; Ahaneku et al., 2013; Xiaohui et al., 2018; Roland et al., 2018; Kazeem & Esther, 2018; Elewa et al., 2021; Joseph & Alo, 2014).

Mild steel is produced in millions of tonnes around the world yearly for different engineering applications. Mild steel has been used to produce automobile panels, structural beams, and other engineering applications as they are readily available and easy to fabricate (Samuel et al., 2021; Melchers, 2005; Burstein & Pistorius, 1995). Heat treatment procedure, which involves a controlled heating temperature; cooling or quenching of the metals improves the material properties without distorting its shape have been researched and documented (Nkhoma et al., 2014; Araoyinbo et al., 2018; Ismail et al., 2016; Bhateja et al., 2012). The heat treatment methods often used to obtain this desired microstructure include the annealing process, normalizing, and tempering (Tukur et al., 2014). The quenching approach is often used to improve steel properties by inducing a martensite transformation, which requires the steel to be cooled rapidly through the eutectoid point, at which the austenite phase becomes unstable (Ismail et al., 2016). Quenching, which is an important process in material property alteration, involves a carefully selected hardening temperature, which is essential before the rapid cooling in water, oil, or other cooling mediums to attain a certain level of hardness or tensile strength, which develops the final mechanical properties and at the same time provides stress relieve in the material.

The carbon and other elements present in the steel composition during the quenching process are trapped within the crystal grain, reducing the dislocation movement and contributing to the improved hardness of the steel (Sharma & Roy, 2014). In this research, low carbon steel is used, which is heat-treated and quenched in four different mediums to observe the effects on the hardness, percentage elongation, yield, and tensile strength. In addition, the heat-treated samples are further subjected to corrosion test by immersion in an aqueous solution of sodium chloride (NaCl) to observe the effect of the heat treatment procedure and subsequently the different quenching mediums on its surface morphology and corrosion behavior.

## **MATERIALS AND METHODS**

### **Preparation of Raw Materials**

The low carbon steel plate was locally purchased for the research, was cut into 85 mm x 18 mm x 3 mm. The samples are cleaned and polished to remove any rust and unevenness on the surface using sandpaper.

### **Heat Treatment Procedure**

For this research, the procedure for the heat treatment process was in three stages, the heating of the samples at specified temperatures; soaking of the heat-treated samples; and cooling or quenching of the samples in water, air, engine oil, and palm oil. First, the tube furnace was utilized as the heating medium in which the cut samples were placed inside, and the temperatures adjusted to 800 °C, 900 °C, and 1000 °C respectively for 1 hour with a soaking time of 30 minutes. Next, the samples were quenched in four mediums of water, air, engine oil, and palm oil.

### **Testing and Characterization**

The testing and characterization of the samples were by XRF to determine the chemical composition, the tensile machine for the percentage elongation, yield, and tensile strength. In contrast, for the hardness values, a Rockwell machine was used. In addition, the morphology of the corrosion test in sodium chloride solution was observed with the use of an optical microscope.

For the tensile testing, the samples were tested using Shimadzu tensile testing machine model AG-XD plus on the heat-treated mild steel with an average of five samples tested for each temperature quenched in water, air, engine oil, and palm oil. The samples were subjected to uniaxial load at a gauge length of 37 mm, and a fixed crosshead speed of 10 mm/min, and the average result of the specimens were recorded. This test method provides readings for the yield strength, tensile strength, and percentage elongation at the break-off for the samples. In addition, for the Rockwell hardness testing, five readings at different positions on the samples were obtained, with a Rockwell hardness machine for all the quenched samples.

The heat-treated mild steel specimens were immersed in sodium chloride solution for two weeks. The solution was prepared by adding 35 grams of sodium chloride to 1 liter of water. After two weeks of immersion, the samples were taken out and dried in an oven at 90 °C for 12 minutes. The morphology of the samples was observed with an optical microscope after the corrosion testing using an optical microscope with a magnification of 40x.

## RESULTS AND DISCUSSION

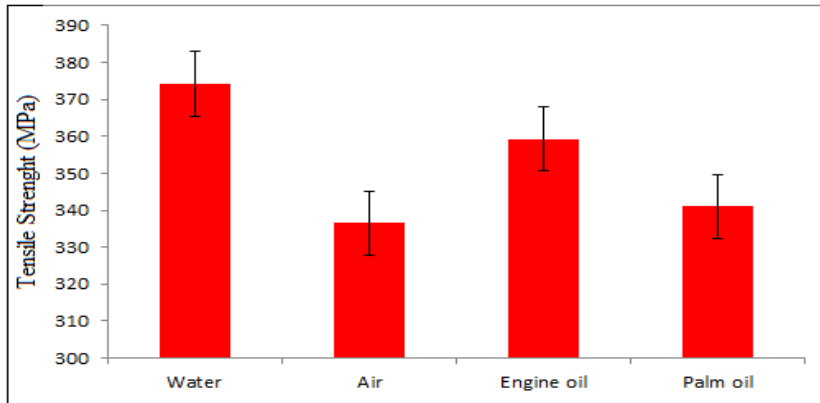
In this study, X-Ray Fluorescence (XRF) was used to characterize the chemical composition of the mild steel. Mild steel consists of many elements, and the main elements present in mild steel are Carbon, Copper, Iron, and Manganese. These elements have a significant effect on the microstructure and the mechanical properties of mild steel. The composition of the mild steel is shown in Table 1, and it shows that the main constituents of the mild steel, which is iron (Fe), has a weight percentage of 98 %, Carbon (C) with a percentage of 0.25 %, Copper (Cu) 0.20 %, Manganese (Mn) 1.03 %, and others 0.52 %.

Table 1

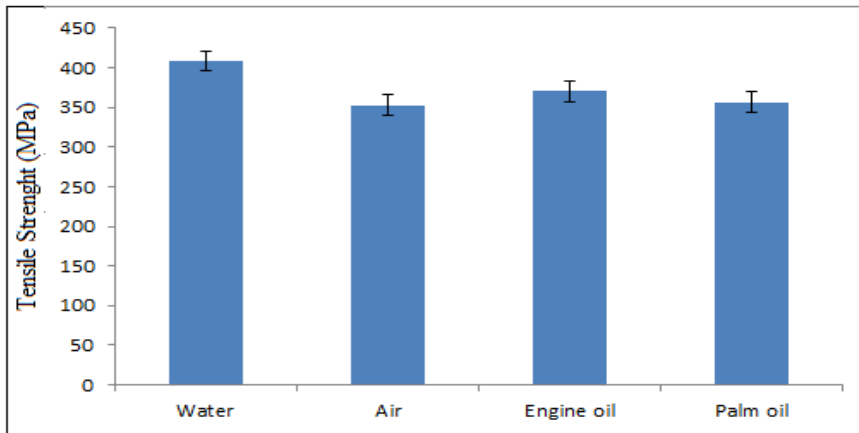
*Chemical composition of the as-received material*

Element	Content (Weight %)
Carbon, C	0.25
Copper, Cu	0.20
Iron, Fe	98.0
Manganese, Mn	1.03
Others	0.52

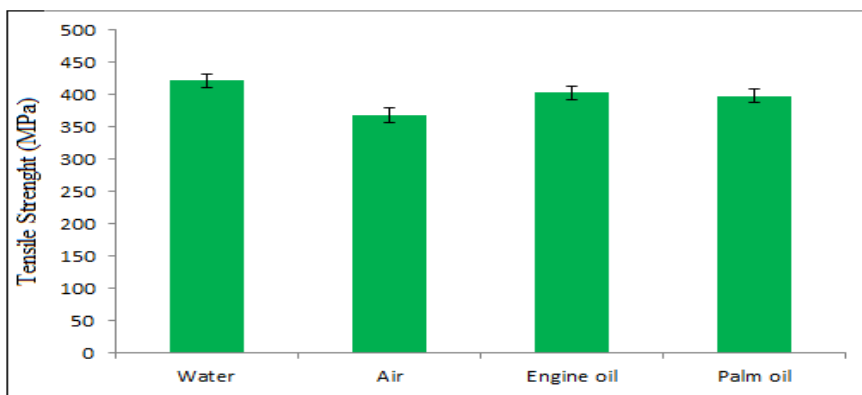
The tensile strength of the quenched steel samples in water, air, engine oil, and palm oil are shown in Figures 1(a), 1(b), and 1(c) at 800 °C, 900 °C, and 1000 °C. There was an improvement in the tensile properties, and the tensile strength results at 800 °C reveal that the sample quenched in water has the highest value of tensile strength of 374.16 MPa, while the sample quenched in the air has the least tensile strength of 336.49 MPa. The samples heat-treated at 900 °C and 1000 °C records the highest tensile strength in both cases to be water quenched samples, which record the tensile strength of 408.42 MPa and 421.80 MPa. The sample quenched in the air still records the lowest tensile strength for both temperatures, which was 352.84 MPa for 900 °C, and 368.5 MPa for 1000 °C. It was observed that as the temperature is increased, all the quenched sample records increased in their tensile strength, including the engine oil and palm oil. The heat treatment process that involves quenching in different mediums provides a means of obtaining certain desirable conditions in mild steel (Tukur et al., 2014). Quenching in the four media allows steel hardening of the mild steel during this process by controlling the heat flow, which also improves the reduction of cracks and distortion that are likely to be obtained from the cooling process (Burstein & Pistorius, 1995).



(a)



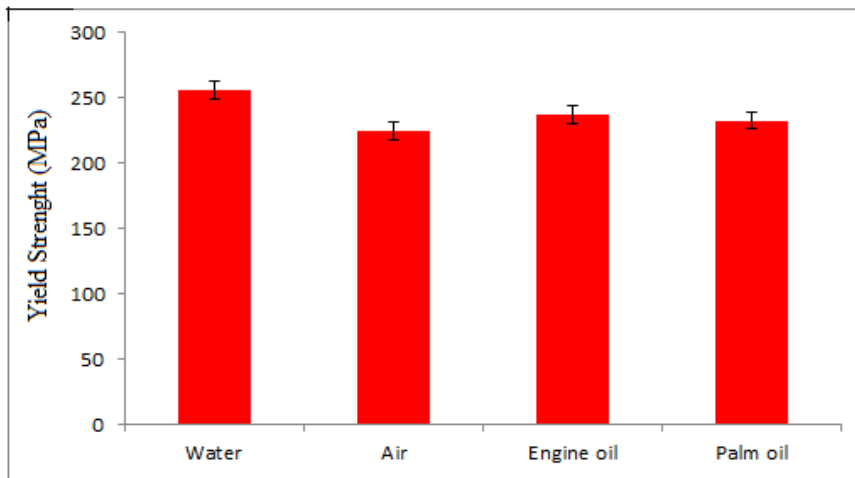
(b)



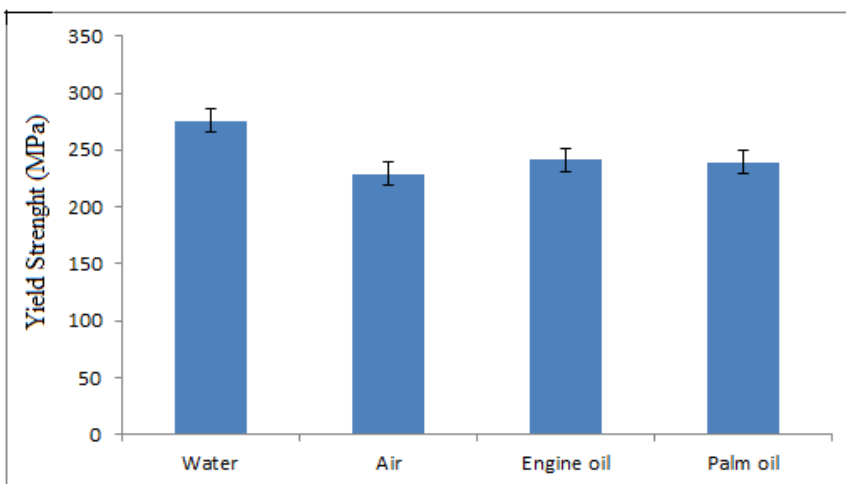
(c)

Figure 1. (a) Tensile strength of samples heat-treated at 800 °C and quenched in four mediums; (b) Tensile strength of samples heat-treated at 900 °C and quenched in four mediums; (c) Tensile strength of samples heat-treated at 1000 °C and quenched in four mediums

Figures 2(a), 2(b), and 2(c) shows the yield strength of the samples heat-treated at 800 °C, 900 °C, and 1000 °C, respectively. The yield strength records the highest strength of 256.31 MPa for 800 °C water quenched sample and 224.70 MPa for 800 °C air quenched sample. The samples heat-treated at 900 °C and 1000 °C records the highest yield strength in both cases to be water quenched samples, which records the yield strength of 275.70 MPa and 286.33 MPa. The sample quenched in the air still records the lowest yield strength for both temperatures, 228.63 MPa for 900 °C and 232.65 MPa for 1000 °C. The values obtained from the three temperatures are indicative of the yield point of the samples, which is indicative of the materials returning to their initial shape or undergoing permanent deformation (Xiaohui et al., 2018).

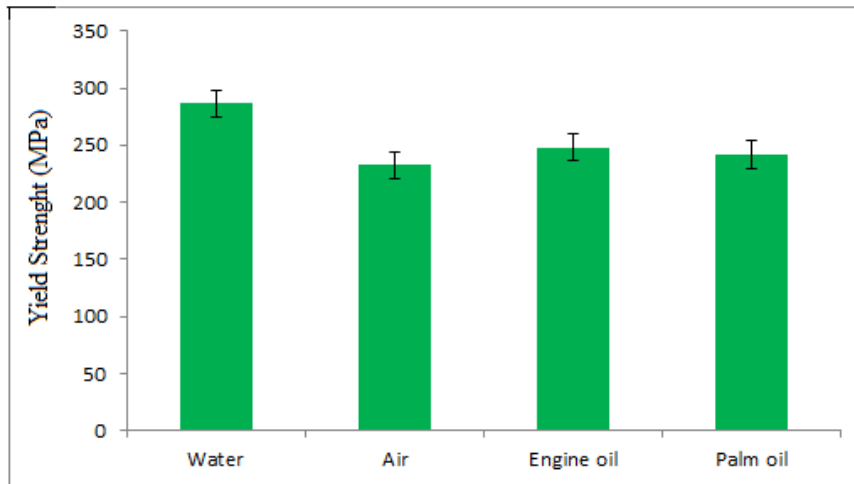


(a)



(b)





(c)

Figure 2. (a) Yield strength of samples at 800 °C and quenched in four mediums; (b) Yield strength of samples at 900 °C and quenched in four mediums; (c) Yield strength of samples at 1000 °C and quenched in four mediums

Figure 3 shows the percentage elongation of heated specimens at 800 °C, 900 °C, and 1000 °C and water quenched, air-cooled, engine oil quenched, and palm oil quenched. Percentage elongation in gauge length measures the ductility of the material, the sample heat-treated at 800 °C in Figure 3, and air-cooled or quenched records the highest elongation of 42.4 %, and water quenched sample records the lowest of 30.2 %. At temperatures of 900 °C and 1000 °C shown in Figure 3, the percentage elongation reduces with increasing temperatures and records 40.48 % at 900 °C and 38.5 % for 1000 °C for air quenched; and 27.4 % at 900 °C and 20.2 % at 1000 °C for water quenched samples. All the quenched samples from the four-quench medium show a significant reduction in percentage elongation as the temperature is increased, which implies that there will be a reduction in its ductility and the ease of machining for the different applications.

The Rockwell hardness machine was used to measure the hardness of the mild steel samples produced from different temperatures of 800 °C, 900 °C, and 1000 °C, and quenched in water, air, engine oil, and palm oil as shown in Tables 2, 3, and 4. This method used to obtain the hardness values offers a less expensive route and is easy to use the approach in relation to other methods (Pillay & Lin, 2014). Tables 2, 3, and 4 show the result of the hardness test obtained from the different specimens quenched in the cooling mediums. Moreover, at 800 °C the water quenched sample records the highest hardness of 22.4 HRA, and the air-cooled records the lowest hardness of 11.2 HRA. At 900 °C and 1000 °C, it was observed that the hardness values increase with increasing temperature. Water quenched samples records the highest in both cases of 24.3 and 28.6 HRA, respectively, while air

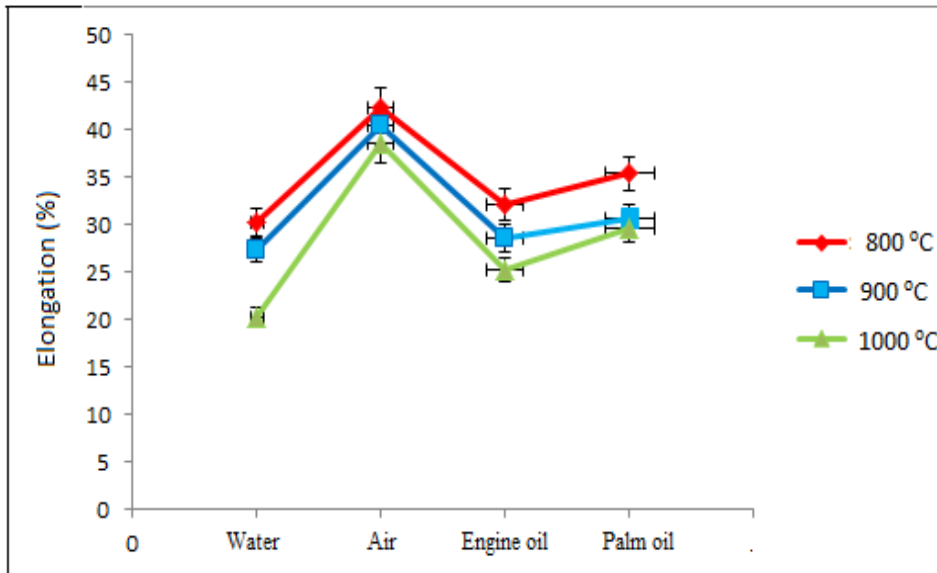


Figure 3. Percentage elongation of samples quenched in four mediums at 800 °C, 900 °C, and 1000 °C.

quenched record the lowest for both temperatures at 16.1 and 20.8 HRA. The higher the hardness, the less ductile the material will be and the likely difficulty to the machine. It was observed that water quenched samples have a higher hardness value when compared with air, engine oil, and palm oil. It may be attributed to the fact that water has a higher cooling rate than the other quenching mediums (Shi et al., 2017).

Table 2

Rockwell hardness values at 800 °C and quenched in four mediums

Sample	Rockwell Hardness (HRA)
800 °C (Water quench)	22.4
800 °C (Air cool)	11.2
800 °C (Engine oil quench)	17.8
800 °C (Palm oil quench)	14.5

Table 3

Rockwell hardness values at 900 °C and quenched in four mediums

Sample	Rockwell Hardness (HRA)
900 °C (Water quench)	24.3
900 °C (Air cool)	16.1
900 °C (Engine oil quench)	20.1
900 °C (Palm oil quench)	18.5

Table 4

*Rockwell hardness values at 1000 °C and quenched in four mediums*

Sample	Rockwell Hardness (HRA)
1000 °C (Water quench)	28.6
1000 °C (Air cool)	20.8
1000 °C (Engine oil quench)	25.4
1000 °C (Palm oil quench)	23.7

Corrosion is known to be a rapid deterioration of materials into a more stable oxide form as a result of exposure to corrosive mediums. This corrosion process involves reducing material thickness which results in a gradual reduction in both tensile and hardness properties. In addition, the presence of pits, which is one form of corrosion, is responsible for stress concentration in the material, which reduces the load-carrying capacity of the steel and further degrades the material until failure occurs (Dauda et al., 2015). Low carbon steel has low resistance to corrosion attacks, and one of the main properties often demanded of steel products is that they should not corrode. A few types of steel provide some form of resistance to corrosion by forming an oxide layer at the surface; the process is called passivation to reduce the corrosion attack on its surface. Figures 4(a), 4(b), 4(c), and 4(d) show the surface morphology of samples heat-treated at 1000 °C and quenched in water, air, engine oil, and palm oil as observed by the optical microscope. Samples heat-treated at 1000 °C are shown only since the 800 °C and 900 °C sample micrographs are similar, and only one temperature is illustrated here. The samples quenched in water, air, engine oil, and palm oil, as shown in Figure 4, shows corrosion attack to be present as the dark pots located on all the metal surfaces due to exposure to the corrosive medium. The corrosion attack spreads over the microstructural surface and is aided by the surface imperfections where the surface has deformities, unevenness, and roughness.

The result shows that when the temperature increases, at the surface of the four quenching mediums, surface corrosion is observed as the pitting spots on the material surface; this might be due to the strong bonding existing in the samples when heat-treated and quenched. The type of corrosion commonly observed on all of these micrographs is the pitting form because the metal is pitted by aerated sodium chloride solution (Seidu & Kutelu, 2013). The different areas on the surface of the mild steel become unstable when a pit is created on the metal surface, and the mild steel samples start to oxidize, and where the pit is created, the corrosion will continue to propagate, and the pits continue to grow (Marlon et al., 2018). The corrosion rate is the rate at which materials deteriorate when in contact with the environment for a known duration of time. The speed or rate of deterioration depends on the environmental conditions and the type and condition of the metal under consideration. The corrosion rate for the samples heat-treated at 1000 °C

shows a marginal difference for all the four quenched samples. Samples quenched in the water had a corrosion rate of 0.142 mmpy, air quenched 0.135 mmpy, engine oil quenched 0.140 mmpy, and palm oil quenched 0.138 mmpy.

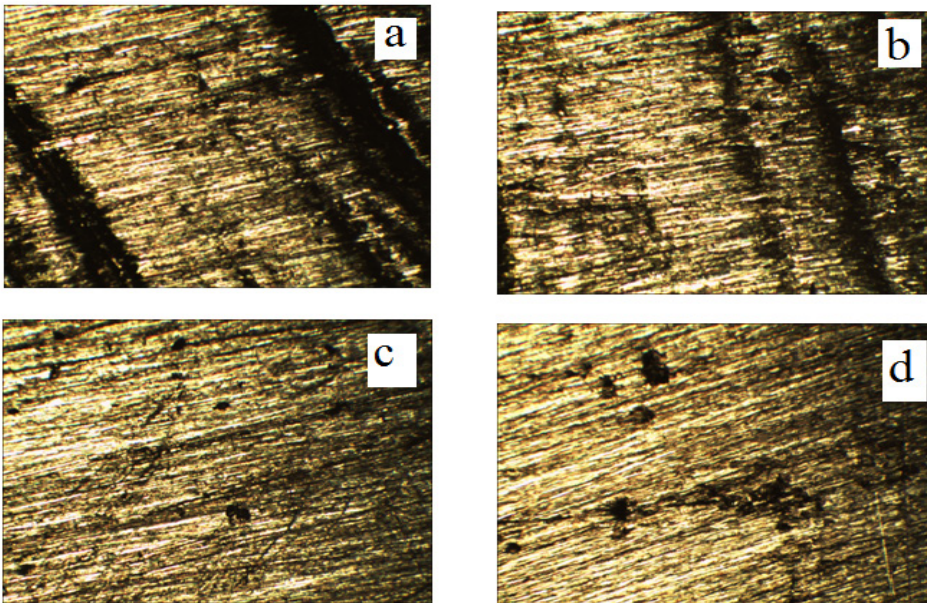


Figure 4. Shows optical microscope (10x) morphology of the samples heats-treated at 1000 °C after immersion test in NaCl (a) Water quench, (b) Air quench, (c) Engine oil quench, and (d) Palm oil quench.

## CONCLUSIONS

The research highlights the impact of high temperature on mild steel's mechanical properties when quenched in water, air, engine oil, and palm oil. It was observed that the samples quenched in engine oil and palm oil produce mechanical properties inferior to water quenched samples. It is a result of water having a faster cooling effect on the mild steel. The results recorded for the tensile strength, yield strength, and hardness show a significant increase when the temperature increases. The water quenched results records the highest tensile strength, yield strength, and hardness, while air quenched indicate the lowest tensile strength, yield strength, and hardness values. The reverse was observed for the percentage elongation as the air quenched samples records the highest percentage elongation and water quenched the lowest percentage elongation. This study further showed that the heat treatment and quenching methods significantly improve the mechanical properties of the material. However, when exposed to corrosive medium, the presence of pitting form of corrosion was observed as a result of the chloride attack on the surface of the metal.

## ACKNOWLEDGMENT

The author is grateful to Covenant University, Ota, Ogun State, Nigeria, for providing research facilities for this project.

## REFERENCES

- Ahaneku, I. E., Kamal, A. R., & Ogunjirin, O. A. (2013). Effects of heat treatment on the properties of mild steel using different quenchant. *Frontiers in Science*, 2(6), 153-158. <https://doi.org/10.5923/j.fs.20120206.04>.
- Alves, V. A., Brett, C. M. A., & Cavaleiro, A. (2013). Influence of heat treatment on the corrosion of high speed steel. *Journal of Applied Electrochemistry*, 31, 65-72. <https://doi.org/10.1023/a:1004157623466>
- Araoyinbo, A. O., Salleh, M. A. A. M., & Jusof, M. Z. (2018). Corrosion protection of mild steel in sea water using chemical inhibitor. In *IOP Conference Series: Materials Science and Engineering* (Vol. 343, No. 1, p. 012012). IOP Publishing. <https://doi.org/10.1088/1757-899x/343/1/012012>.
- Bhateja, A., Varma, A., Kashyap, A., & Singh, B. (2012). Study the effect on the hardness of the three sample grades of tool steel ie EN-31, EN-8 and D3 after heat treatment processes such as annealing, normalizing and hardening and tempering. *The International Journal of Engineering and Science*, 1(2), 253-259. <http://www.theijes.com/papers/v1-i2/AL01202530259>
- Burstein, G. T., & Pistorius, P. C. (1995). Surface roughness and the metastable pitting of stainless steel in chloride solutions. *Corrosion*, 51(5), 380-385. <https://doi.org/10.5006/1.3293603>.
- Dauda, M., Kuburi, L. S., Obada, D. O., & Mustapha, R. I. (2015). Effects of various quenching media on mechanical properties of annealed 0.509wt%C - 0.178wt%Mn steel. *Nigerian Journal of Technology*, 34(3), 506-512. <https://doi.org/10.4314/njt.v34i3.12>
- Elewa, R. R., Araoyinbo, A. O., Fayomi, O. S. I., Samuel, A. U., & Biodun, M. B. (2021). Effect of machining on stainless steel: A review. In *IOP Conference Series: Materials Science and Engineering* (Vol. 1107, No. 1, p. 012084). IOP Publishing. <https://doi.org/10.1088/1757-899x/1107/1/012084>.
- Fadara, T. G., Akanbi, O. Y., & Fadare, D. A. (2011). Effect of heat treatment on mechanical properties and microstructure of NST 37-2 steel. *Journal of Minerals and Materials Characterization and Engineering*, 10(3), 299-308. <https://doi.org/10.4236/jmmce.2011.103020>.
- Hassan, M. F. (2016). Analysis of mechanical behavior and microstructural characteristics change of ASTM A-36 steel applying various heat treatment. *Journal of Material Science & Engineering*, 5(2), 1-6. <https://doi.org/10.4172/2169-0022.1000227>
- Ismail, N. M., Khatif, N. A. A., Kecik, M. A. K. A., & Shaharudin, M. A. H. (2016). The effect of heat treatment on the hardness and impact properties of medium carbon steel. In *IOP Conference Series: Materials Science and Engineering* (Vol. 114, No. 1, p. 012108). IOP Publishing. <https://doi.org/10.1088/1757-899x/114/1/012108>.
- Joseph, O. O., & Alo, F. I. (2014). An assessment of the microstructure and mechanical properties of 0.26% low carbon steel under different cooling media: Analysis by one-way anova. *Industrial Engineering Letters*, 4(7), 39-45.

- Kazeem, O. S., & Esther, T. A. (2018). Experiment on effect of heat treatment on mechanical and microstructure properties of AISI steel. *Materials Today: Proceedings*, 5, 17996-18001. <https://doi.org/10.1016/j.matpr.2018.06.132>.
- Marlon, M. N., Eduardo, M. S., Reny, A. R., & Tarcisio, G. B. (2018). Analysis of quenching parameters in AISI 4340 steel by using design of experiments. *Materials Research*, 4(1), 133-135. <https://doi.org/10.1590/1980-5373-mr-2018-0315>
- Melchers, R. E. (2005). The effect of corrosion on the structural reliability of steel offshore structures. *Corrosion Science*, 47(10), 2391-2410. <https://doi.org/10.1016/j.corsci.2005.04.004>
- Nkhoma, R. K. C., Siyasiya, C. W., & Stump, W. E. (2014). Hot workability of AISI 321 and AISI 304 austenitic stainless steels. *Journal of Alloys and Compounds*, 595, 103-112. <https://doi.org/10.1016/j.jallcom.2014.01.157>.
- Pillay, C., & Lin, J. (2014). The impact of additional nitrates in mild steel corrosion in a seawater / sediment system. *Corrosion Science*, 80, 416-426. <https://doi.org/10.1016/j.corsci.2013.11.047>.
- Roland, T. L., Cleophas, A. L., & Idehai, O. (2018). Effect of heat treatment processes on the localized corrosion resistance of austenitic stainless steel type 301 in chloride/sulphate solution. *Results in Physics*, 11, 570-576. <https://doi.org/10.1016/j.rinp.2018.09.056>
- Samuel, A. U., Araoyinbo, A. O., Elewa, R. R., & Biodun, M. B. (2021). Effect of machining of aluminium alloys with emphasis on aluminium 6061 alloy - A review. In *IOP Conference Series: Materials Science and Engineering* (Vol. 1107, No. 1, p. 012157). IOP Publishing. <https://doi.org/10.1088/1757-899x/1107/1/012157>.
- Seidu, S. O., & Kutelu, B. J. (2013). Effect of heat treatments on corrosion of welded low-carbon steel in acid and salt environments. *Journal of Minerals and Materials Characterization and Engineering*, 1(3), 95-100. <https://doi.org/10.4236/jmmce.2013.13018>
- Sharma, P., & Roy, H. (2014). Pitting corrosion failure of an AISI stainless steel pointer rod. *Engineering Failure Analysis*, 44, 400-407. <https://doi.org/10.1016/j.engfailanal.2014.06.001>
- Shi, D., Kang, K., & Gao, G. (2017). Effect of quenching parameters on the mechanical properties of the 7A04 aluminium alloy. *Materials and Technology*, 51(1), 95-99. <https://doi.org/10.17222/mit.2015.267>
- Tukur, S. A., Dambatta, M. S., Ahmed, A., & Muaz, N. M. (2014). Effect of heat treatment temperature on mechanical properties of the AISI 304 stainless steel. *International Journal of Innovative Research in Science Engineering and Technology*, 3, 9516-9520.
- Xiaohui, C., Jia, L., Xu, C., Huaming, W., & Zheng, H. (2018). Effect of heat treatment on microstructure, mechanical and corrosion properties of austenitic stainless steel 316L using arc additive manufacturing. *Materials Science and Engineering: A*, 715, 307-314. <https://doi.org/10.1016/j.msea.2017.10.002>.

## Tensile Behaviour of Slag-based Engineered Cementitious Composite

Chai Lian Oh<sup>1\*</sup>, Siong Wee Lee<sup>2</sup>, Norrul Azmi Yahya<sup>1</sup>, Gajalakshmi Pandulu<sup>3</sup> and Mohd Raizamzamani Md Zain<sup>1</sup>

<sup>1</sup>*School of Civil Engineering, College of Engineering, Universiti Teknologi MARA, 40450 UiTM, Shah Alam, Selangor Darul Ehsan, Malaysia*

<sup>2</sup>*School of Civil Engineering, College of Engineering, Universiti Teknologi MARA Johor, Pasir Gudang Campus, 81750 UiTM, Masai, Johor, Malaysia*

<sup>3</sup>*School of Infrastructure, B.S. Abdur Rahman Crescent, Institute of Science & Technology (BSACIST) Vandalur, Chennai-600 048, Tamil Nadu, India*

### ABSTRACT

Engineered Cementitious Composites (ECC) have become another alternative in the concrete industry due to their excellent strain capacity under uniaxial tension. Research and development for new ECC mix incorporating wastes remain open to fulfil the industrial needs to produce green and sustainable ECCs. This paper presents the experimental work on the tensile and cracking behaviour of ECCs utilising industrial waste, namely ground granulated blast-furnace slag (GGBS), to replace cement. A total of four slag-based ECC mixes containing 2%–2.5% of PVA fibres and 50%–60% GGBS were investigated under uniaxial compressive and tensile tests. Compressive strength, tensile strength and the

crack behaviours of the slag-based ECCs were evaluated and compared with a control mix. The experimental results show that the slag-based ECCs can achieve tensile strain capacity 2.6 %–2.75 % and ultimate tensile strength 1.43 MPa–2.82 MPa at 28 days. It was also found that the ECCs with GGBS and fibres formed few hairline cracks at the gage of the dog bone compared to brittle fracture in the control specimens.

*Keywords:* Crack, engineered cementitious composites, fibre, slag, tensile

### ARTICLE INFO

#### Article history:

Received: 2 August 2021

Accepted: 12 November 2021

Published: 15 December 2021

DOI: <https://doi.org/10.47836/pjst.30.1.17>

#### E-mail addresses:

[chailian@uitm.edu.my](mailto:chailian@uitm.edu.my) (Chai Lian Oh)

[leesiongwee@uitm.edu.my](mailto:leesiongwee@uitm.edu.my) (Siong Wee Lee)

[norrulazmi@uitm.edu.my](mailto:norrulazmi@uitm.edu.my) (Norrul Azmi Yahya)

[gajalakshmi@crescent.education](mailto:gajalakshmi@crescent.education) (Gajalakshmi Pandulu)

[raizam@uitm.edu.my](mailto:raizam@uitm.edu.my) (Mohd Raizamzamani Md Zain)

\*Corresponding author

## INTRODUCTION

All over the world, the Ordinary Portland Cement (OPC) is used widely as a construction material, especially in concrete buildings and infrastructure. However, the manufacturing process of OPC can release carbon dioxide into the atmosphere, subsequently negatively impacting the environment. In order to lessen the pollution issues and excess embodied energy utilisation, supplementary cementitious material can be utilised for the construction works. The industrial alumina-silicate by-product materials are employed for landfilling purposes, such as fly ash, ground granulated blast furnace slag (GGBS) etc. (Sakulich, 2011). Research works have also been carried out by utilising these aluminosilicate by-product materials in concrete as a partially replacing material to ease the idea of combining the eco-friendly materials, leading to a sustainable built environment.

Engineered Cementitious Composites (ECC), popularly known as bendable concrete, was introduced in the 1990s with the motivation to improve the tensile properties of concrete. The design of the ECC mix requires careful constituent tailoring and optimisation. Important constituents in ECC are cement, Polyvinyl Alcohol (PVA) fibres, silica sand, water and superplasticiser. Superior ductility of the innovation has made it attractive for both seismic and non-seismic applications (Li, 2003).

Many have investigated the tensile properties and cracking behaviour of ECCs. For instance, Kim et al. (2007) investigated strain-hardening behaviour in uniaxial tension of ECC containing GGBS at moderate strength. The tensile strain capacity of slag-based ECC was 50% higher than that of the conventional ECC. It was due to the support of the slag particles in the improvement of dispersion of fibres. Ma et al. (2015) studied the tensile properties of ECCs using local materials, including 2% volume PVA fibre, fly ash and crumb rubber. The authors successfully developed ECCs with up to 5 MPa ultimate tensile strength and up to 6% tensile strain capacity. Also, it was observed that a cost-effective ductile ECC could be designed by using local materials as ingredients. Finally, Chen et al. (2013) tested four ECCs incorporating GGBS at a range of 50% to 80% for the tensile, quasi-static and dynamic compressive performances. The findings from the research showed that the increase of GGBS content in ECCs increased the tensile strain capacity but reduced the ultimate tensile strength and average crack width. Booya et al. (2020) evaluated the mechanical performance of ECC using slag and fly ash as cement replacement materials. The experimental test results showed that both the slag- and fly ash-based ECC displayed similar strain-hardening and ductility characteristics but demonstrated different performance in drying shrinkage strains. Zhu et al. (2012) developed green ECC combination mineral admixtures of fly ash and GGBS with high tensile ductility and good matrix strength at an early age. Nguyễn et al. (2020) evaluated the healing performance of three ECC mixtures utilising a different proportion of Portland cement, CaO-based expansive agent and GGBS. It was found that all the ECCs showed comparative high compressive strength



(> 90MPa), tensile strength (> 8 MPa), and tensile strain (> 4.5%). Kumar and Ranade (2021) developed ECC with slag and calcium carbonate powder. Tensile performance of mixtures with different slag-to-cement weight ratios (1.5 to 3.5) and combination with 25  $\mu\text{m}$  calcium carbonate powder was studied, and it was found that the mixtures with a ratio of slag-to-cement 2.0 to 2.5 demonstrated higher tensile strain capacity and modulus rupture. The authors studied the mechanical properties of ECCs using local constituents from Malaysia (Lee, Oh, & Md Zain, 2019; Lee et al., 2018; Lee, Oh, Zain, et al., 2019). The results showed that the ECC with GGBS of 60% replacing cement achieved higher tensile strength and tensile strain capacity than other percentages (50% and 70%). A review of tensile properties of ECCs could be found in Yu et al. (2018).

Enhancement in tensile strength of ECC after incorporation of slag can be seen through the studies above. However, there are no conclusive results of the slag volume on ECC's tensile strength and cracking behaviour. Thus, this paper investigates experimentally the tensile properties of a series of ECCs containing 50% and 60% local GGBS replacing the cement. The ECCs were also designed to have PVA volume fractions of 2.0 % and 2.5 %. A total of four ECC mixes containing different percentages of PVA fibres and GGBS, as well as a control mix, were prepared and tested under uniaxial compression and tensile tests. This study investigated the effects of slag volume on the tensile properties of ECCs, which were specifically designed for concrete applications.

## METHODOLOGY

This section presents the methodology of the experimental works in four main phases: (1) mix design of ECC, (2) preparation of materials, (3) preparation of specimens and (4) testing.

### Mix Design of ECC

A total of four (4) slag-based ECC mixtures incorporated GGBS were designed. GGBS was chosen as the slag material to replace the cement volumes in the ECCs partially. Several important parameters were considered in the mix design to ensure the strength and durability of the ECCs. In this study, four ECC mixtures were mainly differentiated with the cement ratios to GGBS and the fibre volume fraction. The ECC mixtures were designed with ratios of cement to GGBS of 1.0 and 0.67 as well as the volume fraction of fibre of 2.0% and 2.5%. In addition, the sand-to-cement ratio and water-cement ratio was set to 0.2 and 0.27, respectively. Table 1 shows the mix composition for four (4) ECC mixes (i.e. G50F2.0, G50F2.5, G60F2.0 and G60F2.5) and one control mix (i.e. Control). The name of the mix reflects the mix composition. For instance, G50F2.0 indicates that the mix contains GGBS of 50% replacing cement and PVA fibre 2.0% volume fraction. There was neither GGBS nor PVA fibre applied in the control mix. The design mix resulted in a density of ECCs ranging from 2133 to 2160  $\text{kg/m}^3$ .

Table 1

*Mix composition (kg/m<sup>3</sup>)*

Mix	Cement	GGBS	Silica sand	Water	PVA Fibre	Superplasticizer	Density
<b>G50F2.0</b>	722	722	289	390	26	10	2160
<b>G50F2.5</b>	719	719	288	388	32	10	2156
<b>G60F2.0</b>	575	863	288	388	26	10	2149
<b>G60F2.5</b>	572	858	286	386	32	10	2145
<b>Control</b>	1444	0	289	390	0	10	2133

## Materials

Cement, GGBS, silica sand, PVA fibre, water and superplasticiser are the key materials used in producing ECCs in this study. The specifications of these materials are detailed as follows:

Cement—Ordinary Portland Cement (OPC) type CEM I 42.5N confirming to MS EN 197-1 standard, which is good for general purposes, was used.

GGBS—Ground Granulated Blast Furnace Slag (GGBS), an industrial by-product from the blast-furnaces, is widely known for low embodied CO<sub>2</sub> and acts as a hydraulic binder like cement. GGBS was used to partially replace the cement at 50% and 60% in the study as a sustainable alternative to cement. The chemical compositions and density of both OPC and GGBS are shown in Table 2.

Silica sand—From local silica sand deposits, the silica sand was used as fine aggregate in ECC mixtures. The average particle size of silica sand used is 285 microns.

Fibres—PVA fibre, namely Kuralon™ RECS15 from Kuraray, Japan, was used. The fibre is specified with 40-micron diameter, 12 mm length, 1.6 GPa tensile strength and 40 GPa Modulus. In addition, the Resin-Bundled type fibre with better dispersibility was chosen to prevent any re-aggregation and balling of fibres during the mixing process.

Table 2

*Density and chemical composition*

Chemical compositions	Unit	OPC	GGBS
Silica (SiO <sub>2</sub> )		12.80	35.67
Alumina (Al <sub>2</sub> O <sub>3</sub> )	%	2.13	10.15
Calcium Oxide (CaO)		77.53	43.68
Magnesia (MgO)		0.96	4.03

Table 2 (Continue)

Chemical compositions	Unit	OPC	GGBS
Potassium Oxide (K <sub>2</sub> O)		0.53	0.29
Iron oxide (Fe <sub>2</sub> O <sub>3</sub> )	%	1.61	3.12
Sulphur trioxide (SO <sub>3</sub> )		3.80	2.69

Superplasticizer–Superplasticizer is commonly known as a high range water reducer. The superplasticiser MasterGlenium SKY 8705 was added to the mixture. The superplasticizer contains polycarboxylate ether polymers, Chloride ion content < 0.2%, pH > 6, reddish-brown liquid and complies with BS EN934: Part 3: 1985. It is beneficial to concrete, such as allowing slump retention and enhancing the mechanical properties of concrete produced in hot climates.

### Preparation of Specimens

Cylinder and dog bone specimens were assessed at concrete age of 28 days under uniaxial compressive and uniaxial tensile tests, respectively. Cylinder and dog bone specimens are widely used in uniaxial compression and tensile tests for ECC (Booya et al., 2020; JSCE, 2008; Meng et al., 2017; Yu et al., 2018). JSCE (2008) recommended that the cylinder specimens of 50 mm in diameter and 100 mm in height be used in the uniaxial compression test if the mix does not consist of coarse aggregates. Thus, the cylinder specimens with the recommended size were used since only silica sand was used in the study. For tensile specimens, the dog bone specimens with width, height, the thickness of 40 mm, 320 mm and 13 mm were prepared considering the recommendations in JSCE (2008). Moulds for cylinder specimens were made by PVC type with an inner diameter of 50 mm, whereas dog bone specimens were fabricated in metal form. The specimen moulds and dimensions of dog bone are shown in Figure 1.

After the fabrication of specimen moulds, the casting of ECCs was carried out through a few main steps. First, solid ingredients, such as cement, GGBS and silica sand, were mixed for two minutes using a mixing machine. The water and superplasticiser were then added gradually to obtain a consistent and uniform mixed ECC. This process took about three minutes. Later, the PVA fibre was added slowly to allow good distribution of fibre during the mixing. It was followed by the fresh ECC into the moulds. The mould with fresh ECC was then compacted using the vibration table to expel entrapped air from freshly placed for about one minute. Detachment of the specimens from their moulds took place 24 hours after placement. Finally, the specimens were covered, placed, and cured in dry and normal room condition.

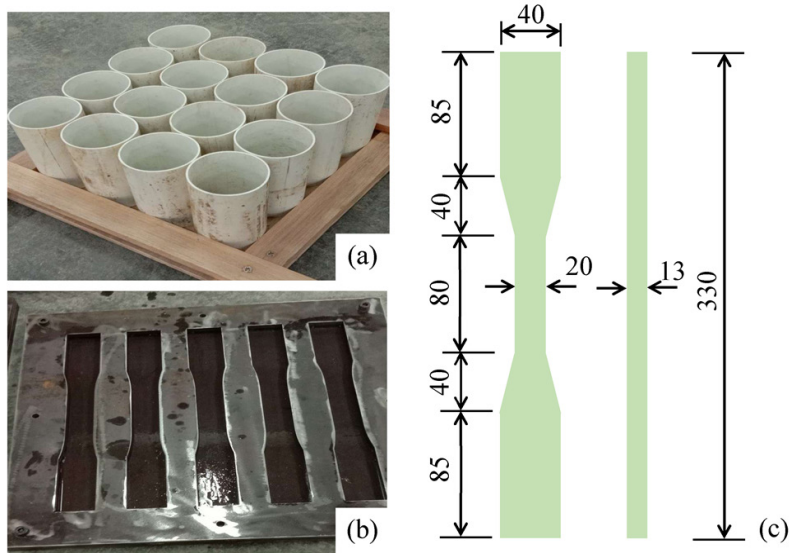


Figure 1. Specimen preparation: (a) cylinder moulds, (b) dog bone moulds and (c) dog bone dimensions (mm)

### Testing

This section presents two main testing in the experimental work: uniaxial compression test and uniaxial tensile test, which are in accordance with (JSCE, 2008). Observing the crack widths using a microscope was also carried out during and after the uniaxial tensile test. JSCE (2008) recommended that at least three specimens be prepared for the uniaxial compression test and at least five for the uniaxial tensile test. The numbers of the test specimen for uniaxial compression and tensile tests in this study are as shown in Table 3.

Table 3  
Numbers of test specimens

Test	G50F2.0	G50F2.5	G60F2.0	G60F2.5	Control
<b>Uniaxial Compression Test</b>	5 nos.	5 nos.	5 nos.	5 nos.	5 nos.
<b>Uniaxial Tensile Test</b>	5 nos.	5 nos.	5 nos.	5 nos.	5 nos.

**Uniaxial Compression Test.** The compression test was conducted for five cylindrical specimens of each mix at 28 days using a UTM-1000 Universal Testing Machine (Figure 2a). First, the surfaces of a cylinder specimen and the bearing surface of the testing machine were cleaned. The cylinder specimen was then placed at the centre of the base plate. Next, the load was applied with a loading rate of 0.5 mm/min. The load was applied incrementally and continuously to the specimen, and the data was stored in a computer.

**Uniaxial Tensile Test.** A tensile test was performed on five dog bone specimens for each mix at 28 days of curing using Shimadzu AGX Universal Testing Machine with a capacity of 50kN. The test set up for the uniaxial tensile test was arranged in accordance with JSCE (2008), which is shown in Figure 2b. The dog bone specimen was placed in the machine with a fixed support at one end and a pin (hinge support) on the other end. The specimen was adjusted and aligned properly vertically between the chucks at the machine so that the tensile load was applied at the centroidal axis of the specimen. The tests were performed at a cross-head displacement rate of 0.3 mm/min. During the tests, the machine continuously recorded the tensile loads (N) and corresponding elongation (mm). Tensile stress was obtained by dividing the load by the initial sectional area, which the area was calculated based on the mean value of three sections at both ends and centre of the specimen. The strain was determined by dividing the elongation of the specimen by the gauge length.



Figure 2. Testing set-up (a) uniaxial compression test and (b) uniaxial tensile test

The crack occurrence was observed during the uniaxial tensile test. Crack widths of the dog bone specimen were measured instantly after the uniaxial tensile test using a Crack Detection Microscope with an optical magnification of X40 and a sensitivity of 0.02mm. Only the maximum and minimum crack widths were recorded. The crack patterns on the dog bone specimens were also observed. The quantities of cracks before and after the test were recorded. It is to ensure the crack observation is properly detailed; either the cracks happen during the hardening process or in the old specimens.

## RESULTS AND DISCUSSION

This section discusses the results obtained from the uniaxial compression and tensile test in the experimental works. The results in terms of compression strength, tensile stress-strain relations and cracking behaviour are presented.

### Compressive Strength

The compressive strength of ECCs and control specimen obtained at concrete age of 28 days is presented in Figure 3. The percentage of differences for the compressive strength of the ECCs compared to the control are shown in Table 4.

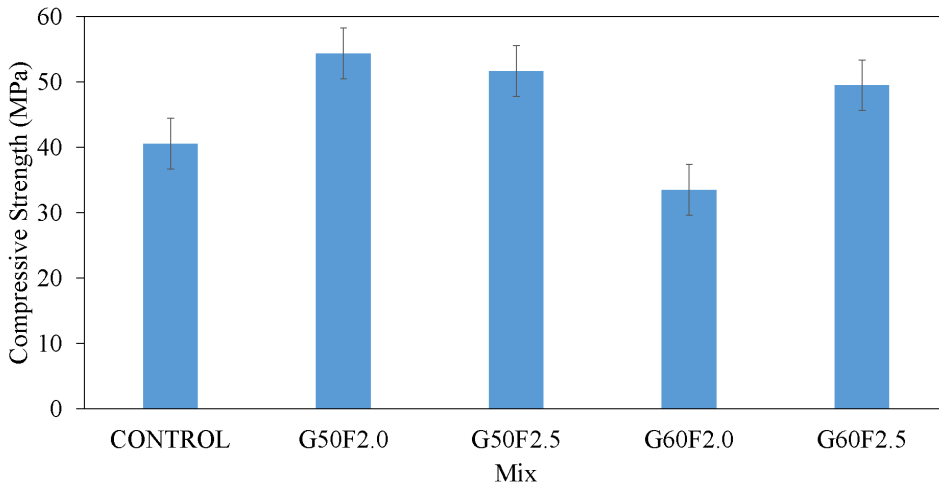


Figure 3. Compressive strength of ECCs

Table 4  
Percentage of difference of ECCs in compressive strength

Mix	Average Compressive Strength (MPa)	Percentage of difference (%)
Control	44.02 (1.33)	-
G50F2.0	57.02 (2.63)	29.5
G50F2.5	54.82 (2.22)	24.5
G60F2.0	35.92 (3.15)	-18.4
G60F2.5	52.69 (2.57)	19.7

It was found that G50F2.0 achieves the highest compression strength of 57.02 MPa (29.5% higher than the control), whereas G60F2.0 achieves the lowest compression strength of 35.92 MPa (18.4% lower than the control). Furthermore, all the ECCs except G60F2.0 have higher compressive strength compared to the control of 19.7–29.5%. It indicates that incorporating fibre at either 2.0% or 2.5% volume fraction in ECCs has generally enhanced the compressive strength of the concrete. Additionally, at same fibre volume fraction, ECCs with 60% percentage GGBS (i.e., G60F2.0 and G60F2.5) achieve lower

compression strength compared to ECCs with 50% GGBS (i.e., G50F2.0 and G50F2.5) in the study. The trend where compression strength of the ECCs decreases as GGBS content in ECC increases is consistent with Kumar and Ranade (2021). The reduction of compressive strength when having beyond 60–80% of GGBS as cement replacement level may be due to inaccessibility free calcium hydroxide for pozzolanic reaction or formation of low-density C-S-H gel by GGBS particles (Kumar & Ranade, 2021).

### Cracks Patterns

The cracking behaviour of the ECC specimen was evaluated based on the uniaxial tensile test. Figure 4 shows the crack patterns for the specimens after failure. Only the control, G50F2.0 and G60F2.0 specimens were presented owing to a similar crack pattern in all the ECC specimens. Occurrence of the first crack at the gage of the dog bone at the first crack strength was observed in ECC specimens. It follows by observing a few hairline cracks formed near the first crack (at the gage of dog bone) in ECC specimens. The formation of hairline cracks was associated with inelastic strain during the test. After the ECC specimens reached the ultimate tensile strength, the composite experienced a localised crack, which caused the composite to fail. Meanwhile, under incremental tensile loading, the control specimens failed in a fracture before any form of cracks. Four out of five control dog bone specimens were broken at the gage, either at the middle or near the shoulder. The tensile stress-strain relation and crack observation reveal that the control specimens are brittle and have low tensile strain compared to the ECCs.

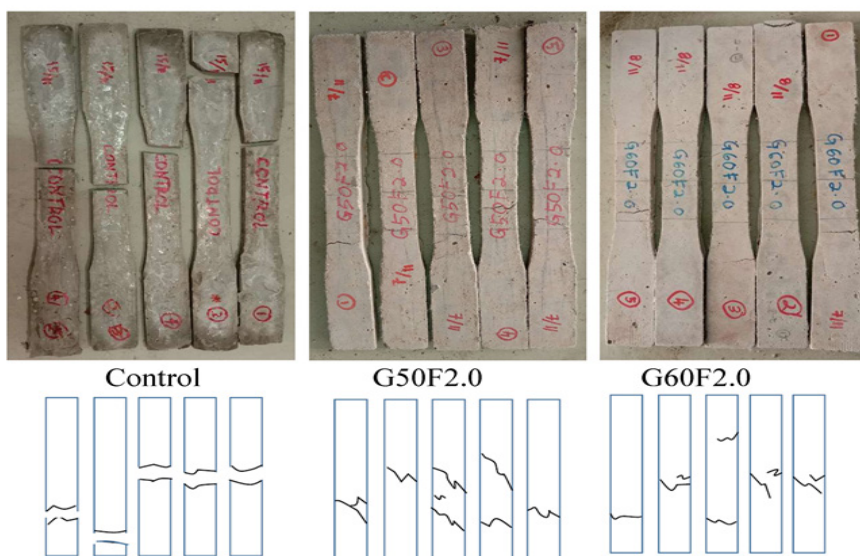


Figure 4. Cracking behaviour of specimens in series Control, G50F2.0 and G60F2.0

Table 5 shows the maximum crack width of the ECCs specimens after failure. Maximum crack widths ranging from 0.5 mm to 1.2 mm were recorded in ECC specimens. The control specimens were broken into two parts (or fracture) during the uniaxial tensile test before any form of cracks; thus, no crack width results were available. The average maximum crack width increased with the increase of the GGBS content from 50% to 60%. Decrement of maximum crack width was observed when the volume fraction of fibre increased from 2.0% to 2.5%. However, the fibre (2.0–2.5%) to the crack control of the ECCs is not as dominant as compared to the effect of GGBS (50–60%) in this study. Therefore, the maximum crack width of the ECCs is higher than the recommendations from JSCE (2008) of 0.1mm for fibre reinforced concrete and EN2 (2004) of 0.3mm for normal reinforced concrete.

Table 5

*Maximum crack width of dog bone specimens*

Mix	Maximum crack width (mm)					Average
	S1	S2	S3	S4	S5	
<b>Control</b>	F	F	F	F	F	NA
<b>G50F2.0</b>	0.6	0.7	-	-	0.6	0.63
<b>G50F2.5</b>	-	0.5	0.5	0.5	0.5	0.50
<b>G60F2.0</b>	1.0	-	1.2	-	1.0	1.07
<b>G60F2.5</b>	-	1.0	-	1.0	1.1	1.03

### Tensile Stress-strain Relation

The typical tensile stress-strain curves of the ECCs and control specimens obtained from the uniaxial tensile test are shown in Figure 5. The first crack strength, ultimate tensile strength and tensile strain capacity were labelled. There are three primary regions in the tensile stress-strain curves of ECCs, regions AB, BC and CD. In region AB, the curve starts to progress in a linearly increasing trend indicating an occurrence of elastic deformation in the specimen at this stage, till the first cracking. The steeper of slope in this region reveals the stiffer the material. Next, the curve in region BC advances in a gradual increasing and nonlinear manner showing pseudo strain hardening behaviour of the material. Fluctuation in the curve in region BC is mainly due to the development of multiple micro-cracks, the propagation of cracks observed associated with the fibre extraction in the specimen at an increasing inelastic strain. When one of the cracks becomes critical, localisation of the crack results in the decrement of tensile stress after C. Region CD presents a descending curve, which is also the effect of the enlargement of the critical crack with continuous application of load. Point D is recorded as the failure of the ECCs. It is clearly seen from



the tensile stress-strain relations that all ECC specimens show pseudo strain hardening behaviour compared to the control specimen. It is expected that the inclusion of the fibre at an optimum volume fraction of and interaction between the fibre-matrix can induce multiple cracking in ECC (Kumar & Ranade, 2021; Meng et al., 2017; Yu et al., 2020). The stress-strain curve for the control specimen illustrates slight fluctuation right after the first cracking; however, it hardly demonstrates the strain hardening behaviour. The curve rises steeply to the peak at a small strain without much fluctuation, indicating no development of other cracks in the specimen. It is supported by the observation of the specimen during the test, where only a critical crack was detected, mostly located at the gauge of the control specimen. Observation of the brittle fracture that suddenly occurred that led to the failure of the control specimen could explain why there is a steep fall in the curve after achieving ultimate tensile strength.

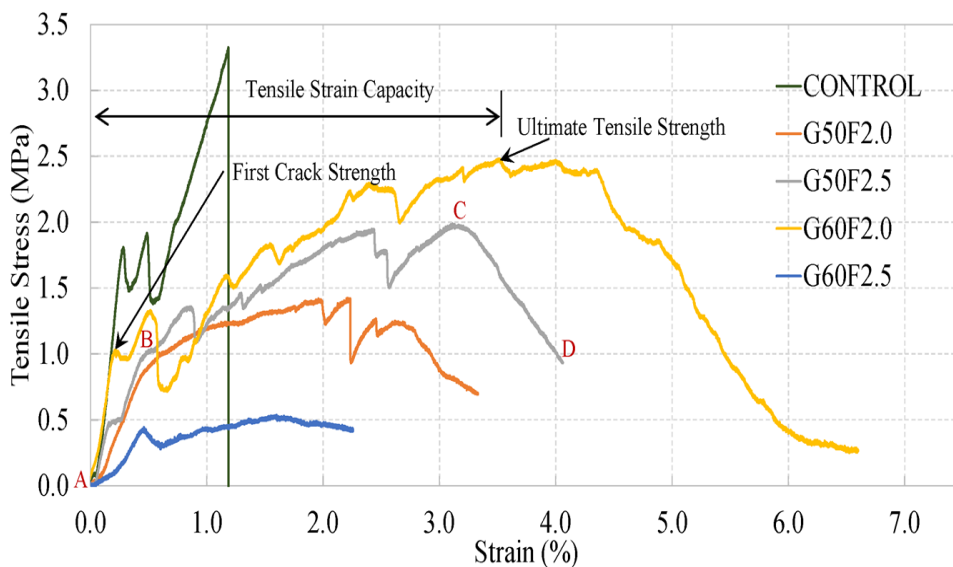


Figure 5. Tensile stress-strain curves

Table 6 shows the uniaxial tensile test of first crack strength, ultimate tensile strength, and ultimate tensile strain capacity. It was found that the control specimen exhibits higher first crack strength and ultimate tensile strength at 28 days compared to the ECC specimen. As expected, the control specimens attained the lowest tensile strain capacity, which explains the observations regarding the brittle fracture in the specimens.

Overall, ECC specimens G50F2.0, G50F2.5 and G60F2.0 demonstrated tensile strain capacity ranging from 2.6 %–2.75 % and with an ultimate tensile strength at a range of

1.43 MPa–2.82 MPa. Effect of fibres can be clearly seen when there was an occurrence of microcracking in ECCs compared to a dominant localised brittle fracture in the control specimen (without fibres). Additionally, ECCs achieve enhanced tensile strain capacity up to 1.6 times higher than the control specimens and about 200–300 times higher than the conventional concrete, which is around 0.01% (Nguyễn et al., 2020). For ECCs with 50% GGBS, when fibre volume fraction increased from 2.0% to 2.5%, increment of 20.6% in first crack strength and 32.9% in ultimate tensile strength was observed, however, with a 7.3% decrement in the tensile strain capacity. The enhanced strength can be supported with the fibre bridging effect, in which the crack propagation is controlled by fibres (Du et al., 2020).

The influence of GGBS can be observed in ECCs with a fibre volume fraction of 2.0%. When GGBS content increased from 50% to 60%, enhancement in tensile properties of ECC were observed, such as 6.5% increment in first crack strength, 97.2% increment in ultimate tensile strength and 5.76% increment in tensile strain capacity. The results are in good agreement with previous experimental works (Chen et al., 2013; Kim et al., 2007; Kumar & Ranade, 2021). According to Chen et al. (2013); Kumar and Ranade (2021), the addition of slag can reduce the toughness of the matrix, which contribute to higher multiple cracking. Furthermore, incorporating slag enhances the fibre-matrix interaction (Kumar & Ranade, 2021) and fibre dispersion (Kim et al., 2007), resulting in higher tensile strain capacity.

In this study, G60F2.5 exhibits relatively low tensile properties compared to other ECC specimens. The variation of the tensile properties is most likely due to variation in fibre bridging properties, matrix flaw randomness and excessive un-hydrated slag particles. Matrix flaws can be affected by the mixing process, vibration time and other factors (Meng et al., 2017). In addition, un-hydrated slag particles due to excessive slag particles can weaken the bonding of fibre-matrix (Kumar & Ranade, 2021).

Table 6

*Tensile properties of ECCs*

Mix	First Crack Strength (MPa)	Ultimate Tensile Strength (MPa)	Tensile strain capacity (%)
Control	1.95 (0.65)	3.27 (0.23)	1.15 (0.15)
G50F2.0	0.92 (0.07)	1.43 (0.07)	2.60 (0.69)
G50F2.5	1.11 (0.91)	1.90 (0.13)	2.41 (0.98)
G60F2.0	0.98 (0.18)	2.82 (0.38)	2.75 (0.93)
G60F2.5	0.50 (0.11)	0.61 (0.08)	1.40 (0.28)

Note: Values between parentheses is the standard deviation of the mean.

## CONCLUSION

This study presents experimental work for the tensile properties and cracking behaviour of ECCs containing different volumes of GGBS and fibre. Few conclusions can be made from the study:

- a. Most slag-based ECCs have higher compressive strength than the control of increment up to 29.5%. ECCs with 50% GGBS have higher compression strength compared to ECCs with 60% GGBS in the study.
- b. All ECC specimens demonstrate pseudo strain hardening behaviour. Most of the ECCs demonstrated tensile strain capacity ranging from 2.6%–2.75% and ultimate tensile strength with a range of 1.43 MPa–2.82 MPa. These ECCs demonstrate tensile strain capacity up to 1.6 times higher than control in this study.
- c. The control specimen demonstrated brittle fractured before any form of cracks, whereas ECCs with GGBS and fibres formed few hairline cracks at the gage of the dog bone. Higher GGBS in the specimen resulted in higher maximum crack width.

Few recommendations were made from the study where research on the effect of different sizes of fibres, silica sand, more variety percentage of replacement materials, different waste materials etc. is needed to gain a deeper understanding of their relationship with tensile and cracking behaviours and to develop more quality and sustainable ECCs for structural applications.

## ACKNOWLEDGMENTS

The Universiti Teknologi MARA funded this research under grant Research Entity Initiative (REI) 600-IRMI/REI 5/3 (012/2018). The authors gratefully acknowledge undergraduate student *Najihah binti Sukri* for assisting in the laboratory works. In addition, the authors would also like to thank the School of Civil Engineering, College of Engineering, Universiti Teknologi MARA, Shah Alam, Selangor.

## REFERENCES

- Booya, E., Gorospe, K., Das, S., & Loh, P. (2020). The influence of utilizing slag in lieu of fly ash on the performance of engineered cementitious composites. *Construction and Building Materials*, 256, Article 119412. <https://doi.org/https://doi.org/10.1016/j.conbuildmat.2020.119412>
- Chen, Z., Yang, Y., & Yao, Y. (2013). Quasi-static and dynamic compressive mechanical properties of engineered cementitious composite incorporating ground granulated blast furnace slag. *Materials & Design*, 44, 500-508. <https://doi.org/https://doi.org/10.1016/j.matdes.2012.08.037>
- Du, Q., Cai, C., Lv, J., Wu, J., Pan, T., & Zhou, J. (2020). Experimental investigation on the mechanical properties and microstructure of basalt fiber reinforced engineered cementitious composite. *Materials*, 13(17), Article 3796. <https://doi.org/10.3390/ma13173796>

- Kim, J. K., Kim, J. S., Ha, G. J., & Kim, Y. Y. (2007). Tensile and fiber dispersion performance of ECC (engineered cementitious composites) produced with ground granulated blast furnace slag. *Cement and Concrete Research*, 37(7), 1096-1105. <https://doi.org/https://doi.org/10.1016/j.cemconres.2007.04.006>
- Kumar, D., & Ranade, R. (2021). Development of strain-hardening cementitious composites utilizing slag and calcium carbonate powder. *Construction and Building Materials*, 273, Article 122028. <https://doi.org/https://doi.org/10.1016/j.conbuildmat.2020.122028>
- Lee, S. W., Oh, C. L., & Zain, M. R. M. (2019). Mechanical properties of engineered cementitious composites using local ingredients. *Journal of Mechanical Engineering (JMEchE)*, 16(2), 145-157. <https://doi.org/10.21491/jmeche.v16i2.15332>
- Lee, S. W., Oh, C. L., & Zain, M. R. M. (2018). Evaluation of the design mix proportion on mechanical properties of engineered cementitious composites. In *Key Engineering Materials* (Vol. 775, pp. 589-595). Trans Tech Publications Ltd.
- Lee, S. W., Oh, C. L., Zain, M. R. M., Yahya, N. A., & Rahman, A. A. (2019). Mechanical performances of green engineered cementitious composites incorporating various types of sand. In *Key Engineering Materials* (Vol. 821, pp. 512-517). Trans Tech Publications Ltd.
- Li, V. C. (2003). On engineered cementitious composites (ECC) a review of the material and its applications. *Journal of Advanced Concrete Technology*, 1(3), 215-230. <https://doi.org/https://doi.org/10.3151/jact.1.215>
- Ma, H., Qian, S., Zhang, Z., Lin, Z., & Li, V. C. (2015). Tailoring engineered cementitious composites with local ingredients. *Construction and Building Materials*, 101, 584-595. <https://doi.org/https://doi.org/10.1016/j.conbuildmat.2015.10.146>
- Meng, D., Huang, T., Zhang, Y., & Lee, C. (2017). Mechanical behaviour of a polyvinyl alcohol fibre reinforced engineered cementitious composite (PVA-ECC) using local ingredients. *Construction and Building Materials*, 141, 259-270. <https://doi.org/10.1016/j.conbuildmat.2017.02.158>
- National Standard Authority of Ireland. (2005). *Eurocode 2: Design of concrete structures-part 1-1: General rules and rules for buildings*. British Standard Institution.
- Nguyễn, H. H., Choi, J. I., Park, S. E., Cha, S. L., Huh, J., & Lee, B. Y. (2020). Autogenous healing of high strength engineered cementitious composites (ECC) using calcium-containing binders. *Construction and Building Materials*, 265, Article 120857. <https://doi.org/https://doi.org/10.1016/j.conbuildmat.2020.120857>
- Sakulich, A. R. (2011). Reinforced geopolymer composites for enhanced material greenness and durability. *Sustainable Cities and Society*, 1(4), 195-210. <https://doi.org/https://doi.org/10.1016/j.scs.2011.07.009>
- Yokota, H., Rokugo, K., & Sakata, N. (2008). JSCE recommendations for design and construction of high performance fiber reinforced cement composite with multiple fine cracks. In *High Performance Fiber Reinforced Cement Composites*. Springer.
- Yu, K. Q., Lu, Z. D., Dai, J. G., & Shah, S. P. (2020). Direct tensile properties and stress - strain model of UHP-ECC. *Journal of Materials in Civil Engineering*, 32(1), Article 04019334. [https://doi.org/10.1061/\(ASCE\)MT.1943-5533.0002975](https://doi.org/10.1061/(ASCE)MT.1943-5533.0002975)

- Yu, K., Li, L., Yu, J., Wang, Y., Ye, J., & Xu, Q. (2018). Direct tensile properties of engineered cementitious composites: a review. *Construction and Building Materials*, 165, 346-362. <https://doi.org/https://doi.org/10.1016/j.conbuildmat.2017.12.124>
- Zhu, Y., Yang, Y., & Yao, Y. (2012). Use of slag to improve mechanical properties of engineered cementitious composites (ECCs) with high volumes of fly ash. *Construction and Building Materials*, 36, 1076-1081. <https://doi.org/https://doi.org/10.1016/j.conbuildmat.2012.04.031>



## A Comparative Effectiveness of Hierarchical and Non-hierarchical Regionalisation Algorithms in Regionalising the Homogeneous Rainfall Regions

Zun Liang Chuan<sup>1\*</sup>, Wan Nur Syahidah Wan Yusoff<sup>1</sup>, Azlyna Senawi<sup>1</sup>, Mohd Romlay Mohd Akramin<sup>2</sup>, Soo-Fen Fam<sup>3</sup>, Wendy Ling Shinyie<sup>4</sup> and Tan Lit Ken<sup>5</sup>

<sup>1</sup>Centre for Mathematical Sciences, College of Computing and Applied Sciences, Universiti Malaysia Pahang, Lebuhraya Tun Razak, 26300 Gambang Kuantan, Pahang DM, Malaysia

<sup>2</sup>Faculty of Mechanical and Automotive Engineering Technology, Universiti Malaysia Pahang, 26600 Pekan, Pahang DM, Malaysia

<sup>3</sup>Faculty of Technology Management and Technopreneurship, Universiti Teknikal Malaysia Melaka, Hang Tuah Jaya, 76100 Melaka, Malaysia

<sup>4</sup>Department of Mathematics, Faculty of Science, Universiti Putra Malaysia, 43400 UPM Serdang, Selangor DE, Malaysia

<sup>5</sup>Takasago Thermal/Environmental Systems Laboratory, Malaysia-Japan International Institute of Technology (MJIT), Universiti Teknologi Malaysia, Jalan Sultan Yahya Petra, 54100 Kuala Lumpur, Malaysia

### ABSTRACT

Descriptive data mining has been widely applied in hydrology as the regionalisation algorithms to identify the statistically homogeneous rainfall regions. However, previous studies employed regionalisation algorithms, namely agglomerative hierarchical and non-hierarchical regionalisation algorithms requiring post-processing techniques to validate and interpret the analysis results. The main objective of this study is to investigate the effectiveness of the automated agglomerative hierarchical and non-hierarchical

regionalisation algorithms in identifying the homogeneous rainfall regions based on a new statistically significant difference regionalised feature set. To pursue this objective, this study collected 20 historical monthly rainfall time-series data from the rain gauge stations located in the Kuantan district. In practice, these 20 rain gauge stations can be categorised into two statistically homogeneous rainfall regions, namely distinct spatial and temporal variability in the rainfall amounts. The

### ARTICLE INFO

#### Article history:

Received: 06 May 2020

Accepted: 01 October 2020

Published: 04 January 2022

DOI: <https://doi.org/10.47836/pjst.30.1.18>

#### E-mail addresses:

chuanzl@ump.edu.my (Zun Liang Chuan)

wnsyahidah@ump.edu.my (Wan Nur Syahidah Wan Yusoff)

azlyna@ump.edu.my (Azlyna Senawi)

akramin@ump.edu.my (Mohd Romlay Mohd Akramin)

famsoofen@utm.edu.my (Soo-Fen Fam)

sy\_ling@upm.edu.my (Wendy Ling Shinyie)

tlken@utm.edu.my (Tan Lit Ken)

\* Corresponding author

results of the analysis show that Forgy  $K$ -means non-hierarchical (FKNH), Hartigan-Wong  $K$ -means non-hierarchical (HKNH), and Lloyd  $K$ -means non-hierarchical (LKNH) regionalisation algorithms are superior to other automated agglomerative hierarchical and non-hierarchical regionalisation algorithms. Furthermore, FKNH, HKNH, and LKNH yielded the highest regionalisation accuracy compared to other automated agglomerative hierarchical and non-hierarchical regionalisation algorithms. Based on the regionalisation results yielded in this study, the reliability and accuracy that assessed the risk of extreme hydro-meteorological events for the Kuantan district can be improved. In particular, the regional quantile estimates can provide a more accurate estimation compared to at-site quantile estimates using an appropriate statistical distribution.

*Keywords:* Anderson Darling statistical test, bootstrap, hierarchical, non-hierarchical, regionalisation algorithm, unbiased statistical test

---

## INTRODUCTION

The rapid advancement of technology and data collection has facilitated organisations and researchers to gather huge amounts of data. However, it is extremely challenging to extract fruitful and reliable insights using conventional statistical analysis techniques (Tan et al., 2006). Therefore, data mining was rapidly growing in performing descriptive and predictive tasks. In principle, descriptive data mining derives patterns, such as associations, trajectories, trends, clusters, and anomalies that summarise principal relationships in the data sets. In nature, descriptive data mining requires post-processing techniques to validate and interpret the results of the analysis. Meanwhile, predictive data mining is used to predict future values of particular attributes in the presence of uncertainty based on historical attributes.

In previous hydrology studies, descriptive data mining tools including agglomerative hierarchical and non-hierarchical regionalisation algorithms have been widely used in identifying homogeneous rainfall regions (Ahmad et al., 2013; Awan et al., 2014; Burn et al., 1997; Chuan et al., 2018a; Chuan et al., 2018b; Guttman, 1993; Hamdan et al., 2015; Ngongondo et al., 2011; Nnaji et al., 2014; Terassi & Galvani, 2017). The principal objective of using descriptive data mining tools in hydrology studies is to extrapolate insights from the gauge into ungauged rainfall stations based on the limited amount of historical rainfall time series data, which can increase the reliability of the risk assessment of extreme hydro-meteorological events. For instance, Guttman (1993) proposed the use of average linkage agglomerative hierarchical (ALAH) and Ward's minimum variance agglomerative hierarchical (WMVAH) regionalisation algorithms to identify the homogeneous precipitation regions in the United States. To identify the homogeneous precipitation regions, they used the Euclidean distance as the dissimilarity measure.



Variables, such as the geographical insights of precipitation gauge stations, mean annual precipitation amount, and average variability of the annual precipitation cycle, were regarded as regionalisation features. In addition, Burn et al. (1997) proposed the use of the agglomerative hierarchical regionalisation algorithm in identifying the homogeneous watersheds in Canada based on Webster and Burrough's distance as the dissimilarity measure. In addition, seasonality measures of the catchments were regarded as regionalisation features. Both previous studies used the L-moments based homogeneity measure to validate the regionalised homogeneous regions. Moreover, Nnaji et al. (2014) proposed the use of the ALAH regionalisation algorithm to identify the homogeneous regions in the Federal Republic of Nigeria based on the coefficient of variation extracted from the historical monthly rainfall time series data and Euclidean distance dissimilarity measure. However, this article does not describe the homogeneity validation of the identified homogeneous rainfall regions. Recently, Terassi and Galvani (2017) proposed identifying the homogeneous rainfall regions in the watersheds of the eastern region of the state of Paraná using the WMVAH regionalisation algorithm. In identifying the homogeneous rainfall regions, they employed the Euclidean distance dissimilarity measure and regionalisation features, such as rainfall variability, relief characteristics, the spatial proximity of pluviometric and meteorological stations.

Ngongondo et al. (2011) proposed the use of WMVAH and MacQueen *K*-means non-hierarchical (MKNH) regionalisation algorithms in identifying the homogeneous rainfall regions in Southern Malawi. First, they define the homogeneous rainfall regions based on the regionalisation features, such as geographical insights of the rain gauge stations and at-site mean annual precipitation. Then, the number of optimum homogeneous rainfall regions is determined using Hubert's gamma coefficient and Dunn internal clustering validation indices. Moreover, they validate the homogeneity of the identified rainfall regions using discordant and L-moments-based homogeneity measures. Awan et al. (2014) conducted a comparison study of the effectiveness between agglomerative hierarchical and non-hierarchical regionalisation algorithms. In particular, they investigated the effectiveness of WMVAH and the MKNH regionalisation algorithms to identify the homogeneous rainfall regions in the East Asia monsoon, including China, Korea, Japan, and Taiwan using the historical monthly rainfall time series data based on the Euclidean distance dissimilarity measure and average annual rainfall amounts. This study employed Calinski–Harabasz, Krzanowski–Lai, and Davies–Bouldin internal clustering validation indices to determine the optimum number of homogeneous regions. The results for the analysis of this study show that the MKNH regionalisation algorithm is superior to the WMVAH regionalisation algorithm.

In Malaysia, previous studies have been extensively employing agglomerative hierarchical regionalisation algorithms in identifying homogeneous rainfall regions. In

particular, Ahmad et al. (2013) proposed identifying the homogeneity of historical annual rainfall time series data recorded from 59 rain gauge stations in Peninsular Malaysia using a complete linkage agglomerative hierarchical (CLAH) regionalisation algorithm and correlation coefficient dissimilarity measure. Their study selected and evaluated a superior regionalisation algorithm from 77 potential agglomerative hierarchical regionalisation algorithms on Malaysia geographical, monsoon limitation, and segregation of stations. They proposed selecting the optimum number of regions using eight internal clustering validation indices. In addition, Hamdan et al. (2015) proposed employing the CLAH regionalisation algorithm to identify homogeneous rainfall regions using the historical annual time series data recorded from 75 rain gauge stations located in Peninsular Malaysia and Euclidean distance dissimilarity measure. However, Ahmad et al. (2013) and Hamdan et al. (2015) did not present the homogeneity validation of the identified homogeneous rainfall regions.

Chuan et al. (2018b) proposed the Technique for Order of Preference by Similarity to Ideal Solution (TOPSIS) multi-criteria decision-making algorithm and internal clustering validation indices, such as C-index, Davies-Bouldin index, Dunn-index, and Gamma index to determine the superior agglomerative hierarchical regionalisation algorithm and the optimum number of homogeneous rainfall regions. Their findings show that the ALAH regionalisation algorithm, which is based on the Altgower dissimilarity measure, had successfully delineated 20 historical monthly rainfall time series data recorded from the rain gauge stations located in the Kuantan district into two coastal and inland regions.

Furthermore, it validated the identified homogeneous regions using a non-parametric Bootstrap-based K-sample Anderson Darling (BKAD) statistical test. Contrariwise, Chuan et al. (2018a) proposed an automated regionalisation algorithm, which integrated the ALAH regionalisation algorithm and multi-scale bootstrap resampling to identify statistically homogeneous rainfall regions. Their proposed automated regionalisation algorithm had regionalised 20 historical monthly rainfall time series data of the Kuantan district in the coastal and inland regions. These two regions show different spatial and temporal rainfall variability. In general, the automated regionalisation algorithm is more advantageous compared to other previously proposed algorithms. The automated regionalisation algorithm is competent to identify and validate the homogeneous rainfall regions and vice versa for the non-automated regionalisation algorithms. In addition, the automated regionalisation algorithm uses an approximately unbiased (AU) statistical test that provides statistical evidence and vice versa for the L-moments based homogeneity measure.

The main objective of this study is to investigate the effectiveness of the automated agglomerative hierarchical and non-hierarchical regionalisation algorithms in identifying the homogeneous rainfall regions based on a new statistically significant difference regionalised feature set. In specific, the agglomerative hierarchical regionalisation algorithms employed in this study include average linkage agglomerative hierarchical (ALAH), complete linkage

agglomerative hierarchical (CLAH), single linkage agglomerative hierarchical (SLAH), and Ward's minimum variance agglomerative hierarchical (WMVAH). The non-hierarchical regionalisation algorithms include Forgy *K*-means (FKNH), Hartigen-Wong *K*-means (HKNH), Lloyd *K*-means (LKNH), and MacQueen *K*-means (MKNH). Moreover, the centred and uncentred inverse correlation coefficients are used as the dissimilarity measure for agglomerative hierarchical algorithms, and Euclidean distance is used as the dissimilarity measure for non-hierarchical algorithms. This study regionalised the homogeneous rainfall regions based on the rainfall distribution characteristics of the historical monthly rainfall time series data. Therefore, the superior regionalisation algorithm is determined based on the accuracy rate of regionalisation. To pursue the main objective of this study, the rest of this paper is organised as follows. Section 2 presents the detailed insights of the rain gauge stations located in the Kuantan district, while Section 3 provides a brief overview of the theoretical background. The results of the analysis and discussion are presented in Section 4. Finally, the concluding remarks are presented in Section 5.

## STUDY AREAS

The Kuantan river basin is about 440 km long and irrigates 29,300 km<sup>2</sup> of the area, and it is located in the eastern part of Peninsular Malaysia. This river is in the Kuantan district that covers 1,630 km<sup>2</sup> of the catchment area starting from the forest reserved area in Mukim Ulu Kuantan; it passes through the agricultural area and the state capital of Pahang before it is discharged into the South China Sea (Saeed et al., 2016; Chuan et al., 2020). Moreover, this river is the main principle tributary, which irrigates the major rural, urban, agricultural, and industrial areas of the Kuantan district. The Kuantan district has a tropical rainforest climate belonging to the Köppen climate classification, which experiences two seasons per year, namely dry and hot seasons during the Southwest Monsoon and rainy seasons during the Northeast Monsoon. However, the anthropogenic emissions of greenhouse gasses are caused by human activities, which are the main contributor to global warming. Consequently, global warming has been increasing the risk of extreme hydro-meteorological events. Therefore, there is a need for a reliable and accurate risk assessment for extreme hydro-meteorological events using sufficient historical rainfall time series data.

This study used 20 historical monthly rainfall time series data (in mm) with 58 months in the Kuantan district to evaluate the regionalisation algorithms. In particular, the historical monthly rainfall time series data cover the period from February 2010 to November 2014, which was collected from the Department of Irrigation and Drainage Malaysia. Figure 1 shows the locations of 20 rain gauge stations in this study. Meanwhile, Table 1 presents the geographical insights of the 20 rain gauge stations and the characteristics of rainfall distribution based on the historical monthly rainfall time series data.

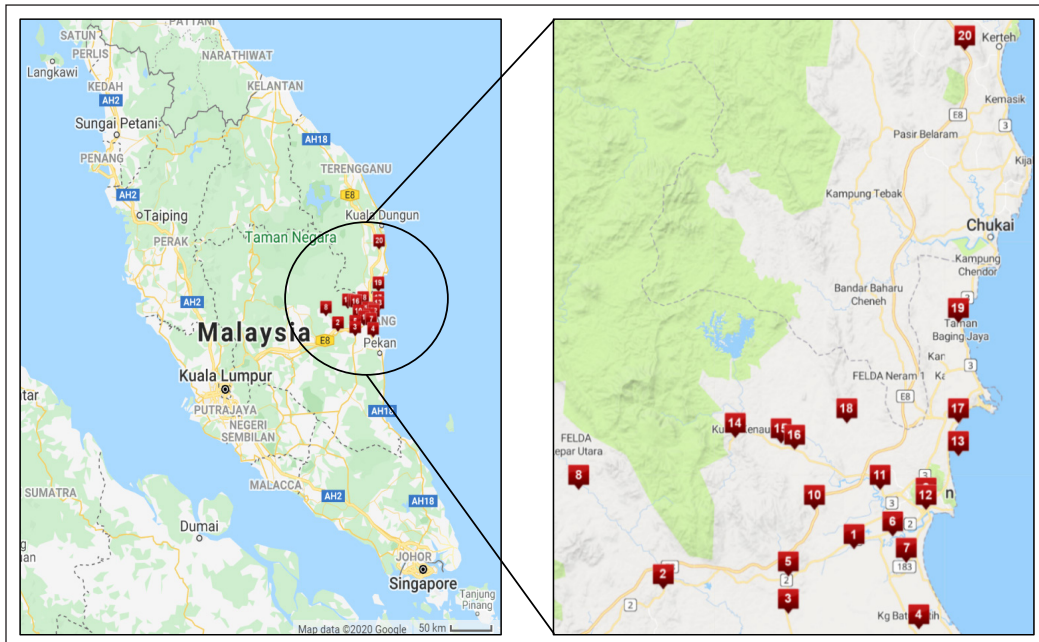


Figure 1. Locations of 20 rain gauge stations located in the Kuantan River Basin for Kuantan District

Table 1

The geographical coordinates insights of the 20 rain gauge stations and the characteristics of the probability distribution of the historical monthly rainfall time series data

Station	Station ID	Station Name	Regionalisation Features						
			$\theta_1$	$\theta_2$	$\theta_3$	$\theta_4$	$\theta_5$	$\theta_6$	$\theta_7$
1	3432001	Sri Damai	3.75	103.22	14.90	90.56	63.94	33.03	16.12
2	3629098	Paya Bungor	3.69	102.93	34.70	158.11	66.46	11.61	10.94
3	3631001	Kg. Pulau Manis	3.65	103.12	37.40	181.52	65.49	13.93	16.31
4	3633104	Kg. Bahru, Penor	3.63	103.32	7.60	179.62	78.90	28.75	24.50
5	3731018	JKR Gambang	3.71	103.12	41.30	234.01	80.29	18.44	19.46
6	3732020	Paya Besar di Kuantan	3.77	103.28	6.00	162.88	76.36	19.23	13.93
7	3732021	Kg. Sg. Soi	3.73	103.30	11.90	210.96	90.27	33.53	28.89
8	3828091	Ldg. Ulu Lepar	3.84	102.80	91.70	167.20	60.28	10.71	10.04
9	3830001	Ldg. Mentiga	3.82	103.33	9.40	199.19	79.08	12.46	13.56
10	3831002	Felda Pancing	3.81	103.16	71.40	234.07	103.13	26.00	19.28
11	3832015	Rancangan Pam Paya Pinang	3.84	103.26	6.70	209.73	90.43	28.47	25.47
12	3833002	Pejabat JPS Negeri Pahang	3.81	103.33	10.30	180.86	83.88	23.27	21.47
13	3833004	Ldg. Jeram di Kuantan	3.89	103.38	-1.40	210.94	109.27	43.74	35.32

Table 1 (continue)

Station	Station ID	Station Name	Regionalisation Features						
			$\theta_1$	$\theta_2$	$\theta_3$	$\theta_4$	$\theta_5$	$\theta_6$	$\theta_7$
14	3930012	Sg. Lembing P.C.C.L Mill	3.92	103.04	33.10	245.67	87.26	7.70	9.68
15	3931013	Ldg. Nada	3.91	103.11	16.90	227.94	87.58	18.06	18.78
16	3931014	Ldg. Kuala Reman	3.90	103.13	29.90	201.86	83.56	9.32	9.73
17	3933003	Balok di Kuantan	3.94	103.38	4.10	220.82	112.23	47.76	33.70
18	4031001	Bkt. Sagu	3.94	103.21	20.90	511.75	193.46	42.31	51.69
19	4033001	Kg. Cherating	4.09	103.38	9.00	221.22	111.61	46.15	30.14
20	4033002	Kg. Sg. Ular	4.50	103.39	58.50	228.74	110.54	45.15	34.24

\*Note:  $\theta_1$  = latitude;  $\theta_2$  = longitude;  $\theta_3$  = altitude;  $\theta_4$  = median;  $\theta_5$  = coefficient of variation;  $\theta_6$  = skewness;  $\theta_7$  = kurtosis

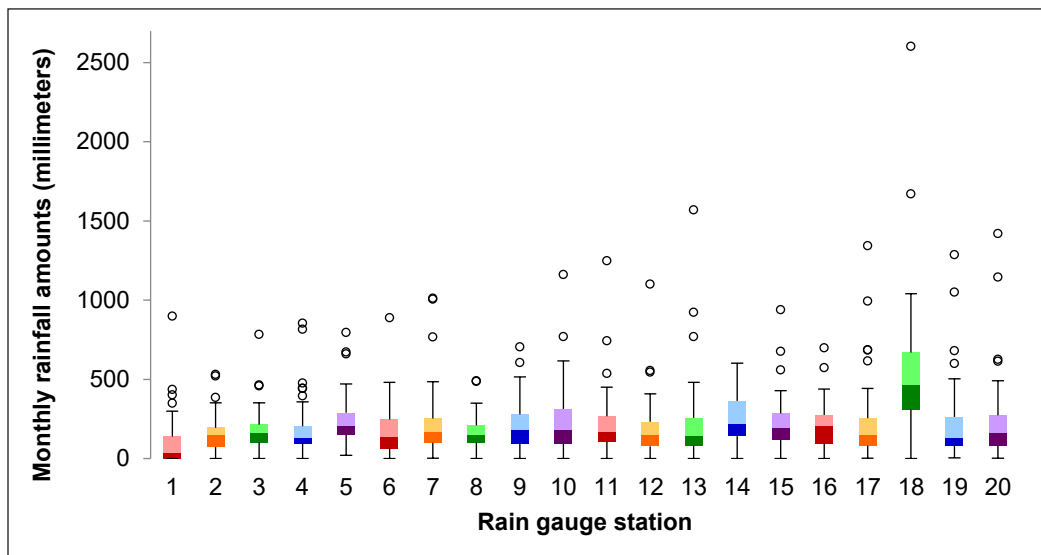


Figure 2. The graphical descriptive summary of twenty historical monthly rainfall amounts recorded from rain gauge stations located Kuantan District

Based on the statistics, the median is more robust than the skewed data and outliers compared to the arithmetic mean (Saeed et al., 2016). Figure 2 and Table 1 show that the employed historical monthly rainfall time series data are highly skewed to the right, and there are outliers in all historical monthly rainfall time series data. In particular, Figure 2 illustrates that the upper box is wider than the lower box for the 20 historical rainfall time series data, while  $\theta_6$  indicates the positive values of skewness. In addition, Figure 2 also presents the presence of outliers (unfilled circle) that excluded the historical monthly rainfall time series data recorded from the 14<sup>th</sup> rain gauge station. Therefore, the most appropriate central value is the median rather than the arithmetic mean.

## METHODOLOGY

This section provides a brief overview of the theoretical background of the agglomerative hierarchical and non-hierarchical regionalisation algorithm employed in this study. In addition, it also presents the theoretical background of the data screening and statistical homogeneity tests, such as approximately unbiased (AU) and non-parametric Bootstrap-based K-sample Anderson Darling (BKAD) statistical test. This study used the AU statistical test to integrate agglomerative hierarchical clustering analysis to establish the automated regionalisation algorithms. The dissimilarity measures include the centred and uncentred inverse correlation coefficient. However, the dissimilarity measure applied in the non-hierarchical regionalisation algorithms is the Euclidean distance. The mechanism of the  $K$ -means non-hierarchical regionalisation algorithm defines the homogeneous rainfall regions by minimising the sum of squared error ( $SSE$ ) based on the Euclidean space. Therefore, the Euclidean distance is appropriately applied in this algorithm.

### Data Screening

Data screening is a preliminary and essential procedure in inspecting and treating errors in data set, such as missing data. In practice, the missing data in the historical monthly rainfall time series data is invertible due to the meteorological extremes, recorded error, and malfunctions of instruments (Chuan et al., 2020; Chuan et al., 2018a; Chuan et al., 2018b; Chuan et al., 2018c; Saeed et al., 2016).  $\mathbf{X}^{incomp}$  is a matrix of size  $I \times J$  of the historical monthly rainfall amount as in Equation 1:

$$\mathbf{X}^{incomp} = \left[ (1 - \pi) X_{ij}^{obs} + \pi X_{ij}^{miss} \right]_{I \times J} \quad (1)$$

where,  $X_{ij}^{obs}$  and  $X_{ij}^{miss}$ , respectively represent the observed and missing historical monthly rainfall amount for  $i$ th month recorded from  $j$ th rain gauge stations.  $\pi \leq 0.3$  represents the rate of missingness and  $i, (j) = 1, 2, \dots, I, (J)$ . To obtain a complete data set, this study employed the column median single imputation algorithm (Saeed et al., 2016) in treating the missing data for the matrix of  $\mathbf{X}^{incomp}$  as in Equation 2:

$$X_j^{miss} = \text{median}_{1 \leq i \leq I} \left[ X_{ij}^{obs} \right] \quad (2)$$

Therefore, this study obtained a complete matrix for the historical monthly rainfall amount,  $\mathbf{X}^{comp}$ . This study employed a column median single imputation algorithm in treating the missing data rather than multiple imputation algorithms. The column median single imputation algorithm requires a low computational cost compared to multiple imputation algorithms. Similar regionalisation results are obtained after treating the missing data using column median single and multiple imputation algorithms.

### Regionalisation Algorithms

Descriptive data mining is used to derive patterns, such as homogeneous rainfall regions that summarise the underlying relationships in  $\mathbf{X}^{comp}$ , which the adequacy of regionalisation of homogeneous rainfall regions is highly dependent on the features extracted from  $\mathbf{X}^{comp}$ . The extraction of the insignificant features from  $\mathbf{X}^{comp}$  can degrade the adequacy of regionalisation results (Dash & Liu, 2003). The regionalisation features set,  $\theta$ , employed in this study include  $\theta_1, \theta_2, \theta_3, \theta_4, \theta_5, \theta_6$  and  $\theta_7$ , which indicate the statistically significant difference results ( $F$  test-statistic = 4,197,057.90; p-value = 0.000) after testing using Roy's greatest root of multivariate analysis of variance (Chuan et al., 2018c; Chuan et al., 2020). Therefore, the homogeneous rainfall regions are identified based on  $\theta$  using the agglomerative hierarchical and non-hierarchical regionalisation algorithms.

**Agglomerative Hierarchical Regionalisation Algorithms.** Previous hydrology studies stated that agglomerative hierarchical regionalisation algorithms are widely employed to define the homogeneous rainfall regions (Ahmad et al., 2013; Burn et al., 1997; Chuan et al., 2018a; Chuan et al., 2018b; Guttman, 1993; Hamdan et al., 2015; Nnaji et al., 2014; Terassi & Galvani, 2017). In principle, agglomerative hierarchical regionalisation algorithms perform  $J - 1$  successive fusion based on predetermined dissimilarity measures to establish a single agglomerative hierarchical dendrogram. Assume that  $\min_{1 \leq j \leq J} [\lambda(\theta_{j_{m0}}, \theta_{j_{n0}})]$  is the minimum distance based on the predetermined dissimilarity measure,  $\lambda$ , for a single cluster,  $\theta_{j_m}$ , which comprises the fused pair of clusters,  $\theta_{j_{m0}}$  and  $\theta_{j_{n0}}$ . By updating ALAH, CLAH, SLAH, and WMVAH regionalisation algorithm mechanism functions in Equations 3 to 6 (Chuan et al., 2018b), it will produce a new hierarchical agglomerative dendrogram,  $\lambda^*(\theta_{j_m}, \theta_{j_n})$ , between cluster  $\theta_{j_m}$  and remaining infused clusters,  $\theta_{j_n}$ .

$$\lambda_{ALAH}^*(\theta_{j_m}, \theta_{j_n}) = \frac{a_{\theta_{j_{m0}}} \lambda(\theta_{j_{m0}}, \theta_{j_m}) + a_{\theta_{j_{n0}}} \lambda(\theta_{j_{n0}}, \theta_{j_n})}{a_{\theta_{j_{m0}}} + a_{\theta_{j_{n0}}}} \quad (3)$$

$$\lambda_{CLAH}^*(\theta_{j_m}, \theta_{j_n}) = \frac{\lambda(\theta_{j_{m0}}, \theta_{j_m}) + \lambda(\theta_{j_{n0}}, \theta_{j_n}) + |\lambda(\theta_{j_{m0}}, \theta_{j_m}) - \lambda(\theta_{j_{n0}}, \theta_{j_n})|}{2} \quad (4)$$

$$\lambda_{SLAH}^*(\theta_{j_m}, \theta_{j_n}) = \frac{\lambda(\theta_{j_{m0}}, \theta_{j_m}) + \lambda(\theta_{j_{n0}}, \theta_{j_n}) - |\lambda(\theta_{j_{m0}}, \theta_{j_m}) - \lambda(\theta_{j_{n0}}, \theta_{j_n})|}{2} \quad (5)$$

$$\lambda_{WMVAH}^*(\theta_{j_m}, \theta_{j_n}) = \frac{\lambda(\theta_{j_{m0}}, \theta_{j_m})(a_{\theta_{j_{m0}}} + a_{\theta_{j_n}}) + \lambda(\theta_{j_{n0}}, \theta_{j_n})(a_{\theta_{j_{n0}}} + a_{\theta_{j_m}}) - \lambda(\theta_{j_{m0}}, \theta_{j_n})(a_{\theta_{j_n}})}{a_{\theta_{j_{m0}}} + a_{\theta_{j_{n0}}} + a_{\theta_{j_n}}} \quad (6)$$

where,  $a_{\theta_{j_{m0}}}$ ,  $a_{\theta_{j_{n0}}}$  and  $a_{\theta_{j_n}}$  represent the number of  $\theta$  extracted from the historical monthly rainfall time series data recorded from the  $j$ th rain gauge that is included in the clusters of  $\theta_{j_{m0}}$ ,  $\theta_{j_{n0}}$  and  $\theta_{j_n}$ , respectively. Moreover, there are two differences of  $\lambda$  employed in this study to investigate their effectiveness in regionalising the homogeneous rainfall regions. They include centred,  $\lambda_1$ , and uncentred,  $\lambda_2$ , inverse correlation coefficients as in Equations 7 and 8:

$$\lambda_1 = 1 - \frac{\sum \left( \text{vec}(\theta_{j_1}) - \overline{\text{vec}(\theta_{j_1})} \right) \left( \text{vec}(\theta_{j_2}) - \overline{\text{vec}(\theta_{j_2})} \right)}{\sqrt{\sum \left( \text{vec}(\theta_{j_1}) - \overline{\text{vec}(\theta_{j_1})} \right)^2 \sum \left( \text{vec}(\theta_{j_2}) - \overline{\text{vec}(\theta_{j_2})} \right)^2}} \quad (7)$$

$$\lambda_2 = 1 - \frac{\sum \left( \text{vec}(\theta_{j_1}) \text{vec}(\theta_{j_2}) \right)}{\sqrt{\sum \left( \text{vec}(\theta_{j_1}) \right)^2 \sum \left( \text{vec}(\theta_{j_2}) \right)^2}} \quad (8)$$

where,  $\text{vec}(\cdot)$  represents the vectorisation function and  $j_1 \neq j_2$ .

**Non-hierarchical Regionalisation Algorithms.** The non-hierarchical regionalisation algorithms, such as  $K$ -means is an iterative regionalisation algorithm with the main principle to regionalise  $J$  rain gauge stations into  $K$  predefined distinct non-overlapping homogeneous rainfall regions,  $C_k$ ;  $k=1,2,\dots,K$ . Based on the mechanism of  $K$ -means non-hierarchical regionalisation algorithm,  $J$  rain gauge stations are delineated into  $K$  homogeneous rainfall regions by minimising the sum of squared error ( $SSE$ ) as in Equation 9:

$$SSE = \sum_{k=1}^K \sum_{j=1}^J \left\| \theta_j^k - \omega_k \right\| \quad (9)$$

where,  $\left\| \theta_j^k - \omega_k \right\|$  represents the Euclidean distance between the infused rain gauge stations and the centre of homogenous rainfall regions,  $\omega$ . On the other hand,  $K$ -means non-hierarchical regionalisation algorithms require prior knowledge in predetermining the  $K$  numbers of  $C_k$ . This study used four distinct non-hierarchical regionalisation algorithms in performing the  $K$ -means process: FKNH (Forgy, 1965), MKNH (MacQueen, 1967), HKNH (Hartigan & Wong, 1979), and LKNH (Lloyd, 1982). The identified homogeneous rainfall regions are based on the regionalisation algorithms validated using BKAD statistical test (Chuan et al., 2018b), which provides statistical evidence.



### Homogeneity Validation Statistical Test

In principle, descriptive data mining requires post-processing techniques in validating and interpreting the results of the analysis. Therefore, this study employed AU and BKAD statistical tests to validate the homogeneity of the identified homogeneous rainfall regions. In particular, the AU statistical test is associated with agglomerative hierarchical regionalisation algorithms to determine the optimum number of homogeneous rainfall regions and validate the homogeneity of identifying rainfall regions. Meanwhile, BKAD statistical test was employed to validate the homogeneity of identifying rainfall regions. Furthermore, AU statistical test is deemed appropriate for the phylogenetic tree selection (Shimodaira, 2002); therefore, two distinct homogeneity tests were used to pursue the main objective of this study.

**Approximately Unbiased Statistical Test.** AU statistical test was introduced by Shimodaira (2002), who employed the multi-scale bootstrap technique to reduce the bias in a statistical test. This statistical test is applied to the maximum likelihood tree selection in acquiring the confidence set of the trees (Shimodaira, 2002). In general, AU statistical test is more advantageous than the L-moments based homogeneity measure to validate the homogeneity of identifying rainfall regions. AU statistical test can provide statistical evidence and vice versa for L-moments based homogeneity measures. The following is the procedure in determining the optimum number of homogeneous rainfall regions and the validation of identifying homogeneity based on the AU statistical test.

**Step 1:** Fix the constants of scaling,  $\Psi_r; r = 1, 2, \dots, R$ , and the number of replicates for the multi-scale bootstrap resampling,  $\Omega_r$ , where  $\Omega_r = 10,000$  is used in this study.

**Step 2:** Generate  $\Omega_r$  bootstrap that replicates with a sequence length of  $\psi^* = \Psi_r J$ , which is denoted as  $\phi^s(\Psi_r)$  for  $\forall r$  and  $s = \Omega_r$ .

**Step 3:** Calculate the bootstrap probability,  $\Pr_{\Omega}(\Psi_r)$ , based on Equation 10.

$$\Pr_{\Omega}(\Psi_r) = \frac{\#\langle \phi^s(\Psi_r) \in H_1 \rangle}{\Omega_r}; H_1 = \sqrt{\sum_{d=1}^D \mu_d} \leq \Lambda_D \tag{10}$$

where,  $\Lambda_D$  represents the region in  $D$ -dimensional parameter spaces.

**Step 4:** Estimate the curvature,  $\xi_1$ , and the signed distance,  $\xi_2$ , by minimising the sum squared of residual ( $SSR$ ) as in Equation 11:

$$SSR(\xi_1, \xi_2) = \sum_{g=1}^G \left( \frac{\frac{\xi_1}{\sqrt{\Psi_r}} + \xi_2 - \Phi^{-1}(1 - \Pr_{\Omega}(\Psi_r))}{\hat{\sigma}_g} \right)^2 \tag{11}$$

where,  $\hat{\sigma}_g = \frac{\Omega_r \varphi(\Phi^{-1} \Pr_{\Omega}(\Psi_r))}{\sqrt{\Pr_{\Omega}(\Psi_r)(1 - \Pr_{\Omega}(\Psi_r))}}$ . Meanwhile,  $\varphi(\cdot)$  and  $\Phi^{-1}(\cdot)$  represent the

density and quantile function of the standard normal distribution, respectively.

**Step 5:** Calculate the p-value of the AU statistical test based on Equation 12.

$$\Pr_{AU} = 1 - \Phi(\xi_2 - \xi_1) \quad (12)$$

**K-sample Anderson Darling Statistical Test.** The BKAD statistical test is the generalisation of the classical  $K$ -sample Anderson Darling statistical test, and this statistical test is free from any statistical assumption (Chuan et al., 2018b). For example, suppose that  $x_{(1)}^{comp} < x_{(2)}^{comp} < \dots < x_{(IK)}^{comp}$  is the pooled order of sample  $C_k$ . Therefore, the BKAD statistical test,  $Q_{BKAD}$ , and its standard deviation,  $Sd(Q_{BKAD})$ , can be defined as Equations 13 and 14:

$$Q_{BKAD} = \sum_{i=1}^{IK-1} \frac{(K \rho_{ik} - i)^2}{i(IK - i)} \quad (13)$$

$$Sd(Q_{BKAD}) = \sqrt{\frac{\Gamma(IK - 3)(\nu_1 + \nu_2 IK + \nu_3 (IK)^2 + \nu_4 (IK)^3)}{\Gamma(IK)}} \quad (14)$$

where,  $\rho_{ik}$  represents the number of historical monthly rainfall amounts in the  $k$  th sample that is not more than the  $j$ th smallest historical monthly rainfall amount in the pooled sample. Meanwhile,  $\nu_1$ ,  $\nu_2$ ,  $\nu_3$  and  $\nu_4$  are expressed as Equations 15 to 18:

$$\nu_1 = 2K \left( 3K + (K - 2) \sum_{i=1}^{IK-1} \frac{1}{i} \right) \quad (15)$$

$$\nu_2 = -\frac{2}{I} \left( IK^2 - 3IK + 3K - (3IK^2 + 2IK + 2I + K) \sum_{i=1}^{IK-1} \frac{1}{i} - IK \sum_{i=1}^{IK-1} \frac{1}{(IK - i)(i + 1)} \right) \quad (16)$$

$$\nu_3 = -\frac{2}{I} \left( 2IK^2 + 3I + 3K - (4IK - 4I - 7K) \sum_{i=1}^{IK-1} \frac{1}{i} - (IK^2 + K + 2I) \sum_{i=1}^{IK-1} \frac{1}{(IK - i)(i + 1)} \right) \quad (17)$$

$$\nu_4 = -\frac{2}{I} \left( 3IK + 3I + 5K - (2IK - 2I - 3K) \sum_{i=1}^{IK-1} \frac{1}{(IK - i)(i + 1)} \right) \quad (18)$$

In principle, the identified rainfall regions are statistically homogeneous if and only if (Equation 19):

$$\eta_{BKAD} = \frac{Q_{BKAD}^2 - K + 1}{Sd^2(Q_{BKAD})} \geq \eta_{K-1, \alpha} \tag{19}$$

where, the upper tail percentage points  $\eta_{K-1, \alpha} = \frac{Q_{K-1}^2 - (K - 1)}{\sqrt{\frac{1.7392(K - 1)}{3}}}$ , and  $Q_{K-1}^2$  is acquired from

fitting Pearson curves (Scholz & Stephens, 1987). Based on Equation (19), the stability property of the BKAD statistical test is questionable. Therefore, the BKAD statistical test was performed based on the ranks of sample historical monthly rainfall amount. In addition, this study employed the non-parametric bootstrap resampling with 10,000 replications in determining the acceptability limit of the BKAD test to overcome this limitation.

### RESULTS AND DISCUSSION

The analysis of this study was mainly conducted using R statistical software. Figure 2 presents the five-number summary of the 20 historical monthly rainfall time series data recorded from the rain gauge stations located in the Kuantan district that includes minimum, first quartile, median, third quartile, and maximum amount of the monthly rainfall. Based on Figure 2, the historical monthly rainfall time series data recorded from the first and 18<sup>th</sup> rain gauge stations show the least and highest rainfall amounts on average, respectively. Meanwhile, the historical monthly rainfall time series data recorded from the fourth and 18<sup>th</sup> rain gauge stations show the least and highest variability of rainfall amounts, respectively. According to Chuan et al. (2018a), the 20 rain gauge stations can be regionalised into two statistically homogeneous rainfall regions, namely the coastal (second, third, fifth, eighth, 10<sup>th</sup>, 14<sup>th</sup>, 15<sup>th</sup>, and 16<sup>th</sup>) and inland regions (first, fourth, sixth, seventh, ninth, 11<sup>th</sup>, 12<sup>th</sup>, 13<sup>th</sup>, 17<sup>th</sup>, 18<sup>th</sup>, 19<sup>th</sup>, and 20<sup>th</sup>) as illustrated in Figure 3. In particular, these coastal and inland regions comprise distinct spatial and temporal variability (Chuan et al., 2018b).

Figures 4 and 5 presented the regionalisation analysis results from the dendrograms (Figures A1 & A2, Appendix) based on ALAH, CLAH, SLAH, and WMVAH regionalisation algorithms using

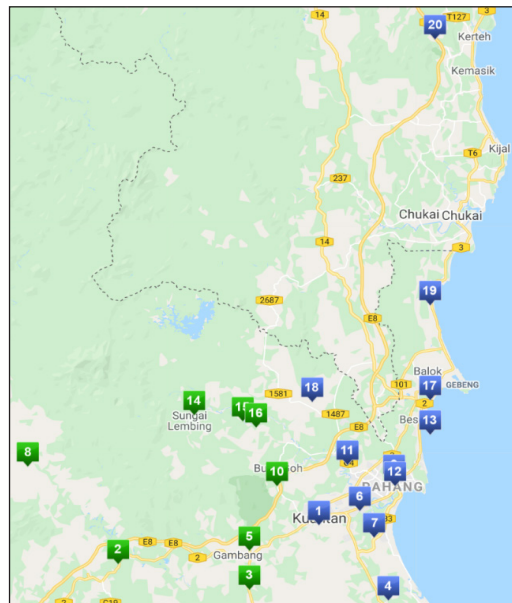


Figure 3. The best regionalised homogeneous rainfall regions, which comprises the coastal and inland regions

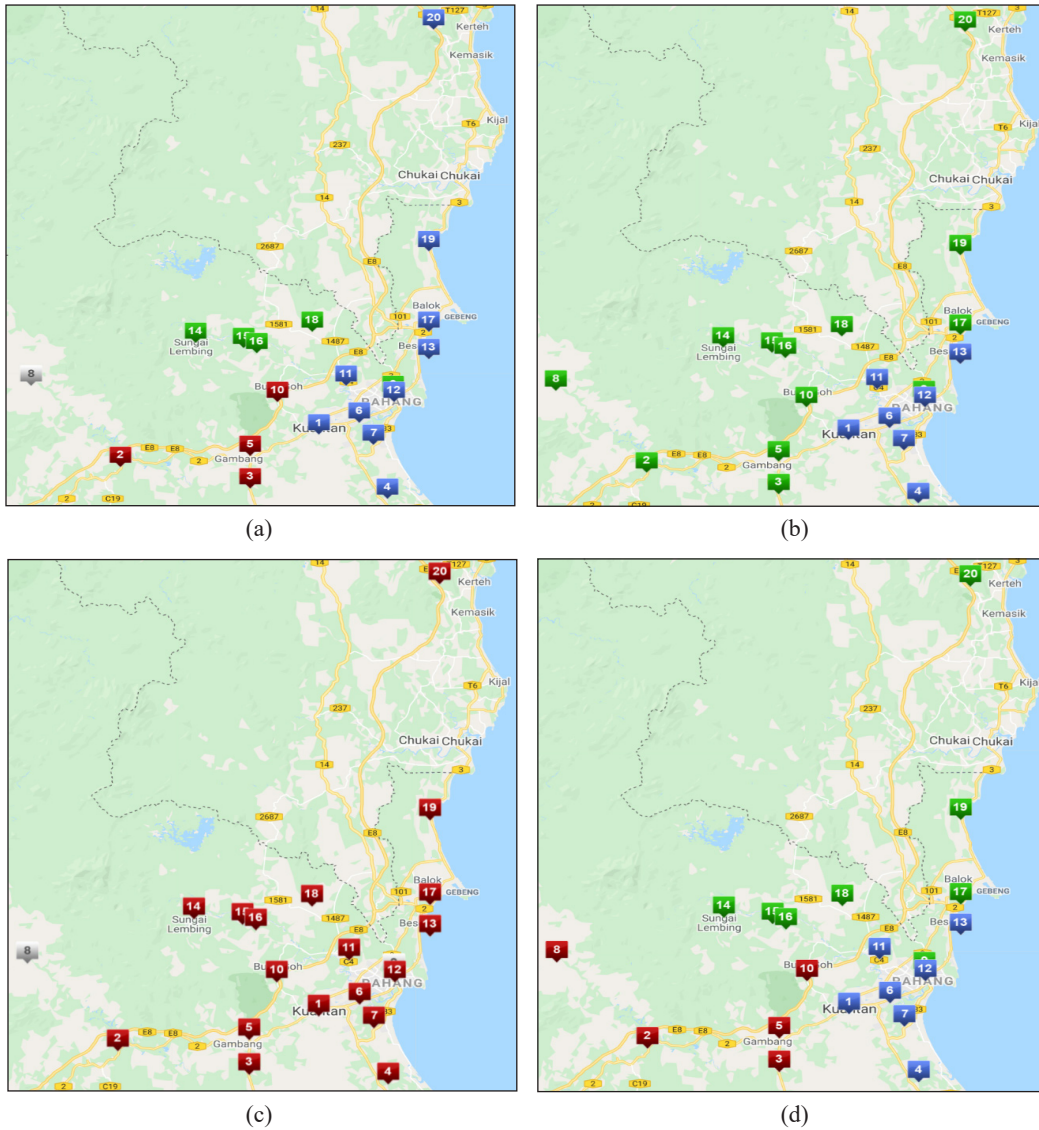


Figure 4. The identified regionalised homogeneous rainfall regions using (a) ALAH, (b) CLAH, (c) SLAH, (d) WMVAH regionalisation algorithm based on  $\lambda_1$

$\lambda_1$  and  $\lambda_2$ , respectively. Meanwhile, Figure 6 presents the regionalisation analysis results based on FKNH, HKNH, LKNH, and MKNH regionalisation algorithms. Based on Figures 4(a) and 4(c), the white marker of the eighth rain gauge station shows that this station is unfit to merge with other statistically homogeneous rainfall regions. A similar representative is also presented in Figures 5(a), 5(b), 5(c), and 5(d). Specifically, the rain gauge stations are unfit to merge with other identified statistically homogeneous rainfall regions represented using white markers.

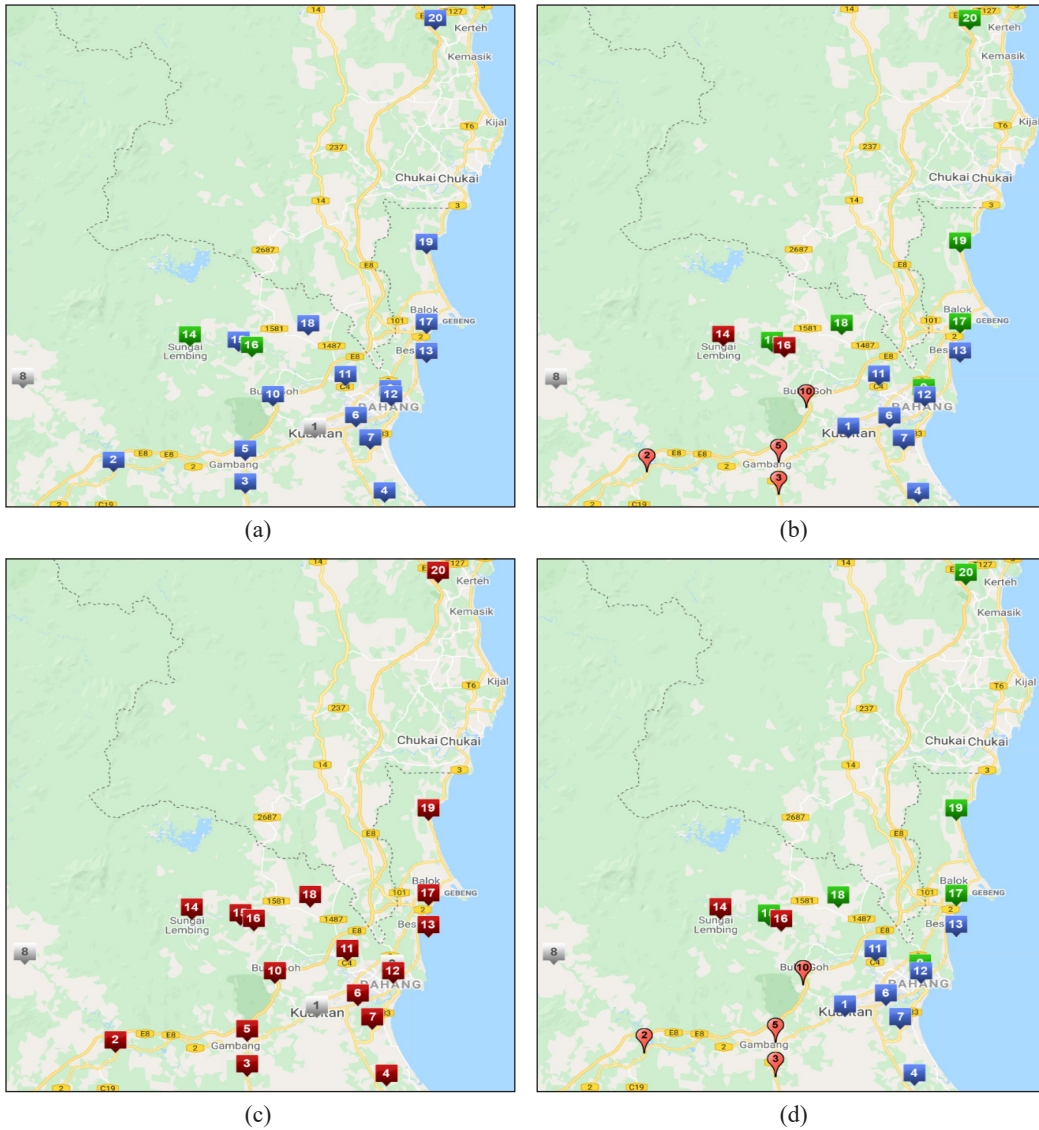


Figure 5. The identified regionalised homogeneous rainfall regions using (a) ALAH, (b) CLAH, (c) SLAH, (d) WMVAH regionalisation algorithm based on  $\lambda_2$

By comparing the regionalisation accuracy rate in Table 2, the automated agglomerative hierarchical regionalisation algorithms using  $\lambda_1$  yielded more adequate regionalisation results than  $\lambda_2$  on average. In particular, the CLAH regionalisation algorithm uses  $\lambda_1$  that yielded high regionalisation with better-fitted regionalisation analysis results and the highest regionalisation accuracy rate compared to other agglomerative hierarchical regionalisation algorithms. However, there is a need to physically relocate the misplaced rain gauge stations from the inland homogeneous rainfall regions to the coastal regions (Sahrin et al., 2018).

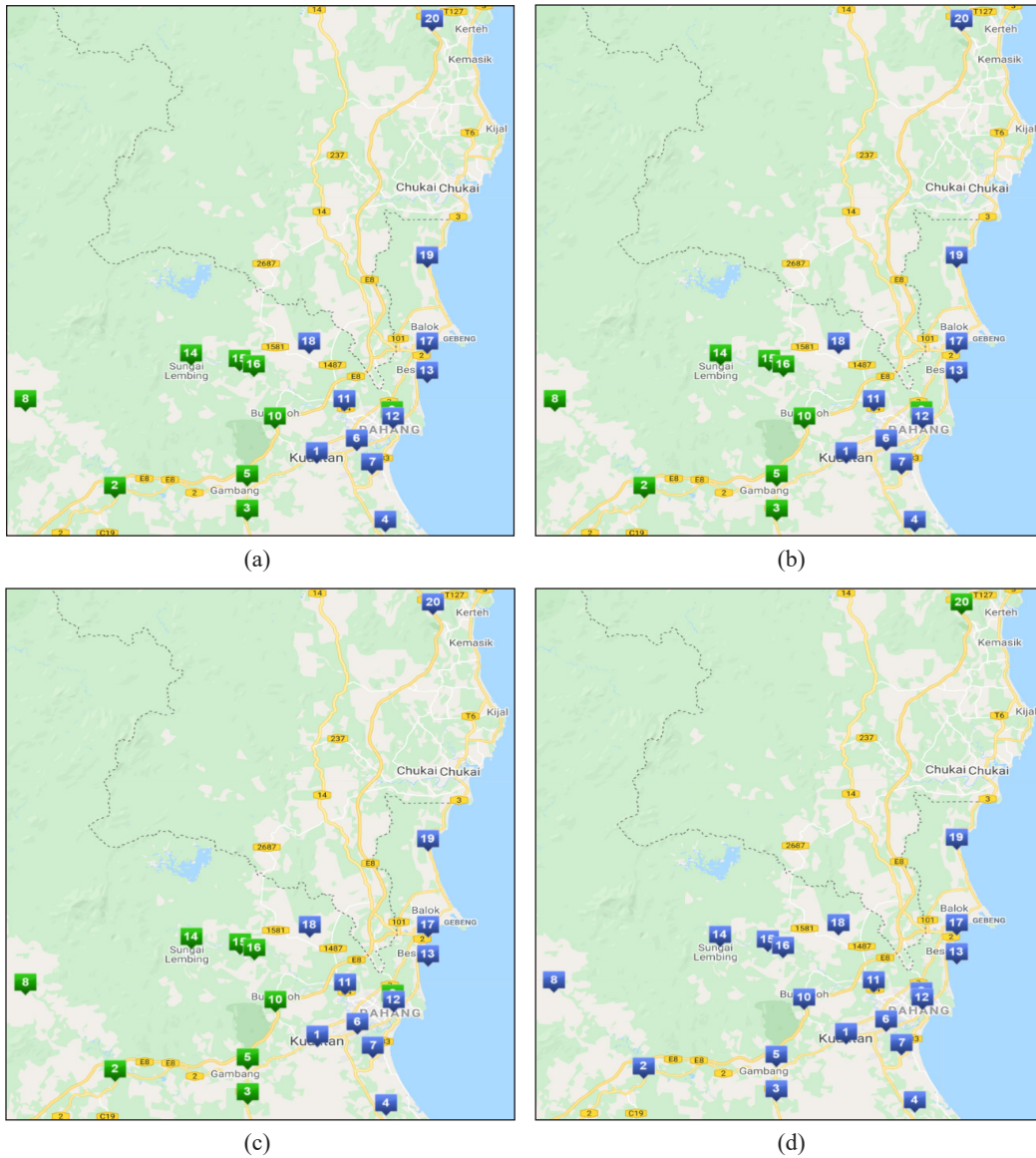


Figure 6. The identified homogeneous rainfall regions using (a) FKNN, (b) HKNN, (c) LKNN, (d) MKNN based on the Euclidean dissimilarity measures

The rain gauge stations that need to be relocated include the ninth, 17<sup>th</sup>, 18<sup>th</sup>, 19<sup>th</sup>, and 20<sup>th</sup>. The relocated misplaced rain gauge stations provide the statistically homogeneous after testing using the BKAD statistical test ( $C_1$  (inland region):  $\eta_{BKAD} = 4.7681$ , p-value = 0.5130;  $C_2$  (coastal region):  $\eta_{BKAD} = 23.6609$ , p-value = 1.0000). The p-value of the BKAD statistical test for  $C_2$  is led to 1.00. This figure (aforementioned p-value) has been rounding up from  $0.\bar{9}$ , which vinculum ( $\bar{\phantom{x}}$ ) represents the recurring decimals. Moreover, Table 2

Table 2  
*The average regionalisation accuracy rate and P-value before physically relocated the misplaced rain gauge stations*

Algorithm	Dissimilarity Distance	Central Value	Regionalisation Accuracy (%)	$\eta_{BKAD}$ (P-value)
ALAH	$\lambda_1$	Mean	28.33	C <sub>1</sub> : null C <sub>2</sub> : 2.7173 (0.8729) C <sub>3</sub> : null C <sub>4</sub> : 0.7985 (0.5913) C <sub>5</sub> : 23.1314 (1.0000)
		Median	33.33	C <sub>1</sub> : null C <sub>2</sub> : 2.7173 (0.8729) C <sub>3</sub> : 2.2541 (0.2129) C <sub>4</sub> : 20.3358 (1.0000)
	$\lambda_2$	Mean	29.17	C <sub>1</sub> : null C <sub>2</sub> : 0.7985 (0.5913) C <sub>3</sub> : null C <sub>4</sub> : 11.2250 (0.8328)
		Median	28.33	C <sub>1</sub> : null C <sub>2</sub> : 0.7985 (0.5913) C <sub>3</sub> : null C <sub>4</sub> : 11.2250 (0.8328)
CLAH	$\lambda_1$	Mean	79.17	C <sub>1</sub> : 16.5523 (1.0000) C <sub>2</sub> : 10.2941 (0.9508)
		Median	79.17	C <sub>1</sub> : 16.5523 (1.0000) C <sub>2</sub> : 10.2941 (0.9508)
	$\lambda_2$	Mean	21.67	C <sub>1</sub> : 2.7173 (0.8729) C <sub>2</sub> : 16.5523 (1.0000) C <sub>3</sub> : null C <sub>4</sub> : 0.7985 (0.5913) C <sub>5</sub> : 3.9347 (0.8414)
		Median	21.67	C <sub>1</sub> : 2.7173 (0.8729) C <sub>2</sub> : 16.5523 (1.0000) C <sub>3</sub> : null C <sub>4</sub> : 0.7985 (0.5913) C <sub>5</sub> : 3.9347 (0.8414)
SLAH	$\lambda_1$	Mean	13.19	C <sub>1</sub> : null C <sub>2</sub> : null C <sub>3</sub> : null C <sub>4</sub> : null C <sub>5</sub> : null C <sub>6</sub> : 8.1221 (0.8786) C <sub>7</sub> : null C <sub>8</sub> : 1.8152 (0.8442)
		Median	34.72	C <sub>1</sub> : null C <sub>2</sub> : null C <sub>3</sub> : 12.9962 (0.9314)
	$\lambda_2$	Mean	23.96	C <sub>1</sub> : null C <sub>2</sub> : null C <sub>3</sub> : null C <sub>4</sub> : 12.9962 (0.9314)

Table 2 (continue)

Algorithm	Dissimilarity Distance	Central Value	Regionalisation Accuracy (%)	$\eta_{BKAD}$ ( $P$ -value)
WMVAH	$\lambda_1$	Median	23.96	$C_1$ : null $C_2$ : null $C_3$ : null $C_4$ : 32.6502 (1.0000)
		Mean	40.28	$C_1$ : 3.0098 (0.7224) $C_2$ : 16.5523 (1.0000) $C_3$ : 6.6316 (0.9640)
		Median	40.28	$C_1$ : 3.0149 (0.7245) $C_2$ : 16.5523 (1.0000) $C_3$ : 2.1053 (0.6921) $C_4$ : 0.7985 (0.5913) $C_5$ : null $C_6$ : null
		Mean	27.08	$C_1$ : 16.5523 (1.0000) $C_2$ : 6.6316 (0.9640) $C_3$ : null $C_4$ : 2.7173 (0.8729)
	$\lambda_2$	Median	21.67	$C_1$ : 16.5523 (1.0000) $C_2$ : 0.7985 (0.5913) $C_3$ : 3.9347 (0.8414) $C_4$ : null $C_5$ : 2.7173 (0.8729)
		Mean	95.83	$C_1$ : 22.3519 (1.0000) $C_2$ : 5.0093 (0.3272)
		Median	95.83	$C_1$ : 22.3519 (1.0000) $C_2$ : 5.0093 (0.3272)
		Mean	95.83	$C_1$ : 22.3519 (1.0000) $C_2$ : 5.0093 (0.3272)
LKNH	Euclidean Distance	Mean	95.83	$C_1$ : 22.3519 (1.0000) $C_2$ : 5.0093 (0.3272)
		Median	95.83	$C_1$ : 22.3519 (1.0000) $C_2$ : 5.0093 (0.3272)
MKNH	Euclidean Distance	Mean	95.83	$C_1$ : 22.3519 (1.0000) $C_2$ : 5.0093 (0.3272)
		Median	54.17	$C_1$ : 16.5523 (1.0000) $C_2$ : 10.2941 (0.9508)

\*Note: null represents the hypothesis testing is invalid. This is because the  $C_k$  merely comprises a single rain gauge station.

reveals that arithmetic means and median as the central value of the regionalised features do not affect the performance of regionalisation accuracy rates, except for ALAH that uses  $\lambda_1$  and  $\lambda_2$ , SLAH uses  $\lambda_1$ , WMVAH uses  $\lambda_2$  and MNKH regionalisation algorithms. In particular, the use of arithmetic means and median as the central value of the regionalised



features for CLAH that uses  $\lambda_1$  and  $\lambda_2$ , SLAH uses  $\lambda_2$ , WMVAH uses  $\lambda_1$ , FKNNH, HKNNH and LKNNH always yield similar regionalisation accuracy rates.

On the other hand, the regionalisation analysis results that use FKNNH [Figure 6(a)], HKNNH [Figure 6(b)], and LKNNH [Figure 6(c)] regionalisation algorithms are superior to MKNNH and automated agglomerative hierarchical regionalisation algorithms. FKNNH, HKNNH, and LKNNH regionalisation algorithms yielded higher regionalisation accuracy rates than MKNNH regionalised algorithms, as presented in Table 2. In addition, the regionalisation analysis results use FKNNH, HKNNH and LKNNH regionalisation algorithms to relocate one misplaced rain gauge station. In particular, the ninth rain gauge station was misplaced in the statistically homogeneous inland region; therefore, the ninth rain gauge station was relocated in the statistically homogeneous coastal region. Furthermore, the BKAD statistical test revealed the statistically significant homogeneity for coastal ( $C_1: \eta_{BKAD} = 4.7681$ , p-value=0.5130) and inland regions ( $C_2: \eta_{BKAD} = 23.6609$ , p-value=1.0000) after relocating the misplaced rain gauge station. Hence, this study concluded that FKNNH, HKNNH, and MKNNH regionalisation algorithms are superior to other agglomerative hierarchical and non-hierarchical regionalisation algorithms with prior knowledge regarding the predetermined  $K$  number of homogeneous clusters. This study recommended using different methods, such as elbow, average silhouette, and gap statistics, in determining the optimal number of homogeneous regions when there is a lack of prior knowledge regarding the predetermined  $K$  number of homogeneous clusters.

## CONCLUSION AND FUTURE WORK

This study evaluated the effectiveness of automated agglomerative hierarchical and non-hierarchical regionalisation algorithms to identify the significant homogeneous rainfall regions for the rain gauge stations located in the Kuantan district. The automated agglomerative hierarchical regionalisation algorithms employed are based on integrating several agglomerative hierarchical regionalisation algorithms, including ALAH, CLAH, SLAH, WMVAH, and the AU statistical test. Meanwhile, the non-hierarchical regionalisation algorithms include FKNNH, HKNNH, LKNNH, and MKNNH regionalisation algorithms. In addition, the dissimilarity measures applied on the automated agglomerative hierarchical regionalisation algorithms are the centred and uncentred inverse correlation coefficients. In contrast, the dissimilarity measures applied on the non-hierarchical regionalisation algorithms are the Euclidean distance. This study used the 20 historical monthly rainfall time series data recorded from the rain gauge stations located in the Kuantan district that comprises the coastal and inland regions with distinct spatial and temporal variability to consolidate the effectiveness of the automated agglomerative hierarchical and non-hierarchical regionalisation algorithms. The analysis results show that FKNNH, HKNNH and LKNNH are the superior non-hierarchical regionalisation algorithms

compared to MKNH regionalisation algorithms. Furthermore, FKNH, HKNH, and LKNH regionalisation algorithms yielded a similar regionalisation accuracy rate.

In summary, this study proposes another regionalised feature set, which can be formed from the combination of geographical insights and the characteristics of rainfall distribution. This study obtained high regionalisation accuracy rates after the features set was applied in the non-hierarchical regionalisation algorithms. Based on the regionalisation results, the reliability and accuracy in assessing the risk of extreme hydro-meteorological events for the Kuantan district can be improved. Furthermore, the regional quantile estimates can provide a more accurate estimation compared to at-site quantile estimates. Finally, this study suggests extending this work in the future by employing other moments bases, such as L-moments, LQ-moments, PL-moments, and TL-moments, in describing the probability distribution of the historical monthly rainfall time-series data that are used as regionalisation features.

## ACKNOWLEDGEMENTS

The authors would like to acknowledge the Department of Irrigation and Drainage Malaysia to provide the historical monthly rainfall time series data employed in this study. The authors would also like to acknowledge the scribble maps developers for providing the software to create maps in this study. A word of appreciation also goes to the reviewers for their constructive comments and suggestions on this paper. Moreover, the authors would like to extend their sincere appreciation to Universiti Malaysia Pahang and the Ministry of Education Malaysia for providing the research funds of this study, namely the UMP internal grants (RDU1703184) and the Fundamental Research Grant Scheme, FRGS/1/2018/ STG06/UMP/02/16 (RDU190134).

## REFERENCES

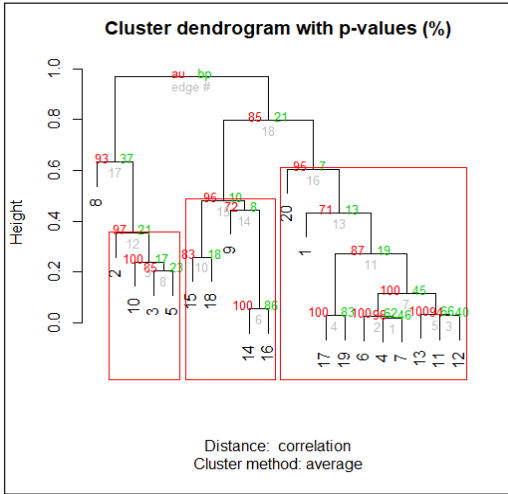
- Ahmad, N. H., Othman, I. R., & Deni, S. M. (2013). Hierarchical cluster approach for regionalisation of Peninsular Malaysia based on the precipitation amount. *Journal of Physics: Conference Series*, 423, 1-10. <https://doi.org/10.1088/1742-6596/423/1/012018>
- Awan, J. A., Bae, D. H., & Kim, K. J. (2014). Identification and trend analysis of homogeneous rainfall zones over the East Asia monsoon region. *International Journal of Climatology*, 35(7), 1422-1433. <https://doi.org/10.1002/joc.4066>
- Burn, D. H., Zrinji, Z., & Kowalchuk, M. (1997). Regionalization of catchments for regional flood frequency analysis. *Journal of Hydrologic Engineering*, 2(2), 76-82. [https://doi.org/10.1061/\(ASCE\)1084-0699\(1997\)2:2\(76\)](https://doi.org/10.1061/(ASCE)1084-0699(1997)2:2(76))
- Chuan, Z. L., Deni, S. M., Fam, S. F., & Ismail, N. (2020). The effectiveness of a probabilistic principal component analysis model and expectation maximisation algorithm in treating missing daily rainfall data. *Asia-Pacific Journal of Atmospheric Sciences*, 56, 119-129. <https://doi.org/10.1007/s13143-019-00135-8>

- Chuan, Z. L., Ismail, N., Shinyie, W. L., Ken, T. L., Fam, S. F., Senawi, A., & Yusoff, W. N. S. W. (2018a). The efficiency of average linkage hierarchical clustering algorithm associated multi-scale bootstrap resampling in identifying homogeneous precipitation catchments. *IOP Conference Series: Materials Science and Engineering*, 342, 1-10. <https://doi.org/10.1088/1757-899X/342/1/012070>
- Chuan, Z. L., Ismail, N., Yusoff, W. N. S. W., Fam, S. F., & Romlay, M. A. M. (2018b). Identifying homogeneous rainfall catchments for non-stationary time series using TOPSIS algorithm and bootstrap k-sample Anderson darling test. *International Journal of Engineering & Technology*, 7(4), 3228-3237.
- Chuan, Z. L., Senawi, A., Yusoff, W. N. S. W., Ismail, N., Ken, T. L., & Chuan, M. W. (2018c). Identifying the ideal number  $Q$ -components of the Bayesian principal component analysis model for missing daily precipitation data treatment. *International Journal of Engineering & Technology*, 7(4.30), 5-10. <https://doi.org/10.14419/ijet.v7i4.30.21992>
- Dash, M., & Liu, H. (2003). Feature selection for clustering. In T. Terano, H. Liu & A. L. P. Chen (Eds.), *Knowledge discovery and data mining current issues and new applications* (pp. 110-121). Springer. [https://doi.org/10.1007/3-540-45571-X\\_13](https://doi.org/10.1007/3-540-45571-X_13)
- Forgy, E. (1965). Cluster analysis of multivariate data: Efficiency versus interpretability of classification. *Biometrics*, 21(3), 768-769.
- Guttman, N. B. (1993). The use of L-moments in the determination of regional precipitation climates. *Journal of Climate*, 6(12), 2309-2325. [https://doi.org/10.1175/1520-0442\(1993\)006<2309:TUOLMI>2.0.CO;2](https://doi.org/10.1175/1520-0442(1993)006<2309:TUOLMI>2.0.CO;2)
- Hamdan, M. F., Suhaila, J., & Jemain, A. A. (2015). Clustering rainfall pattern in Malaysia using functional data analysis. *AIP Conference Proceedings*, 1643, 349-355. <https://doi.org/10.1063/1.4907466>
- Hartigan, J. A., & Wong, M. A. (1979). Algorithm AS 136: A k-means clustering algorithm. *Journal of the Royal Statistical Society: Series C (Applied Statistics)*, 28(1), 100-108. <https://doi.org/10.2307/2346830>
- Lloyd, S. P. (1982). Least square quantization in PCM. *IEEE Transactions on Information Theory*, IT-28(2), 129-137. <https://doi.org/10.1109/TIT.1982.1056489>
- MacQueen, J. (1967). Some methods for classification and analysis of multivariate observations. In L. M. Cam & J. Neyman (Eds.), *Proceedings of the Fifth Berkeley Symposium on Mathematical Statistics and Probability* (pp. 281-297). University of California Press.
- Ngongondo, C. S., Xu, C. Y., Tallaksen, L. M., Alemaw, B., & Chirwa, T. (2011). Regional frequency analysis of rainfall extremes in Southern Malawi using the index rainfall and L-moments approaches. *Stochastic Environmental Research and Risk Assessment*, 25(7), 939-955. <https://doi.org/10.1007/s00477-011-0480-x>
- Nnaji, C. C., Mama, C. N., & Ukpabi, O. (2014). Hierarchical analysis of rainfall variability across Nigeria. *Theoretical and Applied Climatology*, 123(1-2), 171-184. <https://doi.org/10.1007/s00704-014-1348-z>
- Saeed, G. A. A., Chuan, Z. L., Zakaria, R., Yusoff, W. N. S. W., & Salleh, M. Z. (2016). Determine of the best single imputation algorithm for missing rainfall data treatment. *Journal of Quality Measurement and Analysis*, 12(1-2), 79-87.
- Sahrin, S., Ismail, N., & Alias, N. E. (2018). Regional frequency analysis of Peninsular Malaysia using L-moments. *Far East Journal of Mathematical Sciences*, 103(8), 1379-1398. <https://dx.doi.org/10.17654/MS103081379>

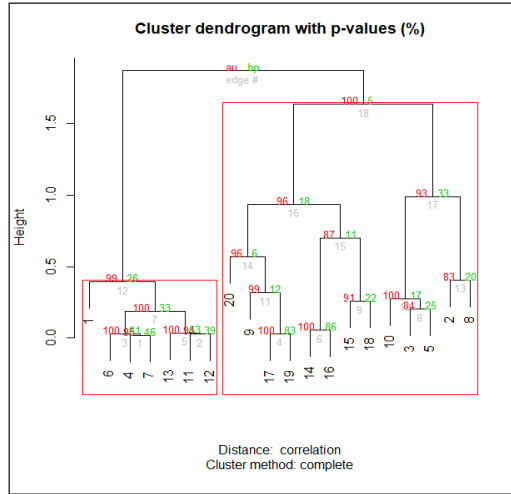
Zun Liang Chuan, Wan Nur Syahidah Wan Yusoff, Azlyna Senawi, Mohd Romlay Mohd Akramin,  
Soo-Fen Fam, Wendy Ling Shinyie and Tan Lit Ken

- Scholz, F. W., & Stephens, M. A. (1986). K-sample Anderson-Darling tests. *Journal of the American Statistical Association*, 82(399), 918-924. <https://doi.org/10.1080/01621459.1987.10478517>
- Shimodaira, H. (2002). An approximately unbiased test of phylogenetic tree selection. *Systematic Biology*, 51(3), 492-508. <https://doi.org/10.1080/10635150290069913>
- Tan, P. N., Steinbach, M., & Kumar, V. (2006). *Introduction to data mining*. Pearson Addison Wesley.
- Terassi, P. M. D. B., & Galvani, E. (2017). Identification of homogeneous rainfall regions in the Eastern watersheds of the State of Paraná, Brazil. *Climate*, 5(3), 1-13. <https://doi.org/10.3390/cli5030053>

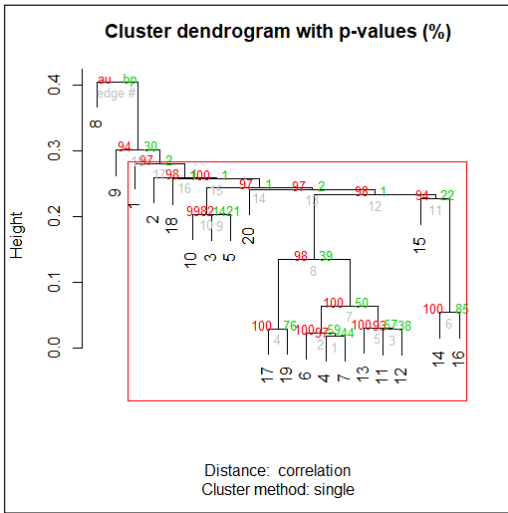
APPENDICES



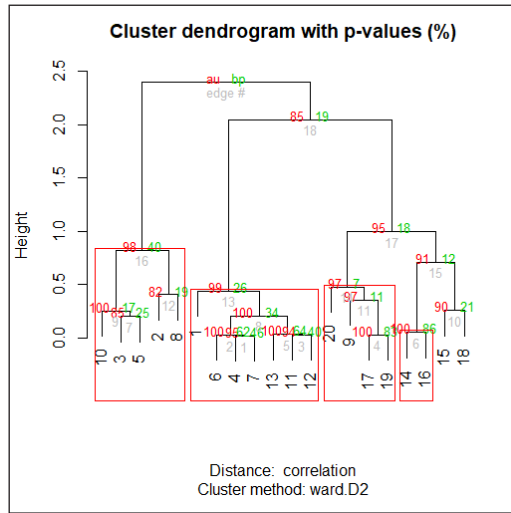
(a)



(b)



(c)



(d)

Figure A1. The dendrograms for the identified regionalised homogeneous rainfall regions using (a) ALAH, (b) CLAH, (c) SLAH, and (d) WMVAH regionalisation algorithm based on  $\lambda_1$

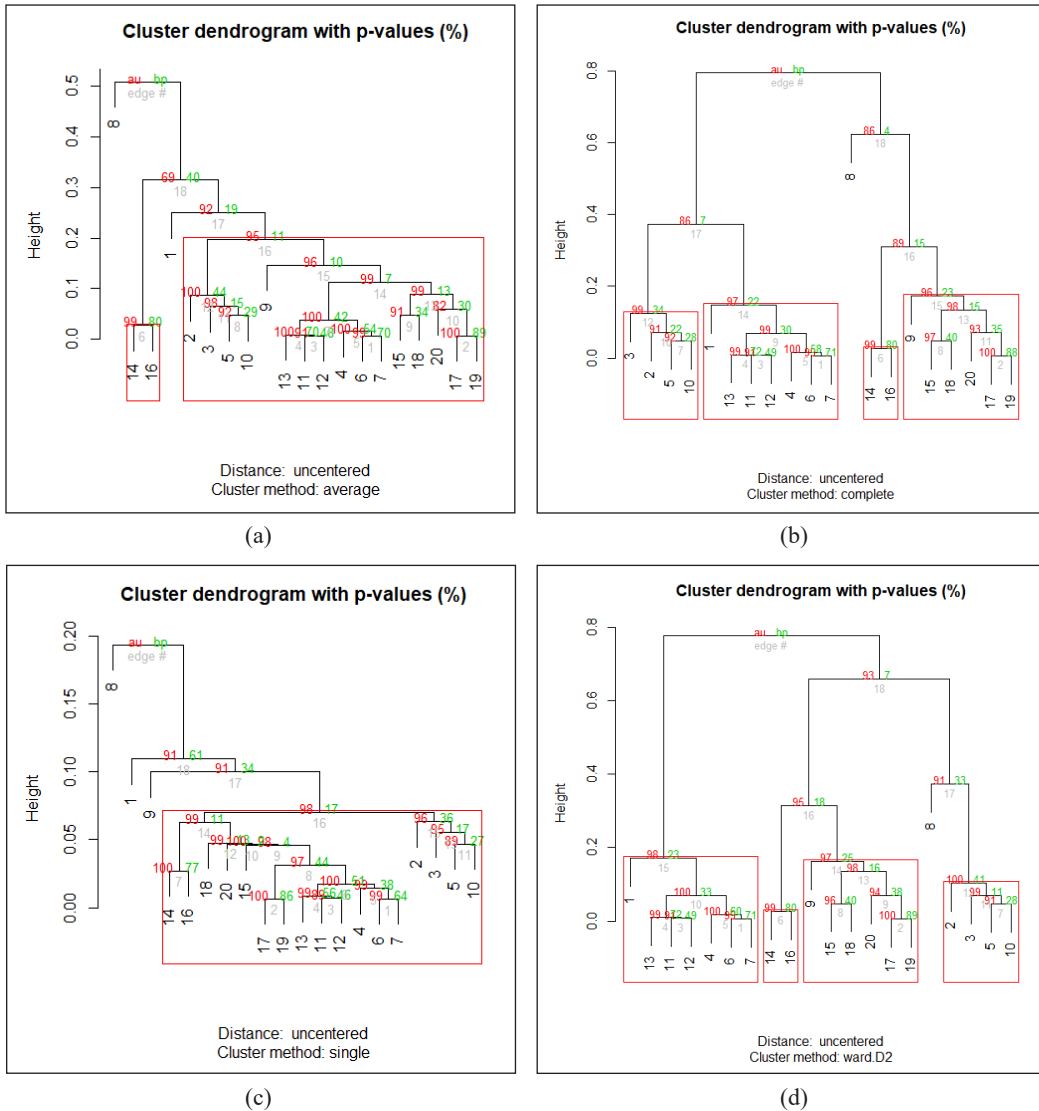


Figure A2. The dendrograms for the identified regionalised homogeneous rainfall regions using (a) ALAH, (b) CLAH, (c) SLAH, and (d) WMVAH regionalisation algorithm based on  $\lambda_2$

## Optical Properties of Cu<sub>2</sub>O Thin Films Impregnated with Carbon Nanotube (CNT)

Oluyamo Sunday Samuel<sup>1</sup>, Ajanaku Olanrewaju<sup>2\*</sup> and Adedayo Kayode David<sup>1</sup>

<sup>1</sup>Department of Physics, Federal University of Technology, PMB 704, Akure, Ondo State, Nigeria

<sup>2</sup>Department of Physical Sciences, Ondo State University of Science and Technology, PMB 353, Okitipupa, Ondo State, Nigeria

### ABSTRACT

This study investigates CNT-doped Cu<sub>2</sub>O thin film deposited by spray pyrolysis technique at a substrate temperature of 100°C. The samples were annealed at temperatures of 200°C and 230°C for 30 minutes. The effect of CNT doping on certain optical properties, such as extinction and absorption coefficients, a refractive index of doped Cu<sub>2</sub>O thin films were examined. The absorbance of the doped samples increases within the visible range and decreases in the ultraviolet range of the electromagnetic spectrum (EM). Both absorbance and extinction coefficients increased with temperature making the samples a good candidate for use as absorbance layer in device fabrication. In addition, there was an increase in direct bandgap with the increase in CNT concentration of the thin films. The result of the study revealed that CNT doping has a significant effect on the properties of Cu<sub>2</sub>O.

*Keywords:* Bandgap, Carbon-nanotube (CNT), Copper (I) Oxide (Cu<sub>2</sub>O), optical characterization, spray pyrolysis

### INTRODUCTION

Semiconducting metal oxides are ideal materials in thin-film technology due to the abundance of their constituent elements in the earth's crust, ease of manufacturing process, and ecologically friendly existence. Copper oxides are strong absorber materials among the various p-types of metal oxides (Farhad et al., 2019; Ruhle et al., 2012). There are two stable copper oxides, namely monoclinic cupric oxide (CuO) or tenorite with a 1.3–1.5 eV energy bandgap (Farhad et

#### ARTICLE INFO

##### Article history:

Received: 30 May 2020

Accepted: 30 September 2020

Published: 10 January 2022

DOI: <https://doi.org/10.47836/pjst.30.1.19>

##### E-mail addresses:

ssoluyamo@futa.edu.ng (Oluyamo Sunday Samuel)

oa.ajanaku@osustech.edu.ng (Ajanaku Olanrewaju)

kbadedayo@yahoo.com (Adedayo Kayode David)

\* Corresponding author

al., 2019; Chatterjee et al., 2016; Rafea & Roushdy, 2009; Daoudi et al., 2018) and cubic cuprous oxide ( $\text{Cu}_2\text{O}$ ) that is a p-type semiconductor with an energy bandgap of 2.0-2.6 eV depending on its method of fabrication and stoichiometry (Farhad et al., 2018; Oluyamo et al., 2014). In photovoltaic research,  $\text{Cu}_2\text{O}$  gets more publicity compared to  $\text{CuO}$  because of its direct bandgap nature, high absorption coefficient ( $\alpha \sim 10^4 \text{cm}^{-1}$ ) in the visible region, higher mobility ( $\mu \sim 100 \text{cm}^2/\text{V.s}$ ) and larger minority carrier diffusion length ( $L_p \sim 1-2 \mu\text{m}$ ) relying on deposition parameters (Farhad et al., 2019). Various endeavors have been made to tune its properties for more innovative applications. Therefore, adding suitable dopants into  $\text{Cu}_2\text{O}$  to maintain multifunctionality is a common occurrence by researchers to overcome the two major drawbacks of  $\text{Cu}_2\text{O}$ , i.e., wide energy bandgap  $\sim 2.2\text{eV}$  and high resistive capacity.

Carbon nanotubes (CNTs) have triggered enormous worldwide interest due to their unique mechanical, electrical, and thermal properties when incorporated into semiconductor materials, which make them conceivably useful in numerous applications in nanotechnology, electronics, optics, and other fields of materials science (Zhu, 2017; Thostenson et al., 2011). Studies have shown that adding CNT to materials may alter carrier concentration and electrical conductivity despite the reduction in carrier mobility, which is comparable to the function of dopants in semiconductors (Yoo et al., 2011).

Various techniques have been applied to prepare  $\text{Cu}_2\text{O}$  this includes high-temperature oxidation of copper, magnetron sputtering, thermal evaporation, pulsed laser deposition (PLD), spin-derived sol-gel coating, chemical bath deposition, electrodeposition, successive ionic layer adsorption and reaction (SILAR), and spray pyrolysis (Farhad et al., 2019; Musa et al., 1998; Figueiredo et al., 2008; Muhibbullah & Ichimura, 2010; Septina et al., 2011; Nair et al., 1999; Mohammed, 2010). In addition, spray pyrolysis has many leading advantages among the other techniques, such as cheap expense, simplicity of experimental operation, and effective controllable deposition settings (Perednis & Gauckler, 2005).

The spray pyrolysis technique consists of directing straight down the precursor solution on top of heated substrates where a thin film of metal oxide is obtained after decomposition and oxidation phenomena (Perednis & Gauckler, 2005).

In this research work,  $\text{Cu}_2\text{O}$  was doped with various concentrations of Carbon nanotubes (CNTs) from 10% to 40% with respect to volume.

## MATERIALS AND METHODS

### Materials

Cupric acetate, 1- Methyl 2- Pyrrolidinone, and short single-wall CNT of purities 98%, 99.5%, and 92% respectively were the reagents used. In contrast, microscopy glass slides were used, while microscopy glass slides were used as a substrate for the deposition of the thin films.



### Substrate Cleaning Process

The substrates were washed with liquid soap, distilled water, and acetone to eliminate noticeable dust. The substrate was dried for 20 minutes at a temperature of 40°C using a hand dryer.

### Preparation of Precursor Solutions

0.15 M of precursor solution was prepared by adding 1.9965 g of Copper (II) acetate (Cu (CH<sub>3</sub>COO)<sub>2</sub> · H<sub>2</sub>O) in distilled water (20 ml) plus N-Methyl-2-pyrrolidone (NMP) (80 ml) stirred vigorously at room temperature using a magnetic stirrer.

For dispersion, 0.2 g of CNT were added to 80 ml of N-Methyl-2-pyrrolidone (NMP) and sonicated for 12 hours to form a dispersive black solution.

### Thin-film Deposition

The substrate temperature for the deposition of all the samples was maintained at 100°C. In contrast, the distance between the spray head and the substrates, precursor flow rate, air pressure were maintained at 10 cm, 500 liter/hr, and 0.05 MPa, respectively. The films were annealed at 200°C and 230°C for 30 minutes. Optical measurements were obtained using a UV-visible spectrophotometer (UV-1601, Shimadzu Corp, Japan) (Nath et al., 2015). The absorption coefficient  $\alpha$  was calculated from the transmission spectra using Equation 1.

$$\alpha = - \frac{2.303A}{t} \quad [1]$$

where, A is the absorbance and  $t$  is the thickness of the film.

According to (Nath et al., 2015), the corresponding bandgap was determined using Equation 2

$$(\alpha h\nu)^2 = h\nu - E_g \quad [2]$$

where  $h$  is Planck's constant, e.g., is the bandgap energy, and  $\nu$  is the frequency of the incident light.

The coefficient of extinction was also obtained with Equation 3

$$k = \frac{\alpha\lambda}{4\pi} \quad [3]$$

A thin-film material's reflectance (R), transmittance (T), and absorbance (A) are connected by using Equation 4:

$$R = 1 - (Te^A)^2 \quad [4]$$

## RESULTS AND DISCUSSION

Figure 1 shows the variation in absorbance at 200°C and 230°C. The absorbance of the doped sample increases within the visible range of the EM spectrum. As the concentration of CNT increases, the absorption peaks were found to decrease within the visible region (Figure 1). It might be attributed to the absorption of photons by CNT in the doped films. The optical properties in the range of 300 nm to 1100 nm at 230°C prove that absorbance is highly dependent on temperature levels. It is in agreement with (Varughese et al., 2014; Siddiqui et al., 2014).

Figure 2 shows the transmittance spectra with a wavelength of the Cu<sub>2</sub>O thin films annealed at 200°C and 230°C. All the films displayed high transmittance within the 600–1000 nm wavelength region. On the other hand, CNT-doped Cu<sub>2</sub>O thin films have lower

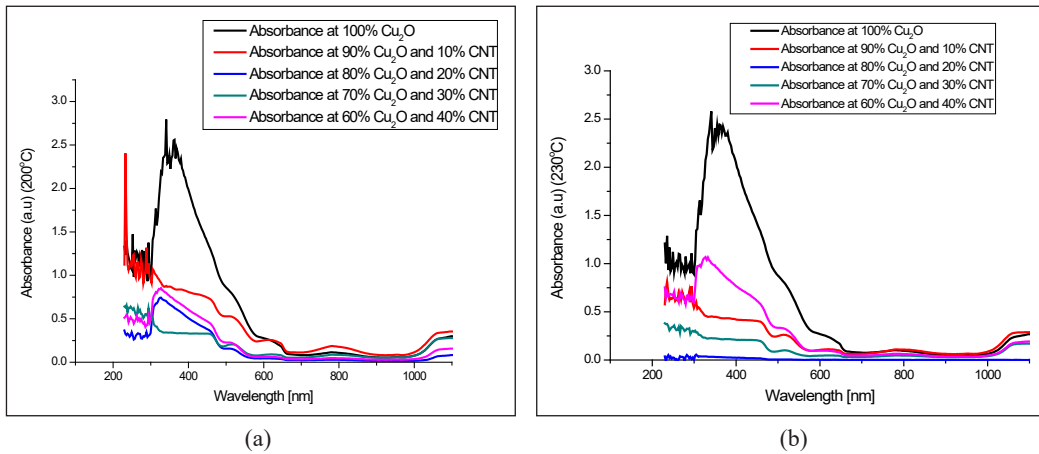


Figure 1. Absorbance spectra of CNT doped Cu<sub>2</sub>O thin films at (a) 200°C and (b) 230°C for various doping concentrations

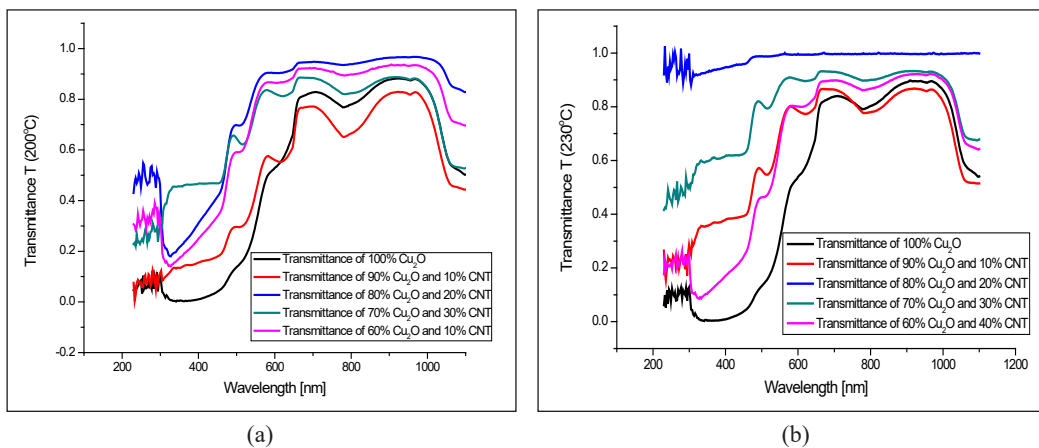


Figure 2. Transmittance spectra of CNT doped Cu<sub>2</sub>O thin films at (a) 200°C and (b) 230°C for various doping concentrations

transmittance within the 200–500nm wavelength range. The increase in transmittance might be due to enhancing scattering of photons owing to an increase in the grain size of Cu<sub>2</sub>O (Mardare & Rusu, 2002; Zhang et al. 2013a; Zhang et al. 2013b). It is important to note that 20% CNT has the maximum transmittance than any other sample for annealed temperatures. The average transmittance in the visible region was found to be greater than 65%.

Figures 3 and 4 show the variation of absorption coefficient and extinction coefficient with energy for the Cu<sub>2</sub>O doped CNT thin films. Both absorption and extinction coefficient increase as the energy increases. The absorption coefficient values were found to be higher than  $10^4 \text{ cm}^{-1}$ , which results in an increase in the probability of occurrence of direct

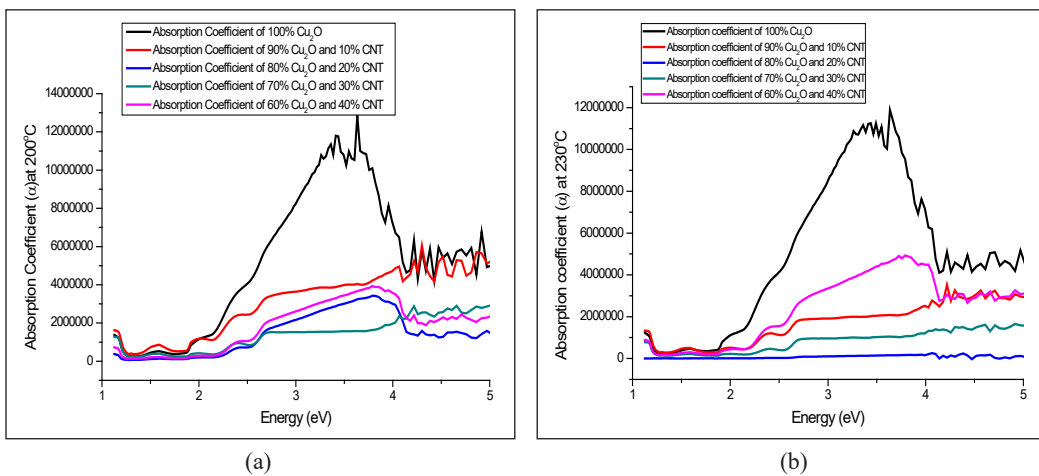


Figure 3. Absorption coefficient against the energy of CNT doped Cu<sub>2</sub>O thin films at (a) 200°C and (b) 230°C for various doping concentrations

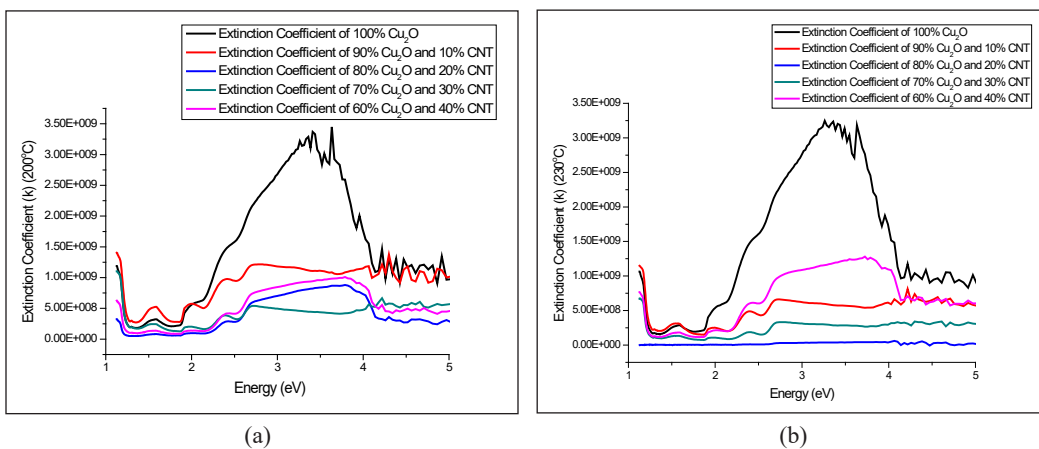


Figure 4. Extinction coefficient against the energy of CNT doped Cu<sub>2</sub>O thin films at (a) 200°C and (b) 230°C for various doping concentrations

transition. Furthermore, materials with high absorption coefficients are known to absorb photons, which excite them into conduction bands readily. Hence the thin film could serve as a good absorbance layer in device fabrication. The direct bandgap value for pure deposited  $\text{Cu}_2\text{O}$  was found to be 2.53 eV, while the CNT doped thin films have values of 1.80, 2.17, 2.18, and 2.27 eV for the samples containing 10%, 20%, 30%, and 40% CNT annealed at 200°C. For film samples annealed at 230°C the bandgap values were 1.68, 2.09, 2.13 and 2.17 eV for 10%, 20%, 30% and 40% CNT concentration. The reduction in the value of the bandgap of the samples annealed at 230°C could be attributed to a reduction of trap ions and an increase in grain size, as earlier stated. The increase in bandgap as CNT percentage increase has attributed this phenomenon to the rich CNT content in the films, which is probably associated with the structural change in  $\text{Cu}_2\text{O}$  induced by CNT doping (Nakano et al. 2009; Zhang et al. 2013a; Zhang et al. 2013b).

## CONCLUSION

In this study, CNT-impregnated  $\text{Cu}_2\text{O}$  thin films were deposited on a glass substrate using the spray pyrolysis technique at a substrate temperature of 100°C. The absorbance of the CNT doped  $\text{Cu}_2\text{O}$  samples increased within the visible range and decreased in the ultraviolet range of the electromagnetic spectrum. The absorption and extinction coefficient was found to increase with increases in energy, making the samples a good candidate as absorbance layer in device fabrication. The average transmittance in the visible region is greater than 65%. The maximum value of the transmittance was 70%, while absorption increases in the wavelength range 300–600 nm, and an increase in some optical constants makes it useful in solar cells application. The bandgap of CNT impregnated  $\text{Cu}_2\text{O}$  thin films was observed to range between 1.80–2.38 eV for samples annealed at 200°C and 1.68–2.17 eV for samples annealed at 230°C.

## ACKNOWLEDGEMENT

The authors wish to appreciate the management of Shelda Institute of Science and Technology (SHESTCO), Abuja, for the usage of the spray pyrolysis machine. The assistance provided by Mr. Noble Alu has been greatly appreciated also the Federal University of Technology, Central Research Laboratory Akure.

## REFERENCES

- Chatterjee, S., Saha, S. K., & Pal, A. J. (2016). Formation of all-oxide solar cells in atmospheric condition based on  $\text{Cu}_2\text{O}$  thin-films grown through SILAR technique. *Solar Energy Materials and Solar Cells*, 147, 17-26. <https://doi.org/10.1016/j.solmat.2015.11.045>
- Daoudi, O., Qachaou, Y., Raidou, A., Nouneh, K., Lharch, M., & Fahoume, M. (2018). Study of the physical properties of  $\text{CuO}$  thin films grown by modified SILAR method for solar cells applications. *Superlattices Microstructure*, 127, 93-99. <https://doi.org/10.1016/j.spmi.2018.03.006>.

- Farhad, S. F. U., Hossain, M. A., Tanvir, N. I., Akter, R., Patwary, M. A. M., Shahjahana, M., & Rahman, M. A. (2019). Structural, optical, electrical, and photo electrochemical properties of cuprous oxide thin films grown by modified SILAR method. *Material Science in Semiconductor Processing*, *95*, 68-75. <https://doi.org/10.1016/j.mssp.2019.02.014>
- Farhad, S. F. U., Webster, R. F., & Cherns, D. (2018). Electron microscopy and diffraction studies of pulsed laser deposited cuprous oxide thin films grown at low substrate temperatures. *Materialia*, *3*, 230-238. <https://doi.org/10.1016/j.mtla.2018.08.032>
- Figueiredo, V., Elangovan, E., Goncalves, G., Barquinha, P., Pereira, L., Franco, N., Alves, E., Martins, R., & Fortunato, E. (2008). Effect of post-annealing on the properties of copper oxide thin films obtained from the oxidation of evaporated metallic copper. *Applied Surface Science*, *254*(13), 3949-3954. <https://doi.org/10.1016/j.apsusc.2007.12.019>
- Mardare, D., & Rusu, G. I. (2002). The influence of heat treatment on the optical properties of titanium oxide thin films. *Materials Letters*, *56*(3), 210-214. [https://doi.org/10.1016/s0167-577x\(02\)00441-x](https://doi.org/10.1016/s0167-577x(02)00441-x)
- Mohammed, K. H. (2010). Effect doping on optical properties film CuO prepared by chemical spray pyrolysis. *Diyala Journal for Pure Sciences*, *2*(6), 106-116.
- Muhibbullah, M., & Ichimura, M. (2010). Fabrication of photoconductive copper oxide thin films by the chemical bath deposition technique. *Japanese Journal of Applied Physics*, *49*(8), Article 081102. <https://doi.org/10.1143/JJAP.49.081102>
- Musa, A.O., Akomolafe, T., & Carter, M. J. (1998). Production of cuprous oxide, a solar cell material, by thermal oxidation and a study of its physical and electrical properties. *Solar Energy Materials and Solar Cells*, *51*(3-4), 305-316. [https://doi.org/10.1016/S0927-0248\(97\)00233-X](https://doi.org/10.1016/S0927-0248(97)00233-X)
- Nair, M. T. S., Guerrero, L., Arenas, O. L., & Nair, P. K. (1999). Chemically deposited copper oxide thin films: Structural, optical and electrical characteristics. *Applied Surface Science*, *150*(1-4), 143-151. [https://doi.org/10.1016/S0169-4332\(99\)00239-1](https://doi.org/10.1016/S0169-4332(99)00239-1)
- Nakano, Y., Saeki, S., & Morikawa, T. (2009). Optical bandgap widening of p-type Cu<sub>2</sub>O films by nitrogen doping. *Applied Physics Letters*, *94*(2), Article 022111. <https://doi.org/10.1063/1.3072804>
- Nath, S. K., Chowdhury, N., & Gafur, M. A. (2015). Effect of Co doping on crystallographic and optoelectronic properties of ZnO thin films. *Journal of Superconductivity and Novel Magnetism*, *28*, 117-123. <https://doi.org/10.1007/s10948-014-2815-6>
- Oluyamo, S. S., Nyagba, M. S., Ambrose, S., & Ojo, S. (2014). Optical properties of copper (I) oxide thin films synthesized by SILAR technique. *IOSR Journal of Applied Physics*, *6*(3), 102-105.
- Perednis, D., & Gauckler, L. J. (2005). Thin film deposition using spray pyrolysis. *Journal of Electroceramics*, *14*(2), 103-111. <https://doi.org/10.1007/s10832-005-0870-x>
- Rafea, A. M., & Roushdy, N. (2009). Determination of the optical band gap for amorphous and nanocrystalline copper oxide thin films prepared by SILAR technique. *Journal of Physics D: Applied Physics*, *42*(1), Article 015413. <https://doi.org/10.1088/0022-3727/42/1/015413>
- Ruhle, S., Anderson, A.Y., Barad, H.N., Kupfer, B., Bouhadana, Y., Rosh-Hodesh, E., & Zaban, A. (2012). All-oxide photovoltaic. *The Journal of Physical Chemistry Letters*, *3*(24), 3755-3764.

- Septina, W., Ikeda, S., Khan, M. A., Hirai, T., Harada, T., Matsumura, M., & Peter, L. M. (2011). Potentiostatic electrodeposition of cuprous oxide thin films for photovoltaic applications. *Electrochimica Acta*, *56*(13) 4882-4888. <https://doi.org/10.1016/j.electacta.2011.02.075>
- Siddiqui, H., Qureshi, M. S., & Haque, F. Z. (2014). One-step, template-free hydrothermal synthesis of CuO tetrapods. *Optik-International Journal for Light and Electron Optics*, *125*(17), 4663-4667. <http://dx.doi.org/10.1016/j.ijleo.2014.04.090>
- Thostenson, E. T., Ren, Z. F., & Chou, T. W. (2001). Advances in the science and technology of carbon nanotubes and their composites: A review. *Composites Science and Technology*, *61*(13), 1899-1912. [https://doi.org/10.1016/S0266-3538\(01\)00094-X](https://doi.org/10.1016/S0266-3538(01)00094-X)
- Varughese, G., Rini, V., Suraj, S. P., & Usha, K. T. (2014). Characterisation and optical studies of copper oxide nanostructures doped with lanthanum ions. *Advances in Materials Science*, *14*(4), 49-60. <https://doi.org/10.2478/adms-2014-0021>
- Yoo, J. J., Yu, J., Song, J. Y., & Yi, Y. (2011). Single-walled carbon nanotubes as a dopant in p-type cuprous oxide films. *Carbon*, *49*(8), 2659-2664. <https://doi.org/10.1016/j.carbon.2011.02.052>
- Zang, Z., Nakamura, A., & Temmyo, J. (2013). Nitrogen doping in cuprous oxide films synthesized by radical oxidation at low temperature. *Materials Letters*, *92*, 188-191. <https://doi.org/10.1016/j.matlet.2012.10.083>
- Zang, Z., Nakamura, A., & Temmyo, J. (2013). Single cuprous oxide films synthesized by radical oxidation at low temperature for PV application. *Optics Express*, *21*(9), 11448-11456. <https://doi.org/10.1364/OE.21.011448>
- Zhu, Z. (2017). An overview of carbon nanotubes and graphene for biosensing applications. *Nano-Micro Letters*, *9*, Article 25. <https://doi.org/10.1007/s40820-017-0128-6>

*Review article*

## **A Review on Synthesis and Characterization of Activated Carbon from Natural Fibers for Supercapacitor Application**

**Thilageshwaran Subramaniam<sup>1</sup>, Mohamed Ansari Mohamed Nainar<sup>1,2\*</sup> and Noor Afeefah Nordin<sup>2</sup>**

<sup>1</sup>Mechanical Engineering Department, Universiti Tenaga Nasional, 43000 UNITEN, Kajang, Malaysia

<sup>2</sup>Institute of Power Engineering, Universiti Tenaga Nasional, 43000 UNITEN, Kajang, Malaysia

### **ABSTRACT**

Supercapacitors have gained much attention in recent years due to their promising characteristics, such as high specific capacitance, high power density, long cycle life, and environment-friendly nature. Usage of natural sources for activated carbon synthesis is a major focus by many researchers worldwide for discovering a replacement of existing supercapacitors. This review summarizes the methods used to synthesize activated carbon (AC) from various natural fiber, their physical and electrochemical characteristics, and the improvement of supercapacitor electrode performance. Previous research studies indicate the practicability of activated carbon derived from various natural fibers with superior electrochemical properties. The effect of activating reagents and temperature on the electrochemical performance for supercapacitor applications are also highlighted in this paper. Since the nature of activated carbon from fibers and its synthesizing methods would result in different properties, the Cyclic Voltammetry (CV) study is

also thoroughly discussed on the specific capacitance together with charge/discharge test to observe the capacitance retention after several cycles. Finally, a detailed approach of converting biowaste materials to activated carbon for energy storage applications with environmental concerns is explored.

#### ARTICLE INFO

*Article history:*

Received: 29 April 2021

Accepted: 05 August 2021

Published: 10 January 2022

DOI: <https://doi.org/10.47836/pjst.30.1.20>

*E-mail addresses:*

thilagesh.97@gmail.com (Thilageshwaran Subramaniam)

ansari@uniten.edu.my (Mohamed Ansari Mohamed Nainar)

afeefahnordin1@gmail.com (Noor Afeefah Nordin)

\* Corresponding author

*Keywords:* Activated carbon (AC), electric double-layer capacitor (EDLC), natural fibers, pseudocapacitor, supercapacitor electrode

## INTRODUCTION

Supercapacitors are devices used to store electrical energy undergoing frequent charge-discharge cycles at high currents in short time duration. It can be used in various applications, including electric vehicles, power grids, and wearable devices, due to its high specific capacitance (Zequine et al., 2017). In the 1950s, the first few ideas of storing electrical charges in an electric double layer were patented. There was much interest in the fact that charge could be stored with the interface between a solid and an electrolyte back then. Standard Oil Company developed the technology in Cleveland, and it was then licensed to Nippon Electric Company (NEC) in 1971. After that, NEC started to manufacture low-powered devices for memory backup with the name “*Supercapacitor*.” Then the technology was developed for military use by the Pinnacle Research Institute (PRJ) in 1982. The development of supercapacitors is carried out till today, where electrochemical double-layer capacitors (EDLCs) are commercially available from several sources (Namisnyk & Zhu, 2003). In the current era, the development of supercapacitors offers a promising method to encounter the growing demands of conventional energy storage applications. With higher power density than batteries and larger energy density compared to conventional capacitors, supercapacitors have an important position to narrow the gap between batteries and conventional capacitors (Liu et al., 2019).

Supercapacitors (SCs) have gained interest in energy storage applications due to renewable energy sources. The burning of fossil fuels causes environmental concerns, and it is non-renewable energy that will eventually get used up. Therefore, renewable energy is being focused on countering the depletion of fossil fuels (Thulasi et al., 2019). Conversely, most renewable energy sources are unstable and continuous, such as wind and solar energy. Therefore, a promising energy storage system is crucial to use these energy sources optimally (Wu et al., 2015). The conventional technique for electrical energy storage uses batteries owing to their high energy density. However, batteries possess low power density, unlike supercapacitors with the superior power density and cycling stability but low energy density. One of the important properties of SCs is the rapid charging and discharging of electrical energy, which makes it a perfect tool for the instant storage of energy (Chowdhury & Grebel, 2019). The advantages of using supercapacitors compared to batteries are its high power density, rapid charging, and discharging abilities, longer life cycles, and safer contrasted to batteries (Enock et al., 2017). Besides high power density and rapid charge-discharge properties, SC also has wide operating temperatures that make it more flexible to be used for various applications (Wei et al., 2019). There are three main supercapacitors categories: electric double-layer capacitors (EDLC), pseudocapacitors, and hybrid capacitors (Rawal et al., 2018). In the case of EDLC, the capacitance is produced as a result of a build-up of static charge at the electrode and electrolyte interface, whereby absorption and desorption occur by charged ions.



Hereafter, large specific surface area (SSA) and high porosity are essential to obtain excellent capacitance for a supercapacitor (Lu et al., 2020). In the case of pseudocapacitance, it attains capacitance by surface-level rapid redox reactions of an electroactive material; meanwhile, the working principle for hybrid supercapacitors is by the combination of electric double-layer capacitors and pseudocapacitors. The electrode materials used in pseudocapacitors are metal oxides and sulfides (Chime et al., 2020; Shinde & Jun 2020). However, the supercapacitors encounter some issues, such as low conductivity of electricity and deprived charge-discharge cycles. Therefore,

various research projects are conducted to improve the electrochemical performance of the material used for supercapacitor electrodes. One of the ways to maximize the performance of EDLCs is by using carbon electrodes, as shown in Figure 1.

Carbon-based materials that are commonly used for the preparation of electrodes are activated carbon (AC), carbon nanotubes (CNT), aerogels, graphene as well as carbon fibers (S. Chen et al., 2020; Lyu et al., 2019; Tsang et al., 2020; Yar et al., 2020). AC is among the highly chosen active materials for supercapacitor electrodes, attributed to high thermal stability and electrical conductivity, corrosion resistance, high surface area after the carbonization process, and low cost (Luo et al., 2021). In addition, AC has a long history of usage and production for various purposes. For example, some of the activated carbons are used for the removal of heavy metals and chromium from solution, carbon dioxide capturing, hydrogen gas storage, air pollution control, and electrical energy applications (Ahmed et al., 2019). In general, the process of producing activated carbon from biomass materials is comparatively easy and cheaper contrasted to other carbon materials (Morali et al., 2018).

The process of producing activated carbon comprises carbonization and is followed by activation. Carbon activation is performed to progress the surface area of the carbon, which increases adsorption and desorption of electrolyte ions from the active surfaces of the activated carbon during the charging and discharging process. In addition, a high degree of randomness and defective graphite structure in the AC leads to the development of a broad range of its porosity. The pore size of AC ranges from visible cracks and crevices to molecular dimensions (Yu et al., 2019). Activating agents are used to increase the pore

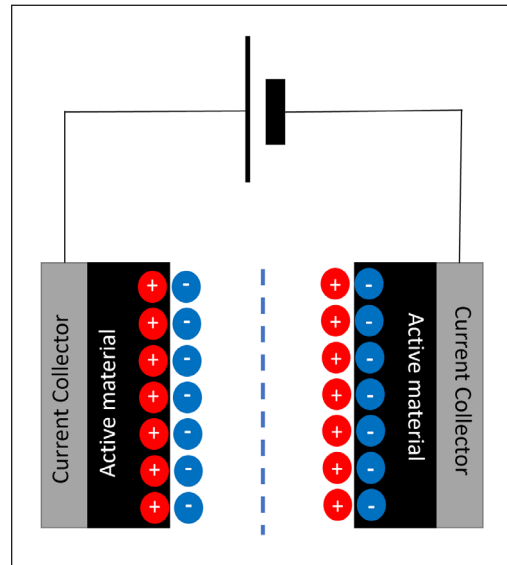


Figure 1. Cross-sectional view of EDLC

numbers in the carbon materials and to remove debris. As a result, the interaction between the active material and the electrolyte is enhanced as the active surface area increases (Musa et al., 2015; Tounsadi et al., 2016). Figure 2 shows the effect of the activating agent before and after the activation process. It can be observed that the fibers are cleaner without the presence of debris, and porosity increases after the activation.

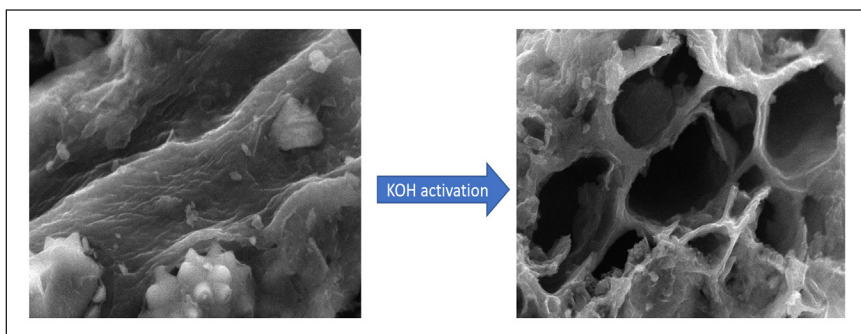


Figure 2. Scanning electron microscopic images of the activated carbon after KOH activation

Considering the recent advancements in technology for the development of supercapacitors, abundant potential renewable sources, and huge demand from various industrial sectors, this review serves to summarize the previous works related to the fabrication of supercapacitor electrode materials from natural fibers and elaborate on the findings obtained during the past five years. In addition, common types of supercapacitor electrodes are also briefly discussed and mainly focused on EDLCs with the usage of activated carbon as active material.

## SUPERCAPACITORS CLASSIFICATION

Supercapacitors can be characterized depending on the energy storage system, primarily alluding to faradaic and non-faradaic electrodes. In non-faradaic electrodes, the electrochemical reaction does not occur; however, only charge adsorption/desorption arises at the interface when charging and discharging take place. On the other hand, faradaic capacitors undergo a fast reduction and oxidation process to store and release charge during charging and discharging of the supercapacitor (Arunachalam et al., 2020).

### Electric Double-Layer Capacitors (EDLC)

EDLC is a non-faradaic capacitor based on an electrolyte and a double layer at the electrode interface. It functions with the build-up of electrostatic charges at the electrolyte/electrode interface, and the charge storage for a high capacitance supercapacitor is very much dependent on the escalation of surface area (Tan & Lee, 2013). Overall, 1000–2000 m<sup>2</sup> g<sup>-1</sup> is the range for a high surface area of carbon electrodes. In comparison with traditional

capacitors, the pore size distribution of EDLC has an increasing effect on the energy density (Gu & Yushin, 2014; Xiong et al., 2014). Furthermore, since EDLCs use aqueous electrolytes, such as H<sub>2</sub>SO<sub>4</sub>, KOH, or organic electrolytes, this could enhance the cycle stability during the charge-discharge processes (Bhat et al., 2021).

### Pseudocapacitor

Pseudocapacitors are faradaic capacitors that store charges through the rapid transfer of charges between the electrolyte and the active material of the electrode (Devillers et al., 2014). The pseudocapacitors charge storage mechanism contrasts with EDLC, whereby the transfer of charge occurring is by voltage-dependent redox reaction, desorption, and adsorption or intercalation of ions. The redox reaction process in pseudocapacitors would result in superior energy density and capacitance. On the other hand, the Faradaic process occurs in dissimilar behaviors whereby the ions in the electrolyte are adsorbed to the metal surface in the initial stage. It was then followed by a reversible redox reaction (reduction and oxidation process) in the oxides/hydroxides of transition metal. The pseudocapacitor electrode surface area is crucial for these two reactions (Sayyed et al., 2019). The third stage involves bulk reversible doping and de-doping processes in the conducting polymers, which are less dependent on the surface area (Devillers et al., 2014).

The faradaic and non-faradaic processes are the primary dissimilarity between EDLCs and pseudocapacitance. Pseudocapacitors have rapid and reversible redox reactions between electrolyte and active material (Simon & Gogotsi, 2008). Therefore, a pseudocapacitor's charge transfer process is similar to a battery during the charging and discharging process. Hence, the capacitance of a supercapacitor can be illustrated as shown in Equation 1. Capacitance (C) is defined as the ratio of stored charge ( $\Delta q$ ) to change in potential ( $\Delta V$ ) (Raju & Ozoemena, 2015).

$$C = \frac{\Delta q}{\Delta V} \quad [1]$$

### Hybrid Supercapacitors

The merging of the Faradaic process and non-Faradaic process forms hybrid supercapacitors. The combination of high pseudocapacitance with capacitance from the electric double layer enables high power density and ensures long cycle life. The hybrid capacitors, which have combined EDLCs and pseudocapacitors, have greater electrochemical performance than EDLCs and pseudocapacitors (Afif et al., 2019). Improved devices can be obtained through the energy storage mechanism of a hybrid supercapacitor, which has a combo of Faradaic and Non-Faradaic processes (Bogeat, 2021). The common types of hybrid supercapacitors and their active materials are as shown in Figure 3 (Saini et al., 2021).

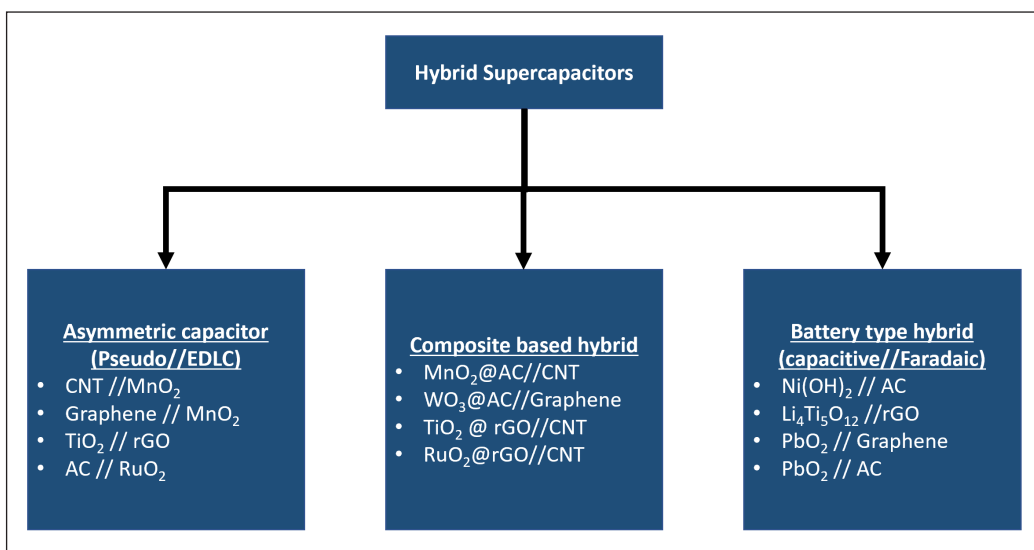


Figure 3. Types of hybrid supercapacitors

## RECOVERY OF CARBON FROM NATURAL FIBRES

Commonly, the process of creating activated carbon is simpler and inexpensive compared to other carbon materials, specifically from biomass materials (Moralı et al., 2018). Thermal treatment of biomass material demonstrates a change in porosity, surface area, and pore structures (Ioannidou & Zabaniotou, 2007). Some research works have proven that AC from natural fibers has adsorption rates of 2 to 50 times faster than AC from coal. It is explained that the fibers with a small diameter (about 10 $\mu$ m) show a larger external surface area (Rombaldo & Lisboa, 2014). The two main steps involved in producing AC are carbonization and activation. Some of the natural fibers discussed in this review are shown in Figure 4.

Carbonization is the process of converting organic matters like natural fibers into carbon. There are two types of activations, which are chemical and physical activation. In physical activation, steam or CO<sub>2</sub> is used to boost the porosity of the AC. Steam is extra effective in producing AC with a practically higher surface area than CO<sub>2</sub> as the smaller molecular size of water molecules helps to enable diffusion within the carbon's porous structure (Im et al., 2019; Qin, 2019). Steam activation is testified to have a faster conversion degree than CO<sub>2</sub> activation (Lei et al., 2018; Ma et al., 2020). On the other hand, chemical activation uses chemical agents, such as KOH (W. Chen et al., 2020; Zhu et al., 2019), ZnCl<sub>2</sub> (Chen et al., 2018; Sun, 2019), NaOH (Hu et al., 2018; Zhang et al., 2019), and H<sub>3</sub>PO<sub>3</sub> to synthesize activated carbon (Yakout & Sharaf El-Deen, 2016). In addition, chemical activation occurs at lower activation temperature compared to physical activation (Nor et al., 2013).

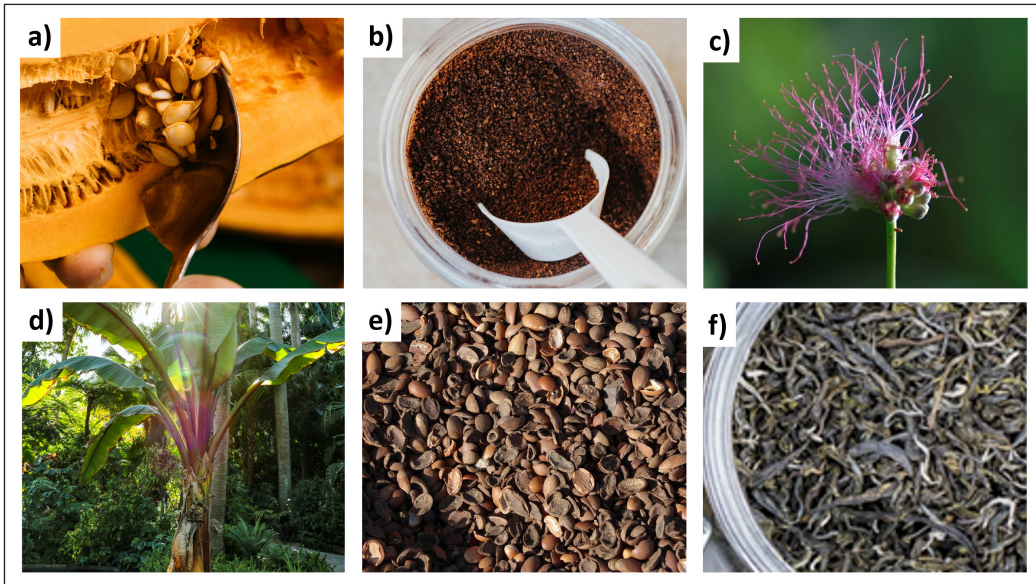


Figure 4. a) *Cucumis melo*, b) coffee grounds, c) *Albizzia* flowers, d) Banana fibers, e) Argan seed shells, and f) Waste tea leaves

Peng et al. (2013) extracted carbon from waste tea leaves (WTL), and the images in Figure 5 show the process involved in the synthesis of activated carbon. Five types of WTL were used to prepare AC, and the recovery process started with soaking the dried tea leaves in boiling water until room temperature. The WTL was then pyrolyzed at 600°C for 2 h with argon flow to produce carbonated products. Next, chemical activation was conducted using KOH solution followed by evaporation at 80°C in a vacuum. The dried carbonized product was then heated at 800°C for one h in an argon atmosphere and was further neutralized using 1 M HCl solution (Peng et al., 2013). The highest specific capacitance achieved was 330 F/g at 1 A/g from the electrode fabricated from WTL AC.

Another study with a similar method was conducted using *Albizzia* flowers (AF) as a precursor, and the process is shown in Figure 6. The carbonization process was done on the dried AFs at 600°C at a rate of 3°Cmin<sup>-1</sup> for three h in an argon gas atmosphere. It was

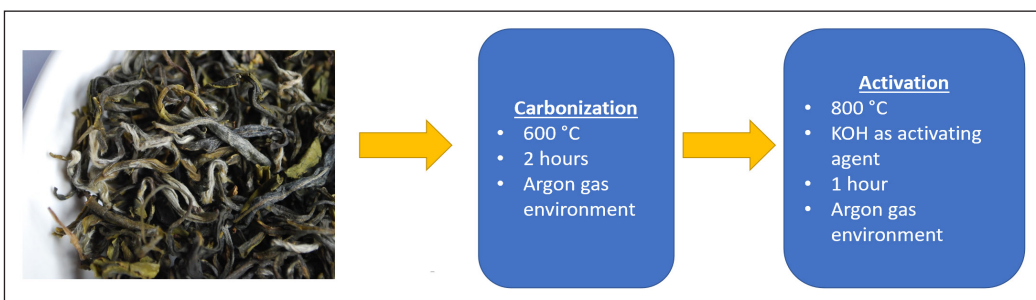


Figure 5. Two-step synthesis of activated carbon from waste tea leaves (Peng et al., 2013)

followed by an activation process using KOH with a ratio of 1:3, KOH: Precarbonized AF (PCAF). The activation temperature used was 700, 800, or 900°C at a rate of 5°C min<sup>-1</sup>. The achieved activated samples were washed with 1 M HCL and deionized water until Ph 7 before it was dried at 80°C for ten h. The fabricated electrode produced 406 F/g at 0.5 A/g in a 6M KOH electrolyte (Wu et al., 2019).

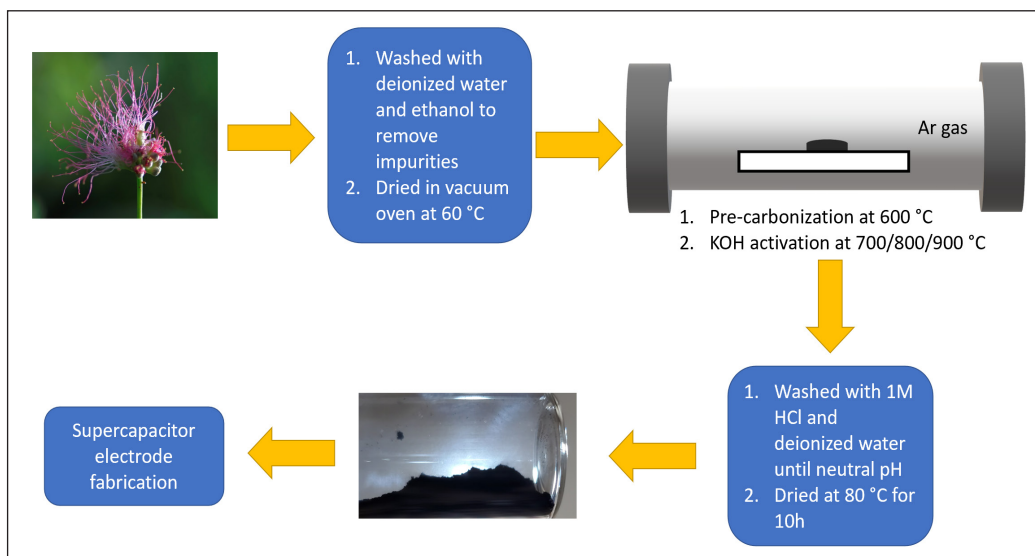


Figure 6. Process of preparing activated carbon from *Albizzia* flowers (Wu et al., 2019)

Apart from that, activated carbon from oil palm kernel shells (PKS) was synthesized by Misnon et al. (2015) to observe the effects of the activation method. Recycling PKS for value-added products is useful as they are abundantly available. This work used two types of activation methods: chemical activation by KOH and physical activation using steam. The PKS was pyrolyzed in a furnace for four h at 500°C, under an oxygen deficit environment. Activated carbon was then produced through chemical activation (AC-C) and physical activation (AC-P). In chemical activation, Pyrolyzed carbon was stirred with KOH in the ratio of 1:4 for four h at 100°C. Another sample was prepared using physical activation through steam. Both samples were then heated in a furnace at 500°C for four h and subsequently washed in 1 M HCl followed by distilled water until pH was neutral before they were further tested as electrodes (Misnon et al., 2015). AC-C and AC-P-based supercapacitor electrodes produced a capacitance of 210 F/g and 123 F/g at 0.5 A/g, respectively in 1 M KOH (Misnon et al., 2015).

Other than two-step synthesis, which is carbonization followed by activation, there is also a one-step synthesis whereby activation and carbonization are done simultaneously. Figure 7 illustrates the difference between one and two-step synthesis.

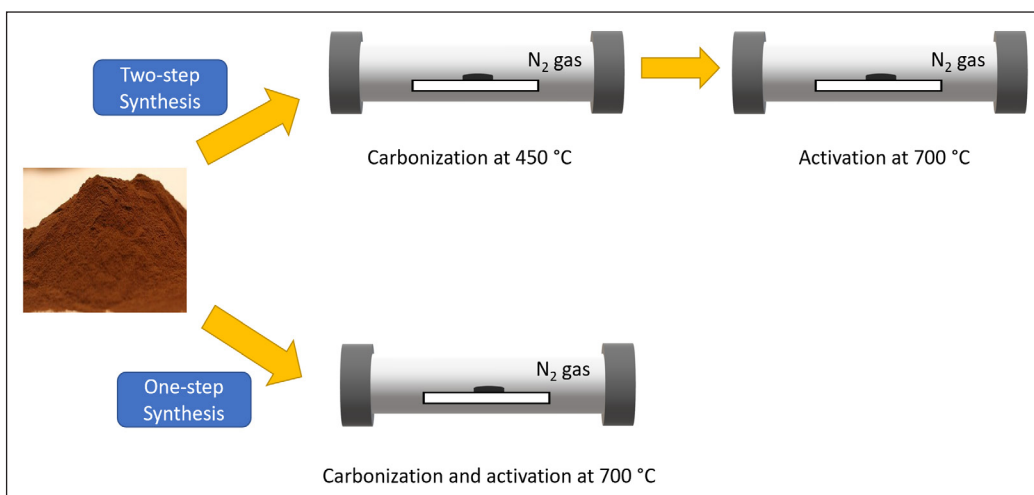


Figure 7. The process of one-step and two-step synthesis of activated carbon (Chiu & Lin, 2019)

One-step synthesis was done to recover carbon from waste coffee grounds and studied the effects of different activation agents on the structural properties of the activated carbon (Chiu & Lin, 2019). First, they dispersed waste coffee grounds in 1 M KOH and stirred for 6 hours. It was followed by washing the prepared powder with deionized water and subsequently drying it in a vacuum oven. Next, the dried powder was dispersed in aqueous solutions containing activating agents and stirred for 15 min during the activation process. The resultant solution was filtered, and the prepared powders were then annealed at 700°C in N<sub>2</sub> for two h. The KOH-activated carbon electrode from coffee grounds resulted in a specific capacitance of 19.28 F/g and obtained the highest energy density of 6.94 Wh/kg at the power density of 350 W/kg (Chiu & Lin, 2019).

Jiang et al. (2013) demonstrated ginkgo shells to produce AC for supercapacitor application. The partially graphitized ginkgo-based activated carbon (GGAC) was prepared by pyrolysis, activation process using KOH, and heat treatment with cobalt nitrate as graphitization catalyst. Ginkgo shell-based activated carbon preparation was initiated by drying the ginkgo shells at 60°C for 24 h. The dried ginkgo shells were then pyrolyzed at 600°C at a rate of 10°Cmin<sup>-1</sup> under nitrogen atmosphere for one h in a tube furnace. Finally, the pyrolyzed ginkgo shells were mixed with KOH at a ratio of 1:2 and heat-treated in a nitrogen gas environment for one h at 700°C. The HCL was used to neutralize the carbonized sample and subsequently rinsed using deionized water a few times until neutral pH was achieved. The product was denoted as ginkgo shell-based activated carbon (GAC). The authors used the same method to produce graphitized ginkgo-based activated carbon (GGAC), with an additional step to impregnate the GAC using cobalt nitrate in a diluted solution form. The GAC was impregnated for 12 h and subsequently heated treated at 900°C at a rate of 10°Cmin<sup>-1</sup> for two h. The findings showed a specific capacitance of

178 F/g at a potential scan rate of 500 mV/s for GGAC, which is significantly higher than commercial activated carbons and ordered mesoporous carbons (Jiang et al., 2013).

Activated carbons from natural fibers are cost-effective. Hence, they have a great advantage in producing electrodes for supercapacitor applications. Simple pyrolysis and activation can produce activated carbon from cheap biomass sources like the *Paulownia* flower (PF). The PF is a widely planted flower in China and is ample with volatile oil and pharmaceutical materials. Generally, PF is disposed of and left to rot without further utilization. For the recovery of activated carbon, the matured PF was collected after it had fallen from *Paulownia* trees. The PF was pyrolyzed for two h at 600°C under a nitrogen atmosphere. The activation process took place after pyrolysis, whereby the carbonized *Paulownia* flower (PFC) was mixed with KOH as an activating agent. In this work, the PFC was mixed with different ratios of 2:1, 3:1, or 4:1 to the KOH to study the effect of activation agent concentration on the properties of supercapacitors. After mixing with KOH, the mixture was further pyrolyzed at 800°C in a nitrogen atmosphere for one h. The activated *Paulownia* flower was washed with 1 M HCl followed by deionized water until neutral pH was achieved. Electrodes were fabricated using the activated carbon from PF by mixing it with active materials, acetylene black, and polytetrafluoroethylene binder in the percentage of 85mw%, 10mw%, and 5mw%, respectively. The supercapacitors were formed via sandwiching hydrophilic cellulose separator between two identical electrodes and immersed in 1 M H<sub>2</sub>SO<sub>4</sub> electrolyte. The symmetric supercapacitor based on a-PFC3 (3 mass ratios of KOH) resulted in a specific capacitance of 297 F/g at a current density of 1A/g within a potential range of 2–3V (Chang et al., 2015).

Subramanian et al. (2007) conducted another study on the electrochemical performance of supercapacitor electrode material using activated carbon from banana fibers. First, they have started to synthesize the activated carbon by washing and drying the banana fibers. Next, they have treated the fibers using KOH or ZnCl<sub>2</sub> at 110°C for five days. The ratio of banana fiber to activating agent was 1:5. After treatment with the activation agent, the samples were pyrolyzed for one h at 800°C with a heating rate of 10°C/min in a nitrogen gas atmosphere. The obtained AC was mixed with 20 wt% of carbon black and five wt% PVdF using NMP as a solvent to form a slurry. The slurry was then coated onto Ni mesh using the brush coating method. After drying for 30 min at 110°C, the mesh was pressed to cohere the active electrode material to the Ni mesh thoroughly.

The coated Ni mesh was used as a working electrode, saturated calomel electrode as reference electrode, and Pt wire was used as a counter electrode during the electrochemical performance test. From CV and GCD studies, the highest specific capacitance has produced the sample produced using ZnCl<sub>2</sub> as an activating agent with the capacitance of 74 F/g at 0.5 A/g in 1 M Na<sub>2</sub>SO<sub>4</sub> electrolyte. In addition, 88% of Coulombic efficiency was exhibited by this sample after 500 Cycles at 0.5 A/g. On the other hand, KOH treated AC produced a



capacitance of 66 F/g at 0.5 A/g. The BET surface area of ZnCl<sub>2</sub> and KOH treated activated carbons are 1097 m<sup>2</sup>/g and 686 m<sup>2</sup>/g, respectively (Subramanian et al., 2007).

## EFFECTS OF ACTIVATION TEMPERATURE ON ELECTROCHEMICAL PERFORMANCE

The performance of activated carbon can be significantly enhanced under appropriate conditions. The initial step in producing activated carbon is carbonization to produce char from the pyrolysis process. Throughout the process, moisture and volatile compounds are removed from the biomass (Ioannidou & Zabaniotou, 2007). The AC can be synthesized using physical and chemical activation after the carbonization process. Physical activation is generally done with gas activating agents, such as CO<sub>2</sub> and steam, while chemical activation involves chemical agents, such as acid, metal oxide, and alkali metal. The activation process finally results in activated carbon with a large surface area, high porosity, and high pore volume (Nor et al., 2013).

Teo et al. (2016) used rice husk as a precursor for AC, and the surface area was studied in detail. The authors varied the activation temperatures and compared the findings with the current data similar to their work. The study also portrayed current studies on the effects of activation temperature on mesopores and micropores of the AC, as shown in Table 1. The rice husk (RH) was treated with 1 M NaOH for 24 h at room temperature and was subsequently dried in the oven. The carbonization was done on the RH in a furnace for four h at 400°C. Silica traces were removed from the carbonized rice husk (RHC) by mixing the RHC with 1 M NaOH solution for 20 minutes to achieve a purer form of RHC. The activation process was initiated by impregnating RHC with KOH. The mass ratio used for the activation process was 1:5 (RHC: KOH), and the mixture was stirred for 30 minutes before leaving it to dry overnight at 100°C. After drying, the mixture was activated at different temperatures, which were 750°C, 850°C, and 950°C in a nitrogen gas atmosphere. Then, the achieved activated carbon was washed until neutral pH was achieved (Teo et al., 2016).

The results indicated that samples activated at higher activation temperatures were porous. However, it must be noted that porosity is an important factor in the production

Table 1  
*Raman spectral values of current studies on activated carbon with different activation temperatures (Teo et al., 2016)*

Sample	S <sub>BET</sub> (m <sup>2</sup> g <sup>-1</sup> )	V <sub>pore</sub> (Total) (cm <sup>3</sup> g <sup>-1</sup> )	V <sub>pore</sub> (micro) (cm <sup>3</sup> g <sup>-1</sup> )	V <sub>pore</sub> (meso) (cm <sup>3</sup> g <sup>-1</sup> )	t-plot micropore area (m <sup>2</sup> g <sup>-1</sup> )
AC750	2121	1.022	0.589	0.243	1426
AC850	2696	1.496	0.274	0.691	486
AC950	1592	1.293	0.052	1.056	-

Note: S<sub>BET</sub>, Brunauer-Emmett-Teller (BET) surface area, V<sub>pore</sub>, pore volume

of activated carbon as it would improve the specific capacitance of the supercapacitor electrodes. Nonetheless, AC850 with the largest BET surface area produced the highest specific capacitance of 147 F/g at 0.1 A/g.

Another investigation was carried out for supercapacitor application using argan seed shells. Argan tree is regularly found in Morocco in the southwest region, and the plant seeds are commonly used to extract oil for cosmetic and culinary uses. A large quantity of argan seed shells (ASS) residues were produced during the oil extraction. The ASS was collected and carbonized for three h at 500°C under a nitrogen gas atmosphere. After carbonization, chemical activation was done using KOH. The ratio for chemical activation used was 1: 4 (sample: KOH). After chemical activation, the samples were heated for 12 h at 60°C; then, the temperature was increased to 110°C to dry the sample. The process was followed by pyrolysis at 300°C for two h. Then, the temperature was increased to 800°C for three h at the rate of 10°Cmin<sup>-1</sup>. In the final stage, the prepared activated carbon was washed using 0.1 M HCl then rinsed using deionized water until no chloride ions were detected (Elmouwahidi et al., 2012). The electrochemical studies were conducted in three electrodes setups with 1 M H<sub>2</sub>SO<sub>4</sub> as electrolyte. The highest capacitance achieved was 355F/g at 125mA/g, while the highest retention was 93% at 1 A/g.

Another potential precursor of activated carbon used in supercapacitor application is oil palm empty fruit bunches that have been studied by Farma et al. (2013). The advantage of using oil palm empty bunches is that it is abundantly available in Malaysia as the oil palm industry is one of the major agricultural sectors in Malaysia. The industry mainly focuses on producing cooking oil from oil palm fruits. During this process of extracting oil, many empty fruit bunches (EFB) were produced and could potentially pollute the environment without a proper disposal method. The burning of EFB for the production of fertilizers is also creating environmental hazards by emitting greenhouse gases from combustion. Therefore, in their study, the EFB was used as a raw material to produce monolithic nanoporous activated carbon for supercapacitor electrodes (Farma et al., 2013). The authors made some comparisons on the specific capacitance achieved with other types of precursors, as presented in Table 2.

The conversion of EFB to activated carbon was initiated by pre-carbonization of EFB fibers at a low temperature of 280°C. It was followed by ball milling for 18 h and subsequently sieved to obtain self-adhesive carbon grains (SACG) powder. The SACG was mixed with KOH in wet conditions using distilled water and stirred for one h to obtain a homogeneous mixture. Green monoliths (GMs) of the SACG and green monolith (GMK) of the KOH-treated SACG were prepared in a mold before it was further carbonized in a nitrogen gas environment at 800°C at a rate of 1.5 liters per minute (Farma et al., 2013).

Elaiyappillai et al. (2019) recovered precursor for AC from *Cucumis melo* (Cm) fruit peel by adapting two stages method (carbonization and activation). First, the Cm

Table 2

Comparison of specific capacitance between other precursors (Farma et al., 2013)

Biomass precursor	Activation method	S <sub>BET</sub> (m <sup>2</sup> g <sup>-1</sup> )	C <sub>sp</sub> (Fg <sup>-1</sup> )
Firewood	KOH	2821	95
Coffee bean waste	ZnCl <sub>2</sub>	1019	368
Cherry stones	KOH	1624	174
Coffee shell	ZnCl <sub>2</sub>	842	156
Recycled wastepaper	KOH	417	180
Cassava peel waste	KOH + CO <sub>2</sub>	1352	153
Sugar cane bagasse	ZnCl <sub>2</sub>	1788	300
Apricot shell	NaOH	2335	348
Coffee endocarp	CO <sub>2</sub>	709	176
Sunflower seed shell	KOH	2509	311
Rubber wood sawdust	CO <sub>2</sub>	912	138
Argan seed shell	KOH	2062	355
Camellia olleifera shell	ZnCl <sub>2</sub>	1935	374
Poplar wood	HNO <sub>3</sub>	416	234
Fibers of palm oil empty fruit bunches	KOH + CO <sub>2</sub>	1704	149

was heated for four h at 300°C at a rate of 5°Cmin<sup>-1</sup> under vacuum conditions. Then, the sample was left to cool to room temperature before being crushed into fine powder form (Elaiyappillai et al., 2019). In the second stage, KOH was used for chemical activation. The authors varied the activation temperature from 600-900°C, and samples were heated for three h. The activated carbon from Cm-900 produced the highest specific capacitance of 404 F/g at 1 A/g with 1 M KOH as electrolyte. As a result, the power density of Cm-900 was 279.78 w/kg, whereas the energy density was 29.30 Wh/kg. Meanwhile, the charge retention obtained after 8000 cycles of charge/discharge was 91%.

Research by Cheng et al. (2020) produced AC from *Laminaria japonica*, a type of seaweed known as brown algae plant and mostly grown on ropes in the sea between Korea and Japan. The synthesis of AC was done using two steps syntheses; pre-carbonization followed by activation using KOH. The varied carbonization temperature was 600°C, 800°C, 1000°C and 1200°C. Most of the previous studies chose activation temperature as the manipulated variable to study its effects on the characteristics of the activated carbon produced. After pre-carbonization, the mixture was activated at 700°C and 800°C under a nitrogen gas atmosphere for two h and subsequently neutralized using 1 M HCL solution and deionized water (Cheng et al., 2020). The overall process is shown in Figure 8. The specific capacitance of the supercapacitor electrode fabricated from *L. japonica* activated carbon was 192 F/g at 0.1 A/g, and the electrode exhibited almost 100% of capacitance retention after 10000 cycles at 1 A/g.

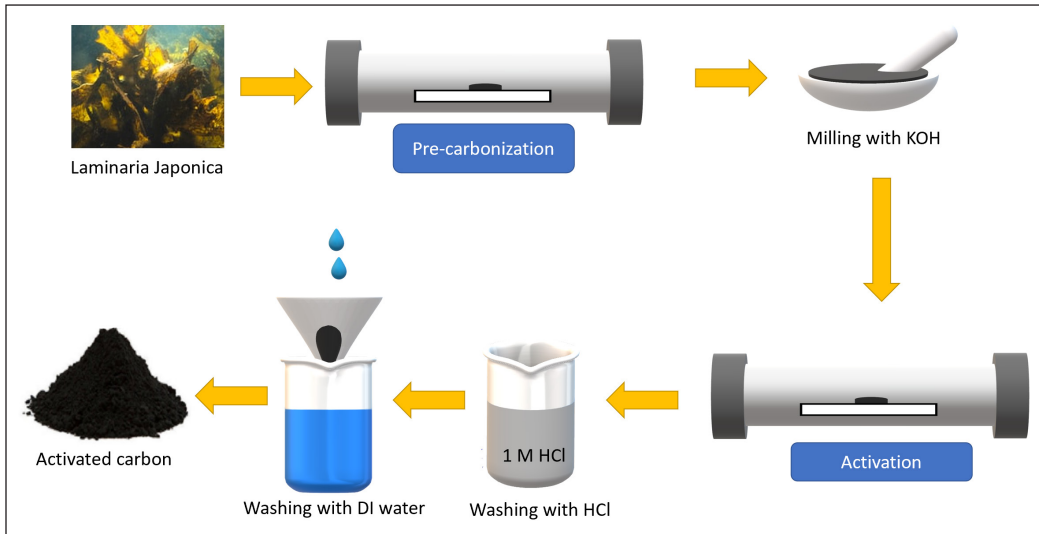


Figure 8. Synthesis of activated carbon from *L. japonica* (Cheng et al., 2020)

Another precursor was discovered from *Saccharum spontaneum* by Samantray and Mishra (2019), containing 48.91% of carbon, as shown in Table 3. Zinc chloride was used as the activating agent in a one-step synthesis process with precursor ratio to the activating agent, 0.5:1. The carbonization temperature used was 400°C to 600°C under a nitrogen gas environment. After carbonization, the samples were neutralized using 0.1 M HCl solution and deionized water. Figure 9 shows the flow chart of activated carbon synthesis. The results from Taguchi analysis in this research prove that optimal conditions to produce high surface area carbon are 600°C, chemical ratio of 1 and 60 min holding time for carbonization process (Samantray & Mishra, 2019).

Table 3  
Analysis of *S. spontaneum* (Samantray & Mishra, 2019)

Analysis	Stem
<b>Proximate (wt%)</b>	
<b>Moisture</b>	9
<b>Volatile matter</b>	72
<b>Ash</b>	3
<b>Fixed carbon</b>	16
<b>Ultimate (wt%)</b>	
<b>Carbon</b>	48.910
<b>Hydrogen</b>	8.341
<b>Nitrogen</b>	0.905
<b>Sulfur</b>	0.18
<b>Oxygen</b>	41.664

### CHARACTERIZATION OF ACTIVATED CARBON-BASED SUPERCAPACITOR ELECTRODE

The commonly used method for characterization of activated carbon is X-ray diffraction (XRD), Field Emission Scanning Electron Microscopy (FE-SEM), Transmission electron microscopy (TEM), Fourier Transform Infrared Spectroscopy (FTIR), Raman spectroscopy, and Brunauer-Emmett-Teller (BET) surface area (Tobi et al., 2019). Meanwhile, the

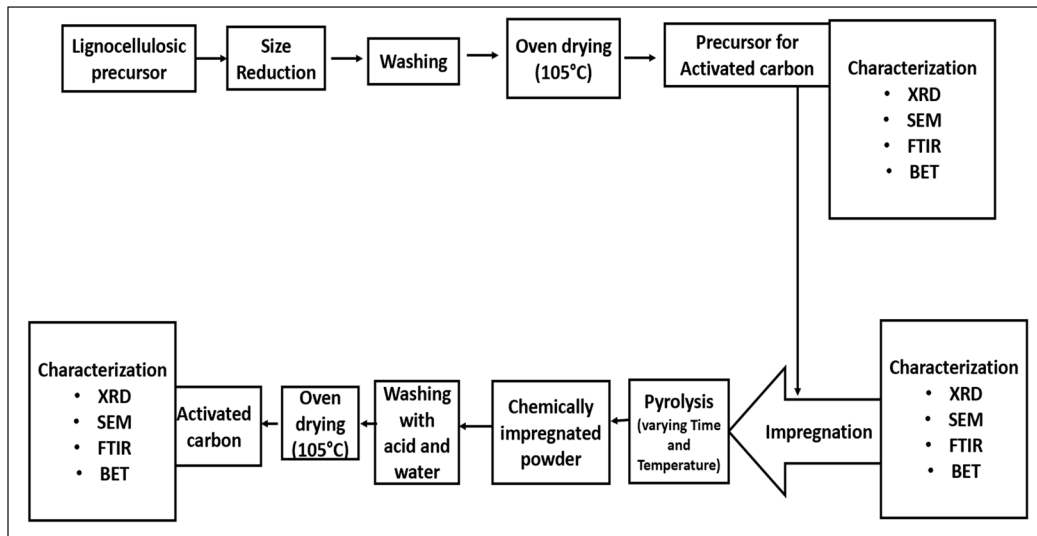


Figure 9. Activated carbon synthesis from *S. spontaneum* (Samantray & Mishra, 2019).

common electrochemical properties are characterized by using Cyclic Voltammetry (CV), galvanostatic charge/discharge (GCD), and electrochemical impedance spectroscopy (EIS).

KOH activation and phosphoric acid-treated carbon derived from the banana stem were compared with other hard carbons derived from corn cob and potato starch. From Raman spectroscopy of these four carbons, it was noted that partial graphitization is observed on all these samples. KOH activated banana stem (KHC) has a more disordered nature. For energy storage applications using carbon, this disordered nature is advantageous owing to the existence of active surfaces. SEM of KHC, phosphoric acid-treated banana stem (PHC), and corn-cob derived carbon (CHC), as shown in Figures 10 (a), (b), and (c), respectively, shows more visible porous structure compared to potato starch derived carbon (SHC), which did not show any evidence of porosity, based on the SEM images as shown in Figure 10 (d). Similar to the conclusions made with SEM, TEM images additionally show that the pore diameters are in the nanometer range except for SHC. When the carbonization temperatures were increased, a greater amount of micro range crystallites were present by various carbon layers. In addition, the micropores and mesopores facilitate the charge

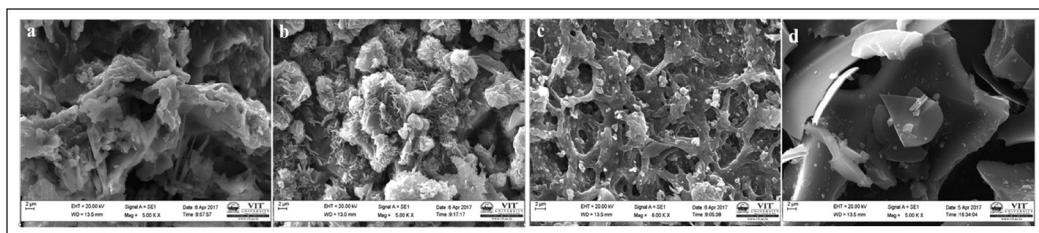


Figure 10. FE-SEM images of (a) KHC, (b) PHC, (c) CHC and (d) SHC (Yao et al., 2015)

transferring process in carbons and subsequently increase the electrochemical performance of the supercapacitor electrode fabricated.

Table 4 shows the specific capacitance achieved by these four samples with the BET surface area of each sample. Based on the BET surface area results, The larger surface area possessed by KHC and CHC attributes to improved performance of supercapacitors. KHC achieved the highest specific capacitance as the improved surface area, lower pore diameter and increased pore volume helped electrochemical performance. The improved surface area is caused by the pore diameter, which is about 1nm as based on literature, better supercapacitor performance is achieved as the pore diameter is close to 1nm (Chmiola et al., 2006; Yao et al., 2015).

Table 4  
Specific capacitance with surface porosity analysis (Yao et al., 2015)

Sample	Specific Capacitance (F/g)	BET Surface area (m <sup>2</sup> /g)	Average pore diameter (nm)	Average pore volume (cc/gm)
KHC	479.23 @1mV/s	567.36	1.205	0.175
CHC	309.81 @2mV/s	215.42	1.199	0.107
PHC	202.11 @2mV/s	177.72	1.789	0.091
SHC	99.9 @2mV/s	42.43	1.363	0.099

The CV curves, as shown in Figure 11, show evident redox peaks for all the samples in 6M KOH electrolyte, especially by KHC. These redox peaks indicate that faradaic reaction related to pseudocapacitance occurs during the charge/discharge process. The samples also exhibit EDLC behavior as the CV curves have quasi-rectangular shapes. These EDLC attributes are caused by the hydrophilic nature of the micro-ordered sheets

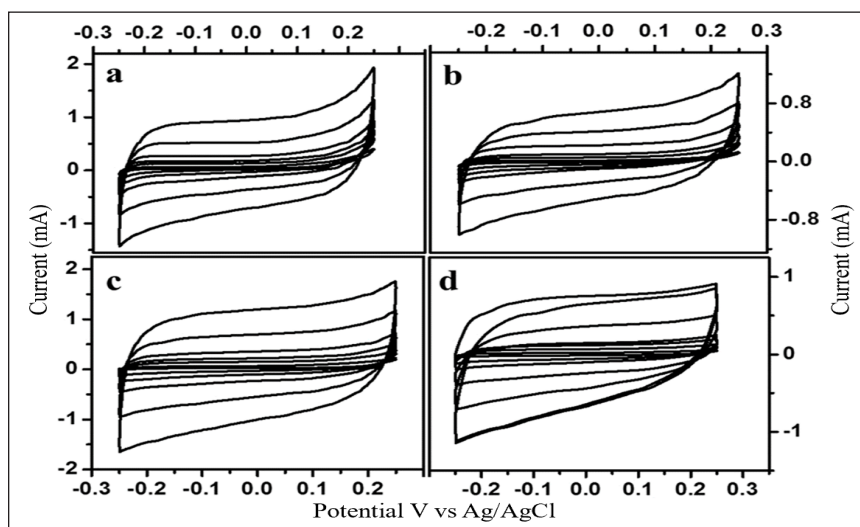


Figure 11. CV curves of (a) KHC, (b) PHC, (c) CHC and (d) SHC (Yao et al., 2015)

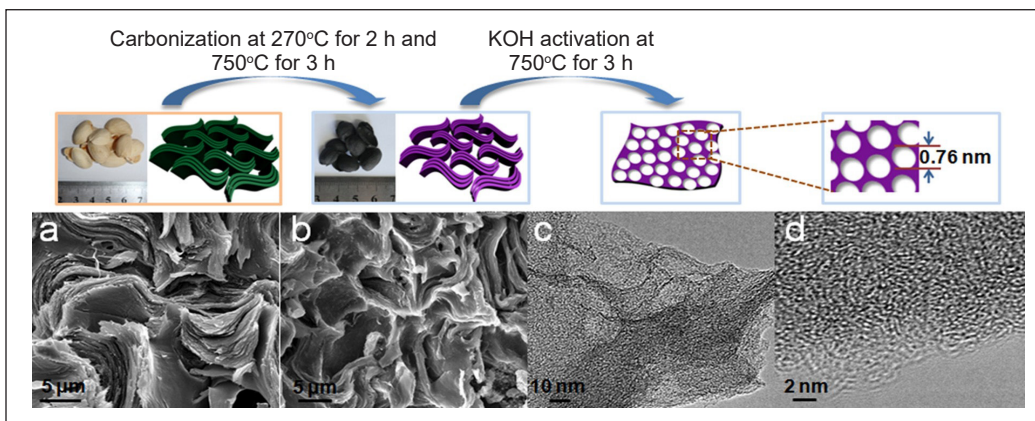


Figure 12. Process of synthesizing AC from pistachio nutshell with a) SEM of natural pistachio shell, b) SEM of C-SPN, c) and d) HRTEM of AC-SPN-3 at different magnification (Xu et al., 2014)

with oxygen on the edge of the structures. In the galvanostatic charge-discharge curve, the EDLC behavior causes a triangular shape, whereas the pseudocapacitance gives a smooth curvilinear shape nearing the triangle's peak (Yao et al., 2015).

Pistachio nutshell was activated at the different mass ratios with KOH as an activating agent with a pyrolysis temperature of 750°C (Xu et al., 2014). The samples were labeled as AC-SPN-X, where X denotes the mass ratio between KOH and carbonized pistachio nutshell (C-SPN). The process of synthesizing activated carbon is described in Figure 12, together with the morphology of the sample at each stage.

From the SEM analysis, C-SPN exhibits a 2D lamellar structure similar to a natural pistachio shell; however, some shrinkage is observed. From HRTEM analysis, AC-SPN-3 possesses interconnected porous structures with a 0.5-1 nm pore diameter. The Raman spectroscopy results shown in Figure 13 confirms that all the samples have defective graphitic structures as the peaks are present about 1320  $\text{cm}^{-1}$  and 1580  $\text{cm}^{-1}$  (Kim et al., 2011; Li et al., 2013; Shimodaira & Masui, 2002). The degree of graphitization depends on the ratio of  $I_G$  and  $I_D$ , which also indicates higher electrical conductivity with a higher ratio value (Bogeat, 2021; Dresselhaus et al., 2005; Mhamane et al., 2011).

Based on Nyquist plots, AC-SPN-3 exhibits the highest electrical conductivity among the other samples, which is supported by the relatively high  $I_G/I_D$  value of AC-SPN-3 compared to AC-SPN-1 and AC-SPN-5. Hence, AC-SPN-3 has the most graphitic layers

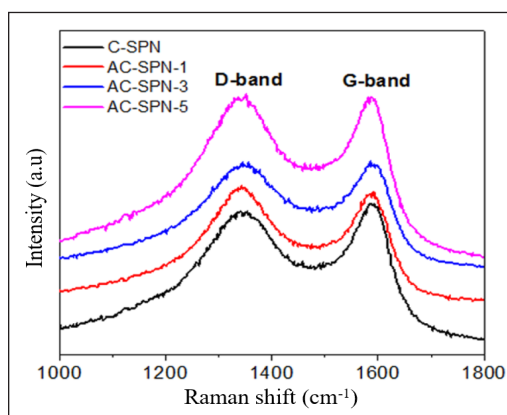


Figure 13. Raman spectroscopy of samples after KOH activation (Xu et al., 2014)

compared to other samples, although it has disordered carbon structures (Shimodaira & Masui, 2002). From the CV curves of AC-SPN-3, as shown in Figure 14(a), a quasi-rectangular shape is observed. Furthermore, AC-SPN-3 has the highest specific capacitance of 313 and 215 F/g in 6M KOH and TMABF<sub>4</sub> electrolytes, respectively, compared to other samples as shown in Figure 14(b).

Gupta et al. (2021) synthesized activated carbon from *Desmostachya bipinnata* (Kusha grass) and studied its electrochemical performance as a supercapacitor electrode (Gupta et al., 2021). The description of steps involved in the DP-AC synthesis is as shown in Figure 15. From the XRD and Raman spectroscopy, as shown in Figure 16, characteristics of activated carbon were confirmed, and an amorphous carbon structure is present (Ghosh

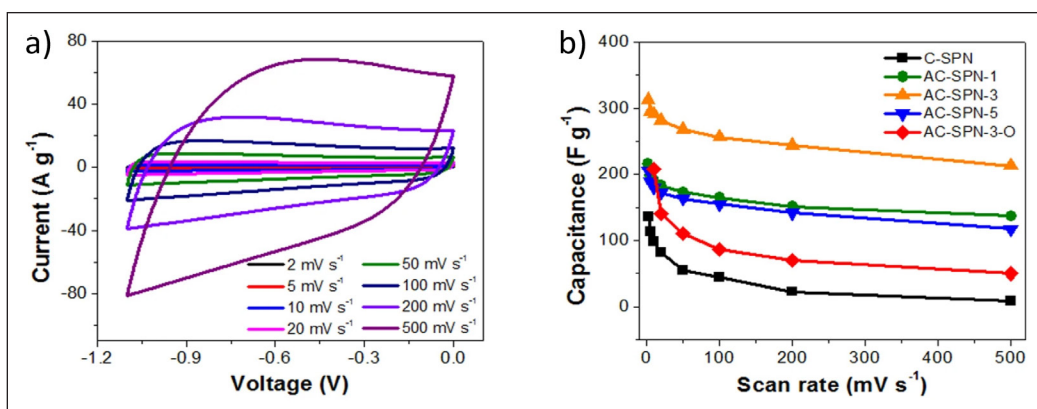


Figure 14. a) CV curve of AC-SPN-3 and b) Specific capacitance of all samples at different scan rates (Xu et al., 2014)

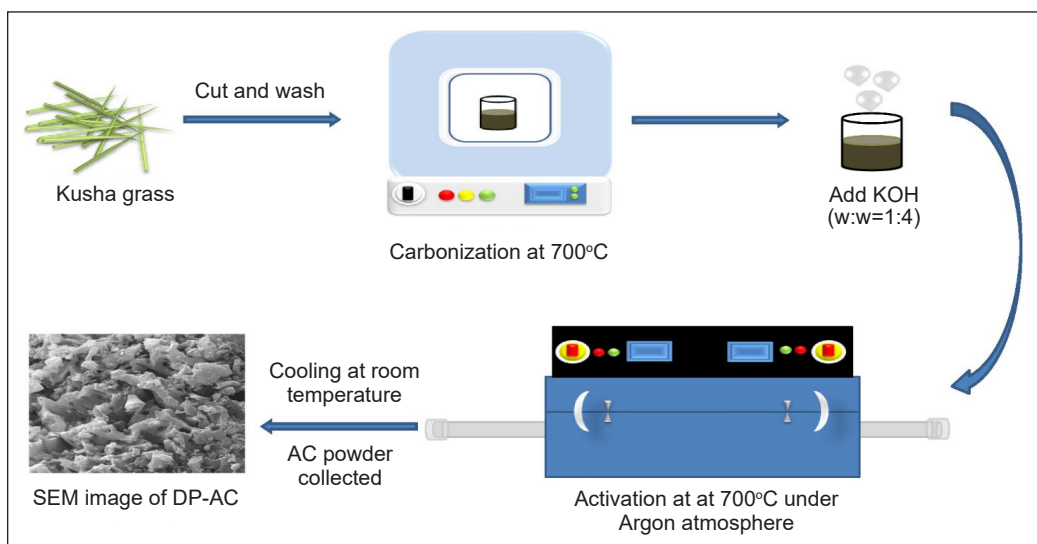


Figure 15. Synthesis of activated carbon from *D. bipinnata* (Gupta et al., 2021)



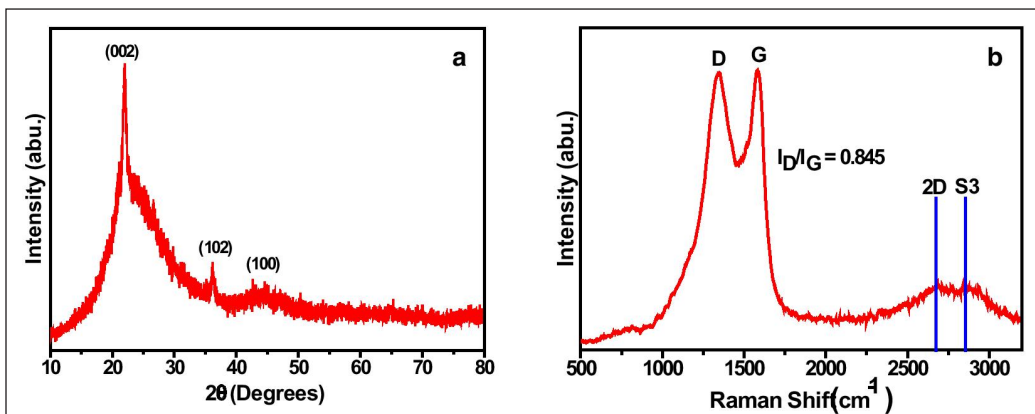


Figure 16. a) XRD pattern and b) Raman spectrum of DP-AC (Gupta et al., 2021)

et al., 2019; Pang et al., 2016). In Raman spectroscopy, the D peak is positioned at  $1346\text{ cm}^{-1}$  and G Peak at  $1587\text{ cm}^{-1}$ . It proves activated carbon with graphitic structure and edge imperfection (Zhang et al., 2013). Another two peaks at  $2678\text{ cm}^{-1}$  and  $2840\text{ cm}^{-1}$  prove the existence of a few layered carbon materials (Purkait et al., 2017). From SEM analysis, it was observed that there is a large, disordered porous structure as a result of an etching by KOH during activation. The BET surface area of DP-AC is  $738.56\text{ m}^2/\text{g}$  with an average pore diameter of  $3.3\text{ nm}$ . The electrochemical study was performed in the three-electrode system with  $6\text{ M KOH}$  as electrolyte. DP-AC achieved the highest specific capacitance of  $220.7\text{ F/g}$  at  $10\text{ mV/s}$  from the CV study and  $218\text{ F/g}$  at  $0.7\text{ A/g}$  from the GCD study. A maximum energy density of  $19.3\text{ Wh/kg}$  was achieved at a power density of  $277\text{ W/kg}$ .

## CONCLUSION

From the findings obtained in previous research works, it was found that there are various sources of carbon that can be converted to activated carbon and used for supercapacitors application. Most of the works used a similar method of activation and carbonization to prepare the AC. Some of the parameters that can be manipulated during the preparation of AC are activation temperature, type of activating agent, the ratio of activated carbon to the activating agent, and activation method. These parameters would vary the electrochemical properties of the electrode in terms of its specific capacitance and capacitance retention. The literature has shown a variety of materials synthesized from heterogeneous natural fiber precursors for supercapacitors based on carbon electrodes. An in-depth comparison has given some indications that natural fibers possess a high potential to be used for high-performance supercapacitor electrodes. Additional studies are essential to minimize the main knowledge gaps in the field of sustainable materials for energy storage applications. This review shows that relatively inexpensive and renewable resources from plants are

highly porous carbon and can be converted into useful products, such as supercapacitors for energy storage applications, which are expected to be in great demand in the future.

## ACKNOWLEDGEMENT

The authors would like to thank the College of Engineering, Universiti Tenaga Nasional (UNITEN), Kajang, Malaysia, and Yayasan Canselor UNITEN (YCU) for the research grant support through iRMC, Grant Number: 201901001YCU.

## REFERENCES

- Afif, A., Rahman, S. M. H., Azad, A. T., Zaini, J., Islan, M. A., & Azad, A. K. (2019). Advanced materials and technologies for hybrid supercapacitors for energy storage - A review. *Journal of Energy Storage*, 25, Article 100852. <https://doi.org/https://doi.org/10.1016/j.est.2019.100852>
- Ahmed, M. B., Johir, M. A. H., Zhou, J. L., Ngo, H. H., Nghiem, L. D., Richardson, C., Moni, M. A., & Bryant, M. R. (2019). Activated carbon preparation from biomass feedstock: Clean production and carbon dioxide adsorption. *Journal of Cleaner Production*, 225, 405-413. <https://doi.org/10.1016/j.jclepro.2019.03.342>
- Arunachalam, S., Kirubasankar, B., Pan, D., Liu, H., Yan, C., Guo, Z., & Angaiah, S. (2020). Research progress in rare earths and their composites based electrode materials for supercapacitors. *Green Energy and Environment*, 5(3), 259-273. <https://doi.org/10.1016/j.gee.2020.07.021>
- Bogeat, A. B. (2021). Understanding and tuning the electrical conductivity of activated carbon: A state-of-the-art review. *Critical Reviews in Solid State and Materials Sciences*, 46(1), 1-37. <https://doi.org/10.1080/10408436.2019.1671800>
- Bhat, V. S., Krishnan, S. G., Jayeoye, T. J., Rujiralai, T., Sirimahachai, U., Viswanatha, R., Khalid, M., & Hegde, G. (2021). Self-activated 'green' carbon nanoparticles for symmetric solid-state supercapacitors. *Journal of Materials Science*, 56(23), 13271-13290. <https://doi.org/10.1007/s10853-021-06154-z>
- Chang, J., Gao, Z., Wang, X., Wu, D., Xu, F., Wang, X., Guo, Y., & Jiang, K. (2015). Activated porous carbon prepared from paulownia flower for high performance supercapacitor electrodes. *Electrochimica Acta*, 157, 290-298. <https://doi.org/10.1016/j.electacta.2014.12.169>
- Chen, H., Wei, H., Fu, N., Qian, W., Liu, Y., Lin, H., & Han, S. (2018). Nitrogen-doped porous carbon using ZnCl<sub>2</sub> as activating agent for high-performance supercapacitor electrode materials. *Journal of Materials Science*, 53(4), 2669-2684. <https://doi.org/10.1007/s10853-017-1453-3>
- Chen, S., Qiu, L., & Cheng, H. M. (2020). Carbon-based fibers for advanced electrochemical energy storage devices. *Chemical Reviews*, 120(5), 2811-2878. <https://doi.org/10.1021/acs.chemrev.9b00466>
- Chen, W., Luo, M., Yang, K., & Zhou, X. (2020). Microwave-assisted KOH activation from lignin into hierarchically porous carbon with super high specific surface area by utilizing the dual roles of inorganic salts: Microwave absorber and porogen. *Microporous and Mesoporous Materials*, 300, Article 110178. <https://doi.org/https://doi.org/10.1016/j.micromeso.2020.110178>

- Cheng, Y., Wu, L., Fang, C., Li, T., & Chen, J. (2020). Synthesis of porous carbon materials derived from *Laminaria japonica* via simple carbonization and activation for supercapacitors. *Journal of Materials Research and Technology*, 9(3), 3261-3271. <https://doi.org/10.1016/j.jmrt.2020.01.022>
- Chime, U. K., Nkele, A. C., Ezugwu, S., Nwanya, A. C., Shinde, N. M., Kebede, M., Ejikeme, P. M., Maaza, M., & Ezema, F. I. (2020). Recent progress in nickel oxide-based electrodes for high-performance supercapacitors. *Current Opinion in Electrochemistry*, 21, 175-181. <https://doi.org/https://doi.org/10.1016/j.coelec.2020.02.004>
- Chiu, Y. H., & Lin, L. Y. (2019). Effect of activating agents for producing activated carbon using a facile one-step synthesis with waste coffee grounds for symmetric supercapacitors. *Journal of the Taiwan Institute of Chemical Engineers*, 101, 177-185. <https://doi.org/10.1016/j.jtice.2019.04.050>
- Chmiola, J., Yushin, G., Gogotsi, Y., Portet, C., Simon, P., & Taberna, P. L. (2006). Anomalous increase in carbon capacitance at pore sizes less than 1 nanometer. *Science*, 313(5794), 1760-1763. <https://doi.org/10.1126/science.1132195>
- Chowdhury, T. S., & Grebel, H. (2019). Supercapacitors with electrical gates. *Electrochimica Acta*, 307, 459-464. <https://doi.org/10.1016/j.electacta.2019.03.222>
- Devillers, N., Jemei, S., Péra, M. C., Bienaimé, D., & Gustin, F. (2014). Review of characterization methods for supercapacitor modelling. *Journal of Power Sources*, 246, 596-608. <https://doi.org/https://doi.org/10.1016/j.jpowsour.2013.07.116>
- Dresselhaus, M. S., Dresselhaus, G., Saito, R., & Jorio, A. (2005). Raman spectroscopy of carbon nanotubes. *Physics Reports*, 409(2), 47-99. <https://doi.org/https://doi.org/10.1016/j.physrep.2004.10.006>
- Elaiyappillai, E., Srinivasan, R., & Johnbosco, Y. (2019). Applied surface science low cost activated carbon derived from *Cucumis melo* fruit peel for electrochemical supercapacitor application. *Applied Surface Science*, 486(April), 527-538.
- Elmouwahidi, A., Zapata-Benabithé, Z., Carrasco-Marín, F., & Moreno-Castilla, C. (2012). Activated carbons from KOH-activation of argan (*Argania spinosa*) seed shells as supercapacitor electrodes. *Bioresource Technology*, 111, 185-190. <https://doi.org/10.1016/j.biortech.2012.02.010>
- Enock, T. K., King'ondo, C. K., Pogrebnoi, A., & Jande, Y. A. C. (2017). Status of biomass derived carbon materials for supercapacitor application. *International Journal of Electrochemistry*, 2017, 1-14. <https://doi.org/10.1155/2017/6453420>
- Farma, R., Deraman, M., Awitdrus, A., Talib, I. A., Taer, E., Basri, N. H., Manjunatha, J. G., Ishak, M. M., Dollah, B. N. M., & Hashmi, S. A. (2013). Preparation of highly porous binderless activated carbon electrodes from fibres of oil palm empty fruit bunches for application in supercapacitors. *Bioresource Technology*, 132, 254-261. <https://doi.org/10.1016/j.biortech.2013.01.044>
- Ghosh, S., Santhosh, R., Jeniffer, S., Raghavan, V., Jacob, G., Nanaji, K., Kollu, P., Jeong, S. K., & Grace, A. N. (2019). Natural biomass derived hard carbon and activated carbons as electrochemical supercapacitor electrodes. *Scientific Reports*, 9, Article 16315. <https://doi.org/10.1038/s41598-019-52006-x>
- Gu, W., & Yushin, G. (2014). Review of nanostructured carbon materials for electrochemical capacitor applications: Advantages and limitations of activated carbon, carbide-derived carbon, zeolite-templated

- carbon, carbon aerogels, carbon nanotubes, onion-like carbon, and graphene. *Wiley Interdisciplinary Reviews: Energy and Environment*, 3(5), 424-473. <https://doi.org/10.1002/wene.102>
- Gupta, G. K., Sagar, P., Pandey, S. K., Srivastava, M., Singh, A. K., Singh, J., Srivastava, A., Srivastava, S. K., & Srivastava, A. (2021). *In Situ* fabrication of activated carbon from a bio-waste *Desmostachya bipinnata* for the improved supercapacitor performance. *Nanoscale Research Letters*, 16(1), 1-12. <https://doi.org/10.1186/s11671-021-03545-8>
- Hu, L., Zhu, Q., Wu, Q., Li, D., An, Z., & Xu, B. (2018). Natural biomass-derived hierarchical porous carbon synthesized by an *in Situ* hard template coupled with NaOH activation for ultrahigh rate supercapacitors. *ACS Sustainable Chemistry & Engineering*, 6(11), 13949-13959. <https://doi.org/10.1021/acssuschemeng.8b02299>
- Im, U. S., Kim, J., Lee, S. H., Lee, S. M., Lee, B. R., Peck, D. H., & Jung, D. H. (2019). Preparation of activated carbon from needle coke via two-stage steam activation process. *Materials Letters*, 237, 22-25. <https://doi.org/https://doi.org/10.1016/j.matlet.2018.09.171>
- Ioannidou, O., & Zabaniotou, A. A. (2007). Agricultural residues as precursors for activated carbon production - A review. *Renewable and Sustainable Energy Reviews*, 11, 1966-2005. <https://doi.org/10.1016/j.rser.2006.03.013>
- Jiang, L., Yan, J., Hao, L., Xue, R., Sun, G., & Yi, B. (2013). High rate performance activated carbons prepared from ginkgo shells for electrochemical supercapacitors. *Carbon*, 56, 146-154. <https://doi.org/10.1016/j.carbon.2012.12.085>
- Kim, H., Cho, J., Jang, S. Y., & Song, Y. W. (2011). Deformation-immunized optical deposition of graphene for ultrafast pulsed lasers. *Applied Physics Letters*, 98(2), Article 21104. <https://doi.org/10.1063/1.3536502>
- Lei, E., Li, W., Ma, C., Xu, Z., & Liu, S. (2018). CO<sub>2</sub>-activated porous self-templated N-doped carbon aerogel derived from banana for high-performance supercapacitors. *Applied Surface Science*, 457, 477-486. <https://doi.org/https://doi.org/10.1016/j.apsusc.2018.07.001>
- Li, Z., Xu, Z., Tan, X., Wang, H., Holt, C. M. B., Stephenson, T., Olsen, B. C., & Mitlin, D. (2013). Mesoporous nitrogen-rich carbons derived from protein for ultra-high capacity battery anodes and supercapacitors. *Energy & Environmental Science*, 6(3), 871-878. <https://doi.org/10.1039/C2EE23599D>
- Liu, P., Yan, J., Guang, Z., Huang, Y., Li, X., & Huang, W. (2019). Recent advancements of polyaniline-based nanocomposites for supercapacitors. *Journal of Power Sources*, 424, 108-130. <https://doi.org/10.1016/j.jpowsour.2019.03.094>
- Lu, W., Cao, X., Hao, L., Zhou, Y., & Wang, Y. (2020). Activated carbon derived from pitaya peel for supercapacitor applications with high capacitance performance. *Materials Letters*, 264, Article 127339. <https://doi.org/10.1016/j.matlet.2020.127339>
- Luo, X., Chen, Y., & Mo, Y. (2021). A review of charge storage in porous carbon-based supercapacitors. *New Carbon Materials*, 36(1), 49-68. [https://doi.org/https://doi.org/10.1016/S1872-5805\(21\)60004-5](https://doi.org/https://doi.org/10.1016/S1872-5805(21)60004-5)
- Lyu, L., Seong, K., Ko, D., Choi, J., Lee, C., Hwang, T., Cho, Y., Jin, X., Zhang, W., Pang, H., & Piao, Y. (2019). Recent development of biomass-derived carbons and composites as electrode materials for supercapacitors. *Materials Chemistry Frontiers*, 3(12), 2543-2570. <https://doi.org/10.1039/C9QM00348G>

- Ma, M., Ying, H., Cao, F., Wang, Q., & Ai, N. (2020). Adsorption of congo red on mesoporous activated carbon prepared by CO<sub>2</sub> physical activation. *Chinese Journal of Chemical Engineering*, 28(4), 1069-1076. <https://doi.org/https://doi.org/10.1016/j.cjche.2020.01.016>
- Mhamane, D., Ramadan, W., Fawzy, M., Rana, A., Dubey, M., Rode, C., Lefez, B., Hannoyer, B., & Ogale, S. (2011). From graphite oxide to highly water dispersible functionalized graphene by single step plant extract-induced deoxygenation. *Green Chemistry*, 13(8), 1990-1996. <https://doi.org/10.1039/C1GC15393E>
- Misono, I. I., Zain, N. K. M., Aziz, R. A., Vidyadharan, B., & Jose, R. (2015). Electrochemical properties of carbon from oil palm kernel shell for high performance supercapacitors. *Electrochimica Acta*, 174(1), 78-86. <https://doi.org/10.1016/j.electacta.2015.05.163>
- Morali, U., Demiral, H., & Şensöz, S. (2018). Optimization of activated carbon production from sunflower seed extracted meal: Taguchi design of experiment approach and analysis of variance. *Journal of Cleaner Production*, 189, 602-611. <https://doi.org/10.1016/j.jclepro.2018.04.084>
- Musa, M. S., Sanagi, M. M., Nur, H., & Ibrahim, W. A. W. (2015). Understanding pore formation and structural deformation in carbon spheres during KOH activation. *Sains Malaysiana*, 44, 613-618. <https://doi.org/10.17576/jsm-2015-4404-17>
- Namnisnyk, A., & Zhu, J. (2003). A survey of electrochemical super-capacitor technology. In *Australian Universities Power Engineering Conference* (pp. 1-6). University of Canterbury.
- Nor, N. M., Lau, L. C., Lee, K. T., & Mohamed, A. R. (2013). Synthesis of activated carbon from lignocellulosic biomass and its applications in air pollution control - A review. *Journal of Environmental Chemical Engineering*, 1(4), 658-666. <https://doi.org/10.1016/j.jece.2013.09.017>
- Pang, P., Yan, F., Chen, M., Li, H., Zhang, Y., Wang, H., Wu, Z., & Yang, W. (2016). Promising biomass-derived activated carbon and gold nanoparticle nanocomposites as a novel electrode material for electrochemical detection of rutin. *RSC Advances*, 6(93), 90446-90454. <https://doi.org/10.1039/C6RA16804C>
- Peng, C., Yan, X. B., Wang, R. T., Lang, J. W., Ou, Y. J., & Xue, Q. J. (2013). Promising activated carbons derived from waste tea-leaves and their application in high performance supercapacitors electrodes. *Electrochimica Acta*, 87, 401-408. <https://doi.org/10.1016/j.electacta.2012.09.082>
- Purkait, T., Singh, G., Singh, M., Kumar, D., & Dey, R. S. (2017). Large area few-layer graphene with scalable preparation from waste biomass for high-performance supercapacitor. *Scientific Reports*, 7, Article 15239. <https://doi.org/10.1038/s41598-017-15463-w>
- Qin, L. (2019). Porous carbon derived from pine nut shell prepared by steam activation for supercapacitor electrode material. *International Journal of Electrochemical Science*, 14, 8907-8918. <https://doi.org/10.20964/2019.09.20>
- Raju, K., & Ozoemena, K. I. (2015). Hierarchical one-dimensional ammonium nickel phosphate microrods for high-performance pseudocapacitors. *Scientific Reports*, 5, Article 17629. <https://doi.org/10.1038/srep17629>
- Rawal, S., Joshi, B., & Kumar, Y. (2018). Synthesis and characterization of activated carbon from the biomass of *Saccharum bengalense* for electrochemical supercapacitors. *Journal of Energy Storage*, 20(October), 418-426. <https://doi.org/10.1016/j.est.2018.10.009>

- Rombaldo, C. F. S., & Lisboa, A. C. L. (2014). Brazilian natural fiber (jute) as raw material for activated carbon production. *Anais da Academia Brasileira de Ciências*, 86, 2137-2144.
- Saini, S., Chand, P., & Joshi, A. (2021). Biomass derived carbon for supercapacitor applications: Review. *Journal of Energy Storage*, 39, Article 102646. <https://doi.org/https://doi.org/10.1016/j.est.2021.102646>
- Samantray, R., & Mishra, S. C. (2019). Saccharum spontaneum, a precursor of sustainable activated carbon: Synthesis, characterization and optimization of process parameters and its suitability for supercapacitor applications. *Diamond and Related Materials*, 101, Article 107598. <https://doi.org/10.1016/j.diamond.2019.107598>
- Sayed, S. G., Mahadik, M. A., Shaikh, A. V., Jang, J. S., & Pathan, H. M. (2019). Nano-metal oxide based supercapacitor via electrochemical deposition. *ES Energy & Environment*, 3, 25-44. <https://doi.org/10.30919/esee8c211>
- Shimodaira, N., & Masui, A. (2002). Raman spectroscopic investigations of activated carbon materials. *Journal of Applied Physics*, 92(2), 902-909. <https://doi.org/10.1063/1.1487434>
- Shinde, P. A., & Jun, S. C. (2020). Review on recent progress in the development of tungsten oxide based electrodes for electrochemical energy storage. *ChemSusChem*, 13(1), 11-38. <https://doi.org/https://doi.org/10.1002/cssc.201902071>
- Simon, P., & Gogotsi, Y. (2008). Materials for electrochemical capacitors. *Nature Materials*, 7(11), 845-854. <https://doi.org/10.1038/nmat2297>
- Subramaniam, V., Luo, C., Stephan, A. M., Nahm, K. S., Thomas, S., & Wei, B. (2007). Supercapacitors from activated carbon derived from banana fibers. *Journal of Physical Chemistry C*, 111(20), 7527-7531. <https://doi.org/10.1021/jp067009t>
- Sun, Q. (2019). Porous carbon material based on biomass prepared by MgO template method and ZnCl<sub>2</sub> activation method as electrode for high performance supercapacitor. *International Journal of Electrochemical Science*, 14, 1-14. <https://doi.org/10.20964/2019.01.50>
- Tan, Y. B., & Lee, J. M. (2013). Graphene for supercapacitor applications. *Journal of Materials Chemistry A*, 1(47), 14814-14843. <https://doi.org/10.1039/C3TA12193C>
- Teo, E. Y. L., Muniandy, L., Ng, E. P., Adam, F., Mohamed, A. R., Jose, R., & Chong, K. F. (2016). High surface area activated carbon from rice husk as a high performance supercapacitor electrode. *Electrochimica Acta*, 192, 110-119. <https://doi.org/10.1016/j.electacta.2016.01.140>
- Thulasi, K. M., Manikoth, S. T., Paravannoor, A., Palantavida, S., Bhagiyalakshmi, M., & Vijayan, B. K. (2019). Ceria deposited titania nanotubes for high performance supercapacitors. *Journal of Physics and Chemistry of Solids*, 135, Article 109111. <https://doi.org/10.1016/j.jpics.2019.109111>
- Tobi, A. R., Dennis, J. O., Zaid, H. M., Adekoya, A. A., Yar, A., & Fahad, U. (2019). Comparative analysis of physiochemical properties of physically activated carbon from palm bio-waste. *Journal of Materials Research and Technology*, 8(5), 3688-3695. <https://doi.org/10.1016/j.jmrt.2019.06.015>
- Tounsadi, H., Khalidi, A., Farnane, M., Abdennouri, M., & Barka, N. (2016). Experimental design for the optimization of preparation conditions of highly efficient activated carbon from *Glebionis coronaria* L.

- and heavy metals removal ability. *Process Safety and Environmental Protection*, 102, 710-723. <https://doi.org/https://doi.org/10.1016/j.psep.2016.05.017>
- Tsang, C. H. A., Huang, H., Xuan, J., Wang, H., & Leung, D. Y. C. (2020). Graphene materials in green energy applications: Recent development and future perspective. *Renewable and Sustainable Energy Reviews*, 120, Article 109656. <https://doi.org/https://doi.org/10.1016/j.rser.2019.109656>
- Wei, H., Wang, H., Li, A., Li, H., Cui, D., Dong, M., Lin, J., Fan, J., Zhang, J., Hou, H., Shi, Y., Zhou, D., & Guo, Z. (2019). Advanced porous hierarchical activated carbon derived from agricultural wastes toward high performance supercapacitors. *Journal of Alloys and Compounds*, 820, Article 153111. <https://doi.org/10.1016/j.jallcom.2019.153111>
- Wu, F., Gao, J., Zhai, X., Xie, M., Sun, Y., Kang, H., Tian, Q., & Qiu, H. (2019). Hierarchical porous carbon microrods derived from albizia flowers for high performance supercapacitors. *Carbon*, 147, 242-251. <https://doi.org/10.1016/j.carbon.2019.02.072>
- Wu, M. B., Li, R. C., He, X. J., Zhang, H. B., Sui, W. B., & Tan, M. H. (2015). Microwave-assisted preparation of peanut shell-based activated carbons and their use in electrochemical capacitors. *Xinxing Tan Cailiao/ New Carbon Materials*, 30(1), 86-91. [https://doi.org/10.1016/S1872-5805\(15\)60178-0](https://doi.org/10.1016/S1872-5805(15)60178-0)
- Xiong, G., Meng, C., Reifengerger, R. G., Irazoqui, P. P., & Fisher, T. S. (2014). A review of graphene-based electrochemical microsupercapacitors. *Electroanalysis*, 26(1), 30-51. <https://doi.org/10.1002/elan.201300238>
- Xu, J., Gao, Q., Zhang, Y., Tan, Y., Tian, W., Zhu, L., & Jiang, L. (2014). Preparing two-dimensional microporous carbon from Pistachio nutshell with high areal capacitance as supercapacitor. *Scientific Reports*, 4, Article 5545. <https://doi.org/10.1038/srep05545>
- Yakout, S. M., & Sharaf El-Deen, G. (2016). Characterization of activated carbon prepared by phosphoric acid activation of olive stones. *Arabian Journal of Chemistry*, 9, S1155-S1162. <https://doi.org/https://doi.org/10.1016/j.arabjc.2011.12.002>
- Yao, F., Pham, D. T., & Lee, Y. H. (2015). Carbon-based materials for lithium-ion batteries, electrochemical capacitors, and their hybrid devices. *ChemSusChem*, 8(14), 2284-2311. <https://doi.org/https://doi.org/10.1002/cssc.201403490>
- Yar, A., Dennis, J. O., Saheed, M. S. M., Mohamed, N. M., Irshad, M. I., Mumtaz, A., & Jose, R. (2020). Physical reduction of graphene oxide for supercapacitive charge storage. *Journal of Alloys and Compounds*, 822, Article 153636. <https://doi.org/https://doi.org/10.1016/j.jallcom.2019.153636>
- Yu, L. J., Rengasamy, K., Lim, K. Y., Tan, L. S., Tarawneh, M., Zulkoffli, Z. B., & Yong, E. N. S. (2019). Comparison of activated carbon and zeolites' filtering efficiency in freshwater. *Journal of Environmental Chemical Engineering*, 7(4), Article 103223. <https://doi.org/10.1016/j.jece.2019.103223>
- Zequine, C., Ranaweera, C. K., Wang, Z., Dvornic, P. R., Kahol, P. K., Singh, S., Tripathi, P., Srivastava, O. N., Singh, S., Gupta, B. K., Gupta, G., & Gupta, R. K. (2017). High-performance flexible supercapacitors obtained via recycled jute: Bio-waste to energy storage approach. *Scientific Reports*, 7(1), 1-12. <https://doi.org/10.1038/s41598-017-01319-w>

- Zhang, Y., Song, X., Xu, Y., Shen, H., Kong, X., & Xu, H. (2019). Utilization of wheat bran for producing activated carbon with high specific surface area via NaOH activation using industrial furnace. *Journal of Cleaner Production*, *210*, 366-375. <https://doi.org/https://doi.org/10.1016/j.jclepro.2018.11.041>
- Zhang, Z. P., Rong, M. Z., Zhang, M. Q., & Yuan, C. (2013). Alkoxyamine with reduced homolysis temperature and its application in repeated autonomous self-healing of stiff polymers. *Polymer Chemistry*, *4*(17), 4648-4654. <https://doi.org/10.1039/C3PY00679D>
- Zhu, Z., Liu, Y., Ju, Z., Luo, J., Sheng, O., Nai, J., Liu, T., Zhou, Y., Wang, Y., & Tao, X. (2019). Synthesis of diverse green carbon nanomaterials through fully utilizing biomass carbon source assisted by KOH. *ACS Applied Materials & Interfaces*, *11*(27), 24205-24211. <https://doi.org/10.1021/acsami.9b08420>



## Esterification of Free Fatty Acid in Palm Oil Mill Effluent using Sulfated Carbon-Zeolite Composite Catalyst

Hasanudin Hasanudin<sup>1\*</sup>, Qodria Utami Putri<sup>1</sup>, Tuty Emilia Agustina<sup>2</sup> and Fitri Hadiah<sup>2</sup>

<sup>1</sup>Department of Chemistry, Universitas Sriwijaya, Palembang, 30662 Indonesia

<sup>2</sup>Department of Chemical Engineering, Universitas Sriwijaya, Palembang, 30662 Indonesia

### ABSTRACT

Free fatty acid esterification (FFA) in palm oil mill effluent (POME) was carried out using a sulfonated carbon-zeolite composite catalyst. The catalyst is synthesized with carbon precursor obtained from molasses, which is adsorbed on the surface of the zeolite and then carbonized and sulfonated with concentrated H<sub>2</sub>SO<sub>4</sub> to form a sulfonated carbon-zeolite catalyst composite, which will be used for the esterification catalyst and the optimization process for the esterification reaction is carried out using the response surface methodology (RSM) and experimental central composite design (CCD). Importantly, the observed independent variables were temperature, catalyst weight, and reaction time to produce fatty acid methyl ester (FAME) products. The catalyst was successfully synthesized, which was shown from the SEM characterization strengthened by the presence of a sulfate group in the FTIR results and the calculation results of high acidity properties. Optimization of FFA esterification with SCZ catalyst obtained optimal conditions with a temperature of 79°C, a catalyst weight of 3.00 g, and a reaction time of 134 minutes with a FAME product of 93.75%, considering that the viscosity of biodiesel is below that required by the API.

*Keywords:* Biodiesel, esterification, palm oil mill effluent, sulfonated carbon

### ARTICLE INFO

*Article history:*

Received: 12 May 2021

Accepted: 15 September 2021

Published: 04 Januari 2022

DOI: <https://doi.org/10.47836/pjst.30.1.21>

*E-mail addresses:*

Hasanudin@mipa.unsri.ac.id; Hasanudinkf@gmail.com

(Hasanudin Hasanudin)

qodriaria@gmail.com (Qodria Utami Putri)

tuty\_agustina@unsri.ac.id (Tuty Emilia Agustina)

fitrihadiah@ft.unsri.ac.id (Fitri Hadiah)

\* Corresponding author

### INTRODUCTION

The crude palm oil (CPO) industry generates a large quantity of liquid waste in the form of POME, available in large quantities with a high content FFA (Hasanudin et al., 2012). It has the potential to be converted to biodiesel through esterification with alcohol. However, the high FFA in POME cannot be processed using a base catalyst

since it reacts to produce soap and might complicate the process of separating esters from glycerol (Aboelazayem et al., 2019; de Jesus et al., 2018). To solve this problem, some researchers use homogeneous acid catalysts for the production of biodiesel derived from ingredients with high FFA content (Encinar et al., 2011; Gebremariam & Marchetti, 2018a). The homogeneous catalysts, such as acids and alkaline homogeneous, can be used in free fatty acid esterification reactions like KOH, NaOH, and H<sub>2</sub>SO<sub>4</sub> (Borugadda & Goud, 2012). However, these alternatives have many drawbacks, such as being economically inefficient, resulting in corrosion of equipment and reactors as well as damaging machinery (Gebremariam & Marchetti, 2018b; Marchetti et al., 2008; Encinar et al., 2011).

Homogeneous acid catalysts can be modified into solid acid catalysts. For example, although the sulfuric acid catalyst is a homogeneous catalyst commonly used to catalyze esterification reactions, sulfuric acid catalysts can also be applied to solids, such as carbon (Mardhiah et al., 2017; Lathiya et al., 2018; Farabi et al., 2019), zeolite (Cheng et al., 2019), resin (Trombettoni et al., 2018; Ma et al., 2015), silica (Hasan et al., 2015) and several other metals including zirconia (Luo et al., 2017) and niobium (Celdeira et al., 2014). In addition, solid acid catalysts have more advantages compared to homogeneous alternatives, such as sulfuric acid. For instance, they do not cause corrosion, withstand high temperatures and pressures, are easily recycled, have a large surface area, and easily separate after the product is formed (Gebremariam & Marchetti, 2018b).

Sulfonated carbon catalyst is used for the production of biodiesel from raw materials with high FFA content, such as palm oil distilled (Farabi et al., 2019; Sangar et al., 2019), and waste cooking oil (Vargas et al., 2019; Maneechakr et al., 2020; Nata et al., 2017). However, it has disadvantages, such as low density, which is difficult to disperse in batch reaction systems (Liu et al., 2010). The sulfonated carbon is applied to the supporting solids, such as silica, to show the excellent catalyst performance (Liu et al., 2010; Wilson & Lee, 2012; Melero et., 2009).

Zeolite is one of the silica compounds that have the potential to be developed as a supporting part of sulfonated carbon. The selection of zeolite to be used as solid support catalyzes chemical reactions because its nature as an acidic solid has a porous crystal structure, large surface area, and good acidity value (Marchetti & Errazu, 2008). Also, it is quite profitable due to its abundant amount and relatively low price, which reduces production costs.

The carbon source embedded in the zeolite solid must be soluble and absorbed on its surface. A cheap and sufficient carbon source is molasses with carbon in the form of dissolved sugars by 50–70%. Therefore, it has the potential to produce strong carbon material. Besides, the disulfonated was carried out to produce stable solids with a large active site, which is referred to as sulfonated carbon (Liu et al., 2010). It is sourced from molasses embedded in zeolites and might be a catalyst material for FFA esterification.

The purpose of this study was to examine the performance of zeolite-sulfonate carbon composite catalysts through esterification reactions with FFA from POME and methanol. The research used an experimental FFA esterification reaction from POME with CCD. This approach shortens the optimization time by reducing the combination variation of independent variables used. Some independent variables, such as temperature, catalyst weight, and reaction time, were used. The processing of response variables, such as FAME yield, acid number, and viscosity, used statistical methods, such as RSM, to obtain the relationship between these responses and the independent variables used in esterification. This method helps determine the optimum conditions due to the simultaneously changed variables used.

## MATERIALS AND METHODOLOGY

### Materials

The apparatus used in this study include analytical balances, hot plates, centrifuges, sets of reflux tools, glass bikers, measuring cups, volume pipettes, drip pipettes, Erlenmeyer 250 mL, burettes, boiling flasks, magnetic stirrers, pycnometers, viscometers, water baths, thermometers, split funnels, stopwatches. The materials used in this study include palm oil waste, Sodium Hydroxide, Methanol p.a, Phenolphthalein Indicator, Akuades, Oxalic Acid, The natural zeolite (Z) clinoptilolite with crystallographic unit cell  $K_{5.17}Mg_{0.16}(Al_6Si_{30}O_{72}) \cdot 24H_2O$  (Suminta & Las, 2018) obtained from Bayah, sulfuric acid, HCl and for the characterization catalyst we used FTIR, SEM, and the acidity analysis.

### Preparation of Sulfonated Carbon-zeolite Composite Catalyst

The natural zeolite (Z) *clinoptilolite* with crystallographic unit cell  $K_{5.17}Mg_{0.16}(Al_6Si_{30}O_{72}) \cdot 24H_2O$  (Suminta & Las, 2018) obtained from Bayah was used. It was pureed and sieved with a size of 200 mesh and soaked with 1.0 M sulfuric acid for two h, then washed with distilled water until it was neutral. Ten grams of pure natural zeolite, which has been smooth and clean, is dispersed into 100 mL of 30% molasses at 80°C while stirring to form a paste. The formed paste is roasted at 120°C to form caramel, then mashed and carbonated for 30 minutes at temperatures between 350°C with  $N_2$  gas. The carbonization results are referred to as Carbon-Zeolite (CZ) composites.

The resulting CZ composite added 50.0 mL of concentrated  $H_2SO_4$  was refluxed at 175°C for 15h and washed with 80°C demineralized water until the filtrate had a neutral pH. The mixture was then centrifuged and dried at 120°C for 24 h. The result is referred to as sulfonated carbon-zeolite (SCZ) composite catalysts and is characterized by the SEM, FTIR, and acidity properties of the catalyst.

### **The Characterization Catalyst with SEM**

SEM was used to determine the structure and shape of the catalyst surface, while to analyze the catalyst using SEM, the catalyst was dried using the oven at 110°C for 4 hours. Then the bentonite was mashed and sifted with a 200-mesh sieve. Finally, the SEM was operated at a voltage of 20 kV (Meçabih, 2016).

### **The Characterization Catalyst with FT-IR**

FT-IR spectrophotometers can analyze the functional groups contained in sulfonated carbon-zeolite composite catalysts with the working principle of vibration of their atoms. For analysis of spectrophotometer, FT-IR sulfonated carbon-zeolite composite catalyst as much as 1 mg each and mixed with 100 mg KBr and then made pellets. Measurements were performed on wave numbers 400 to 4000  $\text{cm}^{-1}$  using the Shimadzu FTIR 8201 infrared spectrophotometer (Ravindra et al., 2013).

### **The Acidity Test of the Sulfonated Carbon-zeolite Composite Catalyst**

One gram of SCZ composite catalyst was immersed in 100 mL 0.5 N NaOH for four h while stirring continuously. The mixture was filtered, and 5.0 mL was taken, and added phenolphthalein indicator before titrating with 0.5 N HCl. The amount of Arrhenius acid site as sulfonate in the catalyst was calculated from the NaOH reacting with the sulfonate group on SCZ. Calculation of the acidity test using the formula below:

$$\text{Total acidity} = m_{\text{NaOH}(a)} - m_{\text{NaOH}(b)}$$

Note:

$m_{\text{NaOH}(a)}$ : initial of mol NaOH

$m_{\text{NaOH}(b)}$ : final of mol NaOH

### **FFA Esterification from POME**

The esterification reaction was carried out using a 250 mL boiling flask equipped with a reflux device. First, 25 g of oil from POME was added to 80 mL methanol, followed by an SCZ catalyst. The process was carried out based on three variables, including temperature, catalyst weight, and reaction time. Next, the resulting product in the form of FAME is separated from the catalyst and water formed by a separating funnel. Afterward, the FAME yield, acid number (by the AOCS Official Method Cd 3d-63), and kinematic viscosity at 40°C (by the ASTM D2270-10 method) were analyzed.

## Experimental Design and Modeling

The experimental design is carried out using the CCD. Three variables that influence the process of FFA esterification with methanol using a catalyst SCZ were observed, namely the temperature, the catalyst weight, and reaction time. The three-factor design is carried out at three levels and dimensionless coded with values -1 (lowest level), 0 (middle level), and +1 (highest level). The variable dimensionless code for temperature, catalyst weight, and reaction time, respectively  $x_1$ ,  $x_2$ , and  $x_3$ , make the same intervals of all variables, making the calculations easier. The second phase experiment with CCD design uses three independent variables, and the rotatability value is:  $(3^2)^{1/4} = 1.7$ . Therefore, value  $\pm 1.7$  includes the value used for coding. The encoding value of the independent variable is calculated using Equations 1-3:

$$x_1 = \frac{\eta_1 - 80^\circ\text{C}}{10^\circ\text{C}} \quad (1)$$

$$x_3 = \frac{\eta_3 - 2.0 \text{ g}}{1.0 \text{ g}} \quad (2)$$

$$x_2 = \frac{\eta_2 - 120 \text{ min}}{30 \text{ min}} \quad (3)$$

Where  $\eta_1$ ,  $\eta_2$  and  $\eta_3$  are the actual temperature values, catalyst weight, and reaction time variables. Based on the Equations 1-3, the coding values for the independent variables ( $x_1$ ,  $x_2$  dan  $x_3$ ) are shown in Table 1. After coding, the experimental design using the CCD method is displayed in Table 2.

The experimental design was carried out with 20 run tests, as shown in Table 2. Afterward, each response variable, including FAME yield ( $y_1$ ), acid number ( $y_2$ ), and kinematic viscosity at 40°C ( $y_3$ ), were obtained. Finally, the optimization model was calculated using MATLAB R2018b in the form of a quadratic polynomial model to determine the interrelationship between the independent variables ( $x_1$ ,  $x_2$ , and  $x_3$ ) formulated in Equation 4.

$$\hat{y} = \beta_0 + \sum_{i=1}^k \hat{\beta}_i X_i + \sum_{i=1}^k \hat{\beta}_{ii} X_i^2 + \sum_{i=1}^k \sum_{j=1}^k \hat{\beta}_{ij} X_i X_j, i > j \quad (4)$$

Table 1  
Variable values and codings

Independent Variable	Unit	Value				
Coding	-	-1.7	-1	0	+1	+1.7
Temperature	°C	63	70	80	90	97
catalyst weight	g	0.3	1.0	2.0	3.0	3.7
Reaction time	minutes	69	90	120	150	171

Table 2  
CCD with three variables

Run	Temperature		catalyst weight		Reaction time	
	Actual (°C)	Code (x <sub>1</sub> )	Actual (g)	Code (x <sub>2</sub> )	Actual (minutes)	Code (x <sub>3</sub> )
1	90	+1	3.0	+1	150	+1
2	90	+1	3.0	+1	90	-1
3	90	+1	1.0	-1	150	+1
4	90	+1	1.0	-1	90	-1
5	70	-1	3.0	+1	150	+1
6	70	-1	3.0	+1	90	-1
7	70	-1	1.0	-1	150	+1
8	70	-1	1.0	-1	90	-1
9	97	+1.7	2.0	0	120	0
10	63	-1.7	2.0	0	120	0
11	80	0	3.7	+1.7	120	0
12	80	0	0.3	-1.7	120	0
13	80	0	1.0	0	171	+1.7
14	80	0	1.0	0	69	-1.7
15	80	0	1.0	0	120	0
16	80	0	1.0	0	120	0
17	80	0	1.0	0	120	0
18	80	0	1.0	0	120	0
19	80	0	1.0	0	120	0
20	80	0	1.0	0	120	0

The estimation of calculated parameters is considered significant in case the p-value <0.05, using the F test. To determine the best reaction conditions leading to the maximum, minimum, or target value of the response variable (in the model), using the global optimization method of the continuous desirability function (Derringer & Suich, 1980). It consists of three forms of functions, such as maximum, minimum, and target value. The desirability function for these three optimization goals is formulated in the following Equations 5-7.

$$d_r^{\max} = \begin{cases} 0 & \text{if, } f_r(x) < A \\ \left( \frac{f_r(x) - A}{B - A} \right) & \text{if, } A \leq f_r(x) \leq B \\ 1 & \text{if, } f_r(x) > B \end{cases} \quad (5)$$

$$d_r^{\min} = \begin{cases} 0 & \text{if, } f_r(x) > B \\ \left( \frac{f_r(x) - B}{A - B} \right) & \text{if, } A \leq f_r(x) \leq B \\ 1 & \text{if, } f_r(x) < A \end{cases} \quad (6)$$

$$d_r^{target} = \begin{cases} \left( \frac{f_r(x) - A}{N_t - A} \right) & \text{if, } A \leq f_r(x) \leq N_t \\ \left( \frac{f_r(x) - B}{N_t - B} \right) & \text{if, } N_t \leq f_r(x) \leq B \\ 1 & \text{if, } A \geq f_r(x) \geq N_t, \text{ or, } N_t \leq f_r(x) \geq B \end{cases} \quad (7)$$

The value of  $d_r^{max}$ ,  $d_r^{max}$  and  $d_r^{target}$  represents the individual desirability function of each  $r$  response arising from changes in independent variables  $x_i$  by producing a response of  $f_r(x)$ . The global desirability ( $D_g$ ) might be determined through individual values using Equation 8. The value  $P$  in Equation 8 is the importance of the response tested. Each individual and global desirability has a scale from the most undesirable value of 0 (zero) to the most desirable (one).

$$D_g = [d_1^{p_1} . d_2^{p_2} \dots d_n^{p_n}]^{1/(p_1+p_2+\dots+p_n)} \quad (8)$$

## RESULT AND DISCUSSION

### Catalyst Characterization

The results of the catalyst surface topology Z, CZ, and SCZ using SEM are shown in Figure 1. The SEM image of Z shows the granular surface structure if it is coated with carbon on the CZ composite. In the SEM images of CZ and SCZ, the CZ composites look smoother, and there are holes on the surface shown by the marked red square in Figure 1(b), which are pores of CZ. Furthermore, the SEM image of the SCZ composite shows that the surface shape of the SCZ composite catalyst has changed to become more trough because the structure of the carbon on the surface of the SCZ has been attached by sulfonate functional groups so that the fine structure of the CZ is lost this occurs because the surface of the SCZ catalyst is modified with some occasional cracks associated with partial oxidation, condensation and partial destruction of the porous structure during

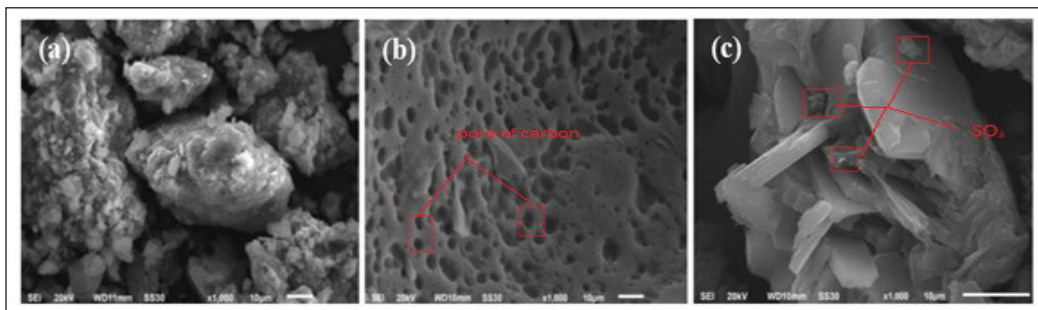


Figure 1. SEM image (a) Z, (b) CZ and (c) SCZ

sulfonation, as reported by Lakhya et al. (2014). Transformation of backbone chemical properties, with a decrease in the number of aliphatic chains, an increase in aromatic rings, and the presence of oxidized groups, obtained after the sulfonation process resulted in a high density of functional groups, such as  $\text{SO}_3\text{H}$ ,  $\text{COOH}$ , and phenolic  $\text{OH}$  groups (Ngaosuwan et al., 2016). Predicted sulfonate atoms to be in Figure 1(c) inside a red square. Prediction of the existence of sulfonate atoms can be determined by comparing images of SEM SCZ results with the results of SEM SCAC (Sulfonate Carbon Active Catalyst) conducted by Ngawosuan et al. (2016).

SCZ identification was also carried out using the FT-IR spectrophotometer to determine the sulfonate functional groups attached to the CZ composite, and the analysis results are shown from the spectrum in Figure 2. According to Xu et al. (2010), the expected absorption of the  $-\text{SO}_3\text{H}$  group was observed in the wave range of  $1037\text{--}1200\text{ cm}^{-1}$ ; the result shows it was seen in the area of  $1080.14\text{ cm}^{-1}$ . The spectrum of the SCZ composite analysis before the sulfonation process contained peaks in the adjacent area of  $1049.28\text{ cm}^{-1}$ , which indicated the C-O vibrational region (Nata et al., 2017). It is due to carbon-based catalysts made through partially carbonized glucose, which form the polycyclic aromatic hydrocarbon compounds with many  $-\text{OH}$  groups. For this reason, no significant difference is seen in the spectrum before and after the sulfonation process in SCZ composites. The second spectrum of the analysis result shows a peak in the vibrational region of  $1635.64$

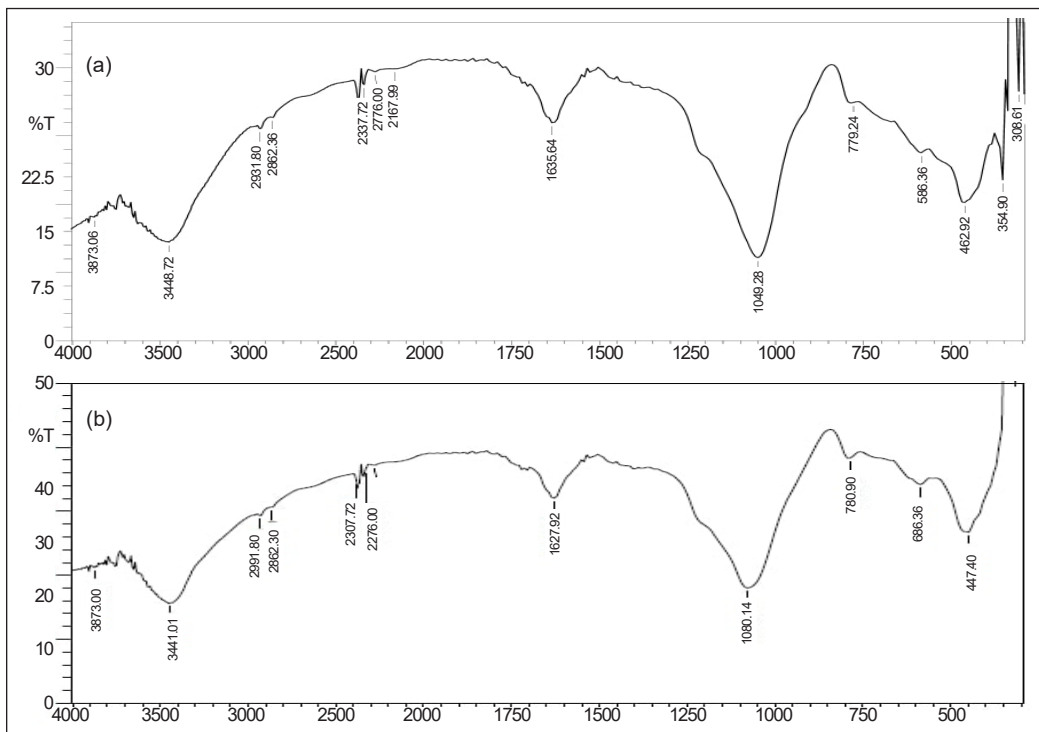


Figure 2. IR Spectrum (a) CZ dan (b) SCZ



$\text{cm}^{-1}$ , which is estimated to be a C=C aromatic region (Mar & Somsook, 2012), and there is also a peak at  $3441.72 \text{ cm}^{-1}$  which is expected for the -OH group. It is confirmed in the spectrum after the sulfonation process produces a peak at  $3441.01 \text{ cm}^{-1}$ , a specific area for free OH. This result was also obtained in the study of Effiyanti et al. (2019).

The acidity test is carried out to determine how much the acidic sites indicate the number of sulfonate groups. It used the acid-base titration with NaOH, which reacts with sulfonate groups on the catalyst, and the results are shown in Table 3. The catalyst acidity of Z, CZ, and SCZ imply SCZ has a much higher acidity,  $9.42 \text{ mmol/g}$ , compared to Z and CZ with  $0.81$  and  $0.57 \text{ mmol/g}$ . It means there is an  $\text{H}^+$  ion on the SCZ catalyst, which reacts with NaOH as the test base reactant. The acidity test results prove SCZ has a better active site than Z and CZ, which is strengthened with FT-IR spectrum data. The  $\text{H}^+$  ions bound to this sulfonate group are expected to act as the active site of the catalyst in the esterification process. It means the SCZ should be used in the next step for the optimization of the esterification process.

Table 3  
*The acidity test of sulfonated carbon-zeolite composite*

No.	Sample	Acidity (mmol/g)
1.	Z	0.81
2.	ZC	0.57
3.	ZSC	9.42

### FAME Identification

The methyl ester product formed from FFA esterification was identified using  $^{13}\text{C}$ -NMR, as evidenced by the formation of the methoxy peak at a shift of  $50\text{-}56 \text{ ppm}$ . The results of the  $^{13}\text{C}$ -NMR analysis of FFA from POME and FAME products are shown in Figure 3. The  $^{13}\text{C}$ -NMR spectrum of FFA from POME not esterified shows the presence of carboxyl groups typical for FFA appearing peak at shift  $180.31 \text{ ppm}$  (Figure 3).

The FAME from the FFA esterification result was also identified by  $^{13}\text{C}$ -NMR spectroscopy and shown in Figure 3. The results obtained in accordance with research conducted by Traiq et al. (2011), shows there is a typical C=O ester, and C-O signal at chemical shifts around  $176 \text{ ppm}$  and  $50.42 \text{ ppm}$  is slightly shifted from the results obtained by Tariq et al., where C carbonyl ester and C-O was identified at  $174.26 \text{ ppm}$  and  $51 \text{ ppm}$ . Tariq et al. get the unsaturation in methyl esters indicated at the peaks around  $131.88$  and  $127.08 \text{ ppm}$ , and on this research, unsaturation in methyl esters indicated at the peaks around  $130.08$  and  $127.92 \text{ ppm}$ . Also, a chemical shift around  $180.31 \text{ ppm}$  does not show the FAME, which indicates an esterification reaction occurs, and the carboxyl group from FFA changes into a FAME product. It is also characterized by the appearance of a C-methoxy signal, which is a typical carbon in the ester with a chemical shift of  $51.45 \text{ ppm}$  (Di Pietro et al., 2020).

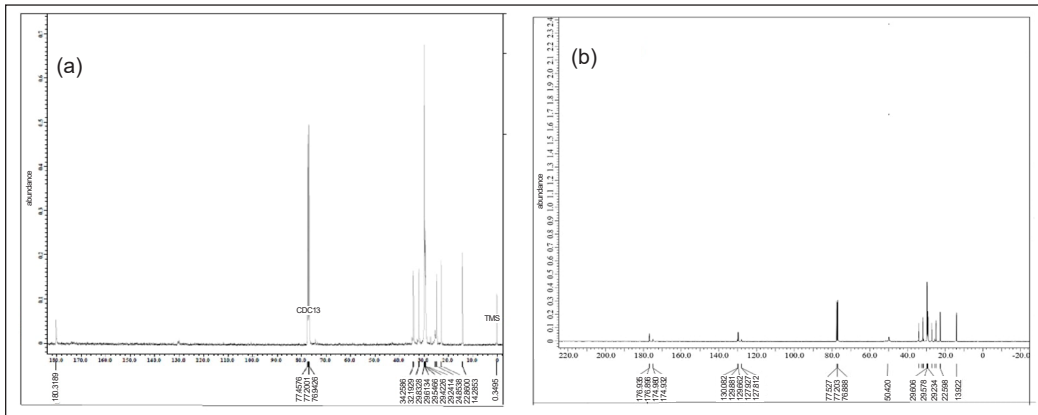


Figure 3. <sup>13</sup>C-NMR of (a) POME and (b) FAME

### Optimization Process

The process of esterifying free fatty acids in POME into methyl ester fatty acids using Composite Sulfonated Carbon Zeolite catalyst is influenced by temperature, reaction time, and weight catalyst. The reaction between the catalyst and FFA in POME with methanol assisted by composite sulfonated carbon zeolite catalyst to produce methyl ester fatty acids (FAME) can be seen in Figure 4. The protonation of the carbonyl group leads to the carbocation, and after the nucleophilic attack of the methanol molecule, a tetrahedral intermediate was generated, which formed the FAME. The catalyst has an active site that is atom hydrogen from -SO<sub>3</sub>H. The hydrogen atom, as a Lewis acid, binds with the FFA, which then weakens the carbonyl bond and makes lower energy activation (Li et al., 2012).

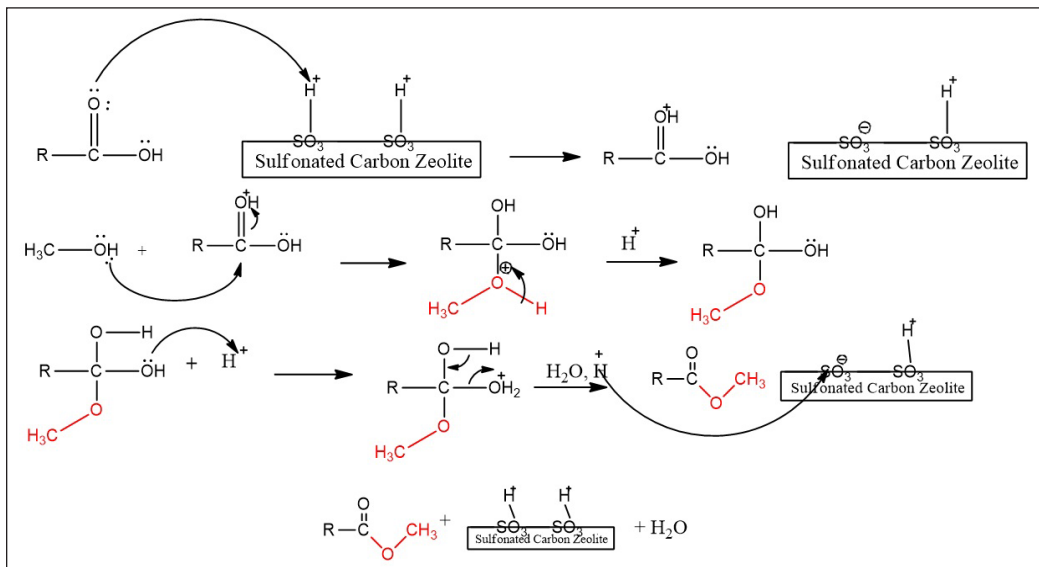


Figure 4. Mechanism of esterification FFA onto sulfonated carbon zeolite catalyst

The FAME product produced from the FFA esterification with CCD for the three independent variables shows the effect on the FAME product. The processing of experimental data with MATLAB R2018b software produces a prediction model equation for the FAME yield response to the treatment of the independent variables of temperature, catalyst weight, and reaction time. The relationship of the three independent variables to the FAME yield response is shown in Figure 5, while the model formulation is in Equation 9.

$$y_1 = 89.64 - 0.46(x_1) + 7.63(x_2) + 2.20(x_3) + 0.66(x_1 \cdot x_2) - 1.50(x_1 \cdot x_3) + 0.78(x_2 \cdot x_3) - 2.30(x_1^2) - 4.15(x_2^2) - 3.60(x_3^2) \quad (9)$$

An analysis of variance shows  $F_{\text{count}} = 10.16$ , while  $F_{\text{table}(9;19;0.05)} = 2.42$ . Since  $F_{\text{count}} > F_{\text{table}}$ , the independent variables make a significant contribution to the model, which shows it affected the optimization model in Equation 9, and therefore, the predicted model should be accepted. Each independent variable affects the FAME yield response, which is shown in the mathematical model obtained.

Furthermore, the catalyst weight and reaction time positively affected the FAME attained. The temperature has a negative effect, but if it is combined with the catalyst weight and reaction time, it has a positive effect. The use of temperatures above the boiling point of the reactants, that is, methanol, in 64.5°C (Gafar, 2012), causes a decrease in FAME yield. The reactants changed to the gas phase, which reduces the reaction between reactants and fatty acids. The amount of FAME yield also increases with the addition of catalyst and reaction time. Nevertheless, the excess catalyst and long reaction time reduce the amount of the products due to the equilibrium and the change in variable conditions,

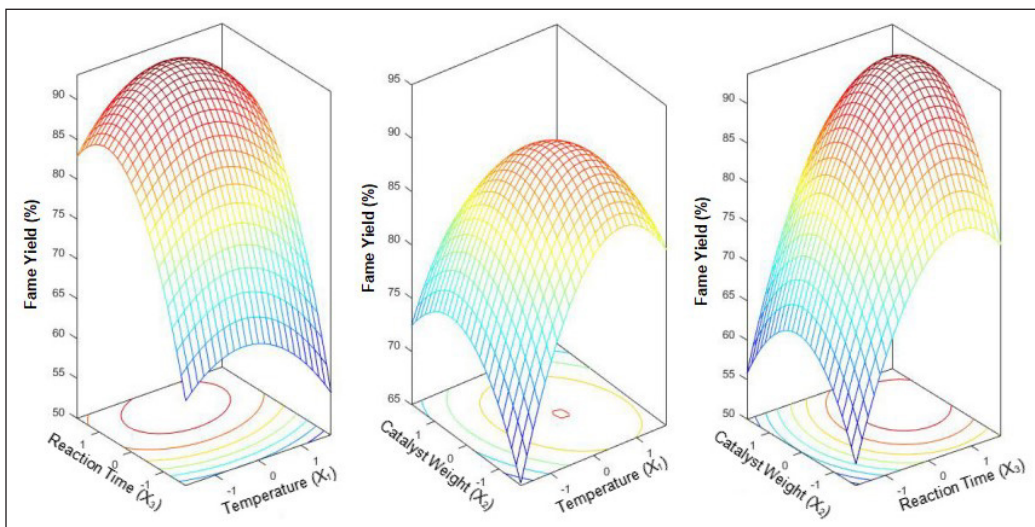


Figure 5. The relationship of the three independent variables to the FAME yield response

which simultaneously causes the reaction to shift toward the reactants side. The optimum conditions for the FAME yield were obtained at a temperature of 79°C, the catalyst weight of 3.00 g, and a reaction time of 134 minutes with the FAME yield of 93.75%. The weight of the catalyst used to get the optimum FAME result is 3.00 g of this result in accordance with the results obtained by Irawati et al. (2019), but the production of methyl ester that Irawati did use palm olein. The optimum temperature and reaction time obtained is close to the results obtained by William et al. (2016), which is 60°C for 3 hours made from distillate palm fatty acids. Optimization of esterification reactions shows that POME esterification reactions are catalyzed by SCZ catalysts at less high temperatures and a period of 120–150 minutes. It happens because the reaction that runs below or above the optimum point of the reaction of the collision theory between molecules will disappear caused by the reactants made less has been converted into products resulting in a small product yield marked by a decreased graph (Ofiofule et al., 2019).

The acid number analyzed the FAME products formed through titration. The smaller the acid number, the higher the quality of the FAME produced. In general, the acid number is the KOH (mg) weight needed to neutralize the FFA contained in one gram of the sample. Additionally, the analysis results with CCD and data processing using the MATLAB 2018b software indicated the effect of the independent variables on the acid numbers, as shown in Figure 6. The optimum conditions were obtained at 79°C, 3.00 g of catalyst, and a reaction time of 134 minutes with acid number 11.66. The results of these observations indicate that there are similarities in the optimum conditions achieved in acid numbers and FAME yield calculations.

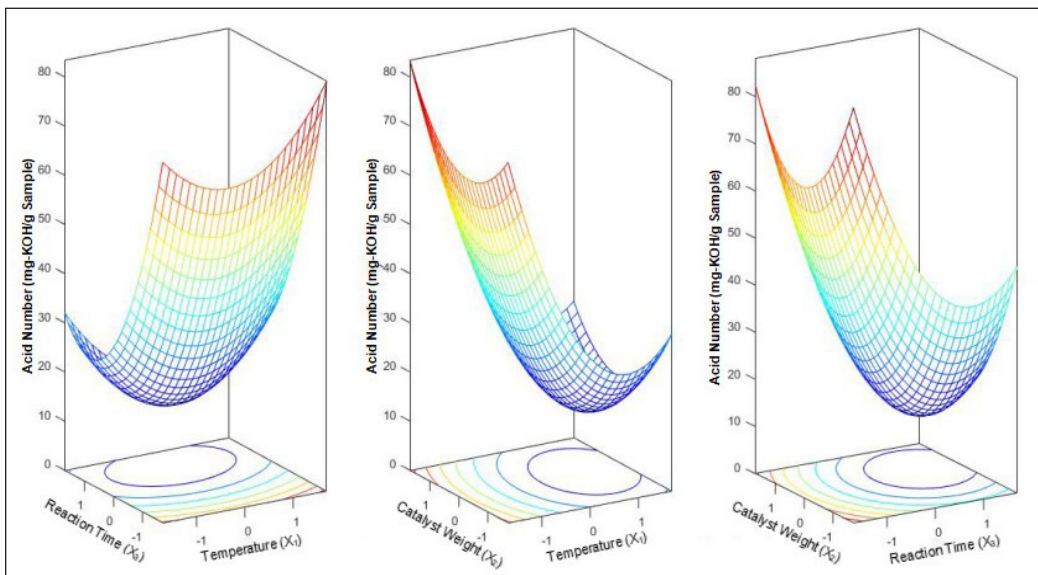


Figure 6. The relationship of the three independent variables to the acid number response

ANOVA analysis results for the model given in Equation 10 show  $F_{\text{count}} = 10.16$ , while  $F_{\text{table}}(9;19;0.05) = 2.42$ . Since  $F_{\text{count}} > F_{\text{table}}$ , the independent variable contributes significantly to the model, influencing the prediction model in Equation 10. Each independent variable affects the response of the acid number of the reaction results shown in the mathematical model obtained.

$$y_2 = 19.35 + 0.85(x_1) - 14.25(x_2) - 4.11(x_3) - 1.24(x_1 \cdot x_2) + 2.80(x_1 \cdot x_3) - 1.46(x_2 \cdot x_3) + 4.30(x_1^2) + 7.76(x_2^2) + 6.73(x_3^2) \quad (10)$$

The viscosity of the FAME produced also influences the quality of FAME as biodiesel fuel. Based on American Petroleum Institute (API), good quality biodiesel is biodiesel, which has a kinematic viscosity at 40°C in the range of values from 2.3 to 6.0 cSt, so optimization is set with the target value in the form of the middle value of viscosity, which is 4.15 cSt. Data was obtained from research with CCD to determine the effect of each process variable on the FAME viscosity response observed. The data processing results of the independent variables studied include temperature, catalyst weight, and reaction time for the FAME viscosity response shown in Figure 7 and the prediction model illustrated in Equation 11.

$$y_3 = 5.43 - 0.76(x_1) - 0.70(x_2) - 0.17(x_3) - 0.25(x_1 \cdot x_2) - 0.21(x_1 \cdot x_3) - 0.25(x_2 \cdot x_3) - 0.18(x_1^2) - 0.25(x_2^2) - 0.35(x_3^2) \quad (11)$$

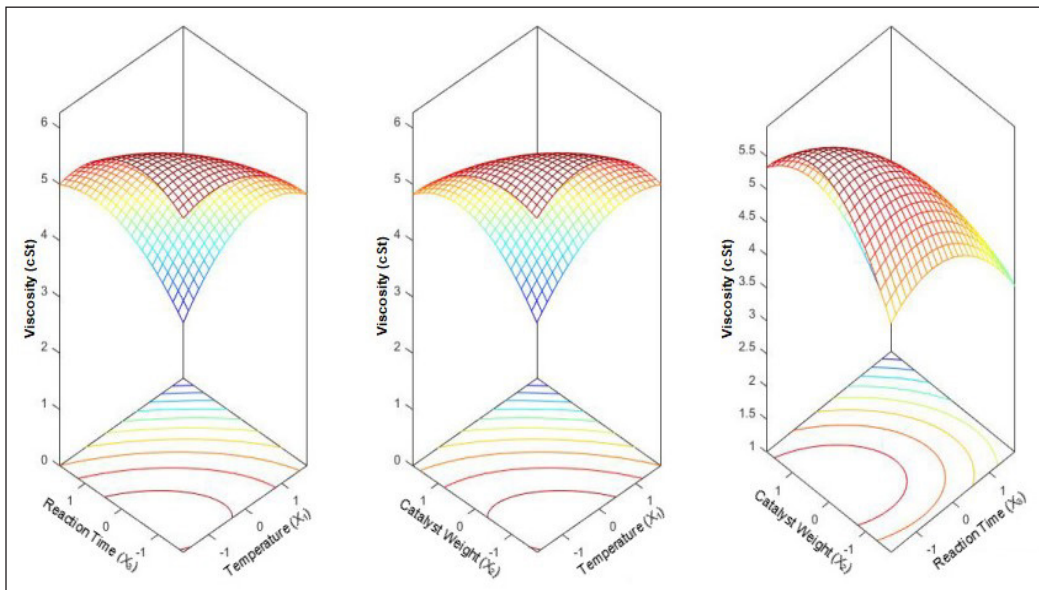


Figure 7. The relationship of the three independent variables to the FAME yield response

The analysis of variance showed  $F_{count} = 18.12$ , while  $F_{table(9; 19; 0.05)} = 2.42$ . Since the  $F_{count} > F_{table}$ , the independent variables significantly influence the model. It shows that the mathematical model obtained should be accepted in explaining the relationship of the independent variables with the FAME viscosity. The optimum conditions for the FAME viscosity include a temperature of 73°C, a catalyst amount of 3.14 g, and a reaction time of 123 minutes with the resulting FAME viscosity of 4.98 cSt.

### Validation of Prediction Model

From the prediction models generated for the four response variables, it is possible to calculate the value of the response variable from each of the experimental conditions. The response obtained from the experimental results and the calculations using the Equations 9-11 are shown in Table 4. The data in Table 4 are then plotted to respond to the experimental results with the model for validation. It is meant to strengthen the mathematical model obtained.

Table 4  
The result of response variables obtained experimentally and model

Run	FAME Product (%)		Acid Number (mg-KOH/g)		Viscosity (cSt)	
	Experiment	Model	Experiment	Model	Experiment	Model
1	88.02	88.89	22.37	20.73	2.39	2.32
2	86.03	85.93	26.09	26.27	3.46	3.57
3	70.29	70.75	55.49	54.63	4.66	4.71
4	71.83	70.91	52.61	54.32	4.69	4.98
5	90.05	91.48	18.58	15.90	4.99	4.77
6	82.46	82.52	32.76	32.65	5.17	5.18
7	75.37	75.99	46.01	44.85	6.21	6.16
8	70.50	70.15	55.09	55.76	5.46	5.60
9	82.14	82.20	33.36	33.23	3.83	3.61
10	84.54	83.76	28.87	30.34	6.05	6.21
11	91.68	90.60	15.54	17.54	3.38	3.53
12	64.31	64.67	66.66	65.99	6.12	5.91
13	84.71	82.97	28.56	31.81	3.93	4.15
14	74.46	75.48	47.71	45.79	5.01	4.73
15	89.96	89.64	18.75	19.35	5.41	5.44
16	89.78	89.64	19.09	19.35	5.48	5.44
17	89.47	89.64	19.67	19.35	5.43	5.44
18	89.37	89.64	19.85	19.35	5.44	5.44
19	89.53	89.64	19.55	19.35	5.39	5.44
20	89.49	89.64	19.86	19.35	5.44	5.44

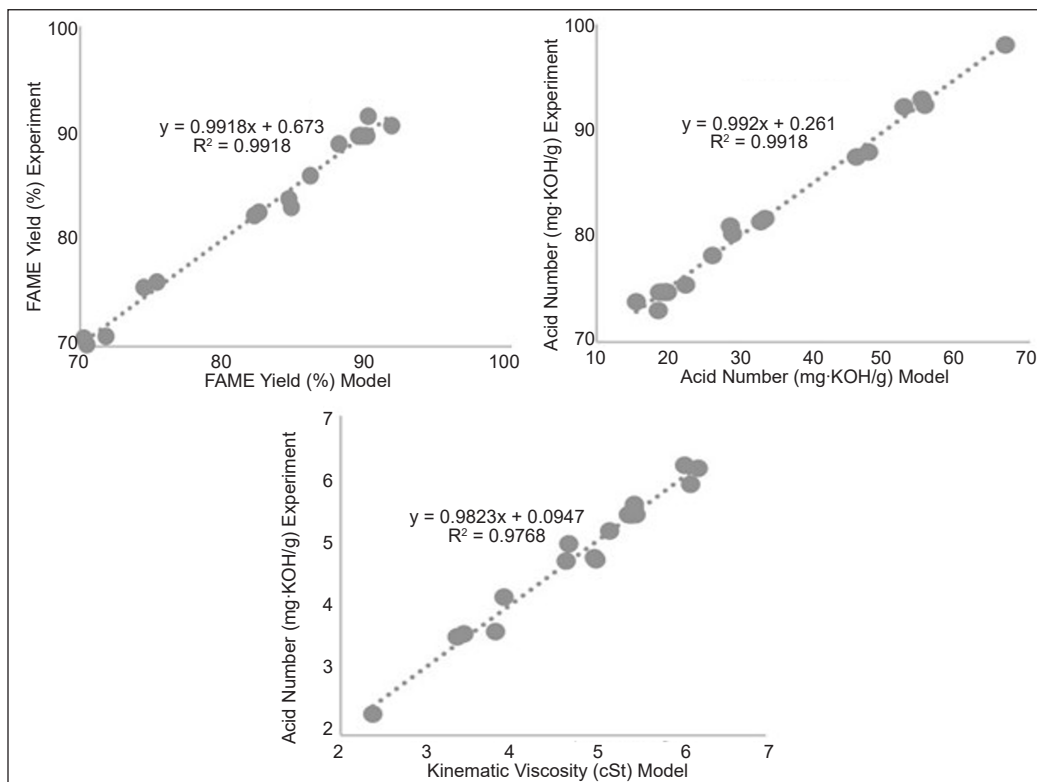


Figure 8. Plotting of response variables based on experimental data and models

Figure 8 shows the regression values for plotting each response variable from experimental data on the calculation of the FAME yield model, acid number, and viscosity, respectively 0.9918, 0.9918, and 0.9768. The regression value obtained is close to 1, and there is a match between the experimental and the model value. Therefore, the model validation results have the potential to predict the FAME yield, acid number, and kinematic viscosity, and the equation is declared useable to predict the response variable.

### The Optimum Conditions Selection using the Desirability Function

The esterification process with temperature, catalyst weight, and reaction time were carried out simultaneously. The determination of the optimum point of FFA to FAME uses the desirability function since it is very compatible with the simultaneous optimization process (Derringer & Suich, 1980). This method uses the maximum function (Equation 5), the target value (Equation 6), and the minimum value (Equation 7). The FAME product reacts as the maximum function, the acid number as the minimum function, and viscosity as the target value function responses. The desirability function for the four optimization objectives is each formulated in Equations 5-7. The results are shown in Table 5.

Table 5  
*The optimum condition desirability test results based on the most desired priorities order*

Optimum condition	Response	Value	Individual desirability	Global desirability
I	FAME yield	93.75	1	0.985
	Acid number	11.66	1	
	Viscosity	4.33	91.26	
II	FAME yield	92.52	94.80	0.967
	Acid number	13.96	94.80	
	Viscosity	4.15	1	

The result of  $D_g$  analysis using Equation 8 shows the optimum condition with the highest value is I with a  $D_g$  of 0.98. Furthermore, the ideal conditions for the FFA esterification process were carried out at 79°C, 3.00 g catalyst, and the reaction time 134 minutes. The esterification under these conditions produces a conversion of 93.75%, the acid number, and the viscosity of 11.66 mg-KOH/g and 4.98 cSt, respectively.

## CONCLUSION

The research results on the manufacture of composite sulfonated carbon zeolite catalysts were successfully conducted, which is shown from the characterization of SCZ catalysts. The characterization of SEM catalyst composite sulfonated carbon zeolite indicates that sulfonated carbon has coated the surface of the zeolites, which is supported by the FT-IR characterization that indicates the presence of sulfonate groups at a wave count of 1080.14  $\text{cm}^{-1}$ . It is also reinforced by the results of calculating high acidity properties of 9.4 mmol /g. Catalyst composite sulfonated carbon zeolite has been applied to the esterification of FFA in POME to produce FAME by using three free variables, namely temperature, weight catalyst, and reaction time and optimization. FFA esterification optimization with SCZ catalysts gets optimal conditions with a temperature of 79°C, catalyst weight of 3.00 g, and a reaction time of 134 minutes with FAME products of 93.75%, given the properties below biodiesel viscosity required by API.

## ACKNOWLEDGMENT

This work was supported by the Ministry of Research, Technology, and Higher Education of the Republic of Indonesia under the Consortium Research Grant of 2020.

## REFERENCES

- Aboelazayem, O., Gadalla, M., & Saha, B. (2019). Derivatisation-free characterisation and supercritical conversion of free fatty acids into biodiesel from high acid value waste cooking oil. *Renewable Energy*, 143, 77-90. <https://doi.org/10.1016/j.renene.2019.04.106>.



- Borugadda, V. B., & Goud, V. V. (2012). Biodiesel production from renewable feedstocks: Status and opportunities. *Renewable and Sustainable Energy Reviews*, *16*(7), 4763-4784. <https://doi.org/10.1016/j.rser.2012.04.010>
- Celdeira, P. A., Gonçalves, M., Figueiredo, F. C. A., Bosco, S. M. D., Mandelli, D., & Carvalho, W. A. (2014). Sulfonated niobia and pillared clay as catalysts in etherification reaction of glycerol. *Applied Catalysis A: General*, *478*, 98-106. <https://doi.org/10.1016/j.apcata.2014.03.037>
- Cheng, J., Zhang, Z., Zhang, X., Liu, J., Zhou, J., & Cen, K. (2019). Sulfonated mesoporous Y zeolite with nickel to catalyze hydrocracking of microalgae biodiesel into jet fuel range hydrocarbons. *International Journal of Hydrogen Energy*, *44*(3), 1650-1658. <https://doi.org/10.1016/j.ijhydene.2018.11.110>
- de Jesus, A. A., de Santana Souza, D. F., de Oliveira, J. A., de Deus, M. S., da Silva, M. G., Franceschi, E., da Silva Egues, S. M., & Dariva, C. (2018). Mathematical modeling and experimental esterification at supercritical conditions for biodiesel production in a tubular reactor. *Energy Conversion and Management*, *171*(April), 1697-1703. <https://doi.org/10.1016/j.enconman.2018.06.108>
- Derringer, G., & Suich, R. (1980). Simultaneous optimization of several response variables. *Journal of Quality Technology*, *12*(4), 214-219. <https://doi.org/10.1080/00224065.1980.11980968>
- Di Pietro, M. E., Mannu, A., & Mele, A. (2020). NMR determination of free fatty acids in vegetable oils. *Processes*, *8*(4), Article 410. <https://doi.org/10.3390/pr8040410>
- Effiyanti, L., Susanto., Hikmah, N., Indrawan, D. A., & Pari, G. (2019). Characterization and potential of wood waste sulfonated activated carbon catalyst based on rice husk hydrolysis reaction using microwave. *Journal of Research Result Forest*, *37*(2), 67-80.
- Encinar, J. M., Sánchez, N., Martínez, G., & García, L. (2011). Study of biodiesel production from animal fats with high free fatty acid content. *Bioresource Technology*, *102*(23), 10907-10914. <https://doi.org/10.1016/j.biortech.2011.09.068>
- Farabi, M. S. A., Ibrahim, M. L., Rashid, U., & Taufiq-Yap, Y. H. (2019). Esterification of palm fatty acid distillate using sulfonated carbon-based catalyst derived from palm kernel shell and bamboo. *Energy Conversion and Management*, *181*(December 2018), 562-570. <https://doi.org/10.1016/j.enconman.2018.12.033>
- Gafar, A. (2012). Síntesis and biodiesel quality test from palm oil plant liquid waste transesterification process. *Journal of Chemical Progress science*, *2*(1), 11-20.
- Gebremariam, S. N., & Marchetti, J. M. (2018a). Biodiesel production through sulfuric acid catalyzed transesterification of acidic oil: Techno economic feasibility of different process alternatives. *Energy Conversion and Management*, *174*(August), 639-648. <https://doi.org/10.1016/j.enconman.2018.08.078>
- Gebremariam, S. N., & Marchetti, J. M. (2018b). Economics of biodiesel production: Review. *Energy Conversion and Management*, *168*(February), 74-84. <https://doi.org/10.1016/j.enconman.2018.05.002>
- Hasanudin., Said, M., Faizal, M., Dahlan, M. H., & Wijaya, K. (2012). Hydrocracking of oil residue from palm oil mill effluent to biofuel. *Sustainable Environment Research*, *22*(6), 395-400.
- Hasan, Z., Yoon, J. W., & Jhung, S. H. (2015). Esterification and acetylation reactions over in situ synthesized mesoporous sulfonated silica. *Chemical Engineering Journal*, *278*, 105-112. <https://doi.org/10.1016/j.cej.2014.12.025>

- Irawati., Kurniawan, C., & Harjono. (2019). Optimization of epoxidation fatty acid methyl esters (FAME) Based on palm olein as a cat filter additive. *Indonesian Journal of Chemical Science*, 8(1), 34-40.
- Lathiya, D. R., Bhatt, D. V., & Maheria, K. C. (2018). Synthesis of sulfonated carbon catalyst from waste orange peel for cost effective biodiesel production. *Bioresource Technology Reports*, 2(2017), 69-76. <https://doi.org/10.1016/j.biteb.2018.04.007>
- Lakhya, J. K., Boro, J., & Deka, D. (2014). Review on latest developments in biodiesel production using carbon-based catalysts. *Renewable and Sustainable Energy Reviews*, 29, 546-564. <https://doi.org/10.1016/j.rser.2013.09.003>
- Li, J., Fu, Y. J., Qu, X. J., Wang, W., Luo, M., Zhao, C. J., & Zu, Y. G. (2012). Biodiesel production from yellow horn (*Xanthoceras sorbifolia* Bunge.) seed oil using ion exchange resin as heterogeneous catalyst. *Bioresource Technology*, 108,112-118. <https://doi.org/10.1016/j.biortech.2011.12.129>
- Liu, X. Y., Huang, M., Ma, H. L., Zhang, Z. Q., Gao, J. M., Zhu, Y. L., Han, X. J., & Guo, X. Y. (2010). Preparation of a carbon-based solid acid catalyst by sulfonating activated carbon in a chemical reduction process. *Molecules*, 15(10), 7188-7196. <https://doi.org/10.3390/molecules15107188>
- Luo, Y., Mei, Z., Liu, N., Wang, H., Han, C., & He, S. (2017). Synthesis of mesoporous sulfated zirconia nanoparticles with high surface area and their applies for biodiesel production as effective catalysts. *Catalysis Today*, 298(November 2016), 99-108. <https://doi.org/10.1016/j.cattod.2017.05.047>
- Ma, L., Han, Y., Sun, K., Lu, J., & Ding, J. (2015). Optimization of acidified oil esterification catalyzed by sulfonated cation exchange resin using response surface methodology. *Energy Conversion and Management*, 98, 46-53. <https://doi.org/10.1016/j.enconman.2015.03.092>
- Maneechakr, P., Samerjit, J., Uppakarnrod, S., & Karnjanakom, S. (2020). Retraction notice to “Experimental design and kinetic study of ultrasonic assisted transesterification of waste cooking oil over sulfonated carbon catalyst derived from cyclodextrin”[*Journal of Industrial and Engineering Chemistry* 32 (2015) 128 - 136]. *Journal of Industrial and Engineering Chemistry*, 87, 264-264. <https://doi.org/10.1016/j.jiec.2020.03.031>.
- Mar, W. W., & Samsok, E. (2012). Sulfonic-functionalized carbon catalyst for esterification of high free fatty acid. *Procedia Engineering*, 32, 212-218. <https://doi.org/10.1016/j.proeng.2012.01.1259>
- Marchetti, J. M., & Errazu, A. F. (2008). Comparison of different heterogeneous catalysts and different alcohols for the esterification reaction of oleic acid. *Fuel*, 87(15-16), 3477-3480. <https://doi.org/10.1016/j.fuel.2008.05.011>
- Marchetti, J. M., Miguel, V. U., & Errazu, A. F. (2008). Techno-economic study of different alternatives for biodiesel production. *Fuel Processing Technology*, 89(8), 740-748. <https://doi.org/10.1016/j.fuproc.2008.01.007>
- Mardhiah, H. H., Ong, H. C., Masjuki, H. H., Lim, S., & Pang, Y. L. (2017). Investigation of carbon-based solid acid catalyst from *Jatropha curcas* biomass in biodiesel production. *Energy Conversion and Management*, 144, 10-17. <https://doi.org/10.1016/j.enconman.2017.04.038>
- Meçabih, Z. (2016). Characterization of pillared clay by SEM-EDX. *Journal of Multidisciplinary Engineering Science and Technology*, 3(6), 5107-5109.

- Melero, J. A., Iglesias, J., & Morales, G. (2009). Heterogeneous acid catalysts for biodiesel production: Current status and future challenges. *Green Chemistry*, 11(9), 1285-1308. <https://doi.org/10.1039/b902086a>
- Nata, I. F., Putra, M. D., Irawan, C., & Lee, C. K. (2017). Catalytic performance of sulfonated carbon-based solid acid catalyst on esterification of waste cooking oil for biodiesel production. *Journal of Environmental Chemical Engineering*, 5(3), 2171-2175. <https://doi.org/10.1016/j.jece.2017.04.029>.
- Ngawosuan, K., Jr Goodwin, J. G., & Prasertdha, P. (2016). A green sulfonated carbon-based catalyst derived from coffee residue for esterification. *Renewable Energy*, 86, 262-269. <https://doi.org/10.1016/j.renene.2015.08.010>
- Ofoefule, A. U., Esonye, C., Onukwuli, O. D., Nwaeze, E., & Ume, C. S. (2019). Modeling and optimization of African pear seed oil esterification and transesterification using artificial neural network and response surface methodology comparative analysis. *Industrial Crops and Products*, 140, Article 111707. <https://doi.org/10.1016/j.indcrop.2019.111707>
- Ravindra, R. T., Kaneko, S., Endo, T., & Lakshmi, R. S. (2013). Spectroscopic characterization of bentonit. *Journal of Laser, Optics & Photonics*, 4(3), 1-4.
- Sangar, S. K., Lan, C. S., Razali, S. M., Farabi, M. S. A., & Taufiq-Yap, Y. H. (2019). Methyl ester production from palm fatty acid distillate (PFAD) using sulfonated cow dung-derived carbon-based solid acid catalyst. *Energy Conversion and Management*, 196, 1306-1315. <https://doi.org/10.1016/j.enconman.2019.06.073>
- Suminta, S., & Las, T. (2018). Smoothing of mordenite crystal cage structure and natural clinoptilolite by rietveld method. *Indonesian Journal of Material Science*, 7(2), 73-78. <https://doi.org/10.17146/jsmi.2006.7.2.5004S>
- Tariq, M., Ali, S., Ahmad, F., Ahmad, M., Zafar, M., Khalid, N., & Khan, M. A. (2011). Identification, FT-IR, NMR (<sup>1</sup>H and <sup>13</sup>C) and GC/MS studies of fatty acid methyl esters in biodiesel from rocket seed oil. *Fuel Processing Technology*, 92, 336-341. <https://doi.org/10.1016/j.fuproc.2010.09.025>
- Trombettoni, V., Lanari, D., Prinsen, P., Luque, R., Marrocchi, A., & Vaccaro, L. (2018). Recent advances in sulfonated resin catalysts for efficient biodiesel and bio-derived additives production. *Progress in Energy and Combustion Science*, 65, 136-162. <https://doi.org/10.1016/j.peccs.2017.11.001>
- Vargas, E. M., Neves, M. C., Tarelho, L. A. C., & Nunes, M. I. (2019). Solid catalysts obtained from wastes for FAME production using mixtures of refined palm oil and waste cooking oils. *Renewable Energy*, 136, 873-883. <https://doi.org/10.1016/j.renene.2019.01.048>
- William., Sanjaya, J., Taslim., Herawan, T., & Rivani, M. (2016). Optimization of biodiesel manufacturing process from distillate palm fatty acids (ALSD) and dimethyl carbonate (DMC) using Novozymes 435 catalyst. *Journal Chemical Engeneering USU*, 5(1), 13-19. <https://doi.org/10.32734/jtk.v5i1.1519>
- Wilson, K., & Lee, A. F. (2012). Rational design of heterogeneous catalysts for biodiesel synthesis. *Catalysis Science and Technology*, 2(5), 884-897. <https://doi.org/10.1039/c2cy20038d>
- Xu, B., Ren, J., Liu, X., Guo, Y., Gou, Y., Lu, G., & Wang, Y. (2010). Novel sulfonated carbonaceous materials from *p*-toluenesulfonic acid/glucose as a high-performance solid-acid catalyst. *Catalysis Communication*, 11, 629-632. <https://doi.org/10.1016/j.catcom.2010.01.010>



## Effect of Water Absorption on Flexural Properties of Kenaf/Glass Fibres Reinforced Unsaturated Polyester Hybrid Composites Rod

Bassam Hamid Alaseel<sup>1</sup>, Mohamed Ansari Mohamed Nainar<sup>1,2\*</sup>, Noor Afeefah Nordin<sup>1</sup>, Zainudin Yahya<sup>1</sup> and Mohd Nazim Abdul Rahim<sup>1</sup>

<sup>1</sup>Mechanical Engineering Department, Universiti Tenaga Nasional, Jalan IKRAM-UNITEN, 43000, Kajang, 43000, Selangor, Malaysia

<sup>2</sup>Institute of Power Engineering, Universiti Tenaga Nasional, Jalan IKRAM-UNITEN, 43000, Kajang, 43000, Selangor, Malaysia

### ABSTRACT

This study investigates the effect of water absorption on the flexural strength of kenaf/glass/unsaturated polyester (UPE) hybrid composite solid round rods used for insulating material applications. Three volume fractions of kenaf/glass fibre 20:80 (KGPE20), 30:70 (KGPE30), and 40:60 (KGPE40) with three different fibre arrangement profiles of kenaf fibres were fabricated by using the pultrusion technique and were aimed at studying the effect of kenaf fibres arrangement profile and its content in hybrid composites. The fibre/resin volume fraction was maintained constant at 60:40. The dispersion morphologies of tested specimens were observed using the scanning electron microscope (SEM). The findings were compared with pure glass fibre-reinforced UPE (control) composite. The water absorption results showed a clear indication of how it influenced the flexural strength of the hybrid and non-hybrid composites. The least affected sample was observed

in the 30KGPE composite type, wherein the kenaf fibre was concentrated at the centre of a cross-section of the composite rod. The water absorption reduced the flexural strength by 7%, 40%, 24%, and 38% of glass/UPE (control), 20KGPE, 30KGPE, and 40KGPE composites, respectively. In randomly distributed composite types, the water absorption is directly proportional to the volume fraction of kenaf fibre. At the same time, flexural properties were inversely proportional to the volume fraction

### ARTICLE INFO

#### Article history:

Received: 23 May 2021

Accepted: 11 August 2021

Published: 10 January 2022

DOI: <https://doi.org/10.47836/pjst.30.1.22>

#### E-mail addresses:

[bsmaq.it@gmail.com](mailto:bsmaq.it@gmail.com) (Alaseel Bassam)

[ansari@uniten.edu.my](mailto:ansari@uniten.edu.my) (Mohamed Ansari Mohamed Nainar)

[afeefahnordin1@gmail.com](mailto:afeefahnordin1@gmail.com) (Noor Afeefah Nordin)

[zai@uniten.edu.my](mailto:zai@uniten.edu.my) (Zainudin Yahya)

[nazim2106@gmail.com](mailto:nazim2106@gmail.com) (Mohd Nazim Abdul Rahim)

\* Corresponding author

of kenaf fibres. Although the influence of water absorption on flexural strength is low, the flexural strength of pultruded hybrid composites was more influenced by the arrangement of kenaf fibre in each composite type than its fibre loading.

*Keywords:* Flexural properties, glass fibres, hybrid composite, insulating material, kenaf fibres, water absorption

---

## INTRODUCTION

The recent advancement in natural fibre-reinforced composites has sparked researchers' interest in utilising these composites to lower the dependency on petroleum-based materials. Manufacturers and scientists are concerned about natural fibre reinforced composites because it is lightweight, relatively more substantial, non-toxic and considered to be excellent products that can be utilised in construction, automotive as well as in furniture industry (Saba et al., 2015). Reducing waste and chemical emissions (produced through using non-degradable materials) by relying on eco-friendly materials, reducing costs, decreasing the insulators' weight, and shortening maintenance time have become areas of attention for environmentalists, manufacturers, and researchers. Furthermore, natural fibre composites are more flexible, stiffer and can withstand high impact stress compared to conventional materials (Sarikaya et al., 2019). Besides, natural fibres are also abundantly available, renewable, possess low density as well as to have thermic insulation properties (Liu et al., 2019).

The origin of natural fibres is classified either as animal or plant-based. Some of the commonly found animal-based fibres are wool and silk, while natural fibres based on plants can be obtained from kenaf, sisal, coir, ramie, jute, bamboo, pineapple and various plant resources (Nunna et al., 2012). These fibres have numerous advantages, including relatively high modulus, lightweight, safe, easy manufacture, and their natural ability to absorb carbon dioxide during their growth process. The dimensional and mechanical characteristics of these fibres determine how well they can be used. These characteristics include the origin, harvest and environment conditions, plant age, and extraction methods (Kabir et al., 2012).

Kenaf plant is well known as a green and sustainable material whereby it is economically cheap and commercially available (Saba et al., 2015). The development of a sustainable product from kenaf fibres is becoming more prevalent for use in the automotive, sports (Seman et al., 2019), food packaging (Hamouda et al., 2019), construction, furniture (Dahy, 2019), textiles, and paper pulp (Sarikaya et al., 2019) sectors. Since kenaf fibre has started to be used in electrical applications, it is crucial for researchers to elucidate its electrical behaviour to identify its merits and demerits (Fares et al., 2019).

The insulator in electricity-transferring power lines is one of the critical components of high voltage networks because it plays a primary role in maintaining the continuity of

the power transmitting system. Insulators could be manufactured from ceramic (glass and porcelain) or non-ceramic (polymer composites). Polymer insulators developed quickly over the past 60 years as an alternative for glass fibres insulators commonly used in the industry. Polymer insulators are also called Fibre-Reinforced Polymer (FRP) insulators and composite insulators. This type of insulator consists of three components: (i) Silicon rubber housing, (ii) FRP rod and (iii) steel end-fitting. It is the most significant part of the power transmission system, whereby a failure in the insulator element can cause system failure, leading to cutting off in power supply (Ghosh et al., 2015). The insulator rod's main aim is to supply mechanical support to a high voltage transferring line by transmitting the conductor load to a tower, thereby providing insulation between the conductor and tower. This insulator rod has traditionally been manufactured from tempered glass or porcelain (Bansal, 1996). Over the past few years, glass-reinforced polymer (GRP) insulator rods have quickly replaced the conventional porcelain in high voltage (HV) power transmission lines (Bansal et al., 1995). Multiple weather sheds and a specific rubber alloy are used to protect the insulator rod. This protection technique is used to protect the insulator rod from moisture and pollution completely. In particular cases, the FRP insulator may be unprotected and allow water to get to the insulator surface. It can happen when the rubber alloy thickness is insufficient, damaged by abrasion, or due to cracks (Kumosa et al., 2004). In some instances, abrasion and cracks occur in the suspension insulator due to bird shooters or during the impact of fragments from a car bomb explosion in war zone regions.

Hybridisation is a combination of different kinds of fibres into one matrix. This combination between kenaf (natural fibre) and glass (synthetic fibre) provides better composites that possess the merits of both components. This method can offer a higher strength-to-weight ratio, longer fatigue life, and better mechanical properties than single-fibre composites. In addition, the alteration of glass fibre by natural fibre will considerably decrease the quantity and proportion of the glass fibre used in production, thus reducing its waste. The crossbreeding of kenaf fibres with glass fibres is widely recognised as a major choice for industrialists and researchers seeking to reduce environmental risks (Hamidon et al., 2018).

Bassam et al. (2019) studied the water absorption of kenaf/glass/UPE pultruded hybrid composites. Three different volume proportions of kenaf fibres with different fibre arrangements were applied to investigate the water absorption of the hybrid composites. Kenaf-glass fibres hybridisation showed that the water absorption of hybrid composites increased up to 10%, as shown in Figure 1. The water absorption was also influenced by kenaf fibres arrangement profiles.

Since numerous studies have found that mechanical properties were influenced by water absorption, this current research describes the leverage of water assimilation on flexural strength of kenaf/glass fibres hybrid composite used in insulator applications as a function

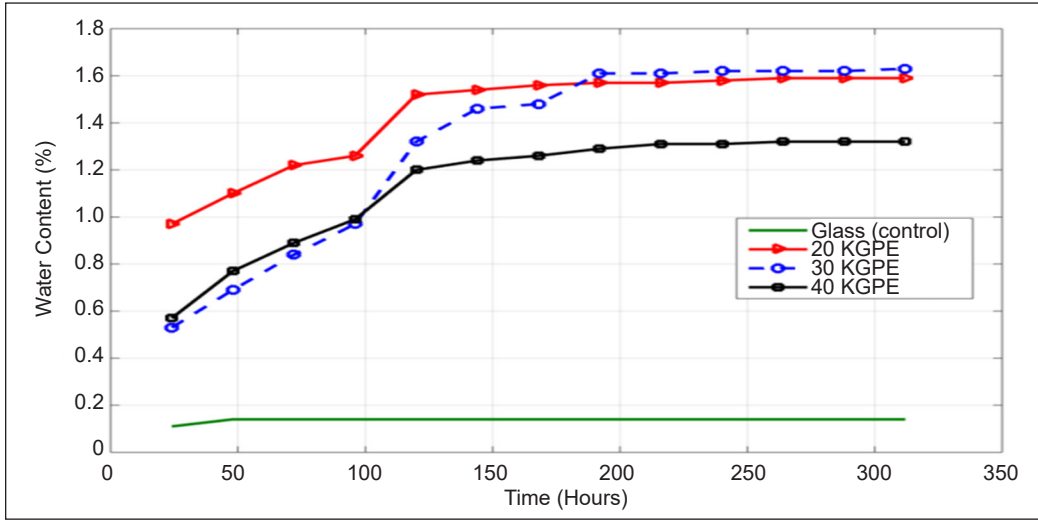


Figure 1. Water absorption of kenaf/glass composites

of genealogical volume proportion of two different fibres (César dos Santos et al., 2020; Hamdan et al., 2019; Khan et al., 2019; Li et al., 2016; Ma et al., 2018; Nayak et al., 2016; Quino et al., 2020; Rajeshkumar, 2020; Swain et al., 2020; Zhang et al., 2020). In addition to this, three-volume fractions of kenaf fibres with three various arrangement profiles had been fabricated, and their flexural properties have been evaluated. The influence of kenaf fibre hybridisation on the water assimilation tendency of hybrid composites was studied.

## METHODS AND MATERIALS

### Materials

Glass fibres (4400 texes) and kenaf yarns (1000 tex) were supplied from the local supplier in Malaysia. UPE resin, hardener, and fillers were purchased from Innovation Pultrusion Sdn. Bhd., Seremban, Malaysia. Kenaf fibres used in this study are made from kenaf bast. It is an economically cheap fibre compared with other natural fibres. Table 1 describes the physical and mechanical properties of glass fibres (GF) and kenaf fibres (KF).

Unsaturated-Polyester (UPE) resin is a common thermoset polymer widely used in engineering industries. UPE is employed to manufacture pultruded composite, utilising

Table 1

Physical and mechanical properties of glass fibres (GF) and kenaf fibres (KF) (Mahjoub et al., 2014, Sanjay et al., 2018, Saba et al., 2016)

Fibres	Density g/cm <sup>3</sup>	Diameter μm	tensile strength MPa	Young's modulus GPa	elongation to break %
GF	2.62	<17	3400	73	3.4
KF	1.19 – 1.4	10-17.7	295 – 600	40-53	1.5-3.5



a pultrusion approach. UPE is being utilised in a wide range of kenaf and glass fibre composite implementations. UPE resin has an excellent chemical resistance property, where its properties are: (3% elongation to break, 3GPa Young's modulus, 50-65 MPa tensile strength, and 1.2g/cm<sup>3</sup> density) (Ouarhim et al., 2019; Soares & Preto, 2016).

### Preparation Process

The volume fraction of fibres (both kenaf and glass fibres together) to UPE resin was 65%. Kenaf/glass fibre reinforced UPE hybrid composites were fabricated using a pultrusion machine (Pultrex Px-1000-6T) at Innovative Pultrusion Sdn. Bhd industry, Seremban, Malaysia. Table 2 demonstrates the hybrid composite types.

Table 2  
*Kenaf/glass/UPE hybrid composite types*

Composite type	Kenaf fibres (vol.%)	Glass fibres (vol.%)
20KGPE	20%	80%
30KGPE	30%	70%
40KGPE	40%	60%

Three Kenaf/glass hybrid composites with different volume fractions were fabricated with a circular cross-section of 24.7mm diameter. The volume fraction of fibres is the main factor for adjusting the flexural properties of hybrid composites (Aslan et al., 2013). Therefore, Equation 1 was used to calculate the number of kenaf and glass fibres according to the constant local fibre volume fraction criterion (Hashemi et al., 2018).

$$\left(\frac{n_{rk}}{n_{rk}^o}\right) + \left(\frac{n_{rG}}{n_{rG}^o}\right) = 1 \quad (1)$$

Where,

$n_{rk}^o$  is the number of kenaf yarns in kenaf/UPE non-hybrid composite,

$n_{rG}^o$  is glass roving in glass/UPE non-hybrid composite,

$n_{rk}^o$  is the number of kenaf yarns in kenaf/UPE non-hybrid composite, and

$n_{rG}^o$  is the number of glasses roving in a hybrid composite.

The gravimetric measurement of weight fraction of fibre and density of composite, matrix, and fibres were used to calculate the volume fraction (Hashemi et al., 2016).

Figures 2(a), 2(b), and 2(c) demonstrates the cross-section of three types of hybrid composites (20KGPE, 30KGPE, 40KGPE) respectively. In 20KGPE composite (a), the volume of kenaf fibres was 20%, and the kenaf/glass fibres were arranged as half of the cross-section. In 30KGPE composite (b), 30vol.% of kenaf fibres were concentrated in the core of the solid rod. In both 20KGPE and 30KGPE composite types, the kenaf fibres were concentrated in the core and surrounded by glass fibres. In the 40KGPE composite type, 40vol.% of fibres was kenaf fibres arranged throughout the whole diameter of the cross-section. Nonetheless, it was shown that the distribution of the kenaf fibre is not consistent because of the nature of the plant fibre, which is twisted, non-uniformity and the discontinuity of its structure (Hashemi et al., 2016).

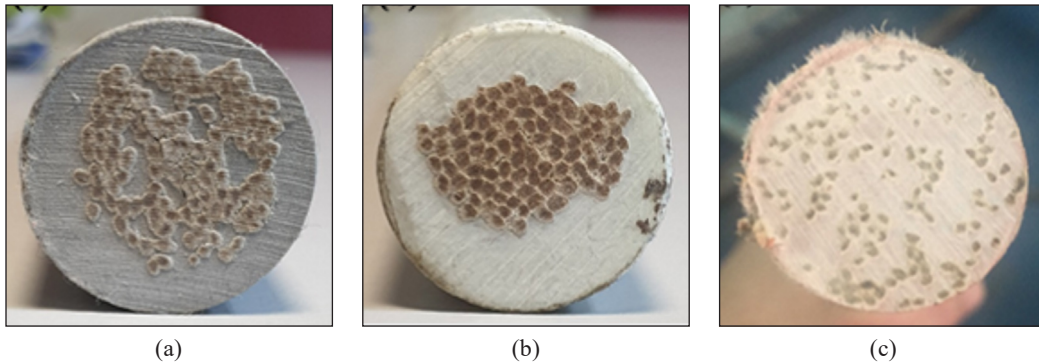


Figure 2. (a) 20KGPE, (b) 30KGPE, and (c) 40KGPE composite types

### Water Absorption Test

A water absorption test was conducted to define the influence of moisture on the composite characteristics (Sanjay et al., 2018) and loss of composite strength (Azwa & Yousif, 2013). Water absorption testing was performed by taking cylindrical bars of length 200 mm and diameter 24.7 mm. The test was done in three replicates for each specimen, specifically following the procedures described in ASTM standard D5229/D5229M-92 (ASTM standard, 2010). All specimens were cleaned to remove contaminants from machining, including the dirt and oil prior to submersion in water. The initial weight of the specimen was measured before they were immersed in distilled water. The weight shift was calculated at regular intervals (every 24 hours) using an analytical balance with 0.1 mg accuracy. The test was continued until the specimens reached an equilibrium state. Then, the water absorption content was calculated using Equation 2:

$$\% \Delta m_w = \frac{m_w - m_d}{m_d} \times 100\% \quad (2)$$

Where,  $m_w$  is the weight of the specimen at the time of collecting data (wet), and  $m_d$  is the weight of the dry specimen. Fick's law has been used to calculate the absorption rate of composites as shown in Equation 3:

$$\frac{M_t}{M_e} = 2 \left( \frac{D}{\pi L^2} \right)^{\frac{1}{2}} \quad (3)$$

Where,  $M_t$  (g) is the mass gain at time  $t$  (s),  $M_e$  (g) is the mass gain at equilibrium,  $2L$  is the thickness of the specimen (cm) and  $D$  is the diffusion coefficient ( $\text{cm}^2 \text{s}^{-1}$ ) (Li et al., 2018).

### Flexural Strength Test

The flexural strength of any material is usually based on the maximum bending that it can tolerate until it breaks (Mishra et al., 2017). The present test was carried out according to the

three-point loading method (ASTM D790-10) by using Zwick/Roell machine following the three-point bending method (Vickers et al., 2014; Sapiai et al., 2015). Every specimen used measures 200 mm in length with a diameter of 24.7 mm. It is held with a steady head speed of 10 mm/min during the whole test. The maximum stress of fibre depends on specimen dimension and the load applied. Equation 4 is used to calculate the maximum stress.

$$S = \frac{3FL}{\pi d^3} \quad (4)$$

where, S = stress (MPa), F=load (kN), L= length (mm), and d= diameter (mm). The mean value of the three results obtained is used to calculate the flexural strength. The flexural tests were carried out on the specimens after water absorption, and the mean value of the specimens of each composite type was recorded.

### Scanning Electron Microscopy (SEM)

Morphological properties of the samples were characterised using SEM to obtain images with high resolution and magnification. The study used SEM to analyse material damage post flexural test by observing the fibre and matrix properties. This method is mandatory since it plays a vital role in understanding the material's physical and mechanical properties. The hybrid composites were properly cleaned and mounted on the stubs, using a silver paste for examination purposes. Morphological properties of each specimen were characterised using a JEOL, JSM-6010PUL/LV scanning electron microscope at Universiti Tenaga Nasional, Kajang, Selangor, Malaysia, with SEM magnification of 300×, 100×, and 30×.

## RESULTS AND DISCUSSION

### Water Absorption

Based on the literature review, the insulator rod that has been in service is possible to be exposed to moisture and rain. The existence of acids on the insulator rod surface was because of acid rain or moist air. Based on the type of polymeric insulator rod, the presence of enough water may lead to failure (Ansari et al., 2021). Therefore, the water absorption test was conducted to calculate the weight of water absorbed by specimens—the test of 20vol.%, 30vol.%, and 40vol.% of kenaf/glass/UPE hybrid composite rod was carried out under room temperature. The findings of hybrid composite rods were compared with pure glass fibre composite rods (control samples). Three samples of each composite type were tested, and the average reading was reported. The hybrid composites rapidly absorbed the water after immersion. After that, water absorption increased significantly during the next three days (days 2–4). All specimens of hybrid composites reached saturation state after 8–10 days, while the non-hybrid composite specimens (control) reached this state after two days. The water absorption of non-hybrid composite (control) was 0.15%; meanwhile,

the water absorption of 20KGPE, 30KGPE, and 40KGPE (pultruded hybrid composites) was 1.59%, 1.63%, and 1.32%, respectively.

Ordinarily, replacing synthetic fibre with natural fibre in hybrid composites increases water absorption, which was observed in past research (Bassam et al., 2019; Saba et al., 2016). Previous studies have proven the type of fibres and their surface, resin viscosity, volume fraction (fibres-fibres and fibres-resin), and temperature-controlled water spreading operation in hybrid composites (Ellyin & Maser, 2004). In addition, the water uptake process is also affected by the orientation and arrangement of the fibres, whereby the kenaf fibres concentrated in the centre of the rod 30KGPE had maximum water absorption. The hybridisation of two or more different fibres utilised in the hybrid composite caused inferior attachment between fibres and resin. This incomplete attachment disabled the fibres to be saturated with resin, and thus, fibres are not in equilibrium for moisture absorption.

The voids inside the material were the main water-storage pathway for the composites. Due to the test occurring at room temperature and using tap water, no cracking mechanism was acting on the FRP. Consequently, the water storage capacity inside composites material remained unchanged. Therefore, constant saturation water uptake may be appropriate for the current four immersion cases. Table 3 illustrates the diffusion coefficient ( $D$ ) for composites.

It was observed that the diffusion coefficient ( $D$ ) of pure glass fibre composite (control) is almost constant for all the testing periods. At the same time, it gradually increased for all the three compositions of kenaf/glass hybrid composites. Additional care was taken during the mixing of raw materials (fibres, resin, and additives) when passing through the die heater in the pultrusion machine during the fabrication process, leading to minimal voids

Table 3  
*Diffusion coefficient ( $D$ ) for kenaf/glass/UPE hybrid composites*

Day	Diffusion coefficient ( $D$ ) ( $\times 10^{-13}$ m <sup>2</sup> /s)			
	Glass (control)	20KGPE	30KGPE	40KGPE
1	0.784	0.761	0.761	0.770
2	0.785	0.776	0.769	0.777
3	0.786	0.778	0.771	0.779
4	0.786	0.780	0.774	0.781
5	0.786	0.781	0.775	0.784
6	0.786	0.785	0.781	0.784
7	0.786	0.785	0.783	0.784
8	0.786	0.785	0.783	0.785
9	0.786	0.786	0.785	0.785
10	0.786	0.786	0.785	0.785
11	0.786	0.786	0.786	0.786
12	0.786	0.786	0.786	0.786
13	0.786	0.786	0.786	0.786

and internal moisture. As a result, it slightly improved the diffusion coefficient, and there is no notable difference in the value 'D' irrespective of the filler volume % (loading level).

### Flexural Properties

The effect of water absorption on the flexural strength of kenaf/glass/ UPE hybrid composite is shown in Figure 3. The average of three samples of each composite type was recorded and analysed in this section. The flexural strength of 20KGPE, 30KGPE, and 40KGPE before water absorption was 148 MPa, 112 MPa, and 190 MPa, while the flexural strength after water absorption was 89.2 MPa, 109 MPa, and 118 MPa, respectively. The standard deviation of error bars with  $\pm 5$  was given out for the average value of every three batches. This deviation of errors was due to the difference of diameters of tex that constitute kenaf fibre and the degree of intertwining between these texes. The fibre with tighter intertwining needs more energy consumption due to mechanical friction, resulting in the difference in flexural strength results.

Unequivocally, water absorption can impair the chemical bonds of composites, causing voids, and dissolve the chemical bonds between the fibres and resins. Voids might produce inner and surface microcracks, resulting in decreased mechanical properties of composites. The findings of the current study revealed that the influence of water absorption on flexural properties of composites with fewer chemical bonds between two different types of fibres (30KGPE) was smaller than the composites that have more chemical bonds between two different types of fibres (20KGPE and 40KGPE). Thus, the composites with fewer contact

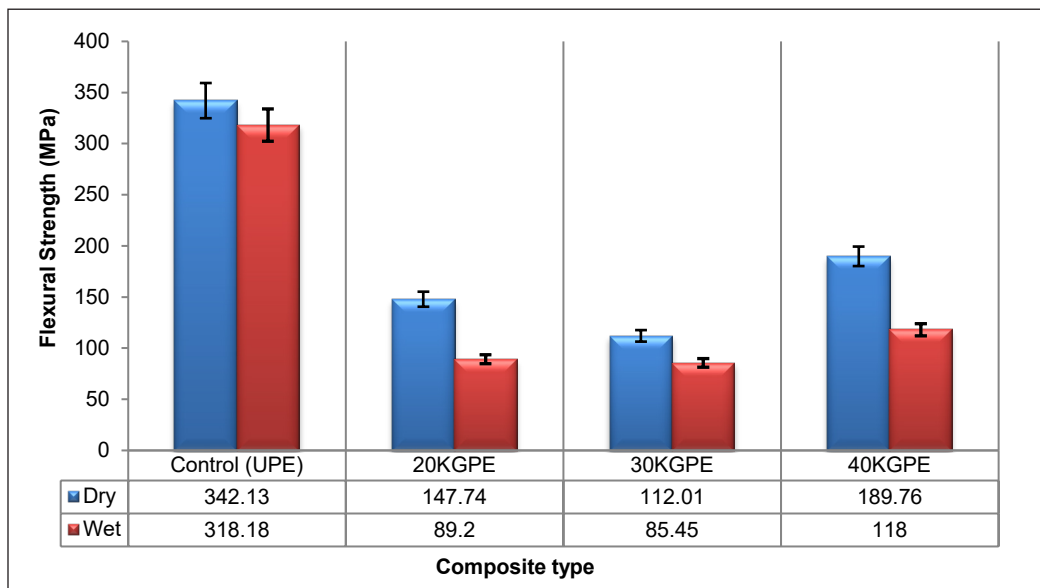


Figure 3. Flexural properties of kenaf/glass fibre hybrid composites reinforced unsaturated polyester, before and after water absorption

areas between two different fibres showed relatively stable flexural strength. The flexural properties of hybrid composites are affected by water absorption and interface adherence with resin when the same fibre, resin, volume fraction, and fibres arrangement were used. Natural fibres essentially contribute to the strength of natural/synthetic hybrid composites. The higher strength fibres give higher strength composites.

Additionally, the higher aspect ratio (length to width) of kenaf fibre supplies methodical stress transfer in the interface of fibres and matrix. A design of an outer layer of glass fibre surrounding a single kenaf fibre enhanced the mechanical properties and decreased the water absorption compared to the other arrangement profiles (Akil et al., 2014). Conversely, increasing the volume fraction of kenaf fibres gives water absorption, which entails an inoperative stress transfer in the matrix/fibre interface. The flexural strength of 20KGPE composite and 40KGPE composite decreases by 40% and 38% after water absorption, respectively, while there is a decrease of only 23.7% for 30KGPE composites. Previous work by Yahya et al. (2016) also reported the same finding whereby kenaf fibre arrangement significantly impacted the flexural properties of the hybrid composite after the water absorption test. The flexural strength of mixed kenaf-glass fibres arrangement is profoundly influenced by water absorption, while concentrated kenaf fibre in the hybrid composite core is only slightly affected. In the flexural test, the failure occurred due to bending and shear failures. As a result of the effect of water absorption on flexural properties, flexural strength decreased after water absorption while shear failure resistance had increased.

### Scanning Electron Microscopy (SEM)

Figures 4(a), 4(b), and 4(c) revealed SEM analysis of flexural fracture surface of kenaf/glass fibre hybrid composites before water absorption and Figures 4(d), 4(e), and 4(f) demonstrated SEM analysis of the flexural surface of kenaf/glass fibre hybrid composites after water absorption test.

From the microscopic images in Figures 4(a) and 4(b), slight debonding and fracture could be noticed in the composites tested before water absorption. In this case, the interfacial relation of fibres to a dry matrix was not very significant, as modes of slight debonding and breakdown of fibre were observed rather than entire fibre pull-out, which is a common thermosetting resins fracture. Therefore, fibre breakage was the primary failure mode for the dry composites. In the meantime, the matrix cracking was observed on the top of Figure 4(c). A close interface between the glass fibres and the UPE matrix produced splits across the extended fibres. Nevertheless, different patterns of surface fractures have been observed in the composites under moisten circumstances. It was evident that the surfaces of the hybrid composites at the fracture area became bumpy and rough. Water absorption might produce matrix delamination and damage to the fibres, where the matrix delamination was very clear, as shown in Figures 4(d) and 4(e). Water absorption

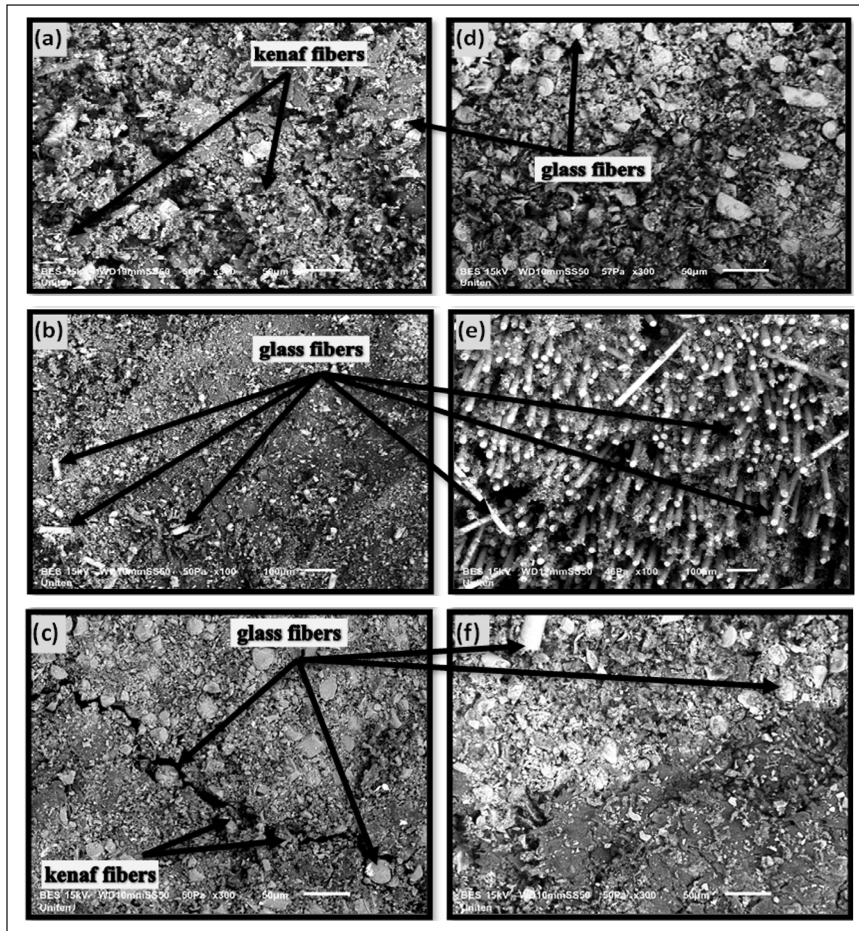


Figure 4. SEM flexural fracture of kenaf/glass fibre hybrid composites ((a), (b), and (c) before water absorption test, (d), (e), and (f) after water absorption test).

debonds the matrix bindings, which decreases the strength of fibre-matrix bonding and enables water to permeate by capillary effect, leading to swelling of the composite. The swelling condition happens in the composite due to water accumulation, which causes stress in the components. An increase of several voids can be observed in the composites after water absorption, as shown in Figures 4(d), 4(e), and 4(f). The increase in the number of voids was due to water absorption by fibres that led to debonding between fibre-fibre and fibres-resin in the composite. These voids work as concentrators of stress, which led to the failure of the composite.

Moreover, the failure of the hybrid composite after water absorption was initiated by the failure of the kenaf fibres due to absorbing more water (hydrophilic fibres). The presence of water molecules in these fibres for a long time made them wet, decreasing the interfacial bindings, thus reducing composites' mechanical and physical characteristics. It

was noted that kenaf fibres in the fracture surface of composites after water uptake did not appear because water absorbed by kenaf fibres reduced the energy absorption resulting in lower toughness and flexural properties of hybrid composites. In addition, water soaking up also increases the amount of kenaf fibre pulled out owing to diminished bonding force between kenaf, glass fibres and matrix. Initially, the applied force was taken up by kenaf fibres and, after it collapsed, the applied load was transferred to the glass fibre, which finally caused the failure of the hybrid composite. From all figures, it can be seen that there is a low kenaf fibre content at the fracture area. Based on morphology attained, the fracture mechanism appeared to encompass different fibres breaking types, macro fracture of fibres and pull-out fibres from the matrix, similar to the result observed by Hojo et al. (2014). Therefore, the water absorption contributes to decreasing the flexural strength of the hybrid composites. The flexural strength reduction depends on the kenaf fibre arrangements more than its volume fraction.

## CONCLUSIONS

Kenaf fibre was chosen and exploited to manufacture hybrid glass fibre reinforced polymer using the pultrusion technique for insulator applications. Water absorption, whether through moisture or rain, is considered the main threat to the mechanical properties of the polymeric insulator rod. Usually, the insulator rod is protected by rubber, silicon, and paint layers to prevent water from entering the insulator surface except for particular situations, such as erosion or abrasion of the protection layers.

In this study, the flexural characteristics of three different types of kenaf/glass reinforced UPE hybrid composite were tested and analysed before and after water absorption. In addition, SEM observation of fractural cross-section was also performed, and the following conclusion points can be drawn:

- The hybridisation kenaf/glass fibre reinforced UPE was successfully fabricated using the pultrusion method.
- The water absorption of kenaf/glass fibre hybrid composite increased from 8 to 10 times compared with pure glass fibre composite.
- The fibre arrangement profiles and their volume proportion influenced water absorption and flexural properties.
- The kenaf fibres in 20KGPE and 40KGPE composite types increased the water absorption by 10% and 8%, which caused a decrease in flexural strength of 40% and 38%, respectively.
- The kenaf fibres arrangement of 30KGPE (concentrated in the centre of the cross-section) decreased the flexural strength to 112MPa (lowest value) compared with other composite types. At the same time, the water absorption was the highest



percentage (10%). Notwithstanding that, the influence of water absorption on flexural strength was very low ( $\approx 2.5\%$ ).

- The SEM morphology observed that the water absorption by kenaf fibre reduced the toughness due to decreased energy absorption and reduced flexural properties.
- The fracture pattern of dry specimens was similar for all composite types but differed in the composites under water-saturated conditions.

## ACKNOWLEDGEMENTS

The authors would like to acknowledge Tenaga Nasional Berhad Malaysia's financial support from a seed fund grant (Project Code: U-TS-RD-18-10), Institute of Power Engineering, Department of Mechanical Engineering, and UNITEN R&D Sdn. Bhd., Universiti Tenaga Nasional, Malaysia, for the funding to publish these project outcomes.

## REFERENCES

- Akil, H. M., Santulli, C., Sarasini, F., Tirillò, J., & Valente, T. (2014). Environmental effects on the mechanical behaviour of pultruded jute/glass fibre-reinforced polyester hybrid composites. *Composites Science and Technology*, 94, 62-70. <https://doi.org/10.1016/j.compscitech.2014.01.017>
- Ansari, M. N. M., Bassam, A., Nazim, A. R. M., Nordin, N. A., & Yahya, Z. (2021). Water absorption of kenaf/glass/epoxy hybrid composites for insulator core. *IOP Conference Series: Materials Science and Engineering*, 1128(1), Article 012027. <https://doi.org/10.1088/1757-899x/1128/1/012027>
- Aslan, M., Mehmood, S., & Madsen, B. (2013). Effect of consolidation pressure on volumetric composition and stiffness of unidirectional flax fibre composites. *Journal of Materials Science*, 48(10), 3812-3824. <https://doi.org/10.1007/s10853-013-7182-3>
- ASTM Standard (2010). *ASTM D5229 – Moisture absorption properties and equilibrium conditioning of polymer matrix composite materials*. Retrieved April 30, 2020, from [https://www.trl.com/astm\\_d5229\\_moisture\\_absorption\\_properties\\_and\\_equilibrium\\_conditioning\\_of\\_polymer\\_matrix\\_composite\\_materials/](https://www.trl.com/astm_d5229_moisture_absorption_properties_and_equilibrium_conditioning_of_polymer_matrix_composite_materials/)
- Azwa, Z. N., & Yousif, B. F. (2013). Characteristics of kenaf fibre/epoxy composites subjected to thermal degradation. *Polymer Degradation and Stability*, 98(12), 2752-2759. <https://doi.org/10.1016/j.polymdegradstab.2013.10.008>
- Bansal, A., Schubert, A., Balakrishnan, M. V., & Kumosa, M. (1995). Finite element analysis of substation composite insulators. *Composites Science and Technology*, 55(4), 375-389. [https://doi.org/10.1016/0266-3538\(95\)00120-4](https://doi.org/10.1016/0266-3538(95)00120-4)
- Bansal, A. (1996). *Finite element simulation and mechanical characterization of composite insulators*. ProQuest Dissertations Publishing.
- Bassam, A., Ansari, M. N. M., Atiqah, A., Begum, S., & Nazim, A. R. M. (2019). Water absorption properties of kenaf/glass reinforced unsaturated polyester composites used in insulator rods. *International Journal of Engineering and Advanced Technology*, 9(2), 4208-4212. <https://doi.org/10.35940/ijeat.b4931.129219>

- César dos Santos, J., Ávila de Oliveira, L., Panzera, T. H., Remillat, C. D. L., Farrow, I., Placet, V., & Scarpa, F. (2020). Ageing of autoclaved epoxy/flax composites: Effects on water absorption, porosity and flexural behaviour. *Composites Part B: Engineering*, 202, Article 108380. <https://doi.org/10.1016/j.compositesb.2020.108380>
- Dahy, H. (2019). Natural fibre-reinforced polymer composites (NFRP) fabricated from lignocellulosic fibres for future sustainable architectural applications, case studies: Segmented-shell construction, acoustic panels, and furniture. *Sensors (Switzerland)*, 19(3), Article 738. <https://doi.org/10.3390/s19030738>
- Ellyin, F., & Maser, R. (2004). Environmental effects on the mechanical properties of glass-fiber epoxy composite tubular specimens. *Composites Science and Technology*, 64(12), 1863-1874. <https://doi.org/10.1016/j.compscitech.2004.01.017>
- Fares, O., AL-Oqla, F. M., & Hayajneh, M. T. (2019). Dielectric relaxation of mediterranean lignocellulosic fibers for sustainable functional biomaterials. *Materials Chemistry and Physics*, 229(November 2018), 174-182. <https://doi.org/10.1016/j.matchemphys.2019.02.095>
- Ghosh, D., Bhandari, S., Chaki, T. K., & Khastgir, D. (2015). Development of a high performance high voltage insulator for power transmission lines from blends of polydimethylsiloxane/ethylene vinyl acetate containing nanosilica. *RSC Advances*, 5(71), 57608-57618. <https://doi.org/10.1039/c5ra08277c>
- Hamidon, M. H., Sultan, M. T. H., & Ariffin, A. H. (2018). Investigation of mechanical testing on hybrid composite materials. In M. Jawaid, M. Thariq & N. Saba (Eds), *Failure analysis in biocomposites, fibre-reinforced composites and hybrid composites* (pp. 133-156). Woodhead Publishing. <https://doi.org/10.1016/b978-0-08-102293-1.00007-3>
- Hamdan, M. H. M., Siregar, J. P., Cionita, T., Jaafar, J., Efriyohadi, A., Junid, R., & Kholil, A. (2019). Water absorption behaviour on the mechanical properties of woven hybrid reinforced polyester composites. *International Journal of Advanced Manufacturing Technology*, 104(1-4), 1075-1086. <https://doi.org/10.1007/s00170-019-03976-9>
- Hamouda, T., Hassanin, A. H., Saba, N., Demirelli, M., Kilic, A., Candan, Z., & Jawaid, M. (2019). Evaluation of mechanical and physical properties of hybrid composites from food packaging and textiles wastes. *Journal of Polymers and the Environment*, 27(3), 489-497. <https://doi.org/10.1007/s10924-019-01369-3>
- Hashemi, F., Brancheriau, L., & Tahir, P. M. (2018). Hybridization and yarns configuration effects on flexural dynamic and static properties of pultruded hybrid kenaf/glass fiber composites. *Composites Part A: Applied Science and Manufacturing*, 112, 415-422. <https://doi.org/10.1016/j.compositesa.2018.05.008>
- Hashemi, F., Tahir, P. M., Madsen, B., Jawaid, M., Majid, D. L., Brancheriau, L., & Juliana, A. H. (2016). Volumetric composition and shear strength evaluation of pultruded hybrid kenaf/glass fiber composites. *Journal of Composite Materials*, 50(17), 2291-2303. <https://doi.org/10.1177/0021998315602948>
- Hojo, T., Xu, Z., Yang, Y., & Hamada, H. (2014). Tensile properties of bamboo, jute and kenaf mat-reinforced composite. *Energy Procedia*, 56, 72-79. <https://doi.org/10.1016/j.egypro.2014.07.133>
- Kabir, M. M., Wang, H., Lau, K. T., & Cardona, F. (2012). Composites: Part B chemical treatments on plant-based natural fibre reinforced polymer composites: An overview. *Composites Part B*, 43(7), 2883-2892. <https://doi.org/10.1016/j.compositesb.2012.04.053>

- Khan, Z., Tehami, W., & Mehmood, Z. (2019). Effect of moisture / liquid absorption on mechanical properties of composites. In *2019 Sixth International Conference on Aerospace Science and Engineering (ICASE)* (pp. 1-8). IEEE Publishing. <https://doi.org/10.1109/ICASE48783.2019.9059227>
- Kumosa, L., Benedikt, B., Armentrout, D., & Kumosa, M. (2004). Moisture absorption properties of unidirectional glass/polymer composites used in composite (non-ceramic) insulators. *Composites Part A: Applied Science and Manufacturing*, 35(9), 1049-1063. <https://doi.org/10.1016/j.compositesa.2004.03.008>
- Li, C., Xian, G., & Li, H. (2018). Water absorption and distribution in a pultruded unidirectional carbon/glass hybrid rod under hydraulic pressure and elevated temperatures. *Polymers*, 10(6), Article 627. <https://doi.org/10.3390/polym10060627>
- Li, H., Xian, Y., Deng, J., Cheng, H., Chen, F., & Wang, G. (2016). Evaluation of water absorption and its influence on the physical-mechanical properties of bamboo-bundle laminated veneer lumber. *BioResources*, 11(1), 1359-1368. <https://doi.org/10.15376/biores.11.1.1359-1368>
- Liu, W., Chen, T., Fei, M. E., Qiu, R., Yu, D., Fu, T., & Qiu, J. (2019). Properties of natural fiber-reinforced biobased thermoset biocomposites: Effects of fiber type and resin composition. *Composites Part B: Engineering*, 171(March), 87-95. <https://doi.org/10.1016/j.compositesb.2019.04.048>
- Ma, G., Yan, L., Shen, W., Zhu, D., Huang, L., & Kasal, B. (2018). Effects of water, alkali solution and temperature ageing on water absorption, morphology and mechanical properties of natural FRP composites: Plant-based jute vs. mineral-based basalt. *Composites Part B: Engineering*, 153(May), 398-412. <https://doi.org/10.1016/j.compositesb.2018.09.015>
- Mishra, K., Pandey, G., & Singh, R. P. (2017). Enhancing the mechanical properties of an epoxy resin using polyhedral oligomeric silsesquioxane (POSS) as nano-reinforcement. *Polymer Testing*, 62, 210-218. <https://doi.org/10.1016/j.polymertesting.2017.06.031>
- Nayak, R. K., Mahato, K. K., & Ray, B. C. (2016). Water absorption behavior, mechanical and thermal properties of nano TiO<sub>2</sub> enhanced glass fiber reinforced polymer composites. *Composites Part A: Applied Science and Manufacturing*, 90, 736-747. <https://doi.org/10.1016/j.compositesa.2016.09.003>
- Nunna, S., Chandra, P. R., Shrivastava, S., & Jalan, A. K. (2012). A review on mechanical behavior of natural fiber based hybrid composites. *Journal of Reinforced Plastics and Composites*, 31(11), 759-769. <https://doi.org/10.1177/0731684412444325>
- Ouarhim, W., Zari, N., & Bouhfid, R. (2019). Mechanical performance of natural fibers-based thermosetting composites. In M. Jawaid, M. Thariq & N. Saba (Eds), *Mechanical and physical testing of biocomposites, fibre-reinforced composites and hybrid composites* (pp. 43-60). Woodhead Publishing. <https://doi.org/10.1016/B978-0-08-102292-4.00003-5>
- Quino, G., Tagarielli, V. L., & Petrinic, N. (2020). Effects of water absorption on the mechanical properties of GFRPs. *Composites Science and Technology*, 199(May), Article 108316. <https://doi.org/10.1016/j.compscitech.2020.108316>
- Rajeshkumar, G. (2020). An experimental study on the interdependence of mercerization, moisture absorption and mechanical properties of sustainable Phoenix sp. fibre-reinforced epoxy composites. *Journal of Industrial Textiles*, 49(9), 1233-1251. <https://doi.org/10.1177/1528083718811085>

- Saba, N., Paridah, M. T., Abdan, K., & Ibrahim, N. A. (2016). Effect of oil palm nano filler on mechanical and morphological properties of kenaf reinforced epoxy composites. *Construction and Building Materials*, *123*, 15-26. <https://doi.org/10.1016/j.conbuildmat.2016.06.131>
- Saba, N., Paridah, M. T., & Jawaid, M. (2015). Mechanical properties of kenaf fibre reinforced polymer composite: A review. *Construction and Building Materials*, *76*, 87-96. <https://doi.org/10.1016/j.conbuildmat.2014.11.043>
- Sanjay, M. R., Madhu, P., Jawaid, M., Sentharamaikkannan, P., Senthil, S., & Pradeep, S. (2018). Characterization and properties of natural fiber polymer composites: A comprehensive review. *Journal of Cleaner Production*, *172*, 566-581. <https://doi.org/10.1016/j.jclepro.2017.10.101>
- Sapiai, N., Jumahat, A., & Mahmud, J. (2015). Flexural and tensile properties of kenaf/glass fibres hybrid composites filled with carbon nanotubes. *Jurnal Teknologi Full*, *11*, 87-95.
- Sarikaya, E., Çallioğlu, H., & Demirel, H. (2019). Production of epoxy composites reinforced by different natural fibers and their mechanical properties. *Composites Part B: Engineering*, *167*(15), 461-466. <https://doi.org/10.1016/j.compositesb.2019.03.020>
- Seman, S. A. H. A., Ahmad, R., & Akil, H. M. (2019). Meso-scale modelling and failure analysis of kenaf fiber reinforced composites under high strain rate compression loading. *Composites Part B: Engineering*, *163*(May 2018), 403-412. <https://doi.org/10.1016/j.compositesb.2019.01.037>
- Soares, B., & Preto, R. (2016). Thermo-mechanical modeling of a high pressure turbine blade of an airplane gas turbine engine Mechanical behavior of basalt fibers in a basalt-UP composite Mechanical behavior of basalt fibers composite. *Procedia Structural Integrity*, *1*, 82-89. <https://doi.org/10.1016/j.prostr.2016.02.012>
- Swain, P. T. R., Das, S. N., Patnaik, P. K., & Purohit, A. (2020). The influence of moisture absorption on the mechanical and thermal properties of chemically treated DPL reinforced hybrid composite. *Materials Science Forum*, *978*, 316-322. <https://doi.org/10.4028/www.scientific.net/MSF.978.316>
- Vickers, L., Rickard, W. D. A., & Van Riessen, A. (2014). Strategies to control the high temperature shrinkage of fly ash based geopolymers. *Thermochimica Acta*, *580*, 20-27. <https://doi.org/10.1016/j.tca.2014.01.020>
- Yahaya, R., Sapuan, S. M., Jawaid, M., Leman, Z., & Zainudin, E. S. (2016). Effect of fibre orientations on the mechanical properties of kenaf-aramid hybrid composites for spall-liner application. *Defence Technology*, *12*(1), 52-58. <https://doi.org/10.1016/j.dt.2015.08.005>
- Zhang, K., Liang, W., Wang, F., & Wang, Z. (2020). Effect of water absorption on the mechanical properties of bamboo/glass-reinforced polybenzoxazine hybrid composite. *Polymers and Polymer Composites*, *29*(1), 3-14. <https://doi.org/10.1177/0967391120903664>

## MYLPHerb-1: A Dataset of Malaysian Local Perennial Herbs for the Study of Plant Images Classification under Uncontrolled Environment

Kalananthni Pushpanathan<sup>1</sup>, Marsyita Hanafi<sup>1\*</sup>, Syamsiah Masohor<sup>1</sup> and Wan Fazilah Fazlil Ilahi<sup>2</sup>

<sup>1</sup>Department of Computer and Communication Systems Engineering, Faculty of Engineering, Universiti Putra Malaysia, 43400 UPM, Serdang, Selangor Darul Ehsan, Malaysia

<sup>2</sup>Department of Agriculture Technology, Faculty of Agriculture, Universiti Putra Malaysia, 43400 UPM, Serdang, Selangor Darul Ehsan, Malaysia

### ABSTRACT

Research in the medicinal plants' recognition field has received great attention due to the need of producing a reliable and accurate system that can recognise medicinal plants under various imaging conditions. Nevertheless, the standard medicinal plant datasets publicly available for research are very limited. This paper proposes a dataset consisting of 34200 images of twelve different high medicinal value local perennial herbs in Malaysia. The images were captured under various imaging conditions, such as different scales, illuminations, and angles. It will enable larger interclass and intraclass variability, creating abundant opportunities for new findings in leaf classification. The complexity of the dataset is investigated through automatic classification using several high-performance deep learning algorithms. The experiment results showed that the dataset creates more opportunities for advanced classification research due to the complexity of the images. The dataset can be accessed through <https://www.mylpherbs.com/>.

*Keywords:* Deep learning, leaf identification, medicinal plants, perennial herbs, plant dataset

### ARTICLE INFO

*Article history:*

Received: 24 May 2021

Accepted: 17 August 2021

Published: 04 January 2022

DOI: <https://doi.org/10.47836/pjst.30.1.23>

*E-mail addresses:*

[kalananthni19@gmail.com](mailto:kalananthni19@gmail.com) (Kalananthni Pushpanathan)

[marsyita@upm.edu.my](mailto:marsyita@upm.edu.my) (Marsyita Hanafi)

[syamsiah@upm.edu.my](mailto:syamsiah@upm.edu.my) (Syamsiah Mashohor)

[wanfazilah@upm.edu.my](mailto:wanfazilah@upm.edu.my) (Wan Fazilah Fazlil Ilahi)

\* Corresponding author

### INTRODUCTION

Medicinal plants have been widely used as an alternative to modern medicine due to their lower negative impact on the human body and affordable price (Lulekal et al., 2008). Asia is a region with enormous biodiversity of medicinal plants; hence, expert knowledge is required for plant

identification, which is tedious and time-consuming. Automatic classification is the best solution for the problem mentioned above, and it has been researched extensively. Nevertheless, to achieve high accuracy, identification systems need to be trained with medicinal plant image datasets that reflect real-life scenarios (Sladojevic et al., 2016; Singh & Misra, 2017; Wäldchen et al., 2018). Accessibility of the standard medicinal plant image datasets is limited despite being researched actively. Most available plant datasets consist of images captured under a controlled environment. The datasets that have been widely used are Swedish Leaf Dataset, Flavia Dataset, Leafsnap dataset and ICL dataset. The examples of studies that used these datasets for automatic identification are Arun et al. (2013), Begue et al. (2017), Dahigaonkar and Kalyane (2018), Harsani and Qurania (2016), Janani and Gopal (2013), Pornpanomchai et al. (2011), Vijayashree and Gopal (2017), Wäldchen and Mäder (2018a). The standard datasets for the studies in the uncontrolled environment are very limited, and until now, the only reliable option is the ImageCLEF datasets. Although great variations of leaf images are available in ImageCLEF, most of the images were captured from wild plant species in Western Europe Flora, and North American. The datasets mentioned above are summarised in Table 1.

Table 1  
*Summary of publicly available datasets*

No	Dataset	No. of images	No. of Plant Species	Website
1	Swedish Leaf Dataset	1125	15	<a href="https://www.cvl.isy.liu.se/en/research/datasets/swedish-leaf/">https://www.cvl.isy.liu.se/en/research/datasets/swedish-leaf/</a>
2	Flavia Dataset	2621	33	<a href="http://flavia.sourceforge.net/">http://flavia.sourceforge.net/</a>
3	Leafsnap dataset	30866	185	<a href="http://leafsnap.com/dataset/">http://leafsnap.com/dataset/</a>
4	ImageCLEF	5436	70	<a href="https://www.imageclef.org">https://www.imageclef.org</a>
5	PlantCLEF 2014	60000	500	<a href="https://www.imageclef.org/node/179">https://www.imageclef.org/node/179</a>
6	PlantCLEF 2015	113205	1000	<a href="https://www.imageclef.org/lifeclef/2015/">https://www.imageclef.org/lifeclef/2015/</a>
7	PlantCLEF 2016	113205	1000	<a href="https://www.imageclef.org/node/198">https://www.imageclef.org/node/198</a>
8	PlantCLEF 2017	1100000	10000	<a href="https://www.imageclef.org/node/218">https://www.imageclef.org/node/218</a>

## METHOD

### Plant Organ Selection

Multiple plant characteristics can be used for analysis in classification, namely flowers, stems, leaves, fruits and even the whole plant. Multiple features can be extracted in each characteristic, such as the leaf shape, vein arrangement, texture, colour, and margins from leaves. Leaves are often favoured among researchers for plant identification studies as they do not undergo major changes throughout the year and exist in abundance for each plant (Wäldchen & Mäder, 2018b). Furthermore, there are more than 40 leaf shapes, and at least 12 types of leaf margins and nine types of venation patterns that can be extracted from leaves (OSU, 2021). Among all the features, leaf shape is the most commonly used

as it is considered the most discriminative feature of a plant. Margins are also useful for plant identification as multiple details can be extracted from the margins, namely the tooth spacing, number of teeth per centimetre and shape of the tooth themselves. The leaf venation patterns are useful as the contrast of veins compared to the rest of the leaves makes them reliable as a feature to be considered for automated plant classification. Veins are vital for the survival of a plant as it is embedded with xylem and phloem cells (Sack & Scoffoni, 2013). Factors such as environmental conditions, biomechanical support and even leaf size affect the vein structure, making vein patterns. Meanwhile, the texture of the leaves is the smoothness or roughness on the surface of the leaves and is often analysed in terms of group pixels as it must visually interpret the roughness or smoothness of the leaves (Wäldchen & Mäder, 2018b). The colours of the leaves are also vital features that can be used in plant identification. Different shades of green, edge/margin colours and hues can all be utilised to differentiate the plant species.

### Asian Local Perennial Herbs

Asian local perennial herbs grow for more than two years compared to biennial plants and annual plants native to the Asian region. These plants mostly require low maintenance, which makes them very favourable. Some of these plants are often used for cooking or decorative purposes. The selected herbs for this dataset are *Andrographis paniculata* (Green chiretta), *Plectranthus amboinicus* (Mexican mint), *Plectranthus amboinicus* 'Variegatus' (Variegated Mexican mint), *Persicaria minor* (Small water-pepper), *Centella asiatica* (Asiatic pennywort), *Gynura pseudochina* (Chinese gynura), *Gynura procumbens* (Longevity spinach), *Orthosiphon aristatus* (Java tea), *Hydrocotyle javanica* (Java pennywort), *Ocimum tenuiflorum* (Holy basil), *Clinacanthus nutans* (Snake grass) and *Ocimum citriodorum* (Lemon basil) as shown in Figure 1. These herbs need to be brought to the attention of the public for their high medicinal value, which has been described in Table 2.

### Data Collection

The introduced MYLPHerbs-1 dataset consists of 34200 images under various imaging conditions. The images were captured at various distances from the camera, illuminations, rotations and scales that reflect real-life scenarios. The acquisition settings for data collection are summarised in Table 3. The settings are based on the situations when capturing the images in real-life scenarios, in which the complexity of the images includes the variation of interclass and intraclass variability that will create more opportunities for developing more advanced machine learning classifiers. The interclass variability is obtained through various plant species, while the intraclass variability is achieved through the various acquisition settings applied to the same plant. Other consideration includes

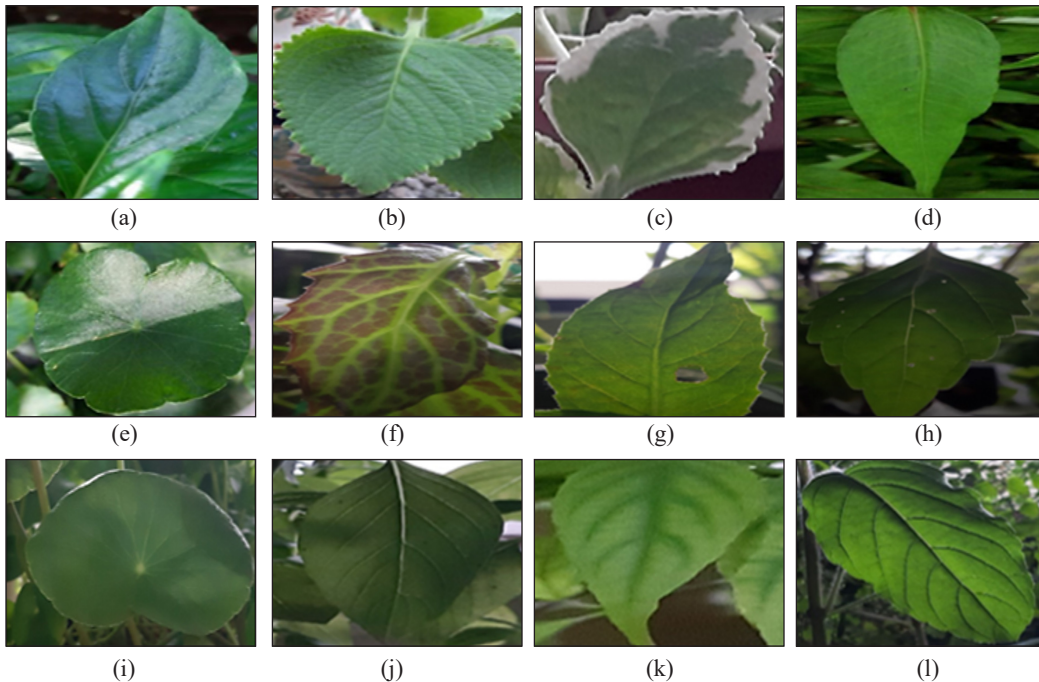


Figure 1. Plants used for the proposed dataset (a) Green chiretta (b) Mexican mint (c) Variegated Mexican mint (d) Small water-pepper (e) Asiatic pennywort (f) Chinese gynura (g) Longevity spinach (h) Java tea (i) Java pennywort (j) Holy basil (k) Snake grass (l) Lemon basil

Table 2  
The medicinal properties of the selected herbs

Plants Species	Medicinal Properties	References
<i>Andrographis paniculata</i> (Green chiretta)	Anti-microbial, anti-inflammatory, antioxidant, anti-diabetic and hepatorenal protective.	Okhwarobo et al. (2014); Kurzawa et al. (2015); Murugan et al. (2020).
<i>Plectranthus amboinicus</i> (Mexican mint)	Antimicrobial, anti-inflammatory, antitumor, antioxidant and analgesic activities.	Bhatt et al. (2013); Swamy et al. (2017); Ashaari et al. (2020)
<i>Plectranthus amboinicus</i> ' <i>Variegatus</i> ' (Variegated Mexican mint)	Antimicrobial, anti-inflammatory, antitumor, antioxidant and analgesic activities.	Bhatt et al. (2013); Swamy et al. (2017)
<i>Persicaria minor</i> (Small water-pepper)	Antioxidant, antibacterial, anti-inflammatory, and anticancer.	Vimala et al. (2012); Christopher et al. (2015); Lau et al. (2020)
<i>Centella asiatica</i> (Asiatic pennywort)	Wound healing, effective for leprosy, lupus, eczema psoriasis, relieving anxiety and improving cognition.	Gohil et al. (2010); Deshpande (2017); Giribabu et al. (2020)
<i>Gynura pseudochina</i> (Chinese gynura)	Haemostatic, antipyretic, regulate menses, to treat breast tumours, herpes infections and sore throats.	Siriwatanametanon et al. (2010); Siriwatanametanon & Heinrich (2011); Proklamasiningsih et al. (2020)



Table 2 (continue)

Plants Species	Medicinal Properties	References
<i>Gynura procumbens</i> (Longevity spinach)	Antihypertensive, antihyperglycemic, anticancer, antimicrobial, antioxidant, and anti-inflammatory activity.	Rahman and Asad (2013); Tan et al. (2016); Ashraf et al. (2020)
<i>Orthosiphon aristatus</i> (Java tea)	Antimicrobial, antioxidant, hepatoprotection, cytotoxic, cardioactive, antidiabetic and anti-inflammatory activities	Abdelwahab et al. (2010); Ashraf et al. (2018); Samidurai et al. (2020)
<i>Hydrocotyle javanica</i> (Java pennywort)	Healing common cold, tonsillitis, cephalitis, enteritis, dysentery, zoster, eczema, period pain, hepatitis, and jaundice.	Mandal et al. (2017); Mandal et al. (2016); Karthika (2020).
<i>Ocimum tenuiflorum</i> (Holy basil)	Analgesics, inflammation relievers, anti-asthmatic, hypoglycemic, hepatoprotective, hypotensive and hypolipidemic	Yamani et al. (2016); Singh and Chaudhuri (2018); Sahu et al. (2020)
<i>Clinacanthus nutans</i> (Snake grass)	Relieving skin rashes, scorpion and insect bites, diabetes mellitus, fever, and diuretics	Alam et al. (2016); Khoo et al. (2018); Haida et al. (2020).
<i>Ocimum citriodorum</i> (Lemon basil)	Antimicrobial, antioxidant, hepatoprotection, antigenotoxic, antiplasmodial, cytotoxic, cardioactive, antidiabetic, anti-inflammatory activities	dos Santos et al. (2016); Majdi et al. (2020)

the utilisation of different camera models. The images were captured using three Android phones, namely Samsung A7, Samsung J1 and Samsung J5, with a camera resolution of 24 Megapixels, 9 Megapixels and 5 Megapixels, respectively. The number of images captured by the Samsung J1 phone is 10920 images, which is 910 images for each herb. Nevertheless, a larger number of images were captured by Samsung J5 and Samsung A7, 970 images for each herb, thus providing 11640 images for each phone. The difference is due to the unavailability of the ISO 800 feature in Samsung J1.

Thus, the total number of considered features in the data collection are 91 features for Samsung J1 and 97 features for Samsung J5 and Samsung A7. Each plant has leaves with different details/features that can be learnt. Different species can be differentiated with a combination of features, namely shape, vein, colour, margin, and texture. The visual characteristics of the leaves are explained in Table 4. The characteristics of the leaves in Table 4 are just a simple explanation of what human eyes could decipher from several examples of each plant. With thousands of examples for each plant, the pre-trained deep learning algorithm would gather information from those examples at a high rate with higher sensitivity towards the features and learn to identify those plants during the testing phase. The example of images in the proposed dataset is illustrated in Figure 2. Figure 3 shows the main page of the proposed dataset that can be accessed through <https://www.mylpherbs.com/>.

Table 3  
*Summary of the image acquisition settings and their description*

Settings	Description
Various distances ranging from 5 cm till 30 cm	The distances of the camera facing the leaf are 5 cm, 10 cm, 15 cm, 20 cm, 25 cm and 30 cm.
Distance with a 45° angle at 10 cm, 20 cm and 30 cm	The camera is tilted at 45° relative to the surface of the leaf, where the images were captured at 10 cm, 20 cm and 30 cm, on both rights and left of the leaf.
Optical Zoom: 1×, 1.5×, 2×, 2.5×, 3×, 3.5× and 4×	Besides various optical zooms, the distance between the camera and leaf is 30 cm.
White balance parameters: Sun, Cloudy, Incandescent and Fluorescent:	The process of removing unrealistic colour cast, thereby improving the captured images under a wide range of lighting conditions. Other considerations include the camera facing the surface of the leaf at 10 cm, 20 cm and 30 cm, and the camera tilted at 45° relative to the right-side surface of the leaf.
ISO: 100, 200, 400 and 800	The sensitivity of the camera to light. Other considerations include the camera facing the surface of the leaf at 10 cm, 20 cm and 30 cm and tilted 45° angle relative to the right-side surface of the leaf.
Exposure: -2, -1, 0, +1, +2	The amount of light that reaches the camera sensor. Other considerations include the camera facing the surface of the leaf at 10 cm, 20 cm and 30 cm and tilted at 45° relative to the right-side surface of the leaf.

Table 4  
*Leaf characteristics of each plant*

Plant species	Leaf Characteristics
Green chiretta	Lanceolate-shaped with arcuate veins
Mexican mint	Ovate-shaped and thick with a cross-venulate type of vein and serrated edges.
Variegated Mexican mint	Similar to Mexican mint with a white edge and thinner.
Small water-pepper	Linear-lanceolate shape with pinnate venation.
Asiatic pennywort	Can range from orbicular to reniform shape
Chinese gynura	The colour is purplish with green veins. Pinnate-shaped veins changes into dichotomous shapes as it reaches the edge of the leaf blade.
Longevity spinach	Ovate-shaped and has a smooth green surface. The venation of the leaves is pinnate-shaped, where the secondary veins are paired in the opposite direction extending from the primary midvein.
Java tea	Small and rhomboid-shaped with serrated edges. The veins are pinnate shaped and have a smooth surface.
Java pennywort	Reniform-shaped with rounded margin.
Holy basil	Ovate-shaped at the base and morphs into a rhomboid shape at its tip. The veins are pinnate shaped with serrated edges.
Snake grass	Lanceolate-shaped leaf with a smooth margin. Smooth texture with arcuate veins.
Lemon basil	Smooth and ovate-shaped with pinnate venation.

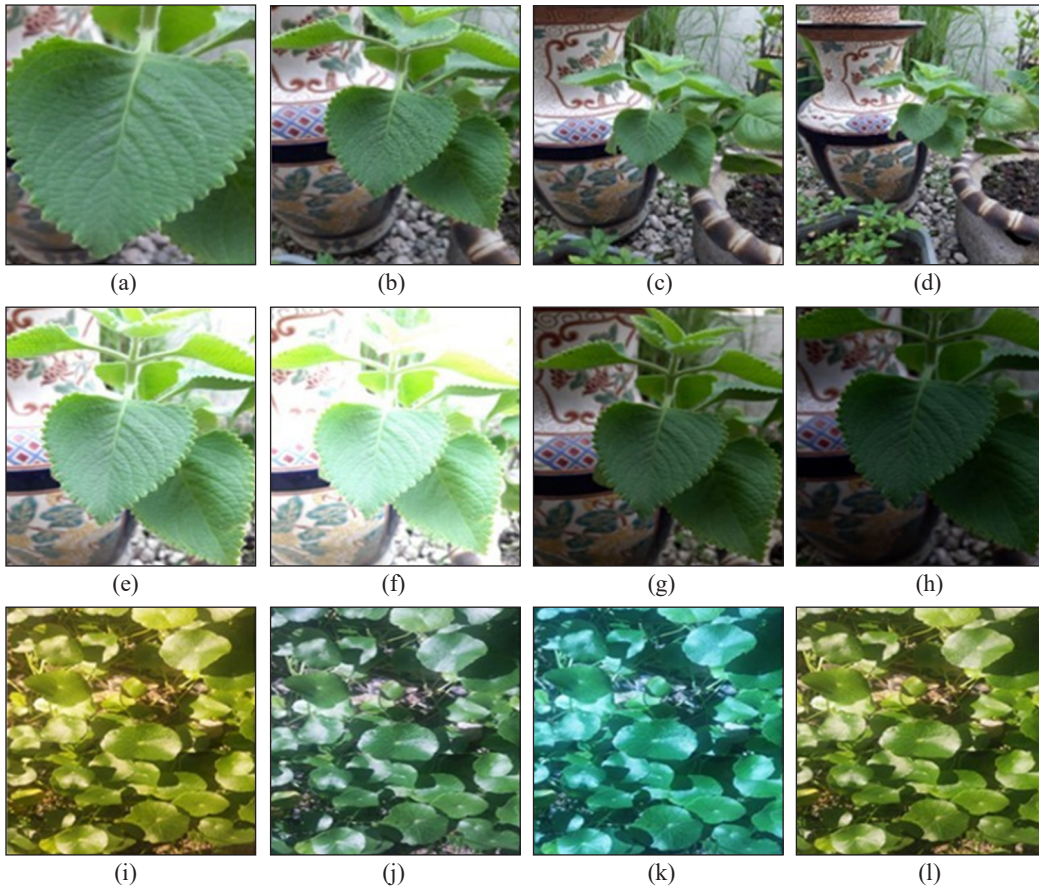


Figure 2. Examples of Mexican mint images that were captured with Samsung A7 at a distance of (a) 5 cm (b) 10 cm (c) 20 cm and (d) 30 cm; Examples of Mexican mints that were captured with Samsung A7 at 10 cm and various exposures namely (e) +1 (f) +2 (g) -1 (h) -2; Examples of Asiatic pennywort captured with Samsung J5 at a distance of 20 cm and various white balance namely (i) cloudy (j) fluorescent (k) incandescent (l) sun

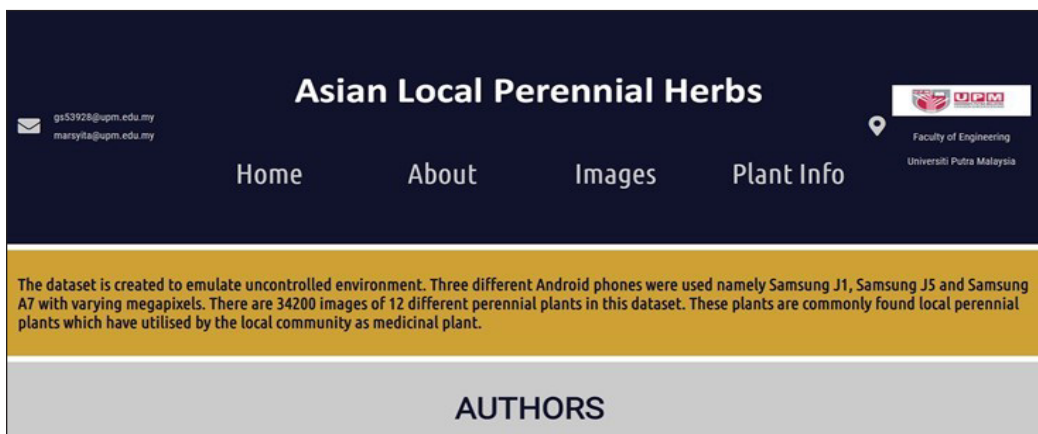


Figure 3. Screenshot of the webpage of the proposed dataset

## Experimental Setup

In this paper, the MYLPHerbs-1 dataset is evaluated using five pre-trained deep learning algorithms, namely VGG16, VGG19, ResNet50, EfficientNet B0 and EfficientNet B7. The findings can be used to create the baseline of a more advanced and reliable deep learning architecture. VGG16 and VGG19 algorithms were chosen for their good performance when classifying leaves or plants (Habiba et al., 2019; Rangarajan & Purushothaman, 2020). The VGG algorithms combine convolutional layers, pooling layers between the convolutional and fully connected layers (FC). According to Simonyan and Zisserman (2014), the algorithms produced more than 90% accuracy when tested with ImageNet with 14 million images and more than 1000 classes. ResNet50 also produced an accuracy of more than 90% when tested with the ImageNet dataset (He et al., 2015). This algorithm has a combination of 50 layers deep of convolutional block and identity block, in which each block has three convolutional layers. Meanwhile, EfficientNet utilises Inverted Residual Blocks or MBConv Block (Sandler et al., 2018), in which in the algorithm, a single convolutional filter is used for each input channel to reduce the number of operations and simultaneously increase the efficiency. There are seven versions of EfficientNet, namely EfficientNet B0, EfficientNet B1, EfficientNet B2, EfficientNet B3, EfficientNet B4, EfficientNet B5, EfficientNet B6 and EfficientNet B7. According to (Tan & Le, 2019), EfficientNet B7 outperformed all the EfficientNet variants as it produced the highest accuracy, namely 84.3%, compared to EfficientNet B0 with only 77.1% accuracy when classifying images from ImageNet.

The experiments were implemented using Python in a Jupyter notebook environment, running on Intel®Core™ i5-8250U, where the base frequency is 1.60GHz, and the maximum frequency is 3.70GHz. Transfer learning has been adopted to run the trials. It means that the architecture of the selected deep learning models has similar architecture as mentioned in Simonyan and Zisserman (2014), He et al. (2015), and Tan and Le (2019) except for the final dense layer where it is changed to 8 for the eight plant species. Adam optimiser is an adaptive learning rate technique is utilised to adapt the learning rate for each weight of the neural network. This technique can minimise the loss function. Other than that, the deep learning models were trained using pre-trained weights. The batch size is set to 32, the number of epoch and the steps per epoch are each set to 10.

Nevertheless, the experiment was conducted on eight plants, namely Green chiretta, Mexican mint, Small water-pepper, Asiatic pennywort, Chinese gynura, Longevity spinach, Java tea and Java pennywort. The acquisition process for the remaining four plants was still ongoing during the experiment. The total number of images for these eight plants is 22800, and each plant species has 2850 images. All the input images were resized to  $224 \times 224$  pixels, and data augmentation was not performed in this experiment. The performance of the deep learning algorithms in classifying a different total number of images is investigated as well. For this purpose, the images were divided into three image classes, namely, full,

half and quarter, in which each class consists of a different number of images, as shown in Table 5. The full class means that there are 22800 images from eight plant species, where there are 2850 images from each plant. As for the half and quarter classes, the total number of images used in the experiment are 1425 images and 713 images, respectively. For these two classes, the total number of images from each plant is 11400 images and 5704 images, respectively. For the purpose of investigating the performance of the deep learning algorithms, the images in each class were split into 70% for training and 30% for testing.

Table 5  
Design parameters used in the experiments

Category	Class	Number of images for training	Number of images for testing
1	Full	15960	6840
2	Half	7976	3424
3	Quarter	4000	1704

## RESULTS AND DISCUSSION

The performances of the selected deep learning algorithms were evaluated based on the accuracy, sensitivity, specificity, precision, and F1-score, as in Equations 1 to 5. Accuracy is defined as the number of correctly identified samples, while sensitivity is the number of positive samples that are accurately identified. Specificity is the number of negative samples that are correctly identified, and precision is the measurement of accurately identified samples among all the correct samples. As for the F1-score, the value represents a harmonic mean between sensitivity and precision.

$$Accuracy = \frac{TP + TN}{TP + TN + FP + FN} \quad (1)$$

$$Sensitivity = \frac{TP}{TP + FN} \quad (2)$$

$$Specificity = \frac{TN}{TN + FP} \quad (3)$$

$$Precision = \frac{TP}{TP + FP} \quad (4)$$

$$F1 - score = \frac{TP}{TP + \frac{1}{2}(TP + FN)} \quad (5)$$

where TP, TN, FP and FN are true positive, true negative, false positive and false negative. The validation accuracy produced by each algorithm is illustrated in Figure 4. It is shown that both VGG16 and VGG19 achieved more than 90% of accuracy when tested on

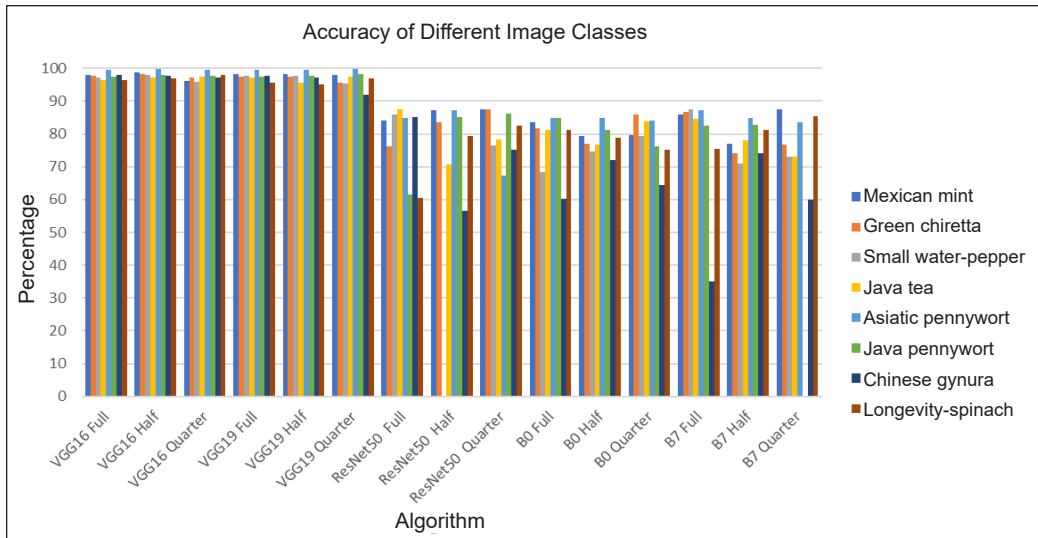


Figure 4. Accuracy performance for different image classes

the full, half and quarter datasets sizes. As for ResNet50, B0 and B7, the accuracy was consistently low. It shows that the dataset's images are very challenging to the three deep learning classifiers, and the classifiers require more images for better performance. It is also shown in He et al. (2016), Simonyan and Zisserman (2014), and Tan and Le (2019), in which the authors showed that ResNet50, EfficientNetB0 and EfficientNetB7 outperformed VGG16 and VGG19 when classifying images from ImageNet dataset that consists of 1000 classes with over 14 million images. Najafabadi et al. (2015) also concluded that some deep learning algorithms are dependent on a high number of data as they need to extract a large number of valuable data points to learn. Their hierarchical architectural nature allows for a better representation of data. Thus, the challenge of classifying images from the MYLPHerbs-1 dataset creates more opportunities for developing advanced classifiers.

The effect of the number of images on the accuracy is further explained through One Way ANOVA Analysis. This test is dependent on the p-value and significance figure. The significance figure set for this experiment is 0.01. The impact of dataset size on accuracy depends on the acceptance or rejection of the null hypothesis. The null hypothesis states that the groups being compared have no significant difference and have the same mean. Therefore, the measured p-value must be lower than the significant figure for the null hypothesis to be rejected and vice versa.

Table 6 shows the p-values for each class. Based on the values, it can be confirmed that the deep learning algorithm affects accuracy. Different deep learning algorithms affect the accuracy differently. As for Table 7, the accuracies achieved by each deep learning algorithm for each class were also compared using ANOVA analysis. The p-values show that the dataset size does not affect the accuracies of each deep learning algorithm.

Table 6  
Comparison of the p-value for each image class

p-value for each image class		
Full	Half	Quarter
$5.77 \times 10^{-24a}$	$4.77 \times 10^{-18a}$	$7.48 \times 10^{-24a}$

Note: a denotes values are significantly different

Table 7  
Comparison of the p-value for each deep learning algorithm

p-value for each deep learning algorithm				
VGG16	VGG19	ResNet50	B0	B7
0.62 <sup>b</sup>	0.62 <sup>b</sup>	0.96 <sup>b</sup>	0.17 <sup>b</sup>	0.25 <sup>b</sup>

Note: b denotes values are not significantly different

As for sensitivity, specificity, precision and F1-score, the results are shown in Figures 5 to 8. Figures 5 to 8 show that both VGG16 and VGG19 can classify the images quite accurately. The graphs also show that for VGG16 and VGG19, the different total number of images does not affect the ability of the deep learning algorithms to classify the images in the dataset. It shows that both algorithms could classify a small number of images. Nevertheless, a different trend is observed for ResNet50, B0 and B7, in which these algorithms are extremely unstable and have poor classification capabilities for this particular dataset. In Figure 5, it can be seen that ResNet50, B0 and B7 have low sensitivity, and this shows that these three algorithms are unable to correctly identify positive images, in which a low percentage of TP and there is also a possibility of a high percentage of FN. Nevertheless,

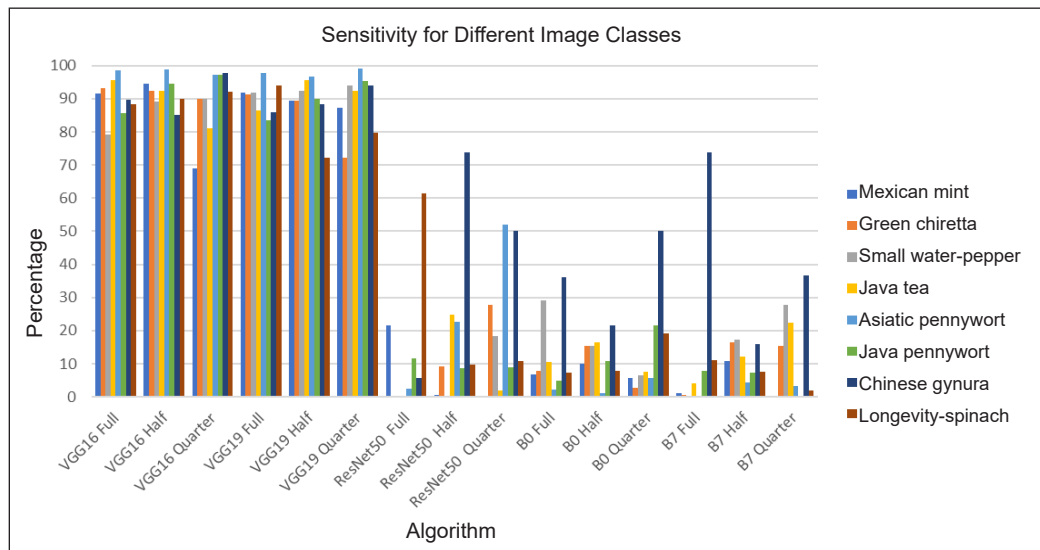


Figure 5. Sensitivity performance for different image classes

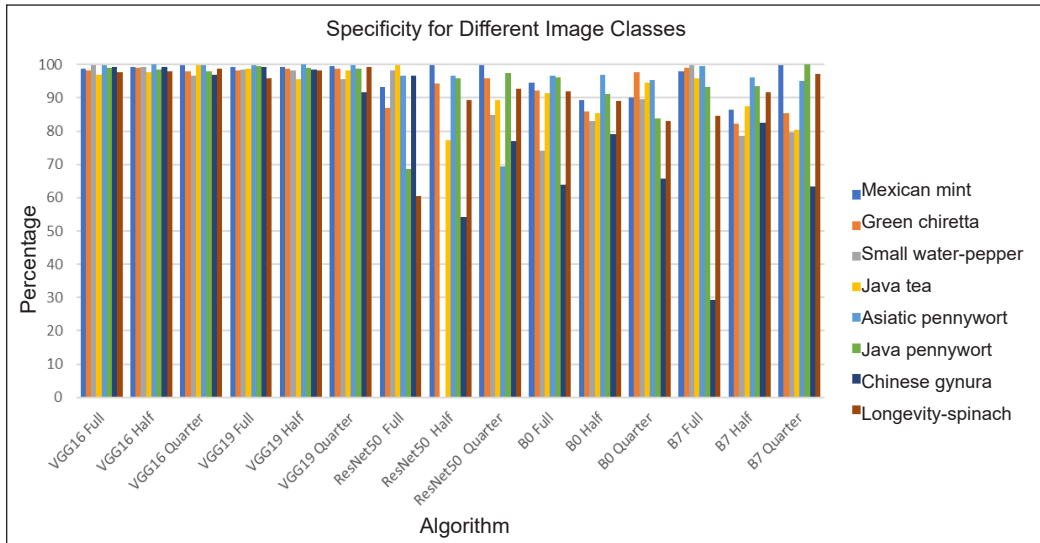


Figure 6. Specificity performance for different image classes

both VGG16 and VGG19 have high accuracy, indicating that these algorithms have high true positives and true negatives. On the other hand, ResNet50, B0 and B7 show a high specificity rate in Figure 6. The specificity rate depends on the value of the true negative.

In Figure 6, it is shown that for most of the herbs, the percentage of specificity produced by all algorithms is much better than the sensitivity rate. It shows that all the algorithms have better performance in identifying negative images. However, for ResNet50, EfficientNet B0 and EfficientNet B7 algorithms, there is a possibility of a high false-positive percentage, especially for Chinese gynura and Asiatic pennywort since the percentage of sensitivity when classifying using ResNet50, EfficientNet B0 and EfficientNet B7 is low. It is also illustrated in Figures 7 and 8, in which the ResNet50, EfficientNet B0 and EfficientNet B7 algorithms produced a low percentage of precision and F1-score. By comparing specificity and precision, it can be seen that the low precision value obtained by ResNet50, EfficientNet B0 and EfficientNet B7 proves that these three algorithms have low true positive and false-positive samples. It shows that the performance of the deep learning models is greatly influenced by the dataset used in the experiment. It must be noted that the challenge faced in this dataset is different from other datasets. Based on the existing works, ResNet50, EfficientNet B0 and EfficientNet B7 models were shown to produce good results using the ImageNet dataset. Hence, the results obtained in this experiment cannot directly reflect the results obtained through the ImageNet challenge as the images used in this dataset are completely different from the images in the ImageNet dataset. Furthermore, the performance of VGG16 and VGG19 models are better than ResNet50, EfficientNet B0 and EfficientNet B7 within the designed parameters in this experiment, where ResNet50 and EfficientNet B0 and B7 may achieve better results if these deep learning models were



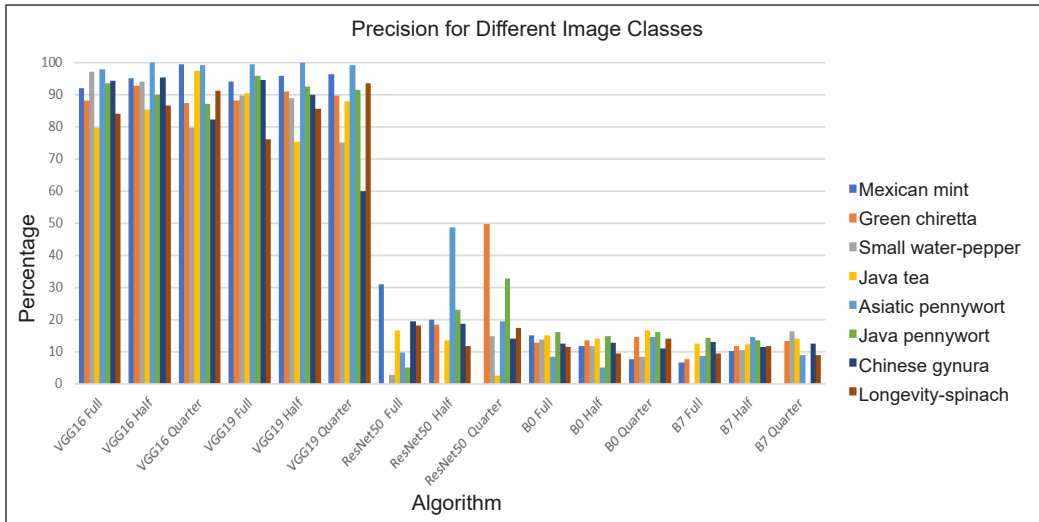


Figure 7. Precision performance for different image classes

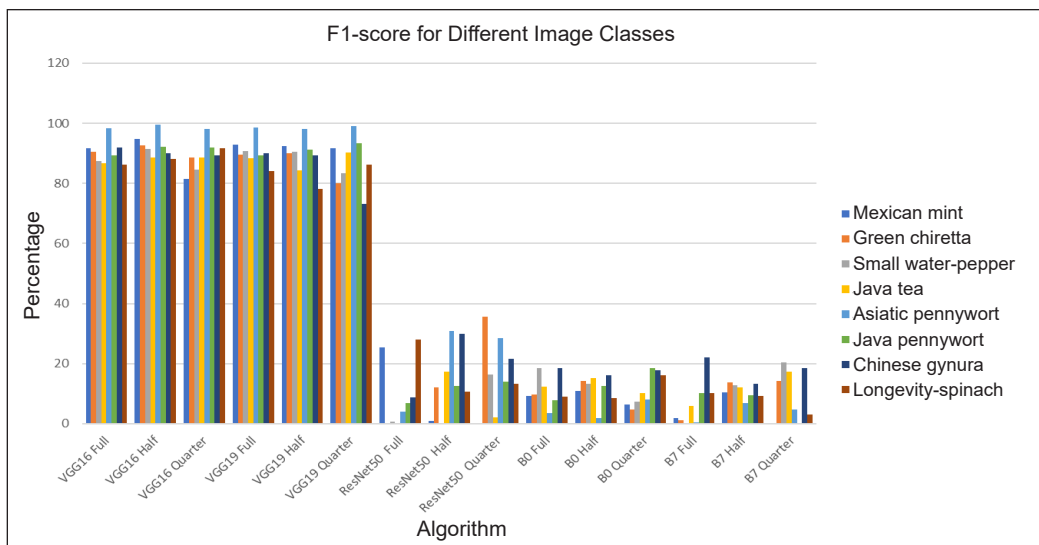


Figure 8. F1-score for different image classes

fine-tuned accordingly. In terms of the architecture of the model, VGG16 and VGG19 models have many weight layers, which could have also contributed to good performance when classifying the images from the proposed dataset.

From the results, it can be concluded that the proposed dataset is challenging. It is due to the complexity of the dataset where some of the plants have approximately similar morphological features, as shown in Figure 9. All four plants have different green tones but have somewhat similar pinnate shapes. The differences among these four plants are the structure of the vein and also the texture. As for Mexican mint, Asiatic pennywort and

Chinese gynura, these three plants have distinctive features, as shown in Figure 10, allowing for deep learning algorithms to learn quickly. Mexican mint is thick and ovate shaped with serrated edges. It also has a deep cross venulate type of vein. As for Asiatic pennywort, it has a very distinctive orbicular shape. Chinese gynura has a purplish shade with light green veins. The vein starting from the midrib are pinnate shaped and subsequently changes to a dichotomous shape as the veins reach the edge of the leaf.

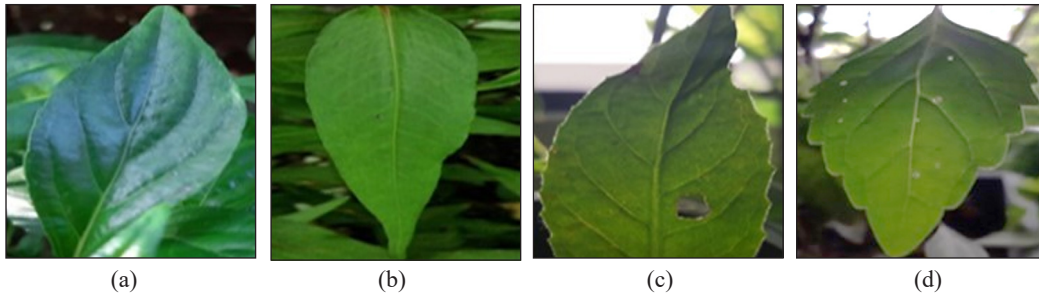


Figure 9. (a) Green chiretta (b) Small water-pepper (c) Longevity spinach (d) Java tea

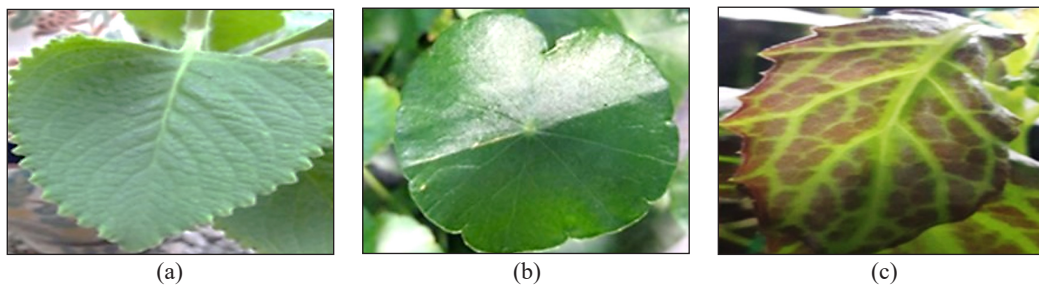


Figure 10. (a) Mexican mint (b) Asiatic pennywort (c) Chinese gynura

## CONCLUSIONS

In conclusion, the experiment showed that some of the images in the proposed dataset are very challenging for classification. It is demonstrated by the selected different deep learning algorithms, namely VGG16, VGG19, ResNet50, EfficientNet B0 and EfficientNet B7, where only the VGG16 and VGG19 algorithms can show high performance when classifying a different number of images from eight plant species in the dataset. Overall, the proposed dataset that consists of 34200 images of twelve different Asian local perennial herbs that were captured in an uncontrolled environment under various imaging conditions, such as various distances from the camera, ambient illuminations and poses, may create abundant opportunities for researchers to study further the classifiers that best suited for automatic identification or recognition of medicinal plants in real-time. The contribution to knowledge is not limited to the research community but also the public recognising the Asian local perennial herbs with high medicinal value.

## ACKNOWLEDGEMENTS

The authors wish to acknowledge the financial support received from Universiti Putra Malaysia under Putra Graduate Initiative (Vot number:9529000 and 9634300) and colleagues for their insight and expertise.

## REFERENCES

- Abdelwahab, S. I., Mohan, S., Elhassan, M. M., Al-Mekhlafi, N., Mariod, A. A., Abdul, A. B., Abdulla, M. A., & Alkharfy, K. M. (2010). Antiapoptotic and antioxidant properties of *Orthosiphon stamineus* benth (Cat's Whiskers): intervention in the Bcl-2-mediated apoptotic pathway. *Evidence-Based Complementary and Alternative Medicine*, 2011, Article 156765. <https://doi.org/10.1155/2011/156765>
- Alam, A., Ferdosh, S., Ghafoor, K., Hakim, A., Juraimi, A. S., Khatib, A., & Sarker, Z. I. (2016). *Clinacanthus nutans*: A review of the medicinal uses, pharmacology and phytochemistry. *Asian Pacific Journal of Tropical Medicine*, 9(4), 402-409. <https://doi.org/10.1016/j.apjtm.2016.03.011>
- Arun, C. H., Emmanuel, W. S., & Durairaj, D. C. (2013). Texture feature extraction for identification of medicinal plants and comparison of different classifiers. *International Journal of Computer Applications*, 62(12), 1-9. <https://doi.org/10.5120/10129-4920>
- Ashaari, N. S., Rahim, M. H. A., Sabri, S., Lai, K. S., Song, A. A. L., Rahim, R. A., Abdullah, W. M. A. N. W., & Abdullah, J. O. (2020). Functional characterization of a new terpene synthase from *Plectranthus amboinicus*. *PloS one*, 15(7), Article e0235416. <https://doi.org/10.1371/journal.pone.0235416>
- Ashraf, K., Halim, H., Lim, S. M., Ramasamy, K., & Sultan, S. (2020). *In vitro* antioxidant, antimicrobial and antiproliferative studies of four different extracts of *Orthosiphon stamineus*, *Gynura procumbens* and *Ficus deltoidea*. *Saudi Journal of Biological Sciences*, 27(1), 417-432. <https://doi.org/10.1016/j.sjbs.2019.11.003>
- Ashraf, K., Sultan, S., & Adam, A. (2018). *Orthosiphon stamineus* Benth. is an outstanding food medicine: Review of phytochemical and pharmacological activities. *Journal of Pharmacy & Bioallied Sciences*, 10(3), 109-118. [https://doi.org/10.4103/jpbs.JPBS\\_253\\_17](https://doi.org/10.4103/jpbs.JPBS_253_17)
- Begue, A., Kowlessur, V., Mahomoodally, F., Singh, U., & Pudaruth, S. (2017). Automatic recognition of medicinal plants using machine learning techniques. *International Journal of Advanced Computer Science and Applications*, 8(4), 166-175. <https://doi.org/10.14569/IJACSA.2017.080424>
- Bhatt, P., Joseph, G., Negi, P., & Varadaraj, M. (2013). Chemical composition and nutraceutical potential of Indian borage (*Plectranthus amboinicus*) stem extract. *Journal of Chemistry*, 2013, 1-7. <https://doi.org/10.1155/2013/320329>
- Christopher, P., Parasuraman, S., Christina, J., Vikneswaran, M., & Asmawi, M. (2015). Review on *Polygonum minus*. Huds, a commonly used food additive in Southeast Asia. *Pharmacognosy Research*, 7(1), 1-6. <https://doi.org/10.4103/0974-8490.147125>
- Dahigaonkar, T. D., & Kalyane, R. (2018). Identification of ayurvedic medicinal plants by image processing of leaf samples. *International Research Journal of Engineering and Technology (IRJET)*, 5, 351-355
- Deshpande, P. (2017). Formulation and evaluation of herbal wound healing formulation of *Centella asiatica*. *World Journal of Pharmaceutical Research*, 1335-1345. <https://doi.org/10.20959/wjpr20176-8658>

- dos Santos, M. S., dos Santos Souza, L. E., Costa, C. A. S., Gomes, F. P., do Bomfim Costa, L. C., de Oliveira, R. A., & da Costa Silva, D. (2016). Effects of water deficit on morpho physiology, productivity and chemical composition of *Ocimum africanum* Lour (Lamiaceae). *African Journal of Agricultural Research*, 11(21), 1924-1934. <https://doi.org/10.5897/AJAR2015.10248>
- Giribabu, N., Karim, K., Kilari, E. K., Nelli, S. R., & Salleh, N. (2020). Oral administration of *Centella asiatica* (L.) urb leave aqueous extract ameliorates cerebral oxidative stress, inflammation, and apoptosis in male rats with type-2 diabetes. *Inflammopharmacology*, 28(6), 1599-1622. <https://doi.org/10.1007/s10787-020-00733-3>
- Gohil, K., Patel, J., & Gajjar, A. (2010). Pharmacological review on *Centella asiatica*: A potential herbal cure-all. *Indian Journal of Pharmaceutical Sciences*, 72(5), 546-556. <https://doi.org/10.4103/0250-474X.78519>
- Habiba, S. U., Islam, M. K., & Ahsan, S. M. M. (2019). Bangladeshi plant recognition using deep learning-based leaf classification. In *2019 International Conference on Computer, Communication, Chemical, Materials and Electronic Engineering (IC4ME2)* (pp. 1-4). IEEE Publishing. <https://doi.org/10.1109/IC4ME247184.2019.9036515>
- Haida, Z., Nakasha, J. J., & Hakiman, M. (2020). *In vitro* responses of plant growth factors on growth, yield, phenolics content and antioxidant activities of *Clinacanthus nutans* (Sabah snake grass). *Plants*, 9(8), Article 1030. <https://doi.org/10.3390/plants9081030>
- Harsani, P., & Qurania, A. (2016). Medicinal plant species identification system using texture analysis and median filter. *Jurnal Ilmiah Kursor*, 8(4), 181-188. <https://doi.org/10.28961/kursor.v8i4.112>
- He, K., Zhang, X., Ren, S., & Sun, J. (2015). *Deep residual learning for image recognition*. arXiv preprint. <https://doi.org/10.1109/CVPR.2016.90>
- Janani, R., & Gopal, A. (2013). Identification of selected medicinal plant leaves using image features and ANN. In *2013 International Conference on Advanced Electronic Systems (ICAES)* (pp. 238-242). IEEE Publishing. <https://doi.org/10.1109/ICAES.2013.6659400>
- Karthika, S. (2020). Investigating apoptotic effects of different extracts of medicinal plants on SH-SY5Y cells. *International Journal of Green Pharmacy (IJGP)*, 14(02), 175-178.
- Khoo, L. W., Kow, S. A., Lee, M. T., Tan, C. P., Shaari, K., Tham, C. L., & Abas, F. (2018). A comprehensive review on phytochemistry and pharmacological activities of *Clinacanthus nutans* (Burm. F.) Lindau. *Evidence-Based Complementary and Alternative Medicine*, 2018, Article 9276260. <https://doi.org/10.1155/2018/9276260>
- Kurzawa, M., Filipiak-Szok, A., Kłodzińska, E., & Szłyk, E. (2015). Determination of phytochemicals, antioxidant activity and total phenolic content in *Andrographis paniculata* using chromatographic methods. *Journal of Chromatography B*, 995, 101-106. <https://doi.org/10.1016/j.jchromb.2015.05.021>
- Lau, H., Shahar, S., Mohamad, M., Rajab, N. F., Yahya, H. M., Din, N. C., & Hamid, H. A. (2020). The effects of six months *Persicaria minor* extract supplement among older adults with mild cognitive impairment: A double-blinded, randomized, and placebo-controlled trial. *BMC Complementary Medicine and Therapies*, 20(1), 1-15. <https://doi.org/10.1186/s12906-020-03092-2>

- Lulekal, E., Kelbessa, E., Bekele, T., & Yineger, H. (2008). An ethnobotanical study of medicinal plants in Mana Angetu District, Southeastern Ethiopia. *Journal of Ethnobiology and Ethnomedicine*, 4(1), 1-10. <https://doi.org/10.1186/1746-4269-4-10>
- Majdi, C., Pereira, C., Dias, M. I., Calhelha, R. C., Alves, M. J., Rhourri-Frih, B., Charrouf, Z., Barros, L., Amaral, J. A., & Ferreira, I. C. (2020). Phytochemical characterization and bioactive properties of cinnamon basil (*Ocimum basilicum* cv. 'Cinnamon') and lemon basil (*Ocimum* × *citriodorum*). *Antioxidants*, 9(5), Article 369. <https://doi.org/10.3390/antiox9050369>
- Mandal, M., Misra, D., Ghosh, N. N., & Mandal, V. (2017). Physicochemical and elemental studies of *Hydrocotyle javanica* Thunb. for standardization as herbal drug. *Asian Pacific Journal of Tropical Biomedicine*, 7(11), 979-986. <https://doi.org/10.1016/j.apjtb.2017.10.001>
- Mandal, M., Paul, S., Uddin, M. R., Mondal, M. A., Mandal, S., & Mandal, V. (2016). *In vitro* antibacterial potential of *Hydrocotyle javanica* Thunb. *Asian Pacific Journal of Tropical Disease*, 6(1), 54-62. [https://doi.org/10.1016/S2222-1808\(15\)60985-9](https://doi.org/10.1016/S2222-1808(15)60985-9)
- Murugan, N. A., Pandian, C. J., & Jeyakanthan, J. (2020). Computational investigation on *Andrographis paniculata* phytochemicals to evaluate their potency against SARS-CoV-2 in comparison to known antiviral compounds in drug trials. *Journal of Biomolecular Structure and Dynamics*, 39(12), 4415-4426. <https://doi.org/10.1080/07391102.2020.1777901>
- Najafabadi, M. M., Villanustre, F., Khoshgoftaar, T. M., Seliya, N., Wald, R., & Muharemagic, E. (2015). Deep learning applications and challenges in big data analytics. *Journal of Big Data*, 2(1), 1-21. <https://doi.org/10.1186/s40537-014-0007-7>
- Okhwarobo, A., Falodun, J. E., Erharuyi, O., Imieje, V., Falodun, A., & Langer, P. (2014). Harnessing the medicinal properties of *Andrographis paniculata* for diseases and beyond: A review of its phytochemistry and pharmacology. *Asian Pacific Journal of Tropical Disease*, 4(3), 213-222. [https://doi.org/10.1016/S2222-1808\(14\)60509-0](https://doi.org/10.1016/S2222-1808(14)60509-0)
- OSU. (2021). *Plant identification: Examining leaves*. Oregon State University. Retrieved January 2, 2021, from <https://landscapeplants.oregonstate.edu/plant-identification-examining-leaves>
- Pornpanomchai, C., Rimdusit, S., Tanasap, P., & Chaiyod, C. (2011). Thai herb leaf image recognition system (THLIRS). *Agriculture and Natural Resources*, 45(3), 551-562.
- Proklamasiningsih, E., Budisantoso, I., Kamsinah, K., & Widodo, P. (2020). Antioxidant activity and flavonoid contents of daun dewa (*Gynura pseudochina*) in various substrates with humic acid treatment. In *IOP Conference Series: Earth and Environmental Science* (Vol. 593, No. 1, p. 012026). IOP Publishing. <https://doi.org/10.1088/1755-1315/593/1/012026>
- Rahman, A., & Asad, M. (2013). Chemical and biological investigations of the leaves of *Gynura procumbens*. *International Journal of Biosciences* 3(4), 36-43. <https://doi.org/10.12692/ijb/3.4.36-43>
- Rangarajan, A. K., & Purushothaman, R. (2020). Disease classification in eggplant using pre-trained VGG16 and MSVM. *Scientific Reports*, 10(1), 1-11. <https://doi.org/10.1038/s41598-020-59108-x>
- Sack, L., & Scoffoni, C. (2013). Leaf venation: Structure, function, development, evolution, ecology and applications in the past, present and future. *New Phytologist*, 198(4), 983-1000. <https://doi.org/10.1111/nph.12253>

- Sahu, P. K., Singh, S., Gupta, A. R., Gupta, A., Singh, U. B., Manzar, N., Bhowmik, A., Singh, H. V., & Saxena, A. K. (2020). Endophytic bacilli from medicinal-aromatic perennial Holy basil (*Ocimum tenuiflorum* L.) modulate plant growth promotion and induced systemic resistance against *Rhizoctonia solani* in rice (*Oryza sativa* L.). *Biological Control*, 150, Article 104353. <https://doi.org/10.1016/j.biocontrol.2020.104353>
- Samidurai, D., Pandurangan, A. K., Krishnamoorthi, S. K., Perumal, M. K., & Nanjian, R. (2020). Sinensetin isolated from *Orthosiphon aristatus* inhibits cell proliferation and induces apoptosis in hepatocellular carcinoma cells. *Process Biochemistry*, 88, 213-221. <https://doi.org/10.1016/j.procbio.2019.09.031>
- Sandler, M., Howard, A., Zhu, M., Zhmoginov, A., & Chen, L. C. (2018). Mobilenetv2: Inverted residuals and linear bottlenecks. In *Proceedings of the IEEE conference on computer vision and pattern recognition* (pp. 4510-4520). IEEE Publishing. <https://doi.org/10.1109/CVPR.2018.00474>
- Simonyan, K., & Zisserman, A. (2014). *Very deep convolutional networks for large-scale image recognition*. arXiv preprint.
- Singh, D., & Chaudhuri, P. K. (2018). A review on phytochemical and pharmacological properties of Holy basil (*Ocimum sanctum* L.). *Industrial Crops and Products*, 118, 367-382. <https://doi.org/10.1016/j.indcrop.2018.03.048>
- Singh, V., & Misra, A. K. (2017). Detection of plant leaf diseases using image segmentation and soft computing techniques. *Information Processing in Agriculture*, 4(1), 41-49. <https://doi.org/10.1016/j.inpa.2016.10.005>
- Siriwatanametanon, N., & Heinrich, M. (2011). The Thai medicinal plant *Gynura pseudochina* var. *hispidula*: Chemical composition and *in vitro* NF- $\kappa$ B inhibitory activity. *Natural Product Communications*, 6(5). <https://doi.org/10.1177/1934578X1100600512>
- Siriwatanametanon, N., Fiebich, B. L., Efferth, T., Prieto, J. M., & Heinrich, M. (2010). Traditionally used Thai medicinal plants: *In vitro* anti-inflammatory, anticancer and antioxidant activities. *Journal of Ethnopharmacology*, 130(2), 196-207. <https://doi.org/10.1016/j.jep.2010.04.036>
- Sladojevic, S., Arsenovic, M., Anderla, A., Culibrk, D., & Stefanovic, D. (2016). Deep neural networks-based recognition of plant diseases by leaf image classification. *Computational Intelligence and Neuroscience*, 2016, Article 3289801. <https://doi.org/10.1155/2016/3289801>
- Swamy, M., Arumugam, G., Kaur, R., Ghasemzadeh, A., Yusoff, M., & Sinniah, U. (2017). GC-MS based metabolite profiling, antioxidant and antimicrobial properties of different solvent extracts of Malaysian *Plectranthus amboinicus* Leaves. *Evidence-Based Complementary and Alternative Medicine*, 2017, Article 1517683. <https://doi.org/10.1155/2017/1517683>
- Tan, H. L., Chan, K. G., Pusparajah, P., Lee, L. H., & Goh, B. H. (2016). *Gynura procumbens*: An overview of the biological activities. *Frontiers in Pharmacology*, 7, Article 52. <https://doi.org/10.3389/fphar.2016.00052>
- Tan, M., & Le, Q. (2019). Efficientnet: Rethinking model scaling for convolutional neural networks. In *International Conference on Machine Learning* (pp. 6105-6114). PMLR.
- Vijayashree, T., & Gopal, A. (2017). Authentication of herbal medicinal leaf image processing using Raspberry Pi processor. In *2017 International Conference on Intelligent Computing and Control Systems (ICICCS)* (pp. 1304-1307). IEEE Publishing. <https://doi.org/10.1109/ICCONS.2017.8250679>

- Vimala, S., Rohana, S., Rashih, A., & Juliza, M. (2012). Antioxidant evaluation in Malaysian medicinal plant: *Persicaria minor* (Huds.) leaf. *Science Journal of Medicine and Clinical Trials*, *1*, 9-16.
- Wäldchen, J., & Mäder, P. (2018a). Machine learning for image-based species identification. *Methods in Ecology and Evolution*, *9*(11), 2216-2225. <https://doi.org/10.1111/2041-210X.13075>
- Wäldchen, J., & Mäder, P. (2018b). Plant species identification using computer vision techniques: A systematic literature review. *Archives of Computational Methods in Engineering*, *25*(2), 507-543. <https://doi.org/10.1007/s11831-016-9206-z>
- Wäldchen, J., Rzanny, M., Seeland, M., & Mäder, P. (2018). Automated plant species identification - Trends and future directions. *PLoS Computational Biology*, *14*(4), Article e1005993. <https://doi.org/10.1371/journal.pcbi.1005993>
- Yamani, H. A., Pang, E. C., Mantri, N., & Deighton, M. A. (2016). Antimicrobial activity of Tulsi (*Ocimum tenuiflorum*) essential oil and their major constituents against three species of bacteria. *Frontiers in Microbiology*, *7*, Article 681. <https://doi.org/10.3389/fmicb.2016.00681>





*Review article*

## The Effect of Elevated Temperature on Engineered Cementitious Composite Microstructural Behavior: An Overview

Mohamad Hakimin Khazani<sup>1</sup>, Oh Chai Lian<sup>1\*</sup>, Lee Siong Wee<sup>2</sup>, Mohd Raizamzamani Md Zain<sup>1</sup> and Norrul Azmi Yahya<sup>1</sup>

<sup>1</sup>School of Civil Engineering, College of Engineering, Universiti Teknologi MARA, 40450 UiTM, Shah Alam, Selangor Darul Ehsan, Malaysia

<sup>2</sup>School of Civil Engineering, College of Engineering, Universiti Teknologi MARA Johor, Pasir Gudang Campus, 81750 UiTM, Masai, Johor, Malaysia

### ABSTRACT

This paper discusses the quantitative bibliographic data derived from scientific publications on Engineered Cementitious Composites (ECC) subjected to elevated temperature, the influence of elevated temperature on the mechanical properties, particularly the compressive strength and microstructure behavior of Engineered Cementitious Composites (ECC) mixtures based on the review of previous pieces of literature. Systematic literature reviews were employed as the methodology in this study. The age of related publications selected to be reviewed was limited to publications for the past ten years, 2010 to December 2020. It was found from available research that exposure of the ECC specimen at the elevated temperature starting from 200°C significantly reduced the compressive strength when the temperature increases, melting of fiber and increase of porosity causes the dramatically increase micro-cracks.

*Keywords:* Cracks, Engineered Cementitious Composites (ECC), elevated temperature, fiber, microstructure, scanning electron microscope (SEM)

### ARTICLE INFO

*Article history:*

Received: 26 May 2021

Accepted: 15 September 2021

Published: 10 January 2022

DOI: <https://doi.org/10.47836/pjst.30.1.24>

*E-mail addresses:*

hakiminkhazani96@gmail.com (Mohamad Hakimin Khazani)

chailian@uitm.edu.my (Oh Chai Lian)

leesiongwee@uitm.edu.my (Lee Siong Wee)

raizam@uitm.edu.my (Mohd Raizamzamani Md Zain)

norrulazmi@uitm.edu.my (Norrul Azmi Yahya)

\* Corresponding author

### INTRODUCTION

Engineered Cementitious Composite (ECC) is a special type of High-Performance Fiber Reinforced Cementitious Composites, distinct for tensile strain-hardening behavior and tensile ductility compared to the quasi-brittle design of conventional concrete

and fiber-reinforced concrete (Huang & Zhang, 2014; Khan et al., 2021). ECC has demonstrated excellent uniaxial tensile strain capacity of 3–5% (about 300–500 times higher than conventional concrete, which is 0.01%) and tight crack width of about 40  $\mu\text{m}$  (Li, 2003; Ma et al., 2015). ECC incorporates industrial waste has also been studied for more greener and sustainable construction materials (Booya et al., 2020; Chen et al., 2013; Lee et al., 2019). The use of ECC has expanded dramatically over the last decade and has been used in a number of systems, such as high-rise buildings (Yang et al., 2021), bridges (Zhang et al., 2021), tunnels (Huang et al., 2021), highways (Guan et al., 2021) and other infrastructures. ECC is suggested in strengthening beam-to-column connections that are recurrently exposed to cyclic loading, a continuous and repeated loading, such as fluctuating stresses, strains, and forces, seismic actions (Lee et al., 2018; Qudah & Maalej, 2014). The ECC-concrete beams with ECC application at the tension region, when subjected to flexural load, displayed a substantial improvement in flexural strength and ductility, proven under both the experimental and theoretical aspects (Yuan et al., 2020; Zhang et al., 2006).

The study of rheological and mechanical properties of the ECC especially dealing with the risk of exposure to elevated temperatures has recently attracted attention. Table 1 shows the previous studies on ECCs subjected to elevated temperature, with different raw materials applications, geometry specifications, experimental testing, and heating parameters. It is found from Table 1 that common raw materials in ECCs are cement, mineral admixtures (i.e., silica fume, limestone powder, fly ash), sand (i.e., river, sand), fibers (i.e., PVA, PE), and superplasticizer. Previous studies investigated strength performances of ECC specimens under room temperature and temperatures at a range of 50°C to 1200°C. The ECC specimens were subjected to a heating rate of 4.4°C/min to 23.5°C with heating exposure for 1–2 hours. High temperature can cause changes in the physical and chemical properties of the ECC, which further affect the mechanical properties and microstructural behavior of the material. The effect of the elevated temperature on mechanical properties, particularly compressive strength and microstructural behavior, such as deterioration of fiber and microcracking that reduce the durability of the ECC, was seen clearly (Şahmaran et al., 2011). It is, therefore, necessary to fully understand the effects of high temperature on ECC so that the applications of ECC could be more effective and sustainable.

This paper presents an overview of the effects of elevated temperature on the microstructural behaviour of ECC. The systematic and integrative reviews were used as the methodology in this study. This study focuses on the selected related research articles limited to recent ten-years publications. This paper consists of four sections. Section 2 presents the methodology of the literature review. Section 3 presents the results of the bibliometric analysis of the topic. Section 4 discusses the effects of elevated temperature on the compressive strength, deterioration of fibers, and microcracking behavior of ECC. Finally, Section 5 presents the conclusions.

Table 1  
*Previous studies on ECCs subjected to high temperatures*

Reference	Raw Materials	Sample size	Experimental testing	Targeted Temperature	Heating Rate	Heat Exposure Time, hour(h)
Bhat et al. (2014)	Type I Ordinary Portland Cement (OPC), class F fly ash (FA), polyvinyl alcohol (PVA) fiber, polycarboxylate-based high range water reducer (HRWR)	229×76.2×12.7mm	Uniaxial tensile test, Uniaxial compressive test	100°C, 200°C, 300°C, 400°C, 600°C	23.5°C/min	2 h
Mohammed et al. (2019)	OPC, nano-silica (NS), class F FA, PVA fiber, washed river sand (average size of 450 µm), HRWR	50mm cubes and dog-bone-shaped	Uniaxial tensile test, Uniaxial compressive test	100°C, 200°C, 300°C, 400°C	15°C/min	1 h
Luo et al. (2019)	OPC, Limestone Powder, Silica Fume (SF), Polyethylene (PE) fiber	40×40×160mm and 40×40×40mm	Uniaxial tensile and compressive test, Flexural test	20°C, 50°C, 100°C, 140°C, 200°C	6.6°C/min	2 h
Abdullah et al. (2013)	Class F FA, alkaline activator	50mm cubes	Uniaxial compressive test	400°C, 600°C, 800°C	4.4°C/min	1 h
Shang and Lu (2014)	Type I OPC, Class F FA, sand, water, PVA fibers, a polycarboxylic ether type HRWR, and hydroxypropyl methylcellulose	Dog-bone-shape	Uniaxial compressive test, Mass Loss	200°C, 400°C, 600°C, 800°C	13.3°C/min	1 h
Şahmaran et al. (2011)	Class F FA, PVA fiber, polycarboxylate-based HRWR	50mm cubes and 200×75×13mm	Uniaxial compressive test, Fire Resistance	200°C, 400°C, 600°C, 800°C	15°C/min	1 h
Wang et al. (2020)	OPC, river sand, PVA fibers	100mm cubes	Uniaxial compressive test	200°C, 400°C, 600°C, 800°C, 1200°C	20°C/min	1 h

**METHODOS**

A systematic literature review approach was employed to overview the microstructural behavior of ECCs after being subjected to elevated temperatures. This approach has been broadly used in many research works and can directly provide important findings from the existing field of knowledge (Ren et al., 2020). In addition to a systematic and comprehensive search to find all previous studies relevant to the research topic, this approach includes explicit criteria that can include or exclude studies to ensure the quality search of the literature. The review protocol for this study is illustrated in Figure 1.

Generally, the protocol consists of two main phases. In the first phase, the data for the bibliographic of the study of microstructure analysis on ECC subjected to elevated temperature was done from a complete retrieval from online databases in Scopus. Scopus is easily accessible, available in the organization subscriptions as well as it is notably with good coverage of publications at sufficiently high quality. The selections were then filtered to obtain the actual trend of the research. The trend of publication year and research work allocation were the data aimed for the retrieval. Computerized databases were used as an approach to obtain this literature because this approach is more efficient and effective.

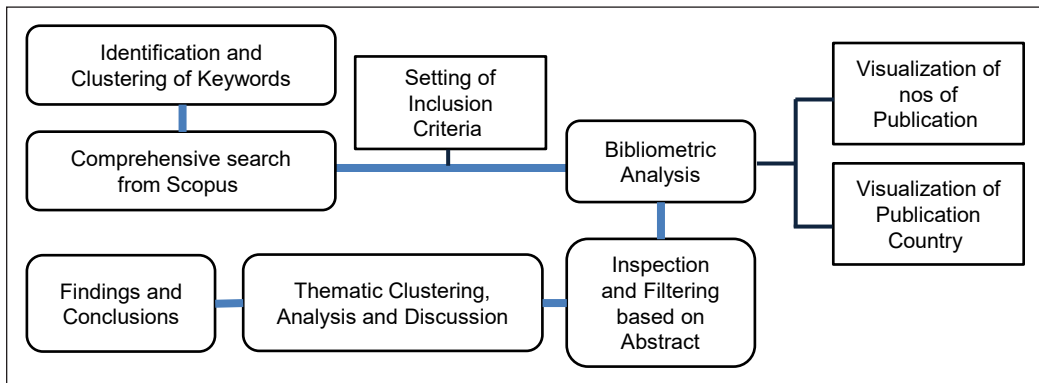


Figure 1. Review protocol

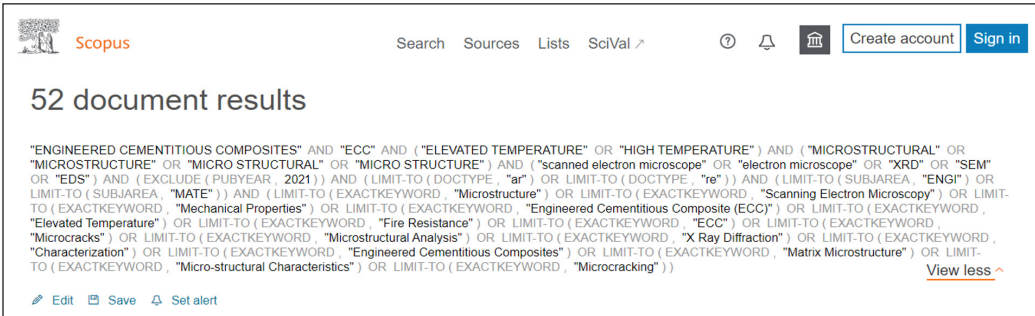
Table 2  
Results of literature retrieval and selection

Steps	Descriptions	Records
Logical Statement in Advance Search	"ENGINEERED CEMENTITIOUS COMPOSITES" AND "ECC" AND ( "ELEVATED TEMPERATURE" OR "HIGH TEMPERATURE" ) AND ( "MICROSTRUCTURAL" OR "MICROSTRUCTURE" OR "MICRO STRUCTURAL" OR "MICRO STRUCTURE" ) AND ( "scanned electron microscope" OR "electron microscope" OR "XRD" OR "SEM" OR "EDS" )	Valid records (first-round filter): 90
Inclusion criteria	Publication years (2010 to Dec 2020), Type of publication: Article, Keywords, subject area: engineering and material science.	Final records (second-round filter): 52

The search started with all the literature based on the topics that related to the research's title. Then, the advanced search function in Scopus online collection database was used to search the related articles. Finally, keywords were used, such as Engineered Cementitious Composites, elevated temperature, microstructural, scanning electron microscope, and electron microscope. The actual coding for the advance search in Scopus is shown in Table 2.

The procedure followed the setting of inclusion criteria. These criteria include the publication years, publication types, refining keywords, and subject matters. Particularly, publication years were limited to 2010 to December 2020. The document types were confined to only research and review articles. Other types of literature, such as the book, conference paper, and book chapter, were not considered. Subject matters, such as engineering and materials science were included, and refining keywords, such as microstructure, scanning electron microscopy, engineered cementitious composite (ECC), elevated temperature, fire resistance, microcracks, microstructural analysis, micropores, x-ray diffraction, fire exposures, matrix microstructure, microstructural characteristics and microcracking were included. Figure 2 shows the number of articles after applying the inclusion criteria.

The entire abstract from 52 articles recorded from the second-round filter was clustered according to the themes. Next, the themes were identified to answer the research questions, such as (1) What are the effects of the temperature on the compressive strength of ECC, and (2) What are the effects of elevated temperature on microstructural behavior of ECC? Finally, the articles that fit the themes of the study were chosen for further analysis, data discussion, and evaluation.



The screenshot shows the Scopus search interface. At the top, there is a search bar and navigation links for Search, Sources, Lists, and SciVal. On the right, there are buttons for 'Create account' and 'Sign in'. The main content area displays '52 document results' and a large, complex logical search statement. The statement is a long string of keywords and operators (AND, OR, EXCLUDE, LIMIT-TO) used to filter the search results. At the bottom of the search statement, there is a 'View less' link. Below the search statement, there are icons for 'Edit', 'Save', and 'Set alert'.

Figure 2. Logical statement and inclusion criteria (Image from Scopus online database)

## RESULTS AND DISCUSSION

### Bibliometric Analysis

Figure 3 shows the publications for the last ten years for the topics as filtered in Figure 2. Research related to the microstructural behavior of ECC after exposure to elevated

temperature has gotten the attention of researchers in recent years. A significant increasing trend of publications can be seen from 2017 to 2020. The highest number of publications (16 nos) was recorded in 2020.

Figure 4 shows the statistical distribution of data number of publications per country for the last ten years. China has actively published articles and showed interest in the research regarding the exposure of ECC to elevated temperature (25 nos of publications), followed by the United States, recorded as 12 publications in years 2010-2020. On the other hand, very few works were done on this study in the countries of the Association of Southeast Asian Nations (ASEAN); only two publications were detected in Malaysia and Singapore, respectively.

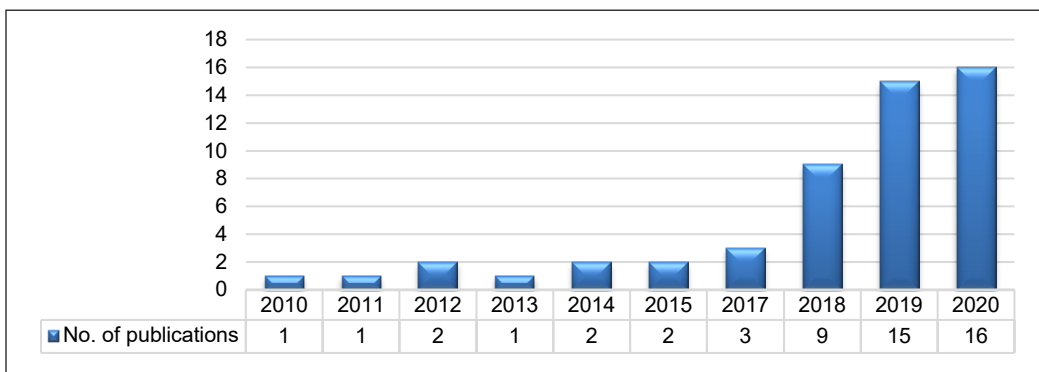


Figure 3. Numbers of publications per year (2010-2020)

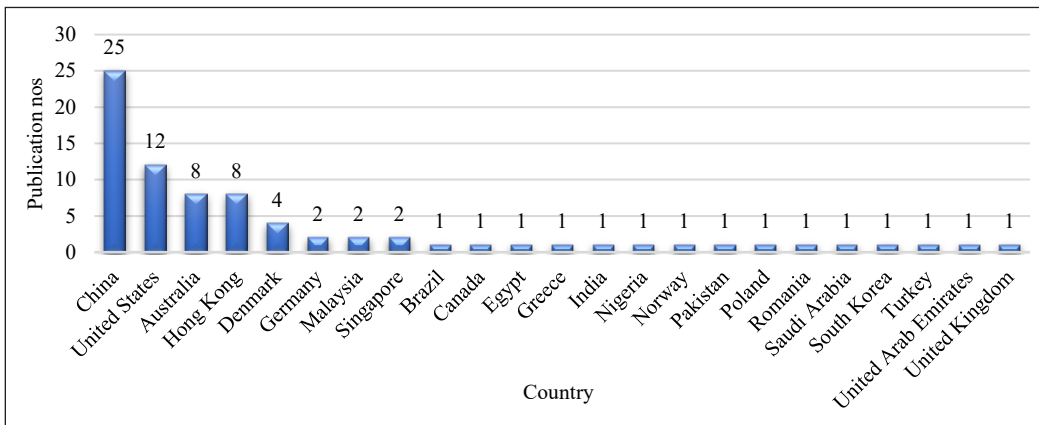


Figure 4. Statistical distribution of data number of publications per country

### Effect of Temperature on Compressive Strength

Table 3 shows the compressive strength of ECCs after exposure to different temperatures. A decreasing trend in the compressive strength is observed when ECCs exposed to elevated temperatures starting from 200°C. The decrement of the compressive strength is obvious

Table 3  
Compressive strength of ECCs after exposure to different temperatures

Reference	Types of mineral admixture (MA/C)	Types of fine aggregate	Types of Fiber	Compressive strength after exposure to different temperatures							
				50°C	100°C	140°C	200°C	400°C	600°C	800°C	1200°C
(Şahmaran et al., 2011)	FA (1.2) for ECC1	110 µm SS	PVA 2% v.f.	-	-	-	-14%	-15%	-47%	-66%	-
(Şahmaran et al., 2011)	FA (2.2) for ECC2	110 µm SS	PVA 2% v.f.	-	-	-	-22%	-23%	-49%	-69%	-
(Shang & Lu, 2014)	FA (0.5)	Sand (size not specified)	PVA 2% v.f.	-	-	-	+1%	-32%	-62%	-77%	-
(Luo et al., 2019)	LP (0.3), SF (0.25), GGBS (1.25)	100 µm SS	PE 2% v.f.	+20%	+15%	-8.3%	-50.5%	-	-	-	-
(Du et al., 2018)	-	-	PVA 2% v.f.	-	-	-	-5.2%	-18.5%	-	-	-
(Yu et al., 2015)	FA	Sand	PVA 2% v.f.	-	-	-	+3.6%	-11%	-32%	-74%	-
(Aslani & Wang, 2019)	FA, SF	150 µm SS	PVA 1.75%	-	+30%	-	-	-26%	-52%	-70%	-
(Wang et al., 2020)	-	River sand 2mm	PVA 2% v.f.	-	-	-	-18.1%	-18.4%	-47.2%	-67%	-89.3

Note: + indicates an increase in compressive strength, - indicates a decrease in compressive strength  
MA, FA, SF, SS denote mineral admixture, Fly ash, Silica Fume, Silica sand, respectively  
v.f. denotes volume fraction (assume density of PVA fiber = 1290kg/m<sup>3</sup>, density PE fiber = 970kg/m<sup>3</sup>)

after 400°C. Şahmaran et al. (2011) found a greater decrement in the compressive strength for ECC with higher fly ash volume at 200°C–400°C, however no significant effect of fly ash volume in the reduction at 600°C–800°C. According to Şahmaran et al. (2011), decreasing in compressive strength when exposed to 200°C is due to the hydration of fly ash particles, whereas at temperature 400°C is due to porosity increase and weight loss. ECC specimens demonstrated a great loss in compressive strength after being exposed at temperatures 600°C to 800°C. A greater reduction in compressive strength, especially at temperature 400°C to 800°C, was reported by Shang and Lu (2014) in their ECC specimens with lower fly ash content. When the ECC specimens were subjected to temperature 1200°C, the decrement up to 89% compared to the one at room temperature was noticed.

Luo et al. (2019) found enhancement in compressive strength when the ECC specimen exposure to a temperature lesser than 100°C. However, decreases steadily started from 50°C to 200°C. The higher temperature increased the pore size and porosity of the specimen. The drastic change in the compressive strength was due to visible minor cracking and increase of porosity (Luo et al., 2019; Şahmaran et al., 2011; Shang & Lu, 2014).

Heating duration can affect the residual mechanical properties of the specimen (Yu et al., 2015). For example, after being exposed for one hour at a temperature of 200°C, the compressive strength increased 3.6%. After two hours of exposure at the same temperature, the compressive strength of the specimen increased 11.5%. The changes in the mechanical properties of the specimen at this temperature may be due to the reinforced hardened cement paste (HCP) during the evaporation of free water, leading to greater Van der Waal forces as the cement gel layers pass closer to each other. The same goes for the study by Aslani and Wang (2019), whereby the compressive strength increases 30% after being exposed to 100°C. The decreasing of the compressive strength at temperature 400 might be due to small microcracks appearing and a drastic decrease of the compressive strength after exposure up to 600, maybe because this temperature level was a critical temperature for strength loss in ECC specimens.

Exposure of ECCs to high temperatures tends to experience moisture loss, and this scenario causes the increment of the initial porosity of ECCs. The increasing porosity resulting from high temperature coarsens the pore size and subsequently gives a remarkably negative effect to the compressive strength (Luo et al., 2019; Şahmaran et al., 2011; Shang & Lu, 2014). Melting of fiber in ECC at high temperature is the reason for the great number of pores and high porosity of the matrix. Figure 5 shows the cumulative pore volume of the ECC specimens after being exposed to the targeted temperature.

Most of the studies mentioned above investigated the strong performances of ECCs at exposure temperature 200°C and onwards. It is supported by Luo et al. (2019), where there are no significant changes in the strength before exposure to a temperature below 200°C. Although many have provided strength performance data at a temperature range from 200°C–800°C, ECCs investigated in these studies mainly incorporated PVA fiber at



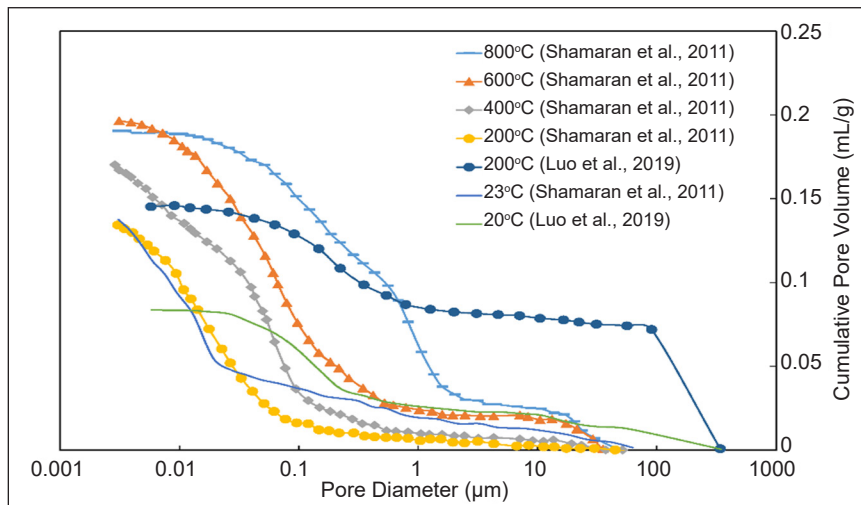


Figure 5. Cumulative pore volume of the sample before and after exposure to elevated temperature by (a) (Şahmaran et al., 2011), and (b) (Luo et al., 2019)

2% volume fraction. Findings on this topic for other fibers (i.e., steel, PE fibers) and their percentages are very limited. Additionally, incorporating the mineral admixtures in these studies is in wide options (i.e., fly ash, silica fume, slag). These findings hardly conclude that they provide a real understanding of the behavior of the ECCs when exposed to elevated temperatures.

### Microcracking and Fibre Deterioration

Table 4 presents the effect of different temperature levels on the deterioration of fiber and the microstructural behavior of ECC. The heating regime is explained based on four main temperature ranges, namely 0°C–200°C, 201°C–400°C, 401°C–600°C, and 601°C–800°C. The melting point of PE fibers in ECC is observed at 150°C, causing the increase of the porosity and the average pore size of the ECC specimen (Luo et al., 2019). On the other hand, the temperature effect on the microstructure of the fiber at 140°C caused the unrecoverable deformation, which affected the mechanical properties of the specimen. On the one hand, PVA fibers started to melt, and micropores began to appear at a temperature of 200°C (Bhat et al., 2014).

At temperature 400°C, the PVA fibers have melted completely and created micropores and interconnected pores in the ECC microstructure (Bhat et al., 2014; Mohammed et al., 2019; Şahmaran et al., 2011; Shang & Lu, 2014). More micropores were observed in the specimen that was exposed to a temperature level of 600°C. The average pore diameter size of the ECC specimen exposed to a temperature of 600°C rapidly changes caused by the totally melted fibers and water evaporation. The magnification of SEM by Bhat et al. (2014) was chosen to illustrate the effect of temperature on the PVA fiber (Figure 6).

For instance, microstructure did not experience any changes at temperature 20°C (Figure 6a). Fiber started to melt, and micropores appeared at 200°C (Figure 6b) while the fiber completely melted, and more micropores appeared at 400°C to 800°C (Figures 6c and 6d). Similar findings were reported by Wang et al. (2020), and three mechanisms were claimed to play roles: the effects of thermal expansion, volume expansion due to chemical reactions, and coarsening of pore structure.

The crystalline calcium hydroxide (CH) started to disappear after the specimen was exposed to a temperature of 100°C (Mohammed et al., 2019). After exposure at a temperature of 200°C, tiny micro-cracks started to visible. The number and size of the micro cracks at this temperature also increase (Shang & Lu, 2014). Conversely, Şahmaran et al. (2011) reported no significant changes in the microstructure, and micro-cracks were not apparent at a temperature of 200°C.

Specimens exposed to the temperature of 300°C and 400°C became porous. The more micro-crack appeared at this temperature level due to the melted PVA fibers, dehydration, and degradation of the cementitious material (Mohammed et al., 2019). However, microcrack only started to be visible at 400°C in ECCs (Abdullah et al., 2013; Şahmaran et al., 2011).

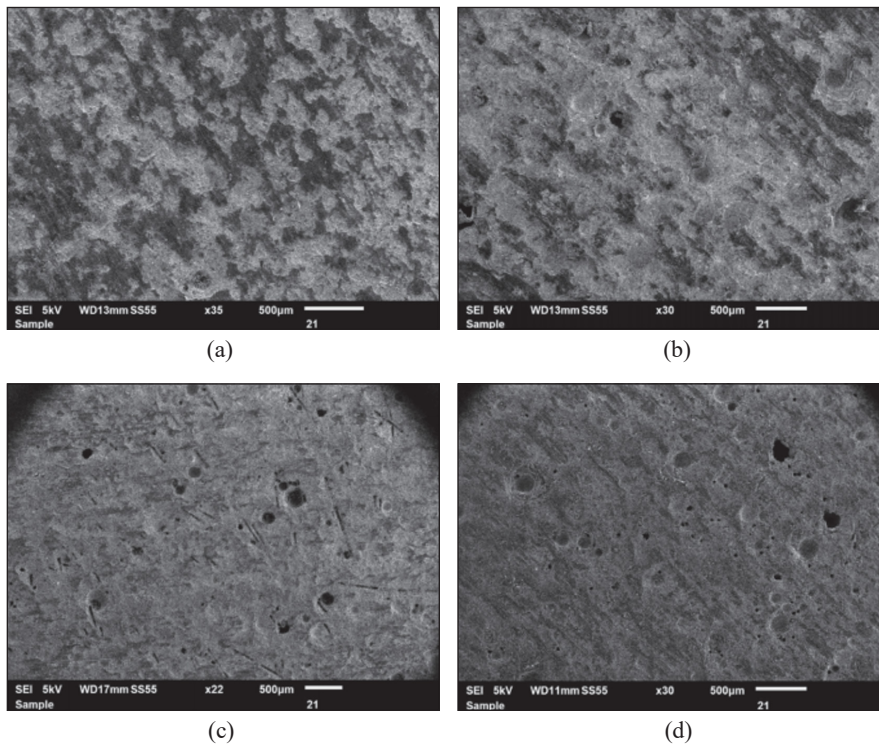


Figure 6. Magnification scanning electron microscopy of ECC subjected to elevated temperature: (a) 20°C; (b) 200°C; (c) 400°C; and (d) 600°C (Bhat et al., 2014)

At a temperature of 600°C and 800°C, rough heterogeneous with a larger proportion of pores appear. The visibility of rough pores at higher temperatures is due to the sintering process (Abdullah et al., 2013). At a higher a temperature of 600°C and 800°C, a wider micro-cracks appearance and a larger pore proportion due to the rate of water evaporation of the sample is high and the sintering process also high (Abdullah et al., 2013). The microstructure of the specimen exposed to a temperature of 800°C started to lose the crystalline strictures characteristic (Şahmaran et al., 2011; Shang & Lu, 2014).

Porosity increased after the specimen was exposed to temperature 200°C due to the pore water in the specimen starting to lose (Du et al., 2018). The melting of the PVA fiber at temperature 300°C created the amount of the pores to become larger. As the temperature increased, the amount of melted fiber also increased. PVA fiber completely melted after exposer at a temperature of 400°C. The surface of the fiber was moderately ruined; however, but the PVA fiber was observed not melting after exposure to a temperature of 200 (Yu et al., 2015). The fiber was completely melted at temperature 400°C, creating more pores and microcracks increased. The specimen loses its crystalline characteristic after being exposed to a temperature up to 800 (Aslani & Wang, 2019; Yu et al., 2015).

## CONCLUSION

This paper presents quantitative bibliographic data derived from scientific publications and an overview of Engineered Cementitious Composites subjected to elevated temperature. There have been very limited studies on this topic for the past ten years. However, an increasing trend in the number of publications over the years reveals the importance and relevancy of the topic in the future, particularly in the construction industry.

The exposure of the ECC specimens to elevated temperatures can influence the mechanical properties of concrete, particularly in compressive strength. Most of the studies showed a decrement in compressive strength after being exposed to a temperature at 200°C onwards. It is found from previous researchers' findings that the decrement in compressive strength is due to the increase of pores, which are mainly caused by the evaporation of water and melting of fibers. The melting point of Polyethylene (PE) fibers at 150°C and Polyvinyl alcohol (PVA) fibers in between 201°C–400°C were reported. After the fibers started to melt, the microstructure behavior of the specimen changed, such as crystalline characteristics, pores, and microcracking was observed.

The residual properties of the specimen drop moderately after the ECC specimen is exposed to elevated temperature. Apparent microcracking and explosive spalling occurred in specimens subjected to elevated temperature compared to the unheated samples. When the temperature increases, micro-crack size dramatically increases and results in plastic behavior and unrecoverable shapes of fibers.

Table 4  
Microcracking behavior

Author	0°C-200°C	201°C-400°C	401°C-600°C	601°C-800°C
Bhat et al. (2014)	-	Micro pores started to appear due to fiber beginning to melt	Fiber has melted and created more micropores. Micro-cracks appear as a “spider web” pattern.	-
Mohammed et al. (2019)	After the exposure at temperature 100°C, the crystalline calcium hydroxide (CH) started to disappear. At a temperature of 200°C, the microstructure started to become pores.	PVA fibers started to melt and cause the microstructural to become more pores and increasing micro-cracks.	-	-
Luo et al. (2019)	At temperature 140°C, PE fibers started to damage. Due to the melting of PE fibers at temperature 200°C, the average pore size increased compared to the specimen at room temperature (104nm to 203.09nm)	-	-	-
Abdullah et al. (2013)	-	Microcracks started to appear at a temperature of 400°C with an average width of microcracks between 0.1m to 0.2m.	After being exposed at a temperature up to 600°C, wider microcracks were noticeable.	At a temperature of 800°C, the average microcracks size became wider.
Shang and Lu (2014)	PVA fiber did not melt. A very small amount of microcracks start to appear.	PVA fibers completely melt at temperature 400°C. The number of microcracks was increased.	-	Specimen lose the characteristic crystalline structure after being exposed at temperature 800°C. The average pore diameter also increases.

Table 4 (continue)

Author	0°C-200°C	201°C-400°C	401°C-600°C	601°C-800°C
Şahmaran et al. (2011)	Microstructure did not experience many changes. Microcrack did not make apparent after being exposed at 200°C.	PVA fibers completely melt at temperature 400°C. Cracking and pores started to visible.	At temperatures over 600°C, the changes in average pore diameter appeared more rapidly. The sample also started losing its crystalline characteristic.	Increasing microcracking after exposure over 800°C. The average pore diameter significantly increases.
Du et al. (2018)	Pore water of the specimen exposed to temperature 200°C was lost, and porosity was observed to be increased.	At a temperature of 300°C, the volume of PVA fibers decreased due to the fiber had reached the melting point. The number of pores increased.	At a temperature of 400°C, melting of the fibers increases the number of pores and causes more cracks to appear.	-
Yu et al. (2015)	At a temperature of 200°C, PVA fibers did not melt, but the surface of the fiber was moderately ruined.	Fibers completely melted at a temperature of 400°C and created pores. Microcracks increased.	-	The number of microcracks increased at temperature 800°C, and the specimen started to lose crystalline structure.
Aslani and Wang (2019)	Temperature below that 100, PVA fiber still undamaged.	The surface of the fiber started to damage at temperature 300, and pores and microcracks started to be visible.	At temperature 600, PVA fiber completely melted, and microstructural became pores.	Specimen lose the characteristic crystalline structure after being exposed at a temperature of 900°C. The number of microcracks increased.
Wang et al. (2020)	Light grey color. No rupture of PVA fibers, but the diameter of fibers was reduced by 43%.	Whitish grey color. Melting of PVA and fibers in longitudinal needle-like channels were observed.	Yellowish grey color. The dents are left by fiber and increase of average pore diameter and total pore volume. Hairline cracks started to be observed.	Light brown color. Channels left by PVA fibers were channels were gradually filled with newly produced.

Based on the previous research findings towards engineered cementitious composite subjected to elevated temperature, the paper makes recommendations on a few future perspectives of research with the aims to improve the current knowledge of findings:

- Advanced engineered cementitious composite. In recent years, significant numbers of smart, green, and innovative materials or techniques, such as hollow glass microspheres (Aslani et al., 2021), ceramic polishing brick powder (Xiong et al., 2021), microbially induced calcium carbonate precipitation using Aerobic non-ureolytic bacteria (Justo-Reinoso et al., 2021) have been utilized into ECC to enhance the material sustainability in the construction industry. However, studies on the effects of these materials on the strength and durability performances of the ECC subjected to elevated temperature are very new research and need to be conducted.
- Advanced microstructural characterization techniques. Many advanced techniques were recently proposed in examining microstructural characteristics of a material, such as the machine-based learning method (Chan et al., 2020; Liu et al., 2021) and deep convolutional neural networks (Dong et al., 2020). New potential methods need to be explored to obtain a better understanding of the microstructural characteristics of the ECC after being exposed to elevated temperatures.

## ACKNOWLEDGMENTS

The Universiti Teknologi MARA funded this research under grant Research Entity Initiative (REI) 600-IRMI/REI 5/3 (012/2018).

## REFERENCES

- Abdullah, M. M. A. B., Kamarudin, H., Nizar, K., Razak, R., Yahya, Z., & Abdullah, A. (2013). Microstructure studies on the effect of the alkaline activators of fly ash-based geopolymer at elevated heat treatment temperature. *Applied Mechanics and Materials*, 421, 342-348. <https://doi.org/10.4028/www.scientific.net/AMM.421.342>
- Aslani, F., Dehghani, A., & Wang, L. (2021). The effect of hollow glass microspheres, carbon nanofibers and activated carbon powder on mechanical and dry shrinkage performance of ultra-lightweight engineered cementitious composites. *Construction and Building Materials*, 280, Article 122415. <https://doi.org/https://doi.org/10.1016/j.conbuildmat.2021.122415>
- Aslani, F., & Wang, L. (2019). Fabrication and characterization of an engineered cementitious composite with enhanced fire resistance performance. *Journal of Cleaner Production*, 221, 202-214. <https://doi.org/https://doi.org/10.1016/j.jclepro.2019.02.241>
- Bhat, P. S., Chang, V., & Li, M. (2014). Effect of elevated temperature on strain-hardening engineered cementitious composites. *Construction and Building Materials*, 69, 370-380. <https://doi.org/https://doi.org/10.1016/j.conbuildmat.2014.07.052>

- Booya, E., Gorospe, K., Das, S., & Loh, P. (2020). The influence of utilizing slag in lieu of fly ash on the performance of engineered cementitious composites. *Construction and Building Materials*, 256, Article 119412. <https://doi.org/https://doi.org/10.1016/j.conbuildmat.2020.119412>
- Chan, H., Cherukara, M., Loeffler, T. D., Narayanan, B., & Sankaranarayanan, S. K. (2020). Machine learning enabled autonomous microstructural characterization in 3D samples. *Computational Materials*, 6(1), 1-9. <https://doi.org/https://doi.org/10.1038/s41524-019-0267-z>
- Chen, Z., Yang, Y., & Yao, Y. (2013). Quasi-static and dynamic compressive mechanical properties of engineered cementitious composite incorporating ground granulated blast furnace slag. *Materials & Design*, 44, 500-508. <https://doi.org/https://doi.org/10.1016/j.matdes.2012.08.037>
- Dong, Y., Su, C., Qiao, P., & Sun, L. (2020). Microstructural crack segmentation of three-dimensional concrete images based on deep convolutional neural networks. *Construction and Building Materials*, 253, Article 119185. <https://doi.org/https://doi.org/10.1016/j.conbuildmat.2020.119185>
- Du, Q., Wei, J., & Lv, J. (2018). Effects of high temperature on mechanical properties of polyvinyl alcohol engineered cementitious composites (PVA-ECC). *International Journal of Civil Engineering*, 16(8), 965-972. <https://doi.org/10.1007/s40999-017-0245-0>
- Guan, Y., Wu, J., Sun, R., Zhang, H., Hu, Y., & Wang, F. (2021). Transverse flexural behaviour of steel-engineering cementitious composites (ECC) composite deck under negative and positive bending forces. *KSCSE Journal of Civil Engineering*, 25(8), 2962-2973. <https://doi.org/10.1007/s12205-021-1053-2>
- Huang, B. T., Dai, J. G., Weng, K. F., Zhu, J. X., & Shah, S. P. (2021). Flexural performance of UHPC–concrete–ECC composite member reinforced with perforated steel plates. *Journal of Structural Engineering*, 147(6), Article 04021065. [https://doi.org/10.1061/\(ASCE\)ST.1943-541X.0003034](https://doi.org/10.1061/(ASCE)ST.1943-541X.0003034)
- Huang, T., & Zhang, Y. X. (2014). Simulation of material behaviour of engineered cementitious composites under uniaxial tension. In L. Ye (Ed.), *Recent Advances in Structural Integrity Analysis - Proceedings of the International Congress (APCF/SIF-2014)* (pp. 539-543). Woodhead Publishing. <https://doi.org/https://doi.org/10.1533/9780081002254.539>
- Justo-Reinoso, I., Heath, A., Gebhard, S., & Paine, K. (2021). Aerobic non-ureolytic bacteria-based self-healing cementitious composites: A comprehensive review. *Journal of Building Engineering*, 42, Article 102834. <https://doi.org/https://doi.org/10.1016/j.jobbe.2021.102834>
- Khan, M., Zhang, Y., & Lee, C. (2021). Mechanical properties of high-strength steel–polyvinyl alcohol hybrid fibre engineered cementitious composites. *Journal of Structural Integrity and Maintenance*, 6(1), 47-57. <https://doi.org/https://doi.org/10.1080/24705314.2020.1823558>
- Lee, S. W., Oh, C. L., & Zain, M. R. M. (2019). Mechanical properties of engineered cementitious composites using local ingredients. *Journal of Mechanical Engineering*, 16(2), 145-157. <https://doi.org/10.21491/jmeche.v16i2.15332>
- Lee, S. W., Tan, K. H., & Yang, E. H. (2018). Seismic behaviour of interior reinforced-concrete beam–column sub-assemblages with engineered cementitious composites. *Magazine of Concrete Research*, 70(24), 1280-1296. <https://doi.org/https://doi.org/10.1680/jmacr.17.00359>
- Li, V. C. (2003). On engineered cementitious composites (ECC) a review of the material and its applications. *Journal of Advanced Concrete Technology*, 1(3), 215-230. <https://doi.org/10.3151/jact.1.215>

- Liu, F., Xu, K., Ding, W., Qiao, Y., & Wang, L. (2021). Microstructural characteristics and their impact on mechanical properties of steel-PVA fiber reinforced concrete. *Cement and Concrete Composites*, 123, Article 104196. <https://doi.org/https://doi.org/10.1016/j.cemconcomp.2021.104196>
- Luo, J., Cai, Z., Yu, K., Zhu, W., & Lu, Z. (2019). Temperature impact on the micro-structures and mechanical properties of high-strength engineered cementitious composites. *Construction and Building Materials*, 226, 686-698. <https://doi.org/https://doi.org/10.1016/j.conbuildmat.2019.07.322>
- Ma, H., Qian, S., Zhang, Z., Lin, Z., & Li, V. C. (2015). Tailoring engineered cementitious composites with local ingredients. *Construction and Building Materials*, 101, 584-595. <https://doi.org/10.1016/j.conbuildmat.2015.10.146>
- Mohammed, B. S., Achara, B. E., Liew, M. S., Alaloul, W. S., & Khed, V. C. (2019). Effects of elevated temperature on the tensile properties of NS-modified self-consolidating engineered cementitious composites and property optimization using response surface methodology (RSM). *Construction and Building Materials*, 206, 449-469. <https://doi.org/https://doi.org/10.1016/j.conbuildmat.2019.02.033>
- Qudah, S., & Maalej, M. (2014). Application of engineered cementitious composites (ECC) in interior beam-column connections for enhanced seismic resistance. *Engineering Structures*, 69, 235-245. <https://doi.org/https://doi.org/10.1016/j.engstruct.2014.03.026>
- Ren, R., Hu, W., Dong, J., Sun, B., Chen, Y., & Chen, Z. (2020). A systematic literature review of green and sustainable logistics: bibliometric analysis, research trend and knowledge taxonomy. *International journal of environmental research and public health*, 17(1), Article 261. <https://doi.org/https://doi.org/10.3390/ijerph17010261>
- Şahmaran, M., Özbay, E., Hasan, E. Y., Lachemi, M., & Victor, C. L. (2011). Effect of fly ash and PVA fiber on microstructural damage and residual properties of engineered cementitious composites exposed to high temperatures. *Journal of Materials in Civil Engineering*, 23(12), 1735-1745. [https://doi.org/10.1061/\(asce\)mt.1943-5533.0000335](https://doi.org/10.1061/(asce)mt.1943-5533.0000335)
- Shang, X., & Lu, Z. (2014). Impact of high temperature on the compressive strength of ECC. *Advances in Materials Science and Engineering*, 2014, Article 919078. <https://doi.org/10.1155/2014/919078>
- Wang, Q., Yao, B., & Lu, R. (2020). Behavior deterioration and microstructure change of polyvinyl alcohol fiber-reinforced cementitious composite (PVA-ECC) after exposure to elevated temperatures. *Materials*, 13(23), Article 5539. <https://doi.org/10.3390/ma13235539>
- Xiong, Y., Xu, G., Wu, D., Fang, S., & Tang, Y. (2021). Investigation of using the ceramic polishing brick powder in engineered cementitious composites. *Journal of Building Engineering*, 43, Article 102489. <https://doi.org/https://doi.org/10.1016/j.job.2021.102489>
- Yang, X., Xu, L., & Pan, J. (2021). Mechanical behavior of full-scale composite steel plate shear wall restrained by ECC panels. *Journal of Building Engineering*, 44, Article 102864. <https://doi.org/https://doi.org/10.1016/j.job.2021.102864>
- Yu, K. Q., Dai, J. G., Lu, Z. D., & Leung, C. K. Y. (2015). Mechanical properties of engineered cementitious composites subjected to elevated temperatures. *Journal of Materials in Civil Engineering*, 27(10), Article 04014268. [https://doi.org/10.1061/\(ASCE\)MT.1943-5533.0001241](https://doi.org/10.1061/(ASCE)MT.1943-5533.0001241)



- Yuan, F., Chen, M., & Pan, J. (2020). Flexural strengthening of reinforced concrete beams with high-strength steel wire and engineered cementitious composites. *Construction and Building Materials*, 254, Article 119284. <https://doi.org/10.1016/j.conbuildmat.2020.119284>
- Zhang, J., Leung, C. K. Y., & Cheung, Y. N. (2006). Flexural performance of layered ECC-concrete composite beam. *Composites Science and Technology*, 66(11), 1501-1512. <https://doi.org/https://doi.org/10.1016/j.compscitech.2005.11.024>
- Zhang, N., Gu, Q., Dong, Y., Qian, J., & Zheng, Y. (2021). Seismic performance of bridges with ECC-reinforced piers. *Soil Dynamics and Earthquake Engineering*, 146, Article 106753. <https://doi.org/https://doi.org/10.1016/j.soildyn.2021.106753>



## Palaeoecologic and Palaeoclimatic Inferences from Calcareous Nannofossils in Western Lobe Offshore, Niger Delta

Bamidele Samuel Oretade\* and Che Aziz Ali

Department of Earth Sciences and Environment, Faculty of Science and Technology, Universiti Kebangsaan Malaysia, 43600 UKM, Bangi, Malaysia

### ABSTRACT

In support of the ongoing temporal palaeoenvironment and palaeoclimatic reconstructions of the Neogene sediments, this study attempts to detail the paleo-proxies recovered from DEL-1 Well, western offshore Niger Delta. The standard smear slide method enabled the recovery of well-preserved calcareous nannofossils that depict early to mid-Miocene (NN4–NN5) sediments. The up-hole relationships between the nannofossil accumulation rate (NAR), the relative abundance of *Discoaster* and coccolith size of *Reticulofenestra* show step by step collapse of sea surface stability from early to middle Miocene. The lower horizons (8000–9460 ft) exhibit a low NAR, relatively high *Discoaster* abundance and relatively large *Reticulofenestra* size to suggest a deep thermocline and nutricline that characterise oligotrophic conditions in less warm-water induced climate. Conversely, upper horizons (5225–6550 ft) exhibit a high NAR, relatively low *Discoaster* abundance and relatively small *Reticulofenestra* size to suggest a shallow thermocline and nutricline that characterise eutrophic conditions in warm-water induced climate. The relative abundance of *Helicosphaera carteri* within the mid-NN5 suggests mesotrophic conditions within a stressed environment, with the possible occurrence of carbonate crash events. The combined parameters indicate gradual eutrophication and collapse of sea surface stability favouring nutrients and influx of terrestrial sediments in the ocean water as it progressed from early to middle Miocene. The abundance of the palaeo-proxies assemblages suggests hyposaline waters in a neritic environment that prevailed during the warm climatic condition.

### ARTICLE INFO

#### Article history:

Received: 06 June 2021

Accepted: 15 September 2021

Published: 04 January 2022

DOI: <https://doi.org/10.47836/pjst.30.1.25>

#### E-mail addresses:

p95743@siswa.ukm.edu.my (Bamidele Samuel Oretade)

samtad@mail.com (Che Aziz Ali)

\* Corresponding author

**Keywords:** Calcareous nannofossils, eutrophic, mesotrophic, Neogene sediments, oligotrophic, sea-surface stratification

## INTRODUCTION

The need for examining deep wells drilled in the offshore portion of the Niger Delta are significantly becoming important to provide oceanic records linked with Gondwana breakup and evolution of the Atlantic Ocean to portrait marine conditions for the Gulf of Guinea relative to another proven world oceanic and palaeoceanographic evolution (Guerra et al., 2011; Adegoke et al., 2017). Notably, recent advancements in exploring coastal to deep waters have aided modern understanding of the use of micropalaeontological studies in deciphering ancient to modern oceanographic evolution, perhaps enhancing hydrocarbon exploration. In addition, several researchers have highlighted the pragmatic approach to nannofossil biostratigraphy over the years (Hay et al., 1967; Erba, 2004; Erba, 2006; Zachos et al., 2004; Brown, 2005; Raffi et al., 2006; Vulc & Silye, 2005) in examining global fields/basins for nannofloral existence and biodiversity in palaeoecological and palaeoceanographical reconstructions.

In the Niger Delta, foundational reports of Oyebamiji (1997) and Fadiya (1999) on calcareous nannofossil were reported for their age determination, occurrences, and distribution patterns to aid exploration processes. Recent documented studies (Ojo et al., 2009; Fadiya & Salami, 2012; Obaje & Okosun, 2013; Ajayi & Okosun, 2014; Sanuade, 2014; Adegoke et al., 2017; Ola, 2018) on the Neogene nanнопlankton in the Niger delta highlighted their phylogenetic and paleobathymetric reconstructions, with limitations to their enigmatic palaeoecological and biogeochemical imprints on the Niger Delta palaeobiogeography (Adegoke et al., 2017). However, calcareous nannofossils are geographically distributed in present ocean columns, from coastal areas to open ocean settings and constitute a large part of marine phytoplanktonic communities along with diatoms, dinoflagellates, and cyanobacteria (Erba, 2006). The use of nannofossils in Neogene palaeoceanographic reconstruction seems challenging due to dearth, ecologically restriction, vulnerability to diagenesis and ongoing extinction to most species as a result of extreme nature and environmental changes (Erba, 2006). Conversely, the authors believe that these challenges are very useful in exploring the complex interplay of ocean chemistry, productivity, climate, and tectonics of ocean water.

The factors mentioned above are considered important for the geographical and vertical distribution of oceanic phytoplankton. Furthermore, these are known to differ between taxa and their respective responses to surface water properties such as light, temperature, salinity, turbidity, and nutrient content (McIntyre & Bé, 1967; Imai et al., 2015), thereby highlighting their importance in palaeoecologic and palaeoceanographic reconstructions. However, this study curiously explores the use of nannofossil accumulation rate (NAR; Flores & Sierro, 1997) and the relationship between ecologic proxies (*Discoaster*, coccolith size of *Reticulofenestra* and *Helicosphaera* species) to construe the palaeoceanographic conditions astronomically driven by climatic cycles during sedimentation within the Gulf of Guinea.

Notably, some studies showed evidence of fluctuating surface water properties with progressive collapse of sea surface stability across different oceans' columns (Zhang et al., 2007; Farida et al., 2012; Imai et al., 2015). Thus, indicate substitution in prevalence and gradual collapse regionally of thermocline and nutricline for prevailing mesotrophic/eutrophic conditions. These are most often responsible for vertical occurrence and distribution of calcareous nannoplankton along with ocean columns (Sato & Chionobu, 2009). Therefore, there is a need to explore local nannofloral response(s) to these changes in ocean chemistry that are often accompanied by dynamic factors. Such as atmospheric-oceanic CO<sub>2</sub> exchange, primary production, and fluxes of biogenic and inorganic particles, which are responsible for either/both fluxes in surface water productivity and carbonate production that could lead to eutrophication or carbonate crash events (Fadiya & Salami, 2012). In this study, the presence of calcareous nannoplankton in DEL-1 Well, offshore Niger Delta will be analysed for their abundance and distribution patterns. With the goals to (1) deduce the stratigraphical age of the well section (2) succinctly examine the relationships between the NAR and ecologic nannofloras to construe the palaeoecologic and palaeoenvironmental inferences, and (3) interpret marine developmental changes to reconstruct palaeoceanographic condition of the studied section.

### **Geological Setting of the Western Detachment Fold Zone**

The field under investigation is located within the western detachment fold zone (DFZ), a subdivision of the offshore depositional belt marginally positioned to the border of the southwestern Niger Delta (Figure 1). The DFZ elongated southward towards the east of the basin. The zone is mapped within the more deep-water region of the Niger Delta, known as the toe of the delta (Bilotti & Shaw, 2005). It comprises numerous thrust faults and thrust-associated folds (Corredor et al., 2005), which constituted some fields within the area that benefited from the structural traps formed by contractional fold. The studied field is classed under the fault-bend fold of the subdivision of the contractional part of the deep-water (Connors et al. 1998; Corredor et al., 2005) in the Niger Delta. The DFZ is an intermediate zone between the inner and outer fold and thrust belts characterised by the province of little or no. Distortion interspersed with broad detachment anticlines accommodates relatively small amounts of shortening aided by faults and folds" (Bilotti et al., 2005). The Opuama Canyon's encroachment on the north-western margin of the delta (Figure 1) created a great influence on the deposited sediment packages in the DFZ area (Ozumba, 2018). The oldest deposited sediments in the western DFZ were dated late Oligocene, while the sedimentation processes were mainly dominated by marine facies, deposited beneath the presented day delta front consisting of Oligocene and Miocene delta fronts (Ozumba, 2018). The deposition of the Akata facies took place in the Oligocene, while the onset deposition of the paralic lithofacies making the Agbada Formation started in the early Miocene age onwards (Figure 2; Ozumba, 2018).

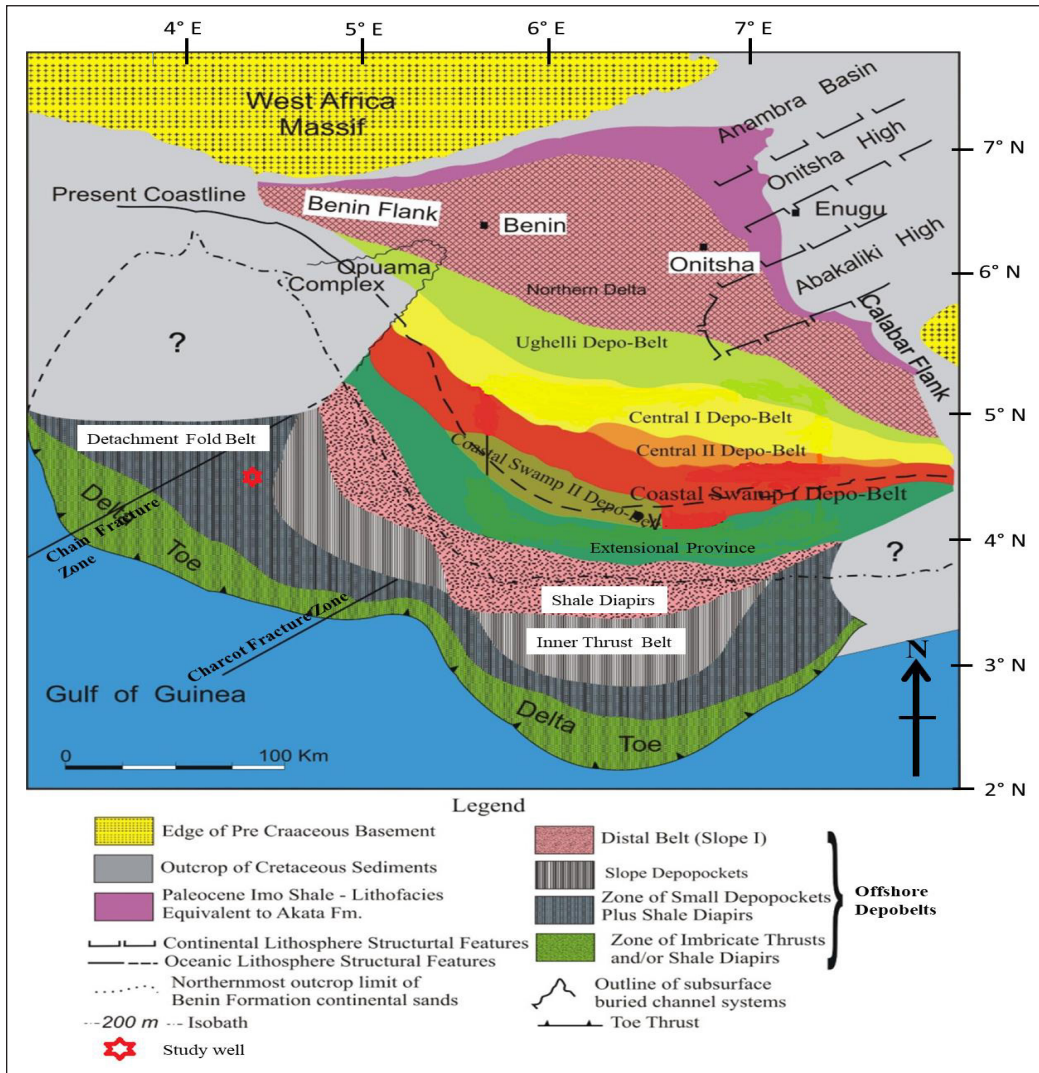


Figure 1. The regional map of the Niger Delta, showing the distribution of main structural elements and depobelts, highlighted in red the study well (modified after Doust and Omatsola, 1990)

The Akata Formation is the basalmost deposit and the major hydrocarbon source rock in the Niger Delta (Reijers, 2011; Ozumba, 2018). It is characteristically made up of marine shale (Figure 2). The Agbada Formation serves as the reservoir unit, and it is the exploration target for conventional hydrocarbon in the Niger Delta. It is lithologically composed of interbeds of sand/sandstone, shale and other constituents often composited as heteroliths in almost equal proportion (Magbagbeola & Willis, 2007; Reijers, 2011). Finally, the youngest lithounit in the basin is the continental deposit of the Benin Formation that is essentially composed of massive sandstone with negligible shale lamina and lignitic intrusions (Reijers, 2011; Momta & Odigi, 2014).

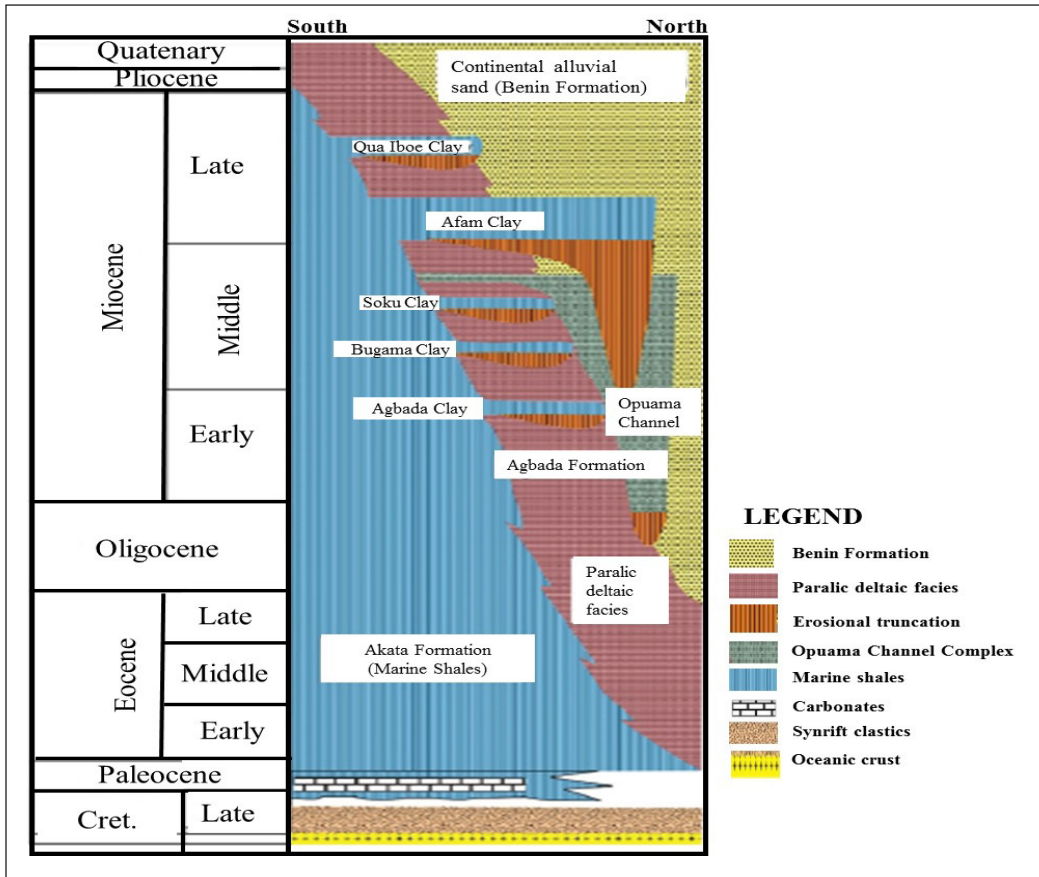


Figure 2. Chrono-stratigraphic diagram showing the three Formations of the Niger Delta Modified after Doust and Omatsola (1990)

## MATERIALS AND METHODS OF STUDY

The lithologic description of each sample was carried out using a stereo-binocular microscope for its constituents and proportions. A graphic sediment log for the well section was created using SedLog 3.1 software (Zervas et al., 2009) to compliment the lithologic description of the samples examined with the interpreted lithologic log from the gamma-ray and resistivity logs. Biostratigraphically, Bown and Young (1998) standard strewn-slide technique was used to process and analyse calcareous nannoplankton in deciphering their biostratigraphical significance and events.

Five grams of each sample was carefully selected from the 25 composite ditch cuttings recovered within a section (4600 - 9460 ft) of DEL-1 Well. Each weighed sample was put on a clean white sheet of paper, folded, and gently crushed because of the fragile nature of nannofossils using a pestle. The crushed materials were dispersed in distilled water inside a glass. Vials were stirred with a stirring rod, after which they were decanted into another

glass tube. Next, the decanted suspensions were pipetted with disposable pipettes onto each 22 × 40 mm coverslips placed on a regulated hot plate to gently dry at a temperature of about 50–60°C. Then, the coverslips were mounted on the labelled glass slides using two drops of Norland optical adhesive mounting medium (Refractive index = 1.56) and cured under ultraviolet light for forty-five minutes. Finally, the prepared slides were examined for their calcareous nannofossils' content under a high-powered Olympus light microscope in cross-polarized and transmitted light in three traverses.

Numbers of different species found were recorded to get their known abundance and diversity. Detailed identification of the assemblages and description is based on previous works (Martini, 1971, Backman, 1984; Perch-Nielsen, 1985) and other relevant texts mentioned in the discussion section. The calcareous nannofossil bio horizons were deduced based on first occurrence (FO), last occurrence (LO), first consistent occurrence (FCO), last consistent occurrence (LCO) and paracme ending (PE) of marker species in accordance with the zonation scheme of Martini (1971). The chronostratigraphic subdivisions were correlated with the geological time scale (GTS) *sensu* (Gradstein et al., 2020). Photographs of the forms were taken using an OLYMPUS CX31PF binocular microscope with a camera attached.

Estimating the absolute abundance of nannofossils was carried out by counting in random visual fields, while the total abundance of nannofossils (*Helicosphaera*, *Reticulofenestra* and *Discoaster* inclusive) using Equation 1 according to Flores and Sierro (1997).

$$N = n * R^2 * V * r^2 * g^{-1} * v^{-1} \quad (1)$$

The “N” represents a number of nannofossils per gram of dry sediments; “n” represents the number of nannofossils in a random scanned area; “R” represents the radius of Petri disk; V represents the volume of water added to the dry sediment in the beaker; “r” represents the radius of the visible field of study; “g” represents the weighted dry sediments, and lastly “v” represents a volume of mixture pipette. Therefore, the Nannofossil Accumulation Rate (NAR) was calculated as accounted by Flores and Sierro (1997) as in Equation 2:

$$NAR = N * d * S \quad (2)$$

Where NAR (nannofossil \* cm<sup>-2</sup> \* ky<sup>-1</sup>); d is the dry density of the sample (g \* cm<sup>-3</sup>), and S is the linear sedimentation rate (cm \* ky<sup>-1</sup>).

## RESULTS

### Sedimentological Overview of DEL–1 Well

The ditch cuttings analysed span the interval of 4500 to 9460 ft that showed a good variation of lithic units to characterise dominant clastic sedimentation. Lithological observations and descriptions of the ditch cuttings from the DEL-1 Well show the well predominantly



penetrated sandstones, shales, silts and paralic sandstone–shale intercalations, which essentially constitute the Agbada Formation (Figure 3). A critical assessment of the studied litho-section revealed the differences between the upper transitional paralic (4500–6750 ft) and lower paralic (6750–9460 ft) horizons of the Agbada Formation.

The lower horizons exhibit paralic thick shale intervals with packets of sandstone beds to be named the lower paralic horizons (Figure 3). The shales are thickly bedded with thickness ranging from 100 to 450 ft and pale grey to greyish. The sandstones are brownish to yellowish-white, dominantly medium-grained, and angular to subangular. However, the shale became grey while the sandstone showed prominent yellowish-white colouration up-hole. The grains are coarser and subangular within the depth interval 7000–7500 ft. On the gamma-ray log signature of the DEL–1 Well, the sandstone is characterised by dominant coarsening upward unit (with typical funnel-shaped log motif) with sand percentages varying from 20–46%, the log motifs suggest delta front, river mouth bar sub-facies environment and crevasse splay sub-facies environment (Selley, 1985). However, the shale-sand heterolithic subunit consists of 20% grains of sand and exhibits slightly serrated coarsening log motifs (7000–7500 ft) upward; this can be interpreted as an intertidal to the tidal sub-facies environment. Conversely, the sandstones in the upper unit of this interval are brownish to off-white, medium to fine-grained and subangular to subrounded (Figure 3).

The upper horizons are interpreted as an upper transitional paralic sequence, characterised by a preponderance of sandstone with interbeds of shale and silts (Figure 3). The thick sandstone beds vary in thickness from 30 to 480 ft. The sandstones are generally medium to fine-grained but occasionally coarse-grained at the upper section of the horizon. However, the sandstone units are yellowish-brown to off white, subangular to subrounded and poorly to moderately sorted. The log analysis shows the gamma-ray log motif for the sandstone are serrated blocky-shaped units with 75–90% sands and could be interpreted to a distributary channel subfacies to channel-fill or submarine canyon-fill subfacies environment (Selley, 1985). The shales are dark grey, platy to occasionally blocky and moderately hard. The silts facies are fine-grained, off-white to brownish-white in colour. The shale exhibited a shelf mud deposition in shallow marine settings.

### **Recognised Calcareous Nannofossils Bioevents**

The detailed analysis of the ditch-cuttings revealed low to moderate species abundance and richness of calcareous nannoplankton over most horizons of the well section. These are evident when some samples yielded a countable taxa abundance and evenness while few samples were barren of calcareous nannoplankton. Forty-seven species from fifteen genera were recognised and dominated by placoliths, helicoliths and nannoliths (Figure 4), while some photomicrographs are presented in Figure 5. The well is inferred to penetrate Middle

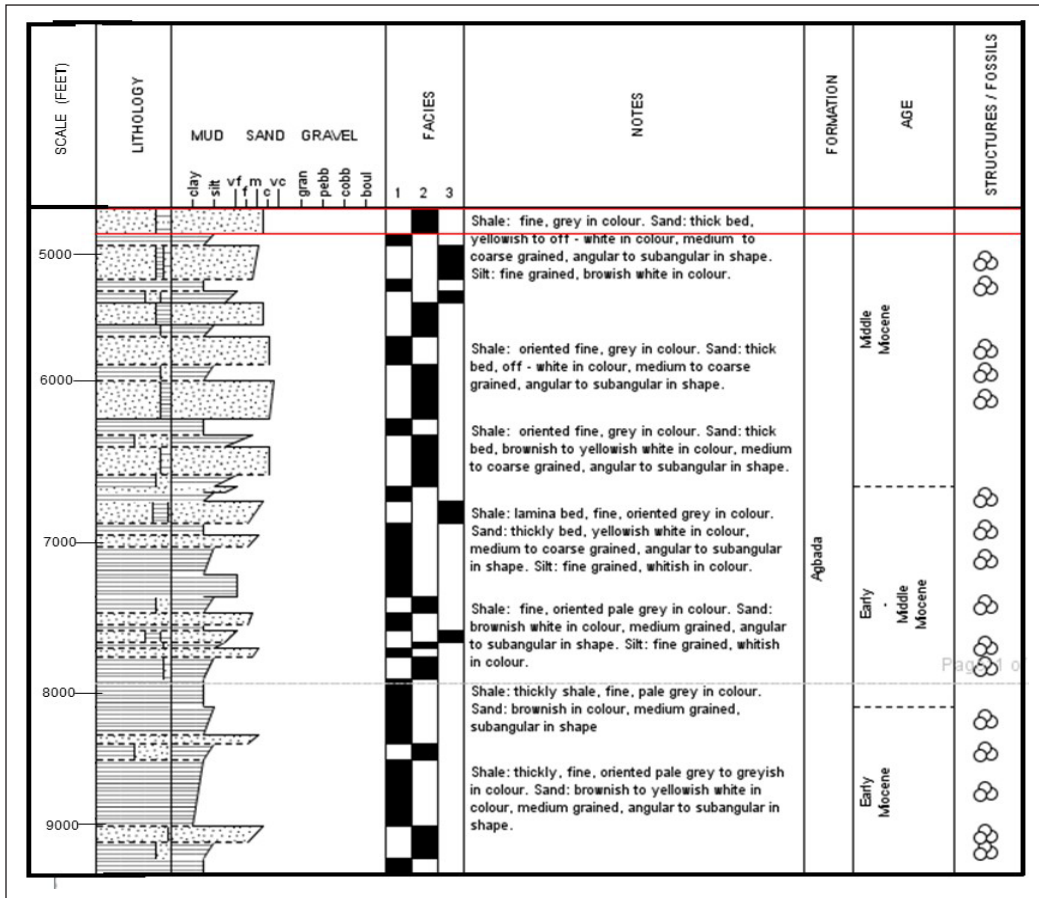


Figure 3. Harmonised down-hole profiling of sedimentological sequences of DEL-1 Well, consisting of the lithology description and lithofacies assemblages

Note. facies assemblages' representation mono-facies, two facies, three facies

to Early Miocene zones (NN5–NN4), while several important calcareous nannofossil bioevents are recorded over the analysed well section (Figure 4) and are described below.

**Nannoplanktons Zone** : *Non-diagnostic*  
**Stratigraphic Interval** : 9025 – 9460 ft  
**Age** : *Early Miocene*

The top of the interval is marked by the probable LDO of *Sphenolithus heteromorphus* at 9025 ft (Figure 4). This interval is marked by moderate abundance and diversity of nannofossils. The abundance/richness peak recorded over the interval 9000–9075 ft is suggestive of a condensed section, which is suspected to be of a post 17.4 Ma. The age is uncertain due to the non-recovery of marker species in this interval. The non-recovery of *Sphenolithus belemnos* used globally to define the NN3 Zone of Martini (1971) supports the evidence that the well did not penetrate sequences older than NN4.

In addition, although species of *Triquetrorhabdulus* were recorded at the upper interval as a key assemblage species for NN2, *Triquetrorhabdulus carinatus* was not observed. The calcareous nannofossils recovered within this interval are *Calcidiscus leptoporus*, *Coccolithus pelagicus*, *Cyclicargolithus floridanus*, *Discoaster deflandrei*, *Discoaster druggii*, *Discoaster* spp. (6 rays), *Helicosphaera ampliaperta*, *Helicosphaera carteri*, *Helicosphaera obliqua*, *Helicosphaera* spp., *Sphenolithus moriformis* and *Sphenolithus* spp. The base of this interval is tentatively placed at the lowest sample analysed (Figure 4).

**Nannoplanktons Zone** : NN4  
**Stratigraphic Interval** : 6775–9025 ft  
**Age** : Early Miocene

The top of this interval is marked with probable LO of *Helicosphaera ampliaperta* (15.6 Ma.) and PE of *Sphenolithus heteromorphus* at depth 6775 ft (Figure 4). The base of this interval is marked by the probable FO of *Sphenolithus heteromorphus* and FCO of *Helicosphaera ampliaperta* at 9025 ft (Figure 4). This interval is marked by increased abundance and diversity of nannofossils with respective abundance or richness peaks recorded within the depth interval 6750–6850 ft, 8200–8350 ft and 8950–9100 ft to suggest candidate condensed sections of Haq et al. (1988) based on their stratigraphic positioning. The age of the condensed basal section (8950–9100 ft.) could not be dated precisely due to the absence of distinctive marker species; however, the probable FCO of *Helicosphaera ampliaperta* characterise the candidate indication. The dominant occurrence of *Helicosphaera ampliaperta* over the enormous abundances of *Sphenolithus heteromorphus*, *Sphenolithus moriformis*, and *Helicosphaera carteri* within the depth interval 8200–8350 ft suggests that this section of the well falls within the basal biohorizon of the NN4 Zone (Young, 1998). Thus, suggest a nannofossil bioevent relative to the 17.4 Ma. (Figure 4). The PE of *Helicosphaera ampliaperta* (dated 15.6 Ma.) within the depth interval 6750–6850 ft could characterise the condensed upper section of this zone. However, the recovery of the following calcareous nannofossils: *Braarudosphaera bigelowii*, *Calcidiscus leptoporus*, *Coccolithus pelagicus*, *Calcidiscus macintyreii*, *Cyclicargolithus floridanus*, *Dictyococcites productus*, *Discoaster deflandrei*, *Helicosphaera ampliaperta*, *Pontosphaera discopora*, among other taxa, characterise the NN4 nannofossil zone.

**Nannoplankton Zone** : NN5  
**Stratigraphic Interval** : 5500–6775 ft  
**Age** : Middle Miocene

The top of the interval is marked by the LO of *Sphenolithus heteromorphus* at 5500 ft (Figure 4). The base of the nannoplankton zone is placed at 6775 ft, the next sample above the LO of *Helicosphaera ampliaperta* and PE of *Sphenolithus heteromorphus*. A moderate abundance of nannofossils characterises this interval. However, the peaks in

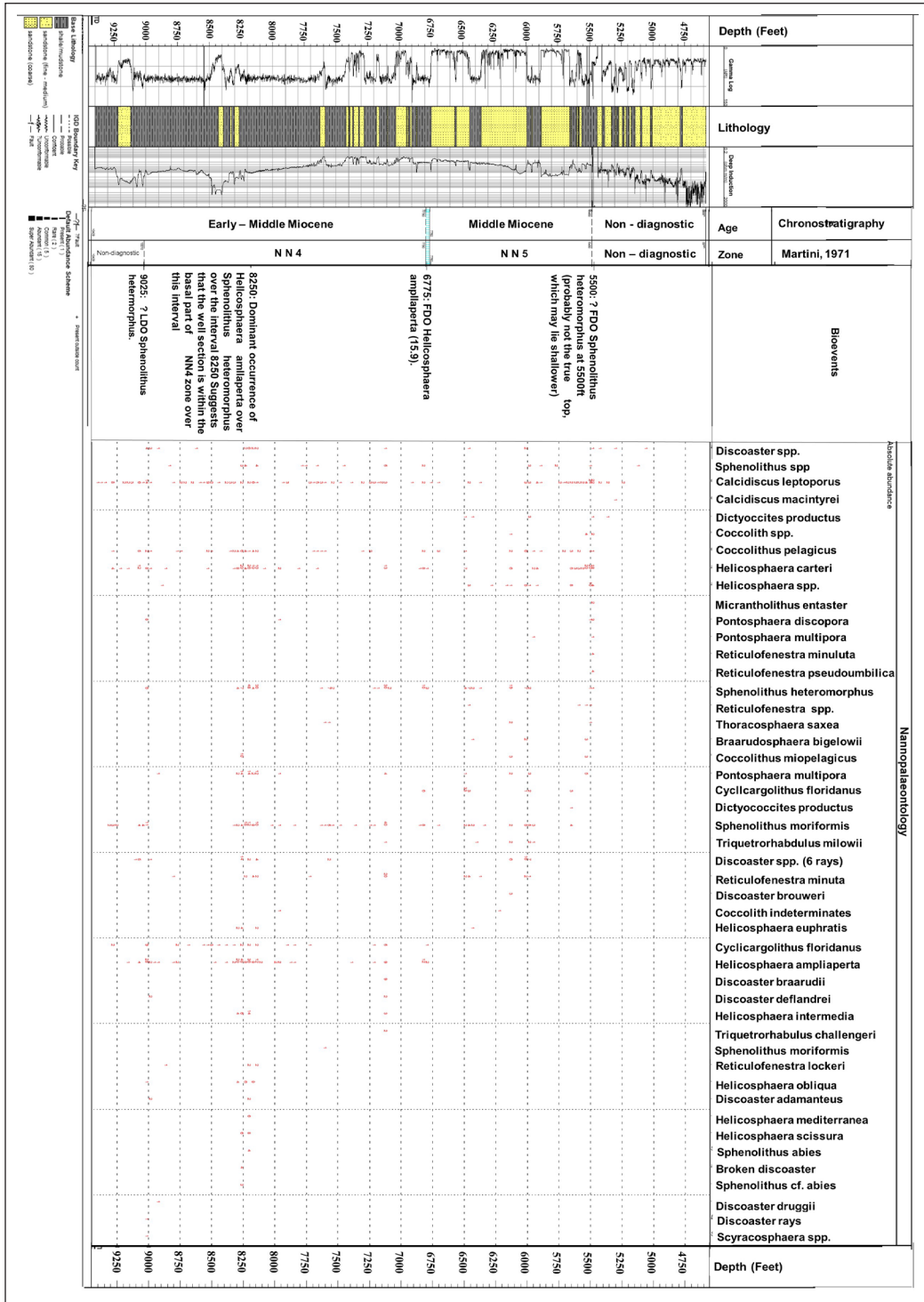


Figure 4. Stratigraphic summation and distribution chart of calcareous nannofossils of DEL-1 Well, with the corresponding gamma-ray log and interpreted lithologic facies

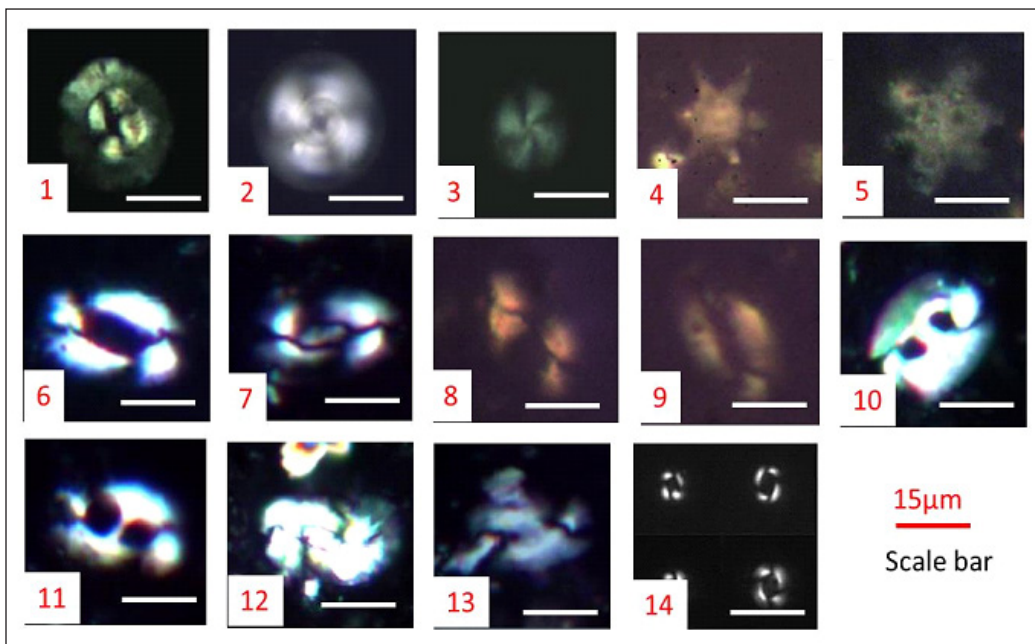


Figure 5. Some nannofloral species recouped from the studied well, including (1) *Coccoliths pelagicus* (Wallich, 1877; Schiller, 1930). (2) *Calcidiscus macintyreii* (Bukry & Bramlette, 1969). (3) *Calcidiscus leptoporus* (Murray & Blackman, 1898; Loeblich & Tappan, 1978). (4) *Discoaster* spp. (6 rays) (Bown & Dunkley, 2012). (5) *Discoaster druggii* (Bramlette & Wilcoxon, 1967). (6) *Helicosphaera ampliapertura* (Bramlette & Wilcoxon, 1967). (7) *Helicosphaera euphratis* (Haq, 1966). (8) *Helicosphaera carteri* (Wallich, 1877; Kamptner, 1954). (9) *Helicosphaera scissura* (Muller, 1981). (10) *Helicosphaera oblique* (Bramlette & Wilcoxon, 1967). (11) *Helicosphaera mediterranea* (Muller, 1981). (12) *Helicosphaera intermedia* (Martini, 1965). (13) *Helicosphaera* spp (Bown & Dunkley, 2012). (14) *Reticulofenestra minuta* (Roth, 1970).

abundance and species count recorded within the stratigraphic interval 5480–5580 ft are probably relics of a condensed section (maximum Flooding Surface) that could be related to the 15.0 Ma. of Haq et al. (1988). The associated calcareous nannofossils recovered within this interval are *Braarudosphaera bigelowii*, *Calcidiscus leptoporus*, *Coccolithus pelagicus*, *Calcidiscus macintyreii*, *Cyclicargolithus floridanus*, *Dictyococites productus*, *Discoaster sanmiguelensis*, *Discoaster* spp. (6 rays), *Helicosphaera carteri*, *Helicosphaera* spp., *Micrantholithus entaster* *Pontosphaera discopora*, *Pontosphaera multipora*, and *Triquetrorhabdulus milowii*.

**Nannoplankton Zone** : *Non-diagnostic*  
**Stratigraphic Interval** : *4500 –5500 ft.*  
**Age** : *Non-diagnostic*

This interval is characterised by scanty occurrences of long-ranging and non-age diagnostic nannoplankton (Figure 4). The nannoplankton species presented here are of sparing distribution within the interval, such as *Calcidiscus leptoporus*, *Calcidiscus macintyreii*, *Dictyococites productus* and *Discoaster* spp.

### Succession of Bioevents

***Discoaster* Bioevents.** Eight distinguished species of *Discoasters* were identified in this study (Figure 4), which belong to the family *Discoasteraceae* with the features of rayed nannoliths. The generally small size ( $\leq 20 \mu\text{m}$ ) of these species made them extremely useful for Tertiary bioevents, evident in their short life span and fast extinction (Perch-Nielsen, 1989; Bown, 1999). *Discoasters* are phytoplankton, notably from their assemblages to reflect microorganism productivity within their niche (Flores & Sierro, 1997; Flores et al., 2005; Sato & Chiyonobu, 2009). The general trend within the studied interval exhibits a relatively low abundance of *Discoasters* showing cyclic distribution up-hole with considerable fluctuating occurrences along some horizons (Figure 4). *Discoaster* species were abundant within the depth interval 8980–9160 ft, with the highest relative abundance exceeding 18 % was recorded at 9040 ft.

At depth interval 8200–8320 ft, the relative abundance exceeding 14% was recorded at depth 8320 ft displaying a gradual decrease in abundance up-hole within the horizons. A sparse occurrence was recorded 6140–8140 ft with an abrupt increase in abundance at depth 7180 ft horizons within the depth interval 5920–6100 ft showed a relative abundance of the species with exceeding 10% recorded at depth 6010 ft. Low relative abundance of *Discoaster* species (typically less than 2%) was recorded at depth interval 5060–5480 ft. to cap its distribution within the studied succession (Figure 4). However, relative occurrences of *Discoaster* species have been documented and interpreted as warm oligotrophic water species (Flores & Sierro, 1987; Aubry, 1992; Flores et al., 2005; Sato & Chiyonobu, 2009; Obaje & Okosun, 2013). Thus, indicate their susceptibility to prevailing surface water stability within the deep section of the well. It suggests an ecological imprint of a lower photic zone (Sato & Chiyonobu, 2009; Obaje & Okosun, 2013).

***Helicosphaera* Bioevents.** The qualitative plot for the studied horizons recorded two major *Helicosphaera* bioevents relative to their occurrence, abundance trend, and size distribution pattern (Figure 4). The measured *Helicosphaera* coccolith size ranged from 6 to 8  $\mu\text{m}$  with modal size at 7  $\mu\text{m}$ ; the maximum size was recorded at depth 8290 ft, while the minimum size was 5620 ft. The occurrence pattern for *Helicosphaera* assemblages shows progressive presence across the horizons, as their abundance is observed in two subdivisions as upper and lower horizons. The lower horizons (8170–9460 ft) show a gradual increase in abundance with continuous occurrence trailing up-hole. The taxa have a more distinct distribution trend that signals ecostratigraphic gains, suggesting a conducive and stable environment favouring an increase in occurrence and abundance with associated species. The assemblage in the lower horizon has its highest relative abundance exceeding 38% recorded at depth 9130 ft followed with abrupt decrease. The relative maximum abundance

(90%) was reached at depth 8260 ft., coincides with the condensed section dated 17.4 Ma. that precede the abrupt decrease in their abundance.

The upper horizons (4600–8140 ft) show low to average (to total number) abundance and discontinuous occurrences with some high abundance 20% and 26% at depth intervals 7150 and 6820 ft., respectively. The *Helicosphaera carteri* is dominant within depth interval 5480–5620 ft to show a progressive occurrence of the taxa with the highest relative abundance of 30% at depth 5480 ft. However, depth interval 4600–5480 ft shows a relative barren section within the upper horizon to cap the bioevents of *Helicosphaera* coccolith in the studied well. Conversely, the abundance pattern of the *Helicosphaera* species within the studied succession supports the putative advantage for the species to be characterised as a diagenetic-resistant species, based on its abundance and widespread elemental factor among the nannofloras (Young, 1990; Gartner, 1992; Flores et al., 2005; Kameo et al., 2010).

**NAR Frequency and Changes in *Reticulofenestra* coccolith Size.** The bioevents of *Reticulofenestra* species in studied sediments generally recorded low occurrences with fluctuating differences with the NAR (Figure 6). The distinguished species show relatively low recording of  $0.9\text{--}12.0 \times 10^9$  specimens/cm<sup>2</sup>/ky across the entire studied section, with depth interval 6520 ft. having the maximum recording. Low frequencies were recorded down-hole within depth interval 8170 ft. to 9460 ft with a variance of  $0.9\text{--}3.9 \times 10^9$  specimens/cm<sup>2</sup>/ky. An increase in NAR has observed up-hole at depth interval 8140 ft, with fluctuations ranging  $4.0\text{--}12.0 \times 10^9$  specimens/cm<sup>2</sup>/ky. A distinct increase in the NAR was recorded within depth interval 6400 ft. to 7030 ft with a record of  $11.9 \times 10^9$  specimens/cm<sup>2</sup>/ky, followed by large fluctuations over the range of  $4.0\text{--}9.0 \times 10^9$  specimens/cm<sup>2</sup>/ky to the top horizon at 5300 ft. In summary, the NAR generally exhibits a gradual increase at the upper horizons of the studied well (Figure 6).

This study put together the modal size of *Reticulofenestra* coccoliths across the stratigraphic changes. The majority of *Reticulofenestra* coccoliths are of the diameter ranging between 6 and 10 μm in a gradual increase pattern in the lower part of the studied interval 8500–9450 ft. An abrupt decrease in modal *Reticulofenestra* size to 7–8 μm was identified at 8140–8460 ft. It was followed by a further decrease in size (3–4 μm) up to depth 7150 ft, where the modal size increased to 6 μm. However, the modal size of *Reticulofenestra* coccoliths gradually decreases with a value ranging 2–4 μm, from a depth of 5480 ft to 6490 ft for the bimodal size distribution. It is specifically critical within the range 6370–6490 ft. Most specimens were found to exhibit a bimodal size of 2–3 or 3–4 μm from 5480 to 5650 ft and followed by an abrupt absence of *Reticulofenestra* coccoliths within depth interval 4500 to 5480 ft. *Reticulofenestra* coccoliths reached the

maximum sizes of 9–10  $\mu\text{m}$  at 8860 ft and the minimum sizes of 2–3  $\mu\text{m}$  at 5490 ft. The summarized results indicate an overall gradual upward decrease in modal and maximum sizes of *Reticulofenestra* coccoliths throughout the studied interval.

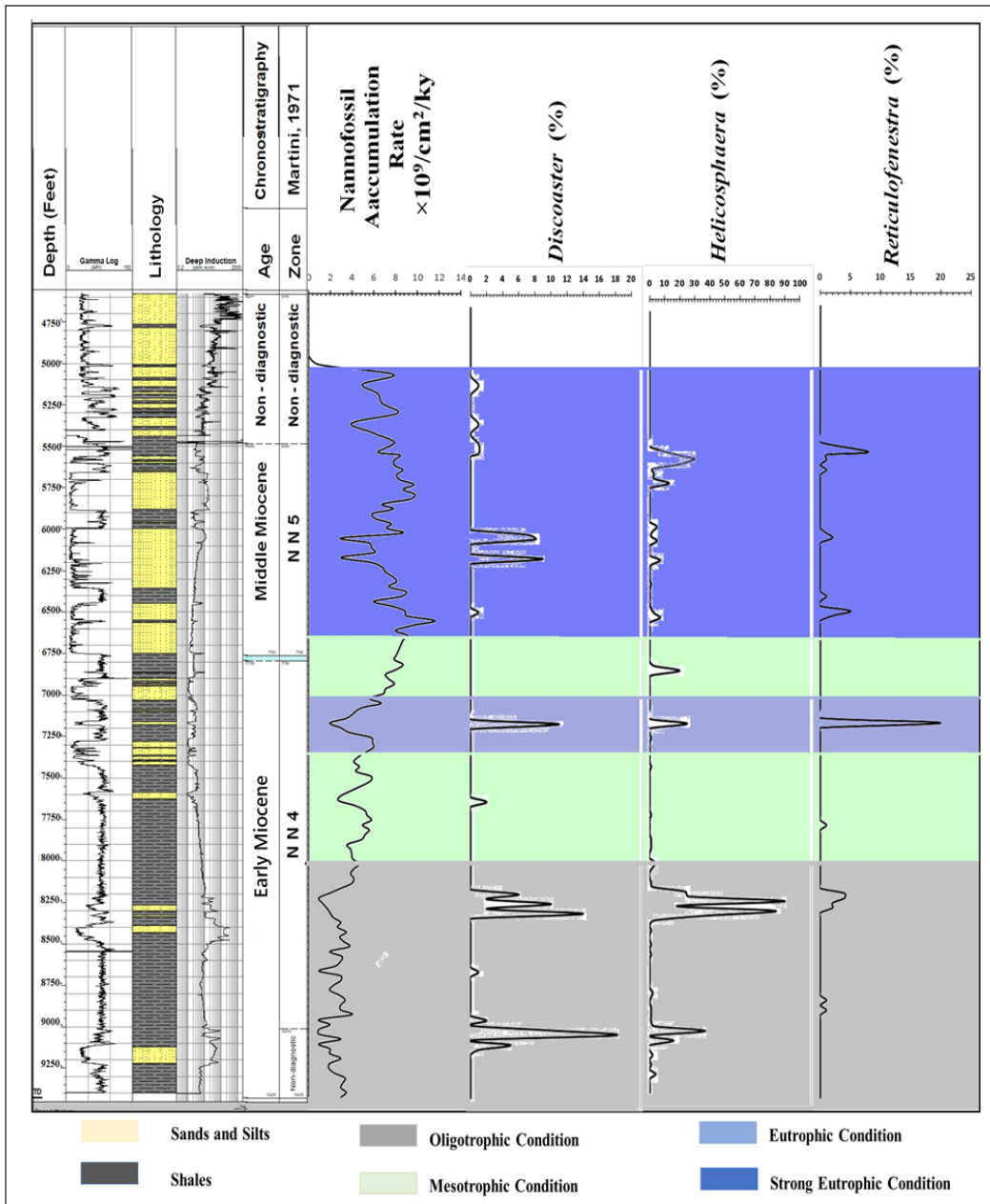


Figure 6. A comparison chart for nannofossil accumulation rate, recouped relative abundances of *Discoaster*, *Helicosphaera* and *Reticulofenestra* species, deciphering the environment and water condition along with the stratigraphic profile. Plotted with the gamma-ray log and interpreted lithological profile.



## DISCUSSION

Eco-stratigraphic deductions were made from integrating some selected calcareous nannoplanktons with the nannofossil accumulation rate tool. The relationship among the NAR, the relative abundance of *Discoaster*, *Helicosphaera* bioevents and *Reticulofenestra* coccolith size distribution (Figures 4 and 6) permits quantitative abundances and fluxes of nannofossils along with the stratigraphic sequences for a better understanding of the sea surface temperature and nutrient variability in palaeoceanographic reconstruction. In line with this concept, the following perspectives were made from the studied sediments: (a) 8500–9450 ft (early Miocene 17.4Ma): This horizon is characterised by the low frequency of NAR, the relative abundance of *Discoaster* spp., and abundant large *Reticulofenestra* coccoliths recorded (Figure 6), suggesting enhanced oligotrophic conditions with a stable sea surface mechanism within the purported depth (Imai et al., 2015) (b) 7780–8500 ft (early Miocene): An increase in NAR, an abrupt increase of *Discoaster* abundance, and decreased modal size of *Reticulofenestra* coccoliths (i.e., continuous decrease in size upward the interval) were recorded for this interval (Figure 5). These characteristics can be suggested as indicative of higher nutrient content compared to the preceding interval (c) 6490–7780 ft (middle Miocene 15.9Ma): This period is characterised by a steady increase in NAR, a diminution in the abundance of both *Discoaster* spp. and a large size of *Reticulofenestra* coccoliths. Also present is a lone abundance of small size *Reticulofenestra* coccoliths within this interval. These combined factors were interpreted as an indicator of increasingly eutrophic conditions predominant at this interval, with the stepwise collapse in sea surface stability favouring nutrient gained (d) 4500–6490 ft. (middle Miocene 15.0Ma): A steady NAR increase, a barely very low abundance of *Discoaster* spp. and predominantly abundance of small *Reticulofenestra* coccoliths were recorded within this interval (Figure 5) to highlight eutrophic conditions. Consideration was taken on the frequency of bimodal size distribution and reduction in maximum size of *Reticulofenestra* coccoliths within this interval, indicative of strong eutrophication at the sea surface.

However, the above local interpretation of the studied succession can be extrapolated central to theoretical facts on biogeochemical and ecological components of the proxies that reflect the temperature and nutrient changes along the ocean column (Sato & Chiyonobu, 2009; Imai et al., 2015). It could be explicitly summarised in the following two major statements. First, horizons characterised with low frequency of NAR and the presence of abundant large *Reticulofenestra* coccoliths with a high relative abundance of *Discoaster* spp., suggest the development of deep fall in thermocline and nutricline that symptomatically induce an oligotrophic condition prevailing at the sea surface (Flores et al., 1995; Farinaciari et al., 2000; Sato & Chiyonobu 2009). Second, horizons characterised with a high frequency of NAR and abundant small *Reticulofenestra* coccoliths with the relative abundance of *Discoaster* spp. suggest the dominance of thermocline and nutricline

at the sea surface, eliciting evident of prevailing eutrophic conditions at the sea surface (Flores et al., 1995; Imai et al., 2015).

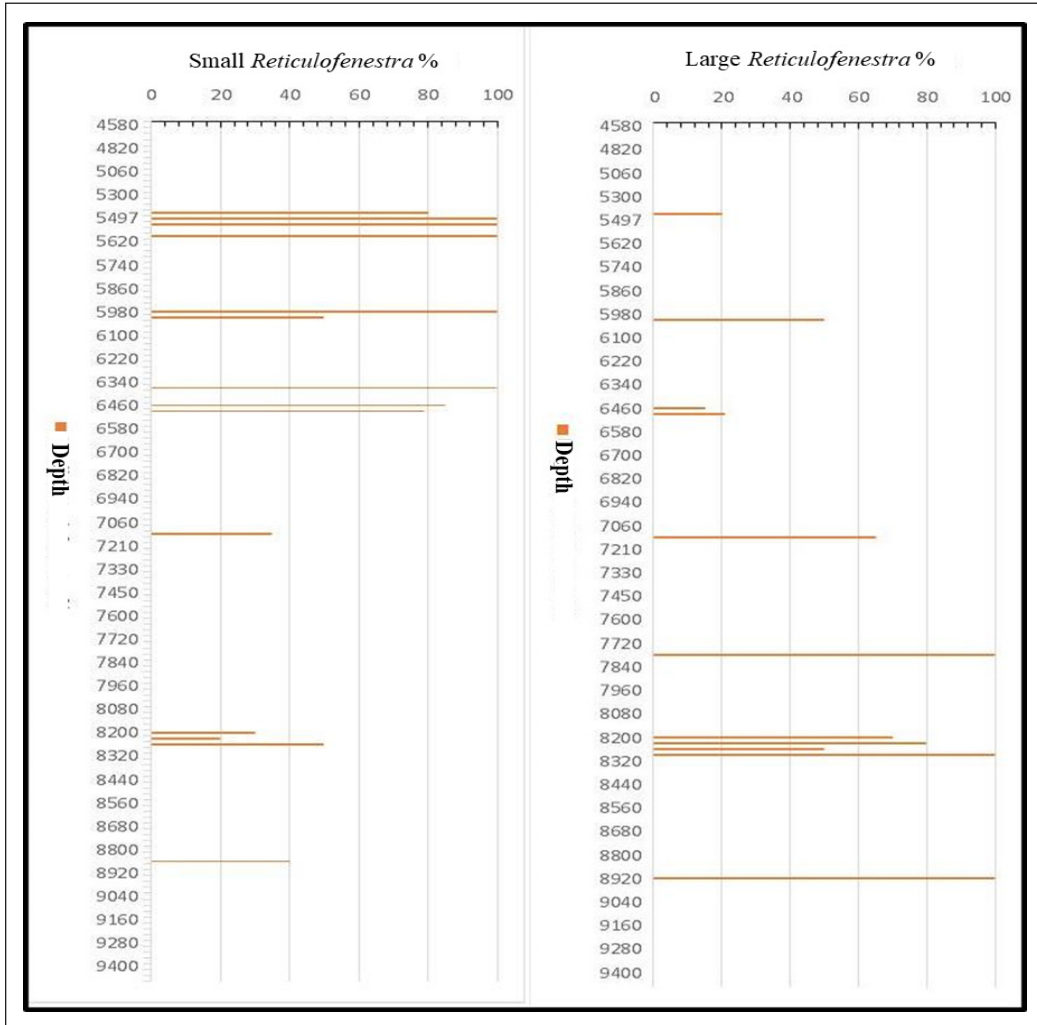


Figure 7. Stratigraphic percentile distribution of coccolith size distribution of *Reticulofenestra* in DEL-1 Well. Small size *Reticulofenestra* increases up-hole while large size *Reticulofenestra* decreases up-hole.

### Miocene Palaeoceanographic Architecture for DEL-1 Well

The interplay between the observed distribution patterns of *Discoaster* species, *Helicosphaera* species and *Reticulofenestra* coccolith sizes within the studied succession allow some insightful deductions to infer possible palaeoceanographic architecture for the studied well. Evident during the period of 17 Ma – older (8500–9450 ft), a steady increase in abundance of lower photic zone species of *Discoaster* (Figures 4 and 6) and dominant abundance of large *Reticulofenestra* coccoliths (Figure 7) show the development

of thermocline and nutricline largely supported by stable ocean water condition, low nutrient content and sun penetration (Gallagher, 1989; Hagino et al., 2000; Herrmann & Thierstein, 2012). Conceivably, it suggests the dominance of oligotrophic oceanographic conditions that influenced the productivity and enhanced size of the *Reticulofenestra* coccoliths. These scenarios are similar to the palaeoceanographic situation described in the western Equatorial Pacific Ocean within NN2–NN5 Zone (Farida et al., 2012) and the NN6–NN8 Zone in the Indian Ocean of DSDP sites (Young, 1990) with a slight difference in the timing of NN4 in this study.

A critical look into horizons within depth interval 7500–8000 ft shows sparse to the low occurrence of nannoliths with *Helicosphaera carteri* and *Calcidiscus leptoporus* standing as a resistant species in their abundances. The bioevents above 17.4 Ma horizons suggest step by step collapse of the thermocline and nutricline that signifies possible dominance of mesotrophic oceanographic condition, which often results in complex nannofloral patterns (Haq, 1980; Young, 1994; Imai et al., 2015). This scenario could be presented as a transitional condition responsible for the observed continuous fluctuating NAR, the relative abundances of *Discoaster* species and the relative abundance of small *Reticulofenestra* species in this study. Moreover, nannofloral diversity and abundance are often favoured by mesotrophic and stable water environments, and by implication, characterize the surface water productivity within the low to middle latitude oceans (Young, 1994; Erba, 2006). Furthermore, these oceanic waters are known for their warm temperature that typifies the Miocene climatic condition (Haq & Lohmann, 1976; Haq, 1980; Imai et al., 2015).

Small *Reticulofenestra* and *Sphenolithus* species are regarded as indicators of eutrophic conditions while typically found in upwelling related areas (Flores et al., 1995; Kameo, 2002; Imai et al., 2015). The bioevents surrounding 15.9 Ma in this study are generally characterized by low and persistent environmental resistance species within intervals 6490–7780 ft. It suggests the interval continuously experience mesotrophic conditions sequel to potential changes at the sea surface. However, the dominant occurrence of small *Reticulofenestra* species and the modal sizes could trigger the overriding effect of eutrophication (Flores et al., 1995; Kameo, 2002). Therefore, the depth interval 4500–6490 ft is regarded as strong eutrophication with the abundant occurrence of small *Reticulofenestra* and gradual decrease in nannofloral abundance and diversity up-hole to characterize the ecostratigraphic events and the bioevents recorded around 15.0 Ma. However, this attests to various emphases placed on small size *Reticulofenestra* species to determine the influence of eutrophication on Miocene palaeoceanographic conditions (Young, 1994; Erba, 2006; Herrmann & Thierstein, 2012; Imai et al., 2015).

LaRiviere et al. (2012) proposed that a continuous relative shoaling of thermocline and reduction in low-latitude gradients in sea surface temperature supports appreciable nutrients could have induced the establishment of eutrophic conditions experienced within depth interval (5000 – 6490 ft). It could have been initiated probably from the low to moderate

abundance and diversity of calcareous nannofossils in mesotrophic habitats that precede the interval. The influence of these factors mentioned above perhaps enlightens the coupling between  $p\text{CO}_2$ , sea surface temperatures, and climatic conditions on the warmth of the Miocene age (Bown et al. 2004). Imai et al. (2015) pointed that strong eutrophication is supported by coastal upwelling or nutrient-rich terrestrial events. Thus, it could be inferred that the fluvial mechanism responsible for the deposition of the encroached Opuama Canyon's (Ozumba, 2018) could enhance the influx of nutrient-rich terrestrial sediments (see deposited sand units in Figure 3) into the western DFZ within the Gulf of Guinea to support the eutrophication of the surface water.

Moreover, this study highlights a decrease in abundance of less-resistant calcareous nannofossils and an overall decrease in species richness within depth interval 4600–8000 ft (Figure 4). Thus, suggest the presence of carbonate crash in reference to its occurrence in another related low to middle latitude oceans (Fadiya & Salami, 2012; Honisch et al., 2012). In this study, this phenomenon is marked within the upper section of NN4 and lower section of NN5 of the studied Miocene succession. In other words, it could be interpreted that the phenomenon is likely ascribed with dissolution or low carbonate productivity effects, coupled with the developmental changes from mesotrophic to eutrophic conditions of the sea surface during the early to middle Miocene experienced in this local area. Moreover, it is widely known that the dissolution of coccoliths is not species-selective; therefore, nannofossils are sensitive indicators to a degree of dissolution and perhaps environmental changes (Boyce et al., 2010; Honisch et al., 2012). Consequently, decrease in abundance of fewer dissolution-susceptible taxa, cyclic decrease in the abundance of *Discoaster* species, and relative abundance of resistant species of *Calcidiscus leptoporus*, *Helicosphaera carteri* and *Sphenolithus* species were highlighted in this study. Thus, suggest the strong influence of carbonate dissolution effect than low surface water productivity on the induced warm waters dominant in the study area (Lyle et al., 1995; Honisch et al., 2012).

### Comparative View with Other Oceans

In this study, the disappearance of Oligocene type species with the replacement of *Discoaster–Sphenolithus–Reticulofenestra* assemblages in the early to middle Miocene (Figure 4) could signal gradual dominance of warm water of induced-climatic events (Haq & Lohmann, 1976; Haq, 1980). It is supported by gradual displacement of large size *Reticulofenestra* species with the dominant presence of small size species in the middle Miocene, similar to the nannoflora event reported in the north-western Pacific and eastern Indian Ocean (Imai et al., 2015). Moreover, this study highlights the dominance of distinct medium to large size *Reticulofenestra* coccoliths with the fluctuating occurrence of *Discoaster* spp., to characterise the early Miocene succession (Figure 4). This scenario suggests the initial gradual collapse of the thermocline at a period when ocean chemistry

and salinity become unstable as a result of terrestrial influxes and possible carbon dissolution (Jiang et al., 2007; Fadiya & Salami, 2012). Perhaps influence the distribution and biodiversity of the associated calcareous nannoplanktons used by Pujos (1985, 1987) to decipher the thermal structure of water masses from the Central Pacific DSDP site within the mid-latitude.

The general observed up-hole changes in *Reticulofenestra* coccoliths size and bimodalisation during the middle Miocene register a trend in this study (Figure 6). This ascribed phenomenon is regarded as a taxonomic marker responsible for ideal variations in nannoliths niches in palaeo-oceans (Backman, 1984; Young, 1994; Farinaciari et al., 2000; Herrmann & Thierstein, 2012). The size variation patterns have been summarized with two extreme possibilities; first, they represent the effect of ecological factors on genetically unchanging populations. Second, that they show evolutionary change without environmental change, the limitation of this study could not allow a distinct definition between the two facts. However, from our observation, since the size range and modal size vary independently, and cyclic dominance of ecologic species like *Discoaster-Sphenolithus-Reticulofenestra-Calcidiscus-Coccolithus* assemblages, thus, suggest the phenomenon would not be as a result of a single external factor, i.e., temperature. Rather, we suggest a combined effect of both evolutionary events of genotypic variation (Bown et al., 2004; Erba, 2004; Erba et al., 2004) and ecological control (Farida et al., 2012; Fadiya & Salami, 2012) might be responsible for the size variation. Seemingly, this phenomenon has been reported in the Atlantic Ocean DSDP site 116 within NN3–NN10 (Haq, 1980), similarly recorded in the western equatorial Pacific Ocean within 5.0–6.0 Ma (Farida et al., 2012), the Indian Ocean at 6.0 Ma (Young, 1990), and north-western Pacific and the eastern Indian Ocean within 6.4–5.0 Ma (Imai et al., 2015).

Some articles on the premise of *Reticulofenestra* size variation and ecological modifications exhibited by *Discoaster-Sphenolithus-Calcidiscus* assemblages in middle Miocene sediments across the oceans mentioned above, are construed to be a widespread low to the middle-latitude event (Young, 1990; Farida et al., 2012; Imai et al., 2015). However, this suggests the oceans might have possibly shared a similar interplay between environmental factors ( $p\text{CO}_2$ , pH, temperature, salinity, light, oxygen, and nutrient levels) and evolutionary control to reflect on the overarching pattern of nannofloras as a result of changes/variability in stability of the sea surface conditions (Young, 1990; Erba, 2006). Conversely, this study noted the presence of bimodality and an abrupt reduction of *Reticulofenestra* coccolith modal size to coincide with an increase in NAR and decrease in *Discoaster* species abundance, which is similar to the nannoflora pattern in the north-western Pacific and the eastern Indian Ocean within 6.4–5.0 Ma (Imai et al., 2015). Though at different timing, thus, suggests a marine event induced by latitudinal climatic changes that resulted in changes in environmental conditions of the surface waters (Young, 1990; Holcová, 2005; Farida et al., 2012, Imai et al., 2015).

## CONCLUSIONS

The studied well has been examined of its palaeoecologic and palaeoceanographic conditions inferred from the recouped calcareous nannofossil assemblages. The biostratigraphic analysis reveals low to moderate abundance and moderate diversity of calcareous nannofossils that enabled the recognition of nannofossil zones NN4 and NN5, which span early to middle Miocene age. The palaeoenvironment is interpreted to range between intertidal to tidal sub-facies to shelf mud deposition in neritic settings. The variances in the relationship among the ecologic proxies suggest that the early Miocene's lower horizons are characterised by deep thermocline and nutricline, a typical representative of dominant oligotrophic conditions.

A short mesotrophic condition, generally characterized with sparse to the low occurrence of nannoliths, aside from the abundance of resistant *Helicosphaera* species in the upper interval of early Miocene, suggests the initial collapse of the thermocline and nutricline of the sea surface water. Consequently, gradual but notably low abundance of dissolution-susceptible taxa within the middle Miocene horizons implies the presence of carbonate crashes like other worlds' oceans. Thus, suggest strong eutrophication with the potential collapse of the surface waters, coupled with the influx of nutrient-rich terrestrial sediments resulting from the prevailed induced-climatic events in the middle Miocene horizons within the Gulf of Guinea axis of the Atlantic Ocean.

The recouped calcareous nannofossil assemblages show a gradual stepwise reduction in nannofossil distribution from early to middle Miocene, thus, suggest a local collapse of the sea surface stratification in the oceanic water around the study area. Moreover, the suggested changes from dominant oligotrophic to short mesotrophic conditions in the early Miocene, finally to a eutrophic condition in the middle Miocene. Thus, construe the oceanic water and the environmental properties of the sea surface water to have engaged in dynamic changes similar to situations in low latitude regions like the Indian Ocean, Caribbean, southern South America, eastern equatorial Pacific and the western coast of Central Africa. However, the timing of the inferred eutrophication in the Gulf of Guinea might slightly differ from other world oceans, suggesting marine events induced by the latitudinal climatic change that influence changes in environmental conditions of the surface waters.

## ACKNOWLEDGEMENT

My sincere appreciation goes to the Geologic Service Unit (SNEPCO) for the provision of ditch cutting samples used for this research. Also, I appreciated Prof. Dr. Che Aziz Ali for his constructive criticism on the research that led to this manuscript. I sincerely appreciate the role played by Dr. Adepehin to suggest different articles to support my findings on the geology of Niger Delta.

## REFERENCES

- Adegoke, O. S., Oyebamiji, A. S., Edet, J. J., Osterloff, P. L., & Ulu, O.K. (2017). *Cenozoic foraminifera and calcareous nannofossil biostratigraphy of the Niger Delta*. Elsevier Incorporation. <http://dx.doi.org/10.1016/C2016-0-03240-0>
- Ajayi, E. O., & Okosun, E. A. (2014). Calcareous nannofossil biostratigraphy of A, B, C, D wells, offshore Niger Delta, Nigeria. *Earth Science Research*, 3(1), 108-123. <http://doi:10.5539/esr.v3n1p108>
- Aubry, M. P. (1992). Late Paleogene calcareous nannoplankton evolution: A tale of climatic deterioration. In D. R. Prothero, & W. A. Berggren (Eds.), *Eocene–Oligocene Climatic and Biotic Evolution* (pp. 272-309). Princeton University Press. <https://doi.org/10.1515/9781400862924.272>
- Backman, J. (1984). Cenozoic calcareous nannofossils and biostratigraphy from the North Eastern atlantic ocean-deep sea drilling project leg 81. In D. G. Roberts, & D. Schnittker (Eds.), *Initials reports of the deep sea drilling project* (Vol. 81, pp. 403-428). Washington U.S. Govt. Office. <http://doi.org/10.2973/dsdp.proc.81.105.1984>
- Bilotti, F., & Shaw, J. H. (2005). Deep-water Niger Delta fold and thrust belt modelled as a critical-taper wedge: The influence of elevated basal fluid pressure on structural styles. *Association American Petroleum Geologists Bulletin*, 89(11), 1475-1491. <https://doi.org/10.1306/06130505002>
- Bilotti, F., Shaw, J. H., Cupich, R. M., & Lakings, R. M. (2005). Detachment fold, Niger Delta. In J. H. Shaw, C. Connors, & J. Suppe, (Eds.), *Seismic interpretation of contractional fault related folds* (Vol. 53, pp. 103-104). Association American Petroleum Geologists.
- Bown, P. R. (1999). *Calcareous nannofossil biostratigraphy*. Kluwer Academic Publication. <https://doi.org/10.1007/978-94-011-4902-0>
- Bown, P. R., & Dunkley, J. T. (2012). Calcareous nannofossils from the Paleogene equatorial Pacific (IODP Expedition 320 Sites U1331-1334). *Journal of Nannoplankton Research*, 32(2), 3-51.
- Bown, P. R., & Young, J. R. (1998). Techniques. In P. R. Bown (Ed.), *Calcareous nannofossil biostratigraphy* (pp. 16-26). Kluwer Academic Publication. [https://doi.org/10.1007/978-94-011-4902-0\\_2](https://doi.org/10.1007/978-94-011-4902-0_2)
- Bown, P. R., Lees, J. A., & Young, J. R. (2004). Calcareous nannoplankton evolution and diversity through time. In H. R. Thierstein, & J. R. Young (Eds.), *Coccolithophores - From molecular processes to global impact* (pp. 481-508). Springer. [https://doi.org/10.1007/978-3-662-06278-4\\_18](https://doi.org/10.1007/978-3-662-06278-4_18)
- Boyce, D., Lewis, M., & Worm, B. (2010). Global phytoplankton decline over the past century. *Nature*, 466, 591- 596. <http://doi:10.1038/nature09268>
- Bramlette, M. N., & Wilcoxon, J. A. (1967). Middle tertiary calcareous nannoplankton of the Cipero section, Trinidad, W.I. *Tulane Studies in Geology and Paleontology*, 5, 93-131.
- Brown P. R. (2005). Paleogene calcareous nannofossils from the Kilwa and Lindi areas of coastal Tanzania (Tanzania Drilling Project 2003-4). *Journal of Nannoplankton Research*, 27, 21-95.
- Bukry, D., & Bramlette, M. N. (1969). Some new and stratigraphically useful calcareous nannofossils of the Cenozoic. *Tulane Studies in Geology*, 7, 131-142.

- Connors, C. D., Denson, D. B., Kristiansen, G., & Angstadt, D. M. (1998). Compressive anticlines of the mid-outer slope, central Niger Delta (abs.). *Association American Petroleum Geologists Bulletin*, 82(10), Article 1903.
- Corredor, F., Shaw, J. H., & Bilotti, F. (2005). Structural styles in the deepwater fold-and-thrust belts of the Niger Delta. *Association American Petroleum Geologists Bulletin*, 89(6), 753-780. <https://doi.org/10.1306/02170504074>
- Doust, H., & Omatsola, E. (1990). Niger delta. In J. D. Edwards & P. A. Santogrossi (Eds.), *Divergent/passive margin basins* (pp. 201-238). American Association of Petroleum Geologists Memoir.
- Erba, E. (2004). Nannofossils and Mesozoic oceanic anoxic events. *Marine Micropaleontology*, 52, 85-106. <https://doi.org/10.1016/j.marmicro.2004.04.007>
- Erba, E. (2006). The first 150 million years history of calcareous nannoplankton: Biosphere-geosphere interactions. *Palaeogeography, Palaeoclimatology, Palaeoecology*, 232, 237-250. <https://doi.org/10.1016/j.palaeo.2005.09.013>
- Erba, E., Bartolini, A., & Larson, R. L. (2004). Valanginian Weissert oceanic anoxic event. *Geology*, 32(2), 149-152. <https://doi.org/10.1130/G20008.1>
- Fadiya, S. L. (1999). Foraminifera and calcareous nannofossils biostratigraphy and well-log sequence Stratigraphic analysis of Opolo-5 and Opolo-6 wells, Niger Delta. (Unpublished Master Thesis). Obafemi Awolowo University, Nigeria.
- Fadiya, S. L., & Salami, M. B. (2012). Middle Miocene carbonate crash in the Niger Delta: Evidence from calcareous nannofossils. *Journal of Nannoplankton Research*, 32(2), 59-70.
- Farida, M., Imai, R., & Sato, T. (2012). Miocene to Pliocene Paleooceanography of the western equatorial Pacific Ocean based on Calcareous nannofossils, ODP Hole 805B. *Open Journal Geology*, 2, 72-79. <https://doi.org/10.4236/ojg.2012.22008>
- Farinaciari, E. S., Rio, A. D., & Negri, A. (2000). Middle Miocene quantitative calcareous nannofossils biostratigraphy in the Mediterranean region. *Journal of Micropalaeontology*, 42, 38-64.
- Flores, J. A., & Sierro, F. J. (1987). Calcareous plankton in the Tortonian/Messinian transition series of the Northwestern edge of the Guadalquivir Basin. *Abhandlungen der Geologischen Bundesanstalt*, 39, 67-84.
- Flores, J. A., & Sierro, F. J. (1997). Revised technique for calculation of calcareous nannofossil accumulation rates. *Marine Micropaleontology*, 43, 321-324. <https://doi.org/10.2307/1485832>
- Flores, J. A., Sierro, F. J., & Raffi, I. (1995). Evolution of the calcareous nannofossil assemblage as a response to the Palaeoceanographic changes in the eastern equatorial Pacific Ocean from 4 to 2 Ma, Leg 138, sites 849 and 852. In N. G. Pisias, L. A. Mayer, T. R. Janecek, A. Palmer-Julson, & T. H. van Andel, T. H. (Eds.), *Proceedings of the Ocean Drilling Program, Scientific Results* (Vol. 138, 163-176). Ocean Drilling Program College Station. <https://doi.org/10.2973/odp.proc.sr.138.109.1995>
- Flores, J. A., Sierro, F. J., Filippelli, G. M., Bárcena, M. Á., Pérez-Folgado, M., Vázquez, A., & Utrilla, R. (2005). Surface water dynamics and phytoplankton communities during deposition of cyclic late Messinian sapropel sequences in the western Mediterranean. *Marine Micropaleontology*, 56, 50-79. <https://doi.org/10.1016/j.marmicro.2005.04.002>



- Gallagher, L. (1989). Reticulofenestra: A critical review of taxonomy, structure and evolution. In J. A. Crux, & S. E. van Heck (Eds.), *Nannofossils and their applications* (pp. 41-75). Ellis Horwood Ltd.
- Gartner, S. (1992). Miocene nannofossil chronology in the north Atlantic, DSDP Site 608. *Marine Micropaleontology*, 18, 307-331. [https://doi.org/10.1016/0377-8398\(92\)90045-L](https://doi.org/10.1016/0377-8398(92)90045-L)
- Gradstein, F. M., Ogg, J. G., Schmitz, M. D., & Ogg, G. M. (2020). *A geologic time scale*. Elsevier. <https://doi.org/10.1016/B978-0-12-824360-2-00001-2>
- Guerra, R. D., Tokutake, L., & Fauth, G. (2011). Cretaceous calcareous nannofossils from Pelotas Basin, Brazil: Biostratigraphic and paleoecological inferences. *Journal of South American Earth Sciences*, 36, 55-71. <https://doi.org/10.016/j.jsames.2011.10.008>
- Hagino, K., Okada, H., & Matsuoka, H. (2000). Spatial dynamics of coccolithophore assemblages in the equatorial Western-Central Pacific Ocean. *Marine Micropaleontology*, 39, 53-72. [https://doi.org/10.1016/S0377-8398\(00\)00014-1](https://doi.org/10.1016/S0377-8398(00)00014-1)
- Haq, B. U. (1966). Electron microscope studies on some upper Eocene calcareous nannoplankton from Syria. *Stockholm Contributions in Geology*, 15, 23-37.
- Haq, B. U. (1980). Biogeographic history of Miocene calcareous nannoplankton and paleoceanography of the Atlantic Ocean. *Marine Micropaleontology*, 26(4), 414-443. <https://doi.org/10.2307/1485353>
- Haq, B. U., & Lohmann, G. P. (1976). Early Cenozoic calcareous nannoplankton biogeography of the Atlantic Ocean. *Marine Micropaleontology*, 1, 111-194. [https://doi.org/10.1016/0377-8398\(76\)90008-6](https://doi.org/10.1016/0377-8398(76)90008-6)
- Haq, B. U., Hardenbol, J., & Vail, P. R. (1988). Mesozoic and Cenozoic chronostratigraphy and eustatic cycles. In C. K. Wilgus, B. S. Hastings, C. G. S. C. Kendall, H. W. Posamentier, C. A. Ross, & J. C. Van Wagoner (Eds.), *Sea-level changes: An integrated approach* (Vol. 42, pp. 71-108). SEPM Special Publication. <https://doi.org/10.2110/pec.88.01.0071>
- Hay, W. W., Mohler, H. P., Roth, P. H., Schmidt, R. R., & Boudreaux, J. E. (1967). Calcareous nannofossils from Nal'chik (northwest Caucasus). *Eclogae Geologicae Helvetiae*, 59, 379-399.
- Herrmann, S., & Thierstein, H. R. (2012). Cenozoic coccolith size changes - Evolutionary and/or ecological controls. *Palaeogeography Palaeoclimatology Palaeoecology*, 333, 92-106. <https://doi.org/10.1016/j.palaeo.2012.03.011>
- Holcová, K. (2005). Quantitative calcareous nannoplankton biostratigraphy of the Oligocene/Miocene boundary interval in the northern part of the Buda Basin (Central Paratethys). *Geological Quarterly*, 49, 263-274.
- Honisch, B., Ridgwell, A., Schmidt, D. N., & Thomas, E. (2012). The geological recorded of ocean acidification. *Science*, 335(6072), 1058-1063. <https://doi.org/10.1126/science.1208277>
- Imai, R., Farida, M., Sato, T., & Iryu, Y. (2015). Evidence for eutrophication in the northwestern Pacific and eastern Indian oceans during the Miocene to Pleistocene based on the nannofossil accumulation rate, *Discoaster* abundance, and coccolith size distribution to *Reticulofenestra*. *Marine Micropaleontology*, 116, 15-27. <http://dx.doi.org/10.1016/j.marmicro.2015.01.001>.
- Jiang, S., Jr Wise, S. W., & Wang, Y. (2007). Cause of the middle/late miocene carbonate crash: Dissolution or low productivity? In D. A. H. Teagle, D. S. Wilson, G. D. Acton, & D. A. Vanko (Eds.), *Proceedings*

- of the Ocean Drilling Program, Scientific Results* (Vol. 206, pp. 1-24). Ocean Drilling Program College Station. <https://doi.org/10.2973/odp.proc.sr.206.013.2007>
- Kamptner, E. (1954) Untersuchungen über den feinaufbau der coccolithen anzeiger [Investigations into the fine structure of the coccoliths. indicator]. Österreichische *Akademie der Wissenschaften. Mathematische-Naturwissenschaftliche Klasse*, 87, 152-158.
- Kameo, K. (2002). Late Pliocene Caribbean surface water dynamics and climatic changes based on calcareous nannofossil records. *Palaeogeography, Palaeoclimatology, Palaeoecology*, 179, 211-226. [https://doi.org/10.1016/S0031-0182\(01\)00432-1](https://doi.org/10.1016/S0031-0182(01)00432-1)
- Kameo, K., Shindo, R., & Takayama, T. (2010). Calcareous nannofossil biostratigraphy and geologic age of the Kiyosumi Formation of the Awa Group, Boso Peninsula, central Japan: Age determination based on size variations of Reticulofenestra specimens (in Japanese with English abstract). *Journal Geology Society of Japan*, 116, 563-574. <https://doi.org/10.5575/geosoc.116.563>
- LaRiviere, J. P., Ravelo, A. C., Crimmins, A., Dekens, P. S., Ford, H. L., & Lyle, M. (2012). Late Miocene decoupling of oceanic warmth and atmospheric carbon dioxide forcing. *Nature*, 486, 97-100. <https://doi.org/10.1038/nature11200>
- Loeblich, A. R., & Tappan, H. (1978) The coccolithophorid genus *Calcidiscus* Kamptner and its synonyms. *Journal of Paleontology*, 52, 1390-1392.
- Lyle, M., Dadey, K. A., & Farrel, J. W. (1995). The Late Miocene (11-8Ma) eastern Pacific carbonate crash: Evidence of reorganization of deepwater circulation by the closure of the Panama Gateway. In N. G. Pisias, L. A. Mayer, T. R. Janecek, A. Palmer-Julson, & T. H. van Andel (Eds.), *Proceedings of the Ocean Drilling Program, Scientific Results* (Vol. 138, pp. 821-838). Ocean Drilling Program College Station. <https://doi.org/10.2973/odp.proc.sr.138.157.1995>
- Magbagbeola, O., & Willis, B. J. (2007). Sequence stratigraphy and syndepositional deformation of the Agbada Formation, Robertkiri field, Niger Delta, Nigeria. *American Association of Petroleum Geologists Bulletin*, 91, 945-958. <https://doi.org/10.1306/02050705150>
- Martini, E. (1965). Mid-Tertiary calcareous nannoplankton from Pacific deep-sea cores. *Colston Papers*, 17, 393-411.
- Martini, E. (1971). Standard tertiary and quaternary calcareous nannoplankton zonation. In A. Farinacci (Ed.), *Proceedings of the Second Planktonic Conference* (Vol. 2, pp. 739-765). CiNii Publication.
- McIntyre, A., & Bé, A. H. (1967). Modern coccolithophoridae of the Atlantic ocean - I. Placoliths and cyrtoliths. *Deep-Sea Research*, 14, 561-597. [https://doi.org/10.1016/0011-7471\(67\)90065-4](https://doi.org/10.1016/0011-7471(67)90065-4)
- Momta, P. S., & Odigi, M. I. (2014, November 9-13). Sequence stratigraphic framework and depositional architecture of MP field, shallow offshore, Niger Delta, Nigeria. In *Proceedings of the NAPE Annual International Conference and Exhibitions* (pp. 9-13). Lagos, Nigeria.
- Müller, C. (1981). Beschreibung neuer Helicosphaera-Arten aus dem Miozän und Revision biostratigraphischer Reichweiten einiger neogener Nannoplankton-Arten [Description of new Helicosphaera species from the Miocene and revision of the biostratigraphic ranges of some neogenic nannoplankton species]. *Senckenbergiana Lethaea*, 61, 427-435.

- Murray, G., & Blackman, V. H. (1898). On the nature of the coccospheres and rhabdospheres. *Philosophical Transactions of the Royal Society*, 190, 27-411. <https://doi.org/10.1098/rstb.1898.0006>
- Obaje, S. O., & Okosun, E. A. (2013). Taxonomic notes on Coccolithophorids from Tomboy Field, offshore western Niger Delta, Nigeria. *International Journal of Science and Technology*, 2(11), 814-821.
- Ojo, E. A., Fadiya, L. S., & Ehinola, O. A. (2009). Biozonation and correlation of BDX-1 and BDX-2 wells of deep offshore Niger Delta using calcareous nannofossils. In *American Association of Petroleum Geologists* (pp. 8-21). Search and Discovery Article.
- Ola, P. (2018). Morphological description of calcareous nannofossils assemblage of a middle-miocene to late-miocene section in the Niger-Delta, Nigeria. *Open Journal of Geology*, 8, 925-936. <http://doi:10.4236/ojg.2018.89055>.
- Oyebamiji, S. A. (1997). *Calcareous nannofossils biostratigraphy of a well in the Niger Delta, Nigeria* (Unpublished Master Thesis). University College, London.
- Ozumba, B. M. (2018). Stratigraphic framework of the Western Central Swamp of the Niger Delta, Nigeria. *Scientific Environment*, 1, 105-114.
- Perch-Nielsen, K. (1985). Cenozoic calcareous nannofossils. In H. M. Bolli, J. B. Saunders, & K. Perch-Nielsen (Eds.), *Plankton stratigraphy* (pp. 427-554). Cambridge University Press.
- Perch-Nielsen, K. (1989). Mesozoic and Cenozoic calcareous nannofossils. In H. M. Bolli, J. B. Saunders, & K. Perch-Nielsen (Eds.), *Plankton stratigraphy* (pp. 329-554). Cambridge University Press.
- Pujos, A. (1985). Cenozoic nannofossils, Central Equatorial Pacific. *Initial Report Deep Sea Drilling Project Leg 85 (IRSDP)*, 15, 581-607. <http://doi:10.2973/dsdp.proc.85.114.1985>.
- Pujos, A., (1987). Late Eocene to Pleistocene medium-sized and small-sized "reticulofenestrads". *Abhandlungen der Geologischen Bundesanstalt*, 39, 239-277.
- Raffi, I., Backman, J., Fornaciari, E., Palike, H., Rio, D., Lourens, L., & Hilgen, F., (2006). A review of calcareous nannofossil astrobiochronology encompassing the past 25 million years. *Quaternary Scientific Review*, 25(23), 3113-3137. <https://doi.org/10.1016/j.quascirev.2006.07.007>
- Reijers, T. J. A. (2011). Stratigraphy and sedimentology of the Niger Delta. *Geologos, The Netherlands*, 17(3), 133-162. <https://doi.org/10.2478/v10118-011-0008-3>
- Roth, P. H. (1970). Oligocene calcareous nannoplankton biostratigraphy. *Eclogae Geologicae Helveticae*, 63, 799-881.
- Sanuade, O. (2014). Calcareous nannofossil biostratigraphic analysis of well 'K-2', deep offshore Niger Delta, Nigeria. *Advances in Research*, 2, 696-711. <http://doi:10.9734/AIR/2014/11364>.
- Sato, T., & Chiyonobu, S. (2009). Cenozoic paleoceanography indicated by size change of calcareous nannofossil and discoaster number (in Japanese with English abstract). *Fossils (Palaeontological Society of Japan)*, 86, 12-19.
- Schiller, J. (1930). Coccolithineae. In L. Rabenhorst (Ed.), *Kryptogamen-Flora* (pp. 89-273). Akademische Verlagsgesellschaft.

- Selley, R. C. (1985). *Ancient Sedimentary Environments*. Cornell University Press. <https://doi.org/10.1002/geo.3340020207>
- Vulc, A., & Silye, L. (2005). Preliminary data on biostratigraphy and paleoecology of calcareous nannofossils and foraminifera in Cepari Quarry (North-Eastern Transylvania, Romania). *Acta Palaentologica Romaniae*, 5, 493-501.
- Wallich, G. C. (1877). Observations on the coccosphere. *Annals and Magazine of Natural History*, 19, 342-350. <https://doi.org/10.1080/00222937708682153>
- Young, J. R. (1990). Size variation of Neogene Reticulofenestra coccoliths from Indian Ocean DSDP cores. *Journal of Micropalaeontology*, 9, 71-86. <http://doi:10.1144/jm.9.1.71>
- Young, J. R. (1994). Functions of coccoliths. In A. Winter, & W. G. Siesser (Eds.), *Coccolithophores* (pp. 63-82). Cambridge University Press.
- Young, J. R. (1998). Neogene. In P. Bown (Ed.), *Calcareous nannofossil biostratigraphy*, (pp. 225-265). British Micropaleontology Society Publication. [https://doi.org/10.1007/978-94-011-4902-0\\_8](https://doi.org/10.1007/978-94-011-4902-0_8)
- Zachos, J. C., Kroon, D., & Blum, P. (2004). *Early Cenozoic extreme climates: The walvis ridge transect*. Oceanographic Institutions Inc.
- Zervas, D., Nichols, G., Hall, R., Smyth, H., Luthje, C., & Murtagh, F. (2009). SedLog: A shareware program for drawing graphic logs and log data manipulation. *Computers and Geosciences*, 35(10), 2151-2159. <https://doi.org/10.1016/j.cageo.2009.02.009>.
- Zhang, J., Wang, P., Li, Q., Cheng, X., Jin, H., & Zhang, S. (2007). Western equatorial pacific productivity and carbonate dissolution over the last 150 kyr: Foraminiferal and nannofossil evidence from ODP Hole 807A. *Marine Micropaleontology*, 64(3-4), 121-140. <https://doi.org/10.1016/j.marmicro.2007.03.003>

## Effect of Chemical Reaction towards MHD Marginal Layer Movement of Casson Nanofluid through Porous Media above a Moving Plate with an Adaptable Thickness

Ganugapati Raghavendra Ganesh and Wuriti Sridhar\*

*Department of Mathematics, Koneru Lakshmaiah Education Foundation, Guntur-522502, Andhra Pradesh, India*

### ABSTRACT

In the current workflow and heat exchange of a Casson nanofluid across a penetrable media above a moving plate with variable thermal conductivity, adaptive thickness and chemical reaction are analyzed. First, the governing nonlinear equations of partial derivative terms with proper extreme conditions are changed into equations of ordinary derivative terms with suitable similarity conversions. Then the resulting equations are worked out using the Keller box method. The effects of various appropriate parameters are analyzed by constructing the visual representations of velocity, thermal, and fluid concentration. The velocity profile increased for shape parameter, and the opposite trend is observed for magnetic, Casson, porosity parameters. Temperature profile increases for magnetic, Casson, Brownian motion parameter, and thermophoresis parameters. Concentration profiles show a decreasing trend for wall thickness, Brownian movement, chemical reaction parameters. Also, skin friction values are calculated and matched with previous literature found in accordance. Also, local parameters Nusselt and Sherwood numbers are calculated and analyzed in detail.

*Keywords:* Adaptive thickness, Casson nanofluid, chemical reaction, porous medium, thermal conductivity, thermal radiation

### ARTICLE INFO

*Article history:*

Received: 06 June 2021

Accepted: 15 September 2021

Published: 04 January 2022

DOI: <https://doi.org/10.47836/pjst.30.1.26>

*E-mail addresses:*

[gr.ganugapati@gmail.com](mailto:gr.ganugapati@gmail.com) (Ganugapati Raghavendra Ganesh)

[sridharwuriti@gmail.com](mailto:sridharwuriti@gmail.com) (Wuriti Sridhar)

\* Corresponding author

### INTRODUCTION

Heat transfer plays a very significant role in many industrial processes. Naturally, the thermal conductivity of traditional fluids is very low. So, to develop the thermal properties of the fluid dispersing nanometer-sized particles in base fluids, a new pioneering class of fluids, which has

outstanding thermal properties and conserving capability, are generated entitled nanofluids. Also, the usage of nanofluids has various applications thermal management of industrial and consumer products. By collaborating nanoparticles in the fluids may reduce erosion and clogging in systems, for long term reliability of the industrial equipment, efficient cooling is most important, so it has application in tribological and biomedical applications as described by Das et al. (2007). Choi (2008) described that nanofluids have very prospective applications in the areas of microelectronics, space, biomedical industries, and defense. Wang and Mujumdar (2008a) go through the recent findings in using nanofluids and their applications and conclude that communication between particle and liquid should show a vital role in the convective heat transfer performance of fluids. Later, Wang and Mujumdar (2008b) reviewed the application of nanofluids and observed a specific application in the biomedical industry like usage in cancer treatment methods to kill tumor cells effectively, safer surgery processes to reduce organ damages. After that, Singh (2008) focuses on the studies related to the thermal conductivity of nanofluids.

Later, Beg et al. (2009) studied nanofluid flow on an oscillating inclined plate with MHD effect concluded that an upsurge in Hartmann magnetic parameter drops velocity and enhances the thickness of the momentum boundary layer. Fang et al. (2012) investigate the momentum boundary layer with non-uniform thickness observes that if the velocity power index is below one, the non-horizontalness presents a mass suction effect, whereas the velocity power index is above one, the non-horizontalness causes an impact of mass injection. Sheikholeslami et al. (2014) discussed 3D nanofluid movement in the middle of two parallel revolving flat surfaces and concluded the degree of the skin friction coefficient increasing function of the magnetic parameter. Malik et al. (2014) describe Casson nanofluid flow on a vertical cylinder using the RK-Fehlberg method. Mahdy and Chamka (2015) take on Buongiorno's model to study Casson nanofluid flow and observe that Casson parameter restrain the velocity field. Besthapu and Bandari (2015) studied Casson nanofluid flow on a nonlinear elongated sheet concluded that enhancement in Grashoff number reduces the temperature of the fluid. Uddin et al. (2015) described Casson fluid flow with slip parameter and observed that increasing thermal slip nanoparticles concentration would be enhanced. Abdel-wahed et al. (2015) observed that the nanosized speck concentration close to the non-flat surface is superior and narrow than on the flat surface. Oyelakin et al. (2016) studied fluid flow with Soret and Dofour effects using the spectral relaxation method. After that, Ibrahim and Makinde (2016) analyzed the stagnation point Casson nanofluid stream and concluded that for growth in Casson and magnetic parameters, thermal boundary thickness enhanced. After that, Ahmad et al. (2017) noted that on increasing Brownian motion parameters, surface temperature rises. Reddy et al. (2017) used the SQLM technique to study Williamson nanofluid flow on the elongated sheet with adaptable thickness concludes for progressive values of Williamson parameter

concentration of fluid enhances. Dharmaiah et al. (2017) considered nanofluid flow on a vertical flat plate and remarked that heat transfer rate would be enhanced by an escalation of heat source parameters. Madaki et al. (2017) examine nanofluid flow on the elongated sheet with radiation and chemical reaction effects using the OHAM technique, and the RK fourth-order method observes that increasing radiation parameter thermal boundary layer thickness increases. Later Biswas and Ahmad (2018) considered the Casson nanofluid flow with hall current and chemical reaction effects observed that increasing magnetic parameter velocity profiles reduces. Mahmood et al. (2018) studied the transfer of the heat and entropy implications on Casson nanofluid flow employing the Cattaneo-Christov model using a finite difference scheme. Later Reddy et al. (2018) considered the slipstream of a Newtonian nanofluid with adaptive surface thickness using RK with shooting technique observes heat transfer ability of various base fluids. Konda et al. (2018) studied mixed convection Casson nanofluid stream observes concentration outline falls with several values of chemical response parameter. Talla et al. (2018) considered Casson fluid flow on exponentially elongated sheet concludes concentration rises for growing values of Casson parameter. Khan et al. (2018) employed the bvp4c procedure to study Casson nanofluid flow on the elongated surface with adaptive thickness concluded coefficient of skin friction will be diminished for enhancement of Casson parameter. Dharmaiah et al. (2019b) used the perturbation method to study rotating frame nanofluid flow and noted that chemical reaction parameter controls the concentration profiles. Later Dharmaiah et al. (2019a) examined viscous dissipation using the perturbation effect, and it was found that the skin friction drag augmented in view of reduction in the concentration buoyancy effects. Dharmaiah et al. (2020) analyzed hall and slip effects in magneto titanium alloy nanofluid concluded that velocity profiles increase increasing values of hall and ion slip parameters. Vijaya et al. (2020) studied liquid thin film flow of Casson nanofluid flow remarks that temperature profile escalates for higher values of magnetic, Casson parameters. Nagalakshmi and Vijaya (2020) used R with bvp4c to study the Carreau nanofluid flow on a nonlinearly stretching sheet. Sridhar and Lakshmi (2020) discussed nanofluid flow on elongating sheet through the double stratified medium using implicit finite difference method concludes that velocity slip parameter reduces concentration profile. Finally, Ismail et al. (2021) analyzed Casson nanofluid flow with variable thermal conductivity, and variable thickness of the fluids concluded that using Casson nanofluid will increase the movement of heat value over the exterior, which will accelerate the cooling process, and this, in turn, leads to improve the heat treatment process. Also, Casson nanofluid increases the shear stress above the surface and the level of mass relocation over the surface. The present work examined the Casson nanofluid flow on a moving surface with adaptable thermal conductivity and irregular thickness with porous media and chemical reaction effects by using Keller box method.

## METHODOLOGY

### Formulation of the Problem

In the present study, two-dimensional Casson nanofluid flow with adaptive thermal conductivity near a moveable surface with irregular thickness is considered. The thickness of the surface is given by  $y = \zeta(x+b)^{\frac{n-1}{2}}$ . Here,  $\zeta$  is small. The plate is movable with irregular velocity  $u_w^* = a\{x+b\}^m$ . The boundary layer is influenced by nonlinear heat generation, thermal radiation and nonlinear transverse magnetic field, chemical reaction effects. Here the moving plate is considered in the path of the x-axis, and the y-axis is upright to the surface. The governing partial differential equations corresponding to 2 dimensional Casson nanofluid stream on a movable surface with radiation, porous medium-plus chemical reaction effects with adaptive thermal conductivity are as in Equations 1-4:

$$u \frac{\partial u}{\partial x} + v \frac{\partial v}{\partial y} = 0 \tag{1}$$

$$u \frac{\partial u}{\partial x} + v \frac{\partial u}{\partial y} = \frac{\nu}{\beta} \frac{\partial^2 u}{\partial y^2} + \nu \frac{\partial^2 u}{\partial y^2} - \frac{\sigma B^2}{\rho} u - \frac{\nu}{k} u \tag{2}$$

$$u \frac{\partial T}{\partial x} + v \frac{\partial T}{\partial y} = \frac{1}{\rho c_p} \frac{\partial}{\partial y} \left( k \frac{\partial T}{\partial y} \right) - \frac{1}{\rho c_p} \frac{\partial q_r}{\partial y} + \tau \left[ D_b \frac{\partial T}{\partial y} \frac{\partial C}{\partial y} + \frac{D_t}{T_\infty} \left( \frac{\partial T}{\partial y} \right)^2 \right] + \frac{Q}{\rho c_p} (T - T_\infty) \tag{3}$$

$$u \frac{\partial C}{\partial x} + v \frac{\partial C}{\partial y} = D_b \left( \frac{\partial^2 C}{\partial y^2} \right) + \frac{D_t}{T_\infty} \left( \frac{\partial^2 T}{\partial y^2} \right) - k^* (C - C_\infty) \tag{4}$$

Magnetic field strength  $B = B_0(x+b)^{\frac{m-1}{2}}$  and heat generation  $Q = Q_0(x+b)^{m-1}$ , and thermal conductivity  $k$  are assumed to be  $k = k_\infty \left( 1 + \frac{\varepsilon(T - T_\infty)}{T_w - T_\infty} \right)$ . Flow-through porous media is represented by  $q = \frac{-kA}{\mu} \left( \frac{dp}{dx} \right)$  where  $k$  is permeability,  $\mu$  is viscosity,  $A$  is the area of a cross-section through porous media.

Constraint set for boundary is (Equation 5):

$$u = u_w^*, v = 0, T = T_w^*, C = C_w^* \text{ at } y = (x+b)^{\frac{1-m}{2}}$$

$$u = 0, T = T_\infty, C = C_\infty \text{ at } y \rightarrow \infty \tag{5}$$

Similarity transformations (Reddy et al., 2017) used are as in Equation 6



$$\left. \begin{aligned} \eta &= \sqrt{\frac{a(m+1)}{v}} \left[ (x+b)^{\frac{m-1}{2}} y - A \right] \\ \varphi &= \sqrt{\frac{2}{m+1}} a v (x+b)^{\frac{m+1}{2}} f \\ T &= T_{\infty} + \theta(\eta) (T_w^* - T_{\infty}) \\ C &= C_{\infty} + \phi(\eta) (C_w^* - C_{\infty}) \end{aligned} \right\} \quad (6)$$

Using similarity transforms governing Equations 2-4 are transformed to Equations 7-9:

$$\left(1 + \frac{1}{\beta}\right) f'''' + f f'' - \frac{2m}{m+1} f'^2 - \frac{2M}{m+1} f' - \frac{2K_1}{m+1} f = 0 \quad (7)$$

$$\left(\frac{3+4Rd}{3Pr}\right) [\theta'' + \varepsilon \theta \theta' + \varepsilon \theta^2] + f \theta' + Nb \theta' \phi' + Nt \theta^2 + \left(\frac{2\lambda}{m+1}\right) \theta = 0 \quad (8)$$

$$\phi'' + Lef \phi' + \frac{Nt}{Nb} \theta' - Sc \gamma \phi = 0 \quad (9)$$

Also, boundary conditions (Equation 5) are transformed into Equation 10

$$\begin{aligned} f(0) &= \frac{1-m}{1+m} \alpha, f'(0) = 1, \theta(0) = 1, \phi(0) = 1 \\ f'(\infty) &= 0, \theta(\infty) = 0, \phi(\infty) = 0 \end{aligned} \quad (10)$$

### Numerical Scheme

Equations 7-9 subject to boundary condition (Equation 10) are solved using the Keller box method, mentioned as in the flow chart. In solving a parabolic system of partial differential equations, and Newton's method is implemented to linearize the system, an adequate initial guess is chosen to get the required solution.

Introducing Equation 11:

$$f' = p, p' = q, g = \theta, g' = t, s = \phi, s' = n \quad (11)$$

Equations 7-9 are converted to the form Equations 12-14:

$$\left(1 + \frac{1}{\beta}\right) q' + f q - \frac{2m}{m+1} p^2 - \frac{2M}{m+1} p - \frac{2K_1}{m+1} p = 0 \quad (12)$$

$$\left(\frac{3+4Rd}{3Pr}\right) [t' + \varepsilon g t' + \varepsilon t^2] + f t + Nbn + Nt t^2 + \left(\frac{2\lambda}{m+1}\right) g = 0 \quad (13)$$

$$n'+Lefn + \frac{Nt}{Nb} t' - Sc\gamma s = 0 \tag{14}$$

Central differences are introduced, and Newton’s method is used to get the system of linear Equations 15-50:

$$\delta f_J - \delta f_{J-1} - \frac{h_J}{2}(\delta p_J) - \frac{h_J}{2}(\delta p_{J-1}) = (r_1)_J \tag{15}$$

$$\delta p_J - \delta p_{J-1} - \frac{h_J}{2}(\delta q_J) - \frac{h_J}{2}(\delta q_{J-1}) = (r_2)_J \tag{16}$$

$$\delta g_J - \delta g_{J-1} - \frac{h_J}{2}(\delta t_J) - \frac{h_J}{2}(\delta t_{J-1}) = (r_3)_J \tag{17}$$

$$\delta s_J - \delta s_{J-1} - \frac{h_J}{2}(\delta n_J) - \frac{h_J}{2}(\delta n_{J-1}) = (r_4)_J \tag{18}$$

$$(a_1)_J \delta q_J + (a_2)_J \delta q_{J-1} + (a_3)_J \delta f_J + (a_4)_J \delta f_{J-1} + (a_5)_J \delta p_J + (a_6)_J \delta p_{J-1} = (r_5)_J \tag{19}$$

$$(b_1)_J \delta t_J + (b_2)_J \delta t_{J-1} + (b_3)_J \delta g_J + (b_4)_J \delta g_{J-1} + (b_5)_J \delta f_J + (b_6)_J \delta f_{J-1} + (b_7)_J \delta n_J + (b_8)_J \delta n_{J-1} = (r_6)_J \tag{20}$$

$$(c_1)_J \delta n_J + (c_2)_J \delta n_{J-1} + (c_3)_J \delta f_J + (c_4)_J \delta f_{J-1} + (c_5)_J \delta t_J + (c_6)_J \delta t_{J-1} + (c_7)_J \delta s_J + (c_8)_J \delta s_{J-1} = (r_7)_J \tag{21}$$

where

$$(a_1)_J = 1 + \frac{\beta h_J}{4(\beta + 1)}(f_J + f_{J-1}) \tag{22}$$

$$(a_2)_J = -1 + \frac{\beta h_J}{4(\beta + 1)}(f_J + f_{J-1}) \tag{23}$$

$$(a_3)_J = \frac{\beta h_J}{4(\beta + 1)}(q_J + q_{J-1}) \tag{24}$$

$$(a_4)_J = (a_3)_J \tag{25}$$

$$(a_5)_J = \frac{-m\beta h_J}{(m+1)(\beta+1)}(p_J + p_{J-1}) - \frac{M\beta h_J}{(m+1)(\beta+1)} - \frac{K\beta h_J}{(m+1)(\beta+1)} \tag{26}$$

$$(a_6)_J = \frac{-m\beta h_J}{(m+1)(\beta+1)}(p_J + p_{J-1}) - \frac{M\beta h_J}{(m+1)(\beta+1)} - \frac{K\beta h_J}{(m+1)(\beta+1)} \tag{27}$$

$$(b_1)_J = 1 + \frac{\varepsilon}{2}(g_J + g_{J-1}) + \frac{\varepsilon h_J}{2}(t_J + t_{J-1}) + \frac{3 \text{Pr } h_J}{4(3 + 4Rd)}(f_J + f_{J-1}) + \frac{3 \text{Pr } Nb h_J}{4(3 + 4Rd)}(n_J + n_{J-1}) + \frac{3 \text{Pr } Nth_J}{2(3 + 4Rd)}(t_J + t_{J-1}) \tag{28}$$

$$(b_2)_J = -1 - \frac{\varepsilon}{2}(g_J + g_{J-1}) + \frac{\varepsilon h_J}{2}(t_J + t_{J-1}) + \frac{3 \text{Pr } h_J}{4(3 + 4Rd)}(f_J + f_{J-1}) + \frac{3 \text{Pr } Nb h_J}{4(3 + 4Rd)}(n_J + n_{J-1}) + \frac{3 \text{Pr } Nth_J}{2(3 + 4Rd)}(t_J + t_{J-1}) \tag{29}$$

$$(b_3)_J = \frac{\varepsilon}{2}(t_J - t_{J-1}) + \frac{3 \text{Pr } \lambda h_J}{(n+1)(3 + 4Rd)} \tag{30}$$

$$(b_4)_J = (b_3)_J \tag{31}$$

$$(b_5)_J = \frac{3 \text{Pr } h_J}{4(3 + 4Rd)}(t_J + t_{J-1}) \tag{32}$$

$$(b_6)_J = (b_5)_J \tag{33}$$

$$(b_7)_J = \frac{3 \text{Pr } Nb h_J}{4(3 + 4Rd)}(t_J + t_{J-1}) \tag{34}$$

$$(b_8)_J = (b_7)_J \tag{35}$$

$$(c_1)_J = 1 + \frac{Le h_J}{4}(f_J + f_{J-1}) \tag{36}$$

$$(c_2)_J = -1 + \frac{Le h_J}{4}(f_J + f_{J-1}) \tag{37}$$

$$(c_3)_J = \frac{Le h_J}{4}(n_J + n_{J-1}) \tag{38}$$

$$(c_4)_J = (c_3)_J \tag{39}$$

$$(c_5)_J = \frac{Nt}{Nb} \tag{40}$$

$$(c_6)_J = -\frac{Nt}{Nb} \tag{41}$$

$$(c_7)_J = -\frac{Sc \gamma h_J}{2} \tag{42}$$

$$(c_8)_J = -\frac{Sc\gamma h_J}{2} \tag{43}$$

$$(r_1)_J = f_{J-1} - f_J + \left(\frac{h_J}{2}\right)(p_J + p_{J-1}) \tag{44}$$

$$(r_2)_J = p_{J-1} - p_J + \left(\frac{h_J}{2}\right)(q_J + q_{J-1}) \tag{45}$$

$$(r_3)_J = g_{J-1} - g_J + \left(\frac{h_J}{2}\right)(t_J + t_{J-1}) \tag{46}$$

$$(r_4)_J = s_{J-1} - s_J + \left(\frac{h_J}{2}\right)(n_J + n_{J-1}) \tag{47}$$

$$(r_5)_J = q_{J-1} - q_J - \frac{\beta h_J}{4(\beta + 1)}(f_J + f_{J-1})(q_J + q_{J-1}) + \frac{2m\beta h_J}{4(m + 1)(\beta + 1)}(p_J + p_{J-1})^2 + \frac{2M\beta h_J}{2(m + 1)(\beta + 1)}(p_J + p_{J-1}) + \frac{2K\beta h_J}{2(m + 1)(\beta + 1)}(p_J + p_{J-1}) \tag{48}$$

$$(r_6)_J = t_{J-1} - t_J - \frac{\varepsilon}{2}(g_J + g_{J-1})(t_J - t_{J-1}) - \frac{\varepsilon h_J}{4}(t_J + t_{J-1})^2 - \frac{3 \text{Pr} \lambda h_J}{(m + 1)(3 + 4Rd)}(g_J + g_{J-1}) - \frac{3 \text{Pr} h_J}{4(3 + 4Rd)}(f_J + f_{J-1})(t_J + t_{J-1}) - \frac{3 \text{Pr} N\beta h_J}{4(3 + 4Rd)}(n_J + n_{J-1})(t_J + t_{J-1}) - \frac{3 \text{Pr} N\theta h_J}{4(3 + 4Rd)}(t_J + t_{J-1})^2 \tag{49}$$

$$(r_7)_J = n_{J-1} - n_J - \frac{Le \text{Pr} h_J}{4}(f_J + f_{J-1})(n_J + n_{J-1}) - \frac{Nt}{Nb}(t_J - t_{J-1}) + \frac{Sc\gamma h_J}{2}(s_J + s_{J-1}) \tag{50}$$

The above linear set of simultaneous will be converted matrix notation (Equation 51). Taking J=1, 2, 3.....

$$\left. \begin{aligned} \{A_1\}\{\delta_1\} + \{C_1\}\{\delta_2\} &= \{r_1\} \\ \{B_2\}\{\delta_1\} + \{A_2\}\{\delta_2\} + \{C_2\}\{\delta_3\} &= \{r_2\} \\ \dots\dots\dots \\ \{B_{j-1}\}\{\delta_1\} + \{A_{j-1}\}\{\delta_2\} + \{C_{j-1}\}\{\delta_3\} &= \{r_{j-1}\} \\ \dots\dots\dots \\ \{B_j\}\{\delta_{j-1}\} + \{A_j\}\{\delta_j\} &= \{r_j\} \end{aligned} \right\} \tag{51}$$

Where

$$A_i = \begin{bmatrix} 0 & 0 & 0 & 1 & 0 & 0 & 0 \\ d & 0 & 0 & 0 & d & 0 & 0 \\ 0 & d & 0 & 0 & 0 & d & 0 \\ 0 & 0 & -1 & 0 & 0 & 0 & d \\ [a_2]_i & 0 & 0 & [a_3]_i & [a_1]_i & 0 & 0 \\ 0 & [b_2]_i & 0 & [b_5]_i & 0 & [b_1]_i & [b_7]_i \\ 0 & [c_6]_i & [c_8]_i & [c_3]_i & 0 & [c_5]_i & [c_1]_i \end{bmatrix}$$

$$A_j = \begin{bmatrix} d & 0 & 0 & 1 & 0 & 0 & 0 \\ -1 & 0 & 0 & 0 & d & 0 & 0 \\ 0 & -1 & 0 & 0 & 0 & d & 0 \\ 0 & 0 & -1 & 0 & 0 & 0 & d \\ [a_6]_j & 0 & 0 & [a_3]_j & [a_1]_j & 0 & 0 \\ 0 & (b_4)_j & 0 & [b_5]_j & 0 & [b_1]_j & [b_7]_j \\ 0 & 0 & 0 & [c_3]_j & 0 & [c_5]_j & [c_1]_j \end{bmatrix}$$

$$B_j = \begin{bmatrix} 0 & 0 & 0 & -1 & 0 & 0 & 0 \\ 0 & 0 & 0 & 0 & d & 0 & 0 \\ 0 & 0 & 0 & 0 & 0 & d & 0 \\ 0 & 0 & 0 & 0 & 0 & 0 & d \\ 0 & 0 & 0 & [a_4]_j & [a_2]_j & 0 & 0 \\ 0 & 0 & 0 & [b_6]_j & 0 & [b_2]_j & [b_8]_j \\ 0 & 0 & 0 & [c_4]_j & 0 & [c_6]_j & [c_2]_j \end{bmatrix}$$

$$C_j = \begin{bmatrix} d & 0 & 0 & 0 & 0 & 0 & 0 \\ 1 & 0 & 0 & 0 & 0 & 0 & 0 \\ 0 & 1 & 0 & 0 & 0 & 0 & 0 \\ 0 & 0 & 1 & 0 & 0 & 0 & 0 \\ [a_5]_j & 0 & 0 & 0 & 0 & 0 & 0 \\ 0 & [b_3]_j & 0 & 0 & 0 & 0 & 0 \\ 0 & 0 & [c_7]_j & 0 & 0 & 0 & 0 \end{bmatrix}$$

$$r_j = \begin{bmatrix} [r_1]_j \\ [r_2]_j \\ [r_3]_j \\ [r_4]_j \\ [r_5]_j \\ [r_6]_j \\ [r_7]_j \end{bmatrix}$$

The tridiagonal system of equations is solved using the block tridiagonal elimination method. These computations are reiterated until the convergence criteria are convinced. Calculations are stopped  $|\delta g^{(i)}| < \epsilon$  with small, prescribed value  $\epsilon = 0.01$ . To confirm the technique's effectiveness, the skin friction values (Table 1) are matched with the previous publications. The outcomes are in accordance with existing literature. Also, temperature and concentration gradients are calculated for different values of heat source parameter and thermophoresis parameter local Nusselt number, and Sherwood numbers are calculated (Tables 2 and 3).

Table 1  
Comparison of  $-f''(0)$  for various values of  $M, \alpha$

$\alpha$	M	Fang et al. (2012)	Madaki et al. (2017)	Present results
0.25	0.5	0.93380	0.92461	0.95576
	1.0	1.00000	1.00000	1.00001
	5.0	1.11860	1.12623	1.08314
0.5	0.5	0.97990	0.96335	0.99724
	1.0	1.00000	1.00000	1.00001
	5.0	1.02340	1.03339	1.01987

Table 2

Values of  $-\theta'(0), -\phi'(0)$  and  $Nu, Sh$  for  $Pfr = 6.2, Rd = 0.3, m = 0.3, \alpha = 0.3, M = 0.3, \beta = \infty, Le = 2, Nb = 0.1, \epsilon = 0$

$\lambda$	$-\theta'(0)$	$-\phi'(0)$	Nu	Sh
-0.5	-2.68098	1.11043	1642	-670
-0.3	-2.36495	0.81090	1448	-497
0	-1.80102	0.28056	1103	-172
0.3	-1.02767	-0.43687	629	268
0.5	-0.19863	-1.19258	122	730

Table 3

Values of  $-\theta'(0), -\phi'(0)$  and  $Nu, Sh$  for  $Pr=6.2, Rd=0.3, m=0.3, \alpha=0.3, M=0.3, \beta=\infty, Le=2, Nb=0.1, \epsilon=0$

Nt	$-\theta'(0)$	$-\phi'(0)$	Nu	Sh
0.1	-1.57612	0.07069	965	-43
0.3	-1.16806	1.32087	715	-809
0.5	-0.85750	1.58877	525	-973

### RESULTS AND DISCUSSION

The velocity, temperature, and concentration visual representations are plotted for various parameters shape parameter ( $m$ ), thickness parameter ( $\alpha$ ), adaptive thermal conductivity parameter ( $\epsilon$ ), magnetic field parameter ( $M$ ), Casson parameter ( $\beta$ ), Brownian motion parameter ( $Nb$ ), thermophoresis parameter ( $Nt$ ) Chemical reaction parameter ( $\gamma$ ), porosity parameter ( $k$ ) are plotted using MATLAB.

Figures 1 and 2 signify velocity and concentration profiles for shape parameter  $m$ ; on increasing, shape parameter velocity and concentration profiles found to increase this is

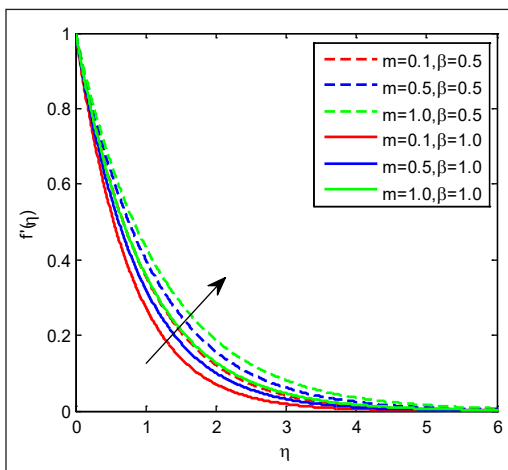


Figure 1. Velocity outlines form,  $\beta$

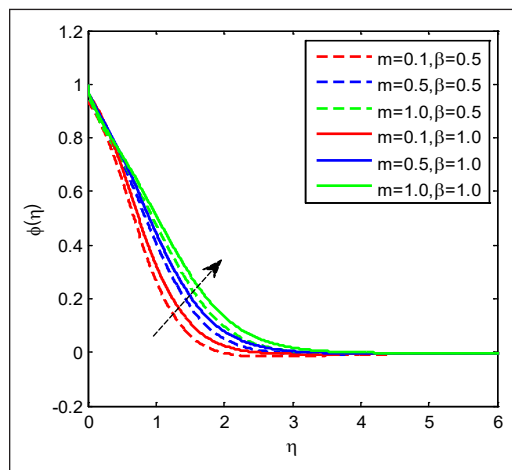


Figure 2. Concentration outlines form,  $\beta$

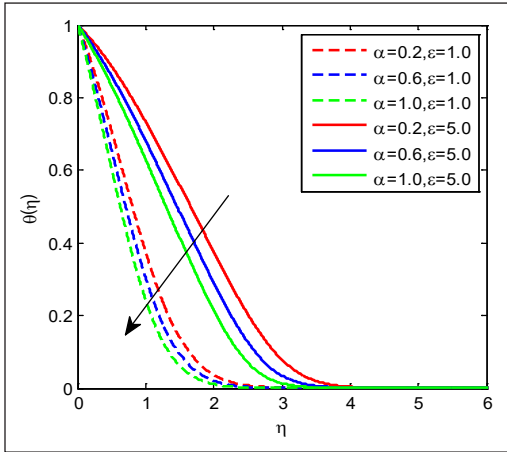


Figure 3. Temperature outlines for  $\alpha, \epsilon$

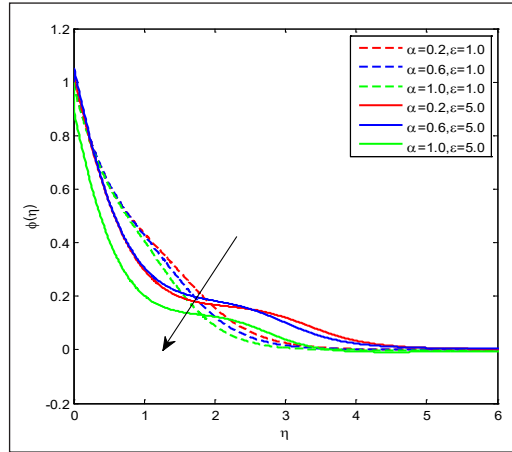


Figure 4. Concentration outlines for  $\alpha, \epsilon$

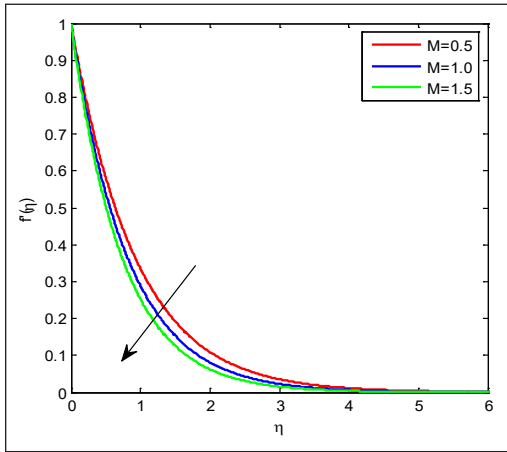


Figure 5. Velocity outlines for  $M$

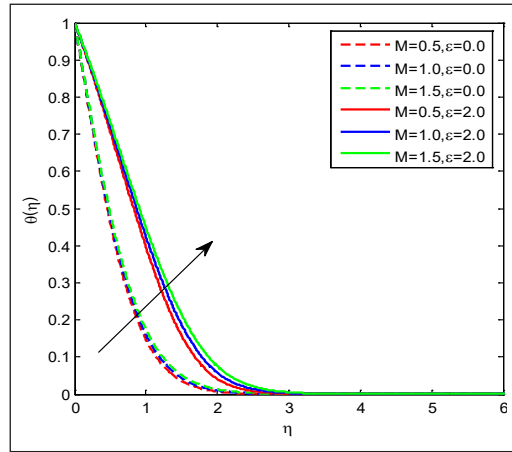


Figure 6. Temperature outlines for  $M, \epsilon$

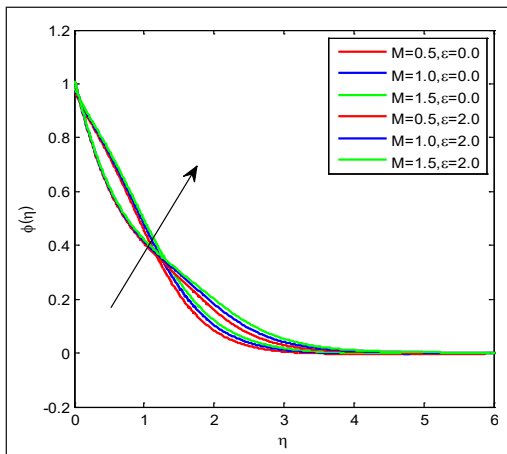


Figure 7. Concentration outlines for  $M, \epsilon$

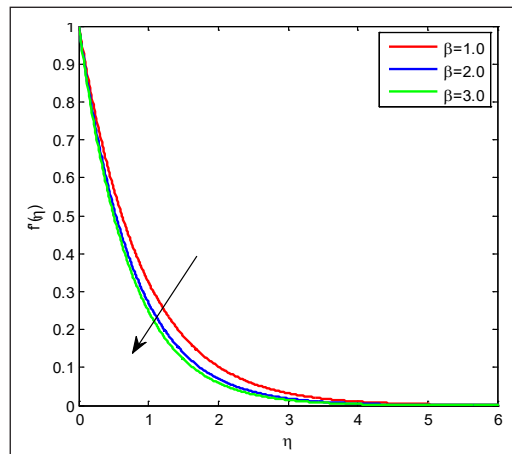


Figure 8. Velocity outlines for  $\beta$

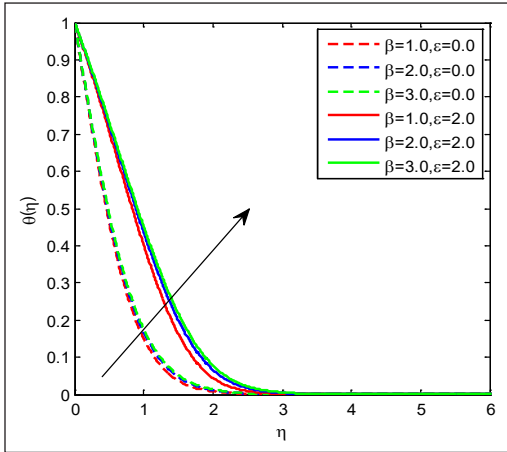


Figure 9. Temperature outlines for  $\beta, \epsilon$

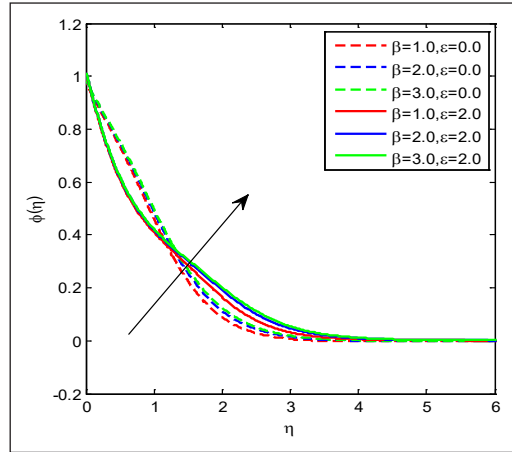


Figure 10. Concentration outlines for  $\beta, \epsilon$

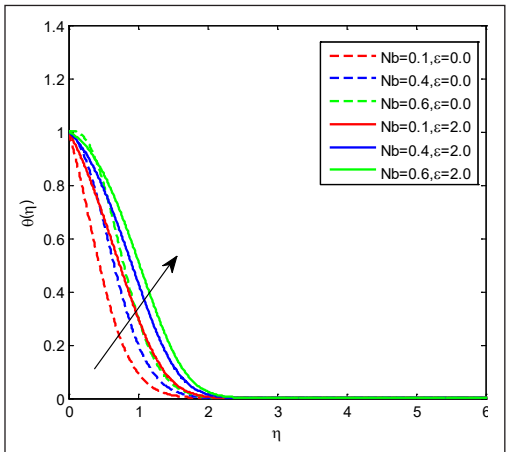


Figure 11. Temperature outlines for  $Nb, \epsilon$

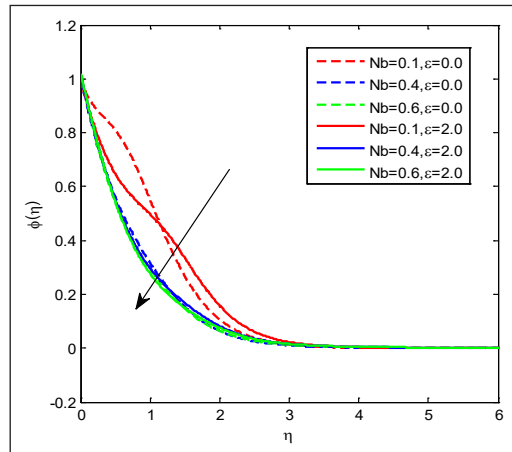


Figure 12. Concentration outlines for  $Nb, \epsilon$

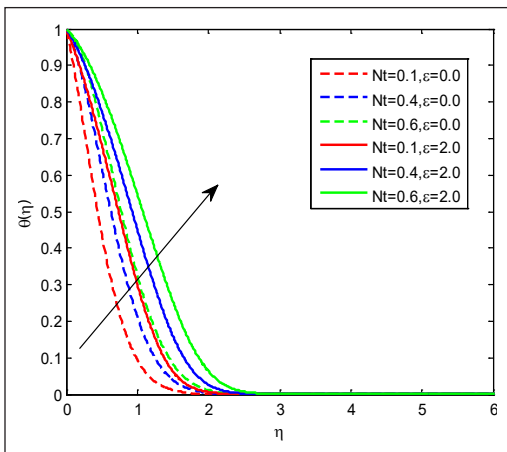


Figure 13. Temperature outlines for  $Nt, \epsilon$

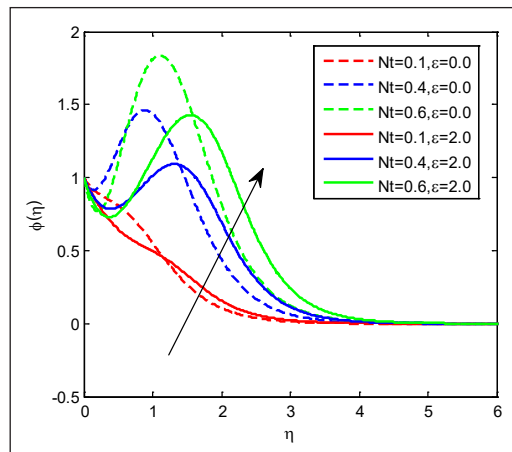


Figure 14. Concentration outlines for  $Nt, \epsilon$



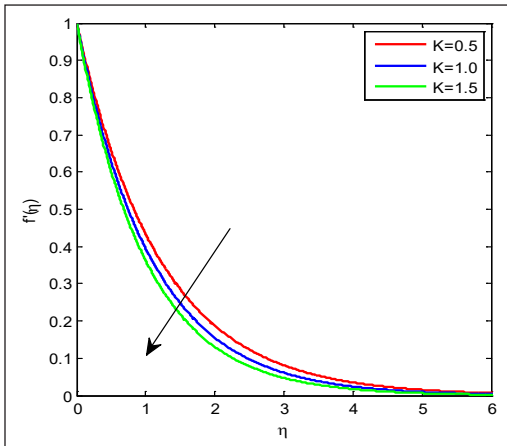


Figure 15. Velocity outlines for K

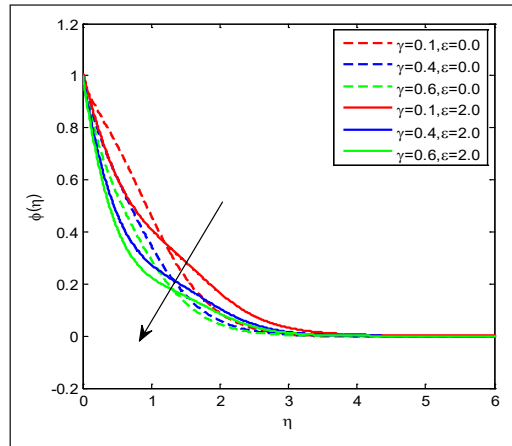


Figure 16. Concentration outlines for  $\gamma$

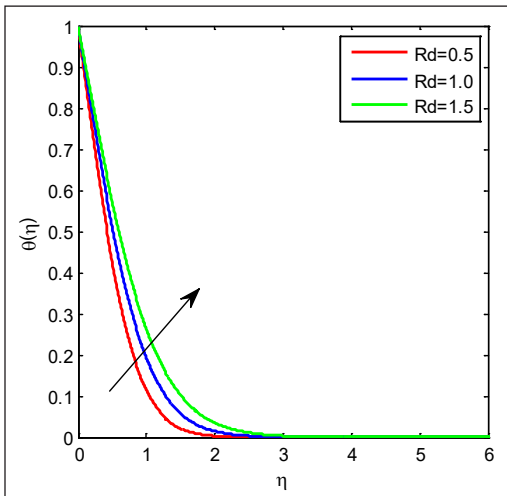


Figure 17. Temperature outlines for Rd

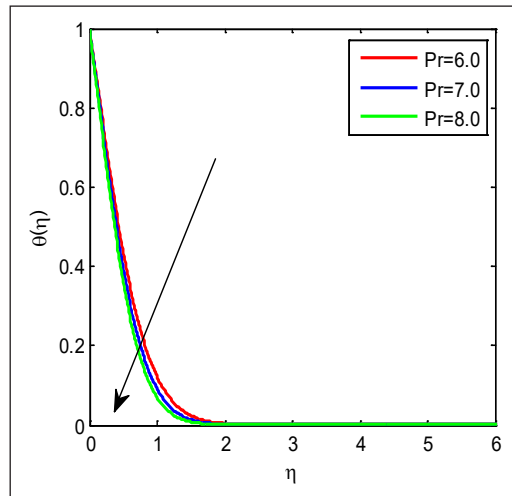


Figure 18. Temperature outlines for Pr

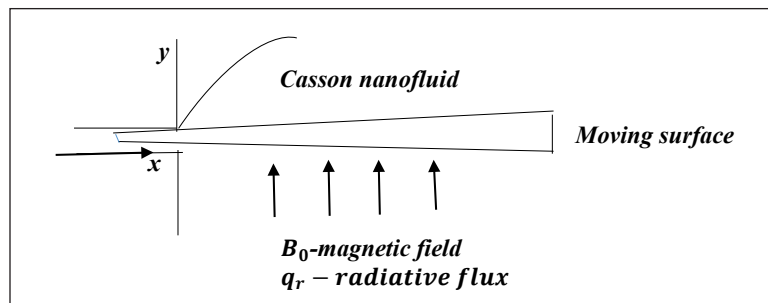


Figure 19. Flow model of the form

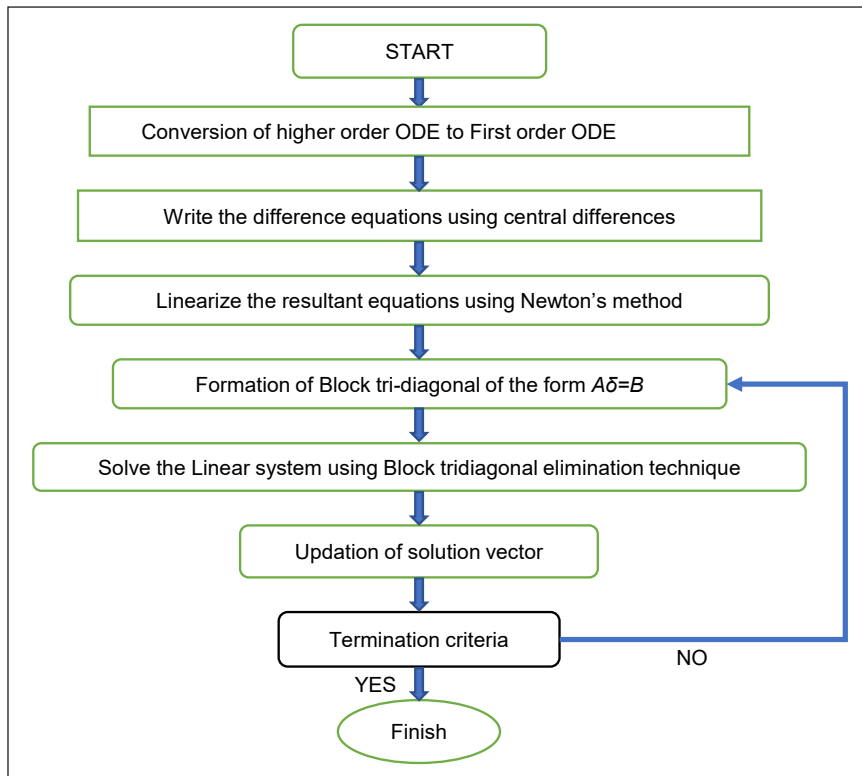


Figure 20. Flow chart of Keller box method

due to increasing values of  $m$  momentum and width of the thermal limit reduces. Also, the velocity of Casson fluid is high when compared with regular nanofluid. An opposite trend is observed in the case of concentration profiles. Figures 3 and 4 corresponds to temperature and concentration profiles for wall width parameter  $\alpha$ , and it is witnessed that for gradual values of wall width parameter, temperature and concentration shows fall tendency this is due to greater values of wall width parameter boundary layer becomes thinner. Also, the influence of variable thermal conductivity studied up variation is observed near the boundary layer in concentration profiles. Figure 5 represents velocity profiles for  $M$ . It is perceived that on increasing  $M$  values, the velocity profile shows decreasing nature because of opposing force named as Lorentz force. Figures 6 and 7 portray thermal and concentration outlines for  $M$ ,  $\varepsilon$ . On intensifying magnetic parameter values, thermal and concentration outlines rose. Also, the influence of thermal conductivity parameter concentration profile shows decreasing nature before  $\eta < 1$  and opposite nature observed after  $\eta > 1$ . Figure 8 shows velocity profiles for  $\beta$ . Increasing Casson parameter appears velocity profiles decline due to an increase in the value of plastic dynamic viscosity, which causes resistance in fluid flow.

Figures 9 and 10 describe graphs of temperature and concentration for  $\beta$ ,  $\epsilon$ . It shows increasing behavior. Also, it is witnessed that variation in heat conductivity causes a rise in the thermal and concentration profiles of the fluid. Figures 11 and 12 represent thermal concentration profiles for Nb. For progressive values of Nb temperature found to increase and concentration profile exhibits decreasing nature. The increase in Brownian motion leads to the movement of particles in a fluid. Hence, activating the movement of particles increases the heat produced, raising the temperature and decreasing the concentration. It is observed that the constant thermal conductivity concentration of molecules turns to a maximum near the surface, and thus, a maximum level will turn to a flat level with variable thermal conductivity. Figures 13 and 14 represent temperature and concentration outlines of Nt. For higher observations of Nt, it guides to increase in temperature, concentration outlines this is because of the force of the thermophoresis was produced by the surface amount of mass relocation builds a far slippery flow on the non-linear elongating surface, hence, with much quantities of thermophoresis the fluid is an extra warm move away across the surface, and because of the thermophoresis force presence the flow is fast from the non-linear surface, and that is lead to increasing the nanoparticle concentration boundary-layer. For growing values of thermal conductivity, concentration was found to increase. Figure 15 represents velocity profiles for porosity parameters. The growth in the absorbent parameter of the liquid enhances the viscosity of the fluid or falls in the elongating rate of the expediting surface, leading to a step-by-step reduction in the velocity of the fluid. Figure 16 represents concentration profiles for chemical reaction parameters. An escalation in chemical reaction values will restrain the concentration of the fluid—greater observations of  $\gamma$  aggregates to a drop in the chemical molecular circulation. Figure 17 portrays temperature profiles of radiation parameters that will deliver more heat to the fluid, resulting in a temperature rise. Figure 18 represents temperature profiles for the Prandtl number. On enhancing the Prandtl number, the heat conductivity of the fluid drops, which causes declination in thermal profiles. Figure 19 represents flow model of the problem while Figure 20 represents flow chart of the Keller box method.

## CONCLUSIONS

In the present investigation, the impact of chemical reaction on magnetohydrodynamic boundary layer of Casson nanofluid flow through permeable media above a moving plate adaptable thickness is studied. As a result, the following results are obtained.

- Velocity profile increases for shape parameter and decreases for the magnetic parameter, Casson parameter, porosity parameter.
- Temperature profile found to decrease wall thickness parameter, Prandtl number. Increases for the magnetic parameter, Casson parameter, Brownian movement parameter, thermophoresis parameter, radiation parameter.

- Concentration profiles were found to increase for shape parameter at various observations of Casson parameter, increases for the magnetic parameter for  $\eta > 1$ , and decreases for  $\eta < 1$ . Decreases for wall thickness, Brownian movement, chemical reaction parameters, increases for thermophoresis parameter at different thermal conductivity values.

## ACKNOWLEDGEMENT

The authors are thankful to Koneru Lakshmaiah Education Foundation, Guntur, India for providing research facilities to complete this project.

## REFERENCES

- Abdel-wahed, M. S., Elbashbeshy, E. M. A., & Emam, T. G. (2015). Flow and heat transfer over a moving surface with non-linear velocity and variable thickness in a nanofluids in the presence of Brownian motion. *Applied Mathematics and Computation*, 254, 49-62. <https://doi.org/10.1016/j.amc.2014.12.087>
- Ahmad, K., Hanouf, Z., & Ishak, A. (2017). MHD Casson nanofluid flow past a wedge with Newtonian heating. *The European Physical Journal Plus*, 132(2), 1-11. <https://doi.org/10.1140/epjp/i2017-11356-5>
- Beg, O. A., Thumma, T., & Sheri, S. R. (2009). Finite element computation of magnetohydrodynamic nanofluid. *Computational Materials Science*, 46(4), 1028-1037.
- Besthapu, P., & Bandari, S. (2015). Mixed convection MHD flow of a Casson nanofluid over a nonlinear permeable stretching sheet with viscous dissipation. *Journal of Applied Mathematics and Physics*, 03(12), 1580-1593. <https://doi.org/10.4236/jamp.2015.312182>
- Biswas, R., & Ahmmed, S. F. (2018). Effects of hall current and chemical reaction on Magnetohydrodynamics unsteady heat and mass transfer of Casson nanofluid flow through a vertical plate. *Journal of Heat Transfer*, 140(9), 1-12. <https://doi.org/10.1115/1.4039909>
- Choi, S. U. S. (2008). Nanofluids: A new field of scientific research and innovative applications. *Heat Transfer Engineering*, 29(5), 429-431. <https://doi.org/10.1080/01457630701850778>
- Das, S. K., Choi, S. U. S., Yu, W., & Pradeep, T. (2007). *Nanofluids*. John Wiley & Sons. <https://doi.org/10.1002/9780470180693>
- Dharmaiah, G., Chamkha, A. J., Vedavathi, N., & Balamurugan, K. S. (2019a). Viscous dissipation effect on transient aligned magnetic free convective flow past an inclined moving plate. *Frontiers in Heat and Mass Transfer*, 12, Article 17. <https://doi.org/10.5098/hmt.12.17>
- Dharmaiah, G., Vedavathi, N., Balamurugan, K. S., & Ramakrishna, K. (2019b). A study on MHD boundary layer flow rotating frame nanofluid with chemical reaction. *Frontiers in Heat and Mass Transfer*, 12, Article 10. <https://doi.org/10.5098/hmt.12.10>
- Dharmaiah, G., Sridhar, W., Balamurugan, K. S., & Kala, K. C. (2020). Hall and ion slip impact on magneto-titanium alloy nanoliquid with diffusion thermo and radiation absorption. *International Journal of Ambient Energy*, 1-11. <https://doi.org/10.1080/01430750.2020.1831597>

- Dharmaiah, G., Vedavathi, N., Balamurugan, K. S., & Prakash, J. (2017). Heat transfer on MHD nanofluid flow over a semi infinite flat plate embedded in a porous medium with radiation absorption, heat source and diffusion thermo effect. *Frontiers in Heat and Mass Transfer*, 9, Article 38. <https://doi.org/10.5098/hmt.9.38>
- Fang, T., Zhang, J., & Zhong, Y. (2012). Boundary layer flow over a stretching sheet with variable thickness. *Applied Mathematics and Computation*, 218(13), 7241-7252. <https://doi.org/10.1016/j.amc.2011.12.094>
- Ibrahim, W., & Makinde, O. D. (2016). Magnetohydrodynamic stagnation point flow and heat transfer of Casson nanofluid past a stretching sheet with slip and convective boundary condition. *Journal of Aerospace Engineering*, 29(2), Article 04015037. [https://doi.org/10.1061/\(asce\)as.1943-5525.0000529](https://doi.org/10.1061/(asce)as.1943-5525.0000529)
- Ismail, H., Abdel-Wahed, M., & Omama, M. (2021). Effect of variable thermal conductivity on the MHD boundary-layer of Casson-nanofluid over a moving plate with variable thickness. *Thermal Science*, 25(1 Part A), 145-157. <https://doi.org/10.2298/tsci190324293i>
- Khan, M., Shahid, A., Salahuddin, T., Malik, M. Y., & Mushtaq, M. (2018). Heat and mass diffusions for Casson nanofluid flow over a stretching surface with variable viscosity and convective boundary conditions. *Journal of the Brazilian Society of Mechanical Sciences and Engineering*, 40(11), 1-10. <https://doi.org/10.1007/s40430-018-1415-y>
- Konda, J. R., Madhusudhana, N. P., & Konijeti, R. (2018). MHD mixed convection flow of radiating and chemically reactive Casson nanofluid over a nonlinear permeable stretching sheet with viscous dissipation and heat source. *Multidiscipline Modeling in Materials and Structures*, 14(3), 609-630. <https://doi.org/10.1108/mmms-10-2017-0127>
- Madaki, A. G., Roslan, R., Kandasamy, R., & Chowdhury, M. S. H. (2017). Flow and heat transfer of nanofluid over a stretching sheet with non-linear velocity in the presence of thermal radiation and chemical reaction. In *AIP Conference Proceedings* (Vol. 1830, No. 1, p. 020014). AIP Publishing LLC. <https://doi.org/10.1063/1.4980877>
- Mahdy, A., & Chamkha, A. (2015). Heat transfer and fluid flow of a non-Newtonian nanofluid over an unsteady contracting cylinder employing Buongiorno's model. *International Journal of Numerical Methods for Heat & Fluid Flow*, 25(4), 703-723. <https://doi.org/10.1108/hff-04-2014-0093>
- Mahmood, A., Jamshed, W., & Aziz, A. (2018). Entropy and heat transfer analysis using Cattaneo-Christov heat flux model for a boundary layer flow of Casson nanofluid. *Results in Physics*, 10, 640-649. <https://doi.org/10.1016/j.rinp.2018.07.005>
- Malik, M. Y., Naseer, M., Nadeem, S., & Rehman, A. (2014). The boundary layer flow of Casson nanofluid over a vertical exponentially stretching cylinder. *Applied Nanoscience*, 4(7), 869-873. <https://doi.org/10.1007/s13204-013-0267-0>
- Nagalakshmi, P. S. S., & Vijaya, N. (2020). MHD flow of Carreau nanofluid explored using CNT over a nonlinear stretched sheet. *Frontiers in Heat and Mass Transfer*, 14(4), 1-9. <https://doi.org/10.5098/hmt.14.4>
- Oyelakin, I. S., Mondal, S., & Sibanda, P. (2016). Unsteady Casson nanofluid flow over a stretching sheet with thermal radiation, convective and slip boundary conditions. *Alexandria Engineering Journal*, 55(2), 1025-1035. <https://doi.org/10.1016/j.aej.2016.03.003>

- Reddy C, S., Naikoti, K., & Rashidi, M. M. (2017). MHD flow and heat transfer characteristics of Williamson nanofluid over a stretching sheet with variable thickness and variable thermal conductivity. *Transactions of A. Razmadze Mathematical Institute*, 171(2), 195-211. <https://doi.org/10.1016/j.trmi.2017.02.004>
- Reddy, J. V. R., Sugunamma, V., & Sandeep, N. (2018). Slip flow of MHD Casson-nanofluid past a variable thickness sheet with joule heating and viscous dissipation: A comparative study using three base fluids. *Journal of Nanofluids*, 7(6), 1113-1121. <https://doi.org/10.1166/jon.2018.1540>
- Sheikholeslami, M., Abelman, S., & Ganji, D. D. (2014). Numerical simulation of MHD nanofluid flow and heat transfer considering viscous dissipation. *International Journal of Heat and Mass Transfer*, 79, 212-222. <https://doi.org/10.1016/j.ijheatmasstransfer.2014.08.004>
- Singh, A. (2008). Thermal conductivity of nanofluids. *Defence Science Journal*, 58(5), 600-607. <https://doi.org/10.14429/dsj.58.1682>
- Sridhar, W., & Lakshmi, G. V. (2020). MHD nanofluid over a stretching surface immersed in double stratified media with radiation and partial slip conditions. *International Journal of Advanced Science and Technology*, 29(9s), 3204-3213.
- Talla, H., Kumari, P., & Sridhar, W. (2018). Numerical study to diffusion of chemically reactive species over MHD exponentially stretching surface of a Casson fluid. *International Journal of Mechanical Engineering and Technology*, 9(10), 470-481.
- Uddin, M. J., Bég, O. A., & Ismail, A. I. (2015). Radiative convective nanofluid flow past a stretching/shrinking sheet with slip effects. *Journal of Thermophysics and Heat Transfer*, 29(3), 513-523. <https://doi.org/10.2514/1.t4372>
- Vijaya, N., Babu, S. G., & Lakshmi, V. N. (2020). Influence of critical parameters on liquid thin film flow of Casson nanofluid over elongated sheet under thermoporesis and Brownian motion. *Frontiers in Heat and Mass Transfer*, 15, Article 23. <https://doi.org/10.5098/hmt.15.23>
- Wang, X. Q., & Mujumdar, A. S. (2008a). A review on nanofluids - part I: Theoretical and numerical investigations. *Brazilian Journal of Chemical Engineering*, 25(4), 613-630. <https://doi.org/10.1590/s0104-66322008000400001>
- Wang, X. Q., & Mujumdar, A. S. (2008b). A review on nanofluids - part II: Experiments and applications. *Brazilian Journal of Chemical Engineering*, 25(4), 631-648. <https://doi.org/10.1590/s0104-66322008000400002>

**List of Symbols**

<i>Symbol</i>	<i>Description</i>	<i>Unit</i>	<i>Dimension</i>
$\nu$	Kinematic viscosity	$m^2s^{-1}$	$L^2T^{-1}$
$\sigma$	Electrical conductivity	$s/m$	$M^{-1}L^{-2}T^3A^2$
$\rho$	Base fluid density	$kg/m^3$	$ML^{-3}$
$\alpha$	Thermal diffusion	$m^2s^{-1}$	$MLT^{-3}K^{-1}$
$C_p$	Heat capacity of fluid at constant pressure	$J.kg^{-1}s^{-1}$	$L^2T^{-2}K^{-1}$
$\varepsilon$	Thermal conductivity	$W/m.k$	$MLT^{-3}K^{-1}$
$D_T$	Thermo-diffusion coefficient	$m^2/s$	
$D_B$	Brownian diffusion coefficient	$m^2/s$	
$u$	Velocity component in x-axis direction		
$v$	Velocity component in y-axis direction		
$\beta$	Casson parameter		
$\tau$	Ratio of nano particle heat capacity and the fluid heat capacity		
$B$	Magnetic field		
$Q$	Heat source parameter		
$a, b$	Constants		
$T_w^*$	Surface temperature		
$T_\infty$	Ambient temperature		
$m$	Shape parameter ( $> -1$ )		
$\varphi$	Stream function		
$M$	Magnetic field parameter		
$Pr$	Prandtl number		
$Nb$	Brownian motion parameter		
$Nt$	Thermophoresis parameter		
$\lambda$	Heat source parameter		
$Sc$	Schmidt number		
$q_r$	Radiative heat flux		





## A New Method to Estimate Peak Signal to Noise Ratio for Least Significant Bit Modification Audio Steganography

Muhammad Harith Noor Azam<sup>1</sup>, Farida Ridzuan<sup>1,2\*</sup> and M Norazizi Sham Mohd Sayuti<sup>3</sup>

<sup>1</sup>Faculty of Science and Technology, Universiti Sains Islam Malaysia, Bandar Baru Nilai, Nilai 71800 USIM, Negeri Sembilan, Malaysia

<sup>2</sup>CyberSecurity and Systems Research Unit, Faculty of Science and Technology, Universiti Sains Islam Malaysia, Nilai 71800 USIM, Negeri Sembilan, Malaysia

<sup>3</sup>Intelligent Cyber-physical System Research Group(iCPS), Faculty of Engineering and Built Environment, Universiti Sains Islam Malaysia, Nilai, 71800 USIM, Negeri Sembilan, Malaysia

### ABSTRACT

Audio steganography is implemented based on three main features: capacity, robustness, and imperceptibility, but simultaneously implementing them is still a challenge. Embedding data at the Least Significant Bit (LSB) of the audio sample is one of the most implemented audio steganography methods because the method will give high capacity and imperceptibility. However, LSB has the lowest robustness among all common methods in audio steganography. To cater to this problem, researchers increased the depth of the embedding level from fourth to sixth and eighth LSB level to improve its robustness feature. However, consequently, the imperceptibility feature, which is commonly measured by Peak Signal to Noise Ratio (PSNR), is reduced due to the trade-off between imperceptibility and robustness. Currently, the lack of study on the estimation of the PSNR for audio steganography has caused the early assessment of the imperceptibility-robustness trade-off difficult. Therefore, a method to estimate PSNR, known as PSNR Estimator (PE), is

introduced to enable early evaluation of imperceptibility feature for each stego-file produced by the audio steganography, which is important for the utilisation of embedding. The proposed PE estimates the PSNR based on the pattern collected from the embedment at different levels. From the evaluation, the proposed method has 99.9% of accuracy in estimating PSNR values at different levels. In comparison with the Mazdak Method,

#### ARTICLE INFO

##### Article history:

Received: 15 June 2021

Accepted: 29 September 2021

Published: 10 January 2022

DOI: <https://doi.org/10.47836/pjst.30.1.27>

##### E-mail addresses:

harithazam.official@gmail.com (Muhammad Harith Noor Azam)

farida@usim.edu.my (Farida Ridzuan)

azizi@usim.edu.my (M Norazizi Sham Mohd Sayuti)

\* Corresponding author

the proposed method performs better in all situations. In conclusion, the proposed PE can be used as a reference for embedding and further reducing the calculation complexity in finding the feasible value to minimise the trade-off between robustness and imperceptibility.

*Keywords:* Audio steganography, Least Significant Bit, peak-signal-to-noise-ratio estimator, trade-off

## INTRODUCTION

This Audio steganography is a method to conceal the secret message by using some method to modify the audio so that only the sender and the intended recipient knows (Alsabhany et al., 2018; Hameed, 2018; Hameed et al., 2019; Jayapandiyani et al., 2020; Sapra, 2016). It exploits Human Auditory System (HAS) to achieve secure communication (Yu et al., 2020). The common audio files used in audio steganography are wave file (.wav) and MPEG-1 Audio Layer III (.mp3) (Sun et al., 2012; Wakiyama et al., 2010).

For any audio steganography method to be successfully implemented, it is important to consider three features: capacity, imperceptibility and robustness (Alsabhany et al., 2020; Amirtharajan & Rayappan, 2013; Hameed, 2018; Zumchak, 2016). First, capacity refers to the amount of secret data embedded inside a cover file (Somani & Madhu, 2015; Srivastava & Rafiq, 2012). Next, the imperceptibility means that the furtive data should not be detected in humans, although there is a difference between cover file and stego-file audio (Somani & Madhu, 2015; Srivastava & Rafiq, 2012). Lastly, robustness refers to the ability of the embedded data to withstand attacks (Somani & Madhu, 2015; Zumchak, 2016). Although audio steganography needs all these features in top conditions simultaneously, there are always trade-offs between all these three features, such as between capacity and robustness (Bhowal et al., 2017; Kumar, 2016), capacity and imperceptibility (Ali et al., 2017; Alsabhany et al., 2019) and lastly, imperceptibility and robustness (Gopalan & Fu, 2015; Xue et al., 2018). The trade-off relationship between audio steganography features is shown in Figure 1. Total disregard for any feature may lead to an unbalanced and impractical audio steganography method (Ali et al., 2017; Gopalan, 2018).

The most common existing audio steganography methods are phase coding, Least Significant Bit (LSB) modification, echo hiding, parity coding, wavelet domain and spread spectrum (Mazdak et al., 2012). This research focuses on the LSB modification because

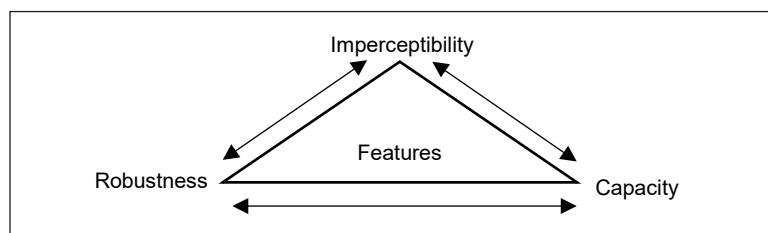


Figure 1. Trade-off relationship among audio steganography features

of its simplicity, flexibility to modification, efficiency, high imperceptibility and capacity (Asad et al., 2011; Djebbar et al., 2011; Tayel et al., 2016; Mazdak et al., 2012). However, although it has numerous advantages, it has low robustness features and is easy to extract (Cvejic & Seppänen, 2005; Kanhe et al., 2015; Meligy et al., 2016). Therefore, researchers proposed to embed the data at a higher level of LSB to increase the robustness features of audio steganography (Ahmed et al., 2010; Priyanka et al., 2012; Cvejic & Seppänen, 2004). However, by doing so, the imperceptibility feature in the LSB method is reduced.

The imperceptibility feature of an audio steganography method is commonly calculated using PSNR. However, to measure the PSNR, a stego-file needs to be produced from the embedding process. In order to find the feasible results that can be used to minimise the trade-off between imperceptibility and robustness feature, the process of embedding the secret data at a different level of LSB and comparing the PSNR value for each stego-file produced is needed. These processes are time-consuming. Therefore, PE is introduced.

The method to estimate the PSNR, also known as PE, will enable early evaluation on imperceptibility feature for each stego-file produced by the audio steganography that can be used as a reference for utilisation of embedding. Additionally, in a real-time application, computational complexity is crucial to ensure an audio steganography implementation (Mazdak et al., 2012). Therefore, PE can avoid repetitive embedding processes in finding the feasible solution for the trade-off, further reducing the computational complexity. Furthermore, we can avoid bad stego-file from being produced, which improves audio steganography efficiency.

The structure of the paper is as follows: the related works are presented in section 2; the proposed method is presented in section 3; the expected results are presented in section 4; and finally, the conclusion and future work are presented in section 5.

## RELATED WORK

Most of the existing research on audio steganography targets only one or two features and discards the other. Hence, PSNR calculation is only carried out at the final stage. Therefore, although several advantages can be achieved by estimating the PSNR, only one research has proposed on PSNR estimation in audio steganography. Mazdak et al. (2012) proposed a PSNR estimation method based on linear interpolation formula. The method uses PSNR value and bit per sample (BPS) rate on existing stego-file to estimate PSNR value of new stego-file that embed different bps rate. This method tries to tackle the trade-off between imperceptibility and capacity features of audio steganography.

PE is also used in image steganography for similar purposes. For example, Li et al. (2014) had proposed PSNR estimation based on Mean Squared Error (MSE) value. It is used to compare the level of distortion between the original signal and the stego-file (Chadha et al., 2013). Suppose  $x = \{x_i | i = 1, 2, 3, \dots, N\}$  is the original signal and

$y = \{y_i | i = 1, 2, 3, \dots, N\}$  is the stego-file signal and where  $N$  is the number of signal samples and  $x_i$  and  $y_i$  are the value of  $i^{\text{th}}$  samples in  $x$  and  $y$ , respectively. The MSE formula is calculated using Equation 1:

$$MSE(x, y) = \frac{1}{N} \sum_{i=1}^N (x_i - y_i)^2 \quad (1)$$

This estimation is also calculated based on bit per sample. However, it is mentioned that the method works best when the BPS rate is less than four because of the size of bit depth in the image sample that is considered small when compared to the audio. This estimation method reduces the expansion of the stego-file needed for the shadow image. The main focus of this method is to improve the imperceptibility feature of image steganography instead of tackling the existing trade-off.

Based on the previous research, it is shown that there is a lack of research conducted for estimating the PSNR value in audio steganography. In addition, the lack of a PSNR estimator focuses on determining the PSNR value to solve the trade-off. The only PSNR estimator in audio steganography is focused on determining the efficiency of a steganography technique for the trade-off between capacity and imperceptibility. Therefore, this research tries to provide a new method for estimating the PSNR value at the different levels of LSB of audio steganography based on PSNR patterns defined from embedding at a different level of LSB to cater to different types of trade-off, which is between imperceptibility and robustness.

## METHODOLOGY

This paper proposes a method to estimate the PSNR value for audio stego-file based on the patterns observed from the PSNR values obtained from embedding at a different level of LSB. A series of experiments are conducted to find patterns in PSNR values. The first experiment was conducted on finding PSNR value at the lowest level of LSB for different sizes of embedded data and the number of audio samples. The second experiment was conducted on finding PSNR values at a different level of LSB for different sizes of embedded data and the number of audio samples. Finally, the new method for estimating PSNR value is proposed based on the patterns from the PSNR values obtained at a different level of LSB embedding.

### PSNR of One Bit per Sample at the First LSB

The objective of this experiment is to observe the similarity of the PSNR value at the lowest level of LSB. The PSNR values between all the stego-file produced should be almost identical to ensure the validity of the pattern. Ten different cover audios ranging

from one to ten seconds with 16-bit depth and 44.1kHz mono are selected from various speech and music .wav audio files to ensure the diversity of the experiment's samples. The ratio of the size of data embedded to number of audio sample is approximately one to two. For each cover audio, a customised size of data is embedded at the first level of LSB of cover audio samples, and the PSNR values for each stego-file produced are recorded. Cover audio name, a total of cover audio samples, size of data embedded and obtained PSNR are tabulated in Table 1.

Table 1 shows that the PSNR for all tested cover audio is between a range of 96.32 dB and 96.34 dB, which indicates that PSNR values are almost the same at the lowest level of LSB.

Table 1  
*Obtained PSNR for one bit per sample at first level LSB*

<i>Cover Audio</i>	<i>Cover Audio Samples</i>	<i>Size of Data (bit)</i>	<i>PSNR</i>
Music 1.wav	44100	22050	96.328
Music 2.wav	132300	66150	96.317
Music 3.wav	220500	110250	96.331
Music 4.wav	352800	176400	96.328
Music 5.wav	441000	220500	96.336
Speech 1.wav	44100	22050	96.292
Speech 2.wav	132300	66150	96.343
Speech 3.wav	220500	110250	96.318
Speech 4.wav	352800	176400	96.323
Speech 5.wav	441000	220500	96.324

### **PSNR of One Bit per Sample at Different Level LSB**

The objective of this experiment is to find the pattern among the PSNR value produced from embedding at a different level of LSB. Therefore, the data is embedded at a different level of LSB. The second, fourth, sixth, seventh and eighth levels of LSB are selected. This experiment is implemented by embedding the data at a different level of LSB of cover audio sample accordingly. Then, the PSNR value for each stego-file is recorded. Cover audio names and obtained PSNR at different LSB levels are tabulated in Table 2.

Based on Table 2, the stego-file produced shows the identical value at all embedding levels. In addition, significant and identical decrement for PSNR value from the lowest level of LSB to the highest level of LSB is shown in all audios. Therefore, it can be concluded that there is a pattern in the difference of PSNR value that can be used to estimate the PSNR at a different level.

Table 2  
Obtained PSNR of one bit per sample at different level LSB

Cover Audio	PSNR Obtained					
	1 <sup>st</sup> level	2 <sup>nd</sup> level	4 <sup>th</sup> level	6 <sup>th</sup> level	7 <sup>th</sup> level	8 <sup>th</sup> level
Music 1.wav	96.328	90.330	78.256	66.215	60.203	54.186
Music 2.wav	96.317	90.289	78.253	66.221	60.216	54.183
Music 3.wav	96.331	90.306	78.243	66.226	60.192	54.171
Music 4.wav	96.328	90.293	78.263	66.253	60.208	54.195
Music 5.wav	96.336	90.299	78.274	66.218	60.226	54.177
Speech 1.wav	96.292	90.315	78.260	66.214	60.150	54.193
Speech 2.wav	96.343	90.322	78.264	66.210	60.191	54.210
Speech 3.wav	96.318	90.289	78.277	66.233	60.231	54.182
Speech 4.wav	96.323	90.288	78.271	66.229	60.205	54.190
Speech 5.wav	96.324	90.308	78.269	66.246	60.205	54.213

### Method on Estimating PSNR Value based on Pattern

In order to estimate the PSNR value for a different level of LSB, the differences between the PSNR value from Table 2 are used as a basis. The PSNR difference at different levels of LSB is shown in Table 3.

Table 3  
Obtained PSNR difference at different level of LSB

Cover Audio	PSNR Difference at Different Level				
	1 <sup>st</sup> & 2 <sup>nd</sup> level	2 <sup>nd</sup> & 4 <sup>th</sup> level	4 <sup>th</sup> & 6 <sup>th</sup> level	6 <sup>th</sup> & 7 <sup>th</sup> level	7 <sup>th</sup> & 8 <sup>th</sup> level
Music 1.wav	5.998	12.074	12.041	6.012	6.017
Music 2.wav	6.028	12.036	12.032	6.005	6.033
Music 3.wav	6.025	12.063	12.017	6.034	6.021
Music 4.wav	6.035	12.03	12.01	6.045	6.013
Music 5.wav	6.037	12.025	12.056	5.992	6.049
Speech 1.wav	5.977	12.055	12.046	6.064	5.957
Speech 2.wav	6.021	12.058	12.054	6.019	5.981
Speech 3.wav	6.029	12.012	12.044	6.002	6.049
Speech 4.wav	6.035	12.017	12.042	6.024	6.015
Speech 5.wav	6.016	12.039	12.023	6.041	5.992

Table 3 shows the obtained PSNR values for ten audio files at different embedding levels. Since the differences are almost identical, ranging from 5.977 to 6.049 at one different level and ranging from 12.01 to 12.074 at two different levels, the average can create a constant in developing a formula for PSNR estimation.

In order to collect the average of PSNR differences between each level, the value of the difference at two levels of embedding should be divided by two to get the average difference

in PSNR value at one difference level. Therefore, a new table is tabulated to display all the differences. Table 4 shows the difference in the PSNR values at all different levels of LSB.

Table 4  
Obtained PSNR difference at all level of LSB

Cover Audio	PSNR Difference at Different Level						
	1 <sup>st</sup> & 2 <sup>nd</sup> level	2 <sup>nd</sup> & 3 <sup>rd</sup> level	3 <sup>rd</sup> & 4 <sup>th</sup> level	4 <sup>th</sup> & 5 <sup>th</sup> level	5 <sup>th</sup> & 6 <sup>th</sup> level	6 <sup>th</sup> & 7 <sup>th</sup> level	7 <sup>th</sup> & 8 <sup>th</sup> level
Music 1.wav	5.998	6.037	6.037	6.021	6.021	6.012	6.017
Music 2.wav	6.028	6.018	6.018	6.016	6.016	6.005	6.033
Music 3.wav	6.025	6.032	6.032	6.009	6.009	6.034	6.021
Music 4.wav	6.035	6.015	6.015	6.005	6.005	6.045	6.013
Music 5.wav	6.037	6.013	6.013	6.028	6.028	5.992	6.049
Speech 1.wav	5.977	6.028	6.028	6.023	6.023	6.064	5.957
Speech 2.wav	6.021	6.029	6.029	6.027	6.027	6.019	5.981
Speech 3.wav	6.029	6.006	6.006	6.022	6.022	6.002	6.049
Speech 4.wav	6.035	6.009	6.009	6.021	6.021	6.024	6.015
Speech 5.wav	6.016	6.02	6.02	6.012	6.012	6.041	5.992

After calculating the difference value at each level, the average difference for PSNR value between each level is 6.02. Hence, a novel formula is proposed, which is based on the average differences retrieved from the pattern shown. The formula is as in Equation 2:

$$y = x - (6.02 * (l_n - l_x)) \tag{2}$$

where  $y$  is the expected PSNR at a different level, while  $x$  is the initial PSNR value at any level, while 6.02 is a constant calculated from the average differences between one upper level and one lower level. Finally,  $l_n$  is the new embedding LSB level, while  $l_x$  is the initial LSB level. The new formula can estimate the PSNR value for stego-file at a different level of LSB embedding. Figure 2 shows the flowchart of the proposed estimation method.

The estimation process starts by selecting the cover audio and secret message that needs to be hidden. Next, the secret message is embedded into one of the least

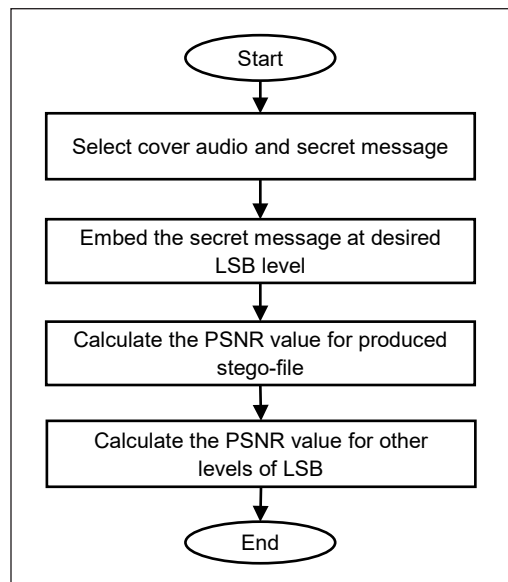


Figure 2. Proposed estimation method flowchart

significant bit levels of the cover audio sample, and modified cover audio is compiled into the stego-file. The stego-file is then evaluated by calculating its PSNR value. Finally, the PSNR value for other levels of LSB can be measured using Equation 2.

## EVALUATION AND DISCUSSION

An accuracy test is carried out to evaluate the proposed method. The average accuracy for the method is calculated using the Equation 3:

$$a = 100\% - \left(\frac{d}{v}\right) * 100\% \quad (3)$$

where  $a$  is the average accuracy,  $d$  is the average absolute difference between estimated PSNR and actual PSNR, and  $v$  is the average of actual PSNR value.

All covers for this evaluation are collected from [www.freesound.org](http://www.freesound.org). They have 44.1 KHz for sample rate, mono channel, wav file format and has 16-bit depth. In addition, speech, music, and silence type audio ranged, which has 1, 3, 5, 8, and 10 seconds are used to give a better view on the capabilities of the method. The number of secret message bits embedded in the cover for this test is at around 50% from the audio sample.

This test compares the estimation of PSNR value for fifteen (15) stego-file at different embedding levels against the actual PSNR value of this stego-file. Furthermore, it estimates two different levels of embedding, which are at the third level of LSB, and the seventh level of LSB, for a better view of the method's performance. Therefore, the proposed Equation 2 is used, and the result for the estimation stego-file PSNR from third level embedding is recorded in Table 5, while the result for the estimation stego-file PSNR from seventh level embedding is recorded in Table 6.

Based on Table 5, the average difference between the estimation and the actual result is 0.0184. For the individual difference, the differences vary between one to the others because of the difference of cover audio files and secret data used. Using different cover audio files and secret data will generate different numbers of bits flipping, leading to the error during the embedding process. Furthermore, if the size of the secret message is big, more modifications will be made to the cover audio sample bit; hence higher error is introduced. In this round, this method can estimate the PSNR value with 99.978% accuracy.

Based on Table 6, the average difference between the estimation and the actual result is 0.0118. The difference is quite similar to the result from Table 5, and both values are considered small. In this round, this method can estimate the PSNR value with 99.98% accuracy.

Based on the result from Tables 5 and 6, this method can estimate the PSNR value with high accuracy. Furthermore, the result shows that the difference between estimation and the actual value is less than 0.1 at different levels.



Table 5  
 Comparison between estimation and actual result of stego-file from 3<sup>rd</sup> level embedding

Audio	Obtained PSNR for 4bps	Estimated PSNR for 3bps	Actual PSNR for 3bps	Absolute difference
Music 1.wav	78.3062	84.3262	84.3459	0.020
Music 2.wav	78.2817	84.3017	84.2983	0.003
Music 3.wav	78.2326	84.2526	84.2813	0.029
Music 4.wav	78.277	84.297	84.2893	0.008
Music 5.wav	78.2686	84.2886	84.3032	0.015
Speech 1.wav	78.2513	84.2713	84.2699	0.001
Speech 2.wav	78.2926	84.3126	84.2652	0.047
Speech 3.wav	78.3005	84.3205	84.2828	0.038
Speech 4.wav	78.2882	84.3082	84.2986	0.010
Speech 5.wav	78.2872	84.3072	84.2963	0.011
Silence 1.wav	78.2864	84.3064	84.3034	0.003
Silence 2.wav	78.3011	84.3211	84.3081	0.013
Silence 3.wav	78.3102	84.3302	84.3067	0.023
Silence 4.wav	78.3133	84.3333	84.3009	0.032
Silence 5.wav	78.3012	84.3212	84.2983	0.023
<b>Average</b>			84.29654667	0.0184
<b>Accuracy of the proposed method to the average actual result</b>				99.978

Table 6  
 Comparison between estimation and actual result of stego-file from 7<sup>th</sup> level embedding

Audio	Obtained PSNR at 5th Level	Estimated PSNR at 7th Level	Actual PSNR at 7th Level	Absolute difference
Music 1.wav	72.2872	60.2472	60.1891	0.0581
Music 2.wav	72.2685	60.2285	60.2065	0.0220
Music 3.wav	72.2662	60.2262	60.2098	0.0164
Music 4.wav	72.2396	60.1996	60.2001	0.0005
Music 5.wav	72.2522	60.2122	60.2034	0.0088
Speech 1.wav	72.2784	60.2384	60.2687	0.0303
Speech 2.wav	72.2568	60.2168	60.2297	0.0129
Speech 3.wav	72.254	60.214	60.2186	0.0046
Speech 4.wav	72.2477	60.2077	60.211	0.0033
Speech 5.wav	72.2573	60.2173	60.2317	0.0144
Silence 1.wav	72.2784	60.2384	60.2372	0.0012
Silence 2.wav	72.3043	60.2643	60.2631	0.0012
Silence 3.wav	72.2952	60.2552	60.254	0.0012
Silence 4.wav	72.2981	60.2581	60.2569	0.0012
Silence 5.wav	72.2829	60.2429	60.2417	0.0012
<b>Average</b>			60.2281	0.0118
<b>Accuracy of the proposed method to the average actual result</b>				99.98

A comparison was made between the proposed method and Mazdak Method (Mazdak et al., 2012). Mazdak Method focuses on estimating PSNR at different bps rates to cater for the trade-off between capacity and imperceptibility. On the other hand, the proposed method focuses on estimating the PSNR value for one bit per sample at a different level to cater for the trade-off between robustness and imperceptibility. Both methods have different objectives, but the accuracy percentage between them can still be compared.

In order to make a comparison, the same audio used in the previous test is used. PSNR values for 3bps and 7bps embedding are estimated using Mazdak Method and compared against the actual PSNR value. The formulation used for Mazdak Method to give a brief idea is presented in Equation 4:

$$y = y_a + (x - x_a) \frac{y_b - y_a}{x_b - x_a} \quad (4)$$

where  $x$  is a given bps rate, and  $y$  is its PSNR. Hence,  $x_a$  represents the bps rate for  $a$ ,  $x_b$  represents the bps rate for  $b$ ,  $y_a$  represents the PSNR of embedding with  $a$  bps rate, and  $y_b$  represents the PSNR of embedding with  $b$  bps rate.

PSNR values from embedding with 4bps and 2bps of 15 audio files are recorded in Table 7. Equation 4 was used to estimate the PSNR value for 3bps. The estimated PSNR value for 3bps, actual PSNR value for 3bps and absolute difference is recorded in Table 7.

PSNR values from embedding with 5bps and 8bps of 15 audio files are recorded in Table 8. The same Equation 4 was used to calculate PSNR to estimate the PSNR value for 7bps. The estimated PSNR value for 7bps, actual PSNR value for 7bps and the absolute difference is recorded in Table 8.

Based on Table 7, the average absolute difference between the estimation and the actual result is 0.2953. Therefore, based on Equation 3, Mazdak Method can estimate the PSNR value with 99.646%.

Based on Table 8, the average absolute difference between the estimation and the actual result is 0.8844, and the estimation accuracy is 98.474%. The differences are higher than the estimation of PSNR value from embedding 3bps secret message, which indicates that the Mazdak method has lower accuracy when estimating PSNR for the embedding at higher bps.

Although Mazdak Method can estimate the PSNR value when embedding with different bps rates, the accuracy is reduced when estimating a higher bps rate. The proposed method obtained higher accuracy than Mazdak Method because the patterns for whole cases were collected and studied, producing stable estimation, which can be maintained around 99.9.

Table 7  
 Comparison between estimation and actual result based on Mazdak Method (3bps)

Audio	Obtained PSNR for 4bps	Obtained PSNR for 2bps	Estimated PSNR for 3bps	Actual PSNR for 3bps	Absolute difference
Music 1.wav	77.6152	89.6416	83.6284	83.1304	0.498
Music 2.wav	77.7262	89.6785	83.70235	83.3395	0.363
Music 3.wav	77.7314	89.7031	83.71725	83.3806	0.337
Music 4.wav	77.7226	89.7036	83.7131	83.3746	0.338
Music 5.wav	77.7247	89.7238	83.72425	83.3948	0.329
Speech 1.wav	77.8145	89.7295	83.772	83.4211	0.351
Speech 2.wav	77.8175	89.7161	83.7668	83.3902	0.377
Speech 3.wav	77.8026	89.7277	83.76515	83.3936	0.372
Speech 4.wav	77.8228	89.7263	83.77455	83.4121	0.362
Speech 5.wav	77.8317	89.7342	83.78295	83.2441	0.539
Silence 1.wav	76.5157	89.7555	83.1356	83.2157	0.080
Silence 2.wav	76.5209	89.6912	83.10605	83.255	0.149
Silence 3.wav	76.5293	89.6974	83.11335	83.242	0.129
Silence 4.wav	76.5236	89.7243	83.12395	83.229	0.105
Silence 5.wav	76.5381	89.7478	83.14295	83.244	0.101
<b>Average</b>				83.3111	0.2953
<b>Accuracy of the proposed method to the average actual result</b>					99.646

Table 8  
 Comparison between estimation and actual result based on Mazdak Method (7bps)

Audio	Obtained PSNR for 5bps	Obtained PSNR for 8bps	Estimated PSNR for 7bps	Actual PSNR for 7bps	Absolute difference
Music 1.wav	71.0445	54.6277	60.0996667	59.0499	1.050067
Music 2.wav	71.2037	54.6757	60.18503333	59.1703	1.014733
Music 3.wav	71.2392	54.7271	60.23113333	59.2143	1.016833
Music 4.wav	71.2929	54.7314	60.2519	59.2527	0.9992
Music 5.wav	71.2967	54.7486	60.26463333	59.2424	1.022233
Speech 1.wav	71.2006	53.1268	59.1514	58.1282	1.0232
Speech 2.wav	71.1503	52.7786	58.9025	57.9722	0.9303
Speech 3.wav	71.2226	53.2252	59.22433333	58.4405	0.783833
Speech 4.wav	71.1999	53.2412	59.22743333	58.3946	0.832833
Speech 5.wav	71.2124	53.1347	59.1606	58.3311	0.8295
Silence 1.wav	69.1936	51.1402	57.158	56.3932	0.7648
Silence 2.wav	69.1907	51.1533	57.16576667	56.4313	0.734467
Silence 3.wav	69.1883	51.1632	57.17156667	56.4236	0.747967
Silence 4.wav	69.1746	51.1607	57.16533333	56.4134	0.751933
Silence 5.wav	69.1861	51.1646	57.17176667	56.4071	0.764667
<b>Average</b>				57.9510	0.8844
<b>Accuracy of the proposed method to the average actual result</b>					98.474

## CONCLUSION

This paper proposes a new method to estimate the PSNR value of any LSB embedding level to cater to the trade-off between imperceptibility and robustness. PSNR values' pattern from embedding at a different level of LSB, which affect the robustness features, can be used to estimate the PSNR specifically for the imperceptibility feature of audio steganography. The estimated PSNR value generated based on the new method has an average of 99.9% accuracy compared to the actual embedding result at a different level of LSB throughout different embedding levels. The proposed method obtained higher accuracy when compared to Mazdak Method and only needed one actual PSNR value compared to Mazdak Method, which needs two actual PSNR values to operate. However, the focus of the proposed method is only on LSB modification. Hence, it is not suitable and accurate to implement the frequency domain in audio steganography.

To conclude, this method can be used as a utilisation tool to refrain from the repetition of embedding processes in finding the feasible solution to cater for the trade-off problem between imperceptibility and robustness features and further reducing the computational complexity of unnecessary repetitive embedding processes. Furthermore, the efficiency of an audio steganography method can be improved as any bad cover audio can be avoided from being produced. Future work that can be considered includes creating a steganography method based on this new estimation method to obtain a method with balanced features in terms of imperceptibility and robustness.

## ACKNOWLEDGEMENT

This work is supported in part by the Ministry of Higher Education (MOHE) Malaysia under a research grant [USIM/FRGS/FST/055002/50117]. The authors would like to express their gratitude to Universiti Sains Islam Malaysia (USIM) and MOHE for the support and facilities provided.

## REFERENCES

- Ahmed, M. A., Kiah, L. M., Zaidan, B. B., & Zaidan, A. A. (2010). A novel embedding method to increase capacity and robustness of low-bit encoding audio steganography technique using noise gate software logic algorithm. *Journal of Applied Sciences*, 10(1), 59-64. <https://doi.org/10.3923/jas.2010.59.64>
- Ali, A. H., Mokhtar, M. R., & George, L. E. (2017). Enhancing the hiding capacity of audio steganography based on block mapping. *Journal of Theoretical and Applied Information Technology*, 95(7), 1441-1448.
- Alsabhany, A. A., Ridzuan, F., & Azni, A. H. (2019). The adaptive multi-level phase coding method in audio steganography for confidential communication. *IEEE Access*, 7, 129291-129306. <https://doi.org/10.1109/ACCESS.2019.2940640>

- Alsabhany, A. A., Ridzuan, F., & Azni, A. H. (2018). An adaptive multi amplitude thresholds embedding algorithm for audio steganography. *Malaysian Journal of Science Health & Technology*, 2 (Special Issue), 7-10. <https://doi.org/10.33102/mjosht.v2i.43>
- Alsabhany, A. A., Ridzuan, F., Ridzuan, F., Azni, A. H., & Azni, A. H. (2020). The progressive multilevel embedding method for audio steganography. In *Journal of Physics: Conference Series* (Vol. 1551, No. 1, p. 012011). IOP Publishing. <https://doi.org/10.1088/1742-6596/1551/1/012011>
- Amirtharajan, R., & Rayappan, J. B. B. (2013). Steganography - Time to time: A review. *Research Journal of Information Technology*, 5(2), 53-66. <https://doi.org/10.3923/rjit.2013.53.66>
- Asad, M., Gilani, J., & Khalid, A. (2011). An enhanced least significant bit modification technique for audio steganography. In *International Conference on Computer Networks and Information Technology* (pp. 143-147). IEEE Publishing. <https://doi.org/10.1109/ICCNET.2011.6020921>
- Bhowal, K., Sarkar, D., Biswas, S., & Sarkar, P. P. (2017). A steganographic approach to hide secret data in digital audio based on XOR operands triplet property with high embedding rate and good quality audio. *Turkish Journal of Electrical Engineering & Computer Sciences*, 25(3), 2136-2148. <https://doi.org/10.3906/elk-162-267>
- Chadha, A., Satam, N., & Sood, R. (2013). An efficient method for image and audio steganography using least significant bit (LSB) substitution. *International Journal of Computer Applications*, 77(13), 37-45. <https://doi.org/10.1109/NSSMIC.2009.5401638>
- Cvejic, N., & Seppänen, T. (2005). Increasing robustness of LSB audio steganography by reduced distortion LSB coding. *Journal of Universal Computer Science*, 11(1), 56-65.
- Cvejic, N., & Seppanen, T. (2004). Increasing robustness of LSB audio steganography using a novel embedding method. In *2004 Proceedings of International Conference on Information Technology: Coding and Computing, ITCC 2004* (Vol. 2, pp. 533-537). IEEE Publishing. <https://doi.org/10.1109/ITCC.2004.1286709>
- Djebbar, F., Ayad, B., Hamam, H., & Abed-Meraim, K. (2011). A view on latest audio steganography techniques. In *2011 International Conference on Innovations in Information Technology* (pp. 409-414). IEEE Publishing. <https://doi.org/10.1109/INNOVATIONS.2011.5893859>
- Gopalan, K. (2018). Audio steganography for information hiding and covert communication - A tutorial. In *2018 IEEE International Conference on Electro/Information Technology (EIT)* (pp. 0242-0243). IEEE Publishing. <https://doi.org/10.1109/EIT.2018.8500167>
- Gopalan, K., & Fu, J. (2015). An imperceptible and robust audio steganography employing bit modification. In *2015 IEEE International Conference on Industrial Technology (ICIT)* (pp. 1635-1638). IEEE Publishing. <https://doi.org/10.1109/ICIT.2015.7125331>
- Hameed, A. S. (2018). High capacity audio steganography based on contourlet transform. *Tikrit Journal of Engineering Sciences*, 25(1), 1-7. <https://doi.org/10.25130/tjes.25.01>
- Hameed, M. A., Hassaballah, M., Aly, S., & Awad, A. I. (2019). An adaptive image steganography method based on histogram of oriented gradient and PVD-LSB techniques. *IEEE Access*, 7, 185189-185204. <https://doi.org/10.1109/ACCESS.2019.2960254>

- Jayapandiyan, J. R., Kavitha, C., & Sakthivel, K. (2020). Enhanced least significant bit replacement algorithm in spatial domain of steganography using character sequence optimization. *IEEE Access*, 8, 136537-136545. <https://doi.org/10.1109/ACCESS.2020.3009234>
- Kanhe, A., Aghila, G., Kiran, C. Y. S., Ramesh, C. H., Jadav, G., & Raj, M. G. (2015). Robust audio steganography based on advanced encryption standards in temporal domain. In *2015 International Conference on Advances in Computing, Communications and Informatics (ICACCI)* (pp. 1449-1453). IEEE Publishing. <https://doi.org/10.1109/ICACCI.2015.7275816>
- Kumar, R. (2016). Audio steganography using QR decomposition and fast Fourier transform. *Indian Journal of Science and Technology*, 6(34), 1-8. <https://doi.org/10.17485/ijst/2015/v8i1/69604>
- Li, P., Kong, Q., & Ma, Y. (2014). Image secret sharing and hiding with authentication based on PSNR estimation. *Journal of Information Hiding and Multimedia Signal Processing*, 5(3), 353-366.
- Mazdak, Z., Azizah, B. A. M., Shahidan, M. A., & Saman, S. C. (2012). Mazdak technique for PSNR estimation in audio steganography. In *Applied Mechanics and Materials* (Vol. 229, pp. 2798-2803). Trans Tech Publications Ltd. <https://doi.org/10.4028/www.scientific.net/AMM.229-231.2798>
- Meligy, A. M., Nasef, M. M., & Eid, F. T. (2016). A hybrid technique for enhancing the efficiency of audio steganography. *International Journal of Image, Graphics and Signal Processing*, 8(1), 36-42. <https://doi.org/10.5815/ijigsp.2016.01.04>
- Priyanka, B. R., Vrushabh, K. R., Komal, P. K., Pingle, S. M., & Mahesh, S. R. (2012). Audio steganography using LSB. *International Journal of Electronics, Communication and Soft Computing Science & Engineering (IJECSCE)*, 2, 90-93.
- Sapra, P. S. (2016). Secured LSB modification using dual randomness. In *2016 International Conference on Recent Advances and Innovations in Engineering (ICRAIE)* (pp. 1-4). IEEE Publishing. <https://doi.org/10.1109/ICRAIE.2016.7939592>
- Somani, H., & Madhu, K. M. (2015). A survey on digital audio steganography techniques used for secure transmission of data. *International Journal of Engineering Development and Research*, 3(4), 236-239.
- Srivastava, M., & Rafiq, M. Q. (2012). A novel approach to secure communication using audio steganography. *Advanced Materials Research*, 408, 963-969. <https://doi.org/10.4028/www.scientific.net/AMR.403-408.963>
- Sun, W., Shen, R., Yu, F., & Lu, Z. (2012). Data hiding in audio based on audio-to-image wavelet transform and vector quantization. In *2012 Eighth International Conference on Intelligent Information Hiding and Multimedia Signal Processing* (pp. 313-316). IEEE Publishing. <https://doi.org/10.1109/IIH-MSP.2012.82>
- Tayel, M., Gamal, A., & Shawky, H. (2016). A proposed implementation method of an audio steganography technique. In *2016 18th international conference on advanced communication technology (ICACT)* (pp. 180-184). IEEE Publishing. <https://doi.org/10.1109/ICACT.2016.7423320>
- Wakiyama, M., Hidaka, Y., & Nozaki, K. (2010). An audio steganography by a low-bit coding method with wave files. In *2010 Sixth International Conference on Intelligent Information Hiding and Multimedia Signal Processing* (pp. 530-533). IEEE Publishing. <https://doi.org/10.1109/IIHMSP.2010.135>

- Xue, P., Liu, H., Hu, J., & Hu, R. (2018). A multi-layer steganographic method based on audio time domain segmented and network steganography. In *AIP Conference Proceedings* (Vol. 1967, No. 1, p. 020046). AIP Publishing LLC. <https://doi.org/10.1063/1.5039018>
- Yu, H., Wang, R., Dong, L., Yan, D., Gong, Y., & Lin, Y. (2020). A high-capacity reversible data hiding scheme using dual-channel audio. *IEEE Access*, 8, 162271-162278. <https://doi.org/10.1109/access.2020.3015851>
- Zumchak, S. M. (2016). *Audio steganography: A comparative study of techniques and tools* (Doctoral dissertation). Utica College, USA.





## Formulation of Polyherbal Carbonated Beverage based on *Halalan Thoyyiban* Principle

Puteri Shazleen Izreena Mohd Shahrin<sup>1</sup>, Norhayati Muhammad<sup>1,2\*</sup> and Nur Fazira Abdul Rahim<sup>1</sup>

<sup>1</sup>Department of Technology and Natural Resources, Faculty of Applied Sciences and Technology, Universiti Tun Hussein Onn Malaysia, UTHM- Campus (Pagoh Branch), Pagoh Education Hub, KM 1, Jalan Panchor, 84600 Muar, Johor, Malaysia

<sup>2</sup>Institut Ahli Sunnah Wal Jamaah, Universiti Tun Hussein Onn Malaysia, 86400, Parit Raja, Batu Pahat, Johor, Malaysia

### ABSTRACT

Herbal products usually have less palatability on their taste even though they are healthy and nutritious. Thus, this study aims to formulate polyherbal carbonated beverages, followed by the evaluation of sensory, physicochemical properties and their compliances with the *halalan thoyyiban* principle. Five formulations were prepared by varying the amount of water and polyherbal extracts that were designated using Design Expert 6.0.4 software. The most accepted formulation was formulation 1 (F1), containing 12.50% polyherbal extract and 87.50% water. F1 was characterised for its physicochemical properties, including carbon dioxide volume, pH, and total acidity, with 3.0 g/L, 4.5, and 1.7%, respectively, and these findings have complied with the *halalan thoyyiban* principle. The antioxidant properties were evaluated by using 2,2-diphenyl-1-picrylhydrazyl (DPPH), ferric reducing antioxidant potential (FRAP), as well as total phenolic content (TPC), and it exhibited 1.25 mg GAE/mL, 1.08 mM Fe (II) and 0.39 mg GAE/mL respectively. Eight Halal Control Point (HCP) were identified along with the production. Moreover, the beverage was found to have antioxidant properties and nutritional content (carbohydrate (0.3%) and energy

content (2.0 kcal/100g)), which can give health benefits to the consumer and proven safe for consumption ( $LC_{50} = 1066.60 \mu\text{g/mL}$ ). To conclude, the formulated polyherbal carbonated beverage is accepted by the consumer and complies with the *halalan thoyyiban* principle.

**Keywords:** Antioxidant, carbonated beverage, *halalan thoyyiban*, polyherbal

### ARTICLE INFO

#### Article history:

Received: 21 June 2021

Accepted: 15 September 2021

Published: 10 January 2022

DOI: <https://doi.org/10.47836/pjst.30.1.28>

#### E-mail addresses:

aw170060@siswa.uthm.edu.my (Puteri Shazleen Izreena Mohd Shahrin)

norhayatim@uthm.edu.my (Norhayati Muhammad)

gw180043@siswa.uthm.edu.my (Nur Fazira Abdul Rahim)

\* Corresponding author

## INTRODUCTION

Malaysia has a wide range of plant species that pose medicinal properties. The herbal plants can be combined as polyherbal to give a more significant effect. This combination can give a more desirable therapeutic effect because the individual plant phytochemical components are insufficient to achieve the beneficial effects (Pandey et al., 2013). *Orthosiphon stamineus* (misai kucing), *Phyllanthus niruri* (dukung anak) and *Strobilanthes crispus* (pecah beling) are herbal plants in a polyherbal combination that exhibited the synergistic effect on 2,2-diphenyl-1-picrylhydrazyl (DPPH) radical scavenging activity. It was proven in a previous study that a combination of these three herbs has similar antioxidant properties and showed a synergistic interaction effect (Rahim et al., 2018). According to Capecka et al. (2005), these herbs are an excellent source of phenolic compounds, which can help prevent various degenerative diseases and exhibit antioxidant effects, making them suitable to be combined as a polyherbal. However, nowadays, people usually refuse to consume herbal plants because they have less palatability even though they are healthy and nutritious. It is due to the presence of antioxidants phytochemicals in the herbal plants or vegetables, which give a noticeable bitter taste (Drewnowski & Gomez-Carneros, 2000).

A formulation is needed to develop a new herbal-based product with high palatability. In Malaysia, there has been a growth in interest in natural herbs for medicinal purposes that indirectly led to rapid growth in the herbal product industry. Herbal products have grown in popularity over the last decade and are now utilised by about 20% of the population, contributing to people's health care (Ya'akob, 2018). In addition, according to Singh (2018), herbal products can meet the tastes and preferences of consumers, which causes many products to have been developed nowadays, such as food supplements (Ekor, 2014), teas (Alexieva et al., 2019) and snacks (Wangcharoen et al., 2006). In this study, the polyherbal carbonated beverage has been developed by formulating the amount of polyherbal extract and water as well as the ingredients. In addition, carbon dioxide gas was added to the beverage by the carbonation process to enhance its taste. In Malaysia, carbonated drinks have become popular because they have a sharp, refreshing taste and quench thirst (Kendra, 2018). The herbal-based carbonated beverage is a novel concept that has the potential to add a unique sparkle effect to the herbal beverage when combined. This concept can increase the consumer preference toward the herbal product. In this study, the best formulation of the product was chosen based on the overall acceptability of the sensory evaluation. The sensory characteristics of food can influence consumer preference of food substances (Kostyra et al., 2016).

In addition, it is important to meet the *halalan thoyyiban* principle's requirements in food production. From an Islamic perspective, *halal* means permissible or allowable and *thoyyiban* is defined as pure, safe, wholesome, and healthy (Yahya et al., 2016). It means that the products identified as *halalan thoyyiban* should not be identified as delicious and pure only. They should also be beneficial to the body and do not cause any harm.

Unfortunately, the food industry has neglected *halalan toyyiban* compliance, which causes many concerns about the questionable status of *halal* food (Salahudin et al., 2015). Thus, the polyherbal carbonated beverage was formulated based on consumer preferences by conducting a sensory evaluation test and developed according to the *halalan thoyyiban* principle, which is safe, healthy and gives health benefits for human consumption, providing antioxidant properties.

## MATERIALS AND METHODS

### Materials

In this study, *O. stamineus*, *P. niruri* and *S. crispus* leaves were used in the form of dried powder. These herbs were purchased from Ethno Resources Sdn Bhd, Sungai Buloh, Selangor. Sucralose, citric acid and sodium benzoate were purchased from Thong Sheng Food Technology Sdn Bhd, Pulau Pinang. DPPH, gallic acid, methanol, Folin-Ciocalteu's phenol reagent have been purchased from (Sigma Aldrich, USA). Sodium carbonate has been purchased from Samchun Chemical Corporation (Pyeongtaek, Korea). Sodium acetate buffer, 2,4,6-tris(2-pyridyl)-s-triazine (TPTZ), iron (III) chloride hexahydrate and iron (III) chloride have been purchased from Sigma Aldrich (St. Louis, MO, USA). All the reagents are food-grade procured from local sources.

### Preparation of Plant Materials

*O. stamineus*, *P. niruri* and *S. crispus* leave powders were used to develop the polyherbal formulations. The herbal extract preparation was done according to Chanthasri et al. (2018), with slight modification. First, an amount of 100 g of each powder (130–150 mesh) was heated slowly by boiling with one litre of distilled water until the volume of the mixture reduced to about a third of the original volume. Then, each type of powder was immersed in hot water at a range of 80°C to 90°C for 20 minutes, as Wijaya (2019) suggested. As a result, it was proven that the optimum condition for extraction herbal for functional drink production was 90°C and 21 minutes, which is expected to give higher antioxidant activity. Then, the extracts were filtered separately using a muslin cloth and sterile grade no. 1 filter paper (Whatman, 1004125-DS, Mexico). Finally, to develop the polyherbal mixture, each extract was mixed in a proportion by referring to the optimised formulation based on antioxidant activity conducted from the previous study (Rahim et al., 2018), as shown in Table 1.

### Formulation of Polyherbal Carbonated Beverage

The components used were the filtered water and the polyherbal extract, and the mixture proportion was designated using Simplex Lattice mixture design of Design Expert 6.0.4 and as shown in Table 2. The low and high values used for filtered water in the formulation

Table 1

*The optimized formulation of polyherbal combination based on antioxidant activity*

Plant samples			Antioxidant activities		
<i>O.stamineus</i>	<i>P. niruri</i>	<i>S. crispus</i>	DPPH	TPC	FRAP
75.42%	0.62%	23.96%	91.23%	141.851 µg GAE/g	148.516 µg/mL

Table 2

*Design layout and experimental results*

Formulation	Volume of filtered water (%)	Volume of polyherbal extract (%)
F1	87.5	12.5
F2	83.75	16.25
F3	80.00	20.00
F4	95.00	5.00
F5	91.25	8.75

Notes: (F1) formulation 1, (F2) formulation 2, (F3) formulation 3, (F4) formulation 4, (F5) formulation 5

were 80% and 95%, respectively. Meanwhile, the low and high values used were 5% and 20% for the polyherbal extract, respectively. The mixture was standardised at 100% of the formulation.

### Carbonation Process

The formulated polyherbal beverages were carbonated using a carbonator machine (Soda Xpress, Malaysia). Therefore, the beverage was needed to be pre-chilled first to ensure the temperature was at the range of 2 to 4°C. This condition helps ease the absorption of carbon dioxide (CO<sub>2</sub>) into the beverage (Abdulkareem et al., 2011).

### Sensory Analysis

Sensory attributes including colour, aroma, taste, sweetness, sourness, sparkling sensation and overall acceptability were determined by hedonic test (untrained panellists). The hedonic test was used to evaluate sensory characteristics and determine the consumer's acceptability for polyherbal carbonated beverages. The samples of five formulations with the control (pure polyherbal extract) were presented in sensory cups coded of F1, F2, F3, F4, F5 and control.

### Physicochemical Analyses

The beverage was analysed for the physicochemical characteristics, including the colour, pH, total acidity, and carbon dioxide volume. A colorimeter (MiniScan EZ, USA) was used to measure the beverage's colour. The pH was estimated using a digital pH meter (Eutech pH 700, India), calibrated according to the method AOAC (2005). The total titratable acidity

of the sample was analysed by a titration method according to AOAC (2000) with slight modification, and the acidity was expressed as citric acid (%). Total acidity was calculated by using Equation 1. A thermometer (SK Sato, Japan) and pressure gauge (Ashcroft, USA) were used to determine the volume of carbon dioxide in the sample. The pressure reading at the constant temperature was converted to the volume of carbon dioxide using a carbonation chart (Thongrote et al., 2016).

$$\text{Total acidity (\%)} = \frac{\text{volume of 0.1 M NaOH (ml)} \times 0.064 \times 100}{\text{volume of sample (ml)}} \quad [1]$$

### Evaluation of Polyherbal Carbonated Beverage with the *Halalan Thoyyiban* Principle Compliance

In order to evaluate the *halalan thoyyiban* compliance, the *halal* status of ingredients used in the beverage development was identified. In addition, the beverage was evaluated to have antioxidant and nutritional content as health benefits. Also, the toxicity test was conducted to ensure the beverage was safe to be consumed.

**Antioxidant Properties.** The antioxidant properties of the formulated polyherbal carbonated beverage were determined by using DPPH, FRAP and TPC assays. In addition, the antioxidant activity of the beverage was compared with the control (polyherbal extract).

**DPPH Assay.** The DPPH assay was carried out according to BehnamNik & Vazifedoost (2020) with minor modifications. The DPPH solution 0.004% was prepared by adding 4 mg DPPH in 100 mL methanol. Then, 0.5 mL of the drink sample was mixed with 3.5 mL of 0.004% prepared DPPH solution. After that, the mixed sample was placed in the dark at room temperature (27°C) for 40 minutes, and then, the sample light absorbance was read at 517 nm. The absorbance values of the samples were compared to the standard curve of the gallic acid. The gallic acid standard curve was drawn in the concentration range of 0.02 and 0.1 mg/mL. The experiment was done in triplicate.

**FRAP Assay.** The FRAP assay was used with slight modifications (Benzie & Strain, 1996). Briefly, the FRAP reagent was prepared by mixing 25 mL of 300 mMol/L acetate buffer (pH 3.6), 2.5 mL of 10 mmol/L TPTZ in 40 mmol/L hydrochloric acid and 20 mmol/L Ferric chloride hexahydrate and then incubated in a water bath at 37°C for five minutes (Memmert/WNB14, Germany). An amount of 300 µL of FRAP reagent was mixed with 10 µL of sample and 30 µL of distilled water. Then, the absorbance of the mixture was measured at 593 nm. The FRAP values of samples were determined using the iron (II) sulphate standard curve (0.2 to 1.0 mM). The antioxidant activity of the sample was expressed as mM iron (II) equivalent.

**TPC Assay.** The content of total phenolic compounds in the carbonated polyherbal beverage was determined by Folin-Ciocalteu colourimetric method. This total phenolic content was measured following BehnamNik and Vazifedoost (2020) with slight modifications. First, an amount of 0.5 mL of drink samples and 2.5 mL of Folin-Ciocalteu reagent 1 N were mixed in the test tube. After that, 2 mL of 7.5% sodium carbonate solution was added to the mixture after ten minutes and then incubated in the dark at room temperature for one hour. The absorbance was measured at 760 nm. For TPC determination, the absorbance values of the samples were compared to the standard curve of the gallic acid. The gallic acid standard curve was drawn in the concentration range of 0.04 and 0.4 mg/mL. The experiment was done in triplicate.

**Nutritional Content Determination.** The polyherbal carbonated beverage was analysed for the presence of the total carbohydrates (AOAC, 2005), protein, energy (Nielsen, 2010) and fat content (Bench et al., 2010).

**Toxicity Assay.** The beverage was tested on its toxicity by using brine shrimp lethality assay with slight modification (Asaduzzaman et al., 2015). Firstly, the brine shrimp eggs, *Artemia salina*, were hatched in artificial seawater prepared by dissolving 38 grams of sea salt in one litre of distilled water in a container with a light source for 24 hours. After 24 hours, the light source was turned off to separate the empty egg float from the brine shrimp. The beverage was prepared at 1600 $\mu$ g/mL concentration as a stock solution by diluting 32 mg of the beverage in 200  $\mu$ L distilled water and was made up the volume to 20 mL with seawater. By using serial dilution, the concentration of 10  $\mu$ g/mL, 100  $\mu$ g/mL, 250  $\mu$ g/mL, 500  $\mu$ g/mL, and 1000  $\mu$ g/mL were made up with the seawater. Ten nauplii were introduced into five mL of the sample in a separate test tube for each concentration. After 24 hours, the test tube was inspected, and the number of deaths of nauplii and the percentage of death in each tube was counted using Equation 2. The concentration killing 50% of the nauplii (LC<sub>50</sub>) was determined using probit analysis and the linear regression method from the plotted graph.

$$\% \text{ Death} = \frac{\text{Number of dead nauplii}}{\text{Total number of nauplii placed in a test tube}} \times 100 \quad [2]$$

### Statistical Analysis

The results were expressed as means $\pm$ standard deviation to show variations in the various experimental. Statistical analyses for the formulation were conducted using Design Expert 6.0.4 (State-Ease Inc., MN, USA). The sensory analysis and antioxidant assay results were analysed by one-way analysis of variance (ANOVA) using commercial statistical

software IBM SPSS Statistics 26 of Tukey-LSD. Differences are considered significant when  $p < 0.05$ .

## RESULTS AND DISCUSSION

### Sensory Evaluation

F1 showed the significantly ( $p < 0.05$ ) highest mean value for overall acceptance with an  $8.2 \pm 1.17$  mean value compared to other samples. F2 had a total of  $7.9 \pm 1.36$  mean score as the second-highest, followed by F3 with a  $6.84 \pm 1.49$  mean score. However, samples coded F4 and F5 were less favourable by panellists with a mean score of  $3.8 \pm 2.25$  and  $4.3 \pm 1.89$ , respectively, as shown in Table 3. The overall acceptability of this beverage is assumed to be affected by the colour and taste attributes of the product. Polyherbal carbonated beverage with a lighter colour than the control with the sweetness and sourness, neither too high nor too low was preferred. According to Saint-Eve et al. (2009), the use of carbon dioxide in the beverage can enhance the flavour. Thus, the sourness in the sample was described due to carbon dioxide content, since F1 accounted for 12.5% of the polyherbal extract, which this amount is neither too high nor too low, resulting in stable sweetness and sourness of the sample. Statistical analysis of data obtained from questionnaires completed by the panellists indicated that the samples had significant differences ( $p < 0.05$ ) among the others for all attributes. F1 was selected to be evaluated for physicochemical properties and its compliance with the *halalan thoyyiban* principle since this formulation obtained the highest overall acceptance among formulations.

### Physicochemical Properties

The results for the physicochemical properties of polyherbal carbonated beverages are shown in Table 4. The pH of carbonated polyherbal beverage was  $4.5 \pm 0.01$ . The lower pH of the beverage could be attributed to the addition of  $\text{CO}_2$  in the sample, which affects the

Table 3  
Mean scores for sensory evaluation

Attributes	F1	F2	F3	F4	F5	Control
Colour	$6.3 \pm 2.12^b$	$6.1 \pm 2.29^b$	$4.8 \pm 1.92^c$	$7.5 \pm 1.22^a$	$6.6 \pm 1.50^{ab}$	$1.8 \pm 1.59^d$
Aroma	$7.0 \pm 1.46^{ab}$	$7.1 \pm 1.66^a$	$7.9 \pm 1.01^a$	$5.9 \pm 1.75^c$	$6.1 \pm 1.40^{bc}$	$2.64 \pm 2.66^d$
Taste	$8.0 \pm 1.34^a$	$6.8 \pm 1.55^{bc}$	$7.2 \pm 2.16^{ab}$	$4.3 \pm 2.16^d$	$6.1 \pm 1.47^c$	$2.08 \pm 1.52^c$
Sweetness	$7.4 \pm 1.23^{ab}$	$7.1 \pm 1.47^{bc}$	$6.4 \pm 1.47^c$	$8.0 \pm 0.92^a$	$7.8 \pm 1.68^{ab}$	$5.0 \pm 0.00^d$
Sourness	$8.0 \pm 0.96^a$	$7.1 \pm 1.52^b$	$5.8 \pm 2.01^c$	$6.4 \pm 1.66^c$	$5.9 \pm 1.67^c$	$5.0 \pm 0.00^d$
Sparkling sensation	$7.8 \pm 1.45^a$	$7.3 \pm 1.47^{ab}$	$6.7 \pm 1.70^b$	$8.0 \pm 1.17^a$	$7.8 \pm 1.17^a$	$5.0 \pm 0.00^c$
Overall acceptance	$8.2 \pm 1.17^a$	$7.9 \pm 1.36^a$	$6.8 \pm 1.49^b$	$3.8 \pm 2.25^c$	$4.34 \pm 1.89^c$	$1.7 \pm 1.10^d$

Notes: a-d Means with different lowercase superscript letters are significantly different ( $p < 0.05$ )

Table 4  
*Physicochemical properties of polyherbal carbonated beverage*

Parameters	Experimental value
pH	4.5±0.01
Total acidity	1.7±0.12 %
Carbon dioxide volume	3.0±0.0 g/L
Colour	L* = 33.00±0.49, a* = 4.10±0.13 and b* = 24.30± 0.71

concentration of the carbonic acid present in the drink (Aslam et al., 2016). Meanwhile, citric acid, an acidulant, gives sourness and increases thirst-quenching effects in the beverage (Steen, 2005). Moreover, the amount of 1.7±0.12 % for total acidity resulted from the polyherbal carbonated beverage. Similar reason with the pH, the addition of citric acid resulted in a high total of acidity could be noticed. The increasing pH value of carbonated beverages is linked to their total acidity (Abdulkareem et al., 2011). Furthermore, the CO<sub>2</sub> volume of the beverage contained 3.0± 0.0 g/L of each 330 mL of bottle drink. The volume for a typical carbonated soft drink ranged between 1 to 5 volumes (2-10 g/L) CO<sub>2</sub> (Abu-Reidah, 2020). Thus, the result for the CO<sub>2</sub> volume of polyherbal carbonated beverages was within the range of the standard carbonated drink. The results for the colour measurement are L\* = 33.00±0.49, a\* = 4.10±0.13 and b\* = 24.30± 0.71. The polyherbal carbonated beverage can be described as brighter, less red and more yellow than control (L\* = 9.71±0.14, a\* = 1.73±0.16 and b\* = 8.09±0.51). It might be because of the addition of water to the polyherbal extract resulting in a lighter colour.

### Compliance of *Halalan Thoyyiban* Principle

**Identification of Halal Control Point (HCP).** Based on Figure 1, eight HCP were identified in developing polyherbal carbonated beverages. HCP 1 begins with the supply of raw materials and ingredients. All the raw materials and ingredients used were purchased from the company that obtained the Halal certificates for their product. Halal certification is an important component in the food and beverages industry in Malaysia as it indicates that the food product is assured in terms of religious compliance, safety, and hygiene. HCP 2, HCP 4, and HCP 6 were involved in the process of mixing the ingredients. During the mixing of ingredients, it was necessary to make sure all ingredients were not contaminated with the *haram* materials to ensure the product was processed in a *halal* manner from raw materials until consumed by the consumers.

On the other hand, HCP 3, HCP 5 and HCP 8 were involved in the equipment used during the process that should be cleaned and not contaminated with any *haram* materials. In addition, the place to store the product was separated from the non-*halal* sources. According to Islamic Law, *halal* foods should be free from contamination and not contain *haram* ingredients during preparation, processed, transported, or stored using any appliance



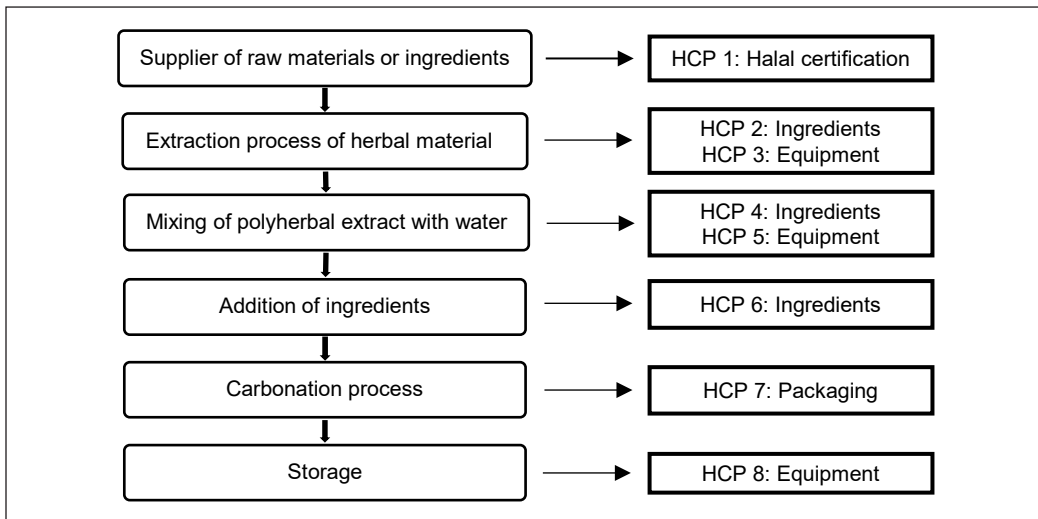


Figure 1. Halal Control Point (HCP) of the process

or facility (Hassan & Awang, 2009). Other than that, the food must also have no direct contact with any non-*halal* materials. Therefore, with the presence of unlawful materials, the polyherbal carbonated beverage can be considered *haram*.

HCP 7 was identified in the carbonation process. During this process, the beverage mixture was transferred into the bottle to allow the carbonation process in the capped bottle. Therefore, the polyherbal carbonated beverage packaging bottle came from *halal* materials and was not contaminated with non-*halal* sources. On the other hand, carbon dioxide addition was not considered as HCP because CO<sub>2</sub> is one of *halal* additive with E-Numbers “E290,” which this additive has been verified its status as *halal* (JAKIM, 2006). So, to simplify, all HCP were successfully identified in the development of polyherbal beverages. Therefore, this product can be considered *halal* as it was not involved with non-*halal* sources along the process.

**Antioxidant Properties.** The results for the antioxidant properties of the beverage are shown in Table 5.

**DPPH Radical Scavenging Activity.** The antioxidant activity referred to as DPPH radical scavenging activity of polyherbal carbonated beverage had obtained a lower value (1.25±0.18 mg GAE/mL) than the control (13.41±0.59 mg GAE/mL). As shown in Table 5, the scavenging activity of polyherbal carbonated beverages and control was significantly different as the *p*-value was less than 0.05. It might be due to the addition of water in polyherbal carbonated beverages, causing the concentration of the sample to become lower than the control. It was noticed that, with an increase in the amount of polyherbal extract,

Table 5  
*Antioxidant properties for polyherbal carbonated beverage and control*

Sample	DPPH (mg GAE/mL)	FRAP (mM Fe (II))	TPC (mg GAE/mL)
Control Polyherbal	13.41±0.59 <sup>a</sup>	1.42 ± 0.03 <sup>a</sup>	3.12 ± 0.18 <sup>a</sup>
Carbonated beverage	1.25±0.18 <sup>b</sup>	1.08 ± 0.04 <sup>b</sup>	0.39 ± 0.22 <sup>b</sup>

Notes: <sup>a,b</sup> Different letters at each column indicates significant different ( $p < 0.05$ )

the antioxidant level was shown to rise. It might be because the increases in the amount of polyherbal extract in the sample caused the concentration of the sample to increase, which led to the stronger action of the scavenging activity (Rusmana et al., 2017). Thus, the higher the amount of polyherbal extract in the formulation, the higher the antioxidant activity of the sample.

**Ferric Reducing Antioxidant Power (FRAP).** The polyherbal carbonated beverage was found to have a significantly lower ( $p < 0.05$ ) FRAP value, which is 1.08 mM Fe (II) equivalent compared to the control 1.42 mM Fe (II) equivalent as presented in Table 5. This result revealed that the control had stronger electron donors and was able to minimise the oxidised intermediates of the lipid peroxidation process. Thus, polyherbal carbonated beverages can be considered to have lower antioxidant activity than the control. The control is 100% pure polyherbal extract, which has more bioactive components, such as phenolic content that correlated with the higher antioxidant properties.

**Total Phenolic Content (TPC).** Based on Table 5, the control had significantly higher ( $p < 0.05$ ) phenolic content of 3.12 mg GAE/mL than the polyherbal carbonated beverage (0.39 mg GAE/mL). Thus, the control can be considered to have higher antioxidant properties than the beverage. It might be because the polyherbal extract has a higher total phenolic content than the polyherbal carbonated beverage. Both edible and non-edible plants have phenolic compounds, which give the biological effects of antioxidant activity (Kahkonen et al., 1999). A study showed that *O. stamineus* aqueous extract has higher antioxidant properties than other herbal plants, such as *P. niruri*, *S. crispus*, and *S. rebudiana*, which might be because the total phenolic content plant is in the appropriate range (Rahim et al., 2018). According to Hasmdia et al. (2015), a higher concentration of the phenolic compound can benefit from preventing the oxidative activities of plant extract. Therefore, it showed that the antioxidant activities for the plant extracts were affected by their phenolic content.

**Nutritional Contents.** Food products that comply with the *halalan thoyyiban* principle must be healthy and nutritious. Besides providing antioxidant properties, the amount of sugar or carbohydrate content needs to be considered; hence all consumers can drink this beverage, including diabetic patients, when it is proven with low sugar or carbohydrate

content. Therefore, the nutritional contents of the beverage were determined to comply with the principle, as shown in Table 6. Based on the result, the beverage contains 0.3% of carbohydrates. According to Kregiel (2015), sucrose, glucose or fructose is used as natural carbohydrate sweeteners in

Table 6

*Nutritional content of polyherbal carbonated beverage*

Nutritional content	Amount
Carbohydrate	0.3%
Protein	0.0%
Fat	0.0%
Energy	2.0 kcal/100g

soft drink. Due to the sugar content in the regular soft drink, the total carbohydrate can be determined as one of the nutritional compositions of the beverage. However, in this study, sugar or sucrose was not included in the formulation of polyherbal carbonated beverages and replaced by sucralose. Therefore, it resulted in a low total carbohydrate in the beverage with only 0.3%. Typically, carbonated beverages have about 10% to 12% sugar content (Abu-Reidah, 2020). Thus, the polyherbal carbonated beverage can be considered lower nutritious than regular carbonated beverages. It indicates that the developed polyherbal carbonated beverage is healthier than regular soft drink as its formulation has no sugar content, which compliance with the *halalan thoyyiban* concept. It is agreed with Hassan (2011) that stated the combination of *halal* and *tayyib* must ensure that the food is *halal*, safe and healthy. Furthermore, the result revealed that the beverage has no protein or fat content. It is because the formulation of the sample does not involve protein and fat sources. Moreover, the beverage contains 2.0 kcal/100 g of energy content. The energy content of soft drinks per 100 mL ranged from 0 kcal to 55 kcal (Iglesias et al., 2016). Thus, the energy content for polyherbal carbonated beverages lies within the range.

**Toxicity.** Food products that comply with the *halalan thoyyiban* principle must be safe to consume and not harmful to our bodies. A toxicity test was performed to determine the  $LC_{50}$  of the polyherbal carbonated beverage to determine its safety. There was a positive linear relationship between mortalities of brine shrimps and concentration of polyherbal carbonated beverage where, as increasing the concentration, the rates of mortalities also increased. The percentages of mortality of brine shrimp nauplii for concentration 10  $\mu\text{g}/\text{mL}$ , 100  $\mu\text{g}/\text{mL}$ , 250  $\mu\text{g}/\text{mL}$ , 500  $\mu\text{g}/\text{mL}$ , and 1000  $\mu\text{g}/\text{mL}$  of polyherbal carbonated beverage were 7%, 23%, 33%, 43% and 47% respectively. In this study,  $LC_{50}$  of polyherbal carbonated beverage was found at 1066.60  $\mu\text{g}/\text{mL}$  concentration. Based on Clarkson's toxicity criterion, a sample with  $LC_{50}$  more than 1000  $\mu\text{g}/\text{mL}$  is non-toxic (Clarkson et al., 2004). Thus, the polyherbal carbonated beverage used in this study was found to have non-toxic properties as deduced from their  $LC_{50}$  values (Dosumu et al., 2010). Therefore, the polyherbal carbonated beverage was found to be safe regarding brine shrimp toxicity assay and since polyherbal carbonated beverage was produced at relatively low concentration due to the combination of polyherbal extract and water.

## CONCLUSION

The addition of carbon dioxide by the carbonation process can enhance the taste of the polyherbal beverage. The most accepted formulation was F1 (12.50% polyherbal extract and 87.50% water). Its physicochemical properties were followed the standard values. The polyherbal carbonated beverage exhibited antioxidant properties and is also nutritious, fulfilling the *halalan thoyyiban* principle as it provides health benefits. Moreover, LC<sub>50</sub> of polyherbal carbonated beverage was found at 1066.60 µg/mL, which can be declared non-toxic and safe for consumption. Thus, the beverage can be considered to comply with the *halalan thoyyiban* principle. Therefore, it can be concluded that the formulated polyherbal beverage is not only accepted by the consumer but was also complied with the *halalan thoyyiban* principle.

## ACKNOWLEDGEMENTS

The Ministry of Higher Education Malaysia supported the research through Fundamental Research Grant Scheme (FRGS/1/2017/WAB11/UTHM/03/01) Vote No. 1646 and partially sponsored by Universiti Tun Hussein Onn Malaysia (UTHM).

## REFERENCES

- Abdulkareem, A. S., Uthman, H., & Jimoh, A. (2011). Development and characterization of a carbonated ginger drink. *Leonardo Journal of Sciences*, 18, 45-54.
- Abu-Reidah, I. M. (2020). Carbonated beverages. In C. M., Galanakis, (Ed.), *Trends in non-alcoholic beverages* (pp. 1-36). Elsevier. <https://doi.org/10.1016/B978-0-12-816938-4.00001-X>
- Alexieva, I., Popova, A., & Mihaylova, D. (2019). Trends in herbal usage - A survey study. *Food Research*, 4, 500-506. [https://doi.org/10.26656/fr.2017.4\(2\).346](https://doi.org/10.26656/fr.2017.4(2).346)
- AOAC. (2000). *Official methods of analysis*. Association of Official Analysis Chemists International.
- AOAC. (2005). *Ash of flour (Direct Method) method 923.03*. Association of Official Analysis Chemists International.
- Asaduzzaman, M., Rana, M. S., Hasan, S. R., Hossain, M. M., & Das, N. (2015). Cytotoxic (brine shrimp lethality bioassay) and antioxidant investigation of *Barringtonia acutangula* (L.). *International Journal of Pharma Sciences and Research*, 6(8), 1179-1185. <https://doi.org/10.9734/EJMP/2015/5400>
- Aslam, M. S., Ahmad, M. S., Mamat, A. S., Ahmad, M. Z., & Salam, F. (2016). An update review on polyherbal formulation: A global perspective. *Systematic Reviews in Pharmacy*, 7(1), 35-41. <https://doi.org/10.5530/srp.2016.7.5>
- BehnamNik, A., & Vazifedoost, M. (2020). Optimizing the formulation of the functional beverage from the co-crystallized powder of *Securigera securidaca* seed extract. *Journal of Food Science and Technology*, 57, 2443-2451. <https://doi.org/10.1007/s13197-020-04279-8>
- Bench, B. J., Whittington, W., Kranz, M., & Guerrero, F. (2010). *Determining total fat content by automated acid hydrolysis*. Springfield.

- Benzie, I. F. F., & Strain, J. J. (1996). The ferric reducing ability of plasma (FRAP) as a measure of “antioxidant power”: The FRAP assay. *Analytical Biochemistry*, 239(1), 70-76. <https://doi.org/10.1006/abio.1996.0292>
- Capecka, E., Mareczek, A., & Leja, M. (2005). Antioxidant activity of fresh and dry herbs of some Lamiaceae species. *Food Chemistry*, 93(2), 223-226. <https://doi.org/10.1016/j.foodchem.2004.09.020>
- Chanthasri, W., Puangkeaw, N., Kunworarath, N., Jaisamut, P., Limsuwan, S., Maneenoon, K., Choochana, P., & Chusri, S. (2018). Antioxidant capacities and total phenolic contents of 20 polyherbal remedies used as tonics by folk healers in Phatthalung and Songkhla, Thailand. *BMC Complementary and Alternative Medicine*, 18(1), 1-11. <https://doi.org/10.1186/s12906-018-2131-y>
- Clarkson, C., Maharaj, V. J., Crouch, N. R., Grace, O. M., Pillay, P., Matsabisa, M. G., Bhagwandin, N., Smith, P. J., & Folb, P. I. (2004). *In vitro* antiplasmodial activity of medicinal plants native to or naturalized in South Africa. *Journal of Ethnopharmacology*, 92(2-3), 177-191. <https://doi.org/10.1016/j.jep.2004.02.011>
- Dosumu, O. O., Oluwaniyi, O. O., Awolola, V. G., & Ogunkunle, O. A. (2010). Toxicity assessment of some tea labels from supermarkets in Ilorin, Nigeria using brine shrimp (*Artemia salina*) lethality assay. *African Journal of Food Science*, 4(5), 282-285. <https://doi.org/10.5897/AJFS.9000302>
- Drewnowski, A., & Gomez-Carneros, C. (2000). Bitter taste, phytonutrients, and the consumer: A review. *The American Journal of Clinical Nutrition*, 72(6), 1424-1435. <https://doi.org/10.1093/ajcn/72.6.1424>
- Ekor, M. (2014). The growing use of herbal medicines: Issues relating to adverse reactions and challenges in monitoring safety. *Frontiers in Pharmacology*, 4, Article 177. <https://doi.org/10.3389/fphar.2013.00177>
- Hasmidia, M. N., Liza, M. S., Syukriah, A. R. N., Harisun, Y., Azizi, C. Y. M., & Adibah, A. M. F. (2015). Total phenolic content and antioxidant activity of *Quercus infectoria* galls using supercritical CO<sub>2</sub> extraction technique and its comparison with soxhlet extraction. *Pertanika Journal of Science & Technology*, 23(2), 287-295.
- Hassan, S. H. (2011). Consumption of functional food model for Malay muslims in Malaysia. *Journal of Islamic Marketing*, 2(2), 104-124. <https://doi.org/10.1108/17590831111139839>
- Hassan, W. M. W., & Awang, K. W. (2009). Halal food in New Zealand restaurants: An exploratory study. *International Journal of Economics and Management*, 3(2), 385-402.
- Iglesias, M. S., de Lourdes Samaniego Vaesken, M., & Moreiras, G. V. (2016). Composition and nutrient information of non-alcoholic beverages in the Spanish market: An update. *Nutrients*, 8(10), Article 618. <https://doi.org/10.3390/nu8100618>
- JAKIM. (2006). *Handbook of halal food additives*. Department of Islamic Development Malaysia.
- Kähkönen, M. P., Hopia, A. I., Vuorela, H. J., Rauha, J. P., Pihlaja, K., Kujala, T. S., & Heinonen, M. (1999). Antioxidant activity of plant extracts containing phenolic compounds. *Journal of Agricultural and Food Chemistry*, 47(10), 3954-3962. <https://doi.org/10.1021/jf990146l>
- Kendra, N. K. (2018). Fruit based carbonated soft drinks for nutritional security and value chain development - A review. *International Journal of Current Microbiology and Applied*, 7(11), 3084-3095. <https://doi.org/10.20546/ijcmas.2018.711.354>
- Kostyra, E., Wasiak-Zys, G., Rambuszek, M., & Waszkiewicz-Robak, B. (2016). Determining the sensory characteristics, associated emotions and degree of liking of the visual attributes of smoked ham.

- A multifaceted study. *LWT Food Science and Technology*, 65, 246-253. <https://doi.org/10.1016/j.lwt.2015.08.008>
- Kregiel, D. (2015). Health safety of soft drinks: Contents, containers, and microorganisms. *BioMed Research International*, 12, 1-15. <https://doi.org/10.1155/2015/128697>
- Nielsen, S.S. (2010). *Food analysis*. Springer. <https://doi.org/10.1007/978-1-4419-1478-1>
- Pandey, M. M., Rastogi, S., & Rawat, A. K. S. (2013). Indian traditional ayurvedic system of medicine and nutritional supplementation. *Journal of Evidence Based Complementary Alternative Medicine*, 2013, 1-12. <https://doi.org/10.1155/2013/376327>
- Rahim, N. F., Muhammad, N., Abdullah, N., Talip, B. A., Jihan, N., & Dasuki, S. (2018). Optimization of the antioxidant properties of the polyherbal formulation. *Journal of Advanced Research in Fluid Mechanics and Thermal Sciences*, 50(1), 16-25.
- Rusmana, D., Wahyudianingsih, R., Elisabeth, M., Balqis, B., Maesaroh, M., & Widowati, W. (2017). Antioxidant activity of *Phyllanthus niruri* extract, rutin and quercetin. *The Indonesian Biomedical Journal*, 9(2), 84-90. <https://doi.org/10.18585/INABJ.V9I2.281>
- Saint-Eve, A., Deleris, I., Aubin, E., Semon, E., Feron, G., Rabillier, J. M., Ibarra, D., Guichard, E., & Souchon, I. (2009). Influence of composition (CO<sub>2</sub>) and (sugar) on aroma release and perception of mint-flavored carbonated beverages. *Journal of Agricultural and Food Chemistry*, 57, 5891-5898. <https://doi.org/10.1021/jf900542j>
- Salahudin, A., Hamdan, M. N., & Ramli, M. A. (2015, November 4-5). Penggunaan teknologi pengesanan halal terhadap produk makanan: Kajian menurut perspektif hukum Islam [The use of halal detection technology on food products: A study from the perspective of Islamic law]. In *Proceeding of the 2nd International Convention on Islamic Management* (pp. 1-6). University of Malaya, Malaysia.
- Singh, R. (2018). Formulation of a carbonated herbal health drink with *Hemidesmus indicus* root extract. *International Journal of Advance Industrial Engineering*, 6, 100-104. <https://doi.org/10.14741/ijaie/v.6.2.1>
- Steen, D. V. (2005). Carbonated beverages. In P. R. Ashurst (Ed.), *Chemistry and technology of soft drinks and fruit juices* (pp. 150-180). Blackwell Publishing Ltd. <https://doi.org/10.1002/9780470995822.ch7>
- Thongrote, C., Wirjantoro, T. I., & Phianmongkhol, A. (2016). Effect of carbonation sources and its addition levels on carbonated mango juice. *International Food Research Journal*, 23(5), 2159-2165.
- Wangcharoen, W., Tipvanna, N., & Wilkinson, B. (2006). Formula optimization for garlic and pepper-flavoured puffed snacks. *Songklanakarin Journal of Science and Technology*, 28(1), 63-70.
- Wijaya, C. H. (2019). Optimization of extraction time and temperature for java tea (*Orthosiphon aristatus* BI. Miq) based functional drink production. *Journal of Food and Nutrition*, 2(2), Article 117. <https://doi.org/10.31021/fnoa.20192117>
- Ya'akob, H. (2018). Current scenario of herbal industry in Malaysia. *Journal of Engineering and Science Research*, 2, 7-13. <https://doi.org/10.26666/rmp.jesr.2018.3.2>
- Yahya, H., Samicho, Z., & Azmi, A. F. M. (2016). A review on application of *halalan toyyiban* risk management plant (HTRMP) and frozen food chain during warehousing activities for maintaining halal, safety and quality. *Journal of Applied Environmental and Biological Science*, 6(11), 96-102.

## Comparative Study on the Social Behavior of Sambar Deer (*Rusa Unicorn*) in Three Selected Captive Facilities in Peninsular Malaysia

Kushaal Selvarajah, Mohd Noor Hisham Mohd Nadzir and Geetha Annavi\*

*Department of Biology, Faculty of Science, Universiti Putra Malaysia, 43400 UPM Serdang, Selangor Darul Ehsan, Malaysia*

### ABSTRACT

Sambar deer was up-listed from Least Concern to Vulnerable by the IUCN Red list in 2015. The local government has initiated *Ex-situ* conservation efforts to boost sambar deer numbers in captivity and reintroduce them into the wild. The reproductive success of sambar deer and their welfare management practices in captivity are important components for effective captive breeding programs. However, there has been a lack of study on sambar deer in recent years, especially about their behavior in captivity. This study aimed to identify environmental factors that may influence the behavior of the captive sambar. Three captive sites were selected and observed for an average of 40 days at each site (minimum 37 days to maximum 43 days, 6 hours/day). A Generalized Linear Model was used to determine the correlation between social behavior and extrinsic parameters. 'Captive sites' showed the strongest correlation in behavioral variability environmental settings, such as the size of the enclosure, could force the deer to spend more time in a herd, which increases the frequency in grooming, which was recorded to be highest in Zoo Negara compared to other captive sites. Time of day also significantly influenced certain behavior skewed towards morning slots. It could be due to an adaptive behavior to the feeding time in the captive sites being often in the morning, which caused the deer to rest towards the afternoon. A

suggestion would be to create a more erratic feeding schedule to ensure that the deer adapt to behavior variations. An extensive study needs to be done on sambar deer to pinpoint the specifics and better understand these possible influential factors in their behavior.

**Keywords:** Captivity, *ex-situ* conservation, generalized linear model, sambar deer, social behavior

### ARTICLE INFO

#### Article history:

Received: 25 June 2021

Accepted: 15 September 2021

Published: 10 January 2022

DOI: <https://doi.org/10.47836/pjst.30.1.29>

#### E-mail addresses:

[kushaal94@gmail.com](mailto:kushaal94@gmail.com) (Kushaal Selvarajah)

[mnhisham@upm.edu.my](mailto:mnhisham@upm.edu.my) (Mohd Noor Hisham Mohd Nadzir)

[geetha@upm.edu.my](mailto:geetha@upm.edu.my) (Geetha Annavi)

\*Corresponding author

## INTRODUCTION

Sambar deer (*Rusa unicolor*) are ungulates defined as hoofed placental mammals distributed across Afro-Eurasia and the New World (Hendrix & Vos, 2019). Unfortunately, due to poaching and deforestation, their status moved from being 'Least Concerned' in 1996 to 'Vulnerable' in 2015 (Timmins et al., 2015). In addition, the population of sambar deer in their native range has been declining, resulting in a regional abundance in areas that are well protected (Timmins et al., 2015). In some countries, such as Australia, sambar deer are considered a pest after being introduced (Gormley et al., 2011). In Sabah, the sambar deer population has been instilled to decline in numbers based on interviews carried out in local communities. The decline was based on the increase in licenses issued to hunt the deer (Wong et al., 2012). This trend shows a need to investigate captive populations as an option for conservation efforts, which is at the center of our research.

Sambar deer are nocturnal species when they are active during the night (e.g., feeding and locomotion) compared to during the day. This behavior was developed as a strategy against predators and to decrease thermoregulatory stress, especially in tropical areas (Semiadi et al., 1993). However, due to the captive environment, they have adapted to grazing more frequently during the day (Couchman, 1978). Other studies have also observed through camera trap data and activity pattern analysis that sambar deer are cathemeral (Tan et al., 2018). In addition, sambar deer have been recorded in the wild to be solitary and rarely in a herd (Wong et al., 2019).

Sambar deer prefer mixed forest habitat as they provide essential shade area, watering holes, and high temperature, especially during daytimes (Chatterjee et al., 2014). Seasonal variation was shown to influence the time budget allocation of female Alpine musk deer to sustain energy lost during pregnancy, lactation, and parturition by increasing its ingestive optimization. It was done by increasing locomotion (standing-gazing and moving) rather than bedding (Meng et al., 2011). The visitor density/frequency was proven to induce higher pacing in jaguars compared to Sellinger and Ha (2005), which showed no association between visitor frequency and pacing. However, they speculated by tying pacing jaguars with other factors (e.g., enclosure size, shrubs/plants) (Vidal et al., 2016).

One of the main threats to sambar deer is poaching. The meat of sambar deer is of high value in Malaysia, contrary to some other species, such as wild boars or tapirs related to superstitious or religious beliefs leading this species towards local extinction due to hunting. In the case of not having sambar deer farms in Peninsular Malaysia, wild sambar meat is sold under the disguise of farmed Javan rusa (*Rusa timorensis*) to escape legal actions (Kawanishi et al., 2014). An interview-based survey across five sites located in Peninsular Malaysia showed that a hunting ban on sambar and muntjac was implemented for the 11-months in 2011, but all studied sites had ignored such restriction, and the hunting was carried out throughout the year (Goldthorpe & Neo, 2011).



Enclosure size and natural substrates (e.g., vegetation, grass, wood chips, water body), which were preferable over concrete flooring, were shown to decrease stereotypic behavior, specifically pacing and increased exploratory behavior (e.g., drinking, grooming, stalking) in tigers (Pitsko, 2003). Shaded areas provide ungulates with a resting place, as they require cooling their bodies in tropical climates, which reduces their foraging activity. The enclosure space should not only fit the functional dimensions of the species housed but, more importantly, permit reactive response and provide a comfortable living situation (Tennessen, 1989). For species with a wide home range, such as carnivores, can influence the frequency of pacing in a captive setting (Clubb & Mason, 2003). Space utilization was observed in leopards in Indian zoos that showed frequent pacing at the edge of the enclosure and high resting towards the back of the enclosure that shied away from the presence of visitors (Mallapur et al., 2002).

Poached species, in particular, tend to be more nocturnal to reduce hunting pressure (Tan et al., 2018). As a comparative, tapirs were found to increase their lip-licking behavior to decrease their internal temperature. It is recommended that the enclosure have a watering pool or mud wallow that allows them to physically reduce their body temperature (Arumugam & Buesching, 2019). Lions in captivity were observed to reduce normal behavior in an environment with minimal facilities compared to lions kept in a larger facility. The receptiveness of female sambar deer was shown to be lower than other ungulates species, and the semen produced by stags varies based on age and health conditions (Muir et al., 1997), which contributes to the difficulty to breed them in captivity. Reproductive success in *ex-situ* environments compared to wild populations could be attributed to poor species-appropriate socio-environmental settings (Lindburg & Fitch-Snyder, 1994).

The research aimed to determine possible extrinsic parameters (captive sites, time of day, temperature, and rain) that may influence the social behavior of sambar deer in the various captive sites in Peninsular Malaysia. An extension of this, an ethogram was updated and modified from a study done by Aun and Rahman (1989) working with the same species.

## MATERIALS AND METHODS

### Study Site and Field Methods

This study was carried out at (a) Zoo Negara, Selangor (3°12'32.8"N 101°45'29.6"E), (b) Zoo Taiping, Perak (4°51'17.9"N 100°45'05.2"E) and (c) Sungkai Captive Wildlife Centre, Perak (4°01'54.3"N 101°22'09.9"E). These sites were categorized into two, captive (permitted to visit by the public) inclusive (a) and (b) and semi-captive (no visitor, located away from human settlements and the habitat is set up close to mimic sambar deer's natural environment) referring to (c). These captive sites were based on availability and permission from each zoo and the Department of Wildlife and National Parks (DWNP). Sungkai Captive Wildlife Center was chosen as it has a reintroduction program for sambar deer.

Zoo Negara was officially opened to the public in 1963 and since then has become one of the main attractions for tourists in Malaysia. The zoo hosts up to over 450 species of wildlife. The sambar deer, *Rusa unicolor*, is kept in an enclosure measuring 100.9 meters (length) x 15 meters (width), as depicted in Figure 1. There are 11 individuals of sambar deer consisting of two stags and nine does. Based on records obtained by the zoo, the two stags were transferred from the Wildlife Conservation Centre in Sungkai, Perak, under the management of the Department of Wildlife and National Parks (DWNP) in the year 2014. The enclosure is shared among two other species, hog deer (*Axis porcinus*) and spotted deer (*Axis axis*). Their numbers and size vary among species. In addition, the enclosure has three moat pools with varying sizes located on the left side of the enclosure. The perimeters of these moats are covered in cement. There are two big huts/shelters labeled as night dens, each on opposite ends of the enclosure and a smaller shelter for the feeding area that was newly built.

In addition, there are two big islands for the deer to rest and take shelter as these 'islands' have moderate-sized trees that provide shade. One of these islands was only constructed in the mid of 2018. The enclosure has sandy and muddy grounds, and not much vegetation can be seen. The perimeter is covered with wired fences. There are two viewing docks for visitors to observe the deer. The enclosure has soil and gravel as their flooring, and only certain areas, such as the feeding hut and shelters, are with cemented flooring. There are a couple of puddles created naturally from heavy rainfalls near the main viewing dock. In addition, there are not many natural covers or shade from trees as there are only a few fully-grown trees in the enclosure. Each of these trees is wrapped with wire fencing around its trunk to avoid debarking from the deer. The newly made "island" has been planted with varying species of flora but is currently not opened to the deer to allow the island to settle in fully. The width of the enclosure runs along a housing area with a small gap in between for the keepers to maneuver through. On the right side of the enclosure is a small patch of unused land overgrown with various flora species.

Zoo Taiping is located towards the northern side of Peninsular Malaysia. The town is surrounded by mountainous terrain sheltering from the harshest weather. The enclosure measures 75.3 meters x 29.5 meters (Figure 2). The enclosure consists of one wallowing pool and five sets of night quarters, each measuring 5.4 meters x 5.7 meters. There are several large trees within the enclosure. The tree barks are wrapped with flexible wire fencing to prevent the sambar deer from debarking the trees. The enclosure is described to be surrounded by greenery. The ground is fully-grown with grass, and the trees provide plenty of shady areas for the deer. Moreover, there are several mud puddles (made naturally) that the deer wallow in during hotter days. The enclosure consists of twelve individuals; three stags, six does, and two younger deer. Just a few days before sampling in Zoo Taiping was completed, one of the does has given birth to a newborn fawn making the total number of individuals is fourteen.

The Sungkai Conservation Centre was built by the Malaysian government body for wildlife (DWNP). This center is dedicated to rescuing wildlife in conflict and captive breeding for endangered species. The area hosts various wildlife species, such as the Malayan tiger, Malayan sun bear, and Seladang/Gaur, aside from sambar deer. Other captive facilities across Malaysia have been built for the same purpose. However, Sungkai Conservation Centre was chosen based on logistics, funding, and, more importantly, accessibility. The enclosure measures 212 meters x 68 meters (Figure 3). Over 60 individuals are in an enclosure, making it difficult to differentiate between individuals. The ground is fully grown with grasses and shrubs alongside large trees. The keeper claimed that the enclosure had more trees when it was newly made. However, due to debarking behavior of the deer, most of the trees had fallen over time. As a result, shaded areas are scarce, and not much wallowing pool can be found unless created naturally from heavy rainfall. The whole area is divided into four different paddocks with varying sizes but located just next to each other. These paddocks are well secured with high fences, with gates and corridors between each of the paddocks. There are huts or shelters in each paddock, hung with salt blocks and huge pails filled with water. The terrain of the paddock is quite uneven, with several places with deeper ends creating holes by which the deer take quick dips.

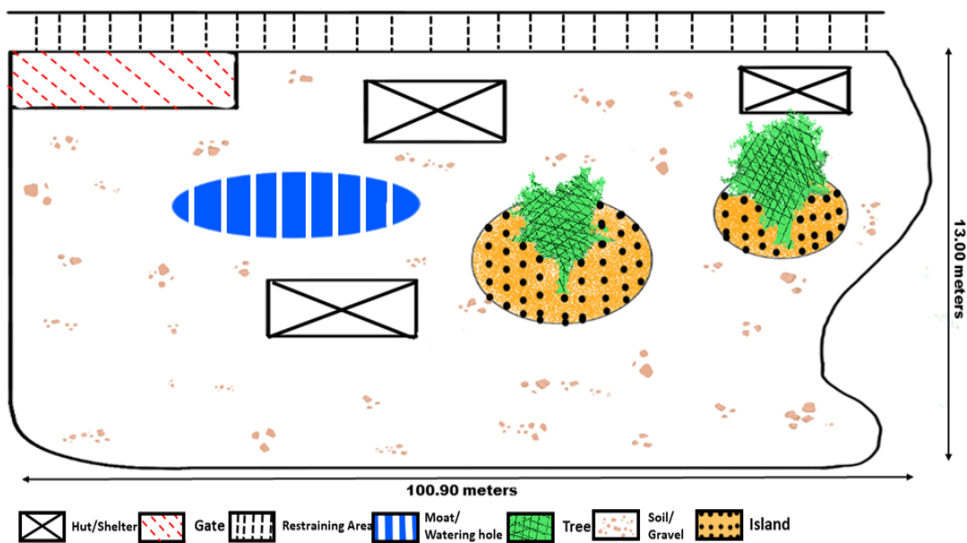


Figure 1. The layout of the sambar deer paddock in Zoo Negara. The layout shows the perimeter of the paddock and the vegetation areas, as well as the moat and feeding area.

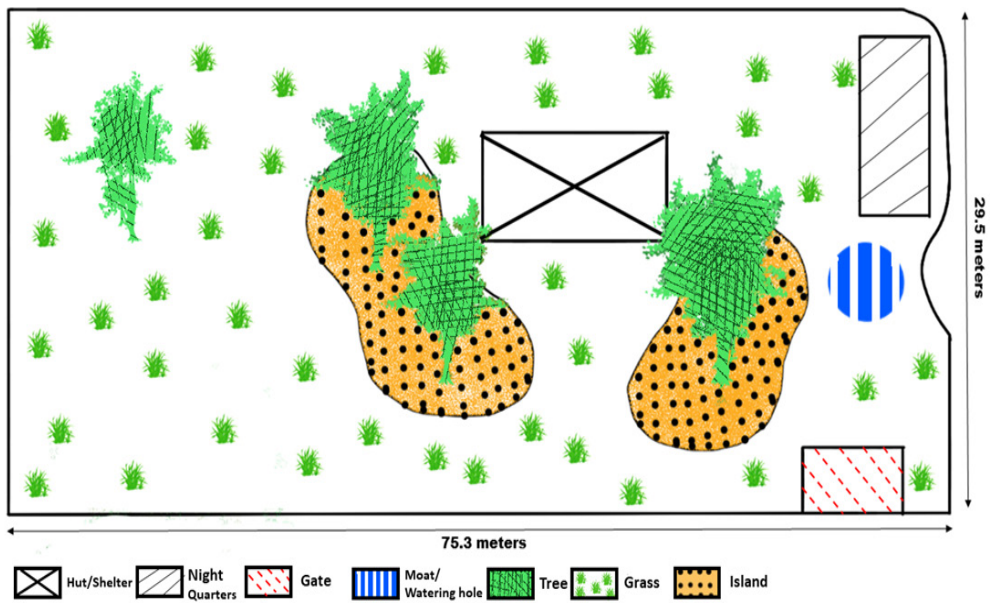


Figure 2. The layout of the sambar deer paddock in Zoo Taiping, Perak. The layout shows the perimeter of the captive area and the feeding hut, as well as vegetation plots.

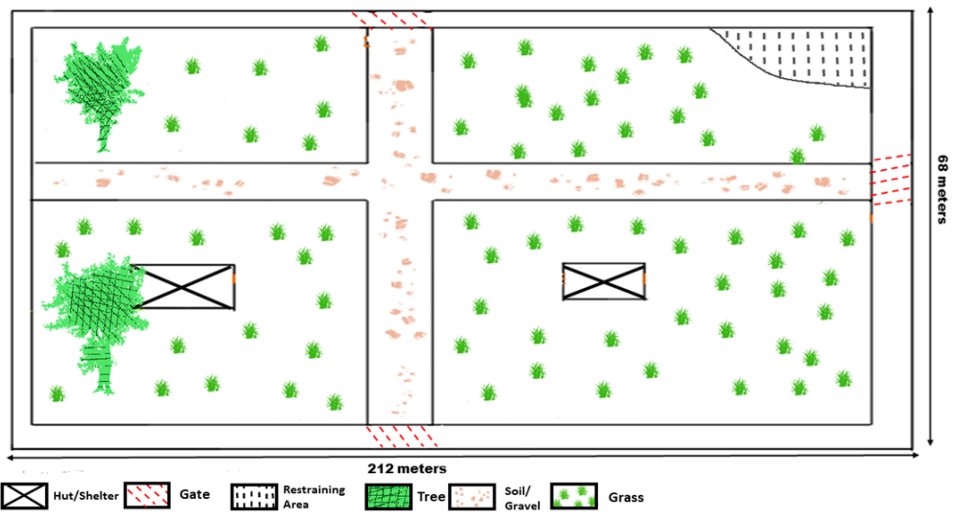


Figure 3. Overview of the Sungkai Conservation Centre managed by the Department of Wildlife and National Parks. There are four separate paddocks where they are rotated from time to time to allow for the vegetation to grow.

## Ethogram and Behavioral Observations

The ethogram used in this study was a modified and adapted list of repertoires of behaviors that are common for ungulates studies (Table 1). The main body of the ethogram was adapted from Aun and Rahman (1989), who also worked on sambar deer in Zoo Melaka, Malaysia studying their behavior in captivity. It was the earliest recorded study on sambar deer behavior in Malaysia. The ethogram was further modified and adapted to current progress and understanding in the animal behavior field (Aun & Rahman, 1989; Semiadi et al., 1994; Semiadi et al., 1995; Lu et al., 2009; Xiaofeng et al., 2011; Powell et al., 2013; Razal et al., 2017; Arumugam & Buesching, 2019: Table 1). Institutional Animal Care and Use Committee, Universiti Putra Malaysia, approved all the methodologies involved in behavior observation and recordings (Ethical approval ref.: UPM/IACUC/AUP-R042/2018). The diurnal observation was carried out through direct observation.

Deer were observed in the enclosure divided into two-time slots in one day. The first slot begins at 0900hrs to 1200hrs (Morning), and the second slot begins at 1400hrs to 1700hrs (Afternoon), three hours of observation per slot total of six hours of observation per day. The three hours slots were broken down into observation points that lasted for ten minutes with a five minutes interval in between points (Aun & Rahman, 1989). Observations were not carried out between 1200hrs and 1400hrs as sambar deer have been known to be least active during these periods (Semiadi et al., 1993) and allowed the observer to have a break between observation periods. A scan sampling method was used to collect these behavioral data. Each frequency of behavior observed is taken as one data point (Table 2), which is accumulated at the end of the ten-minutes observation period. At the beginning of each observation slot, the temperature and humidity were recorded once for each ten-minute observation using a handheld digital thermometer and humidity device. Social behavior was recorded and categorized as interactions between two or more individual deer within the group at any given point of time during observations.

The data points were recorded on a spreadsheet focused on the herd behavior of sambar deer, which focuses on their social behavior. The number of individuals observed varied depending on the study sites. Assumptions were made that these observations would not affect the results. Unfortunately, tagging the deer was not permitted in any of the study sites, providing a challenge and obstacle to identifying or differentiating between individuals unless they have natural markings on the body that can be easily seen. An observation point was established at the beginning of each captive site observation period, and this point did not change throughout as not to influence or affect the behavior of the captive sambar deer.

In addition to observation, the enclosure space and area settings and layout were also recorded alongside informal discussion with their caretaker to take note of general ideas of their daily behavior to aid with the finalization process, for example, the average feeding time and their movement in the enclosure.

Table 1

*Adapted and modified ethogram applied for this study with specifics to social behavior and alertness behavior with extensive definition and description included for each behavior.*

<b>Behavioral Grouping</b>	<b>Behavior Subgroup</b>	<b>Description</b>
<b>Courtship</b>	Low Stretch (LS)	Male approaches female from the rear with head lowered
	Anogenital sniff (AN)	Male approaches female and sniffs and licks vulva
	Follow (FO)	Male follows female after walking away
<b>Receptive</b>	Flehmen (FL)	Head may be raised above horizontal, and lips curled Lips usually opened after smelling dung or urine Lips usually opened after smelling dung or urine
	Urine- Drinking (DU)	Males drink the urine of a female
<b>Pre-mounting</b>	Neck-gripping (NG)	Male anchoring the female by placing the neck on the upper back of the female
	Chin-resting (CR)	Male rest chin/head on the rump of a female
<b>Aggression</b>	Rutting (RU)	Rubbing of antlers (stripping of large areas of barks on trees)
<b>Grooming</b>	Allo-grooming (GR)	Grooming between 2 individuals. One being the groomer and one being the groom.
<b>Defensive</b>	Lookout (LO)	Individuals being attentive to their surrounding Head is usually horizontal or above with eyes open Ears are moving often or aligned with the line of sight Occurs with several positions, including standing and sternal recumbent
	Alarmed (AL)	Tail erected with both eyes and ears towards the direction of a threat

### Generalized Linear Model Analysis

A Generalized Linear Model (GLM) analysis was conducted using R- software Version 3.5.1 for the data recorded. The full average intercept was recorded instead of average condition intercepts. The full average includes every model possible, which further narrows down the estimator and is usually used for variables with weaker correlation in accordance with smaller than “subset” estimators. The parameters were averaged, and only those with  $AICc < 7$  were further analyzed and reported.

The data points obtained were analyzed both as individual behaviors and as subgroups. Subgroups were sorted into six major groups; Courtship (Anogenital Sniff, Low Stretch and Follow), Receptive (Flehmen and Urine Drinking), Pre-mounting (Neck Gripping and Chin Resting), Grooming (Grooming), Defensive (Alertness and Alarmed), and Aggression (Rutting). Models with Delta Akaike's Information Criterion ( $\Delta AICc$ )  $< 7$  were chosen for further analysis. Each behavior (Table 3) and subgroups (Table 4) were tested separately for correlations between variables in all three captive sites. The data were standardized with a model script prior to analysis.

The extrinsic parameters included in the GLM analysis were temperature, rain, captive sites, and time of day. These parameters were chosen to test if they affect the behavior of the deer. Some parameters, for example, the presence or absence of visitors, could not be recorded due to limitations. These parameters were then tested against pre-determined social behaviors with the ethogram modified for this study (Table 1). Time of day was divided into two; Morning (0900hrs-1200hrs) and Afternoon (1400hrs-1700hrs).

## RESULT

A total of 1826 data points obtained (Table 2) from direct observations were recorded over 122 days (ZN = 258 hours, ZT = 222 hours, SCC = 252 hours, Total = 732 hours of observation) between May to December 2018. Among the three sites, the highest collective frequency was recorded in Zoo Negara (ZN) (1177 data points), followed by a close margin between Sungkai Conservation Centre (SCC) (326 data points) and Zoo Taiping (ZT) (323 data points). On the other hand, grooming was recorded to have the highest frequency in all three sites (ZN = 492, ZT = 94, and SCC = 104). These data points were accumulated for various analyses, including the compositions of behavior based on each site and GLM between all three sites for an in-depth comparison.

A total of 1177 data points were recorded at Zoo Negara. Grooming encompassed 42% (492 data points) overall, followed by anogenital sniffing 21% (249 data points). The lowest at only 1% overall are rutting (9 data points) and neck gripping (10 data points). In Zoo Taiping, grooming was at 29% (94 data points) and anogenital sniff at 26% (83 data points). Again, the lowest recorded behavior was chin resting at 1%. There were no observations of rutting and neck gripping from Zoo Taiping; grooming recorded 32% (104 data points) overall in Sungkai Conservation Centre, followed by anogenital sniffing at 17% (56 data points). Again, the lowest was neck gripping and chin resting, resting at  $< 1\%$ .

Captive sites were shown to have the strongest influence on individual behavior, with 73% of the behavior showing significant correlation (Table 3 & Figure 4) and 66% of the subgroups showing strong affiliation to captive sites (Table 4). No subgroups showed any significant correlation to temperature fluctuation, but three behaviors (27%) showed significance: low stretch, follow, and rutting. Receptive grouping was shown to

**Table 2**  
*Mean of each social behavior observed based on individual captive site, average temperature, and the number of days of rain had occurred throughout the study for each captive site. The total frequency of each average site each social behavior to obtain the weighted average of each behavior*

<b>CNC</b>	<b>Temp</b>	<b>Rain (days)</b>	<b>LS</b>	<b>AN</b>	<b>FO</b>	<b>FL</b>	<b>DU</b>	<b>CR</b>	<b>NG</b>	<b>GR</b>	<b>LO</b>	<b>AL</b>	<b>RU</b>	<b>Total Data Points</b>
<b>ZN</b>	29.62	4	0.044	0.213	0.094	0.025	0.030	0.021	0.0008	0.364	0.073	0.067	0.0007	1177
<b>ZT</b>	29.28	6	0.053	0.257	0.086	0.099	0.105	0.0003	0.000	0.291	0.031	0.071	0.000	323
<b>SK</b>	28.50	8	0.080	0.172	0.117	0.071	0.043	0.0003	0.0009	0.319	0.012	0.049	0.126	326 <sup>1</sup>

<sup>1</sup> (LS = Low Stretch, AN = Anogenital Sniff, FO = Follow, FL = Flehmen, UD = Urine Drinking, CR = Chin Resting, NG = Neck Gripping, GR = Grooming, LO = Lookout, AL = Alarmed, RU = Rutting).



be influenced by the presence and absence of rain during the observation period. Time of day (Morning and Afternoon) (Figure 5) resulted in significant influence in less than 40% of the tested individual behavior and only over 30% of the groups.

Table 3

Model-averaged parameters estimate entire sub-models with Delta Akaike's Information Criterion ( $\Delta AICc$ ) < 7 to analyze the relationship between variables and social behaviors. Values in bold are significant.

Explanatory Variables	LS		AN		FO	
	B (CI)	RI	B (CI)	RI	B (CI)	RI
Intercept	-1.64 (-2.06, -1.23)	-	-0.08 (-0.30, 0.15)	-	-1.28 (-1.70, -0.87)	-
Temperature	<b>1.44</b> <b>(0.58, 2.33)</b>	<b>1.00</b>	0.27 (-0.02, 0.83)	0.68	<b>-1.28</b> <b>(-0.43, -2.09)</b>	<b>1.00</b>
Rain	-0.65 (-2.78, 0.46)	0.56	-0.47 (-1.53, 0.10)	0.65	-0.79 (-2.81, 0.30)	0.62
Captive sites	-0.04 (-0.78, 0.49)	0.28	<b>-1.23</b> <b>(-1.63, -0.80)</b>	<b>1.00</b>	<b>-0.56</b> <b>(-1.36, -0.07)</b>	<b>0.78</b>
Morning/ Afternoon	<b>1.67 (0.89,</b> <b>2.45)</b>	<b>1.00</b>	<b>0.48</b> <b>(0.10, 0.90)</b>	<b>1.00</b>	<b>1.28</b> <b>(0.57-1.97)</b>	<b>1.00</b>

Explanatory Variables	FL		UR		CR	
	B (CI)	RI	B (CI)	RI	B (CI)	RI
Intercept	-1.40 (-1.77, -1.04)	-	-1.28 (-1.63, -0.94)	-	-3.59 (-4.60, -2.58)	
Temperature	-0.12 (-0.89, 0.28)	0.39	-0.33 (-1.04, 0.03)	0.66	0.43 (-0.37, 1.98)	0.54 <sup>1</sup>
Rain	-1.67 (-3.90, 0.15)	0.89	-1.02 (-2.46, 0.43)	0.57	0.32 (-0.73, 2.43)	0.37
Captive sites	-0.04 (-0.66, 0.40)	0.28	<b>-0.67</b> <b>(-1.17, -0.16)</b>	<b>0.93</b>	<b>-2.79</b> <b>(-4.33, -1.23)</b>	<b>1.00</b>
Morning/ Afternoon	-0.02 (-0.70, 0.55)	0.28	0.26 (-0.37, 0.87)	0.39	0.08 (-0.96, 1.63)	0.32

Full model: model<-glmer (LS ~ (1|Day) + Captive Sites + Temperature + Time of Day (Morning / Afternoon) + Rain, family = "Poisson", data = Mydata)

<sup>2</sup> (LS = Low Stretch, AN = Anogenital Sniff, FO = Follow, FL = Flehmen, UD = Urine Drinking, CR = Chin Resting, NG = Neck Gripping, GR = Grooming, LO = Lookout, AL = Alarmed, RU = Rutting). B (CI) = Estimated mean (95% Confidence Interval) and RI = Relative Importance.

Table 3 (Continue)

Explanatory Variables	NG		GR		LO	
	B (CI)	RI	B (CI)	RI	B (CI)	RI
Intercept	-1.23 (-6.11, 6.11)		0.40 (0.20, 0.61)		-2.54 (-3.20, -1.89)	
Temperature	7.40 (-8.90, 3.77)	0.52	0.004 (- 0.33, 0.36)	0.26	0.17 (-0.33, 1.26)	0.40
Rain	-4.33 (-1.76, 1.76)	0.28	0.05 (-0.35, 0.66)	0.30	0.06 (-0.74, 1.20)	0.28
Captive sites	-5.27 (-6.24, 2.91)	0.32	<b>-1.51</b> <b>(-1.89, -1.12)</b>	<b>1.00</b>	<b>-2.60</b> <b>(-3.62, -1.60)</b>	<b>1.00</b>
Morning/ Afternoon	-4.63 (-3.04, 1.02)	0.48	<b>0.51 (0.33, 0.70)</b>	<b>1.00</b>	<b>0.59 (0.10, 1.16)</b>	<b>0.93</b>

<sup>3</sup> (LS = Low Stretch, AN = Anogenital Sniff, FO = Follow, FL = Flehmen, UD = Urine Drinking, CR = Chin Resting, NG = Neck Gripping, GR = Grooming, LO = Lookout, AL = Alarmed, RU = Rutting). B (CI) = Estimated mean (95% Confidence Interval) and RI = Relative Importance.

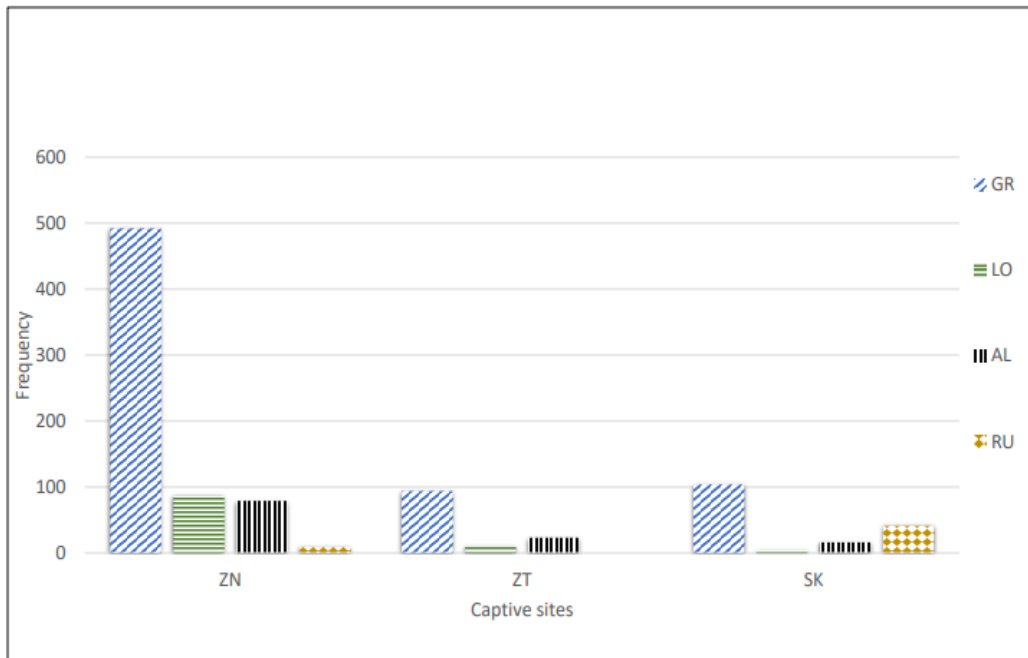


Figure 4. The graphs show the significant behavior recorded in each captive site against the total frequency of observations.

Table 4

Model-averaged parameters estimate entire sub-models with Delta Akaike's Information Criterion ( $\Delta AICc$ ) < 7 to analyze the relationship between variables and grouped social behaviors. Values in bold are significant.

Explanatory Variables	Courtship		Receptive		Pre-mounting	
	B (CI)	RI	B (CI)	RI	B (CI)	RI
Intercept	0.30 (-9.47, 9.47)		-0.90 (-1.22, -0.58)		-3.36 (-4.36, -2.37)	
Temperature	0.73 (-2.73, 1.76)	1.00	-0.24 (-0.79, 0.06)	0.66	0.71 (-0.06, 1.93)	0.75
Rain	-0.89 (-1.47, 1.47)	0.89	<b>-1.25</b> <b>(-2.61, -0.12)</b>	<b>0.91</b>	0.13 (-1.22, 2.07)	0.29
Captive sites	-1.07 (7.52, 4.98)	1.00	<b>-0.40</b> <b>(-1.06, -0.0005)</b>	<b>0.74</b>	-2.29 (-1.15, 1.29)	0.35
Morning/Afternoon	0.85 (-2.07, 1.38)	1.00	0.02 (-0.48, 0.58)	0.35	0.003 (-1.17, 1.29)	1.00

Explanatory Variables	Grooming		Defensive		Aggression	
	B (CI)	RI	B (CI)	RI	B (CI)	RI
Intercept	0.40 (0.20, 0.61)		0.67 (0.48, 0.86)		-6.21 (-9.47, 9.47)	
Temperature	0.004 (-0.33, 0.36)	0.26	0.04 (-0.20, 0.41)	0.31	-8.00 (-2.73, 1.76)	0.65
Rain	0.05 (-0.35, 0.66)	0.30	0.05 (-0.27, 0.57)	0.31	-2.45 (-1.47, 1.47)	0.70
Captive sites	<b>-1.51</b> <b>(-1.89, -1.13)</b>	<b>1.00</b>	<b>-1.53</b> <b>(-1.90, -1.16)</b>	<b>1.00</b>	<b>2.87 (7.52, 4.97)</b>	<b>1.00</b>
Morning/Afternoon	<b>0.51 (0.33, 0.70)</b>	<b>1.00</b>	<b>0.49 (0.31, 0.66)</b>	<b>1.00</b>	-5.97 (-2.07, 1.38)	0.65 <sup>4</sup>

<sup>4</sup> (Courtship, Receptive, Pre-mounting, Grooming, Defensive and Aggression; refer to Table 1). B (CI) = Estimated mean (95% Confidence Interval) and RI = Relative Importance.

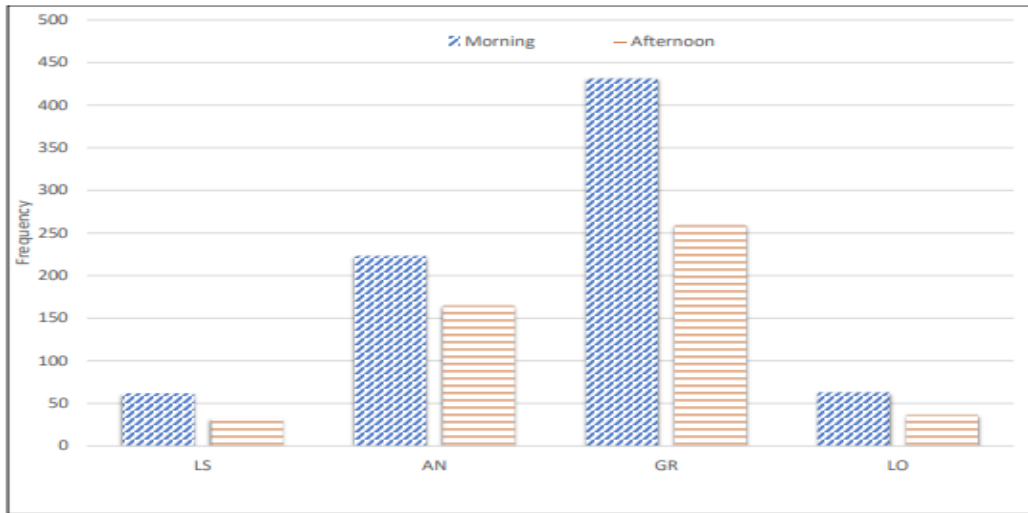


Figure 5. The bar plot is the frequency of each social behavior observed when analyzed according to time of day.

## DISCUSSION

Differences in the behavior of sambar deer across different captive sites are influenced by the varying factors from the external environment. Therefore, it could be suggested that the captive animal tends to react to the change in environment as a form of responsive adaptation (Jaman & Huffman, 2008).

Grooming had the highest frequency in Zoo Negara, followed by Zoo Taiping and Sungkai Conservation Centre (Figure 4 & Table 3). It was an unexpected result given that the individuals in Zoo Negara were the lowest among the three captive sites. An assumption can be made here based on the environmental setting or layout of the paddocks in these captivities. Zoo Negara has arguably the smallest captive area of Zoo Taiping and Sungkai Conservation Centre (Figures 1 to 3). In addition, the paddock in Zoo Negara is shared with two other species, hog deer and spotted deer. Sambar deer have been solitary animals in the wild through camera traps (Wong et al., 2019). However, this could have changed or rather be the opposite in a captive setting. It was seen that the herd in Zoo Negara spend most of their time together around the clock. It is worth noting that this would be higher due to the paddock's sharing with other species of deer, causing them to be in a defensive state constantly. Sambar deer being the bigger species of the other two, could create a territorial space within the paddock. The herd would constantly take shelter or rest after feeding in the shack towards the back end of the paddock, rarely occupied by any other species. Given the time this herd spends together, this could link to the high grooming frequency.

Additionally, all three sites had a high frequency of grooming and anogenital sniffing. Therefore, it could be suggested that grooming could additionally be a form of courting

between a stag and doe and not only shows a display of closeness or hygiene. Moreover, grooming can be seen as a social form of communication (Mooring et al., 2004), which could be related to the behavior of anogenital sniffing as part of the courting process. Grooming, in addition, is a way for the stag to assess the emotion/mood of the targeted doe before moving forward. Being solitary in the wild (Wong et al., 2019), a high frequency of grooming could be an adaptive behavior from their counterpart. However, studies have shown that the relative grooming rate is similar to their wild counterparts in ungulates compared to the rates in a captive population (Hart et al., 1992; Mooring et al., 2000).

The situation is different in the other two captive sites as sambar deer, and no other species only occupied each site. Naturally being solitary animals, it is expected for the herd to spend less time grooming or socializing unless necessary as they would in a wild setting. Sambar tends to travel solitarily or in very small groups in the wild (Bhattarai & Kindlmann, 2018), which would reflect low social behavior as it would in our findings. Sungkai Conservation Centre was categorized as a semi-captive setting in this study, and the behavior of the herd was as expected and observed in the wild. Each individual would pan out on their own for grazing or foraging and only gathered if it was raining or during resting periods. The lack of shelter or shade in the paddock when it was raining was the only time the herd was observed to be huddled together or when there was a reason to be alarmed or under threat.

The courtship grouping can be assumed to be not mutually exclusive of each other and are distinct behavior of their own as there was no significant difference in correlation to temperature but showed otherwise when analyzed separately. It could also be due to the difference in frequency of the behavior. Anogenital sniff is a behavior commonly carried out by the male towards a female in the herd. It is part of the pre-courtship behavior whereby the male 'checks' if the female is receptive and is ready for copulation by sniffing the genital area of the female. Sambar deer are nocturnal species (Hart et al., 1992) in the wild. Therefore, it could explain the higher frequency of anogenital sniff in the morning (possibly early morning) compared to the afternoon. Another influencing factor would be the feeding time of these deer, which relates to captive sites themselves. All three captive sites had a morning feeding ranging between 0900hrs to 1100hrs. Feeding time could potentially affect their instincts during those times and, in extension, affect their behavior in the afternoon period. However, further research can have a much definitive answer compared to nocturnal observation.

Urine drinking and Flehmen (Receptive group) were analyzed and found to be possibly influenced by the presence of rain, which had the highest frequency in Zoo Taiping are the town of Taiping is known to be the "Rain Town" of Malaysia, receiving an annual average rainfall 3000mm, which has the highest humidity in Malaysia (Yusof et al., 2017), which is supported by the high average humidity that is recorded for this study (73.93%).

Flehmen is a responsive behavior that occurs in ungulates as a chemical sensory evaluation. It is carried out before ovulation, whereby the urine from the female has several types of chemosensory response (Rajanarayanan & Archunan, 2011). High humidity could result in an unsuitable environment for the pheromones to travel through the air naturally as it would during a hotter day. Therefore, it could result in the increase of Flehmen by the stag in captivity. Unlike in the wild, it is much easier to access doe urine for the stags to be receptive to the herd's oestrus cycle. It has been observed on several occasions where the male has directly lowered its head into the stream of a urinating female and has a Flehmen response, after which results in a higher frequency.

At the observation time, Zoo Negara was upgrading their deer display area, resulting in a high frequency of lookout and alarming behavior. Hence, this reading could be an inaccurate display of their natural behavior as there were strong external influences. The low frequency of lookout and alarmed in Sungkai Conservation Centre was due to the area not being opened to the public, which clearly can be seen as their surrounding environment much easily triggered them, for example, a falling branch or loud noises as their feed is brought into the paddock usually with a small truck or lorry. The herd tends to stay away from the vehicle (especially the females) until the keepers are a distance from the area. The deer in Sungkai Conservation Centre are kept and conditioned, mimicking as closely to their natural setting as possible. Hence, they are not accustomed to external factors, such as visitors or heavy movement, compared to the herds in Zoo Negara and Zoo Taiping. They are also rarely exposed to any external stimulus, further keeping their instincts compared to their counterparts in full captivity.

Rutting was highest based on the number of frequencies in Sungkai Conservation Centre. It could simply be due to the higher number of stags in the area as compared to the other captive sites. In addition, competition for mating as more does could contribute to increased aggression between stags. In the wild, stags are observed to be purely solitary (Matsubayashi et al., 2007), meaning that they would only be together if a doe is receptive for mating reasons. The abnormal amount of stag could create an area of increased aggression, which shows that the sambar deer in Sungkai Conservation Centre is closer in behavioral similarities to their counterparts in the wild. Rutting was shown to be influenced by temperature and captive sites. Rutting often occurs when there are more competing males in an area, resulting in a higher observation frequency in Sungkai Conservation Centre compared to the other captive sites. Moreover, it is only relevant that rutting occurs at a higher temperature, indicating a sunny day where the deer are more active as compared to on a rainy day.

Variation in captive environments thus proves to affect the behavior of captive sambar. Creating an immersive and suitable display compound is lacking in these captive sites. It could be due to a lack of funds in these sites or expertise and understanding of this species.

In the case of Sungkai Conservation Center, where the reintroduction program takes place, to sustain a healthy captive population in terms that are fitting to be released needs to be addressed and practiced by prioritizing improving the surrounding environment and not solely on just breeding and feeding.

Long-term strategies should include changing these captive holdings to reduce their negative impact on the population. A simple but important change would be to add more shaded areas, especially in Sungkai Conservation Center, to encourage better social interaction between individuals rather than creating scarce shaded areas, which disconnects the population often. We were also informed that the debarking behavior of sambar deer in captivity has proven to be an issue as the trees would eventually rot and fall, contributing to the lack of shaded areas. Captive sites, such as Zoo Negara, have taken the approach of securing the bottom of the tree trunks with wire mesh to prevent debarking from taking place. It is a potential solution, but captive management should also provide a scratch post or debarking trunk to encourage debarking behavior naturally rather than depleting it together. More importantly, creating shaded areas mimics the dense Malaysian forest with a dense canopy cover. For example, Zoo Taiping created shaded and non-shaded areas within their captive sites, which gave the population an opportune environment for both conditions.

It is worth noting that Zoo Negara may have had a higher social frequency, but this was contributed to the smaller captive area and having to share this area with other species of deer rather than having a suitable environment, which could potentially deplete other forms of behavior and induce higher stress levels, which can be studied further. Hence, having a higher level of social interactions between individuals may not necessarily be the best scenario as this means, that sambar being a solitary animal in the wild, may not be able to adapt if need be, reintroduced into the wild.

## CONCLUSION

With current awareness and movements, the ideology separating captive-held animals and the wild is becoming blurred. Aquariums and zoos are becoming more aware and involved in conservation programs in the field while conserved and natural habitats are being intensively managed and diversified (Minteer & Collins, 2013). Zoo's settings should mimic the natural settings of the captive species as closely as possible. Hence, captive management in Malaysia should be aware and understand that the environmental settings affect animals in captivity. Moreover, there needs to be a rally of voices amongst stakeholders to push for better captive management funding as this is often overlooked in national plans and thus has to rely solely on donations and tourism. More in-depth research can be done to pinpoint better and understand how to improve captive enclosures to accommodate captive animals better.

## ACKNOWLEDGMENTS

The authors would like to show their utmost gratitude to the management authorities at these conservation centers for allowing them to conduct this research in their facilities. They would also like to thank the zookeepers in Zoo Negara and Zoo Taiping for aiding them throughout the research and the rangers in Sungkai Conservation Centre for providing a place to stay and aiding the first author in the observations. Unfortunately, there was no funding or grant obtained for the use of this research.

## REFERENCES

- Aun, P. K., & Rahman, S. A. (1989). Ethogram of captive sambar deer *Cervus unicolor* at Zoo Melaka. *The Journal of Wildlife and Parks*, 8, 62-70.
- Arumugam, K. A., & Buesching, C. D. (2019). Lip licking behaviour in captive Malayan Tapirs (*Tapirus indicus*) manifestation of a stereotypic or stress related response? *International Journal of Recent Advances in Multidisciplinary Research*, 6(3), 4724-4727.
- Bhattarai, B. P., & Kindlmann, P. (2018). Factors affecting population composition and social organization of wild ungulates in the Chitwan National Park, Nepal. *Journal of Institute of Science and Technology*, 22(2), 156-167. <https://doi.org/10.3126/jist.v22i2.19608>
- Chatterjee, D., Sankar, K., Qureshi, Q., Malik, P. K., Nigam, P., & Dun, D. (2014). Ranging pattern and habitat use of sambar (*Rusa unicolor*) in Sariska Tiger Reserve. *DSG Newsletter*, 26(May), 60-71.
- Clubb, R., & Mason, G. (2003). Captivity effects on wide-ranging carnivores. *Nature*, 425(6957), 473-474. <https://doi.org/10.1038/425473a>
- Couchman, R. C. (1978). *Deer farming* [Victoria]. Agriculture Bulletin-Department of Agriculture Victoria.
- Goldthorpe, G., & Neo, S. H. (2011). A preliminary investigation into the effects of hunting on three large ungulate species in Peninsular Malaysia, with implications for tiger conservation. *Malayan Nature Journal*, 63(3), 549-560.
- Gormley, A. M., Forsyth, D. M., Griffioen, P., Lindeman, M., Ramsey, D. S. L., Scroggie, M. P., & Woodford, L. (2011). Using presence-only and presence-absence data to estimate the current and potential distributions of established invasive species. *Journal of Applied Ecology*, 48(1), 25-34. <https://doi.org/10.1111/j.1365-2664.2010.01911.x>
- Hart, B. L., Hart, L. A., Mooring, M. S., & Olubayo, R. (1992). Biological basis of grooming behaviour in antelope: The body-size, vigilance and habitat principles. *Animal Behaviour*, 44(4), 615-631. [https://doi.org/10.1016/S0003-3472\(05\)80290-8](https://doi.org/10.1016/S0003-3472(05)80290-8)
- Hendrix, E., & Vos, R. A. (2019). *Differentiation between wild and domesticated Ungulates based on ecological niches*. BioRxiv. <https://doi.org/10.1101/629188>
- Jaman, M. F., & Huffman, M. A. (2008). Enclosure environment affects the activity budgets of captive Japanese macaques (*Macaca fuscata*). *American Journal of Primatology*, 70(12), 1133-1144. <https://doi.org/10.1002/ajp.20612>



- Kawanishi, K., Rayan, D. M., Gumal, M. T., & Shepherd, C. R. (2014). Extinction process of the sambar in Peninsular Malaysia. *Deer Specialist Group Newsletter*, 26, 48-59.
- Lindburg, D. G., & Fitch-Snyder, H. (1994). Use of behavior to evaluate reproductive problems in captive mammals. *Zoo Biology*, 13(5), 433-445. <https://doi.org/10.1002/zoo.1430130506>
- Lu, L., Yan, P., Meng, X., Feng, J., Xu, H., Yang, Q., & Feng, Z. (2009). Behavioral patterns of captive alpine musk deer: Sex-specific behavior comparisons. *Frontiers of Agriculture in China*, 3(3), 300-303. <https://doi.org/10.1007/s11703-009-0055-5>
- Mallapur, A., Qureshi, Q., & Chellam, R. (2002). Enclosure design and space utilization by Indian Leopards (*Panthera pardus*) in four zoos in Southern India. *Journal of Applied Animal Welfare Science*, 5(2), 125-137. <https://doi.org/10.1207/S15327604JAWS0502>
- Matsubayashi, H., Lagan, P., Majalap, N., Tangah, J., Sukor, J. R. A., & Kitayama, K. (2007). Importance of natural licks for the mammals in Bornean inland tropical rain forests. *Ecological Research*, 22(5), 742-748. <https://doi.org/10.1007/s11284-006-0313-4>
- Meng, X., Zhao, C., Hui, C., & Luan, X. (2011). Behavioral aspects of captive alpine musk deer during non-mating season: Gender differences and monthly patterns. *Asian-Australasian Journal of Animal Sciences*, 24(5), 707-712. <https://doi.org/10.5713/ajas.2011.10425>
- Minteer, B. A., & Collins, J. P. (2013). Ecological ethics in captivity: Balancing values and responsibilities in zoo and aquarium research under rapid global change. *ILAR Journal*, 54(1), 41-51. <https://doi.org/10.1093/ilar/ilt009>
- Mooring, M. S., Benjamin, J. E., Harte, C. R., & Herzog, N. B. (2000). Testing the interspecific body size principle in ungulates: The smaller they come, the harder they groom. *Animal Behaviour*, 60(1), 35-45. <https://doi.org/10.1006/anbe.2000.1461>
- Mooring, M. S., Blumstein, D. T., & Stoner, C. J. (2004). The evolution of parasite-defence grooming in ungulates. *Biological Journal of the Linnean Society*, 81(1), 17-37. <https://doi.org/10.1111/j.1095-8312.2004.00273.x>
- Muir, P. D., Semiadi, G., Asher, G. W., Broad, T. E., Tate, M. L., & Barry, T. N. (1997). Sambar deer (*Cervus unicolor*) x red deer (*C. elaphus*) interspecies hybrids. *Journal of Heredity*, 88(5), 366-372. <https://doi.org/10.1093/oxfordjournals.jhered.a023120>
- Pitsko, L. E. (2003). *Wild tigers in captivity: A study of the effects of the captive environment on tiger behavior* (Master Thesis). Virginia Tech, USA. [http://www.carnivoreconservation.org/files/thesis/pitsko\\_2003\\_msc.pdf](http://www.carnivoreconservation.org/files/thesis/pitsko_2003_msc.pdf)
- Powell, D., Speeg, B., Li, S., Blumer, E., & McShea, W. (2013). An ethogram and activity budget of captive Sichuan takin (*Budorcas taxicolor tibetana*) with comparisons to other Bovidae. *Mammalia*, 77(4), 391-401. <https://doi.org/10.1515/mammalia-2012-0076>
- Rajanarayanan, S., & Archunan, G. (2011). Identification of urinary sex pheromones in female buffaloes and their influence on bull reproductive behaviour. *Research in Veterinary Science*, 91(2), 301-305. <https://doi.org/10.1016/j.rvsc.2010.12.005>

- Razal, C., Bryant, J., & Miller, L. (2017). Monitoring the behavioral and adrenal activity of giraffe (*Giraffa camelopardalis*) to assess welfare during seasonal housing changes. *Animal Behavior and Cognition*, 4(2), 154-164. <https://doi.org/10.12966/abc.03.05.2017>
- Sellinger, R. L., & Ha, J. C. (2005). The effects of visitor density and intensity on the behavior of two captive jaguars (*Panthera onca*). *Journal of Applied Animal Welfare Science*, 8(776099595), 233-244. <https://doi.org/10.1207/s15327604jaws0804>
- Semiadi, G., Barry, T. N., Muir, P. D., & Hodgson, J. (1995). Dietary preferences of sambar (*Cervus unicolor*) and red deer (*Cervus elaphus*) offered browse, forage legume and grass species. *The Journal of Agricultural Science*, 125(1), 99-107. <https://doi.org/10.1017/S0021859600074554>
- Semiadi, G., Muir, P. D., & Barry, T. N. (1994). General biology of sambar deer (*Cervus unicolor*) in captivity. *New Zealand Journal of Agricultural Research*, 37(1), 79-85. <https://doi.org/10.1080/00288233.1994.9513043>
- Semiadi, G., Muir, P. D., Barry, T. N., Crush, J. R., & Hodgson, J. (1993). Grazing patterns of sambar deer (*Cervus unicolor*) and red deer (*Cervus elaphus*) in captivity. *New Zealand Journal of Agricultural Research*, 36(2), 253-260. <https://doi.org/10.1080/00288233.1993.10417761>
- Tan, W. S., Hamzah, N. A., Saaban, S., Zawakhir, N. A., Rao, Y., Jamaluddin, N., Cheong, F., Saat, N. I. M., Ee, E. N. Z., Hamdan, A., Chow, M. M., Low, C. P., Voon, M., Liang, S. H., Tyson, M., & Gumal, M. T. (2018). Observations of occurrence and daily activity patterns of ungulates in the Endau Rompin Landscape, Peninsular Malaysia. *Journal of Threatened Taxa*, 10(2), Article 11245. <https://doi.org/10.11609/jott.3519.10.2.11245-11253>
- Tennessen, T. (1989). Coping with confinement - Features of the environment that influence animals' ability to adapt. *Applied Animal Behaviour Science*, 22(2), 139-149. [https://doi.org/10.1016/0168-1591\(89\)90050-6](https://doi.org/10.1016/0168-1591(89)90050-6)
- Timmins, R., Kawanishi, K., Gimán, B., Lynam, A., Chan, B., Steinmetz, R., Baral, H. S., & Kumar, N. S. (2015). *Rusa unicolor*. The IUCN Red List of Threatened Species 2015.
- Vidal, L. S., Guilherme, F. R., Silva, V. F., Faccio, M. C. S. R., Martins, M. M., & Briani, D. C. (2016). The effect of visitor number and spice provisioning in pacing expression by jaguars evaluated through a case study. *Brazilian Journal of Biology*, 76, 506-510. <https://doi.org/10.1590/1519-6984.22814>
- Wong, A., Huaimai, Y., Wong, C., & Shukor, J. A. (2012). A study of hunting activity of sambar deer and bearded pig in Paitan Forest Reserve, Pitas, Sabah, Malaysia. *Journal of Tropical Biology and Conservation*, 9(1), 35-47.
- Wong, S. T., Belant, J. L., Sollmann, R., Mohamed, A., Niedballa, J., Mathai, J., Street, G. M., & Wilting, A. (2019). Influence of body mass, sociality, and movement behavior on improved detection probabilities when using a second camera trap. *Global Ecology and Conservation*, 20, Article e00791. <https://doi.org/10.1016/j.gecco.2019.e00791>
- Xiaofeng, L., Changjie, Z., Cenyi, H., & Xiuxiang, M. (2011). Seasonal variation in the behavior of captive alpine musk deer, *Moschus sifanicus*, in Xinglongshan Musk Deer Farm, of China. *Zoologia (Curitiba)*, 27(6), 848-852. <https://doi.org/10.1590/s1984-46702010000600002>
- Yusof, N. S., Hussain, N. H. M., & Rusli, N. (2017). The relationship of heritage trees in urban heat island mitigation effect at Taiping, Perak, Malaysia. *Malaysian Journal of Sustainable Environment*, 3(2), 157-176. <https://doi.org/10.24191/myse.v3i2.5601>

## Synthesis and Performance of PAFS Coagulant Derived from Aluminium Dross

Shiyi Li<sup>1</sup> and Shafreeza Sobri<sup>1,2\*</sup>

<sup>1</sup>Department of Chemical and Environmental Engineering, Faculty of Engineering, Universiti Putra Malaysia, 43400 UPM, Serdang, Selangor, Malaysia

<sup>2</sup>Institute of Advanced Technology, Universiti Putra Malaysia, 43400 UPM Serdang, Selangor, Malaysia

### ABSTRACT

Polymerised aluminium ferric sulphate (PAFS) was prepared from aluminium dross as a coagulant in wastewater treatment. The effects of leaching time, leaching temperature, and sulfuric acid concentrations on the turbidity removal of the wastewater were investigated, and the optimum conditions were determined using response surface methodology. The results showed that the optimum PAFS preparation conditions were at a leaching time of 60 minutes, a leaching temperature of 65°C, and a sulfuric acid concentration of 1 mol/L. Furthermore, experiments were performed to investigate the effect of coagulant dosages using the PAFS prepared under the optimum leaching conditions, settling time and initial pH of the wastewater on the turbidity removal efficiency. As a result, it was found that the optimum coagulation conditions for PAFS coagulants were at a settling time of 15 minutes, coagulant dosage of 0.5g, and raw water pH 8. Under these optimum conditions, the turbidity removal efficiency of the wastewater was 91.45%. The purpose of this study was to investigate the possibility of aluminium dross utilisation as a coagulant agent for wastewater treatment. Therefore, it can be concluded that PAFS prepared by leaching metal oxides from aluminium dross is an effective wastewater coagulant.

*Keywords:* Aluminium dross, PAFS coagulant, response surface methodology, turbidity

### ARTICLE INFO

*Article history:*

Received: 28 June 2021

Accepted: 13 October 2021

Published: 10 January 2022

DOI: <https://doi.org/10.47836/pjst.30.1.30>

*E-mail addresses:*

[eng.ziva@foxmail.com](mailto:eng.ziva@foxmail.com) (Shiyi Li)

[shafreeza@upm.edu.my](mailto:shafreeza@upm.edu.my) (Shafreeza Sobri)

\*Corresponding author

### INTRODUCTION

Recent developments in the transportation and construction industries, the rapid growth of cities, and the discovery of new potential uses have strengthened the position of aluminium as a key structural material. However, the increasing demand

for aluminium in the coming decades will also release a large proportion of wastes in the form of gaseous emissions and solid residue (Adeosun et al., 2014; Tsakiridis et al., 2013). For example, in 1990, about 28 million tons of aluminium metal were produced globally, but only 8 million tons of scrap were recovered, and in 2010, 56 million tons of aluminium metal were produced, and only 18 million tons of scrap were recovered (Mahinroosta & Allahverdi, 2018). It was estimated that in 2020, global demand for aluminium was 97 million tonnes, and nearly 31 million tons of scrap will need to be recycled.

Aluminium dross is some impure mixed metal produced during the aluminium smelting and contains many aluminium oxides, iron oxides, and other metal oxides. The dross is found to be toxic and hazardous to the environment. Therefore, effective disposal of aluminium dross has become an urgent issue for the aluminium industry worldwide, and abundant work has been done on the separation and recycling of the waste product to reduce the burden of toxic liabilities (Mahinroosta & Allahverdi, 2018; Das et al., 2006).

The current aluminium dross treatment involves the separation of the residual aluminium metal from the aluminium oxide, which can recover between 5%-15% of the initial content and then the waste aluminium dross will be landfilled (Adeosun et al., 2014). However, the landfilled dross can cause leaching of the toxic metals into groundwater, causing pollution of the soil and water resources (Das et al., 2006; Adeosun et al., 2014), heavy metal poisoning of surrounding residents (Xiao et al., 2005; Adeosun et al., 2014), soil salinisation, many crop deaths, and serious environmental pollution. Besides, the reactivity of the leached dross with water results in the formation of flammable gases such as ammonia, hydrogen, and methane (Tsakiridis et al., 2013; Murayama et al., 2012).

Vast attention has been given to finding potential applications and resource reutilisation of aluminium dross. Pepper et al. (2016) studied extraction efficiencies of different acids in the recovery of iron and aluminium from red mud, while Rivera et al. (2018) investigated the extraction of aluminium using a dry digestion method followed by water leaching. A study by Mahinroosta and Allahverdi (2018) extracted alumina nanopowder with 97% purity, suitable for catalytic and adsorption applications. David and Kopac (2013) managed to leach alumina from the dross using sulfuric acid, and the purity of alumina is as high as 99%.

In cement and concrete technology, the substitution of aluminium dross for sand as a filler to produce bricks and other building materials can improve the stiffness and stability of the material (Kim et al., 2010). The use of aluminium dross also increases the compressive strength and porosity of cement as a raw starting material for construction and delays the setting time of concrete (Elinwa & Mbadike, 2011; Mailar et al., 2016; Reddy & Neeraja, 2016; Dai & Apelian, 2016). In addition, the oxide compounds, such as aluminium oxide and magnesium oxide, have great potential as industrial grade refractories (Li et al., 2014).

Many researchers have explored the possibility of using aluminium dross as a coagulant agent in water and wastewater treatment and found that it has excellent coagulation

behaviours (Mahinroosta & Allahverdi, 2018; Mavinkattimath et al., 2017). The dross was dissolved in different acidic solutions to produce different coagulants, such as polymeric aluminium chloride (PAC) (Lei et al., 2009), polymeric ferric aluminium chloride (PAFC) (Yan et al., 2016; Cao et al., 2015; Zhang et al., 2015a; Gao et al., 2019), poly-ferric sulphate (PFS) (Liang et al., 2020) and poly-aluminium ferric sulphate (PAFS) (Chen et al., 2020).

PAFS is developed based on poly-ferric sulphate and poly-aluminium sulphate (Chen et al., 2020). It is mainly trivalent aluminium, supplemented by trivalent iron as an inorganic polymer coagulant formed by cross-hydrolysis and polymerisation (Jiang & Zhu, 2021). Aluminium salt coagulants produce large flocs; however, they have difficulty settling and creating high wastewater turbidity. On the other hand, iron salt coagulants are dense and easy to settle (Yang et al., 2019). The combination effect of aluminium and iron salts in PAFS has the advantages of high base degree, large alum bloom, fast coagulation and sedimentation, low dosage, high removal rate, and wide application fields (Zhang et al., 2015a). It also overcomes the poly-aluminium biological toxicity of the coagulant and solves the shortcomings of unclear water and the high colour of the poly-ferric coagulant (Mohd-Salleh et al., 2020; Zhu et al., 2011; Sun et al., 2012).

In this study, the composite coagulant polymeric aluminium ferric sulphate was synthesised by leaching alumina and iron oxide from aluminium dross with different concentrations of sulfuric acid at different temperatures and times. In order to optimise the performance of the polymeric aluminium ferric sulphate, a response surface methodology was used to investigate the interaction between the individual factors and obtain the optimum synthesis conditions. Finally, the optimal coagulation performance of the PAFS coagulant was investigated by studying the effects of wastewater pH, coagulant dosage, and settling time. This study focuses on the acid leaching-based route of aluminium oxide extraction for use as a coagulant agent in wastewater treatment. Studies on treatment and retrieval processes of aluminium dross will reduce the burden of aluminium production industries in terms of waste generation, disposal cost, and environmental pollution by turning hazardous industrial waste into wealth.

## METHODOLOGY

### Chemical Characterization of Aluminium Dross

The aluminium dross sample was obtained from a waste management company in Malaysia. The sample was stored in a sealed polyethene container. The chemical properties of the aluminium dross were determined by X-ray fluorescence (XRF).

### Preparation of PAFS Coagulant

PAFS coagulant was prepared using analytical grade sulfuric acid ( $H_2SO_4$ ), sodium

hydroxide (NaOH), and dipotassium hydrogen phosphate ( $K_2HPO_4$ ). All solutions were prepared using deionised water.

10g of raw aluminium dross was leached using sulfuric acid with different molarities (0.5 mol/L–2.5 mol/L) in a 250ml beaker. The beaker was placed on a hot plate with a magnetic stirrer, and the temperature was varied between 50°C to 100°C. The leaching duration was set between 60 minutes to 120 minutes, and a stirring speed of 350 rpm was used for all experimental works. First, the experimental data were submitted to regression analysis to predict a significant relationship between the data points. Then, the leached solution was filtered using vacuum pumps, followed by washing with deionised water to wash off the precipitates. Next, 0.35g dipotassium phosphate was added to the filtrate. After 10 minutes, sodium hydroxide solution is added to adjust the pH to 1.5. After stirring for 1 hour at 65°C and ageing for more than 24 hours at room temperature, a liquid PAFS coagulant was obtained. Finally, the liquid coagulant was dried at 60°C for several days to obtain a solid coagulant.

### **Wastewater Collection**

The wastewater was collected from a lake located at the Faculty of Engineering, Universiti Putra Malaysia, using the grab sampling method. The lake water was collected in glass bottles that were earlier washed with dilute soap water, followed by double distilled water. The chemical analysis of the wastewater showed that the pH value and turbidity were within the ranges of 6.0-7.0 and 14.4-26.8 NTU, respectively.

### **Optimisation of Leaching using RSM**

Based on the results of the single-factor experiments, Design-Expert software and RSM Box-Behnken Design were used to investigate further the effects of leaching time, leaching temperature, and sulfuric acid concentrations on the turbidity removal. Fourteen sets of experiments were created using Box Behnken Design (BBD). Model applicability was assessed by analysis of variance and significance tests.

### **Turbidity Removal Test**

PAFS coagulant was prepared under the optimum leaching conditions obtained from experimental and optimisation studies. Coagulation experiments were performed using the jar test method to study the effect of wastewater pH (5-10), coagulant dosages (0.1 grams–0.5 grams) and settling time (5 minutes–25 minutes) on turbidity removal efficiencies. The experimental data were submitted to regression analysis to predict a significant relationship between the data points. 300mL of a mixture of wastewater and coagulant was rapidly stirred at 300 rpm for 30 seconds. Then, the mixture was stirred at

170 rpm for two minutes, followed by 50 rpm for five minutes, and left to settle for 10 minutes. Samples for turbidity measurement were extracted from 2 cm below the water surface in the beaker. The turbidity removal efficiency was calculated using Equation 1.

$$\text{TRE} = \frac{(\tau_0 - T)}{\tau_0} \times 100\% \quad (1)$$

Where:

$T_0$ : Initial turbidity of raw wastewater, NTU

T: Turbidity of coagulated wastewater, NTU

## RESULT AND DISCUSSION

### Chemical Composition of Aluminium Dross

Aluminium dross contains a large number of metal oxides with large proportions of aluminium oxides,  $\text{Al}_2\text{O}_3$ . As shown in Table 1,  $\text{Al}_2\text{O}_3$  constitutes 74.71% of the dross content. In addition, the dross contains minor amounts of oxides of other components, such as  $\text{Fe}_2\text{O}_3$ ,  $\text{SiO}_2$ ,  $\text{CaO}$ ,  $\text{BaO}$ ,  $\text{CuO}$ , and  $\text{ZnO}$ . The chemical composition of aluminium dross differs from one factory to another, depending on the production operating conditions, the technology applied for the production process and the type of furnace (Mahinroosta & Allahverdi, 2018).

Table 1

*Metal oxides analysis of the Al Dross using X-ray Fluorescence (XRF)*

Compounds	$\text{Al}_2\text{O}_3$	$\text{Fe}_2\text{O}_3$	$\text{SiO}_2$	$\text{CaO}$	$\text{BaO}$	$\text{CuO}$	$\text{ZnO}$
%	74.71	4.41	6.15	3.46	5.55	0.23	0.073

### Effect of Leaching Temperature on Turbidity Removal Efficiency

The effect of leaching temperatures on turbidity removal efficiency is shown in Figure 1. The temperatures were chosen based on previous studies by other researchers on the effect of varying temperatures on the dissolution of alumina (Sarker et al., 2015; Feng et al., 2020; David & Kopac, 2013). Regression analysis was performed on the experimental data, and results showed that the leaching temperature (X variable) has a significant influence on turbidity removal rate (Y variable) with analysis of variance  $P < 0.05$ , and therefore Y variable was predicted for different temperature values.

The highest turbidity removal efficiency was found to be 80% at 75°C but decreased to 50% when the temperature was increased to 100°C. Generally, the increase in temperature facilitates the reaction and extraction of alumina (Yan et al., 2016). As the reaction temperature increases, the molecular movement speeds up, and the hydrogen ion

activity increases (Mahinroosta & Allahverdi, 2018). As a result, it causes the solubility of aluminium to increase gradually (Su et al., 2010). However, when the temperature is too high, the water vapour inside the container is released, and the concentration of the solution rises (Zhang et al., 2019), which leads to the breakage of chemical bonds (Jiang & Zhu, 2021; Zhang & Ren, 2013). As a result, it causes large amounts of sulphate ions to form a new molecular layer structure, and the solubility of aluminium is reduced (Zhang et al., 2015b), thus inhibiting the extraction of alumina. In addition, high temperatures consume much energy and increase the operating costs of the extraction process.

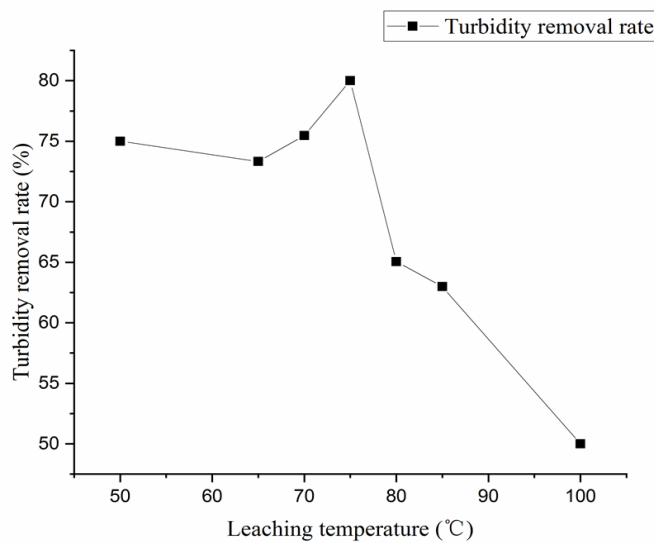


Figure 1. Effect of leaching temperature on turbidity removal efficiency (sulfuric acid concentration: 1 mol/L, leaching time: 60 minutes)

### Effect of Sulfuric Acid Concentrations on Turbidity Removal Efficiency

The effect of sulfuric acid concentrations on turbidity removal efficiency is shown in Figure 2. Regression analysis was performed on the experimental data, and results showed that the sulfuric acid concentrations (X variable) have a significant influence on turbidity removal rate (Y variable) with analysis of variance  $P < 0.05$ , and therefore Y variable was predicted for different acid concentrations. It is evident that the turbidity removal efficiency showed an increasing trend from 68% at 0.5 mol/L to 80% at 1.0 mol/L. It is due to the fact that as the sulfuric acid concentration increases, the sulphate ions increase and the diffusion of hydrogen ions accelerates (Sarker et al., 2015). Aluminium ions form negatively charged ions with sulphate ions (Cui et al., 2015), and the diffusion of aluminium ions start to accelerate (Sarker et al., 2015); thus, the solubility rate increases accordingly (David & Kopac, 2013).



However, the turbidity removal efficiency decreased to 35% when 2.5 mol/L of sulfuric acid was used. When the sulfuric acid concentration is too high, the solubility of basic aluminium sulphate increases (David & Kopac, 2013) and the aluminium ions hinder the diffusion of hydrogen ions (Sarker et al., 2015). Therefore, it causes the aluminium leaching to deteriorate, and turbidity removal becomes erratic. In addition, the liquid thickens, and the solubility of aluminium and iron sulphate decreases.

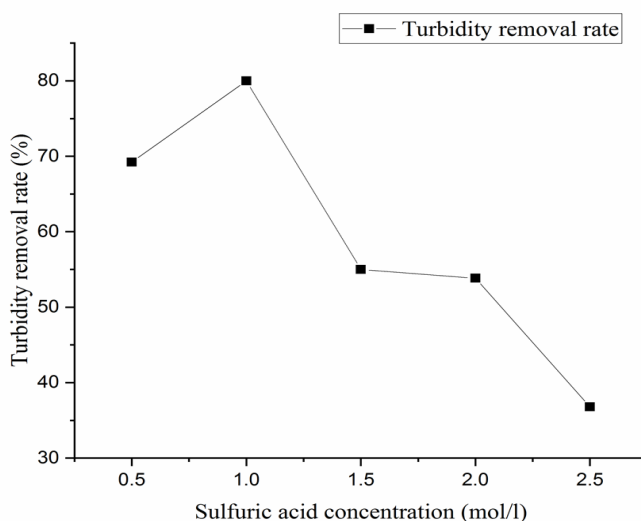


Figure 2. Effect of sulfuric acid concentrations on turbidity removal efficiency (leaching temperature: 75°C, leaching time: 60 minutes)

### Effect of Leaching Time on Turbidity Removal Efficiency

The effect of leaching time on turbidity removal efficiency is shown in Figure 3. Regression analysis was performed on the experimental data, and results showed that the leaching time (X variable) has a significant influence on turbidity removal rate (Y variable) with analysis of variance  $P < 0.05$ , and therefore Y variable was predicted for different leaching times. The time range was chosen because if the reaction time is too short, the reaction will not absorb enough heat, affecting the reaction. However, at prolonged reaction time, the water in the solution evaporates, and the filtrate becomes viscous (Chen et al., 2020), resulting in a loss of some of the leachate during filtration, causing a decrease in turbidity removal efficiency. Based on the results, the highest efficiency was 80% at 60 minutes leaching time but decreased to as low as 45% at longer leaching time.

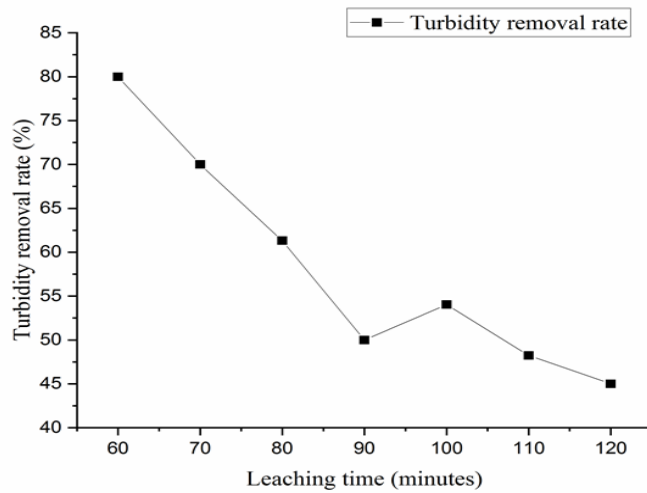


Figure 3. Effect of leaching time on turbidity removal efficiency (sulfuric acid concentration: 1 mol/L, leaching temperature: 75°C)

### Optimisation of Alumina Leaching Conditions Using RSM

Preliminary test results had shown that the leaching temperatures, time, and sulfuric acid concentrations greatly affected the turbidity removal efficiency. Therefore, the upper and lower limit of the three variables were suitable to be chosen as limits for optimisation. The experimental design range showing the levels of the independent variables for the turbidity removal efficiency is shown in Table 2. A total of 14 runs of different conditions were generated in the design matrix. The actual experimental design matrix and results on turbidity removal efficiency are exhibited in Table 3.

Table 2

Experimental factors and levels for optimisation of alumina leaching conditions

Level	Factors		
	A Sulfuric acid concentrations (mol/L)	B Leaching time (minutes)	C Leaching temperature (°C)
1	0.5	60	50
2	1	90	75
3	1.5	120	100

Table 3

*Experimental design matrix and turbidity removal efficiency*

No.	Sulfuric acid concentration (mol/L)	Leaching time (minutes)	Leaching temperature (°C)	Turbidity removal efficiency (%)
1	1	90	50	79.1667
2	1	60	75	83.3333
3	1	120	75	54.1667
4	1	90	100	42.8571
5	1.5	60	100	57.1429
6	1.5	90	75	54.1667
7	1.5	90	75	66.6667
8	1.5	120	50	61.9048
9	1.5	60	50	66.6667
10	1.5	120	100	25.0000
11	0.5	60	75	69.2308
12	0.5	90	100	30.7692
13	0.5	120	75	46.1538
14	0.5	90	50	61.5385

By considering the three independent variables, the maximum turbidity removal efficiency of 82.276% is attainable with PAFS coagulant prepared using one mol/L sulfuric acid at 65°C leaching temperature and 60 minutes leaching time. Table 4 summarises the optimal experimental conditions and the predicted efficiency. A validation experiment at the optimum conditions revealed that the turbidity removal efficiency was 82.353%, which proved that the model is accurate and reliable for predicting optimal conditions for the preparation of PAFS. A conclusion was made based on a small error between the actual and the predicted value, less than 1%.

Table 4

*Optimal experimental conditions and validations*

<b>Sulfuric acid concentration (mol/L)</b>	<b>1.033</b>
<b>Leaching time (minutes)</b>	60
<b>Leaching temperature (°C)</b>	64.804
<b>Predicted turbidity removal efficiency (%)</b>	82.276
<b>Actual turbidity removal efficiency (%)</b>	82.353

Analysis of variance (ANOVA) was employed using Design Expert to evaluate the model's quality statistically, and the result is depicted in Table 5. The most crucial parameter, the Fisher's ratio value (F value) of the model, indicates whether any variable provides a subtle effect on the overall response. The model's F-value was 18.68, indicating that the variance of overall data in the model is 18.68 times greater than the experimental variance and proved that the variables had some effects on the response. However, interpretation of the F value alone is insufficient to determine the variables' significant effect on the response. Based on the p-value (0.0011), the model is considered significant. A p-value of less than 0.05 for the regressions indicates statistically significant model results (Yan et al., 2016). Similarly, the significance of individual terms, such as sulfuric acid concentration, leaching time, and leaching temperature, can be determined from their respective p-value. The most significant term in the current study was B, followed by C, A<sup>2</sup>, C<sup>2</sup>, A, BC, and AC.

Table 5  
*Analysis of variance*

Source	Sum of squares	Degree of freedom	Mean square	F-value	p-value
<b>Model</b>	3453.21	7	493.32	18.68	0.0011
<b>A- sulfuric acid concentration</b>	239.97	1	239.97	9.08	0.0236
<b>B-leaching time</b>	993.43	1	993.43	37.61	0.0009
<b>C-leaching temperature</b>	682.47	1	682.47	25.84	0.0023
<b>AC</b>	29.41	1	29.41	1.11	0.3320
<b>BC</b>	187.43	1	187.43	7.10	0.0373
<b>A<sup>2</sup></b>	312.46	1	312.46	11.83	0.0138
<b>C<sup>2</sup></b>	262.74	1	262.74	9.95	0.0197
<b>Residual</b>	158.49	6	26.41	-	-
<b>Lack of Fit</b>	80.36	5	16.07	0.2057	0.9214
<b>Pure Error</b>	78.12	1	78.12	-	-
<b>Cor Total</b>	3611.69	13	-	-	-

### Effect of Coagulant Dosage on Turbidity Removal Efficiency

The effect of coagulant dosages on turbidity removal efficiency is shown in Figure 4. Different doses of coagulant were added to the wastewater, and the residual turbidity of the treated water samples was measured. Regression analysis was performed on the

experimental data, and results showed that the coagulant dosage (X variable) has a significant influence on turbidity removal rate (Y variable) with analysis of variance  $P < 0.05$ , and therefore Y variable was predicted for different coagulant dosages.

The coagulant becomes more effective as the dosage increases. The turbidity removal efficiency reached 87% with the addition of 0.5g of PAFS coagulant. It is due to the fact that the more coagulant there is, the greater the chance of collision with the particles and the easier it is for the polymer to bond with the particles (Zhu et al., 2011). During the coagulation, the charge on the surface of the particles will bridge with the coagulant (Yan et al., 2016).

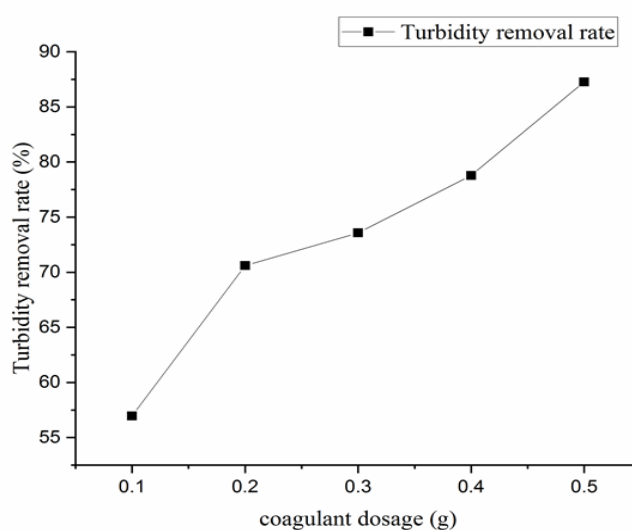


Figure 4. Effect of coagulant dosage on turbidity removal efficiency

### Effect of Wastewater Initial pH on Turbidity Removal Efficiency

The pH of the raw water is an important parameter influencing the removal efficiency of turbidity. In this experiment, the effect of the wastewater pH on the coagulation effect was examined in the range of 5-10. Furthermore, regression analysis was performed on the experimental data, and results showed that the initial pH of the wastewater (X variable) has a significant influence on turbidity removal rate (Y variable) with analysis of variance  $P < 0.05$ , and therefore Y variable was predicted for different pH of the wastewater.

Figure 5 shows that the turbidity removal efficiency increased as the pH increased from 5 to 8, with 86% turbidity removal at a pH of 8. However, as the pH increased to 9, the removal rate decreased significantly. No significant change was observed when the initial pH of the wastewater was increased to 10.

Under acidic conditions, aluminium exists mainly in aluminium ions, which is not conducive to colloidal adsorption and bridging, and flocs are difficult to form (Yang et al.,

2019). However, with increasing pH to alkaline region, the hydrolysis of aluminium ions is accelerated, allowing for enhanced electro-neutralisation (Sun et al., 2017), resulting in more polymers and improved bridging coagulation between ions. At lower alkaline conditions, PAFS coagulants are positively charged, and both coagulants and negatively charged particulate matter are attracted to each other (Zhao et al., 2011), allowing flocs to form easily and turbidity removal to be effective. However, at higher alkaline conditions, the coagulants tend to hydrolyse too quickly (Zhao et al., 2011; Zhu et al., 2011), and the aluminium ions tend to form precipitates, which inhibits the bridging coagulation and therefore has a poor coagulation capacity (Zhao et al., 2016).

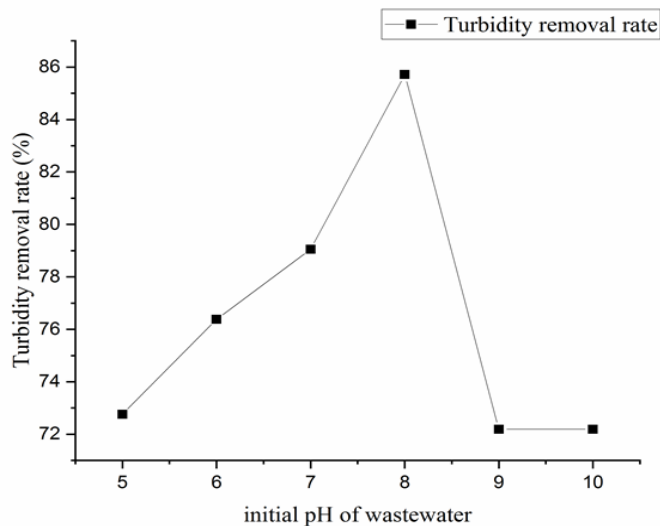


Figure 5. Effect of initial wastewater pH on turbidity removal efficiency

### Effect of Settling Time on Turbidity Removal Efficiency

The effect of settling time on turbidity removal efficiency is shown in Figure 6. Regression analysis was performed on the experimental data, and results showed that the settling time (X variable) has a significant influence on turbidity removal rate (Y variable) with analysis of variance  $P < 0.05$ , and therefore Y variable was predicted for different settling time—the turbidity removal efficiency increases as the settling time increases. As the settling time increases, the chance of collision between coagulants and particles increases, floc formation is complete, and turbidity removal is improved. However, the increment was less significant at a longer settling time. Therefore, 15 minutes was chosen as the optimum settling time.

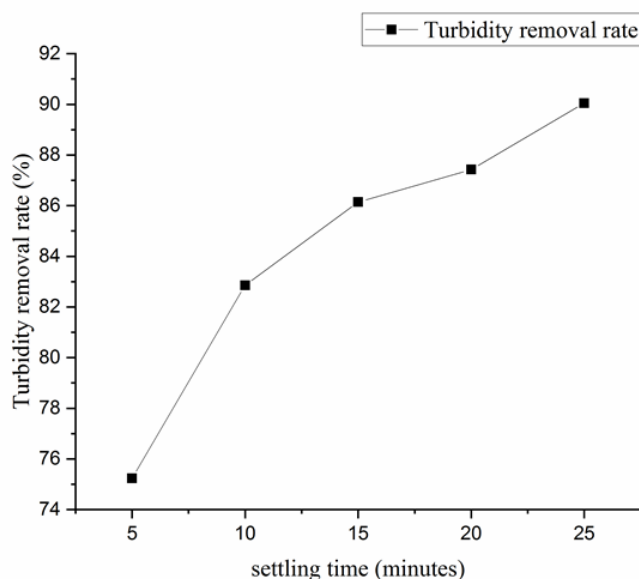


Figure 6. Effect of settling time on turbidity removal efficiency

### Turbidity Reduction Efficiency of Different Coagulants

The investigation was done to compare the performance of the PAFS coagulant obtained from aluminium dross leaching with the commercially available polymeric coagulant. Regression analysis was performed on the experimental data, and results showed that the settling time (X variable) has a significant influence on turbidity removal rate (Y variable) with analysis of variance  $P < 0.05$ , and therefore Y variable was predicted for different settling time.

As shown in Figure 7, both coagulants were able to reduce the turbidity of the wastewater, but it was evident that the PAFS coagulant was more effective than the commercially available coagulant. The turbidity removal efficiency of the PAFS coagulant was recorded to be between 75% to 95%, depending on the settling time. On the other hand, the commercially available polymeric coagulant could only reduce between 41% to 76% of the initial turbidity. This result indicates that the combined action of aluminium and iron salts in the PAFS coagulant can remove a broad range of impurities from wastewater, particularly colloidal particles and dissolved organic substances. The addition of these species to wastewater results in colloidal destabilisation due to the interaction with the negatively charged colloidal particles followed by charge neutralisation (Mwewa et al., 2019).

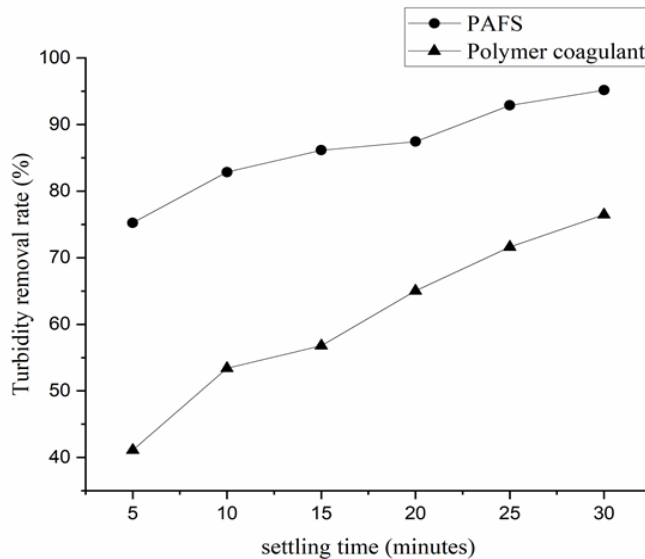


Figure 7. Comparison of turbidity removal efficiency using different coagulants

## CONCLUSION

There is a huge potential to recover alternative coagulants from aluminium dross for wastewater treatment. In this study, acid leaching of aluminium dross was utilised to extract PAFS coagulant from the dross and treatment operations, such as sulfuric acid concentration, leaching temperature and leaching time were considered. The optimum conditions for dissolution of aluminium dross were one mol/L sulfuric acid at 65°C and 60 minutes leaching time. The PAFS coagulants prepared under the optimised leaching conditions were then investigated for their coagulation performance. The turbidity removal efficiency was 91.45% at the optimum coagulant dosage of 0.5 g, raw water pH of 8, and 15minutes settling time. The findings obtained from the present laboratory-scale study may be the basis for the dissolution process on an industrial scale.

## ACKNOWLEDGEMENTS

The authors would like to acknowledge the Master of Environmental Engineering program, Universiti Putra Malaysia under, which this work was funded and completed.

## REFERENCES

- Adeosun, S. O., Sekunowo, O. I., Taiwo, O. O., Ayoola, W. A., & Machado, A. (2014). Physical and mechanical properties of aluminum dross. *Advances in Materials*, 3(2), 6-10. <https://doi.org/10.11648/j.am.20140302.11>



- Cao, B., Gao, B., Wang, M., Sun, X., & Wang, J. (2015). Floc properties of polyaluminum ferric chloride in water treatment: The effect of Al/Fe molar ratio and basicity. *Journal of Colloid and Interface Science*, 458, 247-254. <https://doi.org/10.1016/j.jcis.2015.07.057>
- Chen, J., Li, X., Cai, W., Shi, Y., Hui, X., Cai, Z., Jin, W., & Fan, J. (2020). High-efficiency extraction of aluminum from low-grade kaolin via a novel low-temperature activation method for the preparation of poly-aluminum-ferric-sulfate coagulant. *Journal of Cleaner Production*, 257, Article 120399. <https://doi.org/10.1016/j.jclepro.2020.120399>
- Cui, L., Guo, Y., Wang, X., Du, Z., & Cheng, F. (2015). Dissolution kinetics of aluminum and iron from coal mining waste by hydrochloric acid. *Chinese Journal of Chemical Engineering*, 23(3), 590-596. <https://doi.org/10.1016/j.cjche.2014.05.017>
- Dai, C., & Apelian, D. (2016). Fabrication and characterization of aluminum dross-containing mortar composites: Upcycling of a waste product. *Journal of Sustainable Metallurgy*, 3(2), 230-238. <https://doi.org/10.1007/s40831-016-0071-7>
- Das, B. R., Dash, B., Tripathy, B. C., Bhattacharya, I. N., & Das, S. C. (2006). Production of  $\eta$ -alumina from waste aluminium dross. *Minerals Engineering*, 20(3), 252-258. <https://doi.org/10.1016/j.mineng.2006.09.002>
- David, E., & Kopac, J. (2013). Aluminum recovery as a product with high added value using aluminum hazardous waste. *Journal of Hazardous Materials*, 261, 316-324. <https://doi.org/10.1016/j.jhazmat.2013.07.042>
- Elinwa, A. U., & Mbadike, E. (2011). The use of aluminum waste for concrete production. *Journal of Asian Architecture and Building Engineering*, 10(1), 217-220. <https://doi.org/10.3130/jaabe.10.217>
- Feng, H., Zhang, G., Yang, Q., Xun, L., Zhen, S., & Liu, D. (2020). The investigation of optimizing leaching efficiency of Al in secondary aluminum dross via pretreatment operations. *Processes*, 8(10), Article 1269. <https://doi.org/10.3390/pr8101269>
- Gao, J. Y., Gao, F. Z., Zhu, F., Luo, X. H., Jiang, J., & Feng, L. (2019). Synergistic coagulation of bauxite residue-based polyaluminum ferric chloride for dyeing wastewater treatment. *Journal of Central South University*, 26(2), 449-457. <https://doi.org/10.1007/s11771-019-4017-7>
- Jiang, Z., & Zhu, J. (2021). Preparation, characterization and coagulation performance of a composite coagulant: Polymeric aluminum ferric sulfate. In *IOP Conference Series: Earth and Environmental Science* (Vol. 647, No. 1, p. 012059). IOP Publishing.
- Kim, Y. S., Kim, M. H., & Yoo, C. K. (2010). A new statistical framework for parameter subset selection and optimal parameter estimation in the activated sludge model. *Journal of Hazardous Materials*, 183(1-3), 441-447. <https://doi.org/10.1016/j.jhazmat.2010.07.044>
- Lei, G., Ma, J., Guan, X., Song, A., & Cui, Y. (2009). Effect of basicity on coagulation performance of polyferric chloride applied in eutrophicated raw water. *Desalination*, 247(1-3), 518-529. <https://doi.org/10.1016/j.desal.2008.06.026>
- Li, A., Zhang, H., & Yang, H. (2014). Evaluation of aluminum dross as raw material for high-alumina refractory. *Ceramics International*, 40(8), 12585-12590. <https://doi.org/10.1016/j.ceramint.2014.04.069>

- Liang, J., Wang, W., Liu, H., Wang, E., Zhong, Y., Li, Y., & Luo, K. (2020). Optimization of preparation conditions for liquid polymeric ferric sulfate by response surface analysis. *Advances in Environmental Protection*, 10(01), 85-97. <https://doi.org/10.12677/aep.2020.101010>
- Mahinroosta, M., & Allahverdi, A. (2018). Enhanced alumina recovery from secondary aluminum dross for high purity nanostructured  $\gamma$ -alumina powder production: Kinetic study. *Journal of Environmental Management*, 212, 278-291. <https://doi.org/10.1016/j.jenvman.2018.02.009>
- Mahinroosta, M., & Allahverdi, A. (2018). Hazardous aluminum dross characterization and recycling strategies: A critical review. *Journal of Environmental Management*, 223, 452-468. <https://doi.org/10.1016/j.jenvman.2018.06.068>
- Mailar, G., Sreedhara, B. M., Manu, D. S., Hiremath, P., & Jayakesh, K. (2016). Investigation of concrete produced using recycled aluminium dross for hot weather concreting conditions. *Resource-Efficient Technologies*, 2(2), 68-80. <https://doi.org/10.1016/j.refit.2016.06.006>
- Mavinkattimath, R. G., Kodialbail, V. S., & Govindan, S. (2017). Simultaneous adsorption of Remazol brilliant blue and disperse orange dyes on red mud and isotherms for the mixed dye system. *Environmental Science and Pollution Research*, 24(23), 18912-18925. <https://doi.org/10.1007/s11356-017-9278-9>
- Mohd-Salleh, S. N. A., Shaylinda, M. Z. N., Othman, N., Yashni, G., & Norshila, A. B. (2020). Coagulation performance and mechanism of a new coagulant (polyaluminium chloride-tapioca peel powder) for landfill leachate treatment. *Journal of Engineering Science and Technology*, 15(6), 3709-3722.
- Murayama, N., Maekawa, I., Ushiro, H., Miyoshi, T., Shibata, J., & Valix, M. (2012). Synthesis of various layered double hydroxides using aluminum dross generated in aluminum recycling process. *International Journal of Mineral Processing*, 110, 46-52. <https://doi.org/10.1016/j.minpro.2012.03.011>
- Mwewa, B., Stopić, S., Ndlovu, S., Simate, G. S., Xakalashé, B., & Friedrich, B. (2019). Synthesis of poly-alumino-ferric sulphate coagulant from acid mine drainage by precipitation. *Metals*, 9(11), Article 1166. <https://doi.org/10.3390/met9111166>
- Pepper, R. A., Couperthwaite, S. J., & Millar, G. J. (2016). Comprehensive examination of acid leaching behaviour of mineral phases from red mud: Recovery of Fe, Al, Ti, and Si. *Minerals Engineering*, 99, 8-18.
- Reddy, M. S., & Neeraja, D. (2016). Mechanical and durability aspects of concrete incorporating secondary aluminium slag. *Resource-Efficient Technologies*, 2(4), 225-232.
- Rivera, R. M., Ulenaers, B., Ounoughene, G., Binnemans, K., & Van Gerven, T. (2018). Extraction of rare earths from bauxite residue (red mud) by dry digestion followed by water leaching. *Minerals Engineering*, 119, 82-92. <https://doi.org/10.1016/j.mineng.2018.01.023>
- Sarker, M. S. R., Alam, M. Z., Qadir, M. R., Gafur, M. A., & Moniruzzaman, M. (2015). Extraction and characterization of alumina nanopowders from aluminum dross by acid dissolution process. *International Journal of Minerals, Metallurgy, and Materials*, 22(4), 429-436.
- Su, X., Li, X., & Shen, X. (2010). Experimental study on efficient utilization of aluminum ash. *Journal of Huazhong Normal University (Natural Sciences)*, 44(2), 1000-1190.
- Sun, C., Yue, Q., Gao, B., Cao, B., Mu, R., & Zhang, Z. (2012). Synthesis and floc properties of polymeric ferric aluminum chloride-polydimethyl diallylammonium chloride coagulant in coagulating humic acid-kaolin synthetic water. *Chemical Engineering Journal*, 185, 29-34. <https://doi.org/10.1016/j.cej.2011.04.056>

- Sun, Y., Zhu, C., Zheng, H., Sun, W., Xu, Y., Xiao, X., You, Z., & Liu, C. (2017). Characterization and coagulation behavior of polymeric aluminum ferric silicate for high-concentration oily wastewater treatment. *Chemical Engineering Research and Design*, *119*, 23-32.
- Tsakiridis, P. E., Oustadakis, P., & Agatzini-Leonardou, S. (2013). Aluminium recovery during black dross hydrothermal treatment. *Journal of Environmental Chemical Engineering*, *1*(1-2), 23-32.
- Xiao, Y., Reuter, M. A., & Boin, U. D. O. (2005). Aluminium recycling and environmental issues of salt slag treatment. *Journal of Environmental Science and Health*, *40*(10), 1861-1875. <https://doi.org/10.1080/10934520500183824>
- Yan, L., Wang, Y., Li, J., Shen, H., Zhang, C., & Qu, T. (2016). Preparation of polymeric aluminum ferric chloride (PAFC) coagulant from fly ash for the treatment of coal-washing wastewater. *Desalination and Water Treatment*, *57*(39), 18260-18274. <https://doi.org/10.1080/19443994.2015.1089420>
- Yang, S., Li, W., Zhang, H., Wen, Y., & Ni, Y. (2019). Treatment of paper mill wastewater using a composite inorganic coagulant prepared from steel mill waste pickling liquor. *Separation and Purification Technology*, *209*, 238-245.
- Zhang, P., & Ren, B. (2013). Inverse emulsion polymerization of dimethyl diallyl ammonium chloride and acrylamide for water treatment. *Asian Journal of Chemistry*, *25*(7), 3966-3970. <https://doi.org/10.14233/ajchem.2013.13859>
- Zhang, S., Zhu, W., Li, Q., Zhang, W., & Yi, X. (2019). Recycling of secondary aluminum dross to fabricate porous  $\gamma$ -Al<sub>2</sub>O<sub>3</sub> assisted by corn straw as biotemplate. *Journal of Materials Science and Chemical Engineering*, *7*(12), 87-102. <https://doi.org/10.4236/msce.2019.712010>
- Zhang, Y., Li, S., Wang, X., & Li, X. (2015a). Coagulation performance and mechanism of polyaluminum ferric chloride (PAFC) coagulant synthesized using blast furnace dust. *Separation and Purification Technology*, *154*, 345-350. <https://doi.org/10.1016/j.seppur.2015.09.075>
- Zhang, Y., Li, S., Wang, X., Ma, X., Wang, W., & Li, X. (2015b). Synthesis, purification and characterization of polyaluminum ferric chloride (PAFC) with high (Al+ Fe) b content. *Separation and Purification Technology*, *146*, 311-316. <https://doi.org/10.1016/j.seppur.2015.03.045>
- Zhao, H., Liu, H., & Qu, J. (2011). Aluminum speciation of coagulants with low concentration: Analysis by electrospray ionization mass spectrometry. *Colloids and Surfaces A: Physicochemical and Engineering Aspects*, *379*(1-3), 43-50. <https://doi.org/10.1016/j.colsurfa.2010.11.045>
- Zhao, X., Yang, T., Liu, L., Zhang, X., Fan, L., & Huang, Y. (2016). Effect of aluminum speciation on silica removal during coagulation of heavy-oil wastewater using polyaluminum chloride. *Desalination and Water Treatment*, *57*(25), 11789-11799. <https://doi.org/10.1080/19443994.2015.1044917>
- Zhu, G., Zheng, H., Zhang, Z., Tshukudu, T., Zhang, P., & Xiang, X. (2011). Characterization and coagulation-flocculation behavior of polymeric aluminum ferric sulfate (PAFS). *Chemical Engineering Journal*, *178*, 50-59. <https://doi.org/10.1016/j.cej.2011.10.008>



## Assessment of Domestic Wastewaters as Potential Growth Media for *Chlorella vulgaris* and *Haematococcus pluvialis*

Yeong Hwang Tan<sup>1</sup>, Mee Kin Chai<sup>1\*</sup>, Yang Kai Ooi<sup>2</sup> and Ling Shing Wong<sup>2</sup>

<sup>1</sup>College of Engineering, Universiti Tenaga Nasional, Jalan Ikram-Uniten, 43000 Kajang, Selangor, Malaysia

<sup>2</sup>Faculty of Health and Life Science, INTI International University, Persiaran Perdana BBN, Putra Nilai, 71800 Nilai, Negeri Sembilan, Malaysia

### ABSTRACT

Domestic wastewater contains chemical compounds that can be used as nutrients for microalgae. Removing these chemical compounds from wastewater by microalgae might help in reducing the operation cost of wastewater management while minimizing the cultivation cost for large-scale microalgae metabolite production. In this study, domestic wastewater collected from Indah Water Konsortium (IWK), Kuala Lumpur, Malaysia, was assessed as growth media for two types of microalgae, namely *Chlorella vulgaris* and *Haematococcus pluvialis*. The biomass growth and nutrient removal efficiency of total nitrogen (TN), total phosphorus (TP), and total ammonia (TAN) in different concentrations of diluted wastewater were measured. The results showed that biomass concentration (0.227 g/L), biomass productivity (0.029 g/L/day), and specific growth rate (0.284 d<sup>-1</sup>) yielded by *C. vulgaris* in 14 days of 80% wastewater were comparable to those microalgae grew in standard Bold's Basal medium (BBM). Besides, *C. vulgaris* grew in 50% wastewater to remove TN, TP, and TAN with the highest removal efficiency (>88%). For *H. pluvialis*, the biomass concentration in all wastewater concentrations was lower than BBM. The removal efficiencies of TN and TP were lower than 55%, but more than 80% for removal efficiency of

TAN in 50% and 80% wastewater. Hence, *C. vulgaris* has better growth performance and nutrient removal efficiency than *H. pluvialis*. These findings indicated that IWK domestic wastewater could be used as growth media for microalgae, especially *C. vulgaris*.

### ARTICLE INFO

#### Article history:

Received: 1 July 2021

Accepted: 13 October 2021

Published: 10 January 2022

DOI: <https://doi.org/10.47836/pjst.30.1.31>

#### E-mail addresses:

yeonghwang\_113@hotmail.com (Yeong Hwang Tan)

Mkchai@uniten.edu.my (Mee Kin Chai)

ooiyangkai.oik@gmail.com (Yang Kai Ooi)

lingshing.wong@newinti.edu.my (Ling Shing Wong)

\*Corresponding author

**Keywords:** *Chlorella vulgaris*, *Haematococcus pluvialis*, microalgae, nutrient removal, wastewater treatment

## INTRODUCTION

Wastewater generated from industrial, agricultural, and domestic activities often contains organic matters, metals, and toxic chemicals (Abdullah et al., 2017; Qi et al., 2020). Therefore, wastewater must be treated by sewage treatment plants prior to discharge into the environment. Sewage service needs huge costs on replacement, maintenance, and building of new sewage plant (Aliman, 2019). While the wastewater treatment companies charge expensive bills to the local authorities and clients, they can reduce the operation cost by introducing biological processes on the treatment plant.

Several studies have indicated that microalgae are potential candidates for wastewater treatment due to their ability to utilize the organic and inorganic matters in wastewater (Ramsundar et al., 2017; Kotoula et al., 2020; Umamaheswari et al., 2020). Moreover, the biomolecules produced by microalgae, such as lipid, can be transformed into biodiesel. However, microalgae-based biodiesel is not available in the market today due to its high cultivation cost using freshwater. Therefore, Lu et al. (2015) suggested that harnessing wastewater as a microalgae cultivation medium can minimize the cost of producing the desired products.

Different wastewater has distinct compositions based on their sources. Therefore, the nutrient removal efficiencies vary among different microalgae in the same type of wastewater (Bhatnagar et al., 2011; Ling et al., 2019). Furthermore, even the microalgae strain that showed high nutrient removal efficiency in one wastewater might show different characteristics in another wastewater. For instance, Odjadjare et al. (2018) cultivated *Neochloris aquatica* in two domestic wastewaters collected from different treatment plants. The results showed that the dry biomass weight and metabolite amount were significantly different due to the different physicochemical profiles of wastewater. Therefore, before developing microalgae-based wastewater treatment for a certain area, it is important to study and select the correct type of microalgae for the local wastewater to maximize nutrient removal efficiency and biomass production.

*Chlorella vulgaris* was commonly used in the study of wastewater treatment due to its high growth rate and high nutrient removal efficiency (Cheah et al., 2018; Wang et al., 2015). The harvested biomass could be further used as feedstock for biodiesel, pharmaceutical medicines, and biofertilizers (Ru et al., 2020). *Haematococcus pluvialis* is a high-valued microalga due to its bestowed ability to produce precious astaxanthin, which has a strong antioxidant capacity (Shah et al., 2016). It was reported that astaxanthin has a high market value (USD 2000/kg), and the demand is expected to increase in the future (Ren et al., 2021). However, large-scale *H. pluvialis* cultivation is limited due to the high cost. Shah (2019) suggested that wastewater treatment integration with *H. pluvialis* is a great option in reducing cultivation costs. However, the biomass production by *H. pluvialis* using wastewater was different (Shah, 2019). Hence, the study should be conducted to assess the

wastewater from the certain treatment plant is suitable for *H. pluvialis* to grow to serve its purpose to produce high biomass and remove nutrients from wastewater simultaneously.

The study on the assessment of domestic wastewater collected from Indah Water Konsortium (IWK) as potential growth media for *C. vulgaris* and *H. pluvialis* had not been reported in Malaysia. In this study, *C. vulgaris* and *H. pluvialis* were cultivated in different concentrations of diluted IWK wastewater (10%, 20%, 50%, and 80% of wastewater). The biomass concentration, biomass productivity, and specific growth rate of both microalgae species in each concentration of diluted wastewater were compared to those microalgae grew in standard Bold's Basal medium (BBM). The diluted wastewater samples that stimulated the high biomass concentration and cell density were collected for nutrient removal analysis. The nutrient removal efficiencies of total nitrogen (TN), total phosphorus (TP), and total ammonia (TAN) of both microalgae species were compared to determine the suitable species for IWK water treatment and to access the suitability of IWK domestic wastewater as growth media for *C. vulgaris* and *H. pluvialis*.

## MATERIALS AND METHODS

### Microalgae Strain Cultivation

Microalgae strain *C. vulgaris* was purchased from Culture Collection of Algae and Protozoa (CCAP), United Kingdom, while *H. pluvialis* was attained from the University of Texas (UTEX), United States of America. Both microalgae were initially maintained in Bold's Basal medium (BBM). Then, microalgae cultures were cultivated at room temperature under illumination from cool-white fluorescent tubes with 16 hours of light and 8 hours of the dark cycle. During the cultivation, manual aeration was done twice a day. Hemocytometer (Marienfeld-Superior, Neubauer) with a light microscope (Eclipse E-100 LED, Nikon) was used to investigate the growth phases of the cells by determining the cell density.

### Microalgae Cultivation with Wastewater

Wastewater was collected from Indah Water Konsortium (IWK), Kuala Lumpur, Malaysia. Indah Water Konsortium is a national sewerage and sanitation company in Malaysia. The wastewater sample was filtered to remove solid particles prior to use. The initial pH, total nitrogen (TN), total phosphorus (TP), and total ammonia (TAN) of wastewater was measured according to the method described in the "nutrient removal efficiency" section, and they were approximately 7.33, 33.2 mg/L, 43.8 mg/L, and 10.08 mg/L, respectively. A simple preliminary study was conducted, and the result showed that the original wastewater was not suitable for the direct cultivation of both microalgae due to the high amount of various nutrients. Then, the wastewater was diluted with distilled water to 10%, 20%, 50%, and 80% of wastewater percentages without further process. When *C. vulgaris* and

*H. pluvialis* reached the log phase, 4 mL of the culture (cell density  $6.21 \times 10^6$  cells/mL and  $2.73 \times 10^5$  cells/mL) were transferred into 250 mL of diluted wastewater. Microalgae cultivation with BBM and deionized water were positive and negative control, respectively. The microalgae were cultivated in the 500-mL conical flask at the conditions as previously described in the “Microalgae Strain Cultivation” section.

The cell density and biomass concentration of each sample were measured on the initial day of cultivation and every two days using the method as described in the sections of “Microalgae Strain Cultivation” and “Determination of Microalgae Biomass” until day 14. The microalgae in wastewater during day 0 and day 14 were filtered through a vacuum filter, and the filtrates were collected. The wastewater that had high biomass concentration and cell density was further analyzed to determine the nutrient removal efficiency of TN, TP, and TAN as described in the section of “Nutrient Removal Efficiency.”

### Determination of Microalgae Biomass

The volume of 10 mL aliquots of culture was filtered using mixed cellulose ester membrane filters with absorbent pads. The loaded filter was dried in an oven at 70°C until constant weight. The dry cell weight (DCW) of the microalgae biomass was obtained by subtracting the dry weight of the blank membrane filter with the dry-loaded membrane filter.

The DCW was used to calculate the microalgae growth by biomass concentration, biomass productivity, and specific growth rate using Equations 1, 2, and 3 below:

$$\text{Biomass concentration} = \text{DCW}_t / \text{volume of aliquots} - \text{DCW}_0 / \text{volume of aliquots} \quad [1]$$

$$\text{Biomass productivity, } P_b = (X_f - X_0) / (t_f - t_0) \quad [2]$$

$$\text{Specific growth rate, } \mu = (\ln X_f - \ln X_0) / (t_f - t_0) \quad [3]$$

Where

$\text{DCW}_t$  and  $\text{DCW}_0$  are dry cell weight (g) on the final day of cultivation ( $t_f$ ) and initial day of cultivation ( $t_0$ )

$X_f$  and  $X_0$  are the biomass concentration (g/L) on day  $t_f$  and day  $t_0$ .

### Nutrient Removal Efficiency

The samples for the determination of TN, TP, and TAN were digested and treated according to methods 10071, 8190, and 8038, respectively, described by Hach (Hach, 2021). TN was measured based on the persulfate digestion method using Nitrogen, Total, LR, Test ‘N Tube™ reagent set while TP was measured based on PhosVer® 3 with acid persulfate digestion method using Phosphorus (Total) TNT Reagent Set. TAN was measured based on the Nessler method using the Hach type Nessler nitrogen-ammonia reagent set. The digested samples were put into Hach spectrophotometer DR5000, and the concentration of



each sample was measured using a program set in DR5000. The sample was diluted with deionized water if the concentration was too high to be measured (Hach, 2021).

The nutrient removal efficiency (%) was calculated using Equation 4 below:

$$\text{Nutrient Removal Efficiency (\%)} = (C_0 - C_t) / C_0 \times 100\% \quad [4]$$

$C_0$  and  $C_t$  are the nutrient concentration (mg/L) on day  $t_0$  and day  $t_t$ .

All experiments were repeated in triplicates, and data were presented as means  $\pm$  standard error of the mean. Significance of results, differences between the strains of the microalgae and the wastewater concentrations were evaluated for a duplicate set of data by using one-way analysis of variance (ANOVA) with Post-hoc Turkey's test.

## RESULTS AND DISCUSSIONS

### Effect of Wastewater Concentration on Microalgae Growth

The cell density of *C. vulgaris* and *H. pluvialis* in different wastewater concentrations is shown in Figure 1. The cell density of *C. vulgaris* in 50% and 80% wastewater was notable compared to other wastewater concentrations. The maximum cell density obtained in 50% wastewater was  $1.014 \times 10^7$  cells/mL, and 80% wastewater was  $1.102 \times 10^7$  cells/mL, respectively. These results were comparable to those microalgae that grew in BBM ( $1.132 \times 10^7$  cells/mL). Whereas *C. vulgaris* grew in deionized water, 10% and 20% wastewater reached  $1.28 \times 10^6$ ,  $2.38 \times 10^6$ , and  $4.31 \times 10^6$  cells/mL, respectively. From Figure 1, the lag phase of *C. vulgaris* in all wastewater concentrations was very short, and after that, the microalgae cells initiated the log phase at day 3 with a high specific growth rate. The growth of *C. vulgaris* reached the stationary phase after 7 and 10 days of cultivation in 10%, 20%, 50%, and 80% wastewater, respectively, which were similar to Ryu et al. (2014).

For *H. pluvialis*, the maximum cell density obtained from the culture in BBM was recorded as the highest among all wastewater concentrations on day 14, which is  $2.503 \times 10^7$  cells/mL. The maximum cell density in all wastewater concentrations on day 14 was lower than BBM. On day 3, red nonmotile aplanospore were microscopically observed in 10% and 20% wastewater. The cell number of aplanospore has surged, whereas green vegetative motile cells and palmella cells were diminished along with the increasing cultivation period. The stressed environment, such as nutrient deprivation, prompted the transformation of green vegetative motile cells and palmella cells into red nonmotile aplanospore (Shah et al., 2016). Aplanospore is resting vegetative cells, which means their metabolism rate slows down. The nutrients in 10% and 20% wastewater were lower and probably deprived during the initial cultivation period. As a result, some green vegetative

cells were transformed into red nonmotile aplanospore; therefore, cell density increased slowly.

The biomass concentration of *C. vulgaris* and *H. pluvialis* in different wastewater concentrations during 14 cultivation days is illustrated in Figure 2. Although the biomass concentration of *C. vulgaris* in 80% wastewater showed a similar biomass concentration produced in BBM, there is no significant difference ( $P > 0.05$ ) between these two culture mediums after 14 days of cultivation. It is probably due to rich nutrients in 80% wastewater (Figure 3). Previous studies have reported that *C. vulgaris* survived in the presence of an inflated concentration of nitrogen and reached high biomass concentration (Zhang et al., 2016; Li et al., 2019; Trivedi et al., 2019). However, a high concentration of phosphorus is not favorable for *C. vulgaris* growth through exorbitant nitrogen was available (Zhang et al., 2016).

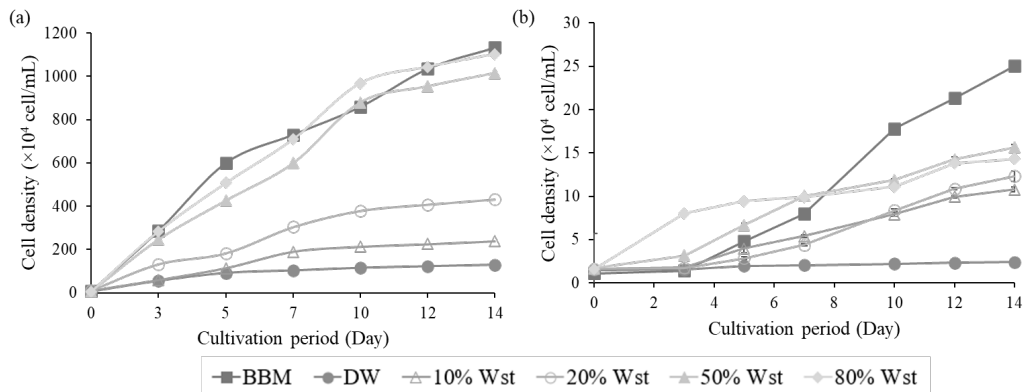


Figure 1. The cell density of (a) *C. vulgaris* and (b) *H. pluvialis* in BBM, deionized water (DW), and different wastewater concentrations (n = 3). 10% Wst: 10: 90 (v/v) of wastewater and distilled water; 20% Wst: 20: 80 (v/v) of wastewater and distilled water; 50% Wst: 50: 50 (v/v) of wastewater and distilled water; 80% Wst: 80: 20 (v/v) of wastewater and distilled water.

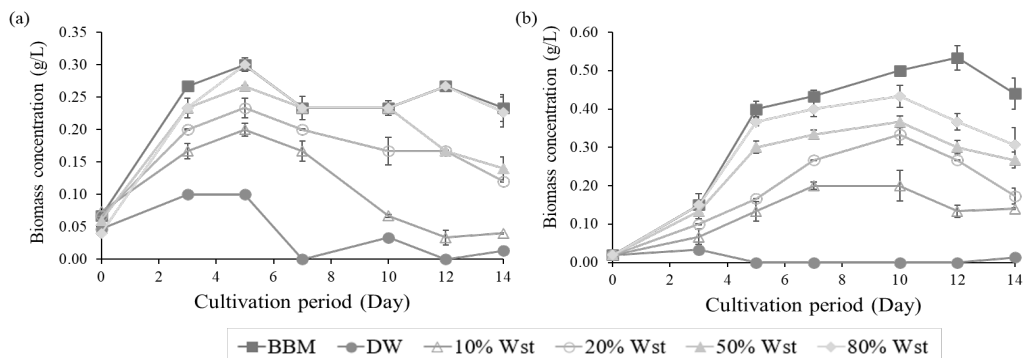


Figure 2. Biomass concentration of (a) *C. vulgaris* and (b) *H. pluvialis* in BBM, deionized water (DW), and different wastewater concentrations (n = 3).

The biomass concentration of *C. vulgaris* in 10% and 20% wastewater was low during the cultivation period. This result was consistent with another study, which too diluted wastewater was not favorable for *C. vulgaris* growth (Wang et al., 2015; Nam et al., 2017). These results indicated that the nutrients in the wastewater must be monitored to obtain a high biomass concentration of *C. vulgaris*.

Figure 2(b) shows that the highest biomass concentration of *H. pluvialis* was observed in BBM standard control media. Although the biomass concentration and cell density increased rapidly from day 2 to day 5, biomass concentration in all wastewater concentrations was significantly lower than in BBM. Moreover, the presence of aplanospore, as described earlier, indicated that *H. pluvialis* was in a stressful environment. However, other studies reported that *H. pluvialis* was able to produce a high amount of biomass concentration (> 600 mg/L) in wastewater containing more than 40 mg/L of total nitrogen and 4.4 mg/L of total phosphorus (Kang et al., 2006; Liu & Yildiz, 2019). Therefore, the low performance of *H. pluvialis* in this study is probably due to inhibitors, such as metals and growth inhibitors in wastewater samples.

Table 1 indicates the biomass concentration, average biomass productivity, and specific growth rate of *C. vulgaris* and *H. pluvialis* in BBM, deionized water, and different concentrations (10%, 20%, 50%, 80%) of wastewater after 14 days of cultivation. The results showed that the biomass concentration, average biomass productivity, and specific growth rate of *C. vulgaris* and *H. pluvialis* in 80% wastewater are comparable to the production in BBM standard culture medium (Table 1). However, compared to *C. vulgaris*, *H. pluvialis* showed higher biomass concentration and productivity. It is probably because of the different cell sizes of microalgae. The cell size of *C. vulgaris* was 2-10  $\mu\text{m}$  (Weil et al., 2017), whereas *H. pluvialis* was 8-50  $\mu\text{m}$  (Li et al., 2019), respectively. Therefore, the larger cell size of *H. pluvialis* probably has a higher weight than *C. vulgaris*, resulting in higher biomass concentration and productivity.

Table 1

*Biomass concentration (BC), average biomass productivity (P<sub>b</sub>), and specific growth rates ( $\mu$ ) of C. vulgaris and H. pluvialis in BBM, deionized water (DW), and different wastewater concentrations (n = 3) after 14 days of cultivation.*

<i>C. vulgaris</i>				
Medium		BC (g/L)	P <sub>b</sub> (g/L/day)	$\mu$ (d <sup>-1</sup> )
BBM		<b>0.233 ± 0.024<sup>a</sup></b>	<b>0.030 ± 0.011</b>	<b>0.212 ± 0.028</b>
DW		0.013 ± 0.033 <sup>b</sup>	0.002 ± 0.001	0.062 ± 0.005
Wastewater	10%	0.040 ± 0.058 <sup>b</sup>	0.011 ± 0.004	0.079 ± 0.005
	20%	0.120 ± 0.057 <sup>c</sup>	0.020 ± 0.001	0.164 ± 0.015

Table 1 (Continue)

<i>C. vulgaris</i>				
Medium		BC (g/L)	P <sub>b</sub> (g/L/day)	μ(d <sup>-1</sup> )
Wastewater	50%	0.140 ± 0.010 <sup>c</sup>	0.025 ± 0.009	0.204 ± 0.038
	80%	<b>0.227 ± 0.010<sup>a</sup></b>	<b>0.029 ± 0.003</b>	<b>0.284 ± 0.043</b>
<i>H. pluvialis</i>				
Medium		BC (g/L)	P <sub>b</sub> (g/L/day)	μ(d <sup>-1</sup> )
BBM		<b>0.440 ± 0.085<sup>d</sup></b>	<b>0.050 ± 0.024</b>	<b>0.421 ± 0.060</b>
DW		0.013 ± 0.015 <sup>e</sup>	0.001 ± 0.002	0.028 ± 0.002
Wastewater	10%	0.140 ± 0.071 <sup>f</sup>	0.016 ± 0.008	0.272 ± 0.040
	20%	0.173 ± 0.048 <sup>f</sup>	0.026 ± 0.005	0.330 ± 0.020
	50%	0.267 ± 0.059 <sup>g</sup>	0.036 ± 0.008	0.380 ± 0.025
	80%	<b>0.307 ± 0.012<sup>g</sup></b>	<b>0.043 ± 0.014</b>	<b>0.404 ± 0.057</b>

Values within the same row having different letters are significantly different ( $P < 0.05$ ).

### Total Nitrogen, Total Phosphorus, and Total Ammonia Removal Efficiency

The nutrient removal efficiency of *C. vulgaris* and *H. pluvialis* in wastewater was assessed to evaluate their potential in wastewater treatment. Samples were taken at the time of inoculation and the end of the cultivation period and analyzed for total residual nitrogen, phosphate, and ammonia. As shown in Figure 3, both microalgae were able to remove TN, TP, and TAN efficiently from 10% wastewater, in which TN, TP, and TAN were reduced more than 85% during the 14<sup>th</sup>-day cultivation of both microalgal species. Compared to *H. pluvialis*, *C. vulgaris* can remove more than 88% of TN, TP, and TAN in 50% wastewater. Interestingly, the TN and TP removal efficiency of both microalgal species in 80% wastewater was the lowest even though their biomass concentrations are the highest compared to other wastewater concentrations. The amount of phosphorus uptake by *C. vulgaris* in 50% and 80% wastewater were 21.9 mg/L and 25.5 mg/L, respectively, resulting in removal efficiency of 100% and 72.89%. These results correspond with the findings from the other studies wherein mediocre removal efficiency of TN (49–60%) and TP in minimally diluted wastewater (Deng et al., 2017; Wen et al., 2017). The low removal efficiency is probably because the phosphorus requirement for *C. vulgaris* has reached a saturated point. Besides, the low nitrogen concentration in the wastewater medium is probably attributed to this result. Phosphorus uptake was mitigated in a low nitrogen environment as protein and ribosome synthesis was reduced (Loladze & Elser, 2011).

Previous work has shown that the unbalance N/P ratio, especially low nitrogen has critical effects on removal efficiency and cell growth (Lee et al., 2013; Whitton et al., 2016; Huang et al., 2021). Beuckels et al. (2015) reported that under a low nitrogen

environment, the uptake of TP by microalgae into the biomass remains low regardless of the TP concentration in the medium. Sufficient nitrogen is essential to ensure no restriction on protein and ribosome synthesis. Alketife et al. (2017) also indicated that TP removal efficiency by *C. vulgaris* was reduced in the medium containing the initial TP concentration of more than 19 mg/L. A longer cultivation period enhanced TN concentration, or higher initial inoculum density probably could enhance the removal efficiency of TP.

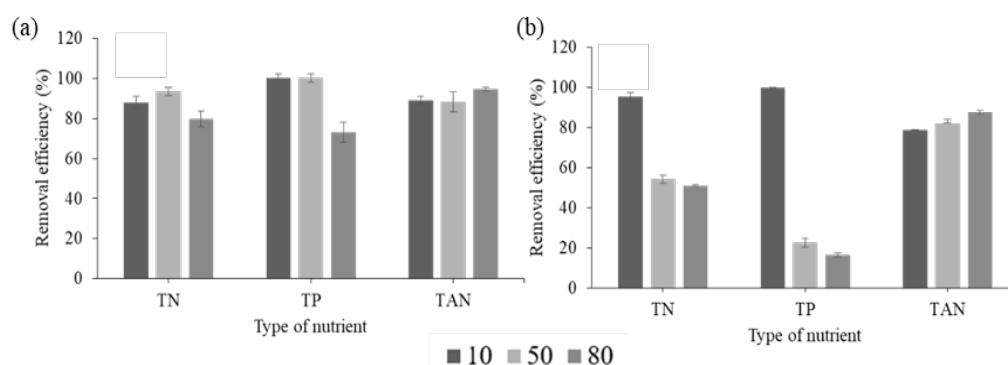


Figure 3. Removal efficiency of (a) *C. vulgaris* and (b) *H. pluvialis* in 10%, 50% and 80% wastewater after 14-day cultivation (n = 3). TN: total nitrogen; TP: total phosphorus; TAN: total ammonia.

For *H. pluvialis*, the results showed that only 5 mg/L and 5.77 mg/L of phosphorus were taken in 50% and 80% wastewater, resulting in removal efficiency of 22.83% and 16.48%, respectively, which much lower than *C. vulgaris*. The reason is underlying these results perhaps due to the slow metabolism of *H. pluvialis*. Pan et al. (2021) revealed that *H. pluvialis* required eight days to reduce 16 mg/L of initial nitrate and 3 mg/L of initial TP to below one mg/L in potato juice wastewater. In another study, 30 mg/L of TN and 4.7 mg/L of TP to 0 mg/L and 0.49 mg/L, respectively, in primary effluent by *H. pluvialis* after 35 days of cultivation (Sato et al., 2015). A longer time is needed to achieve high removal efficiency in low diluted wastewater.

TN removal efficiency of *H. pluvialis* in 50% and 80% wastewater is also lower than *C. vulgaris*. *H. pluvialis* took up 9 mg/L and 13.56 mg/L TN in 50% and 80% wastewater during 14<sup>th</sup> day cultivation, resulting in removal efficiency of 54.52% and 51.05%, respectively. On the one hand, the TAN removal efficiency of *H. pluvialis* in 50% and 80% wastewater was 82.14% and 87.72%, respectively, comparable to the *C. vulgaris*. The preference of nitrogen sources of *H. pluvialis* is varied among the strains. Sipaúba-Tavares et al. (2015) showed that *H. pluvialis* prefers to utilize nitrate, whereas Cifuentes et al. (2003) and Ledda et al. (2016) revealed *H. pluvialis* prefers to consume ammonium. In another study, Wang et al. (2019) pointed out that *H. pluvialis* JNU35

prefers to use urea instead of nitrate and ammonium. In this study, the removal efficiency of TAN is higher than the removal efficiency of TN in both 50% and 80% wastewater for *H. pluvialis*. Therefore *H. pluvialis* prefers to utilize ammonium in this study. Besides strain, light intensity, turbidity, and medium pH might influence the uptake preference of nitrogen sources (Cifuentes et al., 2003; Wang et al., 2019). More research is required to clarify the relationship and mechanisms of these factors on the nitrogen sources uptake.

The amount of TN, TP, and TAN taken by *H. pluvialis* in 50% wastewater was almost closed to 80% wastewater. It is probably because *H. pluvialis* has reached the maximum uptake amount in 50% wastewater. Therefore, the cell density and biomass concentration in 50% and 80% wastewater are also similar. Kang et al. (2006) also observed that the cell density of *H. pluvialis* in two- and four-fold diluted wastewater was higher compared to eight-fold diluted wastewater, but their removal efficiency was much lower than eight-fold diluted wastewater.

However, the removal efficiency of TAN was from 78.67% to 94.54% in all diluted wastewater for microalgal species. It is important to know that the removal of ammonium ions is influenced by confounding factors, including microalgae, volatilization, air-stripping, and the presence of nitrifying and denitrifying bacteria (Podevin et al., 2015; Tao et al., 2017; Tan et al., 2020). Wastewater without sterilization may consist of nitrifying and denitrifying bacteria that convert ammonium ions into nitrogen gas. Previous research also reported that in the presence of various forms of inorganic nitrogen, ammonium is generally favored by many microalgae (Wu et al., 2013; We et al., 2013) because nitrite or nitrate must be converted into ammonium prior to its utilization while no requirement of redox reaction during ammonium assimilation as it can be directly absorbed into amino acids inside the cells (Kim et al., 2016).

Nutrient removal efficiency and biomass productivity by different microalgae grown in domestic wastewater from previous studies were compared in Table 2. Although the biomass productivity of *C. vulgaris* in this study was low, the removal efficiency of TN, TP, and TAN was higher than in other studies. For *H. pluvialis*, the nutrient removal efficiency of TN, TP, and TAN in 10% wastewater were comparable to other studies.

Overall, *C. vulgaris* and *H. pluvialis* achieved high biomass concentration and nutrient removal efficiency in proper dilution of wastewater compared to other microalgae species. Based on the results, *C. vulgaris* shows the better potential for IWK domestic wastewater treatment and simultaneously produces high biomass concentration in 14 days cultivation period.

Table 2

Comparison of nutrient removal efficiency and biomass productivity (mg/L/day) by different microalgae grown in domestic wastewater from previous studies.

Type of system	Treatment	Removal efficiency (%)			P <sub>b</sub>	Day of cultivation	Reference
		TN	TP	TAN			
<i>C. vulgaris</i>	50% diluted	93.37	100	88.29	0.029	14	This study
<i>H. pluvalis</i>	10% diluted	95.48	100	78.67	0.040	14	This study
<i>C. vulgaris</i>	0.02 v/v diluted	85	35	-	0.040	12	Lam et al. (2017)
<i>C. vulgaris</i>	50% diluted	83	100	-	-	18	Thomas et al. (2016)
<i>Chlorella sp.</i>	Autoclaved	-	53.77	95.90	-	10	Kiran et al. (2014)
<i>C. vulgaris</i>	50% autoclaved diluted	73.9	45.4	-	-	12	Pacheco et al. (2021)
<i>H. pluvalis</i>	25% diluted	100	100	-	-	8	Kang et al. (2006)
<i>H. pluvalis</i>	-	93.8	97.3	-	0.028	15	Wu et al. (2013)
<i>Chlorella sorokiniana</i>	municipal wastewaters	28.67	83.3	94.29	0.077	14	Ramsundar et al. (2017)
<i>Scenedesmus acutus</i>	Autoclaved	42.9	92.4	64.3	0.048	16	Alva et al. (2013)

## CONCLUSION

The present study demonstrated that unsterilized IWK domestic wastewater could be used as growth media to cultivate *C. vulgaris* and *H. pluvalis*. The cell density, biomass concentration, average biomass productivity, and specific growth rate of *C. vulgaris* in 80% wastewater were comparable to those grown in BBM but not for *H. pluvalis*. However, the removal efficiencies of TN, TP, and TAN of *C. vulgaris* in 80% wastewater were lower than in 50% wastewater. Nevertheless, the removal efficiency of TN, TP, and TAN of *C. vulgaris* was higher than *H. pluvalis* in 50% and 80% wastewater. Hence, *C. vulgaris* has better growth performance and nutrient removal efficiency than *H. pluvalis*. These findings suggested that *C. vulgaris* is a more suitable candidate for IWK domestic wastewater treatment compared to *H. pluvalis*.

## ACKNOWLEDGEMENTS

The authors want to express their appreciation to the Ministry of Higher Education Malaysia, MOHE: FRGS/1/2020/STG02/UNITEN/02/1 (60%) and UNITEN BOLD Research Grant 2020: RJO10517844/044 (40%) for the financial support and thank Indah Water Konsortium for wastewater samples.

## REFERENCES

- Abdullah, N. A., Ramli, S., Mamat, N. H., Khan, S., & Gomes, C. (2017). Chemical and biosensor technologies for wastewater quality management. *International Journal of Advanced Research and Publications*, 1(6), 1-10.
- Aliman, K. H. (2019, February 28). Tariff review may relieve Indah Water's structural deficit. *The Edge Markets Weekly*. <https://www.theedgemarkets.com/article/tariff-review-may-relieve-indah-waters-structural-deficit>
- Alketife, A. M., Judd, S., & Znad, H. (2017). Synergistic effects and optimization of nitrogen and phosphorus concentrations on the growth and nutrient uptake of a freshwater *Chlorella vulgaris*. *Environmental Technology*, 38(1), 94-102. <https://doi.org/10.1080/09593330.2016.1186227>
- Alva, M. S., Luna-Pabello, V. M., Cadena, E., & Ortíz, E. (2013). Green microalga *Scenedesmus acutus* grown on municipal wastewater to couple nutrient removal with lipid accumulation for biodiesel production. *Bioresource Technology*, 146, 744-748. <https://doi.org/10.1016/j.biortech.2013.07.061>
- Beuckels, A., Smolders, E., & Muylaert, K. (2015). Nitrogen availability influences phosphorus removal in microalgae-based wastewater treatment. *Water Research*, 77, 98-106. <https://doi.org/10.1016/j.watres.2015.03.018>
- Bhatnagar, A., Chinnasamy, S., Singh, M., & Das, K. C. (2011). Renewable biomass production by mixotrophic algae in the presence of various carbon sources and wastewaters. *Applied Energy*, 88, 3425-3431. <https://doi.org/10.1016/j.apenergy.2010.12.064>
- Cheah, W. Y., Show, P. L., Juan, J. C., Chang, J. S., & Ling, T. C. (2018). Enhancing biomass and lipid productions of microalgae in palm oil mill effluent using carbon and nutrient supplementation. *Energy Conversion and Management*, 164, 188-197.
- Cifuentes, A. S., González, M. A., Vargas, S., Hoeneisen, M., & González, N. (2003). Optimization of biomass, total carotenoids and astaxanthin production in *Haematococcus pluvialis* Flotow strain Steptoe (Nevada, USA) under laboratory conditions. *Biological Research*, 36(3-4), 343-357. <http://dx.doi.org/10.4067/S0716-97602003000300006>
- Deng, X. Y., Gao, K., Zhang, R. C., Addy, M., Lu, Q., Ren, H. Y., Chen, P., Liu, Y. H., & Ruan, R. (2017). Growing *Chlorella vulgaris* on thermophilic anaerobic digestion swine manure for nutrient removal and biomass production. *Bioresource Technology*, 243, 417-425. <https://doi.org/10.1016/j.biortech.2017.06.141>
- Hach. (2021, November 19). *Water analysis handbook*. Hach. <https://www.hach.com/wah>
- Huang, Y., Lou, C., Luo, L., & Wang, X. C. (2021). Insight into nitrogen and phosphorus coupling effects on mixotrophic *Chlorella vulgaris* growth under stably controlled nutrient conditions. *Science of the Total Environment*, 752, Article 141747. <https://doi.org/10.1016/j.scitotenv.2020.141747>



- Kang, C. D., An, J. Y., Park, T. H., & Sim, S. J. (2006). Astaxanthin biosynthesis from simultaneous N and P uptake by the green alga *Haematococcus pluvialis* in primary-treated wastewater. *Biochemical Engineering Journal*, 31(3), 234-238. <https://doi.org/10.1016/j.bej.2006.08.002>
- Kim, G., Mujtaba, G., & Lee, K. (2016). Effects of nitrogen sources on cell growth and biochemical composition of marine chlorophyte *Tetraselmis* sp. for lipid production. *Algae*, 31(3), 257-266. <https://doi.org/10.4490/algae.2016.31.8.18>
- Kiran, B., Pathak, K., Kumar, R., & Deshmukh, D. (2014). Cultivation of *Chlorella* sp. IM-01 in municipal wastewater for simultaneous nutrient removal and energy feedstock production. *Ecological Engineering*, 73, 326-330. <https://doi.org/10.1016/j.ecoleng.2014.09.094>
- Kotoula, D., Iliopoulou, A., Irakleous-Palaiologou, E., Gatidou, G., Aloupi, M., Antonopoulou, P., Fountoulakis, M. S., & Stasinakis, A. S. (2020). Municipal wastewater treatment by combining in series microalgae *Chlorella sorokiniana* and macrophyte *Lemna minor*: Preliminary results. *Journal of Cleaner Production*, 271, Article 122704. <https://doi.org/10.1016/j.jclepro.2020.122704>
- Lam, M. K., Yusoff, M. I., Uemura, Y., Lim, J. W., Khoo, C. G., Lee, K. T., & Ong, H. C. (2017). Cultivation of *Chlorella vulgaris* using nutrients source from domestic wastewater for biodiesel production: Growth condition and kinetic studies. *Renewable Energy*, 103, 197-207. <https://doi.org/10.1016/j.renene.2016.11.032>
- Ledda, C., Tamiazzo, J., Borinb, M., & Adani, F. (2016). A simplified process of swine slurry treatment by primary filtration and *Haematococcus pluvialis* culture to produce low cost astaxanthin. *Ecological Engineering*, 90, 244-250. <http://dx.doi.org/10.1016/j.ecoleng.2016.01.033>
- Lee, S. H., Ahn, C. Y., Jo, B. H., Lee, S. A., Park, J. Y., An, K. G., & Oh, H. M. (2013). Increased microalgae growth and nutrient removal using balanced N:P ratio in wastewater. *Journal of Microbiology and Biotechnology*, 23(1), 92-98. <https://doi.org/10.4014/jmb.1210.10033>
- Li, F., Cai, M., Lin, M., Huang, X., Wang, J., Zheng, X., Wu, S., & An, Y. (2019). Accumulation of astaxanthin was improved by the nonmotile cells of *Haematococcus pluvialis*. *BioMed Research International*, 2019, Article 8101762. <https://doi.org/10.1155/2019/8101762>
- Li, H., Zhang, Y., Liu, J., Shen, Z., Li, A., Ma, T., Feng, Q., & Sun, Y. (2019). Treatment of high-nitrate wastewater mixtures from MnO<sub>2</sub> industry by *Chlorella vulgaris*. *Bioresource Technology*, 291(May), Article 121836. <https://doi.org/10.1016/j.biortech.2019.121836>
- Ling, Y., Sun, L. P., Wang, S. Y., Lin, C. S. K., & Sun, Z. (2019). Cultivation of oleaginous microalga *Scenedesmus obliquus* coupled with wastewater treatment for enhanced biomass and lipid production. *Biochemical Engineering Journal*, 148, 162-169. <https://doi.org/10.1016/j.bej.2019.05.012>
- Liu, Y., & Yildiz, I. (2019). Bioremediation of minkery wastewater and astaxanthin production by *Haematococcus pluvialis*. *International Journal of Global Warming*, 19(1-2), 145-157. <https://doi.org/10.1504/IJGW.2019.101778>
- Loladze, I., & Elser, J. J. (2011). The origins of the Redfield nitrogen-to-phosphorus ratio are in a homeostatic protein-to-rRNA ratio. *Ecology Letters*, 14(3), 244-250. <https://doi.org/10.1111/j.1461-0248.2010.01577.x>
- Lu, W., Wang, Z., Wang, X., & Yuan, Z. (2015). Cultivation of *Chlorella* sp. using raw dairy wastewater for nutrient removal and biodiesel production: Characteristics comparison of indoor bench-scale and outdoor pilot-scale cultures. *Bioresource Technology*, 192, 382-388. <https://doi.org/10.1016/j.biortech.2015.05.094>

- Nam, K., Lee, H., Heo, S. W., Chang, Y. K., & Han, J. I. (2017). Cultivation of *Chlorella vulgaris* with swine wastewater and potential for algal biodiesel production. *Journal of Applied Phycology*, 29(3), 1171-1178. <https://doi.org/10.1007/s10811-016-0987-0>
- Odjadjare, E. C., Mutanda, T., Chen, Y. F., & Olaniran, A. O. (2018). Evaluation of pre-chlorinated wastewater effluent for microalgal cultivation and biodiesel production. *Water*, 10, 1-13. <https://doi.org/10.3390/w10080977>
- Pacheco, D., Rocha, A. C. S., Garcia, A., Bóia, A., Pereira, L., & Verdelhos, T. (2021). Municipal wastewater: A sustainable source for the green microalgae *Chlorella vulgaris* biomass production. *Applied Science*, 11(5), 2207-2223. <https://doi.org/10.3390/app11052207>
- Pan, M., Zhu, X., Pan, G., & Angelidak, I. (2021). Integrated valorization system for simultaneous high strength organic wastewater treatment and astaxanthin production from *Haematococcus pluvialis*. *Bioresource Technology*, 326, Article 124761. <https://doi.org/10.1016/j.biortech.2021.124761>
- Podevin, M., Francisci, D. D., Holdt, S. L., & Angelidak, I. (2015). Effect of nitrogen source and acclimatization on specific growth rates of microalgae determined by a high-throughput in vivo microplate autofluorescence method. *Journal of Applied Phycology*, 27, 1415-1423. <https://doi.org/10.1007/s10811-014-0468-2>
- Qi, M., Yang, Y., Zhang, X., Zhang, X., Wang, M., Zhang, W., Lu, X., & Tong, Y. (2020). Pollution reduction and operating cost analysis of municipal wastewater treatment in China and implication for future wastewater management. *Journal of Cleaner Production*, 253, Article 120003. <https://doi.org/10.1016/j.jclepro.2020.120003>
- Ramsundar, P., Guldhe, A., Singh, P., & Bux, F. (2017). Assessment of municipal wastewaters at various stages of treatment process as potential growth media for *Chlorella sorokiniana* under different modes of cultivation. *Bioresource Technology*, 227, 82-92. <https://doi.org/10.1016/j.biortech.2016.12.037>
- Ren, Y., Deng, J., Huang, J., Wu, Z., Yi, Z., Bi, Y. G., & Chen, F. (2021). Using green alga *Haematococcus pluvialis* for astaxanthin and lipid co-production: Advances and outlook. *Bioresource Technology*, 340, Article 125736.
- Ru, I. T. K., Sung, Y. Y., Jusoh, M., Wahid, M. E. A., & Nagappan, T. (2020). *Chlorella vulgaris*: A perspective on its potential for combining high biomass with high value bioproducts. *Applied Phycology*, 1(1), 2-11. <https://doi.org/10.1080/26388081.2020.1715256>
- Ryu, B. G., Kim, E. J., Kim, H. S., Kim, J., Choi, Y. E., & Yang, J. W. (2014). Simultaneous treatment of municipal wastewater and biodiesel production by cultivation of *Chlorella vulgaris* with indigenous wastewater bacteria. *Biotechnology and Bioprocess Engineering*, 19(2), 201-210. <https://doi.org/10.1007/s12257-013-0250-3>
- Sato, H., Nagare, H., Huynh, T. N. C., & Komatsu, H. (2015). Development of a new wastewater treatment process for resource recovery of carotenoids. *Water Science and Technology*, 72(7), 1191-1197. <https://doi.org/10.2166/wst.2015.330>
- Shah, M. M. R. (2019). Astaxanthin production by microalgae *Haematococcus pluvialis* through wastewater treatment: Waste to resource. In S. Gupta & F. Bux (Eds.), *Application of microalgae in wastewater treatment* (pp. 17-39). Springer. [https://doi.org/10.1007/978-3-030-13909-4\\_2](https://doi.org/10.1007/978-3-030-13909-4_2)

- Shah, M. M. R., Liang, Y., Cheng, J. J., & Daroch, M. (2016). Astaxanthin-producing green microalga *Haematococcus pluvialis*: From single cell to high value commercial products. *Frontiers in Plant Science*, 7, Article 531. <https://doi.org/10.3389/fpls.2016.00531>
- Sipaúba-Tavares, L. H., Berchielli-Moraisa, F. A., & Scardoeli-Truzzia, B. (2015). Growth of *Haematococcus pluvialis* Flotow in alternative media. *Brazilian Journal of Biology*, 75(4), 796-803. <https://doi.org/10.1590/1519-6984.23013>
- Tan, X., Meng, J., Tang, Z., Yang, L., & Zhang, W. (2020). Optimization of algae mixotrophic culture for nutrients recycling and biomass/lipids production in anaerobically digested waste sludge by various organic acids addition. *Chemosphere*, 244, Article 125509. <https://doi.org/10.1016/j.chemosphere.2019.125509>
- Tao, R., Kinnunen, V., Praveenkumar, R., Lakaniemi, A. M., & Rintala, J. A. (2017). Comparison of *Scenedesmus acuminatus* and *Chlorella vulgaris* cultivation in liquid digestates from anaerobic digestion of pulp and paper industry and municipal wastewater treatment sludge. *Journal of Applied Phycology*, 29(6), 2845-2856. <https://doi.org/10.1007/s10811-017-1175-6>
- Thomas, D. G., Minj, N., Mohan, N., & Rao, P. H. (2016). Cultivation of microalgae in domestic wastewater for biofuel applications - An upstream approach. *Journal of Algal Biomass Utilization*, 7(1), 62-70.
- Trivedi, T., Jain, D., Mulla, N. S. S., Mamatha, S. S., Damare, S. R., Sreepada, R. A., Kumar, S., & Gupta, V. (2019). Improvement in biomass, lipid production and biodiesel properties of a euryhaline *Chlorella vulgaris* NIOCCV on mixotrophic cultivation in wastewater from a fish processing plant. *Renewable Energy*, 139(3), 326-335. <https://doi.org/10.1016/j.renene.2019.02.065>
- Umamaheswari, J., Kavitha, M. S., & Shanthakumar, S. (2020). Outdoor cultivation of *Chlorella pyrenoidosa* in paddy-soaked wastewater and a feasibility study on biodiesel production from wet algal biomass through in-situ transesterification. *Biomass and Bioenergy*, 143, Article 105853. <https://doi.org/10.1016/j.biombioe.2020.105853>
- Wang, F., Gao, B., Wu, M., Huang, L., & Zhang, C. (2019). A novel strategy for the hyper-production of astaxanthin from the newly isolated microalga *Haematococcus pluvialis* JNU35. *Algal Research*, 39, Article 101466. <https://doi.org/10.1016/j.algal.2019.101466>
- Wang, Y., Guo, W., Yen, H. W., Ho, S. H., Lo, Y. C., Cheng, C. L., Ren, N., & Chang, J. S. (2015). Cultivation of *Chlorella vulgaris* JSC-6 with swine wastewater for simultaneous nutrient/COD removal and carbohydrate production. *Bioresource Technology*, 198, 619-625. <https://doi.org/10.1016/j.biortech.2015.09.067>
- Wen, Y., He, Y., Ji, X., Li, S., Chen, L., Zhou, Y., Wang, M., & Chen, B. (2017). Isolation of an indigenous *Chlorella vulgaris* from swine wastewater and characterization of its nutrient removal ability in undiluted sewage. *Bioresource Technology*, 243, 247-253. <https://doi.org/10.1016/j.biortech.2017.06.094>
- Whitton, R., LeMével, A., Pidou, M., Ometto, F., Villa, R., & Jefferson, B. (2016). Influence of microalgal N and P composition on wastewater nutrient remediation. *Water Research*, 91, 371-378. <https://doi.org/10.1016/j.watres.2015.12.054>
- Wiel, J. B. V., Mikulicz, J. D., Boysen, M. R., Hashemi, N., Kalgren, P., Nauman, L. M., Baetzold, S. J., Powell, G. G., He, H., & Hashemi, N. N. (2017). Characterization of *Chlorella vulgaris* and *Chlorella protothecoides* using multi-pixel photon counters in a 3D focusing optofluidic system. *RSC Advance*, 7, 4402-4408. <https://doi.org/10.1039/C6RA25837A>

- Wu Y. H., Yang, J., Hu, H. Y. & Yu, Y. (2013). Lipid-rich microalgal biomass production and nutrient removal by *Haematococcus pluvialis* in domestic secondary effluent. *Ecological Engineering*, 60, 155-159. <https://doi.org/10.1016/j.ecoleng.2013.07.066>
- Wu, L. F., Chen, P. C., & Lee, C. M. (2013). The effects of nitrogen sources and temperature on cell growth and lipid accumulation of microalgae. *International Biodeterioration and Biodegradation*, 85, 506-510. <https://doi.org/10.1016/j.ibiod.2013.05.016>
- Zhang, L., Lu, H., Zhang, Y., Li, B., Liu, Z., Duan, N., & Liu, M. (2016). Nutrient recovery and biomass production by cultivating *Chlorella vulgaris* 1067 from four types of post-hydrothermal liquefaction wastewater. *Journal of Applied Phycology*, 28(2), 1031-1039. <https://doi.org/10.1007/s10811-015-0640-3>

## FPGA-based Implementation of SHA-256 with Improvement of Throughput using Unfolding Transformation

Shamsiah Suhaili\* and Norhuzaimin Julai

*Department of Electrical and Electronic Engineering, Faculty of Engineering, Universiti Malaysia Sarawak, 94300 UNIMAS, Kota Samarahan, Sarawak, Malaysia*

### ABSTRACT

Security has grown in importance as a study issue in recent years. Several cryptographic algorithms have been created to increase the performance of these information-protecting methods. One of the cryptography categories is a hash function. This paper proposes the implementation of the SHA-256 (Secure Hash Algorithm-256) hash function. The unfolding transformation approach was presented in this study to enhance the throughput of the SHA-256 design. The unfolding method is employed in the hash function by producing the hash value output based on modifying the SHA-256 structure. In this unfolding method, SHA-256 decreases the number of clock cycles required for traditional architecture by a factor of two, from 64 to 34 because of the delay. To put it another way, one cycle of the SHA-256 design can generate up to four parallel inputs for the output. As a result, the throughput of the SHA-256 design can be improved by reducing the number of cycles by 16 cycles. ModelSim was used to validate the output simulations created in Verilog code. The SHA-256 hash function factor four hardware implementation was successfully tested using the Altera DE2-115 FPGA board. According to timing simulation findings, the suggested unfolding hash function with factor four provides the most significant throughput of around 4196.30 Mbps. In contrast, the suggested unfolding with factor two surpassed the classic SHA-256

design in terms of maximum frequency. As a result, the throughput of SHA-256 increases 13.7% compared to unfolding factor two and 58.1% improvement from the conventional design of SHA-256 design.

### ARTICLE INFO

#### Article history:

Received: 1 July 2021

Accepted: 15 September 2021

Published: 10 January 2022

DOI: <https://doi.org/10.47836/pjst.30.1.32>

#### E-mail addresses:

[sushamsiah@unimas.my](mailto:sushamsiah@unimas.my) (Shamsiah Suhaili)

[jnorhuza@unimas.my](mailto:jnorhuza@unimas.my) (Norhuzaimin Julai)

\*Corresponding author

**Keywords:** FPGA implementation, SHA-256, throughput, unfolding technique

## INTRODUCTION

Cryptography is the study of encrypting messages such that only the intended recipient may read them. Cryptographic algorithms are divided into symmetric cryptography, asymmetric cryptography, and hash functions. Asymmetric cryptography employs two separate keys to encrypt and decrypt the message, whereas symmetric cryptography utilizes only one key. The SHA-256 design was the subject of this investigation with no key. Instead, the hash value of a variable-length message was converted to a fixed-length text hash value. Hash functions include various types such as SHA (Secure Hash Algorithm) family, MD5 (Message Digest 5), SHA-1 (Secure Hash Algorithm 1), RIPEMD-160 (RACE Integrity Primitives Evaluation Message Digest 160), and other types.

The hash value results from a hash function where the input depends on the user, which leads to output for a specific algorithm. The hash code is only obtained once the one-way property receives the message input. It is impossible to reverse the process of obtaining the message from the hash code. When the output hash codes M1 and M2 are identical in the second preimage, finding the message M2 is challenging. Finally, collision resistance occurs when two separate messages and two hash function messages digest. Finding the same hash code  $H(M1) = H(M2)$  with two different messages is tough.

One of the approaches for obtaining a new program that runs more than one iteration of the original program is to utilize an unfolding algorithm. The unfolding factor defines the number of iterations in the original program. This methodology is used to increase the performance of the SHA-256 design (Suhaili & Watanabe, 2017). The architecture is referred to as Register Transfer Level, and this strategy focuses on the latency of the designs (RTL). Unfolding transformation factors 2 and 4 were implemented in this paper to minimize the latencies of the SHA-256 hash function. (Parhi, 1999). Both designs were carried out in parallel. The area, on the other hand, grew dramatically. Much research has been done related to SHA-256 using both ASIC and FPGA implementation (Shahid et al., 2011; Sun et al., 2007; Sklavos & Koufopavlou, 2003; Miao et al., 2009; Mestiri et al., 2015; Chaves et al., 2006; McEvoy et al., 2006; Ahmad & Das, 2005; Padhi & Chaudri, 2017; Kahri et al., 2015; Michail et al., 2010; Michail et al., 2005; Phan et al., 2021; Kester & Henry, 2019; Bensalem et al., 2021; He et al., 2018; Zhang et al., 2019; Wu et al., 2020; Li et al., 2019; Li et al., 2020; Brazhinikov, 2020; Chen & Li, 2020).

The inner pipelining with the unfolding of SHA-256 hash functions were designed in this study. Based on Arria II GX, these algorithms were synthesized and implemented. ModelSim was used to verify the simulation results. The following is a breakdown of the structure of the paper: Section 2 presents the proposed SHA-256 design. The implementation results are detailed in Section 3, along with a comparison of alternative SHA-256 solutions. The conclusions are discussed in the final part.

## RELATED WORKS

SHA-2 hash function consists of four different hash functions such as SHA-224, SHA-256, SHA-384, and SHA-512. The output length of these hash algorithms depends on the SHA-2 size ranging from 224 to 512-bit. This paper only focused on the SHA-256 algorithm because of the extension from the SHA-1 algorithm. In addition, previous SHA-256 was implemented using different types of FPGA devices.

Miao et al. (2009) designed and implemented SHA-1, SHA-224, SHA-256, SHA-384, and SHA-512 cryptographic chip on EP2S15F484C3 of Stratix II. These designs were written using Verilog code. Modelsim 6.0c simulator tool was used to simulate and verify the design. From this result, SHA-256 provided 143.16 MHz of maximum frequency and 909.8 Mbps of throughput. In this design, Carry Save Adder (CSA) and Carry Lookahead Adder were implemented into the SHA-256 design to increase execution speed (Miao et al., 2009). Sklavos and Koufopavlou (2003) proposed SHA-256 designs with 83 MHz of maximum frequency and 326 Mbps of throughput. This design was implemented on Xilinx Virtex v200pq240. From this result, the maximum frequency of the SHA-256 algorithm slightly decreases compared with the previous design. This design can be applied efficiently to implement digital signature algorithms, keyed-hash message authentication codes, and random numbers generators architectures (Sklavos & Koufopavlou, 2003).

Ahmad and Das (2005) proposed two types of SHA-2, such as SHA-256 and SHA-512 algorithms. These algorithms were designed and tested based on the Altera Quartus II CAD tool. This paper does not mention which specific programming is used to design and implement the SHA-256 algorithms. Overall, the designs were analyzed and synthesized using Verilog HDL and VHDL, placed and routed in Altera devices of APEX II, Stratix, and Mercury family FPGAs. The maximum frequency of SHA-256 designs was 41.97 MHz (Ahmad & Das, 2005). The maximum frequency of the SHA-256 algorithm decreased significantly compared with other designs.

McEvoy et al. (2006) designed six SHA processors using VHDL and implemented them on Xilinx Virtex II xc2v2000-bf957. For SHA-256, one processor had a basic quasi-pipelined core, one had a 2x-unrolled core, and another had a 4x-unrolled core (McEvoy et al., 2006). These techniques have been proposed to speed up the calculations in the SHA core; Carry Save Adder (CSA), unrolling, quasi-pipelining, which use register break the long critical path within the SHA core, Block RAM, and parallel counter. From the results, unrolled SHA-256 provided low latency compared with the basic design. However, the basic SHA-256 design gave 133.06 MHz of the maximum frequency with 1009 Mbps of throughput.

Chaves et al. (2006) has improved the performance of SHA-2 algorithms. SHA-256 was implemented on Xilinx VIRTEX II Pro (XC2VP30-7) and provided 174 MHz of maximum frequency. This design proposed a rescheduling technique that efficiently uses

a pipelined structure without increasing area and hardware reutilization methods to enable resource-saving. The results showed that the maximum frequency of SHA-256 was 174 MHz with 1370 Mbps of throughput (Chaves et al., 2006). Sun et al. (2007) proposed SHA-2 (256, 384, 512) designs, and the algorithms were written using Verilog code. These designs were simulated and verified using ModelSim 6.0a. The target FPGA device for these designs was the same as the device in Sklavos paper, Xilinx Virtex v200pq240-6. The method of SHA-256 was based on Carry Lookahead Adder (CLA) and Carry Save Adder (CSA). This technique tried to improve the critical path of the design. However, the results showed that the maximum frequency of SHA-256 decreased significantly and only gave 74 MHz with 291 Mbps of throughput (Sun et al., 2007).

Shahid et al. (2011) introduced different hash function algorithms modeled using VHDL. Xilinx and Altera Quartus II were used to synthesize and implement these designs. The designs were divided into: basic and embedded with DSP units and block RAMs. The use of embedded FPGAs resources in the implementation of SHA-2 provided high frequency compared with basic designs. The maximum frequency of SHA-2 increased significantly on Virtex 5 and Stratix III with 218.2 MHz and 205.8 MHz, respectively (Shahid et al., 2011). Kahri et al. (2015) focused on both SHA-256 and SHA-512 designs. The designs showed the results based on a finite state machine with a padded process unit. The FSM performed five states: pad 0, pad 1, pad 2, pad 3, and pad F. The SHA-256 design gave 202.54 MHz of maximum frequency 1.58 Gbps of throughput (Kahri et al., 2015).

Padhi and Chaudhari (2017) designed the optimized pipelined architecture of the SHA-256 hash function. The design has been implemented on Xilinx Virtex-4 FPGA using Verilog HDL code. In this design, CSA was used to enhance the performance of architecture. The maximum frequency of the design was 170.75 MHz with a throughput of 1344.98Mbps (Padhi & Chaudhari, 2017). Michail et al. (2005) proposed an SHA-256 design with 64.1 MHz with 2052.1 MHz. This design was implemented on Virtex E using the pre-computation technique to improve design throughput (Michail et al., 2005). Michail et al. (2010) improved the throughput of optimized SHA-256 design using VHDL based on Virtex FPGA implementation. This design uses partially unrolled operation with pre-calculation and pre-computation. Besides, CSA also is applied in this design to increase the throughput of design (Michail et al., 2010).

He et al. (2018) proposed the SHA-256 design using a three-stage pipeline using Cyclone II FPGA implementation. The throughput obtained for the design was 655.66 MHz with a masking scheme (He et al., 2018). Next, Zhang et al. (2019) and Wu et al. (2020) proposed the SHA-256 design with ASIC implementation. Both inventions have been implemented and synthesized with 14nm technology (Zhang et al., 2019; Wu et al., 2020). Finally, Li et al. (2019) proposed an asynchronous SHA-256 implementation design in SMIC 40nm technology. The result of the design was simulated and verified using Synopsys VCS (Li et al., 2019).



Li et al. (2020) proposed an FPGA-based implementation that gave the implementation results with 100 MHz and 787 Mbps of throughput. This design used neural network and blockchain fusion-based image copyright protection and implemented DNN and SHA-256 on FPGA (Li et al., 2020). Brazhnikov (2020) proposed SHA2 with 28nm CMOS technology. This design produced different results by applying different adder types to the SHA-256 design, such as RCA, CLA, Han-Carlson, Brent-Kung, Kogge Stone, and Sklansky, in terms of delay and area (Brazhnikov, 2020). There is no information related to Maximum frequency and throughput in this paper. The performance of SHA-256 in terms of high-throughput was the main objective of this paper. Chen and Li (2020) proposed a rescheduling method to enhance the throughput. This design was implemented on Virtex-4 with a throughput of 1984 MHz with an area of 979 slices (Chen & Li, 2020).

Bensalem et al. (2021) proposed the latest implementation to improve throughput. Bensalem improved the SHA-256 design implementation on FPGA using OpenCL optimization techniques. These optimization techniques include inserting local memories, loop splitting, loop unrolling, and loop pipelining. This design obtained a throughput of 3973 Mbps (Bensalem et al., 2021). These designs were the previous implementation of SHA-256 based on ASIC and FPGA implementation. In this paper, the improvement of throughput of the SHA-256 hash function was designed and implemented on FPGA to improve the performance by using unfolding transformation techniques. Table 1 depicts a simplified version of the prior SHA-256 design and the proposed SHA-256 design.

Table 1

*Previous design of SHA-256 algorithm and proposed SHA-256 design*

No.	Authors / year	Device	Design Method
1	Miao et al. (2009)	Stratix II–FPGA Implementation	• Iterative CSA and CLA
2	Sklavos and Koufopavlou (2003)	Xilinx Virtex v200pq240–FPGA Implementation	• Iterative
3	Ahmad and Das (2005)	APEX II, Stratix, and Mercury family FPGAs–FPGA Implementation	• Iterative
4	McEvoy et al. (2006)	Xilinx Virtex II xc2v2000-bf957–FPGA Implementation	• CSA Quasi-pipelining
5	Chaves et al. (2006)	Xilinx VIRTEX II Pro (XC2VP30-7)–FPGA Implementation	• Pipelining

Table 1 (Continue)

No.	Authors / year	Device	Design Method
6	Sun et al. (2007)	Xilinx Virtex v200pq240-6-FPGA Implementation	• Iterative CSA and CLA
7	Shahid et al. (2011)	Virtex 5 and Stratix III-FPGA Implementation	• Iterative
8	Padhi and Chaudhari (2017)	Xilinx Virtex-4-FPGA Implementation	• Iterative
9	Michail et al. (2005)	Virtex E-FPGA Implementation	• Iterative (pre-computation technique)
10	Michail et al. (2010)	Virtex-FPGA Implementation	• Iterative partially unrolled operation CSA
11	He et al. (2018)	Cyclone II-FPGA Implementation	• Three-stage pipeline
12	Zhang et al. (2019)	ASIC Implementation	• Iterative
13	Wu et al. (2020)	ASIC Implementation	• Iterative
14	Li et al. (2020)	FPGA-FPGA Implementation	• Iterative neural network blockchain fusion
15	Brazhnikov (2020)	28nm CMOS technology	• Iterative RCA, CLA, Han-carlson, Brent-Kung, Kogge Stone and Sklansky
16	Chen and Li (2020)	Virtex-4-FPGA Implementation	• Iterative (rescheduling method)
17	Bensalem (2021)	FPGA Implementation ASIC Implementation	• OpenCL optimization techniques loop splitting, loop unrolling, and loop pipelining
18	Proposed SHA-256 Design	Arria II GX-FPGA Implementation	• Iterative
19	Proposed SHA-256 Unfolding Design (factor 2)	Arria II GX-FPGA Implementation	• Unfolding factor two
19	Proposed SHA-256 Unfolding Design (factor 4)	Arria II GX and Cyclone IV-FPGA Implementation	• Unfolding factor four

## MATERIALS AND METHODS

These designs were developed to improve throughput performance. SHA-256 was created using Verilog code. The counter SHA-256 module and the other five modules are modules inside this design architecture. The structure of the modules inside the SHA-256 unfolding design is the distinction between two different types of SHA-256 designs. The sequence of constants and messages was identified to be altered when other inputs were used. For input, 15 blocks of 32-bit data were added. Equation 1 was used in this design for the message,  $W_t$ . SHA-256 message,  $W_t$

$$\begin{aligned} W_t &= \text{message input} & 0 \leq t \leq 15 \\ W_t &= \sigma_1^{256}(W_{t-2}) + W_{t-7} + \sigma_0^{256}(W_{t-15}) + W_{t-16} & 16 \leq t \leq 63 \end{aligned} \quad [1]$$

Where,

$$\sigma_0^{256}(x) = ROTR^7(x) + ROTR^{18}(x) + SHR^3(x) \quad [2]$$

$$\sigma_1^{256}(x) = ROTR^{17}(x) + ROTR^{19}(x) + SHR^{10}(x) \quad [3]$$

Equations 2 and 3 were used to generate both functions. The rotation value for x value is shown in Equation 2 for sigma\_0. While for Equation 3, sigma 1 can be obtained by rotating the message x with the value given in Equation 3. It was divided into two portions for the compression function,  $Temp_1$  and  $Temp_2$ . Ch and  $\Sigma_1$  make up  $Temp_1$ , while maj and  $\Sigma_0$  make up  $Temp_2$ . The equations for summation 0 and summation 1, namely  $\Sigma_0$  and  $\Sigma_1$  are shown in Equations 4 and 5. The number of rotation inputs a and e will be based on the number specified in the equations, just like sigma 0 and sigma 1.

$$\Sigma_0(a) = ROTR^2(a) + ROTR^3(a) + ROTR^2(a) \quad [4]$$

$$\Sigma_1(e) = ROTR^6(e) + ROTR^1(e) + ROTR^3(e) \quad [5]$$

The message sequence was generated using a counter module. The final module was developed after finishing all rounds of iteration by the SHA-256 hash algorithm. Before SHA-256 began processing the message, a Multiplexer module assisted in generating eight buffer initializations. 64X32-bit ROM blocks were used to define the constant Kt. Finally, the output module was used to create the SHA-256 message digest. In this model, the final output of the SHA-256 compression function was combined with buffer initialization.

Modifications must be made to each module to improve the performance of the throughput SHA-256 design. For example, two 32-bit parallel inputs with constants were required for the factor two design. Similarly, four parallel 32-bit inputs and four parallel constants were needed in this design. As a result, all information for the following sequence cycle must be changed. Each of the inputs modules has to be changed to achieve this

method. Figure 1 shows the flowchart for this design. It starts with a compilation of RTL designs. Then, the design was evaluated using both functional and timing simulation with both design and testbench file of SHA-256 hash function algorithm before download to FPGA hardware design.

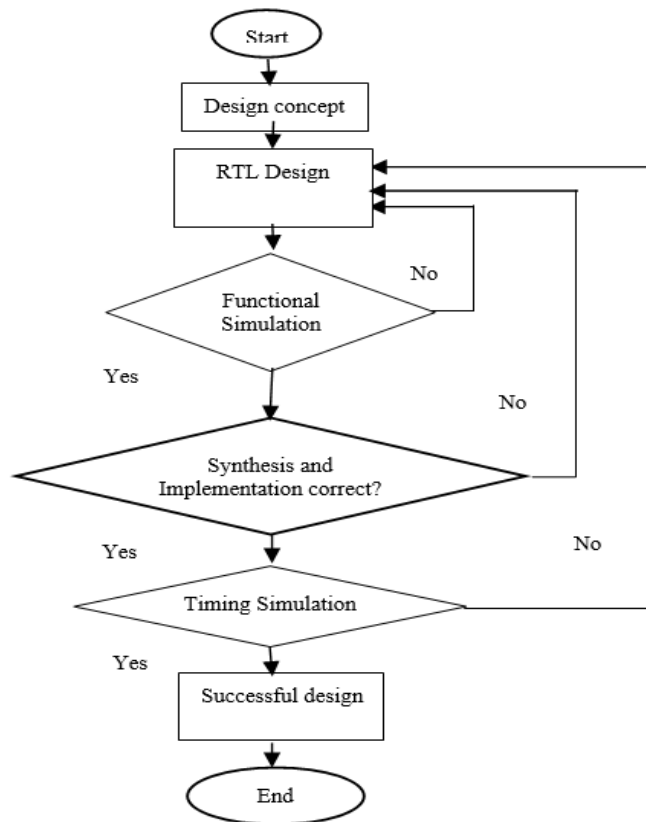


Figure 1. SHA-256 flowchart design

The SHA-256 hash function was improved as a result of these changes. The latency is shortened dependent on the factor J using an unfolding design methodology (Parhi, 1999). Furthermore, this method improves the throughput of the design. For unfolding factor two, the latency reduces to 46.4% from the traditional design, and for unfolding factor four, the percentage reduces around 45.1%. The number of latencies was calculated final results. It was decreased as the design architecture unfolded and changed in response to varied inputs.

In addition, based on modification on modules inside the design, the frequency performance of the design has increased. Compared to the usual design, the frequency of unfolding design rose dramatically with factor two. Compared to two other designs, the

modification of the unfolding method had a large area implementation. However, because of the short latencies, it allowed for high throughput.

The SHA-256 algorithm adjusted message schedule and compression function created the unfolding factor 2 and 4 architecture. This paper used the unfolding technique with factors two and four. Modifications to two modules must be considered. Therefore, it is necessary to consider the alterations to these two modules in the design. The block diagrams of  $Temp_{10}$  and  $Temp_{20}$  are shown in Figures 2 and 3. The following block diagrams and  $\Sigma_{10}$  show how they differed from traditional  $Temp_1$  and  $Temp_2$ . The output of the unfolding design was remade in a different order, with different results. These equations have the SHA-256 algorithm compression function added to them.  $\Sigma_{10}$ ,  $Cho(next\_e, e, f)$ , Message,  $W_{t-1}$  and Constant,  $K_{t-1}$  are found in  $Temp_{10}$ , whereas  $\Sigma_{00}$  and  $Majo(next\_a, a, b)$  are found in  $Temp_{20}$ . A 32-bit adder was used to achieve these results. The  $Temp_{10}$  and  $Temp_{20}$  block diagram design has a different set of data inputs.

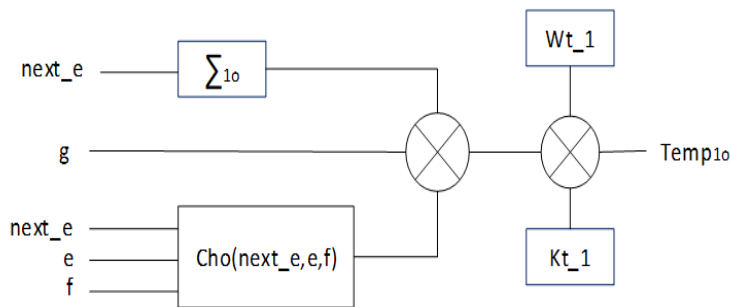


Figure 2. Architecture of  $Temp_{10}$  block diagram

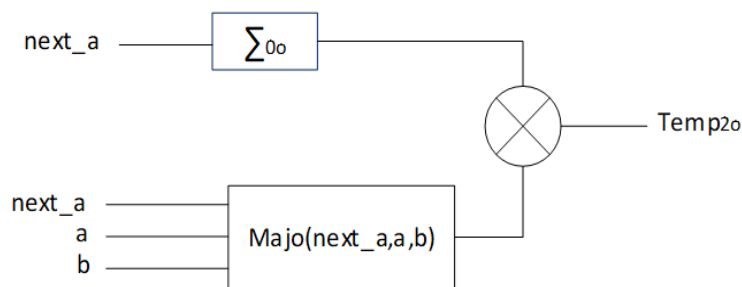


Figure 3. Architecture of  $Temp_{20}$  block diagram

The two architectures inside  $Temp_{10}$  and  $Temp_{20}$  are shown in Figures 4 and 5. The different types of gates are used in both architectures with different location topologies. Both Figures 4 and 5 show that the data inputs differ from the standard function for Cho and Majo. From Figures 4 and 5, it is clearly shown that the new data inputs are applied.

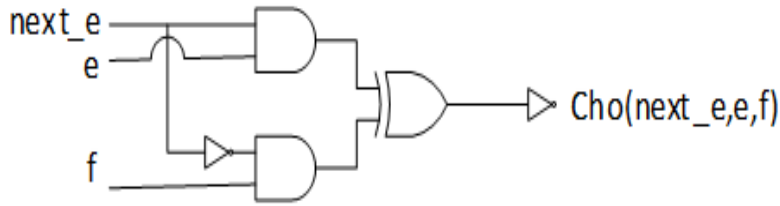


Figure 4. Architectures of Cho Function

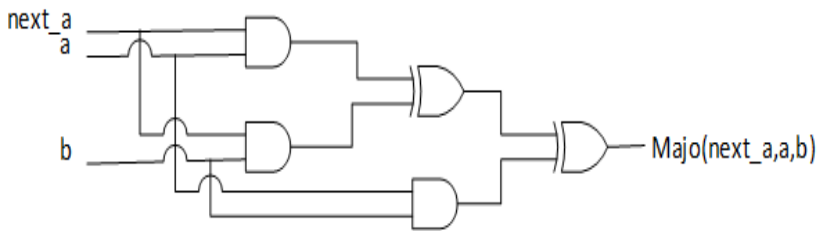


Figure 5. Architectures of Majo Function

The proposed block diagram for summation<sub>0o</sub> and summation<sub>1o</sub> are shown in Figures 6 and 7, respectively. The input next<sub>a</sub> was used to represent, whereas next<sub>e</sub> was used to represent. With a fixed number of values, all rotations in both designs followed the right direction. Finally, using an XOR gate to combine all inputs, the final outputs  $\Sigma_{0o}$  and  $\Sigma_{1o}$  were achieved.

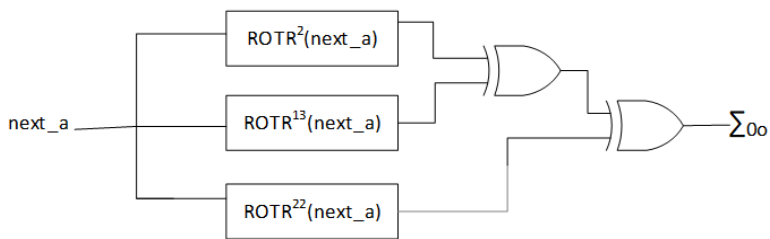


Figure 6. Architecture of  $\Sigma_{1o}(next_e)$

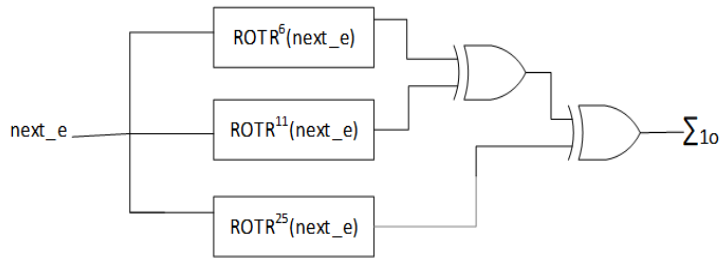


Figure 7. Architecture of  $\Sigma_{10}(next\_e)$

New  $next\_eo$  and  $next\_ao$  were calculated using output  $Temp_{10}$  and  $Temp_{20}$ . Equations 6 and 7 below show the new output value signal.

$$next\_eo = c + Temp_{10} \tag{6}$$

$$next\_ao = Temp_{10} + Temp_{20} \tag{7}$$

Figures 8 and 9 illustrate the revised inner architecture for  $Temp_{11}$  and  $Temp_{21}$ . These two inputs,  $Ch1$  and  $Maj1$  from Figures 8 and 9, are all presented with distinct signals. It is due to factor 4 of the unfolding technique. Similarly, function  $\Sigma_{11}$  and  $\Sigma_{01}$  also use new input to be applied in the new architecture of  $Temp_1$  and  $Temp_2$ . The new equations can be derived from Equations 8 and 9 below by applying the new inputs signal to both equations.

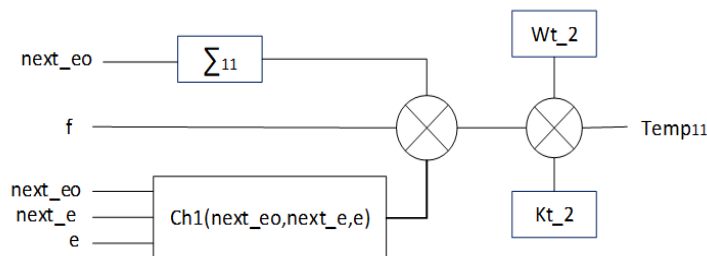


Figure 8. Architecture of  $Temp_{11}$  block diagram

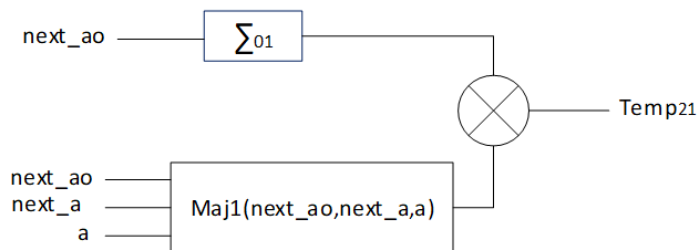


Figure 9. Architecture of  $Temp_{21}$  block diagram

The unfolding factor four was calculated until  $Temp_{12}$  and  $Temp_{22}$  since it required four parallel executions.

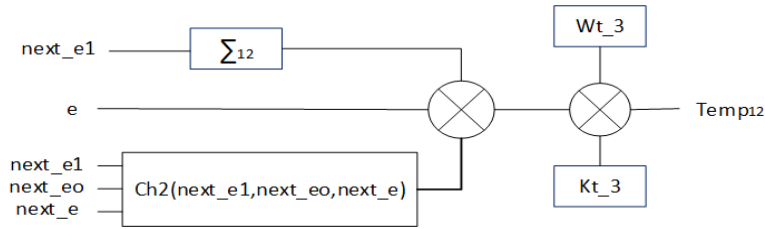


Figure 10. Architecture of  $Temp_{12}$  block diagram

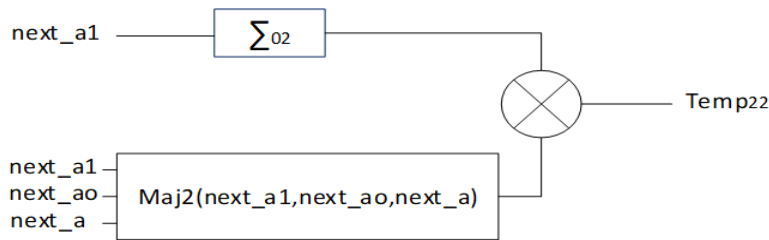


Figure 11. Architecture of  $Temp_{22}$  block diagram

Figures 10 and 11 illustrate the new output for both Temp functions. In both function  $\Sigma_{12}$  and  $\Sigma_{02}$ , two new signal inputs are employed. In addition, the data was relocated to the same place in the input sequence as the one before it. Both Figures 10 and 11 demonstrate these data inputs.

The new signals for Equations 10 and 11 were derived from the  $Temp_{12}$  and  $Temp_{22}$  datasets. The output of  $next\_e2$  and  $next\_a2$  are shown in the equation below.

$$next\_e2 = a + Temp_{12} \tag{10}$$

$$next\_a2 = Temp_{12} + Temp_{22} \tag{11}$$

The message schedule was modified from prior results in the same way the compression algorithm was. The modification of the previous equation for  $\sigma_{0o}$  and  $\sigma_{1o}$  was processed after receiving the signal. The start of this sequence was at  $wt_2$  and concluded at  $wt_{15}$ .

Figures 12 and 13 depict the architectures for the  $\sigma_{0o}$  and  $\sigma_{1o}$  functions, respectively. The fundamental role of these architectures is to generate the SHA-256 message schedule. A constant quantity of value was used to rotate  $w_2$  in the appropriate direction for  $\sigma_{0o}$ , whereas for  $\sigma_{1o}$ , new data input was used. The  $w_2$  was right-shifted with a specific value in  $\sigma_{0o}$  function, and similarly with the  $W_{15}$ . It was right-shifted in  $\sigma_{1o}$  function with a certain value.



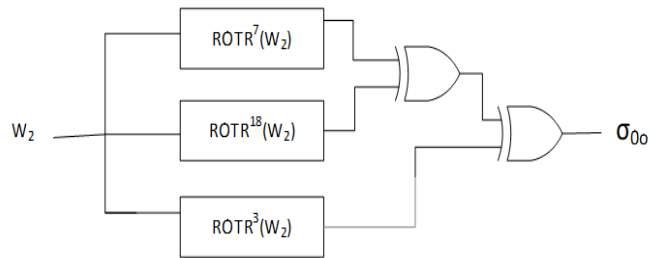


Figure 12. Architecture of  $\sigma_{00}$

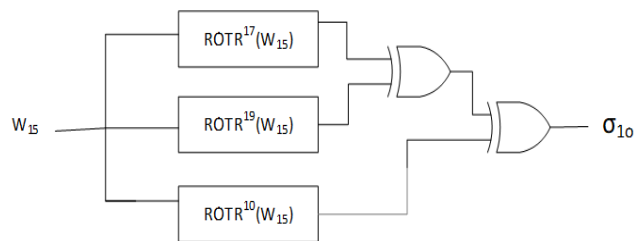


Figure 13. Architecture of  $\sigma_{10}$

With input  $W_3$  and next wt,  $\sigma_{01}$  and  $\sigma_{11}$  were computed for unfolding factor 4. The following Equation 12 was used to calculate next\_wt1.

$$\text{next\_wt1} = W_2 + \sigma_{01} + W_{11} + \sigma_{11} \quad [12]$$

Finally, input  $W_4$  and next\_wto were used to generate the input for  $\sigma_{02}$  and  $\sigma_{12}$ . Figure 13 was used to create the next\_wto. Figure 14 depicts the structure of next\_wt2 and the overall design of unfolding factor 4 for the message schedule. Message input of  $W_0$  data began with  $W_4$  and ended with  $W_{15}$ . The output sequence of next\_wt used in unfolding factor four uses the similar method used in factor two.

Figure 15 illustrates an SHA-256 hash function with an FPGA implementation design. In this phase, functional simulation is used to check the results of the invention. First, Verilog code needs to be converted into gate-level based on an FPGA family device chosen in the early phase of the design. Then, the compilation and synthesis process will be executed to translate the Verilog code into a netlist to represent the actual hardware device. Logic synthesis tools play important roles in digital electronic design automation. After the synthesis process, timing simulation needs to be evaluated in terms of time setup and time hold of the output waveform. Finally, the design can be downloaded to the FPGA device.

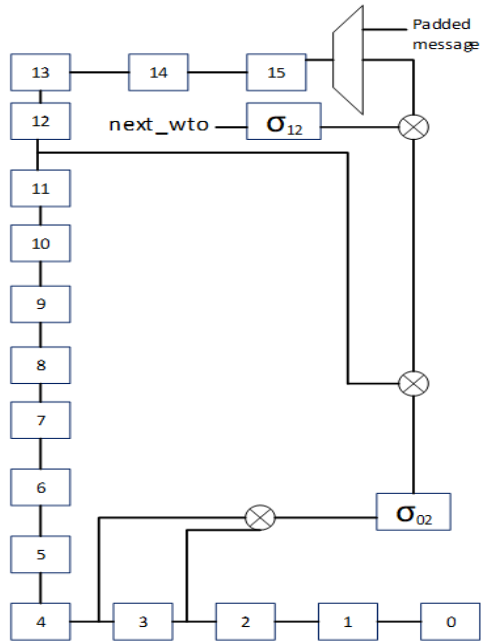


Figure 14. SHA-256 unfolding factor 4 message schedule

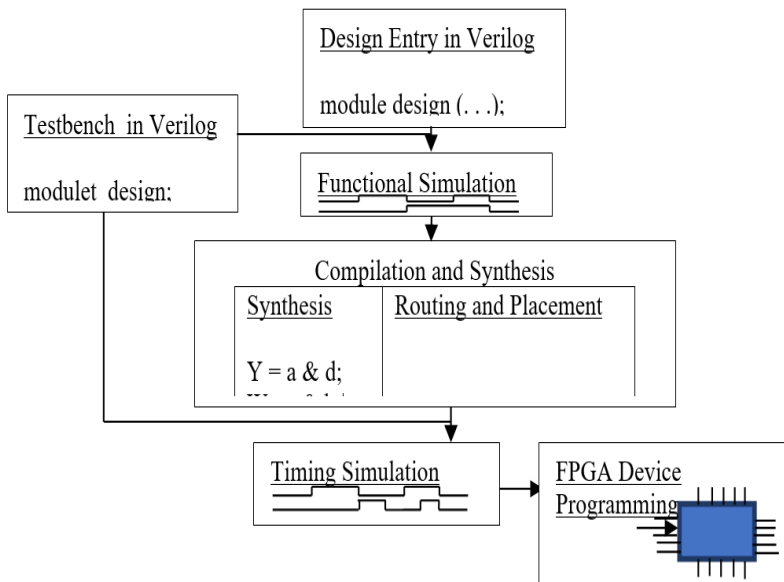


Figure 15. FPGA implementation flow of SHA-256 design

## RESULTS AND DISCUSSION

The proposed SHA-256 unfolding factors two and four have been successfully developed and tested. The Altera Quartus II was used to compile all of the designs written in Verilog code. The functionality of the design was simulated and verified using ModelSim in terms of timing and functional simulation. Finally, the throughput of these designs was calculated using Equation 13.

$$\text{Throughput} = (512 \times \text{FMax}) / \text{Number of Cycle} \quad [13]$$

Table 2 shows a comparison of the proposed SHA-256 designs with previous publications. The design throughput increased significantly by using this unfolding method compared to previous design configurations. Most of the previous SHA-256 algorithms were applied the iterative and pipelining method to design the hash function. Therefore, the area implementation of the designs was smaller than the unfolding method. The unfolding method employs a parallel operation based on the number of unfolding factors. According to the data in Table 2, the unfolding SHA-256 design with factor four design had the highest throughput of all the SHA-256 designs.

Table 2 summarizes the findings of other designs. Iterative and pipelining approaches were applied to the prior SHA-256 algorithm using this table. Different adders, such as CSA and CLA, were applied to the iterative process in the preceding SHA-256 design. Unrolled pipelining was employed in the SHA-256 design of the pipelining method. As a result, three types of SHA-256 algorithms have been proposed to increase the throughput of SHA-256 design: iterative SHA-256 design, unfolding SHA-256 with factor two, and unfolding SHA-256 with factor four. When an unfolding transformation is applied to the SHA-256 algorithm, the design operation improves dramatically because the design is handled in parallel. By minimizing the number of latencies, this strategy can assist in enhancing the performance of SHA-256 designs. Different devices produced different results when the SHA-256 design was implemented. As a result, better results can be obtained by selecting an appropriate family device for implementation.

Table 2

*Other SHA-256 design results in synthesis and implementation comparison*

SHA-256 Hash Function	Area	Device	FMax	Throughput
Proposed SHA-256 Design	855 ALUTs	Arria II GX	228.15 MHz	1756.58 Mbps

Table 2 (Continue)

SHA-256 Hash Function	Area	Device	FMax	Throughput
Proposed SHA-256 unfolding design factor 2	1345 ALUTs	Arria II GX	251.07 MHz	3621.07 Mbps
Proposed SHA-256 unfolding design factor 4	2064 ALUTs	Arria II GX	159.82 MHz	4196.30 Mbps
SHA-2 (Shahid et al., 2011)	320 CLBs	Virtex 5	218.2 MHz	1719 Mbps
SHA-2 (Shahid et al., 2011)	795 ALUTs	Stratix III	205.8 MHz	1621 Mbps
SHA(256,384,512) (Sun et al., 2007)	2207 CLBs	Virtex v200pq 240-6	74 MHz	291 Mbps
SHA-256 (Sklavos & Koufopavlou, 2003)	1060 CLBs	Virtex v200pq240	83 MHz	326 Mbps
SHA-256 (Miao et al., 2009)	2150 ALUTs	Stratix II	143.164 MHz	909.816 Mbps
SHA-256 (Mestiri et al., 2015)	387 Slices	Virtex 5 XC5VFX70T	202.54 MHz	1580 Mbps
SHA-256 (Chaves et al., 2006)	755 Slices	XC2PV-7	174 MHz	1370 Mbps
SHA-256 (MeEvoy et al., 2006)	1373 Slices	Virtex-II xc2v2000- bf957	133.06 MHz	1009 Mbps
SHA-256 (Ahmad & Das, 2005)	-	-	41.97 MHz	335.9 Mbps
SHA-256 (Padhi & Chaudhari, 2017)	610 Slices	Virtex-4	170.75 MHz	1344.98 Mbps
SHA-256 (Kahri et al., 2015)	387 Slices	Virtex-5 XC5VFX70T	202.54 MHz	1580 Mbps
SHA-256 (Michail et al., 2010)	1534 CLBs	Virtex	35.1 MHz	2077 Mbps
SHA-256 (Michail et al., 2010)	1655 CLBs	Virtex E	36.4 MHz	2190 Mbps
SHA-256 (Michail et al., 2005)	-	Virtex E	64.1 MHz	2052.1 Mbps
SHA-256 (Phan et al., 2021)	1895 slice/ LUT	Virtex 5	411.3 MHz	3290.4 Mbps
SHA-256 (Bensalem et al., 2021)	67150 LU	Arria10	243 MHz	3970 Mbps

Table 2 (Continue)

SHA-256 Hash Function	Area	Device	FMax	Throughput
SHA-256 (He et al., 2018)	7219 Cells	Cyclone II	116.2 MHz	875.22 Mbps
SHA-256- cascade (Li et al., 2019)	-	SIMC 40nm technology (Synopsys)	227.27 MHz	3600 Mbps
SHA-256 (Li et al., 2020)	-	Alpha-Data ADMPCIE- 7V3	100 MHz	787 Mbps
SHA-256 (Chen & Li, 2020)	979 Slices	Virtex 4	255.7 MHz	1984 Mbps

The proposed design used 855 ALUTs and had a maximum clock frequency of 228.15 MHz. Thus, the performance of the proposed design was improved significantly by using this technique. According to the results, the proposed design had the highest throughput, with 4196.30 Mbps and a maximum frequency of 159.82 MHz due to the internal pipelining design, which used 1159 registers. Compared to traditional architecture, this technique enhanced the design by eliminating round cycles. As a result, the clock cycle count of the SHA-256 unfolding architecture dropped from 66.5 to 19.5 cycles. The hash function design of SHA-256 with excellent throughput was accomplished using the unfolding transformation approach.

The proposed unfolding SHA-256 design can improve the performance of the hash function design. The design frequency can be considerably increased by employing the unfolding method and following the criteria for developing better HDL coding. In addition, the architecture of the FPGA device plays a vital part in the SHA-256 design. Thus, the performance of the SHA-256 design can be improved by identifying the appropriate FPGA device. The earlier implementation of the SHA-256 design is shown in Table 2. Due to budget and device constraints, it is difficult to locate the same device for the same design. The area implementation of the design increases from iterative design to unfolding design, as shown in this table. The throughput of the SHA-256 unfolding with factor four design, on the other hand, greatly increases. SHA-256 improves throughput by 13.7 percent compared to unfolding factor 2 and by 58.1 percent compared to the traditional SHA-256 design. Figure 16 shows the timing simulation results for the conventional method of SHA-256 design with 64 cycles to generate the final output result. The output of SHA-256 hash function represents by eight 32-bit signal output of {Ha0, Ha1, Ha2, Ha3, Ha4, Ha5, Ha6, Ha7} with the value output of "ba7816bf8f01cfea41410de5dae2223b0036177a9cb410ff61f20015ad".

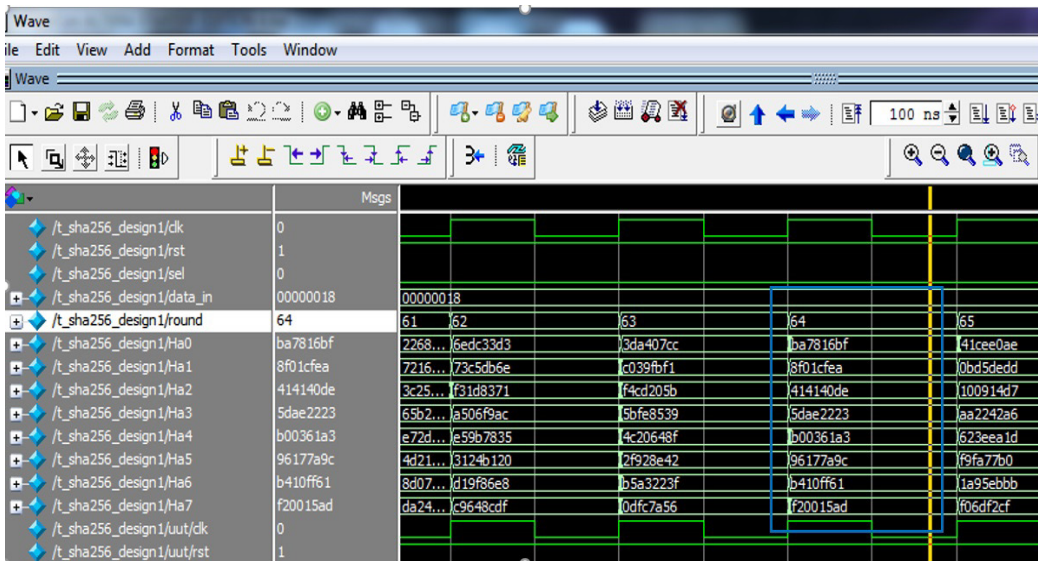


Figure 16. Timing simulation waveform of SHA-256 design

According to Equation 13, the number of cycles for unfolding SHA-256 with factor two is lowered by two, from 64 to 32, as shown in Figure 17. Due to the clock delay in the timing simulation, the number of cycles given in this simulation waveform was 34. Then there will be an increase in throughput of the SHA-256 design.

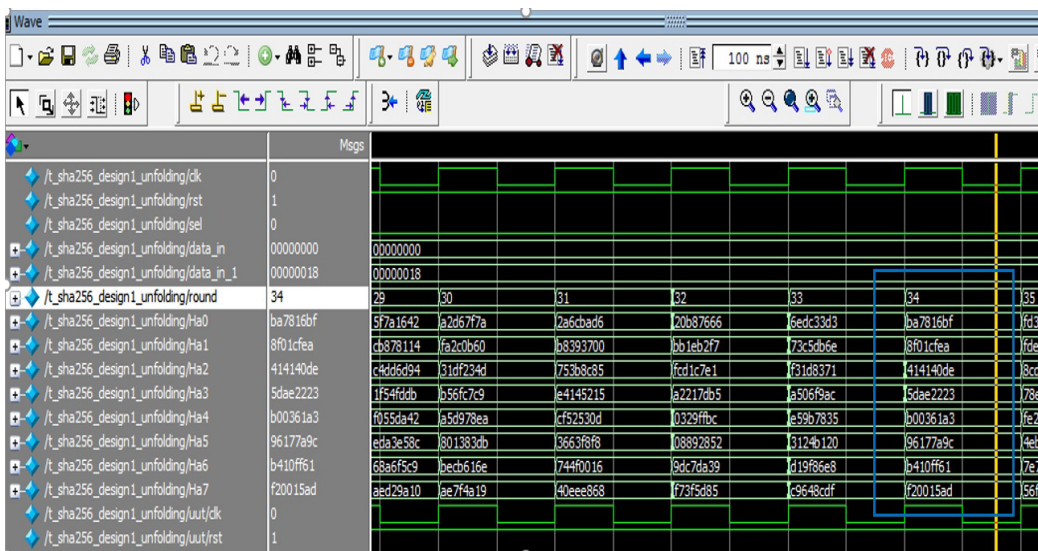


Figure 17. Timing simulation waveform of unfolding SHA-256 with factor two design

Similarly, the cycles of unfolding SHA-256 factor four will decrease by four, bringing the total number of cycles down from 64 to 18. The throughput and performance of the SHA-256 design can benefit from a minimal number of cycles. Figure 18 shows the timing simulation results for unfolding SHA-256 with factor four. Because of the concurrent processing that limits the input-output (I/O) FPGA pads, only 32-bit MSB final results are given in Figure 19(a).

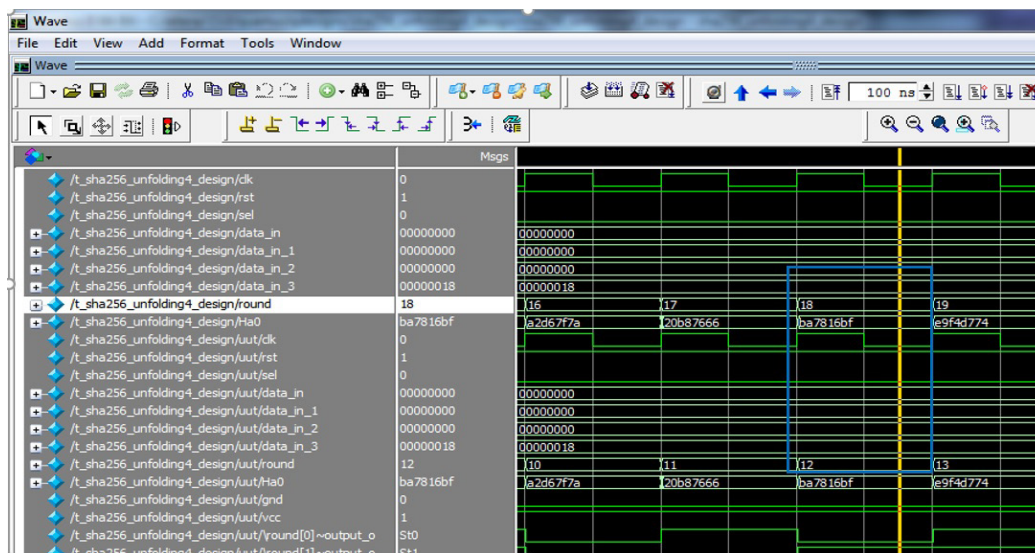


Figure 18. Timing simulation waveform of unfolding SHA-256 with factor four design

The unfolding SHA-256 with factor four design has been downloaded into Cyclone IV E: EP4CE115F29C7 FPGA family device to verify the hardware implementation. The SHA-256 input in this particular instance is the text “abc.” As a result, the text output of the SHA-256 hash function for 256 bits should be “ba7816bf8f01cfea41410de5dae2223b0036177a9cb410ff61f20015ad”.

On the Cyclone IV E family device, Figures 19(a) and 19(b) show the hardware implementation of this hash function. The 32-bit MSB part of the output on the target device EP4CE115F29C7 is “ba7816bf.” The result was evaluated using seven segments, and three red LED bits, yielding 7 in decimal and “111” in binary. If the result of this hash function provides a correct output of 256 bits, the 3 LED outputs will appear 7 in decimal numbers, which is “111” in binary form.

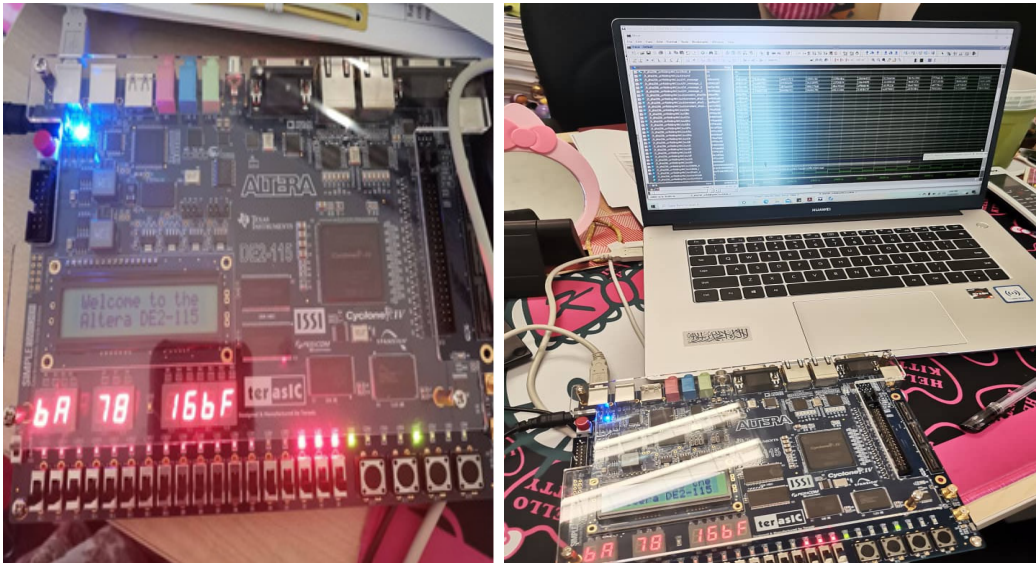


Figure 19. (a) FPGA output implementation display (b) Hardware implementation of SHA-256 hash function

## CONCLUSION

The high-performance design of the hash function is essential in security design. By applying this unfolding method with factor four to the SHA-256 hash function, the throughput of the design increase significantly. It is the best solution to improve the performance of the hash function. The maximum frequency of SHA-256 design implementation illustrates the critical path of the design. In order to obtain the high-performance design, the speed needs to be considered, thus leading to the high throughput of the SHA-256 design. ModelSim was used to simulate the SHA-256 design, then tested on an FPGA device for hardware implementation to verify the hash value output using six blocks of seven-segment and 3 LEDs. The proposed SHA-256 unfolding factors two and four designs are comparable to other SHA-256 methods in the area and maximum frequency. From Table 2, based on the throughput of the previous SHA-256 design with iterative and pipelining, the proposed design with unfolding techniques produced the highest throughput of 4196.30 Mbps with factor four. It is clearly shown that by applying this unfolding method, the SHA-256 design improves significantly in terms of design throughput because the number of latencies reduces four times. For conventional design and unfolding factor two, cycles decreases from 64 to 34. The number of cycles drops from 34 to 18 when the unfolding factor increases to four. As a result, when factor four is applied to the Unfolding SHA-256 design, the throughput dramatically increases. The percentage improvement of SHA-256 unfolding factor four was 13.7% and 58.1% compared to SHA-256 unfolding with factor two and conventional design of SHA-256, respectively. Compared to iterative design, the



proposed unfolding design had the drawback of large area implementation. This design, however, can be enhanced by combining pipelining and unfolding techniques to provide the greatest effect. This design is essential for security applications and could be used in future innovations, such as other hash functions, HMAC, and security applications.

## ACKNOWLEDGEMENTS

This project was supported by Universiti Malaysia Sarawak (UNIMAS) -SGS grant F02/SGS/1785/2018

## REFERENCES

- Ahmad, I., & Das, A. (2005). Hardware implementation analysis of SHA-256 and SHA-512 algorithms on FPGAs. *Computers and Electrical Engineering*, 31(6), 345-360. <https://doi.org/10.1016/j.compeleceng.2005.07.001>
- Bensalem, H., Blaqui re, Y., & Savaria, Y. (2021). Acceleration of the secure hash algorithm-256 (SHA-256) on an FPGA-CPU cluster using OpenCL. In *2021 IEEE International Symposium on Circuits and Systems (ISCAS)* (pp. 1-5). IEEE Publishing. <https://doi.org/10.1109/ISCAS51556.2021.9401197>
- Brazhnikov, S. (2020). A hardware implementation of the SHA2 hash algorithms using CMOS 28nm technology. In *IEEE Conference of Russian Young Researchers in Electrical and Electronic Engineering (EIConRus)* (pp. 1784-1786). IEEE Publishing. <https://doi.org/10.1109/EIConRus49466.2020.9039083>
- Chaves, R., Kuzmanov, G., Sousa, L., & Vassiliadis, S. (2006). Improving SHA-2 hardware implementations. In *International Workshop on Cryptographic Hardware and Embedded Systems* (pp. 298-310). Springer. [https://doi.org/10.1007/11894063\\_24](https://doi.org/10.1007/11894063_24)
- Chen, Y., & Li, S. (2020). A high-throughput hardware implementation of SHA-256 algorithm. In *IEEE International Symposium on Circuits and Systems (ISCAS)* (pp. 1-4). IEEE Publishing. <https://doi.org/10.1109/ISCAS45731.2020.9181065>
- He, Z., Wu, L., & Zhang, X. (2018). High-speed pipeline design for HMAC of SHA-256 with masking scheme. In *12th IEEE International Conference on Anti-counterfeiting, Security, and Identification (ASID)* (pp. 174-178). IEEE Publishing. <https://doi.org/10.1109/ICASID.2018.8693229>
- Kahri, F., Mestiri, H., Bouallegue, B., & Machhout, M. (2015). Efficient FPGA hardware implementation of secure hash function SHA-256/Blake-256. In *2015 IEEE 12th International Multi-Conference on Systems, Signals & Devices (SSD15)* (pp. 1-5). IEEE Publishing. <https://doi.org/10.1109/SSD.2015.7348105>
- Kester, Q. A., & Henry, B. (2019). A hybrid data logging system using cryptographic hash blocks based on SHA-256 and MD5 for water treatment plant and distribution line. In *2019 International Conference on Cyber Security and Internet of Things (ICSIoT)* (pp. 15-18). IEEE Publishing. <https://doi.org/10.1109/ICSIoT47925.2019.00009>
- Li, J., He, Z., & Qin, Y. (2019). Design of asynchronous high throughput SHA-256 hardware accelerator in 40nm CMOS. In *2019 IEEE 13th International Conference on ASIC (ASICON)* (pp. 1-4). IEEE Publishing. <https://doi.org/10.1109/ASICON47005.2019.8983530>

- Li, W., Zhu, Y., Tian, L., Nan, T., & Chen, X. (2020). FPGA-based hardware acceleration for image copyright protection system based on blockchain. In *7th IEEE International Conference on Cyber Security and Cloud Computing (CSCloud)/2020 6th IEEE International Conference on Edge Computing and Scalable Cloud (EdgeCom)* (pp. 234-239). IEEE Publishing. <https://doi.org/10.1109/CSCloud-EdgeCom49738.2020.00048>
- McEvoy, R. P., Crowe, F. M., Murphy, C. C., & Marnane, W. P. (2006). Optimisation of the SHA-2 family of hash functions on FPGAs. In *IEEE Computer Society Annual Symposium on Emerging VLSI Technologies and Architectures (ISVLSI'06)* (pp. 317-322). IEEE Publishing. <https://doi.org/10.1109/ISVLSI.2006.70>
- Mestiri, H., Kahri, F., Bouallegue, B., & Machhout, M. (2015). Efficient FPGA hardware implementation of secure hash function SHA-2. *International Journal of Computer Network and Information Security*, 7(1), 9-15. <https://doi.org/10.5815/ijcnis.2015.01.02>
- Miao, L., Jinfu, X., Xiaohui, Y., & Zhifeng, Y. (2009). Design and implementation of reconfigurable security hash algorithms based on FPGA. In *2009 WASE International Conference on Information Engineering* (pp. 381-384). IEEE Publishing. <https://doi.org/10.1109/ICIE.2009.278>
- Michail, H., Athanasiou, G., Kritikakou, A., Goutis, C., Gregoriades, A., & Papadopoulou, V. (2010). Ultra high speed SHA-256 hashing cryptographic module for ipsec hardware/software codesign. In *2010 International Conference on Security and Cryptography (SECRYPT)* (pp. 1-5). IEEE Publishing.
- Michail, H., Milidonis, A., Kakarountas, A., & Goutis, C. (2005). Novel high throughput implementation of SHA-256 hash function through pre-computation technique. In *12th IEEE International Conference on Electronics, Circuits and Systems* (pp. 1-4). IEEE Publishing. <https://doi.org/10.1109/ICECS.2005.4633433>
- Padhi, M., & Chaudhari, R. (2017). An optimized pipelined architecture of SHA-256 hash function. In *7th International Symposium on Embedded Computing and System Design (ISED)* (pp. 1- 4). IEEE Publishing. <https://doi.org/10.1109/ISED.2017.8303943>
- Parhi, K. K. (1999). *VLSI digital signal processing systems: Design and implementation*. John Wiley & Sons.
- Phan, V. D., Pham, H. L., Tran, T. H., & Nakashima, Y. (2021). High performance multicore SHA-256 accelerator using fully parallel computation and local memory. In *2021 IEEE Symposium in Low-Power and High-Speed Chips (COOL CHIPS)* (pp. 1-3). IEEE Publishing. <https://doi.org/10.1109/COOLCHIPS52128.2021.9410349>
- Shahid, R., Sharif, M. U., Rogawski, M., & Gaj, K. (2011). Use of embedded FPGA resources in implementations of five round three SHA-3 candidates. In *2011 International Conference on Field-Programmable Technology* (pp. 1-9). IEEE Publishing. <https://doi.org/10.1109/FPT.2011.6132680>
- Sklavos, N., & Koufopavlou, O. (2003). On the hardware implementations of the SHA-2 (256, 384, 512) hash functions. In *Proceedings of the 2003 International Symposium on Circuits and Systems, 2003. ISCAS '03* (Vol. 5, pp. 153-156). IEEE Publishing. <https://doi.org/10.1109/ISCAS.2003.1206214>
- Suhaili, S., & Watanabe, T. (2017). Design of high-throughput SHA-256 hash function based on FPGA. In *2017 6th International Conference on Electrical Engineering and Informatics (ICEEI)* (pp. 1-6). IEEE Publishing. <https://doi.org/10.1109/ICEEI.2017.8312449>
- Sun, W., Guo, H., He, H., & Dai, Z. (2007). Design and optimized implementation of the SHA-2(256, 384, 512) hash algorithms. In *7th International Conference on ASIC* (pp. 858-861). IEEE Publishing. <https://doi.org/10.1109/ICASIC.2007.4415766>

- Wu, R., Zhang, X., Wang, M., & Wang, L. (2020). A high-performance parallel hardware architecture of SHA-256 hash in ASIC. In *2020 22nd International Conference on Advanced Communication Technology (ICACT)* (pp. 1242-1247). IEEE Publishing. [https://doi.org/ 10.23919/ICACT48636.2020.9061457](https://doi.org/10.23919/ICACT48636.2020.9061457)
- Zhang, X., Wu, R., Wang, M., & Wang, L. (2019). A high-performance parallel computation hardware architecture in ASIC of SHA-256 hash. In *2019 21st International Conference on Advanced Communication Technology (ICACT)* (pp. 52-55). IEEE Publishing. [https://doi.org/ 10.23919/ICACT.2019.8701906](https://doi.org/10.23919/ICACT.2019.8701906).



## Characterization of Polyvinylidene Difluoride-based Energy Harvesting with IDE Circuit Flexible Cantilever Beam

Khairul Azman Ahmad<sup>1\*</sup>, Noramalina Abdullah<sup>2</sup>, Mohamad Faizal Abd Rahman<sup>1</sup>, Muhammad Khusairi Osman<sup>1</sup> and Rozan Boudville<sup>1</sup>

<sup>1</sup>School of Electrical Engineering, College of Engineering, Universiti Teknologi MARA, Cawangan Pulau Pinang, Permatang Pauh, 13500 UiTM, Pulau Pinang, Malaysia

<sup>2</sup>School of Electric and Electronic Engineering, Universiti Sains Malaysia, Engineering Campus, 14300 USM, Penang, Malaysia

### ABSTRACT

Piezoelectric energy harvesting is the process of extracting electrical energy using energy harvester devices. Any stress in the piezoelectric material will generate induced voltage. Previous energy harvester device with stiff cantilever beam was generated low harvested energy. A flexural piezoelectric energy harvester is proposed to improve the generated harvesting energy. Polyvinylidene difluoride is a polymer piezoelectric material attached to a flexible circuit made of polyimide. Four interdigitated electrode circuits were designed and outsourced for fabrication. The polyvinylidene difluoride was then attached to the interdigitated electrode circuit, and a single clear adhesive tape was used to bind them. Four piezoelectric energy harvesters and ultrasonic ceramic generators were experimentally tested using a sieve shaker. The sieve shaker contains a two-speed oscillator, with  $M1=0.025$  m/s and  $M2=0.05$  m/s. It was used to oscillate the energy harvester devices. The resulting induced voltages were then measured. Design 4, with the widest width of electrode fingers

and the widest gap between electrode fingers, had the highest power generated at an output load of  $0.745 \mu\text{W}$  with the  $M2$  oscillation speed. The oscillation speed of the sieve shaker impacted the energy harvester devices as a higher oscillation speed gave higher generated power.

### ARTICLE INFO

#### Article history:

Received: 19 July 2021

Accepted: 13 October 2021

Published: 10 January 2022

DOI: <https://doi.org/10.47836/pjst.30.1.32>

#### E-mail addresses:

khairulit75@gmail.com (Khairul Azman Ahmad)

eenora@usm.my (Noramalina Abdullah)

faizal635@uitm.edu.my (Mohamad Faizal Abd Rahman)

khusairi@uitm.edu.my (Muhammad Khusairi Osman)

rozan259@uitm.edu.my (Rozan Boudville)

\*Corresponding author

*Keywords:*  $d_{33}$  mode polarization, flexible cantilever beam, interdigitated electrode circuit, polyvinylidene difluoride, vibration piezoelectric energy harvesting

## INTRODUCTION

In recent years, energy harvesting has been an interesting field of study among researchers. Some of the energy harvested were used to keep a large amount of energy for consumption by large-scale electric consumers, and some were used to recycle back the energy capable of supplying energy for sensors or small-scale electric consumers.

Nowadays, many sensors have been installed in various places for measurement. Thus, energy harvesting needs to be done to balance the energy used by these sensors. In the internet of things (IoT) era, sensors were installed on industrial machines, home appliances, and wearable technology for collecting data (Bito et al., 2017; Du et al., 2020; Šolić et al., 2021). In monitoring human health, sensors were installed on the human body (Baloda et al., 2020; Luo et al., 2020). Energy harvester design for human body attachment should be flexible due to the range of human movements. Fakhri et al. (2019) was designed a flexible hybrid structure piezoelectric nanogenerator based on zinc oxide (ZnO) nanorod and polyvinylidene difluoride (PVDF) nanofibers to increase the low generated output. The nanogenerators were tested under load forces of 4, 6.6, 9, and 21 N, and their frequencies were 6 Hz. The generated output was obtained at 356 mV for forces of 4 N, and it was 2.8 times higher than without hybrid piezoelectric.

In this author's work, the energy harvesters were installed on the arm of the human body. They are in amorphous solar cells from Sanyo, which respond to light sources with wavelengths within the 400 nm to 700 nm spectrum range. It is for indoor application. A supercapacitor was used to store the harvested energy. The average indoor power harvested was 7.1  $\mu$ W, and the average outdoor power was 171.4  $\mu$ W (Fan et al., 2018). Piezoelectric fiber composites (PFC) were installed as a head-mounted chin strap to harvest jaw movements' energy. Each PFC was placed under the chin and attached to a head-mounted device by two elastic rubber straps. Any movement of the mouth or face causes side stress and generates voltage. The maximum power transfer obtained was 7  $\mu$ W (Delnavaz & Voix, 2014). Another harvester device was composed of multiple piezoelectric stacks with frame and heel-shaped aluminum plates. The energy harvester was designed to be placed underfoot and harvest energy during walking. The piezoelectric stacks contain lead zirconate titanate (PZT) layers with a thickness of 0.1 mm and silver electrodes with a thickness of 0.1  $\mu$ m. The piezoelectric stack has a length of 32.34 mm with piezoelectric layer sizes of 7.0 mm  $\times$  7.0 mm  $\times$  0.1 mm (length  $\times$  width  $\times$  thickness) as the energy harvesting element of the device. The maximum average power generated with eight piezoelectric stacks were 6 mW, 7 mW, and 9 mW for walking speeds of 4.0 km/h, 4.8 km/h, and 5.6 km/h, respectively (Qian et al., 2018). The piezoelectric-based bridge transducers had a length of 32 mm and a thickness of 2 mm. The maximum power generated by the bridge transducer was 2.1 mW for a weight of 2267.96 kg and a frequency of 5 Hz. The piezoelectric material area has affected the harvested energy (Yesner et al., 2019).

One of the important elements in gaining high generated output is the high conversion performance of mechanical to electrical energy. Azmi et al. (2020) was designed energy harvesting with multi-layered electrospun nanofibers to increase the generated output. The nanofibers have increased the mechanical-to-electrical conversion of sensing elements and improved the generated outputs. The results showed that the piezoelectric materials were based on textile to improve the energy conversion with different piezoelectric coefficients. An electrospun PVDF nanofibers' webs improved 94.49% electrical output conversion with the force of 2.6 N. The results also showed the PVDF nanofibers improved their generated outputs at different angles of forces hit to nanofibers. A further study on nanofibers was by Bafqi et al. (2021) and showed the improvement of output performance. The improved output voltage when applied pressure with a new energy harvesting design with nanofibers piezo-polymers has shown great sensitivity of generated output in the results. PiezoTester was designed to evaluate the performance of an energy harvesting device based on tapping and bending mode. The sensitivity of the device was calculated based on electrical output for the given load, and the unit was mV/N. PiezoTester effectively measured the flexibility of PVDF nanofibers polymers.

Piezoelectric energy harvesters were mostly designed in cantilever beams (Fu et al., 2020; Gao et al., 2017; Li et al., 2014). A piezoelectric vibration energy harvester (PVEH) was designed using a bimorph-type cantilever beam. It consists of the electrodes, two piezoelectric layers, and an elastic layer sandwiched between the piezoelectric layers. PVEH with bimorph improved the bending stiffness by incorporating mesh structure to increase the harvested power. The power generated by PVEH was 12.3  $\mu$ W (Tsukamoto et al., 2018). A mechanically plucked piezoelectric energy harvester (Mech-PEH) was designed to improve the energy output. The Mech-PEH used a cantilever beam as the swing of a beam to generate voltage. A cantilever beam consists of rectangular plectra embedded in the outer ring, made from 125  $\mu$ m thick of polyimide film. The flexible plectra led to a high impact on the bimorph cantilever beam and generated output energy of 0.037 mJ (Kuang & Zhu, 2017). The PVDF-based thin film was used to harvest more energy due to its capacitance of 570 pF. The PVDF cantilever beam has a length of 160 mm, a thickness of 0.9 mm, and a width of 23 mm. The cantilever was attached to a shaker with a frequency of 25 Hz and a maximum power generation of 1.61  $\mu$ J/min (Huang & Chen, 2016). Another design of PVDF cantilever energy harvesting was applied to raindrops. Hao et al. (2020) was an energy harvester device based on a PDVF cantilever and applied to a raindrop. A multi-mode electromechanical was modeled to obtain the dynamic response of the PVDF cantilever due to water droplet impact. A wide range of droplet sizes from 2.4 mm to 4.6 mm and velocities impact range of 0.9 m/s to 3.4 m/s were prepared. The results showed that the droplet splash on a super-hydrophobic beam surface positively affects voltage generation. Small-scaled droplets in splash regime allow higher voltage

from a super-hydrophobic beam surface than from an untreated hydrophilic beam surface. The flexible substrates positively affect droplet splash in generating electric output and are related to Weber number ( $We$ ).

This paper designed the flexible piezoelectric with flexible polymer cantilever beam with flexible IDE circuit, PVDF, and adhesive tape. The next section describes the methodology of flexible piezoelectric with flexible polymer cantilever beam with a design approach and experimental setup. Then, the results and discussion are demonstrated with figures and tables to analyze the results. Lastly, the conclusion of this study is made based on the objective that has been approached.

## METHODOLOGY

### Design of Interdigitated Electrode Circuit with PVDF

An interdigitated electrode (IDE) circuit was designed to improve energy conversion from stress to electrical energy. The  $d_{33}$  mode polarization method, which is a combination of stress inside piezoelectric and IDE circuits, was used, which is shown in Figure 1.

Figure 1 shows the piezoelectric energy harvester (PEH) consisting of an IDE circuit on polyimide thickness of  $161\ \mu\text{m}$ , PVDF with a thickness of  $110\ \mu\text{m}$ , and adhesive tape with a thickness of  $90\ \mu\text{m}$ . The arrow from the negative electrode to the positive electrode shows the direction of polarization inside the PVDF. At both ends of the cantilever, the beam is tightly clamped to the wall, and between the walls, the cantilever beam was in free movement. The movement up and down of the cantilever beam generated stress inside

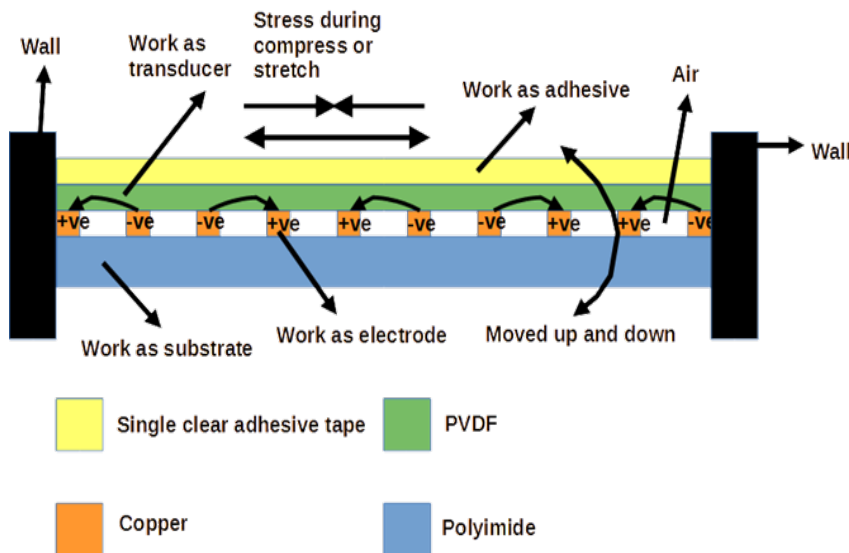


Figure 1. Interdigitated circuit technique with  $d_{33}$  mode polarization method



the PVDF during its compression and stretch. In addition, the process generated induced voltage at the positive terminal electrodes. The substrate used polyimide to reduce stiffness and improve the movement of the cantilever beam. The equation of the induced voltage inside the PVDF is shown in Equation 1 (Shen et al., 2013).

$$V = Es = -\frac{d}{\epsilon_0 \epsilon} Ts \tag{1}$$

where  $V$  is induced voltage,  $E$  is the induced electric field, and  $s$  is the distance between electrodes. Next,  $E$  is equal to  $-(d/\epsilon_0 \epsilon) T$  where  $T$  is stress component,  $d$  is the piezoelectric coefficient,  $\epsilon_0$  is the permittivity of vacuum, and  $\epsilon$  is the relative permittivity of PVDF. The piezoelectric coefficient,  $d_{33}$ , is higher than  $d_{31}$ . So, the induced voltage is higher using the  $d_{33}$  mode polarization compared to  $d_{31}$ . The relative permittivity,  $\epsilon$  of PVDF, is lower than other piezoelectric materials. The parameters of the piezoelectric energy harvesters are shown in Table 1.

Table 1  
*Parameters of piezoelectric energy harvesters*

No	Parameter	Design 1	Design 2	Design 3	Design 4	Ultrasonic piezoelectric ceramic generator
1	IDE electrode width	0.5mm	0.5mm	1mm	1mm	-
2	IDE gap between electrode fingers	0.5mm	1mm	0.5mm	1mm	-
3	IDE electrode length	20.5mm	26mm	25mm	29mm	-
4	Diameter	-	-	-	-	27mm

Four different piezoelectric energy harvesting devices, Design 1, Design 2, Design 3, and Design 4, have been devised based on different IDE electrode finger widths, IDE gaps between electrode fingers, and IDE electrode finger lengths. In addition, the ultrasonic generators bought from the market were used as a reference to compare the efficiency of the PEH. The schematic diagram of the IDE fingers and ultrasonic generators is shown in Figure 2.

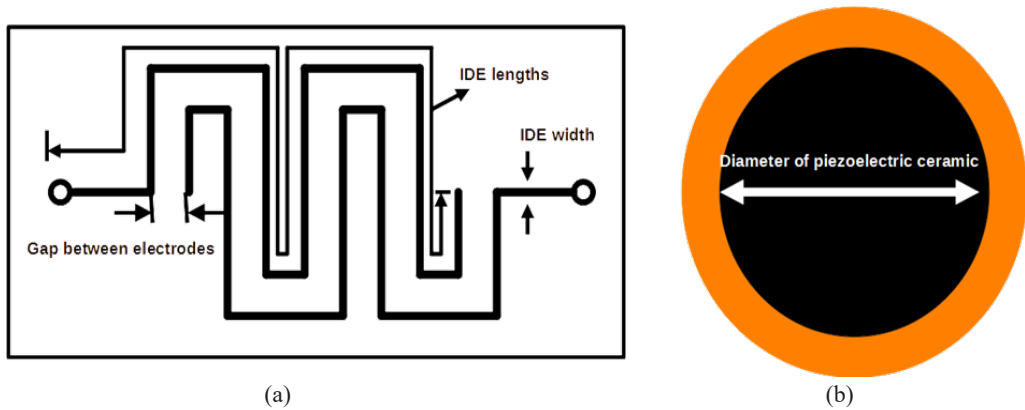


Figure 2. Schematic diagram of piezoelectric energy harvesters, a) top view of IDE circuits, and b) top view of ultrasonic generators

The harvested energy was on the capacitance of piezoelectric ceramic. The interdigitated electrode can be assumed to behave like a parallel plate capacitor. The electric power between the positive finger and the negative finger is given by Equation 2 (Jasim et al., 2018).

$$P = \frac{1}{2} CV^2 . f \tag{2}$$

where,  $P$  is the electric power,  $f$  is the frequency of vibration or wave,  $C$  is the capacitance of piezoelectric ceramic, and  $V$  is the voltage generated during Equation 1. The capacitance generated on the piezoelectric material can be determined from Equation 3 (Jasim et al., 2018).

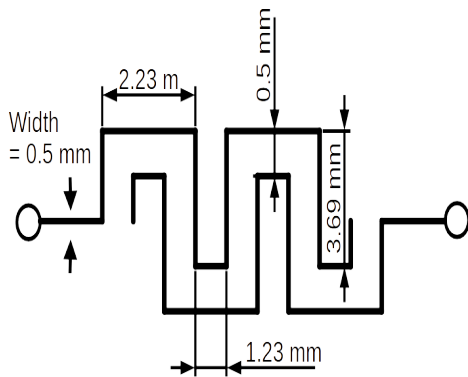
$$C = \frac{\epsilon_o \epsilon_r A}{t} \tag{3}$$

where,  $\epsilon_o$  is the dielectric constant of vacuum ( $8.885 \times 10^{-12}$  Farad/m),  $\epsilon_r$  is the relative dielectric constant of piezoelectric material in the third axial direction,  $t$  is the thickness of the piezoelectric membrane, and  $A$  is an area of the piezoelectric membrane. The gap between electrodes fingers can be affected the harvested energy.

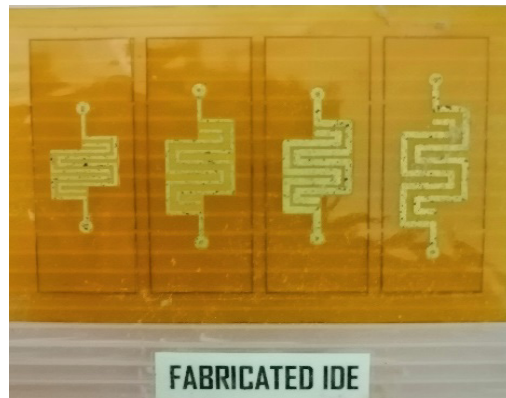
Figure 2 shows the schematic diagram of the IDE circuit, specifically, the top view, which shows the gap between electrode fingers, the width of electrode fingers, and the length of electrode fingers. Next, Figure 2 also shows the top view of the ultrasonic generators, including the diameter of piezoelectric ceramic of ultrasonic generators.

The complete fabricated IDE circuit and piezoelectric energy harvesters are shown in Figure 3. The IDE circuit was designed in Proteus and saved in the Gerber file format. The

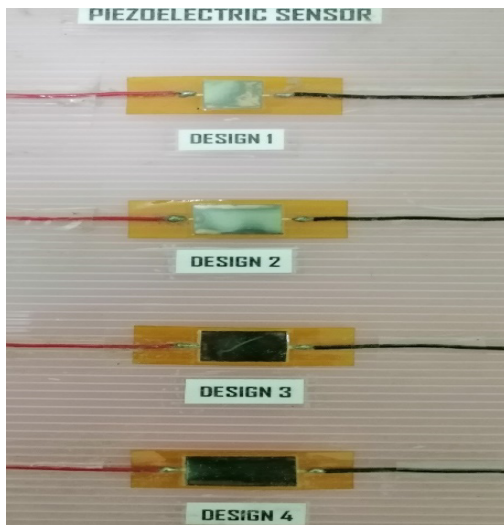
file was then sent to a flexible company for outsourcing fabrication. The schematic and fabrication of IDE circuits are shown in Figure 3a and Figure 3b, respectively. Then, PVDF was placed on top of the IDE circuit, and adhesive tape was used to bond the PVDF to the electrode fingers. The completed piezoelectric energy harvesters are shown in Figure 3c.



(a)



(b)



(c)

Figure 3. Piezoelectric energy harvesting devices, a) schematic diagram of IDE circuit design 1, b) top view of fabrication IDE circuits, and c) photo image of piezoelectric energy harvesting devices

The output of PEH was in alternating current (AC) voltage. Therefore, it needs to be converted to direct current (DC) voltage. The readout circuitry, consisting of a rectifier circuit and an energy storage circuit, was developed and is shown in Figure 4.

The readout circuitry has two parts: the rectifier circuit and the energy storage circuit. The rectifier circuit consists of four diode bridges (1N5817). The storage energy circuit consists of a load capacitor (C) with a value of  $1 \mu\text{F}$  and a load resistor (R) with a value of  $10 \text{ k}\Omega$ . The induced DC voltage was measured across the load resistor (R). The circuit was designed by Motter et al. (2012). The rectifier circuit was tested and suitable for low-frequency energy harvester.

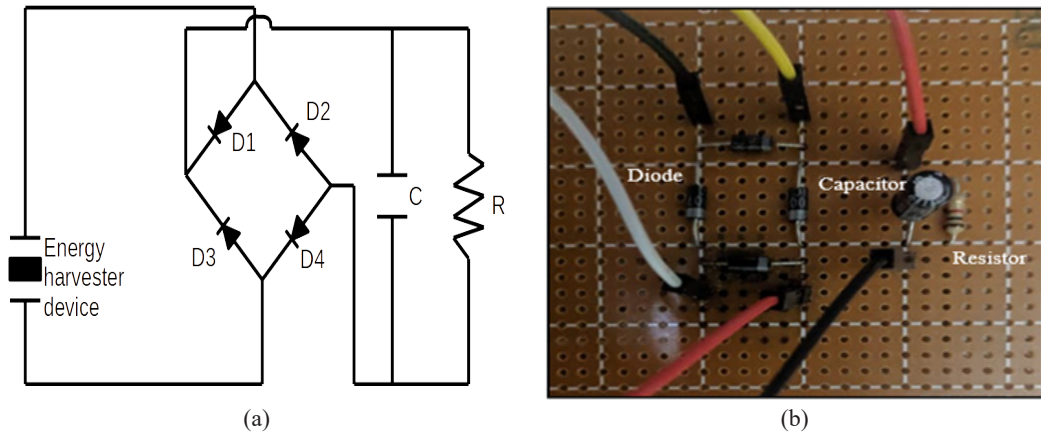
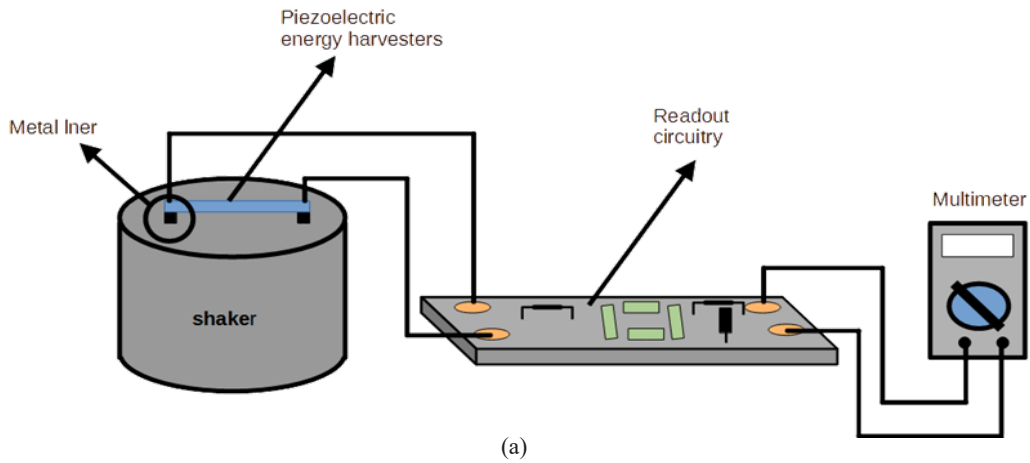
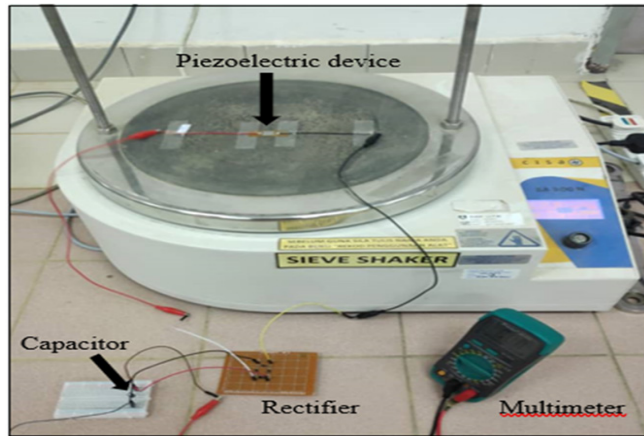


Figure 4. Readout circuitry, a) schematic diagram of bridge rectifier circuit, and b) photo image of bridge rectifier circuit.

### Experimental Setup

The experiment was carried out to investigate and characterize the effect of vibration on piezoelectric energy harvesters. PEH was placed on top of the sieve shaker at the end of both sides. A metal plate is attached under PEH, and PEH is hung in between the metal plate. Figure 5 shows the setup of the vibration experiment on PEH.





(b)

Figure 5. Vibration experimental setup, a) schematic diagram, and b) photo of experimental setup

The experimental vibration setup consists of a sieve shaker, piezoelectric energy harvesters, readout circuitry, and multimeter. The readout circuitry consists of rectifier circuits and storage circuits. The sieve shaker shakes the piezoelectric energy harvesters at a fixed frequency of 50 Hz. The piezoelectric energy harvesters generated voltage from the stress due to shaker vibration. The alternating current (AC) voltage induced at the piezoelectric energy harvester terminals was converted to direct current (DC) voltage by the rectifier circuit, and the energy was stored in the capacitor. A multimeter was used to read the DC voltage at the output terminal of the readout circuitry. Two amplitudes were used for the shaker, namely 1.0 mm and 0.5 mm. These two amplitudes represent the speed of up and down oscillation with distances of 1.0 mm and 0.5 mm. The detailed specification of the vibration setup is shown in Table 2.

Table 2  
*Specification of sieve setup for vibration experiment*

Input frequency	50 Hz
Cycle per second	50 cycle
1 cycle	A1 – 0.0005 m, A2 – 0.001 m
Speed of oscillation: 50 cycle	M1 – 0.025 m/s, M2 – 0.05 m/s

## RESULTS AND DISCUSSION

Four designs of PEH, namely Design 1, Design 2, Design 3, and Design 4, and ultrasonic ceramic generators, were devised to characterize the piezoelectric energy harvesters and ultrasonic ceramic generators. The tabulated results for Design 1 until Design 4 of PEHs and ultrasonic ceramic generators are shown in Table 3. The output voltage results shown in Table 3 were the mean value of three measurement values.

Table 3

*Tabulated results of induced DC voltage and power generated for all energy harvester devices*

Time (min)	Name of energy harvesters	Mean value of voltage stored (mV)		Power ( $\mu$ W)	
		Speed of oscillation, M1=0.025 m/s	Speed of oscillation, M2=0.05 m/s	Speed of oscillation, M1=0.025 m/s	Speed of oscillation, M2=0.05 m/s
1	Design 1	10.4	12.6	0.108	0.159
1	Design 2	15.5	17.1	0.240	0.292
1	Design 3	18.9	20.1	0.357	0.404
1	Design 4	23.0	27.3	0.529	0.745
1	Ultrasonic ceramic generators	8.0	10.2	0.064	0.104

Figure 6 illustrates the power generated by all designs of piezoelectric energy harvester and ultrasonic ceramic generator. Two speeds of the oscillator, which are 0.025 m/s and 0.05 m/s, were applied to the sieve shaker. The impact of the vibrator stressed the energy harvesters, which generated power at the output load. The power generated by the oscillation speed of 0.05 was higher than the oscillation speed of 0.025 for every design of piezoelectric energy harvesters and ultrasonic ceramic generators. The speed of oscillation impacted the harvested vibration energy. Design 4 generated the highest power compared to other piezoelectric energy harvester designs and ultrasonic ceramic generators.

Design 4 has wide electrode fingers and a wide gap between the electrode fingers. This work hypothesized the wide gap between the electrode fingers, and the high power generated by the wide gap design in Design 4 proves that hypothesis. Comparing Design 3 and Design 2, Design 3 has wider electrode fingers but a narrower gap between electrode fingers. Design 3 also generated higher power at the output load compared to Design 2. The surface of the electrode area paired to the surface of the PVDF area generated more induced voltage for the narrow gap between the electrode fingers. The highest

power generated by Design 4 was 0.745  $\mu\text{W}$  using an oscillation speed of  $M2=0.05$  m/s. Ultrasonic ceramic generators generated the lowest power at the output load compared to others. Ultrasonic ceramic generators have a wide piezoelectric ceramic area of 27 mm; however, their harvested energy was low due to no cavity or gap between the electrodes. The targeted hypothesis of the proposed design and the result obtained by the proposed design are summarized in Table 4.

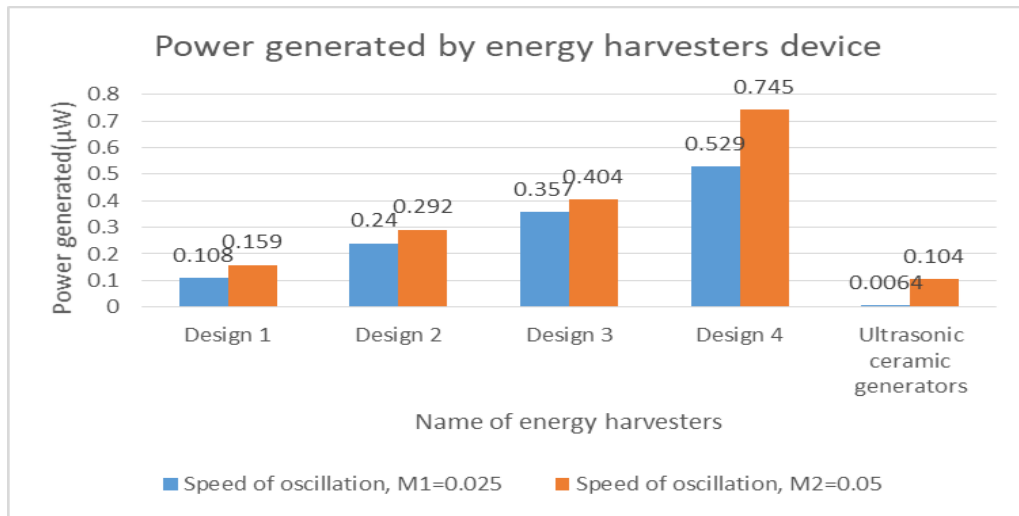


Figure 6. Power generated by energy harvester devices

Table 4

Summary of targeted hypothesis and result obtained by piezoelectric energy harvesters

Parameter	Wide gap between electrodes fingers	Wide width of fingers electrode	Output power generated	Hypothesis
Design 1	No	No	Low	As expected
Design 2	Yes	No	Higher than design 1	As expected
Design 3	No	Yes	Higher than design 2	Not in hypothesis
Design 4	Yes	Yes	The highest compared to others	As expected

Table 4 shows that Design 1, with a narrow gap between electrode fingers and narrow width of fingers, generated low output power as expected in the hypothesis. Meanwhile, Design 2, with a wide gap between electrodes but a narrow width of electrode fingers, generated higher output power compared to Design 1, as expected in the hypothesis. The new finding here was Design 3 with a narrow gap between electrode fingers, but a wide width of fingers generated higher output power compared to Design 2. The observation shows that piezoelectric energy harvesters with a wide width of electrode fingers gave more impact for generating output power compared to the wide gap between fingers. Design 4, with both wide gaps between electrode fingers and width of fingers, generated the highest output power of 0.745  $\mu\text{W}$  with an oscillation speed of 0.05 m/s.

Table 5 shows the performance of previous works using piezoelectric material. Table 5 shows three related works presented; two of them are complicated design and fabrication tools, and one of them is an easy design and fabrication tool similar to this work. Related work no 2 was design pillars fabricated from PDMS and PVDF. Preparation of thin layer of PDMS and PVDF in micro-meter needs a complicated machine and fabrication procedure. A thin layer of PVDF and PDMS gave more flexibility and increased harvested energy. Related work no 3 was designed energy harvester using very thin layer PVDF of 40  $\mu\text{m}$  and mesh-core SU-8 of 200  $\mu\text{m}$ . Fabrication of a thin layer of PVDF needs a complicated machine and process. Furthermore, the fabrication of mesh-core SU-8 needs a complicated process to prepare the mesh-core. This related work also gave high energy harvesting due to flexible mesh-core and a thin layer of PVDF. The related work no 1 was designed to cantilever beam using bimorph PZT with a thickness of 910  $\mu\text{m}$ , and the overall thickness of the cantilever beam was 21 mm. This related work was simple fabrication due to their simple fabrication process. Their work has low harvested energy compared to this work. This work used flexible polymer piezoelectric material, PVDF, flexible IDE circuit, adhesive tape as an efficient, flexible cantilever to increase harvested energy. The design using  $d_{33}$  mode where the piezoelectric coefficient of  $d_{33}$  is higher than the  $d_{31}$  piezoelectric coefficient in PVDF material was improved the energy harvested conversion.

Table 5  
*Summary table of performance related works*

No.	Author	Description	Complexity of design and fabrication tool	Voltage (V)	Power ( $\mu\text{W}$ )	Frequency (Hz)
1.	Motter et al. (2012)	Cantilever beam consist of bimorph lead zirconate titanate (PZT) sandwiched between copper.	Easy	0.020	0.417	58



Table 5 (Continue)

No.	Author	Description	Complexity of design and fabrication tool	Voltage (V)	Power ( $\mu$ W)	Frequency (Hz)
2.	Çetin and Sümer (2015)	Elastomer pillars consist of polydimethylsiloxane (PDMS) and a piezoelectric polymer (PVDF).	Complicated	N/A	58.4	62
3.	Tsukamoto et al. (2018)	Bimorph piezoelectric vibration energy harvester with flexible mesh-core elastic layer (PVDF).	Complicated	14.4	24.6	18.7
4.	This work	Polyvinylidene difluoride-based Energy Harvesting with IDE Circuit Flexible Cantilever Beam	Easy	0.027	0.745	50

## CONCLUSION

Piezoelectric energy harvesters were successfully designed and characterized. Four IDE circuits were designed and outsourced for fabrication. The piezoelectric energy harvesters were also successfully fabricated, and the PVDF was attached to the IDE circuit. All piezoelectric energy harvesters and ultrasonic generators were successfully experimentally investigated in a vibration movement. Design 4, with the widest width of electrode fingers and the widest gap between electrodes, generated the highest power at 0.745  $\mu$ W. It is concluded that the piezoelectric energy harvesters with wider gaps between electrode fingers and wider widths of fingers can harvest higher energy. The observation also shows that piezoelectric energy harvesters with a wider width of electrode fingers gave more impact to energy harvesters compared to piezoelectric energy harvesters with a wider gap between electrode fingers. The oscillation speed of the sieve shaker also impacted all tested energy harvester devices where higher speed generated high power.

## ACKNOWLEDGMENT

The authors would like to thank the Research Division, Community Industry Network & Alumni and Training Department, Human Resources Management of Universiti Teknologi MARA, Cawangan Pulau Pinang, for funding the article fee and the lab technicians for their assistance in some parts of the experiments.

## REFERENCES

- Azmi, S., Varkiani, S. M. H., Latifi, M., & Bagherzadeh, R. (2020). Tuning energy harvesting devices with different layout angles to robust the mechanical-to-electrical energy conversion performance. *Journal of Industrial Textiles*. <https://doi.org/10.1177/1528083720928822>
- Bafqi, M. S. S., Sadeghi, A. H., Latifi, M., & Bagherzadeh, R. (2021). Design and fabrication of a piezoelectric out-put evaluation system for sensitivity measurements of fibrous sensors and actuators. *Journal of Industrial Textiles*, 50(10), 1643-1659. <https://doi.org/10.1177/1528083719867443>
- Baloda, S., Ansari, Z. A., Singh, S., & Gupta, N. (2020). Development and Analysis of graphene nanoplatelets (GNPs)-based flexible strain sensor for health monitoring applications. *IEEE Sensors Journal*, 20(22), 13302-13309. <https://doi.org/10.1109/JSEN.2020.3004574>
- Bito, J., Bahr, R., Hester, J. G., Nauroze, S. A., Georgiadis, A., & Tentzeris, M. M. (2017). A novel solar and electromagnetic energy harvesting system with a 3-D printed package for energy efficient internet-of-things wireless sensors. *IEEE Transactions on Microwave Theory and Techniques*, 65(5), 1831-1842. <https://doi.org/10.1109/TMTT.2017.2660487>
- Çetin, H. G., & Sümer, B. (2015). A flexible piezoelectric energy harvesting system for broadband and low-frequency vibrations. *Procedia Engineering*, 120, 345-348. <https://doi.org/10.1016/j.proeng.2015.08.631>
- Delnavaz, A., & Voix, J. (2014). Flexible piezoelectric energy harvesting from jaw movements. *Smart Materials and Structures*, 23(10), Article 105020. <https://doi.org/10.1088/0964-1726/23/10/105020>
- Du, S., Jia, Y., Zhao, C., Amaratunga, G. A. J., & Seshia, A. A. (2020). A nail-size piezoelectric energy harvesting system integrating a MEMS transducer and a CMOS SSHI circuit. *IEEE Sensors Journal*, 20(1), 277-285. <https://doi.org/10.1109/JSEN.2019.2941180>
- Fakhri, P., Amini, B., Bagherzadeh, R., Kashfi, M., Latifi, M., Yavari, N., Kani, S. A., & Kong, L. (2019). Flexible hybrid structure piezoelectric nanogenerator based on ZnO nanorod/PVDF nanofibers with improved output. *RSC Advances*, 9(18), 10117-10123. <https://doi.org/10.1039/C8RA10315A>
- Fan, D., Ruiz, L. L., Gong, J., & Lach, J. (2018). EHDC: An energy harvesting modeling and profiling platform for body sensor networks. *IEEE Journal of Biomedical and Health Informatics*, 22(1), 33-39. <https://doi.org/10.1109/JBHI.2017.2733549>
- Fu, J., Hou, Y., Zheng, M., & Zhu, M. (2020). Flexible piezoelectric energy harvester with extremely high power generation capability by sandwich structure design strategy. *ACS Applied Materials & Interfaces*, 12(8), 9766-9774. <https://doi.org/10.1021/acsami.9b21201>
- Gao, S., Zhang, G., Jin, L., Li, P., & Liu, H. (2017). Study on characteristics of the piezoelectric energy-harvesting from the torsional vibration of thin-walled cantilever beams. *Microsystem Technologies*, 23(12), 5455-5465. <https://doi.org/10.1007/s00542-017-3336-6>
- Hao, G., Dong, X., Li, Z., & Liu, X. (2020). Dynamic response of PVDF cantilever due to droplet impact using an electromechanical model. *Sensors*, 20(20), Article 5764. <https://doi.org/10.3390/s20205764>
- Huang, H. H., & Chen, K. S. (2016). Design, analysis, and experimental studies of a novel PVDF-based piezoelectric energy harvester with beating mechanisms. *Sensors and Actuators A: Physical*, 238, 317-328. <https://doi.org/10.1016/j.sna.2015.11.036>

- Jasim, A., Yesner, G., Wang, H., Safari, A., Maher, A., & Basily, B. (2018). Laboratory testing and numerical simulation of piezoelectric energy harvester for roadway applications. *Applied Energy*, 224, 438-447. <https://doi.org/10.1016/j.apenergy.2018.05.040>
- Kuang, Y., & Zhu, M. (2017). Design study of a mechanically plucked piezoelectric energy harvester using validated finite element modelling. *Sensors and Actuators A: Physical*, 263, 510-520. <https://doi.org/10.1016/j.sna.2017.07.009>
- Li, H., Tian, C., & Deng, Z. D. (2014). Energy harvesting from low frequency applications using piezoelectric materials. *Applied Physics Reviews*, 1(4), Article 041301. <https://doi.org/10.1063/1.4900845>
- Luo, W., Sharma, V., & Young, D. J. (2020). A paper-based flexible tactile sensor array for low-cost wearable human health monitoring. *Journal of Microelectromechanical Systems*, 29(5), 825-831. <https://doi.org/10.1109/JMEMS.2020.3011498>
- Motter, D., Lavarda, J. V., Dias, F. A., & da Silva, S. (2012). Vibration energy harvesting using piezoelectric transducer and non-controlled rectifiers circuits. *Journal of the Brazilian Society of Mechanical Sciences and Engineering*, 34, 378-385. <https://doi.org/10.1590/S1678-58782012000500006>
- Qian, F., Xu, T. B., & Zuo, L. (2018). Design, optimization, modeling and testing of a piezoelectric footwear energy harvester. *Energy Conversion and Management*, 171, 1352-1364. <https://doi.org/10.1016/j.enconman.2018.06.069>
- Shen, Z., Lu, J., Tan, C. W., Miao, J., & Wang, Z. (2013). D33 mode piezoelectric diaphragm based acoustic transducer with high sensitivity. *Sensors and Actuators A: Physical*, 189, 93-99. <https://doi.org/10.1016/j.sna.2012.09.028>
- Šolić, P., Leoni, A., Colella, R., Perković, T., Catarinucci, L., & Stornelli, V. (2021). IoT-Ready energy-autonomous parking sensor device. *IEEE Internet of Things Journal*, 8(6), 4830-4840. <https://doi.org/10.1109/JIOT.2020.3031088>
- Tsukamoto, T., Umino, Y., Shiomi, S., Yamada, K., & Suzuki, T. (2018). Bimorph piezoelectric vibration energy harvester with flexible 3D meshed-core structure for low frequency vibration. *Science and Technology of Advanced Materials*, 19(1), 660-668. <https://doi.org/10.1080/14686996.2018.1508985>
- Yesner, G., Jasim, A., Wang, H., Basily, B., Maher, A., & Safari, A. (2019). Energy harvesting and evaluation of a novel piezoelectric bridge transducer. *Sensors and Actuators A: Physical*, 285, 348-354. <https://doi.org/10.1016/j.sna.2018.11.013>



*Conceptual Paper*

## A Conceptual Framework for Road Safety Education using Serious Games with a Gesture-based Interaction Approach

Wan Salfarina Wan Husain<sup>1\*</sup>, Syadiah Nor Wan Shamsuddin<sup>2</sup> and Normala Rahim<sup>2</sup>

<sup>1</sup>*Department Computer Science, Faculty of Computer and Mathematical Sciences, Universiti Teknologi MARA, 18500 UiTM, Kelantan Branch, Malaysia*

<sup>2</sup>*Department Informatics and Computing, Universiti Sultan Zainal Abidin, Terengganu 20300, Malaysia*

### ABSTRACT

Road accidents among children are one of the factors that cause mortality. An interactive manual has been developed to solve the problem. However, reports show that most road safety programs are displayed conventionally and unsuitable for almost all target users. In order to minimise the negative effect of road accidents on primary school students, early prevention programs need to be set up to overcome the problem. The natural user interface is a current technology that could be implemented in road safety education. Thus, this research aims to develop a conceptual framework by integrating gesture-based interaction and serious games towards road safety education, which will hopefully meet the road safety syllabus to tackle primary school students. All the proposed conceptual framework elements are identified through a systematic literature review and existing theories and model analysis supported by the experts' review. This research's main finding will be a conceptual framework of user engagement in road safety education through serious games

with a gesture-based interaction technology approach. This conceptual framework would be a reference for road safety designers or developers to build an application for road safety by considering user engagement through gesture-based interaction, learning theory, and serious games at the same time.

### ARTICLE INFO

*Article history:*

Received: 28 July 2021

Accepted: 16 November 2021

Published: 10 January 2022

DOI: <https://doi.org/10.47836/pjst.30.1.34>

*E-mail addresses:*

[salfa457@uitm.edu.my](mailto:salfa457@uitm.edu.my) (Wan Salfarina Wan Husain)

[syadiah@unisza.edu.my](mailto:syadiah@unisza.edu.my) (Syadiah Nor Wan Shamsuddin)

[normalarahim@unisza.edu.my](mailto:normalarahim@unisza.edu.my) (Normala Rahim)

\*Corresponding author

*Keywords:* Gesture-based interaction, road safety education, serious games

## INTRODUCTION

Every day, thousands of people lose their lives on the road. By 2020, the fatality for road crashes in Malaysia is estimated to reach 10,716 deaths if there is no drastic intervention or initiative to address the rising fatality rate (MIROS, 2018). For a long time, road users have seen and read about road accidents on social media, but users are still unaware of the importance of safety education among children. Many child pedestrians killed or seriously injured in road accidents have become a global issue. Hence, more actions need to be taken using various technologies and media. Education through the media only involves one-way communication or communication without interaction. Educating primary school students from an early age using technology is highly suitable because technological devices and connectivity have pervaded all aspects of our lives. The application needs to avoid miscommunication and attract user attention or engagement. User engagement is a key concept in developing user-centred interface applications that refer to the quality of the user experiences while conducting the interaction captured by the technology. Therefore, a new learning environment needs to be set up to increase learners' interest, especially among primary school students.

Serious Games (SG) are related to the Game-Based Learning (GBL) term in teaching approach and skill implemented in various types of domain areas or informal learning while play (Fuchslocher et al., 2011). In general, a serious game offers fun learning that can be applied in life and various fields of knowledge (Bolognesi & Aiello, 2020). Therefore, SG has increasingly been used to enrich learning and development for academic purposes (Mohd et al., 2018). A Natural User Interface (NUI) allows designing products that appear and feel as natural as possible to the user. A NUI aims to create a seamless interaction between humans and machines since one of the characteristics is user-centred. In this study, SG is defined as attributes that embrace game technology that enriches learning development and utilises game technology using the Gesture-Based Interaction (GBI) approach, which is part of natural interaction. Aliprantis et al. (2019) defined the natural interaction interface as the platform that allows users to interact similarly to real life, enables the learning process, and acquire mental load and training. Through this new application framework, the research aim is to implement a NUI through GBI and serious game attributes in handling the road safety problems mapped with learning theories. The Input-Process-Outcome game model inspires the conceptual framework by Garris and Driskell (2002).

## ROAD SAFETY EDUCATION

The increasing number of road accidents and death among children is one of the focus problems in Malaysia (Hamid et al., 2017). Malaysia is one of the countries that participated in the Global Ministerial Conference on Road Safety held in Moscow on 19<sup>th</sup> and 20<sup>th</sup>

November 2009. This conference aimed to overcome issues related to road safety. Our country created the sequel to this conference, Decade Action for Road Safety, or in Malay known as ‘Tindakan Sedekad’. Part of the contents in Decade Action for Road Safety covers from 2011–2020 are focused on the behaviour of road users, education for road safety, and pre-response of road accidents. Many programs have been carried out to change people’s behaviour, including promoting helmets that follow SIRIM standards and mandating vehicle seat belts. Starting from 2019, the road safety department, with the help of the Ministry of Education, has applied these modules for primary and secondary schools. These modules are included in the *Bahasa Melayu* subject and used in 24 selected schools. For secondary school students, the modules were implemented in the year 2020. The modules were implemented based on the Context, Input and Process, and Product (CIPP) model, which is needed to determine the level of knowledge and skill in road safety among primary students.

The study by Kamarudin et al. (2020) found that road safety education, such as crossing the road, is very important to implement for school students, especially students who walk from school to home. One suitable type of education in implementing Road Safety Education (RSE) for primary school students is adventure education. Adventure education implements the experiential learning process in which people construct knowledge through direct experience, practising skills, and strengthening values (Shih & Hsu, 2016). Therefore, to design efficient strategies for road safety, a good framework needs to be applied. According to Hughes et al. (2016), the efficient strategies include two main components, which are; 1) policy tools to improve road safety, such as enforcement and education, and 2) components that involve humans, vehicles, and equipment. Thus, a new conceptual framework might be a potential guideline to develop excellent and effective road safety strategies. The road safety strategies suggested include three main components based on previous research studies, namely:

1. Components of road safety—the components can consist of humans, vehicles, equipment, and the environment, which are the main factors that cause traffic accidents in Malaysia.
2. Characteristics—The critical character in road safety strategies is age. Based on the theories of Jean Piaget, children’s behaviour patterns in road traffic are differentiated between the following four levels of development (Afifah & Hossain, 2016) known as sensorimotor stage, preoperational stage, concrete operational stage and lastly formal operational stage.
3. Policy tools—consist of programs/projects, engineering, education.

More details about road safety strategies are illustrated in Figure 1 below.

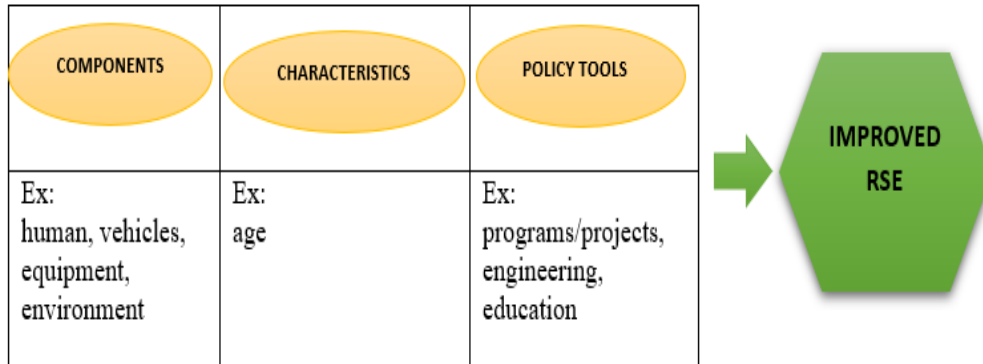


Figure 1. Road Safety Strategies in RSE

One of the components in road safety strategies that have been famously implemented is the Safe System Approaches originate from Haddon Jr (1980), comprising a 9 cases matrix to define the risk factors of an injury in three categories: the individual, the agent, the environment, and the moment of the action: before, during and after the accident. All traffic safety factors could be found in the Haddon matrix: the personality of the driver (before), an agent, such as speed (before and during), environments, such as bad infrastructures (before) or bad emergency services (after) (Assailly, 2017).

The next strategy in RSE is using characteristics that focus on the target audience's age level of development. In Malaysia, based on the CIPP model, the level of development mainly focuses on secondary school and primary school students. It means that RSE in Malaysia focuses on the concrete operational and formal operational stages in development. For concrete operational, the strategies in conveying the materials of RSE need to incorporate inductive logic. Traffic education can be exposed to them at this stage but in actual or simulated conditions rather than theoretically in a classroom. In the formal operational stage, the age of the users is 12 years old and over. On this level, children can think abstractly. They are aware and able to detect their position and assess and avoid risks from their surroundings. In other words, they can understand the complex rules of traffic.

The CIPP model is one of the policy tools implemented in Malaysia. The purpose is to generate the baseline usage for schools, teachers and students. Through this module, the students will be influenced by traffic information, the signals related to road safety, and the next steps to follow, focusing on the youngest generation. In addition, there have been several attempts in the literature to explain the cause of accidents and injury severity.



Another sample of the policy tools in Malaysia is a campaign carried out by Allianz Malaysia. The campaign emphasised the five elements of road safety; understanding basic road safety rules and traffic signage, crossing roads safely and understanding traffic hazards, understanding the traffic light indications, proper wearing of helmets for cyclists and motorcyclists, and getting into the habit of wearing seatbelts. The Allianz Road Safety Tips Booklet is another initiative of Allianz Malaysia that aims to further our efforts to instil road safety awareness among children by reaching a bigger audience. The booklet was developed internally by Allianz Malaysia with consultation from Jabatan Keselamatan Jalan Raya (JKJR). It provides handy tips on road safety for children aged 4 to 12 years old.

## **SERIOUS GAMES**

SG is a game designed for a primary purpose other than pure entertainment. The main aims of SG are learning and behaviour change (Connolly et al., 2012). Based on Mohd et al. (2018), there are 12 basic building blocks according to the educational view as features of the framework of a serious game, which are:

1. Interaction—The engagement in learning explains how the players adapt and manipulate the games' elements. The players need to deal with the situation and implement interaction.
2. Reward—Incentives for the learner, a must-use attribute in games. This attribute will motivate the players to upgrade their knowledge and level in playing the games.
3. Practice and drill—The game structure provides the exercises and games that implement the learning process's repetition concept. This attribute will enforce learner memory and challenge.
4. Incremental learning—The design of learning contents is organised in incremental order. The flow of the game was structured from novice stage to master level.
5. Linearity—Learning is arranged sequentially, which focuses on knowledge delivery (the content of learning).
6. Attention span—Duration time of players, can engage with the content structure and solve the task at the level provided.
7. Transfer of learnt skill—Implementing skills learned previously in novice stage and practice to a new learning environment.
8. Scaffolding—The learning environment splits the learning problem into subproblems and offers support and help during the learning process.
9. Learner control—The learning process can be controlled by the player. The player can repeat or continue the learning process based on try-and-error learning.
10. Accommodating the learner's style—The learning process was structured to match the player's development level.

11. Scenario-based learning—Learning materials for the players were designed based on real-life. The players will gain more knowledge when exploring the contents close to their environment.
12. Intermittent feedback—Just-in-time feedback for learning

One of the models in constructing SG is the Input-Process-Outcome Game Model (Garris & Driskell, 2002), as in Figure 2, which emphasises three main phases.

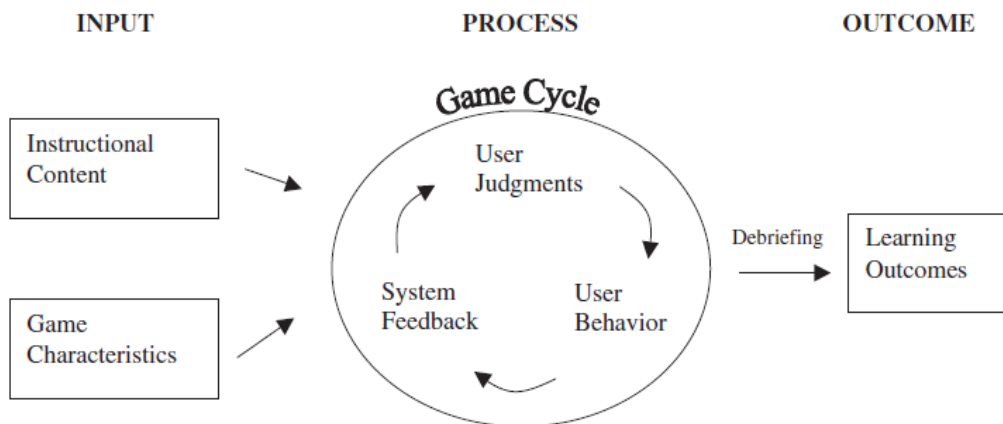


Figure 2. Input-Process-Outcome Game Model (Garris & Driskell, 2002)

First, the learning model’s input consists of two components: instructional content and game characteristics. Instructional content refers to the elements used in the selected contents, which will help the knowledge acquisition process as proper guidance in designing SG (Tsikinas & Xinogalos, 2018). The authors also mentioned that some of the researchers used the term game characteristics as game attributes that assist in the learning process and the learner’s engagement. For example, the use of scaffolding attributes is assistance that the learner might need during gameplay. The second phase is where the process is implemented through games cycles. The cycle will repeat in eliciting the gameplay match with the player (system feedback), for example, like engagement or fun (user judgement) and change learners’ behaviour (user behaviour) towards the given task, which finally brings to the specific learning outcome. Furthermore, in the game cycle, the researchers will extend the pairing contents with appropriate games features. Finally, in the last phase, the learning outcome is achieved. According to Wilson et al. (2008), the learning outcome achieves targeted learning goals beneficial to trainers, instructors, practitioners, and learners.

## LEARNING THEORIES

Learning theories provide a framework for understanding how people learn the contents. Serious gaming is similar to other well-known learning methods that need to be established on prominent learning theories to improve learning outcomes (Pourabdollahian et al., 2012). According to Masethe et al. (2017), traditional learning theories, such as behaviourism, constructivism, and cognitivism, are considered the foundation theories in the teaching and learning process.

Behaviourism theory is well known as the study of behaviour that can be observed and measured. Research has shown that agents can regain attention during drops in engagement. Research by Szafir and Mutlu (2012) found that embodied agents offer great potential to interact using the full range of human communicative behaviour. The behaviour involved is verbal and nonverbal. Verbal acts are, for example directing questions, using humour, and addressing students, while nonverbal acts can be seen through expressions, gestures, eye contact, smiling, posture, and proximity (Velez, 2008). Stavrev (2016) suggested that including new gameplay levels can improve the students' behaviour near and on the road. According to the behaviourism theory, the human mind is considered a 'black box' because responses can be observed quantitatively while completely ignoring thinking processes occurring in the mind (Khowaja, 2017). The game attributes relevant to behaviourism theory are interaction, reward, practice, and drill. In general, there are two interaction strategies in implementing interaction attributes to capture the active user: event-based and state-based (Serrano-laguna et al., 2016). Through the event-based strategy, one way to measure interaction is by analysing the user logs, while in state-based strategy, the specific frequency by users that were played repeatedly in the games state. Meanwhile, reward attributes in the game encourage the learner, keep motivation high, and include scores, permission, property, and reputation (Westera, 2019). The last attribute under this learning theory is practice and drill, which involves repeating learning exercises and practices until the learning goal is achieved (Kurniawan et al., 2019).

Constructivism theory is a learning theory found in psychology that suggests that learners construct knowledge from their experiences (Mohd et al., 2018; Olusegun, 2015). In other words, the students may learn new information and increase what they already know with the idea that students can be taught and can affect the attitudes. Piaget's constructivist learning theory has had a wide-ranging impact on learning theories and teaching methods in education (Olusegun, 2015). When dealing with constructivism, the common nature that we do are asking questions, exploring, and assessing what we know. For example, in the classroom, the constructivist view of learning can implement many different teaching practices. In the most general sense, the learning process encourages students to use active techniques, such as experiments and applying real-world problem solving to create more knowledge. Later on, the students reflect and talk about what they

are doing and how their understanding is changing. Scaffolding is one of the attributes of serious games that allows real-world problem solving while experiencing the game being played by the user. According to Obikwelu (2017), scaffolding is the guidance required in bridging the gap between what a child knows and what he is supposed to know. Basically, the standard game's design that implements scaffolding is divided into subproblems. The last attribute that can be mapped in constructivism is learner control. Learner control is the learner as an active processor of information. In constructivism theory, the learner's role is to construct new ideas from current or past knowledge (Alqurashi, 2018).

Cognitivism theory is the learning process as an internal and active mental process, which develops within a learner and increases mental capacity and skills to learn better (McLeod, 2001). In contrast, ineffective cognitive processes that result in learning difficulties are remembered and impact an individual's lifetime. The literature on interactivity and relative frameworks reviewed by Hart (2014) mentioned that psychology's cognitive model can be drawn and can change over prolonged use and time. As Garris and Driskell (2014) stated, the user gets hooked on cognitive processes that are triggered and beneficial for learning. In developing cognitivist theory instruments, an existing knowledge structure must be present to compare and process new information for education. The attributes that match cognitivism are incremental learning, linearity, attention span and transfer of learnt skills. In incremental learning, the attribute provides the learning materials and introduces the learning activities by increasing the level of knowledge in achieving subject materials learning outcomes (Tsita & Satratzemi, 2018). For example, when the children know numbers, they are taught how to do addition and subtraction processes. Next, linearity is the game design needs to have a start and an end. The execution process will be conducted step-by-step, such as users need to do task A and then task B. Meanwhile, attention span concerns the cognitive processing and short-term memory loads placed upon the learner by the game. These loads need to be carefully calibrated to the target learner. Lastly, the transfer of learnt skills is the support provided by the game to enhance the application of previously learnt knowledge to other game levels.

There have been many conflicts in designing educational games entertaining and sustaining the learning aspects (Ahmad et al., 2015). For this reason, the concept of learning through experience is implanted by embedding the experiential learning theory. Three primary game attributes found from this theory are accommodating the learner's style, scenario-based learning, and intermittent feedback (Mohd et al., 2018). Accommodating learners style attributes refer to the contents in the games, which need to be designed to suit the audience. For example, the medium and sources used need to be suitable to create the game applications for children. Lastly, the intermittent feedback by Tsita and Satratzemi (2018) is the extent to which every interaction that provides feedback should be defined. These feedback attributes are very important to ensure the goal can be achieved by playing the games.

## GESTURE-BASED INTERACTION

User interfaces allow the user to use modalities, such as touch, gestures or voice. Based on Liu (2010), the characteristics of a NUI are: 1) User-centred; 2) Multi-channel; 3) Inexact; 4) High bandwidth; 5) Voice-based interaction; 6) Image-based interaction; and 7) Behaviour-based interaction. The two characteristics relevant to the RSE environment are user-centred and behaviour-based characteristics from the seven characteristics listed. The user-centred characteristic involves a multi-stage problem that requires analysis and how the users see in using the interface and test the validity of their assumptions concerning user behaviour in real-world tests with real users. In a short story, user-centred characteristics study the users' needs, wants, and limitations at each stage of the interface design process. Meanwhile, the behaviour-based characteristic is interactions in the communication process with the user, such as using gestures.

Over a decade, GBI has become the modern interface implemented in various fields. As adapted from Ackad et al. (2014), good approaches to design gesture-based interaction design are: 1) Apply simple and memorable gestures so that passers-by can learn and apply them easily; 2) Gestures need to be quick to allow for fast and accurate navigation through the application; and 3) Gesture set needs to be socially acceptable for use in a public space and within crowds. The researchers also explained that gestures are interesting for communicating with a machine because they are compact and represent human-machine interaction. According to Card (2014), levels of abstraction for gestures can be divided into five: 1) Device abstraction like an application that uses a surface multi-finger stroke device; 2) Transformation that includes application command 3) Signal coding by using gestures, 4) Sensing, such as mutual capacitance; and lastly 5) Physical properties.

Past studies have found that the gesture level of abstraction frequently used by researchers is signal (Bilban et al., 2017; Chang et al., 2015; Chang et al., 2011; Hsu & Iacsit, 2011; Rodriguez, 2015; Savari et al., 2016; Stavrev & Terzieva, 2015). Nevertheless, most of the researchers agree that though the famous gesture level is through signals, the gestures can involve many types of gestures, such as a hand (Bilban et al., 2015; Chang et al., 2011; Rodriguez, 2015), whole-body (Hsu & Iacsit, 2011; Motiian et al., 2015; Savari et al., 2016), and upper-level body (Chang et al., 2015). A sample of simple and easy gestures is shown in Figure 3. As mentioned by Kang et al. (2015), to represent the gestures to the users, many forms can be taken: 1) Using *emblems* like 'thumbs up' or 'ok'; 2) Using *beats* that support structure discourse, such as 'on the other hand' or 'first'; and 3) *Representational* gestures that convey meaning by using *deictic* gestures that point to actual features in the real world, *iconic* like shapes or actions, or *metaphonic* to express meanings and relations.



Figure 3. Simple and easy gestures to follow by children (Ackad et al., 2014)

### METHODOLOGY INSTANCES OF THE PROPOSED FRAMEWORK

The proposed framework consists of three phases. First, instructional content using GBI and serious game attributes is incorporated into the learning model and mapped with the learning theories summarised in Table 1.

Table 1

*The description summary of SG attributes mapped with learning theory and gesture-based interaction*

Serious Game Attributes (SGA)	Learning Theory (LT) / Learning approach	Gesture-based interaction	Description Summary
Accommodating the learner's style (SGA1)	Experiential Learning	User-centred	Learning process using simple gestures to tackle children (focusing on primary school students)
Scenario-based learning (SGA2)	Experiential Learning	User-centred	Learning where the learner can feel like an extension of their body through hand gestures. Players gain knowledge through experience by practising the skills learned.
Scaffolding (SGA3)	Constructivism	Behaviour-based	Support, such as hints, is provided in the game—help solve the question.

Table 1 (Continue)

Serious Game Attributes (SGA)	Learning Theory (LT) / Learning approach	Gesture-based interaction	Description Summary
Learner control (SGA4)	Constructivism	Behaviour-based and User-centred	Self-learning and active learning are based on the learning option chosen by users. There are three levels provided in the prototype.
Interaction (SGA5)	Behaviourism	Behaviour-based and User-centred	Provide the interface elements that are required to deal with interaction. The design interface is designed not to be too crowded with multimedia elements
Incremental learning (SGA6)	Cognitivism	Behaviour-based and User-centred	The games material can be upgraded while playing—one by one level in sequential order.

As indicated in Table 1, the newly founded theories are SGA, learning theory, and GBI can be mapped together to implement RSE. Two SGA that support experiential learning is SGA1 and SGA2, which focus on user-centred where the learning process is using simple gestures as suggested by (Ackad et al., 2014) and by constructing knowledge through direct experience, practising skills, and strengthening values (Shih & Hsu, 2016). SGA3 and SGA4 are mapped with constructivism learning theories that focus on behaviour-based in which SGA3 deals with support in the games and SGA4 learners construct knowledge from their experiences (Mohd et al., 2018; Olusegun, 2015). Meanwhile, SGA5 is mapped with behaviourism learning theory in which the element enhances skills and motivates the user to keep playing the game (Mohd et al., 2018), and SGA6 is mapped with the cognitivism theory where both SGAs focus on behaviour-based and user-centred in different ways in which the learning process is delivered progressively, and the learning is broken into simpler and manageable tasks (Mohd et al., 2018).

In the second phase, learners implement four main functions in the RSE module: *scenario-based environment*, *interactivity gestures*, *module by level*, and *quizzes*. The scenario-based environment focuses on two scenarios that are suitable for children, which are the implementation of traffic safety (Afifah & Hossain, 2016; Ben-bassat & Avnieli, 2016; Chiang et al., 2019; Mark & Al-Mansour, 2018; Salwani & Sobihatun, 2014; Stavrev & Terzieva, 2015) and traffic signs (Rawi et al., 2015; Assailly, 2017; Koekemoer et al.,

2017; Mark & Al-Mansour, 2018; Salwani & Sobihatun, 2014; Stavrev & Terzieva, 2015). Meanwhile, the preparation of gesture conditions is based on the level development as suggested by Jean Piaget, who proposed the development of content based on the age of the user’s level. Considering this theory, there are seven gestures used to cue the users namely (a) CLICK (b) MOVE (c) LEFT (d) RIGHT, (e) MORE, (f) BACK (g) STOP.

Table 2  
*The description of gestures used in the level of application*

Level	Gestures	Action
1	CLICK	to choose answer
	MORE	to get hint/help
2	MORE	to get hint/help
	LEFT	move to the left
	RIGHT	move to the right
	BACK	reverse
	STOP	stop movement
	MOVE	walk/move
3	CLICK	to choose answer
	MORE	to get hint/help
	LEFT	move to the left
	RIGHT	move to the right
	BACK	reverse
	STOP	stop movement
	MOVE	walk/move

In the first level of the games, the users are introduced to two simple gestures to ensure they can practise using gestures before advancing to a higher level. The gestures used are CLICK and MORE. In the second level, users are allowed to use six gestures: MORE, LEFT, RIGHT, BACK, STOP, and MOVE. Meanwhile, in the last level, users can use seven gestures, i.e. MORE, LEFT, RIGHT, BACK, STOP, MOVE, and CLICK. Finally, in LEVEL 1, users are exposed to simple gestures as in Figure 4.

*Quizzes* are a form of games that are applied in this framework in which the goal is to test the knowledge and the engagement in this framework. There are three types of quiz structures implemented to see the growth of knowledge, abilities, and skills in the RSE domain.





Figure 4. Simple gestures for primary school students for level one.

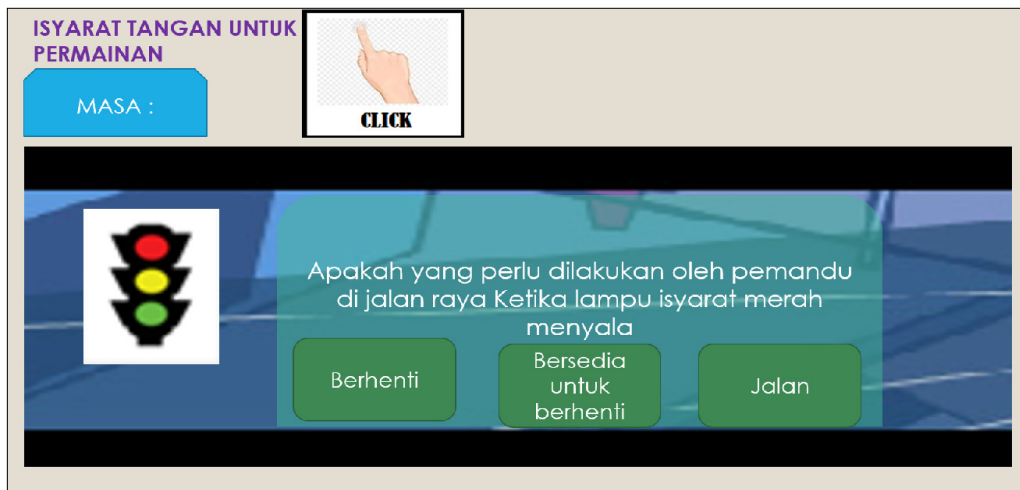


Figure 5. Example of a question in level 2 quiz.

Finally, in the last phase, the learning outcome will be shown on the screen using learning analytics to analyse the score, time, hint, gestures used, and activities view for each user that plays the application.

### **PROPOSED CONCEPTUAL FRAMEWORK FOR ROAD SAFETY EDUCATION USING SERIOUS GAMES WITH GESTURE-BASED INTERACTION APPROACH**

Road Safety Education’s conceptual framework using SG with a GBI approach is inherited from studies about natural user interfaces focusing on gestures and design, SG design and concepts, and learning theories in learning through the games. First, the conceptual framework incorporates certain features or characteristics of natural user interfaces that detail known as GBI include *user-centred* and *behaviour-based interaction*, the attributes

of SG, which are *accommodating the learner's style, scenario-based learning, interaction, learner control, scaffolding, and incremental learning* and supported by learning theories and approaches that match with SG in which the theories embedded in the framework are *experiential learning, constructivism, behaviourism and cognitivism*. Second, the RSE module features content using four main features: *scenario-based environment, interactivity gestures, level and quizzes* in interface design to ensure the users' engagement and in understanding the contents more effectively. All features are extracted based on literature findings that focus on the safety of street crossing and traffic safety signs. Finally, the framework implements learning analytics to capture engagement data by measuring the user performance using the *score, time, hint, and activities view* in the RSE prototype.

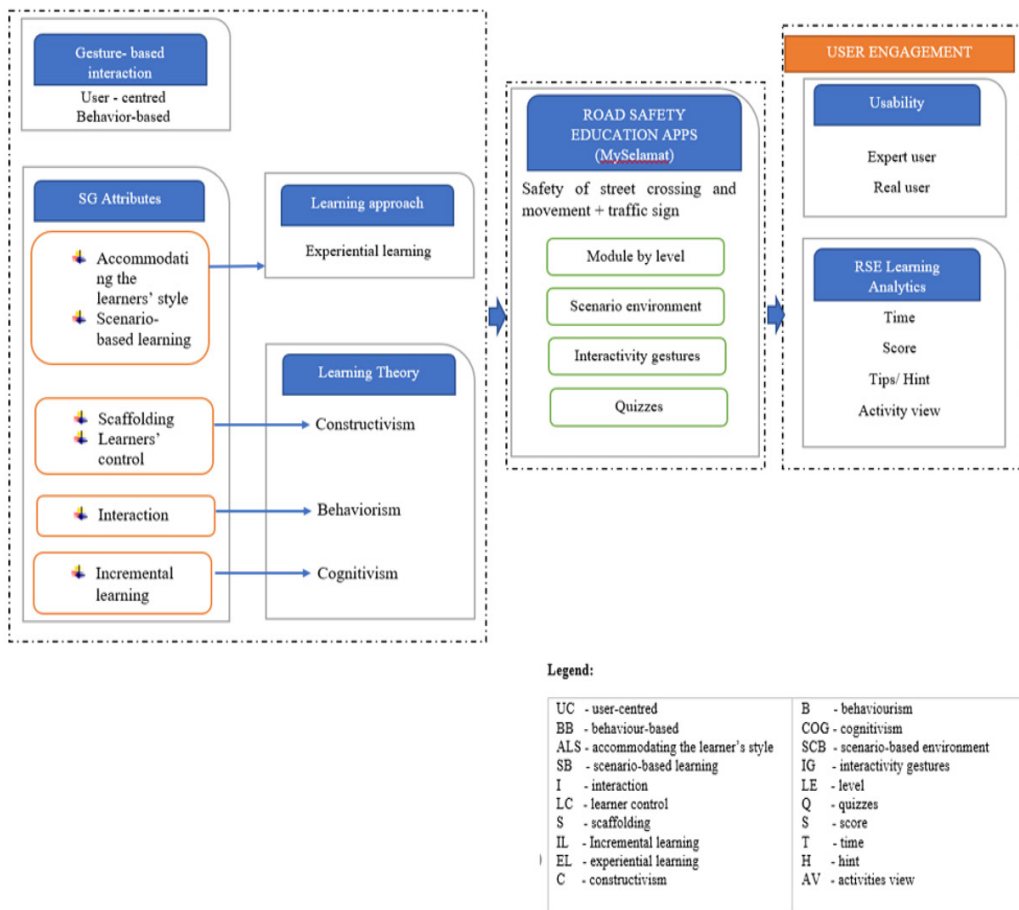


Figure 6. Proposed Conceptual Framework for Road Safety Education using Serious Games with Gesture-based Interaction Approach

The proposed conceptual framework is based on the expert’s review containing five main components: *I. Gesture-based interaction, II. Serious Games Attributes, III. Learning Theories and Approach, IV. Road Safety Education Apps (MySelamat), V. RSE Learning Analytics and usability (User Engagement)*. Each component used here consists of elements and parameters as illustrated in the conceptual framework Figure 6. The expert’s review based on *Natural User Interface, Serious Games, Multimedia, Computer Science, Information Technology, Human-Computer Interface and Road Safety Education* were gathered in giving the opinions and perceptions on the proposed elements and parameters in each component. The selection of experts was based on the research conducted using Google Scholar, ResearchGate and Google search engine. These experts also provided recommendations in helping to clarify the framework. The invitation to participate in the expert review study was sent to several participants, and six experts from 20 showed their willingness and commitment.

The scope of this activity is to find the appropriateness of the proposed elements and parameters in each component. Altogether, the expert review contained 21 quantitative and 21 qualitative questions. The result of the quantitative recommendations is shown in Figure 7 and Figure 8 below, and the names of components used can be referred to in the legend for Figure 6.

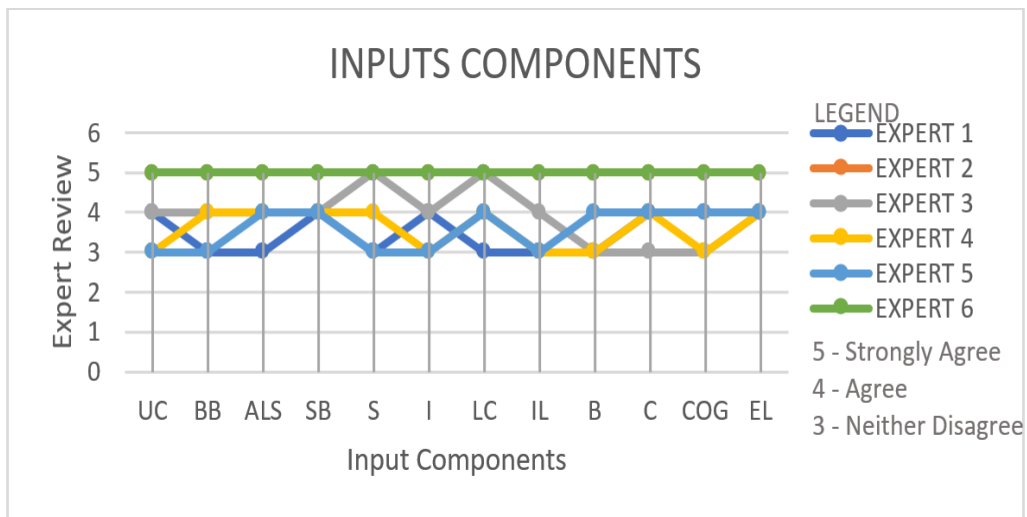


Figure 7. Expert review for input components in the framework

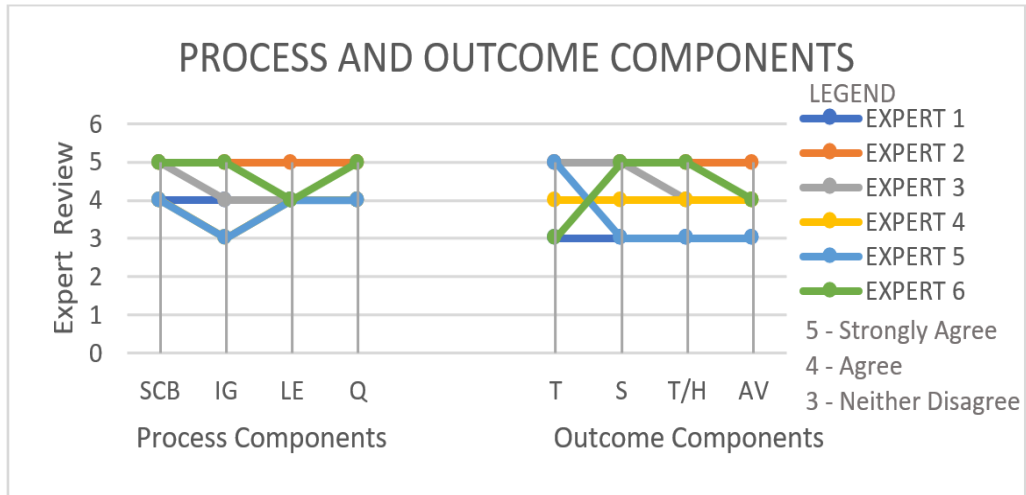


Figure 8. Expert review for process and outcome components in the framework

Table 3  
Frequency of responses selected from expert review feedback

Expert Review Components	Strongly Agree (5)	Agree (4)	Neither Disagree Nor Agree (3)	Total
Input Component	27	26	19	72
Process	8	14	2	24
Outcome Component	9	7	8	24
Total	44	47	29	120
<b>Percentage (%)</b>	36.7	39.2	24.1	100

A total of 120 descriptive responses were collected from the expert feedback. Approximately 36.7% of experts strongly agreed, 39.2% agreed, and 24.1% neither disagreed nor agreed with the suggested components implemented in the conceptual framework—the detailed result of the feedback selected as shown in Table 3 above.

### CONCLUSION AND FUTURE WORKS

Road accidents showed the increasing numbers that bring users to deaths and serious injuries in Malaysia. Therefore, an alternative RSE needs to be done at the early age of the users. The presented framework highlighted the importance of using a GBI to tackle

primary school students by adopting SG attributes mapped with learning theories in the RSE Module features. This paper presented the methodological instances of the proposed framework to produce a learning outcome that effectively manages engagement by using usability test and RSE learning analytics that analyses and report the data about learners and their contexts in the RSE application. The proposed framework is intended to overcome road safety prevention programs displayed conventionally and not suitable for all target users. This paper also discusses the expert's review opinion, whereby 36.7% strongly agree, 39.2% agree, and 24.1% neither disagree nor agree with the components used in the proposed conceptual framework. Therefore, future work should implement the proposed framework by involving GBI with specific body gestures and can be extended with more scenarios of RSE that match the target audience's problem with the help of SG attributes.

## ACKNOWLEDGEMENT

The authors want to express their gratitude to the experts who have participated in the study with their valuable comments.

## REFERENCES

- Ackad, C., Kay, J., & Tomitsch, M. (2014, April 26). Towards learnable gestures for exploring hierarchical information spaces at a large public display. In *CHI'14 Workshop on Gesture-based Interaction Design* (Vol. 49, p. 57). Toronto, Canada.
- Affah, F., & Hossain, M. (2016). The state of road safety education for children in Bangladesh. *IOSR Journal of Mechanical and Civil Engineering*, 13(5), 139-146. <https://doi.org/10.9790/1684-130508139146>
- Ahmad, M., Rahim, L. A. B., & Arshad, N. I. (2015). An analysis of educational games design frameworks from software engineering perspective. *Journal of Information and Communication Technology*, 14, 123-151.
- Aliprantis, J., Konstantakis, M., Nikopoulou, R., Mylonas, P., & Caridakis, G. (2019, January 30). Natural interaction in augmented reality context. In *Visual Pattern Extraction and Recognition for Cultural Heritage Understanding (VIPERC)* (pp. 50-61). Piza, Italy.
- Alqurashi, M. (2018). An exploratory study to identify teaching styles in Saudi Arabia based on three learning theories. *Personal and Ubiquitous Computing International Journal of Social Sciences*, 3(3), 1442-1454. <https://doi.org/10.20319/pijss.2018.33.14421454>
- Assailly, J. P. (2017). Road safety education: What works? *Patient Education and Counseling*, 100, S24-S29. <https://doi.org/10.1016/j.pec.2015.10.017>
- Ben-bassat, T., & Avnieli, S. (2016). The effect of a road safety educational program for kindergarten children on their parents' behavior and knowledge. *Accident Analysis and Prevention*, 95, 78-85. <https://doi.org/10.1016/j.aap.2016.06.024>
- Bilban, M., Uzun, Y., & Arikan, H. (2017). An example with microsoft Kinect : City modeling with Kinect. *Journal of Multidisciplinary Engineering Science and Technology (JMEST)*, 4(July), 7554-7556. <https://www.researchgate.net/publication/318054606%0AAAn>

- Bolognesi, C., & Aiello, D. (2020). Through serious games: A digital design museum for education. In *The International Archives of the Photogrammetry, Remote Sensing and Spatial Information Sciences* (pp. 83-90). Copernicus Publications. <https://doi.org/10.5194/isprs-archives-XLIII-B5-2020-83-2020>
- Card, S. K. (2014). A simple universal gesture scheme for user interfaces. In *Gesture-Based Interaction Design: Communication and Cognition* (pp. 20-24). ACM Publishing. <https://doi.org/10.1145/2559206.2559220>
- Chang, M., Lachance, D., Lin, F., Al-shamali, F., & Chen, N. (2015). Enhancing orbital physics learning performance through a hands-on Kinect game. *Education and Science, 40*(180), 1-12. <https://doi.org/10.15390/EB.2015.3145>
- Chang, Y. J., Chen, S. F., & Huang, J. D. (2011). A Kinect-based system for physical rehabilitation: A pilot study for young adults with motor disabilities. *Research in Developmental Disabilities, 32*(6), 2566-2570. <https://doi.org/10.1016/j.ridd.2011.07.002>
- Chiang, F. K., Chang, C. H., Hu, D., Zhang, G., & Liu, Y. (2019). Design and development of a safety educational adventure game. *International Journal of Emerging Technologies in Learning, 14*(3), 201-219. <https://doi.org/10.3991/ijet.v14i03.9268>
- Connolly, T. M., Boyle, E. A., MacArthur, E., Hainey, T., & Boyle, J. M. (2012). A systematic literature review of empirical evidence on computer games and serious games. *Computers and Education, 59*(2), 661-686. <https://doi.org/10.1016/j.compedu.2012.03.004>
- Fuchslocher, A., Niesenhaus, J., & Krämer, N. (2011). Serious games for health: An empirical study of the game "Balance" for teenagers with diabetes mellitus. *Entertainment Computing, 2*(2), 97-101. <https://doi.org/10.1016/j.entcom.2010.12.001>
- Garris, R., & Driskell, J. E. (2002). Games, motivation, and learning: A research and practice model a research and practice model. *Simulation & Gaming, 33*(4), 441-467. <https://doi.org/10.1177/1046878102238607>
- Haddon Jr, W. (1980). Advances in the epidemiology of injuries as a basis for public policy. *Public Health Reports, 95*(5), 411-421.
- Hamid, H., Low, S. F., Law, T. H., Tan, K. S., Ng, C. P., Nor, N. A. A. M., Ghani, A. H. A., Othman, N., & Wong, S. V. (2017). *Establishing baseline for the 2017 revised road safety education module for primary school through context, input, process and product (CIPP) model*. Malaysian Institute of Road safety Research.
- Hart, J. (2014). *Investigating user experience and user engagement for design*. ProQuest Dissertations Publishing.
- Hsu, H. J., & Iacsit, M. (2011). The potential of Kinect in education. *International Journal of Information and Education Technology, 1*(5), 365-370.
- Hughes, B. P., Anund, A., & Falkmer, T. (2016). A comprehensive conceptual framework for road safety strategies. *Accident Analysis and Prevention, 90*, 13-28. <https://doi.org/10.1016/j.aap.2016.01.017>
- Kamarudin, N. H., Marzuki, M., Rosmiza, M. Z., & Mapjabil, J. (2020). Tahap keselamatan pejalan kaki untuk perjalanan ke sekolah [The level of pedestrian safety for travelling to school]. *Malaysian Journal of Society and Space, 4*(4), 197-212.
- Khowaja, K. (2017). *A serious game design framework for vocabulary learning of children with autism* (Doctoral dissertation). University of Malaya, Malaysia.

- Koekemoer, K., Van Gesselien, M., Van Niekerk, A., Govender, R., & Van As, A. B. (2017). Child pedestrian safety knowledge, behaviour and road injury in Cape Town, South Africa. *Accident Analysis and Prevention*, 99, 202-209. <https://doi.org/10.1016/j.aap.2016.11.020>
- Kurniawan, D. E., Dzikri, A., Widyastuti, H., Sembiring, E., & Manurung, R. T. (2019). Smart mathematics: A kindergarten student learning media based on the drill and practice model. *Journal of Physics: Conference Series*, 1175, Article 012037. <https://doi.org/10.1088/1742-6596/1175/1/012037>
- Liu, W. (2010). Natural user interface - Next mainstream product user interface. In *2010 IEEE 11th International Conference on Computer-Aided Industrial Design and Conceptual Design 1* (pp. 203-205). IEEE Publishing. <https://doi.org/10.1109/CAIDCD.2010.5681374>
- Mark, S., & Al-mansour, A. I. (2018). Development of a new traffic safety education material for the future drivers in the Kingdom of Saudi Arabia. *Journal of King Saud University - Engineering Sciences*, 32(1), 19-26. <https://doi.org/10.1016/j.jksues.2018.11.003>
- Masethe, M. A., Masethe, H. D., & Odunaike, S. A. (2017, October 25-27). Scoping review of learning theories in the 21st century. In *Proceedings of the World Congress on Engineering and Computer Science 2017* (pp. 1-5). San Francisco, USA.
- McLeod, G. (2001). Learning theory and instructional design. *Learning Matters*, 2(2003), 35-43.
- MIROS. (2018). *Laporan tahunan 2018* [Annual report 2018]. Malaysian Institute of Road Safety Research.
- Mohd, N. I., Ali, K. N., Fauzi, A. F. A. A., & Ebrahimi, S. S. (2018). Serious game attributes for the construction of a hazard identification framework. *Journal of Interactive Mobile Technologies*, 12(7), 60-69. <https://doi.org/10.3991/ijim.v12i7.9647>
- Motiian, S., Pergami, P., Guffey, K., Mancinelli, C. A., & Doretto, G. (2015). Automated extraction and validation of children's gait parameters with the Kinect. *BioMedical Engineering OnLine*, 14, Article 112. <https://doi.org/10.1186/s12938-015-0102-9>
- Obikwelu, C. O. (2017). *Evaluating scaffolding in serious games with children* (Doctoral Thesis). University of Central, Lancashire.
- Olusegun, S. (2015). Constructivism Learning Theory: A Paradigm for Teaching and Learning. *IOSR Journal of Research & Method in Education*, 5(6), 2320-7388. <https://doi.org/10.9790/7388-05616670>
- Pourabdollahian, B., Taisch, M., & Kerga, E. (2012). Serious games in manufacturing education: Evaluation of learners' engagement. *Procedia Computer Science*, 15, 256-265. <https://doi.org/10.1016/j.procs.2012.10.077>
- Rawi, N. A., Mamat, A. R., Deris, M. S. M., Amin, M. M., & Rahim, N. (2015). Novel multimedia interactive application to support road safety education. *Jurnal Teknologi*, 77(19), 75-81. <https://doi.org/10.11113/jt.v77.6516>
- Rodriguez, D. (2015). *Natural user interfaces and autostereoscopy for learning in dentistry* (Master Thesis). Valencia Polytechnic University, Spain. <https://doi.org/10.13140/RG.2.1.4080.7846>
- Salwani, H., & Sobihatun, N. (2014, August 12-15). Multimedia courseware of road safety education for secondary school students. In *Knowledge Management International Conference (KMICe) 2014* (pp. 399-404). Langkawi, Malaysia.

- Savari, M., Ayub, M. N. B., Wahab, A. W. B. A., & Noor, N. F. M. (2016). Natural Interaction of Game-based Learning for Elasticity. *Malaysian Journal of Computer Science*, 29(4), 314-327. <https://doi.org/10.22452/mjcs.vol29no4.5>
- Serrano-laguna, Á., Martínez-ortiz, I., Regan, D., Johnson, A., Haag, J., & Fernández-manjón, B. (2016). Applying standards to systematize learning analytics in serious games. *Computer Standards & Interfaces*, 50, 116-123. <https://doi.org/10.1016/j.csi.2016.09.014>
- Shih, J., & Hsu, Y. (2016). Advancing Adventure education using digital motion-sensing games. *Educational Technology & Society*, 19(4), 178-189.
- Stavrev, S. (2016). Natural User Interface for Education in Virtual Environments. *Replay. The Polish Journal of Game Studies*, 3(1), 67-80.
- Stavrev, S., & Terzieva, T. (2015). *Virtual environment simulator for educational safety crossing*. *Computer Science Education & Computer Science Research Journal*, 11, 92-98. <https://doi.org/10.13140/RG.2.1.3057.6808>
- Szafir, D., & Mutlu, B. (2012). Pay attention! Designing adaptive agents that monitor and improve user engagement. In *Proceedings of the SIGCHI Conference on Human Factors in Computing Systems* (pp. 11-20). ACM Publishing. <https://doi.org/10.1145/2207676.2207679>
- Tsikinas, S., & Xinogalos, S. (2018). Designing effective serious games for people with intellectual disabilities. In *2018 IEEE Global Engineering Education Conference (EDUCON)* (pp. 1896-1903). IEEE Publishing. <https://doi.org/10.1109/EDUCON.2018.8363467>
- Tsita, C., & Satratzemi, M. (2018, December). Conceptual factors for the design of serious games. In *International Conference on Games and Learning Alliance* (pp. 232-241). Springer. [https://doi.org/10.1007/978-3-030-11548-7\\_22](https://doi.org/10.1007/978-3-030-11548-7_22)
- Velez, J. J. (2008). The relationship between teacher immediacy and student motivation. *Journal of Agricultural Education*, 49(3), 76-86. <https://doi.org/10.5032/jae.2008.03076>
- Westera, W. (2019). Why and how serious games can become far more effective: Accommodating productive learning experiences, learner motivation and the monitoring of learning gains. *Journal of Educational Technology & Society*, 22(1), 59-69.
- Wilson, K. A., Bedwell, W. L., Lazzara, E. H., Salas, E., Burke, S., Estock, J. L., Orvis, K. L., & Conkey, C. (2008). Relationships between game attributes and learning outcomes: Review and research proposals. *Simulation & Gaming*, 40(2), 217-266. <https://doi.org/10.1177/1046878108321866>



## Arabic Handwriting Classification using Deep Transfer Learning Techniques

Ali Abd Almisreb<sup>1</sup>, Nooritawati Md Tahir<sup>2,3\*</sup>, Sherzod Turaev<sup>4</sup>, Mohammed A. Saleh<sup>5</sup> and Syed Abdul Mutalib Al Junid<sup>2</sup>

<sup>1</sup>Department of Computer Science and Engineering, International University of Sarajevo, Sarajevo, BiH

<sup>2</sup>School of Electrical Engineering, College of Engineering, Universiti Teknologi MARA, 40000, Shah Alam, Selangor, Malaysia

<sup>3</sup>Institute for Big Data Analytics and Artificial Intelligence (IBDAAI), Universiti Teknologi MARA, 40000, Shah Alam, Selangor, Malaysia

<sup>4</sup>Department of Computer Science & Software Engineering, United Arab Emirates University Al Ain, UAE

<sup>5</sup>Collaborative Research on Advanced Cybersecurity Knowledge Research Lab (CRACK), University College of Technology Sarawak (UCTS), 96000 Sibul, Sarawak, Malaysia

### ABSTRACT

Arabic handwriting is slightly different from the handwriting of other languages; hence it is possible to distinguish the handwriting written by the native or non-native writer based on their handwriting. However, classifying Arabic handwriting is challenging using traditional text recognition algorithms. Thus, this study evaluated and validated the utilisation of deep transfer learning models to overcome such issues. Hence, seven types of deep learning transfer models, namely the AlexNet, GoogleNet, ResNet18, ResNet50, ResNet101, VGG16, and VGG19, were used to determine the most suitable model for classifying the handwritten images written by the native or non-native. Two datasets comprised of Arabic handwriting images were used to evaluate and validate the newly developed deep learning models used to classify each model's output as either native or foreign (non-

native) writers. The training and validation sets were conducted using both original and augmented datasets. Results showed that the highest accuracy is using the GoogleNet deep learning model for both normal and augmented datasets, with the highest accuracy attained as 93.2% using normal data and 95.5% using augmented data in classifying the native handwriting.

*Keywords:* Arabic text recognition, deep learning, handwriting classification, transfer learning

### ARTICLE INFO

#### Article history:

Received: 28 July 2021

Accepted: 1 November 2021

Published: 10 January 2022

DOI: <https://doi.org/10.47836/pjst.30.1.35>

#### E-mail addresses:

alimes96@yahoo.com (Ali Abd Almisreb)

noori425@uitm.edu.my; norita\_tahir@yahoo.com (Nooritawati Md Tahir)

sherzod@uaeu.ac.ae (Sherzod Turaev)

mohamed\_oam@ucts.edu.my (Mohammed A. Saleh)

samaljunid@gmail.com (Syed Abdul Mutalib Al Junid)

\*Corresponding author

## INTRODUCTION

About 420 million people speak Arabic in more than 20 countries worldwide. We know, the Arabic alphabet consists of 28 characters (Guellil et al., 2021). Features of Arabic writing include cursive style, connected characters, written right-to-left, and points or marks that will change the word's meaning (Burrow, 2004). Conversely, recognition is a field covering various subjects, including recognising the face, fingerprint, image, character, and many more (Najadat et al., 2019), allowing for identifying specific target items (Savchenko, 2020). Recognition of handwriting can be online (real-time recognition from pen tracing) or offline (recognition from images). Due to the endless variation in the writing styles of individual writers, it is indeed a challenging task to recognise the written text. However, this can be achieved through feature extraction of images to eliminate non-essential variation and only retain recognition-related data (Wong & Loh, 2019).

## LITERATURE REVIEW

Handwriting identification is the process of identifying a writer or a group of writers, with the assumption that the handwriting of each individual or group is specific (Wang, 2019). On the other hand, deep learning (DL) is generally used for image classification. It learns from the trained data, and the model can then be used on new datasets for recognition or classification (Pouyanfar et al., 2019; Goularas & Kamis, 2019; Wang, 2020; Yildiz et al., 2020). Different approaches can be used to build efficient deep learning models, and one of them is transfer learning, specifically applying a pre-trained model on a different problem. In DL, new data of previously unknown classification is provided to the existing network and is adjusted accordingly. Note that transfer learning is indeed valuable for handling insufficient data for a new domain in the neural network, and there is a big pre-existing data pool that can be transferred to the problem to be solved. The benefit of this approach is that much less data is needed, which significantly reduces the computational time (Razak et al., 2020a; Razak et al., 2020b; Wahdan et al., 2020; Yang et al., 2013).

Furthermore, numerous studies have been published on Arabic text with varying degrees of precision. For instance, a geometric recognition system for handwritten Arabic characters was proposed by Abodi and Li (2014). IFN/ENIT dataset was applied, and the outcome was 93.3% as the average accuracy. This study was based on simplifying characters into images containing features, translating images into orthogonal lines, and using them as single vectors. Alharbi (2018) proposed a genetic learning vector quantisation (LVQ) algorithm comprised of two stages: firstly, a method that selected the features, and secondly, the LVQ neural network learning algorithm for classification. Further, the Optical Character Recognition (OCR) system of the handwritten Arabic characters was proposed by Hussien et al. (2016) with an accuracy of 77.25%. The Hopfield neural network was implemented, and only eight Arabic characters were used. In addition, Younis (2017)

used the deep convolutional neural network (CNN) with regularisation parameters, such as batch normalisation, to avoid overfitting. CNN was used to extract features and trained for recognition rather than extracting many gradient or textural features.

Conversely, Elleuch et al. (2016) applied Support Vector Machine (SVM) and CNN with IFN/ENIT as the database to classify 56 classes with an error rate of 7.05%. In addition, Eladel et al. (2015) proposed fast wavelet transform (FWT) and neural network (NN) architecture that is based on multi-resolution analysis (MRA) and the Adaboost algorithm. The Arabic handwriting recognition training and testing were set using IESK-arDB datasets, containing 6000 characters. Moreover, Najadat et al. (2019) obtained 16,800 images of isolated characters from the Arabic Handwritten Character Dataset (AHCD). Thus, to train and check the datasets, CNN's deep learning architecture was developed using a suitable optimisation technique, and results attained showed an accuracy of 94.9% using testing data. Belabiod & Belaïd (2018) implemented a line segmentation method using the RU-net and end-to-end word segmentation approach, namely the CNN followed by the bidirectional long term memory (BLTM) and the connectionist temporal classification (CTC) functions that automatically learned the alignment of text line images with the transcription words.

Based on the previous works mentioned above and to the extent of our knowledge, no studies have reported using more than one Arabic handwritten character for classification, and no studies have reported the deep learning transfer models, specifically the AlexNet, the GoogleNet, the residual neural network (ResNet) 18, the ResNet50, the ResNet101, the VGG16 and the VGG19 for classifying Arabic handwriting images as native writers or otherwise. Hence, findings from this study can assist the non-native writers to confirm and ensuring that their Arabic handwriting is correctly written. Therefore, the main aim of this study is to classify Arabic handwriting images either written by native writers or otherwise with deep learning neural networks as classifiers. The motivation of this study is to investigate if there are differences in writing styles of Arabic handwriting written by foreign and native writers that the human vision could not detect due to the irregular and complex nature of Arabic handwriting. New deep learning algorithms will be developed for this purpose based on the seven transfer learning models mentioned earlier in classifying the Arabic handwriting images as native or foreign (non-native) writers. This study can later be used in the text transcription process application, for instance, ancient or historical documents written in Arabic by the native writers.

## RESEARCH METHOD

This section will elaborate on the methods developed in this study. Firstly, the database used will be explained, followed by the transfer learning models and the performance measure used to evaluate the effectiveness of the proposed method.

## Dataset

As mentioned earlier, large datasets for training were not the main issue in the case of transfer learning, hence in this study, for the handwriting Arabic images dataset, the dataset comprised of handwritten images written by 22 subjects, specifically 11 natives and 11 foreigners. All the participants are male, aged between 22 and 27 years old. Foreign participants are from the following countries: Bosnia and Herzegovina, Turkey, Kenya, Ghana, and Tanzania. On the other hand, the native Arabic participants are from Egypt, Saudi Arabia, Algeria, Lebanon, Palestine, Jordan, Syria, Libya, and Iraq. Each subject was required to write 45 sample images; therefore, 990 handwritten images were generated as the database. All images are captured using a mobile phone. In addition to the original database, the on-the-fly augmentation approach involves the transformation of the database. Two augmentation approaches are utilised by mirroring or creating a mirror image, and the other is augmentation by random crops.

The datasets were categorised into two types, namely the native writers and foreign writers. Figure 1 shows some samples of sentences written by both categories of writers.

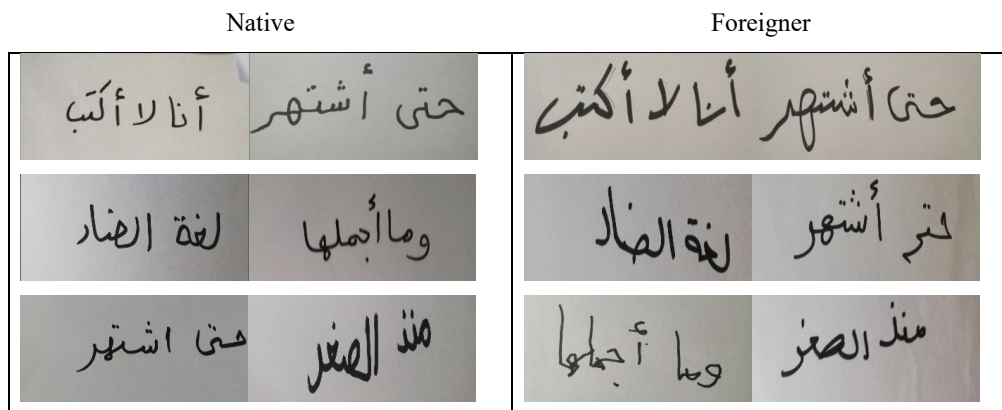


Figure 1. Samples of handwriting images

## Transfer Learning Models

In this section, the seven models of transfer learning methodology used in this study will be discussed. The first one was AlexNet, a CNN designed by Krizhevsky et al. (2017) trained with over one million ImageNet database images. It represented an extensive network structure with sixty million parameters and 650 thousand neurons with eight layers, five convolutional layers and, three fully connected layers. The fully connected layer could classify 1000 classes, and the remainder of the network was regarded as the feature extractor. Next is the GoogleNet. GoogleNet was also known as Inception-V1.

GoogleNet is a pre-trained CNN comprised of 22 layers trained on ImageNet. In the centre of the network, the network architecture is comprised of a 1 to 1 Convolution layer. Further, global average pooling was used at the end of the network rather than fully connected layers (Szegedy et al., 2015). Next, are the ResNet-18, the ResNet-50 and the ResNet-101. Finally, ResNet was proposed by He et al. (2016). The ResNet is a neural network constructed from pyramidal cells in the cerebral cortex. ResNet was applied to skip connections or shortcuts to move across some layers. Regular ResNet models were developed with two or three-layer that skips, including the nonlinearities (ReLU) and batch normalisation in between. ResNet transformed the NN architectural competition by introducing the residual learning concept in the NNs and further included an effective technique for training the deep network. For instance, ResNet-18 is a pre-trained deep learning model for image classification, the network was 18 layers deep and was trained on one million images based on 1000 categories. While the ResNet-50 is a pre-trained model for image classification; the network was 50 layers deep and was trained on one million images of 1000 classes. On the other hand, ResNet-101 is a pre-trained deep learning model for image classification, with 101 layers trained on one million images of 1000 categories.

The sixth transfer learning used is VGG 16. VGG16 is a CNN model presented by Simonyan and Zisserman (2015). This model obtains 92.7% top-5 testing accuracy in ImageNet, comprising 1000 classes with over 14 million images. The name VGG-16 is from the fact that it has 16 layers and the layers include convolutional layers, max-pooling layers, activation layers, and fully connected layers. It has 13 convolutional layers, five max-pooling layers, and three dense layers, which sum up to 21 layers, but there are only 16 weight layers. Lastly is the VGG19, a pre-trained deep learning model for image classification. This network comprises 19 layers and is trained on one million images of 1000 categories from the ImageNet database. As mentioned by Simonyan and Zisserman (2015), the VGG19 has 19 layers, specifically 16 convolutional, three fully connected CNN that utilised 3 by 3 filters with stride and padding of 1, along with 2 by 2 max-pooling layers

Conversely, data augmentation was also developed and used as an additional dataset generated from the existing images. As for data augmentation, two methods were used: augmentation by mirroring or creating a mirror image, and the other is augmentation by random crops. The experimental results and analysis are discussed in the next section.

## RESULTS AND DISCUSSIONS

This section discusses the results attained based on the proposed method. First, all the seven transfer learning approaches were evaluated. Then, the numerical results, specifically, the training loss rates, training accuracy, validation loss rates, and validation accuracy for each model, are reported and elaborated.

### **Training Loss Rate Analysis**

As shown in Figure 2, the training loss rate of AlexNet with and without data augmentation decreases significantly after 100 iterations, while the loss rate for data augmentation decreases after 300 iterations. It is observed that for the GoogleNet, the training loss rate converges after 2000 iterations for the augmented datasets; however, the loss rate significantly decreased at 1000 iteration for normal datasets, and the loss reduces and prolongs until the end of the analysis. As for the ResNet18, the training loss rate for normal datasets decreases significantly after 200 iterations, while the model with data augmentation only shows a decremental pattern after 400 iterations. Further, for the ResNet50, the training loss significantly decreases after 100 iterations for normal datasets; nevertheless, it decreases longer, specifically after 300 iterations for the case of data augmentation. Moreover, the training loss for the ResNet101 decreases to zero after the completion of 100 iterations based on the normal data, while for the augmented dataset, there are decreases after 300 iterations.

Likewise, the training loss rate for VGG16 shows a slight decrease at 200 iterations for the augmented dataset. However, for the normal dataset without augmentation, there is a decrease after 100 iterations. Additionally, the loss rate is unstable after 600 iterations and remains the same until the analysis ends. Finally, for VGG 19, the training loss rate reduces after 100 iterations for the dataset without augmentation. Nonetheless, there is a reduction after 200 iterations, and instability occurs up to 400 iterations for the augmented dataset. Overall, as observed from Figure 2, the training loss for these models mostly converges around 500 epochs. Thus, the loss rate for models without data augmentation can converge to zero earlier as compared to data augmentation. That is due to the less variation amongst the datasets.

### **Training Accuracy Analysis**

In this section, the training accuracy, as depicted in Figure 3 for all seven utilised deep learning models, is described. Firstly, the training accuracy by AlexNet reaches 100% after 100 iterations for normal datasets; however, for data augmentation, AlexNet requires 500 iterations to reach 100%. Again, it is due to the variation in images and the larger number of datasets. Next, is the GoogleNet using both normal and augmented data showing similar trends with both plots reaching 100% accuracy at 2000 iterations. Finally, as for ResNet18, normal datasets reach 100% instantly, compared to data augmentation.

Further, for ResNet50, both models achieve 100% accuracy at less than 200 iterations, with the model for the normal dataset being faster since the datasets are fewer. Moreover, for ResNet101, the training accuracy reaches 100% for normal and augmented datasets before 200 iterations. Additionally, for VGG16, for datasets without data augmentation, the accuracy increases up to 600 iterations but decreases and becomes unstable until the end.

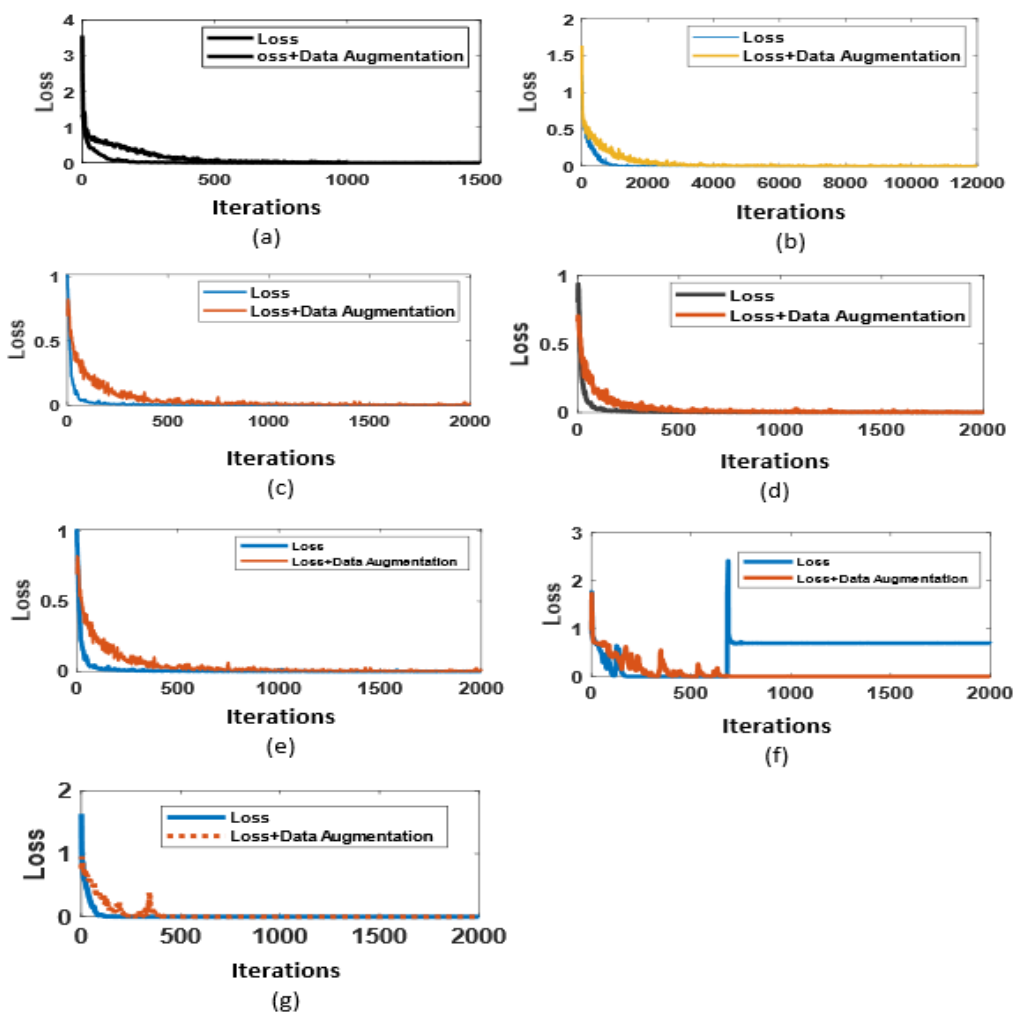


Figure 2. (a) AlexNet, (b) GoogLeNet, (c) ResNet18, (d) ResNet50, (e) ResNet101, (f) VGG16, and (g) VGG19 training loss rates for both original and augmented datasets

As for data augmentation, the accuracy increases to 600 iterations and remains the same until the end. Eventually, for VGG19, the training accuracy increases at 200 iterations for both categories datasets. Nonetheless, the data augmentation becomes unsteady before it stabilises after 400 iterations. Generally, the results show that for all seven deep learning models, the training accuracies for data without augmentation reached 100% accuracy earlier; hence it demonstrates the significant role of data augmentation in classification problems that enrich and enhance the performance of deep learning models that are used in this study.

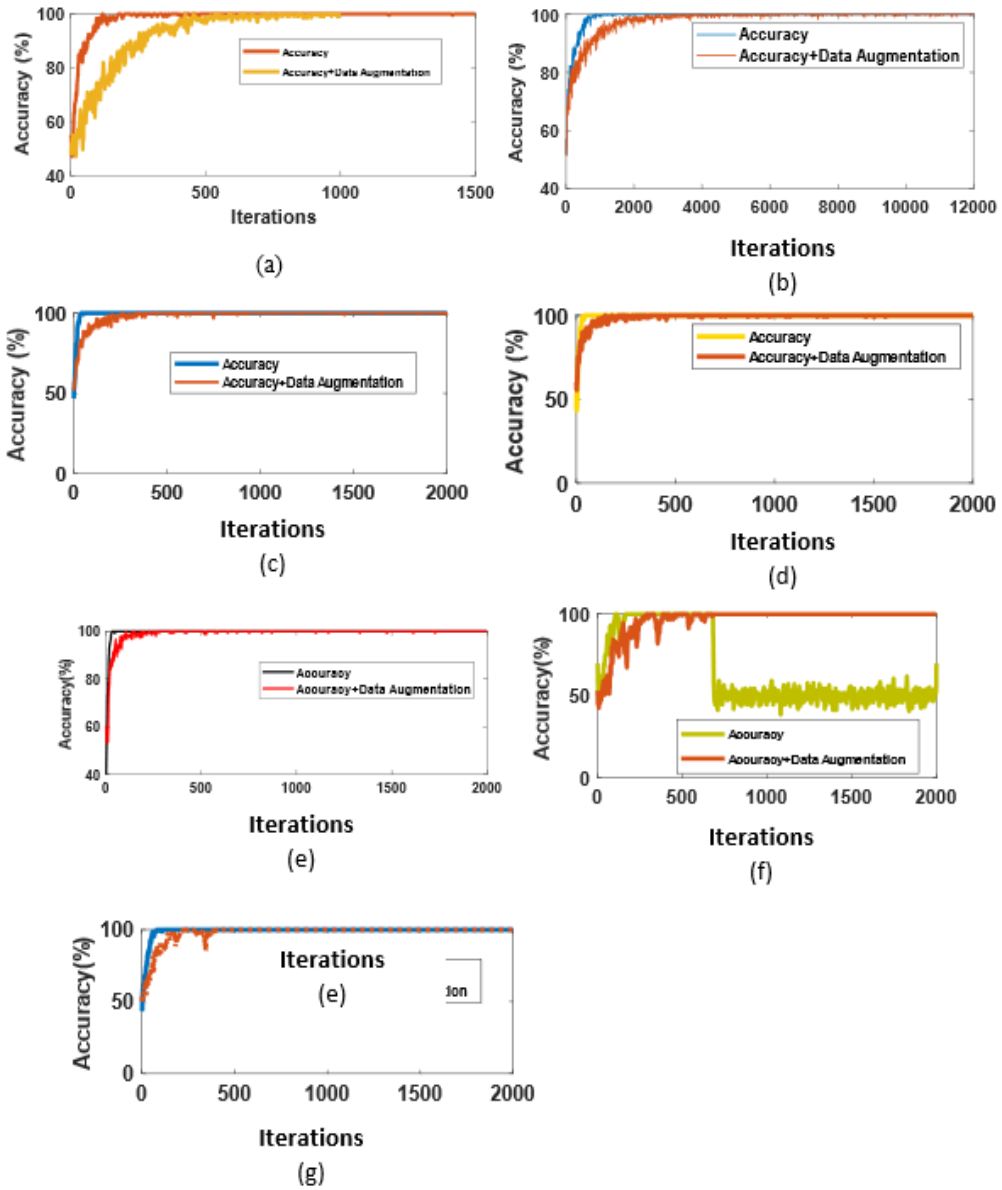


Figure 3(a) AlexNet, (b) GoogLeNet, (c) ResNet18, (d) ResNet50, (e) ResNet101, (f) VGG16, and (g) VGG19 training accuracy for both original and augmented datasets



### Validation Loss Rate Analysis

Another essential point to address is the validation loss rates for each model, shown in Figure 4. Firstly, it is observed that the AlexNet validation loss based on the normal dataset is almost similar to the epoch value at 2; however, for data augmentation, the loss increases for the value of epoch above 2. GoogLeNet shows no significant improvement except for augmented data with a slight decrease for validation loss. Further, it is observed that the loss rate in both models decreases only at iteration value before 50; however, it increases after that until the end of the analysis. Furthermore, for ResNet18 using both datasets, convergence occurs at epoch 5 and remains the same pattern until the numerical analysis is completed.

Additionally, for ResNet50, validation loss converges at the fifth epoch for both datasets but slightly decreases for the normal dataset. Conversely, for ResNet101, validation loss is low and was not improved until the analysis ended. Moreover, as in the case of VGG16, no significant improvement observes for the validation loss. Finally, for the VGG19, the validation loss shows a slight decrease for unaugmented data before epoch 5, but the loss rate increases after that, while for data augmentation, the loss rate is unstable.

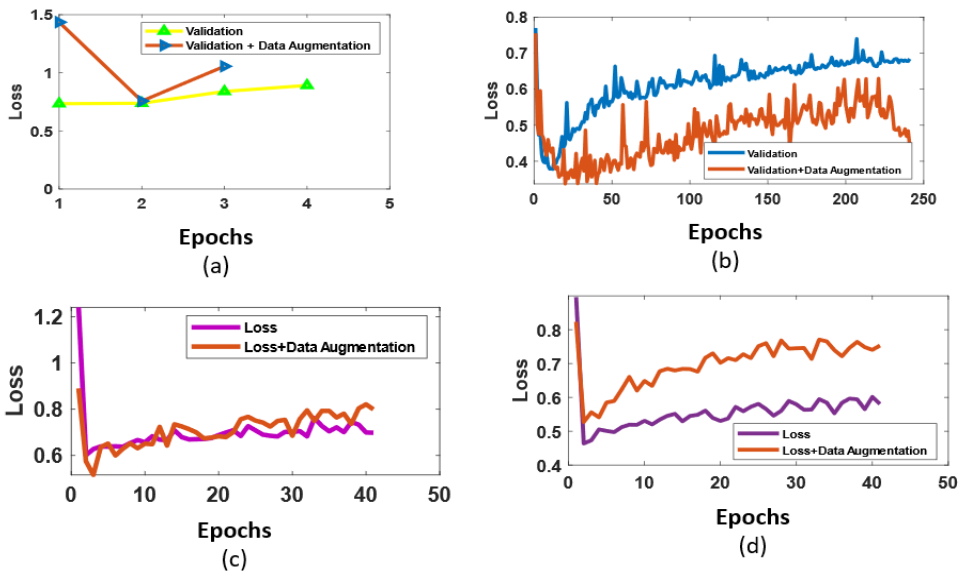


Figure 4. (a) AlexNet, (b) GoogLeNet, (c) ResNet18, (d) ResNet50

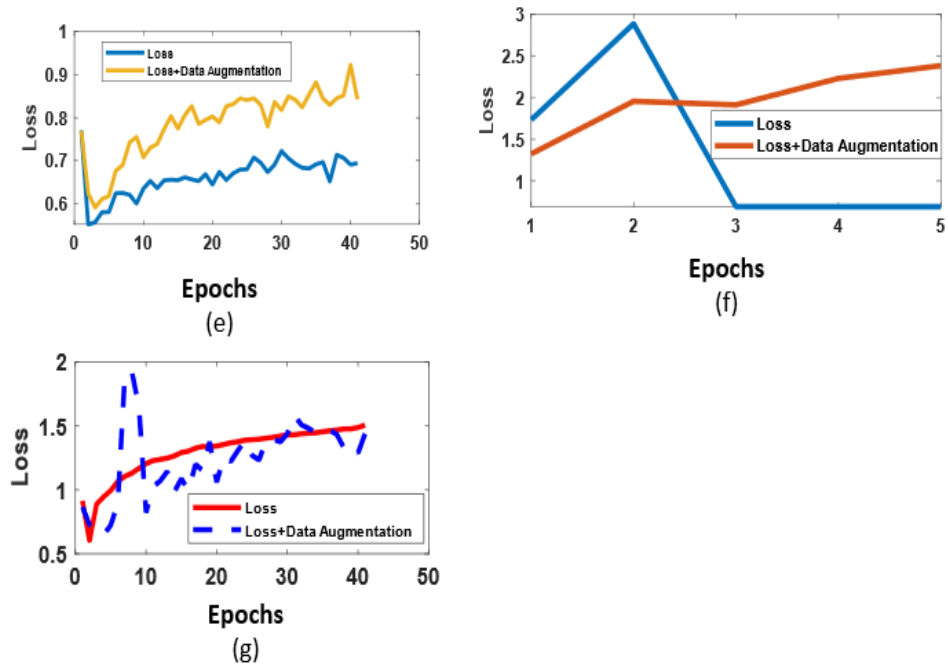


Figure 4. (e) ResNet101, (f) VGG16, and (g) VGG19 validation loss rates for both original and augmented datasets

### Validation Accuracy

Figure 5 depicts the validation accuracy for each deep learning model. As observed, validation accuracy for both datasets using AlexNet shows similar trends, with the accuracy improving and sustaining at epoch values of 2 and above. In the case of GoogleNet, both datasets show similar trends, specifically from 0 to 50 iterations with 80% accuracy. The accuracy increases slightly after that and maintains similar accuracy until the numerical analysis ends. Further, for ResNet18, it is observed that the validation accuracy increases at epoch 5 for both models and demonstrates similar trends until the numerical analysis session ends. Furthermore, the validation accuracy for ResNet50 increases for both datasets up to the fifth epoch and sustain similar values.

On the other hand, for ResNet101, the validation accuracy shows incremental accuracy for both datasets at epoch 5 and maintains the same pattern. As for VGG16, the validation accuracy increases for both normal and augmented datasets at the second epoch. After that, for the augmented dataset, the accuracy increases, while for the normal dataset, the accuracy drops at epoch 3 and maintains a similar accuracy value onwards. Finally, for the VGG19 model, the validation accuracy increases for both datasets at epoch 5, and after the 10<sup>th</sup> epoch, both accuracies achieve stability.

## Performance Measure

The performance measure was used to select the optimum deep transfer learning amongst all seven under evaluation for the Arabic handwriting classification based on the highest accuracy among these models. The performance measures for the two classes are the 'native writer' and 'foreigner writer.' Accuracy (Acc), sensitivity (Sens) and, specificity (Spec) were used in this study as the performance measures. Here, the acc represents the correctness of the deep learning classifier, whilst the sens represents the correctly classified of 'foreigner' handwriting, and the spec represents the correctly classified of the 'native' handwriting. The datasets were partitioned with 60% of the images for training and 40% for testing. All trained models were evaluated and tested using 396 as unseen images for both classes as either 'foreigner' or 'native.' Table 1 tabulates the results of each DL model for both unaugmented and augmented datasets.

Table 1

*Performance measure of each DL model using both original and augmented data*

DL Model	Original Data			Augmented Data		
	Acc	Spec	Sens	Acc	Spec	Sens
AlexNet	78.3	74.2	82.3	75.0	79.3	70.7
GoogleNet	93.2	92.4	93.9	95.5	93.9	97.0
ResNet18	78.8	75.8	81.8	80.6	78.8	82.3
ResNet50	78.5	75.3	81.8	82.8	87.9	77.8
ResNet101	78.5	83.8	73.2	81.6	79.3	83.8
VGG16	50.3	0.6	0.7	78.5	78.3	78.8
VGG19	79.0	74.2	83.8	78.0	91.4	64.6

From Table 1, GoogleNet shows the highest accuracy for both original and augmented data. The same goes for specificity and sensitivity. GoogleNet uses inception modules to decrease the required computation time and replace fully connected layers with global average pooling. AlexNet achieves higher accuracy without data augmentation with an accuracy of 78.3% and 82.3% sensitivity. Consequently, AlexNet could recognise the 'native' handwriting better as compared to 'foreigner' handwriting. Among foreigner and native classes, GoogleNet outperforms for both original and augmented datasets with the highest accuracy using augmented data at 95.5% accuracy, and the class native scores 97.0% as specificity. As for the ResNet18 model, the outcome shows higher accuracy for

augmented data with 80.6% accuracy and 82.3% specificity for the native class. Once again, for ResNet50, the performance of augmented data attains higher accuracy, specifically 82.8% but lower specificity of 77.8% for the class native.

Moreover, for ResNet50, 81.6% accuracy achieves for augmented data compared to 78.5% for the original data. Compared to AlexNet, training the ResNet requires high computation; therefore, AlexNet is the second option for original data. As for VGG16, this deep learning model obtains a higher accuracy rate for augmented data, specifically 78.5%. However, for VGG19, accuracy for unaugmented data is higher that is 79%, as compared to data augmentation accuracy, specifically 78%. Generally, only two deep learning models obtained higher results based on original data, namely AlexNet and VGG19. Although the VGG19 performed slightly better, it requires more memory. The rest of the deep learning models attain higher accuracy using augmented datasets. The overall results prove that GoogleNet is the optimum deep learning model and outperforms other models based on both original and augmented datasets.

## CONCLUSION

In conclusion, handwritten Arabic images classification was analysed in this study using seven deep learning transfer learning to evaluate and validate the ability of each model to distinguish the Arabic handwriting images written by either 'native' or 'foreigner'. Datasets of written Arabic handwriting images were created to train and test these models. The participants in these datasets are Arabic writers and non-Arabic writers. On the whole, training and testing using the seven transfer learning models, namely AlexNet, GoogleNet, Resnet18, ResNet50, ResNet101, VGG16, and VGG19 with both original and augmented datasets, have proven the ability of these models to differentiate the Arabic handwriting according to two categories specifically native writer or foreign writer. In addition, these transfer learnings are also suitable for small-size datasets. Results show that the GoogleNet is the most suitable deep learning model, with 93.2% using the original dataset and 95.5% using augmentation data compared to other transfer learning models. For future work, findings from this study will use a more extensive and diverse database specifically for identifying ancient Arabic handwritten recognition written by the native writer based on deep learning.

## ACKNOWLEDGEMENT

Research Management Centre (RMC), Universiti Teknologi MARA (UiTM), Shah Alam, Selangor, Malaysia, funded this research under Grant No: 600-IRMI/MyRA5/3/BESTARI (041/2017). Sincere appreciation to Prof. Dr AZ Ahmed as a proofreader, Resident Reviewer, UiTM. Also, the authors would like to thank both volunteered participants as contributors in developing the handwriting database.

## REFERENCES

- Abodi, J. A., & Li, X. (2014). An effective approach to offline Arabic handwriting recognition. *Computers Electrical Engineering*, 40(6), 1883-1901. <https://doi.org/10.1016/j.compeleceng.2014.04.014>
- Alharbi, A. (2018). A genetic-LVQ neural networks approach for handwritten Arabic character recognition. *Artificial Intelligence Research*, 7(2), 45-54. <https://doi.org/10.5430/air.v7n2p43>
- Belabiod, A., & Belaïd, A. (2018). *Line and word segmentation of Arabic handwritten documents using neural networks* (Research Report LORIA). Université de Lorraine. <https://hal.inria.fr/hal-01910559>
- Burrow, P. (2004). *Arabic handwriting recognition* (Master of Science). University of Edinburgh, UK. <http://citeseerx.ist.psu.edu/viewdoc/download?doi=10.1.1.67.404&rep=rep1&type=pdf>
- Eladel, A., Ejbali, R., Zaied, M., & Amar, C. B. (2015). Dyadic multi-resolution analysis-based deep learning for Arabic handwritten character classification. In *Proceedings of 2015 IEEE 27th International Conference on Tools with Artificial Intelligence (ICTAI)* (pp. 807-812). IEEE Publishing.
- Elleuch, M., Maalej, R., & Kherallah, M. (2016). A new design based-SVM of the CNN classifier architecture with dropout for offline Arabic handwritten recognition. *Procedia Computer Science*, 80, 1712-1723. <https://doi.org/10.1016/j.procs.2016.05.512>
- Goularas, D., & Kamis, S. (2019). Evaluation of deep learning techniques in sentiment analysis from Twitter data. In *2019 International Conference on Deep Learning and Machine Learning in Emerging Applications (Deep-ML)* (pp. 12-17). IEEE Publishing. <https://doi.org/10.1109/Deep-ML.2019.00011>
- Guellil, I., Saâdane, H., Azouaou, F., Gueni, B., & Nouvel, D. (2021). Arabic natural language processing: An overview. *Journal of King Saud University, Computer and Information Sciences*, 33(5), 497-507. <https://doi.org/10.1016/j.jksuci.2019.02.006>
- He, K., Zhang, X., Ren, S., & Sun, J. (2016). Deep residual learning for image recognition. In *Proceedings of 2016 IEEE Conference on Computer Vision and Pattern Recognition (CVPR)* (pp. 770-778). IEEE Publishing. <https://doi.org/10.1109/CVPR.2016.90>
- Hussien, R. S., Elkhidir, A. A., & Elnourani, M. G. (2016). Optical character recognition of Arabic handwritten characters using neural network. In *Proceedings of 2015 International Conference on Computing, Control, Networking, Electronics and Embedded Systems Engineering (ICCNEEE)* (pp. 456-461). IEEE Publishing. <https://doi.org/10.1109/ICCNEEE.2015.7381412>
- Krizhevsky, A., Sutskever, I., & Hinton, G. E. (2017). ImageNet classification with deep convolutional neural networks. *Communication ACM*, 60(6), 84-90. <https://doi.org/10.1145/3065386>
- Najadat, H. M., Alshboul, A. A., & Alabed, A. F. (2019). Arabic handwritten characters recognition using convolutional neural network. In *Proceedings of 10th International Conference on Information and Communication Systems (ICICS)* (pp. 147-151). IEEE Publishing. <https://doi.org/10.1109/IACS.2019.8809122>
- Pouyanfar, S., Sadiq, S., Yan, Y., Tian, H., Tao, Y., Reyes, M. P., Shyu, M., Chen, S., & Iyengar, S. (2019). A survey on deep learning: Algorithms, techniques, and applications. *ACM Computer Surveys*, 51(5), 1-36. <https://doi.org/10.1145/3234150>

- Razak, H. A., AlMisreb, A. A., Saleh, M. A., & Tahir, N. M. (2020a). Housebreaking crime gait pattern classification using artificial neural network and support vector machine. *Journal of Theoretical and Applied Information Technology*, 98(12), 2185-2198.
- Razak, H. A., Saleh, M. A., & Tahir, N. M. (2020b). Review on anomalous gait behavior detection using machine learning algorithms. *Bulletin of Electrical Engineering and Informatics*, 9(5), 2090-2096. <https://doi.org/10.11591/eei.v9i5.2255>
- Savchenko, A. V. (2020). Probabilistic neural network with complex exponential activation functions in image recognition. *IEEE Transactions on Neural Networks and Learning Systems*, 31(2), 651-660. <https://doi.org/10.1109/TNNLS.2019.2908973>
- Simonyan, K., & Zisserman, A. (2015, May 7-9). Very deep convolutional networks for large-scale image recognition. In *Proceedings of 3rd International Conference on Learning Representations, (ICLR) 2015* (pp. 1-14). San Diego, USA. <https://arxiv.org/abs/1409.1556>
- Szegedy, C., Liu, W., Jia, Y., Arbor, A., Anguelov, D., Erhan, D., Vanhoucke, V., & Rabinovich, A. (2015). Going deeper with convolutions. In *Proceedings of 2015 IEEE Conference on Computer Vision and Pattern Recognition (CVPR)* (pp. 1-9). IEEE Publishing. <https://doi.org/10.1109/CVPR.2015.7298594>
- Wahdan, A., Sendeyah, A. L., Hantoobi, S. A., & Salloum, K. S. (2020). A systematic review of text classification research based on deep learning models in Arabic language. *International Journal of Electrical and Computer Engineering (IJECE)*, 10(6), 6629-6643. <http://dx.doi.org/10.11591/ijece.v10i6.pp6629-6643>
- Wang, G. (2019). The status of Chinese handwriting identification and the improvement of methodologies. *Forensic Science Criminology*, 4(1), 1-7. <http://dx.doi.org/10.15761/FSC.1000129>
- Wang, P. (2020). Research and design of smart home speech recognition system based on deep learning. In *2020 International Conference on Computer Vision, Image and Deep Learning (CVIDL), Chongqing, China* (pp. 218-221). IEEE Publishing. <https://doi.org/10.1109/CVIDL51233.2020.00-98>
- Wong, L. C., & Loh, W. P. (2019). Segregating offline and online handwriting for conditional classification analysis. *IOP Conference Series: Materials Science and Engineering*, 530, Article 012058. <http://dx.doi.org/10.1088/1757-899X/530/1/012058>
- Yang, L., Hanneke, S., & Carbonell, J. (2013). A theory of transfer learning with applications to active learning. *Machine Learning*, 90(2), 161-189. <http://dx.doi.org/10.1007/s10994-012-5310-y>
- Yildiz, A., Almisreb, A. A., Dzakmic, S., Tahir, N. M., Turaev, S., & Saleh, M. A. (2020). Banknotes counterfeit detection using deep transfer learning approach. *International Journal of Advanced Trends in Computer Science and Engineering*, 9(5), 8115-8122. <http://dx.doi.org/10.30534/ijatcse/2020/172952020>
- Younis, K. S. (2017). Arabic hand-written character recognition based on deep convolutional neural networks. *Jordanian Journal of Computers and Information Technology (JJCIT)*, 3(3), 186-200.

*Review Article*

## Adoption of Cloud Computing in E-Government: A Systematic Literature Review

Osama Abied<sup>1\*</sup>, Othman Ibrahim<sup>1</sup> and Siti Nur-Ila Mat Kamal<sup>2</sup>

<sup>1</sup>Department of Information Systems, Azman Hashim International Business School, Universiti Teknologi Malaysia, 81310 Skudai, Johor, Malaysia

<sup>2</sup>Faculty of Information Management, Universiti Teknologi MARA, Jalan Universiti Off KM 12 Jalan Muar, 85000 Segamat, Johor

### ABSTRACT

Cloud computing in governments has become an attraction to help enhance service delivery. Improving service delivery, productivity, transparency, and reducing costs necessitates governments to use cloud services. Since the publication of a review paper on cloud adoption elements in e-governments in 2015, cloud computing in governments has evolved into discussions of cloud service adoption factors. This paper concentrates on the adoption of cloud computing in governments, the benefits, models, and methodologies utilized, and the analysis techniques. Studies from 2010 up to 2020 have been investigated for this paper. This study has critically peer-reviewed articles that concentrate on cloud computing for electronic governments (e-Governments). It exhibits a systematic evaluation of the empirical studies focusing on cloud adoption studies in e-governments. This review work further categorizes the articles and exhibits novel research opportunities from the themes and unexhausted areas of these articles. From the reviewed articles, it has been observed that most of the articles have employed the quantitative approach, with few utilizing qualitative and mixed-method approaches. The results reveal that cloud computing adoption

could help solve problems in learning, such as infrastructure issues, cost issues, and improve service delivery and transparency. This review gives more information on the future directions and areas that need attention, like the trust of cloud computing in e-governments.

*Keywords:* Adoption, cloud computing, cloud services, e-government

### ARTICLE INFO

*Article history:*

Received: 4 August 2021

Accepted: 29 September 2021

Published: 10 January 2022

DOI: <https://doi.org/10.47836/pjst.30.1.36>

*E-mail addresses:*

[mosama@graduate.utm.my](mailto:mosama@graduate.utm.my) (Osama Abied)

[othmanibrahim@utm.my](mailto:othmanibrahim@utm.my) (Othman Ibrahim)

[sitin509@uitm.edu.my](mailto:sitin509@uitm.edu.my) (Siti Nur-Ila Mat Kamal)

\*Corresponding author

## INTRODUCTION

As Information Technology innovation is advancing (Sallehudin et al., 2020), cloud computing in governments is helping improve productivity (Ali et al., 2018b) while enhancing efficiency, transparency, and public service delivery (Mohammed et al., 2016; Nanos et al., 2019). Furthermore, since the evolution of cloud computing in the 2000s (Bayramusta & Nasir, 2016; Senyo et al., 2018), there have been developments in the automation of existing procedures, making infrastructure, software, and platforms easily available on-demand for pay (Sharma et al., 2020). Recently, cloud computing has become a strategic direction for e-governments around the globe because of its benefit in overcoming infrastructure issues as well as attaining cost reduction (Mohammed et al., 2020; Singh et al., 2020).

Cloud computing has also attracted several studies (Senyo et al., 2018). There is no doubt that various large governmental organizations are using cloud computing differently. Apart from becoming popular, it has become a powerful driver for economic and technological changes worldwide (Vu et al., 2020). For instance, in healthcare predictions (Anuradha et al., 2021; Tuli et al., 2020), in smart cities (Wang et al., 2020), in small and medium enterprises (Alismailli et al., 2020), in governments (Zhang, 2020), and education (Vaidya et al., 2020), among other fields. Moreover, the utilization of cloud computing has yielded unprecedented opportunities for organizations to improve their performance. Besides this, the unique properties of cloud computing have made modern governments transparent, efficient, effective in response, and creative (Al Mudawi et al., 2019; Ali et al., 2018a; Nanos et al., 2019).

Hence, with this trend, utilizing cloud computing will create convenience, improve accessibility and quality of delivery of government services, and improve the flow of information and procedures. It will further improve the speed, coordination, and enforcement of activities in the public sector. This paper focuses on existing literature on cloud computing as a supporting technology for e-governments and brings out the themes, methodologies, trends, critical factors, theories, and data analysis techniques in past studies. This paper will critically evaluate existing works and studies on cloud computing in e-governments and highlight new research areas. Three research questions have been developed as explained subsequently to guide this study. The systematic review is complementary to the past studies and gives the following contributions for the researchers interested in cloud computing and e-governments to further their studies. The following research questions will guide this study:

RQ1. What is the research area in focus in cloud computing on e-governments?

RQ2. How is cloud computing used to improve service delivery in e-governments (benefits)?



RQ3. What themes, factors, methods, level of implementation, data analysis techniques, and methodologies are available, and what is the gap for cloud computing in e-governments?

The research identifies primary studies related to cloud computing in e-governments from 2010 to 2020. Other researchers can utilize this list to further their work. The research further selects studies that meet the criteria set for quality assessment. These studies are a good ground for comparing similar works. Comprehensively, this study analyzes the articles and brings out the ideas, themes, methods, methodologies, level of implementation, and factors in the field of cloud computing and e-governments. Finally, a discussion is presented on how to further this work.

This paper is outlined as follows: Section 3 examines the methods used in this study and the primary studies that were systematically chosen for evaluation. Section 4 discusses the findings from the primary studies. Section 5 carries out a discussion as highlighted in the research questions. Lastly, section 6 presents the conclusion and suggestions for further research.

## **PRIOR RESEARCH**

Specifically, and to the best of the researchers' knowledge during this research, the systematic literature reviews (SLRs) concerning the application of cloud computing in e-governments are still limited in number. One of the most recent surveys was on the effect of cloud computing on the sustainability of government services (Mohammed et al., 2020). In this study, the authors identify the gap in incorporating cloud computing as a platform for establishing sustainable services. In the view of this study, the researchers give an important starting point to fellow researchers interested in cloud computing in e-governments. Apart from this, several studies about cloud computing and its extensive use have also been published, and this study will examine them consecutively to extract their differences in the themes chosen by the authors and this research.

A systematic review was done on cloud computing and e-governments (Tsaravas & Themistocleous, 2011). The study highlights the application of Service-Oriented Architecture in e-governments and the utilization of cloud computing in the public sector. In addition, the study highlights the benefits and obstacles of cloud computing, the service models used in cloud computing, and the deployment models. The study also examines the case studies in the cloud in e-governments. However, the study excludes the models, methodologies, level of implementation, themes, and critical factors and focuses mostly on the government organizations in some cities that have adopted cloud computing solutions for improved service delivery.

In 2015, a review was conducted on models of adopting cloud computing in an e-government context (Mohammed & Ibrahim, 2015a). Interestingly the paper highlights the benefits and challenges of cloud computing in e-government structures and examines the proposed cloud computing adoption models. Furthermore, it classifies the models into various categories, such as “layered-based,” “step-based,” “component-based,” and “conceptual/theoretical” models. Since 2016 the application and adoption of cloud computing have grown, and as such, our research seeks to bring out the themes, methodologies, level of implementation, data analysis techniques, and critical factors that have been examined.

A systematic review was also conducted on factors affecting the adoption of cloud computing in e-governments (Wahsh & Dhillon, 2015b). The paper concentrates on the factors affecting cloud adoption in e-governments for public sectors, and this research covers a timeline of up to 2015. The paper suggests an extension of research to include theoretical models. Therefore, our research will seek to highlight the models and factors that have been brought out till 2020. The themes, the level of implementation, methodologies, and data analysis techniques will also be highlighted.

All the past studies mentioned above highlight the wider use of cloud computing; however, they leave out some elements like the methodologies, the level of implementation, data analysis techniques, the factors, and themes used for better adoption solutions. Furthermore, the field of cloud computing in e-governments is growing relatively fast. Hence, it is of significance to provide a summary of the upcoming research studies, more so in cloud computing in e-governments, to act as a guideline for new research studies.

## **RESEARCH METHODOLOGY**

This study conducted a systematic review with the guidance of Kitchenham and Charters (Kitchenham & Charters, 2007) to answer the research questions. The study goes through the planning, execution, and reporting stages of the review while revisiting them back and forth for a thorough examination of the systematic review.

### **Choosing Primary Studies**

The primary studies were selected based on keywords via the search engine or search facility of the journal. The platforms under investigation included IEEE Xplore digital library, Wiley Online, Library, SpringerLink, Google Scholar, ScienceDirect, ACM Digital Library, and Scopus. The exploration was done using the keywords, title, or abstract grounded on each specific platform. The keywords were chosen to enhance the appearance of the study results that would help answer the research questions. The Boolean operators “AND” and “OR” were used where relevant. The search strings used were: (“cloud computing” OR “cloud-computing” OR “cloud service” OR “cloud adoption” OR “cloud implementation”) AND

("e-government"), and ("cloud computing" OR "cloud-computing" OR "cloud service" OR "cloud adoption" OR "cloud implementation") AND ("public service" OR "public sector" OR "public service delivery").

The investigation included any study published from 2010 up to 2020 December. The outcomes were filtered via the inclusion/exclusion measures as presented. The measures enabled the production of outcomes that underwent snowballing from the explanation given (Wohlin, 2014). This study conducted backward and forward snowballing until the inclusion measures were attained.

**Inclusion and Exclusion Measures**

This section describes the inclusion and exclusion measures considered while filtering the study search results for this research. Any literature chosen for this SLR must have given empirical outcomes and should have carried out the study via case research, new technical cloud computing utilization, and commentaries on establishing e-governments through cloud service applications. The research articles should have been peer-reviewed and documented in English. The outcomes from Google Scholar were scrutinized for compliance with the measures as chances could arise for Google Scholar to furnish papers, which are graded lower. The current researched versions were also included in this study. The inclusion and exclusion measures are detailed in Table 1.

Table 1

*Inclusion and exclusion criteria*

The article must have details linked to cloud computing or associated with cloud service technologies in e-government	Articles concentrating on the impact of cloud computing in e-government or public sector
The article must present empirical data linked with the adoption and application of cloud computing in e-government	Grey information like blogs and government documents
The article must be in English, peer-reviewed, and published in a journal or conference proceeding from 2010 to 2020	Non-English articles, outside the year range

**Selection Outcomes**

There were up to 654 studies identified from the initial keyword search on the selected platforms. It was reduced further using the inclusion and exclusion criteria and after removing a lot of duplicate studies. The number of papers that were read in full was 94 papers. The 94 articles were then fully read using the inclusion and exclusion criteria, and

20 papers remained. Applying forward and backward snowballing established eight papers, giving an ultimate figure of 28 papers to be included in this SLR.

### **Quality Assessment**

Evaluation of the quality of the primary research articles was undertaken by following the direction of Kitchenham and Charters (Kitchenham & Charters, 2007). Accordingly, the evaluation was done to extract the relevant articles connected to the research inquiries without any biases and with the validity of the empirical data. The evaluation procedure is grounded on previous research by Hosseini et al. (2017). Five randomly chosen articles were put through the quality evaluation procedure to examine their efficiency. The procedure is as follows:

Step 1: Cloud computing. The article must concentrate on adopting cloud computing or the application of cloud service to a specific, well-mentioned issue.

Step 2: Context. The required context must be given for the study's aim and outcomes. It permits good result interpretation.

Step 3: Cloud computing application. The article must possess the right information for a perfect exhibition concerning the utilization of innovation for a particular problem. It aims to answer RQ1 and RQ2.

Step 4: E-government context. The article must furnish information about the e-government problem to attempt and answer RQ3.

Step 5: Cloud computing performance. It seeks to evaluate cloud service performance in e-government. It will help bring benefits for cloud services.

Step 6: Data gathering. Information about models/frameworks, data collection, measurement, and presentation must be included for precision.

The checklist mentioned above for quality estimation was utilized for every other primary article chosen.

### **Data Extraction**

Every paper that successfully went through quality evaluation underwent data extraction to examine the fullness of data to validate the accuracy of the details gathered in the articles. Data extraction was first done on the first five articles before expansion to incorporate all the articles that successfully underwent the quality evaluation stage. Then, extraction, grouping, and caching of the information were done using excel spreadsheets. The groupings entailed: context details or theme (detailing purpose of the study), methodology (qualitative or quantitative data), level of implementation (organizational or individual), factors (significant elements for adoption), framework or model (information system

models), and data analysis methods (PLS/SEM). Figure 1 exhibits the articles chosen at every phase of the procedure and the rate of every article selected from the keywords utilized in the search to the ultimate choice of the primary articles.

### ANALYSIS AND FINDINGS

The details were compiled within the qualitative and quantitative data groups to answer the research questions. The study also did a meta-analysis of the articles that went to the final extraction procedure. The results are subsequently discussed.

#### Publication Rate

The concept of cloud computing was started as early as 1961 by John McCarthy, but its usage by organizations only began in 2009 (Attaran & Woods, 2018). Hence, this study finds no final primary studies with empirical results published before 2015. It shows that the idea is not fully saturated for e-governments. Figure 2 shows the number of primary studies published every year.

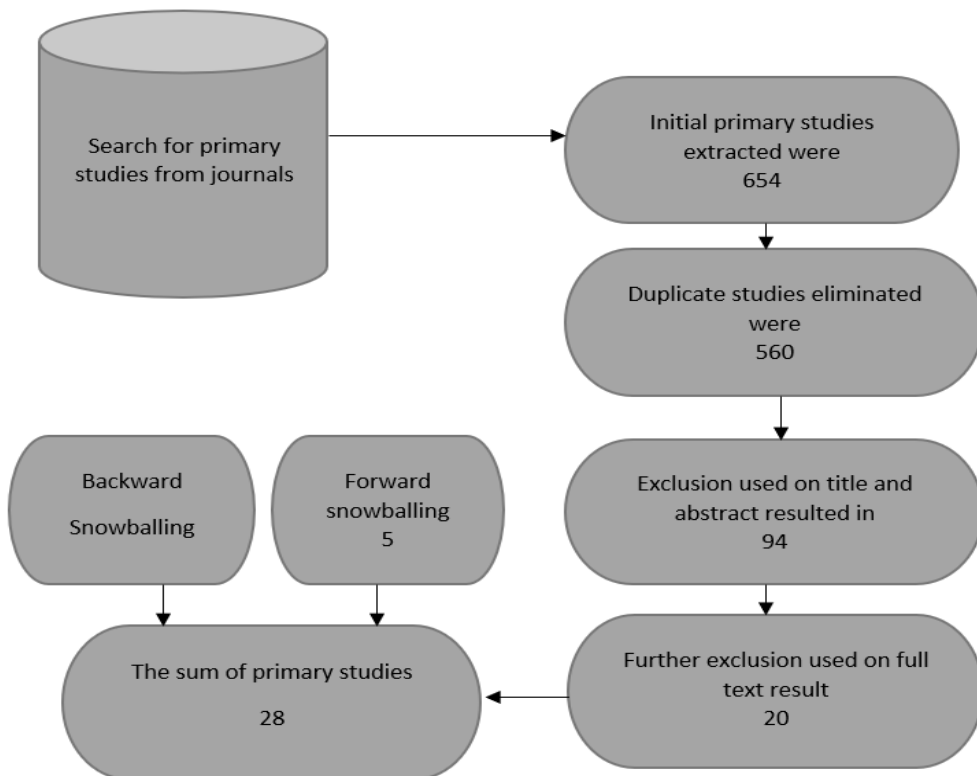


Figure 1. Extraction of the articles through the process

As can be seen from Figure 2, the trend is not consistent, but there were more publications in 2017 compared to all the other years. This study forecasts that there are still many studies coming up on cloud computing in e-governments. The number of publications in 2019 was very low compared to the other years.

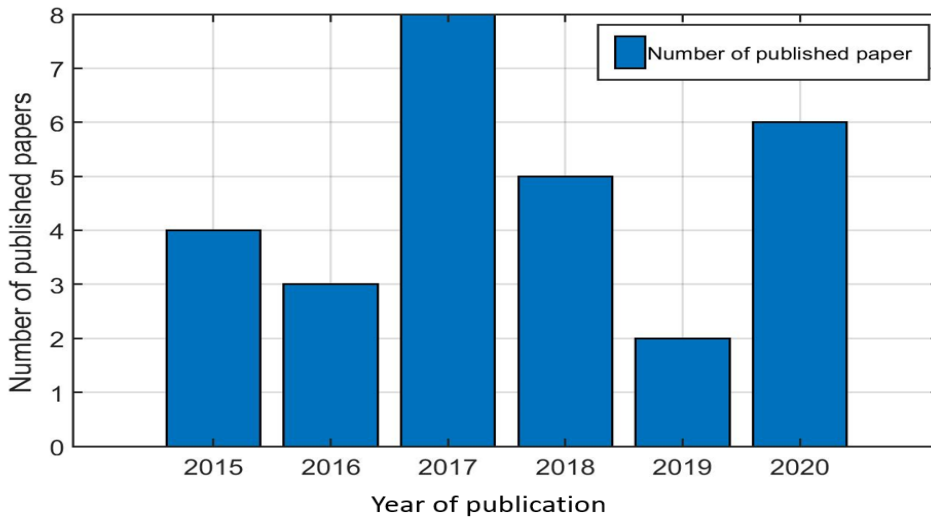


Figure 2. Primary studies published overtime

However, from Figure 2, 2020 has shown an upward trend in the usage of cloud services in e-governments compared to 2019, which received only a few studies. Information and communication technologies still play a role in good governance and public service delivery; hence, the researchers anticipate seeing more studies as years go by.

### The Effect of Keyword Counts

To summarize the common themes in the chosen primary studies, 28 articles were analyzed. Figure 3 shows the word cloud from the 28 studies utilized in this paper.

Furthermore, Table 2 exhibits the number of times specific words were seen in the primary studies.

The analysis of keywords was performed across all the 28 primary studies to summarize the common themes in the primary studies. Table 2 exhibits the number of times specific words appeared in all the primary articles. From Table 2, excluding the keywords that were chosen for this study, which were “cloud computing” and “e-government,” the third keyword that appears most frequently is “adoption,” followed by “information,” and then “model.” It shows an interesting trend in the adoption of cloud computing. Adoption is the



word mentioned most, and in relation to Figure 2, more adoption studies were conducted in 2018. A fluctuation of studies conducted yearly has been observed. Moreover, 2020 has seen a tremendous rise in the adoption of cloud services. Adoption is further highlighted in the discussion section.

Every primary article extracted was read in full, and the qualitative and quantitative details were captured, along with the data analysis technique used, the themes, factors, and the respondents for the study (Appendix A).

All the studies focused on the adoption or usage and factors for the adoption of cloud computing in e-governments. Moreover, some studies mentioned the benefits of the cloud in e-governments, the cloud service models that can be used, as well as the deployment models. Few studies also highlighted the barriers to cloud adoption. Within the extracted papers, some authors also highlighted the benefits of cloud computing in e-governments. This study also extracted the methodologies that every paper has adopted. Figure 3 shows the distribution of the methodologies adopted by the different studies.

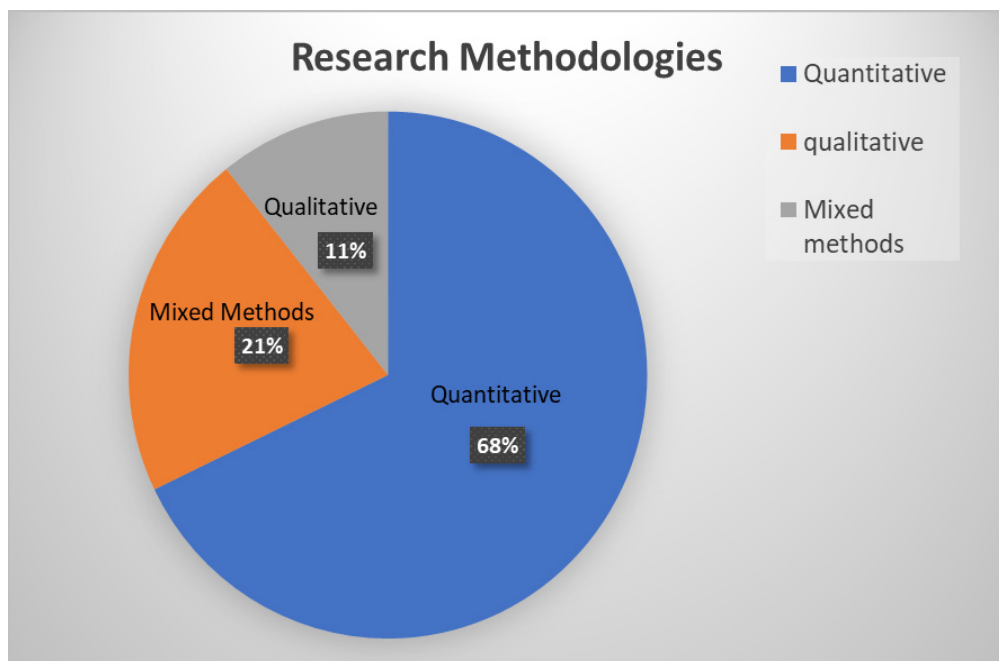


Figure 4. Research methodologies used in the primary studies

According to Figure 2, most studies have used the quantitative method, while very few studies have adopted the mixed method. The information was extracted from the primary studies, and it details the methods used, as shown in Appendix A. While most studies have highlighted the factors for the adoption of cloud computing with models/theories, this



research still highlights that TOE is the most used model for studying cloud adoption in e-governments (13 studies), while DOI (12 studies) follows closely (Appendix A). TOE is a model established to examine technology adoption at the organizational level (Tornatzky et al., 1990). Accordingly, most studies use TOE to study adoption behavior and a holistic approach (Al Hadwer et al., 2021; Alkhalil et al., 2017; Awa et al., 2017). For governments to deliver online services, TOE is appropriate as it helps to investigate the adoption factors for cloud computing in governments (Hsu et al., 2014). It is also a holistic instrument for organization-level studies.

Similarly, DOI has been used by most studies for the adoption and diffusion of innovations, as shown in this study (Appendix A). According to Rogers, this theory can predict the decisions of people in the adoption of new technologies through the examination of patterns and structure (Rogers, 2010). The theory examines adoption through the features of innovation. Furthermore, the model points to the need for exposure to the innovation when the adoption process begins. DOI explains the mechanism of adoption and can predict if a new invention will succeed through the attributes of that innovation (Mohammed et al., 2017a). Most studies have not used the HOT fit model for assessing the human factors in the adoption of cloud computing. Only one study incorporated HOT fit to study the acceptance of cloud in public services. The HOT model highlights the impact of human and organizational elements (Yusof et al., 2008). Accordingly, aligning organization, technology, and humans are significant, as it is a starting point in IT implementation and investment.

Furthermore, the study argues that organizations need to prepare their staff to adopt innovations or any organizational changes (Setiorini et al., 2021). HOT is flexible and fits various fields, stakeholders' perspectives and evaluation systems' life cycles (Yadegaridehkordi et al., 2020). Other researchers have found minimal utilization of HOT (Sallehudin et al., 2019; Sharma et al., 2020). Nevertheless, some studies have merged HOT with other models to study adoption (Alharbi et al., 2016; Lynn et al., 2020). This research found a few studies (6 studies) that have concentrated on individual elements for the adoption of cloud computing. It shows the need to look at the human element in adoption studies. Human employees, for instance, play a great role in internal issues or opportunities related to information technology.

## **DISCUSSION**

The initial keyword searches exhibited that several papers are related to cloud computing. Organizations have adopted cloud computing since 2009; however, it has not yet reached maturity. Most of the papers have highlighted the factors for consideration while bringing the benefits of the technology to governments. The extracted papers have employed different models to extract elements that decision-makers can consider in governments before adopting cloud services.

The studies also highlight how issues like privacy, security, data, infrastructure, cost, and performance can be solved by using cloud computing. It depends on the government's choice to adopt cloud computing. Infrastructure issues can be solved as cloud computing offers reduced costs on the infrastructure acquired and used with remote accessibility. For instance, a study mentions that cloud computing SaaS can improve IT infrastructure costs with fewer management concerns (Hadi & Omar, 2021).

Cloud computing has been highlighted to provide almost readily available hardware that requires no prior capital (Avram, 2014). Besides, several promising upcoming start-ups like Jungle Disk, Gigavox, SmugMug became possible with investments in information technology with a lesser order of magnitude. As such, a cloud service is an adaptive infrastructure that is possible to be shared by various clients, utilizing it in different ways. The flexibility of the infrastructure permits the balancing of computing loads even with many users joining the system. It is an expansion in economies of scale.

RQ1: What is the research area in focus in cloud computing e-government?

It is significant to note that this systematic literature review specifically focuses on adopting cloud services in e-governments but not in other fields like healthcare, manufacturing, or retail. Hence, during the procedure of extracting the primary studies, other fields of research emerged in the literature. The fields also discussed cloud computing in their way; however, the extraction process was mainly on empirical articles that concentrated on e-governments or the public sector. The benefits of cloud services are mentioned when looking at the growth of publications in the public sector or e-governments. It could be because it needs lower infrastructure costs while performing well in ultra-large-scale computing, flexibility, scalability, on-demand services, and virtualization (Li et al., 2021). Therefore, it has become an efficient solution to e-government development issues like rising IT costs. According to the studies extracted, the focus areas were as follows:

Organizational models that will help in adopting cloud services (Mohammed et al., 2017b; Salam & Ali, 2020; Shafique et al., 2017). They specify the determinants to be considered for cloud adoption. Adoption of organizational innovation is key as it improves the productivity of an organization, further enhancing economic growth while lowering inequality (Ali et al., 2018b; Damanpour et al., 2018; park & Choi, 2019). These studies focused on the organizational factors that are significant for adopting cloud services in e-governments. According to a study, the organizational adoption procedure is complex and challenging (Wisdom et al., 2014). Adoption starts from an organization's initial awareness and examination of the innovation. Successful adoption is later seen when the innovation is accepted and integrated into the firm, and individuals continue to use the technology for some time (Hameed et al., 2012).

Behavioral models examine the individual behavior towards the adoption of cloud computing (Alkhwaldi et al., 2017; Lian, 2015; Sivathanu, 2018). It brings out the role of humans in the adoption of e-government cloud services. Employees of an organization play a role in internal issues or opportunities in an organization (Sharma et al., 2020). In adopting innovations, the study points out that apart from the firm's decision to pursue adoption, the staff's acceptance and initiation of their processes are also significant (Wisdom et al., 2014). It is because individuals have difficulty deciding the right innovations for solving specific issues or making adoption decisions. Besides, employee resistance to information technology can be a barrier to innovation adoption (Sharma et al., 2020). Therefore, individual characteristics can provide a comprehensive view of the adoption of cloud services (Ali & Osmanaj, 2020). However, there are not many studies focusing on the individual level of cloud adoption (AlKharusi & Al-Badi, 2016).

A framework for cloud adoption evaluating the procedure and factors for adoption was discussed in a study (Junior et al., 2020; Shukur et al., 2018). From this study, it was seen that very few studies adopted a framework. Frameworks allow organizations to follow policies, standards, and guidelines (Chang et al., 2016). Moreover, they help organizations overcome technical and organizational challenges. For instance, a study had extended the technology acceptance model and TOE for cloud adoption (Gangwar et al., 2015). While for secure cloud adoption, a framework was also developed to protect data (Chang & Ramachandran, 2015)

This study also found some articles from developed countries (Ali et al., 2015; Polyviou & Pouloudi, 2015), with the rest concentrating on developing countries. Accordingly, there have been varying studies on cloud adoption in different parts of the world, with a higher percentage (50%) for developing nations compared to lower than 155 for developed nations (Vu et al., 2020). It may be one reason for the higher number of articles from developing nations. Besides, adoption of cloud services is mentioned to be slow for public sectors, with most being at the initial stages (Kuiper et al., 2014; Nanos et al., 2019). Therefore, the slowness in developing nations is due to the lack of a favorable environment for the utilization of cloud services (Vu et al., 2020). However, current governments are following the adoption trend of cloud services (Mohammed et al., 2020).

RQ2: How is cloud computing used to improve service delivery in e-governments (benefits)?

Cloud computing with its models has a lot to offer for governments and the public sector. Cloud computing is attractive because it eliminates the requirements for clients to plan, allowing utilization of resources only when in demand. Cloud computing promises to furnish every functionality of the existing information technology services model while lowering the upfront costs of computing that make organizations shy away from utilizing

cutting-edge IT services. Cloud pulls resources together like hardware, development platforms, and/or services. It can be exploited via a pay-per-use model through customized service level agreements. Cloud computing hence provides the ability of seamless access to resources. Many governments struggle to manage citizen data, improve service delivery, and enlarge their communication links through e-government. There are issues like data duplication, fragmentation, traditional infrastructure, more costs on modernization, poor performance, security, and privacy. A study agrees that cloud services can help enhance the quality of services provided to citizens from e-government solutions, manage huge data, and offer flexibility and freedom (Ali et al., 2014; Mohammed & Ibrahim, 2015b).

As mentioned in this article, utilizing cloud computing can help handle the issues mentioned above, but the bottom line is adopting the technology for use.

Based on the few issues reviewed, this study mentions how cloud computing can help benefit e-governments in various ways.

- Cost reduction- cloud computing is anticipated to reduce the cost of acquiring physical hardware, hence saving financial resources for organizations (Ali et al., 2015; Lian, 2015; Liang et al., 2017; Shukur et al., 2018). Accordingly, cost reduction is a promise achieved by adopting cloud services in organizations with a positive influence (Aziz et al., 2013; Kuiper et al., 2014; Mohammed & Ibrahim, 2015a; Mohammed & Ibrahim, 2015b). Hence, cloud adoption can lower maintenance and infrastructure costs while enhancing the availability of services. It is possible by using an outsourcing model that permits the renting of resources and paying only for the services used (Alkhater et al., 2014). Any upgrades and maintenance are passed to the third party for responsibility and saving on costs.
- Lower IT infrastructure- this means that the cost of acquiring the hardware will be low (Ali et al., 2015). This factor is linked to the first factor on cost reduction. Accordingly, lowering costs lowers infrastructure costs (Mohammed & Ibrahim, 2015a).
- Provide improved services- cloud computing will help lower risks and enable accessibility of data anytime and anywhere (Ali et al., 2015; Lian, 2015; Shukur et al., 2018). In turn, this will lead to better management of services and improved efficiency. When government services go online, it enhances the quality of services in the areas of accessibility, time, and content (Dash & Pani, 2016). With cloud computing, the increase of user loads only needs the addition and subtraction of network load rather than the addition of hardware (Mohammed & Ibrahim, 2015a).
- Remote accessibility- cloud computing will permit access to rural and remote areas, which increases audience reach (Ali et al., 2015; Liang et al., 2017; Shukur et al., 2018). It also enables sharing of information. According to a study, since cloud

services are web and internet-based, it brings accessibility via various internet-enabled gadgets like tablets, laptops, and traditional computers, among others (Mohammed & Ibrahim, 2015a; Tweneboah-Koduah et al., 2014).

- Backup and disaster recovery- cloud computing will enable functions to operate even amidst unexpected eventualities (Ali et al., 2015; Liang et al., 2017). The backup plan will help provide recovery when such incidents occur. Accordingly, a study adds that backup and restores done on cloud services are easier than those managed on physical storage (Dash & Pani, 2016; Mohammed & Ibrahim, 2015b). Hence, the cloud process is simpler as compared to the traditional process.

RQ3: What factors, methods, levels of implementation, data analysis techniques, and methodologies are available, and what is the gap for cloud computing in e-governments?

All the articles extracted in this study have highlighted significant factors for cloud adoption. It refers to the factors contributing to the successful adoption of cloud services in governments. According to most studies, the elements related to the adoption of cloud services fall into three main categories of technological, organizational, and environmental levels (Ali et al., 2015; Ji & Liang, 2016; Liang et al., 2017; Polyviou & Pouloudi, 2015; Shafique et al., 2017). However, some studies evaluated the factors based on behavioral factors like performance expectancy, social influence, facilitating conditions, perceived risk, trust, and security (Alrashed & Alotaibi, 2017; Lian, 2015; Salam & Ali, 2020; Sivathanu, 2018). Other researchers considered different elements. For instance, Wahsh and Dhillon (2015a) grouped the factors in terms of technical and non-technical elements, where the technical entails elements like security, trust, compatibility, and complexity, and non-technical elements include top management support, IT knowledge, relative advantage, and technological readiness. Additionally, Wu et al. (2016) explained determinants in the form of technological, business, and management factors. One study explores the adoption of cloud from a framework (Junior et al., 2020). Shukur et al. (2018) explore the factors from a framework and highlight the significance of technological, organizational, and environmental elements. Accordingly, other research has also pointed out the significance of environmental, organizational, and technological factors as key factors in the adoption of cloud services (Kuiper et al., 2014). Other researchers have also agreed that organizational, technical, and environmental factors have an impact on the adoption of cloud services (Al Hadwer et al., 2021; Albugmi et al., 2016; Ji & Liang, 2016; Scholtz et al., 2016).

On the level of implementation, the articles extracted for this study fell into two main levels: organizational and individual. Accordingly, 22 articles concentrated on the organizational perspective of adoption, while only six articles considered adoption from the individual perspective (Appendix A). There were no studies that merged both levels. Adoption is a decision by a person to utilize innovation for the first time, impacted by

attributes of the innovation, individual elements, and contextual factors (Sun & Jeyaraj, 2013). Accordingly, the adoption of innovations affects both the organizations as well as the individuals (Hameed et al., 2012; Wisdom et al., 2014). Organizations are deemed complex, while individuals have weights and may fail to choose the right innovation (Wisdom et al., 2014). Different researchers have employed several data analysis techniques. These include Partial Least Squares Structural Equation Modelling (PLS-SEM), factor analysis, Statistical Packages for Social Sciences (SPSS), parsimonious model, MATLAB, Principal component analysis with varimax rotation, ATLAS.ti, Manual & Leximancer visual text tool, and logistic regression. However, PLS-SEM was the most employed analysis tool, as shown in Appendix A. According to a study, PLS-SEM is mostly preferred as it attains high extents of statistical power while exhibiting improved convergence behavior (Hair Jr et al., 2014). In addition, it is good for complex models that may have many relationships (Hwang et al., 2016). Moreover, because most studies were predicting models, PLS-SEM suits the prediction of theories (Hair et al., 2013).

Methodologies have also been utilized in the extracted studies. This study found that several researchers used the quantitative method with surveys for their data collection. At the same time, the qualitative and mixed methods have not been largely used in cloud adoption in e-government specifically (Figure 4). Only three studies employed mixed methods (Al Mudawi et al., 2019; Maluleka & Ruxwana, 2016; Oguntala et al., 2017). Data gathering through surveys and analysis using the SEM method have been the most employed methods. The quantitative method has been relevant in most studies in this article, and a study mentions that this approach is more relevant when studying adoption issues at the organizational level (Choudrie & Dwivedi, 2005). It could be a reason why most studies were quantitative.

## CONCLUSIONS

This study started with the motivation to understand cloud computing in e-governments and how cloud computing can be adopted to support government services. It brought the opportunity to first perform a systematic review on cloud computing in e-governments and know the progress in adoption. This study, in general, analyzed 654 studies from various secondary materials. The articles were narrowed down to 94, and finally to 28 relevant articles for this research. Our analysis reveals that very few empirical studies exist on the adoption of cloud services. The organizational adoption of cloud computing started around 2011, but the researchers could only find the first empirical study from 2015. Therefore, the study sought to explore significant factors for cloud adoption to implement e-governments. While most of our papers are specifically on adoption factors with empirical support, the results reveal that most of these studies were conducted in developing countries. The study also reveals that most studies have concentrated on quantitative methods using

surveys, with only a few using qualitative methods with case studies and semi-structured interviews. This study also notes that the concentration on identifying factors has mostly been done using quantitative procedures like structural equation modeling and regression analysis. The findings indicate that researchers have mostly resorted to employing the TOE (13 studies) and DOI (12 studies) frameworks for studying the adoption factors. Nevertheless, the researchers have also seen studies using UTAUT and TAM. Some studies have equally combined the models for better understanding. Technological, environmental, and organizational factors have been the most cited elements in research. Recent studies have also emphasized the role of trust in cloud services, as this will influence willingness for adoption.

In developing countries, there is significant growth in emerging technologies. The issues mentioned include IT infrastructure, cost reductions, backup and recovery, availability, and accessibility. For instance, cloud adoption for e-invoices in Taiwan mentions access, availability of infrastructure, security, safety mechanisms, privacy, and data confidentiality, among issues hindering adoption. The utilization of cloud services in governments can help handle such issues and bring improved service delivery. Considering the factors identified in this study can help developing nations adopt cloud services.

## **SUGGESTIONS FOR FUTURE WORK**

This study has examined how cloud computing can contribute to e-government issues. The initial keyword searches for this study show that cloud computing has so many possible solutions for healthcare, governments, manufacturing, and retail. This study, however, concentrated on electronic governments. There are many applications for cloud computing in e-governments; however, in a decentralized structure without trust, the issues in e-governments may not be solved. Furthermore, cloud computing has evolved with various service models (IaaS, PaaS, SaaS), and the adoption of a good service will help handle infrastructure and cost issues in e-governments. From the outcomes of this survey and the study observations, this article presents the following research directions for cloud computing in e-governments that are worth considering for further evaluation.

**Trust in Cloud computing:** Trust has been mentioned as an issue in cloud computing, and it is an area that needs much improvement. This study shows that very few studies have considered the element of trust in the adoption of cloud computing in e-governments. Little has been discussed about this factor concerning decisions to adopt cloud services (Alrashed & Alotaibi, 2017). Trust can act as a moderator for the adoption of cloud services. Governments are least trusted in storing confidential and classified details on the internet. There is difficulty controlling sensitive information as a third party provides the services. Trust is related to levels of confidence (Sivapragash et al., 2019; Sivapragash et al., 2012). While there has been a good amount of research evaluating determinants for

cloud computing, very few studies have evaluated the causal elements. Thus, there is a need for future researchers to consider trust as the main factor, moderator, and/or mediator to fill this gap in the literature.

**Human and social factors for adoption:** As mentioned earlier, and from this study, very few researchers have considered the element of humans in the adoption of cloud computing (Alkhwaldi et al., 2017; Lagzian et al., 2018). Furthermore, only one study mentions the social factor as an element for cloud adoption (Alkhwaldi et al., 2017). Hence, there is a need to explore the human and social elements for cloud adoption in governments.

**Behavioral models for adoption:** This study also discovered that only a few researchers did empirical studies on behavioral models for the adoption of cloud services in e-governments (Alrashed & Alotaibi, 2017; Sivathanu, 2018). Hence, research needs to consider these models for government adoption studies.

This study found that most researchers have done quantitative studies. This methodology is very predominant in adoption studies. However, there is a need to consider using mixed methods for research studies related to cloud adoption in e-governments. Information system researchers have promoted the utilization of mixed methods for stronger validity and reliable outcomes (Ali & Osmanaj, 2020).

The SLR shows minimal studies in the domain of cloud computing in e-governments. However, more studies rose in 2020 as compared to 2019. It means there is a need to further grow the research in cloud computing in governments and public sectors.

This study also found frameworks with empirical results. However, very few studies utilized this approach. Frameworks are good for a holistic view at both organizational and individual levels. This study did not find frameworks from an individual perspective with empirical results. The frameworks adopted were from the organizational perspective. It is another worth area consideration. Frameworks with empirical studies can strengthen findings and broaden the application of cloud computing in various contexts.

## ACKNOWLEDGEMENT

The authors would like to express sincere appreciation to everyone who helped this study along the way by providing advice and assistance.

## REFERENCES

- Al-Rawahna, A. S. M., Hung, C. W., & Chen, S. C. (2018). Readiness of government organizations for cloud-computing age: An empirical evidence from Jordan. *Journal of Business and Management Sciences*, 6(4), 152-162. <https://doi.org/10.12691/jbms-6-4-3>
- Al Hadwer, A., Tavana, M., Gillis, D., & Rezanian, D. (2021). A systematic review of organizational factors impacting cloud-based technology adoption using technology-organization-environment framework. *Internet of Things*, 15, Article 100407. <https://doi.org/10.1016/j.iot.2021.100407>



- Al Mudawi, N., Beloff, N., & White, M. (2019). Cloud computing in government organizations-towards a new comprehensive model. In *2019 IEEE SmartWorld, Ubiquitous Intelligence & Computing, Advanced & Trusted Computing, Scalable Computing & Communications, Cloud & Big Data Computing, Internet of People and Smart City Innovation (SmartWorld/SCALCOM/UIC/ATC/CBDCom/IOP/SCI)* (pp. 1473-1479). IEEE Publishing. <https://doi.org/10.1109/SmartWorld-UIC-ATC-SCALCOM-IOP-SCI.2019.00266>
- Albugmi, A., Walters, R., & Wills, G. (2016). A framework for cloud computing adoption by Saudi government overseas agencies. In *2016 Fifth International Conference on Future Generation Communication Technologies (FGCT)* (pp. 1-5). IEEE Publishing. <https://doi.org/10.1109/FGCT.2016.7605063>
- Alharbi, F., Atkins, A., & Stanier, C. (2016). Understanding the determinants of cloud computing adoption in Saudi healthcare organisations. *Complex & Intelligent Systems*, 2(3), 155-171. <https://doi.org/10.1007/s40747-016-0021-9>
- Ali, K. E., Mazen, S. A., & Hassanein, E. (2018a). A proposed hybrid model for adopting cloud computing in e-government. *Future Computing and Informatics Journal*, 3(2), 286-295. <https://doi.org/10.1016/j.fcij.2018.09.001>
- Ali, K. E., Mazen, S. A., & Hassanein, E. E. (2018b). Assessment of cloud computing adoption models in e-government environment. *International Journal of Computational Intelligence Studies*, 7(1), 67-92. <https://doi.org/10.1504/IJCISTUDIES.2018.090168>
- Ali, O., & Osmanaj, V. (2020). The role of government regulations in the adoption of cloud computing: A case study of local government. *Computer Law & Security Review*, 36, Article 105396. <https://doi.org/10.1016/j.clsr.2020.105396>
- Ali, O., Soar, J., & Yong, J. (2014). Impact of cloud computing technology on e-government. In *International conference on information and software technologies* (pp. 272-290). Springer. [https://doi.org/10.1007/978-3-319-11958-8\\_22](https://doi.org/10.1007/978-3-319-11958-8_22)
- Ali, O., Soar, J., Yong, J., McClymont, H., & Angus, D. (2015). Collaborative cloud computing adoption in Australian regional municipal government: An exploratory study. In *2015 IEEE 19th International Conference on Computer Supported Cooperative Work in Design (CSCWD)* (pp. 540-548). IEEE Publishing. <https://doi.org/10.1109/CSCWD.2015.7231017>
- Alismailli, S. Z., Li, M., Shen, J., Huang, P., He, Q., & Zhan, W. (2020). Organisational-level assessment of cloud computing adoption: Evidence from the Australian SMEs. *Journal of Global Information Management (JGIM)*, 28(2), 73-89. <https://doi.org/10.4018/JGIM.2020040104>
- Alkhalil, A., Sahandi, R., & John, D. (2017). An exploration of the determinants for decision to migrate existing resources to cloud computing using an integrated TOE-DOI model. *Journal of Cloud Computing*, 6(1), 1-20. <https://doi.org/10.1186/s13677-016-0072-x>
- AlKharusi, M. H., & Al-Badi, A. H. (2016). IT personnel perspective of the slow adoption of cloud computing in public sector: Case study in Oman. In *2016 3rd MEC International Conference on Big Data and Smart City (ICBDSC)* (pp. 1-8). IEEE Publishing. <https://doi.org/10.1109/ICBDSC.2016.7460364>
- Alkhatir, N., Wills, G., & Walters, R. (2014). Factors influencing an organisation's intention to adopt cloud computing in Saudi Arabia. In *2014 IEEE 6th international conference on cloud computing technology and science* (pp. 1040-1044). IEEE Publishing. <https://doi.org/10.1109/CloudCom.2014.95>

- Alkhwaldi, A., Kamala, M., & Qahwaji, R. (2017). From e-government to cloud-government: Challenges of Jordanian citizens' acceptance for public services. In *2017 12th International Conference for Internet Technology and Secured Transactions (ICITST)* (pp. 298-304). IEEE Publishing. <https://doi.org/10.23919/ICITST.2017.8356405>
- Alrashed, M. A., & Alotaibi, M. B. (2017). The role of trust in the acceptance of government cloud: An empirical study. *International Journal of Technology Diffusion (IJTD)*, *8*(3), 1-19. <https://doi.org/10.4018/IJTD.2017070101>
- Anuradha, M., Jayasankar, T., Prakash, N., Sikkandar, M. Y., Hemalakshmi, G., Bharatiraja, C., & Britto, A. S. F. (2021). IoT enabled cancer prediction system to enhance the authentication and security using cloud computing. *Microprocessors and Microsystems*, *80*, Article 103301. <https://doi.org/10.1016/j.micpro.2020.103301>
- Attaran, M., & Woods, J. (2018). Cloud computing technology: A viable option for small and medium-sized businesses. *Journal of Strategic Innovation & Sustainability*, *13*(2), 94-106.
- Avram, M. G. (2014). Advantages and challenges of adopting cloud computing from an enterprise perspective. *Procedia Technology*, *12*, 529-534. <https://doi.org/10.1016/j.protcy.2013.12.525>
- Awa, H. O., Ojiabo, O. U., & Orokor, L. E. (2017). Integrated technology-organization-environment (TOE) taxonomies for technology adoption. *Journal of Enterprise Information Management*, *30*(6), 893-921.
- Aziz, M. A., Abawajy, J., & Chowdhury, M. (2013). The challenges of cloud technology adoption in e-government. In *2013 International Conference on Advanced Computer Science Applications and Technologies* (pp. 470-474). IEEE Publishing. <https://doi.org/10.1109/ACSAT.2013.98>
- Bayramusta, M., & Nasir, V. A. (2016). A fad or future of IT?: A comprehensive literature review on the cloud computing research. *International Journal of Information Management*, *36*(4), 635-644. <https://doi.org/10.1016/j.ijinfomgt.2016.04.006>
- Chang, V., Kuo, Y. H., & Ramachandran, M. (2016). Cloud computing adoption framework: A security framework for business clouds. *Future Generation Computer Systems*, *57*, 24-41. <https://doi.org/10.1016/j.future.2015.09.031>
- Chang, V., & Ramachandran, M. (2015). Towards achieving data security with the cloud computing adoption framework. *IEEE Transactions on Services Computing*, *9*(1), 138-151. <https://doi.org/10.1109/TSC.2015.2491281>
- Choudrie, J., & Dwivedi, Y. K. (2005). Investigating the research approaches for examining technology adoption issues. *Journal of Research Practice*, *1*(1), D1-D1.
- Damanpour, F., Sanchez-Henriquez, F., & Chiu, H. H. (2018). Internal and external sources and the adoption of innovations in organizations. *British Journal of Management*, *29*(4), 712-730. <https://doi.org/10.1111/1467-8551.12296>
- Dash, S., & Pani, S. K. (2016). E-Governance paradigm using cloud infrastructure: Benefits and challenges. *Procedia Computer Science*, *85*, 843-855. <https://doi.org/10.1016/j.procs.2016.05.274>
- Gangwar, H., Date, H., & Ramaswamy, R. (2015). Developing a cloud-computing adoption framework. *Global Business Review*, *16*(4), 632-651. <https://doi.org/10.1177/0972150915581108>

- Garad, A., & Santoso, J. (2017). Analysis and design of cloud computing for e-government in Yemen. *International Journal of Computer Engineering and Information Technology*, 9(8), 166.
- Hadi, H., & Omar, M. (2021). Investigating the determinants of CC-SaaS adoption in Iraqi's public organisations from the perspective of IT professionals. *International Journal of Engineering and Technical Research*, 14, 130-143.
- Hair, J. F., Ringle, C. M., & Sarstedt, M. (2013). Partial least squares structural equation modeling: Rigorous applications, better results and higher acceptance. *Long Range Planning*, 46(1-2), 1-12. <https://doi.org/10.1016/j.lrp.2013.01.001>
- Hair Jr, J. F., Sarstedt, M., Hopkins, L., & Kuppelwieser, V. G. (2014). Partial least squares structural equation modeling (PLS-SEM): An emerging tool in business research. *European Business Review*, 26(2), 106-121. <https://doi.org/10.1108/EBR-10-2013-0128>
- Hameed, M. A., Counsell, S., & Swift, S. (2012). A conceptual model for the process of IT innovation adoption in organizations. *Journal of Engineering and Technology Management*, 29(3), 358-390. <https://doi.org/10.1016/j.jengtecman.2012.03.007>
- Hosseini, S., Turhan, B., & Gunarathna, D. (2017). A systematic literature review and meta-analysis on cross project defect prediction. *IEEE Transactions on Software Engineering*, 45(2), 111-147. <https://doi.org/10.1109/TSE.2017.2770124>
- Hsu, P. F., Ray, S., & Li-Hsieh, Y. Y. (2014). Examining cloud computing adoption intention, pricing mechanism, and deployment model. *International Journal of Information Management*, 34(4), 474-488. <https://doi.org/10.1016/j.ijinfomgt.2014.04.006>
- Hwang, Y., Al-Arabi, M., Shin, D. H., & Lee, Y. (2016). Understanding information proactiveness and the content management system adoption in pre-implementation stage. *Computers in Human Behavior*, 64, 515-523. <https://doi.org/10.1016/j.chb.2016.07.025>
- Ji, H., & Liang, Y. (2016). Exploring the determinants affecting e-government cloud adoption in China. *International Journal of Business and Management*, 11(4), 81-90. <https://doi.org/10.5539/ijbm.v11n4p81>
- Junior, L. P., Cunha, M. A., Janssen, M., & Matheus, R. (2020). Towards a framework for cloud computing use by governments: Leaders, followers and laggards. In *The 21st Annual International Conference on Digital Government Research* (pp. 155-163). ACM Publishing. <https://doi.org/10.1145/3396956.3396989>
- Kandil, A. M. N. A., Ragheb, M. A., Ragab, A. A., & Farouk, M. (2018). Examining the effect of TOE model on cloud computing adoption in Egypt. *The Business & Management Review*, 9(4), 113-123.
- Kitchenham, B., & Charters, S. (2007). Guidelines for performing systematic literature reviews in software engineering (Technical Report EBSE). Keele University.
- Kuiper, E., Van Dam, F., Reiter, A., & Janssen, M. (2014). Factors influencing the adoption of and business case for cloud computing in the public sector. In *eChallenges e-2014 Conference Proceedings* (pp. 1-10). IEEE Publishing.
- Kyriakou, N., Euripides, L., & Paraskevi, D. (2020). Factors affecting cloud storage adoption by Greek municipalities. In *Proceedings of the 13th International Conference on Theory and Practice of Electronic Governance* (pp. 244-253). ACM Publishing. <https://doi.org/10.1145/3428502.3428537>

- Lagzian, M., Hemmat, Z., Rashki, M., & Aghadavood, S. (2018). *An investigation on effective factors of acceptance of cloud computing in iranian public services* (No. 279). EasyChair.
- Li, G., Zhou, M., Feng, Z., Li, M., & Jiang, H. (2021). Research on key influencing factors of e-government cloud service satisfaction. *Wireless Personal Communications*, 1-19. <https://doi.org/10.1007/s11277-021-08567-0>
- Lian, J. W. (2015). Critical factors for cloud based e-invoice service adoption in Taiwan: An empirical study. *International Journal of Information Management*, 35(1), 98-109. <https://doi.org/10.1016/j.ijinfomgt.2014.10.005>
- Liang, Y., & Qi, G. (2017). The determinants of e-government cloud adoption: Multi-case analysis of China. *International Journal of Networking and Virtual Organisations*, 17(2-3), 184-201. <https://doi.org/10.1504/IJNVO.2017.10004061>
- Liang, Y., Qi, G., Wei, K., & Chen, J. (2017). Exploring the determinant and influence mechanism of e-Government cloud adoption in government agencies in China. *Government Information Quarterly*, 34(3), 481-495. <https://doi.org/10.1016/j.giq.2017.06.002>
- Liang, Y., Qi, G., Zhang, X., & Li, G. (2019). The effects of e-Government cloud assimilation on public value creation: An empirical study of China. *Government Information Quarterly*, 36(4), Article 101397. <https://doi.org/10.1016/j.giq.2019.101397>
- Lynn, T., Fox, G., Gourinovitch, A., & Rosati, P. (2020). Understanding the determinants and future challenges of cloud computing adoption for high performance computing. *Future Internet*, 12(8), Article 135. <https://doi.org/10.3390/fi12080135>
- Maluleka, S. M., & Ruxwana, N. (2016). Cloud computing as an alternative solution for South African public sector: A case for department of social development. In *New Advances in Information Systems and Technologies* (pp. 481-491). Springer. [https://doi.org/10.1007/978-3-319-31232-3\\_45](https://doi.org/10.1007/978-3-319-31232-3_45)
- Mohammed, F., & Ibrahim, O. (2015a). Models of adopting cloud computing in the e-government context: A review. *Jurnal Teknologi*, 73(2), 51-59. <https://doi.org/10.11113/jt.v73.4193>
- Mohammed, F., & Ibrahim, O. B. (2015b). Drivers of cloud computing adoption for e-government services implementation. *International Journal of Distributed Systems and Technologies (IJ DST)*, 6(1), 1-14. <https://doi.org/10.4018/ijdst.2015010101>
- Mohammed, F., Ibrahim, O., & Ithnin, N. (2016). Factors influencing cloud computing adoption for e-government implementation in developing countries: Instrument development. *Journal of Systems and Information Technology*, 18(3), 297-327. <https://doi.org/10.1108/JSIT-01-2016-0001>
- Mohammed, F., Alzahrani, A. I., Alfarraj, O., & Ibrahim, O. (2017a). Cloud computing fitness for e-Government implementation: Importance-performance analysis. *IEEE Access*, 6, 1236-1248. <https://doi.org/10.1109/ACCESS.2017.2778093>
- Mohammed, F., Ibrahim, O., Nilashi, M., & Alzurqa, E. (2017b). Cloud computing adoption model for e-government implementation. *Information Development*, 33(3), 303-323. <https://doi.org/10.1177/0266666916656033>

- Mohammed, F., Olayah, F., Ali, A., & Gazem, N. A. (2020). The effect of cloud computing adoption on the sustainability of e-government services: A review. *International Journal of Advanced Science and Technology*, 29(5), 2636-2642.
- Mousa, M. A. S. (2020). Determinants of cloud based e-government in Libya. *Journal of Critical Reviews*, 7(13), 2239-2248.
- Nanos, I., Manthou, V., & Androutsou, E. (2019). Cloud computing adoption decision in E-government. In *Operational Research in the Digital Era—ICT Challenges* (pp. 125-145). Springer. [https://doi.org/10.1007/978-3-319-95666-4\\_9](https://doi.org/10.1007/978-3-319-95666-4_9)
- Oguntala, G. A., Abd-Alhameed, P., Raed, A., Odeyemi, D., & Janet, O. (2017). Systematic analysis of enterprise perception towards cloud adoption in the African states: The Nigerian perspective. *The African Journal of Information Systems*, 9(4), Article 1.
- Park, H., & Choi, S. O. (2019). Digital innovation adoption and its economic impact focused on path analysis at national level. *Journal of Open Innovation: Technology, Market, and Complexity*, 5(3), Article 56. <https://doi.org/10.3390/joitmc5030056>
- Polyviou, A., & Pouloudi, N. (2015). Understanding cloud adoption decisions in the public sector. In *2015 48th Hawaii International Conference on System Sciences* (pp. 2085-2094). IEEE Publishing. <https://doi.org/10.1109/HICSS.2015.250>
- Rogers, E. M. (2010). *Diffusion of innovations*. Simon and Schuster.
- Salam, N. R. A., & Ali, S. (2020). Determining factors of cloud computing adoption: A study of Indonesian local government employees. *Journal of Accounting and Investment*, 1(2), 312-333. <https://doi.org/10.18196/jai.2102151>
- Sallehudin, H., Aman, A. H. M., Razak, R. C., Ismail, M., Bakar, N. A. A., Fadzil, A. F. M., & Baker, R. (2020). Performance and key factors of cloud computing implementation in the public sector. *International Journal of Business and Society*, 21(1), 134-152. <https://doi.org/10.33736/ijbs.3231.2020>
- Sallehudin, H., Razak, R., Ismail, M., Fadzil, A., & Baker, R. (2019). Cloud computing implementation in the public sector: Factors and impact. *Asia-Pacific Journal of Information Technology and Multimedia*, 7(2-2), 27-42. [https://doi.org/10.17576/apjitm-2018-0702\(02\)-03](https://doi.org/10.17576/apjitm-2018-0702(02)-03)
- Scholtz, B., Govender, J., & Gomez, J. M. (2016). Technical and environmental factors affecting cloud computing adoption in the South African public sector. In *International Conference on Information Resources Management (CONF-IRM)* (pp. 1-14). AISeL.
- Senyo, P. K., Addae, E., & Boateng, R. (2018). Cloud computing research: A review of research themes, frameworks, methods and future research directions. *International Journal of Information Management*, 38(1), 128-139. <https://doi.org/10.1016/j.ijinfomgt.2017.07.007>
- Setiorini, A., Natasia, S. R., Wiranti, Y. T., & Ramadhan, D. A. (2021). Evaluation of the application of hospital management information system (SIMRS) in RSUD Dr. Kanujoso Djatiwibowo using the HOT-Fit method. In *Journal of Physics: Conference Series* (Vol. 1726, No. 1, p. 012011). IOP Publishing. <https://doi.org/10.1088/1742-6596/1726/1/012011>

- Shafique, M. A., Mahmood, Y., Hameed, K., Malik, B. H., Cheema, S. N., & Tabassum, S. (2017). Determinants impacting the adoption of e-government information systems and suggesting cloud computing migration framework. *International Journal of Advanced Computer Science and Applications*, 8(9), 173-182. <https://doi.org/10.14569/IJACSA.2017.080925>
- Sharma, M., Gupta, R., & Acharya, P. (2020). Analysing the adoption of cloud computing service: A systematic literature review. *Global Knowledge, Memory and Communication*, 70(1/2), 114-153. <https://doi.org/10.1108/GKMC-10-2019-0126>
- Shukur, B. S., Ghani, M. K. A., & Burhanuddin, M. (2018). An analysis of cloud computing adoption framework for Iraqi e-government. *Culture*, 9(8), 104-112. <https://doi.org/10.14569/IJACSA.2018.090814>
- Singh, P., Dwivedi, Y. K., Kahlon, K. S., Sawhney, R. S., Alalwan, A. A., & Rana, N. P. (2020). Smart monitoring and controlling of government policies using social media and cloud computing. *Information Systems Frontiers*, 22(2), 315-337. <https://doi.org/10.1007/s10796-019-09916-y>
- Sivapragash, C., Padmanaban, S., Eklas, H., Holm-Nielsen, J. B., & Hemalatha, R. (2019). Location-based optimized service selection for data management with cloud computing in smart grids. *Energies*, 12(23), 1-16. <https://doi.org/10.3390/en12234517>
- Sivapragash, C., Thilaga, S., & Kumar, S. S. (2012). Advanced cloud computing in smart power grid. In *IET Chennai 3rd International Conference on Sustainable Energy and Intelligent Systems (SEISCON 2012)* (pp. 356-361). IET Digital Library. <https://doi.org/10.1049/cp.2012.2238>
- Sivathanu, B. (2018). An empirical study of cloud-based e-governance services adoption in India. *International Journal of Electronic Government Research (IJEGR)*, 14(1), 86-107. <https://doi.org/10.4018/IJEGR.2018010105>
- Sun, Y., & Jeyaraj, A. (2013). Information technology adoption and continuance: A longitudinal study of individuals' behavioral intentions. *Information & Management*, 50(7), 457-465. <https://doi.org/10.1016/j.im.2013.07.005>
- Tornatzky, L. G., Fleischer, M., & Chakrabarti, A. K. (1990). *Processes of technological innovation*. Lexington books.
- Tsaravas, C., & Themistocleous, M. (2011, May 30-31). Cloud computing and Egovernment: A literature review. In *European, Mediterranean & Middle Eastern Conference on Information Systems* (pp. 154-164). Athens, Greece.
- Tuli, S., Tuli, S., Tuli, R., & Gill, S. S. (2020). Predicting the growth and trend of COVID-19 pandemic using machine learning and cloud computing. *Internet of Things*, 11, Article 100222. <https://doi.org/10.1016/j.iot.2020.100222>
- Tweneboah-Koduah, S., Endicott-Popovsky, B., & Tsetse, A. (2014). Barriers to government cloud adoption. *International Journal of Managing Information Technology*, 6(3), 1-16. <https://doi.org/10.5121/ijmit.2014.6301>
- Vaidya, S., Shah, N., Virani, K., & Devadkar, K. (2020). A survey: Mobile cloud computing in education. In *2020 5th International Conference on Communication and Electronics Systems (ICCES)* (pp. 655-659). IEEE Publishing. <https://doi.org/10.1109/ICCES48766.2020.9138053>

- Vu, K., Hartley, K., & Kankanhalli, A. (2020). Predictors of cloud computing adoption: A cross-country study. *Telematics and Informatics*, 52, Article 101426. <https://doi.org/10.1016/j.tele.2020.101426>
- Wahsh, M. A., & Dhillon, J. S. (2015a). An investigation of factors affecting the adoption of cloud computing for E-government implementation. In *2015 IEEE Student Conference on Research and Development (SCORED)* (pp. 323-328). IEEE Publishing. <https://doi.org/10.1109/SCORED.2015.7449349>.
- Wahsh, M. A., & Dhillon, J. S. (2015b). A systematic review of factors affecting the adoption of cloud computing for E-government implementation. *Journal of Engineering and Applied Sciences*, 10(23), 17824-17832.
- Wang, C., Li, S., Cheng, T., & Li, B. (2020). A construction of smart city evaluation system based on cloud computing platform. *Evolutionary Intelligence*, 13(1), 119-129. <https://doi.org/10.1007/s12065-019-00259-w>
- Wisdom, J. P., Chor, K. H. B., Hoagwood, K. E., & Horwitz, S. M. (2014). Innovation adoption: A review of theories and constructs. *Administration and Policy in Mental Health and Mental Health Services Research*, 41(4), 480-502. <https://doi.org/10.1007/s10488-013-0486-4>
- Wohlin, C. (2014). Guidelines for snowballing in systematic literature studies and a replication in software engineering. In *Proceedings of the 18th international conference on evaluation and assessment in software engineering* (pp. 1-10). ACM Publishing. <https://doi.org/10.1145/2601248.2601268>
- Wu, J., Ding, F., Xu, M., Mo, Z., & Jin, A. (2016). Investigating the determinants of decision-making on adoption of public cloud computing in e-government. *Journal of Global Information Management (JGIM)*, 24(3), 71-89. <https://doi.org/10.4018/JGIM.2016070104>
- Yadegaridehkordi, E., Nilashi, M., Shuib, L., Nasir, M. H. N. B. M., Asadi, S., Samad, S., & Awang, N. F. (2020). The impact of big data on firm performance in hotel industry. *Electronic Commerce Research and Applications*, 40, Article 100921. <https://doi.org/10.1016/j.elerap.2019.100921>
- Yusof, M. M., Kuljis, J., Papazafeiropoulou, A., & Stergioulas, L. K. (2008). An evaluation framework for Health Information Systems: Human, organization and technology-fit factors (HOT-fit). *International Journal of Medical Informatics*, 77(6), 386-398. <https://doi.org/10.1016/j.ijmedinf.2007.08.011>
- Zhang, H. (2020). The application of cloud computing in government management. In *IOP Conference Series: Materials Science and Engineering* (Vol. 750, No. 1, p. 012166). IOP Publishing. <https://doi.org/10.1088/1757-899X/750/1/012166>

**APPENDIX A**

No.	Author	Issues/Themes	Factors	Level	Theory/ Model	Methodology	Data Analysis Technique	Respondents
1	Al Mudawi et al. (2019)	Factors affecting cloud adoption	Technological- compatibility, complexity, service quality, security, and relative advantage 2. Organizational- top management support, technological readiness, organizational size 3. Environmental -competitive pressure, regulations 4. Social attitude, trust, awareness	Organizational	TOE & DOI	Mixed method	SEM	400
2	Ali and Osmanaj (2020)	e-government services, Infrastructure, cost of data and applications, IT budget costs, software licensing and support, integration, and management	1. Technological – Cost, security concern 2. Organizational- top management support, organizational size, employees' knowledge 3. Environment – Government regulation, information intensity 4. Innovation characteristics- Compatibility, complexity 5. benefits characteristics- anticipated benefits	Organizational	TOE & DOI & DF	Quantitative	Factor analysis, SEM	480 IT staff



No.	Author	Issues/Themes	Factors	Level	Theory/ Model	Methodology	Data Analysis Technique	Respondents
3	Wahsh and Dhillon, (2015a)	Factors affecting adoption of cloud for e-government implementation	<ol style="list-style-type: none"> <li>1. Technological – Security, Trust, Compatibility, Complexity</li> <li>2. non-technological factors – Top management support, IT knowledge, Technological readiness, Relative advantage</li> </ol>	Organizational	TOE & DOI	Quantitative	SPSS with AMOS	234 IT experts
4	Polyviou and Pouloudi (2015)	Understanding cloud adoption in the public sector	<ol style="list-style-type: none"> <li>1. Technological – Relative advantage, compatibility, complexity</li> <li>2. Organizational – interoperability, business processes, environmental standards, transparency of process standards, security standards</li> <li>3. Environment – Bureaucracy, political matters, legal issues</li> </ol>	Organizational	TOE	Qualitative	Qualitative software	21 interviews across 6 European countries

No.	Author	Issues/Themes	Factors	Level	Theory/ Model	Methodology	Data Analysis Technique	Respondents
5	Wu et al. (2016)	Decision-making determinants on public cloud adoption in e-government	<ol style="list-style-type: none"> <li>1. Technical – alignment, adaptation, security</li> <li>2. Business – cost-effectiveness, operational risk</li> <li>3. Management – IT compliance, management controlling power</li> </ol>	Organizational	Technical adoption theory and IT decision-making	Quantitative	SEM	227 CIOs from public sectors
6	Salam and Ali (2020)	Factors influencing adoption of cloud by government	<ol style="list-style-type: none"> <li>1. Performance Expectations</li> <li>2. Business expectations</li> <li>3. Perception of Availability</li> </ol>	Organizational	UTAUT	Quantitative	SEM	123 employees
7	Mohammed et al. (2017b)	Factors influencing cloud adoption in the public sector	<ol style="list-style-type: none"> <li>1. Fitness- Relative advantage, compatibility, trialability, security</li> <li>2. Viability- return on investment, asset specificity</li> <li>3. Technological readiness- IT infrastructure, IT policy, and regulations</li> </ol>	Organizational	Fit Viability & DOI	Quantitative	PLS SEM	296 IT staff

No.	Author	Issues/Themes	Factors	Level	Theory/Model	Methodology	Data Analysis Technique	Respondents
8	Kandil et al. (2018)	Effect of TOE on cloud adoption in Egypt	<ol style="list-style-type: none"> <li>1. Technology – Relative advantage, Complexity, Compatibility, Security &amp; Trust</li> <li>2. Organizational- Top Management Support, Technology readiness, Maturity &amp; Performance Issues</li> <li>3. Environment- Competitive Pressure, Telecommunication Infrastructure, Internet Service Provider, Trading Partner support, Trading Partner Pressure</li> </ol>	Organizational	TOE	Quantitative	PLS SEM	432 IT employees
9	Maluleka and Ruxwana (2016)	Cloud computing as an alternative for the South African public sector	<ol style="list-style-type: none"> <li>1. Lack of support, user resistance, compatibility, migration cost, lack of approved standards, poor IT infrastructure</li> </ol>	Organizational	DOI	Mixed methods	SPSS	28 questionnaires, 6 interviews
10	Al-Rawahna et al. (2018)	Readiness of government organizations for cloud computing	<ol style="list-style-type: none"> <li>1. Top Management Support</li> <li>2. Organizational Capability</li> <li>3. Government Policy</li> <li>4. Organizational Size</li> <li>5. IT skills and Infrastructure</li> </ol>	Organizational	TOE	Quantitative	PLS-SEM	132 IT staff

No.	Author	Issues/Themes	Factors	Level	Theory/ Model	Methodology	Data Analysis Technique	Respondents
11	Vu et al. (2020)	Predictors of cloud adoption	Legal System Quality, Fixed Broadband Penetration, Advanced Digital Infrastructure, Digital Legacy Large Services	Organizational	Institutional	Quantitative	Parsimonious model	45 countries
12	Oguntala et al. (2017)	Perception toward cloud adoption	On-demand service deliver, guaranteed quality of service, scalability, and flexibility, data security, user-centric interface, user autonomy	Organizational	Literature	Mixed methods	Data processing software and MATLAB	200
13	Liang et al. (2019)	“Effects of e-government cloud assimilation on public value creation”	Depth, breadth, balanced fit, complementary fit, operational public value, strategic public value	Individual	IT assimilation theory, IT value theory, organizational ambidexterity theory	Quantitative	PLS SEM	158 IT directors and senior IS managers

No.	Author	Issues/Themes	Factors	Level	Theory/Model	Methodology	Data Analysis Technique	Respondents
14	Sivathanu (2018)	Elements affecting adoption of Digi Locker cloud-based e-governance	Performance expectancy, effort expectancy, facilitating conditions, social influence, perceived awareness, computer self-efficacy, multilingual option, perceived quality of information, perceived response, perceived trust	Individual	e-GAM and UTAUT models	Quantitative	PLS-SEM	80 citizens and students
15	Junior et al. (2020)	“Towards a framework for cloud computing use by governments”	Cloud characteristics	Individual	DOI and Institutional theory	Qualitative	spreadsheets	17 Managers and engineers in charge of Cloud Gov
16	Kyriakou et al. (2020)	“Factors affecting cloud storage adoption by Greek municipalities	Relative advantage, compatibility, complexity	Organizational	DOI	Quantitative	Principal component analysis	121 municipalities

No.	Author	Issues/Themes	Factors	Level	Theory/ Model	Methodology	Data Analysis Technique	Respondents
17	Mousa (2020)	Determinants of cloud-based e-government	Technological, organizational, IT knowledge	Organizational	TOE & DOI	Quantitative	SEM	279 decision-makers
18	Garad and Santoso (2017)	Impact of using Cloud computing in e-government and infrastructure required	Performance, security and privacy, control, data transfer costs, accuracy and reliability	Organizational	Framework	Quantitative	SPSS	136 managers and IT employees
19	Ji and Liang (2016)	Exploring the determinants affecting e-government cloud adoption in China	Technology, organizational, and environment	Organizational	TOE & DOI	Qualitative	Qualitative analysis software	12 interviews
20	Shafique et al. (2017)	Elements affecting e-government and cloud migration	Technological-perceived benefits, IT infrastructure, complexity, Organizational-size, top management commitment and innovativeness, resource commitment Environmental-external pressure, regulatory environment, work overload	Organizational	TOE	Quantitative	Principal component factor analysis	175 respondents

No.	Author	Issues/ Themes	Factors	Level	Theory/ Model	Methodology	Data Analysis Technique	Respondents
21	Liang et al. (2017)		Technology driving- comparative advantage, technological concern Cloud provider support- cloud provider characteristic, cloud provider competence, cloud provider presence Organizational readiness- top management support, organizational scale, and complexity of informational resource Environmental stimulus- policy & regulation, industry standards, competition pressure, requirement of citizen, best practice, financial fund Cloud trust- initial trust, perceived benefit-based trust	Organizational	Grounded theory	Qualitative	Atlas's	24 government officials
22	Shukur et al. (2018)	Cloud adoption framework for Iraqi e-government	Technological- cost, scalability, flexibility, compatibility, complexity, security & privacy, resource utilization Organizational- top management support, IT infrastructure, IT human resources Environment- reliable, available, ownership, mobile access, migration Ease of use, Regulation issues	Organizational	TOE & TAM	Quantitative	Mean & SD	25 e-government staff

No.	Author	Issues/Themes	Factors	Level	Theory/ Model	Methodology	Data Analysis Technique	Respondents
23	Lian (2015)	Cloud-based e-invoice adoption	Effort expectation, social influence, trust in e-government, perceived risk	Individual	UTAUT2	Quantitative	PLS SEM	251 respondents
24	Alkhwaldi et al. (2017)	Cloud-based e-government acceptance in Jordan	Technological, Human, Social, Finance	Individual	UTAUTA2	Quantitative	SPSS	164 respondents
25	Liang and Qi (2017)	Determinants of e-government cloud adoption in China	Environmental- financial commitment support, completeness of policy & standard, successful cases Organizational- top management support, organizational inertia, scale, and complexity of informational resources Technology task fit Technology-compatibility, competitive advantage, complexity	Organization	DOI, TOE, TAM, TTF	Qualitative: multicas	Atlas's	21 respondents



No.	Author	Issues/Themes	Factors	Level	Theory/Model	Methodology	Data Analysis Technique	Respondents
26	Ali et al. (2015)	Collaborative cloud adoption in Australian municipal government	Technological- Cost, technology readiness, security Organizational- Size, top management support, employee knowledge	Organizational	TOE & DOI	Qualitative	Manual & Leximancer visual text tool	21 interviews
27	Alrashed and Alotaibi (2017)	Trust in acceptance of government cloud	Environment- Competitive pressure, regulation support, information intensity Innovation factors- Relative advantage, complexity, compatibility Performance expectancy, effort expectancy, social influence, trust, perceived risk	Individual	UTAUT	Quantitative	PLS-SEM	310 IT professional and technicians
28	Lagzian et al. (2018)	Effective factors for acceptance of cloud in Iran public services	Human- recipients' innovation, decision makers' knowledge Technological- relative advantage, test capability, compatibility, technology infrastructure, security, and privacy Organizational- information intensity, employee knowledge Environmental- External support, environmental infrastructure, competitive pressure	Organizational	TTF, Hot fit, DOI, & TOE	Quantitative	SPSS & Logistic regression	60 managers and IT experts



## Dose Distribution of $^{192}\text{Ir}$ HDR Brachytherapy Source Measurement using Gafchromic® EBT3 Film Dosimeter and TLD-100H

Nor Shazleen Ab Shukor<sup>1</sup>, Marianie Musarudin<sup>1\*</sup>, Reduan Abdullah<sup>2</sup> and Mohd Zahri Abdul Aziz<sup>3</sup>

<sup>1</sup>School of Health Sciences, Universiti Sains Malaysia, Health Campus, 16150 USM, Kubang Kerian, Kelantan, Malaysia

<sup>2</sup>Hospital Universiti Sains Malaysia, 16150 USM, Kubang Kerian, Kelantan, Malaysia

<sup>3</sup>Advance Medical and Dental Institute, Universiti Sains Malaysia, 13200 USM, Kepala Batas, Penang, Malaysia

### ABSTRACT

This study aims to measure the radial dose function  $g(r)$  and anisotropy function  $F(r, \theta)$  of High Dose Rate (HDR)  $^{192}\text{Ir}$  source in a fabricated water-equivalent phantom using Gafchromic® EBT3 film and TLD-100H and to compare the results obtained with the MCNP5 calculated values. The phantom was fabricated using Perspex PMMA material. For  $g(r)$ , the EBT3 films with a required dimension and TLD-100H chips were placed at  $r=1, 2, 3, 5,$  and  $10$  cm from the source. The  $F(r, \theta)$  measurements were carried out at  $r=1, 2, 3, 5,$  and  $10$  cm with the angle range from  $10^\circ$  to  $170^\circ$ . The result of  $g(r)$  from EBT3 film and TLD-100H was in good agreement ( $2.10\% \pm 1.99$ ). Compared to MCNP5, the differences are within  $0.31\%$  to  $11.47\%$  for EBT3 film and  $0.08\%$  to  $10.58\%$  for TLD-100H. For the  $F(r, \theta)$ , an average deviation with the MCNP5 calculation is  $4.94\% \pm 2.7$ . For both  $g(r)$  and  $F(r, \theta)$ , the effects are prominent at  $r=10$  cm. At this distance, the

response of both Gafchromic® EBT3 film and TLD-100H shows less sensitivity as the dose followed the inverse square law. This work demonstrates that Gafchromic® EBT3 film dosimeter and TLD-100H are suitable dosimeters in  $^{192}\text{Ir}$  dosimetric measurements at a radial distance of  $<5$  cm.

### ARTICLE INFO

#### Article history:

Received: 11 August 2021

Accepted: 21 October 2021

Published: 10 January 2022

DOI: <https://doi.org/10.47836/pjst.30.1.37>

#### E-mail addresses:

shazleen@usm.my (Nor Shazleen Ab Shukor)

marianie@usm.my (Marianie Musarudin)

reduan@usm.my (Reduan Abdullah)

mohdzahri@usm.my (Mohd Zahri Abdul Aziz)

\*Corresponding author

**Keywords:**  $^{192}\text{Ir}$  brachytherapy source, dose distribution, Gafchromic® EBT3 film dosimeter, Monte Carlo simulation, TLD-100H dosimeter

## INTRODUCTION

Brachytherapy is an internal radiotherapy technique in which a sealed radiation source is placed inside or near the treated area. Iridium-192 ( $^{192}\text{Ir}$ ) is the most frequent source used for HDR brachytherapy. The dose distribution around  $^{192}\text{Ir}$  brachytherapy sources is inherently anisotropic and is characterised by steep dose gradients. As the dose gradient near radioactive sources is veer, the dose distribution in the surrounding tissues is difficult to be measured (Hsu et al., 2012). These properties had put a high demand on the dosimetry of  $^{192}\text{Ir}$  brachytherapy source regarding the dosimeter's precision, size, and energy dependence (Kirisits et al., 2014). The American Association of Physicists in Medicine (AAPM) had introduced dose distribution parameters based on the direct dose distribution in a homogenous water medium in which the dose rate constant ( $\Lambda$ ), the radial dose function  $g(r)$ , the geometry factor  $G(r, \theta)$ , and the anisotropy function  $F(r, \theta)$  are the parameters in question (Chandola et al., 2010; Granero et al., 2011; Rivard et al., 2004).

Based on the literature, the most frequently reported dosimetry systems in the determination of the dosimetric function of  $^{192}\text{Ir}$  source are film dosimetry and thermoluminescent dosimeter (TLD) (Ayoobian et al., 2016; Bassi et al., 2020; DeWerd et al., 2014; Sellakumar et al., 2009; Uniyal et al., 2011; Wu et al., 2014). The dosimetric functions of  $^{192}\text{Ir}$  studied by Sellakumar et al. (2009) were measured the  $\Lambda$ ,  $g(r)$ , and  $F(r, \theta)$  for HDR  $^{192}\text{Ir}$  source using Gafchromic® EBT films. Therefore, according to the findings, the Gafchromic® EBT film could be utilised to assess the brachytherapy dosimetric function as defined by the AAPM TG-43. Furthermore, another experimental study found that the TLD and Gafchromic® EBT2 film measured values for  $F(r, \theta)$  are within 4% of each other (Uniyal et al., 2011).

A recent study by Bassi et al. (2020) reported, EBT3 film was energy independent and can be utilised for brachytherapy source dose monitoring despite being calibrated with a 6MV photon beam and could be expanded to be applied in clinical dosimetry brachytherapy. Besides film dosimetry, TLDs also was recommended for dosimetric measurement in brachytherapy because of their excellent sensitivity, miniature, flat energy response, and energy independence. However, according to a prior study, TLD's appropriateness for brachytherapy dosimetry was determined by high-precision measurements using some of the most regularly utilised brachytherapy sources (DeWerd et al., 2014). Apart from these dosimeters, Monte Carlo calculation has been reported as a reliable and preferable dosimetry system, and it is also commonly utilised in obtaining dosimetric data for brachytherapy sources (Patel et al., 2010).

Previously, dosimetry protocols or a set of dosimetry procedures employing film dosimetry and TLD had been published (Ayoobian et al., 2016; Bassi et al., 2020; Faghihi & Street, 2015; Palmer et al., 2013; Sellakumar et al., 2009). However, they reported the properties of Gafchromic EBT, EBT2 and TLD 100 in their study. On the other hand, the

dosimetric properties of the Gafchromic® EBT3 film and TLD-100H in brachytherapy dosimetry has not yet been clarified. Therefore, this study investigates the dose distribution of  $^{192}\text{Ir}$  brachytherapy source for  $g(r)$  and  $F(r, \theta)$  in fabricated Perspex PMMA phantom using Gafchromic® EBT3 film dosimetry and TLD-100H and compared with dose distribution data obtained from MCNP5 calculated values.

## MATERIALS AND METHODS

### Nucletron $^{192}\text{Ir}$ MicroSelectron HDR Source

The Nucletron  $^{192}\text{Ir}$  microSelectron HDR source (HDR, Nucletron Inc., The Netherlands) was modelled using MCNP5 code. The source has a material density,  $\rho$  of  $22.56 \text{ g cm}^{-3}$ , modelled with a 3.5 mm active length and 0.6 mm diameter (Wu et al., 2014). The cover used to enclose this source is stainless steel AISI 316L ( $\rho = 8.027 \text{ g cm}^{-3}$ ) with a diameter of 1.1 mm. At the outer steel cover on the proximal side, a 5 mm AISI 304 stainless steel cable ( $\rho = 4.81 \text{ g cm}^{-3}$ ) extending from the cover was modelled in this calculation. The material compositions of these steel are as described by López et al. (2011). Figure 1 illustrates the detailed model of the source used in this study. The  $^{192}\text{Ir}$  energy spectrum used in this study was adopted from the energy distribution described by Fazli et al. (2013). We have excluded the beta spectrum in the calculation due to its negligible contribution at  $>1 \text{ mm}$  distance to the source.

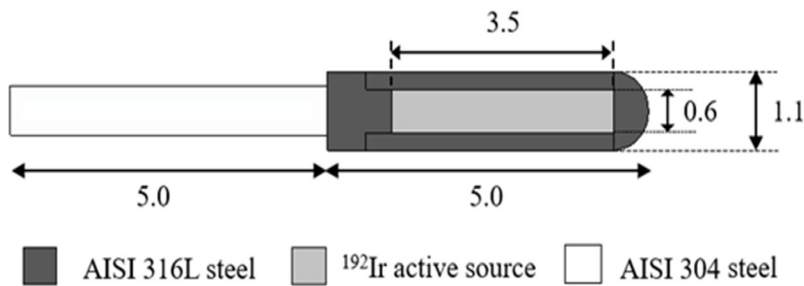


Figure 1. The geometry of Nucletron  $^{192}\text{Ir}$  microSelectron HDR source modelled in MCNP5 calculation (length is in mm units)

### Validation of the MCNP5 Dose Calculation

Identical simulation geometry defined by Wu et al. (2014) has been modelled using MCNP5 code, which is created by the Los Alamos National Laboratory (Los Alamos National Laboratory, Los Alamos, NM). This remodelling aims to compare and verify the dosimetric parameters obtained from our MCNP5 code. Therefore, a 30 cm spherical phantom filled

with homogeneous water ( $\rho=0.997 \text{ g cm}^{-3}$ ) was modelled. The  $g(r)$  and  $F(r;\theta)$  are the two dosimetric parameters considered for this purpose (Shukor et al., 2020). It is in line with the recommendation in AAPM TG-43, whereby the  $g(r)$  is one of the most important dosimetric parameters for source validation and benchmarking (Rivard et al., 2004).

### Fabricated Phantom Design

The phantom designed in this study was invented from a published study by Uniyal et al. (2011). A frequently used Perspex PMMA (polymethylmethacrylate) was selected as the phantom material due to the low effective atomic number ( $Z_{\text{eff}} = 6.5$ ), economical, and widely available (de Almeida et al., 2002; Ghiassi-Nejad et al., 2001; Palmer et al., 2014; Subhalaxmi & Selvam, 2015). The Perspex PMMA slab phantom ( $\rho=1.19 \text{ g cm}^{-3}$ ) was fabricated at the Engineering Physic Workshop, School of Physic, USM (Figure 2).

The dimension of the Perspex PMMA phantom is  $30 \times 30 \times 2 \text{ cm}$ . This slab phantom has an inner diameter of 0.5 cm and was radially machined in the arced of  $0^\circ$  to  $360^\circ$  with a 1 to 10 cm distance from the centre. For TLD chips placement, the TLD holes were machined for 0.2 cm depth with 0.5 cm diameter at 1 to 10 cm radial distance with an angle of  $10^\circ$ ,  $30^\circ$ ,  $60^\circ$ ,  $90^\circ$ ,  $120^\circ$ ,  $150^\circ$ , and  $170^\circ$ . In addition, a horizontal catheter insert was designed for source catheter delivery placement at the centre of the slab phantom.

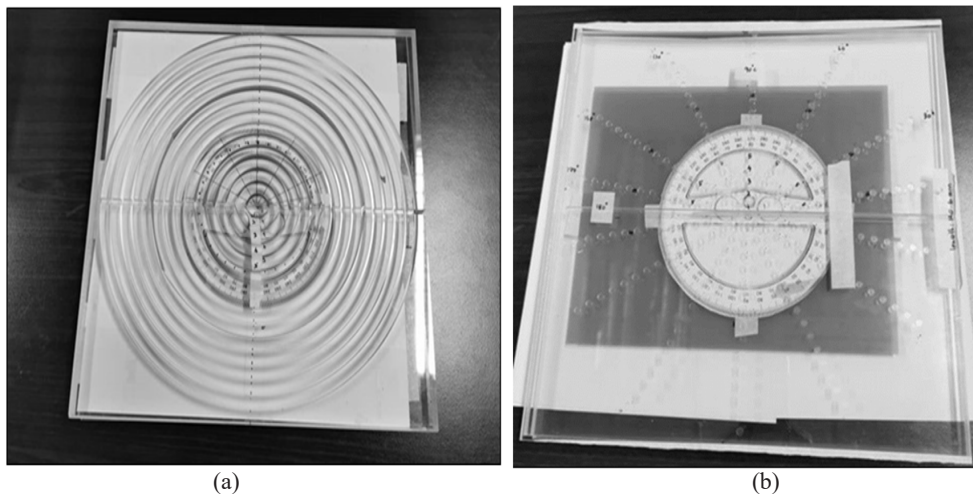


Figure 2. The fabricated slab Perspex PMMA phantom for dose distribution measurement of  $^{192}\text{Ir}$  brachytherapy source (a) with film inserts (b) with TLD holes

## Dosimetry System

**Radiochromic Film Dosimetry.** The third-generation film, Gafchromic® EBT3 film (Ashland ISP, Wayne, NJ), is improved than their predecessor, EBT2, with features, such as symmetrical active layer configuration, with a dose range of 0.1-20 Gy and added matte polyester substrate, which has microscopic silica particles which keep minimising the gap thus preventing the formation of Newton's rings interference patterns (Fiandra et al., 2013; Reinhardt et al., 2012). With the new enhancement, EBT3 film was more robust and easier to handle than EBT2 (Borca et al., 2013; Reinhardt et al., 2012). Film lot #08231801 was used in this study and was handled according to the guidelines in the AAPM TG-55 (Niroomand-Rad et al., 2020).

The first phase of this study involved the calibration of the EBT3 film. As it is known as energy independent, the calibration is done with a 6MV photon beam (Adelnia & Fatehi, 2016; Palmer et al., 2013). A set of 10 pieces of EBT3 films were cut into 3×3 cm squares and marked at the left corner for orientation. For irradiation setup, the film pieces were placed in a full scatter solid water phantom at  $d_{\text{max}}=1.5$  cm, and irradiation of 6MV photon beam was delivered with PRIMUS™ LINAC (Siemens Medical Systems, CA, USA) at SSD=100 cm, the field size of 10×10 cm and a dose range of 100 to 900 cGy. One sample was left unexposed as a background control for base and fog. After 24 hours of irradiation, the irradiated films were scanned in portrait orientation using 10000XL EPSON® Expression flatbed scanner (Epson Seiko Corporation, Nagano, Japan) with PTW-FilmScan software (PTW-Freiburg, Freiburg, Germany) with the setting parameters of positive colour film type, 16-bit grayscale, and 300 digital image resolutions (dpi) in a transmission mode (Figure 3). A curve between the pixel value and the corresponding dose was plotted from the PTW-Film Cal software v2.4 (PTW-Freiburg, Freiburg, Germany) (Figure 4). The film calibration curve was saved as a lookup table or calibration table for dose determination.

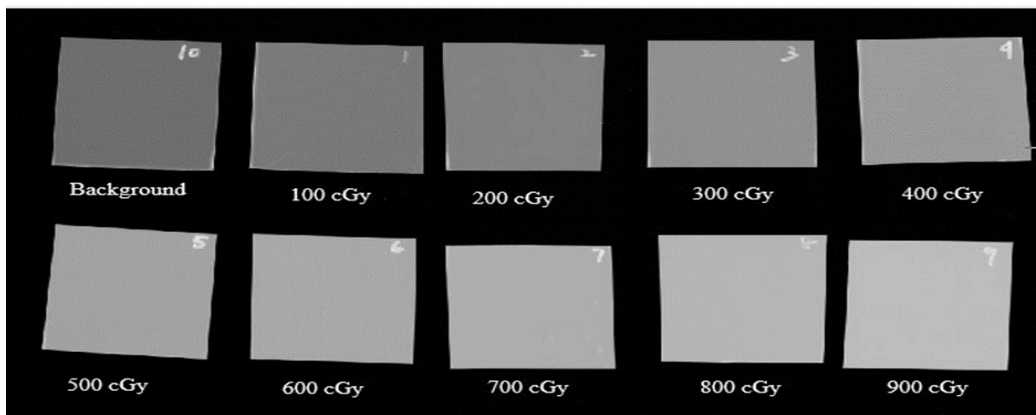


Figure 3. A set of Gafchromic® EBT3 films were digitalised using PTW-FilmScan software

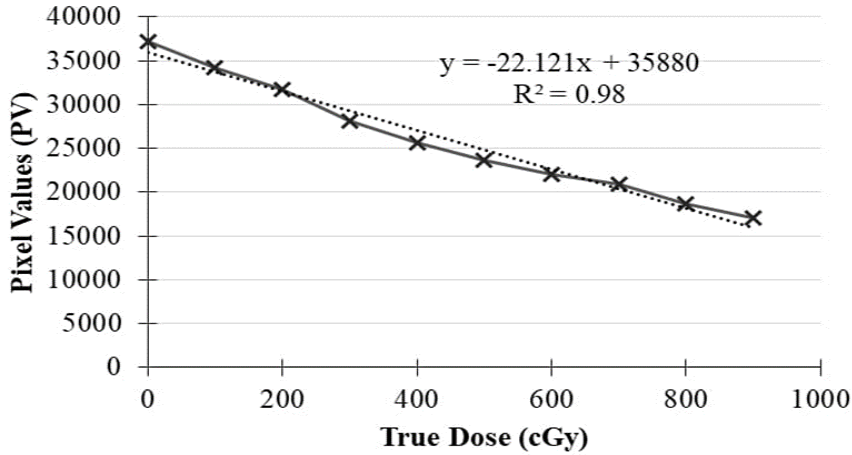


Figure 4. The dose-response of Gafchromic® EBT3 film generated by PTW- FilmCal software v2.4

### Thermoluminescent Dosimeter (TLD) System

TLD measurements were performed with 3×3×1 mm chips of Harshaw TLD-100H (Thermo Fisher Scientific Inc., Waltham, MA). TLD100-H has been reported to be more sensitive, has a simple glow curve and short annealing than TLD100. As the brachytherapy source is known to have a steep dose gradient and will lose its energy in a short distance, it has been interesting to study the properties of TLD100-H towards the source (Freire et al., 2008). Therefore, the sensitivity test was performed by irradiating a group of 60 chips of TLD-100H with 100 cGy of 6MV photon beam using PRIMUS™ LINAC (Siemens Medical Systems, CA, USA) at SSD=100 cm, 10×10 cm field size, and  $d_{max}=1.5$ cm. The TL readout was performed 24 hours after irradiation using a Harshaw 3500 TLD reader (Thermo Fisher Scientific Inc. Waltham, MA).

The sensitivity factor for individual TLD is calculated using Equation 1.

$$Sensitivity = \frac{TLD_i}{TLD_{avg}} \tag{1}$$

Where,  $TLD_i$  is the individual reading of TLD and  $TLD_{avg}$  is the average reading. Since the response of individual TLD to the same delivered dose may be different, only the high sensitivity TLD chips with a sensitivity of >1 were used in this study. The reproducibility test was performed by repeating the same measurement three times. According to Faghihi & Street (2015), the calculation of the coefficient of variation (CV) of TLD measurement obtained using Equation 2 should be less than 10%.

$$CV (\%) = \frac{SD}{mean} \times 100 \tag{2}$$



In addition, an individual Element Correction Coefficient (ECC) was also a required correction that needs to be applied. The characteristic of TL dosimeters could not present with the same TL efficiency (where TL efficiency (TLE) is defined as the emitted TL light intensity per unit of absorbed dose). Therefore, the ECC was calculated using Equation 3.

$$ECC_j = \frac{\langle TLE \rangle}{TLE_j} \quad [3]$$

Where,  $\langle TLE \rangle$  is the average reading of the total TLDs, whereas  $TLE_j$  is an individual reading. Calibration measurement was performed using 20 chips of TLDs with a CV of less than 10%, with the same setup that was used for the sensitivity test. The group calibration factor (CF) of TLD-100H is obtained by dividing the irradiated dose by the average response of the TLDs. From this study, the CF for this group of TLD-100H is 0.59 cGy/ $\mu$ C.

### Radial Dose Function

The measurements setup was prepared by positioning the <sup>192</sup>Ir source inside the catheter at the centre of the Perspex PMMA slab phantom along the Y-axis with the tip of the source toward the +Y axis (Chandola et al., 2010). Before the exposure, source position verification to assess the source placement and a dwell position verification to keep the source at the centre of the film was performed. From the verification, the source position is confirmed to be centred on the field, and the dwell position is precisely placed in line at the centre of the 12.06 cm dwell length. Then, a set of films with the required dimension were placed in the film insert at radial distances ( $r$ ) of 1, 2, 3, 5, and 10 cm from the source with the film facing toward the source at an angle of 90°. A full scattering medium was achieved by placing a Perspex PMMA slab with a thickness of 1 cm on the top of the fabricated phantom. The calculated source strength,  $Sk$  from the treatment planning, is 14911 cGy cm<sup>-2</sup> h<sup>-1</sup>. Referring to the  $Sk$ , the dwell time for completed 300 cGy is 72 s. The post-irradiated films were scanned after 24 hours using a 10000XL EPSON® Expression flatbed scanner (Epson Seiko Corp., Nagano, Japan) with a scanning parameter of 300 dpi and 16-bit grayscale. The film dose then was obtained from PTW-Verisoft software (PTW-Freiburg, Freiburg, Germany). The same irradiation setup also was performed for the TLD-100H measurements, which take place in the fabricated slab phantom with TLD holes as it has the same dimension as the slab phantom for a film. The signal readout was performed 24 hours' post-irradiation.

### Anisotropy Function

The anisotropy function  $F(r, \theta)$  describes the variation in dose distribution around the source as a function of polar angle relative to the transverse plane, including the effects of absorption and scatters in the medium due to; photon scattering in the medium,

self-filtration, and the primary photons' filtration through the encapsulation materials (Sellakumar et al., 2009). For the  $F(r, \theta)$ , the measurements were carried out using the same phantom as described for the  $g(r)$ . However, the dose values were measured at radial distances of 1, 2, 3, 5, and 10 cm with polar angles varied from  $10^\circ$  to  $170^\circ$ .

### Monte Carlo Simulation

The dose distribution of the  $^{192}\text{Ir}$  source was calculated using a validated MCNP5 code (Wu et al., 2014). The data were scored using an F6 tally grid system modelled by 0.5 mm height and ring radius of the cylindrical rings concentric from the source in its longitudinal axis. The concentric rings were positioned at  $r=0.5$  to 14 cm from the centre, and they were fixed at the centre of the active length of the source in each calculation. The tip of the source was modelled to face towards the +Y direction while the cylindrical ring of the tally cells concentric to the Z-axis (Figure 5a). The data, which yielded at  $r=0.5$  to 14 cm in the transverse plane of the source ( $\theta = 90^\circ$ ), allows normalisation to the dose rate at  $r=1$  cm of the same plane. Meanwhile, the data for  $F(r, \theta)$  that measure doses at various angles from the source were tallied at a different angle from  $0^\circ$  to  $180^\circ$  with a  $10^\circ$  increment. The centre of the active  $^{192}\text{Ir}$  core was set as the centre of the angle rotation. The distal end of the stainless-steel cable was assumed as  $0^\circ$ , while the tip end of the source is  $180^\circ$  (Figure 5b).

The F6 tally calculates the amount of energy deposited in a unit of MeV/g. The output is multiplied by  $1.6 \times 10^{-10}$  using the tally multiplier (FM) card, yielding energy deposition in Gy. The photon cut-off was set at 10 keV to speed up the process (Shukor et al., 2020). A simulation boundary modelled by a 100 cm spherical cell was assigned to limit the simulation calculation. The radiation particles were removed from the calculation by force termination of the particles scattered out of the simulation boundary. The total number history of  $5 \times 10^7$  was selected to guarantee a reliable confidence interval  $< 0.1$ .

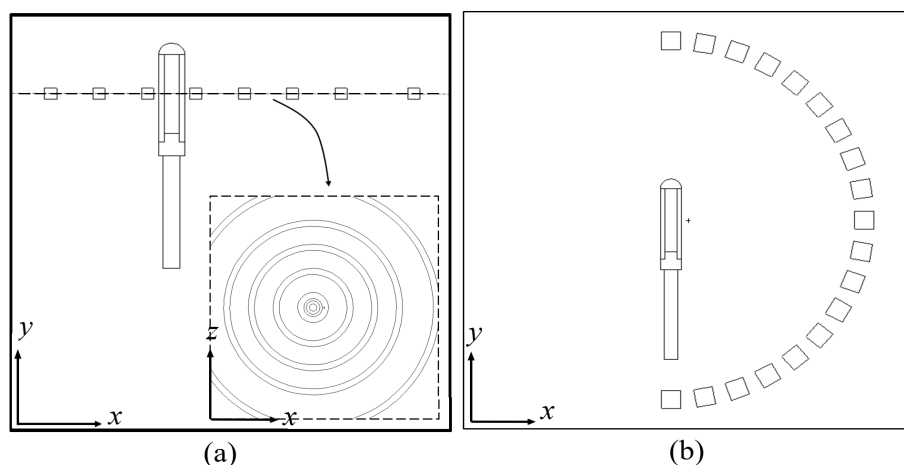


Figure 5. The geometry of the model was developed using MCNP5 code for (a)  $g(r)$  (b)  $F(r, \theta)$

**Dose Calculation Formalism**

According to the AAPM TG-43 recommendation, the dose rate at the point of interest  $P(r, \theta)$  in water is expressed as Equation 4:

$$D(r, \theta) = S_k \Lambda \frac{G(r, \theta)}{G(r_0, \theta_0)} \cdot g(r) \cdot F(r, \theta) \tag{4}$$

Where,  $r$  is the distance (cm) from origin to the point of interest  $P$ ,  $\theta$  is the angle between the direction of radius vector  $r$  and the long axis of the source,  $\theta_0$  defines the source transverse plane and is equal to  $\pi/2$  radians,  $S_k$  is the air kerma strength,  $\Lambda$  is the dose rate constant,  $G(r, \theta)$  is the geometry function,  $g(r)$  is the radial dose function, and  $F(r, \theta)$  is the anisotropy function.  $P(r_0, \theta_0)$  is defined at  $r=1$  cm, ( $\theta = 90^\circ$ )(Figure 6).

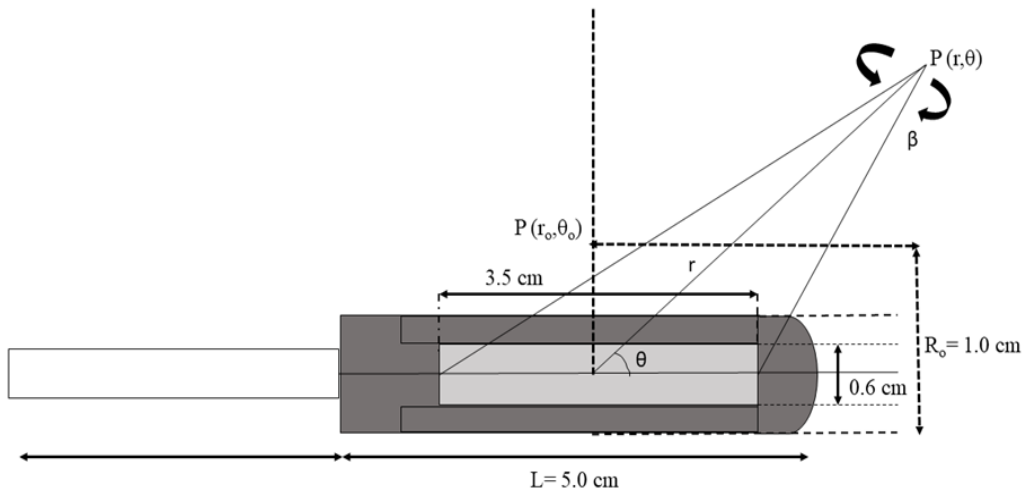


Figure 6. The geometry of line source used in TG-43 formalism

The Excel worksheet and formulas were used to simplify and calculate Equations 5, 6 and 7. The dose measured using TLD100-H and EBT3 film at a particular point has been inserted in the formula. The  $g(r)$  is described as follows Equation 5:

$$g(r) = \frac{D(r, \theta_0) \cdot G(r_0, \theta_0)}{D(r_0, \theta_0) \cdot G(r, \theta_0)} \tag{5}$$

In this study,  $g(r)$  was measured at a particular point using TLD100-H and EBT3 film. Where, dose at point,  $D(r_0, \theta_0)$  is defined at 1 cm,  $\theta=90^\circ$  and  $D(r, \theta_0)$  is defined at  $r=1, 2, 3, 4, 5$  and 10 cm,  $\theta=90^\circ$ . The geometry function,  $G(r, \theta)$  is calculated according to the following Equation 6:

$$G(r, \theta) = \frac{\beta}{Lr \sin \theta} \quad \text{if } \theta \neq 0^\circ \tag{6}$$

Where, for  $g(r)$  calculation,  $G(r_0, \theta_0)$  is defined at  $r=1$  cm,  $\theta=90^\circ$  and  $G(r, \theta_0)$  is defined at  $r=1, 2, 3, 4, 5$  and  $10$  cm,  $\theta=90^\circ$ . Whereas,  $L$  is the line source approximation used for the geometry function,  $\beta$  is the angle in radians, subtended by the tips of the hypothetical line source with respect to the calculation point  $P(r, \theta)$ .

The  $F(r, \theta)$  is defined as in Equation 7:

$$F(r, \theta) = \frac{D(r, \theta) \cdot G(r, \theta_0)}{D(r, \theta_0) \cdot G(r, \theta)} \tag{7}$$

Where,  $D(r, \theta_0)$  is defined at  $r=1, 2, 3, 5$  cm,  $\theta=90^\circ$ ,  $D(r, \theta)$  is defined at  $r=1, 2, 3, 5$  and  $10$  cm,  $\theta=10^\circ-170^\circ$ ,  $G(r, \theta_0)$  is defined at  $r=1, 2, 3, 5$  and  $10$  cm at  $\theta=90^\circ$ ,  $G(r, \theta)$  is defined at  $r=1, 2, 3, 5$  and  $10$  cm at  $\theta=10^\circ-170^\circ$ .

## RESULTS AND DISCUSSION

### Radial Dose Function

Figure 7 compared the measurement  $g(r)$  of  $^{192}\text{Ir}$  source using EBT3 film and TLD-100H with the calculated  $g(r)$  by MCNP5 and published data previously presented by Wu et al. (2014). The average relative difference is  $0.37\% \pm 0.47$ , and a maximum deviation is at  $r=10$  cm (1.30%). A previous study found that a good agreement is achieved when the deviation is within 2% (Buchapudi et al., 2019). Therefore, our MCNP5 code for the  $^{192}\text{Ir}$  HDR brachytherapy dose calculation achieved a good agreement with Wu et al. (2014). We extended the simulation to  $r=0.3, 0.5$  and  $0.7$  cm and observed small deviations to the  $g(r)$  at  $r=1$  cm for the three radial distances (0.48, 0.12 and 0.01% each).

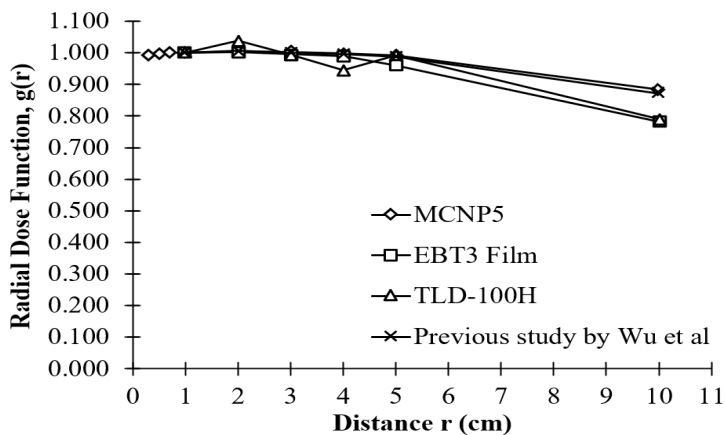


Figure 7. The comparison of measured,  $g(r)$  for EBT3 film and TLD100-H with MCNP5 and a previous study by Wu et al. (2014)

Meanwhile, EBT3 film shows a good agreement with MCNP5 at  $r=1$  to 5 cm with an average relative difference of  $1.03\% \pm 1.25$ . However, a greater relative difference (11.47%) was calculated at  $r=10$  cm. A similar result was observed for the TLD-100H whereby at  $r=1$  to 5 cm, the  $g(r)$  values were  $1.92\% \pm 2.35$ . The maximum difference was also noted at  $r=10$  cm (10.58%). Nevertheless, the experimental  $g(r)$  values obtained between EBT3 film and TLD-100H were in good agreement with a relative difference of  $2.10\% \pm 1.99$ . Even though a similar measurement setup was implemented for both film and TLD, slight variation was noted between the two, most probably due to the different dosimetry properties of film and TLD, e.g. differences in size, range of sensitivities, and measurement's principal (Uniyal et al., 2011). The  $g(r)$  values between measured and calculated are within the tolerance at  $r=1$  to 5 cm, and the differences are significant at  $r=10$  cm. At this position, the response of TLD signal and film is relatively small, possibly because of the lower dose received due to the depth increase as mentioned in inverse square law (Hsu et al., 2012). In addition, the variation occurs because of the dose-response factor of the detector due to the shift of the photon spectrum to lower energies with increasing depth (Haworth et al., 2013).

Table 1

Comparison of the  $g(r)$  measured using film in this study with the previous studies for a homogenous water phantom

Radial distance, $r$ (cm)	This study	Buchapudi et al.	Relative differences (%)	Sellakumar et al.	Relative differences (%)
	EBT3	EBT2		EBT	
1	1.000	1.000	0.00	1.000	0.00
2	1.003	1.004	0.15	1.006	0.37
3	0.995	0.999	0.38	1.077	7.60
4	0.990	0.970	2.06	1.002	1.16
5	0.961	0.966	0.56	0.992	3.17
10	0.782	0.846	8.20	-	-
Relative Uncertainty (%)	3.5 (k=1)	2.4 (k=1)		1.5 (k=1)	

Table 2

Comparison of  $g(r)$  measured using TLD in this study with the previous study for a homogenous water phantom

Radial distance, r (cm)	This study	Buchapudi et al.	Relative differences (%)
	TLD100-H	TLD100	
1	1.000	1.000	0.00
2	1.038	1.010	2.73
3	0.995	1.006	1.13
4	0.945	1.002	6.07
5	0.993	0.989	0.40
10	0.790	0.888	12.43
Relative uncertainty (%)	3.6 (k=1)	1.9 (k=1)	

Table 1 and Table 2 present the comparison between the measured  $g(r)$  obtained in this study with the data previously presented by Buchapudi et al. (2019) and Sellakumar et al. (2009). From Table 1, the average relative difference between the film measurement with the previous studies is  $1.89\% \pm 3.17$  (Buchapudi et al., 2019) and  $2.46\% \pm 3.12$  (Sellakumar et al., 2009). Meanwhile, the comparison between the TLD measurements is shown in Table 2, whereby the relative difference between this study with Buchapudi et al. (2019) is  $3.80\% \pm 4.77$ , with a maximum difference is at  $r=10$  cm (12.43%). A significant difference was observed at  $r=10$  cm, which is 8.20% and 12.43%, respectively. The disparities are probably due to the different phantom materials, dimensions, and the energy dependence of the detector at lower photon energies (Ghiassi-Nejad et al., 2001). Previous studies used EBT, EBT2 and TLD100 in their measurement. Our study shows that the performance of EBT3 film is lower than EBT and EBT2 (Fiandra et al., 2013). As TLD100-H is known to have higher sensitivity than TLD100, it suffers from a fluctuation from the thermal effect of Cu and P materials, which may degrade the TL sensitivity (Chen et al., 2002). Therefore, our measured  $g(r)$  for film and TLD measurements are lower than the previous study but still within tolerance within  $<3.0\%$  deviation. However, this may occur because of the

material of our Perspex PMMA phantom that was denser than water ( $\rho=1.19 \text{ g cm}^{-3}$ ), which caused higher attenuation than water, thus lowering the dose detected by the dosimeters (Sina et al., 2015).

### Anisotropy Function

The measured  $F(r, \theta)$  at radial distances of 1 cm, 2 cm, 3 cm, 5 cm, and 10 cm in a homogenous water medium is illustrated in Figures 8a-8e. Figure 8a shows the  $F(r, \theta)$  at  $r=1$  cm. Compared to the MCNP5 calculation, the average differences are  $4.21\% \pm 2.35$  and  $4.17\% \pm 3.74$  for EBT3 film and TLD-100H, respectively. At  $10^\circ \leq \theta \leq 60^\circ$ , the difference was found to be at  $4.46\% \pm 2.04$  for film and  $4.01\% \pm 1.20$  for TLD. Meanwhile, at  $120^\circ \leq \theta \leq 170^\circ$ , the variation is at  $5.38\% \pm 3.0$  for EBT3 and  $5.72\% \pm 4.54$  for TLD-100H. The same trend was observed for  $r=2, 3, 5,$  and  $10$  cm (Figures 8b-8d). At  $r=5$  cm (Figure 8d) and  $10^\circ \leq \theta \leq 60^\circ$ , the difference was found to be  $6.44\% \pm 1.69$  for EBT3 film and  $6.74\% \pm 5.87$  for TLD-100H. At the larger distance of  $r=10$  cm (Figure 8e), the differences were  $14.99\% \pm 5.81$  for EBT3 film and  $6.41\% \pm 3.50$  for TLD-100H at  $10^\circ \leq \theta \leq 60^\circ$ . At a polar angle of  $120^\circ \leq \theta \leq 170^\circ$ , the variation is at  $6.73\% \pm 5.87$  for EBT3 and  $5.37\% \pm 2.27$  for TLD-100H. The MCNP5 calculated  $F(r, \theta)$  for  $r=0.3, 0.5, 1.0$  and  $2.0$  cm is shown in Figure 8f. As the  $F(r, \theta)$  at  $r=0.3, 0.5, 1.0$  and  $2.0$  cm at  $30^\circ < \theta < 120^\circ$  is in a good agreement with the deviation range within  $0.03\% - 0.86\%$ , which is  $< 1\%$ . Meanwhile, at  $\theta=180^\circ$ , the deviation at  $r=0.3$  cm ( $5.11\%$ ) and  $r=0.5$  cm ( $2.1\%$ ), larger than  $r=2$  cm ( $0.032\%$ ) The deviation for  $r < 0.5$  cm is larger due to the influence of dynamic internal components (DeWerd et al., 2011).

The deviation between the measured  $F(r, \theta)$  and MCNP5 calculation is on the average of  $4.94\% \pm 2.7$ . Similar to  $g(r)$ , the deviation may be caused by the different densities between water and Perspex PMMA. Figure 8 also show that the  $F(r, \theta)$  values in the backward direction are non-symmetrical, possibly due to photon disruption by the drive wires and asymmetry in encapsulation thickness (Ghiassi-Nejad et al., 2001; Sellakumar et al., 2009). In addition, the geometric and activity distribution of the source modelled in MCNP5 simulations may differ from those in the actual distribution of source in EBT3 film and TLD-100H measurements. This minor variation may contribute to the large differences between the measured and calculated doses (Chiu-Tsao et al., 2014).

In comparison, the  $F(r, \theta)$  values measured with EBT3 and TLD-100H show a good agreement with each other within  $1.57\% \pm 1.21$  at  $r=1$  cm. The relative difference of  $F(r, \theta)$  values between these is more prominent as the radial distance increases. The fluctuations occurred because of the effect of the air gap between the slab inserts in the Perspex PMMA phantom. The maximum discrepancy between EBT3 and TLD-100H was at  $10.5\% \pm 7.85$  at  $r=10$  cm. This fluctuation is most probably due to the limited size of the TLD detector, which makes it challenging to obtain unperturbed dose values. As previously proved by Uniyal et al. (2011), diminishing the size of the detector exhibit some limitations related

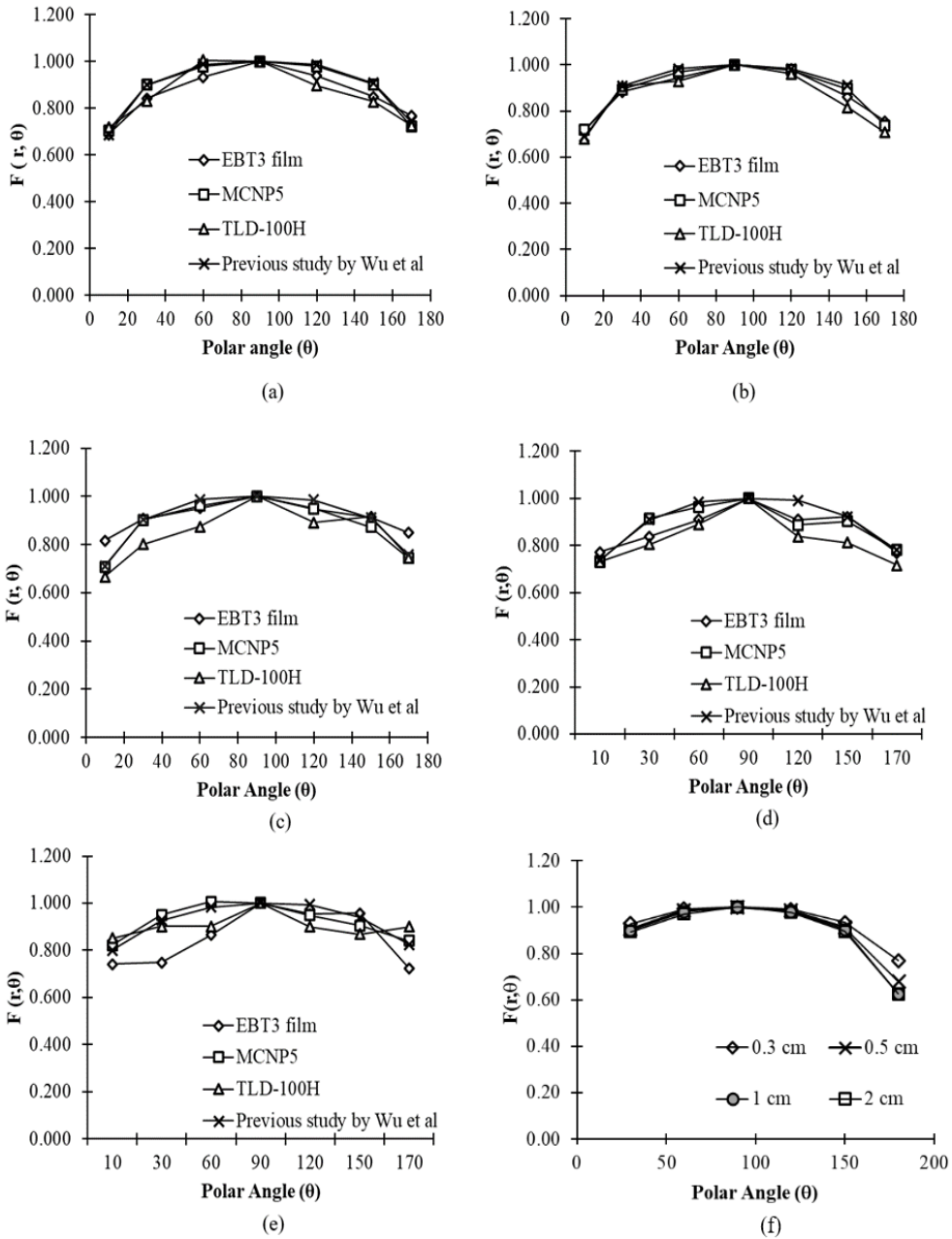


Figure 8. The measured and calculated of anisotropy function,  $F(r, \theta)$  at radial distances of (a) 1 cm, (b) 2 cm, (c) 3 cm, (d) 5 cm, (e) 10 cm in a homogenous water medium and (f) 0.3, 0.5, 1 and 2 cm calculated using MCNP5



to the improper positioning of the phantom measurement accuracy. The EBT3 film utilised in this study provides a high spatial resolution. Therefore, the angular variation of  $F(r, \theta)$  measured using EBT3 is expressed in a good response shape except for  $r=10$  cm. At this distance, the response of both EBT3 film and TLD-100H shows less sensitivity in detecting the dose since the dose followed the inverse square law. Besides that, several factors, such as the probability of film scratches and dirt during the experiment handling, may also contribute to an error in the sensitivity of the EBT3 film and TLD-100H.

### Uncertainty

The uncertainties of measurements and simulation results were calculated using NIST TN 1297. Type A uncertainty estimation is based on the standard error of the mean. For MCNP5, the relative uncertainty is 2.0% ( $k=1$ ), TLD100-H is 3.6% ( $k=1$ ), and for EBT3 measurement 3.5% ( $k=1$ ). As recommended by the previous study, for low-and high-energy brachytherapy sources of low dose rate and high dose rate, a combined dosimetric uncertainty  $<5\%$  ( $k=1$ ) is estimated (DeWerd et al., 2011). The uncertainties between measured and simulations show a small difference but within tolerance for clinical practice.

### CONCLUSION

This work demonstrates that Gafchromic® EBT3 film and TLD-100H are suitable dosimeters in  $^{192}\text{Ir}$  dosimetric measurements at a radial distance of  $<5$  cm. It was proved by a small average relative difference of  $g(r)$  at  $r=1$  to 5 cm between the measured and MCNP5, which is  $1.03\% \pm 1.25$  for EBT3 film and  $1.92\% \pm 2.35$  for TLD-100H. The  $g(r)$  data obtained between TLD and film at  $r=1$  to  $r=10$  are in good agreement with each other within  $2.10\% \pm 1.99$ . The deviation of measured  $F(r, \theta)$  in the fabricated Perspex PMMA phantom with MCNP5 is 4.94%. For both parameters, the effects are prominent at a radial distance of  $r=10$  cm with the maximum average difference of 11.47% for  $g(r)$  and 14.99% for  $F(r, \theta)$ . At this distance, the response of both EBT3 film and TLD-100H shows less sensitivity as the dose followed the inverse square law. In addition, from the comparison between the older dosimeters, the performance of EBT3 film and TLD-100H does not show a significant difference between EBT2 and TLD100.

### ACKNOWLEDGEMENT

Universiti Sains Malaysia supports the study under Short Term Grants number 304/PPSK/6315167.

### REFERENCES

- Adelnia, A., & Fatehi, D. (2016). Estimation and evaluation of tissue inhomogeneity effect on dose distribution for high dose rate iridium 192 source Using Monte Carlo simulation and film dosimetry. *Journal of Nuclear Medicine & Radiation Therapy*, 7(6), Article 1000312. <https://doi.org/10.4172/2155-9619.1000312>

- Ayoobian, N., Asl, A. S., Poorbaygi, H., & Javanshir, M. R. (2016). Gafchromic film dosimetry of a new HDR 192Ir brachytherapy source. *Journal of Applied Clinical Medical Physics*, 17(2), 194-205. <https://doi.org/10.1120/jacmp.v17i2.6005>
- Bassi, S., Cummins, D., & McCavana, P. (2020). Energy and dose dependence of GafChromic EBT3-V3 film across a wide energy range. *Reports of Practical Oncology and Radiotherapy*, 25(1), 60-63. <https://doi.org/10.1016/j.rpor.2019.12.007>
- Borca, V. C., Pasquino, M., Russo, G., Grosso, P., Cante, D., Sciacero, P., Girelli, G., La Porta, M. R., & Tofani, S. (2013). Dosimetric characterization and use of GAFCHROMIC EBT3 film for IMRT dose verification. *Journal of Applied Clinical Medical Physics*, 14(2), 158-171. <https://doi.org/10.1120/jacmp.v14i2.4111>
- Buchapudi, R., Manickam, R., & Chandaraj, V. (2019). Experimental determination of radial dose function and anisotropy function of GammaMed plus 192Ir high-dose-rate brachytherapy source in a bounded water phantom and its comparison with egs-brachy Monte Carlo simulation. *Journal of Medical Physics*, 44(4), 246-253. [https://doi.org/10.4103/jmp.JMP\\_60\\_19](https://doi.org/10.4103/jmp.JMP_60_19)
- Chandola, R., Tiwari, S., Kowar, M., & Choudhary, V. (2010). Monte Carlo and experimental dosimetric study of the mHDR-v2 brachytherapy source. *Journal of Cancer Research and Therapeutics*, 6(4), 421-426. <https://doi.org/10.4103/0973-1482.77068>
- Chen, T. C., Stoebe, T. G., Horowitz, Y. S., & Oster, L. (2002). Role of impurities in the thermoluminescence of LiF:Mg,Cu,P. *Radiation Protection Dosimetry*, 100(1-4), 243-246. <https://doi.org/10.1093/OXFORDJOURNALS.RPD.A005857>
- Chiu-Tsao, S. T., Napoli, J. J., Davis, S. D., Hanley, J., & Rivard, M. J. (2014). Dosimetry for 131Cs and 125I seeds in solid water phantom using radiochromic EBT film. *Applied Radiation and Isotopes*, 92, 102-114. <https://doi.org/10.1016/j.apradiso.2014.06.014>
- de Almeida, C. E., Rodriguez, M., Vianello, E., Ferreira, I. H., & Sibata, C. (2002). An anthropomorphic phantom for quality assurance and training in gynaecological brachytherapy. *Radiotherapy and Oncology*, 63(1), 75-81. [https://doi.org/10.1016/S0167-8140\(02\)00065-8](https://doi.org/10.1016/S0167-8140(02)00065-8)
- DeWerd, L. A., Ibbott, G. S., Meigooni, A. S., Mitch, M. G., Rivard, M. J., Stump, K. E., Thomadsen, B. R., & Venselaar, J. L. M. (2011). A dosimetric uncertainty analysis for photon-emitting brachytherapy sources: Report of AAPM Task Group No. 138 and GEC-ESTRO. *Medical Physics*, 38(2), 782-801. <https://doi.org/10.1118/1.3533720>
- DeWerd, L. A., Liang, Q., Reed, J. L., & Culberson, W. S. (2014). The use of TLDs for brachytherapy dosimetry. *Radiation Measurements*, 71, 276-281. <https://doi.org/10.1016/j.radmeas.2014.05.005>
- Faghihi, R., & Street, M. (2015). Investigation of LiF, Mg and Ti (TLD-100) reproducibility. *Journal of Biomedical Physics & Engineering*, 5(4), 217-222.
- Fazli, Z., Sadeghi, M., Zahmatkesh, M. H., Mahdavi, S. R., & Tenreiro, C. (2013). Dosimetric comparison between three dimensional treatment planning system, Monte Carlo simulation and gel dosimetry in nasopharynx phantom for high dose rate brachytherapy. *Journal of Cancer Research and Therapeutics*, 9(3), 402-409. <https://doi.org/10.4103/0973-1482.119316>
- Fiandra, C., Fusella, M., Giglioli, F. R., Filippi, A. R., Mantovani, C., Ricardi, U., & Ragona, R. (2013). Comparison of Gafchromic EBT2 and EBT3 for patient-specific quality assurance: cranial stereotactic

- radiosurgery using volumetric modulated arc therapy with multiple noncoplanar arcs. *Medical Physics*, 40(8), Article 082105. <https://doi.org/10.1118/1.4816300>
- Freire, L., Calado, A., Cardoso, J. V., Santos, L. M., & Alves, J. G. (2008). Comparison of LiF (TLD-100 and TLD-100H) detectors for extremity monitoring. *Radiation Measurements*, 43(2), 646-650. <https://doi.org/https://doi.org/10.1016/j.radmeas.2007.12.013>
- Ghiassi-Nejad, M., Jafarizadeh, M., Ahmadian-Pour, M. R., & Ghahramani, A. R. (2001). Dosimetric characteristics of <sup>192</sup>Ir sources used in interstitial brachytherapy. *Applied Radiation and Isotopes*, 55(2), 189-195. [https://doi.org/10.1016/S0969-8043\(00\)00375-4](https://doi.org/10.1016/S0969-8043(00)00375-4)
- Granero, D., Vijande, J., Ballester, F., & Rivard, M. J. (2011). Dosimetry revisited for the HDR brachytherapy source model mHDR-v2. *Medical Physics*, 38(1), 487-494. <https://doi.org/https://doi.org/10.1118/1.3531973>
- Haworth, A., Butler, D. J., Wilfert, L., Ebert, M. A., Todd, S. P., Hayton, A. J. M., & Kron, T. (2013). Comparison of TLD calibration methods for <sup>192</sup>Ir dosimetry. *Journal of Applied Clinical Medical Physics*, 14(1), 258-272. <https://doi.org/10.1120/jacmp.v14i1.4037>
- Hsu, S. M., Wu, C. H., Lee, J. H., Hsieh, Y. J., Yu, C. Y., Liao, Y. J., Kuo, L. C., Liang, J. A., & Huang, D. Y. C. (2012). A study on the dose distributions in various materials from an Ir-192 HDR brachytherapy source. *PLoS ONE*, 7(9), Article e44528. <https://doi.org/10.1371/journal.pone.0044528>
- Kirisits, C., Rivard, M. J., Baltas, D., Ballester, F., De Brabandere, M., Van Der Laarse, R., Niatsetski, Y., Papagiannis, P., Paulsen Hellebust, T., Perez-Calatayud, J., Tanderup, K., Venselaar, J. L. M., & Siebert, F. A. (2014). Review of clinical brachytherapy uncertainties: Analysis guidelines of GEC-ESTRO and the AAPM q. *Radiotherapy and Oncology*, 110, 199-212. <https://doi.org/10.1016/j.radonc.2013.11.002>
- López, J. A., Donaire, J. T., & Alcalde, R. G. (2011). Monte Carlo dosimetry of the most commonly used <sup>192</sup>Ir high dose rate brachytherapy sources. *Revista de Física Médica*, 12(3), 159-168.
- Niroomand-Rad, A., Chiu-Tsao, S. T., Grams, M. P., Lewis, D. F., Soares, C. G., Van Battum, L. J., Das, I. J., Trichter, S., Kissick, M. W., Massillon-JL, G., Alvarez, P. E., & Chan, M. F. (2020). Report of AAPM Task group 235 radiochromic film dosimetry: An update to TG-55. *Medical Physics*, 47(12), 5986-6025. <https://doi.org/https://doi.org/10.1002/mp.14497>
- Palmer, A. L., Bradley, D. A., & Nisbet, A. (2014). Dosimetric audit in brachytherapy. *The British Journal of Radiology*, 87(1041), Article 20140105. <https://doi.org/10.1259/bjr.20140105>
- Palmer, A. L., Nisbet, A., & Bradley, D. A. (2013). Semi-3D dosimetry of high dose rate brachytherapy using a novel Gafchromic EBT3 film-array water phantom. *Journal of Physics: Conference Series*, 444(1), Article 012101. <https://doi.org/10.1088/1742-6596/444/1/012101>
- Patel, N. P., Majumdar, B., & Vijayan, V. (2010). Comparative dosimetry of GammaMed Plus high-dose rate <sup>192</sup>Ir brachytherapy source. *Journal of Medical Physics*, 35(3), 137-143. <https://doi.org/10.4103/0971-6203.66761>
- Reinhardt, S., Hillbrand, M., Wilkens, J. J., & Assmann, W. (2012). Comparison of Gafchromic EBT2 and EBT3 films for clinical photon and proton beams. *Medical Physics*, 39(8), 5257-5262. <https://doi.org/10.1118/1.4737890>

- Rivard, M. J., Coursey, B. M., DeWerd, L. A., Hanson, W. F., Huq, M. S., Ibbott, G. S., Mitch, M. G., Nath, R., & Williamson, J. F. (2004). Update of AAPM Task Group No. 43 Report: A revised AAPM protocol for brachytherapy dose calculations. *Medical Physics*, *31*(3), 633-674. <https://doi.org/10.1118/1.1646040>
- Sellakumar, P., Sathish Kumar, A., Supe, S. S., Anand, M. R., Nithya, K., & Sajitha, S. (2009). Evaluation of dosimetric functions for Ir-192 source using radiochromic film. *Nuclear Instruments and Methods in Physics Research Section B: Beam Interactions with Materials and Atoms*, *267*(10), 1862-1866. <https://doi.org/https://doi.org/10.1016/j.nimb.2009.03.003>
- Shukor, N. S. A., Musarudin, M., Abdullah, R., & Aziz, M. Z. A. (2020). Effects of different volumes of inhomogeneous medium to the radial dose and anisotropy functions in HDR brachytherapy. *Journal of Physics: Conference Series*, *1497*(1), Article 012027. <https://doi.org/10.1088/1742-6596/1497/1/012027>
- Sina, S., Lotfalizadeh, F., Karimipourfard, M., Zaker, N., Amanat, B., Zehtabian, M., & Meigooni, A. S. (2015). Material-specific conversion factors for different solid phantoms used in the dosimetry of different brachytherapy sources. *Iranian Journal of Medical Physics*, *12*(2), 109-120. <https://doi.org/10.22038/ijmp.2015.4774>
- Subhalaxmi, M., & Selvam, T. P. (2015). Phantom scatter corrections of radiochromic films in high-energy brachytherapy dosimetry: A Monte Carlo study. *Radiological Physics and Technology*, *8*(2), 215-223. <https://doi.org/10.1007/s12194-015-0310-9>
- Uniyal, S. C., Naithani, U. C., & Sharma, S. D. (2011). Evaluation of Gafchromic EBT2 film for the measurement of anisotropy function for high-dose-rate <sup>192</sup>Ir brachytherapy source with respect to thermoluminescent dosimetry. *Reports of Practical Oncology and Radiotherapy*, *16*(1), 14-20. <https://doi.org/10.1016/j.rpor.2010.11.003>
- Wu, C. H., Liao, Y. J., Liu, Y. W. H., Hung, S. K., Lee, M. S., & Hsu, S. M. (2014). Dose distributions of an <sup>192</sup>Ir brachytherapy source in different media. *BioMed Research International*, *2014*, Article 946213. <https://doi.org/10.1155/2014/946213>

## **Development of Attendance and Temperature Monitoring System using IoT with Wireless Power Transfer Application**

**Noramalina Abdullah\* and Sarah Madihah Mohd Shazali**

*School of Electric and Electronic Engineering, Universiti Sains Malaysia, Engineering Campus, 14300 USM, Penang, Malaysia*

### **ABSTRACT**

Enclosed areas pose a greater risk of transmitting infectious and bacterial diseases. The proposed system helps prevent disease by tracking students' daily body temperature before entering the school premises. Each student will be provided with a unique QR code containing the student information, such as their name and class. The QR code needs to be scanned first by the camera-equipped smartphone before reading the body temperature. The thermometer will record the student's body temperature and send the information to the smartphone via Bluetooth. The student's profile will be updated with the recorded daily temperature. An Android application will be developed to scan the QR code and display the students' profiles and information. In order to design a battery-less system, the system will be integrated with a wireless power transfer circuit. Based on the simulation results, the wireless power transfer circuit can be used as a wireless charger for the smartphone used in the system or for charging the thermometer of the thermometer.

*Keywords:* Android application, Arduino, infrared thermometer, QR code, temperature monitoring, wireless power transfer

### ARTICLE INFO

*Article history:*

Received: 17 August 2021

Accepted: 27 September 2021

Published: 10 January 2022

DOI: <https://doi.org/10.47836/pjst.30.1.38>

*E-mail addresses:*

eenora@usm.my (Noramalina Abdullah)

sarah.madidah@yahoo.com (Sarah Madihah Mohd Shazali)

\*Corresponding author

### **INTRODUCTION**

Viral and bacterial diseases, such as flu and cold, are very common diseases that researchers have been trying to develop a cure for, yet all the medicine available is to alleviate the symptoms instead of curing them (Alkhatay et al., 2015). The best approach for this problem is to avoid contracting the virus carrier to avoid spreading the disease among the community (Lee et al., 2012).

Fever is one of the initial and typical symptoms indicating the presence of viruses in individuals, including SARS and COVID-19 (Addi et al., 2020). Omron, a Japanese electronics company, has mentioned on their website that the most accurate standards are taken from rectal measurement, which is 37.0°C to 37.5°C. In contrast, oral measurement gives a slightly lower reading of 36.8° ± 0.4 °C. Furthermore, measurements were taken on the skin, such as axillary (armpit), tympanic (ear), and forehead, gives the lowest reading out of these types, which is 36.5°C (OmronHealthcare, 2020). Regarding the current pandemic, enforcement is required to record the attendees and their body temperature to detect early signs of fever, as fever is known as one of the symptoms that affect 89% of patients (Guan et al., 2020). A clinical analysis has found that conventional thermometry is better than self-reported fever when seasonal influenza patients are identified (Haghmohammadi et al., 2018).

Several papers propose a temperature monitoring system in detecting body temperature. Alkhatay et al. (2015) and Huang et al. (2016) suggested a fever detection system that uses multiple infrared cameras, which allowed the room temperature to be controlled and identify students that have a temperature higher than 37 °C (Alkhatay et al., 2015; Huang et al., 2016). Apart from that, Somboonkaew et al. (2017) and Haghmohammadi et al. (2018) proposed the usage of thermal imaging from IR cameras. Their system does general screenings on random passers-by and does not collect any details of the person. Zhang (2018) developed a design of a non-contact infrared thermometer to compensate for the drawbacks of the traditional mercury thermometer to measure a single student at a time. MLX90614 infrared temperature sensor was used to collect the body temperature of the individual. Buzzer alarm was also included in his design to alert the user when the body temperature exceeds the set value, which is 37°C. Ebeid et al. (2020) also designed a non-contact forehead thermometer with the purpose of early detection of Coronavirus with the accuracy of ±0.3°C.

This project includes the attendance tracking features with the temperature monitoring system, as the student needs to register themselves before taking their body temperature. There are several taking-attendance apart from the traditional attendance taking method in a class, such as fingerprints scanners, facial recognition, Radio-Frequency Identification (RFID), Bluetooth, and QR code (Monday et al., 2018). Other approaches that used the low-cost setup are Bluetooth, and QR codes did not require the usage of any other additional device apart from a personal-owned smartphone (Raj et al., 2019). As for Bluetooth, the main Bluetooth device detect all the MAC address, which is within its range, and automatically logs their attendance (Gohel, 2018). However, Bluetooth connection struggles in pinpointing the exact attendees, as sometimes, MAC addresses from passers-by can also be detected and included in the attendance data.

Wireless power transfer (WPT) and data communication are important research problems with various applications. However, these two problems are usually studied separately. WPT is useful to electrical power devices where interconnecting wires are inconvenient, hazardous, or impossible. It consists of three mains: the transmitter circuit, receiver circuit, and coils. The transmitter's oscillator circuit transforms the input power into an electromagnetic field, transmitted by an antenna transmitter or coupling system. Similar coupling mechanisms on the recipient side are used to change the received electromagnetic field into an electric current, which the receiver devices may operate (Navin et al., 2017). He also reported that the frequency has a huge effect on the output power rate. A magnetic field will be generated from the WPT of the coils and metal. This project focuses on the magnetic resonant inductive coupling technique for applying a wireless charger system due to the high output power and the range of its distance. As the coil shape also affects the power transfer rate, the circular shape of the transmitter coil and receiver coil was chosen. According to research done by Shah and Abuzneid (2019), spiral coils was found to be more suitable compared to circular coils, as it has a higher Q-factor and consumes less space. With the recent technology and demand for a portable device, we are working on integrating the data communication aspect with WPT for a better consequence.

## METHODOLOGY

### Implementation of Infrared Thermometer with QR code

The proposed system uses a non-contact infrared thermometer and will include a QR code. The flowchart of the system design is shown in Figure 1.

The admin will generate a unique QR code during the student registration. The tag with the QR code, which acts similarly to a matric card and contains the links to the students' profiles, will then be provided to each student. As the student arrives at school, they will be required to scan their tag at the scanner in the smartphone. The phone will display the students' profiles, such as their names and classes. The time and attendance will be recorded as the students scan their tags. In addition, an infrared thermometer will be used to monitor the students' body temperature. There are two situations that the alarm will go off:

- The temperature is lower than 35.5°C. It will prompt the student to retake the reading until the temperature is within the acceptable range (35.5°C–37.5°C).
- The temperature is higher than 37.5°C. It will alert the teacher that the student has a fever and further action needs to be taken by the school.

The whole procedure has practically accomplished and successes.

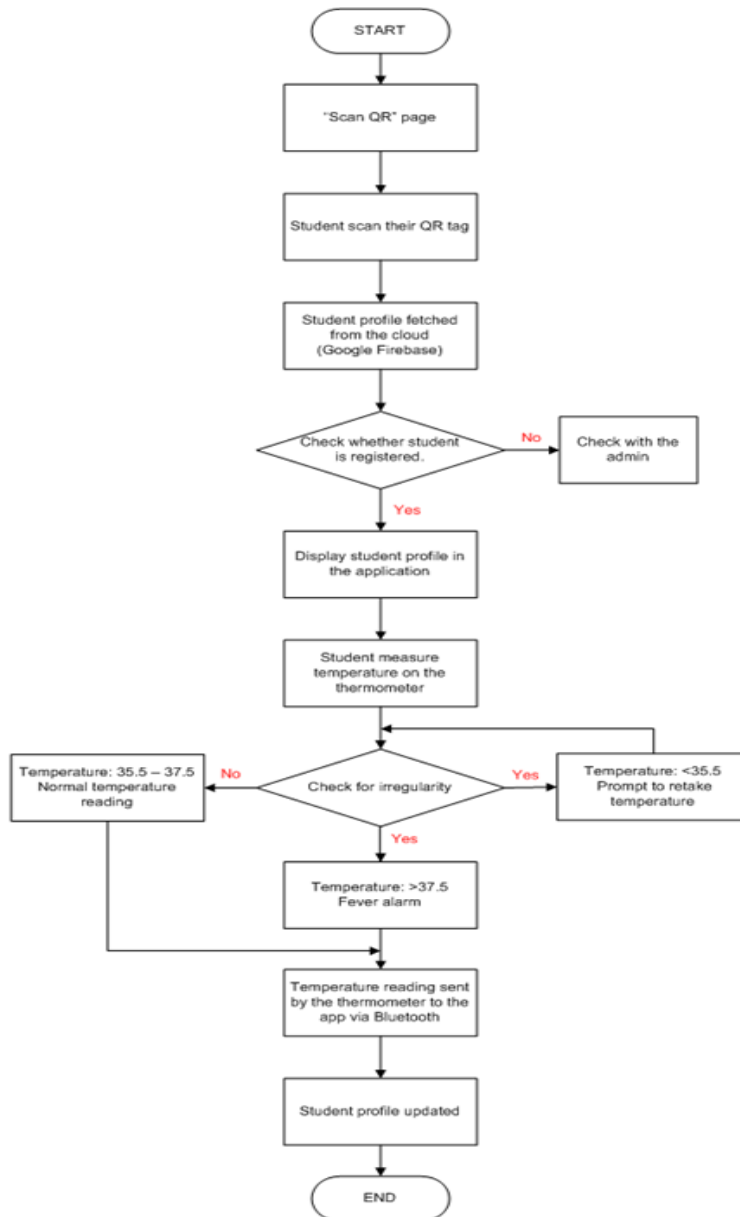


Figure 1. Flowchart of temperature measurement process

### Implementation of Arduino Microcontroller

Figure 2 shows the circuit of the contactless IF thermometer. The thermometer consists of an MLX90614 infrared temperature sensor connected to an Arduino microcontroller. The whole procedure has practically accomplished and successes.



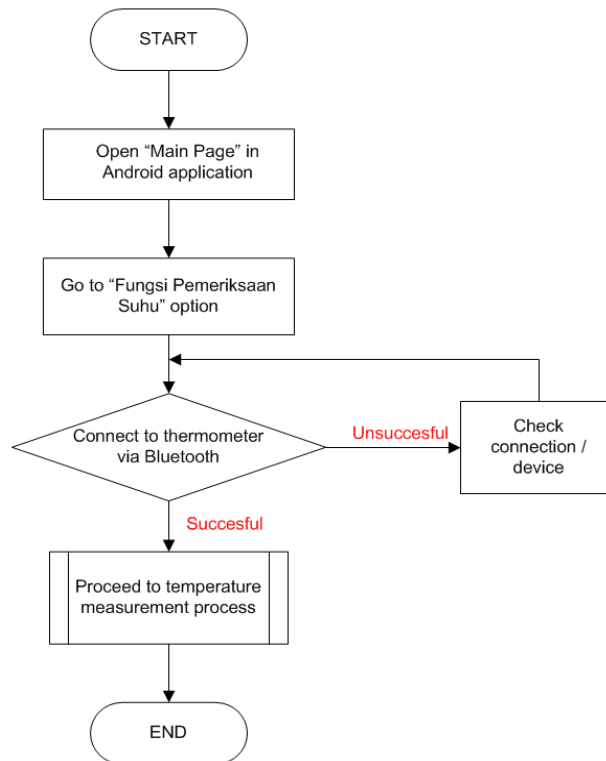


Figure 2. Flowchart of the initial process before temperature measurement process

For normal temperature, the data will automatically be updated to the student's profile and the school's database. When the scanner detects an abnormal temperature, the alarm will go off. In addition, the APDS9960 proximity sensor will be installed on the thermometer. The APDS9960 proximity sensor helps minimise contact, as it can detect the presence of nearby objects without direct physical contact and thus automatically activate the thermometer. It will automatically activate the thermometer once it detects the presence of nearby objects.

An LCD was used to display the body temperature reading. If the thermometer detects an abnormally low-temperature reading, which is less than  $35.5^{\circ}\text{C}$ , the default message of "NOT DETECTED" will be displayed, thus prompting the user to retake their temperature. This message was displayed when the user stood too far for the thermometer to get an accurate body temperature reading. When the thermometer detects a temperature higher than  $37.5^{\circ}\text{C}$ , the LCD will produce a warning message, and the buzzer will produce a loud beep to alert the teacher. In order to test the accuracy of the system thermometer, the body temperature reading taken by the system thermometer was compared with the temperature

taken by the K3 infrared thermometer, which is currently available in the market and widely used in public premises, such as hospitals, restaurants, and shops. In addition, the time to measure the student's body temperature was taken at various times every day to get various ambient temperature readings throughout the day.

### Implementation of Bluetooth

A Bluetooth module (HC-05 Arduino) will also be connected to the circuit to send the data from the thermometer to a smartphone. For scanning the QR code, an Android application was developed in AndroidStudio. The whole procedure has practically accomplished and successes.

The application can be connected to the Bluetooth module in the thermometer circuit, thus allowing the temperature reading to be sent to the smartphone and updated in the student's profile. The process of connecting the thermometer to the application is shown in Figure 3. The application also allows the teacher to install and view the scanned history of any recorded day. The system used Google Firebase as its database. The Android application will only be distributed to teachers and admin, thus allowing teachers to access the student profile just from their mobile phone to check and view the student's details and attendance. However, the registration of new students and the profile editing process can only be done by the admin, as shown in Figure 4.

### Application of WPT

With the advantages of WPT, it will be used as a mobile phone charger. The whole procedure has been completely done by using simulation.

Two circuits are involved: the transmitter (Figure 5) and receiver (Figure 6). These circuits are simulated in the Proteus software. The transmitter circuit consists of an oscillator circuit and transmitter coil used to transmit the voltage wirelessly. For the oscillator circuit, a Royer oscillator is chosen, as it has many advantages, such as the simplicity of the design and lesser components required for the circuit. The operating frequency formula for the resonance circuit (Equation 1),

$$F = \frac{1}{2\pi\sqrt{LC}} \quad [1]$$

The oscillator circuit consists of two n-channel MOSFET, two 1N4148 diodes, two 4.7k $\Omega$  resistors, two 470 $\Omega$  resistors and a 330 $\mu$ H inductor. As for the transmitter coil, it is connected to the oscillator circuit with a 1 $\mu$ F capacitor. The receiver circuit, which receives the wireless voltage from the transmitter circuit, consists of a receiver coil, rectifier circuit and a voltage regulator. The receiver coil, consisting of 7 $\mu$ H inductive coils and a 1 $\mu$ F capacitor, is connected to the receiver circuit. By using Equation 1, the resonance frequency for the circuit was calculated.

$$F = \frac{1}{2\pi\sqrt{(7 \times 10^{-6})(1 \times 10^{-6})}}$$

$$F = 60.15 \text{ kHz}$$

The circuit includes a bridge rectifier which will rectify the input AC voltage to DC voltage. Four individual rectifying diodes are used and connected in a full-wave bridge arrangement. A smoothing capacitor will also be added across the output of the bridge rectifier to convert the full-wave voltage ripple from the rectifier to a smooth DC output voltage. The main advantage of using a full-wave bridge rectifier instead of a half-wave bridge rectifier is that the former produces a smaller AC ripple for the given load, making it more stable. The receiver circuit consists of four diodes, a 1µF capacitor, a 7805-voltage regulator and a 1µF capacitor smoothing capacitor. Seven thousand eight hundred five voltage regulators are used to produce a regulated 5V output from the DC voltage obtained from the rectifier. In addition, the smoothing capacitor will act as a filter to smoothen the DC voltage from the rectifier.

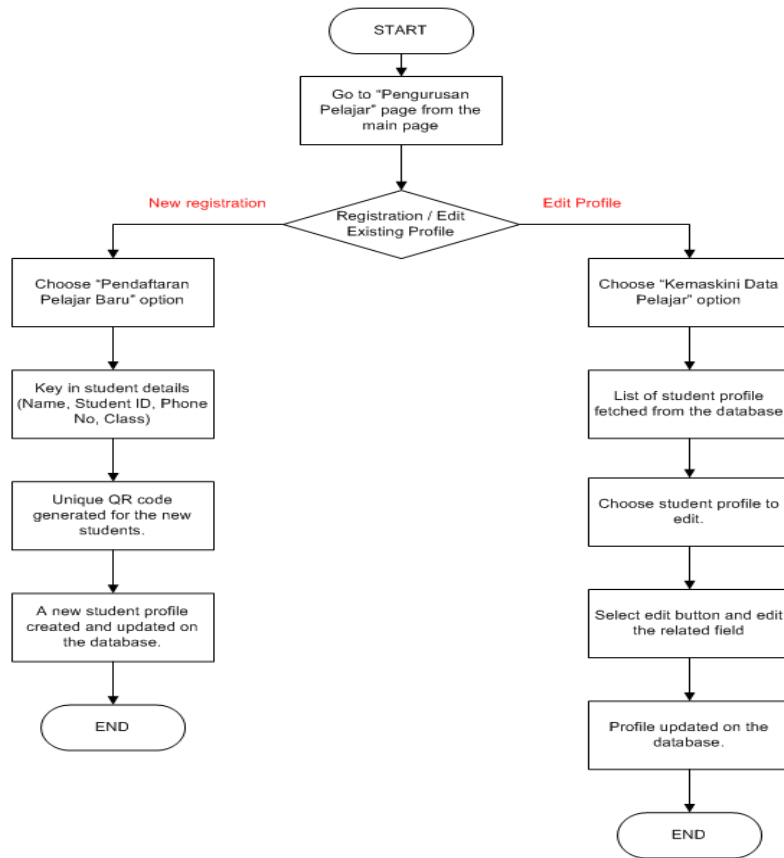


Figure 3. Flowchart for the student management process (can only be accessed by admin)

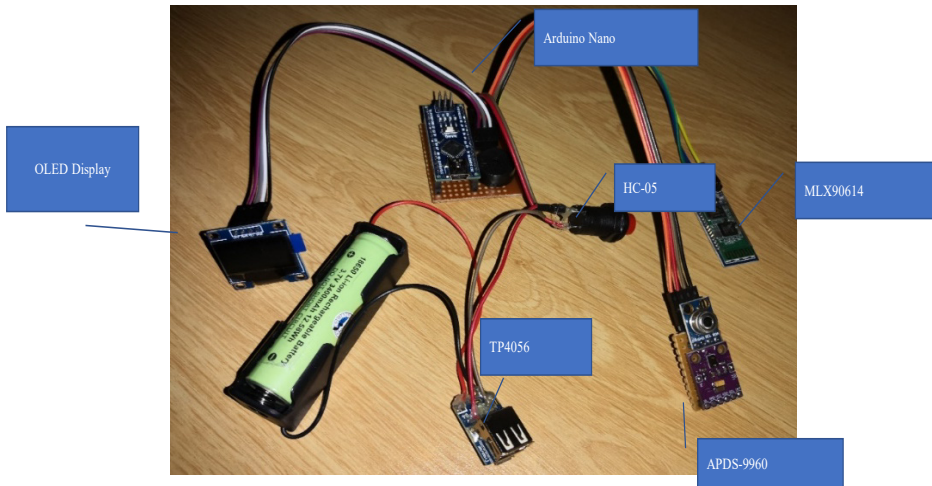


Figure 4. Circuit of the non-contact infrared thermometer

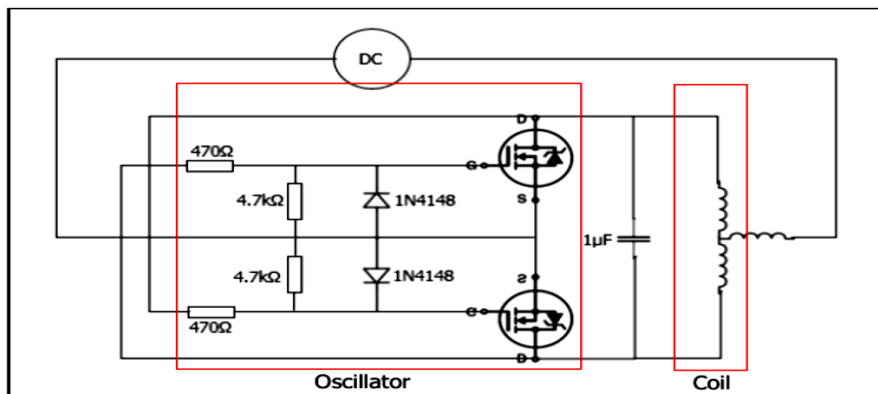


Figure 5. Transmitter circuit

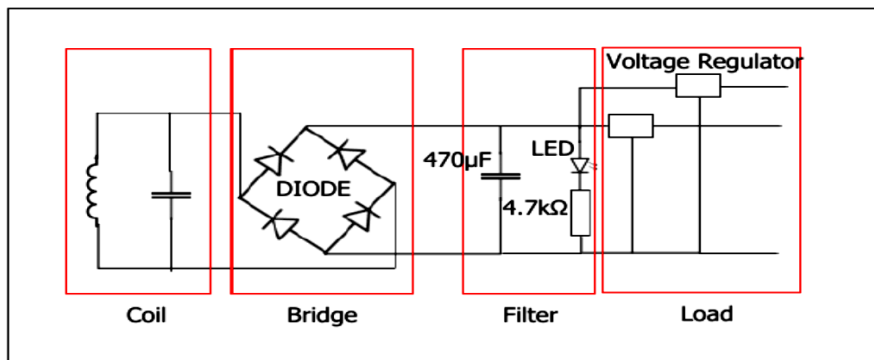


Figure 6. Receiver circuit

## RESULTS AND DISCUSSION

### Results for Temperature Detection and Analysis

When the thermometer takes the body, the temperature detects a reading lower than 35.5°C, the temperature taken will be considered an error, and the temperature will not be recorded into the system. The display will show the “NOT DETECTED” message, as shown in Figure 7 until the thermometer can take a reasonable temperature reading. In contrast, for temperatures above 35.5°C, the measured body temperature will be displayed on the OLED, as shown in Figure 8, and recorded in the student’s profile. The alarm will be triggered for this system, and loud noise will be produced from the buzzer when the body temperature taken by the system thermometer detects a temperature higher than 37.5°C, as shown in Figure 9. It indicates that the student has a fever, as stated in the Ministry of Health guidelines of normal body temperature. The body temperature reading was taken from 4 students. Their average temperature for the day was taken to see the relation between the ambient temperature and the average body temperature. The lowest ambient temperature was at 28.58°C on Day 9. At the same time, the highest ambient temperature reading was at 34.23°C on Day 4.



Figure 7. Default message for when error temperature is detected

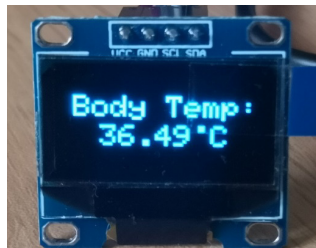


Figure 8. Normal body temperature reading



Figure 9. High body temperature reading

The readings in Figure 10 and Figure 11 show the temperature reading comparison taken by the system’s thermometer (ST) and K3 infrared thermometer (K3). Figure 10 shows the obtained temperature reading when the ambient temperature is highest, while Figure 11 shows the temperature readings when the ambient temperature is lowest. Based on Figure 10 and Figure 11, the average difference in body temperature taken by the system thermometer and K3 thermometer is in the range of  $\pm 0.01$ . Thus, it can be said that the system thermometer is considered reliable and is on par in terms of accuracy, with other available thermometers on the market. The result is further proven statistically using SPSS.

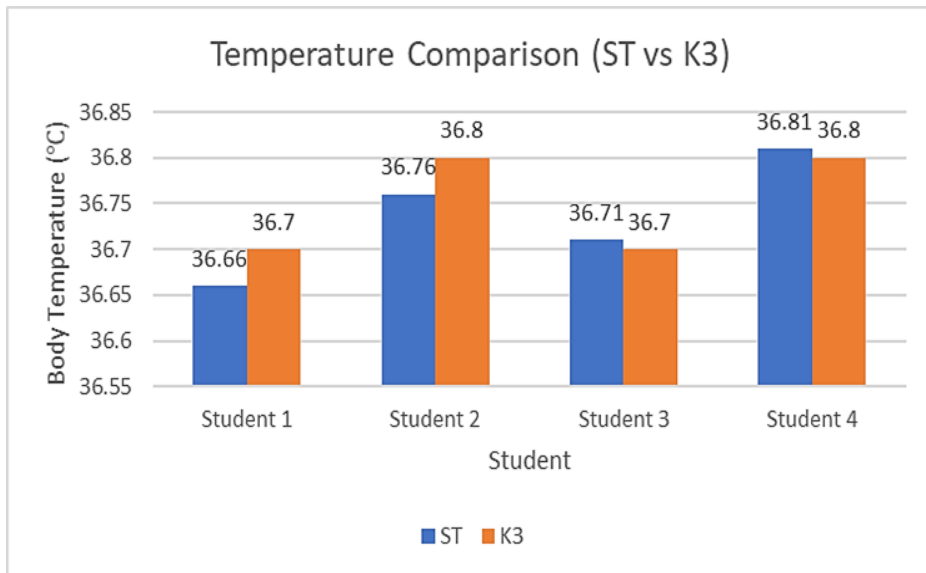


Figure 10. Temperature comparison between system thermometer (ST) and K3 infrared thermometer (K3) when ambient temperature is at the highest (34.23 °C)

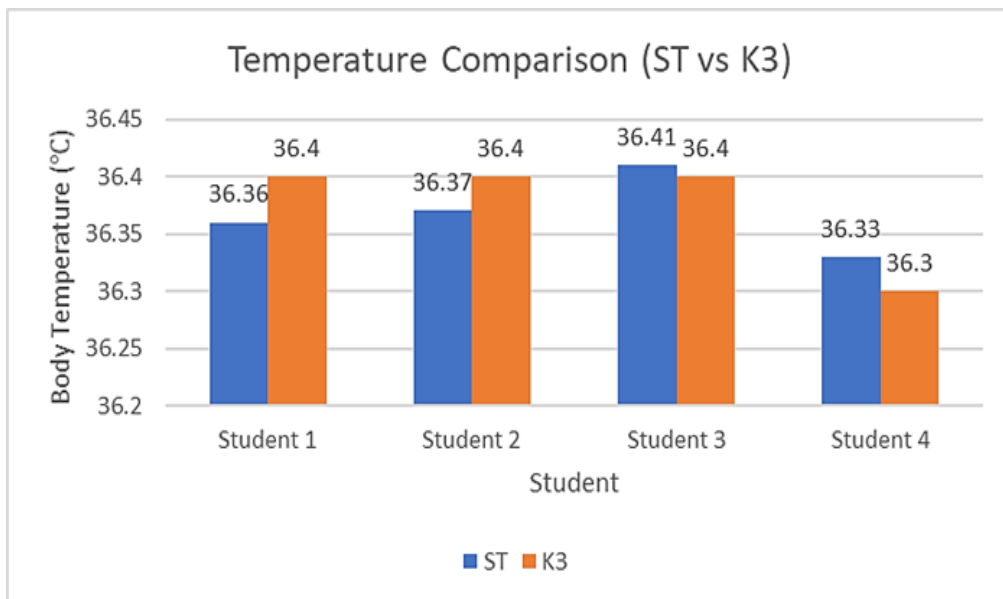


Figure 11. Temperature comparison between system thermometer (ST) and K3 infrared thermometer (K3) when ambient temperature is at the lowest (28.58 °C)

This result found that the mean value of the system thermometer, ST ( $36.53 \pm 0.03^\circ\text{C}$ ), is relatively similar to the mean value of the K3 thermometer ( $36.55 \pm 0.03^\circ\text{C}$ ) with a very small mean difference between these two methods ( $0.03^\circ\text{C}$ ). Statistically, there is no significant difference observed between the mean values of ST and K3 ( $p=0.548$ ). Therefore, it is noted that the reading of both ST and K3 was relatively equal and could be implemented. When the ambient temperature is high at  $34.23^\circ\text{C}$ , the average body temperature is around  $36.74^\circ\text{C}$ . The relation between these two parameters can be seen further seen in Figure 12, where the ambient temperature has shown significant positive correlations with ST ( $r=0.728$ ,  $p<0.01$ ) as well as K3 thermometer ( $r=0.778$ ,  $p<0.01$ ). Therefore, it can be deduced that the increase or decrease of ST and K3 thermometers are significantly associated with the changes in the ambient temperature when the reading is taken, which should be within ten days. Based on the overall reading, the recorded body temperature taken is between  $36.2^\circ\text{C}$  to  $36.9^\circ\text{C}$ . Statistically, using SPSS proves that the ambient temperature strongly affects the temperature reading taken by ST and K3.

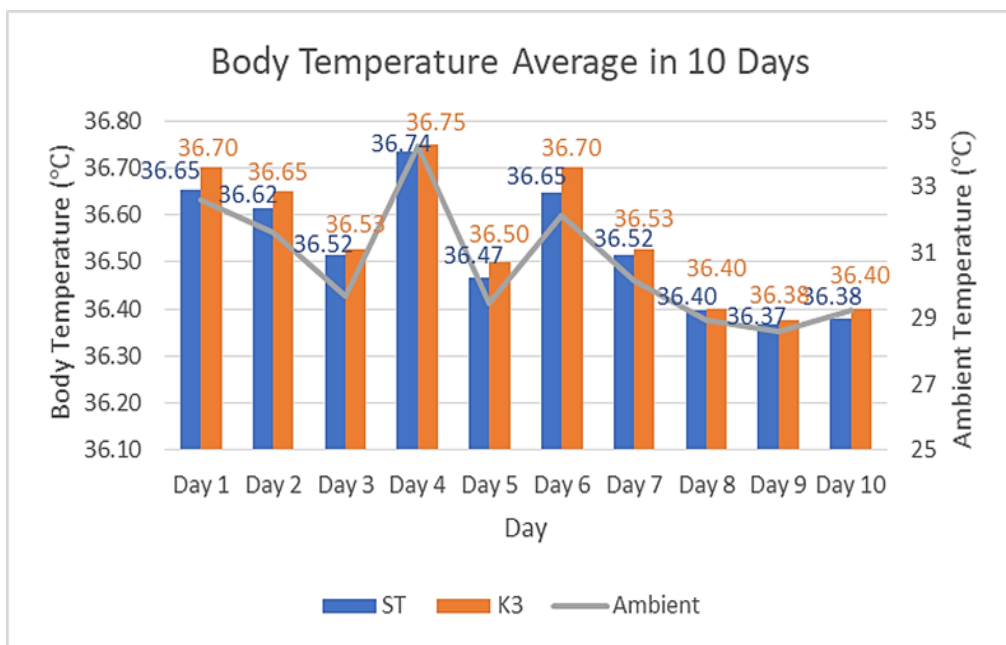


Figure 12. Average body temperature reading in the span of 10 days

### Results with Android Application

There are three main features included in the Android application, which are: (i) Student Management, (ii) Admission History, and (iii) Temperature Checking Function. The “Student Management” feature allows the teacher to register new students or edit the existing students’ information. Once a new student is registered, a unique QR code will be generated automatically. The code can be printed and attached to the tag for the student to use while scanning. Student’s history can be viewed as well, which includes the date and time when the student’s scan their tag and the temperature recorded at that time, as shown in Figure 13 (a), (b) and (c), respectively. Finally, the “Admission History” feature allows the teacher to view the scan history for the day or the overall history. For example, in Figure 13 (c), the list shows the student’s name, class, the temperature recorded by the thermometer, and the date and time when the tag is scanned. In addition, it allows the teacher to check for any lack of punctuality or absentees.

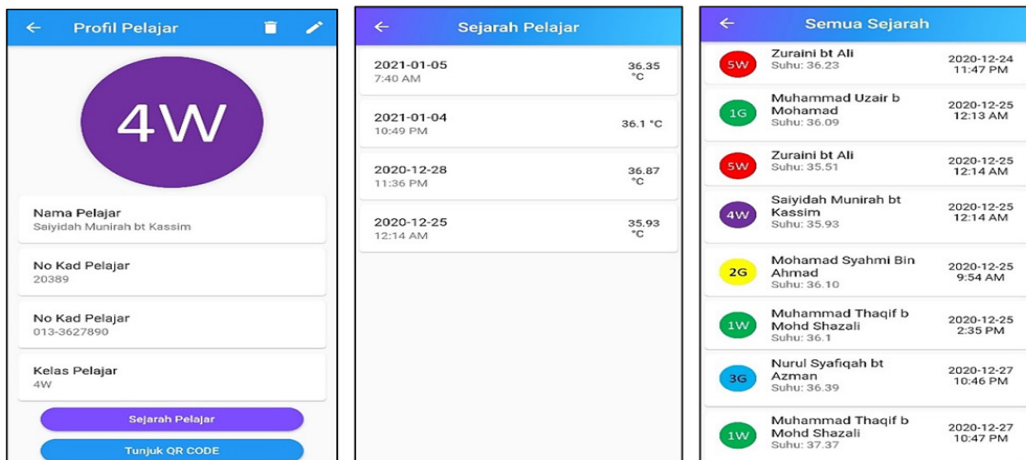


Figure 13. IoT information platform (a) Student’s profile (b) Student history (c) Overall history

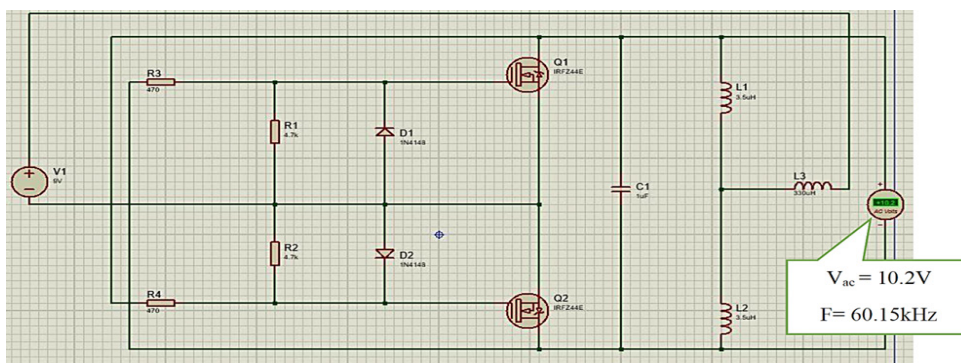


Figure 14. Transmitter circuit with inductive coil of 7μH



### Results with Bluetooth-QR Code Verification

As for the “Temperature Checking Function” feature, it is used for temperature checking. By selecting this option, a Bluetooth configuration page will pop up, which allows the smartphone to connect to the thermometer via Bluetooth. Once the connection is established, the student will be required to scan their forehead, and after the temperature is recorded, a page with a QR scanner will pop up, allowing the student to scan their tag. Next, the detected temperature will then be updated to the profile that belongs to the scanned tag.

### Results with WPT Simulation

The transmitter circuit in Figure 14 will transmit the power wirelessly to the receiver circuit. The testing inductance value used in the simulation is  $7\mu\text{H}$ . By referring to Equation 1, the inductance value is high while the operating frequency is low. As for the receiver circuit illustrated in Figure 15, the input for the voltage source is obtained from the output at the transmitter circuit. A minimum output of 5V is needed to comply with the requirement for the WPT application. The simulation results show that the circuit can produce a voltage output of more than 5V. The output voltage can be tuned based on the value of inductance used in the circuit. The number of turns for the coils can be varied to adjust the inductance value. The results show that the system can be powered using WPT instead of a rechargeable battery.

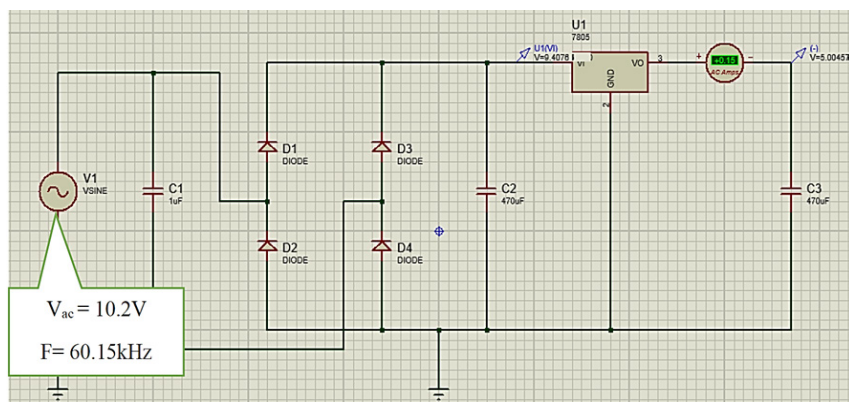


Figure 15. Receiver circuit with inductive coil of  $7\mu\text{H}$

### CONCLUSION

The proposed system included the attendance-taking method using the QR Code to integrate an Android application and simulation for WPT purposes. We have successfully developed the IoT platform with useful information. It is the most contribution we have achieved

compared with other research works. Furthermore, we have successfully investigated the potential integration with wireless power transfer. The wireless power circuit will be practically integrated into the system to make the system more portable and to charge the thermometer's battery. The finding will be further implemented to other premises for an efficient attendance record and monitoring. In the future, a web-based platform can also be included in the system, apart from the current Android application installed in the teacher's phone, for an easier monitoring process.

## ACKNOWLEDGEMENTS

The authors would like to thank the Department of Research and Innovation Universiti Sains Malaysia for giving the opportunity and support throughout the completeness of this work.

## REFERENCES

- Addi, R. A., Bensim, A., Amine, M., & Cherkaoui, M. (2020). Asymptomatic COVID-19 infection management: The key to stop COVID-19. *Journal of Clinical and Experimental Investigations*, 11(3), 1-2. <https://doi.org/10.5799/jcei/7866>
- Alkhayat, A. H., Bagheri, N., Ayub, M. N., & Noor, N. F. M. (2015). Fever detection & classroom temperature adjustment: Using infrared cameras. In *2015 IEEE International Conference on Consumer Electronics-Taiwan* (pp. 240-241). IEEE Publishing. <https://doi.org/10.1109/ICCE-TW.2015.7216876>
- Ebeid, A. G., Selem, E., & El-Kader, S. M. A. (2020). Early detection of COVID-19 using a non-contact forehead thermometer. In *International Conference on Advanced Intelligent Systems and Informatics* (pp. 314-323). Springer. [https://doi.org/10.1007/978-3-030-58669-0\\_29](https://doi.org/10.1007/978-3-030-58669-0_29)
- Gohel, S. (2018). Bluetooth attendance system with android application for ERP. In *2018 International Conference on Computing, Power and Communication Technologies (GUCON)* (pp. 481-484). IEEE Publishing. <https://doi.org/10.1109/GUCON.2018.8674898>
- Guan, W., Ni, Z., Hu, Y., Liang, W., Ou, C., He, J., Liu, L., Shan, H., Lei, C., Hui, D. S. C., Du, B., Li, L., Zeng, G., Yuen, K. Y., Chen, R., Tang, C., Wang, T., Chen, P., Xiang, J., Zhong, N. (2020). Clinical characteristics of Coronavirus disease 2019 in China. *New England Journal of Medicine*, 382(18), 1708-1720. <https://doi.org/10.1056/NEJMoa2002032>
- Haghmohammadi, H. F., Neculescu, D. S., & Vahidi, M. (2018). Remote measurement of body temperature for an indoor moving crowd. In *2018 IEEE International Conference on Automation, Quality and Testing, Robotics (AQTR)* (pp. 1-6). IEEE Publishing. <https://doi.org/10.1109/AQTR.2018.8402698>
- Huang, P. W., Chang, T. H., Lee, M. J., Lin, T. M., Chung, M. L., & Wu, B. F. (2016). An embedded non-contact body temperature measurement system with automatic face tracking and neural network regression. In *2016 International Automatic Control Conference (CACS)* (pp. 161-166). IEEE Publishing. <https://doi.org/10.1109/CACS.2016.7973902>

- Lee, B., Yoon, J., Kim, S., & Hwang, B. Y. (2012). Detecting social signals of flu symptoms. In *8th International Conference on Collaborative Computing: Networking, Applications and Worksharing (CollaborateCom)* (pp. 544-545). IEEE Publishing. <http://dx.doi.org/10.4108/icst.collaboratecom.2012.250355>
- Monday, H. N., Dike, I. D., Li, J. P., Agomuo, D., Nneji, G. U., & Ogungbile, A. (2018). Enhanced attendance management system: A biometrics system of identification based on fingerprint. In *2018 IEEE 9th Annual Information Technology, Electronics and Mobile Communication Conference (IEMCON)* (pp. 500-505). IEEE Publishing. <https://doi.org/10.1109/iemcon.2018.8614776>
- Navin, K., Shanthini, A., & Krishnan, M. B. M. (2017). A mobile based smart attendance system framework for tracking field personals using a novel QR code-based technique. In *2017 International Conference on Smart Technologies for Smart Nation (SmartTechCon)* (pp. 1540-1543). IEEE Publishing. <https://doi.org/10.1109/smarttechcon.2017.8358623>
- OmronHealthcare. (2020). *Does the temperature reading depend on the body part where the reading is taken?* Omron Healthcare. Retrieved November 5, 2020, from <https://www.omronhealthcare-ap.com/my/faqs/temperature-measurement/406>
- Raj, R., Das, A., & Gupta, S. C. (2019). Proposal of an efficient approach to attendance monitoring system using Bluetooth. In *2019 9th International Conference on Cloud Computing, Data Science & Engineering (Confluence)* (pp. 611-614). IEEE Publishing. <https://doi.org/10.1109/confluence.2019.8776978>
- Shah, S. N., & Abuzneid, A. (2019). IoT based smart attendance system (SAS) using RFID. In *2019 IEEE Long Island Systems, Applications and Technology Conference (LISAT)* (pp. 1-6). IEEE Publishing. <https://doi.org/10.1109/LISAT.2019.8817339>
- Somboonkaew, A., Prempre, P., Vuttivong, S., Wetcharungsri, J., Porntheeraphat, S., Chanhorm, S., & Sumriddetchkajorn, S. (2017). Mobile-platform for automatic fever screening system based on infrared forehead temperature. In *2017 Opto-Electronics and Communications Conference (OECC) and Photonics Global Conference (PGC)* (pp. 1-4). IEEE Publishing. <https://doi.org/10.1109/oecc.2017.8114910>
- Zhang, J. (2018). Development of a non-contact infrared thermometer. In *2017 International Conference Advanced Engineering and Technology Research (AETR 2017)* (Vol. 153). Atlantis Press. <https://doi.org/10.2991/aetr-17.2018.59>



## Octave Band Technique for Noise Measurement at the Source, Path, and Receiver of Gas Turbines in Oil and Gas Facilities

Akmal Haziq Mohd Yunos\* and Nor Azali Azmir

*Faculty of Mechanical and Manufacturing Engineering, Universiti Tun Hussein Onn Malaysia, Batu Pahat, 86400, Johor Malaysia*

### ABSTRACT

Noise measurement is essential for industrial usage. However, further attention to preventing noise pollution is needed, especially when working with equipment generating a high noise level, such as gas turbines. This study aims to determine the best way to perform noise measurement and analyze the octave band frequency generated by noise pollution caused by gas turbine equipment. Data from site measurements show that the gas turbines produce more than 85 dB of noise with a Z-weighted measurement. A noise measuring investigation was conducted to obtain the data for the 1/3 octave band. A frequency-domain was used to comprehend the properties of the noise measurement frequency band. The frequency band was classified into three different zones called low, medium, and high frequency, which is useful in noise measurement analysis to identify a viable solution to reduce the noise. On-site sampling was performed at the source, path, and receiver of three separate gas turbine locations within oil and gas operations. The 1/3 octave band data collection results at the sound source, path, and receiver demonstrate the noise level distribution at the perimeter of gas turbine installations in the low and medium frequency ranges. Most of the high noise frequency range is between 250 Hz and 2 kHz for source, path, and receiver. All acquired values are compared to the Department of Safety and Health (Occupational Safety

and Health (Noise Exposure) Regulations 2019 in Malaysia. As a result, oil and gas service operators can monitor and take countermeasures to limit noise exposure at oil and gas facilities.

*Keywords:* Control measure, gas turbines, noise measurement, Octave band, oil and gas facilities

### ARTICLE INFO

*Article history:*

Received: 18 August 2021

Accepted: 1 November 2021

Published: 10 January 2022

DOI: <https://doi.org/10.47836/pjst.30.1.39>

*E-mail addresses:*

[akmalhaziqmy@gmail.com](mailto:akmalhaziqmy@gmail.com) (Akmal Haziq Mohd Yunos)

[azali@uthm.edu.my](mailto:azali@uthm.edu.my) (Nor Azali Azmir)

\*Corresponding author

## INTRODUCTION

A gas turbine is a turbomachinery piece used to generate electricity for industry. In today's world economy, the gas turbine is essential to power up remote areas, such as oil and gas facilities. It is widely used on the platform to generate power for multiple types of equipment. Since it is vital equipment for the oil and gas industry, it is now looking for a highly efficient gas turbine unit. This equipment will be the only option to generate electricity onboard oil and gas facilities, such as offshore platforms. Turbomachinery equipment is referred to as rotating equipment that uses multiple moving components and creates the power to reach its target performance. However, these components produce excessive noise when the gas turbine operates. It could also be considered a noticeable occupational health issue as it affects the workers' hearing health when carrying out jobs near the gas turbines. A previous study shows that Malaysian workers are affected by noise-induced hearing loss (NIHL), and it was the highest occupational health issue in 2014 (Sam et al., 2017).

Noise is a type of occupational hazard, and the industry should set a target to reduce noise to an acceptable level and help conserve workers' hearing health. This action requires the implementation of any countermeasure that could reduce the volume of noise generated or reduce the noise path through the air and its transmission or through the person exposed to the noise path itself. The countermeasures include engineering modification of equipment, the working area operations, and the room layout itself. The best approach for noise control in the workplace is to reduce the exposure or eliminate noise source generation, either by direct action on the source or by its confinement.

Noise from the engine with a turbofan is produced by a few different parts of the gas turbine and the airflow that generates turbulence. Each noise component produced by the different parts of the engine impacts the overall generated noise depending on the type of turbofan (El-Badawy & El-Arna'outy, 2007). Engine noise is caused by all engine parts, such as compressors, rotors, stators, combustors, turbine blades, and exhaust. However, the loudest noise is generated by the air intake and the exhaust (Cumpsty & Marble, 1977). Since the two modules generate the most noise, noise reduction techniques are primarily applied to these modules. A section of gas turbines that is commonly used in the industry is shown in Figure 1.

Noise can cover a broad range of situations, such as excessive vibrations in the structure of mechanical equipment or equipment component failures during operation. The American Academy of Ophthalmology and Otolaryngology has established a sound pressure level that should not exceed 85 dB(A) in low and medium frequency for more than 5 hours (Tiede, 1969). Furthermore, in the Occupational Safety and Health (Noise Exposure) Regulation 2019, Regulation 6(2) states that where it appears to an employer that any of his employees are exposed to an excessive noise exceeding the noise exposure limit of daily noise exposure

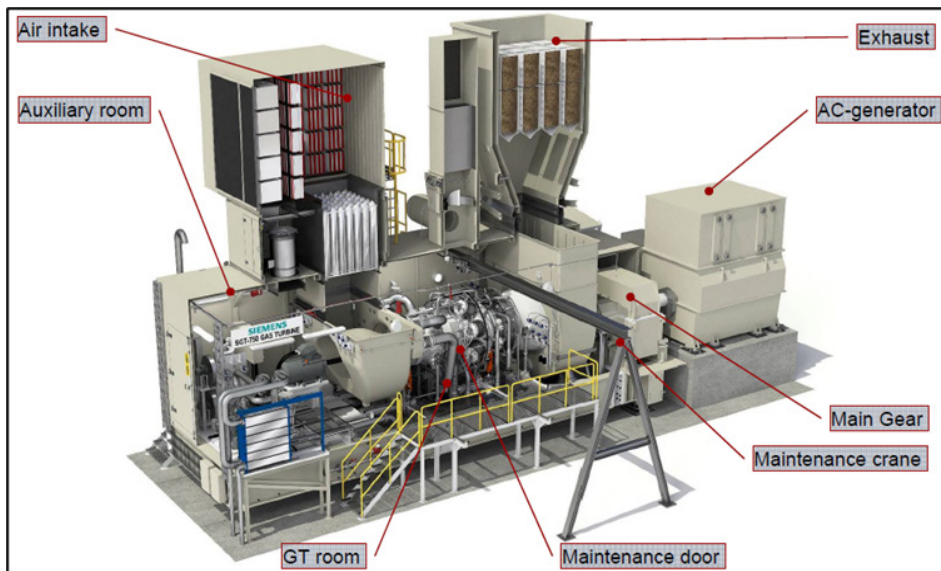


Figure 1. A section of gas turbines (Hellberg et al., 2012)

level of 85 dB(A), the employer shall take a countermeasure to reduce the excessive noise (DOSH, 2019). Therefore, it is essential to reduce such excessive noise by carrying out action plans, such as noise measurement at oil and gas facilities and equipment to suppress or attenuate the noise level below 85 dB(A).

Noise emission can be a problem in a gas turbine as it can tell the equipment's current condition. It also contributes to occupational health hazards where excessive noise can be fatal to human hearing ability. Therefore, the quiet operation of gas turbine packages has become primary importance in every turbine installation. The degree of noise attenuation required, if any, depends on the location of the installation and the noise environment in which it will be operating (McAuliffe et al., 1963). The outcome of this study could provide initial data for future researchers on how to improve the reliability of gas turbine equipment in the future. It may assist the industry in getting the idea to improve noise control programs at the workplace, and it would be advantageous to choose the most practical principle to reduce noise risk. Furthermore, the market for noise control products in Malaysia can be considered small since the industry is still looking for low-cost ways to control noise. The noise control product market could grow by studying and selecting the most feasible solutions based on noise engineering control techniques.

## METHODOLOGY

This study primarily covers noisy sound source, path and receiver survey, and octave band measurement as a sound frequency parameter that will be done prior to analyzing

the frequency band. In addition, this methodology covers the technique used for octave band measurement and details on the selected gas turbines. Generally, three methods were employed to conduct the study: pre-values review, on-site data collection, and post-noise analysis work. The flow chart in Figure 2 portrays the main steps of conducting this study, starting from document review until discussion on how to measure the effectiveness of the noise control option on noisy equipment and areas based on octave band frequency analysis.

A pre-job process is essential to understand how the equipment operates as it helps gather the information required for further evaluation. The operation history of the equipment also increases the chances of developing a strategy to solve noise issues on the equipment. Technical information is gathered, including equipment data sheets, factory acceptance test (FAT) reports, existing noise exposure monitoring (NEM) reports, mechanical drawings, and piping and instrument diagrams (P&ID) before the on-site job.

The on-site job consists of preparing data collection and measurement jobs on site. It will be a process where noise surveying is done using octave band measurement, and the area or location producing noise emission is identified. The octave band data is collected on all points, including the source, noise path, and receiver. Once the octave band data has been measured on-site, it will be analyzed with a theoretical study and calculation. The noise control analysis for the gas turbines plays with noise reduction coefficients to select a suitable material to absorb the noise with a calculation of sound transmission loss.

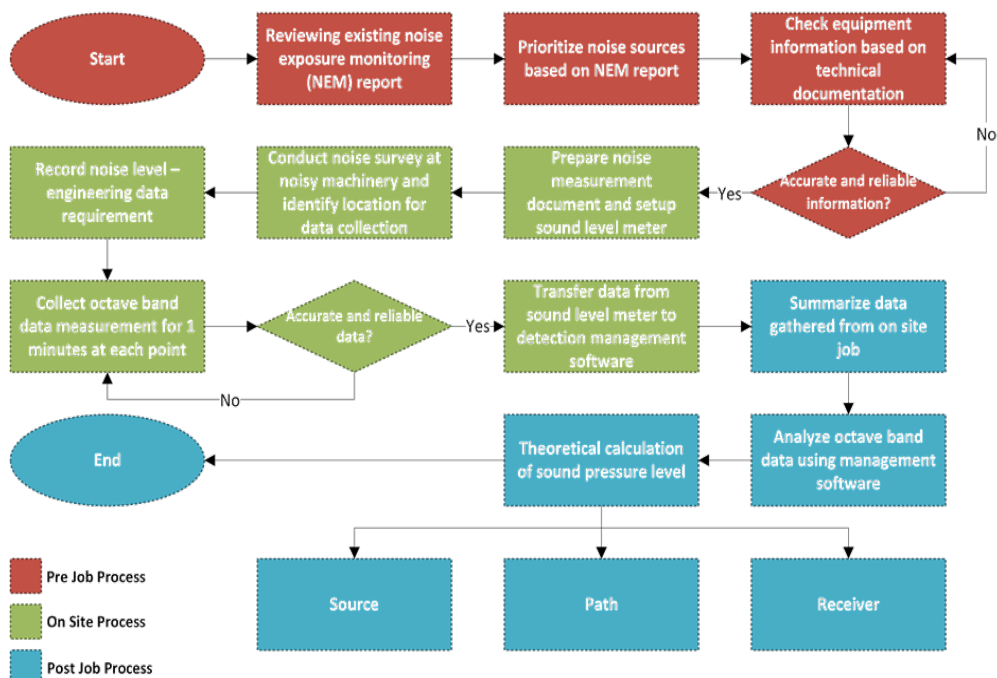


Figure 2. Process flowchart



## Noise Measurement

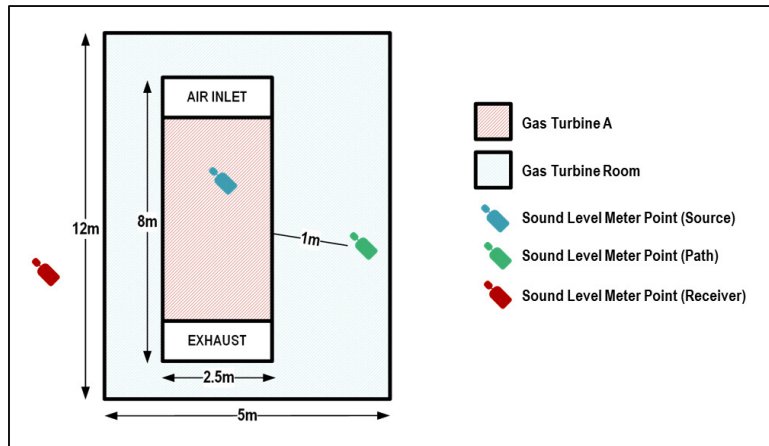
Noise measurement is the only way to gather the data to select a possible way to reduce the sound intensity of gas turbines. Sound is known as vibration energy that transmits through an airwave, while noise is unwanted sound (CCOHS, 2019). The noise is measured in three categories: source, path, and receiver. Anything that emits noise without any engineering control measures will be considered a sound source. However, if any existing engineering control measure is found, it is viewed as a sound path. The sound receiver defines noise emission at a worker's location, such as inside the control room or enclosure where the worker takes a parameter reading or performs an inspection job.

The noise measurement is located as close as (less than 1-meter perimeter) at the gas turbine for each source, path, and receiver location. In addition, the noise inside and outside the gas turbine generator room or enclosure is taken to determine the existing equipment enclosure effectiveness. For this study, one SoundPro SP SE-1-1/3 sound level meter was used with an AC-300 acoustic calibrator to collect the readings. Before on-site noise data collection, the sound level meter is set to the maximum of 140 dB magnitude of noise level with a selection of 1/3 octave bandwidth. The exchange rate used is 3 dB, and Z-weighting and the fast response are chosen. A Z-weighting was used to get a trend for low-frequency noise generation, and 1/3 octave band data collection aimed to determine the dominant frequency band that emits a high noise level (Peters, 2013). In order to achieve more accurate data, the time taken to get a reading on each point was set at 1 minute.

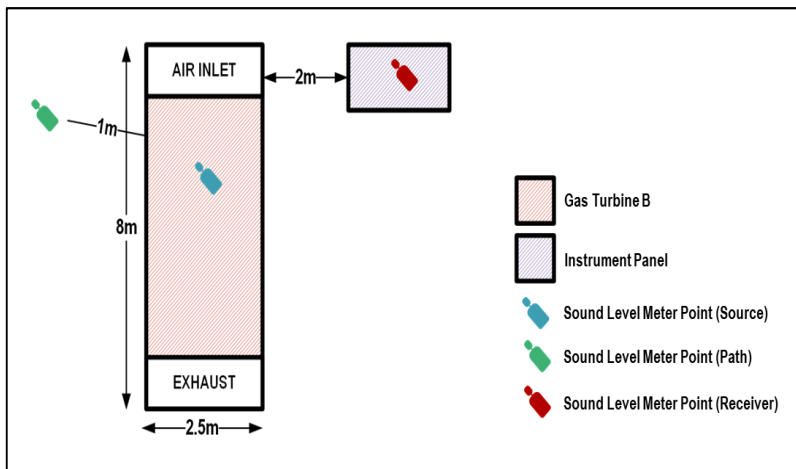
The range of interest of frequency is between 12.5 Hz and 20 kHz, according to the human hearing range. Fundamentally, the noise frequency band is separated into three categories, which are low frequency (12.5 Hz to 200 Hz), medium frequency (200 Hz to 2 kHz), and high frequency (2 kHz to 20 kHz). The measurement of dB(Z) does not filter all noise frequency bandwidths. The standard used to convert dB(Z) to dB(A) measurement is BS 61672-1:2003. The dB(A) level is calculated using the standard magnitude level reduction for each frequency bandwidth. The data gathered from the 1/3 octave band is used as generic data to select the 1/1 octave band, including 63 Hz, 125 Hz, 250 Hz, 500 Hz, 1000 Hz, 2000 Hz, 4000 Hz, and 8000 Hz. These frequencies are used to calculate sound absorption and transmission loss.

For this study, three gas turbines were chosen and nominated Gas Turbine A, Gas Turbine B, and Gas Turbine C. Gas Turbine A is located inside a gas turbine room, while Gas Turbine B and Gas Turbine C are in an open area. The schematic diagram for all three turbines and the data collected is shown in Figures 3(a) to 3(c).

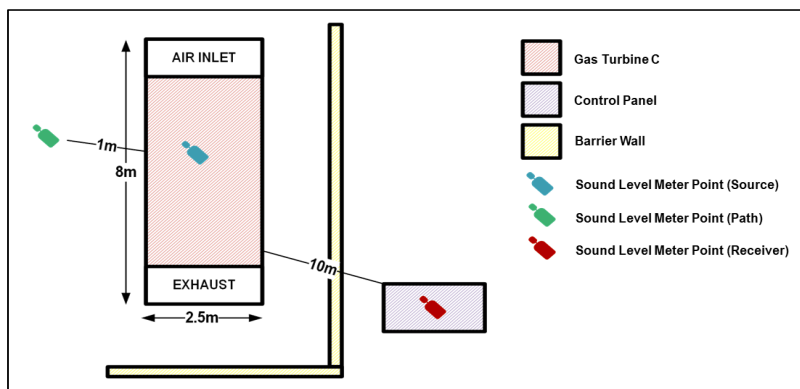
Since Gas Turbine A enclosure is located inside a gas turbine room, the noise measurement at the source will be taken inside the enclosure, while noise at the path will be taken inside the gas turbine room after the enclosure door is closed. The noise measurement at the receiver will be taken outside the gas turbine room.



(a)



(b)



(c)

Figure 3. (a) Diagram of measurement point for Gas Turbine A; (b) Diagram of measurement point for Gas Turbine B; (c) Diagram of measurement point for Gas Turbine C

Gas Turbine B is in an open area where the only noise control measure will be the gas turbine enclosure. Therefore, for Gas Turbine B, the noise source reading will be taken inside the enclosure, and noise along the path will be taken outside the enclosure with a closed door.

A noise reading will be taken at the instrument panel point located 2 meters from the gas turbine enclosure.

For Gas Turbine C, it was in an open area, and a barrier wall was used to split the area of the gas turbine and control room. The noise source reading will be taken inside the enclosure, and noise along the path will be taken outside the enclosure with a closed enclosure door. The receiver data was collected inside the control room, located 10 meters from the gas turbine.

### Noise Control Strategies

Once the data has been collected, the analysis is done based on planned noise measurement strategies. Referring to the principle, acoustical properties continuously reflect, absorb, or transmit the sound that strikes on the component as all materials have some sound-absorbing properties. If a sound wave hits any surface, the energy is divided into several paths. Some energy is reflected, some are absorbed, and others are transmitted through the material. However, the portion for each path of sound energy is not always the same for all conditions. It always depends on the acoustic performance of the material used. Figure 4 shows the phenomenon of sound interaction with acoustic material.

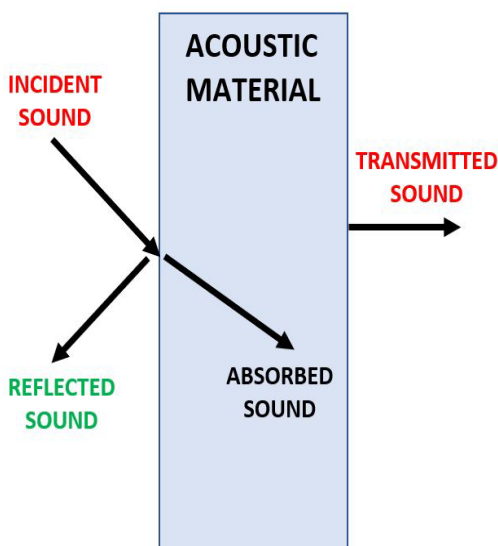


Figure 4. Interaction of sound wave on material

The incident sound energy that is not absorbed by material needs to reflect and be transmitted and dissipated. For acoustical material, acoustic performance can be obtained by three characterizations, namely: Sound absorption coefficient ( $\alpha$ ), noise reduction coefficient (NRC), and sound transmission loss (STL). The sound absorption coefficient ( $\alpha$ ) is a prominent feature in defining the performance of any material used for a specific purpose. As shown in Equation 1, the sound absorption coefficient is determined as the ratio of sound energy absorbed to the incident sound energy striking a material.

$$\alpha = \frac{(I_a + I_t)}{I_i} \quad (1)$$

Where:

$\alpha$  = sound absorption coefficient

$I_a$  = Sound absorbed (W/m<sup>2</sup>)

$I_i$  = Incident sound energy (W/m<sup>2</sup>)

$I_t$  = Sound transmission (W/m<sup>2</sup>)

The sound absorption coefficient is a unitless quantity where the value lies between zero and 1.0. When a material has zero sound absorption value, there is no sound absorption as incident sound energy is being reflected or transmitted. On the other hand, when a material has a value of 1.0, it shows that it absorbs all incident sound energy.

### Noise Reduction Coefficient

The calculation of the Noise Reduction Coefficient (NRC) is one of the parameters used to define material acoustic performance, particularly for sound absorber materials. NRC is the average measured sound absorption coefficient value at several frequencies and provides a more straightforward NRC form. The value is used as an index of the sound-absorbing efficiency of the material. Based on ASTM C423-17 (2017), the Standard Method of Test for Sound Absorption of Acoustic Materials in Reverberant Rooms, NRC's value is calculated as shown in Equation 2 by summing up low, medium, and high-frequency NRC values and dividing them by the number of counts.

$$NRC = \frac{\alpha_{250} + \alpha_{500} + \alpha_{1000} + \alpha_{2000}}{4} \quad (2)$$

### Sound Transmission Loss

Apart from the Noise Reduction Coefficient, another calculation is the Sound Transmission Loss (STL). A transmitted sound wave is commonly used to find out the sound insulation ability. Sound transmission loss is the value that represents the ratio of sound energy transmitted through treatment to the amount of sound energy incident on the source side of the material. This value is measured in decibels (dB), where a material isolates the sound in a specific octave band. The test follows ASTM E90-09 (2009), the Standard Recommendation Practice for Laboratory Measurement of Airborne Sound Transmission Loss of Building Partitions. Similar to sound absorption, the transmission loss is defined by the following Equation 3:

$$STL = 10 \log \left( \frac{W_i}{W_t} \right) \quad (3)$$

Where:

$W_i$  = Incident sound power

$W_t$  = Transmitted sound power

## RESULTS AND DISCUSSION

The results from three different gas turbines located at three different facilities denoted as Gas Turbine A, Gas Turbine B, and Gas Turbine C are presented. The summary from the data collection is discussed with a possible noise control recommendation for each gas turbine unit.

### Gas Turbine A

Octave band frequency data for all sampling points at Gas Turbine A is shown in Table 1 for noise source, path, and receiver location. The highest noise source level is detected in the middle section of the gas turbine equipment, with an average sound radiation level of 100.9 dB(Z) due to gas turbine operation. The frequency of interest contributing to noise is between 50 Hz and 20 kHz. The highest noise path level location is the generator rotor bearing, with an average sound radiation level of 104.6 dB(Z). The frequency of interest contributing to noise is between 80 Hz and 5 kHz. The highest sound level at the receiver is detected outside the generator room, where the gas turbine exhaust silencer duct and stack are located, with a sound level of 100.6 dB(Z). The frequency of interest contributing to noise is between 63 Hz and 250 Hz.

Table 1

*Gas turbine A octave band data*

Location	Octave Band Frequency									Noise Level dB(Z)
	31.5	63	125	250	500	1000	2000	4000	8000	
Source	79	86.9	85.3	88.3	88.1	95.9	87.7	92.7	95.6	100.9
Path	81.7	83.9	92.9	101.2	97.8	96.3	93.9	88.8	81.3	104.6
Receiver	80.8	99.9	90.1	87.8	75.3	73.5	63.6	59.8	48.1	100.6



Figure 5. (a) Gas turbine A source reading; (b) Gas turbine A path reading; (c) Gas turbine A receiver reading

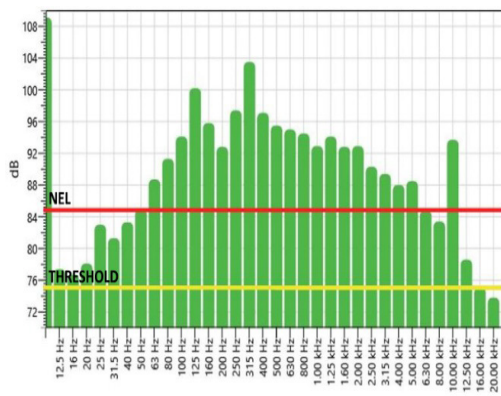
Based on the measurement data shown in Figures 5(a) to 5(c) for the noise source, path, and receiver, the excessive noise localized at the generator rotor rotation area is located at the guarding air inlet. It indicates a very high noise level of 110 dB(Z). The red line indicates the noise level of 85 dB (high), or what can be called the Noise Exposure Limit (NEL), while the yellow line indicates 75 dB (low) of the noise level or noise threshold. The reason to set up the high and low limits is to visualize the distribution of noise levels at each respective frequency of interest. 75 dB was chosen as the low noise level, as any reading below 75 dB will be ignored. The reason is that the numerical difference between the two noise values is zero, and it will not contribute to the whole noise data (CCOHS, 2019). The sound source is measured during the turbine enclosure door is opened, while the sound path is measured at the perimeter of the gas turbine generator machine during the enclosure door is closed. The noise level measured closely at the generator rotor bearing open area (path) exceeds 85 dB (Z) in the frequency band from 80 Hz to 5 kHz, generated by aerodynamic air inlet flow and mechanical centrifugal force. An average attenuation rate calculated from the sound source and sound path difference is around  $\pm 8$  dB. Therefore, the existing enclosure cannot reduce the noise below 85 dB(A) in the Gas Turbine A area.

### Gas Turbine B

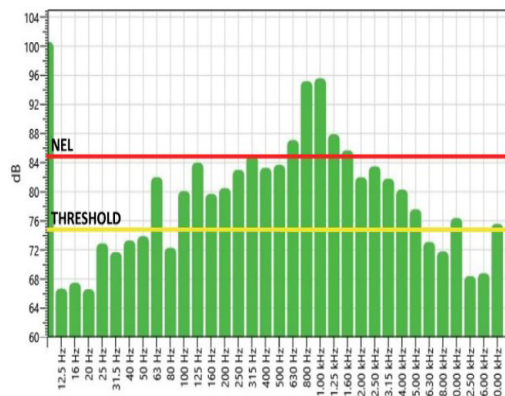
As with Gas Turbine A, the process for data collection at Gas Turbine B will acquire the octave band data at the source, path, and receiver. The measurement data is shown in Table 2. The highest noise source level is located inside the gas turbine generator enclosure with an average sound radiation level of 104.0 dB(Z). Besides that, the highest noise level along the path outside the gas turbine generator is measured at an average sound pressure level of 96.8 dB(Z). It indicates that the noise energy emission is initiated at the gas turbine exhaust vent. The high-frequency aerodynamic noise radiates from the 90-degree exhaust vent design without lagging due to turbulence gas effects. On the receiver side, the noise level is recorded at 90.6 dB(Z).

Table 2  
Gas turbine B octave band data

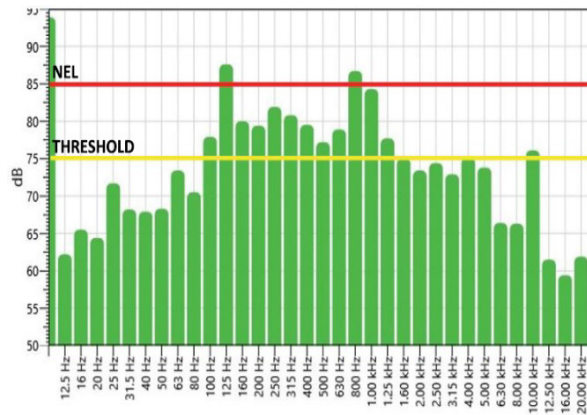
Location	Octave Band Frequency									Noise Level dB(Z)
	31.5	63	125	250	500	1000	2000	4000	8000	
Source	81.3	88.7	100.2	97.4	95.5	92.9	92.9	88	83.4	104.0
Path	71.7	82	84	83	83.	95.6	82	80.3	71.8	96.8
Receiver	68.2	73.4	87.6	81.9	77.2	84.3	73.4	75.1	66.3	90.6



(a)



(b)



(c)

Figure 6. (a) Gas Turbine B source reading; (b) Gas Turbine B path reading; (c) Gas Turbine B receiver reading

Based on the 1/3 octave band data in Figures 6(a) to 6(c), the sound level at the source shows that the noise level is distributed at low-to high-frequency ranges of 63 Hz to 10 kHz inside the gas turbine enclosure. Two pure tone frequencies spike a high noise magnitude at 125 Hz and 315 Hz, reaching more than 100 dB(Z). It is due to the high rotation of the turbine engine and electrical noise. The equivalent noise emission is recorded between 108 dB(Z) and 109.6 dB(Z) at all sampling points. The sampling point at path location shows that the dominant medium frequency of noise bandwidth contributes to accumulating a high level of noise distribution of 90.6 dB(Z) to 100.6 dB(Z). The low-frequency noise distribution comes from the top side gas turbine exhaust vent outlet. The right-left and sides of an enclosure show an average noise attenuation of 15 dB(Z).

### Gas Turbine C

As for the third sample, Gas Turbine C, the octave band frequency data for all sampling points at the gas turbine generator are shown in Table 3 for noise source, path, and receiver location. The highest noise source level is recorded at an average sound radiation level of 103.5 dB(Z).

Most of the noise frequency band distribution ranges from 12.5 Hz to 3.15 kHz. Meanwhile, for the noise path, the highest noise level is measured at 100.2 dB(Z) and is dominant at 1 kHz and 1.25 kHz frequency bandwidths. The sound receiver is recorded at 63.9 dB(Z), indicated below the quiet zone of 80 dB(Z).



Table 3

Gas Turbine C octave band data

Location	Octave Band Frequency									Noise Level dB(Z)
	31.5	63	125	250	500	1000	2000	4000	8000	
Source	94.9	95.9	93.5	98.6	94.3	91.9	90.8	83.6	78.4	103.5
Path	86.2	79.1	81.7	85.3	94.6	97.9	84.4	77.3	82.3	100.2
Receiver	57.4	55.5	56.2	58.7	60.6	53.4	55.5	48.8	42.4	65.9

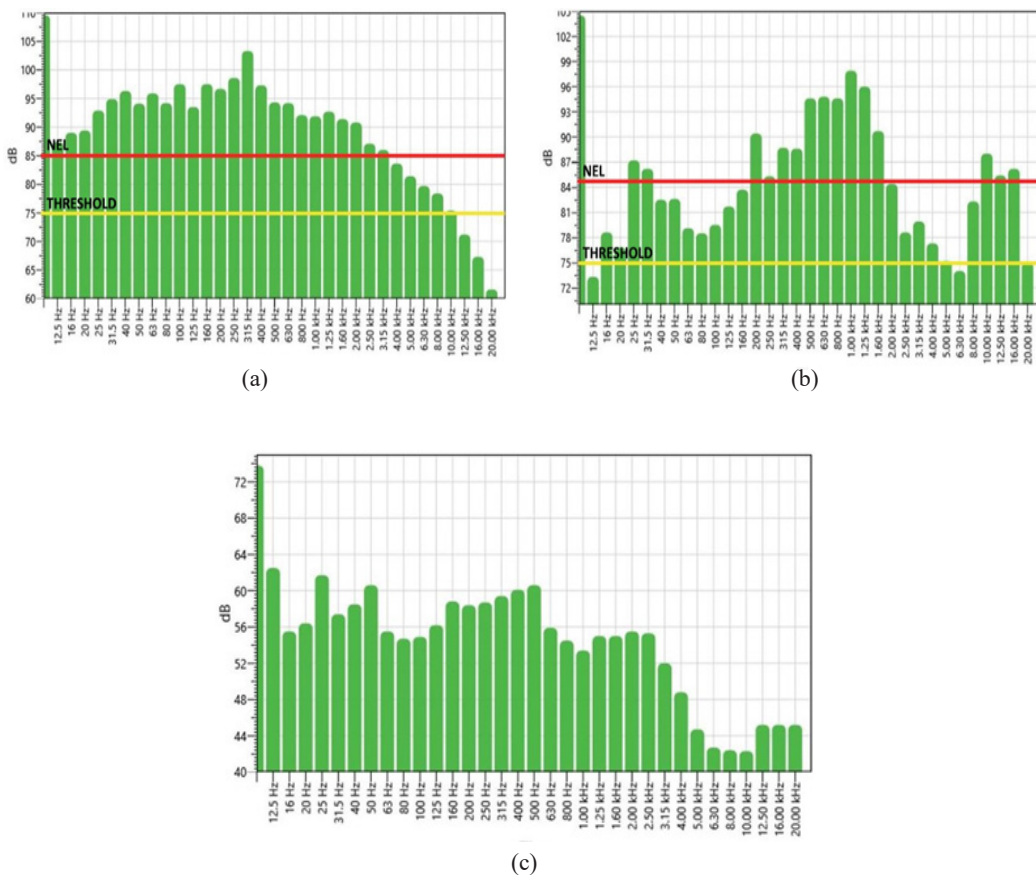


Figure 7. (a) Gas Turbine C source reading; (b) Gas Turbine C path reading; (c) Gas Turbine C receiver reading

The sound source of the 1/3 octave band results indicates that the noise level distributions are at low, medium, and high frequency ranges inside the gas turbine enclosure,

as shown in Figures 7(a) to 7(c). Most noise level magnitude at each frequency band excites more than 85 dB(Z). It is due to the rotation speed of the turbine engine and electrical noise. The sampling point at path location shows that the dominant medium frequency of noise bandwidth contributes to the accumulation of high noise distributions between 90 dB(Z) and 98 dB(Z). The low frequency of noise distribution comes from the topside gas turbine inlet and outlet air vents. However, the dominant 200 Hz to 1.6 kHz frequency band is found at the connecting duct between gas turbine enclosures and exhaust silencers. The sampling point at the receiver location, the gas turbine control room, shows a result below 80 dB(Z).

### Octave Band Calculation

A noise reduction calculation is made by calculating the noise reduction coefficient and sound transmission loss for the equipment. In this study, a modular acoustic panel is used as an example. By utilizing an on-site dimension, the area for acoustic treatment is defined in the calculation. The example of the analysis is shown in Figures 8 to 13. For this example, the noise source reading from Gas Turbine A is an input. The distance from the primary source also needs to consider the directivity factor. Two directivities have been chosen by referring to the gas turbine location inside the enclosure base.

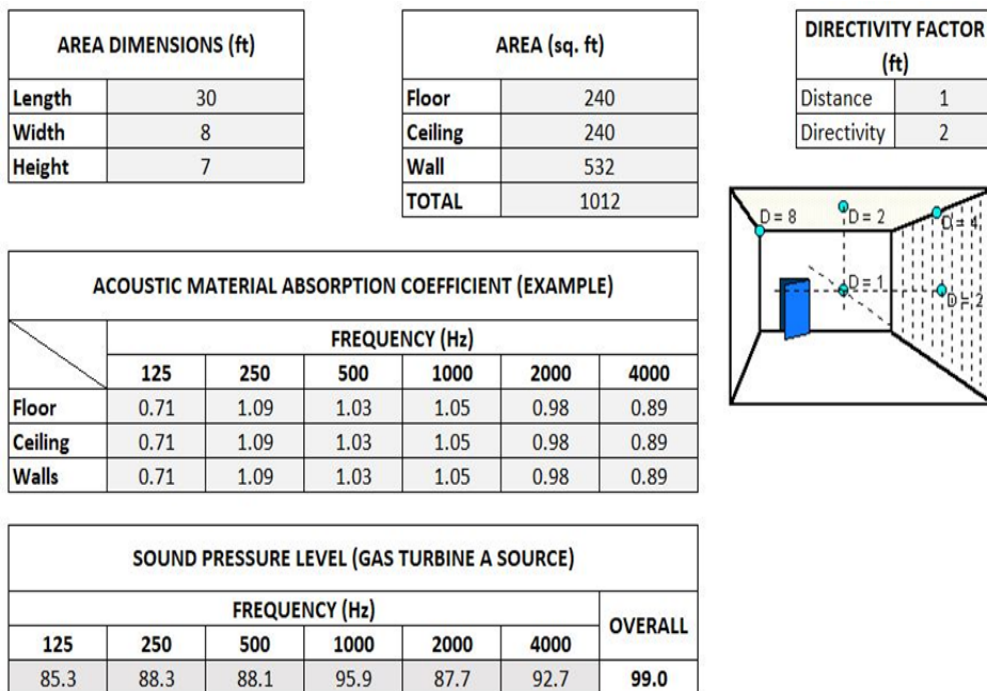


Figure 8. Input data for noise reduction calculation

The overall noise pressure level for Gas Turbine A (Source) was calculated using an equivalent continuous sound energy level ( $L_{eq}$ ) based on the BS 61672 standard. The formula for the equivalent sound level is as follows:

$$L_{eq} = 10 \log \left( 10^{\frac{L1}{10}} + 10^{\frac{L2}{10}} + 10^{\frac{Ln}{10}} \right) \tag{4}$$

$$= 10 \log \left( 10^{\frac{85.3}{10}} + 10^{\frac{88.3}{10}} + 10^{\frac{88.1}{10}} + 10^{\frac{95.9}{10}} + 10^{\frac{87.7}{10}} + 10^{\frac{92.7}{10}} \right)$$

$$= 99 \text{ dBA}$$

The average absorption coefficient and room constant are calculated using the surface area and treated surface with selected acoustic material absorption values at 125 Hz, 250 Hz, 500 Hz, 1000 Hz, 2000 Hz, and 4000 Hz frequencies. Absorption can be calculated by dividing the total room sound absorption by the total surface area of the room. The total room sound absorption can be calculated by multiplying the surface area with the absorption coefficient of the actual surface. The frequency of 125Hz is used as an example for the whole calculation:

$$\begin{aligned} \text{Average Absorption Coefficient} &= [\text{Total Sound Absorption (Floor)} + \text{Total Sound Absorption (Ceiling)} + \text{Total Sound Absorption (Wall)}] / \text{Total Surface Area in the Room} \\ &= [(240 \times 0.71) + (240 \times 0.71) + (532 \times 0.71)] / 1012 \\ &= 0.71 \end{aligned}$$

The result for the average absorption coefficient for the rest of the frequency is as follows:

AVERAGE ABSORPTION COEFFICIENT					
FREQUENCY (Hz)					
125	250	500	1000	2000	4000
0.71	1.09	1.03	1.05	0.98	0.89

Figure 9. Average absorption coefficient result

Once the result of the average absorption coefficient is obtained, the room constant can be calculated as follows:

$$\begin{aligned} \text{Room Constant} &= \text{Total Room Sound Absorption} / (1 - \text{Average Absorption Coefficient}) \\ &= (1012 \times 0.71) / (1 - 0.71) \\ &= 2477.7 \end{aligned}$$

ROOM CONSTANT (sqft)					
FREQUENCY (Hz)					
125	250	500	1000	2000	4000
2477.7	-12256.4	-34745.3	-21252.0	49588.0	8188.0

Figure 10. Room constant result

A reduction when using a modular acoustic panel can be seen once a sound pressure level calculation using the directivity factor is done. Based on the Directivity Factor formula,

$$L_p = L_N + \log \left( \left( \frac{D}{4\pi r^2} \right) + \left( \frac{4}{R} \right) \right) \tag{5}$$

Where:

- $L_p$  = Sound Pressure Level (After)
- $L_N$  = Sound Power Level from source (Before)
- $D$  = Directivity Factor
- $r$  = Distance
- $R$  = Room Constant

$$\begin{aligned} &= 85.3 + \log \left( \left( \frac{2}{4\pi(1)^2} \right) + \left( \frac{4}{2477.7} \right) \right) \\ &= 77.4 \end{aligned}$$

SOUND PRESSURE LEVEL (dB)						
FREQUENCY (Hz)						
125	250	500	1000	2000	4000	Linear
77.4	80.3	80.1	87.9	79.7	84.7	91.1

Figure 11. Sound pressure level result

The sound pressure level can be corrected into A-weighted by using the BS 61672-1:2003 standard, and the outcome can be seen in Figure 12. The overall difference between before (99 dBA) and after applying a modular acoustic panel at the source of Gas Turbine A (90.7 dBA) is about 8.3 dBA.

A-WEIGHTED SOUND LEVEL (dBA)						
FREQUENCY (Hz)						
125	250	500	1000	2000	4000	Linear
61.3	71.7	76.9	87.9	80.9	85.7	90.7

Figure 12. A-Weighted corrected sound level

Figure 13 depicts a comparison of the sound pressure levels of three gas turbines. Gas Turbine B and Gas Turbine C, located in an open area, recorded a higher difference in sound pressure level compared to Gas Turbine A, located in a gas turbine room.

	COMPARISON (dBA)		
	<i>Before</i>	<i>After</i>	<i>Difference</i>
<b>Gas Turbine A</b>	99.0	90.7	<b>8.3</b>
<b>Gas Turbine B</b>	103.8	91.1	<b>12.7</b>
<b>Gas Turbine C</b>	101.8	89.6	<b>12.2</b>

Figure 13. Comparison of noise reduction between three gas turbines

As for the sound transmission loss, the example for the calculation is shown in Figure 14. The same acoustic material is used for sound transmission loss calculation following the noise reduction coefficient analysis. The minimum insertion loss or transmission loss value is used at 125, 250, 500, 1000, 2000, 4000, and 8000 Hz frequencies. The linear sound pressure level and A-weighted sound pressure level are automatically calculated by deducting the sound pressure level from the source with transmission loss. Correcting the linear sound pressure level with an A-weighting correction value from the BS 61672 standard will give out an A-weighted sound level. The overall sound level reduction of 26.8 dB is achieved to reduce the noise level for Gas Turbine A. The main important element in selecting proper noise absorption and transmission material is determining the material properties.

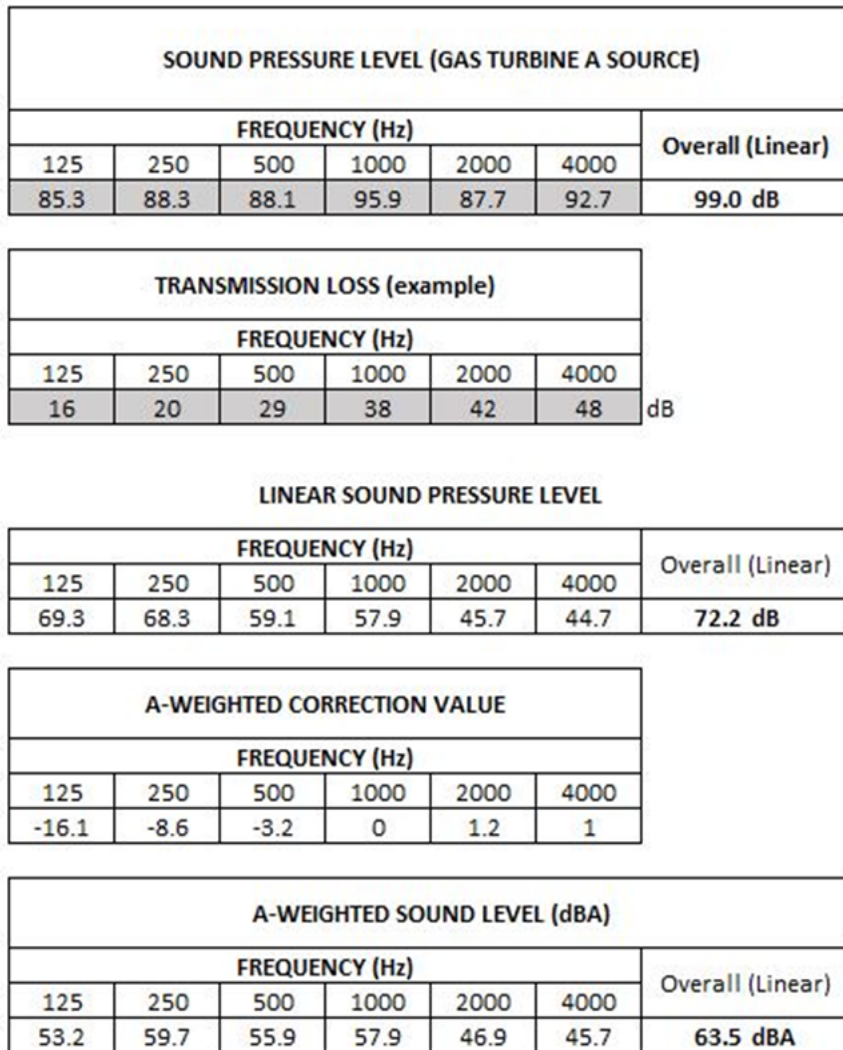


Figure 14. Calculation data for sound transmission loss

Based on the noise data analysis, some options can be implemented on the gas turbine equipment for all three sections, including source, path, and receiver. For example, noise at the source can be reduced by using sound-absorbing material, such as sound foam inside the enclosure. Acoustic foam can be found easily on the market with various materials to absorb the noise. Some researchers study natural materials to be used for sound absorption. For example, Nasidi et al.'s (2021) study use sodium hydroxide concentration on coir fiber (coconut fiber) to increase sound absorption, significantly reducing the impact on medium frequency bands such as 1000 Hz. As a comparison, Gas Turbines B and C show a high

level of noise on the medium frequency band at the source. Other than that, gas turbine end-users can reduce the rotational tip speed of the rotor blades by controlling the gas turbine performance or reducing the fan pressure ratio that could significantly affect fan noise. In addition, the baseplate damper for the gas turbine can be modified to support the equipment during the operation. A survey was done by Krishna (1999) also recommends passive damping inside the turbine engine enclosure. Another study also states that installing an isolation pad between the turbine skid and the enclosure helps in reducing the noise transmission at the source (Lages, 1979).

Other than that, installing an acoustic panel on the gas turbine enclosure could reduce the noise along the path by ensuring the acoustic material used for the enclosure has a good efficiency in attenuating the noise level. Taking noise path reading from Gas Turbine B as an example, the noise comes from a connecting duct between gas turbine generator enclosures and its exhaust silencer. The noise path reading is significant around 250 Hz to 2000 Hz, almost the same as the study done by Uddin et al. (2016). The previous research has modified the silencer, which can be applied to the Gas Turbine B noise path.

Another option could be relocating a gas turbine control panel at an acceptable distance. Depending on the location and area of work, noise at the receiver can be controlled by introducing an online parameter reader that can be monitored directly from a centralized control room (CCR) at the offshore facilities. Developing a program or software that can integrate the information from gas turbine panels can be helpful to operate and monitor the equipment remotely without having to collect the data on-site. Most of the time, industrial players focus on preparing a personal hearing protector for the workers who work near noisy equipment. However, previous research already concludes that hearing protectors used in the industry are only marginally associated with reduced odds of high-frequency hearing shifts, suggesting that hearing protectors provide inadequate noise reduction for many workers (Themann & Masterson, 2019).

## CONCLUSION

This study concludes that gas turbines produce a high volume of noise that could affect the hearing health of offshore workers. All three gas turbines from three different offshore facilities show that the noise level exceeds the noise exposure limit of 85 dB(A). Based on the noise measurement, gas turbine users can take advantage of acoustic materials found in the market to reduce noise emissions at their facilities, such as modular acoustic panels that manage to reduce sound levels by up to 20 dB(A) based on calculation. The analysis shows that usage of acoustic material, such as modular panels, can attenuate the noise level for gas turbine equipment. It means that the high frequency of noise can be reduced by introducing proper materials, and noise measurement could test the effectiveness of the gas turbine noise control materials. Therefore, the objective of noise measurement study for gas turbine equipment at oil and gas facilities is accomplished.

## ACKNOWLEDGEMENT

This research is supported by Universiti Tun Hussein Onn (UTHM) through Tier 1 (vot H767).

## REFERENCES

- ASTM C423-17. (2017). *Standard test method for sound absorption and sound absorption coefficients by the reverberation room method*. ASTM International.
- ASTM E90-09. (2009). *Standard test method for laboratory measurement of airborne sound transmission loss of building partitions and elements*. ASTM International.
- CCOHS. (2019). *Noise - Basic information*. Canadian Centre for Occupational Health and Safety.
- Cumpsty, N., & Marble, F. (1977). Core noise from gas turbine exhausts. *Journal of Sound and Vibration*, 54(2), 297-309. [https://doi.org/10.1016/0022-460X\(77\)90031-1](https://doi.org/10.1016/0022-460X(77)90031-1)
- DOSH. (2019). *Industry code of practice for management of occupational noise exposure and hearing conservation*. Department of Occupational Safety and Health Malaysia.
- El-Badawy, A., & El-Arna'outy, W. (2007, July 9-12). *Passive noise control of a burner-combustor system of a turbo-fan engine*. In 14th International Congress of Sound and Vibration (pp. 1-8). Cairns, Australia. <https://doi.org/10.13140/2.1.1065.5686>
- Hellberg, A., Andersson, T., & Häggmark, A. (2012). Design, testing and performance of the recently developed 37 MW siemens SGT-750. In *Turbo Expo: Power for Land, Sea, and Air* (Vol. 44724, pp. 45-50). American Society of Mechanical Engineers. <https://doi.org/10.1115/gt2012-68249>
- Krishna, C. R. (1999). *Survey of noise suppression systems for engine generator sets*. Brookhaven National Lab. <https://doi.org/10.2172/752962>
- Lages, F. P. (1979). Air filtration and sound control systems for gas turbines-the start of the art. In *Proceedings of the 8th Turbomachinery Symposium* (pp. 83-94). Texas A&M University Libraries. <https://doi.org/10.21423/R1MX05>
- McAuliffe, D., Morlock, H., & Oran, F. (1963). What to do about gas-turbine noise. In *ASME 1963 Aviation and Space, Hydraulic, And Gas Turbine Conference and Products Show* (Vol. 79924, p. V001T01A026). American Society of Mechanical Engineers. <https://doi.org/10.1115/63-ahgt-77>
- Nasidi, I., Ismail, L., & Samsudin, E. (2021). Effect of sodium hydroxide (NaOH) treatment on coconut coir fibre and its effectiveness on enhancing sound absorption properties. *Pertanika Journal of Science and Technology*, 29(1), 693-706 <https://doi.org/10.47836/pjst.29.1.37>
- Peters, R. J. (2013). *Acoustics and noise control* (3rd Ed.). Routledge. <https://doi.org/10.4324/9781315847146>
- Sam, W. Y., Anita, A. R., Hayati, K. S., Haslinda, A., & Lim, C. S. (2017). Prevalence of hearing loss and hearing impairment among small and medium enterprise workers in Selangor, Malaysia. *Sains Malaysiana*, 46(2), 267-274. <http://dx.doi.org/10.17576/jsm-2017-4602-11>



- Themann, C., & Masterson, E. (2019). Occupational noise exposure: A review of its effects, epidemiology, and impact with recommendations for reducing its burden. *The Journal of the Acoustical Society of America*, 146(5), 3879-3905. <https://doi.org/10.1121/1.5134465>
- Tiede, D. (1969). Measurement and control of gas turbine noise from an industrial vehicle. In *ASME 1969 Gas Turbine Conference and Products Show* (Vol. 79832, p. V001T01A025). American Society of Mechanical Engineers. <https://doi.org/10.1115/69-gt-25>
- Uddin, M., Rahman, A., & Sir, M. (2016). Reduce generators noise with better performance of a diesel generator set using modified absorption silencer. *Global Journal of Research in Engineering*, 16(1), 1-14.



## The Detection of Changes in Land Use and Land Cover of Al-Kut City using Geographic Information System (GIS)

Fatima Asaad Tayeb<sup>1\*</sup>, Ahmed Kareem Jebur<sup>1</sup> and Husham H. Rashid<sup>2</sup>

<sup>1</sup>Department of Surveying Techniques, Kut Technical Institute, Middle Technical University, Baghdad, Iraq

<sup>2</sup>Middle Technical University, Institute of Technology, Baghdad, Iraq

### ABSTRACT

Models of digital elevation (DEMs), which provide elevation information for the ground surface of the catchment, are core components of computer-based analyzes for drainage basins. Many production methods are available, including contour interpolation, DGPS (Differential Global Positioning System) interpolation, and digital photogrammetry techniques. However, data on the precision and often contradictory nature of these three techniques are sparse. This study aims at identifying some of the contributing factors and comparing the accuracy of various approaches quantitatively. Changes in land coverage break ecosystem cycles, which may directly affect land ability to sustain human activity resulting in long-term trends of decline and inter-annual variability. It can be monitored at a spatial level of detail to enable the study of human-induced changes. Remote sensing techniques (RS) and geographical information system (GIS) methods have been used to extract the spatial and temporal changes of urban land use in the city of Al-Kut. The land sat satellite images taken in periods encompassing 1997, 2007, and 2017 are used. As a result, the city has lost a large part of its urban specificity and gained randomness and disorder in most of its residential neighborhoods, which was especially exacerbated after the change in the governing system in 2003. The results show an increase of 314% and 219% in industrial and residential areas, respectively, whereas agricultural land and open spaces have decreased by 66 % and 32%. The data analysis reveals a diagnostic relationship between land-use

conversion and socio-economic drivers. This research sheds light on the total area changes of the Al-Kut city before and after 2003. It highlights the significant destruction of the city life, which was established over almost three centuries.

**Keywords:** Chemical impacts, GIS, remote sensing, social factors

### ARTICLE INFO

#### Article history:

Received: 30 March 2021

Accepted: 05 July 2021

Published: 04 January 2022

DOI: <https://doi.org/10.47836/pjst.30.1.40>

#### E-mail addresses:

nooralhudaiairaqi@gmail.com (Fatima Asaad Tayeb)

ahemd.gis@gmail.com (Ahmed Kareem Jebur)

Husham.HRashid@gmail.com (Husham H. Rashid)

\* Corresponding author

## INTRODUCTION

Satellite remote-sensing techniques have been successfully used in detecting and monitoring land cover change at various scales (Xiao & Weng, 2007). However, there is an increasing need to develop the methodology of detecting changes in land cover using satellite imaging with the increasing importance of accurate and timely information that describe the nature of land resources and changes over time, especially in fast-growing urban areas (Popovici et al., 2013).

Land resources are increasingly scarce, and this is particularly true for land available for primary biomass production or purposes related to conservation. As a result, competing land uses are becoming more critical and frequent, resulting in more complex conflicts of interest. In addition, there are ongoing pressures of urban expansion competing with agricultural enterprises and recreational demands on the fringes of the urban areas. Such situations often lead to a rapid increase in the economic value of land, and land tenure becomes an important political issue (Prakasam et al., 2010).

Error analysis of many datasets is often confusing for some users because of not entirely or universally understanding error statistics. The most commonly used root mean squared error measurement (RMS error or RMSE) is at the forefront of this issue. Often users complain and misunderstand this error measure, particularly with regard to Global Positioning Systems (GPS). Error-values are commonly cited as 30 meters, which many consumers consider to be a maximal error, not RMS error, for GPS readings (previous to the elimination of Selective Availability). Many consumers still do not understand that a systemic error is not part of the cited RMSE value if the overwhelming error caused for GPS may be a systemic error. Inappropriate data collection is a classic source for systematic error in GPS systems, which can cause systemic errors in GPS readings of more than 1000 m of magnitude. Differential GPS (DGPS). The reads have errors in various quantities and their mistaken functions (Carry Phase (CP) corrections, the hardware involved, device rounding errors, atmospheric differences, base station-to-rover reach, satellite visibility, and multi-path errors, among others). Differential GPS(DGPS) is not prone to errors. A thorough description of DGPS source errors is given. Failed DEM analysis by interpolation obtained from contour data often continues to focus on the use of RMSE. This value is reasonably easy to calculate and provides an outstanding indicator of the exactness when properly made. Sadly, the end-users who manufacture DEMs have little, if any, the idea of error measuring and problems in this way is frequent.

The production of DMS can also be done with digital photogrammetry. Usually, the user can carry out systematic and thorough error analysis of findings through software developed to collect data from aerial photography. However, such software continues to be sophisticated and requires the expertise of the user. This sophistication and the limited potential demand aim to make this program costly, limiting the use of this DEM production

process further. Other DEM sources such as LIDAR (Light Detection and Ranging) and interferometry radar are also available. However, these are relatively new approaches to DEM and, despite their precision and resolution benefits compared to more conventional approaches, have not yet gained widespread use. In general, the precision and shortcomings of these modern approaches are clearly articulated. However, because few conventional methods users understand the flaw in the actual data they use, they struggle to comprehend the benefits of such data sources, which may be reliable. This study attempts to offer an image of the spatial changes of urban land use in the residential, commercial, industrial areas in the Al-Kut city over four decades and evaluate whether these modifications have been negative or positive. Al-Kut city is the capital of Al-Kut district in Wassit Governorate of Iraq, shown in Figure 1. Al-Kut city is bounded between 45°46'00" to 45°53'20" E and 32°27'00" to 32°34'00" N coordinates. It covers an area of about 5640 km<sup>2</sup>. Al-Kut city is located along the main highway connecting Baghdad with Amarah in the south, about 170 km south-east of Baghdad and 150 km north-west of Amarah city (Boakye et al., 2008).

## MATERIALS AND METHODS

### DGPS Setting

For this study, six datasets had to be generated. It included: (i) several digital contours for interpolation into a DEM from the largest mapping possible, (ii) a digital photogrammetry DEM, and (iii) several DGPS points. They included: Two data sets, one from each of the

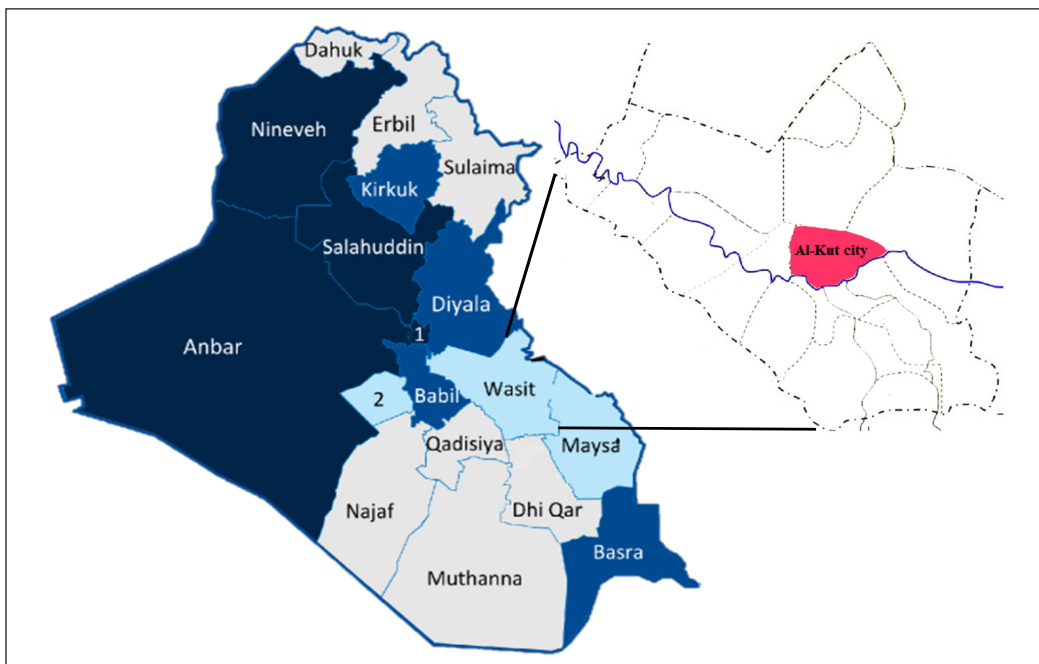


Figure 1. Al-Kut city location within the Wassit Governorate of Iraq

areas of study that were needed. On-screen from the map Ordnance Survey (OS) 1:25000 digitized contours for the KUT region of the study have been digitized. In order to avoid interpolatory border mistakes, a wide margin across the study region is digitized. These contours were digitized via ArcView and then used as a polyline input into the module feature Spatial Analyst.

The three datasets for the Iraqi field of research were developed as the KUT data datasets. Onscreen digitization of 1:10000 maps was given as black and white scanned images. The digital contour data was extracted. In order to minimize interpolation errors in the analysis, a large margin has been digitized across the sample region. The distance between contours on these maps was 10 meters. The same processes mentioned for the KUT data set were followed by interpolation, transformation, and import into imaginary. The digital photogrammetric extraction of data from 1996 for the region of the Iraqi analysis was carried out using OrthoMax software in 1:12000 color aerial photography. Ground correction control was based upon 1:25000 maps because when digital photogramming was performed, a 1:10000 map was not usable. The performance error was considerably higher than in KUT photogrammetry due to the smaller photography size and poor accuracy of maps used.

### **Procedure of Calculation**

In the first step, the x and y coordinates of the points to be analyzed were established. The GPS dataset consultation decided it. The Imagine function was then used to obtain from the relevant points the interpolated and photogrammetric height values. The method output was the X, Y, and Z text files for the points. For collection and statistical analysis, these files were imported into Microsoft Excel.

Different statistics, including maximal error, average (mean) error, and RMSE, can be obtained by directly comparing the height values for the three datasets. Excel also permitted the constructing plots of the points that, when analyzed in addition to field notes, allowed the precise evaluation of high error points or areas and the potential cause for the postulation of error.

### **Detection and Analysis of Land**

Three QuickBird 60 cm global high-resolution satellite images from 1997, 2007, and 2017 were acquired from the United States Geological Survey (USGS). Digital images were processed using conventional processes as follows; (i) ENVI 4.7 suite of programs were used to clip the region of interest in this research (Dewan & Yamaguchi, 2009) (ii) the satellite images were radiometrically corrected using geo-referencing methods for subsequent GIS data integration, and finally, (iii) images were enhanced using Erdas imagine 2014 software.

Each scene was geo-referenced using nine ground control points (GCPs) identified and selected from the Differential Global Positioning System (DGPS), followed by using the corrected image as a reference for image-to-image registration of all other band-images. The random distortion technique was used to correct the pictures geometrically (Kim et al., 2017). For a general knowledge of the study area, the research was supported by field survey inquiry.

## RESULTS AND DISCUSSION

### Detection in the Urban Land-Use Area

Table 1 shows that the town of Al-Kut has a significant spatial change based on the visual interpretation of high-resolution satellite pictures by spatial resolution (1 m and 0.6 m) and spatial resolution (30 m) land satellite images for that city during the period 1997–2017.

Based on the analysis from the outcomes, the first ten years (from 1997–2007). The total area of the urban area in 1997 was 8376.299 hectares, compared to 5824.057 hectares at the end of 2007. At the end of 2017, 12711.035 hectares were recorded. The total area changes for the period 1997–2017 were 4891.984 hectares. This expansion came from several variables, and the most important variable is the increase in population and migration, where the population size of 1997 was 340 thousand, up to 2017 estimates showing the population size of the town 457 thousand, this may result in changes in the type or pattern of use based on scheduling, political, social and other factors (Mengistu & Salami, 2007).

Table 1  
*The percentage of Land use / Land cover change analysis in AL-Kut city in 1997, 2007, and 2017*

Type of use	Year 1997		Year 2007		Year 2017		Amount of change	
	Area (hectare)	Value (%)	Area (hectare)	Value (%)	Area (hectare)	Value (%)	Area (hectare)	Value (%)
Residential	1720.107	13.513	3581.475	28.135	7126.432	55.984	5406.325	314.301
Commercial market	38.492	0.302	62.365	0.489	80.410	0.631	41.918	108.900
Industrial	48.548	0.381	50.698	0.398	154.962	1.217	106.414	219.193
Agricultural lands	6804.550	53.456	3986.049	31.314	2285.406	17.954	-4519.144	-66.413
Vacant land	3841.701	30.180	4655.963	36.577	2604.967	20.464	-1236.734	-32.192
Services								
Educational	65.866	0.517	87.822	0.689	89.760	0.705	23.894	36.276
Recreation	161.881	1.271	253.373	1.99	324.932	2.552	163.051	100.722
Religious places	1.081	0.008	1.081	0.008	1.371	0.010	0.290	26.857
Hospitals	46.976	0.369	50.376	0.395	60.962	0.478	13.986	29.772
Sum	12729.202	100	12729.202	100	12729.202	100	0	737.416

### Change Detection in the Residential Area

Table 1 and Figure 2 indicate that residential use has seen a substantial shift in the area for the period 1997–2017 because of urban expansion, which is one of the reasons that contributed to the land investment has changed, especially the encroachment on land near the city. It is evident in the change in the category of positive use at the expense of agricultural lands and empty spaces, which is used occupied 1486.107 hectares, 12.464% in 1997, a small area relatively due to the small population that affected the residential space and area. During that period, the area allocated for residential use increased by 19.107% from 2007 to 1981.475 hectares, a small area compared with 1997. In 2017, a remarkable increase was observed while the area of the city recorded 6026.432 hectares, with 47.302% of the city’s total area. It is due to a change in the category of positive residential use and its expansion at the expense of empty spaces and agricultural land. Years and the period of economic siege imposed on the Iraqi people, which lasted over 13 years, so that the slight increase in the area is justified, including regulatory, political and population, and other factors (Abd El-Kawy et al., 2011; Verburg et al., 2011)

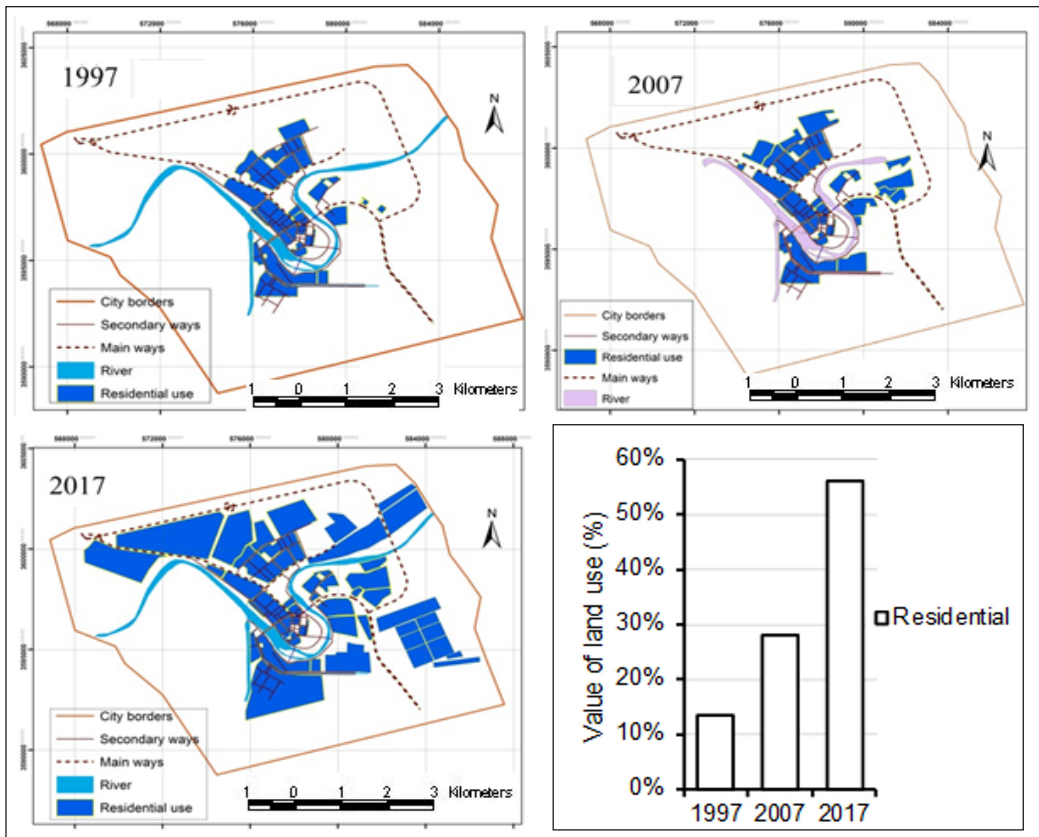


Figure 2. The changes of areas for residential use in Al-Kut city in 1997, 2007, and 2017, and the percentage of residential use change over the same period



The reason for the increase in the area in the combination of many variables coincided with the change of the system in 2003 and its consequences for the deterioration of the security situation and the weakness of the regulators, which encouraged many of the population, particularly from the southern and central provinces and even the North, including the mass exodus to the province of Kut, for two reasons first the state of security calm in the city of Kut, compared to other governorates and second, the economic side, to work and earn a daily living. As a result, the clear increase in the residential area changes for the period 1997-2017 can be seen, noting that the residential area registered an absolute positive change of 4540.325 hectares at a rate of change of 305.518%.

### **Change Detection in the Commercial Area**

The urban expansion in cities is a land change that affects all uses without exception, depending on the importance of this use (Halefom et al., 2018). Therefore, land uses are expanding simultaneously with the expansion of other uses, thus showing a mixture of land uses, including residential, service, industrial, and even commercial. For example, Table 1 and Figure 3 show that, during the period 1997–2017, the commercial use covered the change in the field with a record area of 38.492 hectares by 0.322% in 1997. However, the positive spatial change of this use soon began until the record 45.365 hectares increased by 0.437% in 2007 despite the circumstances of the eight-year war. After that, however, the rate of change in the commercial area increased as a result of a creation of a new revival.

In 2017, for political and economic reasons, the commercial area registered 80.4106 hectares at a rate of 0.631%. From the above, the absolute change in the commercial area is moving towards a positive record of 41.919 hectares with a change rate of 108.903%. This rate is high due to the excessive commercial use of agricultural and empty spaces calculations and changes in housing units, which have changed from the category of use because they have been cut off and annexed for commercial use. However, institutions and commercial markets have rapidly developed over time to the present study, which covers all parts of the city, or the outskirts of the city, or outside the residential neighborhoods (Paul et al., 2016).

### **Change Detection in the Industrial Area**

The present form of distribution of industrial land use is not the result of coincidence; however, it is governed by several factors, including site, land, planning, transport, political and other factors, to achieve the current distribution (Bajocco et al., 2012). Thus, in Table 1 and Figure 4, industrial use reported an area of 48.548 hectares by 0.407% in 1997. However, this increase did not last long but recorded a significant decline during the 1990s following the imposition of economic sanctions (economic blockade and its consequences), which led to the suspension of many industrial projects primarily based on raw materials

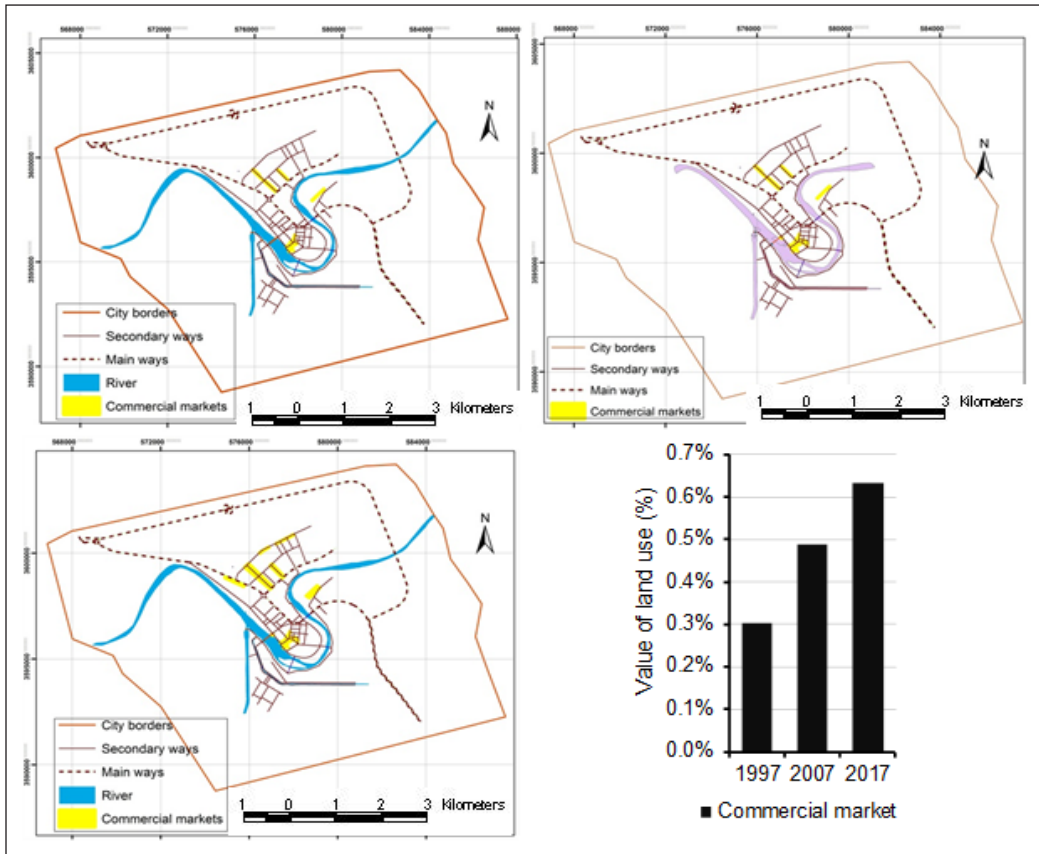


Figure 3. The changes of areas for commercial use in Al-Kut city in 1997, 2007, and 2017, and the percentage of commercial use change over the same period

imported from the outskirts, the industrial use area was 48.548 hectares in 2007 and a 437% increase in the area allocated for industrial use in 2017 to increased to 1.216% of the urban area of 154.962 hectares. It is due to the lifting of the economic sanctions imposed on Iraq and the diversification of industrial products received in the country, especially after the regime changed in 2003. In general, the amount of change in industrial use was recorded +106.414 hectares by the change rate of 219.193%.

### Change Detection in the Service Area

Figure 5 show that there has been a noticeable change in the uses of service land (educational, health, religious, and recreation), particularly with the rise in the area allocated to each of the two dates. Table 1 shows an increase in the rate of change area for service uses. Therefore, the area changes, and the rate of increase changes during the study periods, shifting towards the positive. For example, the change in Education services is 36.276%, health is 31.389%, religion is 26.827%, and recreation is 102.634%.

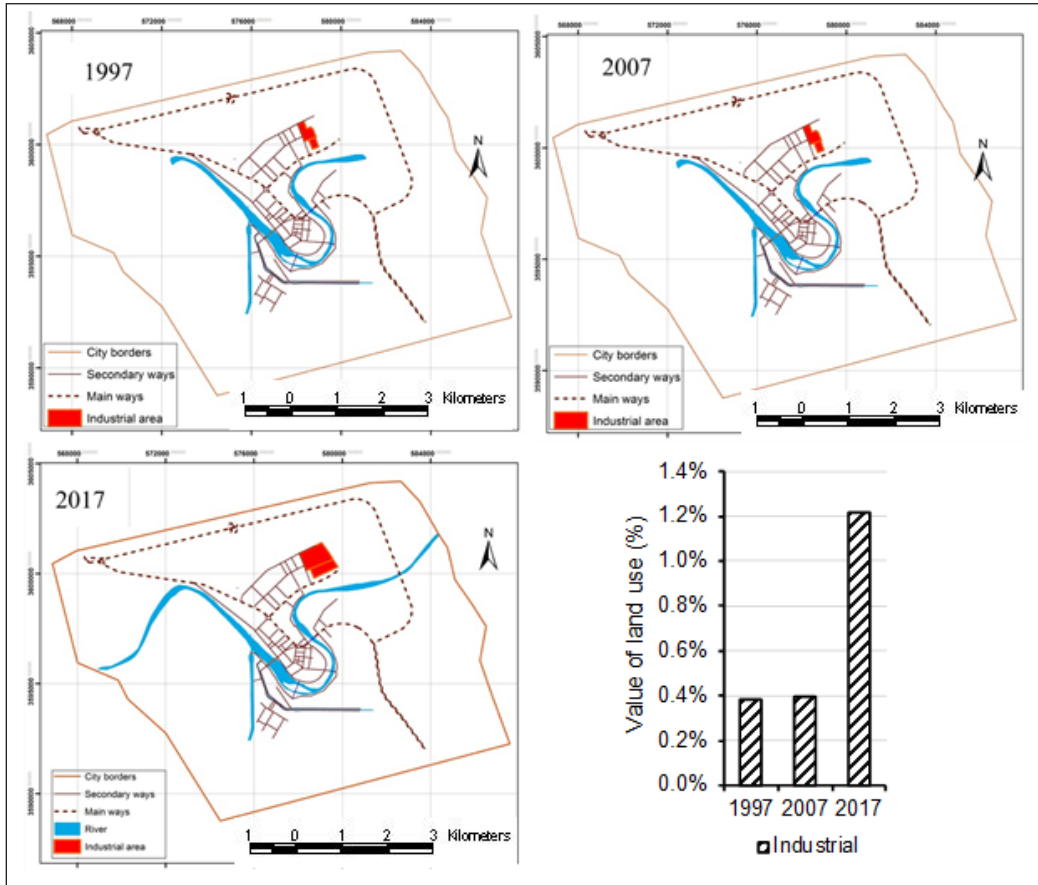


Figure 4. The changes of areas for industrial use in Al-Kut city in 1997, 2007, and 2017, and the percentage of industrial use change over the same period

### Change Detection in the Agricultural Area

Through remote sensing software and satellite image interpretation, it appears that the green area in the northern part of the city and some scattered areas that existed in the 1970s have decreased significantly, as shown in Table 1, which indicates the extent of change in agricultural land. The agricultural land area occupied 6529.453 hectares by 54.763% in 1997. The area decreased to 2285.406 hectares and 17.938% of the total area of the city in 2017. The absolute land change was recorded in -4244.047 hectares with a rate change of 64.998%. This reduction shows that the urban land use, especially the residential use, has been pushed at the expense of agricultural land, which has reduced the size of the current area, as shown in Figure 6. It can be seen in many areas that are presently residential neighborhoods. It can be noted that residential use is the most widespread use at the expense of agricultural land, and many of them have been fully urban, and the rest are still candidates for such use.

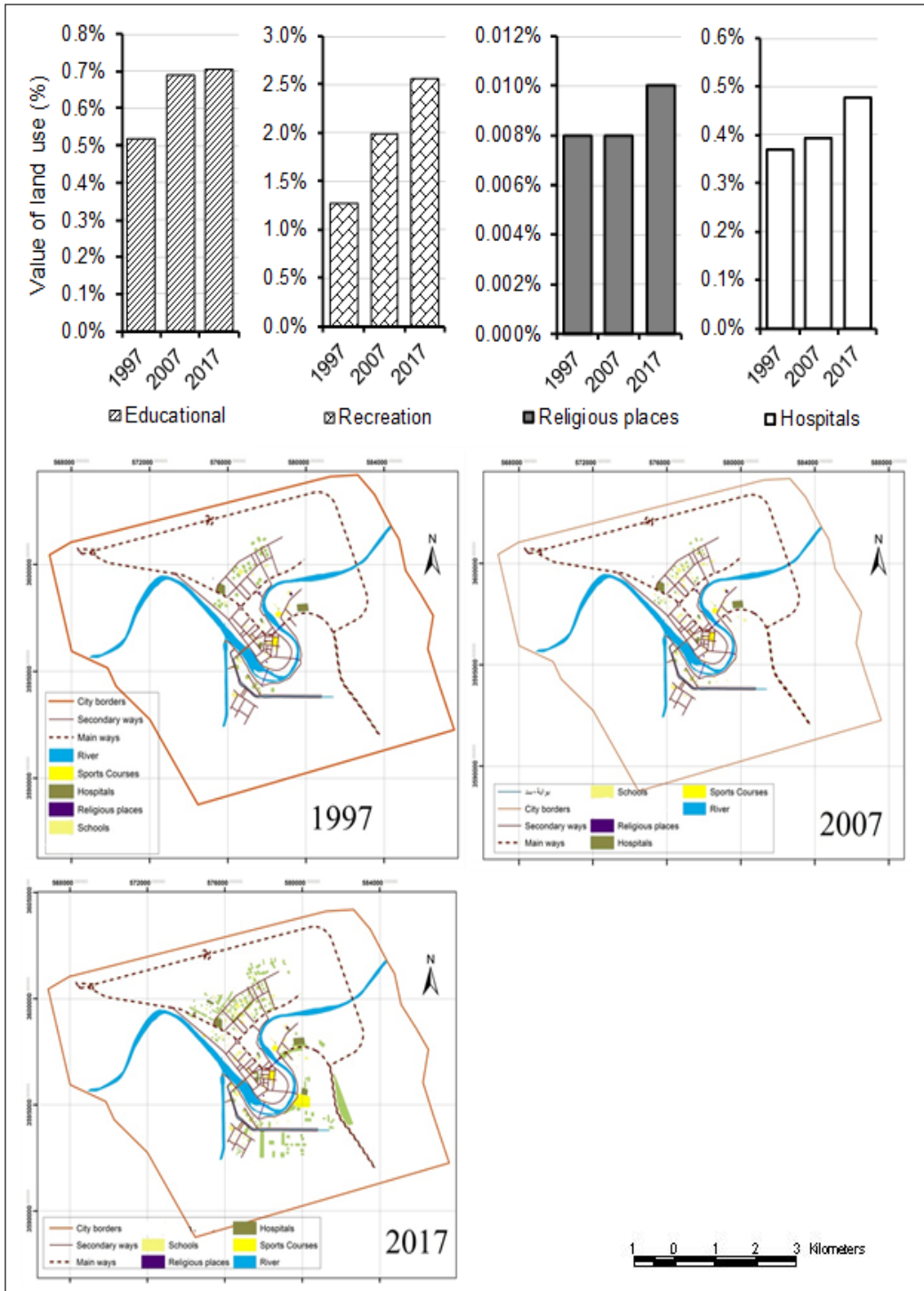


Figure 5. The changes of areas for services use in Al-Kut city in 1997, 2007, and 2017, and the percentage of services changed over the same period

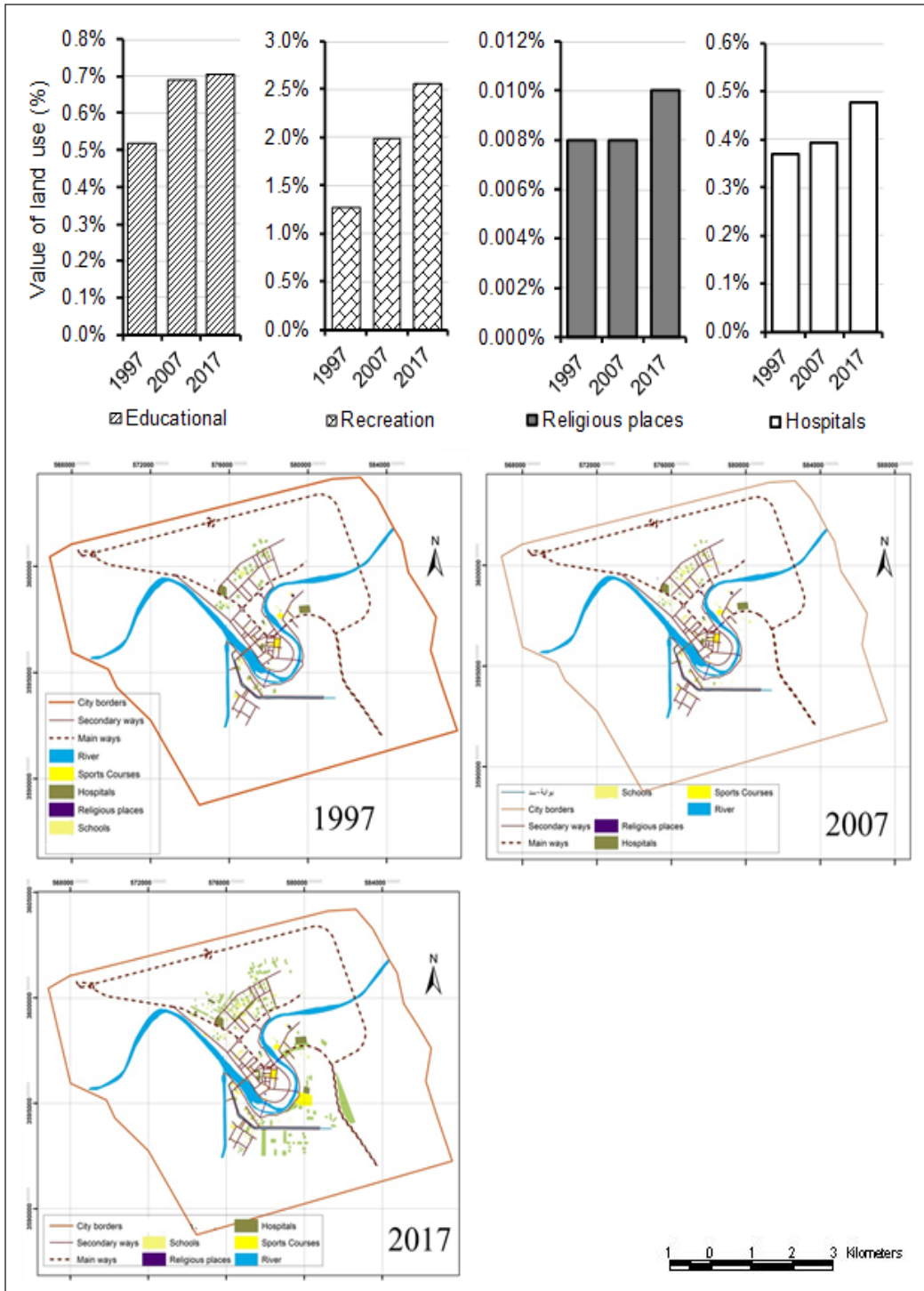


Figure 6. The changes of areas for agricultural use in Al-Kut city in 1997, 2007, and 2017, and the percentage of agricultural use change over the same period

### Change Detection in the Vacant Lands

As shown in Table 1, the vacant lands of the city have been reduced in area. For example, Figure 7 indicates that the empty space in 1997 was about half of the city’s area of 3546.762 hectares and 29.747% while this area reduced in 2017 to 29.167% with an area of 3715.967 hectares, so the change in the area was 169.205 hectares with the change rate of 4.77%.

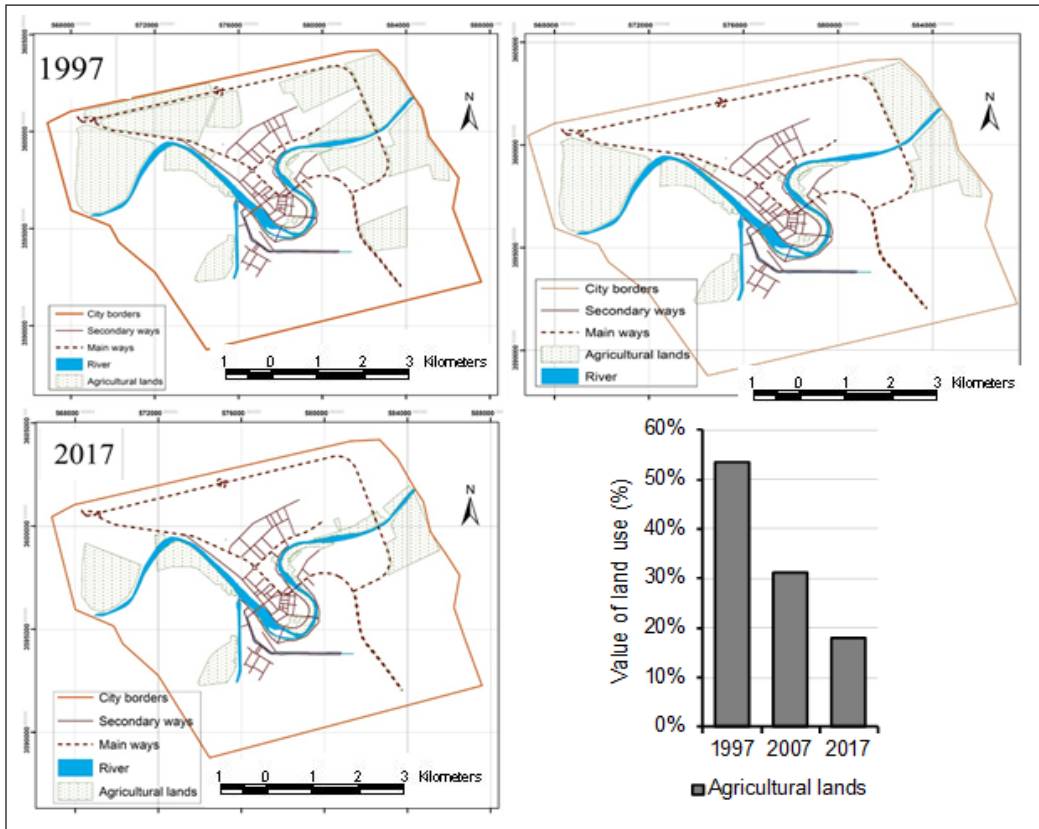


Figure 7. The changes of areas for vacant land in Al-Kut city in 1997, 2007, and 2017, and the percentage of vacant lands change over the same period

### CONCLUSIONS

The study of spatial and digital maps by remote sensing and geographic information systems (GIS) shows that residential use changed in the study period from 1997 to 2017. In 1997, it recorded 1486.107 hectares, which rose to 6026.432 hectares in 2017 with an increase of 4540.325 hectares, which means that the residential use area increased by four times during the mentioned period 305.518% change.

For several years digital photogrammetry was feasible, but the development of inexpensive and efficient desktop computers has led the technique out of the field of

science and into daily use. The methodology is now readily accessible, but many people do not know what the solution would be. Error is quantified in the methodology, and its consequences are discussed.

Data used in this analysis were from two areas of temperature, substrates, and relief contrasting to each other. These are the upland floodplains and river terraces in Wales and the topography of the Badlands in a semi-arid Spanish country. This method makes it possible for any procedure in the areas to make a detailed assessment of the absolute elevation error.

The study showed that urbanization, which highlighted the changes in the residential use category, was at the expense of agricultural land and empty spaces. The area of agricultural land, as shown by the NDVI technique of 1997, recorded 6529.453 hectares, with an area of 2285.406 hectares in 2017, With a negative change of 4244.047 hectares with a negative change of 64.998%, while vacant lands recorded in 1997, 3546.762 hectares expanded in 2017 to 3715.967 hectares, which means an absolute change of record of 169.205 hectares with a change of 4.77%.

Recommendation for the future study: There will be a range of additions to expand this work further and enhance the understanding and comparison of DEM sources. It may be interesting to study various interpolation procedures. Although other sources of DEMs would be more helpful as this would increase the confidence of results significantly. The new Shuttle Radar Topographic Mapping data are one source of potential for another DEM. Data will be accessible from this source in the future.

## ACKNOWLEDGEMENT

The authors gratefully thank Ali Asaad Tayeb for his assistance. Also, we would like to thank the governorate of Wasit for their support and providing the satellite images for the study area.

## REFERENCES

- Abd El-Kawy, O. R., Rød, J. K., Ismail, H. A., & Suliman, A. S. (2011). Land use and land cover change detection in the western Nile delta of Egypt using remote sensing data. *Applied Geography*, 31(2), 483-494. <https://doi.org/10.1016/j.apgeog.2010.10.012>
- Bajocco, S., De Angelis, A., Perini, L., Ferrara, A., & Salvati, L. (2012). The impact of land use/land cover changes on land degradation dynamics: A Mediterranean case study. *Environmental Management*, 49(5), 980-989. <https://doi.org/10.1007/s00267-012-9831-8>
- Boakye, E., Odai, S. N., Adjei, K. A., & Annor, F. O. (2008). Landsat images for assessment of the impact of land use and land cover changes on the Barekese catchment in Ghana. *European Journal of Scientific Research*, 22(2), 269-278.

- Dewan, A. M., & Yamaguchi, Y. (2009). Using remote sensing and GIS to detect and monitor land use and land cover change in Dhaka Metropolitan of Bangladesh during 1960–2005. *Environmental Monitoring and Assessment*, 150(1-4), 237-249. <https://doi.org/10.1007/s10661-008-0226-5>
- Halefom, A., Teshome, A., Sisay, E., & Ahmad, I. (2018). Dynamics of land use and land cover change using remote sensing and GIS: A case study of Debre Tabor Town, South Gondar, Ethiopia. *Journal of Geographic Information System*, 10(02), Article 83580. <https://doi.org/10.4236/jgis.2018.102008>
- Kim, J., Song, J., No, H., Han, D., Kim, D., Park, B., & Kee, C. (2017). Accuracy improvement of DGPS for low-cost single-frequency receiver using modified Flächen Korrektur parameter correction. *ISPRS International Journal of Geo-Information*, 6(7), Article 222. <https://doi.org/10.3390/ijgi6070222>
- Mengistu, D. A., & Salami, A. T. (2007). Application of remote sensing and GIS inland use/land cover mapping and change detection in a part of south western Nigeria. *African Journal of Environmental Science and Technology*, 1(5), 99-109
- Paul, S., Ghosh, S., Oglesby, R., Pathak, A., Chandrasekharan, A., & Ramsankaran, R. A. A. J. (2016). Weakening of Indian summer monsoon rainfall due to changes in land use land cover. *Scientific Reports*, 6(1), 1-10. <https://doi.org/10.1038/srep32177>
- Popovici, E. A., Bălteanu, D., & Kucsicsa, G. (2013). Assessment of changes in land-use and land-cover pattern in Romania using Corine Land Cover Database. *Carpathian Journal of Earth and Environmental Sciences*, 8(4), 195-208
- Prakasam, C. (2010). Land use and land cover change detection through remote sensing approach: A case study of Kodaikanal Taluk, Tamil Nadu. *International Journal of Geomatics and Geosciences*, 1(2), Article 150
- Verburg, P. H., Neumann, K., & Nol, L. (2011). Challenges in using land use and land cover data for global change studies. *Global Change Biology*, 17(2), 974-989. <https://doi.org/10.1111/j.1365-2486.2010.02307.x>
- Xiao, H., & Weng, Q. (2007). The impact of land use and land cover changes on land surface temperature in a karst area of China. *Journal of Environmental Management*, 85(1), 245-257. <https://doi.org/10.1016/j.jenvman.2006.07.016>



## Automation of Psychological Selection Procedures for Personnel to Specific Activities

Ihor Prykhodko<sup>1</sup>, Stanislav Horielyshev<sup>1\*</sup>, Yanina Matsehora<sup>1</sup>, Vasiliy Lefterov<sup>2</sup>, Stanislav Larionov<sup>1</sup>, Olena Kravchenko<sup>1</sup>, Maksim Baida<sup>1</sup>, Olena Halkina<sup>3</sup> and Olena Servachak<sup>4</sup>

<sup>1</sup>National Academy of the National Guard of Ukraine, Kharkiv, 61001, Ukraine

<sup>2</sup>National University "Odessa Law Academy", Odessa, 65009, Ukraine

<sup>3</sup>Kharkiv National University of Internal Affairs, Kharkiv, 61057, Ukraine

<sup>4</sup>Donetsk National Technical University, Pokrovsk, 85300, Ukraine

### ABSTRACT

The article presents a universal method for determining the professional suitability (PS) of a candidate and an algorithm for forming a psychological profile for a specific profession based on determining the psychological potential of personality. The developed method is based on the use of automated support systems. Based on the obtained value of the integral indicator, a decision is made on the PS group of this candidate. This method adapts to the requirements of the profession to candidates, taking into account changes in the conditions of activity by adjusting the typical psychological profile of the personality. The developed method for determining a candidate's PS has been brought to practical implementation in the form of an Automated Psychodiagnostic Complex (APDC) "Psychodiagnostics." APDC has been tested on the example of the psychological selection procedures of personnel for military service in units with law enforcement functions. APDC allows to reduce the time and labor costs for conducting psychodiagnostic studies, increases the reliability of tests

due to a higher degree of standardization of the testing procedure, increases the accuracy of assessing psychological characteristics, and reduces the likelihood of errors in the processing of test results. APDC can be used for recruiting in various sectors of the economy, education, and military sphere.

*Keywords:* Automation, extreme activity, integral indicator, personality characteristics, psychological selection procedures

### ARTICLE INFO

#### Article history:

Received: 06 April 2021

Accepted: 19 November 2021

Published: 04 January 2022

DOI: <https://doi.org/10.47836/pjst.30.1.41>

#### E-mail addresses:

prikhodko1966@ukr.net (Ihor Prykhodko)

port\_6633@ukr.net (Stanislav Horielyshev)

yanina\_gora@ukr.net (Yanina Matsehora)

lefterov.vasil@gmail.com (Vasiliy Lefterov)

larionov1985@gmail.com (Stanislav Larionov)

elena\_diamant@outlook.com (Olena Kravchenko)

maxbayda07@ukr.net (Maksim Baida)

yaen0110@gmail.com (Olena Halkina)

e.v.servachak@gmail.com (Olena Servachak)

\* Corresponding author

## INTRODUCTION

Automation based on artificial intelligence and machine learning has increasingly been used to support managerial tasks and duties to enhance the quality and efficiency of information processing and decision-making (Langer et al., 2020). Solving the problem of determining professional suitability (PS) leads to the determination of a person's inclination to a particular category of professions, where his potential, psychophysiological reactions to external conditions, the ability to make adequate decisions depending on the circumstances are most fully revealed (Prykhodko, 2008). An employee who has developed professionally important psychological traits has better performance indicators (both qualitative and quantitative), is less prone to professional deformation, illness, and injury, his professional age is greater, and the cost of training is much lower (Vorobyova et al., 2012). It becomes the key to the high-quality fulfillment of the tasks set, raising the status of a person in a team and his self-esteem.

It is necessary to consider automation and decision support systems to get a clearer understanding of automated systems for personnel selection procedures (PSP). Sheridan and Parasuraman (2005) propose to consider automation as “a) the mechanization and integration of the sensing of environmental variables (by artificial sensors), b) data processing and decision making (by computers), c) mechanical action (by motors or devices that apply forces on the environment), d) and/or ‘information action’ by communication of processed information to people.” We focus on the data processing and decision-making aspects of automation, followed by information action, where systems provide processed information to human decision-makers. This kind of automation is reflected by four broad classes of functions of automation: a gathering of information, filtering and analysis of information, decision recommendations, and action implementation (Parasuraman et al., 2000). With more of these functions realized within systems, the extent of automation increases. Systems that provide decision recommendations could be trained on previous data to fulfill classification (e.g., distinguishing suitable vs. non-suitable applicants) or prediction tasks (e.g., what applicants will most likely be high-performing employees). The outputs of those tasks can then be presented to human decision-makers. It is precisely the kind of automated system that the current paper refers to automated systems that gather and analyze the information as well as derive inferences and recommendations based on these steps. Such systems can aid hiring managers, psychologists in a large range of their duties (e.g., gathering and integrating of information, applicant screening), and their outputs can be used as an additional (or alternative) source of information for decision-makers (Langer et al., 2020).

Automated support systems for high-level cognitive tasks are an emerging topic in research and practice, especially within PSP. Within human resource management, current practical developments, and recent research point to a future where managers will

collaborate with automated systems to work on tasks as varied as scheduling (Ötting & Maier, 2018), PSP (Campion et al., 2016; Petrescu et al., 2015), including for military personnel (Farina et al., 2019) and law enforcement officers (Zhiltsova et al., 2005). Various automated support systems for PSP have been developed and implemented in the U.S. Armed Services and the Special Forces (Farina et al., 2019), Russian Federation (Zhiltsova et al., 2005), Ukraine (Zlepko et al., 2010), and other countries.

There are different approaches in the methodology of creating automated support systems for determining the PS of candidates. Skorupski et al. (2020) used a computer-generated fuzzy model based on linguistic variables to construct a candidate's PS profile. Anitei and Buzea (2012), Kabak et al. (2012), and Kelemenis and Askounis (2010) have proposed a fuzzy hybrid multicriteria decision-making approach that combines qualitative and quantitative factors. For this, the authors used a combination of Fuzzy ANP, Fuzzy TOPSIS, Fuzzy ELECTRE methods. Grechushkina (2020) developed indicators of the potential effect of introducing software and hardware psychodiagnostic complexes to determine the PS of future officers.

The emerging use of such systems, especially for PSP, might be due to the complexity of personnel selection. Automated decision support systems might help gather and combine information for large applicants, thus making selection procedures more efficient, and there is hope that they can attenuate adverse impact (Langer et al., 2020).

Thus, the problem of the automated support systems for PSP from auxiliary to the sphere of mandatory means of research is relevant since computer technology is increasingly penetrating the sphere of humanitarian disciplines, particularly psychology (Spielberger, 2004). Moreover, their use contributes to the rapid and most reliable determination of human PS to a specific category of professions.

The purpose of the study is to develop the method for determining the candidate's PS for a certain category of professions, taking into account his psychological potential and allowing him to predict success in a particular profession. Therefore, it is necessary to solve the following tasks to achieve the goal: (1) substantiate the methodology for the formation of a psychological profile with given parameters, depending on specialization; (2) to develop a method for calculating the integral indicator of PS based on the obtained test data and a given psychological profile; (3) offer tools for determining and automating the method of calculating candidate's PS for a certain category of professions.

## **MATERIALS AND METHODS**

### **Method of Formation Psychological Selection Procedures for Personnel to Specific Activities**

The method of formation PSP for personnel to specific activities is a system of consistently conducted activities developed by the authors and includes four main stages: studying the characteristics of professional activities and substantiating requirements; formation of a

typical psychological profile; development of a method for calculating the integral indicator of the candidate's PS for a certain category of professions; deciding on PS.

The proposed method is based on the Eastern European classical approach for determining the PSP of specialists (Bodrov, 2007; Prykhodko, 2008), taking into account personality characteristics and features of future professional activity. This method is based on the principles used in the PSP in different countries. The choice of specific psychodiagnostic tests depends on the cultural characteristics of the subjects, the field of professional activity. The list of psychodiagnostic tests is formed based on the most common and recognized tests used for PSP in a particular country.

Several pilot studies were carried out during 2012–2014 to develop the psychodiagnostic tests battery used in this study. The objectives of these studies were to identify the relationship between the personality characteristics of candidates with the success of training in a higher military educational institution and the effectiveness of the professional activity. As a result of these studies, professionally important psychological characteristics and adequate psychological tests for their measurement were identified.

The flowchart of the method of formation PSP to specific activities is shown in Figure 1. Further, the stages of formation of the PSP to specific activities are discussed in more detail.

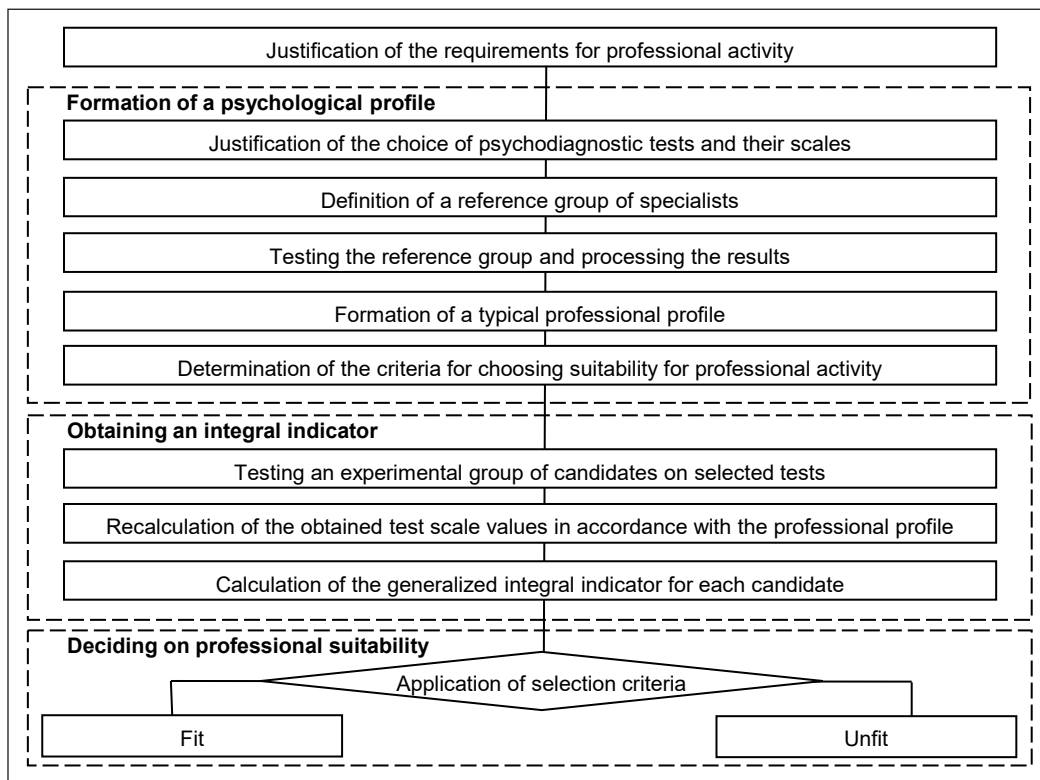


Figure 1. The flowchart of the method of formation psychological selection procedures for personnel to specific activities.

### **Method for Studying the Characteristics of Professional Activity and Justifying Requirements**

At this stage, the features of specific types of professional activity were studied, and the requirements for professionally important psychological characteristics of a personality were determined. The main method of psychological research of professional activity in various specialties is analytical professiography (Bodrov, 2007). Analytical professiography allows to study of the patterns, mechanisms, conditions, and factors of the productive development of personnel and the implementation of the chosen life strategy (Karpilovskaya et al., 1997; Melnyk et al., 2019).

As a result of such a study, the criteria for the success of professional activity are determined; the procedure for choosing psychological tests for assessing professionally important psychological characteristics necessary for the successful mastering of this profession is substantiated. For this, a professiogram (psychogram) is drawn up, which indicates professionally important psychological characteristics that allow the candidate to master a particular specialty successfully and quickly (Prykhodko, 2008). First, the revealed psychological characteristics were assessed on a five-point Likert scale in accordance with the following criteria: (1) the degree of importance of each quality for achieving the final goal (result), performing a specific task (element, operation); (2) the duration and frequency of application of this psychological characteristic to perform all types of activity (work process); (3) the duration and frequency of application of this psychological characteristic when performing a specific task (individual labor operations); (4) the degree of complexity of each psychological characteristic. Next, the average score of professionally important psychological characteristics was calculated. Thus, we obtained quantitative and qualitative indicators of professionally important psychological characteristics necessary for effective professional activity in a particular specialty. Further, these characteristics were assessed during psychodiagnostics of the candidate's PS.

### **Formation of a Psychological Profile with Specified Characteristics Depending on the Category of Professions**

The formation of candidate's PS can be divided into the following stages: (1) definition of a test battery covering all aspects of this category of professions; (2) determination of reference groups of specialists, testing; (3) the formation of a typical psychological profile and the establishment of restrictions.

To determine the candidate's PS level for specific activities, proceed from psychological, psychophysiological, medical, and other criteria. It determines the choice of psychodiagnostic techniques that determine the degree of mastery of professional knowledge and skills (achievement tests) and the level of development of professionally important psychological characteristics.

In accordance with the given characteristics of the profession, several experimental groups are formed: successful professionals, professionals, and low-performing employees. In each group, specialists in different age categories should be represented in approximately equal proportions.

In constructing the psychological profile, statistical data were used, on the one hand, obtained after testing the selected groups, and on the other hand, the ideal model (according to the given characteristics).

If psychological tests are used  $n$ , then a test vector is formed  $\vec{T} = (T_1, T_2, \dots, T_n)$ . Each psychological test is characterized by its own set of scales  $\vec{S}_i = (S_{i1}, S_{i2}, \dots, S_{ik})$ . The number of scales  $k$  in each test may differ. Then the psychological profile can be represented by a set of scales (individual psychological characteristics) in the form of a column vector

$$\vec{P} = \begin{pmatrix} \vec{S}_1 \\ \vec{S}_2 \\ \dots \\ \vec{S}_n \end{pmatrix}, \text{ and the number of scales is calculated as in Equation 1:}$$

$$M = \sum_{i=1}^n k_i, \quad (1)$$

where  $k_i$  – the number of scales in the  $i$ -th test.

In accordance with the key to the test  $T_i$  used, a set of possible values is formed for each scale using Equation 2:

$$S_{ij} = \{a_1, a_2, \dots, a_r\} \quad (2)$$

where  $a_1$  – minimum scale value,  $a_r$  – maximum scale value,  $r$  – number of possible scale values,  $i = 1 \dots n$  – psychological test number,  $j = 1 \dots k$  – scale number of the  $i$ -th psychological test.

Based on the obtained statistical data of testing the experimental groups, for each scale of each test  $S_j$ , the distribution of a random variable of its values  $\mathbf{P}^a$  is constructed and described by the distribution function  $F(a)$  (Ventzel, 2006). Unfortunately, the scale values even in one test can differ by several orders of magnitude. Therefore, to take into account their contribution to the PS value, it is necessary to normalize the distribution  $F(a)$  relative to the general ten-point universal scale  $F_{10}(a)$  and approximate it in accordance with the given requirements for an ideal specialist in this profession.

Thus, for each psychological characteristic of each test, we obtain a distribution of the values of the survey results on a standard ten-point scale  $F_{10_{ij}}(a)$ . The totality of these distributions is the average psychological profile for this specialty. According to the comparison results, by correlation analysis of successful and poorly successful

experimental groups, the most significant qualities in the psychological profile are identified and restrictions on the minimum value in  $F_{10ij}(a)$ .

### **The Method of Calculation the Integral Indicator of Professional Suitability Based on the Obtained Test Data and the Psychological Profiling**

The main task of the study was to develop a comprehensive indicator of the effectiveness of the professional activity, taking into account different aspects of the personality of the candidate. As a result, this made it possible to decide on its distribution into one of three suitability groups: unsuitable, conditionally suitable, and suitable.

The decision criterion used the principle of similarity of the candidate's profile to the average psychological profile of his representative. As an indicator used an integral indicator of PS, the basis of which was the assessment of characteristics on the scales of psychodiagnostic tests, the formation of the average value of the test using the created psychological profile, and the summation of these values over the entire set of tests.

At the first stage for each scale  $S_j$ , its values  $a_j$  were obtained in accordance with the key. Further, to take into account the contribution of all scales to the overall indicator of the psychodiagnostic test  $T_i$ , a generalized indicator for this test  $P_i^0$  was formed by recalculating the values of the scales in accordance with the standard normalized distribution of a given profile  $F_{10ij}(a)$  and further averaging using Equation 3:

$$P_i^0 = \frac{\sum_{j=1}^{k_i} F_{10ij}(a_{ij})}{k_i} . \quad (3)$$

At the second stage after, obtaining the values of the generalized indicators for each test, derived the integral indicator  $PS^*$  of the candidate's PS for a certain category profession by summing them up using Equation 4:

$$PS^* = \sum_{i=1}^n P_i^0 . \quad (4)$$

Depending on the number of selected tests, covering professionally important psychological characteristics, the maximum possible value of the integral indicator of PS was calculated using Equation 5:

$$PS_{\max}^* = 10 * n , \quad (5)$$

where  $n$  – number of psychological tests.

Empirical studies conducted with a control group of specialists in a specific profession (in this study, there were candidates for military service) made it possible to establish the selection criterion at the level  $PS^* > 0.6 * PS_{\max}^*$  (all candidates who scored more than 60% of the maximum possible value). As a result, the selected candidates had the necessary professional qualifications to fulfill their professional duties successfully.

Thus, using the developed method, an integral indicator of PS was obtained, which, in accordance with the selected criterion, made it possible to make an informed decision about the suitability of the candidate for this profession.

### **Automation of the Method for Determining the Professional Suitability of a Candidate for a Certain Category of Professions**

When developing tools of the method for determining PS, the authors of the article paid special attention to the following aspects: automation of the individual and group testing procedures, automation of the processing of test results, their storage, and protection, as well as different ways of presenting individual and group testing results, depending on the tasks facing the psychologist (creation of an individual psychological support card, data transfer to the Word application, transfer of group testing data to the Excel application for further statistical processing) (Arestova et al., 1995; Matsehora et al., 2014; Vorobyova et al., 2012).

The implementation of this method was the creation of an Automated Psychodiagnostic Complex (APDC) “Psychodiagnostics.” The specifics of the solution of the tasks are dictated by the need to build APDC both in the network version and in the local one. The functional diagram of the APDC “Psychodiagnostics” is shown in Figure 2.

In both construction options, two specialized operating modes of APDC are envisaged—the modes “Respondent” and “Psychologist.” The “Respondent” mode allows you to conduct psychological testing of the subject according to a given set of psychological tests. The “Psychologist” mode gives the user full access to all the possibilities of the APDC, for example, the formation of psychodiagnostic tests battery for the given profession, setting the selection criteria and forming a standard psychological profile, obtaining an integral indicator, working with the database of the subjects and the results of their psychological testing.

When the system is deployed on a local computer, the equipment of these terminals coincides; that is, one personal computer (PC) is used. However, in the network implementation, several different PC are used: one is the “terminal” of the psychologist; the other is the terminal of the respondent. The exchange of information between the modules is carried out using a control and data exchange module, which control signals of the complex’s operation, information flows pass.

In the “Respondent” mode, the following modules are used: the module of respondent identification, the module of test dialogue, and the module of automated psychodiagnostic



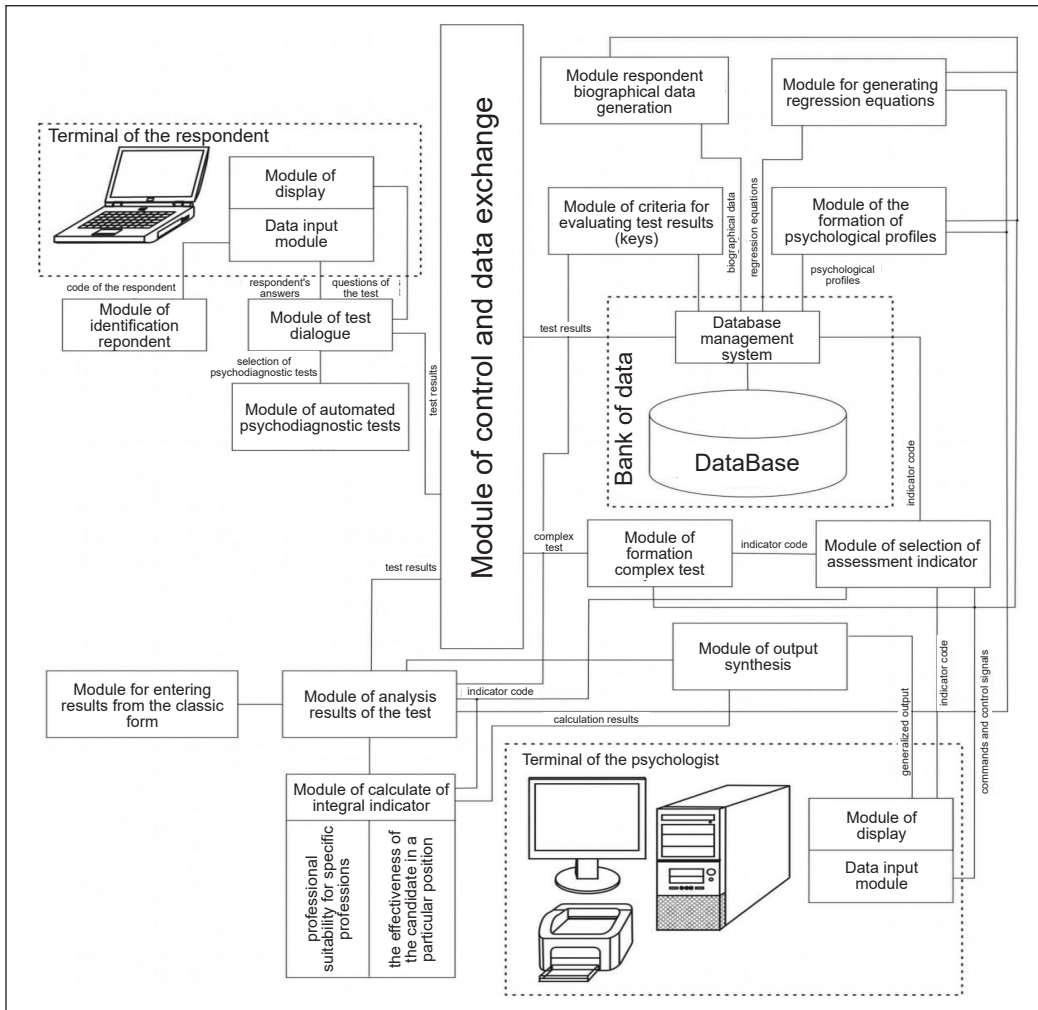


Figure 2. Functional diagram APDC “Psychodiagnosis”

tests. Finally, in the “Psychologist” mode, the functioning of the complex requires additional modules that significantly expand the psychologist’s capabilities in the field of analysis of the results obtained and their display, calculation of various integral indicators (PS, including indicators for specific professions), values of regression equations the effectiveness of the candidate in a particular position, as well as testing.

Thus, the developed method for determining PS is brought to practical implementation based on a PC and tested in practice.

## RESULTS AND DISCUSSION

Consider the use of the method on the example of the PSP of candidates for military service in units with law enforcement functions.

All respondents (N = 186) were divided into three groups in the experiment. Group 1 (n = 62) was formed from the most experienced specialists from units with law enforcement functions (reference group), Group 2 (n = 62) and Group 3 (n = 62) were made up of respondents who were candidates for professional activities with law enforcement functions. The test results of Group 1 were used to form the typical psychological profile of the personality  $F_{10ij}(a)$ . The determination of PS in Group 2 was carried out using the APDK “Psychodiagnostics,” and in Group 3 without its use (testing was carried out on paper by the same methods, but with manual calculation, and the integral index of PS was not determined).

After a detailed study of the activities of the military personnel of such units and substantiation of professional requirements, a test battery was formed (Table 1) that covered almost all aspects of the personality (Matsehora et al., 2014; Vorobyova et al., 2012). The selection of these psychodiagnostic tests was based on PSP principles in post-Soviet countries.

For the selected tests, using the results of Group 1, a typical psychological profile was formed, which consisted of 51 scales ( $T_1$  – 1 scale,  $T_2$  – 5 scales,  $T_3$  – 8 scales,  $T_4$  – 10 scales,  $T_5$  – 9 scales,  $T_6$  – 17 scales,  $T_7$  – 1 scale). For example, for the test  $T_1$ , one indicator,  $S_{11}$ , is evaluated—the intelligence coefficient. Its original range of points varies from 0 to 132. The distribution function  $F(a)$  of intelligence points of the reference sample is shown

Table 1  
*Psychodiagnostic tests battery*

№	Test name	Test focus	Test designation
1	“Progressive Matrices” (J. Raven)	Common abilities that determine the ability to master any activity	$T_1$
2	“Temperament Structure Questionnaire of Self-assessment” (B. Smirnov)	Features of temperament	$T_2$
3	“The Motivation Questionnaire for Professional Choice of Candidates for Service in the Ministry of Internal Affairs of Ukraine”	Features of the choice motivation	$T_3$
4	“Determining the Type of Accentuation of Character Traits and Temperament Questionnaire” (K. Leonhard, H. Schmieschek)	Character traits and accentuations that worsen adaptation to new conditions	$T_4$
5	“Suicidal Risk Questionnaire” (A. Shmelev)	Strong-willed features and suicidal tendency	$T_5$
6	“The Sixteen Personality Factor Questionnaire (16PF)” (R. Cattell)	A generalized characteristic of human traits	$T_6$
7	“Multi-level Personality Questionnaire ‘Adaptability’” (A. Maklakov, S. Chermyanin)	Features of adaptation of a person to new conditions, its tolerance to changes	$T_7$
8	“Luscher Color Test” (modified by L. Sobchik)	Features of the emotional sphere	$T_8$

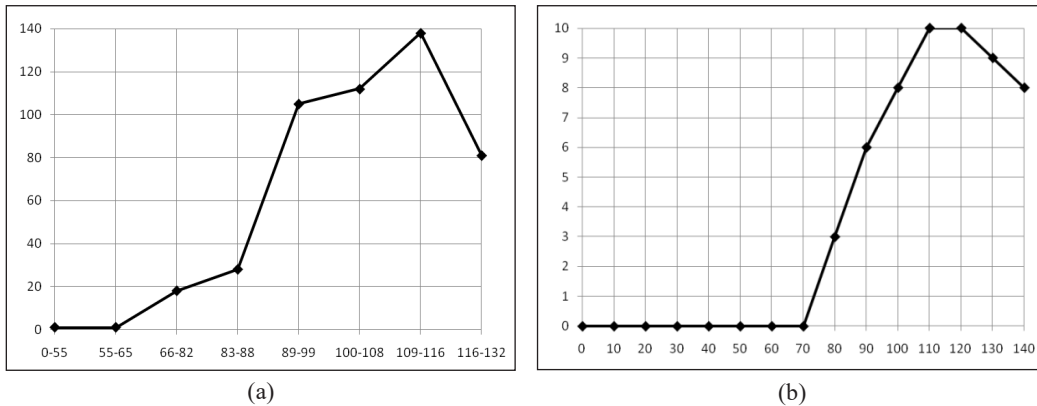


Figure 3. Distribution of intelligence points in the sample: (a) distribution function (maximum ordinate value is 138 points), (b) normalized distribution function (maximum ordinate value – 10, step after abscissa 10).

in Figure 3(a), and the normalized distribution function  $F_{10,11}(a)$ , taking into account the approximation, is shown in Figure 3(b).

A feature of the approximation of this indicator is the fact that an intelligence score of up to 70 “conditional points,” inclusive, is not evaluated on a ten-point scale and is assigned a zero value. In addition, this indicator is professionally important, and the minimum necessary value is set for it in 6 normalized units of a ten-point scale. Let us present data comparing intelligence indicators in highly successful and poorly successful groups of military personnel (Table 2).

The data obtained indicate that highly successful military personnel have significantly higher indicators on the intelligence scale ( $106.57 \pm 12.03$ ) than poorly successful ( $98.82 \pm 12.72$ ), indicators of statistical significance of differences according to the Student’s T-test and Fisher test ( $t=4.42$ ,  $p \leq 0.01$ ). Thus, there is a significant relationship between the index of intelligence and the success of activities, but this relationship is weak. Table 3 shows the discrete normalized distribution function  $F_{10,11}(a)$  after approximation. A similar approach is applied to the remaining scales of the selected tests.

Table 2

*Intelligence indicators of military personnel of units with law enforcement functions (in conditional points)*

Scales	Highly successful military personnel	Weak military personnel	t	p
Intelligence	106,57±12,03	98,82±12,72	4,42	0,01

Table 3

*Discrete values of the normalized distribution function after approximation*

Points	0	10	20	30	40	50	60	70	80	90	100	110	120	130	140	Critical value
$F_{10,11}(a)$	0	0	0	0	0	0	0	0	3	6	8	10	10	9	8	6

Further, with the help of the APDC, the candidates of Group 2 were tested, the results were saved, the integral indicator of PS to service in units with law enforcement functions was calculated, and the candidate's suitability group was determined (I – suitable, II – conditionally suitable, III – not suitable). The results obtained for Group 2 for a small sample ( $n = 8$ ) are shown (for example) in Table 4. In Table 4, columns 2–8 show the results of tests calculated relative to a given psychological profile, in column 9 the integral indicator, and in column 10 the candidate's PS group.

The proposed method for determining a candidate's PS for a particular profession was developed to simplify the decision-making process based on the results of the PS of applicants. Implementing this method with the help of automated support systems contributes to the fastest and most reliable determination PS of a candidate. In addition, the developed method for determining the PS of a candidate involves the use of no more than three candidate suitability groups.

In contrast to the results of the studies Arestova et al. (1995), Grechushkina (2020), Zhiltsova et al. (2005), Zlepko et al. (2010), the developed method for calculating the integral indicator of the candidate's PS for a certain category of professions and the algorithm for forming a psychological profile for a particular profession allows obtaining a more reliable result in determining a person's ability to a certain category of professions. As a result of the conducted studies of Group 2, the time for testing, processing the results obtained, and making a decision on suitability was reduced by 73%, the reliability of the results obtained (the presence of errors in the non-automated calculation of test scale values) improved by 7% compared to the results of Group 3. The effectiveness of the developed method is comparable with similar indicators used in the studies of Anitei and Buzea (2012), Kabak et al. (2012), Kelemenis and Askounis (2010).

The developed method also allows to research a large number of candidates, reduce the time for testing and processing the results, and avoid subjectivity when making a decision (Prykhodko, 2020). However, the reliability of a decision on PS largely depends

Table 4  
Results of determining the PS candidates

Full name	$T_1$	$T_2$	$T_3$	$T_4$	$T_5$	$T_6$	$T_7$	PS*	Group
1	2	3	4	5	6	7	8	9	10
Candidate 1	10	7.899	9	4.999	7.746	7.374	5.000	52.02	II
Candidate 2	10.00	5.200	8	8	9.522	7.374	7.199	55.29	I
Candidate 3	8.799	8.799	7.125	7.900	8.333	7.079	9.599	57.63	I
Candidate 4	9.200	4.900	5.25	4.900	3.251	4.720	1	33.22	III
Candidate 5	6.200	6.799	6.75	8.300	8.634	6.725	9.999	53.41	II
Candidate 6	10	6.300	8.249	8.200	8.895	5.781	7.399	54.82	I
Candidate 7	7	9.299	4.75	8.200	8.999	7.138	7.799	53.18	II
Candidate 8	6.800	6.299	7	7.900	7.635	7.138	5.200	47.97	II

on the accuracy and correctness of research on the formation of the characteristics of the psychological profile based on selected reference groups of specialists of a particular specialization (Prykhodko et al., 2020). Also important is the process of selecting the numerical values of the boundaries of groups of candidates, which depend on the number of selected tests and the given requirements for these groups (Cano, 2018).

All the obtained calculation data of the integral indicator of PS can be presented in text and graphic forms. Generalized data are synthesized for an individual respondent and a group united by a common attribute. Information can be made out in the form of tables according to the results of methods, scales, digital data, and graphs. In addition, a descriptive interpretation is made for each test indicator.

The developed method for determining PSP and APDC was implemented in the practical activities of the psychological service of the National Guard of Ukraine (NGU). In 2014–2016, the basics of the practical use of APDC at NGU were determined, and psychologists were trained to work with it. After the official consolidation of the developed method and the APDC in the regulatory documents in 2016, regulating the activities of the NGU psychological service, its practical use was carried out. To date, with his help, more than 20 000 candidates for military service and NGU military personnel have undergone psychodiagnostic studies. In addition, constant monitoring studies are being carried out, which track the links between the effectiveness of the professional activities of military personnel with personality indicators measured and assessed by the APDC. In these studies, with a large sample of subjects, the reliability of the developed method was confirmed.

Further improvement of the method should improve forming a psychological profile with specified characteristics depending on the category of professions, justification, and correction of the values of the boundaries of the focus groups, and their automation.

## CONCLUSIONS

As a result of the study, for the first time, the method was developed for calculating the integral indicator of the candidate's PS and an algorithm for forming a psychological profile for a specific profession. The developed method differs from the known ones in that the total PS indicator is calculated taking into account the totality of psychological characteristics of personality (cognitive, typological, characterological, neurodynamic, emotional-volitional, motivational). This method adapts the requirements of the profession to candidates, taking into account changes in the conditions of activity by adjusting the typical psychological profile of personality.

The algorithm for forming a psychological profile consists of the following stages: defining a set of tests; definition of reference groups of specialists and their testing; formation of a typical psychological profile of personality. The developed algorithm forming a psychological profile of personality with given characteristics, depending on

the specialization, makes it possible to include an arbitrary number of psychodiagnostic tests. The number of tests and scales is determined when analyzing the requirements for professional activity and compiling a list of psychological characteristics that contribute to the successful mastery of this specialty and effective performance of official duties in real-life conditions.

The developed method for calculating the integral indicator of the candidate's PS is based on obtaining testing data on the selected scales of psychodiagnostic tests; their recalculation in accordance with the created typical psychodiagnostic profile and the summation of the data obtained. Thus, the general integral indicator includes all the characteristics of the candidate's personality, considering their importance.

The practical result of the research is the developed software toolkit for the method of determining the candidate's PS for a given category of professions in the form of an APDC "Psychodiagnosics." It reduces the time and labor costs for conducting psychodiagnostic studies, increases the reliability of tests due to a higher degree of standardization of the testing procedure, increases the accuracy of assessing psychological characteristics, and reduces the likelihood of errors in the processing of test results. In addition, the APDC accelerates the decision-making process based on test results due to the ability to calculate test scores and generate reports on the results quickly.

## ACKNOWLEDGEMENT

The work presented in this paper has been supported by the Main Directorate of the National Guard of Ukraine (research project No. DR 0119U001475).

## REFERENCES

- Anitei, M., & Buzea, E. (2012). Models and applications in psychological selection and evaluation. *Procedia Social and Behavioral Sciences*, 33, 756-760. <https://doi.org/10.1016/j.sbspro.2012.01.223>
- Arestova, O. N., Babanin, L. N., & Voyskunsky, A. E. (1995). *Spetsifika psikhologicheskikh metodov v usloviyakh ispolzovaniya kompyutera* [The specifics of psychological methods in terms of using a computer]. Publishing house of Moscow University.
- Bodrov, V. A. (2007). Razvitiye sistemnogo podkhoda v issledovaniyakh professionalnoy deyatelnosti [The development of a systems approaches in the study of professional activities]. *Psychological Journal*, 28(3), 23-28.
- Campion, M. C., Campion, M. A., Campion, E. D., & Reider, M. H. (2016). Initial investigation into computer scoring of candidate essays for personnel selection. *Journal of Applied Psychology*, 101(7), 958-975. <https://doi.org/10.1037/apl0000108>
- Cano, A. (2018). Use of psychological test in personnel selection processes in consultants of human assumption resources. *Eureka-Revista Cientifica De Psicologia*, 15(1), 108-120.

- Farina, E. K., Thompson, L. A., Knapik, J. J., Pasiakos, S. M., McClung, J. P., & Lieberman, H. R. (2019). Physical performance, demographic, psychological, and physiological predictors of success in the U.S. Army Special Forces Assessment and Selection course. *Physiology & Behavior*, *210*, Article 112647. <https://doi.org/10.1016/j.physbeh.2019.112647>
- Grechushkina, E. (2020). *Ispolzovaniye informatsionnykh tekhnologiy v psikhologo-pedagogicheskoy soprovozhdenii podgotovki ofitserских kadrov* [The use of information technology in the psychological and pedagogical support of the training of officer personnel]. Multipsikhometr.
- Kabak, M., Burmaoğlu, S., & Kazançoğlu, Y. (2012). A fuzzy hybrid MCDM approach for professional selection. *Expert Systems with Applications*, *39*(3), 3516-3525. <https://doi.org/10.1016/j.eswa.2011.09.042>
- Karpilovska, S. Y., Mitelman, R. Y., & Synovsky, V. V. (1997). *Osnovy profesiohrafyyi* [Fundamentals of professiography]. MAUP.
- Kelemenis, A., & Askounis, D. (2010). A new TOPSIS-based multi-criteria approach to personnel selection. *Expert Systems with Applications*, *37*(7), 4999-5008. <https://doi.org/10.1016/j.eswa.2009.12.013>
- Langer, M., König, C. J., & Busch, V. (2020). Changing the means of managerial work: Effects of automated decision support systems on personnel selection tasks. *Journal of Business and Psychology*, *36*, 751-769. <https://doi.org/10.1007/s10869-020-09711-6>
- Matsehora, Y. V., Prykhodko, I. I., Vorobyova, I. V., Horielyshev, S. A., & Kazyanina, N. A. (2014). *Psykhologichnyy monitoring profesiyno vazhlyvykh yakostey kursantiv vyshchykh viyskovykh navchalnykh zakladiv MVS Ukrayiny* [Psychological monitoring of professionally important qualities of cadets of higher military educational institutions of the Ministry of Internal Affairs of Ukraine]. IT MIA of Ukraine.
- Melnyk, Y. B., Prykhodko, I. I., & Stadnik, A. V. (2019). Medical-psychological support of specialists' professional activity in extreme conditions. *Minerva Psichiatrica*, *60*(4), 158-168. <https://doi.org/10.23736/S0391-1772.19.02025-9>
- Ötting, S. K., & Maier, G. W. (2018). The importance of procedural justice in human-machine interactions: Intelligent systems as new decision agents in organizations. *Computers in Human Behavior*, *89*, 27-39. <https://doi.org/10.1016/j.chb.2018.07.022>
- Parasuraman, R., Sheridan, T. B., & Wickens, C. D. (2000). A model for types and levels of human interaction with automation. *IEEE Transactions on Systems, Man, and Cybernetics - Part A: Systems and Humans*, *30*(3), 286-297. <https://doi.org/10.1109/3468.844354>
- Petrescu, M., Burtăverde, V., Mihăilă, T., & Mihaela, A. (2015). Situational judgments tests - A fact in call center personnel selection - Pilot study. *Procedia - Social and Behavioral Sciences*, *187*, 762-766. <https://doi.org/10.1016/j.sbspro.2015.03.161>
- Prykhodko, I. I., Bielai, S. V., Hrynzovskyi, A. M., Zhelaho, A. M., Hodlevskyi, S. O., & Kalashchenko, S. I. (2020). Medical and psychological aspects of safety and adaptation of military personnel to extreme conditions. *Wiadomości Lekarskie*, *LXXIII*(4), 679-683. <https://doi.org/10.36740/WLek202004110>
- Prykhodko, I. I. (2008). *Profesynnyy psikhologichnyy vidbir maybutnikh ofitseriv vnutrishnikh viysk MVS Ukrayiny* [Professional psychological selection of future officers of the internal troops of the Ministry of Internal Affairs of Ukraine]. IT MIA of Ukraine.

- Prykhodko, I. I. (Ed.). (2020). *Avtomatyzatsiya profesijnoho psykholohichnoho vidboru kandydativ na viyskovu sluzhbu v Natsionalnu hvardiyu Ukrainy* [Automation of professional psychological selection of candidates for military service in the National Guard of Ukraine]. National Guard of Ukraine.
- Sheridan, T. B., & Parasuraman, R. (2005). Human-automation interaction. *Reviews of Human Factors and Ergonomics*, 1(1), 89-129. <https://doi.org/10.1518/155723405783703082>
- Skorupski, J., Grabarek, I., Kwasiborska, A., & Czyżo, S. (2020). Assessing the suitability of airport ground handling agents. *Journal of Air Transport Management*, 83, Article 101763. <https://doi.org/10.1016/j.jairtraman.2020.101763>
- Spielberger, C. D. (Ed.). (2004). *Encyclopedia of Applied Psychology*. Academic Press.
- Ventzel, E. S. (2006). *Teoriya veroyatnosti* [Probability theory]. Higher school.
- Vorobyova, I. V., Prykhodko, I. I., Poltorak, S. T., Rutin, V. V., Timchenko, O. V., Lipatov, I. I., Matsehora, Y. V., Horielyshev, S. A., & Poberezhniy, A. A. (2012). *Avtomatyzovanyy psykholohichnyy kompleks vyznachennya profesijnoyi prydatnosti kandydativ na viyskovu sluzhbu u vnutrishni viyska MVS Ukrainy i navchannya u vyshchyykh viyskovyykh navchalnykh zakladakh MVS Ukrainy* [Automated psychodiagnostic complex for determining the professional suitability of candidates for military service in the internal troops of the MIA of Ukraine and education in higher military educational institutions of the MIA of Ukraine]. IT MIA of Ukraine.
- Zhiltsova, V. A., Zarakovsky, G. M., & Ostrovsky, N. P. (2005). *Osnovy voyennogo professionalnogo psikhologicheskogo otbora* [Fundamentals of military professional psychological selection] (V. I. Lazutkin, Ed.). Military Publishing House.
- Zlepko, S. M., Koval, L. H., Petrenko, V. V., & Belzetskiy, P. S. (2010). *Metody i zasoby psykhoфизиологического vidboru kandydativ na sluzhbu za kontraktom v Zbroyni Syly Ukrainy* [Methods and means of psychophysiological selection of candidates for contract service in the Armed Forces of Ukraine]. Vinnytsia National Technical University Publishing House.



## Determination of Putative Vacuolar Proteases, PEP4 and PRB1 in a Novel Yeast Expression Host *Meyerozyma guilliermondii* Strain SO using Bioinformatics Tools

Okojie Eseoghene Lorraine<sup>1,2</sup>, Raja Noor Zaliha Raja Abd. Rahman<sup>1,3,4</sup>, Joo Shun Tan<sup>5</sup>, Raja Farhana Raja Khairuddin<sup>6</sup>, Abu Bakar Salleh<sup>1</sup> and Siti Nurbaya Oslan<sup>1,2,3\*</sup>

<sup>1</sup>Enzyme and Microbial Technology Research Centre, Universiti Putra Malaysia, 43400 UPM, Serdang, Selangor, Malaysia

<sup>2</sup>Department of Biochemistry, Faculty of Biotechnology and Biomolecular Sciences, Universiti Putra Malaysia, 43400 UPM, Serdang, Selangor, Malaysia

<sup>3</sup>Laboratory of Vaccine and Biomolecules (VacBio 5), Institute of Bioscience, Universiti Putra Malaysia, 43400 UPM, Serdang, Selangor, Malaysia

<sup>4</sup>Department of Microbiology, Faculty of Biotechnology and Biomolecular Sciences, Universiti Putra Malaysia, 43400 UPM, Serdang, Selangor, Malaysia

<sup>5</sup>School of Industrial Technology, Universiti Sains Malaysia, 11800 USM, Pulau Pinang, Malaysia

<sup>6</sup>Faculty of Science and Mathematics, Universiti Pendidikan Sultan Idris, 35900 UPSI, Tanjung Malim, Perak, Malaysia

### ABSTRACT

*Meyerozyma guilliermondii* strain SO, a newly isolated yeast species from spoiled orange, has been used as a host to express the recombinant proteins using methylotrophic yeast promoters. However, as a novel yeast expression system, the vacuolar proteases of this yeast have not been determined, which may have contributed to the low level of heterologous protein secretions. Thus, this study aimed to determine intra- and extracellular proteolytic activity and identify the putative vacuolar proteases using bioinformatics techniques. A clear zone was observed from the nutrient agar skimmed milk screening plate. Proteolytic

activity of 117.30 U/ml and 75 U/ml were obtained after 72 h of cultivation for both extracellular and intracellular proteins, respectively. Next, the Hidden Markov model (HMM) was used to detect the presence of the vacuolar proteases (PEP4 and PRB1) from the strain SO proteome. Aspartyl protease (PEP4) with 97.55% identity to *Meyerozyma* sp. JA9 and a serine protease (PRB1) with 70.91% identity to

#### ARTICLE INFO

##### Article history:

Received: 26 April 2021

Accepted: 05 July 2021

Published: 04 January 2022

DOI: <https://doi.org/10.47836/pjst.30.1.42>

##### E-mail addresses:

gs50664@student.upm.edu.my (Okojie Eseoghene Lorraine)

rnzaliha@upm.edu.my (Raja Noor Zaliha Raja Abd. Rahman)

jooshun@usm.my (Joo Shun Tan)

rfrk@fsmt.upsi.edu.my (Raja Farhana Raja Khairuddin)

abubakar@upm.edu.my (Abu Bakar Salleh)

snurbayaoslan@upm.edu.my (Siti Nurbaya Oslan)

\* Corresponding author

*Candida albicans* were revealed. The homology with other yeast vacuolar proteases was confirmed *via* evolutionary analysis. PROSPER tool prediction of cleavage sites postulated that PEP4 and PRB1 might have caused proteolysis of heterologous proteins in strain SO. In conclusion, two putative vacuolar proteases (PEP4 and PRB1) were successfully identified in strain SO. Further characterization can be done to understand their specific properties, and their effects on heterologous protein expression can be conducted *via* genome editing.

*Keywords:* Hidden Markov model, phylogenetic tree, secretion, vacuolar proteases, yeast expression system

---

## INTRODUCTION

Proteases are proteolytic enzymes that can break long chain-like protein molecules into shorter fragments, peptides, and eventually into their component's amino acids (Barrett et al., 1998). Yeast proteases are secreted into the extracellular space, and the majority of which are abundant in the vacuolar, cell wall, plasma membrane, and Golgi apparatus (Delic et al., 2013; Feyder et al., 2015). A major limitation for efficient secretion of heterologous proteins is the undesired travel to the vacuoles where the proteins are degraded and recycled (Forgac, 2000; Li & Kane, 2009). Besides, descriptions of proteolytic degradation of recombinant proteins have been attributed to the release of vacuolar proteases to the exterior as a result of lysis of the cells as opposed to product mistargeting (Kobayashi et al., 2000; Sinha et al., 2005) and could mostly be averted by disruption of the two major vacuolar proteases PEP4 (aspartyl) and PRB1 (serine) or yapsin-type proteases (Gleeson et al., 1998; Idiris et al., 2010; Silva et al., 2011; Wu et al., 2013). Some studies have reported the reduced proteolysis of secreted heterologous proteins using yapsin (vacuolar protease) mutant strains of *Pichia pastoris* and *Saccharomyces cerevisiae* (Copley et al., 1998; Kerry-Williams et al., 1998; Bourbonnais et al., 2000; Egel-Mitani et al., 2000; Yao et al., 2009; Werten & de Wolf, 2005).

In bioinformatics, hidden Markov models are feasibly the most common statistical models (Haussler et al., 1993), whose applications are increasingly popular in the statistical analysis of biological sequences with complex correlations. Some examples of such applications include gene prediction (Krogh et al., 2001), protein modeling (Krogh et al., 1994), copy number reconstruction (Wang et al., 2007), sequence alignment (Hughey & Krogh, 1996), functional segmentation of the genome (Ernst & Kellis, 2012) and identification of ancestral DNA segments (Falush et al., 2003; Tang et al., 2006; Li & Durbin, 2011). In addition, in some studies, it has been used to identify genomic regions that contain regulatory information, such as the *cis*-regulatory modules (CRMs) and transcription factor binding sites (TFBSs) (Crowley et al., 1997; Frith et al., 2001; Rajewsky et al., 2002; Bailey & Nobel, 2003; Sinha et al., 2003).

In addition, several tools are utilized for the recognition of sorting signals as well as the prediction of subcellular localization of proteins from their amino acid sequences

(Imai & Nakai, 2020). For predicting signal peptides and their cleavage sites, many prediction methods, such as SPElip (Fariselli et al., 2003), SignalP 4.0 (Petersen et al., 2011), Phobius (Krogh et al., 2007), and DeepSig (Savojardo et al., 2018), have been developed. Moreover, SignalP has been further elevated as a deep neural network-based method that combines conditional random field classification and optimized transfer learning (SignalP-5.0; Armenteros et al., 2019). Other online tools that are used to predict possible protease cleavage for recombinant proteins include PROSPER (Song et al., 2012), MEROPS peptidase database (Rawlings et al., 2018), and ExpASY PeptideCutter tool (Gasteiger et al., 2005).

In recent times, yeasts have served as an alternative expression system in recombinant gene technology than the insect-baculovirus, bacterial and mammalian hosts (Gellissen et al., 2005). Unlike the prokaryotic expression system, yeasts are easily modified genetically and present a simple large-scale fermentation profile (Mattanovich et al., 2012). Additionally, the secret large amount of glycosylated proteins (Gellissen et al., 2005; Boer et al., 2007; Johanna et al., 2017). Recombinant protein production in yeasts can be targeted for food and non-food industries (Hensing et al., 1995). Furthermore, yeast cells act as an advantageous host for several productions of recombinant proteins in that they are considered as GRAS (Generally Recognized as Safe) by the American Food and Drug Administration (FDA) (Kim et al., 2014; Martinez et al., 2012; Nevoigt, 2008; Ahmad et al., 2014; Gellissen et al., 2005; Madzak et al., 2004; Van Ooyen et al., 2006).

A novel yeast expression system *M. guilliermondii* strain SO, which was isolated from spoiled orange (Oslan et al., 2012), had been reported to be an expression host for thermostable T1 lipase from *Geobacillus zalihae* under the regulation of alcohol oxidase promoter (pAOX1) with 14 (U/ml) in comparison to the commercial expression system, *P. pastoris*, with 81 (U/ml) (Oslan et al., 2014; Oslan et al., 2015). Interestingly, the T1 lipase could also be expressed without methanol induction (Abu et al., 2017). Nevertheless, strain SO had been used to express thermostable  $\alpha$ -amylase using formaldehyde dehydrogenase promoter (pFLD) with a yield of 26 (U/mL) after 24 h of cultivation without induction (Nasir et al., 2020). Furthermore, W200R protease and diamine oxidase had been expressed in strain SO (Mahyon, 2017). Several optimization strategies had been carried out, yet a low expression level of these enzymes was recorded. This limitation has deterred the strain SO from being used widely as the expression host. This occurrence may be due to the proteolytic activity of the native vacuolar protease(s) of strain SO regarding the secretory pathway of heterologous proteins in yeast expression systems. Thus, it is imperative to identify the vacuolar protease(s) gene to enable future genomic disruption that might give a better yield of secreted heterologous proteins in strain SO as an expression host.

Recently, the genome/proteome of strain SO has been deposited in the Genbank (BioProject: PRJNA547962). With the availability of various bioinformatics tools, this

study aimed to determine the proteolytic level of strain SO and identify the putative vacuolar protease(s) of *M. guilliermondii* strain SO.

## **MATERIALS AND METHODS**

### **Strain**

*M. guilliermondii* strain SO was used during this study obtained from the previous study (Oslan et al., 2012) preserved in 80% glycerol stock solution.

### **Inoculum and Production Media Composition**

Strain was grown for biomass production on YPD medium containing 1% (w/v) yeast extract, 2% (w/v) peptone, and 2% (v/v) dextrose; for expressed protease in the culture supernatant and pellet fractions, YPT medium containing 1% (w/v) yeast extract, 2% (w/v) peptone and 0.2% (w/v) tryptic soya broth and  $4 \times 10^{-5}$ % (w/v) biotin were used (Oslan et al., 2015).

### **Preparation of Inoculum**

Wild type strain SO was streaked on YPD plate (1% (w/v) yeast extract, 2% (w/v) peptone, 2% (w/v) Bacteriological agar, and 2% (w/v) dextrose). A 10 mL YPD broth was inoculated using a single colony and incubated at 30°C overnight with an agitation of 250 rpm.

### **Preparation of Skim Milk agar for Qualitative Assay**

The enzyme activity was also screened qualitatively on a skim milk agar plate prepared by dissolving 2.5 g of skim milk into 50 ml distilled water and autoclaved at 115°C for 5 min. Furthermore, 2 g of nutrient agar was dissolved in 50 ml of distilled water and autoclaved at 121°C for 15 min. Finally, the solutions were mixed in sterile conditions and poured into sterile petri-dishes (Rahman et al., 1994).

### **Determination of Protease Activity**

For sample analysis, a prepared inoculum was incubated overnight at 30°C at 250 rpm. Subsequently, 1% (v/v) of the inoculum was transferred into a 100 mL YPD medium in a conical flask for biomass production. First, the culture media were grown for 24 h in an incubator shaker at 30°C with a shaking speed of 250 rpm. Then, the cells were centrifuged at  $3000 \times g$  at room temperature for 10 min and resuspended in 100 ml of YPT. Next, the cell was incubated at 30°C in a shaker at 250 rpm for three days. 5 ml yeast culture from the flask was harvested at  $4000 \times g$  for 10 min at 4°C every 24 h until three days. 5 ml of assay buffer (0.1 M Tris-HCl-2 mM  $\text{CaCl}_2$  at pH 7.0) was used to resuspend the pellet obtained from the initial harvested culture and sonicated for 6 min with pause interval of

10 sec. Next, the sample was centrifuged at  $10\,000 \times g$  for 7 min at 4°C. Then, a protease assay for extracellular and intracellular activity was undertaken.

### **Qualitative Protease Activity**

For screenings, filtered crude extracellular and intracellular enzymes using cellulose acetate membrane filter with a pore size of 0.22  $\mu\text{m}$  were obtained in sterile micro-centrifuge tubes. Furthermore, wells were bored on the skimmed milk agar plate using a sterile wire loop. Subsequently, 100  $\mu\text{l}$  of enzymes was pipetted into the holes and incubated overnight at 30°C (Rahman et al., 1994).

### **Quantitative Protease Assay**

The proteolytic activities were determined based on the method described by Rahman et al. (1994) using azocasein as the protein substrate with slight modification. The substrate mixture was freshly prepared by mixing 0.5% (w/v) azocasein in 0.1 M Tris-HCl-2 mM  $\text{CaCl}_2$  at pH 7.0. A reaction mixture (100  $\mu\text{l}$  of enzyme solution-supernatant and 1 ml of substrate mixture) was shaken in a horizontal water bath shaker for 30 min at 30°C. A 1.1 ml of 10% (w/v) TCA was used, and the sample was incubated at 25°C for 30 min to terminate the reaction. Subsequently, 1ml of the sample was transferred into a 1.5 ml tube and were later centrifuged at  $10\,000 \times g$  for 7 min. Subsequently, 700  $\mu\text{l}$  supernatant was transferred into a 1.5 ml tube and mixed with 700  $\mu\text{l}$  of 1 M NaOH, and the absorbance of the mixture was measured at 450 nm where one unit (U) of protease activity is defined as the rate of the reaction that gives an increase of 0.001 absorbance unit at 450 nm per minute under the assay condition.

### **Statistical Analysis**

The experimental data were further analyzed statistically using a t-test for paired two samples for means of expression level. SPSS version 2.0 was used to compute and evaluate the experimental results.  $P < 0.05$  was considered to indicate a statistically significant difference (Kirkwood & Sterne, 2003).

### **Bioinformatics Tools (Hardware and Software Used)**

The hypothetical protease search was conducted on Windows 7, and the comparative genomic analysis was performed on iMac with MacOs Sierra with 10.12.1 version as the operating system.

**National Center for Biotechnology Information (NCBI).** The reference vacuolar proteases model sequence used for this study were *P. pastoris* aspartyl protease (PEP4) and

serine protease (PRB1) sequences retrieved from NCBI. The sequences were downloaded from <http://www.ncbi.nlm.nih.gov/>.

**Hidden Markov Model.** This installation was used to investigate the sequence obtained from the database for sequence homologies. It was downloaded from <http://hmmer.org/download.html> and installed in iMac. Xcode was also installed as a dependency for HMMER.

**Molecular Evolutionary Genetic Analysis 7(MEGA7).** It was downloaded and installed in Windows 7 from <http://www.megasoftware.net/>. Reported to be suited for analyzing protein and DNA sequence data from different living sources (Kumar et al., 2016). The retrieved proteases sequences from different yeast species from the database, NCBI, were aligned using the MUSCLE tool of MEGA 7.

#### **Identification of the Vacuolar Protease(s) Sequence in *M. guilliermondii* Strain SO**

Bioinformatics analysis of *M. guilliermondii* strain SO genome/proteome was performed using the nucleotide sequences deposited at the NCBI database (<https://www.ncbi.nlm.nih.gov>) BioProject: PRJNA547962. In addition, the *P. pastoris* sequence for PEP4 (accession number: CCA39046) and PRB1 (accession number: CCA36690) obtained from NCBI (Küberl et al., 2011; Valli et al., 2016) were taken as reference vacuolar protease model sequences because they had been well characterized and have been found similar to the aspartyl and serine proteases sequence of *S. cerevisiae* (Van Den Hazel et al., 1996). The position-specific iterated blast PSI-BLAST algorithm was selected using a cut-off E-value=0.01 using the Basic Local Alignment Search Tool (BLAST) with the reference proteins (refseq\_protein) to search the database. From the third iteration values of the blast results, selection of closely related protease sequences of other yeast species was carried out based on percentage identity and alignment coverage ranging from 49%–99%. A total of 27 sequences of serine proteases and 24 sequences of aspartyl proteases were selected. Therefore, multiple sequence alignment (MSA) of the selected sequences for each model was created using MEGA7 software by MUSCLE tool, and the aligned files were saved in a FASTA format as PEP4\_proteinaseA.fas and PRB1\_proteinaseB.fas, respectively.

#### **Identification of Homologous Vacuolar Proteases Sequence using Hidden Markov Model Software**

The whole proteome of *M. guilliermondii* strain SO was obtained from GenBank, BioProject: PRJNA547962. Vacuolar aspartyl and serine protease models were assigned as PEP\_ProteinaseA.hmm and PRB1\_proteinaseB.hmm, respectively, to build the models. Primarily, the models were searched against *M. guilliermondii* strain, SO proteome as the

directory contained the targeted proteome of strain SO. The models were built using a set command with an E-value of 0.01. Subsequently, the search results (hits) were observed using ATOM software.

### Analysis of the Hits Output

The hits output results for both vacuolar protease groups were further analyzed to identify the protein names and species homology. Hence, pairwise sequence alignment was carried out to determine the percentage similarities of the output of the hits with the reference model of *P. pastoris* vacuolar aspartyl and serine proteases, respectively. First, the hits output sequences were searched against the GenBank database NCBI (National Center for Biotechnology Information, National Library of Medicine) to identify similarities using the BLASTp search program. Next, multiple sequence alignment was carried out with the reference sequence used to build the HMM models using MEGA7 software. Subsequently, evolutionary analysis was inferred by constructing a phylogenetic tree using the maximum-likelihood method (Jones et al., 1992).

Furthermore, the molecular weight and theoretical pI of strain SO vacuolar aspartyl and serine proteases were predicted using ExPASy software tools (<http://web.expasy.org/protparam/>). The presence of signal peptide was inferred by using SignalP [<http://www.cbs.dtu.dk/services/SignalP/>]. An *in-silico* prediction of the cleavage sites on thermostable T1 lipase integrated with the identified vacuolar proteases model was also inferred using PROSPER, an online software (<http://lightning.med.monash.edu.au/PROSPER/>).

## RESULTS

### Determination of Native Protease(s) Activities of *M. guilliermondii* Strain SO

The quantitative and qualitative activity of strain SO native protease(s) were determined using azocasein and skimmed milk as the protein substrate. Qualitatively, the proteolysis zones could be directly observed by the presence of the clear halos around the wells for both extracellular and intracellular enzymes of *M. guilliermondii* strain SO native protease after 24 h of incubation time at 30°C (Figure 1a).

*P. pastoris* strain X-33 was used as a positive control. The yeasts were grown in a YPD medium providing the yeast cells with a carbon source for biomass production. After generating mass, the cells were resuspended into a YPT medium (Clare et al., 1991). The cell culture was incubated at 30°C for three days, and protease activity was determined along with the growth incubation time. The fermentation time course in shake flask for protease production by *M. guilliermondii* strain SO using 100µl (2mg) of the crude enzymes showed that the maximum protease activity (117.30 U/ml and 75 U/ml) were obtained after 72 h of cultivation for both extracellular and intracellular samples (Figure 1b). This

study showed that the native protease of *M. guilliermondii* strain SO exhibited a substrate specificity for azocasein and skim milk (Rahman et al., 1994). Suryawanshi and Pandya (2017) reported on the efficacy of screening of proteolytic activity using skimmed milk agar plates for screening and identification of alkaline proteases producing fungi.

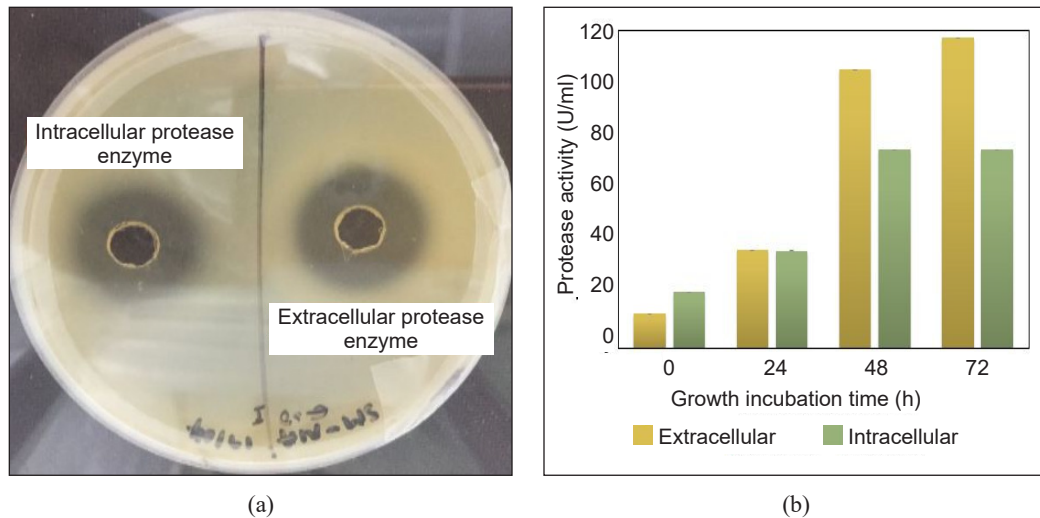


Figure 1. Total protease activity of *M. guilliermondii* strain SO: (a) Qualitative assay showing the clear zones of proteolysis due to the hydrolysis of the peptide bonds of the substrate by the enzymes; and (b) Quantitative native protease activity with standard deviation calculated.

### Identification of the Vacuolar Protease(s) Sequence in *M. guilliermondii* Strain SO Using HMM Strategy

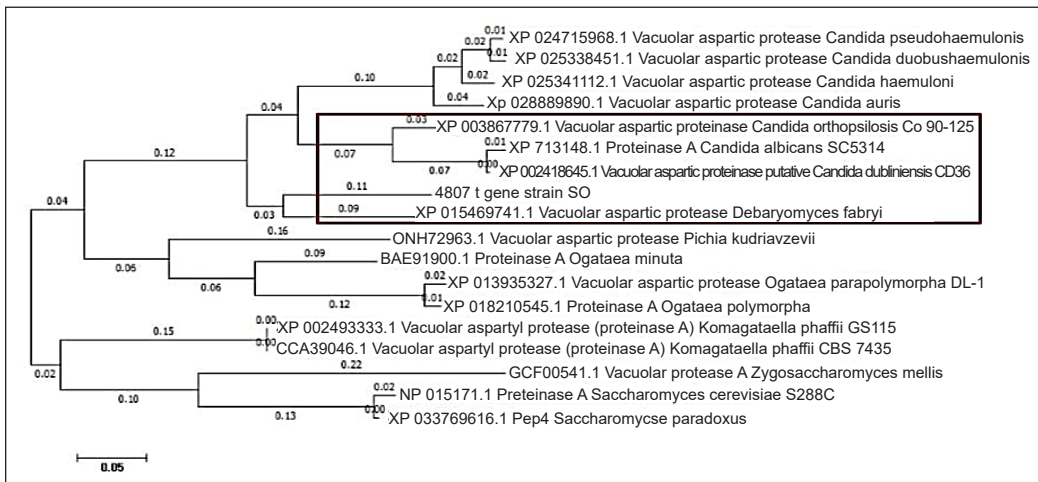
HMM strategy was used to determine and identify the protease(s) sequence in *M. guilliermondii* strain SO proteome deposited in the GenBank with accession number: PRJNA547962. A total of 14 hits were observed from the aspartyl model built, and three hits were observed from the serine model built to detect protease sequence from *M. guilliermondii* proteome. The first hit observed from the results for each group was significantly matched to the multiple sequences aligned file because the E-value was chosen within the cut-off value of 0.01.

### Analysis of the Hidden Markov Model Hits Output

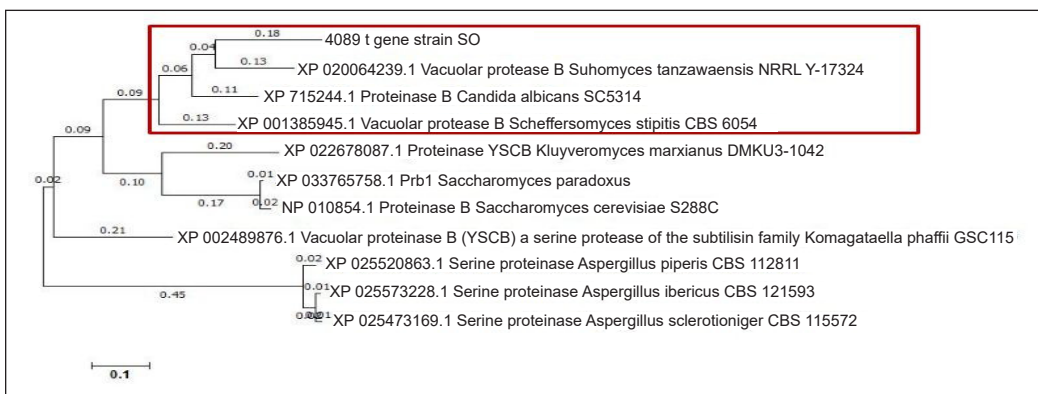
The amino acid sequence of both vacuolar aspartyl and serine proteases were aligned with corresponding amino acids of *P. pastoris* vacuolar aspartic and serine proteases, respectively (Appendix - Tables S2a & S2b). Based on the pairwise alignment tools, the output of the first hit of serine protease and aspartyl protease of strain SO showed that it had 770 and 408 amino acid residues, respectively, and were 40.90% and 68.3% identical to *P. pastoris* PRB1 serine protease and PEP4 aspartyl protease respectively.



The protein BLAST results revealed that the serine protease sequence of strain SO had 70.91% identity with *C. albicans* (accession number: XP7152441). While aspartyl protease sequence of strain SO had 97.55% identity with *Meyerozyma* sp. JA9 (accession number: RLV83957.1). Furthermore, the protein sequences of the two groups of proteases were used to construct a phylogenetic tree with other yeasts vacuolar serine and aspartyl proteases selected from the reference protein sequence database. A query coverage of 80% above, e-value of 1e-15, and types of yeast family, which include Saccharomyceteceae, Debaryomyceteceae, Metschnokowiaceae, Aspergilleceae, Phaffomycetaceae, and Pichiaceae, were used. The phylogenetic trees drawn to scale using the maximum likelihood method (Jones, 1991) (Figures 2a & 2b) showed the nearness of the respective identified vacuolar protease of strain SO (aspartyl 4807t (PEP4) and serine 4089t (PRB1)) to Debaryomyceteceae yeast family.



(a)

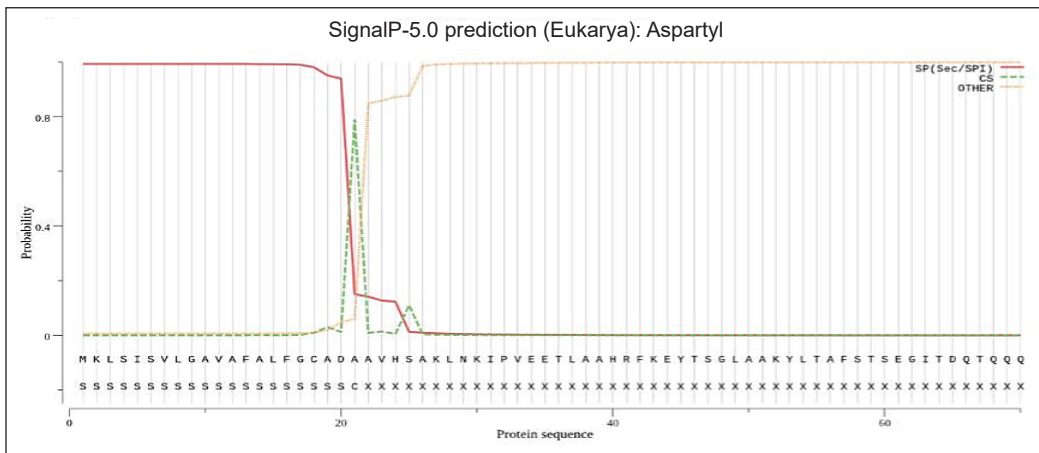


(b)

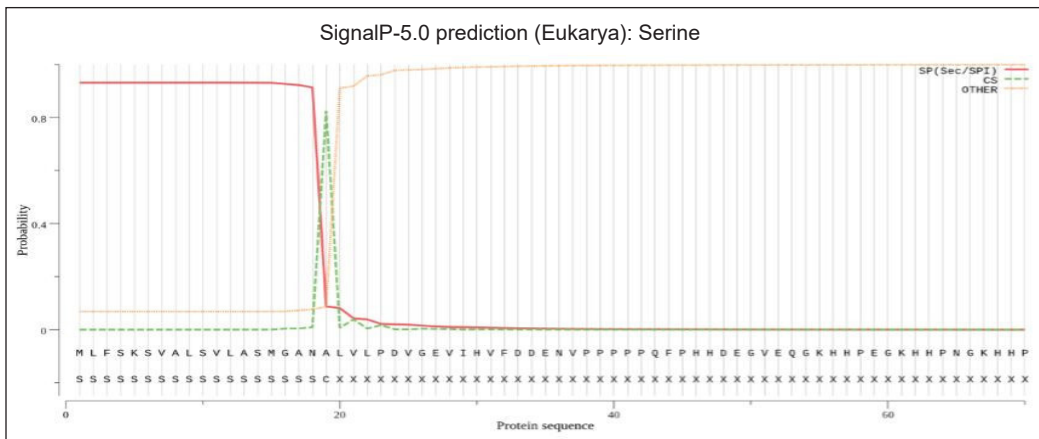
Figure 2. Phylogenetic tree construction: (a) Dendrogram showing the closeness of *M. guilliermondii* strain SO aspartyl protease (4807t gene) with the Debryomyceteceae family; and (b) Dendrogram showing the closeness of *M. guilliermondii* strain SO serine protease (4089t gene) with the Debryomyceteceae family.

### Determination of Signal Peptide of Vacuolar Proteases of Strain SO

The Signal peptide (Sec/SPI) was predicted with the cleavage site for aspartyl protease of strain SO between positions 21 and 22 of the amino acid sequence ADA-AV (Alanine, Aspartic acid, Alanine–Alanine, Valine) with a probability of 0.7896. Furthermore, it showed that the protein was secreted extracellularly with an approximate molecular weight and theoretical pI of 44.2kDa and 4.57, respectively (Gasteiger et al., 2005) (Figure 3a). Likewise, for serine protease, the signal peptide was predicted with the cleavage site between positions 19 and 20 of the amino acid sequence ANA-LV (Alanine, Asparagine, Alanine–Leucine, Valine) with a probability of 0.8258. This result revealed that the protein was secreted extracellularly with approximate molecular weight and theoretical pI of 83.3kDa and 5.50, respectively (Gasteiger et al., 2005) (Figure 3b).



(a)



(b)

Figure 3. Assessment of the signal-peptides (SPs) of *M. guilliermondii* strain SO vacuolar proteases using SignalP software: (a) The signal peptide of aspartyl protease of *M. guilliermondii* strain SO predicted graph; and (b) Signal peptide of serine protease of *M. guilliermondii* strain SO predicted graph

More so, with PROSPER online protease cleave prediction tool, three and five cleavage sites respectively on recombinant protein T1 lipase from *G. zalihae* (Leow et al., 2004) as a substrate used for the integration (Appendix - Tables S3a & S3b) was predicted using model(s) enzymes. The prediction infers the possibility of degradation of the recombinant protein (T1 lipase) into peptides that would invariably reduce the expressed protein.

## DISCUSSION

The native protease(s) activity over time was examined in the wild-type *M. guilliermondii* strain SO. Protease activity was observed to increase as the incubation time increased.

In other studies, the current strategies implemented to considerably reduce the effects of the native protease(s) in yeasts cells for recombinant protein secretion is by identifying the genes of the vacuolar proteases based on the secretory pathway of yeasts expression system and after that developing protease-deficient mutants (Copley et al., 1998; Gonzalez-Lopez et al., 2002; Jonson & Rehfeld 2004; Kang et al., 1998; Chung & Park, 1998). Presently, the proteolytic activities detected in both the extracted crude intra- and extracellular enzymes of *M. guilliermondii* strain SO were the total protease activity. The specific aspartyl and serine protease activities could only be detected once these two proteases are purified and characterized accordingly. Hence in this study, we report on the approach used to identify the two potential vascular proteases using genome/proteomic data of *M. guilliermondii* strain SO (BioProject: PRJNA547962).

Investigation and evaluation of the significant difference between the two variables obtained from the extracellular and intracellular protease activities of strain SO over time were reported. Statistically, according to Kirkwood and Sterne (2003), the null hypothesis is accepted because there is no significant difference between extracellular protease activity and intracellular protease activity as the alpha value of 0.05 is less than the t-value of 0.27 (Appendix - Table S1). HMM has been reviewed by various studies as an efficient and popular statistical tool, which utilizes mathematical principles to analyze data (Singh et al., 2012; Yoon, 2009; Gales & Young, 2007). It is an analytical approach with hidden states (Gomez-lopera et al., 2017). The vacuolar proteases hits from the HMM search yielded results contributing to the construction of vacuolar aspartyl and serine null mutant strain(s) in our future study. Several studies have reported on the identification of the vacuolar proteases (PEP4 and PRB1), which are mainly the bottlenecks of secretory heterologous proteins in a yeast expression system (Gleeson et al., 1998; Van den Hazel et al., 1996), which this study had identified in the novel yeast expression host *M. guilliermondii* strain SO proteome. The phylogenetic trees construction further revealed that the respective identified vacuolar protease of strain SO (aspartyl 4807t and serine 4089t) showed more nearness to the Debaryomyceteceae yeast family.

Signal peptides are short peptides located at the N-terminal of secretory proteins. In several industrial and scientific fields, disease diagnosis, and laboratory techniques, signal peptides have attracted great interest, particularly in producing recombinant protein, which determines efficient translocation from heterologous species (Zamani et al., 2015; Negahdaripour et al., 2017; Mousavi et al., 2017). The presence of the signal peptide in the native vacuolar protease(s) of strain SO has increased the secretion of these proteins in the medium. This finding might have explained why the proteolytic activity was higher in crude extracellular proteins environment as compared to intracellular. Furthermore, other studies have reported that the signal peptides have increased the secretion of the heterologous proteins at significant levels (Low et al., 2013; Mergulhao et al., 2005; Ohmuro-Matsuyama & Yamaji, 2017).

The signal-peptide was assessed by calculating the D-scores of Signal Peptides (SPs) using SignalP 5.0. The software predicts likely cleavage sites in ORF and signals peptides sequences. The web-based software uses an HMM algorithm and a neural network to compute a D-score to the input polypeptide sequence, using an average of the mean and the maximum score, which infers the possibility of a cleavage site.

Furthermore, PROSPER, a tool used for predicting protease substrate cleavage sites (Song et al., 2012), also predicted the possible cleavage sites of the enzyme model(s) for thermostable T1 lipase. Based on the analysis conducted in this study, *M. guilliermondii* strain SO vacuolar proteases have been identified as aspartyl protease and serine protease showing homology with other yeasts vacuolar aspartyl and serine proteases, respectively as inferred by the comparative sequence study, bioinformatics analysis, and evolutionary analysis conducted by the construction of the phylogenetic tree.

## CONCLUSION

This study successfully determined and identified two vacuolar proteases, PEP4 (4807t) and PRB1 (4089t) of *M. guilliermondii* strain SO employing activity assays and bioinformatics analysis approaches. The observed relationship with other yeasts' vacuolar proteases was indicated as the respective identified putative vacuolar proteases of strain SO were clustered among other yeasts' PEP4 and PRB1 proteases, respectively. PROSPER tool detected both PEP4 and PRB1 cleavage sites of the T1 lipase sequence. Signal peptides were also present in these proteases, thus confirming their secretory features. However, for the explicit understanding of their specific properties, the further characterization needs to be conducted in future research.

The identified vacuolar proteases PEP4 and PRB1 can be targeted for gene knockout to develop protease-deficient strains of *M. guilliermondii* strain SO and optimization of the cultivation parameters that may contribute to the numbers of protease mutant strains used to enhance secretion of heterologous proteins in yeast expression systems.

## ACKNOWLEDGEMENTS

The authors wish to thank the Ministry of Education, Malaysia, for the Fundamental Research Grant (Code: FRGS/1/2019/STG05/UPM/02/1) and the Ministry of Education, Nigeria, allowing OEL to develop their career further.

## REFERENCES

- Abu, M. L., Nooh, H. M., Oslan, S. N., & Salleh, A. B. (2017). Optimization of physical conditions for the production of thermostable T1 lipase in *Pichia guilliermondii* strain SO using response surface methodology. *BMC Biotechnology*, *17*, Article 78. <https://doi.org/10.1186/s12896-017-0397-7>
- Ahmad, M., Hirz, M., Pichler, H., & Schwab, H. (2014). Protein expression in *Pichia pastoris*; Recent achievements and perspectives for heterologous protein production. *Applied Microbiology and Biotechnology*, *98*, 5301-5317. <https://doi.org/10.1007/s00253-014-5732-5>
- Armenteros, J. J. A., Tsirigos, K. D., Sønderby, C. K., Petersen, T. N., Winther, O., & Brunak, S. (2019). SignalP 5.0 improves signal peptide predictions using deep neural networks. *Nature Biotechnology*, *37*, 420-423. <https://doi.org/10.1038/s41587-019-0036-z>
- Bailey, T. L., & Noble, W. S. (2003). Searching for statistically significant regulatory modules. *Bioinformatics*, *19*(suppl.2), 1116-1125. <https://doi.org/10.1093/bioinformatics/btg1054>
- Barrett, A. J., Rawlings, N. D., & Woessner, J. F. (1998). *Handbook of proteolytic enzymes*. Academic Press.
- Boer, E., Steinborn, G., Kunze, G., & Gellissen, G. (2007). Yeast expression platforms. *Applied Microbiology and Biotechnology*, *77*, 513-523. <https://doi.org/10.1007/s00253-007-1209-0>
- Bourbonnais, Y., Larouche, C., & Tremblay, G. M. (2000). Production of full-length human pre-elafin, an elastase specific inhibitor, from yeast requires the absence of a functional yapsin 1 (Yps1p) endoprotease. *Protein Expression and Purification*, *20*, 485-491. <https://doi.org/10.1006/prev.2000.1338>
- Chung, B. H., & Park, K. S. (1998). Simple approach to reducing proteolysis during the secretory production of human parathyroid hormone in *Saccharomyces cerevisiae*. *Biotechnology and Bioengineering*, *57*, 245-249. [https://doi.org/10.1002/\(SICI\)1097-0290\(19980120\)57:2](https://doi.org/10.1002/(SICI)1097-0290(19980120)57:2)
- Clare, J. J., Rayment, F. B., Ballantine, S. P., Sreekrishna, K., & Romanos, M. A. (1991). High-level expression of tetanus toxin fragment C in *Pichia pastoris* strains containing multiple tandem intergrations of the gene. *Biotechnology Journal*, *9*, 455-60. <https://doi.org/10.1038/nbt0591-455>
- Copley, K. S., Alm, S. M., Schooley, D. A., & Courchesne, W. E. (1998). Expression, processing and secretion of a proteolytically sensitive insect diuretic hormone by *Saccharomyces cerevisiae* requires the use of a yeast strain lacking genes encoding the Yap3 and Mkc7 endoproteases found in the secretory pathway. *Biochemical Journal*, *330*, 1333-1340. <https://doi.org/10.1042/bj3301333>
- Crowley, E. M., Roeder, K., & Bina, M. (1997). A statistical model for locating regulatory regions in genomic DNA. *Journal of Molecular Biology*, *268*(1), 8-14. <https://doi.org/10.1006/jmbi.1997.0965>
- Delic, M., Valli, M., Graf, A. B., Pfeffer, M., Mattanovich, D., & Gasser, B. (2013). The secretory pathway: Exploring yeast diversity. *FEMS Microbiology Reviews*, *37*(6), 872-914. <https://doi.org/10.1111/1574-6976.12020>

- Egel-Mitani, M., Andersen, A. S., Diers, I. I., Hach, M., Thim, L., Hastrup, S., & Vad, K. (2000). Yield improvement of heterologous peptides expressed in yps1-disrupted *Saccharomyces cerevisiae* strains. *Enzyme and Microbial Technology*, 26, 671-677. [https://doi.org/10.1016/s0141-0229\(00\)00158-7](https://doi.org/10.1016/s0141-0229(00)00158-7)
- Ernst, J., & Kellis, M. (2012). ChromHMM: Automating chromatin-state discovery and characterization. *Nature Methods*, 9, 215-216. <https://doi.org/10.1038/nmeth.1906>.
- Falush, D., Matthew, S., & Jonathan, K. P. (2003). Inference of population structure using multilocus genotype data: Linked loci and correlated allele frequencies. *Genetics*, 164, 1567-1587.
- Fariselli, P., Finocchiaro, G., & Casadio, R. (2003). SPElPip: The detection of signal peptide and lipoprotein cleavage sites. *Journal of Bioinformatics*, 19, 2498-2499. <https://doi.org/10.1093/bioinformatics/btg360>
- Feyder, S., De Craene, J. O., Bär, S., Bertazzi, D. L., & Friant, S. (2015). Membrane trafficking in the yeast *Saccharomyces cerevisiae* model. *International Journal of Molecular Sciences*, 16(1), 1509-1525. <https://doi.org/10.3390/ijms16011509>
- Forgac, M. (2000). Structure, mechanism and regulation of the clathrin-coated vesicle and yeast vacuolar H(+)-ATPase. *Journal of Experimental Biology*, 203, 71-80.
- Frith, M. C., Hansen, U., & Weng, Z. (2001). Detection of cis-element clusters in higher eukaryotic DNA. *Journal of Bioinformatics*, 17, 878-889.
- Gales, M., & Young, S. (2007). The application of hidden Markov models in speech recognition. *Foundation and Trends in Signal Processing*, 1(3), 195-304. <https://doi.org/10.1561/20000000004>
- Gasteiger, E., Hoogland, C., Gattiker, A., Duvaud, S., Wilkins, M. R., Appel, R. D., & Bairoch A. (2005). Protein identification and analysis tools on the ExpASY server. In J. M. Walker (Ed.), *The proteomics protocols handbook* (pp 571-607). Humana Press.
- Gellissen, G., Kunze, G., Gaillardin, C., Cregg, J. M., Berardi, E., Veenhuis, M., & Van Der Klei, I. (2005). New yeast expression platforms based on methylotrophic *Hansenula polymorpha* and *Pichia pastoris* and on dimorphic *Arxula adenivorans* and *Yarrowia lipolytica*—a comparison. *FEMS Yeast Research*, 5(11), 1079-1096. <http://doi.org/10.1016/j.femsyr.2005.06.004>
- Gleeson M. A. G., White C. E., Meininger D. P., & Komives E. A. (1998). Generation of protease-deficient strains and their use in heterologous protein expression. In D. R. Higgins & J. M. Cregg (Eds.), *Pichia protocols* (pp. 81-94). Humana Press. <https://doi.org/10.1385/0-89603-421-6:81>
- Gomez-Lopera, J. F., Matinez-Aroza, J., Roman-Roldan, R., Roman-Galvez, R., & Blanco-Navarro, D. (2017). The evaluation problem in discrete semi-hidden Markov models. *Mathematics and Computers in Simulation*, 137, 350-365. <https://doi.org/10.1016/j.matcom.2016.12.002>
- Gonzalez-Lopez, C. I., Szabo, R., Blanchin-Roland, S., & Gaillardin, C. (2002). Genetic control of extracellular protease synthesis in the yeast *Yarrowia lipolytica*. *Genetics*, 160, 417-427.
- Haussler, D., Krogh, A., Mian, I. S., & Sjolander, K. (1993). Protein modeling using hidden Markov models: Analysis of globins. In *1993 Proceedings of the Twenty-sixth Hawaii International Conference on System Sciences (Vol. 1, pp. 792-802)*. IEEE Publishing. <https://doi.org/10.1109/HICSS.1993.270611>

- Hensing, M. C., Rouwenhorst, M., Heijnen, R. J., Van, J. J., Dijken, J. P., & Pronk, J. T. (1995). Physiological and technological aspects of large-scale heterologous-protein production with yeasts. *Antonie Van Leeuwenhoek*, *67*(3), 261-279. <https://doi.org/10.1007/BF00873690>
- Hughey, R., & Krogh, A. (1996). Hidden Markov models for sequence analysis: Extension and analysis of the basic method. *Bioinformatics*, *12*(2), 95-107. <https://doi.org/10.1093/bioinformatics/12.2.95>
- Idiris, A., Tohda, H., Kumagai, H., & Takegawa, K. (2010). Engineering of protein secretion in yeast: Strategies and impact on protein production. *Applied Microbiology and Biotechnology*, *86*, 403-417. <https://doi.org/10.1007/s00253-010-2447-0>
- Imai, K., & Nakai, K. (2020) Tools for the recognition of sorting signals and the prediction of subcellular localization of proteins from their amino acid sequences. *Frontiers in Genetics*, *11*, Article 607812. <https://doi.org/10.3389/fgene.2020.607812>
- Johanna, M., Smeekens, H. X., & Wu, R. (2017). Global analysis of secreted protein and glycoproteins in *Saccharomyces cerevisiae*. *Journal of Proteome Research*, *16*(2), 1039-1049. <https://doi.org/10.1021/acs.jproteome.6b00953>
- Jones, D. T., Taylor, W. R., & Thornton, J. M. (1992). The rapid generation of mutation data matrices from protein sequences. *Computer Applications in the Biosciences*, *8*, 275-282. <https://doi.org/10.1093/bioinformatics/8.3.275>
- Jones, E. W. (1991). Tackling the proteases problem in *Saccharomyces cerevisiae*. *Methods in Enzymology*, *194*, 428-453. [https://doi.org/10.1016/0076-6879\(91\)94034-a](https://doi.org/10.1016/0076-6879(91)94034-a)
- Jonson, L., & Rehfeld, J. F. (2004). Enhanced peptide secretion by gene disruption of CYM1, a novel protease in *Saccharomyces cerevisiae*. *European Journal of Biochemistry*, *271*(23-24), 4788-4797. <https://doi.org/10.1111/j.1432-1033.2004.04443.x>
- Kang, H. A., Kim, S. J., Choi, E. S., Rhee, S. K., & Chung, B. H. (1998). Efficient production of intact human parathyroid hormone in a *Saccharomyces cerevisiae* mutant deficient in yeast aspartic protease 3 (YAP3). *Applied Microbiology and Biotechnology*, *50*, 187-192. <https://doi.org/10.1007/s002530051275>
- Kerry-Williams, S. M., Gilbert, S. C., Evans, L. R., & Balance, D. J. (1998). Disruption of the *Saccharomyces cerevisiae* YAP3 gene reduces the proteolytic degradation of secreted recombinant human albumin. *Yeast*, *14*, 161-169. [https://doi.org/10.1002/\(SICI\)1097-0061\(19980130\)14:2](https://doi.org/10.1002/(SICI)1097-0061(19980130)14:2)
- Kim, H., Yoo, S. J., & Kang, H. A. (2014). Yeast synthetic biology for the production of recombinant therapeutic proteins. *FEMS Yeast Research*, *15*, 1-16. <https://doi.org/10.1111/1567-1364.12195>
- Kirkwood, B., & Sterne, J. (2003). *Essential medical statistics* (2nd Ed.). Wiley-Blackwell.
- Kobayashi, K., Kuwae, S., Ohya, T., & Ohda, T. (2000). High-level expression of recombinant human serum albumin from the methylotrophic yeast *Pichia pastoris* with minimal protease production and activation. *Journal of Bioscience and Bioengineering*, *89*, 55-61. [https://doi.org/10.1016/s1389-1723\(00\)88050-0](https://doi.org/10.1016/s1389-1723(00)88050-0)
- Krogh, A., Brown, M., Mian, I. S., Sjölander, K., & Haussler, D. (1994). Hidden Markov models in computational biology: Applications to protein modeling. *Journal of Molecular Biology*, *235*(5), 1501-1531. <https://doi.org/10.1006/jmbi.1994.1104>

- Krogh, A., Larsson, B., von Heijne, G., & Sonnhammer, E. L. (2001). Predicting transmembrane protein topology with a hidden Markov model: Application to complete genomes. *Journal of Molecular Biology*, 305(3), 567-580. <https://doi.org/10.1006/jmbi.2000.4315>
- Krogh, A., Sonnhammer, E. L. L., & Ka, L. (2007). Advantages of combined transmembrane topology and signal peptide prediction - The Phobius web server. *Nucleic Acids Research*, 35, W429-W432. <https://doi.org/10.1093/nar/gkm256>
- Küberl, A., Schneider, J., Thallinger, G. G., Anderl, I., Wibberg, D., Hajek, T., Jaenicke, S., Brinkrolf, K., Goesmann, A., Szczepanowski, R., Pühler, A., Schwab, H., Glieder, A., & Pichler, H. (2011). High-quality genome sequence of *Pichia pastoris* CBS7435. *Journal of Biotechnology*, 154(4), 312-320. <https://doi.org/10.1016/j.jbiotec.2011.04.014>
- Kumar, S., Stecher, G., & Tamura, K. (2016). MEGA7: Molecular evolutionary genetics analysis version 7.0 for bigger datasets. *Molecular Biology and Evolution*, 33(7) 1870-1874. <https://doi.org/10.1093/molbev/msw054>
- Leow, T. C., Rahman, R. N. Z. R. A., Basri, M., & Salleh, A. B. (2004). High level expression of thermostable lipase from *Geobacillus specie* strain T1. *Bioscience, Biotechnology, and Biochemistry*, 68(1), 96-103. <https://doi.org/10.1271/bbb.68.96>
- Li, H., & Durbin, R. (2011). Inference of human population history from individual whole-genome sequences. *Nature*, 475(7357), 493-496. <https://doi.org/10.1038/nature10231>
- Li, S. C., & Kane, P. M. (2009). The yeast lysosome-like vacuole: Endpoint and crossroads. *Biochimica et Biophysica Acta*, 1793, 650-663. <https://doi.org/10.1016/j.bbamcr.2008.08.003>
- Low, K. O., Mahadi, N. M., & Ilias, R. M. (2013). Optimization of signal peptide for recombinant protein secretion in bacterial hosts. *Applied Microbiology and Biotechnology*, 97(9), 3811-3826. <https://doi.org/10.1007/s00253-013-4831-z>
- Madzak, C., Gaillardin, C., & Beckerich, J. M. (2004). Heterologous protein expression and secretion in the non-conventional yeast *Yarrowia lipolytica*: A review. *Journal of Biotechnology*, 109, 63-81. <https://doi.org/10.1016/j.jbiotec.2003.10.027>
- Mahyon, N. I. (2017). *Structural investigation of alcohol oxidase from Meyerozyma Guilliermondii and the use of its promoter for recombinant protein expression* (Master thesis). Universiti Putra Malaysia, Malaysia.
- Martínez, J. L., Liu, L., Petranovic, D., & Nielsen, J. (2012). Pharmaceutical protein production by yeast: Towards production of human blood proteins by microbial fermentation. *Current Opinion in Biotechnology*, 23, 965-971. <https://doi.org/10.1016/j.copbio.2012.03.011>
- Mattanovich, D., Branduardi, P., Dato, L., Gasser, B., Sauer, M., & Porro, D. (2012). Recombinant protein production in yeasts. *Methods in Molecular Biology*, 824, 329-358. [https://doi.org/10.1007/978-1-61779-433-9\\_17](https://doi.org/10.1007/978-1-61779-433-9_17)
- Mergulhao, F., Summers, D. K., & Moneri, G. A. (2005). Recombinant protein secretion in *Escherichia coli*. *Biotechnology Advances*, 23(3), 177-202. <https://doi.org/10.1016/j.biotechadv.2004.11.003>



- Mousavi, P., Mostafavi, Z., & Morowvat, M. H. (2017). *In silico* analysis of several signal peptides for the excretory production of reteplase in *Escherichia coli*. *Current Proteomics*, *14*(4), 326-335. <https://doi.org/10.2174/1570164614666170809144446>
- Nasir, N. M., Leow, C., Oslan, S., Salleh, A., & Oslan, S. (2020). Molecular expression of a recombinant thermostable bacterial amylase from *Geobacillus stearothermophilus* SR74 using methanol-free *Meyerozyma guilliermondii* strain SO yeast system. *BioResource*, *15*(2), 3161-3172
- Negahdaripour, M., Nezafat, N., & Hajighahramani, N. (2017). *In silico* study of different signal peptides for secretory production of interleukin- 11 in *Escherichia coli*. *Current Protein and Peptide Science*, *14*(2), 112-121. <https://doi.org/10.2174/1570164614666170106110848>
- Nevoigt, E. (2008). Progress in metabolic engineering of *Saccharomyces cerevisiae*. *Microbiology and Molecular Biology Reviews*, *72*, 379-412. <https://doi.org/10.1128/MMBR.00025-07>
- Ohmuro-Matsuyama, Y., & Yamaji, H. (2017). Modification of a signal sequence for antibody secretion from insect cells. *Journal of Cytotechnology*, *70*(3), 891-898. <https://doi.org/10.1007/s10616-017-0109-0>
- Oslan, S. N., Salleh, A. B., Rahman, R. A., Basri, M., & Chor, A. L. (2012). Locally isolated yeasts from Malaysia: Identification, phylogenetic study and characterization. *Acta Biochimica Polonica*, *59* (2), 225-229.
- Oslan, S. N., Salleh, A. B., Rahman, R. A., Zaliha, R. N., Leow, T. C., Sukamat, H., & Basri, M. (2015). A newly isolated yeast as an expression host for recombinant lipase. *Cellular and Molecular Biology Letters*, *20*(2), 279-293. <https://doi.org/10.1515/cmb-2015-0015>
- Oslan, S. N., Salleh, A. B., Rahman, R. A., Zaliha, R. N., Leow, A. T. C., & Basri, M. (2014). *Pichia pastoris* as a host to overexpress the thermostable T1 lipase from *Geobacillus zalihae*. *Journal of Biosciences*, *3*(1), 7-17. [https://doi.org/10.5176/2251-3140\\_3.1.45](https://doi.org/10.5176/2251-3140_3.1.45)
- Petersen, T. N., Brunak, S., von Heijne, G., & Nielsen, H. (2011). SignalP 4.0: Discriminating signal peptides from transmembrane regions. *Nature Methods*, *8*, 785-786. <https://doi.org/10.1038/nmeth.1701>
- Rahman, R. N. Z. A., Razak, C. N., Ampon, K., Basri, M., Yunus, W. M. Z. W., & Salleh, A. B. (1994). Purification and characterization of a heat stable alkaline protease from *Bacillus stearothermophilus* F1. *Applied Microbiology and Biotechnology*, *40*, 822-827. <https://doi.org/10.1007/BF00173982>
- Rajewsky, N., Vergassola, M., Gaul, U., & Siggia, E. D. (2002). Computational detection of genomic *cis*-regulatory modules applied to body patterning in the early *Drosophila* embryo. *BMC Bioinformatics*, *3*, Article 30. <https://doi.org/10.1186/1471-2105-3-30>
- Rawlings, N. D., Barrett, A. J., Thomas, P. D., Huang, X., Bateman, A., & Finn, R. D. (2018). The MEROPS database of proteolytic enzymes, their substrates and inhibitors in 2017 and a comparison with peptidases in the PANTHER database. *Nucleic Acids Research*, *46*, D624-D632. <https://doi.org/10.1093/nar/gkx1134>
- Savojardo, C., Martelli, P. L., Fariselli, P., & Casadio, R. (2018). DeepSig: Deep learning improves signal peptide detection in proteins. *Journal of Bioinformatics*, *34*, 1690-1696. <https://doi.org/10.1093/bioinformatics/btx818>

- Silva, C. I., Teles, H., Moers, A. P., & Eggink, G. (2011). Secreted production of collagen-inspired gel-forming polymers with high thermal stability in *Pichia pastoris*. *Biotechnology and Bioengineering*, *108*, 2517-525. <https://doi.org/10.1002/bit.23228>
- Singh, B., Kapur, N., & Kaur, P. (2012). Speech recognition with Hidden Markov Model: A review. *International Journal of Advanced Research in Computer Science and Software Engineering*, *2*(3), 401-403.
- Sinha, J., Plantz, B. A., Inan, M., & Meagher, M. M. (2005). Causes of proteolytic degradation of secreted recombinant proteins produced in methylotrophic yeast *Pichia pastoris*: Case study with recombinant ovine interferon-tau. *Biotechnology and Bioengineering*, *89*, 102-112. <https://doi.org/10.1002/bit.20318>
- Sinha, S., van Nimwegen, E., & Sigga, E. D. (2003). A probabilistic method to detect regulatory modules. *Journal of Bioinformatics*, *19*(Suppl. 1), i292-i301. <https://doi.org/10.1093/bioinformatics/btg1040>
- Song, J., Tan, H., Perry, A. J., Akutsu, T., Webb, G. I., & Whisstock, J. C. (2012). PROSPER: An integrated feature-based tool for predicting protease substrate cleavage sites. *PLoS ONE*, *7*(11), Article e50300. <https://doi.org/10.1371/journal.pone.0050300>
- Suryawanshi, H. K., & Pandya, N. D. (2017). Screening, identification of alkaline proteases producing fungi from soil of different habitats of Amalner Tahsil [Maharashtra] and their applications. *International Journal of Applied Sciences and Biotechnology*, *5*(3), 397-402. <https://doi.org/10.3126/ijasbt.v5i3.18304>
- Tang, H., Coram, M., Wang, P., Zhu, X., & Risch, N. (2006). Reconstructing genetic ancestry blocks in admixed individuals. *American Journal of Human Genetics*, *79*, 1-12. <https://doi.org/10.1086/504302>
- Valli, M., Tatto, N. E., Peymann, A., Gruber, C., Landes, N., Ekker, H., Thallinger, G. G., Mattanovich, D., Gasser, B., & Graf, A. B. (2016). Curation of the genome annotation of *Pichia pastoris* (*Komagataella phaffii*) CBS7435 from gene level to protein function. *FEMS Yeast Research*, *16*(6), 1-12. <https://doi.org/10.1093/femsyr/fow051>
- Van Den Hazel, H. B., Morten, C. K. B., & Jakob, R. W. (1996). Biosynthesis and function of yeast vacuolar proteases: Review. *Yeast*, *12*, 1-16. [https://doi.org/10.1002/\(SICI\)1097-0061\(199601\)12:1<1](https://doi.org/10.1002/(SICI)1097-0061(199601)12:1<1)
- Van Ooyen, A. J., Dekker, P., Huang, M., Olsthoorn, M. M., Jacobs, D. I., Colussi, P. A., & Taron, C. H. (2006). Heterologous protein production in the yeast *Kluyveromyces lactis*. *FEMS Yeast Research*, *6*, 381-392. <https://doi.org/10.1111/j.1567-1364.2006.00049.x>
- Wang, K., Li, M., Hadley, D., Liu, R., Glessner, J., Grant, S. F. A., & Bucan, M. (2007). PennCNV: An integrated hidden Markov model designed for high-resolution copy number variation detection in whole-genome SNP genotyping data. *Genome Research*, *17*(11), 1665-1674. <https://doi.org/10.1101/gr.6861907>
- Werten, M. W., & de Wolf, F. A. (2005). Reduced proteolysis of secreted gelatin and Yps1-mediated alpha-factor leader processing in a *Pichia pastoris* kex2 disruptant. *Applied and Environmental Microbiology*, *71*, 2310-2317. <https://doi.org/10.1128/AEM.71.5.2310-2317.2005>
- Wu, M., Shen, Q. M., Yang, Y., & Zhang, S. (2013). Disruption of YPS1 and PEP4 genes reduces proteolytic degradation of secreted HAS/PTH in *Pichia pastoris* GS115. *Journal of Industrial Microbiology and Biotechnology*, *40*, 589-599. <https://doi.org/10.1007/s10295-013-1264-8>
- Yao, X. Q., Zhao, H. L., Xue, C., Zhang, W., Xiong, X. H., Wang, Z. W., Li, X. Y., & Liu, Z. M. (2009). Degradation of HSA-AX15 (R13K) when expressed in *Pichia pastoris* can be reduced via the

- disruption of YPS1 gene in this yeast. *Journal of Biotechnology*, 139, 131-136. <https://doi.org/10.1016/j.jbiotec.2008.09.006>
- Yoon, B. (2009). Hidden Markov Models and their applications in biological sequence analysis. *Current Genomics*, 10(6), 402-415. <https://doi.org/10.2174/138920209789177575>
- Zamani, M., Nezafat, N., & Negahdaripour, M. (2015). *In silico* evaluation of different signal peptides for the secretory production of human growth hormone in *E. coli*. *International Journal of Peptide Research and Therapeutics*, 21(3), 261-268. <https://doi.org/10.1007/s10989-015-9454-z>

## APPENDIX

Table S1

Summary of statistical analysis of native protease activity assay of *M. guilliermondii* strain SO

	Extracellular	Intracellular
Mean	68.16666667	51.91666667
Variance	2604.481481	751.3611111
Observations	4	4
Pearson Correlation	0.994528638	
Hypothesized Mean Difference	0	
df	3	
t Stat	1.357279359	
P(T<=t) one-tail	0.133888423	
t Critical one-tail	2.353363435	
P(T<=t) two-tail	0.267776845	
t Critical two-tail	3.182446305	

Statistical analysis of the two variables obtained from the extracellular and intracellular protease activities of *M. guilliermondii* strain SO over time, shows that the t-value is greater than alpha value of 0.05

Table S2a

Pairwise sequence alignment of aspartyl protease hits from the HMM strategy with reference *P. pastoris* aspartyl protease (PEP4)

Hit(s)	Amino acid count	% identity	% similarity	Gaps	Score
4807	408	68.3%	79.8%	3.4	1510.0
4057	434	18.3%	31.7%	37.4	230
4064	388	20.8%	36.1%	28.3	246
1971	402	23.8%	38.4%	28.2	255
999	393	22.7%	35.8%	32.4	217
4978	414	25.2%	36.7%	26.5	296
4979	384	26.4%	38.6%	28.7	298
4980	446	24.3%	39.9%	19.1	244.5
4707	390	22.9%	41.6%	26.0	307
341	399	19.7%	29.8%	38.3	219
1972	504	23.8%	39.6%	18.1	280
70	549	22.3%	36.6%	28.1	264
57	334	23.7%	40.3%	23.9	259
2	344	19.6%	32.0%	37.8	177.5

Pairwise sequence alignment. **(a)** Showing aspartyl protease sequence hit output. Each hit (14) outputs were pairwise aligned with reference sequence using the EMBL-EBI search and sequence analysis tools. The first hits output from the HMM analysis with the lowest E-value shows the closest similarity with the reference model and has the highest score value. **(b)** Showing serine protease sequence hit output. Each hit (3) outputs were pairwise aligned with reference sequence using the EMBL-EBI search and sequence analysis tools. The first hits output from the HMM analysis with the lowest E-value shows the closest similarity with the reference model and has the highest score value.

Table S2b

*Pairwise sequence alignment of serine protease hits from the HMM strategy with reference P. pastoris serine protease (PRB1)*

Hit(s)	Amino acid count	% identity	% similarity	Gaps	Score
4089	770	40.9%	53.5%	30.7	1574.5
5205	1048	20.3%	27.5%	59.0	987
3337	381	26.3%	37.7%	35.1	542

Table S3a

*Predicted potential cleavage sites (red) on thermostable T1 lipase using PROSPER aspartyl protease model*

Position	Segment	N-fragment	C-fragment	Score
172	TLVN <b>R</b> MVDF	21.40 kDa	26.16 kDa	1.14
156	HFVL <b>R</b> SVTT	19.68 kDa	27.89 kDa	1.11
124	MLVS <b>R</b> LLEN	15.74 kDa	31.82 kDa	1.06

Predicted cleavage sites using PROSPER online tool. **(a)** Showing three (3) predicted potential cleavage sites on thermostable T1 lipase using PROSPER aspartyl protease model. **(b)** Showing five (5) predicted potential cleavage sites on thermostable T1 lipase using PROSPER serine protease model.

Table S3b

*Shows five (5) predicted potential cleavage sites (red) on thermostable T1 lipase using PROSPER serine protease model*

Position	Segment	N-fragment	C-fragment	Score
360	DHLE <b>R</b> IIGV	44.33 kDa	3.24 kDa	1.27
127	SLLE <b>R</b> INGSQ	16.10 kDa	31.47kDa	1.02
149	PLFE <b>R</b> GGHH	18.70 kDa	28.86 kDa	1.02
189	AVLE <b>R</b> AAAV	23.46 kDa	24.11 kDa	1.00
315	RWLE <b>R</b> NDGI	38.70 kDa	8.86 kDa	0.98



## The Asymmetric Impacts of Crude Oil Prices, Inflation, the Exchange Rate, Institutional Quality, and Trade Balance on Tourist Arrivals in Bangladesh: A Nonlinear ARDL Model Approach

Rehana Parvin

*Department of Quantitative Sciences, International University of Business Agriculture, and Technology (IUBAT), 4 Embankment Drive Road, Sector 10, Uttara, Dhaka, Bangladesh*

### ABSTRACT

The nonlinear interaction of oil prices, inflation, the exchange rate, institutional quality, and trade balance on tourist arrivals in Bangladesh is scrutinized in this study. The technique utilized in this study, Nonlinear Autoregressive Distributed Lag (NARDL), is a novel co-integrating strategy. The yearly time series data used in this study spanned 1995 to 2019. The NARDL bound test is performed to assess if variables like oil prices, inflation, the exchange rate, institutional quality, and trade balance on tourist arrivals are co-integrated. Oil prices and exchange rates, according to the findings, have a long-run negative and significant impact on tourism demand, whereas improvements in institutional quality are positively associated with tourist arrivals. Moreover, the study's findings revealed a nonlinear kinship between the trade balance, inflation, and tourism demand across time. The asymmetric results obtained could enable Bangladeshi policymakers to make more precise decisions.

*Keywords:* Asymmetric, exchange rate, inflation, institutional quality, NARDL, trade balance

### INTRODUCTION

Tourism is a significant growth driver in the world economy. In recent years, tourism has become increasingly essential to the global economy. The number of tourists has increased year over year in recent years because of globalization, preventing a significant expansion in both the sector and service quality. It has become one of the economy's most important

#### ARTICLE INFO

*Article history:*

Received: 02 July 2021

Accepted: 19 November 2021

Published: 04 January 2022

DOI: <https://doi.org/10.47836/pjst.30.1.43>

*E-mail address:*

rehana.parvin@iubat.edu

ISSN: 0128-7680

e-ISSN: 2231-8526

© Universiti Putra Malaysia Press

foundations, thanks to population migration, as well as the enormous tourism options and professionalization of the industry. Tourism is one of the world's most significant economic sectors. It is the third-largest export category, trailing behind fuels and chemicals, contributing to 7% of global trade in 2019. According to the World Economy Forum (WEF), it can account for more than 20% of a country's Gross Domestic Product (GDP) in some cases, and it is the world economy's third-largest export sector.

Over the last five decades, the tourism industry has seen explosive growth worldwide. Due to its contributions to global GDP, job creation, poverty alleviation, and inflation reduction, it continues to appear to be a dominant economic engine. Despite hovering in the shadow of terrorism for the past few decades, global tourism has risen to prominence as a fast-growing sector, promoting the development of tourism infrastructure in developing nations in response to local demand. A country with a lower unemployment rate invests in infrastructure and raises per capita income, increasing tax revenue. It increases the country's foreign reserves, boosts economic growth, and attracts international investment, all of which raise living standards (Balcilar et al., 2014; Tang & Abosedra, 2014; Habibi, 2017). Thus, it is vital to understand which microeconomic variables impact the tourism sector to enrich the economy and save the sector. Some worldwide studies look at how the exchange rate, oil prices, and inflation affect tourism demand. Linear trend analysis has been employed in most investigations. However, this research uncovered a non-linear pattern among the research variables by integrating two more crucial components: institutional quality and trade balance.

Exchange rates have been explored repeatedly in the literature as a crucial factor in determining tourism demand. Furthermore, recent research has recommended including the exchange rate in the tourism demand equation to avoid the possibility of a missing component, the exchange rate. Foreigner tourists with strong currencies benefited from the local currency depreciation since their overall tourism expenses were reduced. Due to this, the number of tourists visiting the country is constantly increasing (Vita & Kyaw, 2013). However, when it comes to the exchange rate, there are two schools of thought: some experts argue for appreciation to enhance tourism, while others push for depreciation. Tourism demand is positively influenced by exchange rate appreciation (Toh et al., 2006; Görmüş & Göçer, 2010). On the other hand, exchange rate depreciation is positively correlated with tourism demand, according to Meo et al. (2018), because traveling to a country whose currency has depreciated becomes less expensive.

According to Becken (2008), transportation is crucial to growing tourism, which is strongly reliant on energy sources, such as oil. Inflationary pressures result from higher oil prices, which lower consumer income (Kisswani et al., 2020). Furthermore, as oil prices rise, the cost of production rises in numerous areas, thereby lowering output and increasing unemployment, as well as causing inflation. An increase in oil prices, according to Anoruo



and Elike (2009), has a detrimental impact on economic growth due to demand and supply. Supply-side effects developed because of the huge increase in oil prices, and as a result, the cost of production increased, lowering the supply of items that require a large amount of oil, according to the authors. On the other hand, high oil prices have cut domestic consumption and investment, as well as the purchasing power of the local currency and customers' capacity to purchase products and services. Nigeria's economy, according to Gokmenoglu et al. (2016), is driven by oil. Because tourism is regarded as a luxury item, the trend mentioned above has a significant and unfavorable effect on demand.

Poor institutional quality, among other things, is one of Bangladesh's major impediments. These things are "essential," including legality, ownership rights, anti-exploitation, liability, and government excellence. When it comes to ensuring the success of the tourism industry, organizing activities is critical.

In addition, the tourism industry adds to the economy's growth. Therefore, it is critical to think about how microeconomic variables affect this industry. To this point, most academics have studied the nexus of tourism demand and its drivers in a linear framework. However, in order to investigate structural changes or short-term volatility, linear models cannot be employed. Most studies have looked at the relationship between microeconomic factors (such as oil prices, inflation, and the currency rate) and economic development in a linear context, as previously mentioned. In practice, however, these variables are subject to frequent oscillations and exhibit nonlinear behavior, which has previously been overlooked in research. The basic limitation of a linear model, according to Anoruo (2011), is that it examines linear series, although they are nonlinear in fact. Furthermore, the linear model ignores short-term volatility and structural changes. Furthermore, linear models assume linearity in time series, even though time series is nonlinear in reality. Failure to account for intrinsic nonlinearities, according to the data, can lead to inaccurate conclusions. As a result, the primary goal of this research is to determine how pricing differences (exchange rates, trade balance, inflation, and oil prices) influence tourist arrivals. No previous research has investigated the asymmetric relationship between the variables mentioned above and visitor arrivals, as far as the researchers are aware. In this work, the nonlinear autoregressive distributed lag estimation approach was applied. As a result, this research uses this method to gain a better understanding of the impact of microeconomic variables on Bangladesh's tourism. As a result, this study will make more accurate policy suggestions to decision-makers.

### **Tourism in Bangladesh**

Bangladesh's weather is pleasant, making it a popular tourist destination worldwide. The Ganges, Brahmaputra, and Ganges River delta are all at sea level in Bangladesh. The Ganges, Brahmaputra, and Meghna rivers and their tributaries come together to form this

delta. Natural beauty abounds in Bangladesh. Rivers, beaches, ancient sites, religious sites, hills, forests, waterfalls, and tea gardens are all nearby. Four world heritage sites in Bangladesh are Sundarban, Cox's Bazar Sea beach, the Historic Mosque in Bagerhat, and the Ruins of the Buddhists Vihara at Paharpur, among others 1007 heritage sites in the world. Many local and international tourists visit the country and its tourist attractions to admire the beauty of nature. Around six lakh (600,000) tourists visited Bangladesh in 2012 to see and appreciate its natural beauty.

Bangladesh is ranked 120th out of 140 countries in the Travel and Tourism Competitiveness Report 2019, up from 125<sup>th</sup> last year. In 2018, tourism accounted for 4.4% of Bangladesh's overall GDP. The government allocated Bangladeshi Taka 34 billion to the Civil Aviation (Biman) and Tourism Ministries, doubling the previous fiscal year's budget. As a result, Bangladesh's direct contribution to GDP will increase by 6.2% per year to Bangladeshi Taka 824.0 billion (2.1% of GDP) by 2028, according to the World Travel and Tourism Council (WTTC). Visitor exports mostly determine the direct contribution to GDP. Bangladesh's visitor exports totaled BDT 18.4 billion in 2017, with an estimated value of BDT35.8 billion in spending by international visitors.

By 2024, Bangladesh will have graduated from the Least Developed Countries (LDC) category. As a result, Bangladesh must begin seeking out other sources of foreign revenue before its primary source runs dry. The tourism industry accounts for 10.4% of the global GDP and is growing at 3.9% each year. As a result, if well managed, the tourism business can be a significant source of foreign currency revenues.

These are the only few studies that studied only the improvement of the tourism sector in the Bangladesh context (e.g., Islam, 2015; Mondal & Haque, 2017). There is no study on asymmetric or even symmetric tourism demand behavior in Bangladesh, to the best of the authors' knowledge. This study used nonlinear autoregressive distributed lag (NARDL) model by Shin et al. (2014), which can compute the error correction model (ECM) as well as long-term and short-period asymmetries to fill this gap.

## Literature Review

After oil and gas, tourism is the world's third most significant industry. As a result, the tourist industry is now seen as a crucial component of increasing state revenue and the overall economy. Therefore, several studies have been conducted to determine the factors that contribute to an increase in tourism demand in a specific country.

Several studies have investigated the impact of crude oil prices on tourist arrivals (Yeoman et al., 2007; Becken & Lennox, 2012; Shaeri et al., 2016). According to some research, there is an asymmetric relationship between oil prices and tourist demand (Kisswani et al., 2020; Al-Mulali et al., 2020). Using the NARDL model, Kisswani and Harraf (2021) investigated the asymmetric effects of price variations in the oil market

on tourism demand. The authors conclude that decision-makers in the Middle East and Northern Africa (MENA) countries should pay attention to the asymmetric impact of oil prices on tourism, given that tourism is a significant contributor to GDP and a good source of jobs, and that this information can be useful in developing policies.

Furthermore, rates of exchange conversion are frequently used in research to account for the effect of relative tourism pricing (Cheng, 2012; Yap, 2012; Tang et al., 2016). Exchange rate volatility can be a separate variable in a tourism demand model since customers may react differently to real pricing differences owing to volatility (Dincer et al., 2015; Sharma & Pal, 2020). Using the ARDL model in Iceland, Agiomirgianakis et al. (2015) looked at the currency rate in relation to visitor flows. According to their findings, currency rate fluctuation has a detrimental impact on visitor arrivals.

Inflation or tourist pricing is crucial for forecasting tourism demand (Naidu et al., 2017; Shaari et al., 2018; Pektas & Unluonen, 2020; Achyar & Hakim, 2021). As measured by the price elasticity of demand, rising tourism prices have always been negatively linked to tourism demand. Inflation and the number of visitors are inversely connected, according to Hanafiah and Harun (2010).

Several recent studies have investigated the link between institutional quality and tourism (Kim et al., 2018; Usman et al., 2020). Institutional quality and political stability influence tourism demand. According to the bulk of studies, political stability is necessary for tourism development (Farmaki et al., 2015; Khan et al., 2020; Lee et al., 2020; Mushtaq et al., 2020). According to Haseeb and Azam (2021), a higher level of corruption has a detrimental influence on tourism competitiveness among nations. Ghalia et al. (2019) explored the effects of institutional quality and political risk on tourism demand. According to the authors, the absence of conflict has been proven helpful to tourism development. Therefore, the quality of an institution plays an important role in enhancing tourist traffic.

For the past decade, tourism has been seen as a source of trade balance, particularly in countries gifted with natural beauty. Moreover, the tourist sector, according to Jalil et al. (2013), is economically significant since it generates revenue, creates investment and job opportunities, and improves infrastructure. Terrorism, on the other hand, is more than a financial drain (Liu & Pratt, 2017; Meo et al., 2018).

Because of tourists' spending power, tourism demand responds asymmetrically. Bangladesh is an oil-importing country. Therefore, the relationship between oil prices and tourism demand makes sense. Tourist arrivals are thus adversely affected by rising energy prices. In addition, the quality of Bangladesh's institutions, inflation, trade balance, and exchange rates all play a role in tourist arrivals. To this date, most scholars have examined the nexus of tourism demand and its drivers in a linear framework. However, structural changes and short-term volatility cannot be studied using linear models. According to Raza et al. (2016), non-linearities, such as structural fractures and asymmetric behavior resulting

from bankruptcy or severe credit events, regularly influence market dynamics, especially when the sample period includes financial crises like the global crisis of 2007 and 2008. As a result, earlier research has shown contradictory findings.

Hence, in this study, the nonlinear framework was used in Bangladesh to fill in this gap. In addition, the nonlinear impacts of different microeconomic variables are commonly explored in the literature to study the five key mentioned above components that impact tourist arrivals. As a result, macroeconomic variables, such as the trade balance, exchange rate, institutional quality, inflation, and oil prices, are all possible sources of asymmetric tourism demand. Furthermore, this will be the first study in Bangladesh to look at the asymmetric influence of the above-mentioned microeconomic variables on tourist arrivals, to the best of the authors' knowledge. Shin et al. (2014) created a novel econometric methodology called the nonlinear ARDL technique, which allows us to look at asymmetries between study variables in both the short and long run. Tourist arrivals, the exchange rate, trade balance, inflation, institutional quality, and oil prices are among the six variables used. Yearly secondary time series data from 1995 to 2019 has been used for empirical study.

## METHOD AND MATERIALS

### Data Description

This research has combined key microeconomic factors to look at the asymmetric relationship in the short and long run. Yearly secondary time series data from 1995 to 2019 has been used for this empirical study. Table 1 has shown the description and sources of study variables.

### Methodology

Crude oil prices, inflation, the exchange rate, the trade balance, and the quality of institutions all impacted tourist arrivals in Bangladesh and were investigated using the augmented

Table 1  
*Description and sources of study variables*

Variables	Indicators	Description	Data sources
Tourist arrival	TA	Tourist arrival (in Thousand person)	World Development Indicators (WDI)
Oil Price	OP	Crude Oil Price (in dollar per barrel)	Statistical Review of World Energy, 2020
Inflation	INF	Consumer Price Index (in percentage of the total)	World Development Indicators (WDI)
Exchange rate	EXR	US Dollar/Bangladeshi Taka	Bangladesh Bank
Trade balance	TB	Trade balance (in % of GDP)	World Development Indicators (WDI)
Institutional quality	IQ	Index	ICRG

*Note:* Tourist arrivals, oil prices, and the exchange rate are all expressed as logarithms.

Phillips curve methodology in this research. Ibrahim (2015), Sek (2017), and Abdlaziz et al. (2016) have all investigated an augmented Phillips curve technique. The following linear Equation 1 was proposed to investigate the influence of crude oil prices, inflation, exchange rate, trade balance, and institutional quality on tourist arrivals in Bangladesh:

$$LNTA_t = \alpha_0 + \alpha_1 LNOP_t + \alpha_2 INF_t + \alpha_3 LNEXR_t + \alpha_4 TB_t + \alpha_5 IQ_t + u_t \quad (1)$$

Where, LNTA, LNOP, INF, LNEXR, TB, and IQ represent the logarithmic of tourist arrivals, the logarithmic of oil prices, inflation, and the logarithmic of the exchange rate, trade balance, and institutional quality, respectively, and  $u_t$  is an independent and identically distributed (i.i.d.) component. This study conducted the current investigation in nonlinear settings due to nonlinearities in time series. It could be due to (a) concealed co-integration and (b) the co-integration of series components causing structural fractures and asymmetries. The nonlinear ARDL methodology employs positive and negative changes or partial sum decompositions to determine the asymmetric effects in long and short-run periods. This approach produces superior results with small samples, according to Romilley et al. (2001) and Pesaran et al. (2001). The model's nonlinear functional form of the model to investigate the impact of crude oil prices, inflation, exchange rate, trade balance, and institutional quality on tourist arrivals is as in Equation 2:

$$LNTA = f(LNOP^+, LNOP^-, INF^+, INF^-, LNEXR^+, LNEXR^-, TB^+, TB^-, IQ^+, IQ^-) \quad (2)$$

Based on the previous work of Liang et al. (2020), Ibrahim (2015), and Lacheheb & Sirag (2019), considering the asymmetric relationship between oil prices, inflation, exchange rate, trade balance, institutional quality, and tourist arrivals, the model will be as in Equation 3:

$$LNTA_t = \beta_0 + \beta_1 LNOP_t^+ + \beta_2 LNOP_t^- + \beta_3 INF_t^+ + \beta_4 INF_t^- + \beta_5 LNEXR_t^+ + \beta_6 LNEXR_t^- + \beta_7 TB_t^+ + \beta_8 TB_t^- + \beta_9 IQ_t^+ + \beta_{10} IQ_t^- + e_t \quad (3)$$

Where the  $\beta_i$ 's represent long run parameters and  $e_t$  is an i.i.d. component. Positive changes  $OP^+$ ,  $INF^+$ ,  $EXR^+$ ,  $TB^+$ , and  $IQ$  as well as negative changes  $OP^-$ ,  $INF^-$ ,  $EXR^-$ ,  $TB^-$ , and  $IQ$  respectively, account for the nonlinear influence of research variables. Positive and negative changes in their partial sums in oil prices, inflation, the exchange rate, trade balance, and institutional quality are represented by the following Equations 4-13:

$$OP_t^+ = \sum_{i=1}^t \Delta OP_t^+ = \sum_{i=1}^t \max(\Delta OP_i, 0) \quad (4)$$

$$OP_t^- = \sum_{i=1}^t \Delta OP_t^- = \sum_{i=1}^t \min(\Delta OP_i, 0) \quad (5)$$

$$INF_t^+ = \sum_{i=1}^t \Delta INF_t^+ = \sum_{i=1}^t \max(\Delta INF_i, 0) \tag{6}$$

$$INF_t^- = \sum_{i=1}^t \Delta INF_t^- = \sum_{i=1}^t \min(\Delta INF_i, 0) \tag{7}$$

$$EXR_t^+ = \sum_{i=1}^t \Delta EXR_t^+ = \sum_{i=1}^t \max(\Delta EXR_i, 0) \tag{8}$$

$$EXR_t^- = \sum_{i=1}^t \Delta EXR_t^- = \sum_{i=1}^t \min(\Delta EXR_i, 0) \tag{9}$$

$$TB_t^+ = \sum_{i=1}^t \Delta TB_t^+ = \sum_{i=1}^t \max(\Delta TB_i, 0) \tag{10}$$

$$TB_t^- = \sum_{i=1}^t \Delta TB_t^- = \sum_{i=1}^t \min(\Delta TB_i, 0) \tag{11}$$

$$IQ_t^+ = \sum_{i=1}^t \Delta IQ_t^+ = \sum_{i=1}^t \max(\Delta IQ_i, 0) \tag{12}$$

$$IQ_t^- = \sum_{i=1}^t \Delta IQ_t^- = \sum_{i=1}^t \min(\Delta IQ_i, 0) \tag{13}$$

Under an unrestricted error correction representation, Equation 3 can be included in the following NARDL Equation 14:

$$\begin{aligned} \Delta LNTA_t = & \gamma_0 + \sum_{i=1}^p \gamma_1 \Delta LNTA_{t-i} + \sum_{i=1}^p \gamma_2 \Delta LNOP^+_{t-i} + \\ & \sum_{i=1}^p \gamma_3 \Delta LNOP^-_{t-i} + \sum_{i=1}^p \gamma_4 \Delta INF^+_{t-i} + \sum_{i=1}^p \gamma_5 \Delta INF^-_{t-i} + \\ & \sum_{i=1}^p \gamma_6 \Delta LNEXR^+_{t-i} + \sum_{i=1}^p \gamma_7 \Delta LNEXR^-_{t-i} + \sum_{i=1}^p \gamma_8 \Delta TB^+_{t-i} + \\ & \sum_{i=1}^p \gamma_9 \Delta TB^-_{t-i} + \sum_{i=1}^p \gamma_{10} \Delta IQ^+_{t-i} + \sum_{i=1}^p \gamma_{11} \Delta IQ^-_{t-i} + \theta_1 LNTA_{t-1} + \\ & \theta_2 LNOP^+_{t-1} + \theta_3 LNOP^-_{t-1} + \theta_4 INF^+_{t-1} + \theta_5 INF^-_{t-1} + \theta_6 LNEXR^+_{t-1} + \\ & \theta_7 LNEXR^-_{t-1} + \theta_8 TB^+_{t-1} + \theta_9 TB^-_{t-1} + \theta_{10} IQ^+_{t-1} + \theta_{11} IQ^-_{t-1} + \varepsilon_t \end{aligned} \tag{14}$$

Where p indicate the lag order and  $\beta_1 = \theta_2/\theta_1, \beta_2 = \theta_3/\theta_1, \beta_3 = \theta_4/\theta_1$  and  $\beta_4 = \theta_5/\theta_1, \beta_5 = \theta_6/\theta_1, \beta_6 = \theta_7/\theta_1, \beta_7 = \theta_8/\theta_1, \beta_8 = \theta_9/\theta_1, \beta_9 = \theta_{10}/\theta_1$  and  $\beta_{10} = \theta_{11}/\theta_1$  are long-run asymmetric effects of crude oil prices, inflation, exchange rate, trade balance and institutional quality on tourist arrivals and  $\varepsilon_t$  is an error correction term. Accordingly,  $\sum_{i=1}^p \gamma_i$  's are measures the short run asymmetric effects of crude oil prices, inflation, the exchange rate, the trade balance, and institutional quality respectively.

Pre-testing is required for this research work to estimate Equations 14. First, this work investigated the order of integration of the selected variables using the well-known Augmented Dickey-Fuller (ADF) and Phillips–Perron (PP) tests. The NARDL technique is appropriate regardless of whether the variables are fully I (0) or I (1) integrated, or even fractionally integrated. However, according to some authors, this approach does not apply to the I (2) series because the estimators become invalid for the I (2) series. Second, this study

estimated Equation 14 using Katrakilidis and Trachanas’s (2012) typical Ordinary Least Squares (OLS) approach. Third, this research used a bound testing methodology developed by Pesaran et al. (2001) and Shin et al. (2014) to evaluate the existence of a long-run relationship between variables in a co-integration test. Using the F-test, this study checks the null hypothesis of  $\theta_1 = \theta_2 = \theta_3 = \theta_4 = \theta_5 = \theta_6 = \theta_7 = \theta_8 = \theta_9 = \theta_{10} = \theta_{11} = 0$  jointly. Oil prices, inflation, exchange rates, trade balances, institutional quality, and tourist arrivals are all subjected to the Wald test to evaluate long-run asymmetry. This study uses the NARDL approach to estimate the asymmetric long-run and short-run effects of oil prices, inflation, exchange rates, trade balance, institutional quality, and tourist arrivals after determining the existence of long-run co-integration.

**RESULTS AND DISCUSSION**

The descriptive statistics for all the study variables are presented in Table 2. Bangladesh saw a high of 1016000 visitors, a minimum of 125000, and an average of 294000 visitor arrivals during the study period. The maximum inflation rate was 11.39517% throughout the research period, the lowest inflation rate was 2.007174%, and the average inflation rate was 6.373795%. During the study period, Bangladesh experienced a high exchange rate of 84.58 Bangladeshi taka/Dollar, a low exchange rate of 40.278 Bangladeshi taka/Dollar, and an average exchange rate of 65.30372 Bangladeshi taka/Dollar. The price of crude oil ranged from \$105 per barrel to \$13.05 per barrel, with an average of \$53.764 per barrel over the research period. The institutional quality index in Bangladesh ranged from 2 to 5.39 over the survey period, with an average of 2.6284. According to the calculations, the skewness of tourist arrivals and institutional quality is not between -0.5 and 0.5 (not close to zero). It indicates that the data is not approximately symmetrical and that the Kurtosis is greater than three, indicating that the distribution of tourist arrivals and institutional quality is wider than the normal distribution. According to the findings, the data for the

Table 2  
*Descriptive statistics*

	TA (Thousand person)	OP (dollar per barrel)	EXR (US Dollar / Bangladeshi Taka)	INF (%)	IQ (Index)	TB (% of GDP)
Mean	293.7600	53.76400	65.30372	6.373795	2.628400	-5.940400
Median	207.0000	52.81000	68.87500	6.194280	2.500000	-5.750000
Maximum	1016.000	105.0100	84.58000	11.39517	5.390000	-4.150000
Minimum	125.0000	13.06000	40.27800	2.007174	2.000000	-8.640000
Std. Dev.	221.8572	30.73617	13.96584	2.347536	0.736176	1.215221
Skewness	2.141649	0.359648	-0.339835	-0.035101	2.498626	-0.440069
Kurtosis	6.710256	1.855099	1.876445	2.871849	9.562608	2.240691

*Note.* TA, OP, EXR, INF, IQ, and TB represent tourist arrivals, oil prices, the exchange rate, inflation, institutional quality, and trade balance, respectively.

other parameters is approximately symmetrical, and the Kurtosis for all factors is less than three, suggesting that the distribution is narrower than the normal distribution.

The unit root test, also known as the stationary test, is the most important condition for time series data when looking at the order of integration of variables. The Augmented Dickey-Fuller (ADF) and Phillips–Perron (PP) tests conducted the empirical research. Table 3 summarizes the results of the study. For the best lag structure, involving intercept and linear time trend at level but eliminating time trend from the first difference, the Schwarz information criteria (SIC) was used. Except for the oil price, all variables are stationary at level, showing that they are  $I(0)$  according to the ADF test, whereas all study variables are stationary at the first difference, according to both tests' results, showing that variables are  $I(1)$ . In the absence of  $I(2)$  variables, this study utilized the bound testing methodology to approximate the Equation 14. The effects of each microeconomic variable on tourism demand are depicted in Figure 1. All study factors have a substantial relationship with tourist arrivals in Bangladesh, as seen in the graph.

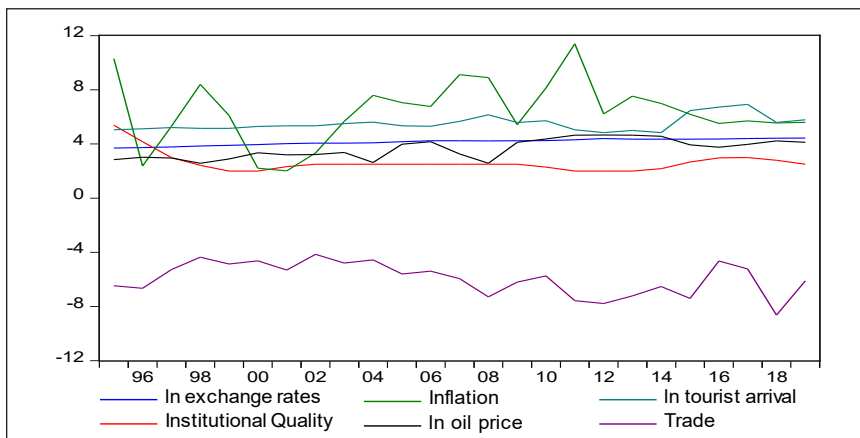


Figure 1. Tourist arrivals versus different study variables

Table 3  
Unit root test results

Variables	Level		First difference	
	ADF	PP	ADF	PP
LNTA	-3.824387**	-2.572581	-4.336694**	-5.014653**
LNOP	-1.558679	-1.589572	-4.463976**	-4.451869**
LNEXR	-3.669183**	-2.536068	-4.361832**	-4.186842**
INF	-3.813030**	-3.888668**	-6.332178**	-12.67836**
IQ	-4.899241**	-5.590900**	-4.612749**	-3.199342**
TB	-3.021265**	-2.957852	-6.129287**	-9.473984**

Note. Significant at 5% levels is denoted by the symbol “\*\*\*”. For optimal lag, order SIC is used, and intercept and time trend are included in level, but only intercept is included in the first difference. LNTA, LNOP, LNEXR, INF, IQ, and TB represent the logarithmic of tourist arrivals, the logarithmic of oil prices, the logarithmic of the exchange rate, inflation, institutional quality, and trade balance, respectively.



The long-run connection is determined by the model’s optimal lag section, according to Bahmani-Oskooee and Bohl (2000). This study used the conventional VAR model for optimal lag order selection and followed the Schwarz information criteria (SIC). Therefore, this study chose lag “1” as the optimal lag. Model estimation results for symmetric and asymmetric co-integration are shown in Table 4. Because the F-statistic result of 2.364730 is smaller than the necessary lower limit of 2.82 at 1% level, the bound test confirms no co-integration in a linear ARDL fashion. However, the F-statistic value of 10.04634 exceeds the upper critical constraint of 3.86 at a 1% level of significance, indicating co-integration for the non-linear ARDL specification.

From the NARDL results, Table 5 explains how to create long-run parameters. Oil prices, exchange rates, inflation, the trade balance, and institutional quality all have a non-linear impact on tourist arrivals, as seen in Table 5. Some diagnostic tests were also undertaken to support the NARDL model’s dependability. The Jarque-Bera (J-B) test, the Ramsey RESET test, the Autoregressive Conditional Heteroskedasticity (ARCH) up to order 2 for heteroskedasticity, and the serial autocorrelation LM test up to level 2 for serial autocorrelation were all used to assess error normality. The results of all the tests are shown on the bottom panel of Table 5. The NARDL model passes all diagnostic tests,

Table 4  
*Bounds test results for co integration*

Model specification	F-Statistic	99% lower bound	99% upper bound	Conclusion
Linear ARDL	2.364730	2.82	4.21	No co integration
Nonlinear ARDL	10.04634	2.54	3.86	Co integration

Note. The critical values are from Narayan (2005), and the SIC criterion is used for optimal lag.

Table 5  
*Nonlinear ARDL estimation and diagnostic test results*

Variable	Coefficient	Std. Error	t-statistic
C	5.329924***	0.847211	6.291143
LNTA(-1)	-1.071399***	0.139152	-7.699467
LNOP <sup>+</sup>	-0.033022**	0.163225	-0.202308
LNOP <sup>-</sup>	-0.856262***	0.164730	-5.197977
LNEXR <sup>+</sup>	-1.758631**	1.414517	-1.243274
LNEXR <sup>-</sup>	-0.969191	5.172185	-0.187385
INF <sup>+</sup>	-0.040615**	0.044209	-0.918699
INF <sup>-</sup>	0.001195	0.041053	0.029106
IQ <sup>+</sup>	1.909432***	0.453803	4.207627
IQ	-0.230186**	0.221506	-1.039185
TB <sup>+</sup>	-0.079228	0.089249	-0.887727
TB <sup>-</sup>	0.253727***	0.059858	4.238855

Table 5 (continue)

CointEq(-1)*	-0.971399
R <sup>2</sup>	0.916795
J-B [p-value]	0.866214
R-R [p-value]	0.0661
LM(1) [p-value]	0.0942
LM(2) [p-value]	0.0825
ARCH(1) [p-value]	0.6722
ARCH(2) [p-value]	0.4568

Note. J-B and R-R refer to the Jarque-Bera test for error normality and the Ramsey-RESET test for model specification, respectively. The LM test is for serial correlation, and the ARCH test is for autoregressive conditional heteroskedasticity, up to the lag order given in the parenthesis. \*\*\*, \*\* refer to significant at 1% and 5% levels of significance, respectively. LN<sub>TA</sub>, LN<sub>OP</sub>, LN<sub>EXR</sub>, INF, IQ, and TB represent the logarithmic of tourist arrivals, the logarithmic of oil prices, the logarithmic of the exchange rate, inflation, institutional quality, and trade balance, respectively.

implying that it is reliable. The speed of adjustment (SOA) is a metric that measures how quickly companies close the difference between their prior year’s leverage and their current period’s desired leverage. The adjustment speed, according to the data, is -0.97, indicating a 97% increase in significance in the prior period to reaching equilibrium. Therefore, Equation 14 can be written with estimated parameters both for short and for the long run as in Equation 15:

$$\begin{aligned} \Delta LN_{TA}_t = & 5.329924 - 1.071399\Delta LN_{TA}_{t-i} - 0.018275\Delta LN_{OP}^+_{t-i} - \\ & 0.693037\Delta LN_{OP}^-_{t-i} - 0.137559\Delta INF^+_{t-i} - 0.028178\Delta INF^-_{t-i} - \\ & 7.160873\Delta LN_{EXR}^+_{t-i} - 8.612820\Delta LN_{EXR}^-_{t-i} + 0.429580\Delta TB^+_{t-i} + \\ & 0.009386\Delta TB^-_{t-i} + 2.135067\Delta IQ^+_{t-i} - 2.829846\Delta IQ^-_{t-i} - \\ & 0.07922LN_{TA}_{t-1} - 0.030821LN_{OP}^+_{t-1} - 0.799200LN_{OP}^-_{t-1} - \\ & 0.037908INF^+_{t-1} + 0.001115INF^-_{t-1} - 1.641434LN_{EXR}^+_{t-1} - \\ & 0.904603LN_{EXR}^-_{t-1} - 0.073949TB^+_{t-1} + 0.236819TB^-_{t-1} + \\ & 1.782185IQ^+_{t-1} - 0.214846IQ^-_{t-1} - 0.971399 \end{aligned} \tag{15}$$

Table 6 shows the findings of the short-run and long-run parameters. Tourist arrivals are lowered by 0.693037% for every 1% fall in crude oil prices, according to the short-run NARDL model, whereas a positive change in oil prices has no significant influence on tourist arrivals. According to the statistics, for every 1% increase in the exchange rate, tourist arrivals decrease by 7.160873% in the short run. Furthermore, tourist arrivals significantly dropped by 0.137559% for every 1% increase in inflation, according to the findings. On

Table 6  
NARDL Short run and long run estimates results

Short run estimates				Long run estimates			
Variable	Coefficient	Std. Error	t-Statistic	Variable	Coefficient	Std. Error	t-statistic
$\Delta LNOP^+$	-0.018275	0.066339	-0.275478	$LNOP^+$	-0.030821**	0.129234	-0.238492
$\Delta LNOP^-$	-0.693037***	0.099823	-6.942675	$LNOP^-$	-0.799200***	0.126911	-6.297341
$\Delta LNXR^+$	-7.160873***	1.025923	-6.979934	$LNXR^+$	-1.641434**	0.873768	-1.878570
$\Delta LNXR^-$	-8.612820	2.735347	-3.148711	$LNXR^-$	-0.904603	3.301046	-0.274035
$\Delta INF^+$	-0.137559**	0.026513	-5.188303	$INF^+$	-0.037908**	0.034259	-1.106522
$\Delta INF^-$	-0.028178	0.021086	-1.336361	$INF^-$	0.001115	0.029331	0.038023
$\Delta IQ^+$	2.135067**	0.201262	10.60838	$IQ^+$	1.782185***	0.283059	6.296151
$\Delta IQ^-$	-2.829846**	0.295685	9.570491	$IQ^-$	-0.214846***	0.109707	-1.958367
$\Delta TB^+$	0.429580**	0.068998	6.225959	$TB^+$	-0.073949	0.054617	-1.353960
$\Delta TB^-$	0.009386	0.045804	0.204915	$TB^-$	0.236819***	0.064636	3.663878

Note. \*\*\*, \*\* refer to significant at 1% and 5% levels of significance, respectively. The terms “+” and “-” refer to positive and negative changes, respectively. LNNTA, LNOP, LNXR, INF, IQ, and TB represent the logarithmic of tourist arrivals, the logarithmic of oil prices, the logarithmic of the exchange rate, inflation, institutional quality, and trade balance, respectively.

the other hand, institutional quality has a significant impact on tourist numbers. According to the findings, every 1% increase in institutional quality resulted in a considerable rise in tourist arrivals of 2.135067%. Conversely, tourist arrivals fell by 2.829846% for every 1% drop in institutional quality. Finally, every 1% increase in the trade balance resulted in a considerable rise in tourist arrivals of 0.429580% in the short run, according to the findings.

Rising or declining oil prices, according to this research, have a significant and negative impact on tourism in the long run. The study’s findings are consistent with Meo et al. (2018) and Hamilton & Tol (2007). Increases in oil prices are expected to raise inflation and slow economic growth. Oil prices directly impact the prices of commodities derived from petroleum products in terms of inflation. Increases in oil prices can put a damper on the supply of other items by raising the cost of production. Tourists are unable to travel anywhere, and tourist arrivals are limited as a result. Because of the influence of shipping costs, energy costs, financial instability, and the flexibility of the exchequer, fluctuations in oil prices could influence financial and tourism activities. From a microeconomic standpoint, rising oil prices result in an immediate drop in disposable income. According to the findings, tourist arrivals are reduced by 0.031% for every 1% increase in crude oil prices, and tourist arrivals are also reduced by 0.79% for every 1% decrease.

Inflation is a major predictor of tourism demand in emerging economies. International tourism is primarily influenced by internal (pricing) and foreign (global economic) trends. According to these findings, a decrease in inflation has a positive but insignificant long-term impact on tourism demand, whereas an increase in inflation, on the other hand, has a

detrimental but significant effect on tourism demand in the long run. Theoretically, inflation is linked to consumer purchasing power because, as inflation rises, tourists' purchasing power declines, and they stop visiting. They live and travel in these areas because it is too expensive to live and travel elsewhere. As inflation falls, more tourists visit the countries they stay in to take advantage of lower living and transportation costs. Tourist arrivals were reduced by 0.038% for every 1% increase in inflation, according to the findings.

According to the study's calculations, the exchange rates have the greatest impact on visitor arrivals. An increase in the exchange rate has a long-term detrimental and significant effect on tourist arrivals, while a fall in the exchange rate has the same but insignificant effect. However, compared to an increase in the exchange rate, it significantly impacts tourist arrivals. One reason for this could be the depreciation of a country's currency, making foreign travel more inexpensive. Increases in the value of a country's currency, on the other hand, will raise the cost of international tourism and reduce the number of visitors from other countries. Our findings align with those of Meo et al. (2018) and Webber et al. (2001). Tourist arrivals significantly dropped by 1.64% for every 1% increase in the exchange rate, according to the findings.

Tourism demand has a strong and positive relationship with the institutional quality. It shows that the country's tourism demand has increased because of improved institutional quality. An increase in institutional quality, according to this research, has a long-term positive and significant effect on tourist arrivals, while a fall in institutional quality has a negative but insignificant effect. Among the specific components of institutional quality, the rule of law, regulatory quality, corruption control, and voice and accountability have all been found to help the tourism industry flourish in the economy. According to the findings, tourist arrivals significantly increase by 1.78% for every 1% increase in institutional quality, but tourist arrivals are reduced by 0.21% for every 1% decrease.

The value of exported items is subtracted from the value of imported products to determine the trade balance. A positive trade balance indicates a surplus, whereas a negative value indicates a deficit. Bangladesh's trade deficit in 2019 was estimated to be at 19.76 billion dollars. Bangladesh had a trade deficit every year during the entire study period. The trade deficit has grown because of COVID-19. According to the findings, a 1% decrease in the trade balance will significantly increase tourist arrivals by 0.23%. When the trade balance is positive, it can aid in the growth of the national economy. Because tourism can contribute to a country's GDP, the government should seek to strengthen this sector. Because of this consequence, tourist arrivals in Bangladesh will increase.

As demonstrated in Table 6, the coefficient sizes of the detrimental and optimistic components of oil prices, inflation, exchange rate, trade balance, and institutional quality are not equal in the long run, indicating an asymmetric relationship. The Wald test was

used to confirm the nonlinearities between the variables under investigation. Table 7 shows the results, which demonstrate the occurrence of asymmetries between variables at a 5% level of significance. The robustness of every statistical study must be checked for parameter stability. Brown et al. (1975) suggested using the stability test for Cumulative Sum (CUSUM) and Cumulative Sum Square (CUSUMSQ) parameters devised by Brown et al. (1975). Thus, the CUSUM and CUSUM Square tests ensured that the model was stable. Figures 2 and 3 show the results of these tests and show that the NARDL model is quite stable.

Table 7  
Testing the presence of asymmetric relationship (Wald test)

Variables	[Chi-square, p-value]	Asymmetric relationship
OP	53.10749 [0.0000]	Asymmetric relationship exist between oil prices and tourist arrivals
EXR	43.61410 [0.0000]	Asymmetric relationship exist between exchange rate and tourist arrivals
INF	6.302883 [0.0428]	Asymmetric relationship exist between inflation and tourist arrivals
IQ	35.708454[0.0000]	Asymmetric relationship exist between Institutional quality and tourist arrivals
TB	22.06879 [0.0000]	Asymmetric relationship exist between Trade balance and tourist arrivals

Note. OP, EXR, INF, IQ, and TB represent oil prices, the exchange rate, inflation, institutional quality, and trade balance respectively.

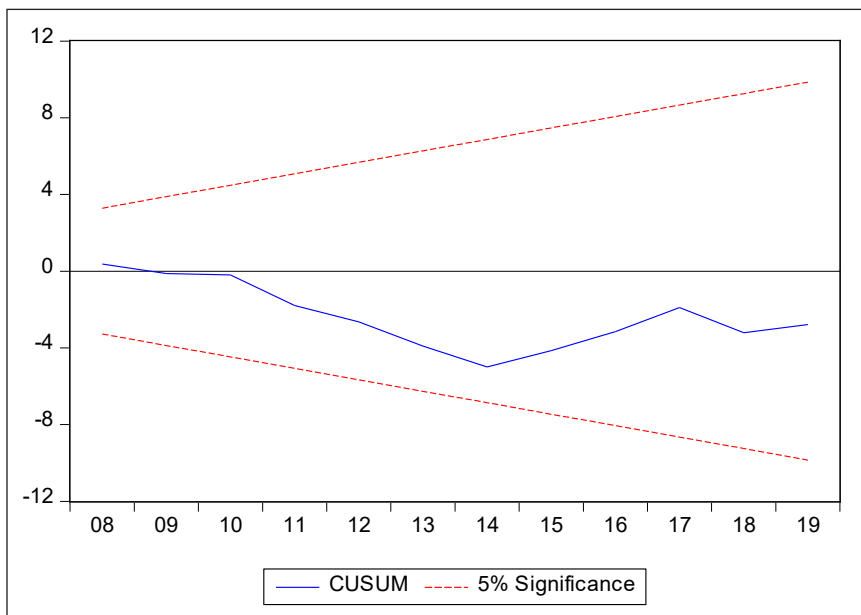


Figure 2. Model stability check using the Cumulative Sum (CUSUM) test

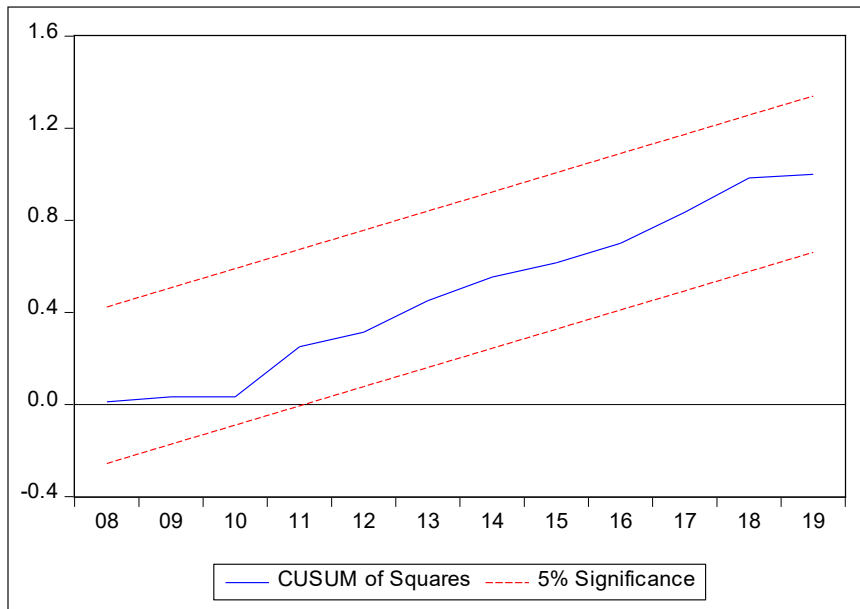


Figure 3. Model stability check using the Cumulative Sum (CUSUM) square test

## CONCLUSION

All around the world, tourism is regarded as a “sunshine” industry. However, in terms of job generation, foreign exchange profits and national revenue have remained a small contributor to the region’s national economy. As a result, tourism has failed to contribute much to poverty reduction in Bangladesh, even though it is a critical need in its economy. This article examines the dynamics of crude oil prices, inflation, the exchange rate, trade balance, institutional quality, and tourist arrivals in Bangladesh using annual data from 1995 to 2019. This study investigated asymmetric impacts in the long and short run using a nonlinear ARDL approach. In both the long and short terms, the findings of this study reveal that the factors analyzed have asymmetric impacts. Rising oil prices have a significant negative impact on tourist arrivals, according to long-run nonlinear results, whereas lowering oil prices has a considerable positive impact, according to the findings. Furthermore, the inflation, the exchange rate, institutional quality, and the trade balance all have a significant non-linear impact on tourism in Bangladesh.

It has been discovered that adopting a linear symmetric model to forecast Bangladesh’s tourism demand could be deceiving. Tourism demand can be better understood using a nonlinear ARDL technique, which can help with forecasting and policymaking by interpreting tourist demand and several macroeconomic determinants that have nonlinear dynamics. Future research that uses an asymmetric framework and panel studies to explore additional macroeconomic variables will be the most suited.

## ACKNOWLEDGEMENT

The author is thankful to Miyan Research Institute, International University of Business Agriculture, and Technology (IUBAT).

## REFERENCES

- Abdlaziz, R. A., Rahim, K. A., & Adamu, P. (2016). Oil and food prices co-integration nexus for Indonesia: A non-linear autoregressive distributed lag analysis. *International Journal of Energy Economics and Policy*, 6(1), 82-87.
- Achyar, D. H., & Hakim, D. B. (2021). Cointegration analysis of tourism sector, inflation, interest rate and economic growth in a special autonomy region of Aceh Province, Indonesia. *International Journal of Scientific Research in Science, Engineering and Technology*, 8(1), 216-221. <https://doi.org/10.32628/IJSRSET218144>
- Agiomirgianakis, G., Serenis, D., & Tsounis, N. (2015). Effects of exchange rate volatility on tourist flows into Iceland. *Procedia Economics and Finance*, 24, 25-34. <https://doi.org/10.1504/IJTP.2015.075128>
- Al-Mulali, U., Gholipour, H. F., & Al-hajj, E. (2020). The nonlinear effects of oil prices on tourism arrivals in Malaysia. *Current Issues in Tourism*, 23(8), 942-946. <https://doi.org/10.1080/13683500.2019.1586844>
- Anorou, E., & Elike, U. (2009). An empirical investigation into the impact of high oil prices on economic growth of oil-importing African countries. *International Journal of Economic Perspectives*, 3(2), 121-129.
- Anoruo, E. (2011). Testing for linear and nonlinear causality between crude oil price changes and stock market returns. *International Journal of Economic Sciences and Applied Research*, 4(3), 75-92.
- Bahmani-Oskooee, M., & Bohl, M. T. (2000). German monetary unification and the stability of the German M3 money demand function. *Economics Letters*, 66(2), 203-208. [https://doi.org/10.1016/S0165-1765\(99\)00223-2](https://doi.org/10.1016/S0165-1765(99)00223-2)
- Balcilar, M., Van Eyden, R., Inglesi-Lotz, R., & Gupta, R. (2014). Time-varying linkages between tourism receipts and economic growth in South Africa. *Applied Economics*, 46(36), 4381-4398. <https://doi.org/10.1080/00036846.2014.957445>
- Becken, S. (2008). Developing indicators for managing tourism in the face of peak oil. *Tourism Management*, 29(4), 695-705. <https://doi.org/10.1016/j.tourman.2007.07.012>
- Becken, S., & Lennox, J. (2012). Implications of a long-term increase in oil prices for tourism. *Tourism Management*, 33(1), 133-142. <https://doi.org/10.1016/j.tourman.2011.02.012>
- Brown, R. L., Durbin, J., & Evans, J. M. (1975). Techniques for testing the constancy of regression relationships over time. *Journal of the Royal Statistical Society: Series B (Methodological)*, 37(2), 149-163. <https://doi.org/10.1111/j.2517-6161.1975.tb01532.x>
- Cheng, K. M. (2012). Tourism demand in Hong Kong: Income, prices, and visa restrictions. *Current Issues in Tourism*, 15(3), 167-181. <https://doi.org/10.1080/13683500.2011.569011>
- Dincer, M. Z., Dincer, F. I., & Ustaoglu, M. (2015). Reel effective exchange rate volatilities impact on tourism sector in Turkey: An empirical analysis of 2003-2014. *Procedia Economics and Finance*, 23, 1000-1008. [https://doi.org/10.1016/S2212-5671\(15\)00352-4](https://doi.org/10.1016/S2212-5671(15)00352-4)

- Farmaki, A., Altinay, L., Botterill, D., & Hilke, S. (2015). Politics and sustainable tourism: The case of Cyprus. *Tourism Management*, 47, 178-190. <https://doi.org/10.1016/j.tourman.2014.09.019>
- Ghalia, T., Fidrmuc, J., Samargandi, N., & Sohag, K. (2019). Institutional quality, political risk and tourism. *Tourism Management Perspectives*, 32, Article 100576. <https://doi.org/10.1016/j.tmp.2019.100576>
- Gokmenoglu, K. K., Bekun, F. V., & Taspinar, N. (2016). Impact of oil dependency on agricultural development in Nigeria. *International Journal of Economic Perspectives*, 10(2), 151-163.
- Görmüş, Ş., & Göçer, İ. (2010). The socio-economic determinant of tourism demand in Turkey: A panel data approach. *International Research Journal of Finance and Economics*, 55(1), 88-99.
- Habibi, F. (2017). The determinants of inbound tourism to Malaysia: A panel data analysis. *Current Issues in Tourism*, 20(9), 909-930. <https://doi.org/10.1080/13683500.2016.1145630>
- Hamilton, J. M., & Tol, R. S. (2007). The impact of climate change on tourism in Germany, the UK and Ireland: A simulation study. *Regional Environmental Change*, 7(3), 161-172. <https://doi.org/10.1007/s10113-007-0036-2>
- Hanafiah, M. H. M., & Harun, M. F. M. (2010). Tourism demand in Malaysia: A cross-sectional pool time-series analysis. *International Journal of Trade, Economics and Finance*, 1(1), 80-83.
- Haseeb, M., & Azam, M. (2021). Dynamic nexus among tourism, corruption, democracy and environmental degradation: A panel data investigation. *Environment, Development and Sustainability*, 23(4), 5557-5575. <https://doi.org/10.1007/s10668-020-00832-9>
- Ibrahim, M. H. (2015). Oil and food prices in Malaysia: A nonlinear ARDL analysis. *Agricultural and Food Economics*, 3(1), 1-14. <https://doi.org/10.1186/s40100-014-0020-3>.
- Islam, M. S. (2015). Study on factors influencing tourism: Way forward for sustainable tourism in Bangladesh. *Journal of Tourism, Hospitality and Sports*, 6, 1-13.
- Jalil, A., Mahmood, T., & Idrees, M. (2013). Tourism-growth nexus in Pakistan: Evidence from ARDL bounds tests. *Economic Modelling*, 35, 185-191. <https://doi.org/10.1016/j.econmod.2013.06.034>
- Katrakilidis, C., & Trachanas, E. (2012). What drives housing price dynamics in Greece: New evidence from asymmetric ARDL cointegration. *Economic Modelling*, 29(4), 1064-1069. <https://doi.org/10.1016/j.econmod.2012.03.029>
- Khan, M. A., Popp, J., Talib, M. N. A., Lakner, Z., Khan, M. A., & Oláh, J. (2020). Asymmetric impact of institutional quality on tourism inflows among selected Asian Pacific countries. *Sustainability*, 12(3), Article 1223. <https://doi.org/10.3390/su12031223>
- Kim, Y. R., Saha, S., Vertinsky, I., & Park, C. (2018). The impact of national institutional quality on international tourism inflows: A cross-country evidence. *Tourism Analysis*, 23(4), 533-551. <https://doi.org/10.3727/108354218X15391984820503>
- Kisswani, K. M., & Harraf, A. (2021). Asymmetric impact of oil price shocks on tourism: Evidence from selected MENA countries. In M. S. B. Ali (Ed.), *Economic Development in the MENA Region: New Perspectives* (pp. 45-63). Springer. [https://doi.org/10.1007/978-3-030-66380-3\\_4](https://doi.org/10.1007/978-3-030-66380-3_4)



- Kisswani, K. M., Zaitouni, M., & Moufakkir, O. (2020). An examination of the asymmetric effect of oil prices on tourism receipts. *Current Issues in Tourism*, 23(4), 500-522. <https://doi.org/10.1080/13683500.2019.1629578>
- Lacheheb, M., & Sirag, A. (2019). Oil price and inflation in Algeria: A nonlinear ARDL approach. *The Quarterly Review of Economics and Finance*, 73(C), 217-222. <https://doi.org/10.1016/j.qref.2018.12.003>.
- Lee, H. S., Lee, S. Y., & Har, W. M. (2020). Roles of institutional quality on the relationship between tourism and economic development in Malaysia. *Journal of Environmental Treatment Techniques*, 8(1), 119-124.
- Liang, C. C., Troy, C., & Rouyer, E. (2020). US uncertainty and Asian stock prices: Evidence from the asymmetric NARDL model. *The North American Journal of Economics and Finance*, 51, Article 101046. <https://doi.org/10.1016/j.najef.2019.101046>
- Liu, A., & Pratt, S. (2017). Tourism's vulnerability and resilience to terrorism. *Tourism Management*, 60, 404-417. <https://doi.org/10.1016/j.tourman.2017.01.001>
- Meo, M. S., Chowdhury, M. A. F., Shaikh, G. M., Ali, M., & Sheikh, S. M. (2018). Asymmetric impact of oil prices, exchange rate, and inflation on tourism demand in Pakistan: New evidence from nonlinear ARDL. *Asia Pacific Journal of Tourism Research*, 23(4), 408-422. <https://doi.org/10.1080/10941665.2018.1445652>
- Mondal, M., & Haque, S. (2017). SWOT analysis and strategies to develop sustainable tourism in Bangladesh. *UTMS Journal of Economics*, 8(2), 159-167.
- Mushtaq, R., Thoker, A. A., & Bhat, A. A. (2020). Does institutional quality affect tourism demand? Evidence from India. *Journal of Hospitality and Tourism Insights*, 4(5), 622-638. <https://doi.org/10.1108/JHTI-05-2020-0088>
- Naidu, S., Chand, A., & Pandaram, A. (2017). Exploring the nexus between urbanisation, inflation and tourism output: Empirical evidences from the Fiji Islands. *Asia Pacific Journal of Tourism Research*, 22(10), 1021-1037. <https://doi.org/10.1080/10941665.2017.1360923>
- Pektas, S. Y., & Unluonen, K. (2020). The evaluation of tourism in Turkey in terms of inflation. *Journal of Tourismology*, 6(1), 111-132. <https://doi.org/10.26650/jot.2020.6.1.0012>
- Pesaran, M. H., Shin, Y., & Smith, R. J. (2001). Bounds testing approaches to the analysis of level relationships. *Journal of Applied Econometrics*, 16(3), 289-326. <https://doi.org/10.1002/jae.616>.
- Raza, N., Shahzad, S. J. H., Tiwari, A. K., & Shahbaz, M. (2016). Asymmetric impact of gold, oil prices and their volatilities on stock prices of emerging markets. *Resources Policy*, 49, 290-301. <https://doi.org/10.1016/j.resourpol.2016.06.011>
- Romilly, P., Song, H., & Liu, X. (2001). Car ownership and use in Britain: A comparison of the empirical results of alternative cointegration estimation methods and forecasts. *Applied Economics*, 33(14), 1803-1818. <https://doi.org/10.1080/00036840011021708>
- Sek, S. K. (2017). Impact of oil price changes on domestic price inflation at disaggregated levels: Evidence from linear and nonlinear ARDL modeling. *Energy*, 130, 204-217. <https://doi.org/10.1016/j.energy.2017.03.152>
- Shaari, M. S., Ahmad, T. S. T., & Razali, R. (2018). Tourism led-inflation: A case of Malaysia. In *MATEC Web of Conferences* (Vol. 150, p. 06026). EDP Sciences. <https://doi.org/10.1051/mateconf/201815006026>

- Shaeri, K., Adaoglu, C., & Katircioglu, S. T. (2016). Oil price risk exposure: A comparison of financial and non-financial subsectors. *Energy, 109*, 712-723. <https://doi.org/10.1016/j.energy.2016.05.028>
- Sharma, C., & Pal, D. (2020). Exchange rate volatility and tourism demand in India: Unraveling the asymmetric relationship. *Journal of Travel Research, 59*(7), 1282-1297. <https://doi.org/10.1177/0047287519878516>
- Shin, Y., Yu, B., & Greenwood-Nimmo, M. (2014). Modelling asymmetric cointegration and dynamic multipliers in a nonlinear ARDL framework. In R. C. Sickles & W. C. Horrace (Eds.), *Festschrift in Honor of Peter Schmidt* (pp. 281-314). Springer. [https://doi.org/10.1007/978-1-4899-8008-3\\_9](https://doi.org/10.1007/978-1-4899-8008-3_9)
- Tang, C. F., & Abosedra, S. (2014). The impacts of tourism, energy consumption and political instability on economic growth in the MENA countries. *Energy Policy, 68*, 458-464. <https://doi.org/10.1016/j.enpol.2014.01.004>
- Tang, J., Sriboonchitta, S., Ramos, V., & Wong, W. K. (2016). Modelling dependence between tourism demand and exchange rate using the copula-based GARCH model. *Current Issues in Tourism, 19*(9), 876-894. <https://doi.org/10.1080/13683500.2014.932336>
- Toh, R. S., Khan, H., & Goh, L. (2006). Japanese demand for tourism in Singapore: A cointegration approach. *Tourism Analysis, 10*(4), 369-375. <https://doi.org/10.3727/108354206776162831>
- Usman, O., Elsalih, O., & Koshadh, O. (2020). Environmental performance and tourism development in EU-28 Countries: The role of institutional quality. *Current Issues in Tourism, 23*(17), 2103-2108. <https://doi.org/10.1080/13683500.2019.1635092>
- Vita, G. D., & Kyaw, K. S. (2013). Role of the exchange rate in tourism demand. *Annals of Tourism Research, 43*, 624-627. [10.1016/j.annals.2013.07.011](https://doi.org/10.1016/j.annals.2013.07.011)
- Webber, A. G. (2001). Exchange rate volatility and cointegration in tourism demand. *Journal of Travel Research, 39*(4), 398-405. <https://doi.org/10.1177/004728750103900406>
- Yap, G. (2012). An examination of the effects of exchange rates on Australia's inbound tourism growth: A multivariate conditional volatility approach. *International Journal of Business Studies: A Publication of the Faculty of Business Administration, Edith Cowan University, 20*(1), 111-132.
- Yeoman, I., Brass, D., & McMahon-Beattie, U. (2007). Current issue in tourism: The authentic tourist. *Tourism Management, 28*(4), 1128-1138. <https://doi.org/10.1016/j.tourman.2006.09.012>

*Short communication*

## Reinvestigation on Assessing the Stability of Mullagulov Tested Steel Rods under Follower Forces

Jakkana Peter Praveen<sup>1\*</sup> and Boggarapu Nageswara Rao<sup>2</sup>

<sup>1</sup>Department of Mathematics, Koneru Lakshmaiah Education Foundation, deemed to be University, Vaddeswaram, Guntur-522 502, India

<sup>2</sup>Department of Mechanical Engineering, Koneru Lakshmaiah Education Foundation, deemed to be University, Vaddeswaram, Guntur-522 502, India

### ABSTRACT

Dynamic instability is an interesting topic in the mechanics of elastic structures. Though the subject has been formed by many analytical, numerical, and experimental investigations, it has many issues, as evidenced from the critical overview of Elishakoff. Furthermore, the controversial articles of Koiter and Sugiyama on unrealistic and realistic follower forces demand experimental verification. Mullagulov has proposed a device for creating the follower forces and tested steel rods under compression. This paper highlights the experimentation of Mullagulov and his observations briefly to examine the influence of material properties on the stability load estimations and to confirm the practical realization of follower forces.

*Keywords:* Beck column, coalescence frequency parameter, concentrated tangential load, critical load parameter

### INTRODUCTION

Elastic structures under non-conservative forces are subject to flutter or dynamical instability. Dissipation plays a fundamental

and destabilizing role in these structures. A large difference is noticed in critical load assuming the absence of dissipation and limit of vanishing dissipation ('the Ziegler paradox'). This subject finds importance in structural mechanics, physics, rotor dynamics, aeroelasticity, and fluid-structure interaction (Mirko, 2018). Space launch vehicles under aerodynamic (drag) forces are modeled as columns under compressive loads, whose structural integrity is assessed by performing an overall stability analysis for the flight conditions.

#### ARTICLE INFO

*Article history:*

Received: 31 July 2021

Accepted: 19 November 2021

Published: 04 January 2022

DOI: <https://doi.org/10.47836/pjst.30.1.44>

*E-mail addresses:*

[jpraveen17@kluniversity.in](mailto:jpraveen17@kluniversity.in) (Jakkana Peter Praveen)

[bnrao52@rediffmail.com](mailto:bnrao52@rediffmail.com) (Boggarapu Nageswara Rao)

\* Corresponding author

The static and dynamic stability of systems loaded with follower forces has attracted many researchers to investigate and contribute. Von Beck has solved analytically the standard problem (namely, a cantilever column subjected to follower force) for the first time. Hence, the problem is referred to as the famous Beck column. Analytical, numerical, and experimental studies are made (after Beck in 1952) on a cantilever column with a tip-concentrated tangential or sub-tangential follower load (Anderson & Thomsen, 2002; Langthjem & Sugiyama, 2000a; Langthjem & Sugiyama, 2000b; Rao & Rao, 1989a; Rao & Rao, 1989b; Rao & Rao, 1990; Rao & Rao, 1991; Madhusudan et al., 2003; Zahharov et al., 2004; Kwasniewski, 2010; Mutyalarao et al., 2012). The controversial articles of Koiter (1996) and Sugiyama et al. (1999) on unrealistic and realistic follower forces remain a matter of debate (Mascolo, 2019).

Timoshenko and Gere (2012) have emphasized experimental validation. Sugiyama et al. (2000), Sugiyama (2002), and Sugiyama et al. (2019) have performed experiments on cantilever columns under a tip-concentrated sub-tangential follower force by mounting a solid rocket motor at free-end. They have demonstrated the stabilization of the system due to rocket thrust. However, their test results cannot be utilized directly to compare critical load estimates (Mutyalarao et al., 2017). Tomski and Uzny (2008) have examined a slender system with force directed toward the positive pole, which falls under the conservative load category. They have also considered a non-conservative load case, in which Beck's load is generated through a reaction engine.

Willems (1966) has adopted a simple procedure and performed experiments. Though the configuration has a critical load close to Beck's problem, theoretical analysis of Huang et al. (1967) and discussion of Augusti et al. (1967) have concluded that Willems test results are not representing the Beck column. Praveen et al. (2021) have revisited the critical load assessment of Huang et al. (1967) and corrected the error in the computed values and confirmed the adequacy of Willems's (1966) approach on the Beck column. Xiong et al. (1989) have considered a centripetally loaded model and simulated Beck's column showing equivalence of the first and second modes individually, whereas Praveen et al. (2020) have demonstrated the equivalence of the first and second modes directly from the dynamic characteristics of the Beck column. The discrepancy in the test data and the dynamic analysis results can be due to assigned values of Young's modulus and density of the material. Praveen et al. (2020) commented on the analysis of Xiong et al. (1989) that there is no necessity to modify the characteristic equation of the Beck column to match the test data. Xiong et al. (1989) have not conducted experiments up to the initiation of instability.

Mullagulov (1994) has made an interesting experimental-theoretical study on the stability of rods compressed by follower forces. This paper briefly presents the critical load evaluation of Beck column, Mullagulov experimentation, and his observations to examine

the influence of material properties on the stability load estimates and confirm follower forces' practical realization.

## METHODS

### Critical Load Evaluation of Beck Column

Based on the moment-curvature relationship, Mutyalarao et al. (2017) have employed a system of non-linear ordinary differential equations assuming harmonic motion to investigate cantilever columns' stability under a sub-tangential follower force. Figure 1 depicts the tip-angle  $\phi(0)$  and a follower force  $P$  with load rotation (or sub-tangential) parameter  $\beta$ . OB and OCA are the un-deformed and deformed positions. The column length is  $L$ .  $(X_a, Y_a)$ , are the tip-coordinates and  $(u, v) = (X - L + s, Y)$ , are the deflections. The angle  $\phi(s)$  is between the tangent to the bent axis and the vertical. Deflection curve length ( $s$ ) of the column is from its tip. The load rotation parameter,  $\beta = 0$  represents the Euler's column, in which  $P$  acts in vertical direction, whereas,  $\beta = 1$  represents the Beck's column, in which  $P$  acts as a tangential force.

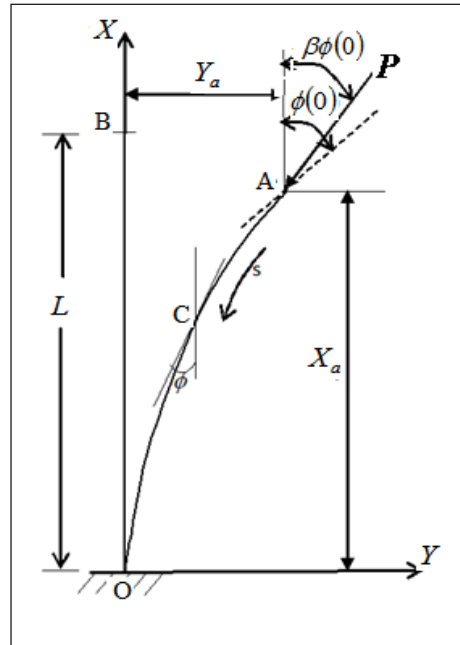


Figure 1. Cantilever column under a tip-concentrated sub-tangential follower force

Mutyalarao et al. (2017) have defined  $x = \frac{X}{L}$ ;  $y = \frac{Y}{L}$ ;  $\eta = \frac{s}{L}$ ; load parameter,  $\lambda = \frac{PL^2}{EI}$ ; frequency parameter,  $\omega = \Omega L^2 \sqrt{\frac{m}{E}}$  and presented the nonlinear differential Equations 1-5 in non-dimensional form as

$$\phi'' + \lambda \sin(\phi - \beta\phi(0)) + \omega^2 (H \sin \phi + V \cos \phi) = 0 \tag{1}$$

$$H' - (1 - \eta - x) = 0, \tag{2}$$

$$V' - y = 0, \tag{3}$$

$$x' + \cos \phi = 0, \tag{4}$$

$$y' + \sin \phi = 0, \tag{5}$$

Here prime denotes differentiation with respect to  $\eta$ .  $m$ , is the mass per unit length of the column.  $\Omega$ , is the circular frequency.  $E$ , is the Young's modulus and  $I$ , is the moment of inertia. The second, third and fourth terms in Equation 1 are due the bending moments produced by the tip –concentrated sub tangential follower load the action of inertia forces. The boundary conditions for Equations 1-5 are as below (Equations 6-7)

$$\phi = \phi(0), \phi' = H = V = 0 \quad \text{at } \eta = 0 \tag{6}$$

$$\phi = x = y = 0 \quad \text{at } \eta = 1 \tag{7}$$

For the case of small deflections ( $\phi \rightarrow 0$ ), replacing  $\frac{\phi}{\phi(0)}$  as  $\tilde{\phi}$  and  $\frac{y}{\phi(0)}$  as  $\tilde{y}$ , the nonlinear ordinary differential Equations are reduced to (Equation 8)

$$\tilde{y}^{iv} + \lambda \tilde{y}'' - \omega^2 \tilde{y} = 0 \tag{8}$$

The boundary conditions are as in Equations 9-10

$$\tilde{y}' = -1, \tilde{y}'' = 0, \tilde{y}''' = \lambda(1 - \beta) \quad \text{at } \eta = 0 \tag{9}$$

$$\tilde{y} = \tilde{y}' = 0 \quad \text{at } \eta = 1 \tag{10}$$

The general solution of the Equation 8 is as stated in Equation 11

$$\tilde{y}(\eta) = A \cosh(\lambda_1 \eta) + B \sinh(\lambda_1 \eta) + C \cos(\lambda_2 \eta) + D \sin(\lambda_2 \eta) \tag{11}$$

$$\text{H e r e } A = -\frac{(B \sinh \lambda_1 + D \sin \lambda_2)}{(\cosh \lambda_1 + \lambda_1^2 \lambda_2^{-2} \cos \lambda_2)} ; B = \frac{\lambda(1 - \beta) - \lambda_2^2}{\lambda_1(\lambda_1^2 + \lambda_2^2)} ; C = \left(\frac{\lambda_1}{\lambda_2}\right)^2 A ;$$

$$D = -\frac{\lambda(1 - \beta) + \lambda_1^2}{\lambda_2(\lambda_1^2 + \lambda_2^2)} ; \lambda_1 = \sqrt{-0.5\lambda + \sqrt{\omega^2 + 0.25\lambda^2}} ; \text{ and } \lambda_2 = \sqrt{0.5\lambda + \sqrt{\omega^2 + 0.25\lambda^2}} .$$

The transcendental equation relating to load parameter ( $\lambda$ ) and the frequency parameter ( $\omega$ ) is of the form Equation 12

$$\beta\lambda^2 + 2\omega^2 + (\lambda^2(1 - \beta) + 2\omega^2)(\cosh \lambda_1 \cos \lambda_2) + (2\beta - 1)\lambda\omega \sinh \lambda_1 \sin \lambda_2 = 0 \tag{12}$$

Equation 12 is solved for  $\omega$  specifying  $\lambda$  and  $\beta$ . Figure 2 shows the variation of  $\omega$  with  $\lambda$  for different values of  $\beta$  ranging from 0 to 1 with an incremental step size of 0.1.

The Eigencurves of the column (namely, the load parameter ( $\lambda$ ) versus frequency parameter ( $\omega$ ) curves) indicate the stability of the equilibrium position of the column. Static stability loads are those at which the Eigencurve meets the load ( $\lambda$ ) axis. The dynamic stability loads are those at which two branches of Eigencurves coalesce. Static stability loads

are possible when the sub-tangential parameter  $\beta = \frac{1}{2}$ . For  $\beta = \frac{1}{2}$ , the first load-frequency curve touches the load axis and later it coalesces with the second Eigencurve of the column. For  $\frac{1}{2} < \beta < 1$ , the two branches of Eigencurves coalesce. From the Eigencurves in Figure 2, it is noticed that the transition of static and dynamic stability takes place at  $\beta = \frac{1}{2}$ . For Euler's column ( $\beta = 0$ ), the critical load parameter,  $\lambda_c = 2.4674$ , whereas,  $\lambda_c = 20.05$  and the coalescing frequency parameter,  $\omega_c = 11.01$  for Beck's column ( $\beta = 1$ ). These results are in good agreement with the numerical solutions (Mutyalarao et al., 2012).

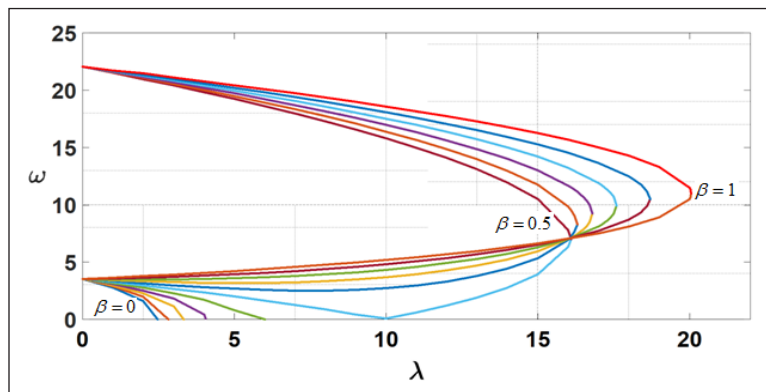


Figure 2. Variation of frequency parameter ( $\omega$ ) with load parameter ( $\lambda$ ) for different sub-tangential parameters ( $\beta$ ) ranging from 0 to 1 with an incremental step size of 0.1

## RESULTS AND DISCUSSION

### Mullagulov Experimentation on Creation of Follower Force

Figure 3 shows a schematic of Mullagulov (1994) stand to create the follower force for the rods through a propeller driven by a high-speed electric motor (having 2.6 kg weight; 1.47 kW power; and the rotational speed limiting to 6000 rpm).

The test rod is mounted horizontally on the stand base and installed with an electric motor (with a propeller). The electric motor is suspended on a ceiling wire to suppress the bending of the test rod from the motor weight. The influence of torque is eliminated by mounting a special carriage at the end of the test rod. The hardened and ground surfaces of the guides are lubricated with machine oil for making the free end of the rod displace freely in the horizontal plane without friction. A balancing device is provided to eliminate the influence of restoring forces (if any) due to the attachment of the electric motor to the test rod, keeping the same length of ceiling wire and the rocker-strut.

Gradual increasing of the electrical voltage increases the compressive follower force smoothly. When it reaches the critical value, oscillations of the test rod with increasing

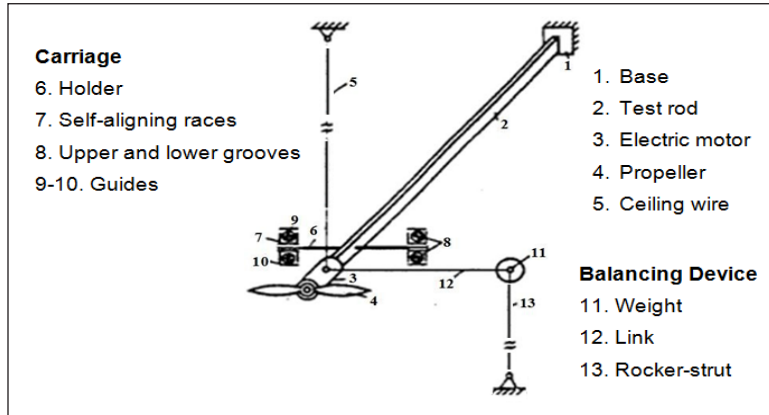


Figure 3. Schematic of stand for creating a follower force (Mullagulov, 1994)

amplitude begin spontaneously without any artificial disturbance. The stand is quite simple in design and fabrication and has no restriction on its operation time. The stability of the column is assessed from the load versus frequency curve (which is nothing but the Eigencurve). The dynamic stability load of a Beck column is the minimum load where two branches of Eigencurve coalesce. Analytical and numerical results on the Beck column are presented in dimensionless parameters. The load parameter ( $\lambda$ ) and the frequency parameter ( $\omega$ ) for the Beck column defined are as in Equation 13-14.

$$\lambda = \frac{PL^2}{EI} \tag{13}$$

$$\omega = \Omega L^2 \sqrt{\frac{m}{E}} \tag{14}$$

Here,  $E$  is the tip-concentrated follower load;  $E$  is the Young's modulus;  $I \left( = \frac{bd^3}{12} \right)$ , is the moment of inertia;  $L$  is the column length;  $b$  and  $d$  are column breadth and depth respectively;  $m$  is the mass per unit length of the column; and  $\Omega$  is the circular frequency. The critical load parameter ( $\lambda_c$ ) and the coalescing frequency parameter ( $\omega_c$ ) for the Beck column obtained are 20.05 and 11.01 respectively. The critical load ( $P_{cr}$ ) for the Beck column can be estimated from Equation 15.

$$P_{cr} = \frac{\lambda_c \times E \times I}{L^2} = 20.05 \times \frac{E \times I}{L^2} \tag{15}$$

It should be noted that the critical load parameter ( $\lambda_c$ ) arrived from the dynamic stability of a Beck column (A uniform cantilever column under a tip-concentrated follower load) is 20.05. The critical load ( $P_{cr}$ ) for the Beck column in Equation 15 is directly



proportional to the stiffness of the column ( $E$ ) and inversely proportional to the square of the column length ( $L^2$ ). Russian Professors/ Scientists have been performed experiments on cantilever hardened steel rods repeatedly in several years. The rods having constant rectangular cross- section with dimensions: Length,  $L = 1000$  mm; Width,  $b = 39.4$  mm; and Depth,  $d = 0.97$  mm. Young's modulus of the hardened steel varies from 190 to 210 GPa. Hence, the bending stiffness of the rod  $EI$  varies from 0.57 to 0.63 N-m<sup>2</sup>. Table 1 gives the critical load of the hardened steel cantilever rod subjected to a tip- concentrated follower force. For the variation of bending stiffness, the estimated range of the critical load ( $P_{cr}$ ) is from 11.43 to 12.63 N for the Beck column from Equation 15. The test results in Table 1 are within the expected range.

Table 1

*Experimental investigations of Russian Professors/Scientists on a cantilever hardened steel rod subjected to a tip-concentrated follower force*

Professor/Scientist	Critical load, $P_{cr}(N)$	
	Test (Mullagulov, 1994)	Estimated range (Eq.15)
K. G. Galimkhanov	12.0	
G. S. Shpire	11.8	
I. Kh. Khairullin	11.7	
M. I. Vil'danov	11.6	11.43 - 12.63
G. Batyrgareev	12.1	
M. Kh. Mullagulov	12.2	

Mullagulov (1994) performed experiments on hardened steel rods with different lengths and rectangular cross-sections to record the critical follower load. Table 2 presents the critical follower loads for the rod lengths varying from 0.7 to 1 m with a different moment of inertia (varying rectangular cross-section). For a constant stiffness of the column, the critical follower load ( $P_{cr}$ ) decreases with increasing column length. In the case of a fixed column length, the critical follower load ( $P_{cr}$ ) increases with increasing the stiffness of the column. The test results in Table 2 are found to be within the expected range.

Assuming all the hardened steel rods tested by Mullagulov (1994) are from the same batch, one test result is used to evaluate Young's modulus ( $E$ ). From Equation 15, one can find Young's modulus (Equation 16),

$$E = \frac{P_{cr} \times L^2}{\lambda_c \times I} = \frac{11.8 \times 1^2}{20.05 \times 3 \times 10^{-12}} = 1.96176 \times 10^{11} \text{ N/m}^2 \approx 196.2 \text{ GPa} \quad (16)$$

The Young's modulus of the hardened steel rods is worked out to be 196.2 GPa, which is within the variation of 190 to 210 GPa. The critical load estimates in Table 2 using Young's modulus value of 196.2 GPa are close to the test results (Mullagulov, 1994).

**Table 2**  
*Comparison of experimental and analytical flutter loads of rods having a constant rectangular cross-section with different lengths and bending stiffness*

Length, $L$ (m)	Flutter or Critical Load, $P_{cr}(N)$		
	Test	Present Analysis	
	(Mullagulov, 1994)	$E = 190 - 210 \text{ GPa}$	$E = 196.2 \text{ GPa}$
Moment of inertia, $I = 3 \times 10^{-12} \text{ m}^4$			
0.7	24.8	23.32 – 25.78	24.08
0.8	19.0	17.86 – 19.74	18.44
0.9	14.8	14.11 – 15.59	14.57
1.0	11.8	11.43 – 12.63	11.80
Moment of inertia, $I = 2.35 \times 10^{-12} \text{ m}^4$			
0.7	19.2	18.27 – 20.19	18.87
0.8	14.6	13.99 – 15.46	14.44
0.9	11.5	11.05 – 12.22	11.41
1.0	9.2	8.95 – 9.89	9.24
Moment of inertia, $I = 1.62 \times 10^{-12} \text{ m}^4$			
0.7	13.2	12.59 – 13.92	13.01
0.8	10.0	9.64 – 10.66	9.96
0.9	8.0	7.62 – 8.42	7.87
1.0	6.23	6.17 – 6.82	6.37

## CONCLUSION

Many researchers have made interesting investigations on the static and dynamic stabilities of the systems loaded with follower forces. Since the critical load of the Beck column (namely, a cantilever column subjected to a tip—concentrated tangential load) is found to be nearly eight times that of the classical Euler column, there is a demand for experimental validation. Willems (1966), Xiong et al. (1989), and Sugiyama et al. (2000) have been partially successful in performing the experiments.

Mullagulov (1994) successfully created the cantilever rod’s follower force and performed tests. This paper reinvestigates on the stability assessment of Mullagulaov tested steel rods under follower forces and the influence of material properties on the critical load evaluation of the Beck column. One of his test results is considered and evaluated Young’s modulus of the hardened steel as 196.2 GPa, which is used for critical load evaluation of other cantilever rods having different lengths and bending stiffness. Estimates of the critical load match well with test results. This study indicates the practical realization of follower forces through a simple design and fabrication involved in Mullagulov experimentation. It should be noted that the destabilizing effect due to damping cannot be expected in short-duration tests (Mutyalarao et al., 2017).

## ACKNOWLEDGEMENT

The authors wish to thank the reviewers and the Editor for their constructive criticisms to improve the paper's clarity in presentation.

## REFERENCES

- Anderson, S. B., & Thomsen, J. J. (2002). Post-critical behavior of Beck's column with a tip mass. *International Journal of Nonlinear Mechanics*, 37, 135-151. [https://doi.org/10.1016/S0020-7462\(00\)00102-5](https://doi.org/10.1016/S0020-7462(00)00102-5)
- Augusti, G., Roorda, J., Herrmann, G., & Levinson, M. (1967). Discussion: Experimental verification of the dynamic stability of a tangentially cantilever column. *Transactions of ASME Journal of Applied Mechanics*, 34, 523-524. <https://doi.org/10.1115/1.3607727>
- Beck, M. (1952). Die Knicklast des einseitig eingespannten, tangential gedrückten Stabes [The buckling load of the cantilevered, tangentially pressed bar]. *Zeitschrift für angewandte Mathematik und Physik ZAMP*, 3(3), 225-228. <https://doi.org/10.1007/BF02008828>
- Huang, N. C., Nachabar, W., & Nemat-Nasser, S. (1967). On Willems experimental verification of the critical load in Beck's problem. *Transactions of ASME Journal of Applied Mechanics*, 34, 243-245. <https://doi.org/10.1115/1.3607646>
- Koiter, W. T. (1996). Unrealistic follower forces. *Journal of Sound and Vibration*, 194(4), 636-638. <https://doi.org/10.1006/jsvi.1996.0383>
- Kwasniewski, L. (2010). Numerical verification of post-critical Beck's column behavior. *International Journal of Nonlinear Mechanics*, 45, 242-255. <https://doi.org/10.1016/j.ijnonlinmec.2009.11.007>
- Langthjem, M. A., & Sugiyama, Y. (2000a). Optimum design of cantilevered columns under the combined action of conservative and non-conservative loads, Part-I: The undamped case. *Computers and Structures*, 74, 385-398. [https://doi.org/10.1016/S0045-7949\(99\)00050-4](https://doi.org/10.1016/S0045-7949(99)00050-4)
- Langthjem, M. A., & Sugiyama, Y. (2000b). Dynamic stability of columns subjected to follower loads: A survey. *Journal of Sound and Vibration*, 238, 809-851. <https://doi.org/10.1006/jsvi.2000.3137>
- Sugiyama, Y., Langthjem, M. A., & Ryu, B. J. (1999). Realistic follower forces. *Journal of Sound and Vibration*, 225, 779-782. <https://doi.org/10.1006/jsvi.1998.2290>
- Madhusudan, B. P., Rajeev, V. R., & Rao, B. N. (2003). Post-buckling of cantilever columns having variable cross-section under a combined load. *International Journal of Non-linear Mechanics*, 38, 1513-1522. [https://doi.org/10.1016/S0020-7462\(02\)00086-0](https://doi.org/10.1016/S0020-7462(02)00086-0)
- Mascolo, I. (2019). Recent developments in the dynamic stability of elastic structures. *Frontiers in Applied Mathematics and Statistics*, 5, Article 516. <https://doi.org/10.3389/fams.2019.00051>
- Mirko, T. (2018). *Flutter instability in structural mechanics: Theory and experimental evidence* (PhD thesis). University of Trento, Italy.
- Mullagulov, M. K. (1994). Experimental-theoretical study of the stability of rods, compressed by follower forces. *Strength of Materials*, 26(6), 441-446. <https://doi.org/10.1007/BF02209415>

- Mutyalarao, M., Bharathi, D., & Rao, B. N. (2012). Dynamic stability of cantilever columns under a tip-concentrated sub tangential follower force. *Mathematics and Mechanics of Solids*, 18(5), 449-463. <https://doi.org/10.1177/1081286512442436>
- Mutyalarao, M., Bharathi, D., Narayana, K. L., & Rao, B. N. (2017). How valid are Sugiyama's experiments on follower forces? *International Journal of Non-linear Mechanics*, 93, 122-125. <https://doi.org/10.1016/j.ijnonlinmec.2014.12.007>
- Praveen, J. P., Rao, B. N., Harnath, Y., Rao, B. V., Narayana, C., & Mahaboob, B. (2021). Revisited the critical load assessment of Huang et al. on the Willems tested Beck column. *Pertanika Journal of Science and Technology*, 29(1), 251-262. <https://doi.org/10.47836/pjst.29.1.14>
- Praveen, J. P., Rao, B. N., Mahaboob, B., Rajaiah, M., Harnath, Y., & Narayana, C. (2020). On the simulation of Beck column through a simple Xiong-Wang-Tabarrok experimental model of centripetally loaded column. *International Journal of Emerging Trends in Engineering Research*, 8(9), 5100-5103. <https://doi.org/10.30534/ijeter/2020/35892020>
- Rao, B. N., & Rao, G.V. (1989a). Post-critical behaviour of a uniform cantilever column under a tip concentrated follower force. *Journal of Sound and Vibration*, 132,350-352. [https://doi.org/10.1016/0022-460X\(89\)90604-4](https://doi.org/10.1016/0022-460X(89)90604-4)
- Rao, B. N., & Rao, G. V. (1989b). Some studies on buckling and post- buckling of cantilever columns subjected to conservative or non conservative loads. *The Journal of the Aeronautical Society of India*, 41(2), 165-182.
- Rao, B. N., & Rao, G. V. (1990). Stability of tapered cantilever columns subjected to a tip concentrated sub tangential follower force. *Forschung Im Ingenieurwesen*, 56(3), 93-96. <https://doi.org/10.1007/BF02560974>
- Rao, B. N., & Rao, G. V. (1991). Post-critical behaviour of a tapered cantilever column subjected to a tip concentrated follower force. *ZAMM-Journal of Applied Mathematics and Mechanics/Zeitschrift für Angewandte Mathematik und Mechanik*, 71(11), 471-473. <https://doi.org/10.1002/zamm.19910711116>
- Sugiyama, Y. (2002). Experimental approach to non-conservative stability problems. In A. P. Seyranian & I. Elishakoff (Eds.), *Modern Problems of Structural Stability* (pp. 341-394). Springer. [https://doi.org/10.1007/978-3-7091-2560-1\\_7](https://doi.org/10.1007/978-3-7091-2560-1_7)
- Sugiyama, Y., Katayama, K., & Kiriya, K. (2000). Experimental verification of dynamic stability of vertical cantilever columns subjected to a sub tangential force. *Journal of Sound and Vibration*, 236(2), 193-207. <https://doi.org/10.1006/jsvi.1999.2969>
- Sugiyama, Y., Langthjem, M. A., & Katayama, K. (2019). *Dynamic stability of columns under non-conservative forces: Theory and experiments*. Springer International Publishing. [https://doi.org/10.1007/978-3-030-00572-6\\_2](https://doi.org/10.1007/978-3-030-00572-6_2)
- Timoshenko, S. P., & Gere, J. M. (2012). *Theory of elastic stability*. Tata McGraw-Hill Education Private Limited.
- Tomski, L., & Uzny, S. (2008). Free vibration and the stability of a geometrically nonlinear column loaded by a follower force directed towards the positive pole. *International Journal of Solids and Structures*, 45(1), 87-112. <https://doi.org/10.1016/j.ijsolstr.2007.07.011>

- Willems, N. (1966). Experimental verification of the dynamic stability of a tangentially loaded cantilever column. *Transactions of ASME Journal of Applied Mechanics*, 33, 460-461. <https://doi.org/10.1115/1.3625073>
- Xiong, Y., Wang, T. K., & Tabarok, B. (1989). On a centripetally loaded model simulating Beck's column. *International Journal of Solids and Structures*, 25(10), 1107-1113. [https://doi.org/10.1016/0020-7683\(89\)90070-X](https://doi.org/10.1016/0020-7683(89)90070-X)
- Zahharov, Y. V., Okhotkin, K. G., & Skorobogatov, A. D. (2004). Bending of bars under a follower load. *Journal of Applied Mechanics and Technical Physics*, 45, 756-763. <https://doi.org/10.1023/B:JAMT.0000037975.91152.01>



*Review Article*

## **A Review of Thermal Design for Buildings in Hot Climates**

**Sahar Najeeb Kharrufa\* and Firas Noori**

*Department of Architecture, Ajman University. University rd, Al Jurf, Ajman, UAE*

### **ABSTRACT**

Most of the developed world currently lives above the tropic of Cancer in cold climate regions. It follows that most of the top architectural firms are from the same countries, and most of their work is based on that experience. Experience that does not travel well to hotter countries. This paper is mainly concerned with the climates of the Middle East region, which are hot in summer and have mild or cold winters, and where the humidity ranges from dry to humid. It is a review of the factors, designs, and solutions that designers sometimes ignore, undervalue, or on the other hand, put too much weight on when working in such climates. An overview of thermal solutions is conducted, and a critique and suitability of each one for hotter climates are offered. Some of the solutions, which are thought to be helpful, have little benefit, especially traditional ones, which are not up to present-day standards and lifestyles. Others, such as courtyards, do more harm than good. A couple of case studies to evaluate houses with and without thermal measures showed improvements of 23-48%. The paper will evaluate architectural, cooling, and building design solutions according to suitability in dry and medium humidity, warm and hot countries.

*Keywords:* Buildings in hot climates, cooling loads, evaporative air conditioning, traditional building designs

### ARTICLE INFO

*Article history:*

Received: 4 August 2021

Accepted: 19 November 2021

Published: 10 January 2022

DOI: <https://doi.org/10.47836/pjst.30.1.45>

*E-mail addresses:*

[s.sulaiman@ajman.ac.ae](mailto:s.sulaiman@ajman.ac.ae) (Sahar Najeeb Kharrufa)

[f.noori@ajman.ac.ae](mailto:f.noori@ajman.ac.ae) (Firas Noori)

\*Corresponding author

ISSN: 0128-7680  
e-ISSN: 2231-8526

### **INTRODUCTION**

Many of the world's top architectural firms are from countries located in cold climates, such as Europe or America. Consequently, their designs for primarily hot regions, such as the Middle East or North African (MENA), are rooted in practices and conventions established in their home countries. It is sometimes difficult to fully

appreciate the differences. Designing for hotter climates is not just about knowing the solutions but also recognizing the priorities (Butera et al., 2014).

A considerable amount of work has been conducted on the various elements involved in designing for hot climates. Al-Homoud (2016) studied the “impact of building envelope thermal design on the effectiveness of thermal performance of buildings in hot climates” in the MENA region. The purpose was to evaluate its effectiveness numerically. Kharrufa (2008) and Derradji and Aiche (2014) studied the use of earth structures and basements. Both reached positive conclusions. However, below-ground spaces are not suitable for every application. Mushtaha and Helmy (2016) studied the effect of building form on thermal conditions in the Gulf city of Sharjah and suggested that it could reduce energy consumption by 10%. Fasi and Budaiwi (2015) was concerned with the contribution windows made to visual comfort and unsurprisingly recommended low energy types.

Evaporative cooling continues to attract attention due to its low energy consumption. Yang et al. (2019) studied the latest developments in this field and recommended several technologies to enhance their potential. Sajjad et al. (2021) conducted a comprehensive review of indirect coolers and concluded that they might be a viable alternative to vapor-compression cycle air conditioners.

Sustainability and energy saving regulations have been introduced in many MENA regions countries. For example, Alalouch et al. (2019) assessed the effect of new sustainability regulations on energy savings in the Gulf country of Oman and concluded that they save up to 48.2% of energy.

Rackes et al. (2016) simulated building parameters to evaluate thermal comfort. He recommended ceiling fans and night ventilation. Garde et al. (2011) made similar conclusions on a specifically built low energy building in La Reunion in the Indian Ocean. Such simple solutions are only sufficient when the weather is reasonably mild. Ceiling fans are one of the cheapest methods of achieving thermal comfort in terms of capital and energy consumption.

Traditional solutions have also been studied. Bagasi and Calautit (2020) investigated the effect of the Mshrabaiy in Jeddah and concluded that it is insufficient to provide thermal comfort even with some evaporative cooling involved. Wind catchers are a prominent feature in many traditional buildings in the middle east. Hedayat et al. (2015) measured their efficiency in a house in Yazd, Iran. They found that it had a significant effect ranging from 17-70%. However, their measurements were taken in the winter.

This paper will review the factors, and solutions that designers sometimes ignore, devalue, or on the other hand, put too much weight on. The emphasis will be on technologies related to designing for the hot, relatively dry areas of the MENA region. More specifically, hot areas require architectural intervention to make the buildings thermally comfortable. For a building design to be “suitable,” it should reduce energy consumption using solutions



relevant to the specific local conditions. The study will review and critique the options available to designers.

## **HOT AND COLD CLIMATE BUILDING DESIGN SIMILARITIES**

If the climate outside is uncomfortable thermally, and the interior requires artificial cooling or heating, many treatments are similar between cold and hot weather. In both cases, the building shell needs to protect the interior environment from the harsh outside. Good thermal insulation, limiting air infiltration, and thermally efficient windows, are recommended in both conditions (Hawkes & Forster, 2002).

## **MILDLY HOT WEATHER**

In warm seasons, the design and treatments vary according to how hot the weather is. If it is relatively mild, good ventilation and a ceiling fan are often sufficient. Ventilation increases the evaporation of human sweat, which cools the body resulting in improved thermal comfort (Nicol et al., 2012). In addition, designing for ventilation and air movement is cheap. The simplest solution, of course, is to use good window and opening designs. However, to ensure that good ventilation can be had at any time, adding a ceiling fan is a cheap, low-energy option and is the next solution to consider.

At the time of writing this paper, a ceiling fan costs in the region of \$60.00 online (Amazon, 2017) and does not use much electricity. Compared to a compressor air conditioner, the \$60.00 fan uses 50 Watt/hr while a small, single room, 12000 BTU air conditioner, needs 3500 Watt/hr (ASHRAE, 2009). Furthermore, a ceiling fan takes up no space and provides air movement for the whole room. Unlike a standing fan, for instance, which needs to rotate to do the same, and then only improves comfort for one part of the space at a time as it does so. It is also noisier, and the air movement is too strong for office work as it disturbs the paper lying around. Nevertheless, a ceiling fan is always a good option in hot weather, whatever the circumstances.

## **HOT WEATHER**

If the climate is hot enough to require air conditioning, then the picture changes considerably. Before solutions are considered, it must first be determined which hot weather is being dealt with, hot humid or hot dry. In all hot conditions, the effect of humidity is more of a concern than in cold climates. High humidity reduces sweat evaporation, reducing thermal comfort (Nicol et al., 2012).

## Hot Dry Weather

If the weather is hot and air conditioning is necessary, especially if the heat is not excessive, and the weather is relatively dry, an evaporative air conditioner can do a good job (Kharrufa & Adil, 2012a). Regrettably, the evaporative cooler is only suitable within certain conditions. Beyond that, a direct expansion compressor air conditioner must be employed.

Literature regarding evaporative coolers is abundant. A large portion of it is concerned with improving efficiency. Most attempt to achieve this is by modifying the wetting media. It is a layer that is moistened with water and whose evaporation leads to cooling. Some papers claim an efficiency of 80% or more (Saleem, 1986). Saleem (1986) tested various wetting media to raise it. He achieved gains of 87% by using honeycomb cardboard corrugated sheet layers (ibid).

The evaporative cooler has a well-deserved reputation as a “green” or “environmentally friendly” appliance. The fresh air it provides is cooled and filtered while using considerably less energy than a phase change compressor air conditioner (Meher et al., 2014; Cuce & Riffat, 2016). Unfortunately, it cannot be relied on to deliver a constant, thermally acceptable air stream. An evaporative cooler’s performance varies depending on climatic conditions, including temperature, relative humidity, and the unit’s efficiency. When the humidity rises, its cooling powers diminish. It is why it is not popular in humid coastal and tropical areas.

In hot, dry climates, the evaporative cooler can increase the gap between the ambient exterior temperature and the cooler’s output when it is hotter outside and the humidity is lower. It seems ideal for hot, dry climates if not for two inherent drawbacks that affect all evaporative systems and reduce thermal comfort.

1. The cooling unit’s output will carry along with it increased moisture.
2. When the outside temperature passes a certain threshold, the temperature difference between the outside and the cooler output air will not be sufficient, even in dry conditions.

Tests were conducted in dry weather on a commercial evaporative cooler, which can provide an output of 7600m<sup>3</sup>/h (4500cfm) and maximum cooling of 16kW (54000 BTU) during the summer of 2006. The results are shown in Table 1 (Kharrufa & Adil, 2012b).

Table 1 shows that while the temperatures were less than the low 30’s, the output air was quite good. When it exceeded the higher thirties, the comfort value results plummeted, as shown in Table 2. Based on residential thermal conditions, which were assumed to be (Ibid):

- Low residential human movement.
- Light summer clothing.
- Moderate ventilation of 0.5m/s.
- A radiant temperature is similar to the ambient.

Table 1

*Performance of evaporative cooler in Baghdad as recorded by Kharrufa. Average cooler efficiency was 67% (Kharrufa & Adil, 2012b)*

Exterior Ambient temp °C	Exterior RH	Outside air WB °C	Output air temp °C
24.9	58.2%	19.2	22.3
27	41%	18	23
32	32%	20	23.8
34.4	27.5%	20.7	25.3
37.5	23.6%	21.8	27
39.8	19.5%	22.1	28.5
3.5	16.2%	24	30.3
44.3	16.4%	23.8	31.3

Table 2

*Thermal comfort conditions from the evaporative cooler output are based on the figures from Table 1. PMV levels are based on ISO 7730-1993 (Kharrufa, & Adil, 2012a)*

Exterior ambient temp. °C	Interior ambient temp. °C	Interior RH	PMV	Dissatisfaction rates
37.5	27	74.8%	0.28	8%
39.8	28.5	73.4%	0.95	24%
44.3	31.3	70.7%	1.80	67%

Tables 1 and 2 show that even in dry weather, if the ambient temperature approaches the 40°C thresholds, the comfort figures start to deteriorate, and at 44°C, it becomes completely unsatisfactory.

By comparison, in the same conditions but without the evaporative cooling, when the outside temperature was 37.5°C, thermal measurements in the room revealed the interior at a very hot 39°C in the daytime (Kharrufa & Adil, 2012a). At this temperature, the PMV rating rises considerably to 4.4 even with a fan working, and the dissatisfaction rate rises to 99% (Ibid).

Comparing a compressor air-conditioner with an evaporative cooler reveals big differences between the two systems. A compressor unit with a capacity of 7kW (24000 BTU) output cooled air to a temperature of 14–16°C, while outside, it was 43°C. The conditioner also dehumidifies the air inside the room. This same unit required around 15 Amperes of electric current, the equivalent of around 3.3kW of electric power. The

evaporative cooler, which was used for the tests, required considerably less at only 2.1 Amps and 220V, which equals 0.45kW of electric power (Ibid).

Table 3

*Comparison of direct expansion compressor and evaporative air conditioners assuming similar airflow output (Kharrufa & Adil, 2012a)*

Cooler type	Flow cfm	Cooling kW	Outside temp°C	Output cooler air temp°C	Electric Power kW
Compressor	600	7	43	15	3.3
Evaporative	600	2	43	30.3	0.066

Finally, a comparison of compressor air conditioner performance relative to an evaporative cooler is provided in Table 3. The measurements of the output flow from the latter have been converted to match those of the direct expansion compressor AC. The data are for an ambient outside temperature of 43°C (Ibid).

The conclusion is that the evaporative cooler is much more energy-efficient and needs considerably less power but within limits. If the temperature or humidity is too high, it will not provide comfort. The only choice in such conditions is to use a direct expansion compressor air conditioner or an indirect evaporative cooler (Sajjad et al., 2021).

### **Excessively Hot Dry and Hot Humid Weather**

Once it is determined that neither ventilation nor an evaporative cooler is sufficient to provide thermal comfort, then direct expansion compressor air conditioners must be used. These use electrical compressors to forcefully induce a phase change in a suitable refrigerant (ASHRAE, 2009). The process can deliver the required cooling capacity, but on the downside, it consumes considerable energy. In many hot countries, such as those in the Middle East, the energy production of the country may use up to 80% of for air conditioning of buildings (DEWA, 2015; DEWA, 2018).

Air conditioning is necessary not just for human comfort but also to cool such facilities as data centers filled with heat-producing electronics, computer servers, and power amplifiers. It is also used to protect and store artwork (McQuiston et al., 2004).

Air conditioners circulate the air, usually through ducts, to the interior space. It improves both thermal comfort and indoor air quality. Electric compressor-based units can be found in many shapes and sizes. The smaller units will only cool a small bedroom and are light enough to be carried by a single person. The larger ones can be massive and installed in dedicated spaces to cool entire buildings (Ibid.).

Considering how much energy this type of air conditioning consumes, as shown in Table 3, it becomes imperative that the designer use all means available to reduce the cooling load. Many of these are similar to treatments in colder weather and include (Hawkes & Forster, 2002):

- a. Add insulation.
- b. Use double glazing and e-energy efficient windows and doors. UPVC windows in walls not facing sunlight are a good option.
- c. Add multiple heavy layers of interior curtains and shades.
- d. Protect against air infiltration

The following sections will review the relevant building parts particular to cooling and explain how each should be treated.

**Windows and Shading.** Windows and doors are sources of air infiltration, lower insulation values, and direct and indirect sunlight. Except for the latter, all the other factors should be treated the same as cold countries. Sunlight, on the other hand, is different and very important. While it has the same effect as in cold countries in that it results in heating the building, this is considered a positive contribution in these climates, and completely the opposite in hot ones. Therefore, the goal here must be to reduce direct and indirect sunlight, which contains significant thermal energy (McQuiston et al., 2004).

1. The best way to protect against direct sunlight is to use exterior shading. Various solutions are used. The following rules of thumb are popular (Arasteh et al., 2003; Lee et al., 2013).
2. North orientations require very little protection and are preferable in the northern hemisphere.
3. South is second best as it is easy to shield using horizontal cantilevers or sunshades.
4. East and West are very difficult to protect completely, but vertical or combined vertical and horizontal sun breakers are preferable. It is difficult to protect windows in these two orientations fully, so it remains the designer's choice to best shade them.

The north and south conditions are reversed in the bottom half of the globe, south of the equator. The south becomes best followed by the north.

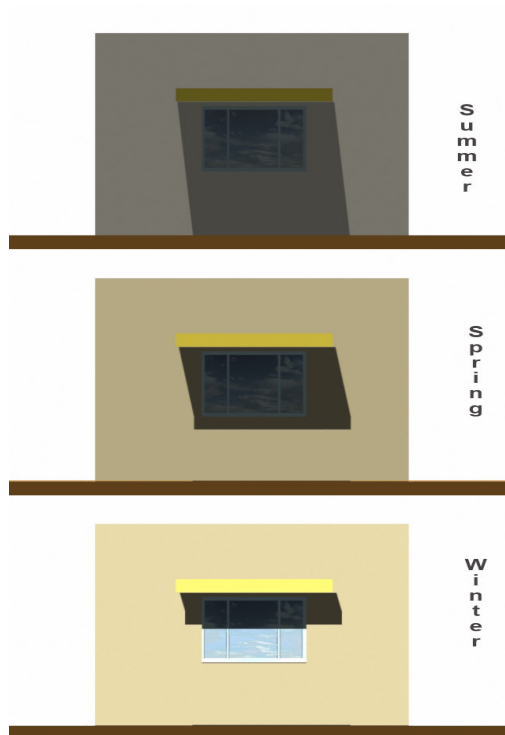


Figure 1. Sunshade from a cantilever protruding 1m and facing south, during the four seasons at 12:00 noon. The geographic position is 25°N. Spring and Fall are the same in terms of shading (Author's images)

The south orientation is especially advantageous as the sun is less intense during the summer and more during the winter. This is due to the earth's tilt and movement around the sun. Figure 1 shows how a cantilever above a window facing south in the northern hemisphere can protect it from sun rays during the four seasons.

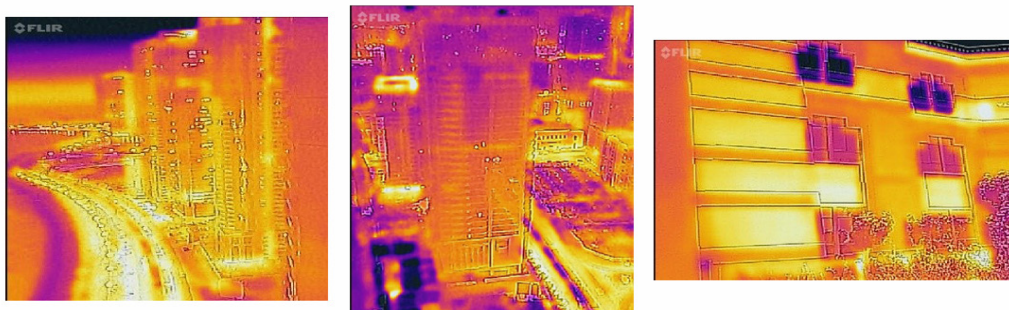


Figure 2. Thermal image of several occupied buildings. Brighter yellow indicates hot, magenta, then blue indicates colder. Upper floors are clearly cooler (taken by the author, June 2016, Sharjah, UAE)

Even after protecting from direct sunlight, indirect or reflected sunlight can still have a considerable heating effect. A series of exterior, infrared thermal images in Figure 2 reveal that lower floors, closer to the ground, are always hot than upper floors, which receive less reflected light, even for three-story buildings. The brighter yellow colors are hotter, magenta then blue are colder. The images were taken in the UAE during June. Plant cover surrounding the buildings help (Kanaan et al., 2021).

**Drapes and Shutters.** Drapes, or any other internal shading devices, are usually less effective compared to exterior ones, as the heat will have already penetrated the glazing into the building. All interior shading devices, such as roller shades, Venetian blinds, and draperies provide less effective shading and thermal insulation. On the other hand, they offer easy operation by room occupants. Traditionally, internal shading devices have been primarily intended to provide a varying degree of privacy from the outside. Fortunately, they also reduce discomfort from radiation through the window. Curtains universally reduce sunlight and provide protection from glare (Bansal & Mathur, 2006; Ariosto et al., 2019). Adding layers of protection can improve insulation. The image in Figure 3 shows a window partially blacked out by a 7mm insulation board, thick dual-layer blinds, then a curtain covering both.



*Figure 3.* Window showing three layers of protection. 1. Insulation covering glass pane (the black surface behind the curtain and the blind) 2. Thick blinds, 3. Curtain (taken by the author, June 2016, Sharjah, UAE)



*Figure 4.* Exterior shutter from the inside. The strap on the right slides it up and down. The slits allow light in but close when the shutters are completely shut, thus improving insulation with the outside. (Taken by author June 2017, Amman, Jordan)

Exterior shutters, on the other hand, can be quite effective. They can be found in many shapes and forms. They cut off the sun before it enters the room and, depending on the type, they may provide some measure of insulation as well. For example, the shutters in

Figures 4 and 5 are outside the window but can be opened and shut from the inside, and they are sealed from the sides too, which improves their thermal performance.

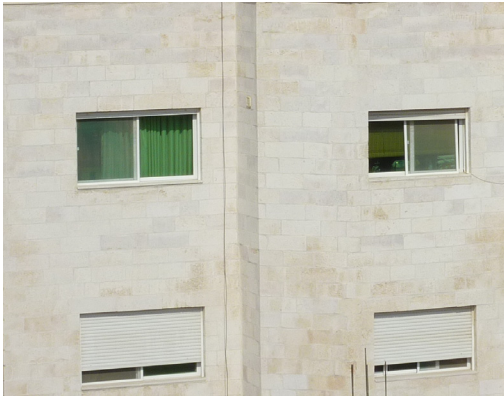


Figure 5. Exterior shutters from the outside. The two at the bottom are partially drawn close, similar to the one in Figure 5. (Picture taken by author June 2009, Amman, Jordan)

Many solutions for cold weather work in hot ones too. These include storm panels, sometimes called secondary glazing, and good drapes. When fitted with a quilt or other insulated backing, conventional draperies become thermal barriers. They will perform as operational insulation shutters located on the interior. They can be in hinged, sliding, folding, or bi-folding. It is important to provide some form of the airtight seal around the edges of any draperies, if possible, to improve its thermal performance and to prevent condensation (Bansal & Mathur, 2006; Buesing, 1981).

**Insulation.** Insulation is just as important in hot climates as cold with a slight change in priorities (Dylewski & Adamczyk, 2011; Kaynakli, 2012). While in cold areas, it is important to insulate the roof and ceiling to prevent the heat escaping by hot air gravitating upwards; the situation is reversed in hot ones. In an air-conditioned room with minimal air movement in a hot climate, the cold air will stay low. The heat transferred through the roof to the layer of air below the ceiling will be stuck close to the top of the room because the light hot air will float above the colder layer under it. That changes when air movement and ventilation are introduced, which is often the case. However, the effect remains relatively less than in cold countries. Insulating floors become important for the same reason. Heavy cold air descends downwards and needs to be protected thermally. That is not to say that insulating the roof is not necessary or important; it is. However, paying more attention to walls and windows reaps a better return for the investment.

**Green Roofs.** Much interest has been shown in green roofs recently. Seeing greenery on top of a roof gives many the impression that the building is “Green.” A green roof rarely becomes cold enough to act as a cooling element. It does, however, have quite a few benefits, as well as a few drawbacks (Vijayaraghavan, 2016). Thermally speaking, it is more useful in a hot climate than in a cold one. Regrettably, in many hot countries, such as those in the Middle East, the water necessary to irrigate the plants is not readily available. So, it is also necessary to find plants that can withstand the regional climate, which becomes even more difficult if it is dry and hot.



Briefly speaking, in hot countries, the pros and cons of a green roof are as follows (idib) (Del Barrio, 1998):

#### Benefits

- Some evaporative cooling
- Thermal mass keeps the interior temperature stable
- Absorb sunrays without much increase in mass temperature by plants, which reduces the heat island effect of the urban surroundings
- Pleasant psychological effect
- Reduced air pollution
- Easier to install since almost all roofs in these areas are horizontal.

#### Drawbacks

- Requires water and maintenance
- Heavy load on the structure
- Requires good waterproofing of the roof construction
- Occupy space on the roof

Roof ponds and roof cooling. Roof ponds can cool the envelope through evaporative cooling, radiant cooling, or through the effect of their heat mass (Kharrufa & Adil, 2008; Sharifi & Yamagata, 2015). In all these processes, the roof acts as a heat exchanger cooled mostly by surface evaporation. Infra-red radiation may also account for some cooling at night. Its thermal mass also functions as a heat sink absorbing the building's heat and keeping the temperature relatively steady. Because the ceiling is thermally coupled to the pond, the interior spaces are cooled by convection and a lower mean radiation temperature (MRT). Since the roof acts as a heat exchanger and is not in direct contact with the interior, roof pond evaporative cooling does not raise the humidity inside the building.

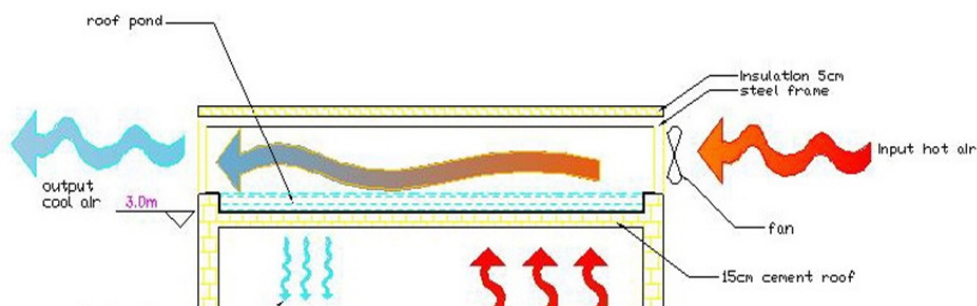


Figure 6. Roof pool with forced ventilation (courtesy of the author, Kharrufa & Adil, 2008)

Encouraging tests were done on a ventilated evaporative roof pond in the hot, dry climate of Baghdad (Kharrufa & Adil, 2008). A diagram of the system is shown in Figure 6. It shows a roof pond in a compartment above the roof with air movement forced mechanically. The results revealed that the pool installation alone, without a fan, lowered the average temperature inside by 3.36°C compared to a lone room with no means of cooling. Adding the fan to ventilate the pond dropped it a further 1.28°C for a final drop of 4.5°C. As a cooling solution, roof ponds are the least popular of all the solutions reviewed in this article.

**Double Skin Walls.** Double exterior curtain wall systems, or double skin facades, consist of an outer glazed skin surrounding the building. The inner wall is usually glazed, fully or partially. A large air gap between the two walls is left. The width of the gap and its ventilation are supposed to have a significant effect on the effectiveness of the envelope. The system often relies on air movement within the gap. Figure 7 shows how such a system may work. It can be natural, mechanical, or both. The outer wall can be either continued along the whole of the façade or interrupted every several floors (Boake et al., 2014).

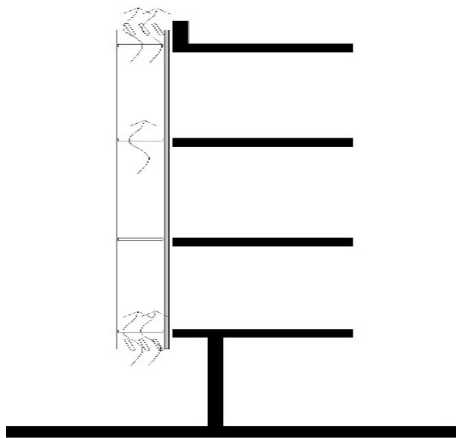


Figure 7. Cross-section of a double skin wall showing ventilation vents at the bottom and top (drawing by author)

Double skin walls were designed for office buildings to gain a wholly glazed facade in the hope that it would, at the same time, conserve heating energy. They were also touted as doing the same for cooling because of the ventilation between the two leaves of the wall. However, research and tests have not been able to verify such claims (Boake et al., 2014; Hashemi et al., 2010).

Boake et al. (2014) wrote that many independent research projects attempted to verify the case for or against this solution. He goes on to say, “*The results seem not to have been gathered into a definitive or conclusive text, meaning that “the jury is still out.”*” However, he goes on to say that

*“the construction of double façade envelope systems has continued to increase and persist in spite of the lack of conclusive hard data to prove the energy benefits”.*

In Iran, for instance, which has a hot arid climate in summer, the cavity walls facing the sun heat up because of the high ambient temperature and the solar incidence. Therefore, it naturally increases the cooling load requirements rather than vice-versa. As a result, it is essential to ventilate the cavity at nighttime to cool down the inner facade (Hashemi et al., 2010).

The Iranian measurements specifically show that in summer, throughout most of the day, the cavity temperature was up to 10°C more than the outside temperature. Shading the cavity has a positive effect on cooling, as might be expected, and reduces such differences (Hashemi et al., 2010).

**Exterior Colors and Surface Reflectivity.** Color has an enormous effect on the amount of heat absorbed and gained by any building. Dark colors reflect less solar energy falling on a surface and thus absorb more heat than light colors. Therefore, using light color paints, or reflective surfaces, in exterior walls and roofs in a hot climate can be considered an important passive strategy to reduce the amount of heat gained by building components and reduce the amount of heat penetrating inside. This strategy can also be used in moderate climates, as using light colors will help reduce the amount of unrequired heat gained during the hot season (Pal et al., 2020; Shi & Zhang, 2011).

Buildings with good insulation will be less affected by exterior color, while light color and reflective surfaces can be more effective when less, or no insulation, is used.

Both roof incline and color can have a combined effect on the process of heat gain. In a cold climate, for example, it is highly recommended to use dark, highly pitched roofs to gain more heat. A hot climate, on the other hand, requires the use of less slope (flat) roof with light color paint. Flat roofs absorb more heat only when the sun is at its highest point in the sky during summer mid-day. In the early morning or late afternoon, the sun will be very low, and a flat white roof will reflect most of the low-angle solar energy falling on it, reducing the amount of heat gain during the hot season (Pal et al., 2020).

**Geothermal Heat Pumps.** Geothermal heat pumps utilize the difference between the temperature above and below ground to improve air conditioning efficiency. The soil temperature near the ground surface is very close to the ambient temperature of the air above. On the other hand, the deeper we move underground, the fewer the temperature variations. It is because earth soil has a large thermal mass. It retains the heat for a longer period the deeper we go. At a depth of 6m, there will be little or no fluctuation, and a relatively steady state is reached. As a result, the soil temperature is almost the same during the whole year. It should be equivalent to the average annual air temperature in the area (Lechner, 2014). Figure 8 shows how depth affects temperature. At 6 meters, the fluctuation year-round is no more than  $\pm 3^{\circ}\text{C}$ . It varies, however, according to the type of earth, cover, and moisture content.

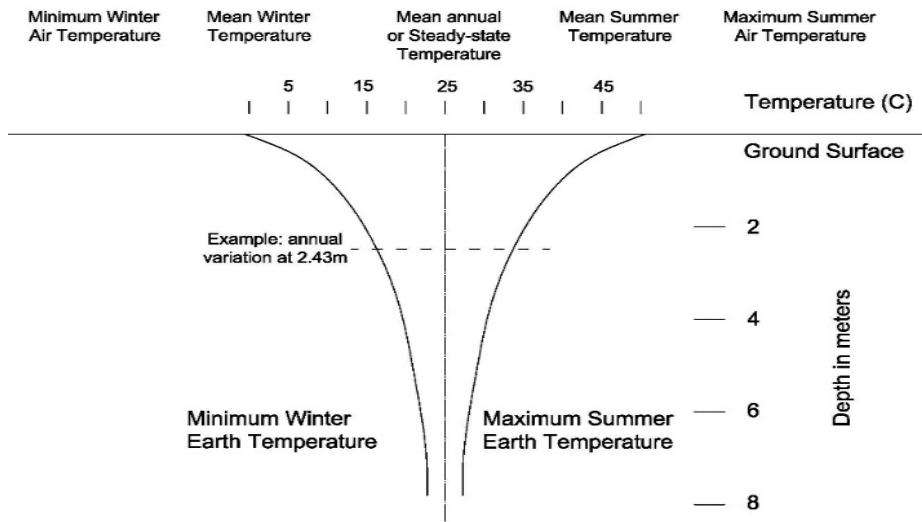


Figure 8. Graph showing the relationship between depth underground and ground temperatures. At 6 meters, the temperature is almost steady at the average yearly ambient temperature (Drawing by the author based on Williams & Gold, 1976)

Depending on the outside temperature and the efficiency of the particular unit, heat pumps can save from 30 to 60% on electric bills, depending on the geographical location and the equipment used (Lechner, 2014).

Earth cooling is efficient if the ground temperatures are cold in summer. However, this happens only if a wide temperature difference between seasons results in cold winters. In such cases, the ground temperature deep in the ground will be significantly less than the ambient temperature in summer and higher in winter.

Table 4 shows the example of two hot cities, Dubai and Baghdad (NCM, 2021; Central Statistics Organization, 2015). Dubai is hot in summer and has mild weather in winter. Baghdad, on the other hand, while also hot in summer, is cold in winter. Table 4 shows that the average yearly temperature, which should be close to the ground temperature deep in the ground, is 28.1°C in Dubai and 22.8°C in Baghdad. During August, the difference between the deep earth temperatures and ambient would be (36–28.1) 7.9°C in Dubai and (34.5–22.8) 11.7°C in Baghdad. A heat pump in summer would be more efficient in the latter, where it can benefit from the more significant temperature difference.

Heat pumps work through the use of heat exchangers in the ground to benefit from the lower temperature. Pipes will extend from the air conditioner compressor unit above ground to the underground heat exchangers. However, it costs money and exposes the equipment and installation to corrosion. In addition, ground temperatures need to be significantly lower than the ambient air temperature to make it feasible.

Table 4

*Monthly average temperatures in Dubai and Baghdad (NCM, 2021; Central Statistics Organization, 2015)*

Month	Dubai °C	Baghdad °C
Jan	19.3	10
Feb	20.6	12.5
Mar	23.2	15.5
Apr	27.2	22
May	31.4	28
Jun	33.6	32
Jul	35.7	34
Aug	36	34.5
Sep	33.4	30.5
Oct	30	25
Nov	25.4	18
Dec	21.3	11.5
Average	28.1	22.8

**Earth Structures.** Earth structures use the same principles as heat pumps. They use the thermal mass to stabilize the temperature. They help keep it close to the daily, or even yearly, average inside a building. Thus, earth sheltering provides a warmer environment in the winter and a cooler one in the summer (Derradji & Aiche, 2014; Kharrufa, 2008).

Light dry soil reaches a near-constant ground temperature at a shallower depth than heavy, damp soil. Earth sheltering can stabilize interior temperature swings during all seasons. Figure 9 shows comparative temperature readings in a building with a basement and no air conditioning. Its floor is 2 meters below ground level, and its ceiling is above ground by 1.5m. The basements' temperature is significantly lower than the ground floor, without climate control.

The graph in Figure 9 illustrates how the basement temperature was consistently lower than the average outside by around 5°C during the whole of the summer period. Considering that summer afternoon in central Baghdad can reach up to 50°C, the basement would be 17–18°C less than that. However, at 32–34°C, it is still not thermally comfortable.

Although the graph in Figure 9 shows some fluctuation in the basement's monthly readings, Figure 10 shows that it is stable throughout a single 24-hour day [ibid].

Basements are not for every region, nor are they a universal solution. However, it must be mentioned that in some places, they are ingrained in the local culture to ease the pain of hot summers. In many areas in Iraq, for instance, the residents would use the basement for the afternoon naps, thus avoiding the hottest times of the day (Akram et al., 2015).

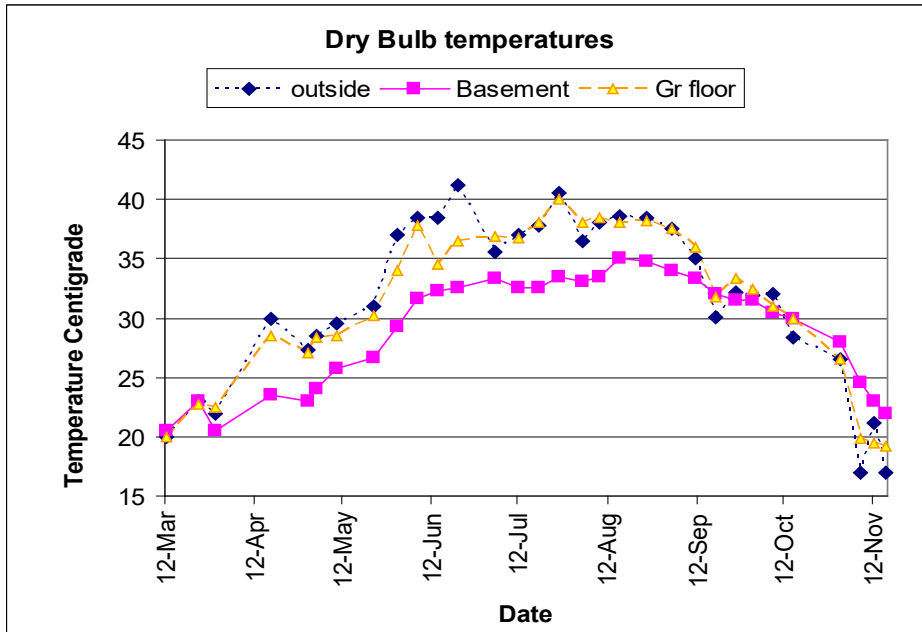


Figure 9. Monthly dry bulb temperature readings for the ambient, ground floor, and basement during the summer of 2006 in Baghdad (Courtesy of the author, Kharrufa, 2008).

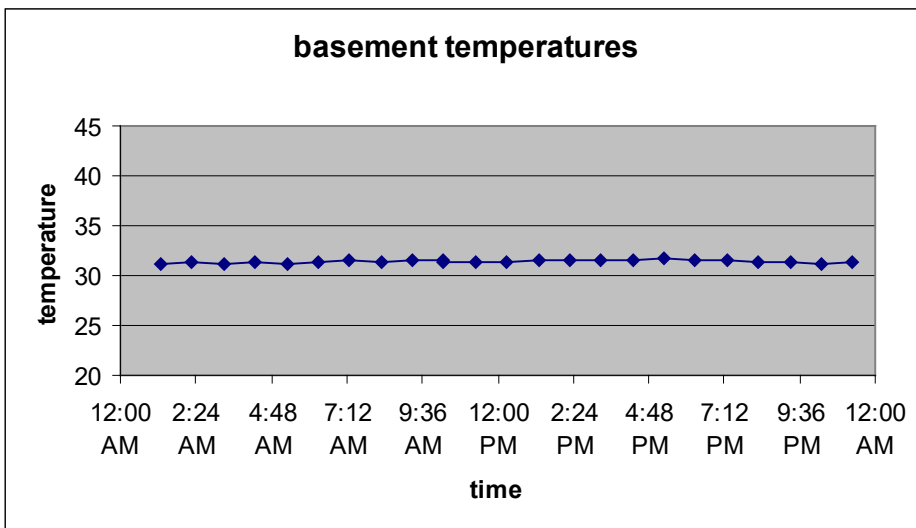


Figure 10. Basement temperature during a 24-hour in September shows a stable temperature reading (Courtesy of the author, Kharrufa, 2008).

**Evaporative Assisted Cooling.** It would be extremely useful if it were possible to use the energy efficiency of the evaporative cooler to supplement the cooling capability of the compressor air conditioner to configure a system that could combine the first's low energy requirements with the second's cooling prowess. Regrettably, these two cannot be used simultaneously to cool an interior space. The evaporative cooler requires that the air be expelled from the room. The compressor air conditioner re-cools return air. These are opposing and conflicting workflows.

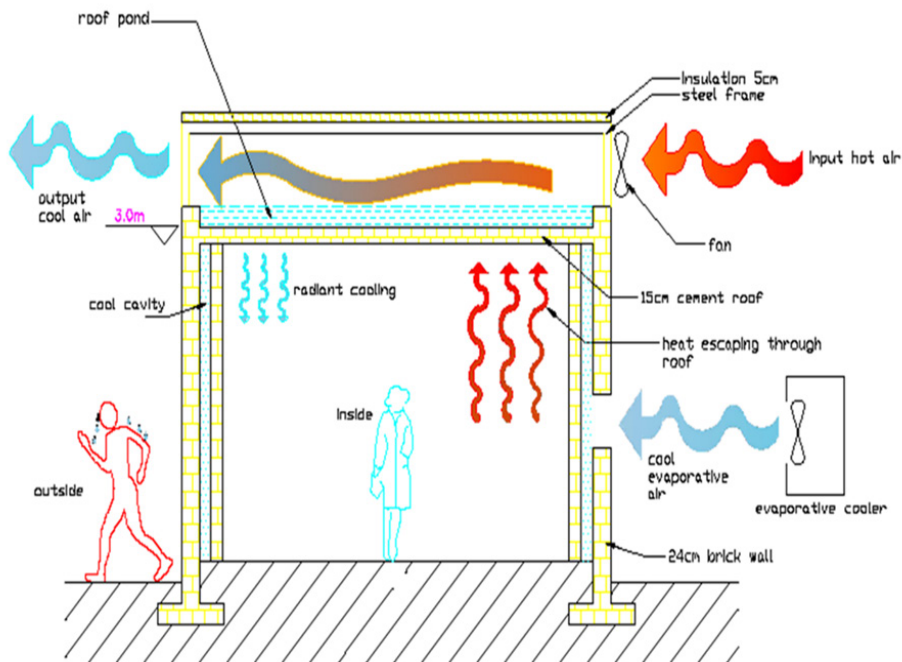


Figure 11. Diagram showing how the building structure can be cooled by evaporation (Courtesy of the author, Kharrufa & Adil, 2012a).

Several researchers have suggested using evaporative systems to cool the building envelope. One such system is shown in Figure 11. It uses evaporative conditioners and roof ponds to cool parts of the structure, not the interior. Compressor air conditioners can support it inside (Kharrufa & Adil, 2012a).

Cooling the walls uses a water spray or output from an evaporative cooler. The roof may be cooled by a pond, evaporative cooler, or a green roof. The results have been encouraging. In suitable conditions, savings of up to 80% of electric power have been calculated through simulation. These are results well worth further investigation (Ibid.).

The system does have some constraints. Primarily because it suffers from the same issues that plague all evaporative systems, it works better in dry climates, and its efficiency varies from region to region. Furthermore, conversion of existing buildings to such a system is difficult.

## MISCONCEPTIONS

Several misconceptions prevail in hot countries about using traditional methods for climate control that date back to pre-air-conditioning days. However, most of these are no longer suitable. The changes to how we conduct our daily routines and modern-day expectations render them obsolete. Often, they may even have an adverse effect.

### Courtyards

In many hot countries, and even cold ones, houses utilize an internal courtyard. Usually included for privacy, it was also part of the thermal solution. The whole house was arranged to be used as a system that relied on occupying certain areas during certain times of the day. These would sometimes include a basement or semi-basement, interior spaces, the roof, a garden, and the courtyard. The roof or the court would be slept on at night when it would be cold outside and hot inside. The courtyard or garden would be occupied in the early morning and evenings—the interior rooms and basements in the afternoons (Kharrufa, 2008). Figure 12 shows such a design. The picture is of the former residence of the ruler of Ajman in the UAE. The view is from the courtyard.



*Figure 12.* The courtyard of the ruler of Ajman's former residence. It is a traditional Emirati house that was occupied until the early eighties (picture taken by author August 2011, Ajman, UAE).



Modern-day life cannot accommodate such an arrangement. Furthermore, installing a courtyard becomes a thermal strain. Small houses add to the exterior surface area considerably and increases the heat transfer into the building.

### Windcatchers

These are special duct-type arrangements that can increase ventilation inside the building (Zarandi, 2009; Hedayat et al., 2015). Before the age of electricity, any design that encouraged ventilation was welcome.

However, during the hot summer months, an ordinary windcatcher introduces hot air from the outside. Figure 13 is of such a system. It is an Emirati windcatcher. Its main purpose is purely ventilation.



Figure 13. Emirati windcatcher (picture taken by the author, October 2009, Dubai, UAE).

More articulate forms of catchers exist. Some will utilize the cooler building mass surrounding it during the day to cool the air that slowly filters down, as shown in Figure 14. This catcher is common in the southern areas of Iraq and Iran. It is designed to face the cooler northern breeze. In addition, a small fountain or porous clay water pitcher is often put at the bottom to cool the air further. Nevertheless, the introduced temperatures remain relatively high by present-day standards and are not suitable for modern-day comfort.

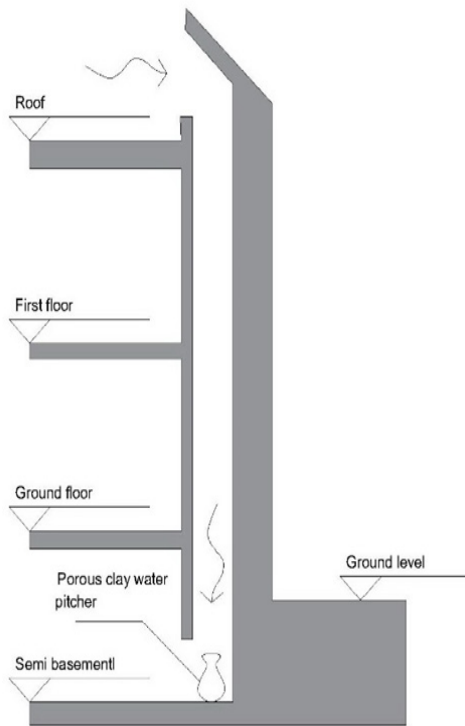


Figure 14. Cross-section of wind tower cooled by building mass (drawing by author).

### Building Mass

Thick 50-80cm walls were the rule rather than the exception before modern construction methods (Kharrufa, 2008). Introduced because of their mass, these benefitted from performing like earth structures. They tended to keep the interior temperatures close to the daily average and delay the heat transfer through the structure. This time lag results in daytime temperatures inside that are lower than the outside, but nighttime and mornings would be higher.

This system is also not suitable for modern-day architecture. Notwithstanding the extra cost and weight of using so much material, the heavy building mass requires considerable energy to cool. It increases the cooling load rather than the other way around.

### BUILDING REGULATIONS AND GUIDELINES

The building guidelines in the countries of the MENA region vary from one to the other. The countries of the Gulf have been more diligent in proposing and implementing thermal and sustainability guidelines. Dubai issued its first decree for thermal insulation in 2003 and followed it by comprehensive green building regulations, 2013 (Dubai Municipality, 2021). These include guidelines for shading and glazing to wall ratio. Other Gulf states followed. In many other countries of the region, no such rules apply (Al-Taie et al., 2014).

The setback rules also vary and significantly affect both the design and thermal transmission. For instance, in both Jordan and the Gulf, most buildings are required to have a three-meter setback on all sides, although the front is sometimes exempt. In Iraq, it is the exact opposite. There are no setback limitations on the sides, while the front varies according to size. In addition, having the buildings adjacent to each other reduces the heat transfer in three of the five exterior surfaces of the building, leaving only the front and the roof exposed.

## CASE STUDIES

Two cases are compared to assess the effectiveness of thermal measures in reducing the cooling load. Each was simulated with and without. The analysis was performed using Ecotect 5.5. The houses are in two cities that represent the main climate zones of the MENA region: the hot, dry city of Baghdad (NCM, 2021; Central Statistics Organization, 2015), and the coastal city of Dubai, which has higher humidity levels (NCM, 2021). By necessity, the design will be different as per municipality rules for each region and city. Primarily, in Baghdad, there are no setbacks except in the front, while in Dubai, in non-freehold land, the setback is required on all four sides. The construction of both houses follows local traditional practices. The design of each is shown in Figure 15.

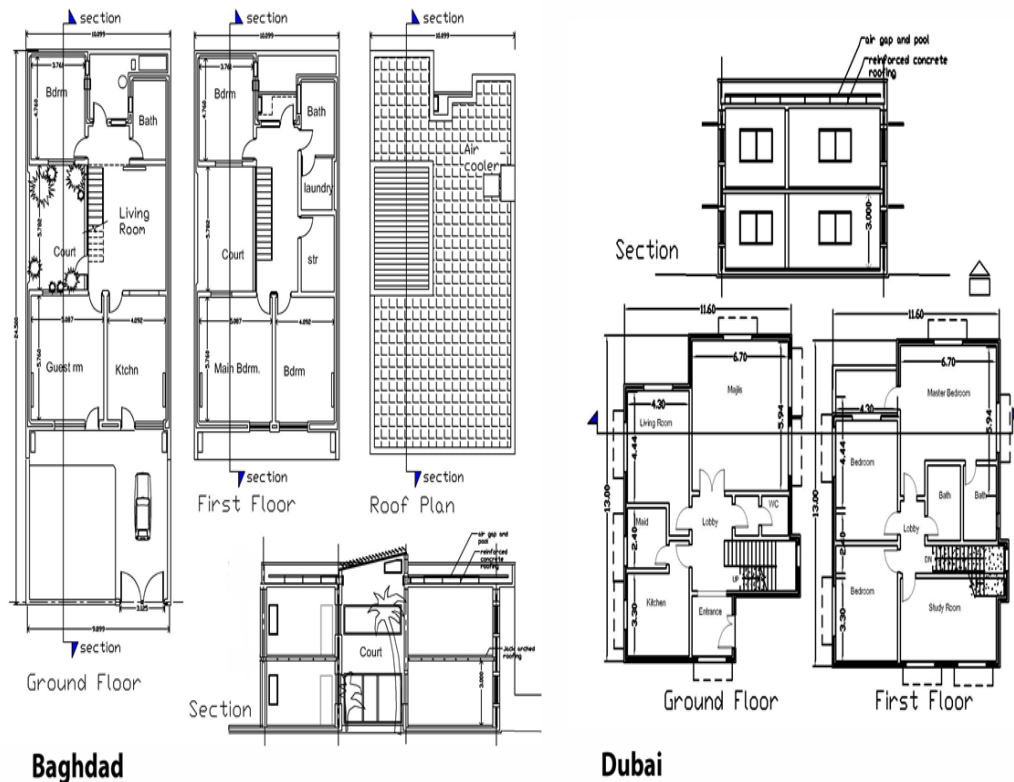


Figure 15. Layout of the two houses that were thermally simulated. The one on the left is designed for Baghdad, and Dubai on the right. The variations in design are primarily due to differences in municipality building guidelines of each city (Drawings by author)

The total built-up floor area for the Dubai house was 261m<sup>2</sup> and 266 m<sup>2</sup> for Baghdad. The indoor temperature was set at 26°C in Dubai, where such a setting results in a Predicted Mean Vote (PMV) of 0.1. In the drier climate of Baghdad, a higher temperature of 27°C was sufficient to achieve the same. All other variables, such as clothing and activity, were set similarly. The weather data was imported from the US Department of Energy, EnergyPlus website ([https://energyplus.net/weather-region/asia\\_wmo\\_region\\_2](https://energyplus.net/weather-region/asia_wmo_region_2)). For simulation, the construction and material are assumed to be:

1. Walls: 20cm thick block concrete with cement plaster finishing and paint on both sides.
2. Roof: 10cm reinforced concrete with cement tile finishing.
3. Exterior doors: low infiltration 7 cm wood
4. Aluminum windows.

The parameters of the thermal simulations were Sedentary activity, light clothing of trousers, and a T-shirt. The air movement was at 0.5m/s, and the radiant temperature was assumed to equal the interior. Figure 16 shows the Ecotect model of the houses.

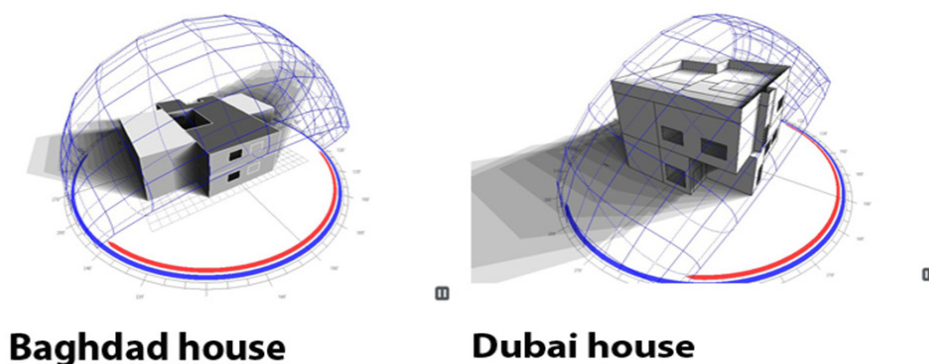


Figure 16. Ecotect models of the thermal simulations

The measures that were added to improve the thermal efficiency were:

1. For the walls, 5–6 cm of polystyrene thermal insulation and 10 cm in the roof.
2. Windows: Double glazed low-e aluminum frame
3. Increased airtightness of the envelope
4. An increase in interior air movement.
5. Horizontal cantilevers for shading above windows

These are moderate changes and do not reflect best-case scenarios but rather financially feasible ones. The u-values of the software were used for both houses, although they differ slightly according to manufacture and raw material. Slight differences may exist between the two countries. There are also differences in construction, although both countries use cement and concrete construction. In Baghdad, the walls are used as load-bearing elements, while in Dubai, thin columns are hidden inside the walls to carry the load. It should have a minimal effect on the thermal conditions. The simulations revealed the results as shown in Table 5.

Table 5

*Thermal simulation results of the cooling load of the two case study houses*

City	Without thermal measures	With thermal measures	Savings
Dubai	46.36 kWh	23.86 kWh	48.5%
Baghdad	28.37 kWh	21.6 kWh	23.86%

The cooling load in Dubai is higher primarily because the differences between night and day are slight, and air conditioning is required almost all year round. In Baghdad, the weather is cool during the night, and temperatures are cold in winter, requiring no cooling.

The savings are significant, especially in Dubai, where they are higher mainly because all four sides of the buildings are exposed, which highlights the effect of the added wall insulation, while in Baghdad, the adjacency to neighboring houses results in less heat gain.

## CONCLUSIONS

The design of buildings in hot countries often requires distinct solutions. Sunlight, as one of the main sources of heat, requires shading and preventive measures to mitigate its effect. The use of white or light colors for the exterior is recommended. Windows should be protected from direct sunlight. Horizontal cantilevers should be used on southern facing walls in the northern hemisphere and on north-facing walls in the southern. Vertical sun-breakers on the east and west-facing walls are better in most cases; vegetation around the building is recommended to reduce reflected sunlight.

Climate variations demand different solutions. In mildly hot climates, the priority is for ventilation. Installing a ceiling fan is both cheap and low on power consumption.

In hot, dry climates, adding evaporative coolers is recommended. If the weather does not allow for comfortable cooling, then energy heavy compressor air conditioners need to be used in tandem with measures that ensure the lowest possible electrical consumption. Insulation should be added; double glazing and e-energy efficient windows and doors.

Using UPVC windows in walls not facing sunlight is a good option as the frame conducts less heat. The possibility of using exterior sliding shutters should be assessed, as well as multiple layers of interior curtains and shades. Protection against air infiltration is also useful. Geothermal heat pumps may be feasible in many regions. Some innovative measures, such as roof ponds and evaporative assisted cooling, should be studied.

## ACKNOWLEDGEMENT

The authors would like to acknowledge the support received from the university of Ajman. We would also like to thank Ms Shafiya Rizwan and Ms Foutoun Daboul for their help in improving the presentation of this article.

## REFERENCES

- Akram, O. K., Ismail, S., Utaberta, N., Yunos, M. Y. M., Ismail, N. A., & Ariffin, N. F. M. (2015). The important values of architectural Baghdadi heritage. *Advances in Environmental Biology*, 9(24), 46-53.
- Alalouch, C., Al-Saadi, S., AlWaer, H., & Al-Khaled, K. (2019). Energy saving potential for residential buildings in hot climates: The case of Oman. *Sustainable Cities and Society*, 46, Article 101442. <https://doi.org/10.1016/J.SCS.2019.101442>
- Al-Homoud, M. S. (2016). The effectiveness of thermal insulation in different types of buildings in hot climates. *Journal of Thermal Envelope and Building Science*, 27(3), 235-247. <https://doi.org/10.1177/1097196304038368>
- Al-Taie, E., Al-Ansari, N., Knutsson, S., Al-Taie, E., Al-Ansari, N., & Knutsson, S. (2014). The need to develop a building code for Iraq. *Engineering*, 6(10), 610-632. <https://doi.org/10.4236/ENG.2014.610062>
- Amazon. (2017). *Ceiling fan price*. Retrieved April 1, 2017, from <https://goo.gl/GYgk1F>
- Arasteh, D., Apte, J., & Huang, Y. (2003). Future advanced windows for zero-energy homes. *ASHRAE Transactions*, 109(2), 871-882.
- Ariosto, T., Memari, A. M., & Solnosky, R. L. (2019). Development of designer aids for energy efficient residential window retrofit solutions. *Sustainable Energy Technologies and Assessments*, 33, 1-13. <https://doi.org/10.1016/J.SETA.2019.02.007>
- ASHRAE. (2009). *2009 ASHRAE handbook: Fundamentals*. American Society of Heating, Refrigeration and Air-Conditioning Engineers.
- Bagasi, A. A., & Calautit, J. K. (2020). Experimental field study of the integration of passive and evaporative cooling techniques with Mashrabiya in hot climates. *Energy and Buildings*, 225, Article 110325. <https://doi.org/10.1016/J.ENBUILD.2020.110325>
- Bansal, N. K., & Mathur, J. (2006). *Energy efficient windows*. Anamaya Publishers.
- Boake, T. M., Bes, B., & Arch, M. (2014). Hot climate double façades: Avoiding solar gain. *Facade Tectonics*, 14, 2-24.

- Buesing, J. W. (1981). *Energy conserving window treatments: Insulated shades and draperies*. Publication-Cooperative Extension Programs.
- Butera, F., Adhikari, R., & Aste, N. (2014). *Sustainable building design for tropical climates: Principles and applications for Eastern Africa*. UN-Habitat.
- Central Statistics Organization. (2015). *Environmental indicators, Iraqi environmental statistics, (Table 3.1) daily average temperature and relative humidity for Baghdad*. Iraqi Ministry of Planning.
- Cuce, P. M., & Riffat, S. (2016). A state of the art review of evaporative cooling systems for building applications. *Renewable and Sustainable Energy Reviews*, 54, 1240-1249. <https://doi.org/10.1016/J.RSER.2015.10.066>
- Del Barrio, E. P. (1998). Analysis of the green roofs cooling potential in buildings. *Energy and Buildings*, 27(2), 179-193. [http://dx.doi.org/10.1016/S0378-7788\(97\)00029](http://dx.doi.org/10.1016/S0378-7788(97)00029)
- Del Barrio, E. P. (1998). Analysis of the green roofs cooling potential in buildings. *Energy and Buildings*, 27(2), 179-193. [https://doi.org/10.1016/S0378-7788\(97\)00029-7](https://doi.org/10.1016/S0378-7788(97)00029-7)
- Derradji, M., & Aiche, M. (2014). Modeling the soil surface temperature for natural cooling of buildings in hot climates. *Procedia Computer Science*, 32, 615-621. <https://doi.org/10.1016/J.PROCS.2014.05.468>
- DEWA. (2015). *Set your AC to 24°C*. Dubai Electricity and Water Authority. Retrieved February 13, 2018, from <https://www.dewa.gov.ae/en/customer/sustainability/spread-the-message/24-degrees-campaign>
- DEWA. (2018). *Abu Dhabi power reduction*. Dubai Electricity and Water Authority. Retrieved February 13, 2018, from <http://www.powerwise.gov.ae/en/section/how-can-i-save-electricity/residential/air-conditioning>
- Dubai Municipality. (2021). *Green building in Dubai*. Retrieved October 14, 2021, from <https://www.dm.gov.ae/municipality-business/al-safat-dubai-green-building-system/green-building-in-dubai/>
- Dylewski, R., & Adamczyk, J. (2011). Economic and environmental benefits of thermal insulation of building external walls. *Building and Environment*, 46(12), 2615-2623. <https://doi.org/10.1016/j.buildenv.2011.06.023>
- Fasi, M. A., & Budaiwi, I. M. (2015). Energy performance of windows in office buildings considering daylight integration and visual comfort in hot climates. *Energy and Buildings*, 108, 307-316. <https://doi.org/10.1016/J.ENBUILD.2015.09.024>
- Garde, F., David, M., Lenoir, A., & Ottenwelter, E. (2011). Towards net zero energy buildings in hot climates: Part 1, new tools and methods. *ASHRAE Transactions*, 117(1), 450-457.
- Hashemi, N., Fayaz, R., & Sarshar, M. (2010). Thermal behavior of a ventilated double skin facade in hot arid climate. *Energy and Buildings*, 42(10), 1823-1832. <https://doi.org/10.1016/j.enbuild.2010.05.019>
- Hawkes, D., & Forster, W. (2002). *Energy efficient buildings: Architecture, engineering, and environment*. WW Norton & Company.
- Hedayat, Z., Belmans, B., Ayatollahi, M. H., Wouters, I., & Descamps, F. (2015). Performance assessment of ancient wind catchers - An experimental and analytical study. *Energy Procedia*, 78, 2578-2583. <https://doi.org/10.1016/J.EGYPRO.2015.11.292>

- Kanaan, A., Sevostianova, E., Donaldson, B., & Sevostianov, I. (2021). Effect of different landscapes on heat load to buildings. *Land*, 10(7), Article 733. <https://doi.org/10.3390/LAND10070733>
- Kaynakli, O. (2012). A review of the economical and optimum thermal insulation thickness for building applications. *Renewable and Sustainable Energy Reviews*, 16(1), 415-425. <https://doi.org/10.1016/j.rser.2011.08.006>
- Kharrufa, S. N. (2008). Evaluation of basement's thermal performance in Iraq for summer use. *Journal of Asian Architecture and Building Engineering*, 7(2), 411-417. <https://doi.org/10.3130/jaabe.7.411>
- Kharrufa, S. N., & Adil, Y. (2008). Roof pond cooling of buildings in hot arid climates. *Building and Environment*, 43(1), 82-89. <https://doi.org/10.1016/j.buildenv.2006.11.034>
- Kharrufa, S. N., & Adil, Y. (2012a). Reducing the cooling load by evaporative cooling of the roof. In *Energy and Buildings: Efficiency, Air Quality, and Conservation* (pp. 235-255). Nova Publishers. <https://doi.org/10.1016/j.enbuild.2012.09.006>
- Kharrufa, S. N., & Adil, Y. (2012b). Upgrading the building envelope to reduce cooling loads. *Energy and Buildings*, 55, 389-396. <https://doi.org/10.1016/j.enbuild.2012.09.006>
- Lechner, N. (2014). *Heating, cooling, lighting: Sustainable design methods for architects*. John Wiley & Sons.
- Lee, J. W., Jung, H. J., Park, J. Y., Lee, J. B., & Yoon, Y. (2013). Optimization of building window system in Asian regions by analyzing solar heat gain and daylighting elements. *Renewable Energy*, 50, 522-531. <https://doi.org/10.1016/j.renene.2012.07.029>
- McQuiston, F. C., Parker, J. D., & Spitler, J. D. (2004). *Heating, ventilating, and air conditioning: Analysis and design*. John Wiley & Sons.
- Mehere, S. V, Mudafale, K. P., & Prayagi, S. V. (2014). Review of direct evaporative cooling system with its applications. *International Journal of Engineering Research and General Science*, 2(6), 995-999.
- Mushtaha, E., & Helmy, O. (2016). Impact of building forms on thermal performance and thermal comfort conditions in religious buildings in hot climates: A case study in Sharjah city. *International Journal of Sustainable Energy*, 36(10), 926-944. <https://doi.org/10.1080/14786451.2015.1127234>
- NCM. (2021). *Climate yearly report 2003-2017*. National Center of Meteorology. Retrieved June 2, 2021, from <https://www.ncm.ae/services/climate-reports-yearly?lang=en>
- Nicol, F., Humphreys, M., & Roaf, S. (2012). *Adaptive thermal comfort: Principles and practice*. Routledge.
- Pal, R. K., Goyal, P., & Sehgal, S. (2020). Thermal performance of buildings with light colored exterior materials. *Materials Today: Proceedings*, 28, 1307-1313. <https://doi.org/10.1016/J.MATPR.2020.04.508>
- Rackes, A., Melo, A. P., & Lamberts, R. (2016). Naturally comfortable and sustainable: Informed design guidance and performance labeling for passive commercial buildings in hot climates. *Applied Energy*, 174, 256-274. <https://doi.org/10.1016/J.APENERGY.2016.04.081>
- Sajjad, U., Abbas, N., Hamid, K., Abbas, S., Hussain, I., Ammar, S. M., Sultan, M., Ali, H. M., Hussain, M., Ur-Rehman, T., & Wang, C. C. (2021). A review of recent advances in indirect evaporative cooling technology. *International Communications in Heat and Mass Transfer*, 122, Article 105140. <https://doi.org/10.1016/J.ICHEATMASSTRANSFER.2021.105140>



- Saleem, J. (1986). Improving performance of evaporative coolers. In *Proceedings of Fifth Annual Scientific Symposium of Iraqi Research Council*. Baghdad, Iraq.
- Sharifi, A., & Yamagata, Y. (2015). Roof ponds as passive heating and cooling systems: A systematic review. *Applied Energy*, 160, 336-357. <https://doi.org/10.1016/j.apenergy.2015.09.061>
- Shi, Z., & Zhang, X. (2011). Analyzing the effect of the longwave emissivity and solar reflectance of building envelopes on energy-saving in buildings in various climates. *Solar Energy*, 85(1), 28-37. <https://doi.org/10.1016/J.SOLENER.2010.11.009>
- Vijayaraghavan, K. (2016). Green roofs: A critical review on the role of components, benefits, limitations and trends. *Renewable and Sustainable Energy Reviews*, 57, 740-752. <https://doi.org/10.1016/J.RSER.2015.12.119>
- Williams, G. P., & Gold, L. W. (1976). *CBD-180 ground temperatures*. National Research Council Canada.
- Yang, Y., Cui, G., & Lan, C. Q. (2019). Developments in evaporative cooling and enhanced evaporative cooling - A review. *Renewable and Sustainable Energy Reviews*, 113, Article 109230. <https://doi.org/10.1016/J.RSER.2019.06.037>
- Zarandi, M. M. (2009). Analysis on Iranian wind catcher and its effect on natural ventilation as a solution towards sustainable architecture (Case Study: Yazd). *World Academy of Science, Engineering and Technology*, 54, 574-579.



## Accuracy of Ultrasound and Magnetic Resonance Cholangiopancreatography Findings in the Diagnosis of Biliary System Stones

Abdullah Taher Naji<sup>1\*</sup>, Ameen Mohsen Amer<sup>1</sup>, Saddam Mohammed Alzofi<sup>1</sup>, Esmail Abdu Ali<sup>2</sup> and Noman Qaid Alnaggar<sup>2</sup>

<sup>1</sup>Department of Medical Radiology and Imaging Technology, Faculty of Medicine and Health Sciences, University of Science and Technology, Sana'a, Yemen

<sup>2</sup>Department of Biomedical Engineering, Faculty of Engineering, University of Science and Technology, Sana'a, Yemen

### ABSTRACT

This study aimed to evaluate the diagnostic accuracy of magnetic resonance cholangiopancreatography (MRCP) and Ultrasound (US) images for the diagnosis of biliary system stones, as well as to assess the consistency between MRCP and US findings. The study sample included 200 cases (90 males and 110 females) with symptomatic biliary system stones between 14 and 82 years. All cases underwent both the US and MRCP imaging for biliary system diagnosis. The study revealed that the most prominent age group with symptoms of biliary system stones was the 33-60-year-old group. It also found that the accuracy of US and MRCP in detecting gallbladder (GB) stones compared with the final diagnosis was 94% and 91%, respectively, with moderate conformity between their results. The accuracy of US and MRCP images in detecting common bile duct (CBD) stones was 61% and 98%, respectively, with fair conformity between their results. In addition, there is

a significant agreement between the MRCP and US results in detecting the GB and CBD stones with an agreed percentage of 74% and 71%, respectively. The study concluded that US is the preferred imaging technique for patients with symptomatic gallbladder stones, whereas MRCP is a trustworthy investigation for common bile duct stones.

### ARTICLE INFO

#### Article history:

Received: 31 August 2021

Accepted: 12 November 2021

Published: 10 January 2022

DOI: <https://doi.org/10.47836/pjst.30.1.46>

#### E-mail addresses:

[a.taher1983@gmail.com](mailto:a.taher1983@gmail.com) (Abdullah Taher Naji)

[aminalfahi@gmail.com](mailto:aminalfahi@gmail.com) (Ameen Mohsen Amer)

[saddamalzofi@gmail.com](mailto:saddamalzofi@gmail.com) (Saddam Mohammed Alzofi)

[Dresmail4@gmail.com](mailto:Dresmail4@gmail.com) (Esmail Abdu Ali)

[Noman\\_qaed@yahoo.com](mailto:Noman_qaed@yahoo.com) (Noman Qaid Alnaggar)

\*Corresponding author

*Keywords:* Accuracy, biliary system stones, diagnosis, MRCP, ultrasound

## INTRODUCTION

The biliary system stones (gallbladder and common bile duct stones) need a specific diagnosis and accurate technique because of the overlapping signs and symptoms. Thus, medical imaging modalities play a key role in establishing biliary lithiasis diagnoses and formulating an ideal treatment (Peixoto et al., 2019).

Some common clinical problems caused by biliary stones, especially in patients older than 60 years, can cause serious clinical complications, such as pancreatitis and acute cholangitis (Alkarboly et al., 2016; Chan et al., 2013). For example, CBD stones were estimated for 10 to 20% of cases with symptomatic gallstones and can cause some health problems, such as infection, jaundice, pain, and acute pancreatitis (Williams et al., 2017). Moreover, gallstones are associated with a higher risk of gastrointestinal cancer (Pang et al., 2021).

Biliary stones are prevalent in women compared to men (Kratzer et al., 2021). Besides, gallbladder (GB) stone is more prevalent in obese patients and associated with upper abdominal pain, nausea, and vomiting in some cases (Kichloo et al., 2021). Costi et al. (2014) mentioned that the biliary stones are collected from the bile salts, cholesterol component, or black pigment. The primary common bile duct stones are formed inside the common bile duct, whereas the secondary common bile duct stones are formed in the gallbladder and migrated to the common bile duct (Williams et al., 2008). While 5% -30% of biliary stones are combined with choledocholithiasis (Wu et al., 2021).

Many researchers have reported that computed tomography can help in detecting GB stones, especially with difficult and inconclusive cases or GB perforation, and is still recommended for abdominal pain evaluation, only if the diagnosis is uncertain (Harraz & Abouissa, 2020; Danse et al., 2018; Wertz et al., 2018). On the contrary, a CT scan is less accurate than ultrasound (US) imaging in detecting biliary stones and debatably the most effective for diagnosing gallbladder condition, especially for gallstone ileus and pancreaticobiliary tract evaluation (Veronica et al., 2019; Alshargi et al., 2018).

Ultrasound imaging is the investigation of choice in confirming or excluding dilated bile ducts, cysts, and calcifications (Liu et al., 2012). In addition, ultrasound should be a valuable first-line imaging modality of choice for biliary system stones diagnosis due to its inherent superiority compared to other imaging modalities. For patients with suspected CBD stones, trans-abdominal US imaging is recommended (Williams et al., 2017). Despite that, US imaging is a highly operator-dependent modality, and difficult to standardize its' findings. Some studies (De Silva et al., 2019; Gurusamy et al., 2015; Şurlin et al., 2014) have revealed varied accuracy of US regarding the detection of common bile duct stones ranging between 44% and 90%.

On the other hand, MRCP imaging (Magnetic resonance imaging for bile duct, gallbladder, and pancreatic duct) is a non-invasive technique to evaluate the pancreatic

ductal system and hepatic biliary tree without ionizing radiation or iodinated contrast material and can provide the diagnostic range equivalent to the endoscopic retrograde cholangiopancreatography (Getsov et al., 2020). MRCP diagnostic performance has proved to be a convenient imaging technique for biliary diseases diagnosis and a valuable alternative to endoscopic retrograde cholangiopancreatography (ERCP) without the risks associated with these procedures. MRCP imaging exploits the biliary and pancreatic ducts fluid as a contrast agent by acquiring MR images using T2 weighted sequences (Griffin et al., 2012).

Many studies have investigated the accuracy of MRCP imaging in the diagnosis of the biliary system; for instance, some studies (Goud et al., 2020; Veronica et al., 2019; Virzi et al., 2018) have stated that MRCP is a highly accurate diagnostic modality in establishing the diagnosis of obstructive biliary pathologies, allowing a detailed evaluation of the biliary and pancreatic ducts, and providing excellent anatomical imaging in both normal and pathologic conditions with the advantage of the improved biliary system for stone detection without ionizing radiation.

Akkuzu et al. (2020) stated that the sensitivity of MRCP for choledocholithiasis detection was 81.5%, other studies have documented vary accuracy rate for MRCP in the diagnosis of biliary system stones and pathologies which ranged between 86.4% and 100% (Yahya et al., 2021; Agha et al., 2018; Giljaca et al. 2015; Limanond et al., 2004; Figueras et al., 2000).

In contrast, some other studies have reported several limitations which may mask various pathologic conditions of the pancreatic or extrahepatic bile duct (Williams et al., 2017; Maccioni et al., 2010).

This research aimed to evaluate the accuracy of US and MRCP modalities in detecting the biliary system stones and estimate the agreement between US and MRCP results. Results of this research can provide updated guidance to specialized professionals with valuable information about the role of US and MRCP modalities in diagnosing biliary system stones to choose the best modality.

## **MATERIALS AND METHODS**

This study was conducted on patients with symptomatic biliary system stones referred to the radiology department at the University of Science and Technology Hospital in Sana'a city, Yemen. A prospective review of 200 cases (90 males and 110 females) suspected of having biliary system stones (gallbladder (GB) stones and common bile duct (CBD) stones). The study's participants are aged between 14–82 years. They all underwent US and MRCP exams for biliary lithiasis diagnosis during the same period (less than one week) for each.

US imaging technique uses high-frequency sound waves to characterize tissue. In the initial examination of the gallbladder and bile ducts, abdominal US imaging was used for

all selected patients. The high-frequency US probe (2-7 MHz) was used to gain adequate penetration.

On the other hand, MRCP with a 1.5 Tesla system was performed for all selected patients fasting for five hours before the examination. As a result, the MRCP imaging technique has high contrast resolution, different plans, and an artifact-free display of anatomy and pathology.

Two radiologists independently reviewed the MRCP and US images to determine the absence or presence of GB and CBD stones. The results of US and MRCP images in the detection of biliary system stones were correlated with the final diagnosis and operative findings as a standard reference. In addition, the diagnostic accuracy of both imaging modalities was compared to assess the agreement between their results.

### **Ethical Consideration**

The ethical approval for conducting this study was obtained from the Medical Research Ethics Committee of the University of Science and Technology, Yemen (MECA No.: EAC/UST202).

### **RESULTS AND DISCUSSION**

The findings of this study showed that the biliary system stones were more frequently occurred among females (55%) than males (45%). Figure 1 shows the classification of the study sample according to gender.

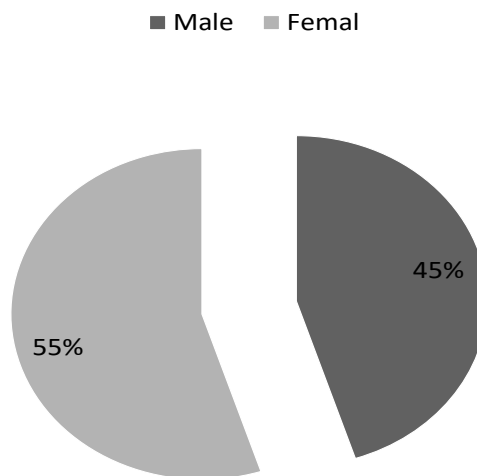


*Figure 1.* Distribution of suspected biliary stones cases according to gender

According to Wu et al. (2021), women are more likely to develop biliary system stones, associated with higher estrogen levels and less exercise.

Regarding age, the mean age of the study sample was 50.2 years, and the predominant age of patients with biliary system stones symptoms was the 33–60 years group. Table 1 shows the classification of the study sample according to age group.

Table 1  
Distribution of ages for suspected biliary stones cases

Age (yrs.)	N	%
<33	32	16%
33–60	110	55%
>60	58	29%
Total	200	<b>100%</b>

The findings of this study are relatively in line with Kolomyitsev et al. (2019), who reported that the mean age of patients suspected of having choledocholithiasis was  $56.4 \pm 15.11$  years and ranged from 19 to 87.

**GB Stones Diagnosis using MRCP and US Imaging**

From 200 cases with cholelithiasis symptoms, gallstones were more detected by US (76%) than MRCP (74%), as shown in Figure 2.

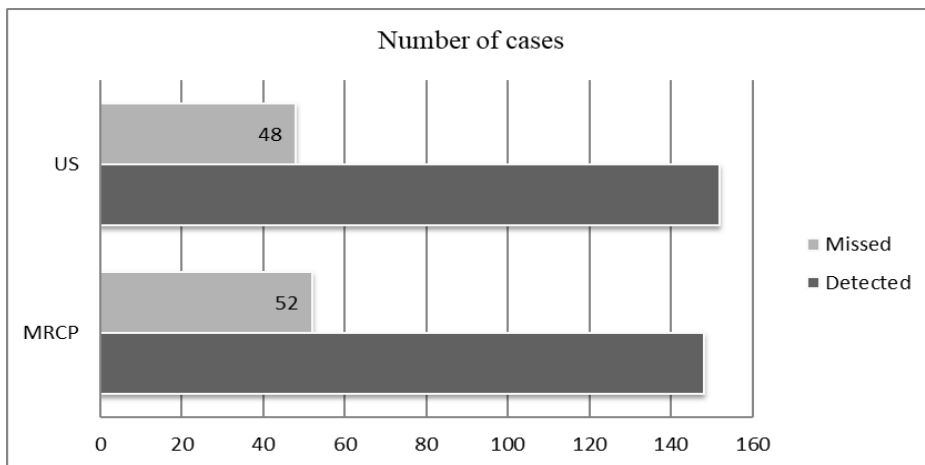


Figure 2. MRCP and US findings for suspected gallbladder stones cases

US imaging showed more sensitivity to detect gallbladder (GB) stones with an accuracy of 94% as well as a positive predictive value over 98% when correlated with the final diagnosis and operative findings. This finding appeared to be better than that reported by Pinto et al. (2013), who revealed high sensitivity of US (88%) in detecting GB stones in patients with suspected acute calculous cholecystitis. Because gallbladder stones are likely to be surrounded by the bile and can be detected by the US accurately, the US is an initial imaging technique for the GB stones diagnosis. This finding is in line with that of Ahmed and Diggory (2011), who documented the superiority of the US in cholelithiasis diagnosis.

In contrast, negative results may be referred to as gallstones with small size (less than 2 mm) because they may not be readily detectable on US imaging or because gallstones that impact the gallbladder’s neck may be silhouetted with the surrounding intraperitoneal fat or echogenic bowel gas. This finding is consistent with Rubens (2007), who stated that ultrasound is a primary imaging modality for the initial diagnosis of suspected biliary disease. On the other hand, MRCP imaging showed an accurate diagnosis of GB stones by 91% and a positive predictive value of 95%. This result is better than that reported by Polistina et al. (2015), who found an MRCP accuracy rate of 80.5% in detecting biliary stones. The MRCP negative results may occur in patients with < 2 mm stones or those with massive ascites. Moreover, MRCP accuracy can be affected by patient cooperation, positioning, and imaging procedures. Consequently, US imaging is considered a reference technique and an initial diagnostic imaging modality for GB stones.

### The Agreement between MRCP and US Results in the GB Stones Diagnosis

Kappa test was used. Table 2 shows the symmetric values between MRCP and US imaging results to evaluate the inter-rate symmetry (agreement) between MRCP and US results in detecting GB stones.

Table 2

*Results of inter-rate agreement between US and MRCP in detecting GB stones*

		GB stones result by MRCP imaging		Measure of Agreement (kappa)	
		Missed	Detected	value	Sig.
GB stones result by US imaging	Missed	24	24	0.31	< 0.001
	Detected	28	124		



Although the overall conformity percentage between US and MRCP results was 74%, the results of the Kappa test showed fair agreement ( $K = 0.31$ ) between US and MRCP in the detection of GB stones by MRCP in comparison with the US.

### Diagnosis of CBD Stones using MRCP and US Imaging

From 200 patients with choledocholithiasis symptoms, common bile duct (CBD) stones were mostly diagnosed by MRCP (67%;  $n=108$ ) compared with US (46%;  $n=66$ ), as shown in Figure 3.

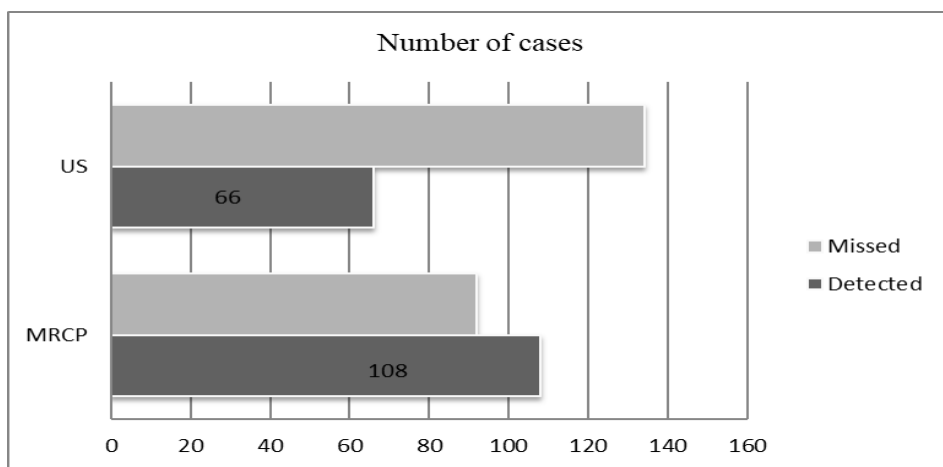


Figure 3. MRCP and US findings for suspected CBD stones cases

The results showed that CBD stones were detected in 108 cases by MRCP with an accuracy rate of over 98% based on the final diagnosis, including histological and surgical findings. This result is similar to those reported by Karwa and Patil (2017), who showed a 95% accuracy rate for the MRCP in the detection of CBD stones, as well as consents with Lee et al. (2018), who documented a 93.3% accuracy rate for MRCP in the diagnosis of CBD. In contrast, this finding is relatively better than those reported by Orman et al. (2018), who found an 86.4% MRCP sensitivity for choledocholithiasis detection, as well as Akkuzu et al. (2020), who reported an 81.5% MRCP sensitivity for hepatobiliary system stones.

In addition, this present study demonstrated that CBD stones larger than 6 mm could be detected with high accuracy without contrast. The results showed that CBD stones were detected in 66 cases by the US with an accuracy rate of 61%; approximately the same results were documented by Kolomiytsev et al. (2019), who reported a 66% accuracy rate for US imaging in the detection of CBD stones. On the contrary, this finding is better than those of Orman et al. (2018), who found a 40.8% US sensitivity in detecting choledocholithiasis.

The number of cases with CBD stones detected by both modalities was less than the number detected for GB stones. Moreover, there were more negative results for the US (i.e., defined as negative findings in the US with positive findings at MRCP and were confirmed in the final diagnosis). However, this result revealed higher diagnostic accuracy for MRCP in detecting CBD stones, which is in line with the findings of Virzi et al. (2019), who reported higher positive predictive values for MRCP in detecting CBD stones compared with the US imaging. This advantage, therefore, can reduce the misdiagnosis of normal US examinations.

The limited accuracy of US in detecting CBD stones may be attributed to many reasons such as the operator skill or lack of fluid around compressed CBD stones against the duct wall, which reduces stone border visibility. In contrast, gallbladder stone is easily seen because it is surrounded by bile. Also, the location of CBD stones at the ampulla of Vater (hepatopancreatic ampulla) may be hidden by bowel gas and difficult to see in US image. In addition, poor acoustic shadows for small stones. This finding is in line with that of Qiu et al. (2015), who revealed low US imaging accuracy in diagnosing CBD stones.

### The Agreement between MRCP and US Results in the Diagnosis of CBD Stones

The Kappa test evaluated the agreement between MRCP and US results detecting GB stones. Table 3 shows the symmetric values between MRCP and US imaging results.

Table 3

*Results of agreement between US and MRCP in the detection of CBD stones*

		CBDS result by MRCP imaging		Measure of Agreement (kappa)	
		Missed	Detected	K – value	Sig.
CBDS result by US imaging	Missed	84	50	0.44	< 0.001
	Detected	8	58		

The MRCP negative results were only shown in 2 cases with a < 2 mm stone which is less than US imaging negative results. MRCP imaging appears to be sensitive and specific for the CBD stone diagnosis. Table 3 revealed that the overall conformity percentage between MRCP and US was 71%, while the Kappa test results showed moderate agreement (0.44) in detecting CBD stones by MRCP compared to the US.

## CONCLUSION

In conclusion, the US is an accurate imaging modality for patients with symptomatic GB stones and is considered as the benchmark investigation because of its better availability, lower costs, and accuracy for GB stones detection. At the same time, MRCP is a more valuable imaging technique for detecting CBD stones. Although there is a statistically significant agreement between MRCP and US findings in biliary diagnosis stones, MRCP and US have a fair agreement in detecting GB stones. In contrast, the findings of this study showed moderate conformity between MRCP results for suspected cases and their US results in the detection of CBD stones.

## ACKNOWLEDGEMENTS

The authors would like to thank the University of Science and Technology Hospital for the permission to the authors to use the hospital facilities during the process of conducting this study. Furthermore, special thanks go to the radiology technologists (Hanan Mogalli, Manal Alsormi, Eman Alshame, Athar Almaqlaleh) who assisted in collecting this research data.

## REFERENCES

- Agha, M., Abougabal, A. M., & Abd Ellatief, H. (2018). The breath-hold 2D MRCP and the respiratory-triggered 3D MRCP sequences, comparative study as regards the possible pitfalls. *The Egyptian Journal of Radiology and Nuclear Medicine*, 49(3), 614-623. <https://doi.org/10.1016/j.ejnm.2018.04.006>
- Ahmed, M., & Diggory, R. (2011). The correlation between ultrasonography and histology in the search for gallstones. *The Annals of The Royal College of Surgeons of England*, 93(1), 81-83. <https://doi.org/10.1308/003588411X12851639107070>
- Akkuzu, M. Z., Altintas, E., Yaras, S., Özdoğan, O., Ucbilek, E., Ates, F., Aydin, F., Balci, H. R., Dirik, Y., & Sezgin, O. (2020). EUS Accuracy Against MRCP for Detection of Pancreaticobiliary Lesions. *Eastern Journal of Medicine*, 25(4), 535-539. <https://doi.org/10.5505/ejm.2020.92195>
- Alkarboly, T. A. M., Fatih, S. M., Hussein, H. A., Ali, T. M., & Faraj, H. I. (2016). The accuracy of transabdominal ultrasound in detection of the common bile duct stone as compared to endoscopic retrograde cholangiopancreatography (with literature review). *Open Journal of Gastroenterology*, 6(10), 275-299. <http://dx.doi.org/10.4236/ojgas.2016.610032>
- Alshargi, A. O., Al-sallami, S. E., Hejazi, H. A. M., & Alahdal, A. I. O. (2018). Accuracy of ultrasound in diagnosis of cholecystitis. *The Egyptian Journal of Hospital Medicine*, 73(7), 7146-7152. <https://dx.doi.org/10.21608/ejhm.2018.17604>
- Chan, H. H., Wang, E. M., Sun, M. S., Hsu, P. I., Tsai, W. L., Tsai, T. J., Wang, K. M., Chen, W. C., Wang, H. M., Liang, H. L., Lai, K. H., & Brugge, W. R. (2013). Linear echoendoscope-guided ERCP for the diagnosis of occult common bile duct stones. *BMC Gastroenterology*, 13, Article 44. <https://doi.org/10.1186/1471-230X-13-44>

- Costi, R., Gnocchi, A., Di Mario, F., & Sarli, L. (2014). Diagnosis and management of choledocholithiasis in the golden age of imaging, endoscopy and laparoscopy. *World Journal of Gastroenterology*, 20(37), 13382-13401. <https://doi.org/10.3748/wjg.v20.i37.13382>
- Danse, E., Jamali, S., & Hubert, C. (2018). Spectral CT detection of entrapped gallstone based on Z-effective Map. *Journal of the Belgian Society of Radiology*, 102(1), Article 53. <https://doi.org/10.5334/jbsr.1515>
- De Silva, S. L., Pathirana, A. A., Wijerathne, T. K., Gamage, B. D., Dassanayake, B. K., & De Silva, M. M. (2019). Transabdominal ultrasonography in symptomatic choledocholithiasis - Usefulness in settings with limited resources. *Journal of Clinical Imaging Science*, 9, Article 31. <https://doi.org/10.25259/JCIS-38-2019>
- Figueras, J., Llado, L., Valls, C., Serrano, T., Ramos, E., Fabregat, J., Rafecas, A., Torras, J., & Jaurrieta, E. (2000). Changing strategies in diagnosis and management of hilar cholangiocarcinoma. *Liver Transplantation*, 6(6), 786-794. <https://doi.org/10.1053/jlts.2000.18507>
- Getsov, P., Siminkovitch, S., Kovacheva-Slavova, M., Vladimirov, B., & Dineva, S. (2020). Anatomical variations of bile ducts. study of their frequency in the Bulgarian population, using magnetic resonance cholangiopancreatography. *Comptes Rendus de l'Academie Bulgare des Sciences*, 73(6), 866-871.
- Giljaca, V., Gurusamy, K. S., Takwoingi, Y., Higgie, D., Poropat, G., Štimac, D., & Davidson, B. R. (2015). *Endoscopic ultrasound versus magnetic resonance cholangiopancreatography for common bile duct stones*. John Wiley & Sons. <https://doi.org/10.1002/14651858.CD011549>
- Goud, S., Devi, B. V., Kale, P. K. G., Lakshmi, A. Y., & Reddy, V. V. R. (2020). To study diagnostic efficacy of ultrasound and magnetic resonance cholangiopancreatography in obstructive jaundice. *Journal of Dr. NTR University of Health Sciences*, 9(2), 217-221. [https://doi.org/10.4103/JDRNTRUHS.JDRNTRUHS\\_43\\_20](https://doi.org/10.4103/JDRNTRUHS.JDRNTRUHS_43_20)
- Griffin, N., Charles-Edwards, G., & Grant, L. A. (2012). Magnetic resonance cholangiopancreatography: The ABC of MRCP. *Insights into Imaging*, 3(1), 11-21. <https://doi.org/10.1007/s13244-011-0129-9>
- Gurusamy, K. S., Giljaca, V., Takwoingi, Y., Higgie, D., Poropat, G., Štimac, D., & Davidson, B. R. (2015). *Ultrasound versus liver function tests for diagnosis of common bile duct stones*. John Wiley & Sons. <https://doi.org/10.1002/14651858.CD011548>
- Harraz, M. M., & Abouissa, A. H. (2020). Role of MSCT in the diagnosis of perforated gall bladder. *Egyptian Journal of Radiology and Nuclear Medicine*, 51, Article 4. <https://doi.org/10.1186/s43055-019-0128-2>
- Karwa, S., & Patil, V. (2017). Role of magnetic resonance cholangiopancreatography in biliary disorders. *International Journal of Radiology & Radiation Therapy*, 2(4), 95-99. <http://doi:10.15406/ijrrt.2017.02.00032>
- Kichloo, A., Solanki, S., Haq, K. F., Dahiya, D., Bailey, B., Solanki, D., Singh, J., Albosta, M., Wani, F., Aljadah, M., Shah, H., Khan, H., & Jafri, S. M. (2021). Association of non-alcoholic fatty liver disease with gallstone disease in the United States hospitalized patient population. *World Journal of Gastrointestinal Pathophysiology*, 12(2), 14-24. <https://doi.org/10.4291/wjgp.v12.i2.14>
- Kolomyitsev V. I., Terletskiy O. M., & Bufan, M. (2019). Comparative evaluation of radiological imaging results of choledocholithiasis in patients with acute calculous cholecystitis. *Bulletin of Problems Biology and Medicine*, 2(150), 236-242. <https://doi.org/10.29254/2077-4214-2019-2-1-150-236-242>

- Kratzer, W., Klysik, M., Binzberger, A., & Schmidberger, J. (2021). Gallbladder stone incidence and prevalence in Germany: A population-based study. *Zeitschrift für Gastroenterologie*, 59(08), 859-864.
- Lee, S. L., Kim, H. K., Choi, H. H., Jeon, B. S., Kim, T. H., Choi, J. M., Ku, Y. M., Kim, S. W., Kim, S. S., & Chae, H. S. (2018). Diagnostic value of magnetic resonance cholangiopancreatography to detect bile duct stones in acute biliary pancreatitis. *Pancreatology*, 18(1), 22-28. <https://doi.org/10.1016/j.pan.2017.12.004>
- Limanond, P., Raman, S. S., Ghobrial, R. M., Busuttill, R. W., & Lu, D. S. (2004). The utility of MRCP in preoperative mapping of biliary anatomy in adult-to-adult living related liver transplant donors. *Journal of Magnetic Resonance Imaging*, 19(2), 209-215. <https://doi.org/10.1002/jmri.10446>
- Liu, L. N., Xu, H. X., Lu, M. D., Xie, X. Y., Wang, W. P., Hu, B., Yan, K., Ding, H., Tang, S. S., Qian, L. X., Luo, B. M., & Wen, Y. L. (2012). Contrast-enhanced ultrasound in the diagnosis of gallbladder diseases: A multi-center experience. *PLoS One*, 7(10), Article e48371. <https://doi.org/10.1371/journal.pone.0048371>
- Maccioni, F., Martinelli, M., Al Ansari, N., Kagarmanova, A., De Marco, V., Zippi, M., & Marini, M. (2010). Magnetic resonance cholangiography: Past, present and future. *European Review for Medical and Pharmacological Sciences*, 14(8), 721-725.
- Orman, S., Senates, E., Ulasoglu, C., & Tuncer, I. (2018). Accuracy of imaging modalities in choledocholithiasis: A real-life data. *International Surgery*, 103(3-4), 177-183. <https://doi.org/10.9738/INTSURG-D-16-00005.1>
- Pang, Y., Lv, J., Kartsonaki, C., Guo, Y., Yu, C., Chen, Y., Yang, L., Bian, Z., Millwood, I. Y., Walters, R. G., Li, X., Zou, J., Holmes, M. V., Chen, J., Chen, Z., & Li, L. (2021). Causal effects of gallstone disease on risk of gastrointestinal cancer in Chinese. *British Journal of Cancer*, 124, 1864-1872. <https://doi.org/10.1038/s41416-021-01325-w>
- Peixoto, S., Lameira, R. P., Sousa, I., & Fonseca-Santos, J. (2019). *Acute biliary disease - Pictorial review*. European Society of Radiology. <http://dx.doi.org/10.26044/ecr2019/C-2752>.
- Pinto, A., Reginelli, A., Cagini, L., Coppolino, F., Ianora, A. A. S., Bracale, R., Giganti, M., & Romano, L. (2013). Accuracy of ultrasonography in the diagnosis of acute calculous cholecystitis: review of the literature. *Critical Ultrasound Journal*, 5(1), 1-4. <https://doi.org/10.1186/2036-7902-5-S1-S11>
- Polistina, F. A., Frego, M., Bisello, M., Manzi, E., Vardanega, A., & Perin, B. (2015). Accuracy of magnetic resonance cholangiography compared to operative endoscopy in detecting biliary stones, a single center experience and review of literature. *World Journal of Radiology*, 7(4), 70-78. <https://doi.org/10.4329/wjr.v7.i4.70>
- Qiu, Y., Yang, Z., Li, Z., Zhang, W., & Xue, D. (2015). Is preoperative MRCP necessary for patients with gallstones? An analysis of the factors related to missed diagnosis of choledocholithiasis by preoperative ultrasound. *BMC Gastroenterology*, 15(1), 1-8. <https://doi.org/10.1186/s12876-015-0392-1>
- Rubens, D. J. (2007). Ultrasound imaging of the biliary tract. *Ultrasound Clinics*, 2(3), 391-413. <https://doi.org/10.1016/j.cult.2007.08.007>
- Şurlin, V., Săftoiu, A., & Dumitrescu, D. (2014). Imaging tests for accurate diagnosis of acute biliary pancreatitis. *World Journal of Gastroenterology*, 20(44), 16544-16549. <https://doi.org/10.3748/wjg.v20.i44.16544>
- Veronica, B., Francesca, C., Luigi, L., De Gaetano, A. M., & Riccardo, M. (2019). Imaging of biliary colic and cholecystitis. In M. Cova & F. Stacul (Eds.), *Pain imaging* (pp. 229-245). Springer. [https://doi.org/10.1007/978-3-319-99822-0\\_13](https://doi.org/10.1007/978-3-319-99822-0_13)

- Virzi, V., Ognibene, N. M. G., Sciortino, A. S., Culmone, G., & Virzi, G. (2018). Routine MRCP in the management of patients with gallbladder stones awaiting cholecystectomy: A single-centre experience. *Insights into Imaging, 9*(5), 653-659. <https://doi.org/10.1007/s13244-018-0640-3>
- Wertz, J. R., Lopez, J. M., Olson, D., & Thompson, W. M. (2018). Comparing the diagnostic accuracy of ultrasound and CT in evaluating acute cholecystitis. *AJR. American Journal of Roentgenology, 211*(2), 92-97. <https://doi.org/10.2214/AJR.17.18884>
- Williams, E. J., Green, J., Beckingham, I., Parks, R., Martin, D., & Lombard, M. (2008). Guidelines on the management of common bile duct stones (CBDS). *Gut, 57*(7), 1004-1021. <http://dx.doi.org/10.1136/gut.2007.121657>
- Williams, E., Beckingham, I., El Sayed, G., Gurusamy, K., Sturgess, R., Webster, G., & Young, T. (2017). Updated guideline on the management of common bile duct stones (CBDS). *Gut, 66*(5), 765-782. <http://dx.doi.org/10.1136/gutjnl-2016-312317>
- Wu, Y., Xu, C. J., & Xu, S. F. (2021). Advances in risk factors for recurrence of common bile duct stones. *International Journal of Medical Sciences, 18*(4), 1067-1074. <https://doi.org/10.7150/ijms.52974>
- Yahya, S., Alabousi, A., Abdullah, P., & Ramonas, M. (2021). The diagnostic yield of magnetic resonance cholangiopancreatography in the setting of acute pancreaticobiliary disease - A single center experience. *Canadian Association of Radiologists Journal, 20*(1), 1-9. <https://doi.org/10.1177/08465371211013786>

# REFEREES FOR THE PERTANIKA JOURNAL OF SCIENCE & TECHNOLOGY

Vol. 30 (1) Jan. 2022

The Editorial Board of the Pertanika Journal of Science and Technology wishes to thank the following:

Abdullah Hisam Omar  
(UTM, Malaysia)

Bong Chih How  
(UNIMAS, Malaysia)

Francesco Tornabene  
(University of Salento, Italy)

Adnan Ashraf  
(MUEP, Pakistan)

C. Sivapragash  
(SCET, India)

Gabriele Ruth Anisah  
Froemming  
(UNIMAS, Malaysia)

Ahmad Hussein Abdul Hamid  
(UiTM, Malaysia)

Chandrabose Selvaraj  
(Alagappa University, India)

Hamid Reza Karimi  
(Polimi, Italy)

Ahmad Khusairi Azemi  
(USM, Malaysia)

Chew Few Ne  
(UMP, Malaysia)

Hanizam Awang  
(USM, Malaysia)

Ahmad Ramli Mohd Yahya  
(USM, Malaysia)

Dzati Athiar Ramli  
(USM, Malaysia)

Hasrizal Shaari  
(UMT, Malaysia)

Ahmad Shukri Yahaya  
(USM, Malaysia)

Edi Syams Zainudin  
(UPM, Malaysia)

Hedzlin Zainuddin  
(UiTM, Malaysia)

Ahmad Sufriil Azlan Mohamed  
(USM, Malaysia)

Elysha Nur Ismail  
(UPM, Malaysia)

Henry Bernard  
(UMS, Malaysia)

Ahmad Taufek Abdul Rahman  
(UiTM, Malaysia)

Eris Elianddy Supeni  
(UPM, Malaysia)

Herni Halim  
(UM, Malaysia)

Ahmad Zhafran Ahmad Mazlan  
(USM, Malaysia)

Ezza Syuhada Sazali  
(UTM, Malaysia)

Ikhlas Abdelaziz  
(Jeddah University, Saudi Arabia)

Ahmad Zulfaa Mohamed Kassim  
(USM, Malaysia)

Fadhilah Mat Yamin  
(UUM, Malaysia)

Jefferson A. Hora  
(MSUIT, Philippines)

Anasyida Abu Seman  
(USM, Malaysia)

Fam Soo Fen  
(UTeM, Malaysia)

John Paul Tan Yusiong  
(UP, Philippines)

Aqilah Baseri Huddin  
(UKM, Malaysia)

Farah Nora Aznieta Abd. Aziz  
(UPM, Malaysia)

Khairul Azlan Mustapha  
(UM, Malaysia)

Azni Zain Ahmed  
(UiTM, Malaysia)

Farzaneh Mohamadpour  
(USB, Iran)

Khairul Hamimah Abas  
(UTM, Malaysia)

Bagherzadeh Roohollah  
(AUT, Iran)

Fathey Mohammed  
(UUM, Malaysia)

Khalid Mohammad  
(Sunway University, Malaysia)

Khanh Le Nguyen Quoc  
(TMU, Taiwan)

Khuzaimah Zailani  
(UPM, Malaysia)

Kwong Qi Jie  
(UiTM, Malaysia)

Lai Kee Huong  
(Sunway University, Malaysia)

Lim Soh Fong  
(UNIMAS, Malaysia)

M. Premkumar  
(PIT, India)

M. Selvakumar  
(MIT, India)

M.C. Manjunatha  
(MITT, India)

Maizatul Hayati Mohamad Yatim  
(UPSI, Malaysia)

Mary Subaja Christo  
(SRMIST, India)

Masnida Hussin  
(UPM, Malaysia)

Md Faisal Md Basir  
(UTM, Malaysia)

Mehdi Hussain  
(NUST, Pakistan)

Mo Kim Hung  
(UM, Malaysia)

Mohamad Faizal Abd. Rahman  
(UiTM, Malaysia)

Mohamad Ikhsan Selamat  
(UiTM, Malaysia)

Mohamadariff Othman  
(UM, Malaysia)

Mohamed Abd Rahman  
(IIUM, Malaysia)

Mohammed Alias Yusof  
(UPNM, Malaysia)

Mohd Nazim Mohtar  
(UPM, Malaysia)

Mohd Sapuan Salit  
(UPM, Malaysia)

Mohd Shahrul Nizam Mohd  
Danuri  
(KUIS, Malaysia)

Mohd Zaidi Omar  
(UKM, Malaysia)

Muhammad Isa Bala  
(FUTMinna, Nigeria)

Mundzir Abdullah  
(USM, Malaysia)

Mus`ab Abd. Razak  
(UPM, Malaysia)

Nasri Sulaiman  
(UPM, Malaysia)

Ng Kok Haur  
(UM, Malaysia)

Nik Nor Liyana Nik Ibrahim  
(UPM, Malaysia)

Noor Haida Mohd Kaus  
(USM, Malaysia)

Nor Azura Husin  
(UPM, Malaysia)

Nor Hasanah Abdul Shukor Lim  
(UTM, Malaysia)

Noramalina Abdullah  
(USM, Malaysia)

Norashikin Mohd Fauzi  
(UMK, Malaysia)

Norshita Mat Nayan  
(UKM, Malaysia)

Nur Ain Ayunni Sabri  
(UMK, Malaysia)

Nur Hartini Mohd Taib  
(USM, Malaysia)

Nuur Alifah Roslan  
(UPM, Malaysia)

Ooi Boon Yaik  
(UTAR, Malaysia)

Ooi Lu Ean  
(USM, Malaysia)

Praveen Kumar Malik  
(LPU, India)

Rahizar Ramli  
(UM, Malaysia)

Reuben Clements Gopalasamy  
(Sunway University, Malaysia)

Riza Wirawan  
(ITB, Indonesia)

Rosmanjawati Abdul Rahman  
(USM, Malaysia)

Ruzinoor Che Mat  
(UUM, Malaysia)

Sarina Sulaiman  
(IIUM, Malaysia)

Sathya Shankara Sharma  
(MIT, India)

Shariza Jamek  
(UMP, Malaysia)

Sinouassane Djearamane  
(UTAR, Malaysia)

Siow Chun Lim  
(MMU, Malaysia)



Solley Joseph  
(Christ University)

Teoh Ying Jia  
(USM, Malaysia)

Zailan Siri  
(UM, Malaysia)

Subhash Bhatia  
(USM, Malaysia)

Vijay Pratap Singh Rathod  
(Government Polytechnic, India)

Zarani Mat Taher  
(UTM, Malaysia)

Suffian Mohamad Tajudin  
(UniSZA, Malaysia)

Viv Djanat Prasita  
(Universitas HangTuah, Indonesia)

Zulaikha Jamalludin  
(UMMC, Malaysia)

Teh Je Sen  
(USM, Malaysia)

Yoon Li Wan  
(Taylor's University, Malaysia)

---

AUT – Amirkabir University of Technology  
FUTMinna – Federal University of Technology Minna  
IUTM – International Islamic University Malaysia  
ITB – Bandung Institute of Technology  
KUIS – Kolej Universiti Islam Antarabangsa Selangor  
LPU – Lovely Professional University  
MIT – Manipal Institute of Technology  
MITT – Maharaja Institute of Technology Thandavapura  
MMU – Multimedia University Malaysia  
MSUIIT – Mindanao State University - Iligan Institute of Technology  
MUET – Mehran University of Engineering and Technology  
NUST – National University of Sciences & Technology  
PIT – Panimalar Institute of Technology  
Polimi – Polytechnic University of Milan  
SCET – Swarnandhra College of Engineering and Technology  
SRMIST – SRM Institute of Science and Technology  
TMU – Taipei Medical University  
UITM – Universiti Teknologi MARA  
UKM – Universiti Kebangsaan Malaysia

UM – Universiti Malaysia  
UMK – Universiti Malaysia Kelantan  
UMMC – University of Malaya Medical Centre  
UMP – Universiti Malaysia Pahang  
UMS – Universiti Malaysia Sabah  
UMT – Universiti Malaysia Terengganu  
UNIMAS – Universiti Malaysia Sarawak  
UniSZA – Universiti Sultan Zainal Abidin  
UP – University of the Philippines  
UPM – Universiti Putra Malaysia  
UPNM – Universiti Pertahanan Nasional Malaysia  
UPSI – University Pendidikan Sultan Idris  
USB – University of Sistan & Baluchestan  
USM – Universiti Sains Malaysia  
UTAR – Universiti Tunku Abdul Rahman  
UTeM – Universiti Teknikal Malaysia Melaka  
UTM – Universiti Teknologi Malaysia  
UUM – Universiti Utara Malaysia

---

While every effort has been made to include a complete list of referees for the period stated above, however if any name(s) have been omitted unintentionally or spelt incorrectly, please notify the Chief Executive Editor, *Pertanika* Journals at [executive\\_editor.pertanika@upm.edu.my](mailto:executive_editor.pertanika@upm.edu.my)

Any inclusion or exclusion of name(s) on this page does not commit the *Pertanika* Editorial Office, nor the UPM Press or the university to provide any liability for whatsoever reason.



# Pertanika Journal of Science & Technology

*Our goal is to bring high-quality research to the widest possible audience*

## INSTRUCTIONS TO AUTHORS

(REGULAR ISSUE)

(Manuscript Preparation & Submission Guide)

*Revised: November 2020*

Please read the *Pertanika* guidelines and follow these instructions carefully. The Chief Executive Editor reserves the right to return manuscripts that are not prepared in accordance with these guidelines.

### MANUSCRIPT PREPARATION Manuscript Types

*Pertanika* accepts submission of mainly 4 types of manuscripts

- that have not been published elsewhere (including proceedings)
- that are not currently being submitted to other journals

#### 1. Regular article

Regular article is a full-length original empirical investigation, consisting of introduction, methods, results, and discussion. Original research work should present new and significant findings that contribute to the advancement of the research area. *Analysis and Discussion* must be supported with relevant references.

*Size:* Generally, each manuscript is **not to exceed 6000 words** (excluding the abstract, references, tables, and/or figures), a maximum of **80 references**, and **an abstract of less than 250 words**.

#### 2. Review article

A review article reports a critical evaluation of materials about current research that has already been published by organising, integrating, and evaluating previously published materials. It summarises the status of knowledge and outlines future directions of research within the journal scope. A review article should aim to provide systemic overviews, evaluations, and interpretations of research in a given field. Re-analyses as meta-analysis and systemic reviews are encouraged.

*Size:* Generally, it is expected **not to exceed 6000 words** (excluding the abstract, references, tables, and/or figures), a maximum of **80 references**, and **an abstract of less than 250 words**.

#### 3. Short communications

Each article should be timely and brief. It is suitable for the publication of significant technical advances and maybe used to:

- (a) reports new developments, significant advances and novel aspects of experimental and theoretical methods and techniques which are relevant for scientific investigations within the journal scope;
- (b) reports/discuss on significant matters of policy and perspective related to the science of the journal, including 'personal' commentary;
- (c) disseminates information and data on topical events of significant scientific and/or social interest within the scope of the journal.

*Size:* It is limited to **3000 words** and have a maximum of **3 figures and/or tables, from 8 to 20 references, and an abstract length not exceeding 100 words**. The information must be in short but complete form and it is not intended to publish preliminary results or to be a reduced version of a regular paper.

#### 4. Others

Brief reports, case studies, comments, concept papers, letters to the editor, and replies on previously published articles may be considered.

### Language Accuracy

*Pertanika* emphasises on the linguistic accuracy of every manuscript published. Articles can be written in **English** or **Bahasa Malaysia** and they must be competently written and presented in clear and concise grammatical English/Bahasa Malaysia. Contributors are strongly advised to have the manuscript checked by a colleague with ample experience in writing English manuscripts or a competent English language editor. For articles in Bahasa Malaysia, the title, abstract and keywords should be written in both English and Bahasa Malaysia.

Author(s) **may be required to provide a certificate** confirming that their manuscripts have been adequately edited. **All editing costs must be borne by the authors.**

Linguistically hopeless manuscripts will be rejected straightaway (e.g., when the language is so poor that one cannot be sure of what the authors are really trying to say). This process, taken by authors before submission, will greatly facilitate reviewing, and thus, publication.

## MANUSCRIPT FORMAT

The paper should be submitted in **one-column format** with 1.5 line spacing throughout. Authors are advised to use Times New Roman 12-point font and *MS Word* format.

### 1. Manuscript Structure

The manuscripts, in general, should be organised in the following order:

#### Page 1: Running title

This page should **only** contain the running title of your paper. The running title is an abbreviated title used as the running head on every page of the manuscript. The running title **should not exceed 60 characters, counting letters and spaces.**

#### Page 2: Author(s) and Corresponding author's information

**General information:** This page should contain the **full title** of your paper **not exceeding 25 words**, with the name of all the authors, institutions and corresponding author's name, institution and full address (Street address, telephone number (including extension), handphone number, and e-mail address) for editorial correspondence. **The corresponding author must be clearly indicated with a superscripted asterisk symbol (\*).**

**Authors' name:** The names of the authors should be named **in full without academic titles**. For Asian (Chinese, Korean, Japanese, Vietnamese), please write first name and middle name before surname (family name). The last name in the sequence is considered the surname.

**Authors' addresses:** Multiple authors with different addresses must indicate their respective addresses separately by superscript numbers.

**Tables/figures list:** A list of the number of **black and white/colour figures and tables** should also be indicated on this page. See **"5. Figures & Photographs"** for details.

*Example (page 2):*

#### **Fast and Robust Diagnostic Technique for the Detection of High Leverage Points**

**Habshah Midi<sup>1,2\*</sup>, Hasan Talib Hendi<sup>1</sup>, Jayanthi Arasan<sup>2</sup> and Hassan Uraibi<sup>3</sup>**

<sup>1</sup>*Institute for Mathematical Research, Universiti Putra Malaysia, 43400 UPM, Serdang, Selangor, Malaysia*

<sup>2</sup>*Department of Mathematics, Faculty of Science, Universiti Putra Malaysia, 43400 UPM, Serdang, Selangor, Malaysia*

<sup>3</sup>*Department of Statistics, University of Al-Qadisiyah, 88 -Al-Qadisiyah -Al-Diwaniyah, Iraq*

*E-mail addresses*

habshah@upm.edu.my (Habshah Midi)

h.applied.t88@gmail.com (Hasan Talib Hendi)

jayanthi@upm.edu.my (Jayanthi Arasan)

hssn.sami1@gmail.com (Hassan Uraibi)

\*Corresponding author

*List of Table/Figure: Table 1.*

*Figure 1.*

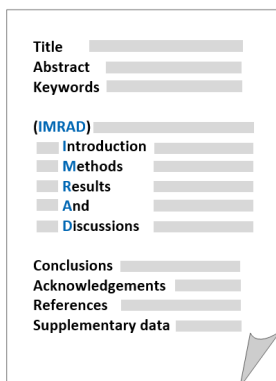
#### Page 3: Abstract

This page should **repeat** the **full title** of your paper with only the **Abstract**, usually in one paragraph and **Keywords**.

**Keywords:** *Not more than 8 keywords in alphabetical order must be provided to describe the content of the manuscript.*

#### Page 4: Text

A regular paper should be prepared with the headings *Introduction, Materials and Methods, Results and Discussions, Conclusions, Acknowledgements, References, and Supplementary data* (if any) in this order. The literature review may be part of or separated from the *Introduction*.



#### MAKE YOUR ARTICLES AS CONCISE AS POSSIBLE

Most scientific papers are prepared according to a format called IMRAD. The term represents the first letters of the words Introduction, Materials and Methods, Results, And, Discussion. It indicates a pattern or format rather than a complete list of headings or components of research papers; the missing parts of a paper are: Title, Authors, Keywords, Abstract, Conclusions, and References. Additionally, some papers include Acknowledgments and Appendices.

The Introduction explains the scope and objective of the study in the light of current knowledge on the subject; the Materials and Methods describes how the study was conducted; the Results section reports what was found in the study; and the Discussion section explains meaning and significance of the results and provides suggestions for future directions of research. The manuscript must be prepared according to the Journal's instructions to authors.

### 2. Levels of Heading

Level of heading	Format
1 <sup>st</sup>	<b>LEFT, BOLD, UPPERCASE</b>
2 <sup>nd</sup>	<b>Flush left, Bold, Capitalise each word</b>
3 <sup>rd</sup>	<b>Bold, Capitalise each word, ending with .</b>
4 <sup>th</sup>	<b>Bold italic, Capitalise each word, ending with .</b>

### 3. Equations and Formulae

These must be set up clearly and should be typed double-spaced. Numbers identifying equations should be in square brackets and placed on the right margin of the text.

### 4. Tables

- All tables should be prepared in a form consistent with recent issues of *Pertanika* and should be numbered consecutively with Roman numerals (Table 1, Table 2).
- A brief title should be provided, which should be shown at the top of each table (APA format):

Example:

Table 1

*PVY infected Nicotiana tabacum plants optical density in ELISA*

- Explanatory material should be given in the table legends and footnotes.
- Each table should be prepared on a new page, embedded in the manuscript.
- Authors are advised to keep backup files of all tables.

**\*\* Please submit all tables in Microsoft word format only, because tables submitted as image data cannot be edited for publication and are usually in low-resolution.**

### 5. Figures & Photographs

- Submit an original figure or photograph.
- Line drawings must be clear, with a high black and white contrast.
- Each figure or photograph should be prepared on a new page, embedded in the manuscript for reviewing to keep the file of the manuscript under 5 MB.
- These should be numbered consecutively with Roman numerals (Figure 1, Figure 2).
- Provide a brief title, which should be shown at the bottom of each table (**APA format**):

Example: *Figure 1. PVY-infected in vitro callus of Nicotiana tabacum*

- If a figure has been previously published, acknowledge the original source, and submit written permission from the copyright holder to reproduce the material.
- Authors are advised to keep backup files of all figures.

**\*\* Figures or photographs must also be submitted separately as TIFF or JPEG, because figures or photographs submitted in low-resolution embedded in the manuscript cannot be accepted for publication. For electronic figures, create your figures using applications that are capable of preparing high-resolution TIFF files.**

### 6. Acknowledgement

Any individuals and entities who have contributed to the research should be acknowledged appropriately.

### 7. References

References begin on their own page and are listed in alphabetical order by the first author's last name. Only references cited within the text should be included. All references should be in 12-point font and double-spaced. If a Digital Object Identifier (DOI) is listed on a print or electronic source, it is required to include the DOI in the reference list. Use Crossref to find a DOI using author and title information.

**NOTE:** When formatting your references, please follow the **APA-reference style** (7<sup>th</sup> edition) (refer to the examples). Ensure that the references are strictly in the journal's prescribed style, failing which your article will **not be accepted for peer-review**. You may refer to the *Publication Manual of the American Psychological Association* (<https://apastyle.apa.org/>) for further details.

Examples of reference style are given below:

Books		
	Insertion in text	In reference list
Book/E-Book with 1-2 authors	<p><b>Information prominent' (the author's name is within parentheses):</b></p> <p>... (Staron, 2020)</p> <p>... (Darus &amp; Rasdi, 2019)</p> <p>... Or</p> <p><b>'Author prominent' (the author's name is outside the parentheses):</b></p> <p>(Starron, 2020)...</p> <p>Darus and Rasdi (2019) ...</p>	<p>Staron, M. (2020). <i>Action research in software engineering</i>. Springer International Publishing. <a href="https://doi.org/10.1007/978-3-030-32610-4">https://doi.org/10.1007/978-3-030-32610-4</a></p> <p>Darus, A., &amp; Rasdi, I. (2019). <i>Introduction to occupational health a workbook</i>. UPM Press.</p>
Book/E-Book with 3 or more authors	<p><i>For all in-text references, list only the first author's family name and followed by 'et al.'</i></p> <p><b>Information prominent' (the author's name is within parentheses):</b></p> <p>... (Yusof et al., 2020)</p> <p>... Or</p> <p><b>'Author prominent' (the author's name is outside the parentheses):</b></p> <p>Yusof et al. (2020) ...</p>	<p>Yusof, N. A., Azmi, U. Z. M., Ariffin, N., &amp; Rahman, S. F. A. (2020). <i>Biosensors and chemical sensors: A practical approach</i>. UPM Press.</p>
Book/E-Book with more than 20 authors		<p>For books with more than 20 authors, please follow the guidelines for journal articles with more than 20 authors.</p>
Chapter in an edited Book/E-Book	<p><b>Inform ation pr ominent' (the author 's name is within parentheses):</b></p> <p>... (Mainzer, 2020) ...</p> <p>... (Tang et al., 2020) ...</p> <p>Or</p> <p><b>'Author prominent' (the author's name is outside the parentheses):</b></p> <p>Mainzer (2020) ...</p> <p>Tang et al. (2020) ...</p>	<p>Mainzer, K. (2020). Logical thinking becomes automatic. In K. Mainzer (Ed.), <i>Artificial intelligence-When do machines take over?</i> (pp. 15-45). Springer. <a href="https://doi.org/10.1007/978-3-662-59717-0_3">https://doi.org/10.1007/978-3-662-59717-0_3</a></p> <p>Tang, W., Khavarian, M., Yousefi, A., &amp; Cui, H. (2020). Properties of self-compacting concrete with recycled concrete aggregates. In R. Siddique (Ed.), <i>Self-Compacting Concrete: Materials, Properties, and Applications</i> (pp. 219-248). Woodhead Publishing. <a href="https://doi.org/10.1016/B978-0-12-817369-5.00009-X">https://doi.org/10.1016/B978-0-12-817369-5.00009-X</a></p>

	Insertion in text	In reference list
Editor	<p><b>Information prominent' (the author's name is within parentheses):</b>                      ... (Kesharwani, 2020) ...                      ... (Lanza et al., 2020) ...                      Or  <b>'Author prominent' (the author's name is outside the parentheses):</b>                      Kesharwani (2020) ...                      Lanza et al. (2020) ...</p>	<p>Kesharwani, P. (Ed.). (2020). <i>Nanotechnology based approaches for tuberculosis treatment</i>. Academic Press.</p> <p>Lanza, R., Langer, R., Vacanti, J. P., &amp; Atala, A. (Eds.). (2020). <i>Principles of tissue engineering</i>. Academic press. <a href="https://doi.org/10.1016/C2018-0-03818-9">https://doi.org/10.1016/C2018-0-03818-9</a></p>
Several works by the same author in the same year	<p><b>Information prominent' (the author's name is within parentheses):</b>                      ... (Aggarwal &amp; Aggarwal, 2020a, 2020b) ...                      Or  <b>'Author prominent' (the author's name is outside the parentheses):</b>                      Aggarwal &amp; Aggarwal (2020a, 2020b) ...</p>	<p>Aggarwal, P., &amp; Aggarwal, Y. (2020a). Strength properties of SCC. In R. Siddique (Ed.), <i>Self-Compacting Concrete: Materials, Properties, and Applications</i> (p. 83-115). Woodhead Publishing. doi: <a href="https://doi.org/10.1016/B978-0-12-817369-5.00004-0">https://doi.org/10.1016/B978-0-12-817369-5.00004-0</a></p> <p>Aggarwal, P., &amp; Aggarwal, Y. (2020b). Carbonation and corrosion of SCC. In R. Siddique (Ed.), <i>Self-Compacting Concrete: Materials, Properties, and Applications</i> (p. 147-193). Woodhead Publishing. doi: <a href="https://doi.org/10.1016/B978-0-12-817369-5.00007-6">https://doi.org/10.1016/B978-0-12-817369-5.00007-6</a></p>
<b>Journals</b>		
Journal article with 1-2 authors	<p><b>Information prominent' (the author's name is within parentheses):</b>                      ... (Laan &amp; Fox, 2019) ...                      Or  <b>'Author prominent' (the author's name is outside the parentheses):</b>                      Laan and Fox (2019) ...</p>	<p>Laan, E., &amp; Fox, J. W. (2019). An experimental test of the effects of dispersal and the paradox of enrichment on metapopulation persistence. <i>Oikos</i>, 129(1), 49-58. <a href="https://doi.org/10.1111/oik.06552">https://doi.org/10.1111/oik.06552</a></p>
Journal article with 3 or more authors	<p><i>For all in-text references, list only the first author's family name and followed by 'et al.'</i>  <b>Information prominent' (the author's name is within parentheses):</b>                      ... (Midi et al., 2020) ...                      ... (Shagufta et al., 2017) ...                      Or  <b>'Author prominent' (the author's name is outside the parentheses):</b>                      Midi et al. (2020) ...                      Shagufta et al. (2017) ...</p>	<p>Midi, H., Hendi, H. T., Arasan, J., &amp; Uraibi, H. (2020). Fast and Robust Diagnostic Technique for the Detection of High Leverage Points. <i>Pertanika Journal of Science &amp; Technology</i>, 28(4), 1203-1220.</p> <p>Shagufta, B., Sivakumar, M., Kumar, S., Agarwal, R. K., Bhilegaonkar, K. N., Kumar, A., &amp; Dubal, Z. B. (2017). Antimicrobial resistance and typing of Salmonella isolated from street vended foods and associated environment. <i>Journal of Food Science and Technology</i>, 54(8), 2532-2539. doi: <a href="https://doi.org/10.1007/s13197-017-2698-1">https://doi.org/10.1007/s13197-017-2698-1</a></p>
Journal article with more than 20	<p><b>Information prominent' (the author's name is within parentheses):</b>                      ... (Wiskunde et al., 2019) ...                      Or  <b>'Author prominent' (the author's name is outside the parentheses):</b>                      Wiskunde et al. (2019) ...</p>	<p>Wiskunde, B., Arslan, M., Fischer, P., Nowak, L., Van den Berg, O., Coetzee, L., Juárez, U., Riyaziyyat, E., Wang, C., Zhang, I., Li, P., Yang, R., Kumar, B., Xu, A., Martinez, R., McIntosh, V., Ibáñez, L. M., Mäkinen, G., Virtanen, E., ... Kovács, A. (2019). Indie pop rocks mathematics: Twenty One Pilots, Nicolas Bourbaki, and the empty set. <i>Journal of Improbable Mathematics</i>, 27(1), 1935–1968. <a href="https://doi.org/10.0000/3mp7y-537">https://doi.org/10.0000/3mp7y-537</a></p>
Journal article with an article number	<p><b>Information prominent' (the author's name is within parentheses):</b>                      ... (Roe et al., 2020) ...                      Or  <b>'Author prominent' (the author's name is outside the parentheses):</b>                      Roe et al. (2020) ...</p>	<p>Roe, E. T., Bies, A. J., Montgomery, R. D., Watterson, W. J., Parris, B., Boydston, C. R., Sereno, M. E., &amp; Taylor, R. P. (2020). Fractal solar panels: Optimizing aesthetic and electrical performances. <i>Plos One</i>, 15(3), Article e0229945. <a href="https://doi.org/10.1371/journal.pone.0229945">https://doi.org/10.1371/journal.pone.0229945</a></p>
Journal article with missing information	<p><b>Information prominent' (the author's name is within parentheses):</b>                      ... (Alfirevic et al., 2017) ...                      ... (Hayat et al., 2020) ...                      ... (Fan et al., 2020) ...</p>	<p><b>Missing volume number</b>                      Alfirevic, Z., Stampalija, T., &amp; Dowswell, T. (2017). Fetal and umbilical Doppler ultrasound in high-risk pregnancies (review). <i>Cochrane Database of Systematic Reviews</i>, (6), 1-163. <a href="https://doi.org/10.1002/14651858.CD007529.pub4">https://doi.org/10.1002/14651858.CD007529.pub4</a>. Copyright</p>

	Insertion in text	In reference list
Journal article with missing information	Or <b>'Author prominent' (the author's name is outside the parentheses):</b> Alfirevic et al. (2017) ... Hayat et al. (2020) ... Fan et al. (2020) ...	<b>Missing issue number</b> Hayat, A., Shaishta, N., Mane, S. K. B., Hayat, A., Khan, J., Rehman, A. U., & Li, T. (2020). Molecular engineering of polymeric carbon nitride based Donor-Acceptor conjugated copolymers for enhanced photocatalytic full water splitting. <i>Journal of colloid and interface science</i> , 560, 743-754. <a href="https://doi.org/10.1016/j.jcis.2019.10.088">https://doi.org/10.1016/j.jcis.2019.10.088</a> <b>Missing page or article number</b> Fan, R. G., Wang, Y. B., Luo, M., Zhang, Y. Q., & Zhu, C. P. (2020). SEIR-Based COVID-19 Transmission Model and Inflection Point Prediction Analysis. <i>Dianzi Keji Daxue Xuebao/Journal of the University of Electronic Science and Technology of China</i> , 49(3). <a href="https://doi.org/10.12178/1001-0548.9_2020029">https://doi.org/10.12178/1001-0548.9_2020029</a>
Several works by the same author in the same year	<b>Information prominent' (the author's name is within parentheses):</b> ... (Chee et al., 2019a, 2019b) ... Or <b>'Author prominent' (the author's name is outside the parentheses):</b> Chee et al. (2019a, 2019b) ...	Chee, S. S., Jawaid, M., Sultan, M. T. H., Alothman, O. Y., & Abdullah, L. C. (2019a). Accelerated weathering and soil burial effects on colour, biodegradability and thermal properties of bamboo/kenaf/epoxy hybrid composites. <i>Polymer Testing</i> , 79, Article 106054. <a href="https://doi.org/10.1016/j.polymeresting.2019.106054">https://doi.org/10.1016/j.polymeresting.2019.106054</a> Chee, S. S., Jawaid, M., Sultan, M. T. H., Alothman, O. Y., & Abdullah, L. C. (2019b). Evaluation of the hybridization effect on the thermal and thermo-oxidative stability of bamboo/kenaf/epoxy hybrid composites. <i>Journal of Thermal Analysis and Calorimetry</i> , 137(1), 55-63. <a href="https://doi.org/10.1007/s10973-018-7918-z">https://doi.org/10.1007/s10973-018-7918-z</a>
<b>Newspaper</b>		
Newspaper article – with an author	... (Shamshuddin, 2019) ... Or ... Shamshuddin (2019) ...	Shamshuddin, J. (2019, September 23). Lynas plant waste residue can be used to boost oil palm growth? <i>New Straits Times</i> . <a href="https://www.nst.com.my/opinion/letters/2019/09/523930/lynas-plant-waste-residue-can-be-used-boost-oil-palm-growth">https://www.nst.com.my/opinion/letters/2019/09/523930/lynas-plant-waste-residue-can-be-used-boost-oil-palm-growth</a>
Newspaper article – without an author	("Zoonotic viruses," 2017). OR "Zoonotic viruses" (2017) ... Use a shortened title (or full title if it is short) in Headline Case enclosed in double quotation marks.	Zoonotic viruses like swine flu are ticking time bombs, say experts. (2020, July 4). <i>New Straits Times</i> , 3.
<b>Dissertation/Thesis</b>		
Published Dissertation or Thesis References	... (Rivera, 2016) ... Or ... Rivera (2016) ...	Rivera, C. (2016). <i>Disaster risk management and climate change adaptation in urban contexts: Integration and challenges</i> [Doctoral dissertation, Lund University]. Lund University Publications. <a href="https://lup.lub.lu.se/search/ws/files/5471705/8570923.pdf">https://lup.lub.lu.se/search/ws/files/5471705/8570923.pdf</a>
Unpublished Dissertation or Thesis References	... (Brooks, 2014) ... Or ... Brooks (2014) ...	Brooks, J. D. (2015). <i>Bamboo as a strengthening agent in concrete beams for medium height structures</i> [Unpublished Doctoral dissertation]. The University of Washington.
<b>Conference/Seminar Papers</b>		
Conference proceedings published in a journal	... (Duckworth et al., 2019) ... Or Duckworth et al. (2019) ...	Duckworth, A. L., Quirk, A., Gallop, R., Hoyle, R. H., Kelly, D. R., & Matthews, M. D. (2019). Cognitive and noncognitive predictors of success. <i>Proceedings of the National Academy of Sciences, USA</i> , 116(47), 23499-23504. <a href="https://doi.org/10.1073/pnas.1910510116">https://doi.org/10.1073/pnas.1910510116</a>
Conference proceedings published as a book chapter	... (Bedenel et al., 2019) ... Or Bedenel et al. (2019) ...	Bedenel, A. L., Jourdan, L., & Biernacki, C. (2019). Probability estimation by an adapted genetic algorithm in web insurance. In R. Battiti, M. Brunato, I. Kotsireas, & P. Pardalos (Eds.), <i>Lecture notes in computer science: Vol. 11353. Learning and intelligent optimization</i> (pp. 225-240). Springer. <a href="https://doi.org/10.1007/978-3-030-05348-2_21">https://doi.org/10.1007/978-3-030-05348-2_21</a>



	Insertion in text	In reference list
Online	... (Gu et al., 2018) ... Or Gu et al. (2018) ...	Gu, X., Yu, J., Han, Y., Han, M., & Wei, L. (2019, July 12-14). <i>Vehicle lane change decision model based on random forest</i> . [Paper presentation]. 2019 IEEE International Conference on Power, Intelligent Computing and Systems (ICPICS), Shenyang, China. <a href="https://doi.org/10.1109/ICPICS47731.2019.8942520">https://doi.org/10.1109/ICPICS47731.2019.8942520</a>
<b>Government Publications</b>		
Government as author	<b>First in-text reference: Spell out the full name with the abbreviation of the body.</b> ... National Cancer Institute (2019) ... Or ... (National Cancer Institute, 2019) ... <b>Subsequent in-text reference:</b> ... NCI (2019) ... Or ... (NCI, 2019) ...	National Cancer Institute. (2019). <i>Taking time: Support for people with cancer</i> (NIH Publication No. 18-2059). U.S. Department of Health and Human Services, National Institutes of Health. <a href="https://www.cancer.gov/publications/patient-education/takingtime.pdf">https://www.cancer.gov/publications/patient-education/takingtime.pdf</a>

## 8. General Guidelines

**Abbreviations:** Define alphabetically, other than abbreviations that can be used without definition. Words or phrases that are abbreviated in the *Introduction* and following text should be written out in full the first time that they appear in the text, with each abbreviated form in parenthesis. Include the common name or scientific name, or both, of animal and plant materials.

**Authors' Affiliation:** The primary affiliation for each author should be the institution where the majority of their work was done. If an author has subsequently moved to another institution, the current address may also be stated in the footer.

**Co-Authors:** The commonly accepted guideline for authorship is that one must have substantially contributed to the development of the paper and share accountability for the results. Researchers should decide who will be an author and what order they will be listed depending upon their order of importance to the study. Other contributions should be cited in the manuscript's *Acknowledgements*.

**Similarity Index:** All articles received must undergo the initial screening for originality before being sent for peer review. *Pertanika* does not accept any article with a similarity index exceeding **20%**.

**Copyright Permissions:** Authors should seek necessary permissions for quotations, artwork, boxes or tables taken from other publications or other freely available sources on the Internet before submission to *Pertanika*. The *Acknowledgement* must be given to the original source in the illustration legend, in a table footnote, or at the end of the quotation.

**Footnotes:** Current addresses of authors if different from heading may be inserted here.

**Page Numbering:** Every page of the manuscript, including the title page, references, and tables should be numbered.

**Spelling:** The journal uses American or British spelling and authors may follow the latest edition of the Oxford Advanced Learner's Dictionary for British spellings. Each manuscript should follow one type of spelling only.

## SUBMISSION OF MANUSCRIPTS

All submissions must be made electronically using the **ScholarOne™ online submission system**, a web-based portal by Clarivate Analytics. For more information, go to our web page and click "**Online Submission (ScholarOne™)**".

### Submission Checklist

#### 1. MANUSCRIPT:

Ensure your manuscript has followed the *Pertanika* style particularly the first-4-pages as explained earlier. The article should be written in a good academic style and provide an accurate and succinct description of the contents ensuring that grammar and spelling errors have been corrected before submission. It should also not exceed the suggested length.

## 2. DECLARATION FORM:

Author has to sign a declaration form. In signing the form, authors declare that the work submitted for publication is original, previously unpublished, and not under consideration for any publication elsewhere.

Author has to agree to pay the publishing fee once the paper is accepted for publication in *Pertanika*.

## 3. COVER LETTER:

In Step 6 of the ScholarOne system, author is asked to upload a cover letter in *Pertanika* format. Please ignore this instruction and replace the cover letter with the **Declaration Form**.

*Note:*

**COPYRIGHT FORM:** Author will be asked to sign a copyright form when the paper is accepted. In signing the form, it is assumed that authors have obtained permission to use any copyrighted or previously published material. All authors must read and agree to the conditions outlined in the form and must sign the form or agree that the corresponding author can sign on their behalf. Articles cannot be published until a signed form (original pen-to-paper signature) has been received.

Visit our Journal's website for more details at <http://www.pertanika.upm.edu.my/>.

## ACCESS TO PUBLISHED MATERIALS

Under the journal's open access initiative, authors can choose to download free material (via PDF link) from any of the journal issues from *Pertanika*'s website. Under "**Browse Journals**" you will see a link, "*Regular Issue*", "*Special Issue*" or "*Archives*". Here you will get access to all current and back-issues from 1978 onwards. No hard copy of journals or offprints are printed.

Visit our Journal's website at:

[http://www.pertanika.upm.edu.my/regular\\_issues.php](http://www.pertanika.upm.edu.my/regular_issues.php) for "Regular Issue"  
[http://www.pertanika.upm.edu.my/cspecial\\_issues.php](http://www.pertanika.upm.edu.my/cspecial_issues.php) for "Special Issue"  
[http://www.pertanika.upm.edu.my/journal\\_archives.php](http://www.pertanika.upm.edu.my/journal_archives.php) for "Archives"

## PUBLICATION CHARGE

Upon acceptance of a manuscript, a processing fee of RM 750 / USD 250 will be imposed on authors; RM 750 for any corresponding author affiliated to an institution in Malaysia; USD 250 for any corresponding author affiliated to an institution outside Malaysia. Payment must be made online at <https://paygate.upm.edu.my/action.do?do=>

---

Any queries may be directed to the **Chief Executive Editor's** office via email to [executive\\_editor.pertanika@upm.edu.my](mailto:executive_editor.pertanika@upm.edu.my)

---



Dose Distribution of <sup>192</sup> Ir HDR Brachytherapy Source Measurement using Gafchromic® EBT3 Film Dosimeter and TLD-100H <i>Nor Shazleen Ab Shukor, Marianie Musarudin, Reduan Abdullah and Mohd Zahri Abdul Aziz</i>	691
Development of Attendance and Temperature Monitoring System using IoT with Wireless Power Transfer Application <i>Noramalina Abdullah and Sarah Madihah Mohd Shazali</i>	709
Octave Band Technique for Noise Measurement at the Source, Path, and Receiver of Gas Turbines in Oil and Gas Facilities <i>Akmal Haziq Mohd Yunos and Nor Azali Azmir</i>	725
The Detection of Changes in Land Use and Land Cover of Al-Kut City using Geographic Information System (GIS) <i>Fatima Asaad Tayeb, Ahmed Kareem Jebur and Husham H. Rashid</i>	747
Automation of Psychological Selection Procedures for Personnel to Specific Activities <i>Ihor Prykhodko, Stanislav Horielyshev, Yanina Matsehora, Vasily Lefterov, Stanislav Larionov, Olena Kravchenko, Maksim Baida, Olena Halkina and Olena Servachak</i>	761
Determination of Putative Vacuolar Proteases, PEP4 and PRB1 in a Novel Yeast Expression Host <i>Meyerozyma guilliermondii</i> Strain SO using Bioinformatics Tools <i>Okojie Eseoghene Lorraine, Raja Noor Zaliha Raja Abd. Rahman, Joo Shun Tan, Raja Farhana Raja Khairuddin, Abu Bakar Salleh and Siti Nurbaya Oslan</i>	777
The Asymmetric Impacts of Crude Oil Prices, Inflation, the Exchange Rate, Institutional Quality, and Trade Balance on Tourist Arrivals in Bangladesh: A Nonlinear ARDL Model Approach <i>Rehana Parvin</i>	781
<i>Short communication</i>	
Reinvestigation on Assessing the Stability of Mullagulov Tested Steel Rods under Follower Forces <i>Jakkana Peter Praveen and Boggarapu Nageswara Rao</i>	801
<i>Review article</i>	
A Review of Thermal Design for Buildings in Hot Climates <i>Sahar Najeeb Kharrufa and Firas Noori</i>	813
Accuracy of Ultrasound and Magnetic Resonance Cholangiopancreatography Findings in the Diagnosis of Biliary System Stones <i>Abdullah Taher Naji, Ameen Mohsen Amer, Saddam Mohammed Alzofi, Esmail Abdu Ali and Noman Qaid Alnaggar</i>	841

A New Method to Estimate Peak Signal to Noise Ratio for Least Significant Bit Modification Audio Steganography <i>Muhammad Harith Noor Azam, Farida Ridzuan and M Norazizi Sham Mohd Sayuti</i>	497
Formulation of Polyherbal Carbonated Beverage based on <i>Halalan Thoyyiban</i> Principle <i>Puteri Shazleen Izreena Mohd Shahrin, Norhayati Muhammad and Nur Fazira Abdul Rahim</i>	513
Comparative Study on the Social Behavior of Sambar Deer ( <i>Rusa unicolor</i> ) in Three Selected Captive Facilities in Peninsular Malaysia <i>Kushaal Selvarajah, Mohd Noor Hisham Mohd Nadzir and Geetha Annavi</i>	527
Synthesis and Performance of PAFS Coagulant Derived from Aluminium Dross <i>Shiyi Li and Shafreeza Sobri</i>	547
Assessment of Domestic Wastewaters as Potential Growth Media for <i>Chlorella vulgaris</i> and <i>Haematococcus pluvialis</i> <i>Yeong Hwang Tan, Mee Kin Chai, Yang Kai Ooi and Ling Shing Wong</i>	565
FPGA-based Implementation of SHA-256 with Improvement of Throughput using Unfolding Transformation <i>Shamsiah Suhaili and Norhuzaimin Julai</i>	581
Characterization of Polyvinylidene Difluoride-based Energy Harvesting with IDE Circuit Flexible Cantilever Beam <i>Khairul Azman Ahmad, Noramalina Abdullah, Mohamad Faizal Abd Rahman, Muhammad Khusairi Osman and Rozan Boudville</i>	605
<i>Conceptual paper</i> A Conceptual Framework for Road Safety Education using Serious Games with a Gesture-based Interaction Approach <i>Wan Salfarina Wan Husain, Syadiah Nor Wan Shamsuddin and Normala Rahim</i>	621
Arabic Handwriting Classification using Deep Transfer Learning Techniques <i>Ali Abd Almisreb, Nooritawati Md Tahir, Sherzod Turaev, Mohammed A. Saleh and Syed Abdul Mutalib Al Junid</i>	641
<i>Review article</i> Adoption of Cloud Computing in E-Government: A Systematic Literature Review <i>Osama Abied, Othman Ibrahim and Siti Nuur-Ila Mat Kamal</i>	655

A Comparative Effectiveness of Hierarchical and Non-hierarchical Regionalisation Algorithms in Regionalising the Homogeneous Rainfall Regions <i>Zun Liang Chuan, Wan Nur Syahidah Wan Yusoff, Azlyna Senawi, Mohd Romlay Mohd Akramin, Soo-Fen Fam, Wendy Ling Shinyie and Tan Lit Ken</i>	319
Optical Properties of Cu <sub>2</sub> O Thin Films Impregnated with Carbon Nanotube (CNT) <i>Oluayamo Sunday Samuel, Ajanaku Olanrewaju and Adedayo Kayode David</i>	343
<i>Review article</i>	
A Review on Synthesis and Characterization of Activated Carbon from Natural Fibers for Supercapacitor Application <i>Thilageshwaran Subramaniam, Mohamed Ansari Mohamed Nainar and Noor Afeefah Nordin</i>	351
Esterification of Free Fatty Acid in Palm Oil Mill Effluent using Sulfated Carbon-Zeolite Composite Catalyst <i>Hasanudin Hasanudin, Qodria Utami Putri, Tuty Emilia Agustina and Fitri Hadiah</i>	377
Effect of Water Absorption on Flexural Properties of Kenaf/Glass Fibres Reinforced Unsaturated Polyester Hybrid Composites Rod <i>Bassam Hamid Alaseel, Mohamed Ansari Mohamed Nainar, Noor Afeefah Nordin, Zainudin Yahya and Mohd Nazim Abdul Rahim</i>	397
MYLPHerb-1: A Dataset of Malaysian Local Perennial Herbs for the Study of Plant Images Classification under Uncontrolled Environment <i>Kalananthni Pushpanathan, Marsyita Hanafi, Syamsiah Masohor and Wan Fazilah Fazlil Ilahi</i>	413
<i>Review article</i>	
The Effect of Elevated Temperature on Engineered Cementitious Composite Microstructural Behavior: An Overview <i>Mohamad Hakim Khazani, Oh Chai Lian, Lee Siong Wee, Mohd Raizamzamani Md Zain and Norrul Azmi Yahya</i>	433
Palaeoecologic and Palaeoclimatic Inferences from Calcareous Nannofossils in Western Lobe Offshore, Niger Delta <i>Bamidele Samuel Oretade and Che Aziz Ali</i>	451
Effect of Chemical Reaction towards MHD Marginal Layer Movement of Casson Nanofluid through Porous Media above a Moving Plate with an Adaptable Thickness <i>Ganugapati Raghavendra Ganesh and Wuriti Sridhar</i>	477

Towards Adoption of Smart Contract in Construction Industry in Malaysia <i>Dewi Noorain Bolhassan, Chai Changsaar, Ali Raza Khoso, Loo Siawchuing, Jibril Adewale Bamgbade and Wong Ngie Hing</i>	141
Person Verification based on Multimodal Biometric Recognition <i>Annie Anak Joseph, Alex Ng Ho Lian, Kuryati Kipli, Kho Lee Chin, Dyg Azra Awang Mat, Charlie Sia Chin Voon, David Chua Sing Ngie and Ngu Sze Song</i>	161
Development of Stand-Alone DC Energy Datalogger for Off- Grid PV System Application based on Microcontroller <i>Mohd Ruzaimi Ariffin, Suhaidi Shafie, Wan Zuha Wan Hasan, Norhafiz Azis, Mohammad Effendy Yaacob and Eris Elianddy Supeni</i>	185
Performance of a HAWT Rotor with a Modified Blade Configuration <i>Tabrej Khan, Balbir Singh, Mohamed Thariq Hameed Sultan and Kamarul Arifin Ahmad</i>	201
Acceptance Ratio Analysis in Grid-Connected Photovoltaic System: Is There Any Difference between DC and AC? <i>Fatin Azirah Mohd Shukor, Hedzlin Zainuddin, Jasrul Jamani Jamian, Nurmalessa Muhammad, Farah Liyana Muhammad Khir and Noor Hasliza Abdul Rahman</i>	221
A Dashboard-based System to Manage and Monitor the Progression of Undergraduate IT Degree Final Year Projects <i>Nooralisa Mohd Tuah, Ainnecia Yoag, Dinna@Nina Mohd Nizam and Cheang Wan Chin</i>	235
Pectinase Production from Banana Peel Biomass via the Optimization of the Solid-State Fermentation Conditions of <i>Aspergillus niger</i> Strain <i>Nazaitulshila Rasit, Yong Sin Sze, Mohd Ali Hassan, Ooi Chee Kuan, Sofiah Hamzah, Wan Rafizah Wan Abdullah@Wan Abd. Rahman and Md. Nurul Islam Siddique</i>	257
Compression and Flexural Behavior of ECC Containing PVA Fibers <i>Lee Siong Wee, Mohd Raizamzamani Md Zain, Oh Chai Lian, Nadiyah Saari and Norrul Azmi Yahya</i>	277
The Effect of Quenching on High-Temperature Heat Treated Mild Steel and its Corrosion Resistance <i>Alaba Oladeji Araoyinbo, Ayuba Samuel, Albakri Mohammed Mustapha Abdullah and Mathew Biodun</i>	291
Tensile Behaviour of Slag-based Engineered Cementitious Composite <i>Chai Lian Oh, Siong Wee Lee, Norrul Azmi Yahya, Gajalakshmi Pandulu and Mohd Raizamzamani Md Zain</i>	303

# Pertanika Journal of Science & Technology

## Vol. 30 (1) Jan. 2022

### Content

- Foreword  
*Chief Executive Editor*
- Deep Learning to Detect and Classify the Purity Level of Luwak Coffee Green Beans 1  
*Yusuf Hendrawan, Shinta Widyaningtyas, Muchammad Riza Fauzy, Sucipto Sucipto, Retno Damayanti, Dimas Firmanda Al Riza, Mochamad Bagus Hermanto and Sandra Sandra*
- Review article*  
Data Acquisition and Data Processing using Electroencephalogram in Neuromarketing: A Review 19  
*Annis Shafika Amran, Sharifah Aida Sheikh Ibrahim, Nurul Hashimah Ahamed Hassain Malim, Nurfaten Hamzah, Putra Sumari, Syaheerah Lebai Lutfi and Jafri Malin Abdullah*
- Multi-band Antenna with CSRR Loaded Ground Plane and Stubs Incorporated Patch for WiMAX/WLAN Applications 35  
*Palanivel Manikandan, Pothiraj Sivakumar and Nagarajan Rajini*
- Review article*  
A Survey on Model-based Fault Detection Techniques for Linear Time-Invariant Systems with Numerical Analysis 53  
*Masood Ahmad and Rosmiwati Mohd-Mokhtar*
- Work Performance of Extension Agents: Skills of Transfer of Technology and Human Resource Development in Cocoa Industry 79  
*Murni Azureen Mohd Pakri, Salim Hassan, Oluwatoyin Olagunju, Mohd Yusoff Abd Samad and Ramle Kasin*
- Sliding Window and Parallel LSTM with Attention and CNN for Sentence Alignment on Low-Resource Languages 97  
*Tien-Ping Tan, Chai Kim Lim and Wan Rose Eliza Abdul Rahman*
- The Relationships of Interleukin-33, Ve-Cadherin And Other Physiological Parameters in Male Patients with Rheumatoid Arthritis 123  
*Khalid F. AL-Rawi, Hameed Hussein Ali, Manaf A. Guma, Shakir F.T. Alaaraji and Muthanna M. Awad*



Pertanika Editorial Office, Journal Division,  
Putra Science Park,  
1st Floor, IDEA Tower II,  
UPM-MTDC Center,  
Universiti Putra Malaysia,  
43400 UPM Serdang,  
Selangor Darul Ehsan  
Malaysia

<http://www.pertanika.upm.edu.my>  
Email: [executive\\_editor.pertanika@upm.edu.my](mailto:executive_editor.pertanika@upm.edu.my)  
Tel. No.: +603- 9769 1622

PENERBIT  
**UPM**  
UNIVERSITI PUTRA MALAYSIA  
PRESS

<http://www.penerbit.upm.edu.my>  
Email: [penerbit@upm.edu.my](mailto:penerbit@upm.edu.my)  
Tel. No.: +603- 9769 8851

